ICENS

4TH INTERNATIONAL CONFERENCE ON ENGINEERING AND NATURAL SCIENCES

BOOK OF PROCEEDINGS 2018

www.icens.eu

May 2-6 2018 Kyiv Ukraine

Organized by

Partners

IV INTERNATIONAL CONFERENCE ON ENGINEERING AND NATURAL SCIENCES (ICENS)

ISBN 978-605-67955-3-4

BOOK OF PROCEEDINGS OF THE
IV INTERNATIONAL CONFERENCE ON ENGINEERING AND NATURAL SCIENCES (ICENS)

02-06 MAY 2018, UKRAINE

Edited by

Prof. Dr. Özer Çınar

Published, 2018

info@icens.eu
www.icens.eu

This work is subject to copyright. All rights are reserved, whether the whole or part of the material is concerned. Nothing from this publication may be translated, reproduced, stored in a computerized system or published in any form or in any manner, including, but not limited to electronic, mechanical, reprographic or photographic, without prior written permission from the publisher.

info@icens.org

The individual contributions in this publication and any liabilities arising from them remain the responsibility of the authors.

The publisher is not responsible for possible damages, which could be a result of content derived from this publication.

SCIENTIFIC COMMITTEE

1. Prof. Dr. Adisa Parić - University of Sarajevo - Bosnia and Herzegovina
2. Prof. Dr. Ahmet Doğan – Yıldız Technical University - Turkey
3. Prof. Dr. Aleksandar Dimitrov - Ss. Cyril and Methodius University - Macedonia
4. Prof. Dr. Alexander Golub - National University of Kyiv-Mohyla Academy - Ukraine
5. Prof. Dr. Alexander Litvinenko - National University of Food Technologies (Kyiv) - Ukraine
6. Prof. Dr. Anita Grozdanov - Ss. Cyril and Methodius University - Macedonia
7. Prof. Dr. Arslan Saral – Yıldız Technical University - Turkey
8. Prof. Dr. Asif Šabanović – International University of Sarajevo - Bosnia and Herzegovina
9. Prof. Dr. Bekir Erol Ak - Harran University - Turkey
10. Prof. Dr. Cem Şensöğüt - Dumlupınar University - Turkey
11. Prof. Dr. Christos Douligeris - University of Erlangen-Nurnberg - Germany
12. Prof. Dr. Dragutin T. Mihailović - University of Novi Sad - Serbia
13. Prof. Dr. Evgeniy Shtefan - National University of Food Technologies (Kyiv) - Ukraine
14. Prof. Dr. Falko Dressler - University of Paderborn - Germany
15. Prof. Dr. Harry Miller – International University of Sarajevo - Bosnia and Herzegovina
16. Prof. Dr. Houssam Toutanji – Western Michigan University - USA
17. Prof. Dr. Ian F. Akyıldız – Georgia Institute of Technology - USA
18. Prof. Dr. İsmail Usta - Marmara University - Turkey
19. Prof. Dr. Kateryna Derevska - National University of Kyiv-Mohyla Academy - Ukraine
20. Prof. Dr. Liljana Gavrilovska - Ss Cyril and Methodius University - Macedonia
21. Prof. Dr. Lukman Thalib - Qatar University - Qatar
22. Prof. Dr. M. Asghar Fazel – University of Environment - Iran
23. Prof. Dr. Mikhailov Volodymyr - Taras Shevchenko National University of Kyiv - Ukraine
24. Prof. Dr. Mykola Glybovets - National University of Kyiv-Mohyla Academy - Ukraine
25. Prof. Dr. Muammer Koç - Hamad bin Khalifa University - Qatar
26. Prof. Dr. Nadia Bilko - National University of Kyiv-Mohyla Academy - Ukraine
27. Prof. Dr. Özer Çınar – Yıldız Technical University - Turkey
28. Prof. Dr. Perica Paunovik - Ss. Cyril and Methodius University - Macedonia
29. Prof. Dr. Rifat Škrijelj – University of Sarajevo - Bosnia and Herzegovina
30. Prof. Dr. Samir Đug - University of Sarajevo - Bosnia and Herzegovina
31. Prof. Dr. Tanju Karanfil – Clemson University - USA
32. Prof. Dr. Ümit Alver – Karadeniz Technical University - Turkey
33. Prof. Dr. Wolfgang Gerstacker - University of Erlangen-Nurnberg - Germany
34. Prof. Dr. Vladyslav Sukhenko - National University of Life and Environmental Sciences of Ukraine (Kyiv) - Ukraine
35. Prof. Dr. Yılmaz Yıldırım - Bülent Ecevit University - Turkey
36. Prof. Dr. Yousef Haik - Hamad bin Khalifa University - Qatar
37. Assoc. Prof. Dr. Alaa Al Hawari - Qatar University - Qatar
38. Assoc. Prof. Dr. Izudin Dzafic - International University of Sarajevo - Bosnia and Herzegovina

39. Assoc. Prof. Dr. Kateryna Syera - National University of Life and Environmental Sciences of Ukraine (Kyiv) - Ukraine
40. Assist. Prof. Dr. Muhamed Hadziabdic - International University of Sarajevo - Bosnia and Herzegovina
41. Assoc. Prof. Dr. Nusret Drešković - University of Sarajevo - Bosnia and Herzegovina
42. Assoc. Prof. Dr. Polina Vakuliuk - National University of Kyiv-Mohyla Academy - Ukraine
43. Assoc. Prof. Dr. Senija Tahirovic - International University of Sarajevo - Bosnia and Herzegovina
44. Assoc. Prof. Dr. Victor Karamushka - National University of Kyiv-Mohyla Academy - Ukraine
45. Assoc. Prof. Dr. Victoria Konovalova - National University of Kyiv-Mohyla Academy - Ukraine
46. Assoc. Prof. Dr. Yuriy Kravchenko - National University of Life and Environmental Sciences of Ukraine (Kyiv) - Ukraine
47. Assist. Prof. Dr. Fatih Taktak - Uşak University - Turkey
48. Assist. Prof. Dr. Fouzi Tabet - German Biomass Research Center - Germany
49. Assist. Prof. Dr. Haris Gavranovic - International University of Sarajevo - Bosnia and Herzegovina
50. Assist. Prof. Dr. Sasan Rabieh - Shahid Beheshti University - Iran
51. Assist. Prof. Dr. Ševkija Okerić - University of Sarajevo - Bosnia and Herzegovina
52. Dr. Zsolt Hetesi - National University of Public Service, Budapest - Hungary
53. Dr. Zsolt T. Németh - National University of Public Service, Budapest - Hungary

ORGANIZATION COMMITTEE

Chairman of the Conference

Prof. Dr. Özer Çınar – Yıldız Technical University

Members of the Committee

Prof. Dr. Ümit Alver (Co-Chairman) - Karadeniz Technical University - Turkey
Prof. Dr. Mikhailov Volodymyr - Taras Shevchenko National University of Kyiv - Ukraine
Assoc. Prof. Dr. Kateryna Syera - National University of Life and Environmental Sciences of Ukraine (Kiev) - Ukraine
Assoc. Prof. Dr. Lukman Thalib - Qatar University - Qatar
Assoc. Prof. Dr. Yuriy Kravchenko - National University of Life and Environmental Sciences of Ukraine (Kiev) - Ukraine
Assist. Prof. Dr. Sasan Rabieh - Shahid Beheshti University - Iran
Alma Ligata - Zenith Group - Bosnia and Herzegovina
Ismet Uzun - Zenith Group - Bosnia and Herzegovina
Musa Kose - Zenith Group - Bosnia and Herzegovina

WELCOME TO ICENS 2018

On behalf of the organizing committee, we are pleased to announce that the 4rd International Conference on Engineering and Natural Sciences (ICENS 2018) will be held from May 2 to 6, 2018 in Kiev, Ukraine. ICENS 2018 provides an ideal academic platform for researchers to present the latest research findings and describe emerging technologies, and directions in Engineering and Natural Sciences issues. The conference seeks to contribute to presenting novel research results in all aspects of Engineering and Natural Sciences.

The conference aims to bring together leading academic scientists, researchers and research scholars to exchange and share their experiences and research results about all aspects of Engineering and Natural Sciences. It also provides the premier interdisciplinary forum for scientists, engineers, and practitioners to present their latest research results, ideas, developments, and applications in all areas of Engineering and Natural Sciences. The conference will bring together leading academic scientists, researchers and scholars in the domain of interest from around the world.

The scientific program will focus on current advances in the research, production and use of Engineering and Natural Sciences with particular focus on their role in maintaining academic level in Engineering and Applied Sciences and elevating the science level.

The conference's goal will to provide a scientific forum for all international prestige scholars around the world and enable the interactive exchange of state-of-the-art knowledge. The conference will focus on evidence-based benefits proven in clinical trials and scientific experiments.

Best regards,

Prof. Dr.Özer ÇINAR

ICENS 4TH INTERNATIONAL CONFERENCE ON ENGINEERING AND NATURAL SCIENCE
2-6 May 2018 KIEV UKRAINE

Content	Page
Optimization and Estimated Pareto Front of the Maximum Lift/Drag Ratio and Roll Stability Coefficient	1
Recipe Optimization for Synthesis of ZnO and Al2O3 Thin Film by Using Atomic Layer Deposition	8
Data Dependent Techniques for Initialization of Cluster Prototypes in Partitioning Cluster Analysis	13
Comparing Depth Values of GEBCO Bathymetry and Wavelet Tomography Results in the Challenger Deep Point of Marianna Trench and Surroundings	25
An Analysis of Occupational Incidents, Prioritization of Factors Causing These by Using Multi Criteria Decision Making Methods and Identification of Ways for Reducing These: Case Study In Oil And Gas Fields	30
Determination of UAVs Thrust System Parameters by Artificial Bee Colony Algorithm	36
The Use Of Chicken Feather Fibers As Insulation Material For Winter Top Clothing	41
A Literature Review for Applications of Soft Computing On Aeronautics	47
Adsorption of Methylene Blue on Mesoporous Nano Silica Obtained From Quartzite	55
Post-Seismic Surface Deformation of 2017 Mexico Earthquakes	62
Investigation Of Hygroscopic Properties For Fibers Obtained From Chicken Feathers	70
A Study on Usage of Urban Parks: Case of Pamukkale-Denizli, Turkey	79

Determination of Current Situation in Vocational High School Gardens: A Case of Civril-Denizli, Turkey 84

Removal of Ammonium Nitrogen from the DAF-Pretreated Poultry Slaughterhouse Wastewater by Lemna Minor 90

Biological Solid Waste Management In Turkey and Other Countries 95

Effects of Different Nitrogen Sources and Doses on Yield, Yield Components and Some Technologic Properties in Cotton (Gossypium hirsitum L.) 101

A Research on to Effective on Yield and Earliness of Different Sowing Times and Growing Techniques in Sweet Corn (Zea mays saccarata Sturts) in Kahramanmaras Conditions 109

Thermo-hydraulic Performance of Different Nanofluids in a Helical Coiled Tube 120

Shape Factor of Nanofluid on the Thermal Performance of a Double Pipe Heat Exchanger 129

Nonlinear Seismic Response of Masonry-Infilled Reinforced Concrete Frames with Typical Window and Door Openings 137

NAR based forecasting interface for time series analysis: T-seer 145

Experimental Investigation Of The Effect Of Feed Rate On Geometrical Tolerances In Turning Of 7075 Aluminum Alloy 151

The Dyeing of Wool Fabrics with Barberry Shrub Branches 156

Determination of Flame Retardant in Vegetable Tanned Leathers by Tri Butyl Phosphate (TBP) 160

Estimation of Flow Series using Discrete Wavelet Analysis and Artificial Neural Networks 168

Design of PID Controlled-Automatic Voltage Regulator System Based on a New Neighborhood Strategy of Simulated Annealing 175

Two-Dimensional Flow Simulation in Spillways by Computational Fluid Dynamics (CFD) 183

Determining Of Forearm Muscular Strengths By Using Forearm Anthropometric Measurements And Emg Signals 193

Buckling Analysis of Beams with Varying Flexural Rigidity on Elastic Foundation 199

Stability Analysis of Beams Subjected to Distinct Loading Types on Elastic Foundation 204

Investigation of Optimum Longitudinal Transport Limit in Vehicles Fighting Against Snow 209

Determination of the Optimum Number of the Heavy Equipment Used Regions with Heavy Snowfall 216

The Abrasion Resistance of Mortars Containing Natural Zeolite Analcime 223

Consideration of Urbanization Impact for Sustainable Modeling of Kagithane River Floods in Istanbul 230

Evaluation of Wastewater and Produced Leather Quality of Simulated Vegetable Leather Tannery Using Myrobalan Tannin 237

Usability of Alkaline Protease Enzyme in Pretreatment of Polyamide Fabrics 243

Testing the Equisetum Arvense L. Plant for Coloration of Cotton Fibers 247

Selection of Optimal Fiducial Point Locations on Faces with Genetic Algorithm for Down Syndrome Identification 250

Rocks Having High Potentially Toxic Elements Contents and Interaction With Environment 257

Designing and Evaluating Map Symbols for Elementary School Students 271

Protection and Improvement of Wild Sheeps with Photogrammetry Techniques 277

Investigation of The Effect Ratios of Cutting Parameters on The Surface Roughness 284

Experimental Investigation of The Cutting Forces In The Machining of AISI 4140 Steel By Using The CNC Turning Machine 292

Determination of The Effect Ratios of The Cutting Parameters on The Cutting Forces Using The Variance Analysis 299

Investigation of The Effects of Cutting Parameters on The Surface Roughness in The Turning of AISI 1050 Steel 306

An Alternative Method for Long-Term Land Cover Change Detection: A Case Study of Hasanlar Dam 312

Numerical Simulation Of Thermoacoustic In A Rijke Tube And Application Of Nonlinear Analysis Tools 321

Cfd (Computational Fluid Dynamics) Investigation of Effect of Sloped Labyrinth Teeth on Leakage Flow 327

Determination Of The Hip Stem Loosening Using Vibration Method 335

Water Injection Effect on Performance of Gasoline Engine 340

Rock Bit Application Parameters In Geothermal Drilling Works And Cost Analysis 350

The Effect of B4C Reinforcement Ratio on Mechanical Properties of Steel / Al-B4C Circular Layered Composites 359

Investigation of Heat Transfer from Heated Square Patterned Surfaces in a Rectangular Channel with an Air Jet Impingement 367

Investigation on Fatigue Behavior of B4C Powder Size in Al 6061-B4C Composites 377

Anaysis Of Recent Occupational Accidents At Seyitomer Thermal Power Plant (Turkey) 385

Evaluation Of Work Accidents Recently Occurred In Seyitomer Lignite Corporation (Turkey) 392

Evaluation of Physical and Mechanical Specifications of Natural Building Stones in Terms of Water Saturation 399

The Effect of Freeze-Thaw Cycles on Physical-Mechanical Properties of Tuff 406

Analysis of Cooling of the Heated Circle Patterned Surfaces by Using an Air Jet Impingement 411

Modeling the Weight and Length Changes of the Concrete Exposed to Sulfate using Artificial Neural Network 421

The factor of optimum angle of carbon fiber reinforced polymers 432

Designing a web based data acquisition system for battery-powered wireless sensor nodes: WiFiLab 439

A Review on Low Voltage Analog Circuit Design 448

Quality Function Deployment Approach for Evaluation Parameters of Highway Pavement 453

Determination of Mixing and Compaction Temperatures of Polymer Modified Bitumens Containing Nanoclays 461

Turkish Construction Firms' Perceptions of Recycled Materials 468

Construction and Demolition Waste Recycling Plants in Turkey 476

Investigation of Notch Root Strain Behaviors Under Combined Loadings 483

Numerical Simulation of Heat Exchanger for Jatropha Oil Biodiesel Fuel Preheating 492

Analysis Of The Positioning Performance Of Beidou 501

Estimation of machining outputs in drilling of AISI 430 stainless steel by numerical analysis 506

Investigation of the hole quality during fiber laser drilling of ferritic stainless steel 512

Influence Of Ethanol And Methanol Additives On A Diesel Engine Performance Characteristics: 1-D Modelling 518

Effect of LED Position on Mass Transfer of Hazelnut (Corylus Avellana L.) 526

The Effect Of Different Type Of Fibers On Strength Properties Of Clay Samples 533

An Alternative Versatile Machining Process: Abrasive Waterjet Machining and Its Remarkable Applications 540

Finite Element Analysis for Compression Behaviour of Polymer Based Honeycomb and Re-entrant Structures 549

A Traffic Systematic Proposal for Manned and Unmanned Aerial Vehicles Encounter 557

Decision Mechanism for Glaucoma Disease via Classification Techniques by Employing Data Reduction 561

Differential Diagnosis of Erythemato-Squamous Diseases via Machine Learning and Data Reduction Techniques 568

The Effect of Lead-Zinc on the Strength of Clay Soil with Fly Ash 573

Analytical Solution and Comparison of Slip Fluid Flow in a Circular Micro-Channel with First and Second Order Boundary Conditions 582

Simulated Annealing – Based Metaheuristic Approach for Pilot Tones Design in OFDM-IDMA System 593

Low-Velocity Impact Response of Pre-Stressed GRP Tubes Reinforced with Carbon Nanotubes 601

Determination of Soil Moisture Content and Soil Penetration Resistance According To Different Soil Tillage 607

Geochemical Characteristics of Listvenites in the Dagkuplu Ophiolite (Eskisehir, NW Turkey) 612

Marker-Assisted Selection in Determining of Resistant Varieties against Plant Diseases in the Breeding Process 618

Effect of Electric Field on Inter-subband Second Order Nonlinear Transitions in Single, Double and Triple Delta-Doped GaAs Structures 624

Depending on Al and In Concentration of the Electronic Properties of Asymmetric Double GaAlAs/GaAs and GaInAs/GaAs Quantum Wells 630

Chemical Fixation of Automotive Industry Coating Sludge Containing Nickel and Zinc Using Silica Fume as an Alternative Binder to Portland Cement 636

Economic Analysis of Wind-Hydro Pumped Storage Power System 642

Power System Analysis and Application for The Aircraft At The Different Altitudes 650

Measurement of Orange Size and Volume Using Microsoft Kinect Camera 660

The Investigation and Comparison of friction stir spot welding and Electrical Resistance Spot Welding of AA2024 Aluminum Alloy Joints 666

Optimization of Steady State Flight Parameters for a Given Trim Condition 672

BER Performance of Precoded OSTBC MIMO System with and without Antenna Selection in Rayleigh Fading Channels 680

Assessing Physical Properties of Denim Fabrics Including Wool/Elastane Dual-Core Yarns as Weft 685

Usability of Kinect Camera on Outdoor Conditions for Agricultural Mobile Robots 689

Design of Low Power 6-Bit DACs using 180nm CMOS Technology 697

Magnetic Levitation System Analysis 706

Adapted Cooling Channels for Different Wall Thickness of Plastic Parts 715

Optimal Location Determinations For Different Types Of Mandibular Fractures 720

Text Preprocessing for an Experiment Code on the Internet Assisted Laboratory System 727

Genetic Algorithm and Fuzzy Logic Based Auto-Test System for Distance Education 734

Detection of Sleep States from EEG Signals by Using Convolutional Filter Features Based on Wavelet and Short Time Fourier Image Patterns 739

An Investigation of Increase the Effectiveness of Ohmic Cooking of Meat by Using with Ultrasound Treatment 745

Effect of Ohmic Cooking Alone on Moisture Content and Total Aerobic Mesophilic Count of Beef Muscle 749

Encapsulation of Synthesized Hydroxyapatite in PCL Microspheres by Using Electrospraying Method 753

Web Based Intelligent Tutorial Systems: BILZOS 761

Usage of different machine learning algorithms in the classification of Epileptic Seizure based on EEG signals without feature extraction 766

Optimization of Coating Parameters for Water Vapour Resistance of Denim Fabrics by Using Taguchi Method 773

Static Stability Analysis of Clay Core Rockfill Dam 780

Combined Heat Transfer in an Enclosure with Different Side Wall Geometry 786

Tissue Engineering and Textile Materials 795

Using Newmark Beta Method For Quarter Car Analysis 798

Earthquake Resistant Wall Material Production “Puzzle Bims” 807

Experimental Investigation of Effect of n-hexane Fuel Additive in Diesel Fuel on Engine Performance and Emissions 813

Alternative Natural Formaldehyde Scavenger for Leather Industry: Colloidal Amino Acid Filler in Retanning Process 818

Dyeing of Wool Fabrics with an Extract Mixture of Madder and Alkanet Roots 823

Experimental Investigation of Heat Transfer and Development of Shell Side Heat Transfer Correlation in a Mini-Channel Shell and Tube Heat Exchanger 827

Solar And Biogas Hybrid Energy

836

Resources Used With An Example Of Hospital Building Project In Turkey

Acoustic Improvement Design: University Conference Hall 841

Flood Analysis of a Part of Dicle (Tigris) River by HEC-RAS Program 849

Development of off-shore wind energy in Turkey 858

Vibration Analysis of a Multiple-line Welded Aluminum Plate under Compression 862

Hardness Effect on Vibration Characteristics of a Three-Layered Composite Beam with Viscoelastic Core 865

Investigation on flammability and mechanical properties of polypropylene/red mud polymer composites 870

Tribological Properties of HDPE/Urea Formaldehyde Polymer Blends 878

Input Variance Constrained Control of Morphing Tactical Unmanned Aerial Vehicles (TUAVs) 885

Unmanned Aerial Vehicles (UAVs) by Engine Type 890

Development of Ecological Biodesign Products by Bacterial Biocalcification 900

A Novel Optimization Algorithm; Fox Hunting Algorithm (Fha) And Antenna Array Pattern Synthesis Aplication 908

Use Of A Vertical Take-Off And Landing (Vtol) Unmanned Aerial Vehicle (Uav) In The Control Of Highways 915

Analysis of Preseismic and Postseismic Deformation of Gulbahce and surroundings with Sigacik (Izmir-Turkey) Earthquake (2005) 926

Magnetic Anomaly of The Mid-Atlantic Ridge and Its Surroundings Obtained From Swarm Constellation 931

Accuracy Analysis of Matrakci Nasuh's Kutahya Miniature 936

Some New Results on Soft n-T4 Spaces 943

Structural Analysis of Historic Houses of Bitlis 949

The Determination of the Effect of Wheels and Fender Gap on Drag Force on a Bus Model by Computational Fluid Dynamics (CFD) Method 955

Desıgn Of A Robotıc Pneumatıc Pruner For Robotıc Apple Harvestıng 965

Diffusion Welding of Nodular Cast Iron to Copper 974

Determination of Parameters Affecting Hardness of AA7075 Aluminum Alloy by Response Surface Method 980

Resistance Spot Welding Of Fe3Al Alloy 989

Lateral and Longitudinal Dynamics Control of a Fixed Wing UAV by using PID Controller 994

Geosynthetic Material Applications Used In Mining Sector – A Case Of Emet Boron Works 1003

Rock Bıt Applıcatıon Parameters In Geothermal Drıllıng Works And Cost Analysıs 1008

Considerations on Maximum Penetration Levels of Fixed Speed Wind Energy Conversion Systems Operating in Unbalanced Non-Sinusoidal Environments 1017

E-Learning at Work 1029

Investigation of Flood Risk for Istanbul Gürpınar Stream 1034

Treatment of industrial wastewaters with anaerobic membrane bioreactors 1043

Membrane bioreactors application in textile wastewater treatment 1048

ICENS 4TH INTERNATIONAL CONFERENCE ON ENGINEERING AND NATURAL SCIENCE
2 - 6 May 2018 KIEV UKRAINE

Optimization and Estimated Pareto Front of the Maximum Lift/Drag Ratio and Roll Stability Coefficient

Seda Arik[1], Tugrul Oktay[2], Ilke Turkmen[3]

Abstract

This work presents a new method based on soft computing methods for calculating the optimum values of roll stability coefficient and maximum lift/drag ratio. For this purpose, the Artificial Neural Network (ANN) is integrated into the Artificial Bee Colony (ABC) algorithm and a new method is developed. ABC algorithm is a fast and simple algorithm that is frequently preferred in engineering problems. ANN can produce an appropriate solution for a given problem using a dataset without the need for a function. However, the network structure and parameters that give the most appropriate result for each dataset in ANN can change, and this feature is disadvantageous in terms of calculating the optimum values of roll stability coefficient and maximum lift/drag ratio using only ANN. The ABC algorithm requires an objective function to calculate the best solution for any problem. In order to find the optimum values in this study, ANN based objective function is embedded into ABC algorithm. Thus, when ANN trained with data containing values of roll stability coefficient and maximum lift/drag ratio, the ABC algorithm determines the best solution. However, in multi-objective optimization problems there can be more than one optimum solution that optimizes all objectives and these solutions are expressed in a set of non-dominated solutions or Pareto-optimal solutions. In this study, the results obtained using the new method as well as the Pareto front of the problem solutions is presented.

Keywords: Fuselage Drag Coefficient, Soft Computing Techniques, Pareto Front, Optimization.

1. INTRODUCTION

The designs of Unmanned Aerial Vehicle (UAV) are attracted interest by many researchers. Researchers use wind tunnel experiments and/or Computational Fluid Dynamics (CFD) methods to design the UAVs [1-4]. However, changing any parameter on the UAV requires consideration of the design from the beginning. Thus, the parameters to be affected by the change are recalculated, which is costly. In the last decades, preliminary studies on the UAV design by using computer based numerical methods such as gradient based algorithm, soft computing methods etc. to reduce time and cost have presented [5-11].

The concept of soft computing was proposed by Zadeh in 1993, the founder of the fuzzy logic [12]. Soft computing methods refers to the total of the methods defined for solving problems that are not mathematically be modeled or difficult to model. That is, it refers to combinations of various methods such as Artificial Neural Network (ANN), fuzzy logic and evolutionary algorithms [13]. Soft computing methods are not focused on a single solution; they have interdisciplinary compatibility and quality analysis [14]. They also have features such as nonlinear programming, intelligent control, decision making and optimization. Therefore, they are widely preferred in engineering problems. Soft computing methods, and hybrid approaches based on soft computing methods have become a popular method in aeronautics as well as in many other areas. ANN based applications [8, 15-18], fuzzy logic based applications [19-23], and applications based on evolutionary algorithms [24-28] are available in the literature.

[1] *Corresponding author: Erciyes University, Department of Aircraft Electrical and Electronics, 38030, Melikgazi/Kayseri, Turkey. arikseda@erciyes.edu.tr*

[2] *Erciyes University, Department of Aeronautical Engineering, 38030, Melikgazi/Kayseri, Turkey. oktay@erciyes.edu.tr*

[3] *Erciyes University, Department of Aircraft Electrical and Electronics, 38030, Melikgazi/Kayseri, Turkey. titi@erciyes.edu.tr*

When the studies in literature are examined, it is seen that such topics as lift and drag coefficients, airfoil design etc. are frequently considered [5-28]. In this study, the optimization of the maximum lift/drag ratio and the roll stability coefficient with respect to the dihedral angle and taper ratio are discussed. The optimization process was carried out for our UAV called as ZANKA-II manufactured at Erciyes University and the data belong to ZANKA-II was used [29, 30]. The data set were produced in limited by using CFD methods due to time-consuming nature of the CFD method. ANN was trained with the obtained data. That is, ANN is trained with data set containing the maximum lift/drag ratio and roll stability coefficient in response to the dihedral angle and taper ratio. Thus, since there is no single expression for this multi-objective problem, the objective function required for optimization by using the features of ANN such as learning and generalization is designed with ANN-based. Then, ANN-based this objective function was optimized with the ABC algorithm by embedding into the ABC algorithm. Finally, Pareto front for this multi-objective problem was presented.

2. MATERIALS AND METHODS

The parameters and methods used in this study are briefly explained in this section.

2.1. Parameters

The dihedral angle (φ) is described as the angle at which the wing is connected to the aircraft relative to the horizontal ground plane. Dihedral angle illustrated in Figure 1 has effect on the rolling moment of the aircraft. The resultant rolling moment is also about dihedral ratio [31]. Dihedral angle is generally selected experience-based in aircraft designs. In this study, the dihedral angle is one of two input parameters.

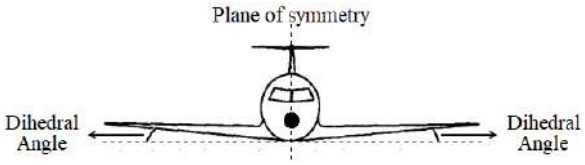

Figure 1. Dihedral angle illustration

Taper ratio (λ) is defined as the ratio of the chord length at the wing tip to the wing root length and shown in Figure 2. It has effect on lift distribution across the entire wing. When the shape of wingplanform is ellipse, drag coefficient in response to lift coefficient is minimum, but it is difficult and costly. When the wing type is untapered rectangular, it has extreme chord towards the tip and more lift force at the tip compared to the ideal situation. In the same aspect ratio, the untapered rectangular wing has about 7% more drag force in response to lift force than the elliptical wing. In addition, when the rectangular wing is tapered, this effect reduces [31]. Thus, taper ratio is one of the important parameters affecting lift/drag ratio and is selected as one of the two input parameters in the study.

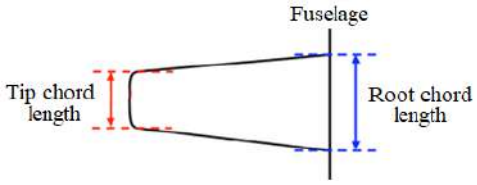

Figure 2. Taper ratio illustration

Lift/Drag Ratio is one of the important parameters for aerodynamic shapes. It is desirable to have a maximum value of lift/drag ratio (E_{max}) in aircraft design. E_{max} is calculated by the equation set given in Equation 1. In this study, E_{max} is one of two output parameters. Here, E is the lift/drag ratio, c_{D_0} is initial drag force, c_L is lift force, c_D is drag force, k is a constant, E_{max} is maximum lift/drag ratio.

$$\begin{cases} E = \frac{c_L}{c_D} = \frac{c_L}{c_{D_0} + k \cdot c_L^2} \\ \frac{dE}{dc_L} = 0 \rightarrow c_L = \sqrt{\frac{c_{D_0}}{k}}, \quad c_D = 2 \cdot c_{D_0} \\ E_{max} = \frac{1}{2 \cdot \sqrt{k \cdot c_{D_0}}} \end{cases} \quad (1)$$

Static roll stability occurs on aircraft only if a restoring moment is generated toward disturbance from wings-level attitude and defines as a function of sideslip angle (β) given in Equation 2. Sideslip angle described as the angle between total velocity and lateral velocity. $C_{l_\beta} < 0$ is the condition required for stability. When an aircraft shows a tendency to sideslip, the roll moment occurred on aircraft depends on dihedral angle, wing sweep, vertical tail and position of wing on fuselage [32].

$$C_{l_\beta} = \left(\frac{c_{l_\beta}}{\varphi}\right) \cdot \varphi + \Delta C_{l_\beta} \quad (2)$$

2.2. Methods

Artificial Neural Network (ANN) is expressed as the mathematical model of biological cells. ANN's, which basic processing unit is neurons, consist of three layers: input, hidden and output. The input layer receives information from the outside world and transmits it to the hidden or output layer. The hidden layer makes this information available to the output layer. At the output layer, information is processed to determine the network output. The number of neurons in the layers is determined by the designers' experience. In feedforward ANN, which preferred in this study, the output of one layer is applied as input over the weights to the next layer, and there is no feedback. As there are many learning algorithms for feed-forward ANN, this structure is often preferred in engineering problems. In addition to this, ANN processes information with some properties such as non-linearity, learning with example, generalization depending on examples [33-35].

The Artificial Bee Colony (ABC) Algorithm was presented by Karaboga in 2005 by modeling the behavior of honey bee's food search. As the ABC algorithm has several control parameters, its working principle is simple and is easy to implement. ABC algorithm with these features is widely used in many optimization problems [36, 37]. The processing steps of the ABC algorithm are as follows: first, the initial food sources are randomly generated. Employed bees select a food source. Employed bees store the nectar at this source, and employed bees return to the hive. Onlooker bees watch the dance of the employed bees returning and select new sources. They store nectar like employed bees and then become scout bees when sources are exhausted, and search for new sources. These steps continue until reaching the stop criteria determined for the algorithm.

Multi-objective optimization problems are defined as the simultaneous optimization of multiple objectives. For example, assume that two different objective functions. Obtained values when optimized these objectives individually are different from the obtained values when optimized simultaneously. In this case, the optimal set of solutions called pareto set or pareto front gives an appropriate set of solutions for both objective. In order to select the most appropriate design from this set, the user applies the decision process according to the importance of each objective. Equivalent weighting coefficients have been applied for objectives in this study. The representive pareto front for optimization problem with dual objectives is shown in Figure 3 [38, 39]

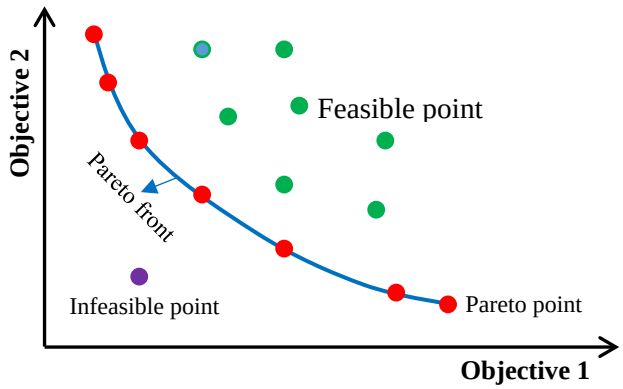

Figure 3. Example of a Pareto front

3. RESULTS AND DISCUSSION

In this section, the process of the study given the block diagram in Figure 4 is explained. Firstly, input and output parameters are selected. The dihedral angle and taper ratio were chosen as input parameters; the maximum lift/drag ratio and roll stability coefficient were chosen as output parameters. Then, data set consist of these parameters is obtained in a limited number by using Computational Fluid Dynamics (CFD) for ZANKA-II given in the Figure 5. Artificial Neural Network (ANN) was trained with this limited number of data. In order to obtain the most suitable ANN structure, the weight values in ANN are adjusted by the Artificial Bee Colony (ABC) algorithm. The obtained optimal weighted ANN structure is integrated into the ABC algorithm for the calculation of the objective function needed in the optimization process. That is, the ABC algorithm is used here for two different optimization purposes: first, it optimized the weights for the most suitable ANN structure. After optimal ANN structure obtained is integrated into ABC algorithm, it used for optimization the original purpose of this study. The main purpose of this study is get to the optimal values of maximum lift/drag ratio and roll stability coefficient depending on the optimal dihedral angle and taper ratio. Mean Square Error (MSE) is chosen as the performance criterion for ANN and ABC.

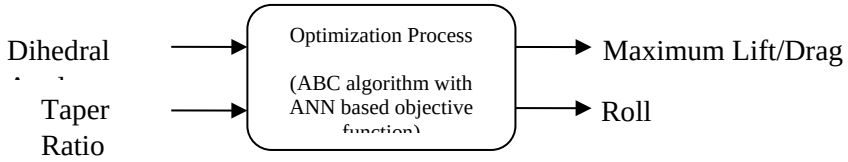

Figure 4. The block diagram of the process of this study

Figure 5. The block diagram of the process of this study

The optimal ANN structure used in the study was obtained by testing for different activation functions and neuron numbers. The most suitable structure was obtained as an input layer with 2 neurons, a hidden layer with 5 neurons and an output layer with 2 neurons for each of the logsig, purelin and tansig activation functions. The values of the best MSE error and standard deviation for these simulations are given in the Table 1. The most suitable ANN structures were integrated into the ABC algorithm and optimization was performed separately for the three activation functions. The control parameters of ABC algorithm are 30 colony sizes and 50 iterations. The values of the optimization process performed by ABC algorithm are presented in the Table 2. Pareto front belonging to this multi-objective problem is given in the Figure 6.

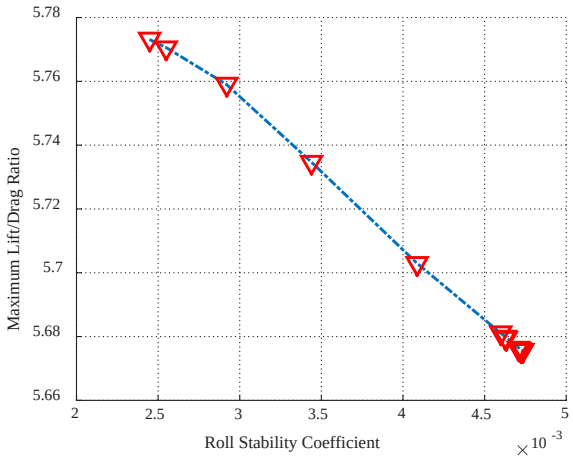

Figure 6. Pareto Front for multi-objective problem

4. CONCLUSIONS

There is no equation involving maximum lift/drag ratio and roll stability coefficient together. Therefore, an alternative hybrid method based on soft computing has been proposed to optimize these two objectives in this study. For this purpose, a dataset consisting of maximum lift/drag ratio and roll stability coefficient outputs corresponding to dihedral angle and taper ratio inputs is obtained. With this data set, Artificial Neural Network (ANN) was trained. Weights of ANN have been optimized to achieve optimum ANN structure. ANN alone is not enough to get optimum output values, since ANN only deals with the input-output relationship. These values need to be optimized in order to achieve optimum results. Therefore, the ANN-based objective function is integrated into the ABC algorithm. Thus, ABC algorithm determines the best solution. However, there is not a single solution for such multi-objective problems, there can be more than one solution set. The results obtained in this study are presented with Pareto front. When the results are examined, it is seen that MSE value is very small. It can be said that the proposed approach compared to the theoretical calculations is a simple, fast and effective method. This approach can be used as an alternative method for researchers in UAV designs.

Table 1. MSE and standard deviation values obtained of different activation functions for the most suitable ANN structures

Performance Criteria	**Logsig (2x5x2)**	**Purelin (2x5x2)**	**Tansig (2x5x2)**
MSE	**0.0012**	**0.0008**	**0.0035**
Standard deviation	**0.0007**	**0.0018**	**0.0049**

Table 2. Colony size and iteration for ABC algorithm, and MSE values of problem optimization process

Activation Function	**Optimization Error (MSE)**
Logsig	0.1707
Purelin	0.2012
Tansig	0.1414

ACKNOWLEDGMENT

This work was supported by Research Fund of The Scientific and Technological Research Council of Turkey (TUBITAK) under Project Number: 214M282

This work was supported by Research Fund of Erciyes University Scientific Research Projects (BAP) Coordination Unit under Project Number: FBA-2015-6286.

REFERENCES

[1]. C. W. Jr. Acree and W. Johnson, "Performance, Loads and Stability of Heavy Lift Tiltrotors," in *AHS Vertical Lift Aircraft Design Conference*, San Francisco, California, American Helicopter Society International, 2006.
[2]. W. Wisnoe, R.E.M. Nasir, W. Kuntjoro, and A.M.I. Mamat, "Wind Tunnel Experiments and CFD Analysis of Blended Wing Body (BWB) Unmanned Aerial Vehicle (UAV) at Mach 0.1 and Mach 0.3," in *13. International Conference on Aerospace Sciences & Aviation Technology*, 2009.
[3]. H. Yeo and W. Johnson, "Performance and Design Investigation of Heavy Lift Tilt-Rotor with Aerodynamic Interference Effects," *Journal of Aircraft*, vol. 46, no. 4, pp. 1231-1239, 2009.
[4]. J. Mariens, "Wing Shape Multidisciplinary Design Shape," Master Thesis, Delft University of Technology, 2012.
[5]. G. W. Burgreen and O. Baysal, "Aerodynamic Shape Optimization Using Preconditioned Conjugate Gradient Methods," *AIAA Journal*, vol. 32, no. 11, pp. 2145–2152, 1994.
[6]. J. Mohanga and O. Baysal, "Gradient-Based Aerodynamic Shape Optimization Using Alternating Direction Implicit Method," *Journal of Aircraft*, vol. 34, no. 3, pp. 346–352, 1997.
[7]. A. Jameson and S. Kim, "Reduction of the Adjoint Gradient Formula for Aerodynamic Shape Optimization Problems," *AIAA Journal*, vol. 41, no. 11, pp. 2114-2129, 2003.
[8]. M. M. Rai and N. K. Madavan, "Aerodynamic Design Using Neural Networks," *AIAA Journal*, vol. 38, no. 1, pp. 173-182, 2000.
[9]. X. Wang, M. Damodaran, and S. L. Lee, "Inverse Transonic Airfoil Design Using Parallel Simulated Annealing and Computational Fluid Dynamics," *AIAA Journal*, vol. 40, no. 4, pp. 791-794, 2002.
[10]. A. Hacioglu and I. Ozkol, "Transonic airfoil design and optimisation by using vibrational genetic algorithm," *Aircraft Engineering and Aerospace Technology*, vol. 75, no. 4, pp. 350-357, 2003.
[11]. E. Vatandas and I. Ozkol, "Dynamic Mesh and Heuristic Algorithms for the Design of a Transonic Wing," *Aircraft Engineering and Aerospace Technology*, vol. 78, vo. 1, pp. 39–44, 2006.
[12]. L. A. Zadeh, *Fuzzy Logic, Neural Networks and Soft Computing*, In: Safety Evaluation Based on Identification Approaches Related to Time-Variant and Nonlinear Structures. Vieweg+Teubner Verlag, 1993.
[13]. L. A. Zadeh, "Fuzzy Logic, Neural Networks and Soft Computing," *Communications of the ACM*, vol. 37, no. 3, pp. 77-84, 1994.
[14]. I. Kroo, "Aeronautical Applications of Evolutionary Design," *VKI Lecture Series on Optimization Methods & Tools for Multicriteria/Multidisciplinary Design*, 2004.
[15]. S. Huang, L. Miller, and J. Steck, "An exploratory application of neural networks to airfoil design," in *32nd Aerospace Sciences Meeting and Exhibit, Aerospace Sciences Meetings*, Reno, NV, USA, 1994.
[16]. M. Norgaard, C. C. Jorgensen, and J. C. Ross, "Neural Network Prediction of New Aircraft Design Coefficients," NASA Ames Research Center, Moffett Field, California 94035-1000, Technical Report 112197, 1997.
[17]. M. Santos, B. Mattos, and R. Girardi, "Aerodynamic Coefficient Prediction of Airfoils Using Neural Networks," in *46th AIAA Aerospace Sciences Meeting and Exhibit, Aerospace Sciences Meetings*, 2008.
[18]. I. Turkmen and S. Arik, "A New Alternative Air Data Computation Method Based On Artificial Neural Networks," *Havacilik ve Uzay Teknolojileri Dergisi*, no. 1, pp. 21-29, 2016.
[19]. M. Konar and A. Bagis, "Ucus Kontrol Sistemi Hiz Parametresinin Adaptif Ag Yapili Bulanik Sonuc Cikarim Sistemi Kullanilarak Belirlenmesi," *IEEE 17. Sinyal Isleme ve Iletisim Uygulamalari Kurultayi (SIU'2009)*, Antalya, TURKEY, 2009.
[20]. Z. A. Ali, D. wang, and M. Aamir, "Fuzzy-Based Hybrid Control Algorithm for the Stabilization of a Tri-Rotor UAV," *Sensors*, vol. 16, no. 5, 2016.
[21]. I. N. Ibrahim and M. A. Al Akkad, "Exploiting an Intelligent Fuzzy-PID system in Nonlinear Aircraft Pitch Control," in *2016 International Siberian Conference on Control and Communications (SIBCON)*, Moscow, Russia, 2016.
[22]. A. G. Roy and N. K. Peyada, "Aircraft parameter estimation using Hybrid Neuro Fuzzy and Artificial Bee Colony optimization (HNFABC) algorithm," *Aerospace Science and Technology*, vol. 71, pp. 772-782, 2017.
[23]. O. Castillo and Leticia Cervantes, "Genetic Design of Optimal Type-1 and Type-2 Fuzzy Systems for Longitudinal Control of an Airplane," *Intelligent Automation & Soft Computing*, vol. 20, no. 2, pp. 213-227, 2014.
[24]. D. C. M. Tse and L. Y. Y. Chan, "Application of Micro Genetic Algorithms and Neural Networks for Airfoil Design Optimization," *RTO MP-035 Aerodynamic Design and Optimization of Flight Vehicles in a Concurrent Multi-Disciplinary Environment*, Canada, 1999.
[25]. B. R. Jones, W. A. Crossley, and A. S. Lyrintzis, "Aerodynamic and Aeroacoustic Optimization of Rotorcraft Airfoils via a Parallel Genetic Algorithm," *Journal of Aircraft*, vol. 37, no. 6, pp. 1088-1096, 2000.
[26]. A. Hacioglu, "Yapay Sinir Agi ile Guclendirilmis Genetik Algoritma ve Tersten Kanat Profili Dizayni," *Journal of Aeronautics and Space Technologies*, vol. 1, no. 3, pp. 1–7, 2004.
[27]. A. C. Marta, "Parametric Study of a Genetic Algorithm using a Aircraft Design Optimization Problem," Stanford University, Tech. Report, 2008.
[28]. S. Bagassi, F. Lucchi, and F. Persiani, "Aircraft Preliminary Design: Genetic Algorithm Based Optimization Method," in *29th Congress of The International Council of The Aeronautical Sciences*, Petersburg, Russia, 2014.

[29]. T. Oktay, M. Konar, M. A. Mohamed, M. Aydin, F. Sal, M. Onay, and M. Soylak, "Autonomous Flight Performance Improvement of Load-Carrying Unmanned Aerial Vehicles by Active Morphing," *International Journal of Mechanical, Aerospace, Industrial, Mechatronic and Manufacturing Engineering*, vol. 10, no. 1, pp. 123-132, 2016.
[30]. T. Oktay, M. Uzun, I. Yilmaz, and M. Konar, "Aerodynamic Nose Shape Optimization for Performance Maximization of Morphing Autonomous Aerial Robot," *2nd International Conference on Engineering and Natural Sciences (ICENS 2016)*, Saraybosna, Bosnia And Herzegovina, 2016.
[31]. D. P. Raymer, *Aircraft design: A conceptual approach*, American Institute of Aeronautics and Astronautics, Inc., Washington, D.C, p.56, 1992.
[32]. R. C. Nelson, *Flight stability and automatic control*, Vol. 2, New York: WCB/McGraw Hill, 1998.
[33]. S. Haykin, *Neural Networks: A Comprehensive Foundation*, Prentice Hall PTR, USA, 1994.
[34]. D. R. Hush and B. G. Horne, "Progress in Supervised Neural Networks," *IEEE Signal Processing Magazine*, vol. 10, no. 1, pp. 8-39. 1993
[35]. E. Oztemel, *Yapay Sinir Aglari*, Istanbul, Papatya Yayincilik, 2003.
[36]. D. Karaboga, "An idea based on honey bee swarm for numerical optimization," Erciyes University, Engineering Faculty, Computer Engineering Department, Technical Report-TR06, 2005.
[37]. D. Karaboga and B. Basturk, "A powerful and efficient algorithm for numerical function optimization: artificial bee colony (ABC) algorithm," *Journal of Global Optimization*, vol. 39, no. 3, pp. 459–471, 2007.
[38]. L. Ozbakir, "Cok objektifli esnek atolye cizelgeleme problemlerinin sezgisel yontemlerle modellenmesi: analizi ve cozumu," PhD Thesis, Erciyes Universitesi, Sosyal Bilimler Enstitusu, Kayseri, 2004.
[39]. E. Ergul, "Cok amacli genetik algoritmalar: temelleri ve uygulamalari," PhD Thesis, Ondokuz Mayis Universitesi, Fen Bilimleri Enstitusu, Samsun, 2010.

BIOGRAPHY

Seda ARIK received a BS in Electrical and Electronics Engineering from Erciyes University (2010) and a MS in Aviation from Erciyes University (2014) and also other MS in Electrical and Electronics Engineering from Erciyes University (2015). She is pursuing a PhD for Aviation at Erciyes University and is currently Research Assistant with the Faculty of Aeronautics and Astronautics, Aircraft Electricals and Electronics, Erciyes University. Her main research areas are artificial intelligence, optimization methods, chaos and electronic circuit applications, semiconductor materials.

ICENS 4TH INTERNATIONAL CONFERENCE ON ENGINEERING AND NATURAL SCIENCE
2-6 May 2018 KIEV UKRAINE

Recipe Optimization for Synthesis of ZnO and Al_2O_3 Thin Film by Using Atomic Layer Deposition

Mert Sonmez[1], Mert Yuksel[1], Ismail Kupa[1], Ersin Bahceci[2], Tolga Depci[2], Meryem Polat Gonullu[1], Hakan Ates[1]*

Abstract

Developments in microelectronics and thin film devices require the advancement of new materials and new deposition methods. In particular, the driving role of some devices, such as silicon devices, will require SiO_2 transition oxide layers with a thickness of several nanometers in the near future. Similarly, recipe optimization for synthesis of ZnO and Al_2O_3 thin films in atomic layer deposition is also important. In this study, ZnO and Al_2O_3 thin film were deposited at 200 ºC on silicon substrates with atomic layer deposition (ALD) technique. The study was repeated ten times with different parameters. The thicknesses of the films were measured with an ellipsometer to determine whether they were homogeneous or not. XRD pattern of thin film was investigated to determine crystal structure and homogeneity also; its electrical properties were characterized. Optimum recipe for atomic layer deposition of ZnO and Al_2O_3 were optimized.

Keywords: ZnO, Al_2O_3, ALD, Film, Recipe

1. INTRODUCTION

Atomic Layer Deposition (ALD) is a deposition technique; develop out of Chemical Vapor Deposition to synthesize ultrathin and conformal films with an accurate control of thickness and material properties onto a substrate [1-3]. The ALD mechanism is based on the consecutive exposure of a surface to two reactants into a vacuum chamber. These precursor vapors react with the surface using self-limiting and saturated reactions which lead to the formation of one monolayer of film per deposition cycle. ALD films are produced by exposing the substrate surface with the precursors cyclically. A definite amount of material is deposited onto the substrate surface in each cycle, known as “growth per cycle” which is between 0.1 and 3 Å. This consecutive behavior of the precursors also helps avoid the formation of gas-phase particles that sometimes plague other gas phase deposition techniques in order to create high purity, density, thin and continuous films which are essential to the nano-community [4-7]. Higher quality films can be produced under optimized conditions like dosage; purge, temperature and pressure are often interdependent with one another [8]. As a result, processes must be optimized to achieve self-limiting saturated surfaces and avoid CVD-like reactions to maintain thickness control and achieve uniformity and conformity at the atomic level while preserving the preferred materials properties (structural, optical, electrical, etc.) [9-10]. As a result of its ability to deposit films with excellent uniformity and conformity with unique thickness control, ALD has emerged as a significant technology used in semiconductor devices, optoelectronics, catalysis, energy devices, micro-electro-mechanical systems (MEMS) and nanotechnology [11-17]. Nevertheless, ALD is a complex technique since it depends on the nature of the reactants and on the process conditions, and so, research on the surface reactions and growth mechanisms is still continuing. Accurate thickness control, excellent uniformity and unique conformity are assumed as essential parameters for ALD process. Also, several parameters such as precursors, temperature window, purge window, saturating exposures, pressure regime and etc. can highly influence the performance of the process [18-19].

A number of thin films can be synthesized using ALD, such as binary oxides (Al_2O_3, TiO_2, ZnO, ZrO_2, HfO_2, and Ta_2O_5), are the most common oxides that have been widely investigated by using ALD [20].

In this work, depositing ZnO and Al_2O_3 films were carried out via the DZE/H_2O and TMA/H_2O process on Si substrates. The aim of this work is to determine the optimum pulse time reveal a recipe for DZE, TMA and H_2O precursors.

2. MATERIALS AND METHOD

ZnO and Al_2O_3 thin films were deposited in a Okyay Tech. ALD reactor. The deposition was done on p-type Si (100) wafer. Diethylzinc (DEZ) and Trimethylaluminum (TMA) was chosen as precursor materials and water as a reactant, while nitrogen as a carrier gas. The pulse time for ZnO; Al_2O_3 and H_2O were 10; 20 and 30 ms after that the purge time was 10 s for all which are given in Table 1. The process temperature was 200 °C and gas flow rate 20 sccm. The growth rate per cycle (GPC) was 0.43 Å/cycle for ZnO and 1.29 Å/cycle for Al_2O_3.

Spectroscopic Ellipsometry (SE) measurements of ALD ZnO and Al_2O_3 thin films were carried out using a UVISEL Jobin Yvon SE at a room temperature in 0.59 - 4.6 eV photon energy region and the incidence angle of 70°. Structural analysis of the ZnO and Al_2O_3 films was made with the use of the Bruker D8 Discover High Resolution X-ray diffractometer (CuK_α radiation source). The I–V measurements of the ZnO and Al_2O_3 thin films have been performed using a Keithley 2400 Current/Voltage Source. Electrical measurements of ZnO and Al_2O_3 thin films deposited on silicon substrates were taken at room temperature at a 10V.

3. RESULTS AND DISCUSSION

3.1. SE Ellipsometry Measurements

Thicknesses of the produced ZnO and Al_2O_3 films under different pulse time were determined by SE technique which is modeled with DeltaPsi software.

Table 1. Pulse times of film precursors.

Sample	DEZ pulse (ms)	TMA pulse (ms)	H_2O pulse (ms)	N_2 purge (s)
S1	10	10	10	10
S2	20	20	20	10
S3	30	30	30	10

There is a need for a model to determine film thickness, optical constants and etc. The model made up of a Si substrate and produced film compositions. Table 3 and Table 4 show that the change of ZnO and Al_2O_3 film thicknesses with respect to pulse time for nine different points. As a result of the measurement, the film thicknesses ZnO and Al_2O_3 were found to be between ~ 5-19 nm and ~ 5-17 nm, respectively.

Table 2. Thickness values of ZnO thin films at different points.

Sample/Pulse Time (ms)	P1	P2	P3	P4	P5	P6	P7	P8	P9
S1/10	5.35	8.66	6.54	6.88	7.32	5.49	8.16	9.69	9.25
S2/20	13.40	12.46	12.57	12.88	13.12	13.18	12.40	13.27	12.70
S3/30	15.99	17.14	16.25	18.65	15.35	15.26	17.35	17.18	18.25

Table 3. Thickness values of Al_2O_3 thin films at different points.

Sample/Pulse Time (ms)	P1	P2	P3	P4	P5	P6	P7	P8	P9
S1/10	5.99	7.20	8.53	6.08	5.74	6.37	8.74	5.44	7.97
S2/20	12.84	13.68	13.00	12.21	13.78	12.11	13.91	12.82	12.06
S3/30	15.64	16.45	17.70	15.84	15.11	15.60	17.83	16.34	15.03

3.2. X-Ray Diffractometry Measurements

The crystal structures of the materials were characterized by XRD diffraction pattern. The XRD measurements of ALD ZnO films has showed hegzagonal wurtzite structure at a <002> preferred orientation according to literature [21] and ALD Al_2O_3 films deposited at 200 °C were amorphous character for 20 pulse. The broad peak matched the amorphous Al_2O_3 by ALD reported in the literature [22], indicating the successful coating of amorphous Al_2O_3 layer whose crystallization take place after annealing at 825 °C.

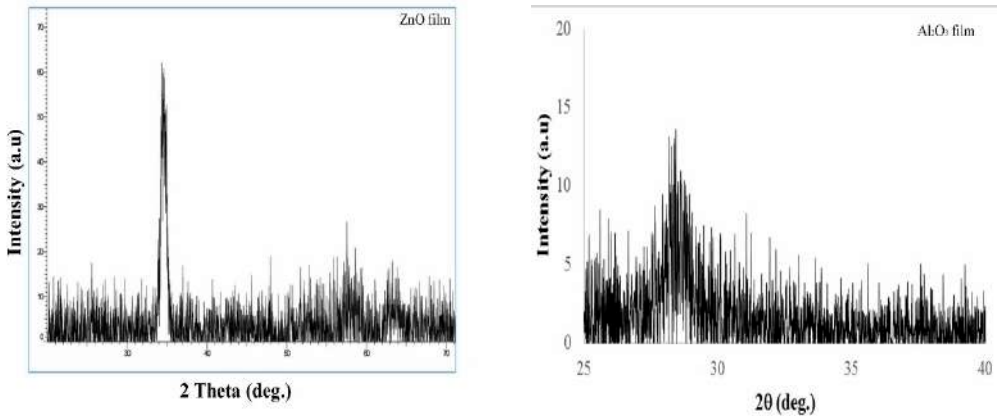

Figure1. XRD pattern of ALD ZnO and Al_2O_3 thin films produced at 20 time pulse.

3.3. Electrical Conductivity Measurements

ALD ZnO and Al2O3 thin films deposited on silicon substrates were examined and their electrical conductivity was investigated at room temperature. In figure 2, I-V curve characteristics demonstrated that ZnO and Al2O3 films were homogeneously deposited on the Si substrate. As can be seen from the electrical analysis of ZnO and Al2O3 thin films grown on Si substrate, thin film layers exhibit stable ohmic behavior. However, it is possible to say that the small curve deviations in some areas of ZnO in the graph originate from ambient noise or dust.

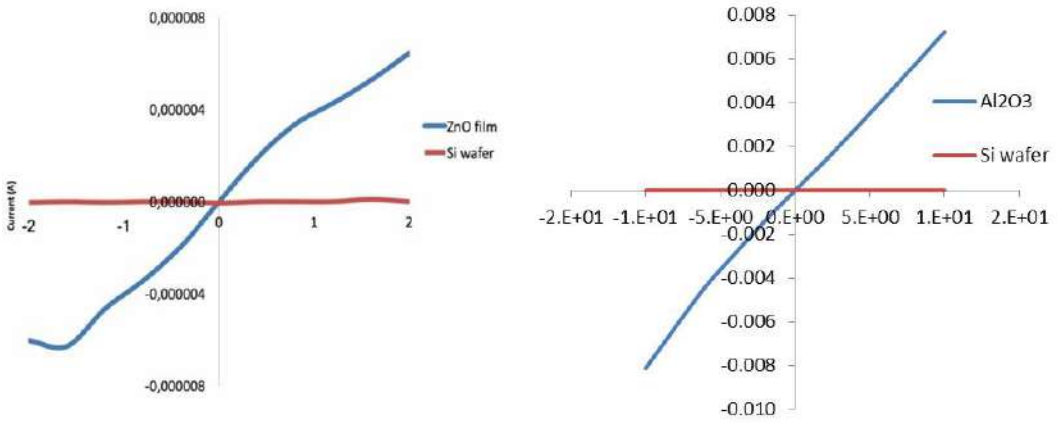

Figure2. I-V curve of ALD ZnO and Al_2O_3 thin films.

4. CONCLUSION

In this work, the ZnO and Al_2O_3 thin films were deposited on the Si substrate by ALD process under different pulse times in order to create new recipes. The properties of the ZnO and Al_2O_3 thin films prepared by thermal ALD were investigated with SE, XRD and I-V characterization techniques. As a result of characterization, it is seen that the S2 samples of the films were more homogeneous than the others and show few nanometer thickness difference in itself according to thickness values from received different areas. Also, XRD and I-V measurements show that better structure for S2 samples for 20 ms pulse time for both films. In conclusion, it can be say that the thickness was controlled by ALD and the films with desire thickness were successfully achieved under the conditions of: ***Substrate temperature 200 ºC, Cycle 300, N_2 flow 20 sccm, purge time 20 s, H_2O Pulse time 0.02s, DEZ and TMA pulse time 20 ms***.

ACKNOWLEDGMENT

Authors would like to thank to Gazi University Scientific Research Unit, Iskenderun Technical University and Okyay Tech. Res.& Eng.

REFERENCES

[1]. M. Knez, K. Nielsch, and L. Niinisto, “Synthesis and surface engineering of complex nanostructures by atomic layer deposition,” Adv. Mater., vol. 19, pp. 3425–3438, 2007.
[2]. D. Riihelä, M. Ritala, R. Matero, and M. Leskelä, “Introducing atomic layer epitaxy for the deposition of optical thin films,” Thin Solid Films., vol. 289, pp .250–255, April 1996.
[3]. R.W. Johnson, A. Hultqvist, and S.F. Bent, “A brief review of atomic layer deposition: from fundamentals to applications,” Mater. Today., vol. 17 (5), pp. 236–246, June 2014.
[4]. M.R. Saleem, A. Rizwan, M. B. Khan, S. Honkanen and J. Turunen, “Impact of atomic layer deposition to nanophotonic structures and devices,” Front. Mater., vol.1, pp. 1-13, October 2014.
[5]. M.R. Saleem, A. Rizwan, Honkanen and J. Turunen, “Determination of thermo-optic properties of atomic layer deposited thin TiO2 films for athermal resonant waveguide gratings by spectroscopic ellipsometry,” Proc. SPIE 2014, 9130, 1–8.
[6]. N. Cheng, and X. (Andy) Sun, “Single atom catalyst by atomic layer deposition technique,” Chin. J. Catal., vol. 38, pp. 1508–1514, September 2017.
[7]. H. Li, D. Han , J. Dong , W. Yu, Yi Liang, Z. Luo, S. Zhang, X. Zhang, and Yi Wang, “Enhanced electrical properties of dual-layer channel ZnO thin film transistors prepared by atomic layer deposition,” Appl. Surf. Sci., vol.439, pp. 632–637, January 2018.
[8]. S.M. George, “Atomic layer deposition: An overview,” Chem. Rev., vol. 110 (1), pp. 111–131, February 2010.
[9]. H. Kim, “Atomic layer deposition of metal and nitride thin films: Current research efforts and applications for semiconductor device processing,” J. Vac. Sci. Technol. B: Microelectron. Nanometer Struct., vol. 21 (6), pp. 2231-2261, September 2003.
[10]. H. Kim, Han Bo Ram Lee, and W. J. Maeng, "Applications of atomic layer deposition to nanofabrication and emerging nanodevices," Thin Solid Films, vol. 517, pp. 2563-2580, September 2009.

[11]. P. Caban, R. Pietruszka, K. Kopalko, B.S. Witkowski, K. Gwozdz, E. Placzek-Popko, and M. Godlewski, "ZnO/GaAs heterojunction solar cells fabricated by the ALD method," Optik., vol. 157, pp. 743–749, 2018.
[12]. J. Phillips, W. Bowen, E. Cagin, and W. Wang, "Electronic and Optoelectronic Devices Based on Semiconducting Zinc Oxide," Comprehensive Semiconductor Sci. Tech., vol. 6, pp. 101-127 (2011)
[13]. A. Di Mauroa, M. Cantarella, G. Nicotra, V. Privitera, and G. Impellizzeri, "Low temperature atomic layer deposition of ZnO: Applications in photocatalysis," Appl. Catal., B: Environ., vol. 196, pp. 68–76, May 2016.
[14]. P. Banerjee, I. Perez, L. Henn-Lecordier, S.B. Lee, and G.W. Rubloff, "ALD basedmetal-insulator-metal (MIM) nanocapacitors for energy storage,"ECS Transactions., vol. 25 (4), pp. 345-353, 2009.
[15]. R. L. Puurunen, J. Saarilahti, and H. Kattelus, "Implementing ALD Layers in MEMS processing," ECS Transactions, vol. 11 (7), pp. 3-14, September 2007.
[16]. S. Zhuiykova, T. Kawaguchi, Z. Hai, M. K. Akbari, and P. M. Heynderickx, "Interfacial engineering of two-dimensional nano-structured materials by atomic layer deposition," Appl. Surf. Sci., vol. 392, pp. 231–243, 2017.
[17]. R. Artzi-Gerlitz, K. D. Benkstein, D. L. Lahr, J. L. Hertz, C. B. Montgomery, J.E. Bonevich, S. Semancik, and M. J. Tarlov, "Fabrication and gas sensing performance of parallel assemblies of metal oxide nanotubes supported by porous aluminum oxide membranes," Sens. Actuators, B., vol. 136, pp. 257-264, October 2009.
[18]. H. Salami, A. Poissant, and R.A. Adomaitis, "Anomalously high alumina atomic layer deposition growth per cycle during trimethylaluminum under-dosing conditions," J. Vac. Sci. Technol. A., vol. 35, pp. 01B101, September 2017.
[19]. R. A. Wind, and S. M. George, "Quartz Crystal Microbalance Studies of Al2O3 Atomic Layer Deposition Using Trimethylaluminum and Water at 125 °C," J. Phys. Chem. A., vol. 114, pp. 1281–1289, 2010.
[20]. Adib Abou Chaaya, "Design of oxide based nanomaterials by ALD : from sensors to membrane application", Material chemistry, Université Montpellier II - Sciences et Techniques du Languedoc, 2014.
[21]. D. Kim, H. Kang, Jae-Min Kim, and H. Kim, "The properties of plasma-enhanced atomic layer deposition (ALD) ZnO thin films and comparison with thermal ALD," Appl. Surf. Sci., vol. 257, pp. 3776–3779, November 2011.
[22]. H. Liu , Ren Bin Yang, S. Guo, Coryl J.J. Lee, N.L. Yakovlev, "Effect of annealing on structural and optical properties of ZnO/Al2O3 superlattice structures grown by atomic layer deposition at 150 ºC," J. Alloy. Comp., vol. 703, pp. 225-231, January 2017.

Biography:

Dr. Hakan Ates was born in 1971, in Ankara, Turkey. He is Professor and works for Gazi University in the Department of Metallurgical and Materials Engineering. He is an international welding engineer and inspector (comprehensive level), and is also vice manager of the Gazi KABTEM application and research center. He is a member of KATED (Welding Technology Society) and TPMA (Turkish Powder Metallurgy Association). He has had many papers published on nanotechnology, nanomaterials, powder metallurgy and welding processes.

ICENS 4TH INTERNATIONAL CONFERENCE ON ENGINEERING AND NATURAL SCIENCE
2-6 May 2018 KIEV UKRAINE

Data Dependent Techniques for Initialization of Cluster Prototypes in Partitioning Cluster Analysis

Zeynel Cebeci[1], Mustafa Sahin[2], Cagatay Cebeci[3]

Abstract

The quality of final clustering obtained from partitioning cluster algorithms is closely related to the initialization of cluster prototypes. Hence, choosing an appropriate initialization technique is the first key step in prototype-based clustering analyses. In this paper, based on required iteration counts and computing time we compared the performances of three new simple data-dependent initialization techniques (random samples averaging, systematic sampling and prototyping around the center of a selected feature) vs. two widely used initialization techniques (K-means++ and simple random sampling). According to the results obtained with Fuzzy C-means algorithm on one synthetic and three real datasets, systematic sampling and prototyping around the center of a selected feature were evaluated to be promising techniques in order to reduce the required iterations by the partitioning clustering algorithms.

Keywords: *cluster analysis, partitioning clustering, prototype-based clustering, initialization of prototypes, data sampling, fuzzy c-means*

1. INTRODUCTION

Cluster analysis partitions data instances into homogenous groups based on some similarity measures. Due to its unsupervised, descriptive and summarizing nature, clustering has become a core analysis in data science [2] for several purposes such as image segmentation, anomaly detection, data classification and compression, and many others. The goal of clustering is that the instances within a cluster be more similar to each other, and different from the instances in other clusters.

Although there is a large number of clustering algorithms being hierarchical and partitioning [13], the partitioning clustering algorithms are mostly used in cluster analysis of large and multidimensional numerical data sets because they often have lower complexity [7]. They partition data into a pre-defined number of clusters (*c* clusters) which are as compact as possible and well separated from each other, and create a one-level partitioning of the data instances using a relevant objective optimizing function. As a dominant group of partitioning-based clustering algorithms, the prototype-based clustering algorithms assume that the characteristics of the instances in a cluster can be represented with a cluster prototype which is a point in the data space. These algorithms assign the *n* instances in data space to the nearest clusters by using their proximities to the prototypes of clusters.

In a partitioning cluster analysis, the choice of initial prototypes be either centroids or medoids is an important task because the quality of final clustering result is very closely related to the appropriate selection of initial cluster prototypes.

[1] *Corresponding author: Cukurova University, Faculty of Agriculture, Division of Biometry & Genetics Adana, Turkey, zcebeci@cu.edu.tr*
[2] *Kahramanmaras Sutcu Imam University, Faculty of Agriculture, Division of Biometry & Genetics Kahramanmaras, Turkey, ms66i@ksu.edu.tr*
[3]*University of Strathclyde, Dept. of Electronic & Electrical Eng. Technology and Innovation Centre, Glasgow, UK, cagatay.cebeci@strath.ac.uk*

Different initializations of prototypes can lead to different clustering results because the partitioning algorithms do not converge to global minima but only to local minima. For finding an optimal solution, multiple runs of an algorithm are required with different initialization settings for handling the smallest squared error, and these runs lead to increase in computational cost. So, choosing an appropriate initialization technique is the first key step in prototype-based clustering tasks. Although there are many data independent and dependent initialization techniques which can be used in initialization of cluster prototypes, some of them are often inefficient to find the appropriate prototypes and some are too sophisticated to apply. It is believed that simple and data dependent initialization techniques may contribute to fast convergence to final clustering, and thus, decrease the computational cost. For this reason, in this paper, we aimed to propose some simple data dependent techniques to initialize the cluster prototypes in partitioning cluster analysis.

2. FUZZY C-MEANS CLUSTRING

In this paper, for testing the performances of the studied initialization techniques we used the basic Fuzzy C-means Clustering (FCM) algorithm [4] as the representative of prototype-based clustering algorithms. As one of the most widely used soft clustering algorithms, FCM differs from hard K-means algorithm with the use of weighted squared errors instead of using squared errors only. Therefore, the proposed initialization techniques in this paper can be applied not only for FCM but also for all hard, fuzzy, possibilistic clustering algorithms and their variants in the same way. In this section, we briefly introduce the basic terminology and FCM algorithm for an easy walkthrough of the studied initialization techniques.

Let $\boldsymbol{X} = \{\boldsymbol{x}_1, \boldsymbol{x}_2, \dots, \boldsymbol{x}_n\}$ be a dataset to be analyzed, and $\boldsymbol{V} = \{\boldsymbol{v}_1, \boldsymbol{v}_2, \dots, \boldsymbol{v}_c\}$ be a set of the prototypes (centroids or medoids) of clusters in multidimensional dataset $\boldsymbol{X}$ ($\boldsymbol{X} \in \mathbb{R}^{np}$) where n is the number of instances, p is the number of features, and c is the number of partitions or clusters. For dataset $\boldsymbol{X}$, FCM minimizes the objective function in Eq. (1).

$$J_{FCM}(\boldsymbol{X};\ \boldsymbol{U}, \boldsymbol{V}) \ = \ \sum_{i=1}^{c} \sum_{k=1}^{n} u_{ik}^{m}\, d_{ik\boldsymbol{A}}^{2} \tag{1}$$

As shown in Eq. (2), $\boldsymbol{U}$ of $n \times c$ dimension is the membership matrix for a fuzzy partition of dataset $\boldsymbol{X}$.

$$\boldsymbol{U} = [u_{ik}] \in M_{FCM} \tag{2}$$

The element u_{ik} is the membership degree of k^{th} instance to i^{th} cluster. Thus, the i^{th} column of matrix $\boldsymbol{U}$ contains the membership values of n instances to i^{th} cluster. $\boldsymbol{V}$ is a cluster prototypes matrix given in Eq. (3).

$$\boldsymbol{V} = \{\boldsymbol{v}_1, \boldsymbol{v}_2, \dots, \boldsymbol{v}_c\},\ \boldsymbol{v}_i \in \mathbb{R}^p \tag{3}$$

In Eq. (1), $d_{ik\boldsymbol{A}}^2$ is the distance between k^{th} data instance and the prototype of i^{th} cluster. It is computed using a squared inner-product distance norm in Eq. (4).

$$d_{ik\boldsymbol{A}}^2 = \|\boldsymbol{x}_k - \boldsymbol{v}_i\|_{\boldsymbol{A}}^2 = (\mathbf{x}_k - \mathbf{v}_i)^T \boldsymbol{A} (\boldsymbol{x}_k - \boldsymbol{v}_i) \tag{4}$$

In Eq. (4), $\boldsymbol{A}$ is a positive and symmetric norm matrix, and the inner product with norm $\boldsymbol{A}$ is a measure of distances between data points and cluster prototypes. When $\boldsymbol{A}$ is equal to $\boldsymbol{I}$, $d_{ik\boldsymbol{A}}^2$ is obtained in squared Euclidean norm. In Eq. (1), m is a fuzzifier parameter (or weighting exponent) whose value is chosen as a real number greater than 1 ($m \in [1, \infty)$, usually chosen as 2 in the literature). While m approaches to 1, clustering tends to become crisp like K-means but when it approaches to the infinity clustering becomes more fuzzified. The objective function J_{FCM} is minimized using the update formulas in Eq. (8) and (9) in each iteration step subject to the constraints in Eq. (5), (6) and (7).

$u_{ik} \in [0,1];\ 1 \le i \le c, 1 \le k \le n$ (5)

$\sum_{i=1}^{c} u_{ik} = 1;\ 1 \le k \le n$ (6)

$0 < \sum_{k=1}^{n} u_{ik} < n;\ 1 \le i \le c$ (7)

FCM stops when the iteration counts has reached to a predefined maximum iteration counts, or when the difference between the sums of membership values in $\boldsymbol{U}$ obtained two consecutive iterations is less than a predefined convergence value (ε). The steps involved in FCM are:

1) Initialize the prototype matrix $\boldsymbol{V}$ and the membership matrix $\boldsymbol{U}$.
2) Update the cluster prototypes:

$\mathbf{v}_i = \frac{\sum_{k=1}^{n} u_{ij}^{m} \boldsymbol{x}_k}{\sum_{k=1}^{n} u_{ik}^{m}};\ 1 \le i \le c$ (8)

3) Update the membership values with:

$u_{ik}^{(t)} = \frac{1}{\sum_{k=1}^{c} \left(d_{ikA}/d_{jkA}\right)^{2/(m-1)}};\ 1 \le i \le c\ , 1 \le k \le n$ (9)

4) If $\left\| \boldsymbol{U}^{(t)} - \boldsymbol{U}^{(t-1)} \right\| < \varepsilon$ then stop else go to the step 2, where t is the iteration number.

3. DATA DEPENDENT INITIALIZATION TECHNIQUES

Initialization of the cluster centers takes place in the first step of the partitioning algorithms. It is a process to assign initial values of prototype matrix $\boldsymbol{V}$ in Eq. (3). For initialization of $\boldsymbol{V}$, some comprehensive reviews of a large number of techniques are available according to the related ([6], [5], [7]).The existing initialization techniques have been categorized as data independent, simple data dependent and sophisticated data dependent techniques in Reference [5]. The data independent techniques ignore the locations of the data instances. On the other hand, the simple data dependent techniques basically consider the data instances while the sophisticated methods initialize the prototypes in more complex ways accordingly to the techniques provided in the clustering algorithms themselves.

In this paper, we do not present an overview of the existing techniques but compare the performances of two widely used initialization techniques (k-means++ and simple random sampling) to those of two the newly proposed data sampling approaches (random samples averaging and systematic sampling) plus a novel simple data-dependent technique named prototyping around the center of a selected feature.

3.1 Simple random sampling

Simple random sampling (without replacement), is the sampling technique in which each instance in a dataset has an equal probability of being sampled. This ordinary technique, known as McQueen method [20] in K-means, has been probably the most commonly used technique for initialization of cluster prototypes because of its simplicity. Unlike its data independent counterparts, it avoids to assign the locations in empty regions of the data space as the prototypes do but it can result with the cluster prototypes that are not well spread out over analyzed dataset. Moreover, there is also the risk to select the outliers rather than the instances in dense regions (clusters). In this technique, as shown in Eq. (10), prototype vector for each cluster is initialized with a data instance vector that is drawn from *n* data instances randomly.

$\boldsymbol{v}_i = rand(\boldsymbol{x}_k)\ ;\quad 1 \le i \le c\ , 1 \le k \le n$ (10)

3.2 Random samples averaging

As a solution for the above mentioned problem of the simple random sampling, a set of random data samples is drawn and their average can be used as the prototype instead of using only one random sample. This technique may be better to avoid the possible biases due to possible outliers in datasets. To achieve this, simple random data sampling is repeated for *r* times, and the average of samples is assigned as the cluster prototype as seen in Eq. (11). This approach is different from the Forgy method [15] which is used for finding the minimum objective function value with multiple runs of in K-means algorithm. Here, with the proposed technique, multiple random data samples are drawn and averaged before starting the clustering algorithm instead of multiple runs of the clustering algorithm itself. It is expected that the use of the average of *r* random samples on *p* features may be helpful to decrease the effect of outliers and contribute to increment in the initialization quality.

$$\boldsymbol{v}_i = \frac{\sum_{j=1}^{r} rand(\boldsymbol{x}_k)}{r} \;\; ; \quad 1 \le i \le c \,, 1 \le k \le n \tag{11}$$

3.3 Systematic sampling

Systematic sampling is another random sampling technique in which data instances are sampled at a given equal width interval systematically. Although it is often used in many applications for its simplicity and efficiency over the simple random sampling, surprisingly there has not been research work which has introduced this technique in the literature related to the initialization problems. Whereas, it may improve the quality of initialization because it tries to determine prototypes far enough from each other by using an equal width interval. In this technique, the prototype of first cluster is the data instance randomly sampled from the top *R* instances (Eq. (12)) located in the first sampling interval of dataset. The index of second cluster prototype is determined by adding *R* to the index of the first data sample. Then, the process is successively repeated for determining the prototypes of remaining clusters by adding the sampling interval *R* to the index of previously chosen data sample as formulated in Eq. (13). In such way, the prototypes are not only randomly determined but also are equally far from each other for improving the quality of initialization process.

$$\boldsymbol{v}_1 = rand(\boldsymbol{x}_j) \,; 1 \le j \le R, \;\; R = n/c \tag{12}$$

$$\boldsymbol{v}_i = \boldsymbol{x}_{(k+(i-1)R)} \;\; ; \; 2 \le i \le c, \;\; k = row_index(\boldsymbol{x}_j) \tag{13}$$

3.4 Prototyping around the center of a selected feature

In this paper, we propose a novel data-dependent deterministic technique so called "*prototyping around the center of a selected feature*" (called *pacsf* in this paper). It resembles Ball and Hall's method [3] for assignment of the first cluster prototype but differs by the use of two different interval values (R_1 and R_2) instead of using only one fixed threshold (*T*) value for determining the prototypes of remaining clusters. Additionally, our proposed technique does not require to sort the dataset. The above mentioned intervals are calculated by using the descriptive statistics of the selected feature according to the formulas shown in Eq. (14) and Eq. (15). In Eq. (14), R_1 is an interval which is calculated by dividing the distance between the center and minimum of the selected feature ($\boldsymbol{x}_{,f}$) by half of the number of clusters minus 1. Similarly, R_2 is an interval which is calculated by dividing the distance between the maximum and center of the selected feature by half of the number of clusters minus 1. These two intervals become equal to each other if the selected feature is normally distributed, and thus, cluster prototypes are located in equidistant positions from each other in the *p*-dimensional space of *n* data instances. On the other hand, the intervals become different when the distribution of the selected feature is left or right skewed.

$$R_1 = \frac{center(\boldsymbol{x}_{,f}) - min(\boldsymbol{x}_{,f})}{(c-1)\,/2} \tag{14}$$

$$R_2 = \frac{\max(\boldsymbol{x}_{.f}) - center(\boldsymbol{x}_{.f})}{(c-1)/2} \quad (15)$$

In the proposed technique *pacsf*, depending on the distribution of selected feature, the mean or median of the selected feature can be used to determine the prototype of first cluster. For this purpose, the nearest data instance to the center of the selected feature is searched on the selected feature column, and assigned as the prototype of first cluster as shown in Eq. (16). Afterwards, the prototypes of remaining clusters are determined by using formulas in Eq. (17), alternately. For example, the prototype of an even-numbered cluster is determined by adding the value of R_1 times the cluster index minus 1 to the first cluster prototype as seen in the first row of Eq. (17). On the other hand, R_2 is used to calculate the prototypes of odd-numbered clusters as seen in the second row of Eq. (17).

$$\boldsymbol{v}_1 = \boldsymbol{x}_k \;;\; k = row_index\ of\ the\ nearest\ \ data\ instance\ to\ center(\boldsymbol{x}_{.f}) \quad (16)$$

$$\boldsymbol{v}_i = \begin{cases} \boldsymbol{x}_{k+(i-1)\,R_1} & if\ i\ mod\ 2 = 1 \\ \boldsymbol{x}_{k-(i-1)\,R_2} & otherwise \end{cases} ; 2 \le i \le c \quad (17)$$

In order to apply the technique *pacsf*, a feature selection process is required for determining the feature to be used to calculate the centers in Eq. (14) and Eq. (15). Although one of existing feature selection algorithms could be applied for this purpose, we recommend to use a simple single feature selection approach which is introduced in Section 4 due to its simplicity.

3.5 K-means++ clustering

The K-means++ introduced in Reference [1] is reported as an efficient approximation algorithm in overcoming the poor clustering problem, which may be encountered in the standard K-means algorithm. K-means++ initializes the cluster centroids by finding the data instances that are farther away from each other in a probabilistic manner. In K-means++, the first cluster center is randomly assigned. The remaining centers are determined with a probability of $mindist(x')^2 / \sum_{k=1}^{n} mindist(x_k)^2$, where $mindist(x')$ is the minimum distance from a data instance *x* to the previously selected centers. In this paper we included K-means++ in our experimental works for comparison purposes.

4. FEATURE SELECTION FOR INITIALIZATION OF PROTOTYPES

The irrelevant and redundant features lead to difficulties in identification of the existing structures in datasets. Therefore, as the process of selecting a subset of relevant features in data mining applications, feature selection is usually an important task for dimension reduction based on the various wrapper, filter and embedded methods ([16] [24]). According to the literature on feature selection, the research works have mainly focused on either predictive model construction using different clustering algorithms or dimension reduction for clustering of big data ([10] [11] [17] [9] [25] [26] [8] [21]). However, in this paper, we consider the feature selection not for selecting a subset of features but for selecting only one relevant feature in order to use in prototype initialization in cluster analyses. So, we call this kind of processes as the "*feature selection for initialization of prototypes (FSIP)*". FSIP is mainly based on the assumption that a selected feature should be the feature which is the most predictive in the formation of cluster structures. According to that assumption a feature can be a possible candidate in prototype initializations if it is the feature with the highest variance or is the multimodal feature with the highest number of peaks (modes).

In the variance based FSIP techniques, one should select the features with higher variances because they may be more relevant in the formation of the cluster structures in datasets. Research works on FSIP are relatively recent, and there are some attempts to use variance based techniques in the literature. One of the algorithms using variance based FSIP has been introduced by Reference [23]. They proposed a new algorithm using a feature selection technique based on variance to build a reduced dataset containing relevant features. In their algorithm they determined the initial prototypes of clusters using the medoids of each cluster by running K-means algorithm on reduced dataset.

In our proposed technique, the assumption is that the modes of a feature are useful indicators of different mass tendency locations or the centers of different dense regions, namely the clusters in a data space. Thus, a feature with the highest number of modes is expected to be more predictive for determining the initial cluster prototypes in partitioning clustering tasks. In fact, this approach so-called "*feature selection based on mode counts*" is actually based on the assumption that clusters are continuous regions of a *p*-dimensional space containing relatively high density of instances, separated from other such regions by regions containing relatively low density of instances as defined in Reference [12].

Algorithm 1: **findpolypeaks**

Input:

xc, vector for the frequencies of classes of a frequency polygon

xm, vector for the middle values of classes of a frequency polygon

tc, threshold frequency value for filtering frequency polygon data, default value is 1

Output:

PM: Peaks matrix for a feature

Init:

1: *xm* ← *xm*[*xc* >= *tc*] ; *xc* ← *xc*[*xc* >= *tc*] //Filter *xm* and *xc* for the class frequencies >= *tc*

2: *pfreqs* ← {} // Vector for the frequencies of peaks

3: *pvalues* ← {} // Vector for the values of peaks

4: *nc* ← length of *xc* //Number of classes (bins)

5: *pidx* ← *1* //Index of the first peak

Run:

6: **IF** *nc* > 1 **THEN**

7: **IF** *xc*[*1*] > *xc*[*2*] **THEN**

8: *pvalues*[*1*]← *xm*[*1*] ; *pfreqs*[*1*]← *xc*[*1*]

9: *pidx* ← *2*

10: **ENDIF**

11: **FOR** *i* = 2 to *nc-1* **DO**

12: **IF** *xc*[*i*] not equal to *xc*[*i-1*] **THEN**

13: **IF** *xc*[*i*] > *xc*[*i-1*] AND *xc*[*i*] >= *xc*[*i+1*] **THEN**

14: *pvalues*[*pidx*] ← *xm*[*i*]

15: *pfreqs*[*pidx*] ← *xc*[*i*]

16: *pidx* ← *pidx* + 1

17: **ENDIF**

18: **ENDIF**

19: **ENDFOR**

20: **IF** *xc*[*nc*] > *xc*[*nc-1*] **THEN**

21: *pvalues*[*pidx*]← *xm*[*nc*] ; *pfreqs*[*pidx*]← *xc*[*nc*]

22: **ENDIF**

23: **ELSE**

24: *pvalues*[*pidx*]← *xm*[1] ; *pfreqs*[*pidx*]← *xc*[1]

25: **ENDIF**

26: *np* ← length of *pvalues*

27: PM_{npx2} ← 0 //Create peaks matrix

28: *PM*[,1] ← *pvalues* ; *PM*[,2] ← *pfreqs*

29: **RETURN** *PM, np*

The number of modes of features can be found by counting the peaks in their frequency polygons. For this purpose, a peaks counting algorithm can be used. In this paper we use a peak counting algorithm called *findpolypeaks* (Algorithm 1) that has been introduced in a recently submitted paper of the authors. The input arguments of this algorithm are the frequencies (*xc*) and middle values (*xm*) of the classes of frequency polygon for the analyzed feature, and a threshold counts value (*tc*) for tuning the height of peaks. The output of algorithm is a peaks vector (*PM*) which shows the peaks values associated with the features. In this paper, we apply the peaks counting approach because the variance based approach may be problematic when the selected feature has normal (unimodal) distribution and contains the outliers.

5. EXPERIMENT ON A SYNTHETIC DATA SET

For evaluating the performances of proposed initialization techniques we implemented the R scripts in R environment [22] on a computer with i7-6700HQ CPU (2.60 GHz) and 16GB RAM. In order to easily demonstrate the performances of the studied prototype initialization techniques, we generated a five-dimensional synthetic dataset (*5p4c*) as our experimental dataset. The dataset *5p4c*, which was created by using *rnorm* function in the base *stats* library of R consisted of five features and four clusters with the descriptive statistics shown in Table 1. In this dataset having 400 data instances (*n=400*), the first feature (*p1*) was unimodal, the second feature (*p2*) was four modal, the third feature (*p3*) was bimodal, the fourth feature (*p4*) was three modal and the fifth feature (*p5*) was bimodal as seen in Fig. 1.

Table 1. Descriptive statistics of the features in the dataset 5p4c

Features	mean	median	std.dev.	min	max	Number of peaks
p1	12.41	12.62	2.86	2.86	20.36	1
p2	69.47	69.72	22.84	29.58	109.43	4
p3	134.01	140.02	21.87	86.38	167.50	2
p4	48.67	47.83	22.57	8.70	88.58	3
p5	20.42	20.24	1.39	16.43	24.55	2

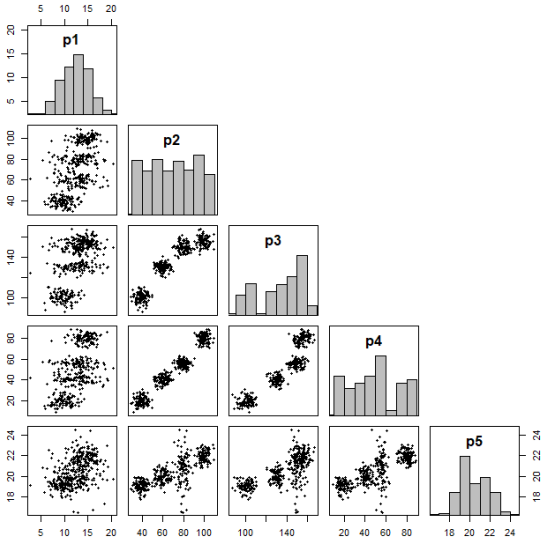

Fig.1. Histograms and scatter plots of the feature pairs in the dataset 5p4c

In our experiments, we ran FCM for seven levels of number of clusters (c = 2,…,8) with the five initialization techniques: K-means++ (*kmpp*), simple random sampling (*rsamp*), random samples averaging (*arsamp*), systematic sampling (*ssamp*) and prototyping around center of selected feature (*pacsf*). For each level of number of clusters, FCM was re-started for ten times because the first four techniques assign different initial centroids in different runs because of their non-deterministic nature.

In order to avoid the possible biases due to different initializations of membership matrix $\boldsymbol{U}$, we used the same $\boldsymbol{U}$ matrix in each level of number of clusters in the successive runs of FCM. For this purpose, we set the seed of random number generator to a predefined constant (*seed=123*). In order to calculate the random sample averages, we arbitrarily sampled data instances for five times (r=5) with the technique *arsamp.* For selecting the feature with the highest number of peaks we used the *findpolypeaks* algorithm (Algorithm 1). The inputs of the algorithm were the middle values and counts of classes obtained from the histograms using Sturge's rule. The algorithm successfully found that *p2* was the multimodal feature having the highest number of peaks with four peaks as seen in Fig. 1. Here we note that when there are multiple features with the highest number of peaks, although they could be interchangeably used as the selected feature with *pacsf* technique, we recommend to use the feature whose variance is also greater than the others.

Good initializations often lead to faster converge, and thus, clustering algorithms require less iterations. Therefore, in order to compare the performances of the studied initialization techniques we used the average iteration counts for reaching to final clustering result in FCM runs. In order to test the differences between the studied initialization techniques we applied Chi-square test, which is a non-parametric statistical test, on the average iteration counts at each level of number of clusters.

Table 2. Iteration counts by the number of clusters for the dataset 5p4c

c	stats	*kmpp*	*rsamp*	*arsamp*	*ssamp*	*pacsf*	*P*
c=2	*min*	34	31	35	25	37	0.9979
	avg	36	36	36	34	37	
	max	36	37	37	37	37	
c=3	*min*	79	79	80	79	85	0.9986
	avg	84	83	83	81	85	
	max	85	83	83	81	85	
c=4	*min*	11	13	13	11	14	0.8586
	avg	18	18	16	13	14	
	max	33	24	16	13	14	
c=5	*min*	32	37	56	33	116	0.0013
	avg	64	96	76	86	116	
	max	146	141	78	122	116	
c=6	*min*	57	58	46	49	112	0.3834
	avg	99	104	92	86	112	
	max	104	106	96	86	112	
c=7	*min*	61	62	59	75	135	0.0033
	avg	108	115	91	83	135	
	max	186	116	91	92	135	
c=8	*min*	72	78	89	77	110	0.0722
	avg	123	130	122	90	110	
	max	124	162	124	91	110	

The results obtained from the FCM runs on the dataset *5p4c* are shown in Table 2. In the table, *min*, *avg* and *max* respectively stand for the minimum iteration counts, the average iteration counts, and the maximum iteration counts in ten runs of FCM. As seen in the last column of Table 2, according to Chi-squared tests (*df=4*) there were no significant differences between the studied initialization techniques except the clustering done for the number of clusters of five and seven (*c=5, c=7*). Although there are no statistically significant differences, the minimum iteration counts were obtained with *ssamp* in FCM runs done for all levels of number of clusters except for those of five (*c=5*). For only this exception, *kmpp* was better than the others although it has been reported that it can converge rapidly. On the other hand, since there is the possibility to select the outliers as the first prototype with *kmpp*. The distance calculations for remaining cluster centroids can be affected by the first prototype determined by *kmpp*. These occasions may lead to more iterations to converge to final clusters. As seen in Table 2, for all the techniques, the iteration counts significantly decreased in the FCM runs done for the number of clusters of four (*c=4*), which is the actual number of clusters in the dataset *5p4c*.

Table 3. Average computing time (miliseconds) per FCM run for the dataset 5p4c

c	*kmpp*	*rsamp*	*arsamp*	*ssamp*	*pacsf*
c=2	343.27	330.09	323.67	325.67	345.31
c=3	993.73	943.64	929.01	927.63	970.69
c=4	333.65	312.14	278.03	238.03	259.60
c=5	1249.43	1714.69	1415.23	1564.98	2093.00
c=6	2198.50	2166.91	1963.15	1826.63	2425.14

c=7	2833.79	2945.35	2267.45	2055.28	3408.19
c=8	3544.67	3671.45	3470.41	2540.79	3125.14

As another performance criteria, the results for average computing time per FCM run obtained from the ten runs of FCM by the initialization techniques are shown in Table 3. Although there were no statistically significant differences between the studied techniques (*F=0.15735; df=4,30; P=0.9581*), *ssamp* gave the minimum average computing time in the clustering runs done for most of the number of clusters (*c=3, c=4, c=6, c=7* and *c=8*). Based on the initializations with *arsamp*, FCM required the minimum computing time for completing the clustering done for the number of clusters of two (*c=2*). The minimum computing time was required with *kmpp* for the clustering done for the number of clusters of five (*c=5*).

6. EXPERIMENT ON THE REAL DATASETS

Based on the required iteration counts by FCM, we also examined the performances of the studied techniques on three real datasets, which are listed with their characteristics in Table 4. All of these datasets were imported from UCI Machine Learning Repository [19].

Table 4. Real datasets used for evaluation of the studied prototype initialization techniques

Data set	Size of dataset	Number of features	Number of classes
Iris	150	4	2,3
Wine	178	13	3
Foresttype	326	27	4

Fisher's Iris dataset [14] is probably one of the most widely used datasets in testing of data mining algorithms. Iris dataset (*Iris*) contains 3 classes of 50 instances each, where each class refers to an iris flower species. In this dataset, one of the species classes is linearly separable while two of them are not linearly separable from each other.

Wine dataset (*Wine*) contains the results of a chemical analysis of three different wine cultivars grown in the same region in Italy. The dataset consists of 178 records with 13 features and 1 class variable with 3 classes.

Forest type mapping training dataset (*Foresttype*) contains remote sensing data which mapped different forest types based on their spectral characteristics at visible-to-near infrared wavelengths by using the Aster satellite images [18]. The dataset consists of 27 features and one class variable with 4 forest types.

In Table 5, the average iteration counts obtained from the FCM runs at the different levels of number of clusters on the studied real datasets were shown by the initialization techniques. According to Chi-square tests on the average iteration counts there were no significant differences between the initialization techniques at the small levels of number of clusters as seen in the last column of Table 5. On the other hand, at the upper levels of number of clusters the average iteration counts tended to be in favor of *ssamp*, *pacsf* and *arsamp*. Since *ssamp* converged to the final clusters with the minimum iterations counts for seven times and the *pacsf* eight times, they were considered more useful when compared to the others.

Table 5. Iteration counts by the initialization techniques for the studied real datasets

c	Datasets	*kmpp*	*rsamp*	*arsamp*	*ssamp*	*pacsf*	*P*
c=2	*Iris*	16	15	15	15	15	0.9997
	Wine	25	24	24	24	26	0.9980
	Foresttype	45	47	46	46	45	0.9995
c=3	*Iris*	42	40	42	36	47	0.8219
	Wine	68	72	71	66	71	0.9855
	Foresttype	50	51	50	49	50	0.9998
c=4	*Iris*	55	59	55	69	41	0.1230
	Wine	54	56	56	64	60	0.8937
	Foresttype	150	150	154	150	162	0.9501
c=5	*Iris*	73	71	71	50	45	0.0210

	Wine	169	189	166	268	270	1.6e-10
	Foresttype	96	98	98	92	98	0.9909
c=6	*Iris*	116	101	112	122	**77**	0.0181
	Wine	134	151	127	74	70	6.2e-10
	Foresttype	174	185	177	178	163	0.8326
c=7	*Iris*	90	93	75	94	96	0.5277
	Wine	120	79	89	323	279	2.2e-16
	Foresttype	184	189	181	189	178	0.9721
c=8	*Iris*	150	81	82	96	89	1.0e-06
	Wine	138	160	136	235	193	3.2e-08
	Foresttype	185	197	180	191	200	0.8384

7. CONCLUSIONS

Based on iteration counts and computing time to converge to the final cluster results, the systematic sampling seemed slightly better than the other techniques for most of the results obtained on the studied synthetic and real datasets. According to the results obtained on the real datasets, the prototyping around the center of a selected feature was also considered to be a successful technique to build prototypes that are well-separated. Due to its deterministic nature, the technique can contribute to increase in the computational efficiency of prototype initializations because it does not require repeated initializations in the successive runs of the clustering algorithms. Although it is a promising initialization technique, further studies are required to examine its performance on the larger datasets with different cluster configurations. Therefore, we plan to conduct research in the future for both testing the performance on larger data sets and comparison with some other data-dependent techniques.

ACKNOWLEDGMENT

This research was supported by the Scientific Research Projects Coordination Unit at the Cukurova University (Grant #: FBA-2017-9730).

REFERENCES

[1]. Arthur D & Vassilvitskii S (2007) “K-means++: The advantages of careful seeding”, In *Proc. of the 18th Annual ACM-SIAM Symposium on Discrete Algorithms*, p. 1027-1035.
[2]. Äyrämo S & Kärkkäinen L (2006), “Introduction to partitioning based clustering methods with a robust example”, Reports of the Department of Mathematical Information Technology (University of Jyväskylä); Series C: Software and Computational Engineering, C1, p. 1-36.
[3]. Ball GH & Hall DJ (1967), “A clustering technique for summarizing multivariate data”, *Systems Researchs and Behavioral Science*, vol. 12, no. 2, p. 153–155.
[4]. Bezdek JC (1981), Pattern recognition with fuzzy objective function algorithms. Plenum, NY, 256 p.
[5]. Borgelt C (2005), Prototype-based Classication and Clustering, Habilitationsschrift zur Erlangung der Venia legendi fuer Informatik, vorgelegt der Fakultaet fuer Informatik der Ottovon-Guericke-Universitaet Magdeburg, Magdeburg.
[6]. Burks S, Harrell G & Wang J (2015), “On initial effects of the k-means clustering”. In *Proc. of the Int. Conf. on Scientific Computing (CSC)*, p. 200-205.
[7]. Celebi ME, Kingravi HA & Vela PA (2013) “A comparative study of efficient initialization methods for the k-means clustering algorithm”. *Expert Systems with Applications*, vol. 40, no.1, p. 200-210.
[8]. Covões T F & Hruschka ER (2011), “Towards improving cluster-based feature selection with a simplified silhouette filter”. *Information Sciences*, vol. *181*, no. 18, pp. 3766-3782.
[9]. Dash M & Liu H (2000), “Feature selection for clusterings”. In *Pacific-Asia Conf. on Knowledge Discovery and Data Mining*, p. 110-121. Springer: Berlin, Heidelberg.
[10]. Dash, M., Choi, K., Scheuermann, P., & Liu, H. (2002), “Feature selection for clustering-a filter solution” In *Proc. of IEEE Int. Conf. Data Mining 2002*, pp. 115-122.
[11]. Dy JG & Brodley CE (2004). “Feature selection for unsupervised learning”. *Journal of Machine Learning Research*, vol. *5*, p. 845-889.
[12]. Everitt B (1980), *Cluster analysis* 2nd ed. London: Halsted Press.
[13]. Fahad A, Alshatri N, Tari Z, Alamri A, Khalil I, Zomaya A, Foufou S & Bouras A (2014). “A survey of clustering algorithms for big data: taxonomy and empirical analysis”. *IEEE Trans Emerg Topics Comp.*, vol. 2, no.3, p.267–279.
[14]. Fisher RA (1936), “The use of multiple measurements in taxonomic problems", Annual Eugenics, 7, Part II, 179-188 (also in "Contributions to Mathematical Statistics", John Wiley, NY, 1950).
[15]. Forgy E (1965), “Cluster analysis of multivariate data: Efficiency vs. interpretability of classification”, *Biometrics*, vol. 21, p. 768-769.

[16]. Guyon I & Elisseeff A (2003), "An introduction to variable and feature selection", *Journal of Machine Learning Research*, vol. *3*, pp. 1157-1182.
[17]. Hsu HH & Hsieh CW (2010), "Feature Selection via Correlation Coefficient Clustering". *Journal of Software*, vol. *5*, no. 12, pp. 1371-1377.
[18]. Johnson B, Tateishi R & Xie Z (2012). "Using geographically-weighted variables for image classification", *Remote Sensing Letters*, vol. 3, no. 6, p. 491-499.
[19]. Lichman M (2013), UCI Machine Learning Repository [http://archive.ics.uci.edu/ml]. Irvine, CA: University of California, School of Information and Computer Science.
[20]. MacQueen J (1967), "Some methods for classification and analysis of multivariate observations", in Proc. of the 5th Berkeley Symposium on Mathematical Statistics and Probability, p. 281–297.
[21]. Pok G, Liu JCS & Ryu KH (2010), "Effective feature selection framework for cluster analysis of microarray data". *Bioinformation*, vol. 4, no. 8, pp. 385-389.
[22]. R Development Core Team (2017). R: A language and environment for statistical computing. R Foundation for Statistical Computing, Vienna, Austria. URL https://www.R-project.org/.
[23]. Rajoot DS, Singh PK & Bhattacharya M. (2010), "A new technique for feature selection and cluster center initialization", In *Proc. of Int. Conf. on Data Mining (DMIN)*, p. 119-125.
[24]. Saeys Y, Inza I& Larrañaga P (2007), "A review of feature selection techniques in bioinformatics", *bioinformatics*, vol. *23*i no. 19, pp.2507-2517.
[25]. Witten DM & Tibshirani R (2010), "A framework for feature selection in clusterings", *Journal of the American Statistical Association*, vol. 105, no. 490, p. 713-726.
[26]. Zhao Z, Morstatter F, Sharma S, Alelyani S, Anand A & Liu H (2010). "Advancing feature selection research", *ASU feature selection repository*, p. 1-28.

ICENS 4TH INTERNATIONAL CONFERENCE ON ENGINEERING AND NATURAL SCIENCE
2-6 May 2018 KIEV UKRAINE

Comparing Depth Values of GEBCO Bathymetry and Wavelet Tomography Results in the Challenger Deep Point of Marianna Trench and Surroundings

Fikret Dogru[1], Oya Pamukcu[2], Ayca Cirmik[2,*]

Abstract

The deepest point of the world, Marianna Trench, is formed as a result of the thrusting Pacific Plate to the Philippines Plate. Mariana Trench stretches for more than 2,540 km with a mean width of 69 km. The greatest depths are reached in Challenger Deep (~11 km), a smaller steep-walled valley on the floor of the main trench southwest of Guam. In this study, depth values which are obtained from the General Bathymetric Chart of the Oceans (GEBCO) and by applying wavelet tomography to the World Gravity Map (WGM2012) Complete Spherical Isostatic gravity anomaly were compared. The most important convenience of the Wavelet Tomography method is that it does not require any inversion technique. As a result, the deepest point of the GEBCO data was obtained 10.8 km. The result of the wavelet tomography again reached a depth value of about 11 km. In addition, profiles were taken from different places for comparison and values were examined. In this study, it is seen that WGM2012 data will present knowledge about base topography by applying Wavelet Tomography method.

Keywords: Marianna Trench, Wavelet Tomography, GEBCO, WGM2012, Challenger Deep.

1. INTRODUCTION

The Mariana Trench is an actively opening basin that lies at the eastern edge of the Philippine Sea plate. It is bounded by the West Mariana Ridge and the Mariana island arc (an active volcanic arc). The deepest part of Marianna Trench, the Challenger Deep, lies in the Southern Mariana Trench almost 360 km southwest of Guam Island and 2700 km south of the Japanese Islands [1], [2]. The location map is shown in the Fig. 1.

The World Gravity Map (WGM 2012) which were compiled by the Bureau Gravimetrique International (BGI) with the support of the United Nations Educational Scientific and Cultural Organization (UNESCO) in association with the International Gravity Field Services (IFGS), computed from the Earth Spherical Model (EGM 2008) [4] instead of the conventional Bouguer slab correction and have a spatial resolution of ~9 km [5], [6].

General Bathymetric Chart of the Ocean (GEBCO) [7] that has 30 arc-second resolution was generated by combining ship depth soundings, with the interpolation between the sounding points being guided by satellite gravity data [8]. GEBCO bathymetry mostly relied upon ship soundings and only 6.5% of all 30 arc-second depth cells are constrained by soundings, with the rest being indirectly mapped using some interpolation scheme [8].

[1] fikretjfm@gmail.com, *Ataturk University, Oltu Earth Sciences Faculty, Geophysical Engineering, 25400, Oltu, Erzurum*
[2] oya.pamukcu@deu.edu.tr, *Dokuz Eylul University, Engineering Faculty, Geophysical Engineering, 35400, Buca,Izmir*
ayca.yurdakul@deu.edu.tr, *Dokuz Eylul University, Engineering Faculty, Geophysical Engineering, 35400, Buca, Izmir*
[*] *Corresponding author:* ayca.yurdakul@deu.edu.tr

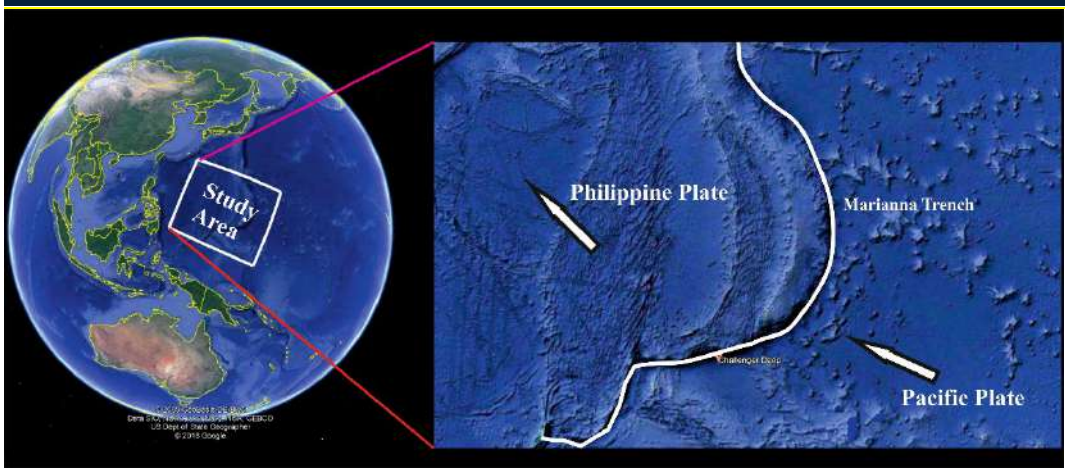

Figure 1. The location map of the study area (The figure exported from Google Earth Pro [3]).

Wavelet transform and its multi-scale tomography application have been used to localize the buried magnetic structures, to determine the depth of hydrothermal systems on self-potential data, edge detection signal processing [9], [10], [11], [12].

2. METHODS

2.1. Wavelet Transform

The wavelet transform has contributed significantly to the study of many processes/signals in almost all areas of earth science. Different applications of wavelet transform have also shown its important role while dealing the complex behaviour of real geophysical data. Wavelet transform can be given following formula;

$$\psi(a,\tau)(t) = \frac{1}{\sqrt{a}}\psi\left(\frac{t-\tau}{a}\right) \qquad (a,\tau \in R \qquad a > 0) \tag{1}$$

where a is the dilation factor, τ is the translation factor and $\psi_{(a,\tau)}(t)$, is the mother wavelet depending on parameters a and τ [13]. In the wavelet transform, instead of holding constant time and frequency resolutions, both can be used as a variable to obtain multi-resolution analysis in the time-frequency domain. Thus, increases in the frequency show improvement in time resolution. Likewise, decreases in frequency show improvement in the frequency resolution.

2.2. Continuous Wavelet Transform (CWT)

The continuous wavelet transform was developed as an alternative approach to the short time Fourier transform (STFT) to overcome the resolution problem. The wavelet analysis is done in a similar way to the STFT analysis, in the sense that the signal is multiplied with a function, similar to the window function in the STFT, and the transform is computed separately for different segments of the time-domain signal.

However, there are two main differences between the STFT and the CWT:

1. The Fourier transforms of the windowed signals are not taken, and therefore single peak will be seen corresponding to a sinusoid, i.e., negative frequencies are not computed.

2. The width of the window is changed as the transform is computed for every single spectral component, which is probably the most significant characteristic of the wavelet transform.

The continuous wavelet transform is defined as follows:

$$CWT_x^{\psi}(\tau,s) = \Psi_x^{\psi}(\tau,s) = \frac{1}{\sqrt{s}}\int x(t)\,\psi^*\left(\frac{t-\tau}{s}\right) \tag{2}$$

the transformed signal is a function of two variables, tau (τ) and s, the translation and scale parameters, respectively.$\Psi_x^{\psi}(\tau,s)$ is the transforming function, and it is called the mother wavelet [14].

2.3. Multi-Scale Wavelet Tomography (MSWT)

In this study, complex Gaussian wavelet (cgau1) was used for estimation of the buried structure. Then wavelet modulus was calculated following formula:

$$mod = \sqrt{reel(coef(cwt))^2 + imag(coef(cwt))^2} \quad (3)$$

where reel and imag are reel and imaginer parts of the continuous wavelet transform. Local maximums were determined from coefficients of CWT. In addition, derivative of anomaly was calculated and then CWT was applied on this anomaly.

3. RESULTS

In this study, WGM2012 Isostatic Bouguer Gravity (IBG) anomaly was used in the wavelet tomography application for determining the deepest point in the Marianna Trench. For this purpose, the wavelet tomography was applied on profiles that were taken from IBG anomaly and vertical derivative was applied on profiles then the wavelet tomography was carried out on these profiles. The results were compared with the GEBCO bathymetry data. In figure 2, Isostatic Bouguer Gravity anomaly and GEBCO bathymetry map are shown. The values changes -240 to 120 mGal in the Bouguer anomaly. The bathymetry values changes between -10804 to 263 meter in the GEBCO data (Fig 2a and 2b). The lowest anomaly values are on the collision boundary of the Pacific and Philippines Plates. Also the deepest point in this area is located in this collision boundary.

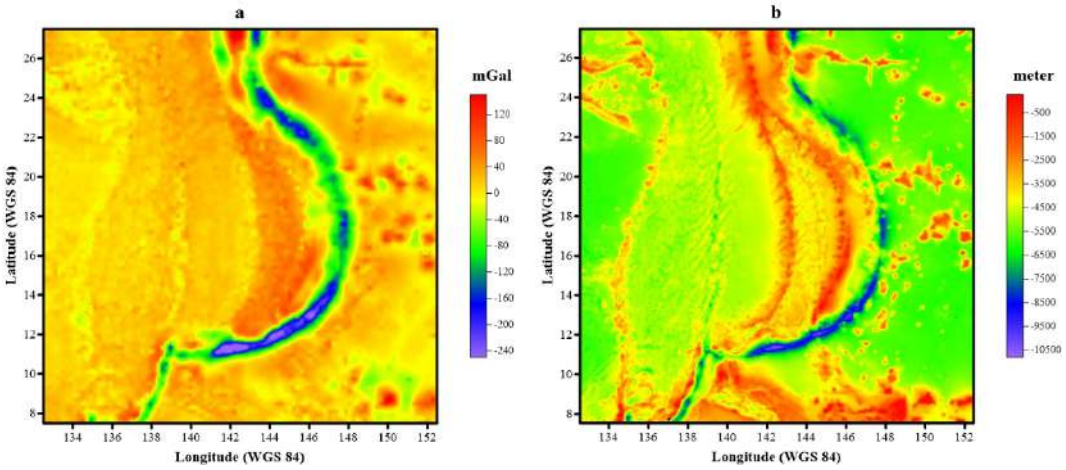

Figure 2. a) Isostatic Bouguer Gravity Anomaly, b) GEBCO bathymetry map.

In the wavelet tomography stage, three profiles were taken for comparison of depth values of GEBCO and obtained from wavelet tomography (Fig. 3). First profile, A-A', was taken from the deepest point ever known on earth, the Challenger Deep point. Then wavelet tomography applied on this profile and ~ 11km depth value was obtained. The deepest point in the GEBCO bathymetry data is 10.804 meter. Then, the other two profiles, B-B' and C-C', were taken and the same method was applied to these profiles. The wavelet tomography result of profile 1 shows that there is no solution but 11km depth value was obtained after the taken vertical derivative of profile 1. On the other hand, the wavelet tomography results of profiles 2 and 3 were almost obtained two times more than known. But vertical derivative improved the solutions of profile 2 and 3. The results are also shown in table 1.

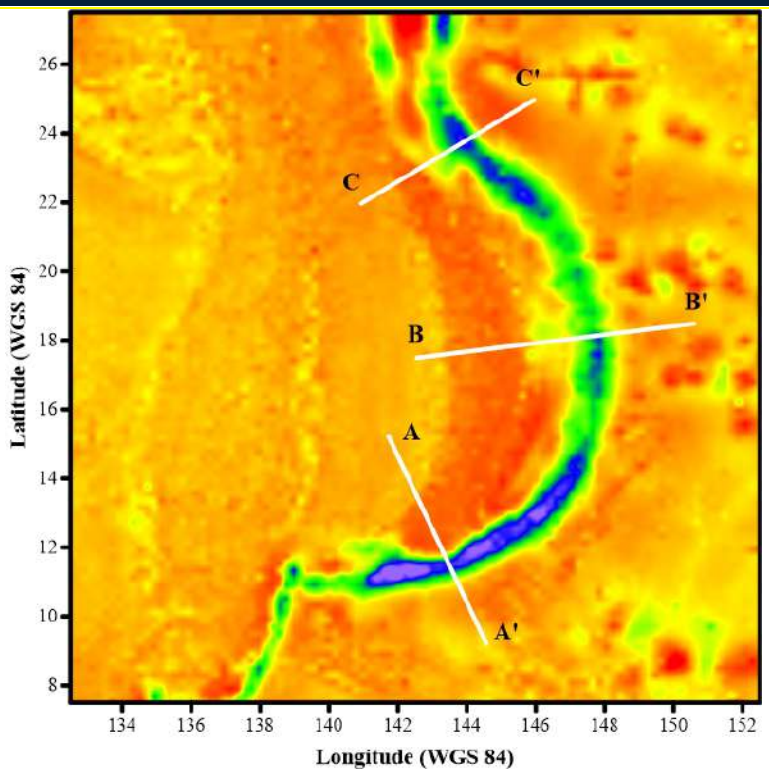

Figure 3. Profiles are shown in IBG anomaly.

Table 1. The comparison of the GEBCO bathymetry and the wavelet tomography results with and without derivative.

		The Wavelet Tomograpy Results		
	GEBCO (m)	Without Derivative (m)	With derivative (m)	Half of Without Derivative (m)
Profile 1	10804	-	11000	-
Profile 2	7700	15060	7320	7530
Profile 3	8463	16900	8290	8450

CONCLUSIONS

In this study, wavelet tomography was applied to the profiles which were taken from Marianna Trench that was the deepest point in the world. Also obtained depth values from wavelet tomography were compared with the GEBCO bathymetry data. The results show there is not so much difference (not more than 380 meters) between GEBCO and wavelet tomography results (with derivative). The results also show that wavelet tomography without derivative gave 2 times more depth values than known from GEBCO. Half of the results are much closer the known values. The most important feature of wavelet tomography method is that it does not require a model such as a cylinder, sphere, etc. and without inversion technique to estimate depth value.

REFERENCES

[1]. P., Fryer, Evolution of the Mariana convergent plate margin system, Rev. Geophys., 34, 89–125, 1996.

[2]. Y., Ohara and T., Ishii, Peridotites from the southern Mariana forearc: Heterogeneous fluid supply in mantle wedge, The Island Arc, 7, 541–558, 1998.

[3]. Google earth Pro V 7.3.1.4507. Data: SIO, NOAA, U.S. Navy, NGA, GEBCO, TerraMetrics 2012, DigitalGlobe 2012. http://www.earth.google.com

[4]. N.K., Pavlis, S.A., Holmes, S.C., Kenyon and J.K., Factor, An earth gravitational model to degree 2160: EGM2008. EGU General Assembly, 10, 13-18, 2008.

[5]. G., Balmino, N., Vales, S., Bonvalot and A., Briais, Spherical harmonic modelling to ultra-high degree of Bouguer and isostatic anomalies. Journal of Geodesy, 86(7), 499-520, 2012

[6]. S., Bonvalot, G., Balmino, A., Briais, M., Kuhn, A., Peyrefitte, N., Vales, and M., Sarrailh, World Gravity Map, 1: 50000000 map. Eds. BGI-CGMW-CNES-IRD, 2012.

[7]. J.J., Becker, D.T., Sandwell, W.H.F., Smith, J., Braud, B., Binder, J., Depner and R., Ladner, Global bathymetry and elevation data at 30 arc seconds resolution: SRTM30_PLUS. Marine Geodesy, 32(4), 355-371, 2009.

[8]. R.L., Fisher, M.J., Jantsch and R.L., Comer, General bathymetric chart of the oceans (GEBCO). Canadian Hydrographic Service, Ottawa, Canada, 1982.

[9]. G., Saracco, F., Moreau, P.E., Mathé, D., Hermitte and J.M., Michel, Multiscale tomography of buried magnetic structures: its use in the localization and characterization of archaeological structures. Geophysical Journal International, 171(1), pp.87-103, 2007.

[10]. G., Mauri, G., Williams-Jones and G., Saracco, Depth determinations of shallow hydrothermal systems by selfpotential and multi-scale wavelet tomography. Journal of Volcanology and Geothermal Research, 191(3), pp.233- 244, 2010.

[11]. F., Guo, Y., Yang, B., Chen and L., Guo, A novel multi-scale edge detection technique based on wavelet analysis with application in multiphase flows. Powder Technology, 202(1), pp.171-177, 2010.

[12]. E., Foufoula-Georgiou and P. Kumar, Wavelets in geophysics. Vol. 4. Academic Press, 2014 eds.

[13]. S.G.A., Mallat, Theory for multiresolution signal decomposition: the wavelet representation. IEEE transactions on pattern analysis and machine intelligence, 11(7), pp.674-693, 1989.

[14]. I., Daubechies, Ten lectures on wavelets. Society for industrial and applied mathematics, 1992.

ICENS 4TH INTERNATIONAL CONFERENCE ON ENGINEERING AND NATURAL SCIENCE
2-6 May 2018 KIEV UKRAINE

An Analysis of Occupational Incidents, Prioritization of Factors Causing These by Using Multi Criteria Decision Making Methods and Identification of Ways for Reducing These: Case Study In Oil And Gas Fields

Ece Gokpinar[1], Can Elmar Balas[2]

Abstract

The aim of the Occupational Health and Safety studies conducted in the oil and gas sector is; to protect workers and to ensure occupational safety in works performed on drilling fields. The aforementioned studies of the companies operating in this field in Turkey are inadequate and are not given due importance to. In such companies, occupational incidents become inevitable for that reason. A vast number of studies have been conducted in many other countries around the world to reduce the number of occupational incidents, and those have led to a substantial reduction in those incidents. In Turkey, it is necessary to take measures to reduce the number of occupational incidents in the oil and gas sector. In this study, occupational incidents occurred in the company investigated as a case study and the other occupational incidents occurred in similar companies and the measures taken to reduce them have been discussed in detail. This study aims to explain what occupational incidents occur in the sector, what the root causes of them are and how to reduce the occupational incidents by taking measures.

Keywords: Multi Criteria Decision Making, Occupational Health and Safety, Occupational Incident, Petroleum and Natural Gas Drilling.

1. INTRODUCTION

It is difficult, costly and dangerous work to extract various mines by drilling. However, there is a great energy deficit increased with technology and progress in the world. For this reason, countries are resorting to a variety of ways to extract oil and similar products to meet this energy deficit. Those drilling works, as significant element of the energy sector, bear the risk of occupational incidents. Because natural or legal entities with exploration licenses, who would like to conduct drilling work which is highly expensive, prefer to hire small companies that are not the experts in that field, in order to get their drilling works done in a more economical way. In drilling works, as one of the most hazardous sectors of activity alongside with mining, lots of occupational incidents and occupational injuries and deaths occur where the occupational health and safety regulations are not applied. In the literature, there are various reports and studies conducted by various institutions that address the various aspects of occupational incidents in oil and gas sector concentrated in extractive works. For example, in the study of Hill, it has been identified that the rate of occupational incidents occurred in USA's oil and gas extraction sector between 2003 and 2009 was seven times higher than the occupational incidents occurred in all other sectors [1]. According to the statistics of U.S. Department of Labor's Bureau of Labor Statistics (US BLS), 823 people working in extractive activity in the oil and gas sector lost their lives between 2003 and 2010 [2]. This figure is seven times higher than the rate of occupational incidents in all other industries of USA. According to a report of the Centers for Disease Control and Prevention (CDC), work-related mortality rates in the oil and gas extraction sector have increased by 27.6% between 2003 and 2013 [3]. The report International Labor Organization (ILO) published in 2016 indicates that the hard labor

[1] Corresponding author: Gazi University, Department of Environmental and Technical Research of Accidents, Ankara, Turkey. ecegokpinar@gmail.com

[2] Gazi University, Department of Civil Engineering, Ankara, Turkey. cbalas@gazi.edu.tr

of oil and gas extraction sector shows itself in the form of occupational incidents [4]. According to the report published by Stromme in ISHN magazine in 2013, 50% of the accidents in the oil and gas drilling sector are caused by two reasons: struck by (36%), caught-in or between (21%) [5]. According to a report published by Petroleum Safety Authority Norway in 2011, the staff working in the oil and gas sector are generally inexperienced. It is found that the vast majority of accidents are occurred due to human factors. The use of new technology has a great importance [6]. Another cause of accidents is identified as crashing-shearing-trapping. According to OSHA, 3 of every 5 casualties caused as a result of crashing-shearing-trapping [7]. American federal statistics of US BLS show that fire accidents are more common in this sector than in other sectors [8]. According to Canadian Center for Occupational Health and Safety (CCOHS), another kind of occupational incident is fall accidents [9]. According to statistics of US BLS related to fall accidents, in 2014 247,120 non-fatal cases involving slips and falls and around 800 fatalities were reported. According to the data of CCOHS, more than 42,000 people are injured at work due to fall accidents. In this study, what kind of occupational incidents occur in oil and gas sector in Turkey and what the root causes of them are will be identified by using TOPSIS method. On the other hand, a statistical comparison between the occupational incidents occurred in the firms at other countries within the same sector and occupational incidents in Turkey will be presented. This study aims to contribute the occupational health and safety studies of Turkey in oil and gas sector; to provide a guideline document that explains what occupational incidents occur in the sector, what the root causes of these incidents are and how to reduce these incidents by taking measures for the companies operating in petroleum, natural gas, geothermal drilling sector in Turkey in order for them can benefit from.

2. MATERIALS & METHODS

2.1. Statistics Of Occupational Incidents

The statistical comparison between Turkey and other countries regarding the occupational incidents occurred in Oil, Geothermal, Gas Drilling Sector, has been made by using the incident analysis provided in International Association of Drilling Contractors (IADC) Incident Statistics Program. IADC is an organization, which is working actively worldwide since 1940. Among the IADC studies, the Incident Statistics Program (ISS) was created to monitor the occupational safety and occupational incident data for the drilling industry. The aim of using the IADC data in this study is to benefit from this organization, which provides a comprehensive study by using the data of many different firms operating worldwide [10]. There are many methods for calculating incidence rate described in the literature in order to make comparisons between occupational incidents statistics. These methods for calculating incidence rate have been developed to be able to make comparison independently of the size and structure of a firm. For example, there is a difference between the probability of 1 worker per 100 full-time workers involved in a recordable occupational incident in 1 year within an establishment with 100 employees and the probability of 1 worker per 50 full-time workers involved in a recordable occupational incident in 1 year within an establishment with 50 employees. In order to be able to compare the probability of occupational incidents between the two firms, various "incident rate" calculations have to be used. For the comparisons between the data of IADC member countries and the data of Turkey, the incident rate calculation formulas, examples of which are provided in Table 1, are used. More detailed information can be found on the website regarding the incident rate calculation data published by OSHA, which is provided below in the References [11]. The formulas given in Table 1 are used to find the number of incidents per 1,000,000 or 200,000 labor hours. Incidence Rate represents the formula using the 1,000,000 ratio, and frequency rate represents the formula using the 200,000 ratio. Depending on the type of the occupational accident, various incidence rate or frequency rate calculations can be made. For example, incidence rate and frequency rate calculations can be made for lost time incidence rate. Making such calculations allow making comparison with the situation at other countries, as described above. Figure 1 shows the comparison of lost time incident rate between Turkey and Europe and lost time incident rate of the firm from Turkey, which is chosen as an example case for this study. These calculations are made by using the formulas regarding lost time incident rate provided in Table 1.

Table 1 Incident Rate Calculations Formula

Incident Rate Criteria	**Formula**
Accident Frequency Rate [12]	Total Accidents X 1,000,000/ MAN-HOURS
Accident Incidence Rate [12]	Total Accidents X 100,000/ MAN
Lost Time Incidence Rate	Lost Time Cases X 200,000 / MAN-HOURS
Lost Time Frequency Rate	Lost Time Cases X 1,000,000 / MAN-HOURS

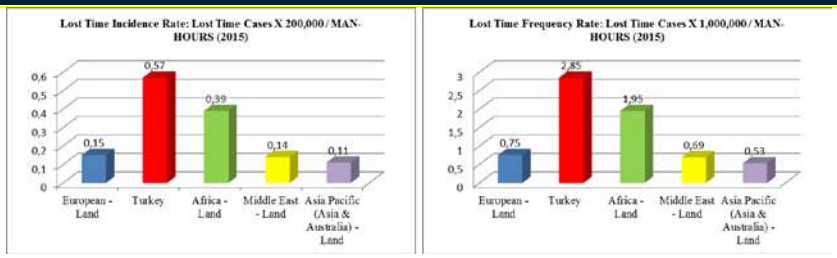

Figure 1. Comparison between lost time incident rates of Europe,Africa, Middle-East, Asia Pacific and Turkey, 2015. The European average data was adopted from the ISP reports by IADC, retrieved from http://www.iadc.org/isp/iadc-2015-isp-program-annual-report-index/[11]

As can be observed here, there is a significant difference between lost time incident rate occurred in oil and gas sector in Europe, Africa, Middle-East, Asia Pacific and Turkey average. The data received in Turkey's case indicates the need for more effective implementation of occupational health and safety management systems. Lost time incident rates occurred in other years also provide similar results.

2.2. Multi Criteria Decision Making Methods

One of the multi criteria decision making methods, TOPSIS (Technique for Order Preference by Similarity to Ideal Solution) method was presented with reference to the study of Hwang and Yoon (1981)[13]. The basic idea of this method is to select the alternative closest to the positive ideal solution while maximizing benefit criteria of the solution whereas minimizing its cost criteria. In the same way, the aim is to obtain the solutions, which are selecting the criteria having farthest distance from the negative ideal solution while maximizing the cost criteria whereas minimize the benefit criteria. The application of the TOPSIS method consists of 6 steps. These steps can be listed respectively as constructing decision matrix, constructing standard decision matrix, calculating weighted decision matrix, determining ideal and negative ideal solutions, calculating the separation measures and calculating the relative closeness to the positive ideal solution.

2.3. TOPSIS Method

Technique for Order Preference by Similarity to Ideal Solution (TOPSIS); which was developed by Hwang and Yoon in 1981 as a method to sort alternatives by calculating their proximity to the ideal and negative ideal solutions. The application steps of the TOPSIS method tailored for this study are presented below [14]:

Step 1: $A = \begin{bmatrix} a_{11} & a_{12} & \dots & a_{1m} \\ a_{21} & a_{22} & \dots & a_{2m} \\ \dots & \dots & \dots & \dots \\ a_{n1} & a_{n2} & \dots & a_{nm} \end{bmatrix}$ (1)

Step 2: *Obtaining the normalized decision matrix (R):* The normalized decision matrix (eq'n (3)) is determined by using eq'n (2):

$r_{ij} = \frac{a_{ij}}{\sqrt{\sum_{i=1}^{n} a_{ij}^2}}$ (2) and, $R = \begin{bmatrix} r_{11} & r_{12} & \dots & r_{1m} \\ r_{21} & r_{22} & \dots & r_{2m} \\ \dots & \dots & \dots & \dots \\ r_{n1} & r_{n2} & \dots & r_{nm} \end{bmatrix}$ (3)

Step 3: *Obtaining the weighted normalized decision matrix (V):* In this step, firstly, the weights (importance values) of the ten criteria (w_j; $j=1,\dots,m$) are assigned. The weighted decision matrix V is formed by multiplying elements in each column in the normalized decision matrix (r_{ij}, $i=1,\dots,n$) and its corresponding criterion weight (w_j, $j=1,\dots,m$):

$V = \begin{bmatrix} w_1 r_{11} & w_2 r_{12} & \dots & w_m r_{1m} \\ w_1 r_{21} & w_2 r_{22} & \dots & w_m r_{2m} \\ \dots & \dots & \dots & \dots \\ w_1 r_{n1} & w_2 r_{n2} & \dots & w_m r_{nm} \end{bmatrix}$ (4)

Step 4: *Identification of ideal and negative ideal solutions:* In order to obtain an ideal (A^*) solution, Eq. (5) is used to determine the highest value for each column of the matrix V (the lowest value if the relevant criterion has the minimization direction) and to obtain the negative ideal (A^-) solution, Eq. (6) is used to determine the lowest values for each column of the matrix V (the highest value if the corresponding criterion has the minimization direction).

$$A^* = \left\{ \left(\max_i v_{ij} \middle| j \in J \right), \left(\min_i v_{ij} \middle| j \in J' \right) \right\} \rightarrow A^* = \{v_1^*, v_2^*, \dots, v_m^*\} \quad (5)$$

$$A^- = \left\{ \left(\min_i v_{ij} \middle| j \in J \right), \left(\max_i v_{ij} \middle| j \in J' \right) \right\} \rightarrow A^- = \{v_1^-, v_2^-, \dots, v_m^-\} \quad (6)$$

Step 5: Calculation of distance to the ideal solution (S^+_i), distance to the negative ideal solution (S^-_i) and performance score (C^*_i) for criteria. Distances to the ideal solution and negative ideal solution and performance scores for the years are obtained according to Eq. (7), Eq. (8), and Eq. (9) respectively. C^*_i gets a value between 0 and 1 ($0 \leq C^*_i \leq 1$)).

$$S_i^* = \sqrt{\sum_{j=1}^m (v_{ij} - v_j^*)^2} \quad (7)$$

$$S_i^- = \sqrt{\sum_{j=1}^m (v_{ij} - v_j^-)^2} \quad (8)$$

$$C_i^* = \frac{S_i^-}{S_i^- + S_i^*} \quad (9)$$

Values in table indicate that nearest distance to '1' shows that the influence of the causes of accidents on the related solution is high (absolute), that nearest distance to '0' shows that the influence is low (ineffective when it has the value of 0). The factors that caused the accidents in this study are selected as follows:

- Number of accidents that occurred during night shift
- The place of the accident (location / Derrick / Mast)
- The profile of the employee experiencing the occupational accidents mostly (the number of rig workers)
- Accident type (caught between, struck by)
- Rig type drilling where the occupational accidents seen mostly
- Age average of employees experienced the occupational accident
- Number of inexperienced employees (less than 1 year) experienced the occupational accidents
- Number according to the most injured body part (finger)
- Number of the occupational accident related to equipment (car / truck, bus, casing, pipe, tubular, drill collar)
- Number of the occupational accident related to operation (material handling - forklift, installation, maintenance, drilling routine)

There is a need for the use of multi criteria decision making (MCDM) methods in the joint evaluation of ten selected measurement criteria. In this study, factors that lead to lost time incidents occurred in a real firm operating in Turkey are analyzed by using TOPSIS.

Table 2. Decision Matrix Constructed Regarding Lost Time Incidents Occurred 2012-2015

Criteria	Equ	Opr	Tim	Loc	Ocp	Ict	Mon	Age	Tis	Bod
Equ	21	33,5	47,5	44,5	56,5	51,5	39,5	45,5	42,5	33
Opr	35,5	25	51,5	46,5	58,5	53,5	41,5	47,5	44,5	36,5
Tim	63,5	65,5	53	70	76	67,5	55,5	61,5	58,5	50,5
Loc	44,5	42	60,5	34	63	58	46	52	49	41
Ocp	56,5	58,5	72,5	63	46	66,5	52	63,5	62	58
Ict	51,5	53,5	67,5	58	64	41	55,5	58,5	57	53
Mon	39,5	41,5	55,5	46	60,5	49,5	29	49,5	45	38,5
Age	45,5	47,5	70,5	52	58	58,5	46,5	35	49,5	47
Tis	42,5	41	69	50	62	57	45	51	32	40
Bod	34,5	37	65	46	58	53	41	47	44	24

Note. Criteria = Incidents Root Cause. LTI = Lost time incidence Equ= LTI's by Equipment (car/truck, bus, Casing ve Drill Collar). Opr = LTI's by Operation (Rig/Equip. Repairs/Maint., Routine Drilling Operations.) Tim = LTI's by Time Of Day (Morning/Day Shift) Loc. = LTI's by Location (Rig Floor/Derrick/Mast) Ocp. = LTI's by Occupation (Floorman, Roustabout). Ict =. LTI's by Injury Cause Type (caught between, struck by) Mon = LTIs by Months (January, February, June) Age= LTI's by Average of Age. Tis= LTIs by Time in Service For Company (>1 yr. < 5 yrs.) Bod= LTI's by Body Part (fingers). All numbers are count and the matrix is made by average numbers.

Table 3.Weighted Normalized Decision Matrix

Criteria	Equ	Opr	Tim	Loc	Ocp	Ict	Mon	Age	Tis	Bod
Equ	0,0185	0,0288	0,0270	0,0301	0,0205	0,0202	0,0189	0,0270	0,0342	0,0235
Opr	0,0312	0,0215	0,0293	0,0315	0,0212	0,0209	0,0199	0,0282	0,0358	0,0260
Tim	0,0559	0,0563	0,0301	0,0474	0,0275	0,0264	0,0266	0,0366	0,0471	0,0359
Loc	0,0392	0,0361	0,0344	0,0230	0,0228	0,0227	0,0221	0,0309	0,0394	0,0292
Ocp	0,0497	0,0503	0,0412	0,0426	0,0167	0,0260	0,0249	0,0377	0,0499	0,0412
Ict	0,0453	0,0460	0,0384	0,0392	0,0232	0,0161	0,0266	0,0348	0,0459	0,0377
Mon	0,0348	0,0357	0,0315	0,0311	0,0219	0,0194	0,0139	0,0294	0,0362	0,0274
Age	0,0400	0,0409	0,0401	0,0352	0,0210	0,0229	0,0223	0,0208	0,0398	0,0334
Tis	0,0374	0,0353	0,0392	0,0338	0,0224	0,0223	0,0216	0,0303	0,0257	0,0284

Bod	0,0304	0,0318	0,0369	0,0311	0,0210	0,0207	0,0197	0,0279	0,0354	0,0171

The decision matrix, which is the first step of the TOPSIS method, is constructed by using Table 2 and the normalized decision matrix is obtained by normalizing the numerical values by using Eq. (2) in the first step of the method. For the criteria provided in Table 1, average number of the accidents occurred has been considered. On the other hand, in order to identify the weights of the each mentioned criterion, three experts of the firm were asked to evaluate each criterion with a score from 1 to 10 (1 refers to the least important; 10 refers to the most important) and then the criteria weights were identified by considering the averages of the expert evaluations by rounding them up to nearest whole numbers. Then, the table of normalized criteria weights was obtained (Table 3). Then, weighted normalized matrix was obtained as a result of multiplying normalized decision matrix by the normalized criteria weights identified for each criterion. At the last step, by using Eq.(5-8) in the in the implementation steps of TOPSIS method the distances to the ideal and negative ideal solutions; by using Eq.(9), the influence of the causes of occupational accidents on lost time incidents, TOPSIS ranking scores were obtained.

RESULTS AND DISCUSSION

As a result of the analysis, the causes of the accident are mathematically expressed by ranking the causes of the accidents according to the accident results. In Figure 2, ranking scores can be seen clearly. Values in table indicate that nearest distance to '1' shows that the influence of the causes of accidents on the related solution is high (absolute), that nearest distance to '0' shows that the influence is low (ineffective when it has the value of 0). As observed from these calculation results, as the factors determined as the cause of the accidents, Equipment (Pipes/Collars/Tubulars/Csg., Material, Engine/Pump, Machinery), Operation *(Rig/Equip. Repairs / Maint., Routine Drilling Operations.)*, Body Part (fingers) shines out as the highest scores in the results of total lost time incidents. There three causes are followed by Month, Time in Service for the Company, Location, Age, Incident cause type, Occupation, Time in Service respectively. In the analysis provided in the appendix, most seen ones are Pipe, tubular, casing tubing in equipment-related accidents. At the same time, the finger injuries are within the first three ranks in TOPSIS analysis in analysis provided in appendix. These results show that engineering measures are required to reduce occupational accidents in oil drilling. It is thought that it would be beneficial to make the drilling works by using the machines, that is to say, by transition to new technology; rather than by using hands. In the risk analysis to be applied to the oil and gas drilling fields, addressing the high risk areas mentioned here will reduce the occupational accidents

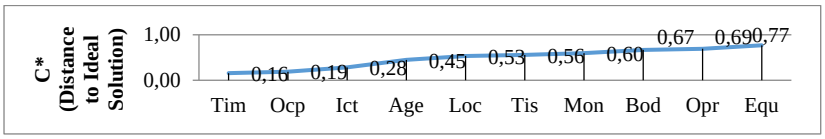

Figure 2. TOPSIS Ranking Scores of Criteria of Occupational Accidents (C^*)

4. CONCLUSION

The calculation of the TOPSIS analysis in the results and the discussion sections are recalculated by appointing equal weights. The results of the analysis are shown in Figure 3. There have not been any changes in the results. In other words, the highest 3 criteria given in the results section are same here.

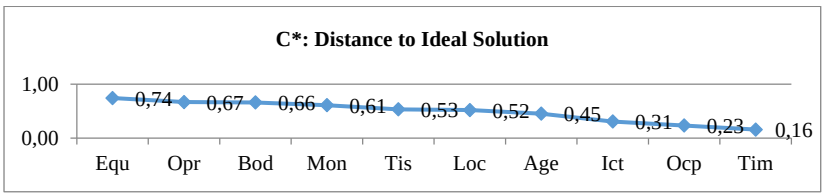

Figure 3. TOPSIS Ranking Scores of Criteria of Occupational Accidents (C^*)with the same weight.

REFERENCES

[1] Hill, R. (2012). Improving safety and health in the oil and gas extraction industry through research and partnerships. Presentation at the MAP ERC Energy Summit, April 12, Denver.
[2] Bureau of Labor Statistics Census of Fatal Occupational Injuries Charts, 1992–2012. Retrieved May 3, 2017 from www.bls.gov/iif/oshwc/cfoi/cfch0011.pdf.
[3] The Centers for Disease Control and Prevention. Retrieved April 12, 2017, from http://www.cdc.gov/mmwr/preview/mmwrhtml/mm6420a4.htm
[4] International Labour Organization. Retrieved April 12, 2017, from http://www.ilo.org/wcmsp5/groups/public/ed_dialogue/sector/documents/publication/wcms_438074.pdf.
[5] Industrial Safety and Hygiene News. Retrieved May, 21, 2017, from https://www.ishn.com/articles/96330-how-to-prevent-struck-by-and-caught-in-hazards-from-causing-injuries
[6] Petroleum Safety Authority Norway, Risk Level in Norwegian Petroleum Activities Development Trends 2011 - The Norwegian Shelf Retrieved May,12, from https://www.sintef.no/globalassets/upload/teknologi_og_samfunn/sikkerhet-og-palitelighet/well-control-incidents_study_2011.pdf
[7] OSHA IMIS Database. Retrieved May, 21, 2017, from https://www.osha.gov/pls/imis/establishment.html.
[8] U.S. Bureau of Labor Statistics. Retrieved April 14, 2017, from http://www.bls.gov/iag/tgs/iag211.htm
[9] Canadian Centre for Occupational Health and Safety. Retrieved April 12, 2017, from https://www.ccohs.ca/oshanswers/safety_haz/falls.html
[10] IADC. Retrieved May 3, 2017, from http://www.iadc.org/isp/iadc-2015-isp-program-annual-report-index/
[11] Formulas For Calculating Rates. Retrieved April 14, 2017, from http://www.nmmcc.com/wp-content/uploads/FORMULAS_for_CALCULATING_RATES1.pdf
[12] 16th International Conference of Labour Statisticians, Geneva, 1998. Retrieved April 14, 2017, from http://www.ilo.org/global/statistics-and-databases/meetings-and-events/international-conference-of-labour-statisticians/WCMS_087574/lang--en/index.htm
[13] Hwang, C.L. & K. Yoon, (1981). Multiple attribute decision making lecture notes in economics and mathematical systems 186, Springer-Verlag, Berlin
[14] Ic, Y. T., Tekin, M., Pamukoglu, F. Z., & Yildirim, S. E. (2015). Development of a financial performance benchmarking model for corporate firms. *Journal of The Faculty of Engineering and Architecture of Gazi University*, *30*(1), 71-85.
[15] United States Department of Labor, Bureau of Labor Statistics. Retrieved April 12, 2017, from https://www.bls.gov/iif/oshwc/osh/os/osch0057.pdf.
[16] U.S. Department of Labor Occupational Safety and Health Administration. Retrieved April 14, 2017, from https://www.osha.gov/SLTC/oilgaswelldrilling/.

ICENS 4TH INTERNATIONAL CONFERENCE ON ENGINEERING AND NATURAL SCIENCE
2-6 May 2018 KIEV UKRAINE

Determination of UAVs Thrust System Parameters by Artificial Bee Colony Algorithm

***Mehmet Konar*[1]**

Abstract

With the development of technology, Unmanned Aerial Vehicles (UAVs) have become a popular application in aviation engineering and are now used for many purposes in military and civil aviation. While usage areas for military purposes of UAVs are such as defense, mapping, and attack; usage areas for civil purposes of UAVs are such as disinfection of agricultural land, search and rescue in emergency, traffic control, cargo transportation, fire extinguishing. The importance of the UAV design has increased with the expansion of the field of applications. One of the most important aims in UAV designs is the design of the thrust system. Selection of the propeller is one of the main parameter of the thrust system design. In selecting the propeller, two basic parameters are considered, namely the diameter and the pitch of the propeller. In this study, the calculation of the maximum thrust force required during a straight flight was considered. For this purpose, an approach based on the Artificial Bee Colony (ABC) algorithm is proposed for the design of UAV with maximum thrust force. In this approach, the diameter and the pitch of the propeller and current flight speed used in the power system design of the UAV is determined as the input parameters. The maximum thrust force versus these mentioned input parameters also is determined the output parameter. In order to obtain the maximum thrust force, effective results were obtained in determining the optimum input parameters with the ABC algorithm. The results of the study showed that the proposed approach would make it easier for designers to design UAV thrust systems.

Keywords: UAVs, Thrust System Design, ABC Algorithm, Optimization.

1. INTRODUCTION

There are many innovations that technology adds to today's life. One of the most popular of this innovation is the Unmanned Aerial Vehicles (UAVs). The UAVs appeal to all military or civilian users due to their low risk for human life and their ability to specific tasks. Hence, the uses of UAVs become widespread and begin to realize different purposes. With the widespread use of UAVs, many designers and researchers have turned to this topic. As a result, many UAVs are designed for military and civil aviation use. While UAVs are used for military purposes in the field such as defense, mapping and attack, they are used for civil purposes in the field such as agricultural land, medication, emergency search and rescue, traffic control, transfer, fire extinguishing etc. The most common of these applications today are cargo transportation, mapping, defense, film industry and traffic control. Along with the increasing of UAVs usage, the important of the UAV design also has come to the fore [1].

One of the important elements of the UAV design is the determination of the thrust system. Depending on the requirements, either electrical engine or piston engine is used in order to obtain thrust. However, electric motors have begun to be used more widespread because of the significant reduction of noise in UAVs [2-6].

In this study, the calculation of the maximum thrust force required during a straight flight is considered. One of the main parameters in the design of the thrust system of electric UAVs is propeller selection. In selecting the propeller, two basic parameters are considered, namely the diameter of the propeller and the pitch of the propeller. Therefore, this study aims to calculate the optimal thrust production by considering the propeller diameter, the propeller pitch and speed variables of the UAVs. In computing, the Artificial Bee Colony (ABC) algorithm, which is one of the heuristic algorithms, is utilized. When computing with ABC, the values of the propeller diameter and propeller pitch were selected as at the recommended value intervals for the engine used. The speed information was selected as at the range of optimum stall and maximum speed of the UAV used as a reference [7].

The other parts of the study are as follows: In the second part, the UAV thrust system is explained. In the third chapter, the formulation used for the optimum thrust problem is given and the parameters used in the formulation are explained. However, the ABC algorithm used in the optimization process is also described in this section. In the fourth chapter, the results obtained in the optimization process with ABC algorithm are presented with tables and graphs. In the last part, the results and discussions are given.

2. UAV THRUST SYSTEM

UAVs have flight phases consisting of its take-off, straight flight and landing. The thrust system enables the UAV to achieve these flight phases and to attain the required distance. The electric thrust system consists of Electronic Speed Control (ESC) unit, battery, engine and propeller. While ESC adjusts the speed of the engine, the battery supplies the required energy. The propeller is used to turn the turning power obtained from the engine to thrust force. Depending on the airfoil structure of the propeller, the air is collected and thrown backwards to either pull or push the UAV [8].

The propeller has two important parameters as pitch and diameter. The propeller pitch is defined as the angle of attack of the propeller. The pitch angle can be fixed or variable according to the UAV used. In the case of variable-pitch UAV, while the UAV is in the air, it can remain in the air even with a high-speed, low-RPM (Revolutions per Minute) rotating propeller. The diameter of the propeller is defined as the diameter of the circle formed by the propeller blades [8].

A propeller is formed by joining two or more blades. These blades start to rotate with the energy they get from the engine. The rotating blades absorb the air from the its front and spray it quickly towards the its back side. As a result of this case, the thrust occurs. Due to the resulting thrust, the UAV is accelerated. Since the wing bottom surface and top surface areas of the accelerated UAV are different, a lift force occurs and the UAV flies.

The components forming the thrust system control are given in Figure 1. The first component here is the ground control. The commands sent from the ground control are received by the receiver on the UAV. Received commands are sent to the ESC unit. Depending on the commands sent from the ground control, the ESC unit drives the electric engine with the energy it receives from the battery. As a result, thrust is occurred with the propeller connected to the electric engine.

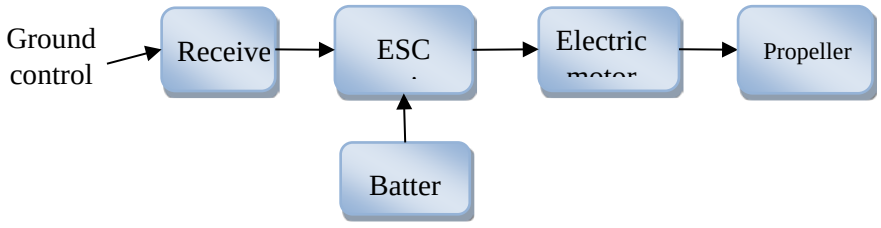

Figure 2. UAV Thrust System Components

3. CALCULATION OF UAV THRUST AND ABC ALGORITHM

3.1. Calculation of UAV Thrust

In the design of the UAV thrust system, the optimum thrust force is calculated taking into account the propeller diameter, propeller pitch and speed variables of the UAV engine. The formula given in Equation 1 is used for the calculation of thrust force [9-10].

$$F = 4.3924 * 10^{-8} * rpm * \frac{d^{3.5}}{\sqrt{pitch}} \left(4.2333 * 10^{-4} * rpm * pitch - V_0\right) \quad (1)$$

The rpm given in Equation 1 is the number of revolutions performed by the propeller in 1 minute. The performance of the thrust force increases in parallel with the increase of rpm value. The d parameter in Equation 1 is the propeller diameter. The propeller diameter varies depending on the engine specifications, as determined by the manufacturer, and has a positive impact on thrust force. The pitch parameter defines the propeller pitch. Pitch refers to the circular distance taken by a full turn of the propeller. The increase in the value of the pitch also has a positive effect on the thrust force. However, these parameters need to be chosen at optimal values depending on the engine characteristics used. Finally, V_0 is the current flight speed of the aircraft. Depending

on the design of the aircraft, the speed value changes. Flight at optimum speed is one of the most important factors for maximum thrust force.

3.2. ABC Algorithm

The ABC algorithm based on swarm intelligence was developed in 2005 by Karaboga with modeling the food search behavior of honey bees. The ABC algorithm provides simplicity and efficiency in solving optimization problems [11-12].

In the ABC algorithm, the honeybees are divided into three groups as employed, onlooker and scout bees according to their tasks. The employed bees provide communication and information sharing between bees in the colony. After collecting the nectars from the discovered food sources, they share information about the food source they have benefited with other bees in the colony. The onlooker bees receives the information by observing the dances of the employed bees. The onlookers make a choice according to the quality of the food sources. The last group, the scout bees, starts looking for random resources regardless of the dances of the employed bees and continues to work as an employed bee after finding the resources. Thus, on the one hand nectar is collected and consumed; on the other hand new nectar resources for the colony are explored.

Karaboga made some assumptions when modeling the ABC algorithm. The first of these assumptions is that the number of employed bees is equal to the total number of food sources. Thus, the nectar of a source is taken only by an employed bee. The second assumption is that the number of employed bees is equal to the number of onlooker bees.

In the ABC algorithm, the positions of food sources correspond to the possible solutions of the optimization problem to be solved, and the nectar quantities of the resources correspond to the quality of the solutions related to those resources. ABC algorithm tries to find the position of the source having the most nectar while it finds the minimum or maximum solution of the optimization problem to be solved. In the ABC algorithm, three basic control parameters are used as colony size, limit value and maximum cycle. Investigation and selection of appropriate values of these control parameters according to the optimization problem will be of great benefit in increasing the quality of the solution.

4. SIMULATION RESULTS

In this study, the design of the thrust system of an electric engine is considered. For this purpose, optimum thrust force is calculated according to Equation-1 by taking into consideration the propeller diameter, the propeller pitch, and flight speed variables of the UAV. In the calculation process, ABC algorithm was used. It is aimed to obtain maximum thrust force in response to optimum input values with ABC algorithm. For this purpose, a model with three inputs and one output was created and the generated model structure is given in Figure 2.

While the thrust force was calculated, the values of the propeller diameter and the propeller pitch that the manufacturer company refers to were used. The speed information was chosen as at the range of optimum stall and maximum speed of the UAV used as a reference.

The normalization intervals for the data were determined as [13, 17], [6, 12], and [30, 80], respectively by taking into account the minimum and maximum values of the input data used in the generated system model (Table 1). Thus, it is aimed to achieve more successful results in the model by normalizing the real values in the interval [0, 1]. The Mean Squared Error (MSE) value was chosen as the evaluation criterion in order to demonstrate the model success [13].

Table 1. The range values of input parameters for ABC model.

	Parameters	**Range Values**
Inputs	Propeller diameter	13-17
	Propeller pitch	6-12
	Propeller forward airspeed	30-80

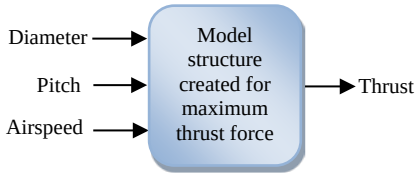

Figure 2. Model structure created for maximum thrust force

Control parameters of the ABC algorithm used for optimization: The colony size was 50, the number of iterations was 500, and the runtime was 30. The best values obtained by the optimization performed with the ABC algorithm are given in Table 2.

Table 2. MSE, input and output values obtained in the optimization process.

Obtained Input Values			**Obtained Output Values**
Propeller		**Propeller forward airspeed**	**Maximum thrust force**
Diameter	**Pitch**		
16,77	**11,98**	**30,89**	**13,16**

The values of the maximum thrust force versus the optimum input values obtained by 30 runtime with the ABC algorithm are presented in Figure 3. As can be seen from figure, the ranges of the propeller diameter, the propeller pitch and speed obtained in the ABC optimization process is [15.04, 16.94], [11.03, 11.99] [30.02, 33.48] respectively, while the maximum thrust force range is [6.82, 13.16]. This can be a reference value for designers.

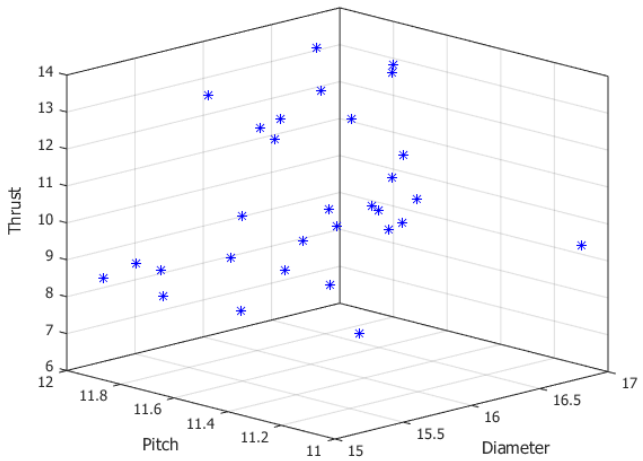

Figure 3. The optimum input-output values obtained at 30 runtime by the ABC algorithm.

The results obtained during the optimization show that the ABC algorithm has a very good performance in achieving optimum input parameters for calculating the maximum thrust force. Thus, it is seen that the proposed approach can facilitate the design of the thrust system

5. CONCLUSIONS

With the expansion of the field of application, the importance of the design of the UAV has increased. Since one of the important issues in UAV design was the design of thrust system, it was chosen as the subject of this work. In this study, the calculation optimum values of the propeller diameter, the propeller pitch and the current flight-speed, in response to the maximum propulsive force required during a straight flight are considered. For this purpose, an approach based on the ABC algorithm is proposed for the design of UAV with maximum

thrust. With the presented approach, for the UAV with maximum thrust, the diameter and the pitch of the propeller, and the current flight speed values were calculated. The ABC algorithm has shown very effective results in determining the parameters in the thrust system design. Considering the results of the study, it can be said that the models based on the ABC algorithm are one of the most important and effective alternatives that can help to design the UAV thrust system. Based on this work, the design of the different systems in the UAVs can also be realized with different heuristic approaches.

Author

Mehmet Konar is an Assistant Professor at Erciyes University. He received an MS in Aviation from Erciyes University (2010) and PhD for Electrical and Electronical Engineering at Erciyes University (2018). He is working on fuzzy logic theory, autopilot systems and unmanned aerial vehicles (UAVs) design and production.

REFERENCES

[1]. R. Austin, *Unmanned Aircraft Systems: UAVS Design, Development and Deployment*, John Wiley & Sons, 2010.
[2]. O. Gur and A. Rosen, “Optimizing electric propulsion systems for unmanned aerial vehicles”, Journal of Aircraft, Vol.46, No.4, July-August 2009.
[3]. D. A. Lawrence and K. Mohseni, “Efficiency analysis for long-duration electric MAVs”, 2005, Arlington, Virginia.
[4]. T. Chang and H. Yu, “Improving electric powered UAVs’ endurance by incorporating battery dumping concept”, Procedia Engineering 99, pp.168-179, 2015.
[5]. B. Elkhedim, E. Benard, M. Bronz, N. Gavrilovic and V. Bonnin, “Optimal design of long endurance mini UAVs for atmospheric measurement”, 2016 Applied Aerodynamics Conference , Jul 2016, Bristol, United Kingdom.
[6]. L. W. Traub. "Range and endurance estimates for battery-powered aircraft", Journal of Aircraft, Vol. 48, No. 2, pp. 703-707, 2011.
[7]. T. Oktay,M. Uzun, “Aerodynamic tailcone shape optimization for autonomous navigation performance maximization of morphing aerial robot”, 2nd International Conference on Engineering and Natural Sciences (ICENS 2016), 2016, Saraybosna.
[8]. Integrated Training System. Module 17 propeller for EASA part- 66. Licence Category A, B l and B 2. TTS Integrated Training System, 2011.
[9]. H. Sahin, T. Oktay, "Powerplant system design for unmanned tricopter", International Conference on Technology, Engineering and Science (IConTES), Antalya, pp.1-14, 2017.
[10]. Gabriel Staples (2007) , Propeller static and dynamic thrust calculation, 16 July 2013. [Online]. Available: http://www.electricrcaircraftguy.com
[11]. D. Karaboga,B. Akay, A comparative study of artificial bee colony algorithm. Applied Mathematics and Computation, 214(1): 108-132.,2009
[12]. D. Karaboga, Artificial bee colony algorithm. Scholarpedia, 5(3): 6915, 2010
[13]. A. Bagis, M. Konar, "Comparison of sugeno and mamdani fuzzy models optimized by artificial bee colony algorithm for nonlinear system modelling", Transactions of The Institute of Measurement and Control, vol.38, no.5, pp.579-592, 2016

ICENS 4TH INTERNATIONAL CONFERENCE ON ENGINEERING AND NATURAL SCIENCE
2-6 May 2018 KIEV UKRAINE

The Use Of Chicken Feather Fibers As Insulation Material For Winter Top Clothing

Nazim Pasayev[1], Onur Tekoglu[1], Sureyya Kocatepe[1]

Abstract

Since ancient times, natural materials such as cotton, wool and bird feathers have been used for thermal insulation in winter clothes. Today, although more artificial materials are used for this purpose, natural insulation materials especially lower feathers of water birds have not lost their importance as waterproofing materials. These materials with high heat protection, lightness, softness and long serviceability are very expensive. In contrast, especially recently developed artificial fibers exhibit superior properties than natural fibers at some angles, but they are not as useful as natural fibers in terms of heat insulation, softness and long service. This makes the water bird feathers more expensive, especially the puffer and goose feathers.

Accordingly, as the chicken feathers material is abundant, easily accessible and cheaper than the water bird feathers, the use of chicken feathers in winter clothes as filling material has attracted more attention. On the other hand, about 22 million tons of chickens are obtained as by-products each year in the world, and more than 4 million tons are wasted. This chemically resistant material is buried or burnt.

Chicken feathers are natural heat insulation materials. However, it is not possible to utilize chicken feathers like geese and ducks feathers. Unlike the goose and ducks, there are no down feathers in chickens as non-flying birds. On the other hand, the roughness, weight, fragility and low elasticity of the chicken feather appears to be a problem. In order to overcome these problems, we proposed to utilize the "fibers" obtained by separating the "barbs" part of the chicken feather from the "rachis" part by mechanical cutting as the filling material in the winter clothes. Research has shown that the chicken feather fibers have porous internal structure, which gives them high insulation properties. Our research has shown that the use of chicken fiber as insulation material in winter clothes is not only economical but technically a good alternative to other insulation materials. The winter coats made from chicken feather fibers have the same appearance as the goose down in terms of insulation, yet they have a beautiful appearance.

Keywords: chicken feather, chicken feather fibers, insulation properties of chicken feathers, filling material.

1. INTRODUCTION

For hundreds of years people have been using down feathers of water birds as filling material in winter tops. However, the reasons why these materials have such a high heat retention capability are not fully clarified. There are not enough studies in this regard. In one of these very few studies, the high insulation property of down feathers of water birds is explained in two respects. In the first place, the physical structure (configuration) of down is recorded, so that the down can store plenty of air inside the feather. Air is, as is well known, the best thermal insulation material. The second one is the high elasticity and durability of the feather, which allows the compressed feather to return to its original state [1].

In another study to investigate the features of some of the water birds feather cover, the mechanical and structural properties of down feathers were more likely to be examined.

In this study, the heat-protective properties of the down feathers are linked to the mechanical and structural properties and the lightness of these feathers [2]. According to the study, down feathers of water birds have a complicated configuration consisting of barbs branched from a tiny stem, while the internal structure of the barbs is empty (Fig 1).

[1] *Corresponding author: Erciyes University, Department of Textile Engineering, 38039, Melikgazi/Kayseri, Turkey, npasayev@erciyes.edu.tr*

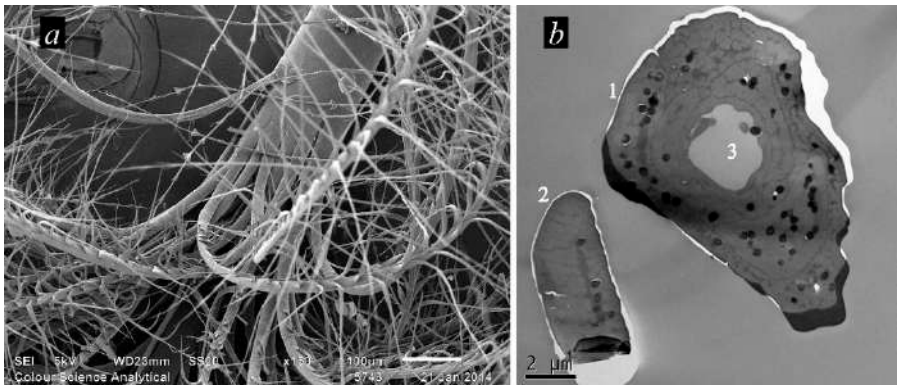

Figure 1. SEM images of the outer (a) and inner structure (b) of the goose down feather [2]

Chickens are lack of down feather because they live on land and can't fly. These birds generally have none or even very few down feathers. But like water birds, chicken feathers also have protein content and they have the same chemical properties.

Chicken feather emerging as a by-product in chicken meat production, which is the most spread animal species in the world, is not widely used. Protein feed is produced from these feathers and the feathers are also used in the construction and furniture sector. An important part of the emerging feather is burnt or buried. It is true that, in recent years, scientists have been paying attention to chicken feathers as a row material and trying to develop products with high added value from this inexhaustible material.

Even though the birds' feathers are the first of them to be used as fillers, their roughness, weight, fragility and low elasticity make it impossible to use chicken feathers as quality filling material. In order to overcome these problems, we proposed to utilize the "fibers" as filler material for winter clothes. These fibers are obtained by separating the "barbs" part of chicken feather from the "rachis" part by mechanical cutting.

The fibers obtained from chicken feathers are not as useful as down feathers of water birds in terms of elasticity and structural configuration. However, in response to this, they have a developed micro-porous internal structure. In Figure 2, SEM images of internal and external structure of chicken feather fibers are given by us. According to us, the micro-pored interior of these kinds of fibers as given in Figure 2b should significantly compensate for the low elasticity of these fibers in terms of insulation.

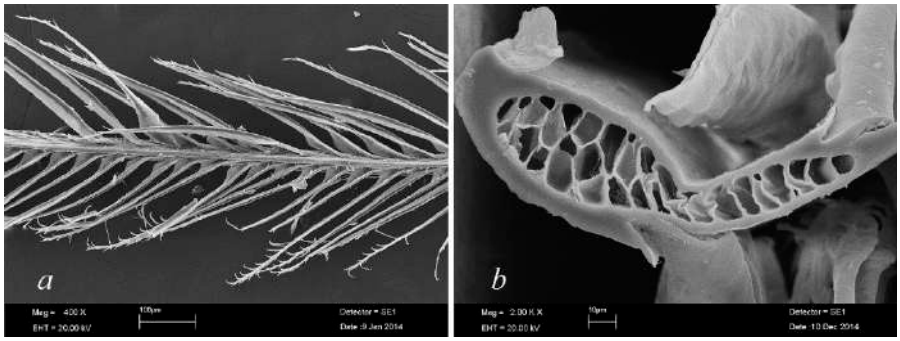

Figure 2. SEM images of external (a) and internal (b) chicken feather fiber [3]

In our unpublished work, a comparative analysis of the thermal properties of chickens, goose down, and some natural and synthetic fillers have been done. Goose down and chicken feather fibers were used as filler material and samples were made of the same size and weight. Measurement results have showed that the thermal conductivity coefficient and specific thermal resistance values of these samples were approximately the same (Figure 3).

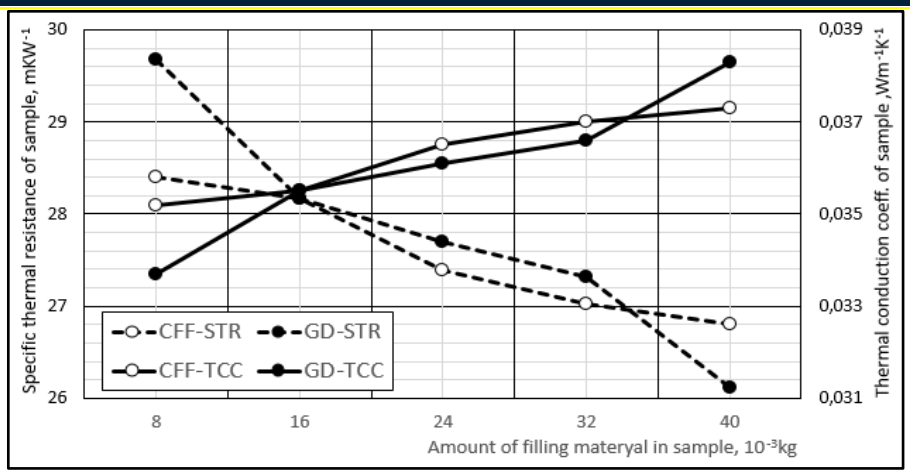

Figure 3. Change of thermal parameters of CFF and GD according to the amount of filler material

In this study, the use of the fiber obtained from chicken feathers as filling material in winter clothes was experimentally performed and the prototype produced product was evaluated by expert method.

2. MATERIALS AND METHODS

2.1. Materials

Two seasonal coats have been made to test the chicken feather fibers as a filling material. Both of the coats have the same medium size and models were produced in the same industrial conditions by one of the leading manufacturers, Maya Textile, in Turkey. On one side, goose feather was used as filling material and on the other side chicken feather fiber was filled (Figure 4).

Figure 4. Experimentally produced coats

2.2. Methods

The expert method was used to evaluate the properties of the product. For this purpose, 10 experts with the same body measurements were selected and they were offered to conduct an active trial of both products at the same climatic conditions for one hour and to evaluate the results.

The following criteria were selected for evaluation:

1. Heat comfort K1
2. Moisture comfort K2
3. Motion freedom K3
4. Weight of product K4
5. Softness K5
6. Body wrap and comfort K6
7. Aesthetic K7
8. Satisfaction K8
9. The price K9

The questionnaire including Table 1 was arranged to determine the weight order of the evaluation criteria. In the questionnaire, it was proposed to rank the evaluation criteria given to each expert according to the degree of importance. The results of these surveys will be used to determine the weight of each criterion in the overall assessment.

Table 1. Table to determine weight order of evaluation criteria

Experts (*j*=1…10)	**Evaluation Criteria K_i (*i*=1…9)**							
	K_1	K_2	K_3	K_4	K_5	K_6	K_7	K_8
1	a_{11}	a_{12}	a_{13}	a_{14}	a_{15}	a_{16}	a_{17}	a_{18}
2	a_{21}	…	…	…	…	…	…	…
...	a_{j1}	…	…	…	…	…	…	a_{ji}

Here, each value of a_{ij} expresses the significance rank determined by the expert *j* for the criterion *i*. The most important criterion is marked with 1, the least important criterion with 9. All values are exact and vary in the range 1 to 9. Separate criteria can be equivalent and at the same time they can be given the same value.

The following formula has been used to calculate the weight of each *i* criterion:

$$A_i = \frac{\sum_1^m a_{ij}}{\sum_1^k \sum_1^m a_{ij}}.$$

In this form, with the weight value given by the expert *j* to the *i* criterion, *aij* is i = 1 ... k, j = 1 ... m,.

In the questionnaire, each expert was asked to make an assessment out of 10 according to the criteria given. The survey results were transferred to the table (Table 2 and Table 3). For each criterion, the arithmetic mean of the expert opinions is taken and the weight coefficient of the criterion is multiplied and divided by the weights of the criteria. Thus, the weighted average for all the criteria is calculated so that the value is the general value given to the product by the experts:

$$\bar{K} = \frac{\sum_{i=1}^k \bar{K}_i A_i}{\sum_1^k A_i}.$$

The compliance score of the expert opinion was evaluated by the concordance correlation coefficient. Kendall W test was applied to the evaluation results. The significance of the concordance correlation coefficient was tested with the *f=k-1* degree of freedom according to the Pirson criterion $\chi 2$.

3. DISCUSSION

Table 2 shows the results of the survey and the processing of the results to determine the evaluation order of expert opinions. In the last row of the table, which is the overall assessment, the weight of the product calculated according to the expert opinion of each evaluation criterion was given.

In Table 3 and Table 4, the evaluation matrices of coats produced from chicken feather fibers and goose down were given.

According to the evaluation results, general evaluation was made for each product based on expert opinions. The overall assessment was calculated based on the average values of the criteria according to experts and

weighted average based on the weights in Table 2. Overall assessment for the coat made from chicken feathers was 8,0 and for the coat made from goose down was 8,7. The compatibility of expert opinions is evaluated by the coefficient of concordance. For this purpose, Kendall W test was applied to the data in Table 3 and Table 4 by using IBM SPSS 25 program. Test results were given in Table 5.

Table 2. Survey results to determine the rank of evaluation

Experts (j=1…10)	**Evaluation Criteria K_i (i=1…9)**								
	K_1	K_2	K_3	K_4	K_5	K_6	K_7	K_8	K_9
1	1	6	5	7	8	3	2	9	4
2	9	8	7	6	5	1	2	3	4
3	1	7	2	4	3	5	6	8	9
4	1	6	3	2	7	5	4	8	9
5	6	7	3	4	8	2	1	9	5
6	3	9	4	8	7	5	2	6	1
7	7	8	6	9	4	3	1	5	2
8	1	3	2	4	5	7	6	8	9
9	2	7	1	4	9	3	5	8	6
10	4	5	1	8	9	6	2	7	3
$\sum_1^m a_{ij}$	35	66	34	56	65	40	31	71	52
$\sum_1^k \sum_1^m a_{ij}$	450								
$A_j = \frac{\sum_1^m a_{ij}}{\sum_1^k \sum_1^m a_{ij}}$	0,08	0,15	0,08	0,12	0,14	0,09	0,07	0,16	0,12

Table 3. Evaluation matrix of the coat produced from chicken feather fibers

Evaluation Criteria K_i (i=1…9)	**Experts (j=1…10)**										$\bar{K}_i$
	1	**2**	**3**	**4**	**5**	**6**	**7**	**8**	**9**	**10**	
Heat comfort K_1	8	5	9	9	9	10	9	9	8	8	8,4
Moisture comfort K_2	8	6	10	10	7	7	7	8	8	7	7,8
Motion freedom K_3	10	10	8	10	10	9	10	10	9	9	9,5
Weight of product K_4	10	9	10	8	10	9	10	10	10	9	9,5
Softness K_5	8	7	10	9	10	9	10	10	9	8	9,0
Body wrap and comfort K_6	6	10	9	10	10	8	10	9	9	9	9,0
Aesthetic K_7	5	4	10	10	8	8	9	7	4	8	7,3
Satisfaction K_8	10	5	10	10	10	8	9	9	8	8	8,7
The price K_9	8	8	10	8	9	10	9	9	9	9	8,9

Table 4. Evaluation matrix of the coat produced from goose down

Evaluation Criteria K_i (i=1…9)	**Experts (j=1…10)**										$\bar{K}_i$
	1	**2**	**3**	**4**	**5**	**6**	**7**	**8**	**9**	**10**	
Heat comfort K_1	10	9	10	10	9	10	9	10	10	9	9,6
Moisture comfort K_2	10	6	10	9	7	7	7	6	9	6	7,7
Motion freedom K_3	7	2	5	8	7	7	9	9	7	6	6,7
Weight of product K_4	9	3	10	9	8	8	10	9	8	8	8,2
Softness K_5	10	5	10	10	8	8	10	10	7	9	8,7
Body wrap and comfort K_6	9	3	8	7	9	8	9	8	7	7	7,5
Aesthetic K_7	8	9	7	10	10	7	9	7	5	8	8,0
Satisfaction K_8	9	10	9	10	8	8	8	9	7	7	8,5
The price K_9	4	4	10	10	7	7	7	8	7	7	7,1

According to the evaluation results, general evaluation was made for each product based on expert opinions. The overall assessment was calculated based on the average values of the criteria according to experts and weighted average based on the weights in Table 2. Overall assessment for the coat made from chicken feathers was 8,0 and for the coat made from goose down was 8,7. The compatibility of expert opinions is evaluated by the coefficient of concordance. For this purpose, Kendall W test was applied to the data in Table 3 and Table 4 by using IBM SPSS 25 program. Test results were given in Table 5.

Table 5. Kendall test results for the evaluation of the coat produced from TTL (a) and goose down (b)

Kendall's W Test — *a*

Test Statistics

N			9
Kendall's W[a]			,285
Chi-Square			23,091
df			9
Asymp. Sig.			,006
Monte Carlo Sig.	Sig.		,004[b]
	99% Confidence Interval	Lower Bound	,002
		Upper Bound	,005

a. Kendall's Coefficient of Concordance

b. Based on 10000 sampled tables with starting seed 2000000.

Kendall's W Test — *b*

Test Statistics

N			9
Kendall's W[a]			,321
Chi-Square			25,993
df			9
Asymp. Sig.			,002
Monte Carlo Sig.	Sig.		,001[b]
	99% Confidence Interval	Lower Bound	,000
		Upper Bound	,002

a. Kendall's Coefficient of Concordance

b. Based on 10000 sampled tables with starting seed 2000000.

As it is seen on Table 5a, it is χ^2=23,091. The critical value of the distribution of χ^2, which corresponds to confidence level *df = 9* and *P = 0.99*, is 21.67. It can be found on the standard table. 23,091> 21,67 [*df = 6 and P = 0,99*] indicates that the calculated value of the criterion χ^2 is greater than the table value which shows that the expert opinion is compatible. On table 5b, it is χ^2=25,993. 25,993>21,67 [*df*=6 and *P*=0,99] also indicates that the calculated value of the criterion χ^2 is greater than the table value. Accordingly, the conclusion is that the expert opinions are compatible.

4. RESULTS

When we look at the results of the evaluation of coats produced from chicken feather fibers filling material and coats produced from goose down filling material, it is seen that the coat made from chicken feather fibers has a higher score than the goose down in general evaluation. It is observed that goose down coat scores are higher for heat comfort and product aesthetics than the coats produced from chicken feather fibers, humidity comfort and satisfaction of the product scores are close to each other and goose down coats have lower scores for the rest of the evolution.

The compliance of the opinions of the experts was evaluated by the Kendall W test, and it is found compatible.

As can be seen, the fibers obtained from chicken feather are similar to goose down as filler material, but they are more advantageous than goose down in some other indicators, especially in cost indicators.

ACKNOWLEDGMENT

The project has been supported by Erciyes University Scientific Research Projects Coordination Unit, with the project number FDK-2016-6385. Because of the help Maya Textile Trade LTD Company showed in prototype production, the writers express their thanks to the Maya Textile.

REFERENCES

[1]. J. Gao, W. Yu& N. Pan. “Structures and Properties of the Goose Down as a Material for Thermal Insulation”. *Textile Research Journal*, vol 77, 8; pp. 617-626, 2007

[2]. M.E. Fuller. The structure and properties of down feathers and their use in the outdoor industry. (Un published doctoral dissertation). Leeds University, Leeds, 2015.

ICENS 4TH INTERNATIONAL CONFERENCE ON ENGINEERING AND NATURAL SCIENCE
2-6 May 2018 KIEV UKRAINE

A Literature Review for Applications of Soft Computing On Aeronautics

Seda Arik[1], Tugrul Oktay[2], Ilke Turkmen[3]

Abstract

This study discusses the works done by using soft computing techniques in the field of aeronautics. Zadeh proposes soft computing in 1994 and the role model of the soft computing is human intelligence. Soft computing techniques produce tolerant results in unclear, uncertain, and partially accuracy situations and aims to solve the problem of full intersection sets. They also produce effective results in real world problems that ideal models cannot develop. Aeronautics is a field that is constantly improving and innovative field. In this study, the place and importance of soft computing techniques in aeronautics will discussed. For this purpose, besides our own studies, the articles available in the literature will examined and interpreted. In addition to the available articles, a different and simple study based on soft computing techniques will also do. This study will compare with the other studies in the literature and the results will presented. In addition, it was discussed what could be done in the light of these studies in the future.

Keywords: Aeronautics, Soft Computing Techniques, Artificial Neural Network, Optimization.

1. INTRODUCTION

Both military and civil aviation is a field that is constantly improving. Along with the production of unmanned aerial vehicles in particular, aeronautics have been incorporated into daily life with applications such as traffic monitoring, mapping for land registry and cadastre, and meteorology [1-5]. The expansion of aviation applications has greatly increased the interest in aircraft design. While advances in computer technology have increased the use of numerical simulation methods in many engineering design problems, aircraft designs have also been influenced by this trend. Especially Computational Fluid Dynamics (CFD) is a numerical simulation program often used in aircraft designs. CFD provides both time saving and low cost compared to aircraft designs made with wind tunnel. However, the CFD method is time consuming in itself even though it saves time compared with the wind tunnel. Therefore, to minimize the time problem mentioned in aircraft designs, researchers have begun to use the CFD method by combining with numerical optimization methods such as gradient-based methods [6-12] and metaheuristic methods [13-21].

Gradient-based methods are preferred in aerodynamic shape optimization due to their low computational complexity as well as the ability to work with many design variables. Since gradient-based methods require continuity and predictability, it is very important to define a limited set of functions with well-defined gradients in these methods. In addition, continuity and uncertainty are disadvantage of gradient-based methods [22]. The problem is that there will be non-continuous topological and local flow changes in the geometrically changing search space during aerodynamic design. For example, discontinuity and convergence in the turbulence model considerably reduces the robustness of gradient-based methods [22, 23]. There is no certain and clear definition of metaheuristic methods, but it can be said that these methods define the intersection of artificial intelligence, soft computing and mathematical programming [24]. Many metaheuristic methods mimic natural phenomena to solve optimization problems (bee colony, evolution of species, ant colony, simulated annealing, etc.). Metaheuristic methods do not require continuity and predictability, and these methods have a high probability of finding global optimum. Therefore, it can be said that metaheuristic methods with mentioned properties are more advantageous than gradient-based methods [22].

[1] *Corresponding author: Erciyes University, Department of Aircraft Electrical and Electronics, 38030, Melikgazi/Kayseri, Turkey. arikseda@erciyes.edu.tr*

[2] *Erciyes University, Department of Aeronautical Engineering, 38030, Melikgazi/Kayseri, Turkey. oktay@erciyes.edu.tr*

[3] *Erciyes University, Department of Aircraft Electrical and Electronics, 38030, Melikgazi/Kayseri, Turkey. titi@erciyes.edu.tr*

In this study, the applications of soft computing methods that are one of metaheuristic methods on aeronautics will be presented. Zadeh, the founder of the fuzzy logic, proposed soft computing in 1993 [25]. Soft computing methods provide tolerant results for uncertain and partially accurate states and provide effective results in real world problems that cannot have ideal models. Soft computing refers to the sum of the methods defined for solving problems that are not mathematically modeled or difficult to model, and consists of a combination of various methods such as fuzzy logic, artificial neural networks, and evolutionary algorithms [26]. Therefore, soft computing methods have become popular in aeronautics as in many field with features such as nonlinear programming, intelligent control, decision-making and optimization. In this study, the applications of soft computing methods on aeronautics will be presented, the works in the literature will be compared and a simple example will be presented.

2. APPLICATIONS OF SOFT COMPUTING METHODS ON AERONAUTICS

Since a small change in aircraft geometry brings about a major change in the characteristics of the aircraft, aircraft designs in the aeronautics are usually redesigned with improvements on existing aircraft. In order to design a new aircraft from scratch, many analyzes, experience and cost are required. Hence, in designs made in this way, not all possibilities for improvements can be used. Metaheuristic based optimization methods can be considered as effective methods for using these possibilities. Soft computing methods, swarm-based methods, and other metaheuristic optimization methods are computer-based, not a single solution-oriented and can be characterized by a combination of continuous, discrete or integer variables [27]. These methods have quality analysis ability and interdisciplinary compatibility, and are therefore preferred to improve the performance of design processes with these features [28]. Therefore, during aircraft design, broad combinations of basic design parameters are assessed using metaheuristic methods and a preliminary idea can be obtained to find the best design [29]. In this study, the scope of study instead of all metaheuristic methods was limited to the aeronautical applications (such as (aerodynamic design, flight control design, etc.) of soft computing methods (i.e. fuzzy logic, Artificial Neural Network (ANN) and evolutionary algorithms) and of hybrid approaches based on soft computing. For this purpose, many articles, theses and conference papers, etc. were examined. This work takes a basic look at approaches and studies based on soft computing on the aeronautics and includes references that describe the practical application areas of soft computing for researchers.

Huang et al. have used the ANN in multi-point inverse airfoil design [30]. They have calculated the lift coefficient, drag coefficient and pitching moment as a function of angle of attack for different airfoil structures. The necessary data for ANN were obtained with Eppler airfoil design code [31].

Norgaard et al. have utilized the neural network during the wind tunnel experiments to determine the coefficient of aircraft design and examined the effectiveness of the method [32]. For this purpose, to find the optimal flap schedules, they have calculated the lift coefficient, drag coefficient, moment of inertia (pitching moment) and lift/drag ratio depending on angle of attack and flap settings. They have produced a limited number of training datasets from wind tunnel experiments. They have tested the obtained results on SHARC (model of the USAF/NASA Subsonic High Alpha Research Concept aircraft) and indicated that the estimated results of the trained networks were within tolerance limits. As a result, they have emphasized that the proposed method reduces wind tunnel experiments and is faster, more realistic and more cost-effective than conventional methods.

Greenman and Roth have used the ANN to optimize the high-lift performance of multi-element airfoil [33]. In their study, for each of the two different slat deflection settings, they have calculated 27 different flap riggings with Computational Fluid Dynamics (CFD) for 10 different angles of attack and used this data in the training of the neural network. For the neural network, they have selected the flap riggings and the angle of attack as inputs, and the aerodynamic force as output. Finally, they have emphasized that the proposed method reduces the average cost by 83%.

Tse and Chan have optimized the airfoil design by using ANN and Genetic Algorithm (GA) [34]. They have used the neural network to predict the airfoil surface pressure distribution. For this purpose, they have selected the coordinates of the B-spline control nodes as inputs, and the pressure values on the airfoil surface as outputs. They have pointed out that ANN is more efficient than CFD by comparing estimates made with neural network and CFD. Then, they have used micro-GA, a derivative of GA, to determine the optimum airfoil design.

Jones et al. have used the GA to maximize the L/D ratio and minimize the noise on the rotor airfoil [35]. They have realized aerodynamic and aeroacoustic analysis using the parameters they obtained.

Rajkumar and Bardina have preferred the ANN for estimating aerodynamic coefficients [36]. As a function of Mach number and angle of attack, lift, drag and pitching moment coefficients were estimated with the artificial neural networks. In this study, which they obtained training data from wind tunnel experiments and numerical

simulations, they have emphasized that the ANN based method is a good potential to develop the aerodynamic models for flight simulations.

Hacioglu and Ozkol have realized the transonic airfoil design using vibrational GA, a derivative of GA [17]. They ran the algorithm for three different situations: first one is inverse airfoil design in incompressible, inviscid flow; second one is inverse airfoil design in transonic flow; third one is airfoil optimization in transonic flow. As a result, they noted that the usage of vibrational GA is a major effect on CFD calculations (reduced by more than 45%). In another study, Hacioglu used GA and ANN together in inverse airfoil design [37]. In his study, the target solution was estimated directly using ANN instead of approximate calculation of the objective function, thus it was aimed to accelerate the design process.

Santos et al. have preferred the neural network to predict aerodynamic coefficients for different airfoil geometries [38]. The data base belonging to different airfoils for the neural network was generated by XFOIL as the function of angle of attack for fixed Mach and Reynolds numbers [39].

Marta has implemented a preliminary aircraft design using GA [40]. He has aimed to maximize the aircraft range using wing, fuselage geometry, tail, and design parameters. For this purpose, he has used limited design variables and Breguet equation as the objective function in the GA. He has evaluated the performance of the GA for six different runtimes. Bagassi et al. have performed a similar study [41]. They have used the Breguet equation to maximize the aircraft range.

Gern et al. have used ANN in control allocation optimization of aircraft called as Hybrid Wing Body (HWB) [42]. They have aimed to minimize control power, hinge moments and actuator forces by keeping system weights within accepted limits. They have produced training data for ANN by using Nastran® aeroservoelastic finite element model. In conclusion they have presented that ANN estimates have been improved by more than 12% from the best Nastran® solution [43].

Haryanto et al. have proposed an approach based on ANN and GA to maximize lift/drag ratio on airfoil [44]. They have trained the ANN using the data obtained by the CFD method to determine the relationship between the airfoil geometry (input) and its aerodynamic coefficients (output). Thus, they have showed that the coefficients of lift and drag can be computed with the ANN by entering airfoil geometry to the program. In addition, they have realized optimization with GA to find the airfoil geometry that has the maximum lift/drag ratio for a fixed Reynolds number, and have confirmed the results with CFD.

Husek and Narenathreyas have proposed an approach based on fuzzy logic to control the longitudinal motion of the aircraft [45]. Ali et al. have used a fuzzy-based algorithm for the stabilization of the tri-rotor Unmanned Aerial Vehicle (UAV) [46]. In another fuzzy logic based study, Ibrahim and Al Akkad designed a fuzzy logic based controller for pitch control of the aircraft [47].

Roy and Peyda used the Adaptive Neuro-Fuzzy Inference System (ANFIS) and Artificial Bee Colony (ABC) algorithm together to predict aircraft parameters [48]. They trained the ANFIS by using the angle of attack, pitch angle, pitch rate, airspeed and accelerations. They produced the flight data according to the aerodynamic model by keeping the initial conditions the same, and used the ABC algorithm to find the optimum values.

Many other applications based on soft computing methods on aeronautics are available in the literature, but the details of them are not mentioned here [49-56]. When the studies available in the literature are examined, it can be observed that approaches based on soft computing methods make the preliminary aircraft design easier in terms of time and cost. In addition, it can be seen that CFD or wind tunnel experiments can be performed in a shorter time and more effectively by using the data obtained by soft computing methods. In summary, soft computing methods allow to simulate aircraft designs, which are very complex and based on many parameters, in almost real timely with acceptable error values. In addition to the works in the literature, we have implemented a simple application in this study as an example. In the next section, the process of our studying is presented.

3. A SIMPLE APPLICATION OF SOFT COMPUTING METHODS ON AERONAUTICS

In this section, a simple approach based on the soft computing method is presented in the calculation of the optimal fuselage drag coefficient. Artificial Neural Network (ANN) and Adaptive Neuro-Fuzzy Inference System (ANFIS) as soft computing methods have been trained with data that were produced optimally by using Artificial Bee Colony (ABC) algorithm, and have provided successful results in producing optimum results in designs.

The ANN is formed by mathematically modeling of biological cells called as neurons. ANNs are information-processing systems that have some features such as nonlinearity, learning with examples, generalization according to examples, adaptability [57-59]. In this study, feedforward ANN structure is preferred. In a

feedforward ANN, the cell output on one layer is applied as the input to the next layer with weights. ANN consists of three layers called as input, hidden and output. The input layer receives information from the outside world and transmits it to the hidden or output layer. This information is processed at hidden or output layer to determine the desired network output. Each layer in the ANN can contain one or more neurons and is determined by the designer according to problem. There are many learning algorithms to train the feedforward ANN structure and therefore, it is a neural network model that is often used in the solutions of engineering problems and applications.

The basic structure of ANFIS is composed of Sugeno type fuzzy systems and a network with neural learning ability [60]. This network structure consists of nodes placed in layers to perform certain functions. ANFIS structure consists of nodes placed in layers to perform certain functions and has five layers. In the first layer, the membership grade is determined according to the input values and the membership function used. In the second layer, the firing strengths of the rules is calculated by multiplying the membership grades. In the fourth layer, the normalized firing strength of rule calculated in the third layer is multiplied by first order Sugeno fuzzy rule. In the fifth layer, overall output of the ANFIS is obtained by summing the output values of each node in the other four layers.

ABC algorithm presented by Karaboga in 2005 is widely preferred by researchers for solving a wide variety of optimization problems because of its simple working principle, having a few control parameters, and its easy implementation [61, 62]. The ABC algorithm, which models the intelligent food search behaviors of honeybees, has three types of bees called as employed, onlooker, and scout bees. In the ABC algorithm, first, the initial food sources are randomly generated. Employed bees select a food source, stores nectar and returns to the hive. The onlookers choose the food source by following the dancing of the employed bees returning to the hive and go to the source. The onlookers starting to store nectar like employed bees become scout bee to search for new food sources when food sources are exhausted. At the same time, scout bees find a random food source and continue to store nectar. The algorithm cycle that has these steps continues until reaching the stop criteria.

In this study, ANN and ANFIS have used to calculate the minimum fuselage drag coefficient given in Equation 1. Here, C_{Df} is the fuselage drag coefficient, l_f is length of the fuselage, and d_f is frontal average diameter of the fuselage. For the Unmanned Aerial Vehicle (UAV) called as ZANKA-II produced at Erciyes University, l_f was determined in the range [114, 126] cm, and d_f values was determined in the range [19, 22] cm. In this ranges of values, 300 input data corresponding to the minimum fuselage drag coefficient was generated by using ABC algorithm. The reason for using the ABC algorithm is to determine the optimum input values that minimize the fuselage drag coefficient. That is, a data set based on optimum input data corresponding to the minimum drag coefficient has been obtained. In the simulation studies made with ANN and ANFIS, l_f and d_f are selected as input parameters, and C_{Df} is selected as output parameter. The Mean Square Error (MSE) expressed in Equation 2 was selected as the performance criteria for ANN and ANFIS trained by these obtained data [63, 64].

$$C_{Df} = 0.0003\left[3 \cdot \frac{l_f}{d_f} + 4.5 \cdot \sqrt{\frac{d_f}{l_f}} + 21 \cdot \left(\frac{d_f}{l_f}\right)^2\right] \quad (1)$$

$$MSE = E(w) = \frac{1}{n}\sum_{i=1}^{n} e_i^2(w) \quad (2)$$

For ANN, 50% of the data were used as training data to train the network, 25% as the test data to evaluate network performance and 25% as validation data to prevent over-learning. As the learning algorithm for ANN, Levenberg-Marquardt (LM) algorithm was preferred with the reason that it is frequently preferred in the literature and that provides fast learning and good convergence in ANN training [65-67]. After selecting the learning algorithm, simulations were made for 1000 epochs by changing the number of hidden layers and the number of neurons in these layers in the range of [1,10] to find the most suitable network structure. The logarithmic sigmoid (logsig) and tangent sigmoid (tansig) activation functions in hidden layers and the linear (purelin) activation function in output layer were preferred depending on experiments and our experiences. The most suitable structures and MSE values made with single-layer ANN and multi-layered ANN to minimize C_{Df} are given in Table 1. As can be seen from Table 1, the optimal structure to minimize C_{Df} is an input layer with two neurons, two hidden layers each with 5 neurons (made with logsig) and an output layer with a single neuron (2x5x5x1).

For ANFIS, 75% of the data were used as training data to train the network, 25% as the test data to evaluate performance. As the membership functions for ANFIS, Gaussian curve (gaussmf), generalized bell-shaped (gbellmf) and triangular-shaped (trimf) were preferred separately with the reason that it is frequently preferred in the literature. After selecting the membership functions, simulations were made for 1000 epochs by changing the number of rules for inputs in the range of [2, 5] to find the most suitable ANFIS structure. The simulation results made with ANFIS to minimize C_{Df} are given in Table 2. As can be seen from Table 2, the most appropriate ANFIS structure was obtained in simulations made with the trimf membership function. Here, 3, 2

membership functions are defined for the input parameters l_f and d_f, respectively. Thus, an ANFIS model consisting of a total of 6 (3x2=6) rules has been determined as the most suitable structure.

Table 1. The most suitable structures and MSE values for ANN based simulations with single-layer and multi-layered

Network Structure	The Most Suitable ANN Structures and The Number of Neurons in Each Layer	Activation Function	Data Sets	MSE Values
Single-layer	2x10x1	Logsig (for hidden layer) Purelin (for output layer)	Training	3.000e-21
			Test	5.1888e-19
			Validation	7.9576e-17
	2x3x1	Tansig (for hidden layer) Purelin (for output layer)	Training	4.6607e-19
			Test	7.6077e-19
			Validation	8.4132e-18
Multi-layered	2x5x5x1	Logsig (for hidden layers) Purelin (for output layer)	Training	3.1882e-23
			Test	3.0479e-22
			Validation	5.1755e-19
	2x4x7x1	Tansig (for hidden layers) Purelin (for output layer)	Training	2.5529e-23
			Test	2.0007e-21
			Validation	3.5381e-17

Table 2. The most suitable number of rules for two inputs and MSE values for ANFIS based simulations

Membership Function	The Number of Rules for Two Inputs	Data Sets	MSE Values
Gaussmf	3x5=15	Training	9.5506e-17
		Test	4.1469e-16
	4x4=16	Training	5.4346e-17
		Test	6.9387e-17
Gbellmf	3x2=6	Training	8.8192e-16
		Test	1.0835e-15
	3x5=15	Training	1.1123e-15
		Test	9.9337e-15
Trimf	3x2=6	Training	5.5524e-19
		Test	7.8998e-19
	4x2=8	Training	5.6199e-20
		Test	5.8279e-12

Figure 1 compares the actual test data with the test outputs obtained with ANN and ANFIS. The test outputs are important in observing the performance of the proposed models. As can be seen from Figure-1, test outputs obtained with ANN and ANFIS compatible with the actual test outputs.

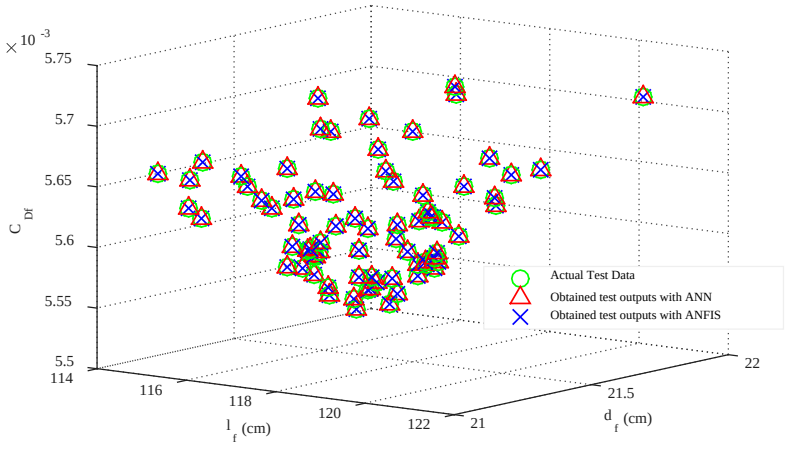

Figure 3. Comparison of actual test data with the test outputs obtained with ANN and ANFIS

4. CONCLUSION

The application of soft computing methods on aeronautics has also been preferred alongside of experimental methods in recent years. This study is a basic overview of the literature on soft computing methods on aeronautics. For this aim, it was examined many articles, conference papers, etc. In addition to the reviews, a simple application based on soft computing and demonstrating the effectiveness of this method has been realized. For this purpose, ANN and ANFIS based modeling has been presented in calculating minimum fuselage drag coefficient of ZANKA-II. When examining the results, very small error values were obtained and it was seen that minimum fuselage drag coefficient obtained with ANN or ANFIS were compatible with the actual outputs. The implementation of these proposed approaches is very simple and useful. In this study, the training data is produced by used the ABC algorithm to obtain the minimum fuselage drag coefficient. After an appropriate training process, ANN and ANFIS produce results without complicated iterative processes for new situations presented to them. In other words, ANN and ANFIS can calculate important parameters such as fuselage drag coefficient more simply than nonlinear equations that are difficult to realize electronically. When this calculation, instead of giving a direct result according to the purpose of the problem, optimum values can be produced by training with optimum data. These methods provide a simple, high precision and flexible alternative to designer application by quickly solving complex problems.

ACKNOWLEDGMENT

This work was supported by Research Fund of The Scientific and Technological Research Council of Turkey (TUBITAK) under Project Number: 214M282.

REFERENCES

[1]. A. Puri, “A Survey of Unmanned Aerial Vehicles (UAV) for Traffic Surveillance,” University of South Florida, Tech. Report, 2004.
[2]. S. C. Jay, R. Lawrence, K. Repasky, and C. Keith, “Invasive species mapping using low cost hyperspectral imagery,” in *ASPRS 2009 Annual Conference*, Baltimore, Maryland, 2009.
[3]. A. A. Dervishsefat, T. W. Kellenberger, and K. I. Itten, “Application of hyperspectral data for forest stand mapping,” in *Symposium on Geospatial Theory, Processing and Applications*, Ottowa, 2002.
[4]. L. Zongjian, “UAV for Mapping-Low Altitude Photogrammetric Survey,” *The International Archives of the Photogrammetry, Remote Sensing and Spatial Information Sciences*, Vol. XXXVII. Part B1, Beijing, 2008.
[5]. A. C. Watts, J. H. Perry, S. E. Smith, M. A. Burgess, B. E. Wilkinson, Z. Szantoi, P. G. Ifju, and H. F. Percival, “Small Unmanned Aircraft Systems for Low-Altitude Aerial Surveys,” *Journal of Wildlife Management*, vol. 74, no. 7, pp. 1614-1619, 2010.
[6]. G. W. Burgreen and O. Baysal, “Aerodynamic Shape Optimization Using Preconditioned Conjugate Gradient Methods,” *AIAA Journal*, vol. 32, no. 11, pp. 2145–2152, 1994.
[7]. J. Mohanga and O. Baysal, “Gradient-Based Aerodynamic Shape Optimization Using Alternating Direction Implicit Method,” *Journal of Aircraft*, vol. 34, no. 3, pp. 346–352, 1997.
[8]. G. Carrier, D. Destarac, A. Dumont, M. Méheut, I. Salah El Din, J. Peter, S. Ben Khelil, J. Brezillon, and M. Pestana, “Gradient-Based Aerodynamic Optimization with the elsA Software,” in *52nd Aerospace Sciences Meeting, AIAA SciTech Forum*, 2014.
[9]. D. D. Santis, M. J. Zahr, and C. Farhat, “Gradient based aerodynamic shape optimization using the FIVER embedded boundary method,” in *54th AIAA Aerospace Sciences Meeting, AIAA SciTech Forum*, 2016.
[10]. A. Jameson, “Aerodynamic Design via Control Theory,” *Journal of Scientific Computing*, vol. 3, no. 3, pp. 233-260, 1988.
[11]. I. H. Tuncer and M. Kaya, “Optimization of Flapping Airfoils for Maximum Thrust and Propulsive Efficiency,” *AIAA Journal*, vol. 43, no. 11, pp. 2329-2336, 2005.
[12]. A. Jameson and S. Kim, “Reduction of the Adjoint Gradient Formula for Aerodynamic Shape Optimization Problems,” *AIAA Journal*, vol. 41, no. 11, pp. 2114-2129, 2003.
[13]. S. Obayashi and T. Tsukahara, “Comparison of Optimization Algorithms for Aerodynamic Shape Design,” *AIAA Journal*, vol. 35, no. 8, pp. 1413-1415, 1997.
[14]. B. R. Jones, W. A. Crossley, and A. S. Lyrintzis, “Aerodynamic and Aeroacoustic Optimization of Rotorcraft Airfoils via a Parallel Genetic Algorithm,” *Journal of Aircraft*, vol. 37, no. 6, pp. 1088-1096, 2000.
[15]. M. M. Rai and N. K. Madavan, “Aerodynamic Design Using Neural Networks,” *AIAA Journal*, vol. 38, no. 1, pp. 173-182, 2000.
[16]. X. Wang, M. Damodaran, and S. L. Lee, “Inverse Transonic Airfoil Design Using Parallel Simulated Annealing and Computational Fluid Dynamics,” *AIAA Journal*, vol. 40, no. 4, pp. 791-794, 2002.
[17]. A. Hacioglu and I. Ozkol, “Transonic airfoil design and optimisation by using vibrational genetic algorithm,” *Aircraft Engineering and Aerospace Technology*, vol. 75, no. 4, pp. 350-357, 2003.
[18]. E. Vatandas and I. Ozkol, “Dynamic Mesh and Heuristic Algorithms for the Design of a Transonic Wing,” *Aircraft Engineering and Aerospace Technology*, vol. 78, vo. 1, pp. 39–44, 2006.
[19]. M. Santos, B. Mattos, and R. Girardi, “Aerodynamic Coefficient Prediction of Airfoils Using Neural Networks,” in *46th AIAA Aerospace Sciences Meeting and Exhibit, Aerospace Sciences Meetings*, 2008.
[20]. S. R. Reddy, H. Sobieczky, G. S. Dulikravic, and A. Abdoli, “Multi-Element Winglets: Multi-Objective Optimization of Aerodynamic Shapes,” *Journal of Aircraft*, vol. 53, no. 4, pp. 992-1000, 2016.

[21]. Ney Rafael Secco and Bento Silva de Mattos, "Artificial neural networks to predict aerodynamic coefficients of transport airplanes," *Aircraft Engineering and Aerospace Technology*, vol. 89, no. 2, pp. 211-230, 2017.
[22]. S. N. Skinner and H. Zare-Behtash, "State-of-the-art in aerodynamic shape optimisation methods," *Applied Soft Computing*, vol. 62, pp. 933-962, 2018.
[23]. Z. Lyu, Z. Xu, and J. R. R. A. Martins, "Benchmarking Optimization Algorithms for Wing Aerodynamic Design Optimization," in *The Eighth International Conference on Computational Fluid Dynamics (ICCFD8)*, 2014.
[24]. E. G. Talbi, *Metaheuristics: From Design to Implementation*, John Wiley & Sons, Inc., Hoboken, New Jersey, 2009.
[25]. L. A. Zadeh, *Fuzzy Logic, Neural Networks and Soft Computing*, In: Safety Evaluation Based on Identification Approaches Related to Time-Variant and Nonlinear Structures. Vieweg+Teubner Verlag, 1993.
[26]. L. A. Zadeh, "Fuzzy Logic, Neural Networks and Soft Computing," *Communications of the ACM*, vol. 37, no. 3, pp. 77-84, 1994.
[27]. A. Hacioglu, "Fast Evolutionary Algorithm for Airfoil Design via Neural Network," *AIAA Journal*, vol. 45, no. 9, pp. 2196-2203, 2007.
[28]. I. Kroo, "Aeronautical Applications of Evolutionary Design," *VKI Lecture Series on Optimization Methods & Tools for Multicriteria/Multidisciplinary Design*, 2004.
[29]. M. F. Nita, "Contributions to Aircraft Preliminary Design and Optimization," PhD. Thesis, Politehnica University of Bucharest, 2012.
[30]. S. Huang, L. Miller, and J. Steck, "An exploratory application of neural networks to airfoil design," in *32nd Aerospace Sciences Meeting and Exhibit, Aerospace Sciences Meetings*, Reno, NV, USA, 1994.
[31]. R. Eppler and D. M. Sommers, "A Computer Program for the Design and Analysis of Low-Speed Airfoils," NASA TM-80210, Technical Report, 1980.
[32]. M. Norgaard, C. C. Jorgensen, and J. C. Ross, "Neural Network Prediction of New Aircraft Design Coefficients," NASA Ames Research Center, Moffett Field, California 94035-1000, Technical Report 112197, 1997.
[33]. R. M. Greenman and K. R. Roth, "High-Lift Optimization Design Using Neural Networks on a Multi-Element Airfoil," *Journal of Fluids Engineering*, vol. 121, no. 2, pp. 434-440, 1999.
[34]. D. C. M. Tse and L. Y. Y. Chan, "Application of Micro Genetic Algorithms and Neural Networks for Airfoil Design Optimization," *RTO MP-035 Aerodynamic Design and Optimization of Flight Vehicles in a Concurrent Multi-Disciplinary Environment*, Canada, 1999.
[35]. B. R. Jones, W. A. Crossley, and A. S. Lyrintzis, "Aerodynamic and Aeroacoustic Optimization of Rotorcraft Airfoils via a Parallel Genetic Algorithm," *Journal of Aircraft*, vol. 37, no. 6, pp. 1088-1096, 2000.
[36]. T. Rajkumar and J. Bardina, "Prediction of Aerodynamic Coefficients using Neural Networks for Sparse Data," in *FLAIRS-02 Proceedings*, 2002.
[37]. A. Hacioglu, "Yapay Sinir Agi ile Guclendirilmis Genetik Algoritma ve Tersten Kanat Profili Dizayni," *Journal of Aeronautics and Space Technologies*, vol. 1, no. 3, pp. 1–7, 2004.
[38]. M. C. dos Santos, B. S. de Mattos, and R. da M. Girardi, "Aerodynamic Coefficient Prediction of Aircraft Using Neural Network," in *Proceedings of COBEM 2007, 19th International Congress of Mechanical Engineering*, Brasilia, 2007.
[39]. M. Drela, "XFOIL: An Analysis and Design System for Low Reynolds Number Airfoils," In: Mueller T.J. (eds) Low Reynolds Number Aerodynamics. Lecture Notes in Engineering, vol 54. Springer, Berlin, Heidelberg, 1989.
[40]. A. C. Marta, "Parametric Study of a Genetic Algorithm using a Aircraft Design Optimization Problem," Stanford University, Tech. Report, 2008.
[41]. S. Bagassi, F. Lucchi, and F. Persiani, "Aircraft Preliminary Design: Genetic Algorithm Based Optimization Method," in *29th Congress of The International Council of The Aeronautical Sciences*, Petersburg, Russia, 2014.
[42]. F. H. Gern, D. D. Vicroy, S. B. Mulani, Rupanshi Chhabra, R. K. Kapania, J. A. Schetz, D. Brown, and N. H. Princen, "Artificial Intelligence Based Control Power Optimization on Tailless Aircraft," NASA/TM–2014-218671, Technical Report, 2014.
[43]. W. P. Rodden, and E. H. Johnson, *MSC.Nastran Version 68, Aeroelastic Analysis User's Guide*, MSC Software, 2009.
[44]. I. Haryanto, MSK T. S. Utomo, N. Sinaga, C. A. Rosalia, and A. P. Putra, "Optimization Of Maximum Lift To Drag Ratio On Airfoil Design Based On Artificial Neural Network Utilizing Genetic Algorithm," *Applied Mechanics and Materials*, vol. 493, pp. 123-128, 2014.
[45]. P. Husek and K. Narenathreyas, "Aircraft longitudinal motion control based on Takagi–Sugeno fuzzy model," *Applied Soft Computing*, vol. 49, pp. 269-278, 2016.
[46]. Z. A. Ali, D. wang, and M. Aamir, "Fuzzy-Based Hybrid Control Algorithm for the Stabilization of a Tri-Rotor UAV," *Sensors*, vol. 16, no. 5, 2016.
[47]. I. N. Ibrahim and M. A. Al Akkad, "Exploiting an Intelligent Fuzzy-PID system in Nonlinear Aircraft Pitch Control," in *2016 International Siberian Conference on Control and Communications (SIBCON)*, Moscow, Russia, 2016.
[48]. A. G. Roy and N. K. Peyada, "Aircraft parameter estimation using Hybrid Neuro Fuzzy and Artificial Bee Colony optimization (HNFABC) algorithm," *Aerospace Science and Technology*, vol. 71, pp. 772-782, 2017.
[49]. O. Castillo and Leticia Cervantes, "Genetic Design of Optimal Type-1 and Type-2 Fuzzy Systems for Longitudinal Control of an Airplane," *Intelligent Automation & Soft Computing*, vol. 20, no. 2, pp. 213-227, 2014.
[50]. R. Wallach, B. S. Mattos, and R. da Mota Girardi, "Aerodynamic Coefficient Prediction of a General Transport Aircraft Using Neural Network," 25th International Congress of the Aeronautical Sciences, Hamburg, Germany, 2006.
[51]. M. Konar and A. Bagis, "Ucus Kontrol Sistemi Hiz Parametresinin Adaptif Ag Yapili Bulanik Sonuc Cikarim Sistemi Kullanilarak Belirlenmesi," *IEEE 17. Sinyal Isleme ve Iletisim Uygulamalari Kurultayi (SIU'2009)*, Antalya, TURKEY, 2009.
[52]. I. Turkmen and S. Arik, "A New Alternative Air Data Computation Method Based On Artificial Neural Networks," *Havacilik ve Uzay Teknolojileri Dergisi*, no. 1, pp. 21-29, 2016.
[53]. R.M. Namal Bandara and S. Gaspe, "Fuzzy Logic Controller Design for an Unmanned Aerial Vehicle," in *2016 IEEE International Conference on Information and Automation for Sustainability (ICIAfS)*, pp. 1-5, 2016.

[54]. Y. Wei, G. Q. Sun, and S. Wang, "A Novel Four Rotor Aircraft Adaptive Control Algorithm Based on the Optimized Fuzzy Neural Network," in *5th International Conference on Machinery, Materials and Computing Technology (ICMMCT 2017)*, Beijing, China, 2017.
[55]. A. G. Roy and N. K. Peyada, "Lateral Aircraft Parameter Estimation Using Neuro-Fuzzy and Genetic Algorithm Based Method," in IEEE Aerospace Conference, pp. 1-11, USA, 2017.
[56]. F. Boria, B. Stanford, S. Bowman, and P. Ifju, "Evolutionary Optimization of a Morphing Wing with Wind-Tunnel Hardware in the Loop," *AIAA Journal*, vol. 47, no. 2, pp. 399-409, 2009.
[57]. S. Haykin, *Neural Networks: A Comprehensive Foundation*, Prentice Hall PTR, USA, 1994.
[58]. D. R. Hush and B. G. Horne, "Progress in Supervised Neural Networks," *IEEE Signal Processing Magazine*, vol. 10, no. 1, pp. 8-39. 1993
[59]. E. Oztemel, *Yapay Sinir Aglari*, Istanbul, Papatya Yayincilik, 2003.
[60]. J. S. R. Jang, "ANFIS: Adaptive-Network Based Fuzzy Inference Systems," IEEE Trans. on Systems, Man, and Cybernetics, vol. 23, no. 3, pp. 665-685, 1993.
[61]. D. Karaboga, "An idea based on honey bee swarm for numerical optimization," Erciyes University, Engineering Faculty, Computer Engineering Department, Technical Report-TR06, 2005.
[62]. D. Karaboga and B. Basturk, "A powerful and efficient algorithm for numerical function optimization: artificial bee colony (ABC) algorithm," *Journal of Global Optimization*, vol. 39, no. 3, pp. 459–471, 2007.
[63]. M. Kantardzic, *Data Mining: Concepts, Models, Methods, and Algorithms*, John Wiley & Sons, 2003.
[64]. K.S. Narendra and K. Parthasarathy, "Identification and Control of Dynamic System Using Neural Networks," *IEEE Trans. On Neural Networks*, vol. 1, no. 1, pp. 4-27, 1990.
[65]. M. T. Hagan and M. Menjah, "Training feedforward networks with the Marquardt algorithm," *IEEE Trans. on Neural Networks*, vol. 5, no. 6, pp. 989-993, 1994.
[66]. K. Levenberg, "A method for the solution of certain nonlinear problems in least squares," *Quarterly Journal of Applied Mathmatics*, vol. 2, no. 2, pp. 164-168, 1944.
[67]. D.W. Marquardt, "An algorithm for least-squares estimation of nonlinear parameters," *Journal of the Society for Industrial and Applied Mathematics*, vol. 11, no. 2, pp. 431-441, 1963.

BIOGRAPHY

Seda ARIK received a BS in Electrical and Electronics Engineering from Erciyes University (2010) and a MS in Aviation from Erciyes University (2014) and also other MS in Electrical and Electronics Engineering from Erciyes University (2015). She is pursuing a PhD for Aviation at Erciyes University and is currently Research Assistant with the Faculty of Aeronautics and Astronautics, Aircraft Electricals and Electronics, Erciyes University. Her main research areas are artificial intelligence, optimization methods, chaos and electronic circuit applications, semiconductor materials.

ICENS 4TH INTERNATIONAL CONFERENCE ON ENGINEERING AND NATURAL SCIENCE
2-6 May 2018 KIEV UKRAINE

Adsorption of Methylene Blue on Mesoporous Nano Silica Obtained From Quartzite

Ersin Bahceci[1], Volkan Aylikci[1], Meryem Polat Gonullu[2], Hakan Ates[2], A.Gurhan Celik[3] and Tolga Depci[1,4]

Abstract

Due to rapid growing in the textile industry, in recent years, dyes contamination of surface and subsurface water sources has been major problem, since many dyes are not biodegradable and tend to accumulate in living organisms causing various diseases and disorders. In order to remove the toxic dyes from waste water, many researches on synthesis of porous materials have been conducted. In the present study, mesoporous nano amorphous silica was prepared using quartzite by leaching process to remove the Methylene Blue from waste water. The chemical structure, surface property and morphological properties of the nano amorphous silica were determined by XRD, IR, SEM, EDX, BET and zeta sizer. The characterization studies indicated that the high purity of nano silica was successfully obtained from quartzite with a remarkable surface area (348.56 m^2/g). In the adsorption studies, the adsorption isotherm data were better fitted by Langmuir model and the main adsorption mechanism between the dye and nano silica was defined as electrostatic interaction.

Keywords: Nano silica, Mesoporous, Methylene Blue, Adsorption

1. INTRODUCTION

Due to rapid industrialization, contamination of surface and subsurface water sources has been major problem. Especially, depending on the developments in the textile, rubber, paper, food and drug industry, dye-containing wastewater is become one of the main pollutant sources worldwide. As known that most of dyes are not biodegradable, since they resist breakdown by aerobic digestion, light, heat, and oxidizing agents [1], [2]. Methylene blue (MB) is a cationic and an aniline-based dye for the chemistry, biology, medical applications and textile industries and it is originally synthesized in 1876 [3]. Its long term exposure can cause detrimental effects for human health and tend to accumulate in living organisms causing various diseases and disorders, like vomiting, nausea, anemia and hypertension [4], [5].

There are various treatment methods, like chemical precipitation, biosorption, membrane technology, coagulation/flocculation, ozonation and adsorption for removal of dye [6]- [8] . Adsorption has been universally accepted as one of the dye removal process from wastewater and granular/powdered activated carbon as adsorbent is mostly preferred [9], [10]. However, the preparation and regeneration of activated carbons have the high cost and tedious procedures. This problem has prompted researchers to find new adsorbents which are especially cheap and locally abundant and naturally occurring materials. In the present study, mesoporous nano amorphous silica as a porous material was prepared using quartzite (obtained from ceramic industry) by leaching process to remove the Methylene Blue from waste water. The main composition of the quartzite is composed of the SiO_2 (93%) and Al_2O_3 (4.6%) and it is a metamorphic rock derived from sandstone [11], [12]. Due to the chemical composition, it is an ideal candidate for production of nano silica with high yield. In the literature, various methods such as sol–gel method [13], precipitation method [14] and low-temperature alkali extraction method [15] have been used to synthesize the nano silica. In this study, the low-temperature alkali extraction method was preferred due to its simplicity, eco-friendly method and giving mesoporous product with narrow size. Using this method, nano silica is obtained from fly ash [16], rice-husk ash [17], biomass [18] and local silica rich ore, like pyrophyllite and pumice [19], [20]. The nano silica is used in the waste water treatment

[1] *Iskenderun Technical University, Dept. of. Metallurgical and Materials Engineering, 31200 Hatay, Turkey*

[2] *Gazi University, Faculty of Technology, Dept. of. Metallurgical and Materials Engineering, Ankara, Turkey*

[3] *Giresun University, Dept. of. Civil Engineering, Giresun, Turkey*

[4] *Corresponding author: Iskenderun Technical University, Dept. of. Engineering Science, 31200 Hatay, Turkey.* tolga.depci@iste.edu.tr

[21] – [24], but it is the first time, the synthesized mesoporous nano silica was used for removing the Methylene blue from water.

2. MATERIALS AND METHOD

2.1. Materials

Methylene Blue (MB) was purchased from MERCK (101458, CI = 52015). The stock solution of MB was prepared dissolving the dye powder in deionized water and desired dye concentrations (20 – 50 mg/L) were obtained using it by successive dilutions. The quartzite as a source was brought from the ceramic industry in Turkey. After sampling operation, the ore was crushed, ground and sieve to obtain the particle size of quartzite as – 180 μm (80–85 mass% passing). NaOH, H_2SO_4 and HCl (from Merck) were used as chemicals to adjust the leaching process and also pH of the solutions.

2.2. Preparation of the Amorphous Silica

In this section, the experimental procedure which was suggested by Mourhly et al., [15] was based on and some modifications were done by us [19]. 5 gr of quartzite was put into 500 ml 3 neck flasks and 300 ml of NaOH solutions (3 M) was poured into the flask. The system was placed on the magnetic stirrer with heating mantle and heated at 100 °C for 12 hours to dissolve the silica and produce sodium silicate. In order to prevent the water from evaporating, the reflux condenser was used. 12 hour later, the solid and liquid part was separated by centrifuge and filtration. Depending on the pH of the solution and leaching process, the siliceous part passed into the liquid and the liquid was titrated with H_2SO_4 (5M) until obtaining the silica gel which was occurred at pH 7. The obtained gel form was kept at room temperature for one day and then filtered using filter paper and washed several times to remove the sulphate salt. The solid was dried in electrical furnace at 80°C for 24 hours. In order to remove the soluble minerals Al and K at high pH values, the obtained solid part was leached using hydrochloric acid HCl solution (1M) at 110°C for three hours. Finally, after the separation of the solid part, it was washed several times and dried at 110°C overnight and then calcinated at 800 °C for two hours. All experiments were duplicated.

2.3. Characterization

The chemical composition and morphological properties of the quartzsite and the obtained nano amorphous silica were determined by XRD (Rigaku Miniflex 600 with Cu Kα), FTIR (Perkin Elmer Spectrum One FTIR-ATR), SEM (Zeiss, Supra55), EDX (Leo Evo-40x VP Electron Microscope), BET (A Tri Star 3000, Micromeritics, USA) and zeta potential (PMalvern Lambda 850 UV/Vis). The spectrophotometric determination of methylene blue concentration in the solution was done using UV-VIS spectrophotometer (Malvern).

2.4. Adsorption experiments

Methylene Blue adsorption study was carried out in routine manner, following by batch technique. The dye adsorption onto the amorphous nano silica with respect to initial dye concentrations (10 – 50 mg/L) was determined at natural pH of the dye solution at 60 minutes. The amount of dye q (mg/g.) adsorbed on the nano silica was calculated using the following mass balance equation (1).

$$q = (C_0 - C) * V / W \quad (1)$$

Where, C_0 (mg/l) is the initial dye concentration and C(mg/l) is unadsorbed dye concentration in solution at time t, V (L) and W (g) is the volume of the solution and the weight of the dry nano silica used respectively. In the present study, adsorption isotherms, Langmuir [25] and Freundlich [26] models, were explained using non-linear method which was determined using the solver add-in with Microsoft's spreadsheet, Microsoft Excel. The models equations(Eq. 2-3) are given in below:

$$q_e = \frac{(Q_0 b C_e)}{(1 + b C_e)} \quad (2)$$

$$q_e = k_f (C_e)^{1/n} \quad (3)$$

C_e is the equilibrium concentration (mg/L), and qe is the adsorption capacity (mg/g). The Langmuir constants are b (L/mg) and the theoretical monolayer capacity, Q_0 (mg/g). The Freundlich constants are the rate constant k_f (L/g) and the dimensionless heterogeneity factor, 1/n.

3. RESULTS AND DISCUSSION

3.1. Characterization of the Ore and Amorphous Silica

The crystal structure, the functional groups and the morphologies of the quartzite and the amorphous nano silica were determined by XRD, IR and SEM.. Figure 1-a shows that the main composition of the quartzite is identified as an amorphous structure and consisted of almost completely of the mineral quartz (more than 90 %). It is very compatible with the literature data [11]. The XRD pattern of the silica indicates the strong broad hump which is recorded between 15 and 30° at 2θ values [15], [27], suggesting the completely amorphous silica structure.

The functional groups of the quartzite and nano silica are presented in Figure 1-b, showing that the quartzite and the amorphous silica have nearly same IR spectra. The wide peak which is observed between 3600 and 3450 cm^{-1} on the spectra can be attributed to the silanol groups (Si-OH) [28] and the sharp and insensitive peaks at 1021 cm^{-1} and 752 cm^{-1} associated with the stretching-vibrations of Si-O-Si [29]. The IR spectra confirm the XRD patterns, which show the predominance of the silica structure in the composition of both compounds.

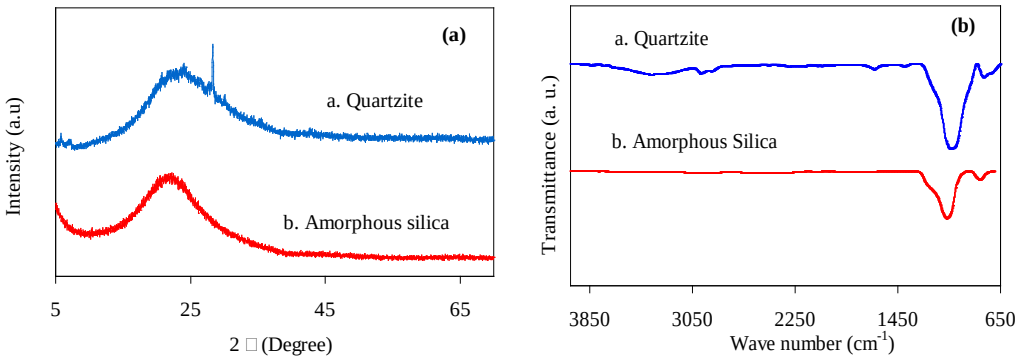

Figure 4. The powder X-ray diffraction patterns (a) and IR spectrum (b) of the quartzite and amorphous silica

The BET surface area of the amorphous nano silica is determined as 348.56 m2/g and the pore size distribution (Figure 2-a) shows the wide range mesoporous structure. The pH of solutions was adjusted manually to the desired value by dropwise addition of dilute NaOH (0.5%) or HCl (0.1 N) and three zeta potential measurements were done at each pH value and the average value was taken. The zeta potential variation of amorphous nano silica was estimated considering the pH of solution and this variation is given in Figure 2-b. The zeta potential value increases in the negative direction with increasing pH. Dougherty et al. [30] declare that nanoparticles will remain in suspension at the higher magnitude of the zeta potential otherwise they will aggregate. The zeta potential results indicate that the amorphous silica nanoparticles are stable due to the electrostatic repulsion.

The SEM image of the quartzite (Figure 3-a.) showed the irregular shape of the quartz grains which is the main structure of the quartzite [12]. The SEM images confirmed the XRD pattern and IR spectrum of the quartzite. The SEM image of the amorphous silica (Figure 3-b.) shows the nearly same particle size glassy form regular shape particles. The particle sizes of extracted amorphous and highly pure silica are a nanometre scale. The purity of the amorphous silica was checked using SEM mapping options and also EDX. The mapping (Figure 3-c and d) shows that the main structure of the amorphous silica occurs from silica and oxygen. The EDX result proves the mapping and also XRD, IR analysis and SEM image, giving that the composition is consisted of 99 % silisium oxide.

The characterization studies show that the amorphous nano size mesoporous silica can be obtained easily and cheaply by the alkaline method with high purity.

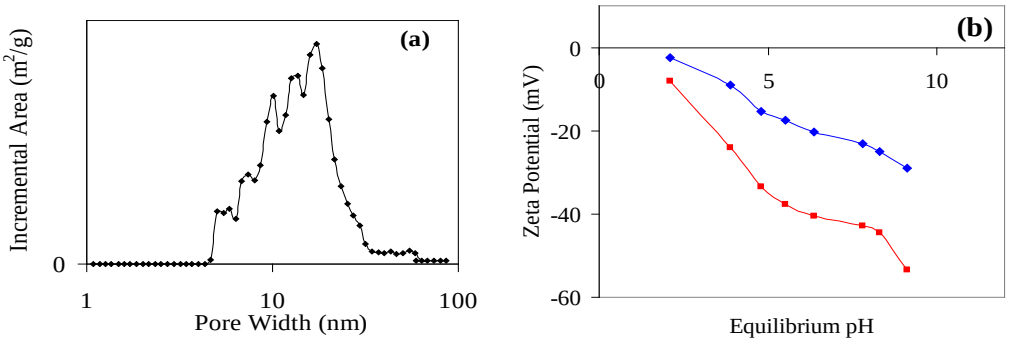

Figure 5. Pore size distribution and zeta potential of the nano amorphous silica

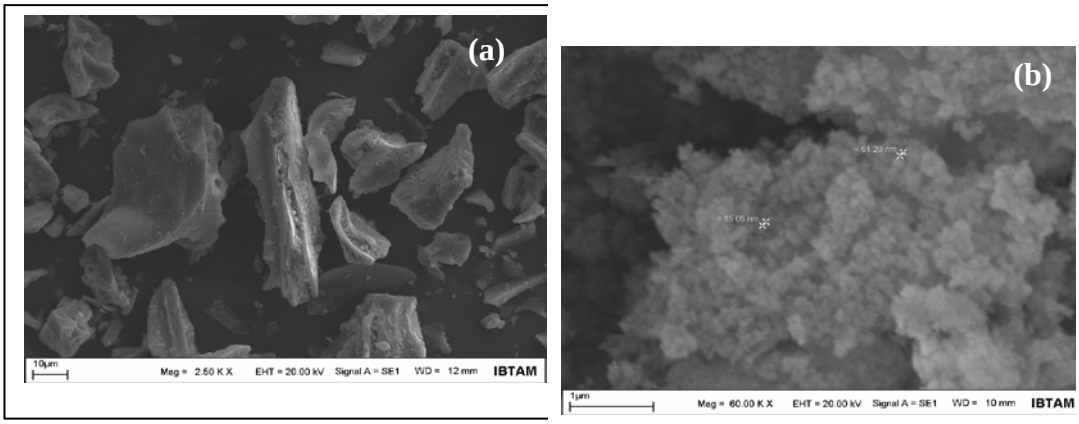

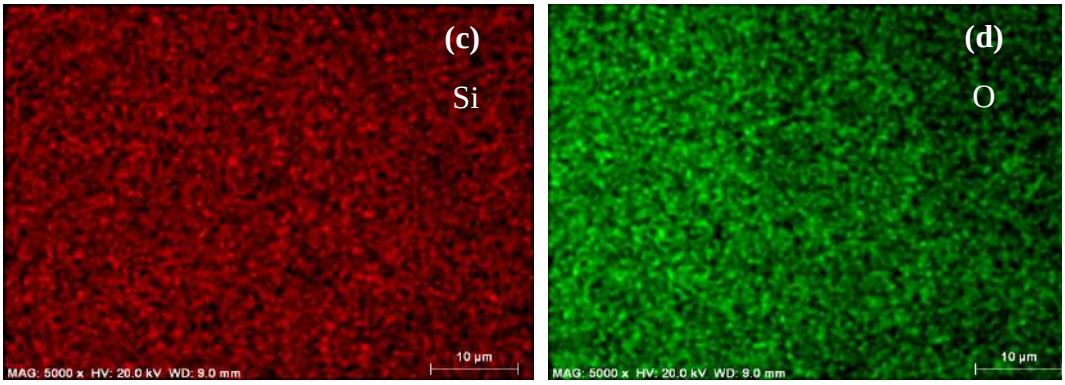

Figure 3. SEM image of the quartzite (a) and amorphous silica (b) and mapping shows the Silica (c) and Oxygen concentration (d)

3.2. Adsorption of Methylene Blue

Adsorption mechanism of the dye on the amorphous mesoporous nano silica is tried to explain and investigate using the Langmuir and Freundlich isotherms at room temperature. The plots of non-linear isotherms Langmuir and Freundlich models are represented in Figure 4- a and b, respectively. The obtained results show that the both models can be described the adsorption mechanism. However, Langmuir model has highest R^2 value and also lowest level of the values of error function in terms of the nonlinear Chi-square test (X^2), meaning that the dye covers the monolayer the silica surface and each dye molecules has equal sorption activation energy. The maximum monolayer adsorption capacity was found as 21.45 mg/g. In addition, aforementioned, the zeta (ζ) potential shows that the surface charge of the amorphous silica is negative charge. As known that Methylene Blue is a cationic dye and it carries a positive charge in their molecule [1]. It is expected that due to different surface charge, the positive charge dye molecules are attracted to the negative surface of the mesoporous amorphous silica. This behaviour also affects the adsorption process.

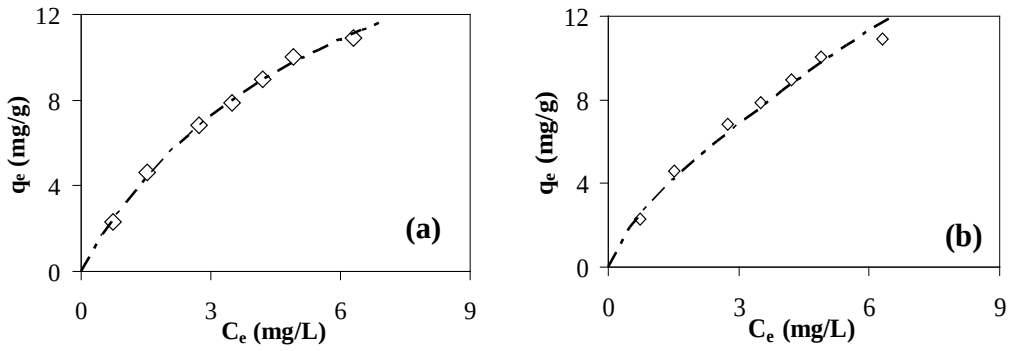

Figure 4. The plots of non-linear isotherm Langmuir and Freundlich models for the removal of the Methylene blue

4. CONCLUSION

In the present study, using the alkaline leaching process, the amorphous silica was extracted from the quartzite with high purity (99 % silica). The BET surface area was determined as 348.56 m^2/g with the wide range

mesoporous structure. The result of the zeta potential of the mesoporous amorphous nano silica indicates the negative surface charge. It means that the positive charge dye molecules are attracted to the silica surface, showing the major role of the surface charge in the basic dye adsorption. In terms of the adsorption isotherm models, the adsorption of the dye on the amorphous silica is is quite well consistent with the Langmuir models. The monolayer adsorption capacity was calculated as 21.45 mg/g. It can be said that the extracted amorphous mesoporous nano silica is a promising adsorbents for removal of the basic dye from wastewater. On the other hand, considering the high purity and particle size, the extracted silica may be also used for catalytic applications, and high tech ceramic synthesis process

REFERENCES

[1]. Sanjay K. Sharma, Ed. *Green Chemistry for Dyes Removal from Waste Water: Research Trends and Applications*: *Dye Adsorption on Expanding Three-Layer Clays*, ISBN: 978-1-118-72099-8, 496 pages, April 2015
[2]. Q. Sun and L. Yang, "The adsorption of basic dyes from aqueous solution on modified peat-resin particle," *Water Res.* vol. 37(7), pp. 1535-1544, Apr. 2003.
[3]. H. Berneth, *Azine dyes*. In: Ullmann's Encyclopedia of Industrial Chemistry. Weinheim, Germany: Wiley-VCH Verlag GmbH & Co. KGaA, pp. 475–514, 2008.
[4]. K.Y. Foo, "Preparation, characterization and evaluation of adsorptive properties of orange peel based activated carbon via microwave induced K_2CO_3 activation," *Bioresour. Technol.* vol. 104, pp. 679–686, 2012.
[5]. B.H. Hameed, "Spent tea leaves: a new non-conventional and low-cost adsorbent for removal of basic dye from aqueous solutions," *J. Hazard. Mater.* vol. 161, pp. 753–759, 2009.
[6]. A. Kausar, M. Iqbal, A. Javed, K. Aftab, Z.H. Nazli, H. N. Bhatti and S. Nouren, "Dyes adsorption using clay and modified clay: A review" *J Mol. Liq.* vol 256, 15, pp. 395-407, Apr. 2018.
[7]. A. M. Ghaedi and A. Vafaei , "Applications of artificial neural networks for adsorption removal of dyes from aqueous solution: A review,".Cis(2017), doi: 10.1016/j.cis.2017.04.015, *Adv. Colloid Interface Sci.(*Article in press)
[8]. M. T. Yagub, T. K.S. Sen, S. Afroze and H.M. Ang, "Dye and its removal from aqueous solution by adsorption: A review," *Adv. Colloid Interface Sci.* vol. 209, pp. 172-184, July 2014.
[9]. M. Goswami and P. Phukan, "Enhanced adsorption of cationic dyes using sulfonic acid modified activated carbon" *J Environ Chem Eng*, vol.5 (4), pp. 3508-3517, Aug. 2017
[10]. A. Murray and B. Ormeci. "Competitive effects of humic acid and wastewater on adsorption of Methylene Blue dye by activated carbon and non-imprinted polymers," *J. Environ. Sci.* vol. 66 pp. 310-317, Apr. 2018
[11]. S. Mishra, T. Chakraborty and V. Matsagar, "Dynamic Characterization of imalayan Quartzite Using SHPB," *Procedia Eng.*, vol 191, pp. 2 – 9, 2017.
[12]. B. A. Blomme, P. Degr, P.Vanpeer and J. Elsen, "The characterization of sedimentary quartzite artefacts from Mesolithic sites, *Geol. Belgica*, vol. 15/3, pp. 193-199, 2012.
[13]. W. Fan and L. Gao, "Synthesis of silica hollow spheres assisted by ultrasound," *J. Colloid Interface Sci.*vol. 297' pp. 157–160, 2006.
[14]. M. Monshizadeh, M. Rajabi, M.H. Ahmadi and V. Mohammadi, "Synthesis and characterization of nano SiO2 from rice husk ash by Precipitation method," *3rd National Conference on Modern Researches in Chemistry and Chemical Engineering*, 2015
[15]. A. Mourhly, M. Khachani, A. El Hamidi, M. Kacimi, M. Halim, and S. Arsalane, "The Synthesis and Characterization of Low-cost Mesoporous Silica SiO_2 from Local Pumice Rock" *Nanomater. Nanotechnol*, pp. 1-7, 2015
[16]. N. Moreno, X. Querol, F. Plana, J.M. Andres, M. Janssen and H. Nugteren,. 'Pure zeolite synthesis from silica extracted from coal fly ashes," *J. Chem. Technol. Biotechnol.* Vol. 77, pp. 274–279, 2002.
[17]. R. Patil, R. Dongre and J. Meshram, "Preparation of silica powder from rice husk," *J. Appl. Chem.* Vol. 27, pp. 26–29, 2014.
[18]. F. Adam, T.S. Chew and J. Andas, "A simple template-free sol-gel synthesis of spherical nanosilica from agricultural biomass,". J. Sol-Gel Sci. Technol. Vol, 59, pp. 580–583 2011.
[19]. M. Sarikaya, T. Depci, R. Aydogmus, A. Yucel and N. Kizilkaya, "Production of nano amorphous SiO_2 from Malatya pyrophyllite," *Earth Env. Sci.* 44 052004, 2016.
[20]. M. Sarikaya, M. D. Turan, R. Aydogmus, A. Yucel, N. Kizilkaya and T. Depci, "Extraction of Meso-pores Amorphous SiO_2 from Van Pumice" *Curr. Phys. Chem.*Vol. 7 , Issue 4 , 2017
[21]. V.B. Arce, R.M. Gargarello, F. Ortega, V. Romañano and M., Mizrahi, "EXAFS and DFT study of the cadmium and lead adsorption on modified silica nanoparticles," *Spectrochim. Acta A* Vol 151, pp. 156–163, 2015
[22]. X. Gao, Q.L. Yu and H.J.H., Brouwers, "Characterization of alkali activated slag–fly ash blends containing nano-silica," *Const. Buil. Mater.* Vol. 98, pp. 397–406, 2015.
[23]. A. Farooq, R. Al-Jowderb, R. Narayanaswamy, M. Azzawi, P. Roche and D.E. Whitehead, "Gas detection using quenching fluorescence of dye-immobilised silica nanoparticles," *Sens. Actuators, B,* vol. 183, pp. 230– 238, 2013.
[24]. M. M. Hessien, M. M. Rashad, R. R. Zaky, E.A. Abdel-Aal and K.A. El-Barawy, "Controlling the synthesis conditions for silica nanosphere from semi-burned rice straw," *Mater. Sci. Eng., B,* vol. 162, pp. 14–21, 2009.
[25]. I. Langmuir, "The adsorption of gases on plane surfaces of glass, mica and platinum," *J. Am. Chem. Soc.* Vol. 40, pp. 1361–1403, 1918.
[26]. H. Freundlich, "Adsorption in solution," *Phys. Chem. Soc.* Vol. 40, pp. 1361–1368, 1906.
[27]. G.Li, J. Zeng, J. Luo, M. Liu, T. Jiang and G. Qiu, "Thermal transformation of pyrophyllite and alkali dissolution behavior of silicon" *App. Clay Sci.* vol. 99, pp. 282–288, 2014.
[28]. J. Yang and E. Wang, "Reaction of water on silica surfaces," *Curr. Opin. Solid State* Mater. Sci. vol. 10, pp. 33-39, 2006.

[29]. Y. Jemmal, N. Zaria, and M. Maaroufi, "Experimental characterization of siliceous rocks to be used as filler materials for air-rock packed beds thermal energy storage systems in concentrated solar power plants," *Sol. Energy Mater Sol. Cells*, vol 171, pp. 33–42, 2017.

[30]. G.M. Dougherty, K.A. Rose, JB. Tok, SS. Pannu, FY. Chuang, MY. Sha, G. Chakarova and SG. Penn, "The zeta potential of surface –functionalized metallic nanorod particles in aqueous solution," *Electrophoresis*, vol. 29, pp.1131 – 1139, 2008.

ICENS 4TH INTERNATIONAL CONFERENCE ON ENGINEERING AND NATURAL SCIENCE
2 - 6 May 2018 KIEV UKRAINE

Post-Seismic Surface Deformation of 2017 Mexico Earthquakes

Fikret Dogru[1], Oya Pamukcu[2], Ayca Cirmik[2,]*

Abstract

On June 14 and 22, 2017, earthquakes with magnitudes 6.9 and 6.8 respectively hit Mexico City and caused the death of more than 50 people. Also on September 8, 19 and 23, 2017, earthquakes with magnitudes 8.2, 7.1 and 6.1 respectively occurred in the Mexico City and caused the death of more than 300 people according to initial reports. In this process, about 800 aftershocks have occurred. In this study, it was aimed to determine the surface deformations caused by these earthquakes using Sentinel-1B SAR data. In this context, 32 SAR data those dates between 10 October 2016 and 17 October 2017 were used as slaves. The SAR data for the day of October 28, 2016, proposed by the Optimal InSAR Master Selection module, was selected as the master. As a result of the evaluations, a DEM error between -0.02 and 0.02 rad/m was observed. In addition, reference Line of Sight (LOS) deformation values of 20 to -30 mm/year were obtained. In the unwrapped phase results, phase values in the interferograms were observed to decrease to 7.7 rad values after the earthquake.

Keywords: SAR, InSAR, Sentinel, Mexico, master, earthquake.

1. INTRODUCTION

The interferometric SAR techniques (InSAR) use the information contained in the phase of two SAR images. The InSAR phase is sensitive to the terrain topography and to relative changes in elevation occurring between two SAR antenna passes over the same area. If the terrain topography is known, i.e. a DEM (Digital Elevation Model) of the imaged scene is available, the corresponding phase component can be subtracted from the InSAR phase, leaving the component due to the terrain surface deformation. This is the so-called differential InSAR technique (DInSAR) [1].

Since the first description of the technique [2], many InSAR applications have been developed. The most important results have been obtained in a different branch of geophysics: ice and glacier dynamics [4], [3]; earthquakes [6], [5]; volcanoes [7], [8]; and landslides [9], [10]. Besides the geophysical applications, many studies have been conducted in urban areas [11], [12], [13], [14], [15], [16].

2. METHODS

2.1. Interferometry

InSAR techniques consist of the combination of two SAR SLC images of the same area acquired from slightly different positions, see Fig. 1.

[1] fikretjfm@gmail.com, *Ataturk University, Oltu Earth Sciences Faculty, Geophysical Engineering, 25400, Oltu, Erzurum*
[2] oya.pamukcu@deu.edu.tr, *Dokuz Eylul University, Engineering Faculty, Geophysical Engineering, 35400, Buca, Izmir*
ayca.yurdakul@deu.edu.tr, *Dokuz Eylul University, Engineering Faculty, Geophysical Engineering, 35400, Buca, Izmir*
[*]*Corresponding author:* ayca.yurdakul@deu.edu.tr

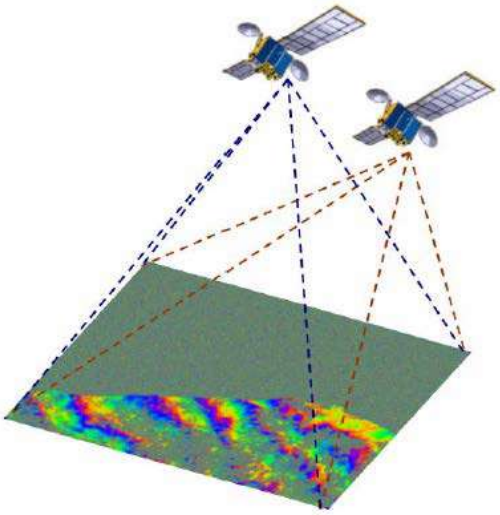

Figure 1. Acquisition of two SAR SLC images with different positions [17].

The result of this combination is a new image known as an interferogram, whose phase component is formed by the following terms:

$$\Delta\Phi_{Int} = \Phi_{Topo} + \Phi_{Mov} + \Phi_{Atm} + \Phi_{Noise} \quad (1)$$

where Φ_{Topo} is the term related with topography, Φ_{Mov} is the phase component of terrain deformation, Φ_{Atm} is the noise component caused by different atmospheric conditions for both SAR acquisitions and Φ_{Noise} is the thermal noise [17].

The European Space Agency (ESA) supplied a Sentinel-1B ASAR dataset on Mexico area including 33 descending pass single look complex (SLC) images. The data span 28th September 2016 to 17th October 2017. 28th September 2016 SLC data was selected as a master and the others are as a slave. The more information about SLCs are shown in table 1. The SLC data were processed by using the *Sentinel* Application Platform (SNAP) [18] and Stanford Method for Persistent Scatterers (StaMPS) [19] programs together.

Table 1. Sensor date, orbit and track number of the SAR images selected for this study.

Sensor	Mst/Slv	Date	Track	Orbit	Number of days from the first date
Sentinel-1B	Master	28.9.2016	143	2269	**0**
Sentinel-1B	Slave	10.10.2016	143	2444	**12**
Sentinel-1B	Slave	22.10.2016	143	2619	**24**
Sentinel-1B	Slave	3.11.2016	143	2794	**36**
Sentinel-1B	Slave	15.11.2016	143	2969	**48**
Sentinel-1B	Slave	27.11.2016	143	3144	**60**
Sentinel-1B	Slave	9.12.2016	143	3319	**72**
Sentinel-1B	Slave	21.12.2016	143	3494	**84**
Sentinel-1B	Slave	2.1.2017	143	3669	**96**
Sentinel-1B	Slave	14.1.2017	143	3844	**108**
Sentinel-1B	Slave	26.1.2017	143	4019	**120**
Sentinel-1B	Slave	7.2.2017	143	4194	**132**
Sentinel-1B	Slave	19.2.2017	143	4369	**144**

Sentinel-1B	Slave	3.3.2017	143	4544	**156**
Sentinel-1B	Slave	15.3.2017	143	4719	**168**
Sentinel-1B	Slave	27.3.2017	143	4894	**180**
Sentinel-1B	Slave	8.4.2017	143	5069	**192**
Sentinel-1B	Slave	20.4.2017	143	5244	**204**
Sentinel-1B	Slave	2.5.2017	143	5419	**216**
Sentinel-1B	Slave	14.5.2017	143	5594	**228**
Sentinel-1B	Slave	26.5.2017	143	5769	**240**
Sentinel-1B	Slave	7.6.2017	143	5944	**252**
Sentinel-1B	Slave	19.6.2017	143	6119	**264**
Sentinel-1B	Slave	1.7.2017	143	6294	**276**
Sentinel-1B	Slave	13.7.2017	143	6469	**288**
Sentinel-1B	Slave	25.7.2017	143	6644	**300**
Sentinel-1B	Slave	6.8.2017	143	6819	**312**
Sentinel-1B	Slave	18.8.2017	143	6994	**324**
Sentinel-1B	Slave	30.8.2017	143	7169	**336**
Sentinel-1B	Slave	11.9.2017	143	7344	**348**
Sentinel-1B	Slave	23.9.2017	143	7519	**360**
Sentinel-1B	Slave	5.10.2017	143	7694	**372**
Sentinel-1B	Slave	17.10.2017	143	7869	**384**

3. RESULTS

In this study, InSAR applications were applied on all 33 SAR SLCs (VV components) by using SNAP program. The study area (Figure 2) is so active in terms of earthquake and there are 5 big earthquakes from 6th June 2017 to 9th September 2017. On 6th June, 6.9 Mw, on 22th June 6.8 Mw, on 8th September, 8.2 Mw, on 19th September, 7.1 Mw and on 23th September, 6.1 Mw earthquakes occurred. The flowchart of SNAP processing steps is shown in Figure 3. After the SNAP PSI exporting StaMPS program was used and the results are shown in Figure 4 to 7.

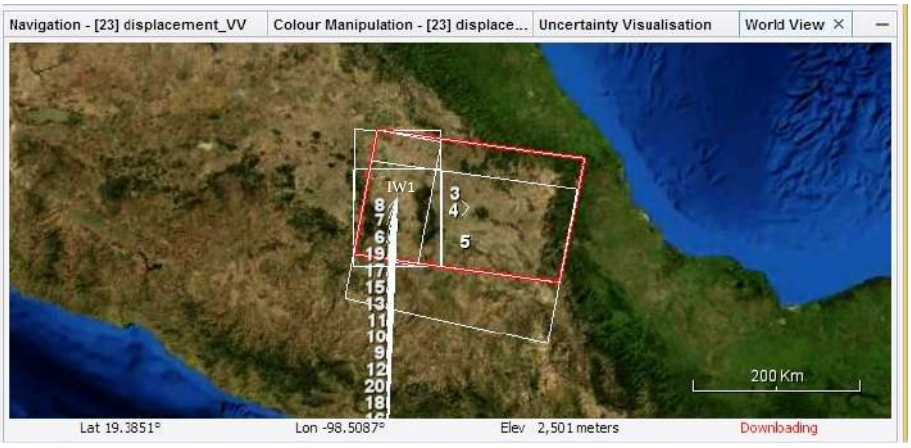

Figure 2. The location of selected two of the SLCs (IW1 data selected in this figure but IW2 middle swath was selected for PSI processing) (Screenshot was taken from SNAP).

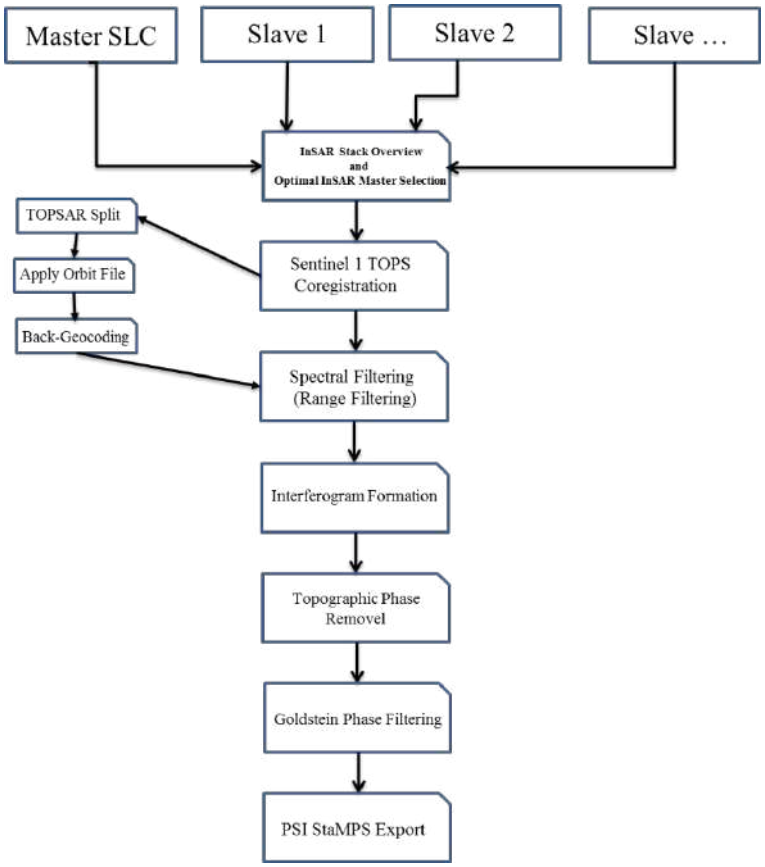

Figure 3. The flowchart of SNAP PSI Export steps.

The DEM error values change between 0.0271 to -0.0209 rad/m (Figure 4). The error was subtracted when calculating mean LOS velocity values (MLV). The MLV values also change between 20 to -30 mm/year (Figure 5). The SAR SLCs are VV component and the MLV negative values show reference subsidence areas. Also, positive values in MLV results indicate the uphill areas after big earthquakes. In figure 6 and 7, the deformation and displacements are clearly shown after the earthquakes. Especially, after the 6.9 Mw earthquake that was occurred on 14th June 2017, and 7.1 Mw earthquake that was occurred on 19th September 2017, the mass displacements and deformation are higher than the other earthquakes. 8.2 Mw earthquake which was occurred on 8th September 2017, its epicentre is the farthest distance to study area and occurred in the sea, thus we think that its effect isn't recognized the most for this reason.

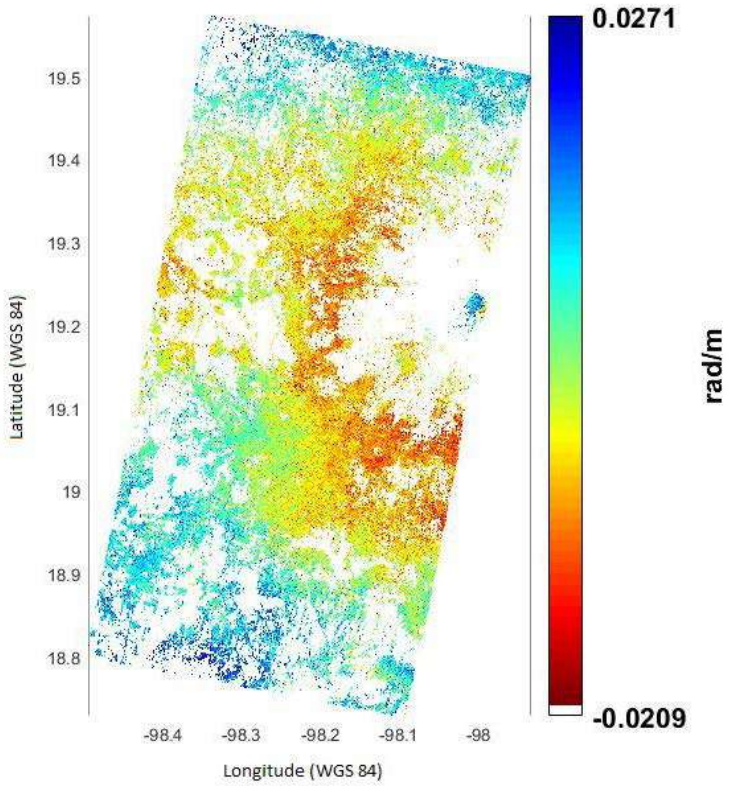

Figure 4. The result of DEM error.

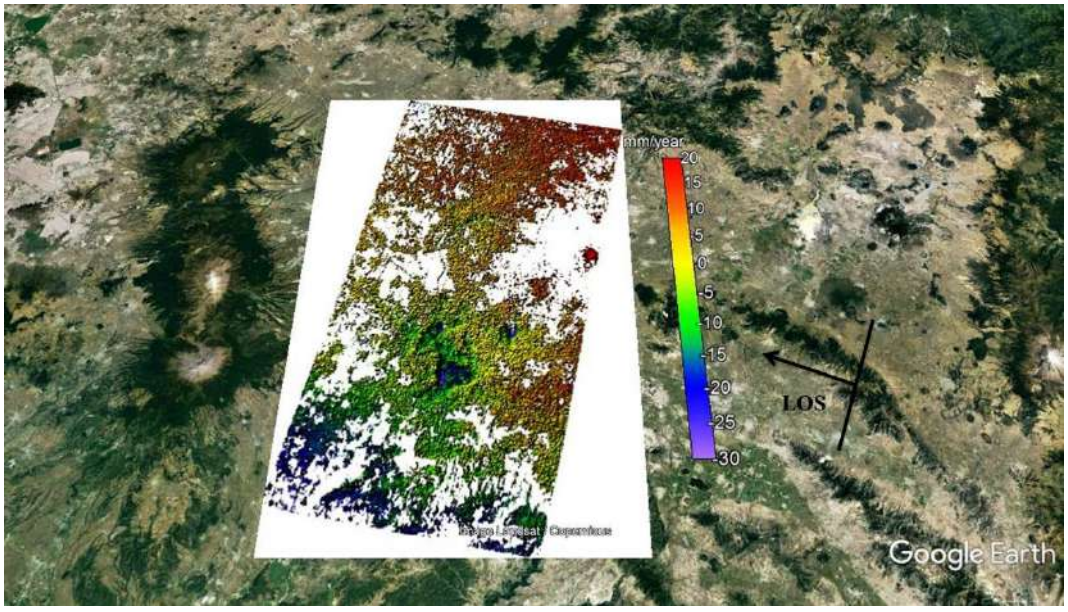

Figure 5. The result of mean LOS velocity rate.

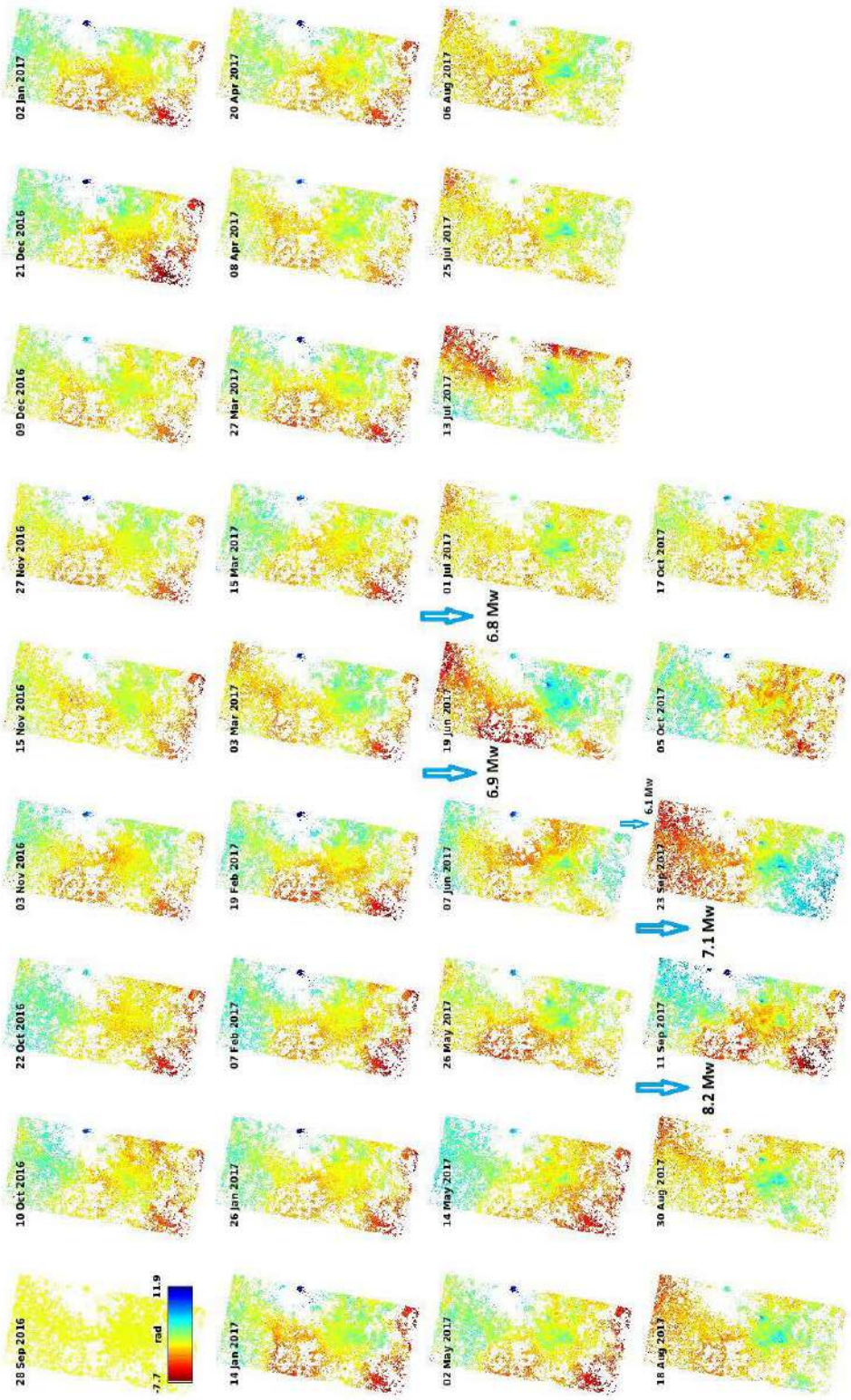

Figure 6. The unwrapped phase results of 32 SLC data according to master data.

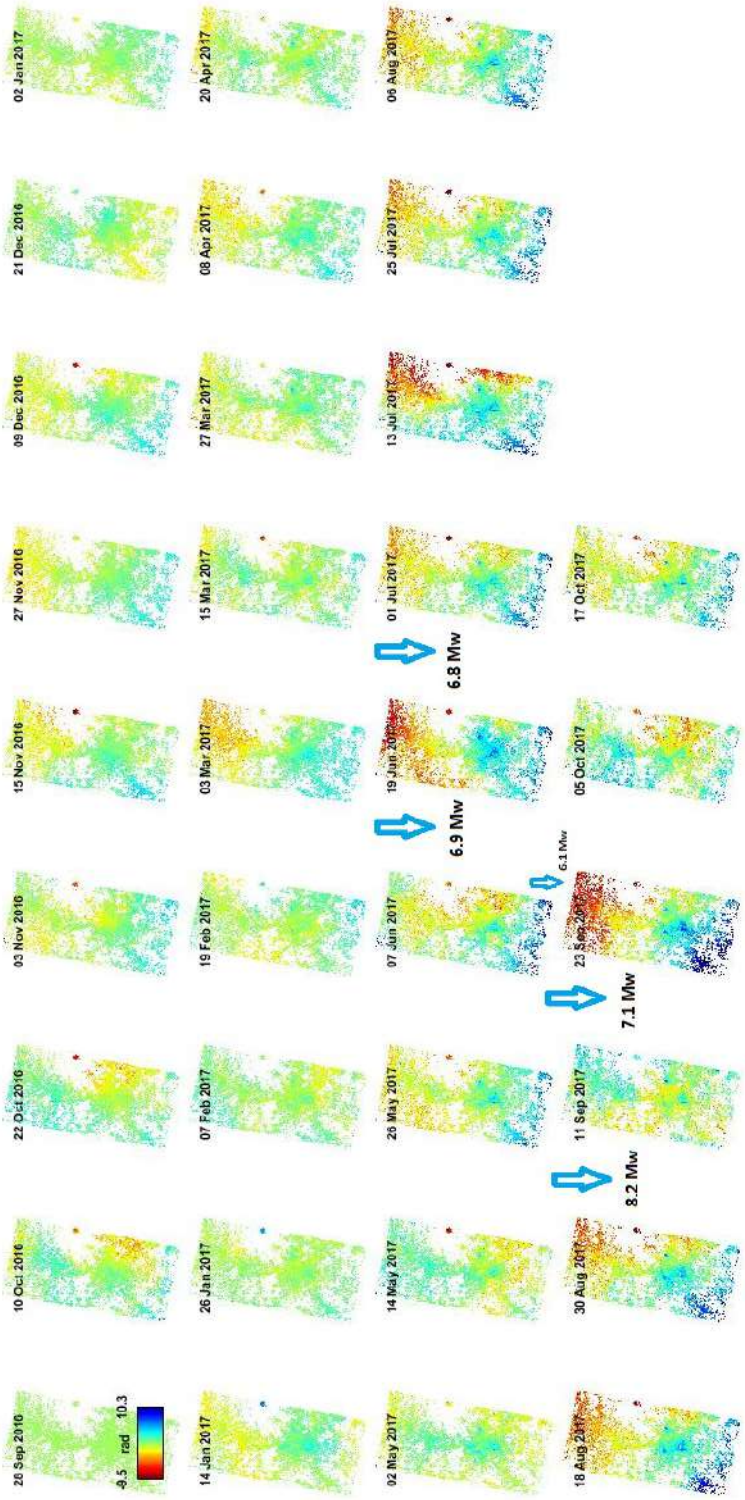

Figure 7. The unwrapped phase results minus dem error of 32 SLC data according to master data.

REFERENCES

[1]. M., Crosetto, A., Arnaud, J., Duro, E., Biescas, and M., Agudo, Deformation monitoring using remotely sensed radar interferometric data. In Proc., 11th FIG Symposium on Deformation Measurements, Santorini, 2003.
[2]. A.K., Gabriel, R.M., Goldstein and H.A., Zebker, Mapping small elevation changes over large areas: differential radar interferometry. J. of Geophys. Research, 94(B7), 9183-9191, 1989.
[3]. R.M., Goldstein, H., Englehardt, B., Kamb and R.M., Frolich, Satellite radar interferometry for monitoring ice sheet motion: application to an Antarctic ice stream. Science, 262, 1525-1530, 1993.
[4]. R., Kwok, and M.A., Fahnestock, Ice sheet motion and topography from radar interferometry. IEEE Transactions on Geoscience and Remote Sensing, 34(1), 189-200, 1996.
[5]. D., Massonnet, M., Rossi, C., Carmona, F., Adragna, G., Peltzer, K., Feigl and T., Rabaute, The displacement field of the Landers earthquake mapped by radar interferometry. Nature, 364, 138-142, 1993.
[6]. D., Massonnet, K., Feigl, M., Rossi and F., Adragna, Radar interferometry mapping of deformation in the year after the Landers earthquake. Nature, 369, 227-230, 1994.
[7]. D., Massonnet, P., Briole and A., Arnaud, Deflation of Mount Etna monitored by spaceborne radar interferometry. Nature, 375, 567-570, 1995.
[8]. F., Amelung, S., Jonson, H.A., Zebker and P., Segall, Widespread uplift and 'trapdoor' faulting on Gal_pagos volcanoes observed with radar interferometry. Nature, 407, 993-996, 2000.
[9]. C., Carnec, D., Massonnet and C., King, Two examples of the use of SAR interferometry on displacement fields of small spatial extent. Geophys. Research Letters, 23(24), 3579-3582, 1996.
[10]. R., Hanssen, Radar interferometry. Kluwer Academic Publishers, Dordrecht, Holland, 308p, 2001.
[11]. F., Amelung, D.L., Galloway, J.W., Bell, H.A., Zebker and R.J., Laczniak, Sensing the ups and downs of Las Vegas: InSAR reveals structural control of land subsidence and aquifersystem deformation. Geology, 27(6), 483-486, 1999.
[12]. M., Tesauro, P., Berardino, R., Lanari, E., Sansosti, G., Fornaro and G., Franceschetti, Urban subsidence inside the city of Napoli (Italy) observed by satellite radar interferometry. Geophys. Research Letters, 27(13), 1961-1964, 2000.
[13]. A., Ferretti, C., Prati and F., Rocca, Nonlinear subsidence rate estimation using the Permanent Scatterers in differential SAR interferometry. IEEE Transactions on Geoscience and Remote Sensing, 38(5), 2202-2012, 2000.
[14]. T., Strozzi, U., Wegmuller, L., Tosi, G., Bitelli and V., Spreckels, Land subsidence monitoring with differential SAR interferometry. Photogrammetric engineering and remote sensing, 67(11), 1261-1270, 2001.
[15]. M., Crosetto, Tscherning, C.C., B., Crippa and M., Castillo, Subsidence Monitoring using SAR interferometry: reduction of the atmospheric effects using stochastic filtering. Geophys. Research Letters, Vol. 29(9), 26-29, 2002.
[16]. M., Crosetto, M. Castillo and R., Arbiol, Urban subsidence monitoring using radar interferometry: Algorithms and validation. Photogrammetric engineering and remote sensing, in press, 2003.
[17]. O., Mora, R., Arbiol, and V., Palà, Advanced DInSAR techniques for monitoring terrain displacements. In *5th European Congress on Regional Geoscientific Cartography and Earth information and systems water*, 2006.
[18]. M., Zuhlke, N., Fomferra, C., Brockmann, M., Peters, L., Veci, J., Malik and P., Regner, SNAP (Sentinel Application Platform) and the ESA Sentinel 3 Toolbox. In *Sentinel-3 for Science Workshop*, Vol. 734, p. 21, 2015.
[19]. A., Hooper, D., Bekaert, K., Spaans, and M., Arikan, Recent advances in SAR interferometry time series analysis for measuring crustal deformation, Tectonophysics, 514-517, pp.1-13. doi: 10.1016/j.tecto.2011.10.013, 2012.

ICENS 4TH INTERNATIONAL CONFERENCE ON ENGINEERING AND NATURAL SCIENCE
2-6 May 2018 KIEV UKRAINE

Investigation Of Hygroscopic Properties For Fibers Obtained From Chicken Feathers

Nazim Pasayev[1], Sureyya Kocatepe[1], Nesli Maras[1], Onur Tekoglu[1]

Abstract

Chicken feathers aren't suitable to use with current form unlike feathers obtained from water birds. The fragility, heavy, rough structure and low elasticity characteristics make unfavourable to get advantage from the chicken feathers. However, the material obtained from chicken feathers and called "chicken feather fibers" is more useful than fibers. These protein fibers that result from processing of chicken feathers, much of which is a waste product, have lots of valuable properties. In this study, hygroscopic properties of chicken fibers have investigated. Chicken feather fibber's ability of absorb moisture from air, ability to absorb water and swelling feature under the influence of water have investigated when compared to goose down, cotton and wool fibers, which used as a natural filling material in winter clothes. At the end of researches, it has revealed that the chicken feather fibers have high hygroscopic properties.

Keywords: chicken feathers; chicken feather fibers; hygroscopity of chicken feathers fibers; hygroscopity of goose down

1. INTRODUCTION

The facilities of benefiting from the current form of chicken feathers are not large. This has several reasons. Chicken feathers are selected because of the specialties which have roughness, weight and more fragile and from goose and duck feathers used widely as a filling material. All of these make it unsuitable to utilize as a filter material from chicken feathers. Chicken feathers which are obtained by separation of barbules from the rachis are more universal in terms of usage. According to the studies, obtaining fibers from chicken feathers attracts the scientists and studies about the chicken feather fibers reveal the important features of these feathers [1]-[5].

This study is related to hygroscopic properties of the fibers obtained from chicken feathers. These characteristics are significantly determined by the chemical composition and microstructure of chicken feathers. In one study, it is said that about 30 different feathers type are available because of the organization differences of keratin molecules which is chemical content of chicken feathers [6]. Of course, these feathers have to selected from each other's according to various characteristics. Moisture content and hygroscopic properties of feathers have an important place between these characteristics.

Even though most of amino acids which constituent of polypeptide chains forming the chicken feathers have hydrophobic features, some of among them have hydrophilic properties [7]. Amino acids which interact strongly with water and have polar groups exhibit hydrophilic properties. Researches have shown that 35 of 95 amino acids in keratin monomers are hydrophilic [8]. The most important amino acid is serine, the ration is about 16% in chicken feathers. Serine has ability to absorb moisture from the air with OH groups [9]. When the hydrophobic amino acids and hydrophilic amino acids in chicken feathers compare, the ratio is 60:40. This is because of chicken feathers also have hydrophilic properties as well as hydrophobic properties [7].

Hygroscopicity is a very important feature of feathers. Because, moisture effects the properties of feathers from many perspectives. For example, mechanical properties of feathers are varied under the influence of moisture. Studies have shown that elasticity and tensile strength of feathers decrease with increasing in humidity, increase the stiffness of feathers [10].

Different values about the moisture content of chicken feathers are given in literature. In one study, has shown that content of chicken feathers form has about 8% of moisture [11]. In another study, it has indicated that

[1] *Corresponding author: Erciyes University, Department of Textile Engineering, 38039, Melikgazi/Kayseri, Turkey, npasayev@erciyes.edu.tr*

fibers obtained from chicken feathers have 12-13% moisture [12]. One author has implied that chicken feather fibers have a moisture content of about 7% [3]. From this it is clear that the moisture in chicken feathers although it has a determinative feature, it has a variable character. Although this variable character depends on ambient conditions and manufacturing feathers, it is probably also depending the chicken genus and growing conditions.

In a study, the fiber sample obtained from chicken feathers was kepted at 23 °C and 50% relative humidity. At the end of the measurement results, moisture content in fibers is same as well as the moisture content in feathers, it is in the range of 16%...20%. It is observed that this humidity ration is varied according to the type of feathers [8].

Research related to changes in humidity chicken feathers, depending on the environmental conditions have not been conducted. However, it was noted that ostrich feathers had have 17% humidity at 50% relative humidity condition and 28,4% humidity at 100% relative humidity condition [10]. In one study, it is shown that moisture had leaved from chicken feather fibers between 100….110°C temperature [13].

One of the most important properties of natural fibers is the swelling under the influence of water. Different types of fibers have shown a different amount of swelling in aqueous media. This feature of chicken feathers has not investigated. The swelling transverse and longitudinal values of some fibers are given under the influence of water at Table 1 [14].

Table 1. The swelling ratios of some natural fibers in water

Fiber types	**Swelling ratio of fibers, %**	
	Length direction	Cross section
Cotton	1,0…1,2	22…42
Linen	1,0…1,2	25…40
Wool	1,2…1,5	18…38
Natural silk	1,5	20

As seen in literature, although there have been many studies about chicken feathers and hygroscopic properties of chicken feather fibers, the changes of hygroscopic properties depending on environmental conditions have not been investigated. Swelling effect of chicken feathers fibers have not been investigated under water. In this study, it is aimed that investigation of chicken feather fibers about the change of moisture content for chicken feather fibers, changes of feathers for ability of getting humidity from air according to environmental temperature when compared with cotton, wool and goose down. Besides these, swelling the chicken feathers under effect of humidity has been researched.

2. EXPERIMENTAL STUDY

2.1. Material

Chicken feathers fibers used in this study were produced from chicken feathers obtained from two different companies in Samsun and Bolu in Turkey. Feathers were washed with a brand Rucogen Yes 5% solution of a nonionic detergent, which's company Rudolf Group, at pH 6,0-7,0 for 60 min at 40°C and rinsed three times for 20 minutes each in pure water. Before this wash, feathers were treated by pre-washing with a 2% sodium hypochlorite for 20 minutes at 40C for the purpose of disinfection. After the main wash, feathers were dried for 72 hours in dry machine. Fibers were obtained by cutting the fibers from 'beard' portion of dried feathers (Figure 1).

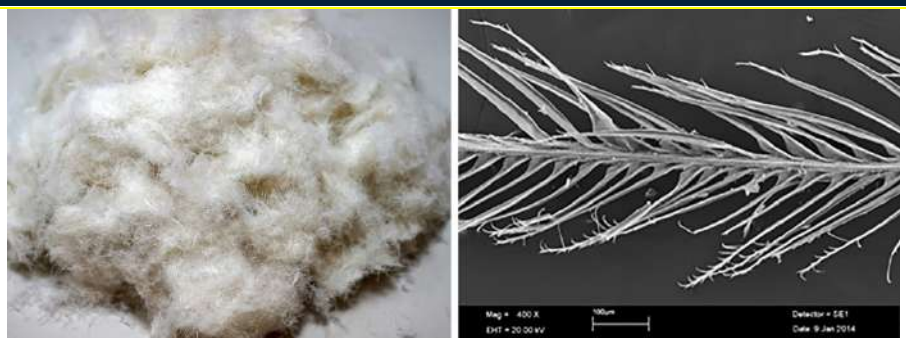

Figure 1. Fibers obtained from chicken feathers

2.2. Method

Investigation of the moisture absorption capability of the chicken feather fibers from air

In order to investigate the chicken feather fiber's ability of absorb moisture from air, weighing method was used to determine the moisture content of the fibers. In this study, the environment temperature and the relative humidity of the environment were chosen as a changing factor. The variation intervals of these factors are given in Table 2.

Table 2. Varying factors of two-factor experiment for examining moisture absorption ability of fiber samples from air

Free varying levels	Levels of factor changes		
Environment temperature, ºC	20	40	60
The relative humidity of the environment, %	65	80	95

3g fiber was taken from fiber mass kept in conditions for 2 hours at 20°C and 65% relative humidity to use in experiments. After holding samples under determined conditions for 2 hours according to the experimental plan, the weight of samples was determined by weighing and results were written to the table. Chicken feather, goose down, cotton and wool fibers were used in experiment to compare according to the experimental results. Moisture content of fiber samples at determined conditions were studied for 2 hours was evaluated by following formula according to the dry weight of sample:

$$W = \frac{m_{wet} - m_{dry}}{m_{dry}}$$

In this formula, W - moisture content of the dry weight of sample (%), m_{wet} - wet weight of sample (g), m_{dry} - dry weight of sample (g).

To determine dry weight of fiber sample were kept under normal conditions (20°C temperature and 65% relative humidity) for 2 hours and taken 3g fiber from sample. Then, this fiber was kept for 120 minutes at 105°C according to the TS 467 standard (Table 3).

Table 3. Dry weight of the fiber samples used in experiment

	Chicken feather fiber	Goose feather	Cotton fiber	Wool fiber
Dry weight of the fiber samples, g	2,73	2,73	2,81	2,71

Investigation of water absorption ability of chicken feather fibers

Water-soaked chicken feather fibers were tested to determine how much water was retention of structure. In order to be able to make comparison with other natural fibers, the same test has been done for goose feather, cotton and wool fibers apart from chicken feather fibers. To determine water absorption properties of chicken feather fibers, the "Water Immersion Method" was based on which is proposed by the standard of TS 866 "Determination of Water Absorption Properties of Cotton Textile Products". Because of the material to be tested, chicken feather fibers is not a standard material, it has to adapt to the standard's requirements to the test object.

The test specimens were prepared as follows; after weighing some goose feather, cotton, wool and chicken feather fibers with precision scale, the fibers were conditioned according to TS 240 standard. Three grams of conditioned samples were weighed and placed in sample bags.

During the experiment, the special experimental setup, which is shown in Figure 2, was prepared to immerse the samples in the water. The fibers, which was weighed as 3gr, were placed in the strainer apparatus, and the apparatus was placed in a 2lt glass beaker. Distilled water, which was a 21±3°C, was added to the beaker. Filter apparatus was designed so that it can be hanged in the middle of the beaker. The apparatus was suspended in water and the stopwatch was turned on by placing it in a test cabinet designated for the required level of temperature. At the end of the 30, 90, 150 minutes' period, the apparatus was removed from the water, and it was suspended for 10 minutes in order to remove the water, which is mechanically related to the fibers. At the end of the experiment, the values, which are related the weight of the weighed fibers, were written in table 5. The experiment was repeated at 20°C, 40°C, and 60°C temperature for each fiber. New fiber was used for each experiment.

Figure 2. Experimental setup for testing the water absorption properties of the fibers

Investigation of swelling ability of chicken feather fibers under the influence of water

To examine of swelling ability of chicken feather fibers under water influence, how the fiber diameter increases were tested as a result of fiber's interaction with water. For this purpose, 5 fibers are selected, similar in thickness and length, of the mass seasoned 2 hours under normal conditions. Test samples were prepared by gluing tape on both edge to prevent fibers slipping from slipping on glass lamellae. Fiber diameter was measured. Then a drop of water dribbled the fiber on lamellae and put in the microscope and 1-minute time was started. The diameter of the fiber absorbed water was measured again at the end of the 1 minutes. This

process was repeated for 2, 3 and 5 minutes. The chances in the fiber's diameter depending on the time were observed and fiber diameter values were recorded in the table.

3. EXPERIMENTAL RESULTS

Investigation of the moisture absorbsion ability of chicken feather fibers from the air

Chicken feather fiber, goose down, cotton and wool fibers were hold under different environmental conditions determined at Table 2, then weighing method was used to determine the moisture which they received. The weight of moisture from the air was calculated according to the dry weight of the sample and the results were written at Table 4.

Table 4. Experimental results for examining moisture absorption ability of fiber samples from air

Experiment number	Temperature, °C	The moisture of air, %	Chicken feather fiber		Goose down		Wool fiber		Cotton fiber	
			m_{dry} = 2,73g		m_{dry} = 2,73g		m_{dry} = 2,71g		m_{dry} = 2,81g	
			Wet weight of fiber mass, g	Humidity received by the fiber mass, %	Wet weight of fiber mass, g	Humidity received by the fiber mass, %	Wet weight of fiber mass, g	Humidity received by the fiber mass, %	Wet weight of fiber mass, g	Humidity received by the fiber mass, %
1	20	65	3,00	9,89	3,00	9,89	3,00	10,70	3,00	6,01
2		80	3,10	13,55	3,19	20,15	3,07	13,28	3,10	9,54
3		95	3,26	19,41	3,43	25,64	3,37	24,35	3,25	14,84
4	40	65	2,94	7,69	3,24	18,68	3,01	9,22	3,07	8,48
5		80	3,17	16,12	3,28	20,15	3,08	13,65	3,16	11,66
6		95	3,33	21,98	3,76	37,73	3,39	21,03	3,36	18,73
7	60	65	2,89	5,86	2,96	11,72	2,88	6,27	2,98	5,30
8		80	2,90	6,23	3,13	14,65	2,96	9,22	3,05	7,77
9		95	2,96	8,42	3,06	12,09	3,09	14,02	3,15	11,31

At Figure 3, the diagrams are given which are related moisture ratio of fibers taken from air and environment humidity. As seen in these diagrams, ability of dehumidification from air for both keratin and cotton fibers, which are cellulose-based fibers, varies according to the environmental conditions. In other words, studied all fibers are defined as "breathable" fibers. These fibers get moisture from air when the relative humidity of environment increase and give back when humidity of environment reduce.

According to Table 4 and diagrams in Figure 3, at a constant temperature with increasing ambient relative humidity increases the amount of moisture absorbed from the air fibers. However, this increase is not the same for all fibers. In Figure 4, for the same fibers, diagrams of the moisture content, which are taken from the air, of the fibers are given with changing the temperature in a constant environment humidity. As seen from these diagrams, in the temperature range of 20...60°C, with temperature rise to 40°C, in any environmental conditions increases the amount of moisture, absorbable fibers. At higher values of the temperature, further increasing the relative humidity of the environment also increases the amount of moisture absorbable fibers. However, these increases have small values. At 60°C the fibers absorb less moisture than 20°C and 40°C temperatures. This is a result of the activation of water molecules by increasing the temperature. As the temperature increases due to the destruction of some of the bonds between the macromolecules the fibers under the action of heat, the absorption of moisture from the air increases. The water molecules, the energy of which also increases with increasing temperature contribute to this. Certainly, there is a temperature at which the fibers absorb the greatest amount of moisture.

If evaluated according to the ability of the "breathe" or the amount of moisture taken from the air, as seen the fibers obtained from the chicken feathers are only worse than goose feathers.

Investigation of water absorption ability of chicken feather fibers

After kept the wool, cotton, chicken feather and goose feather samples in 20°C, 40°C and 60°C temperature in water for 30, 90 and 150 minutes, the amount of water retained in the structure is given in Table 5.

The ration of the amount of water taken by the fibers at different temperatures to the dry weight of the fibers is given in Figure 5.

Table 5. Test results of the water absorption capacity of the fibers

Experiment number	Temperature, °C	Dipping time of the fibers in water, minute	Chicken feather fiber		Goose down		Wool fiber		Cotton fiber	
			m_{dry} = 2,73gr		m_{dry} = 2,73gr		m_{dry} = 2,81gr		m_{dry} = 2,71gr	
			Wet weight of fiber mass, g	The water content of the fiber mass according to dry weight, %	Wet weight of fiber mass, g	The water content of the fiber mass according to dry weight, %	Wet weight of fiber mass, g	The water content of the fiber mass according to dry weight, %	Wet weight of fiber mass, g	The water content of the fiber mass according to dry weight, %
1	20	30	8,92	226,74	15,16	455,31	6,92	144,52	17,02	528,04
2		90	10,00	266,30	16,86	517,58	8,35	195,05	18,79	593,36
3		150	10,61	288,64	18,76	587,18	9,51	236,04	19,07	603,69
4	40	30	10,86	297,80	17,37	536,26	7,93	180,21	18,49	582,29
5		90	11,46	319,78	18,11	563,37	8,84	212,37	19,62	623,99
6		150	13,01	376,56	19,98	631,87	11,21	296,11	20,82	668,27
7	60	30	18,00	559,34	21,59	690,84	9,49	235,33	25	822,51
8		90	16,43	501,83	20,21	640,29	11,12	292,93	23,14	753,87
9		150	15,97	484,98	20,51	651,28	14,38	408,13	22,82	742,07

As can be seen from Table 5 and Figure 5, the amount of water retained on the structure of all tested fibers and goose feather, which were tested to 40C°, increases according to the temperature with increasing water dipping time. So, wool and goose feathers show the highest water absorption ability, while cotton fibers have the lowest water absorption. Because of the temperature rises, the situation has change. Thus, after 40°C for protein-based materials including goose feathers, this increase is reversed. The fibers that receive the maximum amount of water in the first 30 minutes, give back a portion of the water they have taken over time, thus keeping the amount of water in their bodies lower. This situation is not same for the cellulose-based cotton fibers. The amount of water taken by the cotton fibers continues to increase with the prolongation of the water immersion time of the fibers. The water amount of protein-based materials is much higher than cotton fibers at all levels. Between the goose feathers, chicken feather fibers, cotton and wool fibers tested, the moisture absorb ability from air is higher in goose feathers, but the water absorb ability of wool fibers is greater in aqueous environment. Although chicken feather fibers exhibit close values to the wool fibers in terms of moisture absorption from the air, they are worse than wool fibers in terms of water absorb ability. Cotton fibers have a relatively low absorbency in all cases.

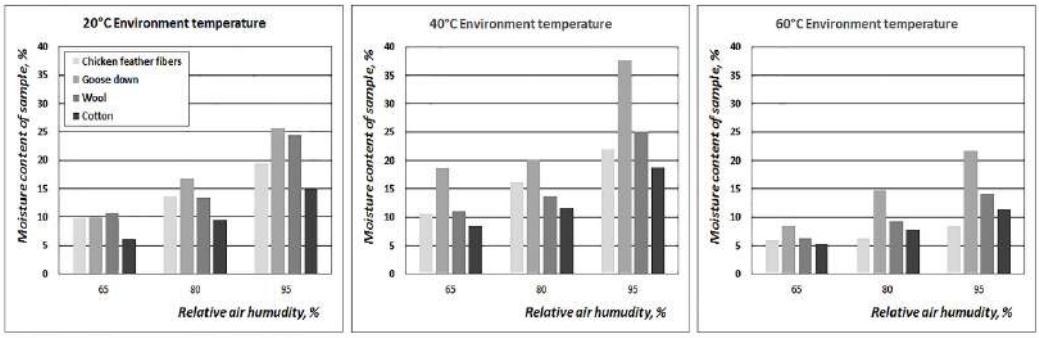

Figure 3. The changing moisture absorption of fibers depending on the ambient humidity

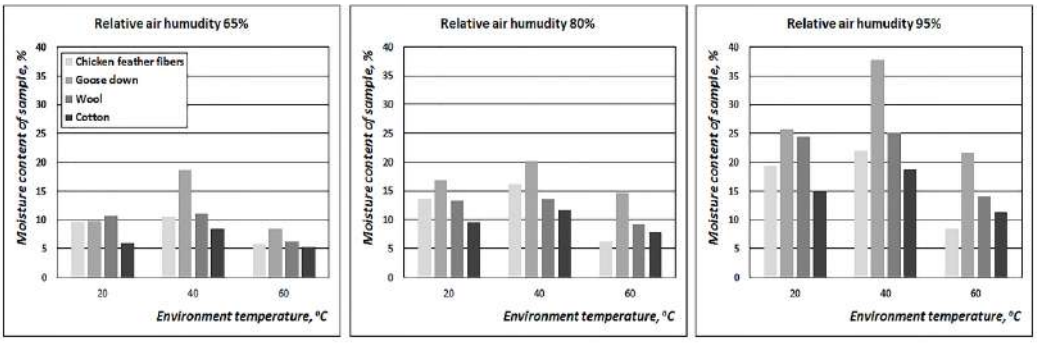

Figure 4. The changing moisture absorption of fibers depending on the ambient temperature

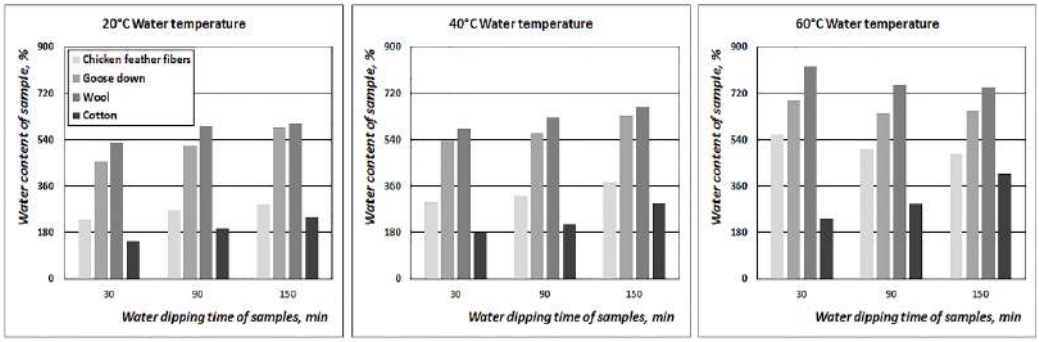

Figure 5. The amount of water that different fibers receive at different temperatures

Investigation of swelling ability of chicken feather fibers under the influence of water

Swelling values of fibers depending on the time under water was observed and written in Table 6 to see any changes that may occur in the fiber structure due to interaction with water during use of the products which will make by chicken feather fibers.

To determine changes in the structure of the chicken fibers in contact with water, the experiment was conducted where the observed degree of swelling of the fibers versus time. The experimental results are shown in Table 6.

The swelling of chicken feather fibers was observed as all natural fibers at the end of wetting. This is because of penetrating the water molecules in to polymer macro-molecular, then this swelling remove some of the links between them and create links with macromolecules. As a result, it is arising the swelling in fibers.

As seen the values in Table, the diameter of the fiber samples reached the maximum level at first minute of wetting and were stabilized. This means that chicken feather fibers have a high wetting speed. Length of the fibers have not shown significant change under the water.

4. CONCLUSION

As a result, chicken feather fibers obtained from chicken feathers have a highly hygroscopic property such as other natural fibers. These fibers are only behind goose down according to the ability of absorbing moisture from air.

Table 6. The diameter changes of chicken feather fibers as a result of swelling under the water effect

The number of measurements (units)	**Values of measured fiber diamater, µm**					
	Untreated sample	After wetting for 1min	After wetting for 2 min	After wetting for 3 min	After wetting for 4 min	After wetting for 5 min
1	138,70	171,95	171,48	171,48	171,48	172,43
2	135,85	168,63	172,43	171,95	172,90	170,53
3	135,90	171,75	171,00	173,38	172,90	171,48
4	133,48	168,63	172,43	173,38	171,00	170,53
5	135,85	169,52	171,48	173,38	172,43	170,05
Average	135,96	170,90	171,76	172,71	172,14	171,00
Swelling ratio according to fiber diameter in normal conditions		0,26	0,26	0,27	0,26	0,26

Water absorption ability of chicken feather fibers, which are dipped in water, is lower than wool fibers and goose feathers, but is closer to the cotton fibers. However, chicken feather fibers' water absorption ability is approaching protein-based materials with increasing environment temperature.

Chicken feather fibers exhibit high swelling properties at aqueous environment. Fibers in aqueous environment nearly swell up about one quarter of diameter in about 1 minute. The length of chicken feathers fibers has not shown significant change under the experimental conditions.

ACKNOWLEDGMENT

This study was supported by The Scientific and Technological Research Council of Turkey (TUBITAK) with 115M725 numbered researching project.

REFERENCES

[1]. A.L. Martínez-Hernández & Velasco-Santos C. "Keratin Fibers From Chicken Feathers: Structure and Advances in Polymer Composites". In R. Dullaart and J. Mousquès (Eds.), *Keratin: Structure, Properties and Applications* (pp. 149-211). Nova Science Publishers, Inc. New York, 2012.

[2]. J.R. Barone & Schmidt W.F. "Effect of formic acid exposure on keratin fiber derived from poultry feather biomass". *Bioresource Technology*, 97, 233–242, 2006. DOI: 10.1016/j.biortech.2005.02.039.

[3]. X. Fan. *Value-Added Products from Chicken Feather Fibers and Protein* (Unpublished doctoral dissertation). Auburn University, Alabama, 2008.

[4]. K.B. Jagadeeshgouda, Reddy P.R. & Ishwaraprasad K. "Experimental Study of Behaviour of Poultry Feather Fiber - A Reinforcing Material For Composites". *International Journal of Research in Engineering and Technology* **03**, 362-371, 2014. DOI: 10.15623/ijret.2014.0302065

[5]. F.C.J. Tseng & Verbeek C.J.R. *Biofibre Production from Chicken Feather*. Paper presented at the SCENZ-IChemE annual conference in New Zealand, University of Waikato, New Zealand, 2011.

[6]. W.F. Schmidt & Line, M. J. *Physical and chemical structures of poultry feather fiber fractions in fiber process development.* Proceedings of the TAPPI Nonwovens Conference, Charlotte, NC Atlanta, 1996.

[7]. K. Saravanan. "Exploration on Amino Acid Content and Morphological Structure in Chicken Feather Fiber". *Journal of Textile and Apparel Technology and Management*, **7**, 3, 1-6, 2012.

[8]. J.W. Kock. *Physical and Mechanical Properties of Chicken Feather Materials* (Unpublished master's thesis). Georgia Institute of Technology, Atlanta, 2006.

[9]. B. Alberts, Bray D., Lewis J., Raff M., Roberts K. & Watson J.D. *Molecular Biology of the Cell*: 3rd. ed. Garland Publishing, New York and London, 1994.

[10]. A.M. Taylor, Bonser R.H.C. & Farrent J.W. "The Influence of Hydration on The Tensile and Compressive Properties of Avian Keratinous Tissues". *Journal of Materials Science*, 39, 939-942, 2004. DOI:10.1023/B:JMSC.0000012925.92504.08

[11]. C. Arunkumar, Megwal H.S., Borkar S.P. & Bhongade A.L. "Recycling of Chicken Feather and Wool Fibre Waste into Reinforced Multilayer Composite - A Review". *Technical Textile*, 2, 371-378, 2013.

[12]. P. Kar & Misra M. "Use of Keratin Fiber for Separation of Heavy Metals From Water". *Journal of Chemical Technology and Biotechnology*, 79, 1313-1319, 2004.

[13]. J.W. Kock, Barbieri R.J., Justice J.M., Kurtis K.E., Gentry T.R. & Nanko H. *Characterization of Chicken Feather Materials for Use in Biocomposites*. Proceedings of the American Society for Composites: Twentieth Technical Conference, Philadelphia, PA, American Society for Composites, CD-ROM – 15, 2005.

[14]. Г.Н. Кукин, Соловьев А.Н. & Кобляков А.И. *Текстильное материаловедение (текстильные полотна и изделия)*. Легпромбытиздат: Москва, 1992.

ICENS 4TH INTERNATIONAL CONFERENCE ON ENGINEERING AND NATURAL SCIENCE
2-6 May 2018 KIEV UKRAINE

A Study on Usage of Urban Parks: Case of Pamukkale-Denizli, Turkey

Cengiz Yucedag[1], Latif Gurkan Kaya[2], Huseyin Samet Asikkutlu[3]

Abstract

In the study, usage of parks in Pamukkale-Denizli, Turkey is determined through a face-to-face questionnaire survey with 100 respondents. 52% of respondents live in Pamukkale county for more than 10 years. The majority of them come to parks with their family and children for playgrounds on foot in all seasons which weather is warm and visit the parks several times a week and spend 1-2 hours for every visit. They mostly prefer Camlik park within the boundaries of Pamukkale county. The cleanliness, safeness and lighting of the parks are found to be inadequate by more than half of the respondents. Half of them think that the number of playgrounds are not adequate in the neighborhood where they live. 44% of respondents state that buffets and cafes around parks have a positive impact on their visit to parks. The majority of visitors consider that trash bins, seating equipment and playgrounds in the parks are inadequate. They would like parks with particularly playgrounds and seating equipment. 59% of the respondents, 62% of whom are female, play sports (mostly walking) in the parks. As considered all results, the cleanliness, safeness and lighting of the parks should be improved by the relevant groups and additionally the furniture deficiencies must be completed as soon as possible.

Keywords: Furniture, Pamukkale, Park, Respondent

1. INTRODUCTION

In recent years, urban areas allowed a lot of immigration, particularly in the developing countries. This case resulted in heavy air and noise pollution together with the increasing traffic congestion in cities. Also, these environmental problems have adversely affected physical and psychological health of city' dwellers. In this sense, open-green lands play an important role in reducing adverse impacts of cities on urban people.

Urban open-green lands, particularly urban parks, are the most critical areas for meeting the physical and psychological needs of people, as well as improving the users' quality of life in urban areas by creating areas for people to escape from the built environment. The user density is defined by the activity opportunities that are served by urban parks and the location and accessibility of the parks. Moreover, these factors are also effective for defining the level of user satisfaction [1].

One of the open-space lands, parks which provide opportunities to feel nature and recreation for centuries, have gained increasing importance and value with the opportunities they offer, especially in urban areas. Urban parks that are formed by cultural values, political and socio-economical structures of the societies are formed with social changes and with these qualities, they also became the reflectors of them [2]. Furthermore, parks have vital contributors to the achievement of wider urban policy objectives, including job opportunities, youth development, public health, and community building-all of which help strengthen the neighborhoods in which parks are located [3]. Good parks provide a place for resting, but more importantly they are places for spontaneous social interaction. [4]. Therefore, urban social life currently requires urban outdoor areas that are right designed, managed and maintained, and also financially supported. Contemporary planning and designs has to focused on the formation of cities in the parks rather than the formation of parks with in a city [5].

The aim of this study is to determine the usage of parks in Pamukkale-Denizli, Turkey.

[1] *Mehmet Akif Ersoy University, Department of Landscape Architecture, 15030, Burdur, Turkey. yucedagc@gmail.com*

[2] *Corresponding author: Mehmet Akif Ersoy University, Department of Landscape Architecture, 15030, Burdur, Turkey. lgkaya@gmail.com*

[3] *Mehmet Akif Ersoy University, Department of Landscape Architecture, 15030, Burdur, Turkey. sametasikkutlu@gmail.com*

2. MATERIALS AND METHODS

Pamukkale district of Denizli, Turkey was selected as case area in the current study (Figure 1). A face-to-face questionnaire survey was conducted to determine the satisfaction levels of users and the usage of parks in the district. The number of respondents in the questionnaire was determined as 100. The questionnaire consisted of questions about socio-economic characteristics of respondents, park preferences, information on their use and satisfaction with the parks and their demands. The obtained data were analyzed by SPSS program.

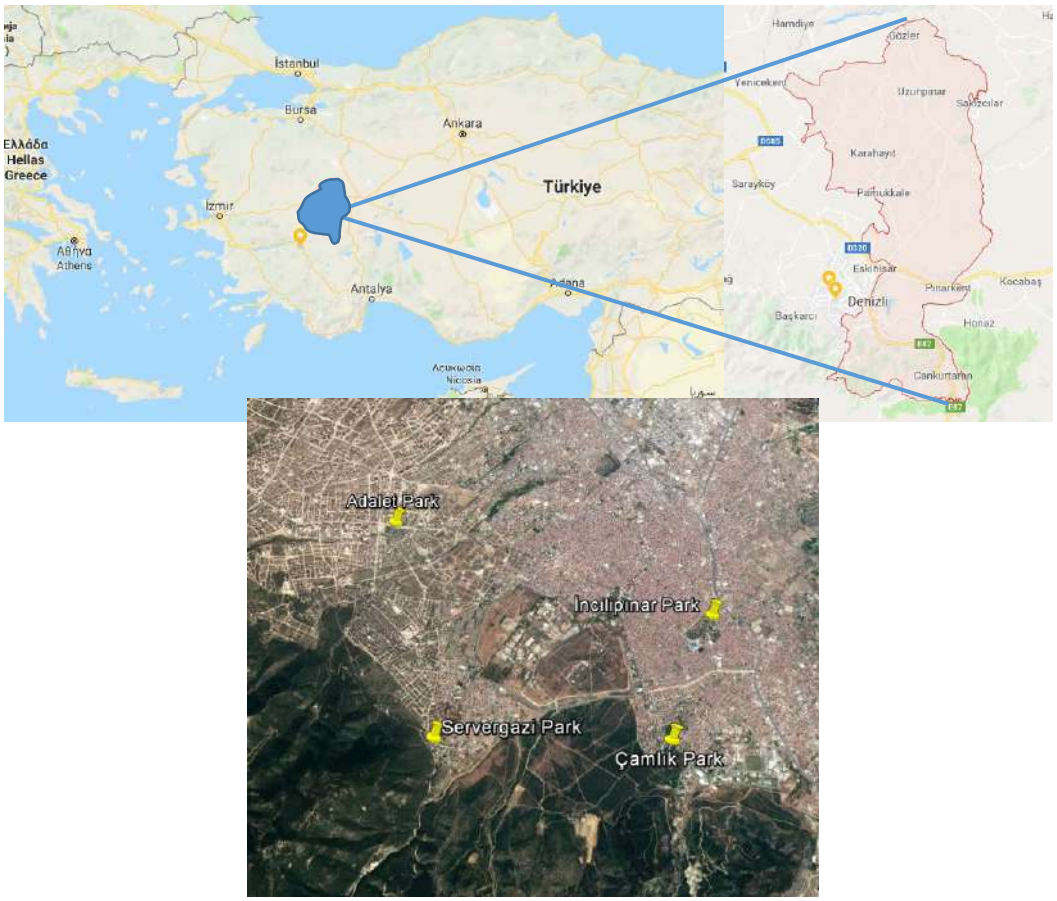

Figure 1. Case area and the preferred parks

3. RESULTS AND DISCUSSION

Socio-economic profiles of respondents

In this study, 69% of the respondents are female and 77% of the respondents are married. The majority of respondents (more than 70%) are 26 to 45 years old and have one or two children. 69% of the respondents have bachelor degree. The job of the respondents is highly self-employment (engineer, architect etc.). 72% of the respondents have a monthly income over 2501 Turkish Liras. The majority of respondents have stayed at their home and lived in Pamukkale for more than 5 years. They came to Pamukkale for their family (Table 1).

Table 1. Socio-economic profiles of respondents

Variables	Percent	Variables	Percent
Gender:		Job:	
Female	69	Officer	17
Male	31	Worker	10
Marital Status:		Self-employment	55
Single	23	Retired	4
Married	77	Housewife	11
Age:		Student	3
15-25	3	Unemployment	0
26-35	43	Monthly Income (TL):	
36-45	44	Under 1000	4
46-55	9	1001-2500	24
56-65	1	2501-4000	32
Over 66	0	4001-5000	16
Child Status:		Over 5001	24
0	25	Do you stay a rental house?:	
1	33	Yes	29
2	37	No	71
3	5	Do you live in Pamukkale?:	
Education:		Yes	80
Illiterate	0	No	20
Primary School	2	How long have you been living in Pamukkale?:	
Secondary School	2	Under 5 years	19
High School	11	5-10 years	29
Bachelor Degree	69	Over 10 years	52
Graduate	16	Why did you come to Pamukkale?:	
		For family	50
		For a work	39
		For others (education, travel etc.)	11

Visit related characteristics

The majority of the respondents visit the parks for playground on foot with their family for 1-2 hours several times a week in hot weathers of every season (Table 2). Aksoy and Akpinar [6] reported similar results in terms of visit related characteristics without the purpose of visit (for resting and walking). Gurer and Ugurlar [1], Chiesura [7], Polat and Gungor [8] and Lee and Kim [9] also stated that people mostly visited the parks for resting and walking. The prevalence of visit by foot show that the parks are close to city center. This result was also supported by Aksoy and Akpinar [6], Bekci and Taskan [10], Saglik and Kelkit [11], Cetinkaya et al. [12] and Shrinagesh and Markandey [13] indicating that the most important factor affecting the satisfaction of park users was accessibility. Forest visitors in Denmark spent an hour or less in the forest on their visits [14].

Table 2. Visit related characteristics

Variables	Frequency	Variables	Frequency
Visit the park for:		Preferred visit time:	
Playground	63	Summer	27
Walking	40	Spring	21
Sport	20	Winter	1
Resting	26	Hot weathers	51
Visit with:		Visit frequency:	
With my family	73	Everyday	3
With my friends	18	Several times a week	39
Alone	9	Once a week	30
Go to park by:		Once a month	28
Foot	64	Visit duration:	
Car	33	Less than one hour	12
Bus	3	One to two hours	80
		Half day	8
		Full day	0

Park related characteristics

The majority of respondents have visited Camlik and Incilipinar parks (Figure 2) because they located within the boundaries of Pamukkale district. Most respondents stated that cleanliness, safety and lighting of the parks were inadequate (Table 3). Cetinkaya et al. [12] and Yucel [15] stressed that cleanliness is an important factor for satisfaction of park users. Ozturk Kurtaslan [2] stated that women, children and the elders can use the Teardrop Park (New York) extensively because its safety and lighting are sufficient.

Figure 2. Views from Camlik and Incirlipinar parks

On the other hand, they indicated that playground number of parks were enough. It was found that cafes in the park have no effect on respondents' visit (Table 3). On the contrary, Yucedag and Kaya [16] indicated that visitors preferred a recreational area with indoor and outdoor culture facilities. The majority of respondents thought that sitting bench, playground equipment and trash can in the parks were insufficient (Table 3). Erdogan et al. [17] also indicated that sitting bench and trash cans were inadequate in the parks. Gurer and Ugurlu [1] found that the adequacy of sitting bench in the park was more important factor than the access to the area in terms of visitors. Bekci and Taskan [10] emphasized that the sitting bench is important in terms of the preference of the park. Playgrounds were the most requested furniture by most respondents, which correlates lacks in the park. 59% of the respondents, 62% of whom were female, played sports (mostly walking) in the parks (Table 3). Shrinagesh and Markandey [13] found that people would like to visit the park due to availability of Paths (walking). Cetinkaya et al. [12] indicated that the satisfaction levels of female park users were to be higher than those of male park users. It was determined that 64% of respondents, 67% of whom were female, did not have a picnic in the parks. On the other side, more than 70% of respondents playing sports and not having a picnic in the parks were single individuals (Table 3).

Table 3. Park related characteristics

Variables	Frequency	Variables	Frequency
Visited park:		Lacks in the park:	
Camlik	50	Sitting bench	47
Incilipinar	41	Playground equipment	46
Adalet	15	Basketball and football fields	37
Servergazi	4	Lighting	35
Cleanliness:		Trash can	57
Yes	42	Requested furniture:	
No	58	Sitting bench	50
Safety:		Sport equipment	35
Yes	29	Playgrounds	54
No	71	Do you play sport in the parks?:	
Lighting:		Yes	59
Yes	35	No	41
No	65	Preferred sport in the park:	
Adequacy of playground number:		Sport equipment	30
Yes	53	Football	2
No	47	Basketball	5
Effect of cafes in the park on visit:		Walking	63
Yes	44	Do you have a picnic in the park?:	
No	56	Yes	36

4. CONCLUSIONS

As considered all results, the cleanliness, safeness and lighting of the parks should be improved by the relevant groups and additionally the furniture deficiencies must be completed as soon as possible. Especially, the numbers of sitting bench and playground equipment should be increased and improved. Furthermore, socio-economic profiles of visitors should be taken into consideration in the design of new parks. The elements of the park should be in harmony when all these design and improvement studies are done.

REFERENCES

[1]. N. Gurer and A. Ugurlar, "Kent Parklarinda Kullanici Memnuniyeti:Ankara Kugulu Park Ornegi," *MEGARON*, vol. 12, pp. 443-459, 2017.
[2]. B. Ozturk Kurtaslan, "Basarili Kent Parki Planlama ve Yonetimi Yaklasiminin Teardrop Park (New York) Orneginde Arastirilmasi," *Uluslararasi Toplum Arastirmalari Dergisi*, vol. 7, pp. 1-19, 2017.
[3]. C. Walker, "*The Public Value of Urban Parks*," The Urban Institute, Washington, USA, 2004.
[4]. S. Shafer and J. Jacob, (2012) Urban Parks: The Value of Small Urban Parks, Plazas and Other Outdoor Spaces. [Online]. Available: http://agrilife.org/urbannature/files/2012/06/UrbanParks_4.pdf.
[5]. I. Cinar, "Kent Parklarinin Rekreasyonel Yonden Yeterliligi Uzerine Fethiye-Mugla Kent Parklari Orneginde Bir Arastirma," *ADU Ziraat Fakultesi Dergisi*, vol. 5, pp. 33-38, 2008.
[6]. Y. Aksoy and A. Akpinar, "Yesil Alan Kullanimi ve Yesil Alan Gereksinimi Uzerine Bir Arastirma Istanbul Ili Fatih Ilcesi Ornegi," *Istanbul Ticaret Universitesi Fen Bilimleri Dergisi*, vol. 10, pp. 81-96, 2011.
[7]. A. Chiesura, "The role of urban parks for the sustainable city," *Landscape and Urban Planning*, vol. 68, pp. 129-138, 2004.
[8]. A.T. Polat and S. Gungor, "Konya Ili Kent Parklari Kullanici Demografik Ozellikleri Ile Park Ziyareti Arasindaki Iliskiler," in *Proc. 5th Landscape Architecture Congress*, 2013, pp. 882-893.
[9]. Y-G. Lee and K-H. Kim, "Attitudes of Citizens towards Urban Parks and Green Spaces for Urban Sustainability: The Case of Gyeongsan City, Republic of Korea," *Sustainability*, vol. 7, pp. 8240-8254, 2015.
[10]. B. Bekci and G. Taskan, "Acik Yesil Alanlardaki Kent Donatilarinin Kisisel Mekan Uzakligina Etkisi: Bartin Kenti Ornegi," *Bartin Orman Fakultesi Dergisi*, vol. 14, pp. 61-71, 2012.
[11]. A. Saglik and A. Kelkit, "Canakkale Kent Parklarinin Yasam Kalitesi Uzerine Etkilerinin Belirlenmesi," *COMU Ziraat Fakultesi Dergisi*, vol. 2, pp. 41-53, 2014.
[12]. G. Cetinkaya, A. Erman and M.S. Uzun, "Determination of the recreational park users satisfactions and dissatisfactions factors," *International Journal of Human Sciences*, vol. 12, pp. 851-869, 2015.
[13]. B. Shrinagesh and K. Markandey, "Rethinking urban space in cities – A study of parks in Hyderabad, India," *IOP Conf. Series: Earth and Environmental Science*, vol. 37, pp. 1-8, 2016.
[14]. F. Søndergaard Jensen, "Monitoring outdoor recreation trends in Denmark," in *Proc. The 6th International Conference on Monitoring and Management of Visitors in Recreational and Protected Areas*, 2012, pp. 78-79.
[15]. G.F. Yucel, "Park alanlarinda kullanici memnuniyeti acisindan bakimin onemi," *YTU Mimarlik Fakultesi E-Dergisi*, vol. 2, pp. 176-187, 2007.
[16]. C. Yucedag and L.G. Kaya, "Recreational Trend and Demands of People in Isparta-Turkey. Chapter 104, H. Arapgirlioglu, A. Atik, R.L. Elliott and E. Turgeon, Ed., In Researches on Science and Art in 21st Century, Gece Publishing, pp. 927-934, Ankara, Turkey.
[17]. R. Erdogan, H.E. Oktay and C. Yildirim, "Antalya-Konyaalti Parklarinda Kullanilan Donati Elemanlari Tasarimlarinin Kullanici Gorusleri Dogrultusunda Degerlendirilmesi," *Artvin Coruh Universitesi Orman Fakultesi Dergisi*, vol. 12, pp. 1-8, 2011.

ICENS 4TH INTERNATIONAL CONFERENCE ON ENGINEERING AND NATURAL SCIENCE
2-6 May 2018 KIEV UKRAINE

Determination of Current Situation in Vocational High School Gardens: A Case of Civril-Denizli, Turkey

Latif Gurkan Kaya[1], Cengiz Yucedag[2], Huseyin Samet Asikkutlu[3]

Abstract

Despite the fact that school gardens play important role for helping students develop physical, social, cognitive, and emotional skills they have been generally overlooked. This study examined current situation in vocational high school gardens in Civril county of Denizli, Turkey based on landscape design principles. For this purpose, general information, school entrance and equipment element, sport areas, furniture, parking lots for education and socio-cultural activities of four vocational high school were evaluated in terms of their adequacy. In general, Beycesultan Vocational and Technical Anatolian High School out of four schools was adequate from the standpoint of most design principles. On the other hand, Kadir Kameroglu Vocational and Technical Anatolian High School was the most inadequate among case schools. Sport areas, seating equipment and parking lots were virtually inadequate in the schools. In conclusion, improving conditions of school gardens with the help of educators, spatial planning and design experts and local community would contribute to the youths' physical and psychological development.

Keywords: Denizli, Landscape design, School garden, Vocational High school

1. INTRODUCTION

Education is the most important factor, which forms the futures of individuals and society. In the beginning of 21st century, this strategically importance of education has more increased. Today, the development levels of societies are determined by how much they integrate with the world economy and they carry the characteristics of an information society. The initial investment, which will be made for the development and improvement of a country, is to provide the best education opportunities given to children and young people [1]. The supply of the best education relies on the improvement of the school gardens as well as the increase of the qualifications of the school buildings.

With the intensive urbanization, outdoor playgrounds are destroyed, existing or newly constructed children's playgrounds are inadequate, and the child is growing far from the gaming activity, which is crucial to development of the child. It is a known fact that the game is absolutely necessary in the physical, mental and social development of the child [2]. In general, the school gardens where children spend most of their time are the safest places for children since they are often within walking distance and isolated from motorized traffic. Consequently, these areas are accepted as one of remaining places in the urban environment where children can make contact with their peers in a natural open space. It has also been determined by studies that school grounds designed with natural elements have positive effects on the development of children [3]. In this sense, the school gardens in the cities have very important role for partially preventing the negative impressions, knowing and enjoying the nature, enhancing the green area and growing up a healthy population. Furthermore, students will meet not only their needs for play and recreation but the knowledge and experience as well as in these environments [4]. According to the researches on child behavior, children who play and spend time in school gardens with natural

[1] *Mehmet Akif Ersoy University, Department of Landscape Architecture, 15030, Burdur, Turkey. lgkaya@gmail.com*

[2] *Corresponding author: Mehmet Akif Ersoy University, Department of Landscape Architecture, 15030, Burdur, Turkey. yucedagc@gmail.com*

[3] *Mehmet Akif Ersoy University, Department of Landscape Architecture, 15030, Burdur, Turkey. sametasikkutlu@gmail.com*

characteristics and high landscape values, are more creative, and their learning and perception styles are more effective [5].

This study examined the current situation in vocational high school gardens in Civril county of Denizli, Turkey based on landscape design principles.

2. MATERIALS AND METHODS

The research material is composed of four vocational high schools in Civril county of Denizli, Turkey (Figure 1). Data collection, analysis and synthesis methods were used in the study. The sizes (m^2) of school gardens were determined, and then this value was proportioned to the number of existing students to calculate the garden area per student. The garden areas per student in the current study were assessed based on the values (25 m^2) and (5 m^2) suggested by Akdogan [6] and for minimum conditions by Kelkit and Ozel [1], respectively. In addition, school gardens have been assessed in terms of structural and plant material, deficiencies have been identified by taking into consideration their current conditions, and recommendations have been developed.

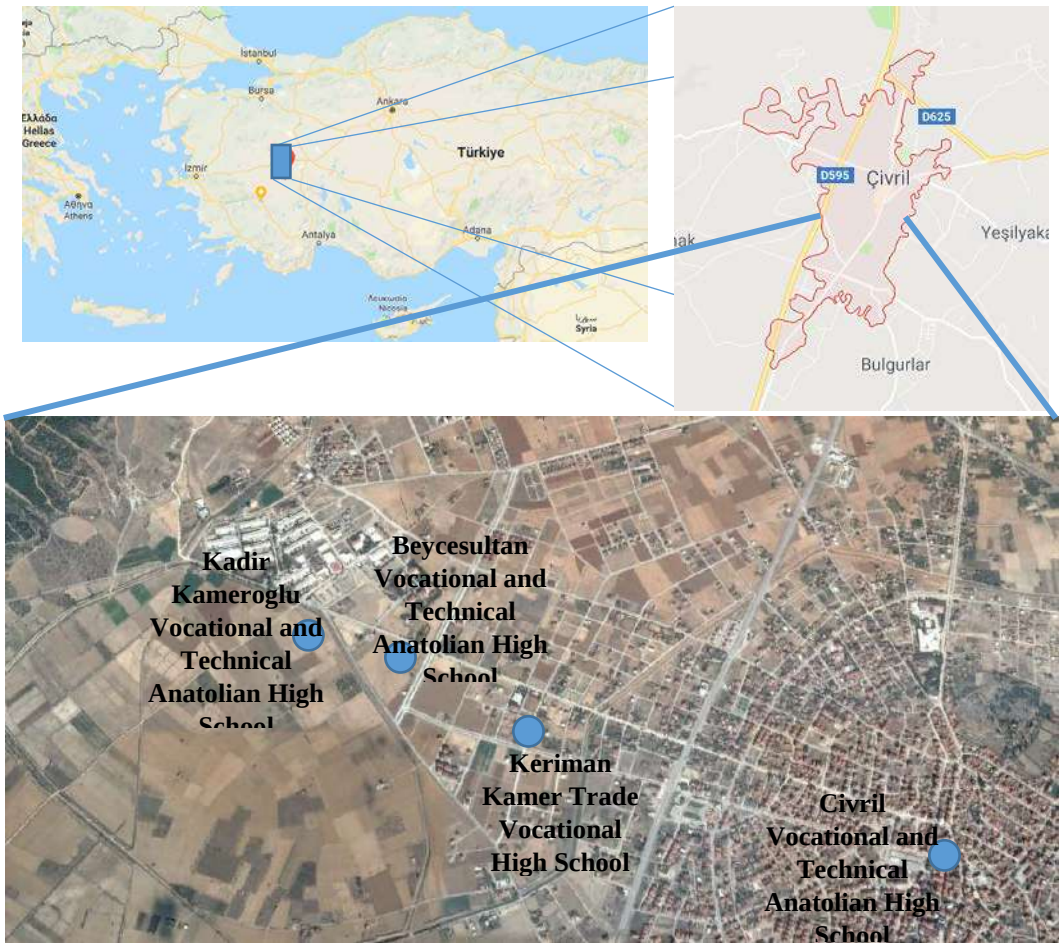

Figure 6. Case areas

3. RESULTS AND DISCUSSION

The data regarding assessments of the use of space and outdoor space of four vocational high schools in Civril county of Denizli were presented in Table 1. Accordingly, the total number of students in the studied schools was 1722. The total area of the school gardens was 29059 m². The mean garden area per student is 18.2 m². As considered the interschool range, the highest and lowest garden areas per student were 39.8 m² (Beycesultan Vocational and Technical Anatolian High School) and 7.2 m² (Kadir Kameroglu Vocational and Technical Anatolian High School), respectively. Although garden areas per student of all the studied schools were higher than that (5 m²) pointed out for minimum conditions by Kelkit and Ozel [1] the other three schools with the exception of Beycesultan Vocational and Technical Anatolian High School were lower garden area per student than that (25 m²) suggested by Akdogan [6]. Only garden area per student of Kadir Kameroglu Vocational and Technical Anatolian High School was under the value (10 m²) in the 3194 number law on construction [7].

Table 2. Land uses of vocational high schools and assessment of their furniture

	Schools	Beycesultan Vocational and Technical Anatolian High School	Kadir Kameroglu Vocational and Technical Anatolian High School	Keriman Kamer Trade Vocational High School	Civril Vocational and Technical Anatolian High School
General Information	Number of Students	339	208	315	860
	School garden (m^2)	13500	1500	4773	9286
	School garden per capita (m^2)	39.8	7.2	15.1	10.7
School Entrance and Equipment Element	Entrance Doors	■			■
	Planting Equipment	■		■	
	Structural Equipment	■	■	■	■
Sport Areas	Basketball	■			
	Football	■	-		-
	Volleyball	■			
Furniture	Lighting equipment	■			
	Trash Bins	+	+	+	+
	Information and Communication Boards	+	-	-	-
	Seating Equipment				
Parking lots	Parking lots		-	-	■
Areas for Education and Socio-cultural activities	Small Amphitheatre	-	-	-	-
	Ceremony and Assembly Area	+	+	+	+
	Small Zoo	-	-	-	-

■ Adequate, Inadequate, + Available, - Unavailable (Adequacy and inadequacy were evaluated according to the number of students and garden area)

All schools were adequate in terms of structural equipment but planting equipment of only Beycesultan Vocational and Technical Anatolian High School and Keriman Kamer Trade Vocational High School gardens were adequate. In Beycesultan Vocational and Technical Anatolian High School garden, the road sides and the sitting areas were limited to the vegetation fence (Figure 2). Only Civril Vocational and Technical Anatolia School garden had unplanted areas. School gardens are an important part of the urban open-green areas and are indicative of both school and urban identity. For this reason, the concept of green school gardens needs to be improved by moving away from classical gardening [2].

Figure 2. A view from Beycesultan Vocational and Technical Anatolian High School Garden

On the other side, all schools had insufficient basketball, volleyball and football areas (Table 1; Figure 3-4). It was observed that in only Beycesultan Vocational and Technical Anatolian High School sports areas were located in different points. This case was also stated by Karakaya and Kiper [8] for the primary schools in Edirne.

Figure 3. A view from Kadir Kameroglu Vocational and Technical Anatolian High School Garden

Figure 4. A view from Keriman Kamer Trade Vocational High School Garden

The majority of the studied schools had inadequate lighting and seating equipment. They had trash bins but no information and communication boards. In the school gardens, important design principles such as color, texture, form, material, and size were not paid attention in sitting elements, lighting elements, trash can, entrance doors, etc. There are also problems in the union of the furniture elements proving the results of the previous studies [1, 2, 4, 8]. Neglected, unsafe and unhealthy equipment made from poor quality materials pose a danger for the students (Figure 5-7). Moreover, there are no equipment for disabled students (Table 1). The used furniture materials in school gardens should not resulted in possible injuries [9].

Figure 5. Views from Civril Vocational and Technical Anatolian High School Garden

Figure 6. A view from Keriman Kamer Trade Vocational High School Garden

Figure 7. A view from Beycesultan Vocational and Technical Anatolian High School Garden

Every school has had a ceremony and assembly areas but none has small amphitheatre and small zoo. The ceremony and assembly areas of schools have been simultaneously used as a playground. These areas also function as parking lots due to the lack of parking lots. Civril and Beycesultan Vocational and Technical Anatolian High Schools had parking lots (Table 1; Figure 8). Similarly, Aksu and Demirel [2] and Arslan Muhacir and Yavuz Ozalp [10] reported that the primary schools in Trabzon and Artvin had either no or inadequate parking lots. Similarly, Kelkit and Ozel [1] and Sisman and Gulturk [11] indicated that parking lots in school gardens of Canakkale and Tekirdag were used for various purposes.

Figure 8. A view from Kadir Kameroglu Vocational and Technical Anatolian High School

4. CONCLUSIONS

In general, Beycesultan Vocational and Technical Anatolian High School out of four schools was adequate from the standpoint of most design principles. On the other hand, Kadir Kameroglu Vocational and Technical Anatolian High School was the most inadequate among the case schools. Sport areas, seating equipment and parking lots were virtually inadequate in the schools. In conclusion, improving conditions of school gardens with the help of educators, spatial planning and design experts and local community would contribute to the youths' physical and psychological development.

REFERENCES

[1]. A. Kelkit and A.E. Ozel, "A Research on the Determination of Physical Planning of School Gardens in Canakkale City," *Pakistan Journal of Applied Sciences*, vol. 3, pp. 240-246, 2003.
[2]. O. V. Aksu and O. Demirel, "Trabzon Kenti Ilkogretim Okul Bahcelerinde Tasarim ve Alan Kullanimlari," *SDU Orman Fakultesi Dergisi*, vol. 12, pp. 40-46, 2011.
[3]. O. Tandogan, "Cocuklar Icin Daha Yasanilir Okul Bahceleri," *MEGARON*, vol. 11, pp. 629-637, 2016.
[4]. H. Yilmaz, "Erzurum Kenti Okul Bahcelerinin Peyzaj Mimarligi Ilkeleri Yonunden Incelenmesi," *Ataturk Universitesi Ziraat Fakultesi Dergisi*, vol. 26, pp. 537-547, 1995.
[5]. A. Ozdemir and O. Yilmaz, "Ilkogretim Okullari Bahcelerinin Cocuk Gelisimi ve Saglikli Yasam Uzerine Etkilerinin Incelenmesi," *Milli Egitim Dergisi*, vol. 181, pp. 121-130, 2009.
[6]. G. Akdogan, *Bes Buyuk Sehirde Cocuk Oyun Alanlari, Okul Bahceleri ve Spor Alanlarinin Yeterlilikleri ve Planlama Prensipleri Uzerinde Bir Arastirma*, Ankara Universitesi Ziraat Fakultesi Yayinlari: 522, Ankara, 1972.
[7]. Anonymous, 3194 number law on construction, 2 September 1999.
[8]. B. Karakaya and T. Kiper, "Edirne Kent Merkezindeki Bazi Ilkogretim Okul Bahcelerinin Peyzaj Tasarim Ilkeleri Acisindan Mevcut Durumunun Belirlenmesi," *Tekirdag Ziraat Fakultesi Dergisi*, vol. 10, pp. 59-71, 2013.

[9]. I. M. O. Erdonmez, "Ilkogretim Okul Bahcelerinde Peyzaj Tasarim Normlari," *Istanbul Orman Fakultesi Dergisi*, vol. 1, pp. 108-120, 2007.

[10]. E. S. Arslan Muhacir and A. Yavuz Ozalp, "Artvin Kenti Ilkogretim Okul Bahcelerinin Nitelik ve Niceliksel Durumunun Cografi Bilgi Sistemleri Kullanilarak Belirlenmesi," *Artvin Coruh Universitesi Orman Fakultesi Dergisi*, vol. 12, pp. 172-184, 2011.

[11]. E. E. Sisman, P. Gulturk, "Ilkogretim Okul Bahcelerinin Peyzaj Planlama ve Tasarim Ilkeleri Acisindan Incelenmesi: Tekirdag Ornegi," Tekirdag Ziraat Fakultesi Dergisi, vol. 8, pp. 53-60, 2011.

ICENS 4TH INTERNATIONAL CONFERENCE ON ENGINEERING AND NATURAL SCIENCE
2 - 6 May 2018 KIEV UKRAINE

Removal of Ammonium Nitrogen from the DAF-Pretreated Poultry Slaughterhouse Wastewater by *Lemna Minor*

F. Ilter Turkdogan [1], Kaan Yetilmezsoy[2], Bulent I. Goncaloglu[2], Necmiye Keskintimur[2], Melike Gungordu[2], Cagri Akyol[2]

Abstract

In this study, ammonium, COD, color and turbidity removal with using Lemna Minor (duckweed) was searched in Poultry Slaughterhouse (PS) wastewaters. Reason of poultry slaughterhouse (PS) wastewaters contains high concentration of organic compounds, ammonia and fats. Wastewater was taken from effluent of Dissolved Air Flotation (DAF) unit, then using MAP process, upper phase was given to reactor which Lemna Minor was being. COD , ammonia, color, turbidity parameters were analyzed after hydraulic retention time of 7 days. The result of the study showed that Lemna Minor is effective in treatment of poultry slaughterhouse wastewaters. In this study especially ammonia removal was investigated. At the same time COD, color and turbidity removal were researched. In this study, ammonia removal efficient was around % 30.08±4.67, Lemna minor was effective in COD, color and turbidity removal as 26.58 ± 8.35; 35.06 ± 15:20; and 51.07 ± 18.77 respectively removal.

Keywords: ***Lemna Minor (duckweed), Poultry slaughterhouse wastewater,***

1. INTRODUCTION

The poultry slaughtering industry has enormous economic importance as the quickly developed among Turkey's other industries. According to the Ministry of Food, Agriculture and Livestock, consumption has grown from 10.5 kg/person in 2002 to 20.3 kg/person in 2015 (Republic of Turkey Ministry of Food, Agriculture and Livestock, 2016).

The poultry slaughtering industries generate large volume of wastewaters containing very high concentrations of organic matter (Quinn and McFarlane, 1989; Sandogoyin and Agbawhe, 1992). Slaughterhouse wastewaters contain different kinds of chemical substances, including dissolved organic compounds and total suspended solids (TSS) including fat, grease, feather, manure, flesh, grit, hair, and undigested feed as well (Bull et al. 1982; Tritt and Schuchardt, 1992). Slaughterhouse wastewaters contain high concentrations of ammonia with many pollutants and direct discharge of these waters cause serious environmental problems. Discharge of such wastewater leads to undesirable aquatic growth and eutrophication. For this reason, these wastewaters should be given receiving conditions after the appropriate criteria are provided according to the characteristics and legislation to be discharged by the treatment.

[1] *Corresponding author: Yildiz Technical University, Department of Environmental Engineering, 34220, Esenler/Istanbul, Turkey. ilter@yildiz.edu.tr*

2 Yildiz Technical University,, Department of Environmental Engineering, 34220, Esenler/Istanbul, Turkey. yetilmezsoy@yildiz.edu.tr, goncal@yildiz.edu.tr

Biological processes are economical and effective in these type of wastewater treatment. But it needs large area and long hydraulic retention time. Physico-chemical treatments are sometimes preferred for some wastewater treatment, due to the shorter hydraulic retention time. Physico-chemical processes such as dissolved air flotation

(DAF) and coagulation–flocculation (CF) are widely used for the removal of TSS, colloids, and fats from slaughterhouse wastewaters (Massé and Masse, 2000). In PS wastewaters, which are also very rich in nitrogen concentration, lowering nitrogen concentrations can prevent possible eutrophication problems in the receiving environment. If PS wastewater is kept in "polishing units" as *Lemna* pools in the last stage of the process, nitrogen levels could be decreased to much lower levels. Duckweed is a low-cost process and efficient method for the treatment of water and wastewater. The purpose of this work is to use duckweed in treating poultry slaughterhouse wastewater after DAF and MAP process. Purification mechanisms such as sedimentation, adsorption, bacterial decomposition and vegetal use are effective in the treatment process with water plants. Organic matter removal is increased by providing surface area for both oxygen and bacterial growth by *Lemna minor* (Korner et al., 1998). Ammonium is the primary source of nitrogen in *Lemna minor* (Yilmaz et al. 2005). Earlier studies have shown the possibility of simultaneously removing of TSS, BOD and COD from slaughterhouse wastewaters. It was tested successfully removal rate of NH4 and COD 41-48% and 17-20%, respectively (Oron et al, 1987). In another study conducted with urban wastewater, the COD removal rates in three parallel units were 61%, 72% and 63%, respectively and TSS removal rate of 82% and 80% was observed (Mandi 1994). Yilmaz et al. (2005) investigated *Lemna minor* activity was at laboratory scale in the treatment of campus wastewater. The last settling basin in *Lemna minor* was compared to the last settling basin in which there is no *Lemna minor* basin. In the last sedimentation pool located in *Lemna minor*; COD removal yield was found to be 15%, BOD5 removal yield 25%, ammonium removal yield 35%, and phosphate removal yield 45% higher (Gurtekin and Sekerdag, 2008). Although studies have been carried out to remove a wide range of wastewater with *Lemna minor*, there is not yet a study in the literature on PS wastewater.

In the present work, *Lemna minor* was used to treat the polishing units and to remove the fine oxide particles. Experimental conditions of the process and effluent wastewater quality before and after treatment were determined. The main objective of the present study was to examine the feasibility of *Lemna minor* after the DAF unit process in treating PS effluent before discharge into urban sewer.

2. MATERIALS AND METHODS

2.1. Characterization of PS Wastewater

PS wastewater was obtained from a local poultry processing plant (Mudurnu Pilic) located in Dilovasi, Izmit (TURKEY). The wastewater samples were taken from the effluent of the dissolved air flotation (DAF) unit at the poultry processing plant (Table 1).

Table 1. Characteristics of the DAF pretreated PSW

nstituent	**Value (mean ± S.D.)**
tal Chemical Oxygen Demand, TCOD (mg/L)	1032.57± 5.35
latile Suspended Solids, VSS (mg/L)	49 ± 17.4
tal Suspended Solids, TSS (mg/L)	58 ± 15.63
‹alinity (mg $CaCO_3$/L)	205 ± 12.8
ımonium Nitrogen, NH_4^+-N (mg/L)	123.75± 4.23
	7.1 ± 0.20

2.2. $MgNH_4PO_4.6H_2O$ (MAP) Precipitation Tests

Due to high NH_4^+-N and COD in PS wastewater may causes some toxic effect on the *Lemna minor*, in order to the toxic effect was studied MAP precipitation. After the precipitation of the MAP, the values of COD 300-350 mg/l and NH_4^+-N 60-70 mg /l were obtained.

Amounts of chemicals used to precipitate the ammonium nitrogen in the wastewater of slaughterhouse in MAP form were determined according to Equations (1) - (3) and as a source of magnesium and phosphate were added to the PSW at stoichiometric ratio (Mg^{2+}: NH_4^+-N: PO_4^{3-} P = 1: 1: 1).

$$MgCl_2.6H_2O + KH_2PO_4 + NH_4^+ \rightarrow MgNH_4PO_4.6H_2O \downarrow + K^+ + 2Cl^- + 2H^+ \quad (1)$$

$$MgSO_4.7H_2O + Na_2H_2PO_4.2H_2O + NH_4^+ \rightarrow MgNH_4PO_4.6H_2O \downarrow + Na^+ + SO_4^{2-} + 2H^+ + 7H_2O \quad (2)$$

$$MgOHCO_3 + 85\%\ H_3PO_4 + NH_4^+ \rightarrow MgNH_4PO_4.6H_2O \downarrow + H_2O + HCO_3^- \quad (3)$$

2.3. *Lemna Minor*

Lemna Minor was collected from Istanbul University Botanical Garden, Istanbul-Turkey (Figure 1). Working with the *Lemna minor* plant was started immediately, but it was kept in a container with the original water for one day before starting to work.

Figure 1. Image of Lemna Minor with stereomicroscope (Prior-James Swift, 240V.AC, F80 mA)

2.4. Analytical Procedure

The pH of wastewater samples was measured by a pH meter (Jenway 3040 Ion Analyser). Ammonium nitrogen (NH_4^+-N), total chemical oxygen demand (TCOD), total suspended solids (TSS), volatile suspended solids (VSS), and alkalinity were conducted by the procedures described in the Standard Methods (2005). Samples were ignited at 550°C by using an ashing furnace (Lenton) for VSS analyses. Absorbance values were recorded at 425 nm by using a spectrophotometer (Pharmacia Biotech LKB Novaspec® II) for NH_4^+-N analysis. Color and Turbidity were measured by the HACH LANGE DR5000 spectrometer.

2.5. System Design

In the study, a reactor with a volume of 6L and an active volume of 5.6 L was used from Plexiglas material. A weir structure has been placed between the wastewater so that the wastewater can be delivered equally to the system. Sluice was placed in order to ensure mixing and better distribution in the reactor. At the exit of the reactor, a wire plate was placed in the outlet pipe to prevent the *Lemna minor* escaping. During the study conducted under this work, a modulated fluorescent lamp (Panlight daylight lamps, 3011 T8 36W) was used as artificial light in the cultivation experiment setting. The system was operated in a daily continuous mode by feeding with a SEKO® peristaltic pump. Hydraulic retention time (HRT) was set to 7 days for reactor. A detailed schematic of the experimental set-up is depicted in Fig. 2

3. RESULTS AND DISCUSSION

3.1 NH_4^+-N and COD Removal of MAP

Table 2 shows the NH_4^+-N and COD values obtained as a result of MAP sedimentation in the samples taken from the DAF unit of slaughterhouses wastewater.

Table 2. NH_4^+-N and COD values of MAP

Parameter	***MAP Inffluent***	***MAP Effluent***	***Removal Rate %***
NH_4^+-N	*123.75±4.23*	*83,6±23,1*	*32.44±3.97*
COD	*1032.57±5.35*	*348,1±40*	*66.29±2.58*

3.2. NH_4-N, COD, Color and Turbidity Removal of *Lemna Minor*

Table 3 shows the NH_4^+-N, COD, color and Turbidity values after *Lemna minor*.

Fig.2. A detailed schematic of the experimental set-up.

Table 3. NH_4^+-N, COD, Color and Turbidity values of Lemna Minor

Parameter	*Inffluent*	*Effluent*	*Removal Rate %*
COD	*348,1±40*	*255.57±25.07*	*26.58±8.35*
NH_4^+-N	*83,6±23,1*	*58.45±5.06*	*30.08±4.67*
Color	*72.83±12.29*	*24.33±16.62*	*35.06±15.20*
Turbidity	*25.01±2.72*	*12.22±4.54*	*51.07±18.77*

4. CONCLUSIONS

High ammonia concentrations are a problem for wastewater if the receiving environment standards are low. This type of wastewater needs to be well treated before the discharge. Existing methods add cost in the treatment plants. Low-cost systems added to the output of existing plants are getting interest. The use of *Lemna minor* pools, which is a natural method, provides an important treatment without energy cost. With this study, it was demonstrated that *Lemna minor* pools can be used as a "polishing" step.

Acknowledgements

The authors would like to thank Istanbul University Botanical Garden, Istanbul-Turkey for supplying the *Lemna Minor* used in this work.

REFERENCES

[1] Republic of Turkey Ministry of Food, Agriculture and Livestock, 2016 Internet: https://www.tarim.gov.tr/HAYGEM/Belgeler/Hayvancilik/Kanatli_Yetistiriciligi/TURKIYE_VE__DUNYADA KANATLI_SEKTORUNUN_GENEL_DURUMU-2016.pdf
[2] Quinn J.M. and McFarlene P.N. (1989) Effects of slaughterhouse and dairy factory wastewaters on epilithon: A comparison in laboratory streams, Water Research 23-10 pp 1267-1273
[3] Sandogoyin AD and Agbawhe OM (1992). Environmental study on surface and ground water pollutants from slaughterhouse effluents, Bioresource Technology, 41 pp 193-200
[4] Bull M.A. , Sterritt R.M. , Lester J.N. (1982) The treatment of wastewaters from the meat industry: a review, Environ. Technol. Lett., 3 (1982), pp. 117-126
[5] Tritt WP and Schuchardt F., (1992), Materials flow and possibilities of treating liquid and solids from slaughterhouses in Germany, Bioresour. Technol., 41 pp. 235-245
[6] Masse D. and Masse L. (2000) The effect of temperature on slaughterhouse wastewater treatment in anaerobic sequencing batch reactors, Bioresource Technology 76-2 pp 91-98
[7] Korner S. and Vermaat, J.E., 1998, The relative importance of Lemna gibba L., bacteria and algae for the nitrogen and phosphorus removal in duckweed-covered domestic wastewater, Water Res., 32, 12, 3651-3661.
[8] Yilmaz Z. Gur K. Tarlan E. (2005), S.U. Atiksularinin Karakterizasyonu ve Su Mercimegi ile Aritilabilirligi , S.U.Muh.-Mi.Fak.Dergi.cilt:20,sayi:4, Konya.
[9] Oron, G. vd., (1987), Performence of the Duckweed Species Lemna Gibba on Municipal Wastewater for Effluent Renovation and Protein Production, Botech. And Bioeng., 29 (2), 258 – 268, (1987).
[10] Mandi L. (1994) Marrakesh Wastewater Purification Experiment Using Vascular Aquatic Plants Eichhornia crassipes and Lemna gibba, Water Science and Technology 29 (4) pp 283-287
[11] Gurtekin E., Sekerdag N. (2008), Son Cokeltme Havuzlarinda Su mercimeginin (L.Minor L.) Rolu, SAU. Fen Bilimleri Dergisi, cilt:12,Sayi:1,Syf:28-31,Elazig.
[12] American Public Health Association (APHA), (2005), Standard Methods for the Examination of Water and Wastewater, 21st Ed., Washington, DC.

ICENS 4TH INTERNATIONAL CONFERENCE ON ENGINEERING AND NATURAL SCIENCE
2-6 May 2018 KIEV UKRAINE

Biological Solid Waste Management In Turkey and Other Countries

Gurdal Kanat[1], Bulent Ilhan Goncaloglu[2] And Gokhan Onder Erguven[3]

Abstract

Today, the world is facing many serious challenges, including ever-growing human population and the consequent security for food, energy, and water. In addition, the greenhouse gas emissions and various other pollutants are posing a serious threat to mankind due to anthropogenic climate change. As a result, the gap between environmental sustainability and economic growth is increasing. Therefore, the need for sustainable technologies and policies to mitigate climatic change and provide a constant supply of energy and feed has become critical for enabling circular economies in the developing countries. The sustainable disposal of waste is still in infancy in most of the developing countries due to limited allocated budgets, infrastructure and maintenance facilities. The high generation rates of organic waste and its disposal to open dumpsites or non-sanitary landfills are resulting in adverse environmental, economic and social problems. Reduction of landfills and dealing with the waste are among the key elements of the cleaner production and advanced environment policy. Composting represents one of the cleaner technologies in diverting organic waste from landfill. In the study, details of solid wastes management problems and success stories in Turkey and other similar countries are also been examined and results are discussed.

Keywords: Composting, developing countries, municipal solid waste, recycle

1. INTRODUCTION

Municipal Solid Waste (MSW) is an unavoidable by-product due to population growth, increasing urbanization and socio-economic development of the countries. MSW is by far the most heterogeneous kind of refuse, being a direct result of the multiplicity of activities in urban environments. Appropriate waste management is therefore a crucial matter, not only because of environmental and human health concerns, but also as a step ahead towards sustainable production and consumption. The management of MSW is currently one of the most serious and controversial issues faced by the local and regional authorities of developed countries.

Biodegradable material, primarily food waste, normally includes 40-70% weight of MSW in developing countries. Therefore, to establish a sustainable waste management system, it is essential to separate and recycle biodegradable organic material. There has been increasing attention on improving the management of the organic fraction of municipal solid waste. Thus, diversion of organic material from the waste stream, by either source separation or centralized mechanical separation, is a prerequisite for further treatment by more environmentally friendly and economic methods, such as composting.

The member countries of the European Union (EU) are required to implement waste management systems that comply with a hierarchy of options, over the following order of priority: prevention (in waste generation), preparing for reuse, recycling, other types of recovery (including energy) and, finally, disposal (Directive on Waste, 2008/98/EC). Moreover, sending biodegradable organic matter to landfill must be phased out gradually. Nevertheless, despite improved legislation and regulatory systems, public acceptance of the location of new waste disposal and treatment facilities is still very low, due to concerns about adverse effects on the environment and human health. Within this context, sustainable MSW management needs support by suitable environmental assessment methods that evaluate the environmental feasibility of waste management strategies. The European

[1] *Corresponding author: gkanat@gmail.com*

[1-2] *Yildiz Technical University, Department of Environmental Engineering, 34220, Esenler/Istanbul, Turkey.*

[3] *Department of Environmental Engineering, Faculty of Engineering, Munzur University, Tunceli, Turkey.*

Commission calls for increased use of Life Cycle Thinking (European Parliament and Council, 2008) to complement the waste hierarchy of priorities.

2. METHODOLOGY

The methodology of the study followed to achieve a case study analysis of selected countries and composting applications and reasons of failure in Turkey. The UK, USA, Japan, and China were selected for the case study given their geographical, socio-economic, waste composition, and waste management profiles.

3. BIOLOGICAL SOLID WASTE MANAGEMENT

Municipal solid waste (MSW) is largely made-up of kitchen and yard waste, and its composting has been adopted by some municipalities. Composting of MSW is seen as a method of diverting organic waste materials from landfills while creating a product, at relatively low-cost, that is suitable for agricultural purposes [1,2].

Adding compost to soil provides nutrients for plant growth, improves the soil structure, increases the water retention capacity, and reduces the reliance on fossil-fuel-based fertilizers. In recent years, Compost has been widely studied for soil remediation and has been identified as the cheapest and most suitable material for in situ heavy metal removal, immobilization of pesticides, and removal of emerging pollutants.

Centralized composting has been adopted in many regions worldwide to divert organic waste (e.g., green waste, kitchen waste, etc.) from landfills and incinerators. Removing green waste, such as yard trimmings, sweeping waste, and garden waste from the municipal waste stream has long been implemented in North America and some European countries, including the UK, Germany, and Spain. However, food waste diversion lags far behind green waste diversion. Regardless, great efforts to recycle food waste for composting have been undertaken, especially in several European countries. In the past two decades, EU member states have adopted more stringent landfill tax policies to minimize the biodegradable municipal waste sent to landfills.

However, various environmental issues may arise during the composting process, including the formation of malodorous or toxic gases, bioaerosols, and dust, resulting in occupational health risks or disturbance to nearby residents [3-5]. It is known that composting has some health problems, such as biological risks, bacteria (mainly gram-negative), fungi (mainly A. fumigatus), endotoxins, parasitic protozoa or chemical risks such as volatile organic compounds (VOCs). However, those problems are mainly in or around near area of the plants. Moreover, waste-derived compost may elevate heavy metal concentrations in soil and food products cultivated in soil amended with MSW compost.

Composting, when managed appropriately, is a sustainable waste management option that has various benefits, including reducing greenhouse gas production and improving soil quality when used as a soil amendment. However, when improperly managed and performed, composting may lead to some environmental issues. In general, the major environmental concerns associated with MSW composting include malodor, bioaerosol, dust, noise, and leachate generation during various composting operations, as well as their release to the surrounding environment beyond the composting facilities (together with potential exposure to heavy metals, organic pollutants, and pathogenic agents in the case of compost application to soil. Of these concerns, odors, bioaerosols, and heavy metals have been most intensively studied due to their high potential risks.

Among the environmental factors associated with MSW composting, odor has attracted great attention due to its substantial impact on environmental health and quality of life. In 2005, the Taiwan Environmental Protection Administration legislated mandatory recycling and composting of household food waste. However, malodors from food waste composting plants present another problem. In 2004 and 2005, four food waste composting plants located in north and central Taiwan were forced to shut down due to protests from nearby residents. Malodors are probably the most demanding challenge for emerging environmental policy in Taiwan [3].

MSW compost containes heavy metal concentrations greater than the background soil levels and there is a risk of heavy metals from MSW compost applied to land. . Therefore, applying MSW compost to soils could increase metal concentrations, resulting in an increased uptake of labile elements, such as zinc (Zn) and copper (Cu), by crops [3].

3.1. Waste Management in Some Countries

Composting rate and food waste management in some countries are listed below [3,4]:

- MSW composted in EU increased from 8% to 15% from 1999 to 2013
- In UK, mandatory targets => landfill tax, from 7 to 84 GBP/ton in 1996 to 2016

- In England, only 0.8 million tons household waste (3% of total) was composted in 2000. But in 2014, 4 million tons (19%)
- Food waste collected separately increased over 20 times from 2006 to 2012, to nearly 350,000 tons
- 1990 to 2010, approx. 180 mechanical-biological treatment plants were installed in EU to divert biodegraded waste from landfills.
- In Spain, capacity was increased by 5 million tons through the installation of 50 new MBT plants.
- In USA, in 1990, 4.2 million tons of MSW (2% of total) was composted.
- Increase to 20.6 million (8.4%) in 2005 => by encourage yard trimmings compost. MSW composting stagnated in the 10 years after 2005
- From 1985 to 1995, landfill tax increased by 177% but in 2013 it was $50/ton, only 1.58 % higher => no motivation to recycle/compost
- In 2013; yard trimmings was 37, food waste was 37 million tons, only 58% and 5% were composted
- In Canada, MSW composting facilities in Guelph, Ontario, and Lunenburg, Nova Scotia have shown landfill diversion rates in excess of 70 and 67%, respectively
- MSW composting rate in China decreased from 10% to less than 2% in the past 15 years and similar trends may exist in other developing countries
- In Canada, MSW composting facilities in Guelph, Ontario, and Lunenburg, Nova Scotia have shown landfill diversion rates in excess of 70 and 67%, respectively,
- But, MSW composting rate in China decreased from 10% to less than 2% in the past 15 years, and similar trends may exist in other developing countries.

Therefore, it is essential to identify the barriers that impede waste composting and predict developing trends.

3.2. Composting applications and failures in Turkey

In the past years, composting plants were built in a few cities in Turkey. Composting applications and reasons of operation failure in Turkey in the past years are seen in Table 1.

Table 1. Composting applications and reasons of failure in Turkey.

CITY	**PROBLEMS**
Mersin	-Not considered the local waste characteristics,
* 160 t/h	-No local material market,
* %50 of city waste	-Using old technology, no spare parts
* by French GONDAT firm	-No work in rainy weather because the floor is not concrete
	-Political reasons, personnel change, etc.
	-In winter, compost cannot pass through the screen
Antalya	-Very high electricity demand-operating cost
50 t/day	-Foreign matter in the compost is also high
Izmir	- Problems in machines
500 t/day	- High operation cost
Marmaris	- Only a few days operation

Giresun 60 ton/day	-Only 5 years, non-continuous operation -Compost is given free of charge -Bad operation, low quality compost -Consumers, farmers were not happy with this compost -Especially odor complaints -No operation due to precipitation in winter conditions -Separated waste is not well marketed -Frequent machine problems -Work of inexperienced technicians

As seen from the Table, composting was planned and built in a few cities. Almost all of these plants were planned by the central authority and built by a company, but as seen, there have been many problems related to design and local conditions as well as the operation. As a result, it is seen that the most important problems are engineering problems and the municipalities do not pay enough attention to this issue.

It is not easy to say that municipalities in Turkey do not have very high quality construction for infrastructure investments, such as water and sewer facilities but have enough success for infrastructure in the cities where public (voters) directly affected. However, there are some, or even many problems in sanitary landfilling of solid waste or operating the composting plants, or even built and operating wastewater treatment plants. Municipalities and the ministry cannot show sufficient success in solving these problems and its organization.

Table 2. Composting plants in Turkey in recent years.

PROVINCES	**Waste capacity tonnes/year**	**Amount of transferred tonnes/year**	**Amount of composted* tonnes/year**
Izmir	127750	64499	38866
Istanbul	365000	139346	71243
Antalya	54750	71348	32385
Denizli	3000	544	544

* Real data is different than this reported data (explained in the text)

In the Table, capacity of the facilities is seen as high but actually these values are lower. For example, the information about the facility in Istanbul is reported as 20,000 tons/year.

3.3. Waste Management in Istanbul and Turkey

Istanbul city has performed improvement in solid waste management in the last decades and do plans for next years. For example, sanitary landfill was built after 1994 and will supply 25 years energy production from landfill gas. Municipal solid waste is rising up to 20,000 tons per day. The city can evaluate only %15 of the waste, recycle/recover only %4.5 and landfill of the remaining %85. An incineration facility, capacity with 3,000 tons/day was planned in 2009 and will be operation in 2021. Also, 100 tons/day biomethanization plant is planned to be in operation in 2024. Then, electricity of about 1.5 million people will be supplied and, landfill

will be lower to ~%50. Average annual compost production is 19,000 tons/year in a 1,000 ton/day capacity plant. Compost is used in green park areas, but municipality has a sale price of 45 TL/ton (1$ = ~4 TL) in 2018 [6].

According to the latest report published by the Ministry of Environment, the amount of municipal waste generated in Turkey in 2014 was 27.1 million tons [7]. Recycled municipal waste was 6% while 64% was disposed of in sanitary landfills and 30% in open dumping areas. Similar to other countries, it is planned to dispose of municipal wastes in Turkey with the most appropriate and economical methods. MSW in 2018 was 30 million tons, and it is expected to be 33 million tons in 2023. In the plan, it is targeted to reach to 65% landfill and 35% recovery in 2023. For this purpose, separately collected packaging waste at the source in 2014 (5.3%) is planned to reach 12% in 2023. Biological methods for municipal waste, which is 0.2% in 2014, will be raised to 4%. Rate of the MBP processes, 5.4% in 2014, will be increased to 11%. Then, landfilling rate of municipal waste, which was 88.7% in 2014, will be reduced to 65% in 2023.

The present situation of the 81 provinces was determined and waste management strategies prepared for 2023 in Turkey. Facility types for planned waste management activities, capacities and investment costs arise on a regional basis. Municipal waste management planning was based on the objectives of the Waste Landfill Regulation and Packaging Wastes Control Regulation.

In the present case, there are 8 biological waste processing facilities in Turkey. The provinces of Amasya, Aydin, Balikesir, Canakkale, Denizli and Kutahya have compost process while in Kocaeli and Sakarya provinces, biomethanization process was used. Moreover, there are 6 mechanical-biological pre-treatment and recycling facilities where mixed municipal waste is processed. These are 2 compost and bioprocessing facilities in Istanbul, and 4 biomethanization processes in Ankara, Adana and Samsun.

When the data are examined, waste amount in Turkey in 2014 was averagely 0.96 kg/person-day. Calculations of estimation of waste generated show that municipal waste in 2018 was 30 million tons, and it is expected to be 33 million tons in 2023. In the management plans, the waste formed in 2023 was targeted to 65% landfilled and 35% recovery. For this purpose;

- Packaging waste, 5.3% separately collected at the source in 2014 will be planned to reach 12% in 2023
- Biological methods for municipal waste, which is 0.2% in 2014, will be raised to 4% in 2023
- Rate of the MBP processes, 5.4% in 2014, will be increased to 11% in 2023
- Landfilling rate of municipal waste, which was 88.7% in 2014, will be reduced to 65% in 2023.

Vermicomposting: Vermicomposting is increasing in Turkey. It is not easy to say that it is correct or not, because there is no technical data but in media news, people say that they have a good amount/sufficient money by vermicomposting (small or larger scale-up to 2-3000 tons/month). Those plants are operated mainly by using organic waste, not mixed municipal waste.

Recently, Ministry of Environment activated a National “Zero waste” plan which will be firstly applied in governmental agencies and later, in shopping malls, hospitals, schools, universities and large workplaces (> 1000 employees) until 2023 (anniversary of Turkish Republic). It is applied in Ministry’s Main Building for 3 months and reported that 45 tons paper, 11 tons plastic, 2.5 tons glass, 1 ton metal and in total approximately 60 tons waste was a gain in the economy [8]. There are only few details about organic material composting. JK6200 compost machine (Sweden) is used to produce 180-200 kg compost from 1000 kg waste in 30 days.

3.4. Recommendations for Waste Management and Composting

In different studies, it is advised do not or do for a successful composting:

- Separated organic collection system,
- Big plants should not be constructed before getting experience,
- Automatic installations should be well examined and, if possible, not preferred in terms of operating and maintenance costs
- It should not be misunderstood that the compost product is the material that can be used and sold very easily
- Optimal technology choice should be investigated
- Very good planning should be done, not believe in magic technologies like enzyme or special bacteria species.

- Development of adequate strategies and the identification of market are prerequisites for successful and long term operation of composting.
- It is recommended that municipalities ensure: Political will and continuity of policy, Development of action plans on how to ensure appropriate organic waste management, Education and training of the entire MSW personnel.

In Turkey, following points can be listed in composting activities:

- The Ministry is unable to provide adequate, sufficient coordination
- The municipalities are inexperienced and irrelevant/uninterested (planning and operation phases of plants)
- The municipalities, for various reasons, hastily prepared plans, politics, etc. Do not get enough knowledge (or cannot) from the other experienced institutions.
- There is very little cooperation between the universities and public/private institutions.
- Composting requires great support and involvement from the government as well as initiatives and commitment from business corporations and other private sectors.
- Good cost benefit analyze is a must before deciding to construct composting plants,
- Business persons do not see composting as a business venture
- MBT had weak economic performance and required an economic support policy
- Turkish farmers should be educated about benefits of compost as a fertilizer and/or soil conditioner.

4. CONCLUSION

This article provides a critical review of MSW composting practices in developed and less-developed countries. Such information may be particularly useful in assisting less developed countries seeking to upgrade their sustainable waste management strategies.

Similar to other developing countries, biological solid waste management, except landfilling has not been successful in Turkey until recent years due to some problems.

The Life Cycle Assessment (LCA) studies increased in recent years but still very complex to give a clear result to choose any waste management alternative. Those studies are not yet an excellent framework for evaluating waste management strategies and not yet helpful in identifying appropriate solutions for managing solid waste.

REFERENCES

[1]. Hargreaves, J.C., Adl, M.S., Warman, P.R., 2008. A review of the use of composted municipal solid waste in agriculture. Agric. Ecosyst. Environ. 123, 1–14.
[2]. Laurent, A., Bakas, I., Lavreul, J., Bernstad, A., 2014. Review of LCA studies of solidwaste management systems – part I: lessons learned and perspectives. WasteManage. 34, 573–588.
[3]. Wei et al. (2017) Environmental challenges impeding the composting of biodegradable municipal solid waste: A critical review, Resources, Conservation and Recycling, 122, 51–65.
[4]. Pearson, C., Littlewood, E., Douglas, P., Robertson, S., Gant, T.W., Hansell, A.L., 2015.Exposures and health outcomes in relation to bioaerosol emissions fromcomposting facilities: a systematic review of occupational and communitystudies. J. Toxicol. Environ. Health B Crit Rev. 18 (1), 43–69.
[5]. Domingo, J.L., Nadal, M., 2009. Domestic waste composting facilities: a review of human health risks. Environ. Int. 35, 382–389.
[6]. Istac, webpage available: www.istac.istanbul, April 2018.
[7]. Csb, Ministry of Environment, 2017 Annual Report, webpage available: webdosya.csb.gov.tr, April 2018.
[8]. Csb, Ministry of Environment, webpage available: sifiratik.csb.gov.tr, April 2018.

ICENS 4TH INTERNATIONAL CONFERENCE ON ENGINEERING AND NATURAL SCIENCE
2-6 May 2018 KIEV UKRAINE

Effects of Different Nitrogen Sources and Doses on Yield, Yield Components and Some Technologic Properties in Cotton (*Gossypium hirsitum* L.)

***Cuneyt Cesur*[1]**

Abstract

In this study it was used three different nitrogen sources (AN, AS and Urea) and five different doses (0, 5, 10, 15 and 20 kg/da) in order to Show the effect in fibre technological characteristic of cotton plant (Maras – 92) yield and yield components. In research it was analised what plant height, number of monopodial branches, number of sympodial branches, number of bolls per plant, cotton weight per boll, 100 seed weight, ginning out turn, boll weight, seed cotton yield, fibre finenes, fibre lenght and fibre strenght

In this research, the pozitive effect of nitrogen sources except cotton seed yield were not significant in all of the characters which were investigated, it was seen that the best yield of cotton with seed was available in plot of hand in urea application. In this study, was effect of significant analysed to other properties of different nitrogen doses, except plant height and seed cotton weight per boll. The seed cotton yield was determined in 20 kg/da nitrogen application (310 kg/da) and the highest yield was determined 15 and 20 kg/da nitrogen application. Again, the result of this study was effect of not significant interactions of different nitrogen sources and doses plant height, number of monopodial branches, number of bolls per plant, seed cotton yield, ginning out turn, seed cotton weight per boll, fibre finenes, fibre lenght and fibre strenght

According to the determined characteristic interactions of different nitrogen sources and nitrogen doses was effect of significant, 100 seed weight and fibre strenght and it was determined effect of significant fort he other characteristics.

Keywords: *Cotton, Gossypium hirsutum L., fertilizier, doses*

1. INTRODUCTION

In times when the population of the world was low, the possibilities of nature were sufficient for people. As population grew, wilderness agricultural lands were opened and new agricultural lands were being created. However, despite the increase population in today, it is obvious that no new agricultural areas can be created. while it was 21 million according to the 1950 years,Turkey's population reached about 56 million in 1990 census. While our agricultural areas were about 10 million hectares in 1950, 19 million hectares were discovered in 1990 due to the opening of new agricultural areas [1]. Population will continue to grow, although new agricultural areas are very difficult to form.

In the light of these data, these actuals show up: If mankind makes great developments in industry and technology and does not reach important developments in agricultural activities that are fundamental to life, it will not be able to endure its life.

All cultivated plants are a wealth for humanity. However, the importance of some plants like cotton is much more strategic. Countries which have climatic conditions for cotton farming, thanks to this plant they get great gains. Cotton plant is open plant to multiple use as fiber, oil, human food and animal nutirtion. China, U.S.A. and India have the world's largest economy, while Turkey is ranked 7th in cotton production [2]. Therefore,

[1] *Corresponding author: Bozok University,Agriculture Faculty, Department of Field Crops, 66100, Yozgat, Turkey.* *cuneyt.cesur@bozok.edu.tr*

Increasing the efficiency of cotton plant, which is very important for both Turkey and World should be continued to work unabated.

The point of aggregation of all agricultural studies related to soil in vegetable aquaculture is to take measures to protect and increase the productivity characteristics of the soil and to give productivity to the soil. It is seen that the largest share among the inputs that increase the product belongs to the fertilizer, and the fertilization increases the product increase by 60% [3]. For this, it is necessary to continuously follow the soil structures. Because the nutrients are constantly reduced due to the nutrients and climatic factors from the cultivated soil [4]. Preventing these losses and restoring the missing nutrients by fertilization is a prerequisite for efficient farming.

The character of the soil to be fertilized, climate of the region, the nutrients requirement of grown plants, fertilizer x soil interactions, time of giving fertilizer and giving methods are important for good yield [5]. If the lack of nutrient matter in the soil is not remedied, the crop is decrease, product quality due to malnutrition and marketing are reduced [3].

Kahramanmaras is in gateway between Akdeniz region and east Anadolu region. While central district is in Akdeniz region, other districts is in east Anadolu region. Intense cotton sowing is seen in districts where are Akdeniz climate's dominate. Cotton trade and industry are developed in this district because of these plantations. As seen, Kahramanmaras region have important potential in terms of cotton farming.

In this study, it was determined which is the most appropriate nitrogen sources (A.N., A.S., U) and dosages (0, 5, 10, 15, 20 kg/da) on yield, yield components and technologic properties in Maras – 92 cotton variety in Kahramanmaras region.

2. MATERIAL AND METHODS

2.1. Materials

In the study, Maras - 92 cotton variety, which was improved for the regional conditions, was used as seed. Maras - 92 variety, Caroline - Queen and Tashkent - 1 cotton varieties were breeded and Kahramanmaras Field Crops Breeding Station Directorate was rehabilitated and registered in 1992. Table - 1 shows the technological properties of this kind.

Table – 1. Some technological properties of boll and fiber of Maras - 92 variety

Boll weight (g)	Ginning out turn (%)	100 seed weight (g)	Fibre length (mm)	Fibre finenes (mic.)	Fibre strenght
6.0	39.0	9.5	29.5	3.6	93.5

In this study were utilized A.N., A.S., and urea as fertilizer sources.

2.2. Experiment area properties

2.2.1. Climate properties

The long-term climate values of Kahramanmaras province between April and September are shown in table 2; Table 3 gives the data for the year 1994 when it was established.

When the climate datas of the experiment site is compared with the table 2 and 3, it is seen that the minimum temperature averages are high compared to the average of long years but the maximum temperature averages are low. The mean temperatures were considerably lower in the test year than in the long years. When the precipitation totals are examined, it is determined that the precipitation totals for April are 68.6 mm in April, and the test year is 11.1 mm in April.

Table 2 The long-term climate values of Kahramanmaras province between April and September

Gozlemler	Nisan	Mayis	Haziran	temmuz	agustos	eylul
Min.sic.ort (°C)	4.4	7.8	13.1	17.6	17.8	12.8
Max.sic.ort (°C)	27.2	32.5	36.4	39.4	38.9	36.7
Ortalama sic. (°C)	14.5	19.8	24.5	27.8	28.0	25.1
Oransal nem (%)	59.8	55.5	49.5	49.2	50.9	49.5
Yagis top. (mm)	68.6	36.2	7.1	1.1	0.9	5.9
5 cm. top. Sic. (°C)	17.1	22.4	28.9	33.3	33.6	29.4
10 cm. top. Sic. (°C)	17.2	22.3	28.4	32.6	33.0	29.4

Source: Kahramanmaras Ili Meteorology Station Monthly Weather Reports, 1994

Table - 3. The climate values of Kahramanmaras province between April and September in 1994 year.

Gozlemler	Nisan	Mayis	Haziran	temmuz	agustos	eylul
Min.sic.ort (°C)	12.3	14.9	18.7	22.2	22.3	20.5
Max.sic.ort (°C)	25.2	28.2	32.0	34.9	36.2	36.1
Ortalama sic. (°C)	8.6	11.4	15.5	18.7	18.5	16.5
Oransal nem (%)	51.2	54.8	52.2	57.4	47.6	49.9
Yagis top. (mm)	11.1	55.8	6.6	0.0	0.0	0.4
5 cm. top. Sic. (°C)	21.2	24.6	30.9	33.7	33.5	31.5
10 cm. top. Sic. (°C)	21.0	23.9	29.1	23.5	33.1	31.4

Source: Kahramanmaras Ili Meteorology Station Monthly Weather Reports, 1994

2.2.2. Soil properties

Table 4 shows that the test site soil is neutral with high clay content. There is no problem in terms of salinity, but it can be observed that the organic matter contained therein differs considerably in terms of beneficial P_2O_5 and K_2O. From the same chart, it seems that the site of the test site is very poor in terms of organic matter.

Table - 4. Some physical and chemical properties of the test soil

Properties	Depth (30 cm)	Method
Sand (%)	21.44	Bouyucus, 1952
Silt (%)	33.67	Bouyucus, 1952
Clay (%)	44.89	Bouyucus, 1952
Lime (%)	20.71	Caglar, 1949
Saturation (%)	46.00	Yesilsoy, 1966
Soluble total salt (%)	0.073	Staff, 1954

Organic matter (%)	0.600	Jackson, 1959
pH	7.43	Jackson, 1959
Useful phosphorus (P_2O_5 kg/da)	5.15	Olsen, 1963
Useful potassium (K_2O ppm)	220.00	Blume, 1966

2.3. Method

2.3.1. Experimental method

The trial was established as 4 replications according to the parcel trial design divided in irrigable trial field by Kahramanmaras Agriculture Directorate, Field Crops Production Station Directorate. The trial parcel size (2.8 x 12 m) was determined as 33.6 m2. Fertilizer sources (Ammonium nitrate, ammonium sulphate, Urea) were applied as sub-parcels in the main plot and doses (0,5,10,15 and 20 kg / da).

2.3.2. Soil preparation and aquaculture operations

In the autumn, the deeply plowed field was treated several times until planting, 6 kg of P_2O_5 was applied before planting, and the bottom was pulled to make ready to plant. The sowing process was carried out on 12 May 1994 with a sowing machine, each parcel was arranged in 4 rows and 70 cm between rows. The plants were diluted by hand as they would be 20 cm above the row after the exit. Half of the nitrogenous fertilizers constituting the study were distributed homogeneously by hand before rowing and before the first irrigation after the first row, and the tractor was pulled over and mixed with the soil, followed by irrigation. Other maintenance procedures in the trial were made according to the soil operations performed in the area. During the growing, the cotton plant was watered 6 times, 4 times hand hoeand 5 times tractor hoe respectively. Work done is given in table-5 according to date order.

Table – 5. Cultural activities during the cultivation period

Aquaculture activities	Date
1.irrigation	22.05.1994
1.hoe (hand hoe)	02.06.1994
2.hoe (tractor hoe)	19.06.1994
2.irrigation	05.07.1994
3.hoe (hand hoe)	08.07.1994
4. hoe (tractor hoe)	20.07.1994
3. irrigation	27.07.1994
4. irrigation	03.08.1994
5. irrigation	15.08.1994
6. irrigation	01.09.1994
1.harvest	15.09.1994
2.harvest	25.09.1994

2.3.3. Investigation properties and method in experiment

Investigated characteristics were determined by studying 20 plants randomly selected from the plants which were 1'er m from the beginning and end of each parcel and two remaining plants after the two rows on the edge, according to the method of Reference [6].

3. RESULT AND DISCUSSION

The values of the different fertilizer sources and doses used in the research are shown in Table 6, which show the interactions on some plant and technological properties of cotton plant. According to the table, it is understood that different fertilizer sources used in the study have a 1% significance effect on the massive cotton yield of the cotton plant, but it does not have a statistically significant effect on the other properties investigated in the study.

While fertilizer doses were found to have a 1% level of effect on plant height, number of boll and massive cotton yield, it is understood that there are no statistical effects on other characteristics examined. In terms of the fertilizer type and fertilizer doze interactions, ginning efficiency, 100 seed weight and boll weight were found to have a significant effect on the 5% level, while the fiber strength was found to be 1%.

It can be observed that the plant height was increased with increasing nitrogen dose and the highest plant height pattern was obtained with 15-20 kg / da N application. These results have supported by the findings of reference [7]-[10].

Table - 6 shows that the number of boll was affected by 1% of different fertilizer doses. As the fertilizer doses will be seen in the grouping of the effect on the number of boll, the number of boll in the control dose was determined as 9,747 pcs / plant, whereas the number of boll detected at 15 kg / da application was 12,507 pcs / plant. As seen that obtained this results have supported with studies of [11]-[15].

Table – 6. The mean values of the effects of different fertilizer sources and doses on some characteristics of the cotton plant

Fertilizer Doses	Control	5 kg/da	10 kg/da	15 kg/da	20 kg/da	LSD	LSD (%5)
p.h:	63.724 b	65.425 b	65.574 b	71.615 a	74.758 a	(%1) 3.64	(%5) O.D
n.m.b:	0.586	0.713	0.698	0.759	0.752	(%5) O.D	(%5) O.D
n.s.b:	6.069	6.386	6.275	6.469	6.081	(%5) O.D	(%5) O.D
n.b:	9.747c	11.231 ab	10.952 bc	12.507 a	11.452 ab	(%1) 1.462	(%5) O.D
s.c.y:	234.0 b	275.6 a	276.1 a	291.0 a	310.2 a	(%1) 34.65	(%1) 28.98
g.o.t:	40.456	40.594	40.166	40.581	39.887	(%5) O.D	(%5) O.D
100.s.d:	10.094	10.153	10.075	10.229	10.293	(%5)O.D	(%5)O..D
c.w.p.b:	5.593	5.692	5.644	5.734	5.702	(%5)O.D	(%5)O.D
	7.130	7.171	7.172	7.267	7.193	(%5)O.D	(%5)O.D
	4.546	4.453	4.344	4.467	4.400	(%5)O.D	(%5)O.D
	29.426	29.357	29.884	29.607	28.901	(%5)O.D	(%5)O.D
	89.600	88.167	91.392	88.992	92.483	(%5)O.D	(%5)O.D

p.h: plant height, **n.m.b:** number of sympodial branch, **n.s.b:** number of sympodial branch, **n.b:** number of boll, **s.c.y:** seed cotton yield, **g.o.t:** ginning out turn, **100.s.d:** 100 seed weight, **c.w.p.b:** cotton weight per

applications	p.h	n.m.b	n.s.b	n.b	s.c.y	g.o.t	100s.w	c.w.p.b	b.w	f.f	f.l	f.w	
Fertilizer varieties													
Ammoniu m nitrate	68.384	0.707	6.400	11.446	260.1 b	40.141	10.225	5.791	7.341	4.457	29.289	90.120	
Ammonium sulphate	67.484	0.754	6.085	11.160	275.1 ab	40.668	10.163	5.673	7.184	4.459	29.378	89.631	
Urea (U)	66.791	0.645	6.274	10.928	297.0 a	40.201	10.119	5.555	7.034	4.410	29.638	90.625	

When we look at the seed cotton yield in the same table, it can be seen that both different fertilizer sources and different fertilizer doses have significant (1%)and positive effect. The highest seed cotton yield was obtained from urea application with 297.0 kg / da in different fertilizer sources and the highest seed cotton yield was obtained from 310.2 kg / da in 20 kg / da fertilizer doses according to different fertilizer doses. The lowest yield was obtained from control applications as 234.0 kg / da. It can be said that the increase of fertilizer doses in the light of this information increases the yield of the seed cotton yield. we were discovered that showed compatibility with finding of [16]-[19]. Although there is no significant difference between the N doses of non-control according to the research results, it is seen that the highest density of cotton yield is obtained by application of 20 kg / da. Although increasing nitrogen doses in the literature seem to increase the yield of seed cotton yield, the determined doses of optium nitrogen vary according to the investigators. These values were obtained from reference [16] at 15.8 kg / da; reference [20] 12 kg / da; reference [21] reported that the optimum nitrogen doses ranged from 3.6 to 9 kg / da, whereas [22] determined that they were 16 kg / da.

In the study, it is seen that different fertilizer sources and fertilizer doses interactions have a significant effect (1%) on seed weight and boll weight and (5%) on fiber strength.

Table – 7. Mean values of 100 seed weights and different fertilizer sources and different fertilizer doses interactions

Fertilizer doses	**A.N**	**A.S**	**Urea**	**Means**
Control	10.265 ^{ab}	10.123^{ab}	9.985^{b}	10.094
5 kg/da	9.865^{b}	10.208^{ab}	10.388^{ab}	10.153
10 kg/da	9.820^{b}	10.510^{ab}	9.895^{b}	10.075
15 kg/da	10.440^{ab}	10.203^{ab}	10.040^{ab}	10.229
20 kg/da	10.733^{a}	9.770^{b}	10.377^{ab}	10.293
Means	10.225	10.163	10.119	
L.S.D.: fertilizer variety * fertilizer doses interactions (%1) = 0.78				

From Table - 7 shows the interaction of different fertilizer sources and different fertilizer doses on 100 seed weights. As can be seen from the table, the highest 100 seed weight was obtained from 20 kg / da (A.N) application of the fertilizer as 10,733 (g). Although no statistical difference can be seen between fertilizer sources averages, the highest 100 seed weights was obtained from A.N applications as 10.225 (g). It was also found that the highest yield was obtained from 20 kg / da dose in average between doses as 10.293 (g).

Table – 8: Mean values of boll weight and different fertilizer sources and different fertilizer doses interactions

Fertilizer doses	**A.N**	**A.S**	**Urea**	**Means**
Control	7.245^{abcd}	7.400^{abcd}	6.745^{e}	7.130
5 kg/da	7.600^{a}	6872de	7.040^{bcde}	7.171
10 kg/da	6.938^{cde}	7.385^{abcd}	7.192^{abcde}	7.172
15 kg/da	7.505^{ab}	7.368^{abcd}	6.929^{cde}	7.267
20 kg/da	7.420^{abc}	6.895^{cde}	7.265^{abcde}	7.193
Means	7.341	7.184	7.034	
L.S.D.: Fertilizer variety * fertilizer doses interactions (%1) = 0.53				

From Table - 8 shows,the effect of different fertilizer sources and different fertilizer dose interactions on boll weight. As can be seen from the table, the highest boll weight was obtained from A.N application (5 kg / da fertilizer dose) as 7,600 (g). According to the average among the different fertilizer sources, Although there is no significant difference between them, the highest boll weight was found from A.N as 7.341 (g). According to the average among fertilizer doses, the highest boll weight was obtained from doses of 15 kg / da as 7.267 (g). There was no statistical difference in the order of fertilizer doses.

Table 9 shows the effect of different fertilizer sources and different fertilizer dose interactions on fiber strength. As tablodan can be examined, applications of Urea (5 kg / da, A.S 15 kg / da and A.N 20 kg / da) constitute the highest group while other applications are in the same group. These findings were show similarity with working of [7], [17], [19].

The other features investigated in the study were not found to be an important effect of both different fertilizer sources and different nitrogen doses.

Table – 9:Means values of fibre strenght and different fertilizer sources and different fertilizer doses interactions

Fertilizer doses	**A.N**	**A.S**	**Urea**	**Means**
Control	88.150^{ab}	92.675^{a}	87.935^{ab}	89.600
5 kg/da	87.025^{ab}	83.225^{b}	94.250^{a}	88.167
10 kg/da	94.275^{ab}	90.075^{ab}	89.825^{ab}	91.392
15 kg/da	87.475^{ab}	91.700^{a}	87.800^{ab}	88.992
20 kg/da	93.675^{a}	90.500^{ab}	93.275^{a}	92.483
Means	90.120	89.631	90.625	
L.S.D.: Fertilizer variety* fertilizer doses interactions (%1) = 7.347				

4. CONCLUSION

This research was carried out to investigate the effects of different fertilizer sources and different nitrogen doses on the yield and technological properties of cotton plant in Kahramanmaras conditions.

According to the results obtained, the highest cotton seed yield was obtained from urea application and it was found out that a good cotton seed yield could be obtained with 15 - 20 kg nitrogen application. It was also determined that the number of boll and plant height increased with nitrogen ratio and that the proper dose rate was 15-20 kg / da nitrogen application. 100 seed weight, boll weight and fiber strength were significantly influenced by the interactions of different fertilizer sources and doses.

As a result, it can be said that a good crop of cottonseed can be obtained with Kahramanmaras plain preference as a nitrogen source and with the application of 15 - 20 kg / da fertilizer at the time of the necessary cultural processes.

ACKNOWLEDGMENT

This article was written from thesis of post graduate which is title “Effects of Different Nitrogen Sources and Doses on Yield, Yield Components and SomeTechnologic Properties” at the science institute of Kahramanmaras Sutcu Imam University in 1995.

REFERENCES

[1]. Anonymous, Turkiye istatistik yilligi, T.C. D.I.E yayin no:1620 Ankara, 1993.
[2]. Anonymous, Kahramanmaras tarla bitkileri uretme istasyonu mudurlugu 1991 yili arastirma, preje sonuc raporu, Kahramanmaras, 1992.
[3]. Sezen, V., Gubreler and gubreleme, A.U. Yayinlari nu:679, Ziraat Fakultesi yayinlari nu:303 ders Kitabi Serisi nu:555, Erzurum, 1991.
[4]. Aktas, M., Bitki besleme ve toprak verimliligi, A.U.Ziraat Fak. Yayin Nu:1202, Ders kitabi:347, Ankara, 1991.
[5]. Zabunoglu, S. and Karacal, I. Gubreler ve gubreleme. Ankara Unv., Ziraat Fak. Yayin Nu:993, Ders Kitabi:293 Ankara, 1986.
[6]. Gencer, O., Sinan, S., Yelin, D., Kaynak, M.A. and Gormus, O., 1992. GAP Bolgesinde yuksek verimli, lif teknolojik ozellikleri ustun pamuk cesitlerinin saptanmasi uzerinde bir arastirma. C. U. Ziraat Fakultesi GAP Tarimsal Arastirma Inceleme ve Gelistirme Proje Paketi Kesin Sonuc Raporu, C.U.Z.F. Genel Yayin No: 31, GAP Yayin No:60, Adana
[7]. Cura, V. and Karadal, O., Azot doz denemesi., Nazilli Bolge Pamuk Arastirma Enstitusu., pamuk Arastirma Proje ve Sonuclari, Nazilli, 1977.
[8]. Gencer, O., 1995. Buyume duzenleyicisi 1.1 dimethyl piperididinium chloride farkli gubrelenmis pamugun tarimsal ve teknolojik ozelliklerine etkisi uzerine bir arastirma., C.U. Ziraat Fak. Tarla Bitkileri Bol. Yayin Nu:421
[9]. Francisco, N., Performance of different varieties of cotton interacting with levels of nitrogen., *CLSU Scientific Journal*., 5(2); p.80., 1986
[10]. Reevers, D.W., Touchtion, J.T. ve Rickerl, D.H., Effect of nitrogen source and dicyondiamide an growth and water relations of cotton., Soil Science Society of America Journal 52:1, 231 – 235, 1986.
[11]. Abuldahap, A. and Hassanan, M.A., Analitical study of yield and its components of Egyption cotton under different n levels and plant population dencities., Field Crops Abstract, p.45,4,7312, 1992.
[12]. El – shinnawy, A.H.M. and Mohamed, H.M.H., Effect of foliar spraying of urea, super phosphate and microelements on growth, flowering boll setting and yield of cotton. Egyption Journal of Agronomy. 11(1-2), 13 – 24, 1985.
[13]. Sawan, Z.M., Effect of nitrogen, phosphorus fertilization and growth regulators on cotton yield and fiber propeties., *Journalof Agronomy and Crop Science*, 156:4, 237 – 245.
[14]. Faziullaev, S. and Gafurov, A., 1991. Yield components plant breeding abstr., 061, 0828, 1991.
[15]. Boquet, D.T., Moser, C.B. and Breitenbeck, G.A., Nitrogen effect on boll production of field grown cotton., *Agronomy Journal*, 85(1); 34 – 39, 1993.
[16]. Bicer, Y. and Yenigun, A.R., Pamukta gubreleme denemeleri sonuc raporu. T.C. Koyisleri ve Kop. Baskanligi, Toprak – Su Genel Mud. Tarsus Bolge Toprak – Su Arastirma Enstitusu Mud. Yay. No:62, 1974.

[17]. Ogunlela, V.B. and Abed, S.M., Nitrogen fertilization of upland cotton (Gossypium hirsutum L.) in a ferruginous tropical soil: 1.Seed Yield Seed Oil Content and Dry Matter Yield Cotton Fibers Tropicales 39:3, 75 - 81
[18]. Mascagni, H.J. and Mapples, R., Effect of nitrogen rate on four cotton cultivars grown on a clay soil., research Series Arkansas Agricultural Experiment Stations., 1990.
[19]. Elayan, S.E.D., A comparative study on yield components and nitrogen fetilization of some cotton varieties. Assiut Journal of Agricultural Science 23(1) 153 – 165., 1992.
[20]. Guzel, N., Toprak verimliligi and gubreler., (ceviri) C.U.Ziraat Fak. Yay. Nu:168, Ders Kitabi No:13, 1992.
[21]. Maples, R. and Frizzel, L., Bulletin agricultural experiment station., University of Arkansas., Nu:882, 19 pp, 21 ref., 15 tab., 1985.
[22]. Gencer, O. and Oglakci, M., Farkli sira arasi uzakligi ve azot gubrelemesinin pamuk bitkisinin (G.hirsutum L.) verim ve kalite unsurlarina etkisi uzerinde arastirmalar., C.U. Ziraat Fak. Yilligi, Yil:14, sayi 3-4, 1983.

ICENS 4TH INTERNATIONAL CONFERENCE ON ENGINEERING AND NATURAL SCIENCE
2-6 May 2018 KIEV UKRAINE

A Research on to Effective on Yield and Earliness of Different Sowing Times and Growing Techniques in Sweet Corn (Zea mays saccarata Sturts) in Kahramanmaras Conditions

Cuneyt Cesur[1], Veyis Tansi[2]

Abstract

In order to investigate the effect of different sowing times and growing techniques. On yield and earliness of two sweet corn varieties, this study, was done in Kahramanmaras conditions in 1997 – 1998 growing years. Kahramanmaras research station conditions. Field trials arranged in split – split plot design with there replications, varieties sowing times and growing techniques were used an as main, sub and sub – sub plots, respectively. In this study, Merit and Jubilee varieties used as sweet corn varieties.

According to result obtained from the experiment interm of starch ration, number of grain per ear and number of plant per unit Merit variety was found to be superior but interm of days two maturity ear lenght Jubilee was superior. It was determined that earliness sweet corn growing was possible by using covered growing techniques on that covered growing techniques possitively influenced the all characteristic studied starch ratio and ear lenght. Effect of sowing times on days the maturity wasn't significant. If the temperature is low plant adapted itself till the temperature research optimum. But days the maturity increased vice verse decreased. The optimum sowing times for the Kahramanmaras conditions was 30 March.

Keywords: *Sweet corn (Zea mays saccarata Sturts), sowing dates, growing techniques*

1. INTRODUCTION

We are in the century where agricultural research will become more important every day. In the last three centuries people have exploited the natural resources irresponsibly by the development of industry and technology. This exploitation is unfortunately still going on. The inexhaustible performance of the western countries, especially in the hands of technology, has brought the whole world to a catastrophic threshold. At the current point, they are talked which about issue such as global warming, decline of biological diversity, climate change than incresing productivity.

Until today, it was tried to fulfill the cultivation of forest and grassland for food needs with the help of agriculture. Even if these processes are continued in some parts of the world, it is also stated that the places that were opened as farming areas in the past, should be abandoned in favor of forest and grassland, according to some researchers, even to the end of new fields to be opened. We understand from this information that the new field areas is no longer in the world. It is then necessary to obtain high efficiency from the unit side in order for the feeding population. Research should develop in this direction. In other words, it is essential to produce more in both quantities and varieties from unit area during the breeding period. For this purpose, many

[1] Corresponding author: Bozok University, Department of Field Crops, 66100, Yozgat, Turkey. cuneyt.cesur@bozok.edu.tr
[2] Cukurova University, Department of Field Crops, 1170, Adana, Turkey.

methods of cultivating and renewing crops such as co-cultivation, intercropping, sliver cultivation, sub-cropping, cover cropping and mixed cultivation are carried out in many parts of the World (1).

It is directly related to the genetic structure of plant production material, soil characteristics and climate movements. Climate conditions play the most important role in the selection of crops to be cultivated in a region (2). Light, temperature, day length and precipitation are the most important factors (3). Temperature is one of the most important issues with the transport of photosynthesis, the determination of the developmental periods and especially the effect of filling the grains (4).

As the seeds of corn are used as feed for human beings and pulp as well as the sugar corn types for fresh consumption, the market value can be two or three times higher when they are introduced to the first market. Therefore, it is extremely important for economic reasons to be able to produce as early as possible. In order to increased productivity and earliness in production, unveiled agriculture technique has emerged in recent years (5, 6,7,8).

The main factor limiting early planting in corn is temperature. Early seeding is possible when the temperature environment required for corn is provided. Early planting can be done by creating low tunnels. In sugar corn which can be obtained earliness for 10 - 21 days according to common sowing method (8,9,10,11).

Polyculture farming can be done easily in the large lands of Kahramanmaras in Mediterranean climate. Many of the plants can continue their development if the necessary environment can be prepared in terms of temperature even from February to March. Plant seedling and low tunnel applications will make it possible to make more efficient farming with earliness.

Figure 1. General view of research area

This study was carried out to investigate the effects of different sowing times and growing techniques on yield and earliness of sugar corn in Kahramanmaras conditions.

2. MATERIAL AND METHOD

2.1. Material

2.1.1. Used material in experimental area

In the study, jubile and merit sugar corn varieties which are suitable for region conditions were used. Seeds are germinated in small nylon tubes. Mixed soils were used to germinate seeds. Pure nitrogen was used at 20 kg / da. 10 kg / da ammonium nitrate (A.N.) was used as fertilizer and 10 kg / da was used as urea as top fertilizer.

2.1.2. Soil characteristics of experimental area

Some physical and chemical analysis characteristics experimental area soil which in taken from 0-30 cm depth are given in Table 1.

Table 1. Some physical and chemical analysis characteristics of experimental area

Depth	Tekstur class	Ph	Lime (%)	Convenient P (P^2O^5)	Organic matter (%)	Saturation with water (%)
0-30 cm	Clay - loamy	7.50	20.24	5.9	0.95	54

*Soil analysis, K.S.U Agricultural Faculty Soil Department laboratory

2.1.3. Climatic properties of experimental area

The climate data for Kahramanmaras province between March and July 1997, 1998 and long years are given in the Table - 2. According to the table, the highest and lowest temperature values for March and April were unusual for many years. Rainfall totals differed in April and May.

Table 2. Climatic datas of March – July months in Kahramanmaras province

Months	Minimum temperature (°C)	Maximum temperature (°C)	Average temperature (°C)	Proportional humidity (%)	Total precipitation (mm)
March 1997	3.4	13.4	6.2	53.3	46.8
1998	4.6	14.5	4.9	61.0	134.0
Long years average	-6.0	25.6	10.4	63.2	90.4
April 1997	6.2	17.3	12.0	62.5	105.3
1998	10.8	22.4	16.6	57.8	166.7
Long years average	-1.8	32.6	14.9	69.8	68.7
May 1997	15.0	28.7	21.7	55.1	88.2
1998	14.3	25.7	19.8	57.0	39.4
Long years average	15.4	36.3	19.9	55.5	35.0
June 1997	18.4	31.6	24.6	51.4	14.9
1998	19.5	33.4	25.9	54.9	15.6
Long years average	20.3	39.6	24.3	49.5	7.0
July 1997	22.3	34.5	27.6	48.6	-
1998	23.1	44.3	29.8	55.6	2.0
Long years average	16.4	41.6	27.8	51.7	3.0

* Kahramanmaras meteorological station 1997, 1998 years with (1940 – 1990) long years average datas.

2.2. Method

2.2.1. Experimental Method

This research was carried out on Kahramanmaras Agricultural Research Center Provincial Directorate. The trials were established in March and July 1997 and 1998. In the experiment, three different times (March 15, March 30 and April 15) were planted seedling on the tubes, seedling under cover and seeding techniques in open field. To cover the plots, a low tunnel roof was made of thin construction iron and covered with transparent plastic linoleum (*Figure 2*). The trial was established according to divided into three divided trials plan.

Varieties were formed in the main parcels, planting times in the sub - parcels, and cultivating techniques in the sub – sub parcels. The planting distances of the plants were determined as 70 cm x 20 cm the rows, and the parcel area (sub-bottom) was 5 × 24 = 12 m2, with each parcel being in 5 m lenght and in 2.4 m width. Closed parcels were opened and ventilated opening in sunny times by following the temperature condition of the air and fully opened towards the end of April.

Figure 2. Low tunnel in used experimental area

2.2.2. Investigated properties in experimental

In this study were investigated properties as ear lenght, ear diameter, number of grain per ear, number of plant per unit, number of ear per unit, ratio and starch ratio. While the Polarimeter method was used for Starch analysis in the laboratories of the Faculty of Agriculture, the other characteristics were determined in the 10 samples of plants obtained from each plot. Statistical analyzes of the obtained datas were calculated on the MSTATC package program.

Figure 3. Outlook of two different applications in experiement.

3. RESULT AND DISCUSSION

3.1. Ear lenght (cm)

The mean values and formed groups of two years (1997 - 1998) showing the effect of cultivar, sowing time and growing techniques on the ear lenght were given in *Table 3*.

Table 3 Two-year mean values indicating the effect on the ear lenght of cultivar, sowing time and growing techniques used in the experiment.

Growing techniques	Merit			
	15 march	30 march	15 april	c x g.t
Covered plant	18.0^{ef}	19.3^{abcde}	18.8^{abcdef}	18.7^{b}
Covered seed	19.1^{abcde}	18.5^{bcdef}	18.1^{ef}	18.6^{b}
Normal sowing	19.9^{abc}	19.3^{abcde}	19.4^{abcde}	19.6^{a}
c x e.z	19.0	19.0	18.8	**18.9**
Growing techniques	Jubile			
	15 march	30 march	15 april	c x g.t
Covered plant	18.7^{abcdef}	17.5^{f}	18.6^{bcdef}	18.2^{b}
Covered seed	18.4^{def}	19.6^{abcd}	20.1^{a}	19.4^{a}
Normal sowing	18.5^{bcdef}	20.0^{ab}	20.0^{abc}	19.5^{a}
c x s.t	18.5^{b}	19.0^{ab}	19.5^{a}	**19.0**
LSD	g.t (%1):0.6070; c x g.t (%5):0.6435; cx s.t x g.t (%1):1.487			

c: cultivar, g.t: growing techniques, s.t: sowing time

According to the table, in the merit coltivar, the c x s.t interaction is not significant, whereas the highest ear lenght (19.0 cm) was obtained from 15 and 30 March sowings.

While the c x g.t interactions of the Merit cultivar was important, the highest value of the study, which was found in the merit cultivar from normal cultivation as 19.6 cm(14). In the jubilee cultivar, the c x s.t interactions were significant (15), while the highest ear lenght was obtained as 19.5 cm in the April 15 plantations. In the jubilee cultivar, the value of the obtained ear lenght was obtained as 19.5 cm from the normal sowing while it was important in the c x g.t. The interactions c x s.t x g.t between the Merit and the jubilee cultivars were not important.

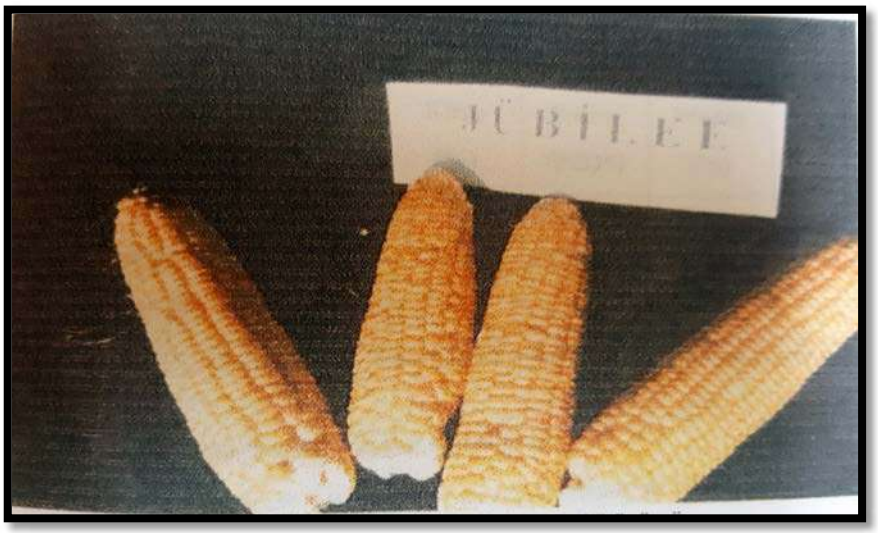

Figure 4. Ear lenght of jubile cultivar

Although the difference is insignificant, the highest ear lenght was obtained from the jubilee cultivar as 19 cm. As can be seen from the values, higher ear lenght was obtained from normal cultivation according to the other cultivation techniques. These results seem to be consistent with studies that indicate that the ear length is higher in normal sowing than in other techniques (12), and that the ear lenght is lower in the plant seedling techniques(13). When sowing time is considered, the time of sowing in merit cultivar was not important but the ear lenght was decreasing, it has increased in the jubilee cultivar. It can be said that this is a cultivar feature, and that the cultivar of jubilee is generally longer than the ear lenght of cultivar merit (14).

3.2. Ear diameter (cm)

In *Table 4* was shown the mean values and formed groups of two years (1997 - 1998) showing the effect of cultivar, sowing time and growing techniques on the ear diameter. When the Table 4 is examined, it is possible to observe that the ear diameter was smaller as the sowing time was delayed, although there was no statistical significance among the factors.

Table – 4. Two-year mean values indicating the effect on the ear diameter of cultivar, sowing time and growing techniques used in the experiment.

Growing techniques	Merit			
	15 march	30 march	15 april	c x g.t
Covered plant	5.0	4.8	4.8	4.9
Covered seed	5.0	4.9	4.5	4.8
Normal sowing	4.1	4.9	4.5	4.5
c x s.t	4.7	4.9	4.6	**4.7**
Growing techniques	Jubile			
	15 march	30 march	15 april	c x g.t
Covered plant	5.0	4.6	4.6	4.7
Covered seed	5.0	4.5	4.8	4.7
Normal sowing	4.3	4.5	4.5	4.5
c x s.t	4.8	4.5	4.7	**4.7**
LSD	Sowing time: n.s, cultivar: n.s			

c: cultivar, y.t: growing techniques, s.t: sowing time, n.s: no significant

Both the merit and the jubile cultivars were found to have a diameter of 5 cm in the March 15 plantings and a drop of 4.5 cm in the April 15 plantings.

According to the cultivation techniques, it is understood that the diameter of the cocoon in normal cultivation (5 cm) was thicker than that of covered cultivation (4.1 cm). The interactions of cultivar x sowing time x growing techniques were to 4.7 cm. It see that the ear diameter was decreasing as the sowing time was delayed, and it seems that the datas werecompatible with similar studies (12,13,17,18). According to the results obtained in our study, it was seen that the cultivation techniques do not have a significant effect on the eardiameter. However, some researchers report that direct sowing forms a thicker ear diameter than other applications (12,13). It can be said that this contrast is made according to the genetic material and ecological regions used in the studies.

3.3. Number of grain per ear

In *Table 5* was shown the mean values and formed groups of two years (1997 - 1998) showing the effect of cultivar, sowing time and growing techniques on the number of grain per ear.

It is seen that cultivar, sowing time and growing techniques have a statistically significant effect on the number of grain per ear at 1% level, cultivar x sowing time, cultivar x growing techniques and x cultivation time x growing techniques interactions is significantly at 5% level.

Table – 5. Two-year mean values indicating the effect on the number of grain per ear of cultivar, sowing time and growing techniques used in the experiment.

Growing techniques	Merit			
	15 march	30 march	15 april	c x g.t
Covered plant	566.7^{def}	617.9^{abcd}	621.1^{abcd}	601.9^{ab}
Covered seed	640.7^{ab}	630.5^{abc}	570.1^{def}	613.8^{a}
Normal sowing	505.5^{gh}	642.3^{ab}	565.9^{def}	569.6^{bc}
c x s.t	569.3^{b}	630.2^{a}	585.7^{b}	**595.1^{a}**
Growing techniques	Jubile			
	15 march	30 march	15 april	cx g.t
Covered plant	519.7^{fg}	512.6^{fgh}	533.1^{efg}	521.8^{d}
Covered seed	551.2^{efg}	615.0^{abcd}	655.6^{a}	607.3^{a}
Normal sowing	455.7^{h}	572.0^{cdef}	585.2^{bcde}	537.6^{cd}
c x s.t	508.9^{c}	566.5^{b}	591.3^{b}	**555.6^{b}**
LSD	s.t(%1):37.03; c(%1):428.3; cxs.t(%5):38.01; g.t (%1):34.51; cxs.txg.t(%5):59.78; cxg.t(%5):34.51			

c: cultivar, g.t: growing techniques, s.t: sowing time

From the obtained data, according to interactions of c x g.t x s.t , it can be seen that the number of grain per ear obtained in merit cultivar (595.1) is higher than the number of jubilee cultivar (555.6). In the c x g.t interactions, the highest value was obtained as 613.8 per from covered seed application of merit cultivar. It was understood that the application of covered seed in the jubilee cultivar showed the highest value as 607.3 per. It was seen that the highest value was obtained from the March 30 application of the highest the number of grain per ear of merit cultivar in the c x s.t interactions, while the highest value of the jubilee cultivar was found on the 15 April cultivars as 591.3 per. According to these results, it can be said that the most suitable sowing technique is the covered seed technique and the most suitable sowing time is between March 30 and April 15(12). According to the c x e.z x y t interaction, it can be said that the merit cultivar has better values than the jubile cultivar compared to the climate and application conditions (14, 29). This result is consistent with the findings of researchers who say that very genotypic is effective (16,20). In the area where the experiment was established, the March climate values averaged around -6 ° C for the long years and 3.4 - 4.6 ° C for the years when the tests were conducted. Therefore, it is expected that the 15 March applications will not be suitable for the cultivation of corn plants. Minimum temperature requirements for maize plant are 13 - 15 ° C(3).

3.4. Number of plant per unit (per/da)

In *Table 6* was given the mean values and formed groups of two years (1997 - 1998) showing the effect of cultivar, sowing time and growing techniques on the number of plant per unit. In Table – 6, it can be observed to be effective of year, sowing time, variety, variety x sowing time and growing techniques on number of plant per unit (per/da) at 1% level.

Table – 6. Two-year mean values indicating the effect on the number of plant per unit (per/da) of cultivar, sowing time and growing techniques used in the experiment.

Growing techniques	Merit			
	15 march	30 march	15 april	c x g.t
Covered plant	5094.8	4154.5	5761.5	5003.6
Covered seed	3844.6	6904.3	6083.0	5610.6
Normal sowing	1833.1	5.47.5	5499.6	4126.7
c x s.t	3590.8^{d}	5368.7^{ab}	5781.3^{a}	**4913.6^{a}**
Growing techniques	Jubile			
	15 march	30 march	15 april	c x g.t
Covered plant	4844.8	3880.5	5440.0	4721.7

Covered seed	4321.0	4666.3	4487.8	4491.7
Normal sowing	2178.1	4368.6	4333.6	3626.8
c x s.t	3781.3^{d}	4305.1^{cd}	4753.8^{bc}	**4280.1^{b}**
LSD	year(%1):5646.7; g.t(%1):544.4	s.t(%1):559.4;	c(%1):5646.7;	cxs.t(%1):791.1;

c: cultivar, g.t: growing techniques, s.t: sowing time

While the highest number of plant per unit was obtained as 4913 from the merit cultivar according to c x y.t x e.z interaction, this data could be obtained from the jubile cultivar as 4280.1. According to the c x s.t interaction, The highest value of the Merit cultivar was obtained from the April 15 plantations as5781 pieces, and this value was realized as 4753.8 pieces in the jubile cultivar from the April 15 plantations. According to c x g.t Interaction, the highest number of plant per unit was obtained from covered seed applications, although statistically insignificant in both types. While the number of plant per unit obtained from the Merit cultivar was 5610.6, the number of plant per obtained from the jubile cultivar was 4491.7. The fact that there is no difference between covered sowing and planting shows compatibility with literature studies (12,21). According to the results obtained by experiment, the covered seed application of April 15 plantings of merit cultivar indicates the most efficient application. It can be said that the merit cultivar had different values according to the jubilee cultivar, indicating that genotypes given different responses (23).

As can be seen from Table-6, the number of plants increases in late sowing. This is due to the increase in temperatures. As temperature increases, the germination power of seeds and the germination fidelity increase (21, 22). Sweetcorn varieties are affected by temperatures too much. The opinions of Cross and Zuber (1972), which states that the most useful classification method of temperature-dependent classification is supporting our data(24).

3.5. Number of ear per unit

In *Table 7* was shown the mean values and formed groups of two years (1997 - 1998) showing the effect of cultivar, sowing time and growing techniques on the number of ear plant per unit. According to *table 7*, year, cultivar, cultivar x sowing time and growing techniques are effective at 1% level and at 5% level of sowing time on number of ear per unit. The highest number of ear per unit according to c x e.z x y.t interaction was 5269.9 (per/da) from the jubile cultivar. According to the cultivation techniques of the cultivars, it can be said that the most suitable cultivation is covered plant application. The highest number of ear plant per unit from covered plant of March 15 application of Merit cultivar was 6737.8 (per/da). The jubile cultivar also gave the highest yield from the covered plant application. It is also say from datas that more the number of ear plant per unit (per/da) are obtained than covered sowing and planting. It is seen from the literature that these values are compatible with previous studies (25, 11).

Table – 7. Two-year mean values indicating the effect on the number of ear plant per unit (per/da) of cultivar, sowing time and growing techniques used in the experiment.

Growing techniques	Merit			
	15 march	30 march	15 april	c x g.t
Covered plant	6737.8^{ab}	5083.0^{de}	5702.0^{bcd}	5840.9
Covered seed	4583.0^{e}	5856.6^{bcd}	5249.6^{cde}	5229.7
Normal sowing	2083.0^{f}	5190.3^{de}	5190.5^{de}	4154.6
c x s.t	4467.9	5376.6	5380.7	**5075.1**
Growing techniques	Jubile			
	15 march	30 march	15 april	c x g.t
Covered plant	6321.1^{abc}	5702.0^{bcd}	7130.8^{a}	6384.6
Covered seed	5497.0^{cde}	4856.6^{de}	4761.6^{de}	5038.4
Normal sowing	2999.8^{f}	5214.0^{cde}	4892.5^{de}	4368.7
c x s.t	4939.3	5257.5	5595.0	**5263.9**
LSD	year(%1):467.80; s.t(%5):520; cxs.txg.t(%1):1109; g.t(%1):452.7			

c: cultivar, g.t: growing techniques, s.t: sowing time

3.6. Cab ration (%)

In Table 8 was given mean values and formed groups of two years (1997 - 1998) showing the effect of cultivar, sowing time and growing techniques on the cab ratio (%).

Table – 8. Two-year mean values indicating the effect on the cab ratio (%) of cultivar, sowing time and growing techniques used in the experiment.

Growing techniques	Merit			
	15 march	30 march	15 april	c x g.t
Covered plant	19.6^{bc}	20.2^{bc}	18.4^{c}	19.4
Covered seed	19.7^{bc}	21.6^{bc}	21.7^{bc}	21.0
Normal sowing	22.6^{b}	20.1^{bc}	22.8^{b}	21.9
c x s.t	20.7	20.6	21.0	**20.8**
Growing techniques	Jubile			
	15 march	30 march	15 april	c x g.t
Covered plant	18.7^{c}	19.6^{bc}	19.9^{bc}	19.4
Covered seed	21.6^{bc}	20.4^{bc}	19.7^{bc}	20.6
Normal sowing	28.5^{a}	22.7^{b}	20.1^{bc}	23.8
c x s.t	22.9	20.9	19.9	**21.2**
LSD	g.t(%1):2.364, cxg.txs.t(%5):3.559			

c: cultivar, g.t: growing techniques, s.t: sowing time

While the effect of growing techniques techniques on the cab ratio was found to be significant at the 1% level, the interactions of c x growing techniques x sowing times techniques appeared to be effective at 5% level. While the cab ratio of the Merit cultivar was determined as 20.8%, this ratio was 21.2% in the jubilee cultivar. According to datas, covered agriculture and early sowing in sweetcorn which cab ratio is be decrease, this state effects to grain yield positively. It is a negative situation that the cab ratio in normal sowing is high. Because it can be said that grain yield decreases in ear of sweetcorn affected by cold (26, 14).

3.7. Starch ratio (%)

In *Table 9* was given the mean values and formed groups of two years (1997 - 1998) showing the effect of cultivar, sowing time and growing techniques on the starch ratio (%). As can be seen from the *table 9*, the highest starch ratio was obtained from the merit cultivar, according to c x g.t x s.t interactions as 54.1% (26). It can be said that the cultivation techniques did not have a statistically significant effect on the starch ratio. The highest starch ratio was found to be 55.9% on 30 March cultivars compared to the cultivar x sowing time interaction. April 15 plantations were in the same group with 54.0%.

Table – 9. Two-year mean values indicating the effect on the starch ratio (%) of cultivar, sowing time and growing techniques used in the experiment.

Growing techniques	Merit			
	15 march	30 march	15 april	c x g.t
Covered plant	52.7	57.3	52.0	54.0
Covered seed	53.0	55.0	54.8	54.2
Normal sowing	51.4	55.4	55.2	54.0
c x s.t	52.4^{bc}	55.9^{a}	54.0^{ab}	**54.1a**
Growing techniques	Jubile			
	15 march	30 march	15 april	c x g.t
Covered plant	53.7	52.0	53.5	53.1
Covered seed	50.2	51.8	54.7	52.0
Normal sowing	51.0	52.5	51.8	51.8
c x s.t	51.6^{c}	51.9^{c}	53.3^{bc}	**52.3b**
LSD	cultivar(%1):15.21, s.t(%5):1.468, cxs.t(%5):2.076			

c: cultivar, g.t: growing techniques, s.t: sowing time

4. CONCLUSION

This study was carried out to investigate the effect of different growing techniques and sowing times on yield and earliness of two sweet corn cultivars. According to result covered seedlings growing techniques provided earlinest and in the years covered seeding and plantings could be performed. It was founded when climatic factors was optimum covered seeding and plantings coluld be performed between 15 – 30 March. Also founded merit cultivar more adapted than jubile cultivarDepth. Also, open seeding is only possible after 30 March. When deciding the proper growing techniques aconomic analysis including addition cost caused by plaastic, seedling procedurs compared to addition income from the earliness should be considered.

ACKNOWLEDGMENT

This article was written from (proje number of FBE 97 D-48) thesis with code no 51 of post graduate which is title “A research on to effective on yield and earliness of different sowing times and growing techniques in sweet corn (Zea mays saccarata Sturts) in Kahramanmaras conditions” at the science institute of Cukurova University in 1999.

REFERENCES

[1]. V. Tansi. “Cukurova bolgesinde misir ve soyanin ikinci urun olarak degisik ekim sistemlerinde birlikte yetistirilmesinin tane ve hasil yem verimine etkisi uzerinde arastirmalar”. C.U Fen Bilimleri Enstitusu Tarla Bitkileri Anabilim Dali Doktora Tezi. 1987.
[2]. Bilgen. “Antalya ovasi kosullarinda iklim faktorlerinin misirda (Zea mays) gelisme ve verim fizyolojisi uzerine etkileri”. C.U. Fen Bilimleri Enstitusu Tarla Bitkileri Anabilim Dali Doktora Tezi, Adana, 1996.
[3]. D. Esen, “Tarimsal ekoloji”, A.U Ziraat Fak. Yay. No:287
[4]. W.G.Duncan, and J.D.Hesketh, “Net photossynthetic rates, relative leaf growth rates and leaf number of 22 races of maize grown at eight temperatures”, Crop Science, 8:670 – 674, 1968.
[5]. S.J.Mc Cormik, “The effects of sowing date of maize developments and yields of silageand grain”, Proc.Inst.Ann.Cong.Agron.Soc. 1971.
[6]. M.A.Dillion, and R.E.Gwin, “How planting date and full season or early hybrids affect corn yields, Field Crop Abst Vol.31 No.3, 1978.
[7]. J.M.White, “Effect of plant spacing and planting date on sweetcorn grown on muck soil in the spring, Field Crop Abst . Vol.39 No.6, 1984.
[8]. S.U.Park, K.Y.Park, Y.G.Kang, H.G.Moon and S.K.Jong, “Effect of plant densityon growth and yield of sweetcorn hybrid” Korean Journal of Crop Science, 32(1)92-96, 1987.
[9]. J.E.Wyatt and J.A.Mullins, “Production of sweetcorn from transplant”, Hortscience, 24(6):1039, 1989.
[10]. H.Walicora, “Development and yield of sweetcorn grown in soil covered with plastic film. Katedra Uprawny Roli Roslin ar Poznan, Poland, 1995.
[11]. S.Ozer, S.Gokmen and M.Idi, “Seker misiri (Zea mays saccharata Sturt) agronomik ozelliklerine ekim zamani ve yetistrime takniklerinin etkisi”, J.of Agriculture and Forestry, (21):65-71 (Tubitak), 1997.
[12]. J.E.Wyatt and J.A.Mullins, Transplanted sweetcorn, Hortscience, 23(5):824, 1988.
[13]. J.E.Wyatt and M.C.Akridge, Yield and quality of direct seeded and transplanted supersweet sweetcorn hybrids, Department of Plant and Soil Science, University of Tennessee Experiment Station, Jackson TN 38301.
[14]. R.Ozel and V.Tansi, Cukurova kosullarinda iki sekermisiri cesidinde sasirtmanin ve farkli ekim zamanlarinin verim ve diger bazi ozelliklere etkisi, Tarla Bitkileri Kongresi, c.I, s.300 – 312, 1994.
[15]. M.Okant, Y.Silbir, T.Saglamtimur and V.Tansi, Ceylanpinari tarim isletmesi akrepli istasyonunda ekim zamanlari, bes misir cesidinde verim ve bazi tarimsal karakterlere etkisini saptamak amaciyla yapilan arastirma. Turkiye II. Cayir – Mer’a ve Yem bitkileri Kongresi, 1991.
[16]. H.Gokcora, Turkiye’de yetistirilen misir cesitlerinin baslica vasiflari uzerine arastirmalar, A.U. Ziraat Fak. Yay. 86 s.143, 1956.
[17]. M.A.Sharkawy, F.A.Sorour, K.Sgater and M.E.Yousef, Effect of dowing date on growing and yield of locale and imported mazie varieties (Zea mays L.) Field Crop.Abst. Vol.31, No.1, 1987.
[18]. C.Koylu and S.Yanikoglu, Samsun ekolojik sartlarinda misir (Zea mays L.) cesit ekim zamani uzerinde bir arastirma. Turkiye’de Misir Uretiminin Gelistirilmesi, Problemler ve Cozum yollari Sempozyumu, 1987.
[19]. L.Cesurer, Kahramanmaras kosullarinda ekim zamani ve ekim sikliginin sekermisirda taze kocan verimine ve diger bazi tarimsal ve bitkisel ozelliklere etkisi. Cukurova Universitesi Fen Bilimleri Enstitusu Tarla Bitkileri Ana Bilim Dali Doktora tezi Adana, 1995.
[20]. M.Derieux, R.Bonhamme, J.B.Dubureq and F.Ruget, Variation in the number of grains in different maize genotypes. Maize Abst.2(1) p.3, 1985.
[21]. L.J.R. Waters, R.L.Burrows, M.A.Bennett and J.Schoenecker, Seed moisture and transplant management techniques influence sweetcorn stand establishment, growth, development and yield, J.Arner.Soc.Hort Sci 115(6):888-892, 1990.
[22]. T.Nakui, K.Nonaka, S.Hara and M.Shinoda, The effect of plastic mulch on the growth of corn plants and their TDN yield of silage in the tokachi district(Hokkaido, Japan). Research bulletion of the hokkaido national agricultural experiment station no:161, p.73-80, 1995.
[23]. M.Furter, H.A Venter, and A.Vande, A comparasion of parameters for the assesment of relative cold tolerance of germinating kernels of maize (Zea mays L.), South African Journal of Plant and Soil 7(4)207 – 21, 1990.

[24]. H.Z.Cross and M.S.Zuber, Prediction of flowering dates in maize based on different methods of estimating thermal units, Agron.J. 64:351 – 355, 1972.
[25]. S.U.Park, K.Y.Park, Y.K.Kang, H.G.Moon and S.K.Jong, Effect of plant density on growth and yield of sweetcorn hybrid, Korean journal of Crop Science 32(1)92-96,1987.
[26]. R.Ozel, Cukurova kosullarinda farkli ekim yontemleri ve zamaninin bazi sekermisiri cesitlerinde verim ve bitkisel ozelliklere etkisi, Cukurova Universitesi Fen Bilimleri Enstitusu Yuksek Lisans Tezi kod no:889, 1994.

ICENS 4TH INTERNATIONAL CONFERENCE ON ENGINEERING AND NATURAL SCIENCE
2-6 May 2018 KIEV UKRAINE

Thermo-hydraulic Performance of Different Nanofluids in a Helical Coiled Tube

Selma Akcay[1], Unal Akdag [2]

Abstract

In this study, the flow and heat transfer characteristics of nanofluids in a three dimensional helical coiled tube under laminar flow conditions are investigated numerically. The governing equations are solved using the Finite Volume Method (FVM) with SIMPLE algorithm. In studies, the effects on heat transfer performance and friction factor of different nanoparticle types (Al_2O_3, CuO, TiO_2, SiO_2) with varying particle volume fractions (φ=1%, 2%, 3%) in specific range of Reynolds number (200≤Re≤1200) under steady flow conditions are analyzed and geometric parameters are kept constant. The average Nusselt number, friction factor and thermo-hydraulic performance along the tube are calculated for tested parameters. The numerical results indicate that heat transfer performance enhances with increasing Reynolds number and particle volume fraction, at the same time the friction factor also increased. It is observed that the thermo-hydraulic performance is significantly affected from nanoparticle type, particle volume fraction and Reynolds number. The nanoparticle volume fraction and Reynolds number that provide the best thermo-hydraulic performance are determined for each nanofluid. The obtained results are given as a function of dimensionless parameters. It is shown that helical coiled tubes have a good potential to enhance heat transfer, if optimum nanofluid parameters under steady laminar flow conditions are used.

Keywords: *Helical tube, Nanofluids, Numerical study, Heat transfer, Friction factor*

1. INTRODUCTION

Alternative methods have been investigated to improve the cooling efficiency of thermal devices for a long time. The main purpose for design of these devices is to minimize the flow resistance while improving the cooling efficiency. The applications as turbulators, rough surfaces, expanded surfaces, vortex generators, coiled pipes, surface tension devices, nanofluids, boiling and condensation are among the most studied topics contains. These applications are known as passive heat transfer enhancement methods. These methods do not require external power and their production is quite simple [1-7].

One of passive method to increase heat transfer is the use of nanofluids instead of traditional working fluids in channels. It is known that nanofluids have the potential to improve thermal performance. The flow characteristics and heat transfer of the nanofluids have been investigated experimentally and numerically for different channel geometries and different parameters (nanoparticle type, particle volume fraction, *Re* number etc.) in the literature. It was declared that heat transfer improved with increasing of nanoparticles volume fraction, but also the use of nanoparticles are increase the pressure drop due to create the flow resistance [8-12].

Flow and heat transfer in the helical coiled tubes are different than conventional flat tubes. Secondary flows occur in the helical tubes due to the centrifugal force, and these formations can improve significantly the heat transfer performance. However, the pump power increase in helical tubes compared to flat tubes.

Corresponding author: Selma Akcay; Institute of Science and Technology, Aksaray University, 68100 Aksaray, Turkey. selma.352@hotmail.com
[2]Unal Akdag: Mechanical Engineering Department, Aksaray University, 68100 Aksaray, Turkey. uakdag@gmail.com

Helical geometries have higher heat transfer coefficient, lowest thermal expansion and lower production cost because they have more surface area in given volume. Helical tubes are widely used in various heating and cooling applications. Many researchers have experimentally and numerically studied the flow and heat transfer characteristics in helical tubes. All these studies shown that heat transfer improvement in helical tubes is higher than in straight tubes [13-21].

Wang et al. [22] numerically investigated flow and heat transfer for helical channels with different helix height-to-diameter ratios and different pitch-to-diameter ratios for the turbulent flow regime. As a result, they reported improvement of swirl flow with increase of helix height and decrease of helix pitch. They also noted that the maximum value of the local *Nu* number and the friction factor was obtained at a specific value. Chen et al. [23] numerically analyzed flow and heat transfer for a wide parameter range in square-section helical tubes and examine in detail the effects of rotation and twisting on *Nu* number and friction factor. Poskas et al. [24] conducted an experimental study to investigate the heat transfer through the concave and convex walls of rectangular-shaped helical grooves in different flow regimes using different geometric parameters. As a result of the study, it was reported that the average *Nu* number in helical channels increased by 50% in laminar flow conditions and 20% in turbulent flow conditions when compared to flat channels. Sheikholeslami et al. [25] presented a review of passive methods involving the effects of the use of swirl flow devices on heat transfer improvement.

Kurnia et al. [26] numerically analyzed the heat transfer performance for the laminar flow in helically twisted tubes with different cross-sectional areas such as circular, ellipse and square. They investigate the influences of different *Re* numbers, wall temperature and geometric parameters for the heating / cooling state. It was also reported that in applications where the heat transfer performance was extremely important, a straight tube heat exchanger of circular cross section may be preferred and a helical pipe heat exchanger of square cross section may be recommended to reduce the pump power. Wu et al. [27] experimentally examined the flow and heat transfer characteristics of alumina-water nanofluid at different particle concentrations for laminar and turbulent flow in a helical twist heat exchanger. They proposed new correlations for laminar flow in helically twisted tubes and reported no significant improvement in heat transfer for laminar and turbulent flow. Naphon [28] experimentally studied the flow and heat transfer behavior of nanofluids in a spiral curved horizontal pipe and analyzed the influence of fluid temperature, nanoparticle concentration and curvature on pressure drop and heat transfer of nanofluids. It was indicated that, the increase in the particle volume ratio increased the *Nu* number compared with pure water, but also caused an increase in the surface friction value. Khoshvaght-Aliabadi et al. [29] experimentally examined laminar flow and heat transfer of Cu-water nanofluid for different ring diameters in a helical microchannel. They reported that heat transfer increased with the increase in pressure drop the addition of Cu particles compared to the base fluid. As a result, they suggested new correlations to estimate friction factor and *Nu* number at the helical microchannels. Nazari et al. [30] experimentally investigated the effect of heat exchanger geometry on heat transfer using CuO/water nanofluid for various particle volume ratios. They used different geometries such as metal foam embedded pipe, helical pipe and straight pipe in their studies. Experimental results shown that the use of CuO-water nanofluid at particle volume ratio of 0.2% provided heat transfer improvement as 42% and 45% for helical pipe and metal foam containing pipe compared to flat pipes, respectively.

In the literature, studies on the effects of nanofluids on the flow and heat transfer in helical channels have been carried out but the hydrodynamic structure of the flow through the coiled channels has not yet been fully understand because the flow behavior in the coiled channels is more complicated than the smooth channels due to torsional and curvature caused by rotation and centrifugal force, and new researches are needed. In this study, the effects on the flow and heat transfer of different particle types in varying particle volume fractions and Reynolds numbers under steady laminar flow conditions in a helical coiled channel are numerically investigated.

2. NUMERICAL STUDY

2.1. Description of the Numerical Model and Governing Equations

Fig. 1. shows the basic geometry of the helical coiled tube used in the present study. The helical tube is circular cross section and the diameter (*d*) is 10mm, the helical diameter (*D*) is 165 mm, distance between two helix pitch (*a*) is 32.5 mm, the numerical model consists of 10 windings in total, the problem is considered three dimensional. All geometric parameters are kept constant.

The nanofluid flow is assumed as a Newtonian fluid, fully developed, laminar, incompressible, three-dimensional, the single phase and steady. The mixture of water and nanoparticles is homogenous and enters the channel at the same flow and thermal conditions. Gravity and radiation heat transfer are negligible.

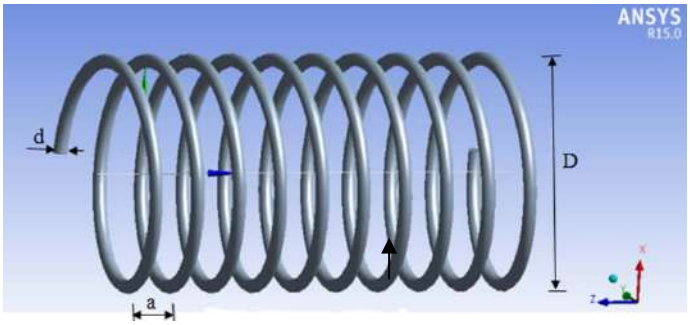

Fig.1. The basic geometry of the helical coiled tube

Therefore the governing equations based on these assumptions are as follows:

$$\nabla(\rho u) = 0 \quad (1)$$

$$\frac{\partial(u_i u_j)}{\partial x_i} = -\frac{\partial p}{\partial x_i} + \frac{1}{\mathrm{Re}}\nabla^2 u_j \quad (2)$$

$$u_i \frac{\partial T}{\partial x_i} = \frac{1}{\mathrm{Re}\,\mathrm{Pr}}\nabla^2 T \quad (3)$$

2.2. Numerical Method and Grid Testing

For the solutions of present problem are used the *CFD* code *ANSYS Fluent* 15.0 [31]. A finite volume method is applied for discretizing the governing equations and they are solved by using the *SIMPLE* algorithm. The convergence criterion for each equation is determined to be 10^{-8}. Several tests are applied for grid independence and in Table 1 is given Nu numbers obtained for different element numbers.

Table 3. Grid independence testing

Element number	Nusselt number
298163	12.85
327287	14.07
390945	**14.59**
437609	14.82

It is found that the element numbers of 390945 is sufficient for the calculation of *Nu* number.

2.3. Thermo- physical Properties of the Nanofluids

Thermo-physical properties include thermal conductivity, viscosity, density and heat capacitance. By assuming the nanoparticles are well dispersed within the base fluid, the effective thermo-physical properties of the nanofluids can be evaluated using some classical appropriate formulas. In Table 2 is given the thermo-physical properties of water and the tested nanoparticles.

Table 2. Thermo-physical properties of the nanoparticles and water

	H_2O	SiO_2	CuO	Al_2O_3	TiO_2

ρ [kg/m^3]	998	2550	6500	3880	4240
C [j/kgK]	4182	710	540	733	686
k [W/mK]	0.62	1.4	18	46	30.77
μ [kg/ms]	0.001003	-	-	-	-

Using these properties, the thermo-physical properties of nanofluids are obtained by the following equations;

$$\rho_{nf} = (1-\varphi)\rho_{bf} + \varphi\rho_{pt} \quad (4)$$

$$C_{nf} = (1-\varphi)C_{bf} + \varphi C_{pt} \quad (5)$$

$$k_{nf} = \frac{k_{np} + 2k_{bf} - 2\varphi(k_{bf} - 2k_{np})}{k_{np} + 2k_{bf} + 2\varphi(k_{bf} - 2k_{np})} \quad (6)$$

$$\mu_{nf} = \mu_{bf}(1+1.25\varphi) \quad (7)$$

where the subscript *nf*, *pt* and *bf* indicate the nanofluid, the nanoparticle and base fluids, respectively. Different equations applied in literature studies are tested especially to calculate thermal conductivity, viscosity and heat capacitance values from thermo-physical properties of the nanofluids. It was observed that there was not so much changed values of this thermo-physical properties [32]-[34].

3. RESULTS AND DISCUSSION

Present study is validated by an experimental study of Hashemi and Akhavan-Behabadi [35]. In the Reference paper, a helical coiled tube geometry with circular cross section with diameter of D_h= 10mm is used, a constant heat flux of q"=1500 W/m^2 is applied to the channel walls and the average heat transfer coefficient of the base fluid is calculated for Reynolds numbers in the range $12 \leq Re \leq 84$. In Fig. 2 is shown the comparison between the two sets of results that a good agreement has been found.

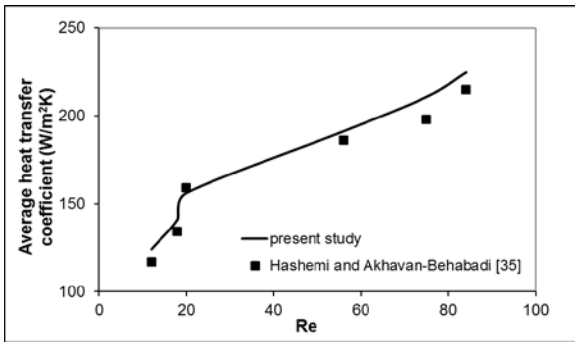

Figure 2.Verification of present study with reference [35]

The effects on heat transfer and thermo-hydraulic performance of different nanofluid types with varying particle volume fractions and Reynolds numbers under steady flow conditions in the helical coiled tube are analyzed. The investigations are performed with four different nanofluid type as Al_2O_3, TiO_2, CuO and SiO_2, for varying nanoparticle volume fractions (φ=1%, 2%, 3%) in the range of Reynolds number from 200 to 1200. Water is used as base fluid. The numerical solution parameters are given in Table.3. The geometric parameters are kept constant for all cases. The Nusselt number, friction factor and thermo-hydraulic performance are calculated for these parameters.

Table 3. The numerical solution parameters

Nanofluid	**Volume fraction: (φ %)**	**Reynolds Number: *Re***
Al_2O_3- water	1, 2, 3	200, 500, 800, 1200
CuO-water	1, 2, 3	200, 500, 800, 1200
SiO_2 -water	1, 2, 3	200, 500, 800, 1200
TiO_2-water	1, 2, 3	200, 500, 800, 1200

The fluids enters the tube with uniform temperature T_o=293K. At the inlet of tube is defined "velocity inlet" boundary condition. At the outlet of tube is performed "outflow" boundary condition. The constant heat flux condition is applied for all tube walls. The tube walls are kept at a uniform heat flux (q") of 2000 W/m^2. At the walls are used the usual no-slip boundary conditions.

The Nusselt numbers are calculated for different case studies of nanofluids. For this purpose, the local heat transfer coefficient (Eqn. 8) and average heat transfer coefficient (Eqn.9) are defined as:

$$h = \frac{q''}{(T_w - T_f)} \quad (8)$$

where, T_w is wall temperature of helical tube and T_f ($T_f=(T_g+T_c)/2$) is the film temperature of fluid in the tube.

$$\bar{h} = \frac{1}{L}\int_0^L h(z)dz \quad (9)$$

The Nusselt number by using the average heat transfer coefficient is defined by Eqn. (10):

$$\overline{Nu_{nf}} = \frac{\bar{h}d}{k_{nf}} \quad (10)$$

The heat transfer performance ε is obtained by Eqn. (11).

$$\varepsilon = \frac{Nu_{nf}}{Nu_w} \quad (11)$$

where Nu_{nf} is Nusselt number for nanofluids, Nu_w is Nusselt number for pure water.

The helical tubes and particle concentration contributes to a significant increase in the shear stress because of the interaction and collision among particles, fluid and the flow passage surfaces. It has been clearly known in the literature that the addition of nanoparticles into a base fluid has produced an adverse effect on the wall shear stress. Because nanofluids have a higher viscosity value in comparison with base fluids. For the evaluation of pressure drop in helical tube, the relative skin friction ratio is defined as $r=f_{nf}/f_w$. Where f_{nf} is the friction factor for nanofluid and the f_w is the friction factor for base fluid.

Thermo-hydraulic performance (*THP*) is defined as the ratio of the heat transfer performance to the friction ratio (Eq.12).

$$THP = \frac{(Nu_{nf}/Nu_w)}{(f_{nf}/f_w)^{1/3}} = \frac{\varepsilon}{r^{1/3}} \quad (12)$$

If the thermo-hydraulic performance is greater than 1, there is an improvement in heat transfer despite friction which is caused by the nanofluid in the tube.

Fig. 3a and 3b demonstrate the variation of heat transfer performance and thermo-hydraulic performance with varying *Re* number and particle volume fraction for Al_2O_3-water nanofluid, respectively. As *Re* number and particle volume fraction increase the heat transfer performance increases but the *THP* decreases when

compared to base fluid. The improvement in *THP* is observed at φ =1% and φ =2%, but no improvement in *THP* at φ=3%. This indicates that there is extremely friction in the tube for φ=3%.

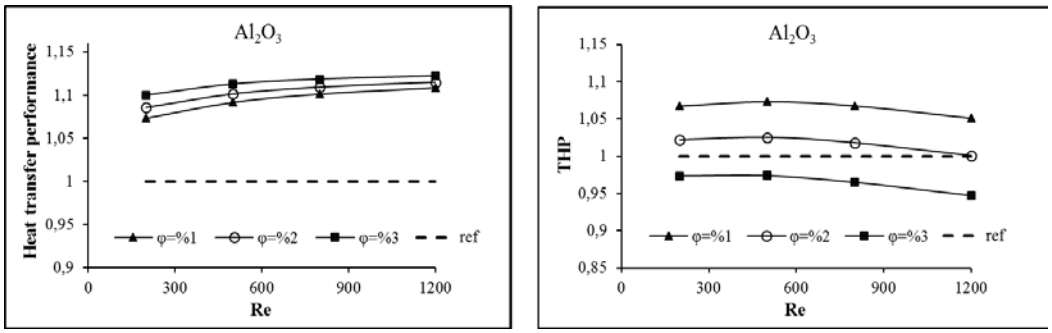

a b

Figure 3. The heat transfer performance (a) and thermo-hydraulic performance (b) for Al_2O_3-water nanofluid

Fig. 4a and 4b indicate the variation of heat transfer performance and thermo-hydraulic performance with varying *Re* number and particle volume fraction for TiO_2-water nanofluid, respectively. TiO_2 –water nanofluid shows similar properties to Al_2O_3-water nanofluid. As *Re* number and volume fraction increase the heat transfer performance increases but the *THP* decreases.

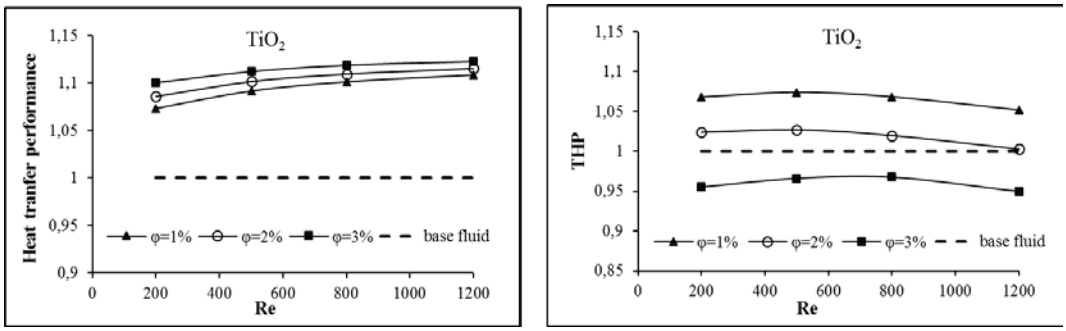

a b

Figure 4. The heat transfer performance (a) and thermo-hydraulic performance (b) for TiO_2-water nanofluid

Fig. 5a and 5b show the variation of heat transfer performance and *THP* with varying *Re* number and particle volume fraction for CuO-water nanofluid, respectively. As *Re* number and volume fraction increase the heat transfer performance increases but the *THP* decreases when compared to base fluid.

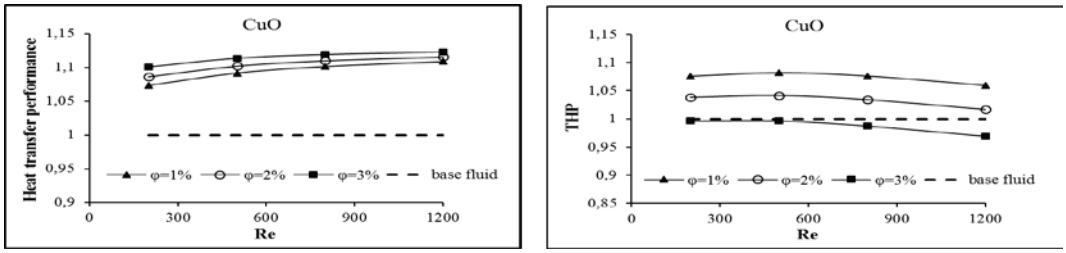

a b

Figure 5. The heat transfer performance (a) and thermo-hydraulic performance (b) for CuO–water nanofluid.

Fig. 6a and 6b demonstrate the variation of heat transfer performance and *THP* with varying *Re* number and particle volume fraction for SiO_2-water nanofluid, respectively. The improvement in *THP* is observed only at φ = %1. There was no improvement in the other cases.

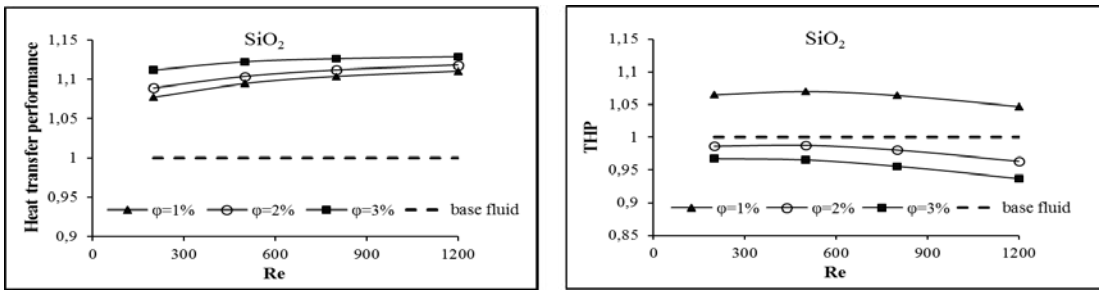

a b

Figure 6. The heat transfer performance (a) and thermo-hydraulic performance (b) for SiO_2-water nanofluid.

In Fig. 7 is shown the variation of heat transfer performance (a) and friction factor (b) with different nanofluids and *Re* numbers for φ=3%. The heat transfer performance and friction factor for each nanofluid increase as *Re* number increases. The maximum heat transfer performance and friction factor are obtained of 1.132 and 1.78 at *Re*=1200 and φ=3%, for SiO_2-water nanofluid, respectively. The heat transfer performance for the other nanofluids is found to be close to each other. The lowest friction factor is obtained for the CuO-water nanofluid.

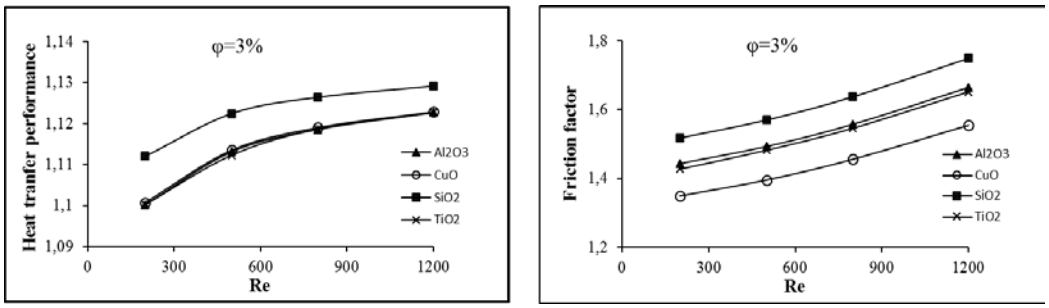

a b

Figure 7. The heat transfer performance (a) and friction factor (b) for φ=3%.

Fig. 8 shows the variation of heat transfer performance (a) and the thermo-hydraulic performance (b) for different nanofluids and particle volume fractions at *Re*=500. The heat transfer performance increase for each nanofluid as particle volume fraction increase but *THP* decreases. There is not improve *THP* by φ=3% for all tested nanofluids.

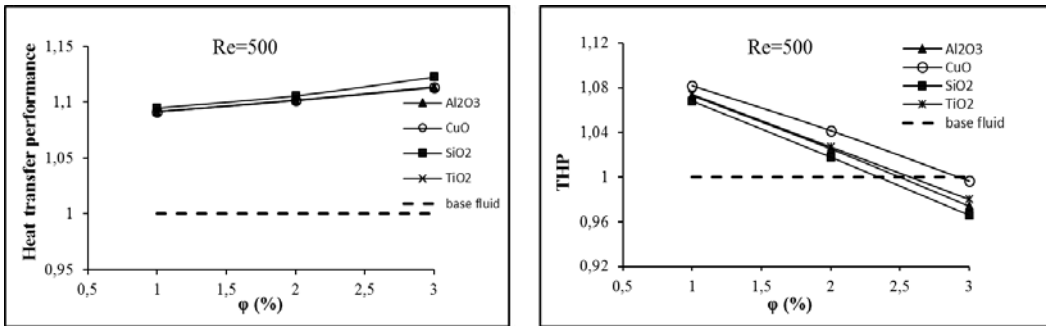

a b

Figure 8. The heat transfer performance (a) and THP (b) for Re=500

The numerical results shown that the heat transfer performance improves under steady flow by using nanofluids in the helical coiled tube. It observed that the heat transfer performance increases with increasing particle volume fraction of nanofluids and *Re* number, but there is an increase in friction factor. Despite heat transfer performance increased, there was no improvement in *THP* at φ=3% because there are too many frictions in the tube. As a result, significant improvement in the thermo-hydraulic performance can be achieved when low *Re* numbers and particle volume fractions are used in helical coiled tubes.

4. CONCLUSIONS

In this study, the effects of nanofluids on thermo-hydraulic performance in the helical coiled tube under laminar steady flow conditions are investigated by using control volume based CFD solver. Numerical results show that the heat transfer performance and the thermo-hydraulic performance are influenced by nanoparticle type, particle volume fraction and *Re* number. While the highest heat transfer is obtained for SiO_2-water nanofluid at high particle volume fractions and increasing *Re* numbers, the best the thermo-hydraulic performance is obtained at low particle volume fractions and Reynolds numbers. The study results show that nanoparticles may improve thermo-hydraulic performance if appropriate parameters are used in a helical coiled channel.

REFERENCES

[1]. P.R. Chandra, V.R. Alexander, and J.C. Han, "Heat transfer and friction behavior in rectangular channels with varying number of ribbed walls",*Int. J. Heat and Mass Transf*., vol. 46, pp. 481–495, 2003.

[2]. S. Gunes, V. Ozceyhan, O. Buyukalaca, "The experimental investigation of heat transfer and pressure drop in a tube with coiled wire inserts placed separately from the tube wall", *Applied Thermal Engineering*, vol. 30, pp. 1719-1725,2010.

[3]. U. Akdag, S. Akcay, and D. Demiral, "Heat transfer enhancement with laminar pulsating nanofluid flow in a wavy channel", *Int. Commun. Heat Mass Transfer*, vol. 59, pp. 17–23, 2014.

[4]. T. Alam, R.P. Saini, and J.S. Saini, "Use of turbulators for heat transfer augmentation in an air duct—a review", *Renew Energy*, vol. 62, pp. 689–715, 2014.

[5]. M. Akbarzadeh, S. Rashidi, and J.A. Esfahani, "Influences of corrugation profiles on entropy generation, heat transfer, pressure drop, and performance in a wavy channel", *Applied Thermal Engineering*, vol. 116, pp. 278–291, 2017.

[6]. A. Saysroy, and S. Eiamsa-ard, "Periodically fully-developed heat and fluid flow behaviors in a turbulent tube flow with square-cut twisted tape inserts", *Applied Thermal Engineering*,vol. 112, pp. 895–910, February 2017.

[7]. P. B. Jasiński, "Numerical study of thermo-hydraulic characteristics in a circular tube with ball turbulators. Part 3: Thermal performance analysis", *International Journal of Heat and Mass Transfer*, vol. 107, pp. 1138–1147,April 2017.

[8]. K.V. Sharma, L.S. Sundar, and P.K. Sarma, "Estimation of heat transfer coefficient and friction factor in the transition flow with low volume concentration of Al_2O_3 nanofluid flowing in a circular tube and with twisted tape insert, Int. Commun. Heat Mass Transfer 36 (2009) 503–507.

[9]. M. Chandrasekar, S. Suresh, and A.C. Bose, "Experimental studies on heat transfer and friction factor characteristics of Al_2O_3/water nanofluid in a circular pipe under laminar flow with wire coil inserts", *Expt. Thermal Fluid Sci*. vol. 34, issue 2, pp.122–130, 2010.

[10]. L. S. Sundar, N.T. R. Kumar, M.T. Naik, and K.V. Sharma, "Effect of full length twisted tape inserts on heat transfer and friction factor enhancement with Fe_3O_4 magnetic nanofluid inside a plain tube: An experimental study", *International Journal of Heat and Mass Transfer*, vol. 55, pp.2761–2768, 2012.

[11]. W.H.Azmi, K.V. Sharma, P.K. Sarma, R. Mamat, S. Anuar and L. S. Sundar, "Numerical validation of experimental heat transfer coefficient with SiO_2 nanofluid flowing in a tube with twisted tape inserts", *Appl. Therm. Eng*. vol. 73, pp.296–306, 2014.

[12]. Y. Yang, H. Tang, B. Zeng and M. Jian, "Numerical simulation and optimization of turbulent nanofluids in a three-dimensional arc rib-grooved channel", *Numerical Heat Transfer, Part A: Applications, An International Journal of Computation and Methodology*, vol. 70, issue 8, pp. 831-846,2016.

[13]. H. Chen, B. Zhang, and J. Ma, "Theoretical and numerical analysis of convective heat transfer in the rotating helical pipes", *Int. J. Heat Mass Transfer*, vol. 46, pp. 4899–4909, 2003.

[14]. E.M. Paloka, and L. Pazanin, "Modelling of heat transfer in a laminar flow through a helical pipe", *Mathematical and Computer Modelling*, vol. 50, pp. 1571-1582, 2009.

[15]. Z. Yang, , Z. Zhao, Y. Liu, Y. Chang, and Z. Cao, "Convective heat transfer characteristics of high-pressure gas in heat exchanger with membrane helical coils and membrane serpentine tubes", *Experimental Thermal and Fluid Science*, vol. 35, pp. 1427–1434, 2011.

[16]. J.Y. San, C.H. Hsu, and S.H. Chen, "Heat transfer characteristics of a helical heat exchanger", *Applied Thermal Engineering*, vol. 39, pp. 114-120, 2012.

[17]. T. Srinivas, and A.V. Vinod, "Performance of an agitated helical coil heat exchanger using Al_2O_3/water nanofluid", *Experimental Thermal and Fluid Science*, vol. 51, pp. 77–83, 2013.

[18]. S.S. Pawar, and K.S. Vivek, "Experimental studies on heat transfer to newtonian and non-newtonian fluids in helical coils with laminar and turbulent flow", *Exp. Thermal Fluid Sci*., vol. 44, pp. 792–804, 2013.

[19]. G. Xia, and X. Liu, "An investigation of two-phase flow pressure drop in helical rectangular channel", *International Communications in Heat and Mass Transfer*, vol. 54, pp. 33–41, 2014.
[20]. Z. Shi, and T. Dong, "Thermodynamic investigation and optimization of laminar forced convection in a rotating helical tube heat exchanger", *Energy Conversion and Management*, vol. 86, pp. 399–409, 2014.
[21]. B.K. Hardik, P.K. Baburajan, and V.S. Prabhu, "Local heat transfer coefficient in helical coils with single phase flow", *International Journal of Heat and Mass Transfer*, vol. 89, pp. 522–538, 2015.
[22]. W. Wang, Y. Zhang, B. Li, H. Han, and X. Gao, "Influence of geometrical parameters on turbulent flow and heat transfer characteristics in outward helically corrugated tubes", *Energy Conversion and Management*, vol. 136, pp. 294–306, 2017.
[23]. Y. Chen, H. Chen, B. Zhang, and H.T. Hsieh, "Fluid flow and convective heat transfer in a rotating helical square duct", *International Journal of Thermal Science*s, vol. 45, pp. 1008–1020, 2006.
[24]. P. Poskas, V. Simonis, and V. Ragaisis, "Heat transfer in helical channels with two-sided heating in gas flow", International *Journal of Heat and Mass Transfer*, vol. 54, pp. 847–853, 2011.
[25]. M. Sheikholeslami, M. Gorji-Bandpy, and D.D. Ganji, "Review of heat transfer enhancement methods: focus on passive methods using swirl flow devices", *Renewable and Sustainable Energy Reviews*, vol. 49, pp. 444–469, 2015.
[26]. J.C. Kurnia, A.P. Sasmito, T. Shamim, and A.S. Mujumdar, "Numerical investigation of heat transfer and entropy generation of laminar flow in helical tubes with various cross sections", *Applied Thermal Engineering*, vol. 102, pp. 849–860, 2016.
[27]. Z. Wu, L. Wang, and B. Sundén, "Pressure drop and convective heat transfer of water and nanofluids in a double-pipe helical heat exchanger", *Applied Thermal Engineering*, vol. 60, pp. 266-274, 2013.
[28]. P. Naphon, "Experimental investigation the nanofluids heat transfer characteristics in horizontal spirally coiled tubes", *International Journal of Heat and Mass Transfer*, vol, 93, pp. 293–300, 2016.
[29]. M. Khoshvaght-Aliabadi, S. Pazdar, and O. Sartipzadeh, "Experimental investigation of water based nanofluid containing copper nanoparticles across helical microtubes", *International Communications in Heat and Mass Transfer*, vol. 70, pp. 84–92, 2016.
[30]. M. Nazari, N.B. Baie, M. Ashouri, M.M Shahmardan, and A. Tamayol, "Unsteady heat transfer from a reservoir fluid by employing metal foam tube, helically tube and straight tube: A comparative experimental study", *Applied Thermal Engineering*, vol. 111, pp. 39–48, 2017.
[31]. ANSYS Fluent user guide & theory guide- Release 15.0, Fluent Ansys Inc, USA, 2015
[32]. A.A. Minea, "Effect of microtube length on heat transfer enhancement of a water/Al_2O_3 nanofluid at high Reynolds numbers", *International Journal Heat and Mass Transfer*, vol. 62, pp. 22–30, 2013.
[33]. S. Kakac, and A. Pramuanjaroenkij. "Review of convective heat transfer enhancement with nanofluids". *International Journal Heat and Mass Transfer*, vol. 52, pp. 3187–3196, 2009.
[34]. B.C. Pak and Y.I. Cho, "Hydrodynamic and heat transfer study of dispersed fluids with submicron metallic oxide particles", *Experimental Heat Transfer*, vol. 11, issue (2), pp. 151–170, 1998.
[35]. S.M. Hashemi, and M.A. Akhavan-Behabadi, "An empirical study on heat transfer and pressure drop characteristics of CuO–base oil nanofluid flow in a horizontal helically coiled tube under constant heat flux", *International Communications in Heat and Mass Transfer*, vol. 39, pp. 144–151, 2012.

Selma Akcay, She was born in 1975 in Kayseri. In 2000, she completed the Department of Mechanical Engineering at Erciyes University, Turkey. She graduated from Aksaray University, Institute of Science and Technology in 2015. She is continuing her PhD education at Aksaray University, Turkey. She is working as a Mechanical Engineer at Kayseri Provincial Health Directory. Heat transfer, pulsating flow, computational fluid dynamics, nanofluids and microflow topics are of interest.

Unal Akdag, He was born in 1970 in Aksaray. In 1992, he completed the Department of Mechanical Engineering at Erciyes University,Turkey. He graduated from Nigde University in 1997 with a Master's degree in Institute of Science and Technology, in 2005 with Istanbul Technical University, Institute of Science Mechanical Engineering and Energy Program Doctorate. In 2006, he was a scholarship researcher at Texas A & M University (USA). He is working as a Professor at Aksaray University, Mechanical Engineering Department. Heat and mass transfer, heat transfer in oscillating/pulsating flow, computational fluid dynamics, nanofluids and microflow topics are of interest.

ICENS 4TH INTERNATIONAL CONFERENCE ON ENGINEERING AND NATURAL SCIENCE
2-6 May 2018 KIEV UKRAINE

Shape Factor of Nanofluid on the Thermal Performance of a Double Pipe Heat Exchanger

Fatih Selimefendigil[1], Hakan F. Oztop[2]

Abstract

In this study, thermal performance of a double pipe heat exchanger with SiO_2-water nanofluid of various particle shapes was numerically investigated. Various nanoparticle shapes such as cylindrical, blade and spherical are added to the water in the range of particle volume fraction between 0% and 5%. Numerical simulations were performed by using Galerkin weighted residual finite element method. The numerical simulations were performed by using a commercial code COMSOL. Effects of nanoparticle volume fraction, shape of the particles, mass flow rate on the variation of heat transfer and fluid flow characteristics were examined. It was observed that overall heat transfer coefficient enhances by using nanofluid. Among various particle shapes, cylindrical ones were found to perform better in terms of heat transfer enhancement and spherical ones perform the worst.

Keywords: double pipe heat exchanger, nanofluid, SiO2 nanoparticles, finite element method

1. INTRODUCTION

Nanofluids technology is implemented in various thermal engineering problems [1-4]. As compared to conventional heat transfer fluids, small addition of the nano size particles results in higher heat and mass transfer coefficients. Nanofluid is used as the base fluid such as water, ethylene glycol, engine oil and small amount of metallic or non-metallic nano sized additives. Particle size is less than 100 nm and various type and shape of the particles are utilized. Application of the nanofluid technology includes solar power, refrigeration, heat exchangers, thermal energy storage and manty others.

When nanofluids are used in heat exchangers, it is possible to obtain higher heat transfer coefficient with little pressure drop and more compacts heat exchangers can be obtained. In the literature, there are many studies that uses nanofluid technology in heat exchangers. In a recent study, Bahmani et al. [5] performed numerical study for the simulation of a double pipe heat exchanger with nanofluid. They used k-e turbulence model and nanofluid was used in the inner tube for the hot water. They obtained thermal efficiency enhancement of 30% with nanofluid. In the study of Shirvan et al. [6], a double pipe heat exchanger with Al_2O_3 nanofluid was numerically simulated by using finite volume method. Simulations were performed for Reynolds number in the range of 50 and 200. Response surface method was used to performed a sensitivity analysis. It was observed that the heat exchanger effectiveness increase with nanoparticle addition. Sarafraz et al. [7] performed experimental work on carbon nanotube water-based nanofluids in a double pipe heat exchanger. Effects of various operating parameters such as mass flow rate, nanofluid mass concentration, inlet temperature of nanofluid on the heat transfer and pressure drop characteristics were analyzed for both in laminar and turbulent regime. Significant enhancements in the thermal performance of the heat exchanger with carbon-nanotube nanofluid was reported. In the experimental study of Hussein [8], hybrid nanofluid was utilized in a double pipe heat exchanger with particle size of 30 nm and for volumetric concentration of 1 and 4%. The experimental study was performed for various flow rates and for Reynolds number between 500 and 1750. It was observed that addition of the hybrid nanofluid with low volume fractions results in heat transfer efficiency enhancements

[1] *Corresponding author: Department of Mechanical Engineering, Celal Bayar University, 45140 Manisa,Turkey. fthsel@yahoo.com*

[2] *Department of Mechanical Engineering, Technology Faculty, Firat University, 23119 Elazig, Turkey hfoztop1@gmail.com*

sup to 160% as compared to base fluid. In the literature, it was shown that particle shape has also significant effects on the thermal performance in heat transfer engineering problems.

In this study, we numerically examined the particle shape effect on the performance of a double pipe heat exchanger. The numerical simulations were performed in the turbulent regime for various values of flow rates, nanoparticle volume fraction and particle shapes.

2. NUMERICAL MODELLING

A schematic view of the double pipe heat exchanger was illustrated in Figure 1. A 2D axisymmetric model was used and SiO_2-water nanofluid with various volume concentrations were used in the inner tube as the hot fluid and in the annulus side cold fluid circulates. The cold fluid enters the annulus side at a flow rate of 0.5 kg/sec with temperature of 300 K while the in the inner tube hot fluid enters with temperature of 340 K. The inner flow rate was changed such that the inner Reynolds number was varied between 5000 and 10^5. A low carbon steel was used for the interface material which has a thermal conductivity of 44 W /m K. At the entrance of the inner tube and annulus uniform velocity and temperature with neglected entrance region was assumed and the exit fully developed conditions were utilized. Effects of viscous dissipation and thermal radiation were neglected. The energy exchange was assumed between the counter flow streams where the surface of the outer pipe was assumed to be adiabatic.

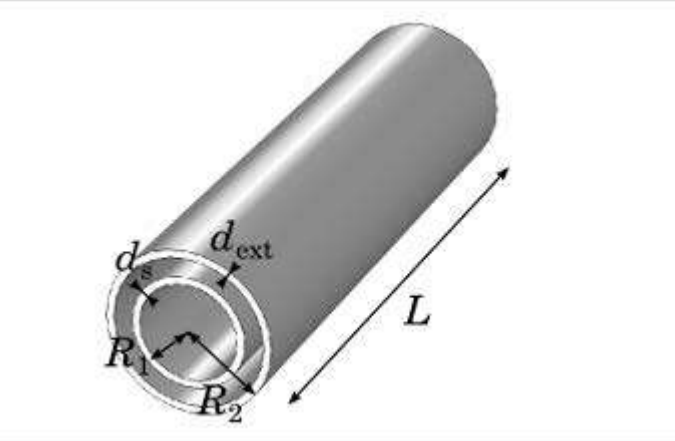

Figure 1 – Schematic view of double pipe heat exchanger

2.1. Governing Equations

Standard k-e turbulence model was utilized. Conservation of mass, momentum and energy equations are expressed as:

$$\frac{\partial(\rho u_i)}{\partial x_i} = 0 \tag{1}$$

$$\frac{\partial(\rho u_i u_j)}{\partial x_j} = -\frac{\partial P}{\partial x_i} + \frac{\partial}{\partial x_j}\left[\mu\left(\frac{\partial u_i}{\partial x_j} + \frac{\partial u_j}{\partial x_i} - \frac{2}{3}\delta_{ij}\frac{\partial u_i}{\partial x_j}\right)\right] + \frac{\partial}{\partial x_j}\left(-\rho u' u'_j\right) \tag{2}$$

$$\frac{\partial\left(u_i\left(E\rho+P\right)\right)}{\partial x_j}=\frac{\partial}{\partial x_j}\left[k_{eff}\left(\frac{\partial T}{\partial x_j}\right)\right],\quad E=h-\frac{P}{\rho}+\frac{u^2}{2} \tag{3}$$

The k-e turbulence model is expressed with the following expressions:

$$\frac{\partial(\rho k u_i)}{\partial x_i}=\frac{\partial}{\partial x_j}\left(\left(\mu+\frac{\mu_t}{\sigma_k}\right)\frac{\partial k}{\partial x_j}\right)+G_k-\rho\varepsilon \tag{4}$$

$$\frac{\partial(\rho\varepsilon u_i)}{\partial x_i}=\frac{\partial}{\partial x_j}\left(\left(\mu+\frac{\mu_t}{\sigma_\varepsilon}\right)\frac{\partial \varepsilon}{\partial x_j}\right)+C_{1\varepsilon}\frac{\varepsilon}{k}G_k-C_{2\varepsilon}\frac{\varepsilon^2}{k}\rho G_k \tag{5}$$

with turbulent viscosity and other constants defined as:

$$\mu_t=C_\mu\frac{k^2}{\varepsilon}\rho,\quad C_\mu=0.09,\sigma_\varepsilon=1.3,\sigma_k=1,C_{1\varepsilon}=1.44,C_{2\varepsilon}=1.92 \tag{6}$$

2.2. Nanofluid effective properties

The density and specific heat of the nanofluid can be described by using the following formulas:

$$\rho_{nf}=\phi\rho_p+(1-\phi)\rho_f \tag{7}$$

$$\left(\rho C_p\right)_{nf}=\phi\left(\rho C_p\right)_p+(1-\phi)\left(\rho C_p\right)_f \tag{8}$$

where the subscripts f, nf and p denote the base fluid, nanofluid and solid particle, respectively. Effect of Brownian motion was included in the description of the effective thermal conductivity of the nanofluid which considers the effects of particle size, particle volume fraction and temperature dependence [32]:

$$k_{nf}=k_f\left[\frac{\left(k_p+2k_f\right)-2\phi\left(k_f-k_p\right)}{\left(k_p+2k_f\right)+\phi\left(k_f-k_p\right)}\right]+5\times10^4\times1.9526\times(100\phi)^{-1.4594}\phi\rho_f C_{p,f}\sqrt{\frac{\kappa_b T}{\rho_p d_p}}f'(T,\phi) \tag{9}$$

The effective viscosity of the nanofluid is given with the following expression:

$$\mu_{nf}=\mu_f\left[\frac{1}{1-34.87\left(\frac{d_p}{d_p}\right)^{-0.3}\phi^{1.03}}\right] \tag{10}$$

with particle size d_p.

In this study, we consider particle shapes other than the spherical ones. The above mentioned correlations for the thermophysical properties were defined for spherical ones. The thermal conductivity and viscosity of the nanofluid considering various shapes (blade, cylinder and brick) were given by using the following correlations:

$$\mu_{nf}=\mu_f\left(1+A_1\phi+A_2\phi^2\right) \tag{11}$$

$$k_{nf} = k_f\left(1 + C_k\phi\right) \tag{12}$$

where the values of different constants in the expressions (A, C) are given in ref. [4].

2.3. Solution methodology

Galerkin weighted residual finite element method was used for the solution of governing system equations along with the boundary conditions. Each of the flow variables were approximated by using the interpolation functions within elements as:

$$u = \sum_{k=1}^{N^u} \psi_k{}^{u,v} U_k, \quad v = \sum_{k=1}^{N^v} \psi_k{}^{u,v} V_k,$$
$$p = \sum_{k=1}^{N^p} \psi_k{}^{p} P_k, \quad T = \sum_{k=1}^{N^T} \psi_k{}^{T} T_k \tag{13}$$

where $\psi_k{}^{u,v}$, $\psi_k{}^{p}$ and $\psi_k{}^{T}$ denote the shape functions of velocity, pressure and temperature, receptively. *U,V,P* and *T* represent the values of the respective variables at the nodes of the element. When the approximated field variables are inserted into the governing equations residual *R* results for each of the governing equations and the weighted average of this residual will be forced to be zero over the computational domain:

$$\int_{\Omega} W_k R d\Omega = 0 \tag{14}$$

where W_k is the weight function. In the Galerkin method, the weight function is chosen from the same set of functions as of the trial functions. Newton-Raphson method was utilized for the solution of the resulting system of nonlinear ODE system.

3. RESULTS AND DISCUSSIONS

In the present study, nanofluid shape effect on the performance of a double pipe heat exchanger was examined with numerical simulations. Effects of various particle shapes (cylindrical, blade and brick) on the performance enhancement of the heat exchanger was analyzed. Reynolds number for the inner tube was varied between 5000 and 10^5 while nanoparticle solid volume fraction was taken between 0% and 5% for different particle shapes. The inlet temperature of the inner and outer tubes is considered to be constant at 340 K and 300 K while the mass flow rate of the outer tube (the annulus side) was considered to be 0.5 kg/sec.

Following formulations are used to evaluate the heat transfer capacity and to find the overall coefficient of the double pipe heat exchanger:

Amount of heat transfer; $Q = mc_p(T_2 - T_1)$ (15)

Overall heat transfer coefficient; $U = \dfrac{1}{\dfrac{1}{h_i} + \dfrac{1}{h_o} + R_w}$ (16)

Logarithmic temperature difference; $\Delta T_{lm} = \dfrac{\Delta T_1 - \Delta T_2}{\ln\left(\dfrac{\Delta T_1}{\Delta T_2}\right)}$ (17)

Total heat transfer; $Q = \dfrac{2\pi L \Delta T_{lm}}{\dfrac{1}{r_i h_i} + \dfrac{1}{r_o h_o} + \dfrac{\ln(r_2 / r_1)}{k}}$ (18)

Figure 2 shows the effect of nano-particle volume fraction on the temperature variation for the cold flow (outer tube) and hot fluid (inner tube) with cylindrical shape particles at Reynolds number of 10000. As the value of the nanoparticle volume fraction rises, the outlet temperature of the cold fluid enhances. Figure 3 presents the results of temperature variation for various particle shapes at the highest value of particle volume concentration. The outlet temperature of the cold fluid enhances most for the nanofluid contacting cylinder particles and least for the spherical ones.

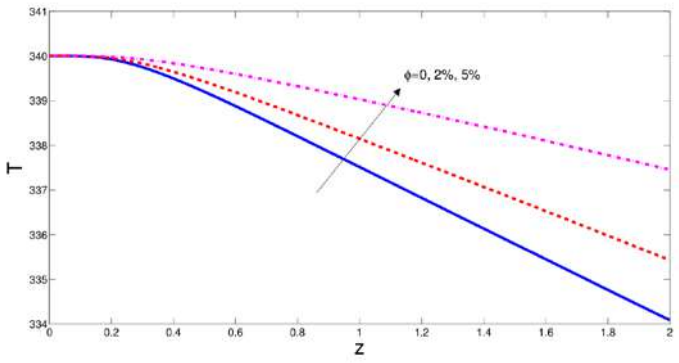

a) Hot fluid

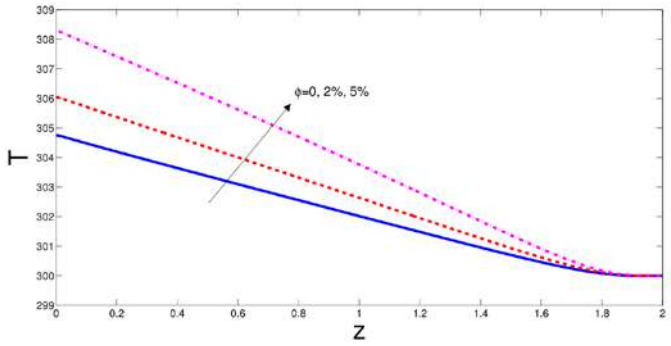

b) Cold fluid

Figure 7. Effect of particle volume fraction on the temperature variation for the cold flow and hot fluid (cylindrical shape, Re*=10000)*

Figure 4 shows the overall heat transfer coefficient of the double pipe heat exchanger versus Reynolds number at the highest particle volume fraction considering various particle shapes. The overall heat transfer coefficient enhances with Reynolds number. The highest value of U is obtained with cylindrical ones since the thermal conductivity enhancement is the highest for this particle shape. Brick and blade shape particles follow the cylindrical ones and the spherical ones show the least value of overall heat transfer coefficient. The discrepancy between the U values for various particle shapes is higher at the intermediate values of Reynolds number and becomes lower for the lowest and highest values of Reynolds number.

Figure 5 present the values of overall heat transfer coefficient for various particle shapes and different solid particle volume fraction at Reynolds number of 10000. The overall heat transfer coefficient enhances significantly with solid particle volume fraction for all particle shapes due to the thermal conductivity enhancement of nanofluid. The discrepancy between U values of various particle shapes is higher as the value of φ increases.

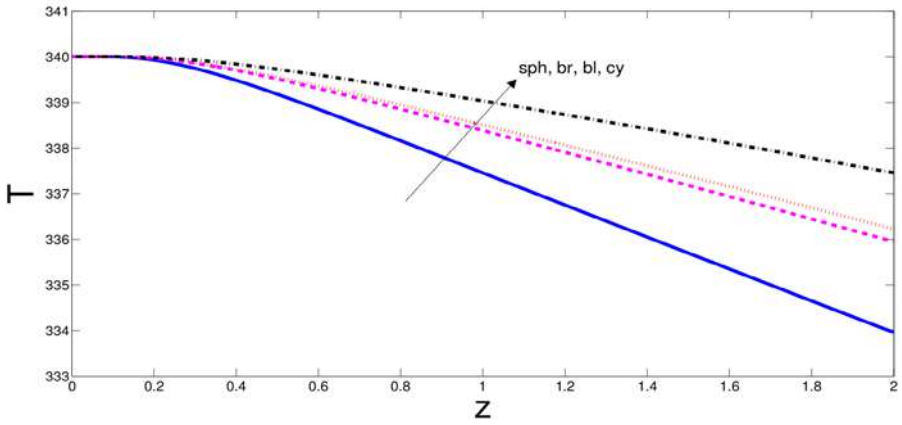

a) Hot fluid

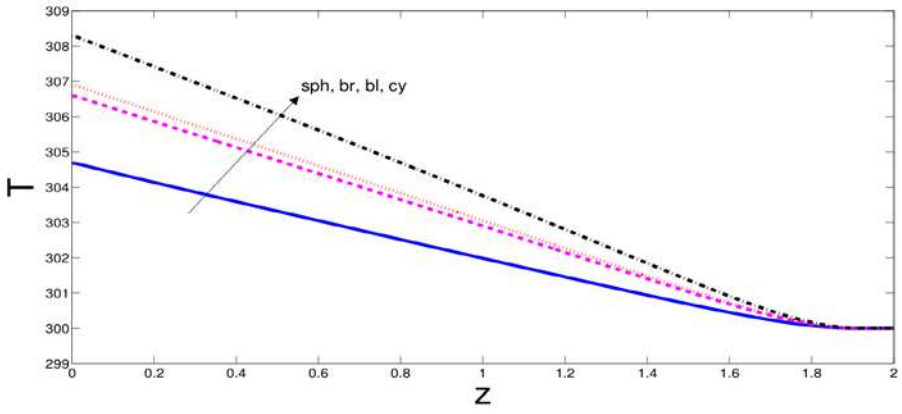

b) Cold fluid

Figure 3. Effect of particle shape on the temperature variation for the cold flow and hot fluid (φ=5%, Re=*10000)*

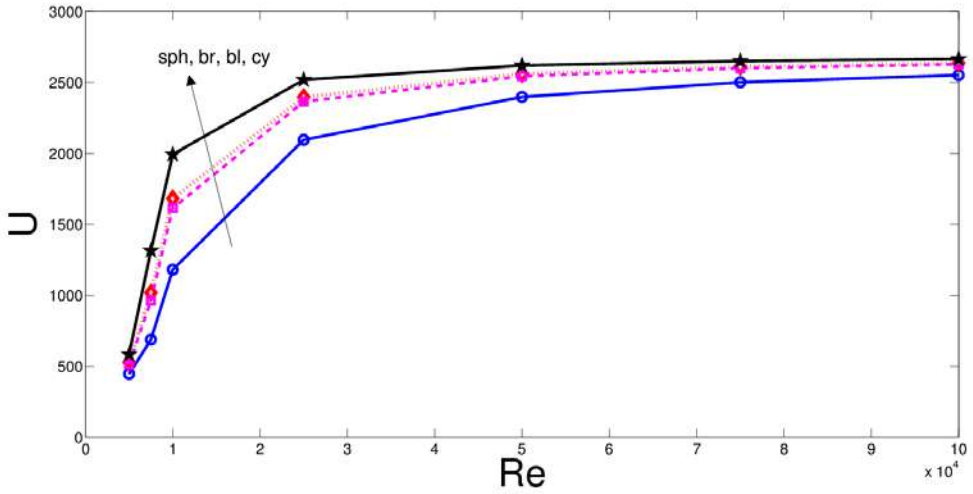

Figure 4. Effects of particle shape on the overall heat transfer coefficient for various values of Reynolds number (φ=5%)

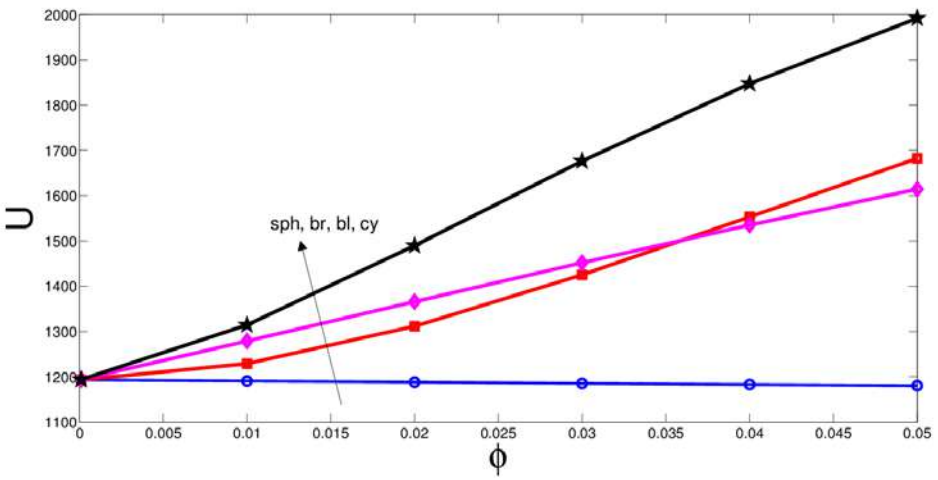

Figure 5. Effects of particle shape on the overall heat transfer coefficient for various values of particle volume fraction (Re=10000)

4. CONCLUSIONS

Numerical simulations for the particle shape effect of nanofluid in a double pipe heat exchanger was performed for the turbulent regime. It was observed that the heat transfer performance of the double pipe heat exchanger was significantly influenced by the shape factor of nanoparticles and cylinder shaped ones show the best performance following the blade, brick shapes while the lowest heat transfer coefficients are achieved for the spherical shape particles.

ACKNOWLEDGMENT

This study is supported by Scientific Research Projects Unit (BAP) of Manisa Celal Bayar University for the project no: 2017-010 whose support is gratefully acknowledged.

REFERENCES

[1] F. Selimefendigil and Hakan F. Oztop, ‘’ Modeling and optimization of MHD mixed convection in a lid-driven trapezoidal cavity filled with alumina–water nanofluid: Effects of electrical conductivity models’’, *International Journal of Mechanical Sciences*, vol. 136, pp. 264-278, 2018.

[2] F. Selimefendigil and Hakan F. Oztop, ‘’Mixed convection of nanofluids in a three dimensional cavity with two adiabatic inner rotating cylinders’’,*International Journal of Heat and Mass Transfer*, vol. 117, pp. 331-343, 2018.

[3] B.H. Chun, H.U. Kang and S. H. Kim 2008, Effect of alumina nanoparticles in the fluid on heat transfer in double-pipe heat exchanger system, *Korean Journal of Chemical Engineering*, vol. 25 (5), pp. 966–971, 2008

[4] I.M. Mahbubul, S.A. Fadhilah, R. Saidur, K.Y. Leong and M. A. Amalina,. ‘’Thermophysical properties and heat transfer performance of Al2O3/R-134a nanorefrigerants‘’, *International Journal of Heat and Mass Transfer*, vol.57, pp.100–108, 2013.

[5] M. H Bahmani, G. Sheikhzadeh, M. Zarringhalam, O. A. Akbari, A. A.A.A. Alrashed, G.A. Shabani, M. Goodarzi, ‘’Investigation of turbulent heat transfer and nanofluid flow in a double pipe heat exchanger’’, *Advanced Powder Technology*, vol. 29, pp.273–282, 2018

[6] K. M. Shirvan,M. Mamourian, S. Mirzakhanlari, R. Ellahi, "Numerical investigation of heat exchanger effectiveness in a double pipe heat exchanger filled with nanofluid: A sensitivity analysis by response surface methodology ", *Powder Technology*, vol.313, pp. 99–111, 2017.

[7] M.M. Sarafraz, F. Hormozi and V. Nikkhah, " Thermal performance of a counter-current double pipe heat exchanger working with COOH-CNT/water nanofluids ", *Experimental Thermal and Fluid Science*, vol. 78, pp. 41–49, 2016.

[8] A. M. Hussein, "Thermal performance and thermal properties of hybrid nanofluid laminar flow in a double pipe heat exchanger", *Experimental Thermal and Fluid Science*, vol. 88, pp. 37-45, 2017

ICENS 4TH INTERNATIONAL CONFERENCE ON ENGINEERING AND NATURAL SCIENCE
2-6 May 2018 KIEV UKRAINE

Nonlinear Seismic Response of Masonry-Infilled Reinforced Concrete Frames with Typical Window and Door Openings

Onur Ozturkoglu[1], Taner Ucar[2]

Abstract

In current construction practice, reinforced concrete (RC) framed structures are usually infilled with unreinforced masonry panels. The composite behavior of the resulting infilled frame under lateral loading is different to that of bare frames, since both the presence of infill panels and the interaction between the bounding frame and infill highly affect the dynamic response of the structure. Besides, prevalent openings for functional reasons, such as windows and doors, may lead to substantial uncertainty in order to assess the seismic response of infilled RC frames depending on their size, position and shape. Therefore, the ability to assess the nonlinear seismic behavior of such structures considered as one of the most complicated issues in the area of structural engineering is of great importance. This paper investigates the nonlinear behavior of masonry-infilled RC frames with rectangular window and door openings by means of pushover analysis. Three different positions of window and door openings in infill wall commonly encountered in construction practice are taken into consideration in numerical models. The lateral stiffness and strength of infill wall influenced by the position and percentage of the opening is taken into account through stiffness reduction factors (SRFs) obtained from finite element analysis of infilled frames under monotonic loading, where infill-frame interaction is modeled by gap elements. The constitutive model and the width of equivalent diagonal compression strut are modified by the derived SRFs. The resulting capacity curves constructed using a displacement controlled pushover analysis are illustrated by graphs both for infilled frames with window and door openings. The variation in characteristic base shear forces and top displacements of capacity curves, and also in interstory drift ratios reveal the effect of window and door openings on nonlinear behavior. It is found that openings upon diagonal are more influential, since diagonal compression strut mechanism cannot effectively develop.

Keywords: *Infilled RC frames, window and door openings, stiffness reduction factor, equivalent compression strut, pushover analysis.*

1. INTRODUCTION

The large population of the existing building stock all over the world, as well as in Turkey, composes of reinforced concrete (RC) framed structures, which are usually infilled with unreinforced masonry panels used as both exterior and interior partitions. It appears that this popular structural form for the buildings in seismic regions will also be used in the future construction practice and infill walls will maintain their functional and architectural efficiencies in RC structures. Besides their role as non-structural architectural components, it has been recognized for long that the seismic response of the resulting infilled frame structure with high in-plane stiffness and strength is different to that of bare frames [1]–[5].

One of the most important lessons learned from destructive earthquakes in the past is that ignoring the mechanical contribution of infill walls in structural analysis and design may lead to significant underestimation of the expected dynamic response of structures. Accordingly, the mismatch between the theoretical and observed seismic response of infilled RC framed structures, in particular of structures with irregular distribution of masonry infills in elevation or plan, should come as no surprise to structural engineers. The observations and experiences from the post-earthquake damage assessment of RC buildings have clearly revealed that the failure mechanism and the overall seismic performance of RC frames are significantly influenced by the infill walls

[1] *Corresponding author: Dokuz Eylul University, Department of Civil Engineering, 35160, Buca/Izmir, Turkey.* onur.ozturkoglu@deu.edu.tr

[2] *Dokuz Eylul University, Department of Architecture, 35160, Buca/Izmir, Turkey.* taner.ucar@deu.edu.tr

[2]–[4], [6]–[11]. Therefore, the importance of including infill walls in numerical models and seismic design has been widely accepted.

On the other hand, the composite behavior the resulting infilled frame under lateral loading is complicated because the modelling of the mechanical characteristics of nonhomogeneous and anisotropic quasi-brittle masonry material is not an easy issue. Since infill walls are not isolated from the bounding frame, they tend to interact with the frame under earthquake excitation. This interaction makes the extremely nonlinear seismic response of infilled RC frames more complicated. Furthermore, prevalent openings, such as windows and doors, are provided in many infill walls for functional reasons, and in particular, they may decisively alter the earthquake response of infilled RC frames depending on their size, position and shape.

Extensive experimental [5], [9], [12]–[17] and analytical [1]–[4], [7], [10], [11], [18]–[25] studies have been performed on seismic behavior of masonry-infilled RC frames with or without openings. Meanwhile, micro-modeling techniques based on discretization of infills by finite elements [1], [3], [11], [12], [18], [20] and macro modelling techniques, where masonry infills are simulated by one or more equivalent compression struts [4], [6]–[8], [10], [21], [22], [24] are widely adopted for consideration of infills. Due to controversial issues regarding the complex composite behavior of masonry-infilled RC frames and the necessity of using infill walls in the residential and commercial structures of today and tomorrow, the effort towards investigating the seismic response of masonry-infilled RC framed structures still presents a relevant challenge.

This paper attempts to investigate the nonlinear seismic behavior of masonry-infilled RC frames with typical window and door openings by means of pushover analysis, which has become a popular tool for evaluating the seismic response of structures in recent years. Three different positions of rectangular window and door openings within the infill wall that are commonly encountered in construction practice are taken into consideration in numerical model of one-story one-bay RC frame. The lateral stiffness and strength of the infill wall influenced by the position and percentage of window and door openings is taken into account through stiffness reduction factors (SRFs) obtained from finite element (FE) analysis of infilled frames under monotonic loading within the elastic region. In FE analyses, infill-frame interaction is modeled by gap elements that transfer axial compression loads. For nonlinear static (NLS) analyses, the brick masonry infills are simulated by means of an equivalent compression strut using the multi-linear constitutive force–displacement (F–D) laws proposed by Dolsek and Fajfar [26], [27]. To take account of the presence of openings, both the strength and stiffness parameters of the constitutive model and the width of the compressive equivalent diagonal strut are modified by the derived SRFs in relation to opening percentage. Displacement controlled pushover analyses are performed and the resulting capacity curves (the base shear force versus roof lateral displacement curves) are illustrated by graphs both for infilled frames with window and door openings. The variation in characteristic base shear force and lateral top displacement of capacity curves, as well as in interstory drift ratio, are considered as main parameters in order to assess the effect of window and door openings on nonlinear seismic response of brick masonry-infilled RC frames.

2. STRUCTURAL DETAILS OF PROTOTYPE INFILLED FRAMES WITH OPENINGS

One-story one-bay moment resisting frame is seismically designed and detailed according to the requirements of TSDC [28] and TS500 [29]. The story height (H) is 3 m and the span length (L) is 5 m of the frame model. The frame is assumed to be located in seismic zone 1 and on Z3 soil group. Uniformly distributed dead (g) and live (q) loads in the span are taken as g = 18.5 kN/m and q = 5 kN/m, respectively. Concentrated dead load (G) of 70 kN and live load (Q) of 12.5 kN acting on the beam-column joints are taken into consideration. Rectangular beams and square columns are considered in RC design of the bare frame. The uniaxial compressive strength of concrete is assumed to be 20 MPa and the uniaxial yield strength of longitudinal reinforcement is taken as 420 MPa. RC design of frame is performed using the structural analysis program SAP2000 [30].

Various configurations of window and door openings in the infill commonly encountered in construction practice wall are considered. Accordingly, infilled frames with upper-left and upper-right window openings are abbreviated as W1 and W3, respectively, whereas infilled frame with a central window opening is abbreviated as W2. Infilled frames with a door opening located at the bottom-left, at the bottom-middle and at the bottom-right are abbreviated as D1, D2 and D3, respectively. Only one position of a window opening, as well as of a door opening, is considered in each case. Thereby, totally six analytical models of RC frames with different positions of window and door openings are implemented. The length of the infill wall (L_{in}) is 4.6 m and the height of the infill wall (H_{in}) is 2.5 m. The infill thickness (t_w) is assumed to be 100 mm in all analytical models. Length (L_{ow}) of 2000 mm and height (H_{ow}) of 1200 mm are assumed for the window opening. The door size is H_{od} = 900 mm and L_{od} = 2100 mm, where H_{od} and L_{od} are height and length of door opening, respectively. The details of the prototype models are shown in Figure 1.

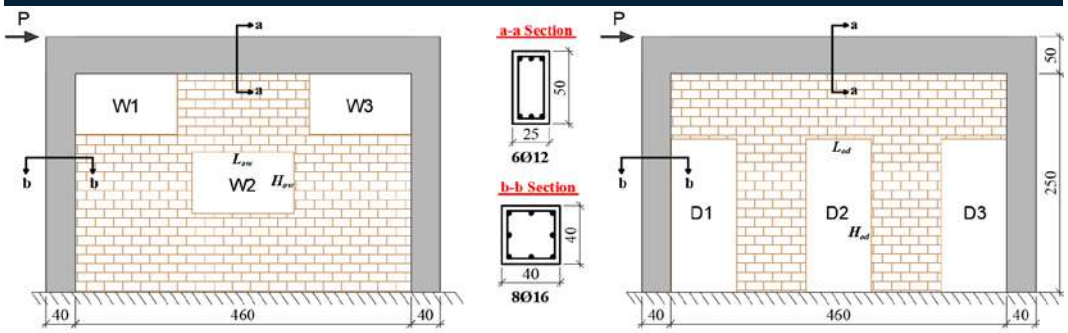

Figure 1. Structural details of prototype RC frames with typical window and door openings

3. MATHEMATICAL MODELLING, ANALYSIS DETAILS AND RESULTS

3.1. Influence of Openings on Stiffness and Strength of Infill Wall

The possible influence of window and door openings on the lateral stiffness and strength of infill panel is taken into account through a stiffness reduction factor (SRF). In the present work, SRFs are obtained by means of FE analysis of infilled frames under monotonic loading within the elastic region.

The infill panels are composed of 250x100x190 mm vertically cored brick units and 10 mm thick mortar joints. The condition of masonry is taken as fair, based on the observations of the authors on construction quality for ordinary residential buildings in Turkey. Following the default lower-bound masonry properties of FEMA 356 [31], the expected compressive strength of the masonry (f_{me}) is calculated as 5.38 MPa. The expected modulus of elasticity of infill wall (E_{me90}) in horizontal direction is determined as a function of horizontal expected compressive strength of masonry (f_{me90}) and is found to be 1479 MPa. The shear modulus (G_w) used to calculate the initial stiffness of the infill wall is taken to be 592 MPa.

RC beam and columns are discretized as linear elastic frame members and infill walls as two dimensional shell elements in FE modelling and, window and door openings are provided by erasing the related finite elements. The mutual interaction of fame and infill is modeled through gap elements which transfer the distributed compression between the frame and infill interfaces. Thereby, the influence of the structural interaction between the infill panel and the surrounding frame is reflected in the derived SRFs. The modelling technique implemented herein is illustrated in Figure 2.

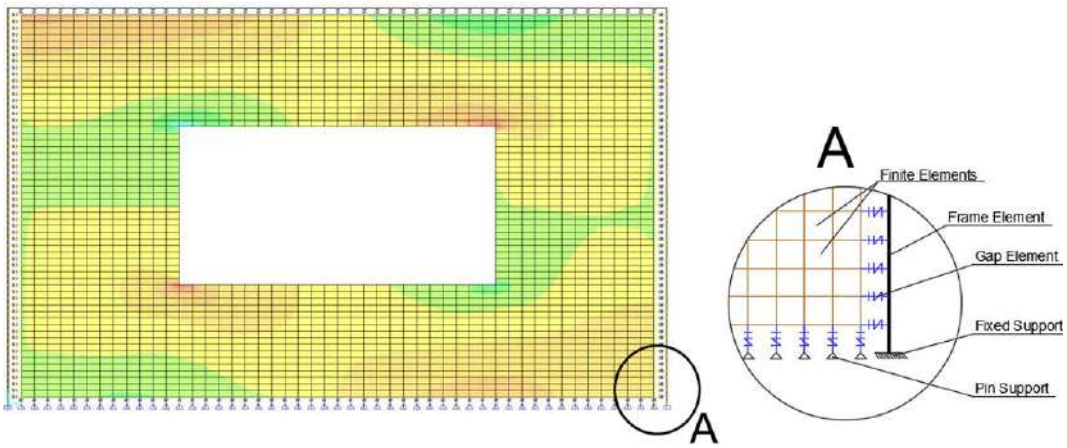

Figure 2. FE modelling of infilled RC frame with opening

Having completed the analytical models, SRF accounting for possible reduction in the initial lateral stiffness and strength of the infill wall due to the presence of opening is obtained as the ratio of the lateral stiffness of infill wall with opening to the lateral stiffness of solid infill wall. Lateral stiffnesses of both infilled frames with and without openings are achieved by means of FE analysis of frames horizontally loaded at the top. Since the structural interaction between the frame and the infill is considered in the analytical model, the derived SRFs also reflect the influence of this interaction. The analyses are performed using the software SAP2000. As a

result, the variation of SRFs in relation to opening percentage is plotted in Figure 3 both for infill walls with window and door openings.

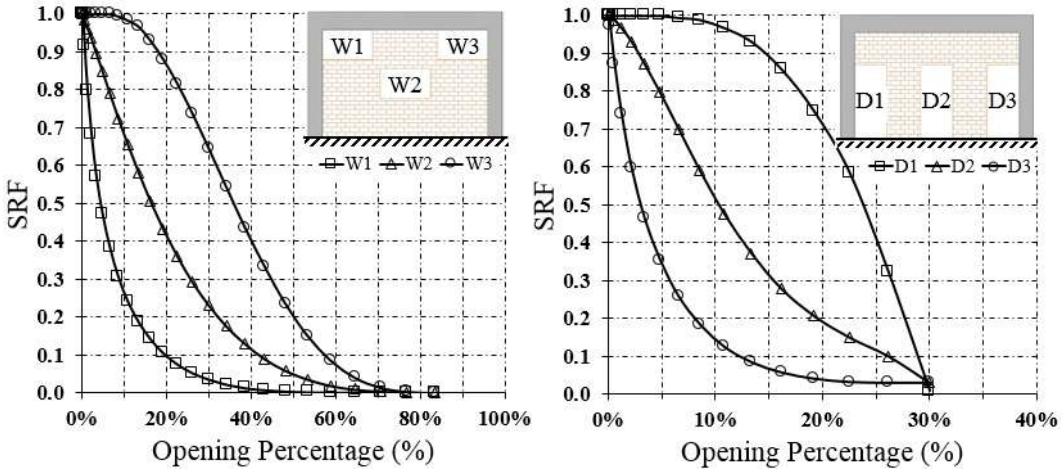

Figure 3. (a) SRFs for infill wall with window opening *(b)SRFs for infill wall with door opening*

The particular values of SRFs are λ_{oW1} = 0.11, λ_{oW2} = 0.43 and λ_{oW3} = 0.88 for W1, W2 and W3, respectively. Similarly, the SRFs of λ_{oD1} = 0.94, λ_{oD2} = 0.44 and λ_{oD3} = 0.10 for D1, D2 and D3, respectively, may be read directly from the above given graphs. As expected, the presence of opening significantly reduces the initial elastic stiffness of the infill panel. Meanwhile, the reduction of stiffness depends mostly on opening position and percentage. Upper-left window opening (W1) and bottom-right door opening (D3) are found to be the most influential on the lateral stiffness, since they are directly located at the corners where a high concentration of compressive stresses develops. In particular, a sharp decrease in initial stiffness of D1 is observed when the opening percentage exceeds 15. The same trend is also observed for W3 with a less sharp decrease. The last two results indicate that the extension of opening to load transfer mechanism results in a considerable decrease in stiffness. In the case of small upper-right window opening and bottom-left door opening (e.g., opening percentage up to 15), the lateral stiffness of the perforated infill panel can be taken as same as that of solid infill panel, which means that there is no need to account for openings. The influence of central openings on lateral stiffness is found to be between the influence of other positions. The contribution of infill walls with openings can be neglected if the opening ratio exceeds 50-60% in the case of window openings and 25-30% in the case of door openings.

3.2. Constitutive Laws of Masonry Infill Walls with Openings

Constitution of F–D envelopes representing the nonlinear behavior of the equivalent strut, which simulates the global mechanical behavior of infill wall, is one of the most crucial issues due to large uncertainties and many different proposals are available regarding this issue. In this study, the widely acceptable three-linear constitutive F–D laws proposed by Dolsek and Fajfar [26], [27] are implemented. Accordingly, the initial stiffness of the infill (K_1), i.e. the slope of the first branch, is calculated as:

$$K_1 = \frac{G_w \cdot L_{in} \cdot t_w}{H_{in}} \tag{1}$$

where G_w is the shear modulus of the wall, L_{in} and H_{in} are the length and the height of the infill, respectively, and t_w is the thickness of the wall. The strength of the infill wall (F_m) is determined according to Eq. (2):

$$F_m = 0.818 \cdot \frac{L_{in} \cdot t_w \cdot f_{tp}}{C_I} \cdot \left(1 + \sqrt{C_I{}^2 + 1}\right) \tag{2}$$

where f_{tp} is the tensile strength of the infill obtained from the diagonal compression test and is taken to be 0.36 MPa in this study. C_I term in Eq. (2) is estimated by:

$$C_I = 1.925 \cdot \frac{L_{in}}{H_{in}} \tag{3}$$

The ratio between the cracking force (F_c) and the strength is 0.6. The lateral drift corresponding to the strength (D_m) is 0.2% in the case of infill without opening, 0.15% in the case of infill with a window opening and 0.10% in the case of infill with a door opening. The lateral drift at collapse state is arbitrarily taken as $5 \cdot D_m$.

It should be noted that for the constitutive F–D law of compressive equivalent diagonal strut, the constitutive parameters (i.e., stiffness, strength and lateral drift) determined in the horizontal direction have to be transformed to the direction of the diagonal by using the angle between the equivalent compression strut and horizontal plane.

The influence of window and door openings on the F–D envelope of the diagonal strut is taken into account by using the derived SRFs in the previous section and the strength and stiffness parameters of constitutive relationship of the infill wall without openings are conveniently reduced. Accordingly, the modified constitutive relationships of the diagonal strut are shown in Figure 4, where displayed on the vertical axis is the axial force (N) and displayed on the horizontal axis is the axial shortening (Δ). Both the strength and the cracking force of infill panel, as well as the initial elastic stiffness, decrease as opening percentage increase. The same trend is observed for the stiffness of the second branch and the softening branch (i.e.., the third branch) of the constitutive laws. In particular, the slope of the second and the third branches is greater in the case of door opening in comparison to window openings. The axial shortening corresponding to the cracking of infill panel does not depend on shape and percentage of the opening.

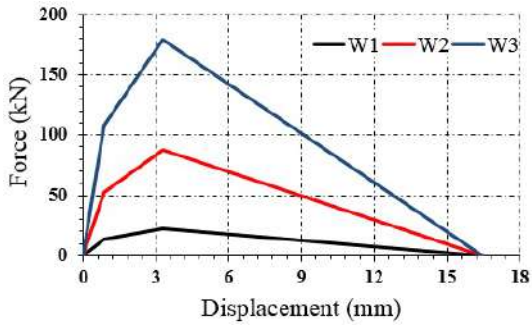

Figure 4. (a) F–D law of strut in the case of window opening

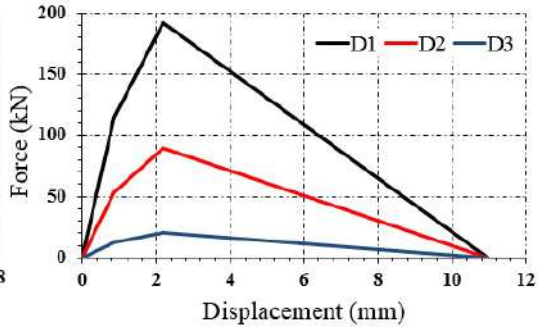

(b) F–D law of strut in the case of door opening

3.3. Nonlinear Static Analysis (NLS) of Frames

The influence of typical window and door openings on seismic response of masonry-infilled RC frame is investigated through NLS analysis, or so-called pushover analysis. The beam and columns are modelled as frame elements with two translational and one rotational degree of freedom at each node. The initial effective stiffness of beam is taken as 40% of the uncracked stiffness of the section and the effective flexural stiffness of columns is reduced according to TSDC [28]. Nonlinear behavior structural element is considered by adopting a lumped plasticity model. Default bending moment–rotation envelopes of SAP2000 are assumed for plastic hinges assigned at both ends of elastic structural members. Bending moment–rotation envelopes for beam and column elements is illustrated in Figure 5, where M/M_p is normalized bending moment, θ_y is yield rotation and θ is rotation angle in radians.

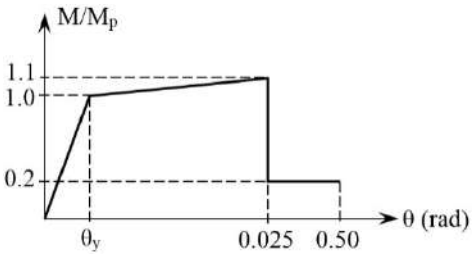

Figure 5. (a) M–θ relations for beam

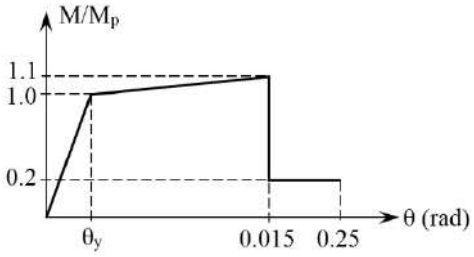

(b) M–θ relations for columns

In NLS analyses of the present study, infill walls are simulated by adopting the model of equivalent compression strut referred to as the most simplified yet reasonably accurate macro-model. The strut is connected between the beam-column joints and moment releases are specified at both ends of the strut in order to prevent the transfer of bending moments from frame to infill (Figure 6). Consequently, the diagonal pin jointed strut can transfer only axial force. The modified cross sectional and mechanical properties of infill walls with opening are assigned to compressive equivalent diagonal strut. The equivalent strut assumed to have the same thickness and modulus of elasticity as the infill panel it represents, whereas its width (a) is reduced by means of a SRF (λ_o). Accordingly, the particular values of equivalent widths of struts are a_{W1} = 76 mm, a_{W2} = 297 mm and a_{W3} = 608 mm for W1, W2 and W3 specimens (i.e., for infill walls with window opening), respectively. The

equivalent strut widths for D1, D2 and D3 specimens (i.e., for infill walls with door opening) are calculated as a_{D1} = 649 mm, a_{D2} = 304 mm and a_{D3} = 69 mm, respectively.

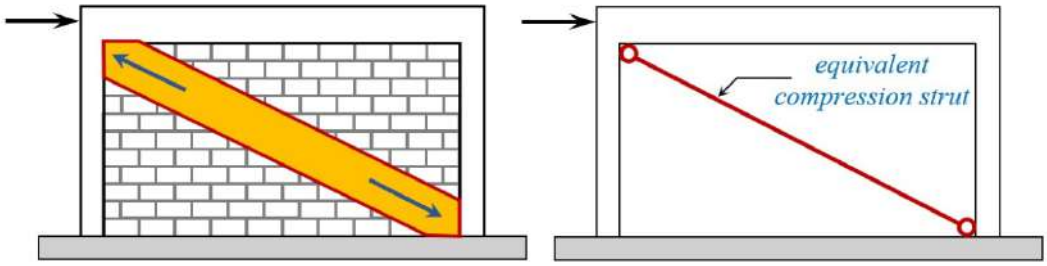

Figure 6. Equivalent diagonal strut model

The results of NLS analysis performed considering only seismic masses are assumed to be the initial conditions of displacement controlled pushover analysis. The seismic masses are concentrated at floor levels and determined as the combination of dead loads and 30% of live loads. Lateral strength and displacement profile of frames is estimated by NLS analyses carried out using SAP2000. The resulting capacity curves (the base shear force versus roof lateral displacement curves) are shown in Figure 7.

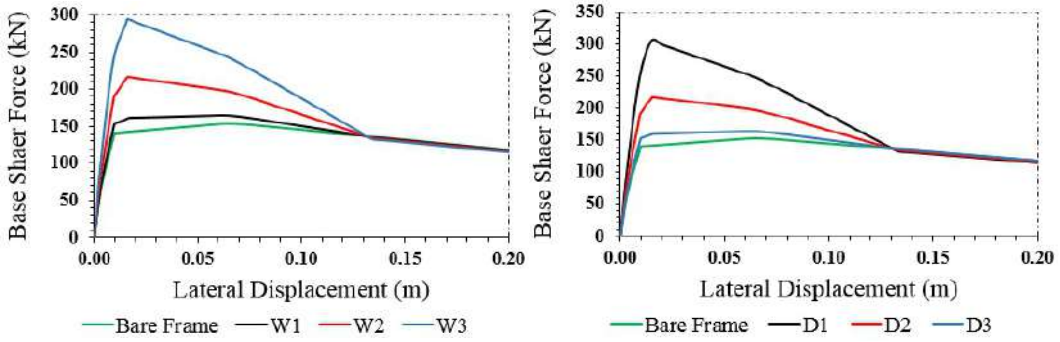

Figure 7. (a) Capacity curves of frames with window opening (b) Capacity curves of frames with door opening

Furthermore, some of the main parameters related to nonlinear seismic response of the frames are summarized in Table 1, where V_{max} is the maximum base shear force, V_y is the yield base shear force, Δ_y is the yield displacement, Δ_y/H is the yield drift ratio, V_a is the base shear force corresponding to complete failure of infill, Δ_u is the ultimate displacement and Δ_u/H is the ultimate drift ratio. There is no universal consensus on defining the yield point of infilled frames. In the present study, the yield point of the infilled frames with opening is specified as the point where a clear departure from linear elastic behavior occurs. Meanwhile, the ultimate displacement is estimated as the displacement when the rotation capacity of any base column hinge is exceeded.

Table 1. Main parameters of capacity curves

Specimen	V_y (kN)	V_{max} (kN)	V_a (kN)	Δ_y (mm)	Δ_u (mm)	Δ_y/H (%)	Δ_u/H (%)
Bare Frame	140.1	152.9	-	9.7	65.6	0.353	2.385
W1	150.8	164.6	135.0	9.3	65.6	0.338	2.385
W2	190.0	216.7	134.2	9.4	70.6	0.342	2.567
W3	253.2	295.1	133.0	9.5	70.6	0.345	2.567
D1	270.5	305.3	133.0	9.3	70.6	0.338	2.567
D2	191.8	218.3	134.4	9.6	70.6	0.349	2.567
D3	149.8	163.3	135.3	9.5	65.6	0.345	2.385

A considerable effect of opening position is monitored for the same opening percentages. Although relatively small opening percentages (15-20%) are taken into consideration, the capacity curves of W1 and D3 are very close to that of a bare frame, indicating that the behavior of infilled frame becomes identical to behavior of a bare frame. Approximately 42% increase in V_{max} and 36% increase in V_y values of infilled frames with central window and door openings are observed. Both the yield and the maximum strength of the frames with off-diagonal window and door openings are found to be greater in comparison to those of other specimens. A complete failure of infill panel occurs at around 134 kN for all specimens. The reduction in base shear force (i.e., in strength) is approximately 55% for W3 and D1 specimens, and 38% for W2 and D2 specimens after infill panel completely collapsed. This reduction is not obvious for W1 and D3.

It is found that all infill walls attain their cracking strength by approximately 0.25% lateral drift ratio. When the maximum strength of the infill wall is reached, the lateral drift ratio is monitored to be between 0.5% and 0.6%. The specimens yield at about 0.35% lateral drift ratio and the lateral drift ratio is approximately 2.5% at the ultimate displacement.

4. SUMMARY AND CONCLUSIONS

Seismic response of brick-infilled RC frames with typical window and door openings is investigated analytically through nonlinear static analysis where infill walls are simulated by adopting the compression strut analogy. The influence of the openings on the overall seismic response is introduced by means of SRFs obtained from FE analysis.

The results indicate that the first cracking of infill wall with typical window and door openings occurs at relatively small lateral drift ratio. The lateral stiffness and strength of infilled frames with openings generally increase in comparison to that of a bare frame. However, this increase is mostly influenced by the position of the window or door opening. It can be concluded that, opening located at the diagonally opposite corners of the compression strut substantially reduces the stiffness of the infill wall and the nonlinear seismic response of RC frames with openings becomes identical to response of bare RC frames. Recognizing this behavior, there is no need to include infill walls in the analytical model in the presence of such openings. The initial lateral stiffness and the maximum base shear force of frames with off-diagonal openings are considerably high. It is also notable that, the off-diagonal openings considered in this study do not directly restrain the development of the load transfer path by intersecting the compression strut. While RC frames with central window and door openings exhibit similar behavior in terms of capacity, the influence of infill wall on the nonlinear seismic response is also remarkable in these frames.

In contrast to their dominant influence on lateral stiffness and strength, the influence of typical window and door openings on the yield and the ultimate drift ratios of infilled RC frames is found to be insignificant. However, this result should not be generalized without extending the analyses beyond prototype one-story one-bay RC frames.

REFERENCES

[1]. A. Mohebkhaha, A. A. Tasnimia, and H. A. Moghadamb, “Nonlinear analysis of masonry-infilled steel frames with openings using discrete element method”, *Journal of Constructional Steel Research*, vol. 64(12), pp. 1463–1472, 2008.
[2]. P. G. Asteris, D. M. Cotsovos, C. Z. Chrysostomou, A. Mohebkhah, and G. K. Al-Chaar, “Mathematical micromodeling of infilled frames: State of the art”, *Engineering Structures*, vol. 56, pp. 1905–1921, 2013.
[3]. Y. P. Yuen and J. S. Kuang, “Nonlinear seismic responses and lateral force transfer mechanisms of RC frames with different infill configurations”, *Engineering Structures*, vol. 91, pp. 125–140, 2015.
[4]. G. Uva, F. Porco, and A. Fiore, “Appraisal of masonry infill walls effect in the seismic response of RC framed buildings: A case study,” *Engineering Structures*, vol. 34, pp. 514–526, 2012.
[5]. D. J. Kakaletsis and C. G. Karayannis, “Influence of masonry strength and openings on infilled R/C frames under cycling loading”, *Journal of Earthquake Engineering*, vol. 12(12), pp. 197–221, 2008.
[6]. K. Thinley and H. Hao, “Seismic assessment of masonry infilled reinforced concrete frame buildings in Bhutan”, in *Proc. Tenth Pacific Conference on Earthquake Engineering (PCEE)*, 2015, paper 111, Sydney.
[7]. G. Uva, D. Raffaele, F. Porco, and A. Fiore, “On the role of equivalent strut models in the seismic assessment of infilled RC buildings,” *Engineering Structures*, vol. 42, pp. 83–94, 2012.
[8]. P. M. Pradhan, “Equivalent strut width for partial infilled frames”, *Journal of Civil Engineering Research*, vol. 2(5), pp. 42-48, 2012.
[9]. M. Valente, “Seismic performance assessment of a masonry infilled ductile RC structure”, *IACSIT International Journal of Engineering and Technology*, vol. 4(6), pp. 701–704, 2012.
[10]. A. Fioren, F. Porco, D. Raffaele, and G. Uva, “About the influence of the infill panels over the collapse mechanisms active under pushover analyses: Two case studies”, *Soil Dynamics and Earthquake Engineering*, vol. 39, pp. 11–22, 2012.
[11]. G. Mondal and S. K. Jain, “Lateral stiffness of masonry infilled reinforced concrete (RC) frames with central opening,” *Earthquake Spectra*, vol. 24(3), pp. 701–723, 2008.
[12]. I. Koutromanos, A. Stavridis, P. B. Shing, K. Willam, “Numerical modeling of masonry-infilled RC frames subjected to seismic loads”, *Computers and Structures*, vol. 89(11–12), pp. 1026–1037, 2011.
[13]. A. A. Tasnimi and A. Mohebkhah, “Investigation on the behavior of brick-infilled steel frames with openings, experimental and analytical approaches”, *Engineering Structures*, vol. 33(3), pp. 968–980, 2011.
[14]. L. Cavaleri and F. D. Trapani, “Cyclic response of masonry infilled RC frames: Experimental results and simplified modeling”, *Soil Dynamics and Earthquake Engineering*, vol. 65, pp. 224–242, 2014.
[15]. V. Sigmund and D. Penava, “Influence of openings, with and without confinement, on cyclic response of infilled R-C frames–An experimental study”, *Journal of Earthquake Engineering*, vol. 18(1), pp. 113–146, 2014.
[16]. D. J. Kakaletsis, and C. G. Karayannis, “Experimental investigation of infilled reinforced concrete frames with opening,” *ACI Structural Journal*, vol. 106(2), pp. 132–141, 2009.

[17]. J. S. Kuang and H. Zhang, "Shake table tests of infilled RC frames with different column-to-infill connections", in *Proc. Second European Conference on Earthquake Engineering and Seismology*, 2014, Istanbul.
[18]. D. Celarec, P. Ricci, and M. Dolšek, "The sensitivity of seismic response parameters to the uncertain modelling variables of masonry-infilled reinforced concrete frames", *Engineering Structures*, vol. 35, pp. 165–177, 2012.
[19]. S. Lagomarsino, A. Penna, A. Galasco, and S. Cattari, "TREMURI program: An equivalent frame model for the nonlinear seismic analysis of masonry buildings", *Engineering Structures*, vol. 56, pp. 1787–1799, 2013.
[20]. X. Chen and Y. Liu, "Numerical study of in-plane behaviour and strength of concrete masonry infills with openings", *Engineering Structures*, vol. 82, pp. 226–235, 2015.
[21]. M. Sukrawa, "Earthquake response of RC infilled frame with wall openings in low-rise hotel buildings", Procedia Engineering, vol. 125, pp. 933–939, 2015.
[22]. L. D. Decanini, L. Liberatore, and F. Mollaioli, "The influence of openings on the seismic behaviour of infilled framed structures", in *Proc.* 15*th World Conference on Earthquake Engineering*, 2012, Lisboa.
[23]. L. D. Decanini, L Liberatore, and F. Mollaioli, "Strength and stiffness reduction factors for infi lled frames with openings", *Earthquake Engineering and Engineering Vibration*, vol. 13(3), pp. 437–454, 2014.
[24]. E. Martinelli, C. Lima, and G. D. Stefano, "A simplified procedure for nonlinear static analysis of masonry infilled RC frames," *Engineering Structures*, vol. 101, pp. 591–608, 2015.
[25]. E. Smyrou, C. Blandon, S. Antoniou, R. Pinho, and F. Crisafulli, "Implementation and verification of a masonry panel model for nonlinear dynamic analysis of infilled RC frames," *Bulletin of Earthquake Engineering*, vol. 9(5), pp. 1519–1534, 2011.
[26]. M. Dolsek and P. Fajfar, "Mathematical modelling of an infilled RC frame structure based on the results of pseudo-dynamic tests", *Earthquake Engineering & Structural Dynamics*, vol. 31(6), pp. 1215–1230, 2002.
[27]. M. Dolsek and P. Fajfar, "The effect of masonry infills on the seismic response of a four-storey reinforced concrete frame-a deterministic assessment," *Engineering Structures*, vol. 30(7), pp. 1991–2001, 2008.
[28]. *Turkish Seismic Design Code (TSDC)*, Ministry of Public Works and Settlement, Ankara, Turkey, 2007.
[29]. *Requirements for Design and Construction of Reinforced Concrete Structures (TS*500*)*, Turkish Standards Institution, Ankara, Turkey, 2000.
[30]. *SAP2000 Integrated Structural Analysis and Design Software, Ver.16.0.0*, Computer and Structures Inc., USA, 2017.
[31]. *Prestandard and Commentary for the Seismic Rehabilitation of Buildings (FEMA 356)*, Federal Emergency Management Agency, Washington, D.C., 2000.

ICENS 4TH INTERNATIONAL CONFERENCE ON ENGINEERING AND NATURAL SCIENCE
2-6 May 2018 KIEV UKRAINE

NAR based forecasting interface for time series analysis: T-seer

Ismail Kirbas[1]

Abstract

Today time series are widely used in many scientific areas. Determination of the magnitudes that vary with time, and later estimates of future with these values is a matter that has been closely related to human beings for centuries. In the analysis of the time series, generally ARIMA-like statistical methods are preferred. However, advances in artificial intelligence studies show that artificial neural networks may be more successful than well-known statistical approaches in pattern recognition and forecasting. MATLAB software that is widely preferred by many scientists contains an artificial neural network toolbox. Our work is the development of a NAR-based time series analysis and forecasting software using the MATLAB App Designer programming environment, which was first introduced in 2016. With the developed application, data files stored in CSV format can be easily analyzed via interface and a novice user to make predictions, to calculate estimation performance and to produce graphical results, can easily change all parameters related to estimation.

Keywords: Forecasting, Interface, Matlab, NAR, nonlinear autoregressive neural networks, prediction, software, time series, T-seer.

1. INTRODUCTION

Nowadays, time series are widely used in many scientific areas. Determination of the magnitudes that vary with time, and later estimates of future with these values is a matter that has been closely related to human beings for centuries. In the analysis of the time series, generally ARIMA-like statistical methods are preferred. However, advances in artificial intelligence studies show that artificial neural networks may be more successful than well-known statistical approaches in pattern recognition and forecasting.

When the literature is examined, it is seen that the time series has a wide application area. For this reason, it is a hot topic that attracts many researchers. Kirbas published two studies [1], [2] on short-term wind-speed forecasting using ARIMA and artificial neural networks. Ruiz et al. [3] used nonlinear autoregressive neural networks to predict energy consumption in public buildings. Caswell [4] proposed a nonlinear autoregressive approach to statistical prediction of disturbance storm time geomagnetic fluctuations using solar data. Sayfeddine [5] utilized NAR network with exogenous inputs based solution for local minimum problem. Al-Sbou and Alawasa [6] developed an NAR network model for solar radiation prediction. Shen and Chang [7] suggested online multistep-ahead inundation forecasts by recurrent NARX networks. Sanam and Eros [8] offered a NARX model for outdoor temperature forecasting. Kirbas and Kerem [9] analyzed neural network performances for wind-speed prediction. Thielbar and Dickey [10] published a book on neural networks for time series forecasting and practical implications. Buitrago [11] has been written a doctorate thesis on short-term forecasting of electric loads using NARX networks. Dietz [12] suggested a method for the analysis of nonlinear economic time series, which is based on artificial neural networks.

The second section of the paper mentions the artificial neural network based nonlinear forecasting approach and the third section explains the developed interface for NAR based forecasting. Finally, the outcome of the study is also summarized in conclusion section.

2. ARTIFICIAL NEURAL NETWORK BASED NONLINEAR FORECASTING

Nonlinear autoregressive neural networks is designed to forecast a time series from past values [13]. Time delay differential equation can be formulated by time delay differential equation in Equation 1, where α, β and c are

[1] *Corresponding author: Mehmet Akif Ersoy University, Department of Computer Engineering, 15100, Merkez/Burdur, Turkey. ismailkirbas@mehmetakif.edu.tr*

parameters and τ is the delay time [14]. When τ increases solution turns from periodic to chaotic, equation is solved using Runge-Kutta integration method, and the series to predict is shaped by sampling values with a given interval.

$$\hat{y}(t) = \frac{\alpha y(t-\tau)}{1+y^c(1-\tau)} - \beta y(t) \quad (1)$$

The neural network used is a time lagged feed-forward networks type. The neural network topology comprises of I_x inputs, one hidden layer of H_0 neurons, and one output neuron as presented Figure 1. Z denotes the one-step delay operator.

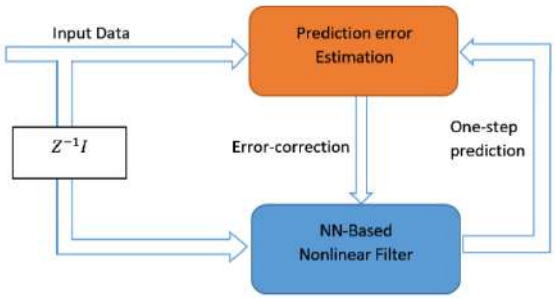

Figure 1. Block scheme of the NN-based nonlinear forecasting process.

Figure 2 shows the block scheme of the NN-based nonlinear prediction filter. The prediction device is designed such that starting from a given sequence $\{X_n\}$ at time n corresponding to a time series it can be obtained the best prediction $\{X_e\}$ for the sequence. For this reason, an estimator filter is proposed with an input vector I_x obtained by applying the delay operator Z^{-1} to the sequence $\{X_n\}$.

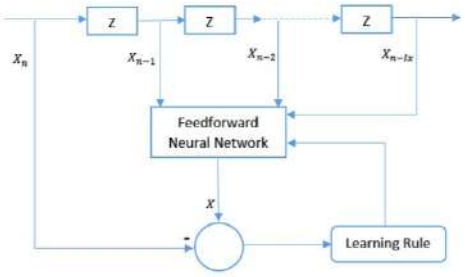

Figure 2. The block scheme of NN-based nonlinear prediction filter.

To estimate the sequence $\{X_e\}$ one-step ahead, the first delay is taken from line X_n and used as input. Hence, the output prediction can be denoted by where, F_p is the nonlinear predictor filter operator, and $X_e(n+1)$ the output prediction at $n+1$.

$$X_e(n+1) = F_p(Z^{-1}I(\{X_n\}) \quad (2)$$

Mean Square Error (MSE) and Root Mean Square Error (RMSE) metrics are generally used to evaluate the performance of the generated artificial neural network. MSE value can be calculated using Equation 3 and Equation 4 is used for RMSE value.

$$MSE = \frac{1}{N}\sum_{i=1}^{N}(\varepsilon_i)^2 = \frac{1}{N}\sum_{i=1}^{N}[y(t) - \hat{y}(t)]^2 \quad (3)$$

$$RMSE = \sqrt{\frac{1}{N}\sum_{i=1}^{N}[y(t) - \hat{y}(t)]^2} \quad (4)$$

3. THE DEVELOPED INTERFACE FOR NAR BASED FORECASTING

Our main study object, the NAR based interface, was developed using the app designer programming environment of Matlab software [15]. The standard Matlab commands are executed in the application. NAR based networks can be built trained and predict future values using the Matlab programming language. However, this requires Matlab programming skills. Our goal is for users who do not have any programming experience to predict future values over a time series.

As an application example, the wind speed measurements of Antalya international airport for 6 months in 2016 were examined. Figure 3 depicts the developed NAR based forecasting interface.

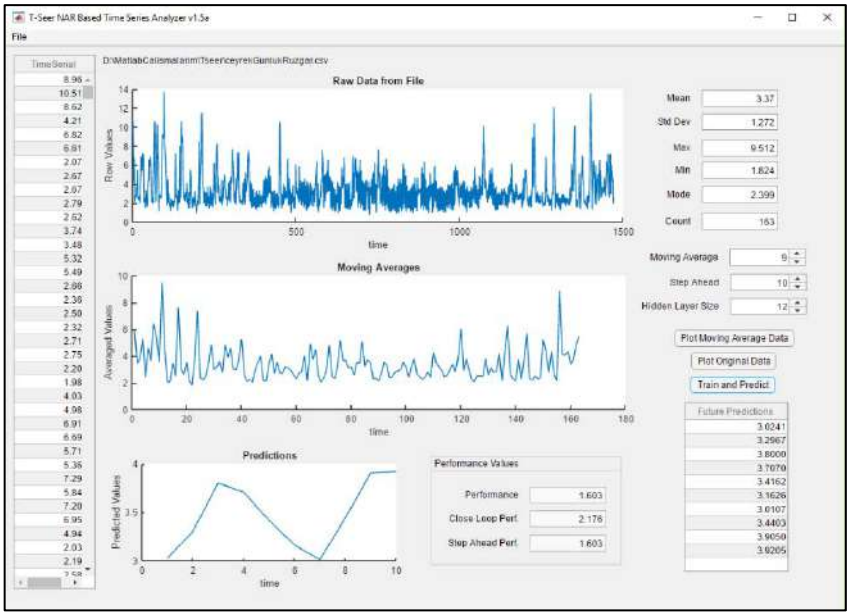

Figure 3. A screenshot of T-seer, NAR based time-series analyzer tool.

The file containing the time series is loaded from the file menu. The file extension must be CSV. In the section to the left of the screen, the values read from the file are displayed. After the file is uploaded, the data is automatically drawn as a time series graph in the top center of the screen. The statistical calculations for raw data are made and displayed in the text boxes in the upper right part of the screen. Basic statistical calculations include data count, mean, standard deviation, maximum and minimum values, and mode.

In the part below the statistical data, softening of the data with the moving average is ensured. You can enter numbers directly to the textboxes or use the up and down keys to increment or decrement one by one. In the step-ahead box, the user can enter the number of steps to forecast. The number of neurons in the hidden layer that forms the network is entered in the hidden layer size section. There is a button below the these textboxes that allows you to draw the moving average graph. When the value of the moving average box is changed, the moving average graph is redrawn automatically.

In order to make future predictions "train and predict" button is clicked. After this step, a network is created and 70 percent of the moving avarage data is used to train the network. After this stage, the popup screen, which is shown in Figure 4, displays the network training and performance metrics. This screen displays a summary of the network structure. At the same time, the training method, number of iterations, elapsed time and performance values are displayed. If desired, analysis results such as performance, training state, error histogram, and time series response can be accessed on this screen. Then the future values and performance values are calculated and displayed at the bottom of the screen.

Figure 4. A screenshot of Matlab Neural Network Training screen.

According to the iterations, the performance button is clicked to display the training performance. Figure 5 shows the performance graph obtained for the sample application.

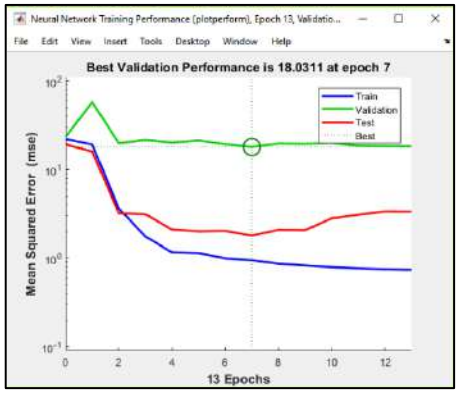

Figure 5. A screenshot of Matlab Neural Network Training Performance screen.

Closed-loop training form of the created neural network is shown in figure 6.

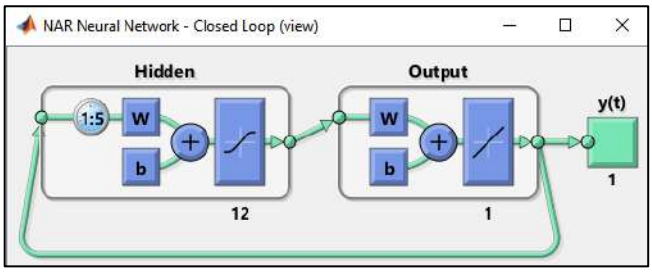

Figure 6. The closed-loop view of the developed NAR neural network.

After closed-loop training period one step ahead form is created and shown in Figure 7.

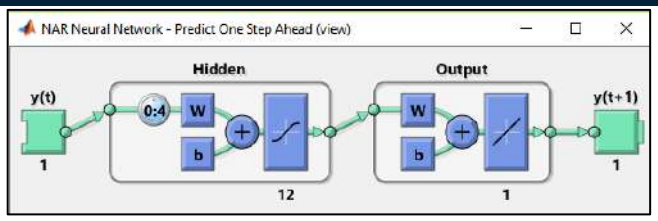

Figure 7. The One Step Ahead view of the developed NAR neural network.

Using neural network training popup screen, error histogram in Figure 8 and time-series response in Figure 9 can be analyzed.

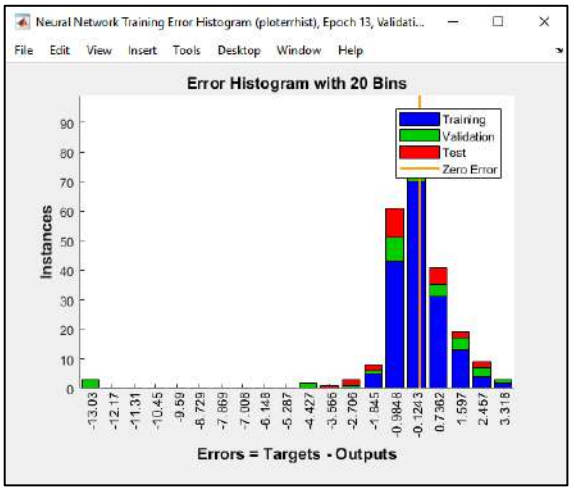

Figure 8. A screenshot of Matlab Neural Network Training Error Histogram screen.

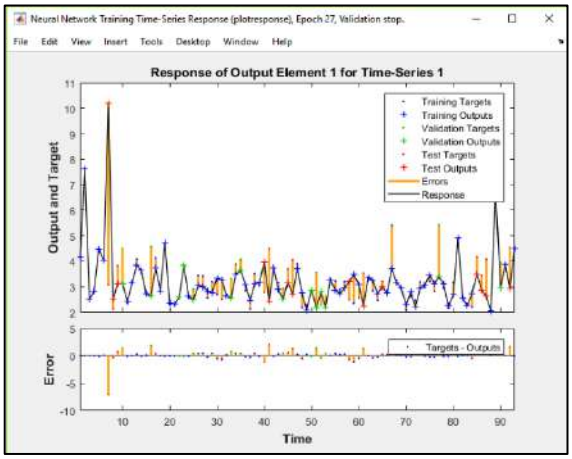

Figure 9. A screenshot of Matlab Neural Network Training Time-Series Response screen.

4. CONCLUSION

Our work is the development of a NAR-based time series analysis and forecasting software using the MATLAB App Designer programming environment, which was first introduced in 2016. With the developed application, data files stored in CSV format can be easily analyzed via interface and a novice user to make predictions, to calculate estimation performance and to produce graphical results, can easily change all parameters related to estimation.

REFERENCES

[1] I. Kirbas, "Short-Term Multi-Step Wind Speed Prediction Using Statistical Methods And Artificial Neural Networks," presented at the International Science and Technology Conference, 2016, vol. 1, p. 1064.
[2] I. Kirbas, "Istatistiksel metotlar ve yapay sinir aglari kullanarak kisa donem cok adimli ruzgâr hizi tahmini," *Sak. Univ. J. Sci.*, vol. 22, no. 1, pp. 24–38, Feb. 2018.
[3] L. Ruiz, M. Cuéllar, M. Calvo-Flores, and M. Jiménez, "An Application of Non-Linear Autoregressive Neural Networks to Predict Energy Consumption in Public Buildings," *Energies*, vol. 9, no. 9, p. 684, Aug. 2016.
[4] J. M. Caswell, "A Nonlinear Autoregressive Approach to Statistical Prediction of Disturbance Storm Time Geomagnetic Fluctuations Using Solar Data," *J. Signal Inf. Process.*, vol. 05, no. 02, pp. 42–53, 2014.
[5] D. Sayfeddine, "Nonlinear autoregressive neural network with exogenous inputs based solution for local minimum problem of agent tracking using quadrotor," *Инженерный Вестник Дона*, vol. 29, no. 2, 2014.
[6] Y. A. Al-Sbou and K. M. Alawasa, "Nonlinear Autoregressive Recurrent Neural Network Model For Solar Radiation Prediction," *Int. J. Appl. Eng. Res.*, vol. 12, no. 14, pp. 4518–4527, 2017.
[7] H.-Y. Shen and L.-C. Chang, "Online multistep-ahead inundation depth forecasts by recurrent NARX networks," *Hydrol. Earth Syst. Sci.*, vol. 17, no. 3, pp. 935–945, Mar. 2013.
[8] S. Narejo and E. Pasero, "Time Series Forecasting for Outdoor Temperature using Nonlinear Autoregressive Neural Network Models," *J. Theor. Appl. Inf. Technol.*, vol. 94, no. 2, p. 451, 2016.
[9] I. Kirbas and A. Kerem, "Short-Term Wind Speed Prediction Based on Artificial Neural Network Models," *Meas. Control*, vol. 49, no. 6, Jul. 2016.
[10] M. Thielbar and D. A. Dickey, *Neural Networks for Time Series Forecasting: Practical Implications of Theoretical Results*. 2011.
[11] J. H. Buitrago, "Short-Term Forecasting of Electric Loads Using Nonlinear Autoregressive Artificial Neural Networks with Exogenous Multivariable Inputs," PhD Thesis, University of Miami, Open Access Dissertations, 2017.
[12] Sebastian Dietz, "Autoregressive Neural Network Processes Univariate, Multivariate and Cointegrated Models with Application to the German Automobile Industry," PhD Thesis, Passau University, Passau University, 2010.
[13] M. T. Hagan, H. B. Demuth, and M. H. Beale, *Neural network design*, 1st ed. Boston: PWS Pub, 1996.
[14] J. A. Pucheta, C. M. Rodríguez Rivero, M. R. Herrera, C. A. Salas, H. D. Patiño, and B. R. Kuchen, "A feed-forward neural networks-based nonlinear autoregressive model for forecasting time series," *Comput. Sist.*, vol. 14, no. 4, 2011.
[15] *MATLAB and Neural Network Toolbox Release 2016b*. Massachusetts, United States: The MathWorks, 2016.

BIOGRAPHY

Ismail KIRBAS,got his bachelors' degree in the Computer Education Department in Technical Education Faculty at Kocaeli University, Kocaeli/Turkey in 2000, his master degree in the Electronics and Computer Education at Kocaeli University in 2008, PhD degree in Electronics and Computer Education Department at Sakarya University in 2013. He is still an academic member of the Computer Engineering Department at Burdur Mehmet Akif Ersoy University. His major areas of interests are: Wireless Sensor Networks, Embedded Systems, Design of Experiments, Time Series Predictions and Mobile Programming.

ICENS 4TH INTERNATIONAL CONFERENCE ON ENGINEERING AND NATURAL SCIENCE
2-6 May 2018 KIEV UKRAINE

Experimental Investigation Of The Effect Of Feed Rate On Geometrical Tolerances In Turning Of 7075 Aluminum Alloy

Ismail Tekaut[1], *Seven Bozkurt*[2], *Halil Demir*[3], *Ulvi Seker*[4]

Abstract

Machine parts often combine with other parts to form systems. Production is very important between the dimensional and geometric tolerance values stated on the manufacturing drawing so that these parts constituting the systems can be installed without errors and fast. Particularly in moving systems in industries with narrow tolerance values such as aviation, defense, automotive, etc., parts must be produced between geometric tolerance values to minimize problems such as vibration, balance, high heat due to friction. The choice of manufacturing method and conditions are very important for the capture of these tolerance values. Generally, the machining method is preferred for machining parts and the turning operation is about one third of machining. Thus, while machine parts are shaped by turning, knowing the appropriate cutting conditions and cutting parameters know in advance about the end product quality, dimensional accuracy and geometric tolerance values. By knowing the ideal cutting conditions and cutting parameters, time and economic losses are prevented, the manufacturer and operator have many advantages. For this reason, the AA 7075 T651 Aluminum alloy, which is frequently used in many industries in this work, has a cutting speed of 100 m/min, a feed rate of three different feedrates (0.05, 0.1, 0.25 mm /rev) and combinations of 0.5, 1.5 and 3 mm cutting depth parameters the effect of geometric tolerances (cylindricality, circularity, linearity) of the amount of advance was investigated. As a result, feed rate increase has led to increased geometric tolerance.

Keywords: *Turning, Cutting speed, Cylindricality, Circularity, Linearity*

1. INTRODUCTION

The geometric dimension and tolerance relationship between the parts creating the machines is very effective in the long life and functional operation of the machine elements. For this reason, the production is required on desired measurements, tolerances, surface quality and geometry that is specified on the technical drawing of the part. The precise measurement and geometric tolerances are critical to fulfill the exact functions of especially moving systems, slides and hole-shaft mechanisms. Problems such as improper mounting, rapid wear, excessive vibration, overheating decrease the life span of the mechanisms and cause economic loss. Therefore, the calculated measurement and geometric tolerance values increase the strength and motion sensitivity of the mechanisms. However, it is difficult to produce a machine part exactly in the dimensions, shapes and tolerances specified in the technical drawing. For this reason, it is very important to choose the best manufacturing method and determine the optimum cutting conditions. Machining is preferred in industrial sectors such as aviation, automotive and defense where the production is desired in precision measurements. Parts can also be produced in geometries that are rapid and difficult to produce by machining. Turning, among the machining methods, is the most preferred method of forming parts in cylindrical, conical geometries. Thus, many researchers investigate the turning and machining conditions. It is seen that studies on turning operations usually involve cutting parameters (cutting speed, feed rate, cutting depth), cutting tool material, chip form and surface roughness. It is emphasized that cutting parameters are important in the formation of quality criteria such as surface quality, dimensional and formal accurateness. It is known that the change in cutting forces causes to vibration on the cutting tool although it is desired that cutting force values should remain stable without changing during turning [1]. It is also known that the vibrations in the turning operation are occurred due to the structure of the machine tool, the gaps and abrasion in the bearings, the attachment type of the part, the geometrical structure of the cutting tool, the applied cutting parameters

[1] *Corresponding author: Gazi University, Technical Sciences Vocational School, 06374, Ostim/Ankaral, Turkey.* ismailt@gazi.edu.tr

and the environmental effects [2]. It is indicated that the formation of BUE (Built-up edge) on the cutting tool makes the surface quality worse and causes vibrations by increasing the dynamic forces acting on the cutting insert. It is also confirmed that the control of vibrations occurring on machine tools can be done by selecting the appropriate cutting parameters [3-6]. It is implied that the vibration values generated during turning are an important factor in determining surface roughness, dimensional and geometrical deviations and BUE formation increase the surface roughness [7]. It is emphasized that cutting forces and surface roughness increase with increasing feed rate through cutting parameters. It is also stated that surface roughness depends not only on cutting parameters and but also vibration. It is emphasized that the BUE formation at the low feed rate and the cutting speed also showed a significant increase [8]. It is explained that increase on the feed rate, cutting forces and chip depth increase the vibration. It is emphasized that although the increase in cutting speed decreases the cutting forces, it increases the vibration [9]. It is indicated that increasing feed rate increases the surface roughness and radial vibration [10]. From the literature, it is seen that the increase in the feed rate in the turning process is an effective parameter in making the surface quality worse and increasing the vibration. It is emphasized that the change in cutting force during machining and the BUE generated in the cutting tool cause the vibration. The work to be done is generally seen to be on surface roughness. For this purpose, in this study, the effect of geometric tolerances (cylindricality, circularity, linearity) on the feed rate was investigated by turning with AA 7075 T651 Aluminum alloy which is widely used in many industries.Both oral and poster presentations will be published on a CD in order to be distributed to participants at the time of registration in the conference.

2. MATERIAL AND METHOD

AA7075-T651 aluminum alloy having diameter of 50mm and according to ASTM B221M-12 Standard is used in the work. The hardness of the part was measured via Burton GOKO SEIKI manual hardness tester, which is located in TUBITAK SAGE dimensional and quality control laboratory, by applying HRB type 1/16 "ball tip and 100 kg load. The physical properties and chemical composition of the workpiece are shown in Table 1. The samples having diameter of 48 mm and length of 45 mm were turned on the face of the samples and a centre hole was opened from one side. In the experiments, VCGT 160404-AS coded insert and SVJCR 2020K 16 coded tool holder were used in according to the ISO 3685 standard recommended for aluminum materials in the catalog of ISKAR. The properties of insert are given in Fig.1. Cutting parameters were selected with three different feed rate (0.05, 0.1, 0.25 mm /rev), three different depth of cut (0.5, 1.5 and 3 mm) and 100 m/min feed rate recommended by the tool manufacturer. Machining experiments were carried out on The SPINNER-TC65 CNC tuning lathe. CIMCOOL Cimperial 806 semi-synthetic emulsion (5%) was used as cutting fluid in the experiments. The new inserts were used for each test, and the cylindricality, circularity, linearity measurements of the parts after experiments were performed on the CMM device (Fig. 2).

Table 1. The physical properties and chemical composition of the workpiece(AA7075-T651).

The chemical composition								
Cr	**Cu**	**Fe**	**Mg**	**Mn**	**Si**	**Ti**	**Zn**	**Al**
0.19	1.4	0.19	2.5	0.22	0.17	0.08	5.4	89.85
The physical properties								
Density (g/cm3)	**Hardness (HRB)**	**Ultimate Strength (MPa)**	**Yield Strength (MPa)**	**Strain (%)**	**Elastic Modulus (GPa)**	**Poisson's ratio**	**Melting Temperature (°C)**	**Thermal conductivity (W/mK)**
2.81	99.5	572	503	11	71.7	0.33	635	130

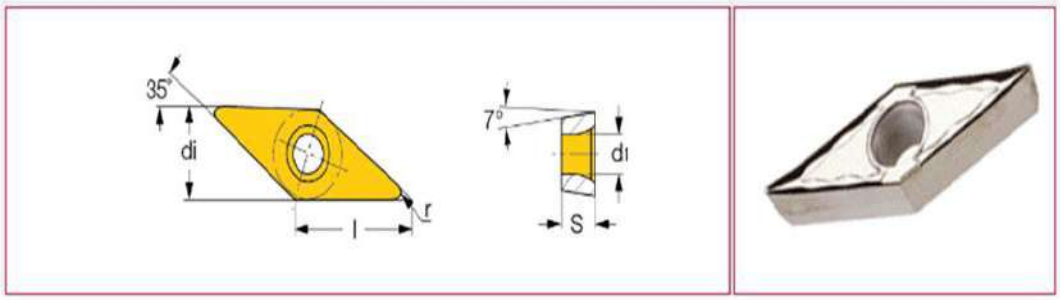

Designation	l	di	S	r	d1	ap (min)	ap (max)	ft (min)	ft (max)	Tough ⟵⟶ Hard Grade & Vc
VCGT 160404-AS	16.60	9.52	4.76	0.40	4.40	0.50	3.00	0.05	0.25	IC20 IC520

Figure 1. ISKAR branded VCGT 160404-AS coded insert.

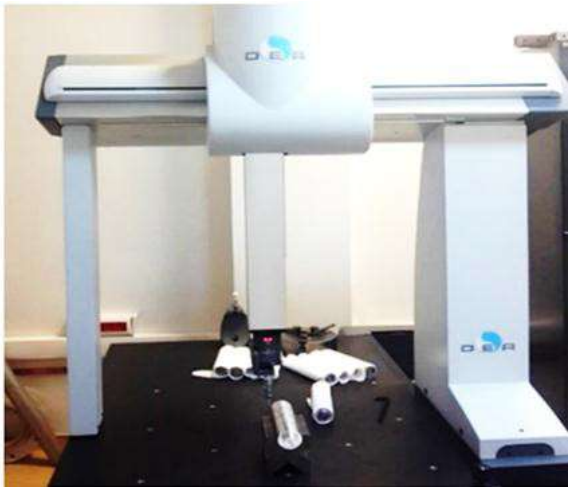

Figure 2. CMM device.

3. RESULTS AND DISCUSSION

In the study, the effect of the feed rate on geometric tolerances (cylindricality, circularity, linearity) in turning of AA 7075 T651 aluminum alloy was investigated. The measurement results from the CMM device were converted to graphs (Figure 3-a, b, c). When Figure 3 are examined, it is seen that the increase in the feed rate generally leads to the increase in cylindricality, circularity and linearity deviation values. This situation can be attributed to the increase in the chip volume removed at a unit time by increasing feed rate, and consequently the increase in machine tool-insert vibration by increasing cutting forces [1-6]. The fluctuations in large cutting forces cause the vibration amplitude to increase, and so the geometric tolerance deviation values increase, too. When the graphics are examined in terms of depth of cut, the increase in depth of cut causes an increase in the deviation values. This situation can be interpreted as increasing cutting forces and the vibrations of fluctuations on these cutting forces as a result of increasing the chip volume removed at a unit time. Increasing the geometric tolerance values by increasing the feed rate and the depth of cut proves that increasing cutting forces increases the vibration amplitude of the fluctuation. The high cylindricality and linearity deviations at the feed rate of 0.05 mm/rev, the long, unbroken chips and BUE formation (see Figure 4) around the cutting tool and workpiece due to the low amount of feed rate cause fluctuations in cutting forces [7-10]. Force fluctuations also increase the deviation values by increasing the amplitude of vibration

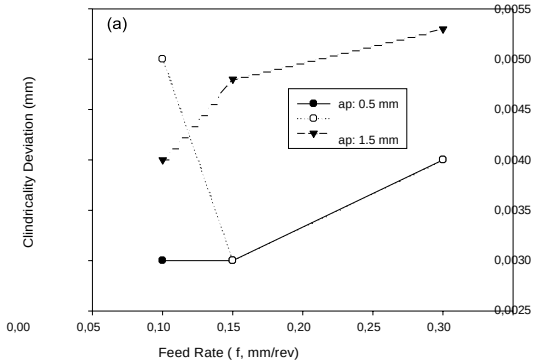
(a)
Clindricality Deviation (mm)
ap: 0.5 mm
ap: 1.5 mm
0,0055
0,0050
0,0045
0,0040
0,0035
0,0030
0,0025
0,00
0,05
0,10
0,15
0,20
0,25
0,30
Feed Rate (f, mm/rev)

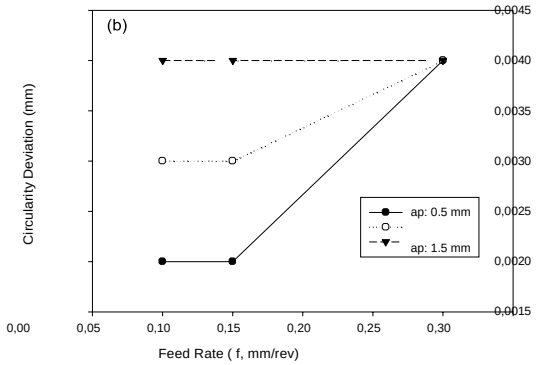
(b)
Circularity Deviation (mm)
ap: 0.5 mm
ap: 1.5 mm
0,0045
0,0040
0,0035
0,0030
0,0025
0,0020
0,0015
0,00
0,05
0,10
0,15
0,20
0,25
0,30
Feed Rate (f, mm/rev)

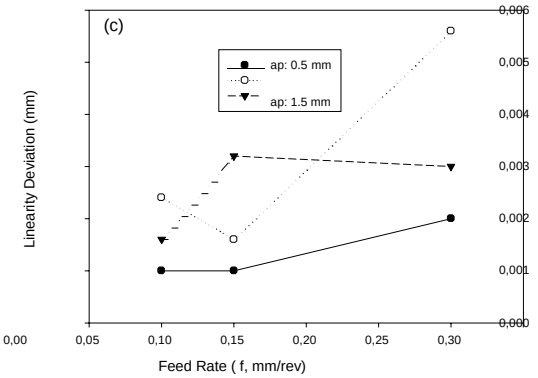
(c)
Linearity Deviation (mm)
ap: 0.5 mm
ap: 1.5 mm
0,006
0,005
0,004
0,003
0,002
0,001
0,000
0,00
0,05
0,10
0,15
0,20
0,25
0,30
Feed Rate (f, mm/rev)

4. CONCLUSIONS

The effect of feed rate on geometric tolerances (cylindricality, circularity, linearity) in turning of AA 7075 T651 aluminum alloy was investigated.

Consequently;

Increasing the feed rate and depth of cut is an effective parameter in increasing the geometric tolerance value. This situation led to increase in cutting forces by increasing the chip removal rate in unit time with the help of the increase in feed rate. The increase in vibration as a reult of the fluctuation of increasing cutting forces can be interpreted as an increase in the geometric tolerance values.

BUE formation and chip wrapping on the cutting tool cause the cylindricality, circularity and linearity deviation values to increase. This situation can be construed as increasing vibration of the machine tool-insert and so increasing the geometric tolerance values as a result of the fluctuations of cutting forces during the machining.

The feed rate where the cylindricity, circularity, and linearity tolerance values is the lowest is 0.1 mm/rev for cylindricality and 0.05 mm/rev for circularity and linearity.

The depth of cut is 0.5 mm in which the cylindricity, circularity, and linearity tolerance values is the lowest.

REFERENCES

[1]. Tekaut, I.,"Takim Tezgahlarindaki Kesici Takim Titresiminin Yuzey Puruzlulugune Etkisi", Master Thesis, Gazi University Graduate School of Natural and Applied Sciences, 65-89 (2008).
[2]. Neseli,S., Yaldiz, S., "Tornalamada Takim Geometrisi ve Tirlama Titresimlerinin Yuzey Puruzlulugune Etkisi'', Master Thesis, Selcuk University, 49-53(2006).
[3]. Lin, S.C., Hu, M.R., "Low vibration control system in turning", International Journal of Machine Tools& Manufacture, 32: 627-629 (1992).)
[4]. .M. Wegmuller, J. P. von der Weid, P. Oberson, and N. Gisin, "High resolution fiber distributed measurements with coherent OFDR," in *Proc. ECOC'00*, 2000, paper 11.3.4, p. 109.
[5]. Choudhury, S.K., Sharath, M.S., "On line control of machine tool vibration during turning", Journal of Materials Processing Technology, 47: 250-251(1995). (2007)
[6]. Choudhury, S.K., Goudimenko, N.N., Kudinov, V.A., "On-line control of machine tool vibration in turning", International Journal of Machine Tools& Manufacture, 37: 801-811 (1997).
[7]. Thomas, M., Beauchamp, Y., Youssef Y.A., Masounave, J., "Effect of tool vibrations on surface roughness during lathe dry turning process", Computers and Industrial Engineering, 31:637-644. (1996).
[8]. *M. Seeman, G. Ganesan, R. Karthikeyan ve A. Velayudham, 2010. Study on tool wear and surface roughness in machining of particulate aluminum metal matrix composite-response surface methodology approach. The International Journal of Advanced Manufacturing Technology, 48: 613-624.* "PDCA12-70 data sheet," Opto Speed SA, Mezzovico, Switzerland.
[9]. V. Wayal, N. Ambhore, S. Chinchanikar ve V. Bhokse, 2015. Investigation on Cutting Force and Vibration Signals in Turning: Mathematical Modeling Using Response Surface Methodology. Journal of Mechanical Engineering and Automation, 5: 64-68.
[10]. K. Risbood, U. Dixit ve A. Sahasrabudhe,. Prediction of surface roughness and dimensional deviation by measuring cutting forces and vibrations in turning process. Journal of Materials Processing Technology, 132: 203-214.(2003).

ICENS 4TH INTERNATIONAL CONFERENCE ON ENGINEERING AND NATURAL SCIENCE
2-6 May 2018 KIEV UKRAINE

The Dyeing of Wool Fabrics with Barberry Shrub Branches

Huseyin Benli[1], M.Ibrahim Bahtiyari[2], Fazlihan Yilmaz[3]

Abstract

*In this study, barberry shrub branches (Berberis vulgaris) were investigated as natural dye source. Four different metal salts; iron (II) sulfate, copper (II) sulfate, alum and tin (II) chloride, were used to make the dyeing more efficient. All the dyeing applications were carried out for one hour at boiling temperature. The color efficiencies (K/S) and CIE L*a*b* results of the naturally dyed samples were determined and in addition to this, the dyed wool fabrics were tested in terms of fastness properties too. Consequently, it has been seen that satisfactory colors and fastnesses could be obtained by dyeing the wool fabrics with barberry shrub branches.*

Keywords: Natural dyes, Wool fabric, Berberis vulgaris, Textile, Mordanting agent

1. INTRODUCTION

Natural dyes are non-toxic, non-allergic and non-carcinogenic and also these dyes can be obtained from animals or vegetable materials without chemical processes but during the manufacturing of synthetic dyes, many carcinogenic chemicals are used [1]. Application of natural dyes for textiles is increasing due to awareness of environment, ecology, and pollution control [2]. In this research, Barberry shrub branches, as natural colorants, are used in dyeing of wool fabrics. Barberry (*Berberis vulgaris* L., Var. asperma Don., family Berberidaceae) grows in Asia and Europe; It is well known medicinal plants in traditional medicine, the fruits has also been used as food [3]. Berberine is a natural antimicrobial agent and can be used as a colorant known as natural yellow 18 [4]. Berberine is a cationic natural colorant and the chemical structure of berberine chloride has shown in Figure 1[5].

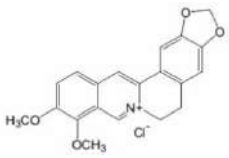

Figure 1. Chemical structure of Berberine chloride [5]

Freile et al. (2003) reported that Berberine displayed a significant antibacterial and antifungal activity against *Staphylococcus aureus* and different *Candida spp*. [6] So, different studies on the usability of this feature (antibacterial and antifungal) of berberine has been investigated in terms of textile applications as well. Haji et al. emphasized that the plasma treated and copper sulfate mordanted nylon 6 fibers showed acceptable antibacterial activity against both gram negative and gram positive bacteria when dyed with an extract from *B. vulgaris*, berberine [7]. In another study, Nylon 66 was successfully treated with berberine, a natural cationic

[1] *Corresponding author: Erciyes University, Mustafa Cikrikcioglu Vocational School, 38039, Kayseri, Turkey.* hbenli@erciyes.edu.tr

[2] *M. Ibrahim Bahtiyari Erciyes University, Department of Textile Engineering, 38039, Kayseri, Turkey.,* ibahtiyari@yahoo.com

[3] *Fazlihan Yilmaz, Erciyes University, Department of Textile Engineering, 38039, Kayseri, Turkey.,* fazyilmaz@hotmail.com

yellow dyes as well as antimicrobial agent and it was observed that berberine treatment provides very strong antimicrobial functions [8].

2. MATERIALS AND METHODS

a. Materials

Wool fabrics were used in this study. Barberry shrub branches (Figure 2) were collected in autumn in Kayseri province and then they were dried. In dyeing processes, these dried form of the plants were used after a grinding process.

Figure 2. The dried branches of barberry shrub plant

b. Methods

In the all experiments, as mordanting agents, 3% (w/w) iron (II) sulfate, copper (II) sulfate, tin (II) chloride or 20% (w/w) alum were used. During the study, simultaneously mordanting method was applied. So the fabric, mordanting agent and the natural dye source (in the same amount with the fabric weight) were all together added to the bath. In the experiments, the dyeing process shown in Figure 3 has been carried out. After dyeing, a cold rinsing, a washing in boiling with soap, a warm washing and then drying at room temperature were done respectively.

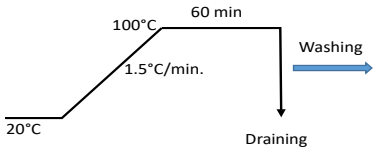

Figure 3. Dyeing diagram for woolen fabrics

After dyeing processes, all the dyed samples were tested in terms of color efficiencies (*K/S*) and color values (CIE *L*a*b**) by using Konica Minolta 3600d spectrophotometer. In addition, the washing fastness with ISO 105-C10 [9], rubbing fastness with ISO 105-X12 [10] and light fastness with ISO 105-B02 [11] were evaluated.

3. RESULTS AND DISCUSSION

The colors obtained from wool fabrics dyed with barberry plants are shown in Table I. As seen from the table with the change of the mordanting agent, the obtained colors have been varied. So after dyeing with barberry shrub branches brown colors by using copper sulfate, gray colors by using iron sulfate, beige colors by using alum, and yellow colors by using tin (II) chloride were obtained.

Moreover the spectral measurements for the dyed samples were managed too. In the CIE *L*a*b** space, L^* indicates lightness; colors with $a^* > 0$ represent redness, and those with $a^* < 0$ greenness; $b^* > 0$ indicates yellowness, and $b^* < 0$ blueness [12]. From the table, it can be easily said that the lightest color was obtained from sample naturally dyed by using tin (II) chloride mordanting agent. In that case, the highest b* value (b*=37.86) was obtained as well and the color was yellow. On the other hand, the darkest color was obtained from the sample dyed by using iron (II) sulfate (L*=47.2) and the lowest redness (a*=1.44) was obtained in this situation. In case of using alum as mordanting agent the color is in light orange/beige shade and the hue angle was 74.27.

The color efficiencies of the samples were analyzed too. It was observed that the highest color efficiency was obtained from the dyeings with copper (II) sulfate and the lowest color efficiencies were observed from the natural dyeing by using alum. The values were 8.55 and 4.27 respectively.

The dyed samples were analyzed in terms of fastnesses as well. For the light fastness, the best result was obtained by using copper sulfate as a mordanting agent; in that case the light fastness was 5. On the other hand, in the use of iron sulfate, alum, tin chloride, the obtained light fastness values were 3, 3, 2 respectively.

Moreover, it was observed that for the all dyed samples, the washing and the rubbing fastnesses were very good.

*Table 1. Scanned photos, color fastness and CIE L*a*b* values of dyed samples.*

Mordant agent	Dyed sample	CIE *L*a*b**	Fastness properties				
			Rubbing		Washing		Light
			Wet	Dry	Sta.	C.C.	
$CuSO_4.5H_2O$		***L**** 51.57 ***a**** 5.07 ***b**** 25.36 ***C**** 25.86 ***h°*** 78.69 ***K/S*** 8.55	5	5	5	5	5
$FeSO_4.7H_2O$		***L**** 47.2 ***a**** 1.44 ***b**** 10.51 ***C**** 10.61 ***h°*** 82.22 ***K/S*** 5.47	5	5	5	5	3
$KAl(SO_4)_2.12H_2O$		***L**** 62.04 ***a**** 7.3 ***b**** 25.93 ***C**** 26.94 ***h°*** 74.27 ***K/S*** 4.27	5	5	5	5	3
$SnCl_2.2H_2O$		***L**** 73.68 ***a**** 5.8 ***b**** 37.86 ***C**** 38.3 ***h°*** 81.29 ***K/S*** 5.34	5	5	5	5	2

Sta.: Staining on cotton; C.C.: Color Change

4. CONCLUSIONS

In this study, it was planned to introduce barberry shrub branches as a natural dye source for the coloration of the wool fabrics. As a result of the study; it was determined that barberry shrub branches could be used in dyeing of wool fabrics and depending on the used mordanting agents different colors and light fastnesses can come across. So it is thought that it can be used in coloration of wool fabrics and can find different opportunities in coloration of different fibers as well. So for the further studies, it is recommended to investigate the usability of this plant in dyeing of synthetic fibers.

ACKNOWLEDGMENT

This work was supported by the Research Fund of Erciyes University. Project Number: FBA-2017-7416.

REFERENCES

[1]. N. Pruthi, G.D. Chawla, and S. Yadav, "Dyeing of silk with barberry bark dye using mordant combination", *Natural Product Radiance*, vol. 7, issue 1, pp. 40-44, January/February 2008.
[2]. A. Davulcu, H. Benli, Y. Sen, M.I. Bahtiyari, "Dyeing of cotton with thyme and pomegranate peel", *Cellulose*, vol.21, pp. 4671-4680, Dec. 2014.
[3]. R. Khosrokhavar, A. Ahmadiani, and F. Shamsa, "Antihistaminic and Anticholinergic Activity of Methanolic Extract of Barberry Fruit (Berberis vulgaris) in the Guinea- Pig Ileum", *Journal of Medical Plants*, vol. 9, no 35, pp. 99-105, 2010.
[4]. K. Ravikumar, S.H. Kim, and Y.A. Son, "Design of experiments for the optimization and statistical analysis of Berberine finishing of polyamide substrates", *Dyes and Pigments*, vol. 75, issue 2, pp. 401-407, 2007.
[5]. T. K. Kim, and Y. A. Son, "Effect of reactive anionic agent on dyeing of cellulosic fibers with a Berberine colorantdpart 2: anionic agent treatment and antimicrobial activity of a Berberine dyeing", *Dyes and Pigments*, vol. 64, issue 1, pp. 85-89, Jan. 2005.
[6]. M.L. Freile, F. Giannini, G. Pucci, A. Sturniolo, L. Rodero, O. Pucci, V. Balzareti, and R.D. Enriz, "Antimicrobial activity of aqueous extracts and of berberine isolated from Berberis heterophylla", *Fitoterapia*, vol. 74, pp. 702–705, Dec. 2003.
[7]. A. Haji, A. M. Shoushtari, and M. Mirafshar, "Natural dyeing and antibacterial activity of atmospheric-plasma-treated nylon 6 fabric", *Coloration Technology*, 130, pp. 37-42, Feb. 2014.
[8]. Y. A. Son, B. S. Kim, K. Ravikumar, and T. K. Kim, "Berberine finishing for developing antimicrobial nylon 66 fibers: % exhaustion, colorimetric analysis, antimicrobial study, and empirical modeling," *Journal of Applied Polymer Science*, vol. 103, issue 2, pp. 1175-1182, Jan. 2007.
[9]. ISO 105-C10:2006 Textiles - Tests for color fastness - Part C10: Color fastness to washing with soap or soap and soda, Test Condition:Test A(1), International Organization for Standardization, Geneva Switzerland, 2006.
[10]. ISO 105-X12:1993 Textiles–tests for color fastness. Part X12: color fastness to rubbing, International Organization for Standardization, Geneva Switzerland, 1993.
[11]. ISO 105-B02:1994 Textiles - Tests for color fastness-Part B02: Color fastness to artificial light: Xenon arc fading lamp test, International Organization for Standardization, Geneva, Switzerland, 1994.

[12]. K. J. Smith, *Colour order systems, colour spaces, colour difference and colour scales*, In: R. McDonald (Ed.), *Colour Physics for Industry*, 2nd ed. Bradford, England: JSDC, pp. 121-208, 1997.

ICENS 4TH INTERNATIONAL CONFERENCE ON ENGINEERING AND NATURAL SCIENCE
2-6 May 2018 KIEV UKRAINE

Determination of Flame Retardant in Vegetable Tanned Leathers by Tri Butyl Phosphate (TBP)

Safiye Meric Acikel[1], Cem Celik[2], Demet Gurbuz[3], Adem Cinarli[3]

Abstract

Tributyl Phosphate (TBP) is classified as organophosphorus compounds and shows a fire retardant effect in different material. In this work, lime splitting cattle leathers was tanned two type vegetable tannings, Mimosa (Group 1) and Tara (Group 2) and then TBP was applied to the non-finished vegetable tanned leathers at different concentrations. (0%, 7%, 14%, 21%) After the flame retardant mixture applied to the vegetable tanned leathers, samples were finished with a standard finishing recipe. Fire retardant effect on TBP treated leathers was determined by LOI test. Also morphological properties of leathers by SEM, molecular binding characterization of leathers by ATR-FTIR Analysis and color properties of leathers by CIE Lab Color Analysis were researched. The results showed that TBP treated vegetable tanned leathers were good flame retardant effect.

Keywords: Leather, Fire, Flame Retardant, Vegetable Tanned, Tributyl Phosphate

1. INTRODUCTION

There are several methods for tanning leather, but not all of them are the right choice for your health or environment. Chrome-tanning is the most popular and controversial, due to its widespread use in the fashion industry. But the use of chromium salts is harmful to the human and environmental health. Vegetable-tanning is the true "chromium-free" method, and does not have harmful chemicals. [1] In this way leather industry latterly have been increased to use vegetable tannins to be healthier than chrome tanned leathers. In vegetable tanning production, various types of vegetable tannins which are known as hydrolysis and condensation molecular structures, gives to the leathers different color tone (brown, red brown, yellow brown, red ,etc.). Thus color and light fastness of the vegetable tanned leather can be affected according to their chemical properties. [2],[3] The production of flame retardant leather is important for some leather types as motorcyclist jackets, flight or automotive upholstery leathers. If these type leathers ignite lately, the retardant property of material will provide gain in time to rescue humans and animals during the fire. [4],[5] Flame retardants can have classified as halogen containing flame retardants and halogen-free flame retardants. Phosphorus based flame retardant chemicals are one of these categories and there are many written work about the effects of flame retardants in literature. Tributyl Phosphate (TBP) is classified as organophosphorus compounds and shows a fire retardant effect in different materials. [6],[7],[8] Vegetable-tanned leathers contains more water ions than other leather types due to the hydroxyl groups present in the molecular structures. For this reason, it is known that Vegetable-tanned leathers burn more later than the other types of leather in the initial stage during fire. [9],[10],[11] In this study, it was aimed to increase the flame retardancy properties of vegetable tanned leathers with TBP. Furthermore, the effects of color fastness of TBP on the vegetable tanned leathers were also investigated.

[1] *Istanbul University, Vocational School of Technical Sciences, Leather Technology Program, Istanbul, Turkey, +90212 473 70 00-18596. e-mail: safiye.acikel@istanbul.edu.tr*

[2] *Istanbul University, Leather Research and Application Center, Istanbul, Turkey, +90212 473 70 00-18596, e-mail: ccelik@istanbul.edu.tr*

[3] *Istanbul University, Faculty of Engineering, Department of Chemistry, 34320, Avcilar, Istanbul, Turkey, +90212 473 70 00, e-mail: adem@istanbul.edu.tr, demet@istanbul.edu.tr*

2. MATERIAL AND METHOD

2..1. Material

Lime Splitting Cattle Leathers were supplied from Tuzla Leather Industrial Area. Tributyl Phosphate- TBP (97%) was obtained from Sigma (St. Louis, USA), 2-Propanol (≥99.5%) was obtained from Sigma (St. Louis, USA). In the finishing recipe; different chemicals were used, Sarpur 317 (Sarchem b.v.) aspolyurethanebinder, Saracryl 588 (Sarchem b.v.) as acrylic binder, Sarfill 8537 (Sarchem b.v.) as filler, Sarkol K Black (Sarchem b.v.) as black Pigment, Sarwaks 8147 (Sarchem b.v.) as wax, Selladerm Black (TFL Company) asanilin dye, Sartop 118 (Sarchem b.v.) as protein binder, Melio EW 348B (Clariant b.v.) as hydrolacque, Melio WF 5226 (Clariant b.v.) as feeling agent.

2.2 Method

Lime Splitting Cattle Leathers were produced as vegetable tanning methods and recipe of leathers was given in Table 1. In tanning process was divided two groups as mimosa Tannins and Tara tannins. Mimosa was the condensed tannin group, having lower light fastness and Tara was the hydrolyzed tannin, having good light fastness property. Vegetable tanned leathers did not make the finishing process before TBP application. Tributyl Phosphate-2-Propanol (TBP-IPA) mixtures were prepared at different concentrations for the flame retardant application. (0%, 7%, 14%, 21%).

Table 1. Recipe of Leather Process

Leather Process	Chemical Additives	T (ºC)	Rate (%)	Time (min)	Remarks
Weight					
Deliming	Water	35	200		
	(NH4)2SO4		0.3	60	pH 8
	Bemanol DLFA		3		
Bating	Bemanol 5BN	35	0,5	40	
Washing	Water	25	300	10	Drain
Pickle	Water	22	80		
	Common salt		8	10	7 ºBé
	HCOOH		1,6	(3X15min)+30	
	Corilene HLG		0,5	30	
	H_2SO_4		0,2	(3x10min)+90 min	pH:2.8
Tanning	Synektan BEH	22	1		
	Mimosa(Group1)		5	30	
	Tara (Group 2)				
	Corilene N-60		0,5	60	
Washing	Water	25	30		Drain, 48 h
					horse up
Bleaching	Water	30	200		
	Funguside	20	0,3	20	
	EDTA		0,3		
	Oxalic Acid		1	60	Drain
Washing	Water	35	200	15	Drain
Neutralization	Water	35	150	15	
	Sodium formate		2		
	Neutraktan D		0,8	90	pH: 5-5.2, Drain
Washing	Water	20	200	15	Drain

Retanning	Water	20	50		
	Synektan BEH		2	15	
	Mimosa (Group 1)		8		
	Tara (Group 2)				
	Corilene N-60		1	90	
Fatliquaring-1	Water	45	100		
	Salem GC		4		
	Corilene N-60		2		
	Corilene F-265		3	60	
	HCOOH		0,4	30	Drain
Washing	Water	45	200	15	Drain
Fatliquaring-2	Water	45	100		
	Salem GC		3		
	Corilene F-265	40	2		
	HCOOH	10	0,2		Drain
Washing	Water	20	200	15	
	EDTA		0,2		Drain

Also 0% group leather samples were only applied IPA solution for the homogenous application. Surface of leather samples were treated with TBP-IPA solutions by Leather Padding Technique which is a kind of finishing technique, made by hand and is used for the intense or decorative pattern finishing applications. All leathers were dried in the room temperature for 24 h and then same application was repeated once again. After the proposed flame retardant mixture applied, samples were finished with a standard finishing recipe. (Table 2.)

Table 2. Finishing Recipe of TBP Applied Leathers0

Chemical	**Rate**	**Finishing Application**
Polyurethane Binder (g)	100	2x Spray
Acrylic Binder (g)	100	Press
Protein Binder (g)	25	(70 atm, 90 ^{o}C,1sn)
Filler (g)	35	1 x Spray
Casein Binder (g)	25	Press
Waks (g)	30	(70 atm, 90 ^{o}C,1sn)
Pigment Dye (g)	80	
Anilin Dye (g)	20	
Water (g)	500	
Hydrolaque (g)	100	1 x Spray
Feeling Agent (g)	10	Press
Water (g)	150	(70 atm, 90^{o}C, 1 sn)

a. Measurements

Limit oxygen index (LOI) tests were performed on a limiting oxygen index chamber with strips of fabrics according to ASTM D 2863-77. [12] pieces leather samples for each group (140 mm x 60 mm) were taken from flame-retardant leather and were used for parallel tests. For SEM analysis the samples were placed on a scanning electron microscope (Fei-Quanta Feg 250) and their images were taken at 100 µm and 20 µm magnifications. FTIR analysis was conducted in order to determine the differences in the chemical properties of leather treated with TBP and control group (0%). FTIR studies were conducted on Bruker-Vertex70 ATR device with ATR equipment. For this purpose, the leather samples were scanned with IR spectrums at a wavelength of 4000-600 cm-1 and the results were evaluated in the FTIR Spectrum Software and compared with the spectrums in the literature. A Konica Minolta CM-508D brand global spectrophotometer with an 8 mm diameter measurement area was used in the measurement of the leather dyes. Measurements were taken from 10 different areas of each leathers according to CIE Lab (1976) and the color differences were determined between treated and untreated leathers in CIE 100 standard observer angle and CIE standard D65 light source. In the components of the CIE Lab color space, L* is the lightness of color, and a* and b* indicate the color. If L* has a negative value, it means that the color of sample has darkened, while if it has a positive value, it means that the sample color has turned lighter. If a* has a negative, it means that the sample color has turned greener, and if it has a positive value, it means that the sample color has turned redder. If b* has a negative value, it means that the sample color has become bluer, and if it is positive, it means that the sample color has turned yellower. ΔL is difference darkness of lightness, Δa is difference redness and greenness and Δb is difference yellowness and blueness between samples and standard samples. [13],[14] ΔE which is total color difference, is calculated below equation. (1)

$$\Delta E = [(\Delta L^*)2+(\Delta a^*)2+(\Delta b^*)2]1/2 \quad (1)$$

3. RESULTS

3.1 LOI Results

Limiting Oxygen Index (LOI) which is probably the most well-known of the standard fire tests and required specification for all type materials, is the per cent concentration of oxygen at a sample. LOI results of Mimosa and Tara Vegetable Tanned Leathers were given in Table 3. According to the results, the LOI values of mimosa-tanned leathers were higher than tara-tanned leathers. While mimosa tanned leathers were increased from %39.2 to 39.4; tara tanned leather were raised from %33.1 to %34.1. %7 and %14 TBP rates did not show flame retardant effect both types of leathers. In addition, LOI values in all groups were higher than other natural polymers or textiles such as wool, cotton, silk because of their high hydrophilic hydroxyl groups in the molecular structure of vegetable tannins. In other words, their burning behavior of leathers have delayed because of the moisture or water. [9]

Table 3. LOI Results of TBP Treated Vegetable Tanned Leathers

Group	LOI (%)
Mimosa	
0%	39.2
7%	39.2
14%	39.2
21%	39.7
Tara	
0%	33.1
7%	33.1
14%	33.1
21%	34.9

3.2 CIE Lab Results

Table 4. shows the results of CIE Lab after TBP was applied to vegetable tanned leathers in different concentration.

Table 4. CIE Lab Results of TBP Treated Vegetable Tanned Leathers

Group	L*(D65)	a*(D65)	b*(D65)	ΔL	Δa	Δb	ΔE
Mimosa							
%0	50.03	23.78	25.78				
%7	52.9	23.84	24.09	2.87	0.06	-1.69	3.33
%14	52.2	23.32	22.7	2.17	-0.46	-3.71	4.32
%21	52.37	22.82	21.79	2.34	-0.96	-3.99	4.72
Tara							
%0	66.39	16.04	52.28				
%7	66.22	15.78	49.15	-0.17	-0.26	-3.13	3.14
%14	65.38	15.25	46.91	-1.01	-0.79	-5.37	5.52
%21	67.78	13.4	46.7	1.39	-2.64	-5.58	6.32

Since the vegetable tannins used in leather production give their own colors to the leathers, there are problems in adjusting the color tone of the leathers during the dying process. For this reason, it is important to bleach the leather or lightness the color to obtain the desired color. [15] From this point of view, ΔL values was increased 2 unit after TBP application to the mimosa tanned vegetable leathers. Δa values, being redness and greenness, was changed from 0.06 to -0.96. It is mean that greenness effect of mimosa tanned vegetable leathers was raised by TBP effect. Δb values, being yellowness and blueness, was observed -2 unit decreasing and the blue color of mimosa tanned vegetable leathers was increased by TBP. When CIE Lab values of tara tanned leathers was examined; it was seen that ΔL values was increased from -0.17 to 1.39. Δa values was changed negative direction by TBP and was decreased from -0.26 to -2.64 in tara tanned vegetable leathers. Similarly Δb values was changed negative direction by TBP and was decreased from -3.13 to -5.58 in tara tanned vegetable leathers. When it is compared both mimosa and tara tanned vegetable leathers; TBP shows lightness effect better result than mimosa tanned leathers. This difference can be related with molecular structure of tannins, being hydrolysis or condense.

3.3 ATR-FTIR Results

ATR-FTIR Results of mimosa and tara tanned vegetable leathers were given in Figure 1. According to results of TBP treated mimosa tanned vegetable leathers, FTIR spectrums shows 3300 cm-1, 2923 cm-1, 2850 cm-1, 1730 cm-1, 1643 cm-1, 1540 cm-1, 1377 cm-1, 1449 cm-1, 1277 cm-1, 1027 cm-1, 838 cm-1, 536 cm-1. The mimosa condensed tannin gave at 1277 cm-1 C-O stretching of flavonoid pyran. Hydroxyl groups appeared in 3284 cm-1 and 1377 cm-1 peaks which are coming from tannin extract and leather molecular structure. [16] The region of 2923 cm-1 is related the CH, CH2, and CH3 stretching vibrations which are occurred because of leather structure or carbohydrates and sugars derivates of tannin. [17],[18] The stretching of the C=C-C aromatic bond appeared in the region of 1643-1449 cm-1 which is based on aromatic structure of vegetable tannins. [18]

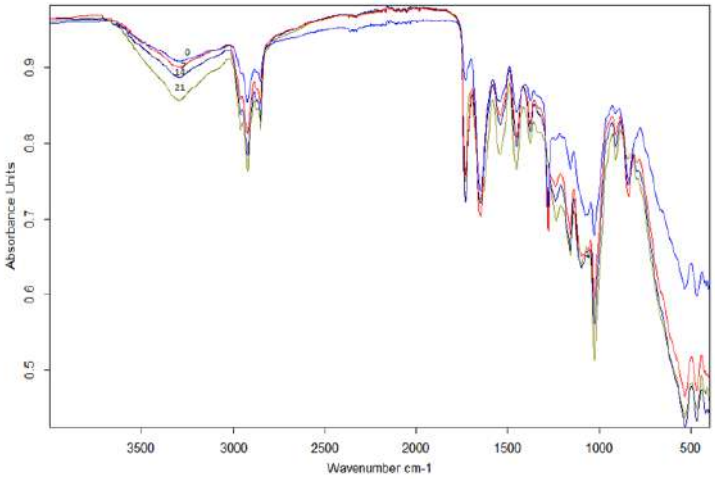

Figure 1. ATR-FTIR Results of Mimosa Tanned Vegetable Leathers

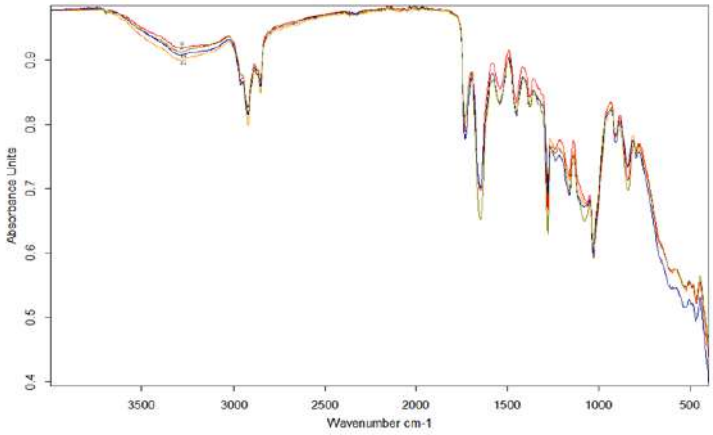

Figure 2. ATR-FTIR Results of Tara Tanned Vegetable Leathers

According to results of TBP treated tara tanned vegetable leathers, FTIR spectrums shows 3284 cm-1, 2917 cm-1,2850 cm-1,1728 cm-1,1650 cm-1, 1540 cm-1 , 1448 cm-1 ,1377 cm-1, 1279 cm-1, 1161 cm-1, 1027 cm-1, 907 cm-1, 841 cm-1. Tara is a hydrolysed tannin which is from gallotannins class and in this way 1728 cm-1 peak showed the C=O stretching of esters of hydrolysable tannins, derivatives of gallic acid. [19] However %21 TBP treated mimosa and tara tanned vegetable leathers gave strong stretch P=O in 1320-1140 cm-1 peaks because of phosphate compounds of TBP. [20]

SEM RESULTS

SEM images 100 µm and 20 µm magnifications of TBP treated mimosa and tara tanned leathers after finishing application is given in Figure 3 and Figure 4. These images show that in 0%, 7% and 14% TBP applied mimosa and tara vegetable tanned leather samples have not observed significantly changing and the deformations on the surfaces of the leathers are similarly same. So TBP showed that it does not cause damage problems in these application rates for the leathers and it can be used easily for vegetable leathers.

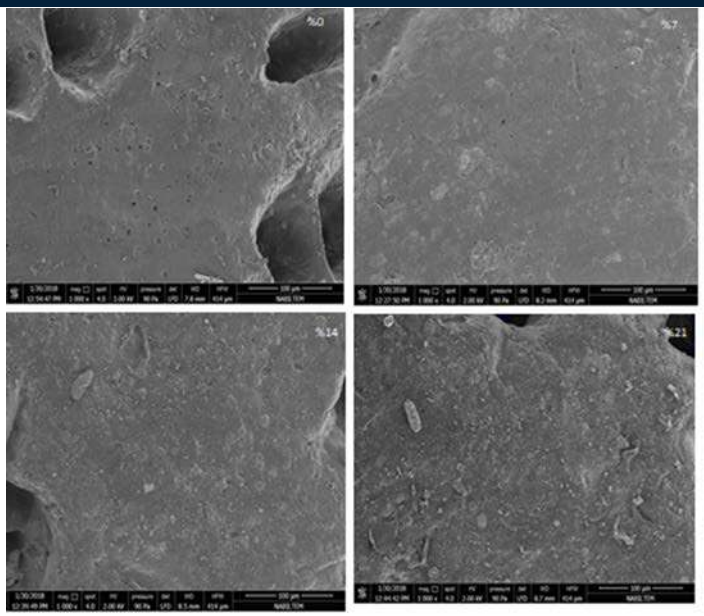

Figure 3. SEM Results of TBP Applied and Mimosa Tanned Vegetable Leathers in 100 µm

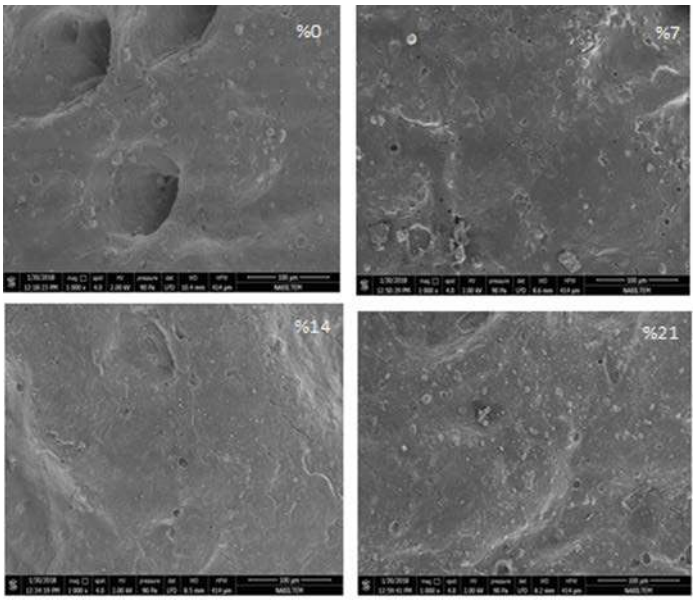

Figure 4. SEM Results of TBP Applied and Tara Tanned Vegetable Leathers in 100 µm

4.CONCLUSIONS

In this work, the color effect and of TBP in surface of mimosa and tara vegetable tanned leathers were studied. After TBP application while mimosa tanned leather was appeared %39.7 LOI result in %21 TBP, tara tanned leathers gave %34.9 LOI value in %21 TBP. In this way; TBP chemical increased the flame retardant property of vegetable leathers. However interesting result was obtained in CIE Lab and ΔL values were increased in the mimosa and tara vegetable leathers by TBP application. In SEM results; TBP applied vegetable leather samples have not observed significantly changing and harmful effect on the surfaces of the leathers were seen similarly same.

ACKNOWLEDGMENT

This study was financially supported by Istanbul University Scientific Research Projects Coordination Unit for Financial Support (Project Number: FYD-2017-24510)

REFERENCES

[1]. A.D. Covington, *Tanning Chemistry: The Science of Leather*, Cambridge, UK, 2009, p.384.
[2]. M. Kite and R. Thomson, *Conservation of Leather and Related Materials*, Butterworth-Heinemann, Elsevier, Oxford, 2006.
[3]. R.L. Sykes, *The Principles of Tanning, in Leather its composition and changes with time*, C. Calnan and B. Haines eds., The Leather Conservation Centre, Northampton, 1991.
[4]. Z. Huang, L. Li, W. Chen, *Influence of retanning on the flammability of leather*, China Leather, 2005, vol:34(3), pp:1-4.
[5]. Z. Huang, L. Li, W. Chen W., *Influence of fatliquoring on the flammability of leather*, Journal of The Society of Leather Technologists and Chemists, 2006, vol:90, pp:155-158.
[6]. S.M. Acikel, C. Celik, A.S. Gultek, A. Aslan, *The Flame Retardant Effect Of Tributyl Phosphate on the Leathers*, International Journal of Scientific and Technology Research, 2017, vol:6(10), pp:44-48.
[7]. E. Schmitt E. *Flame retardants Phosphorus-based flame retardants for thermoplastics*, Plastics Additives and Compounding, 2007, vol:9(3), pp:26–30.
[8]. S. Gaan, G. Sun, K. Hutches, M.H. Engelhard, *Effect of nitrogen additives on flame retardant action of tributyl phosphate: Phosphorusenitrogen synergism*, Polymer Degradation and Stability, 2008, vol:93, pp:99-108.
[9]. A. Bacardit, M.D. Borràs, J. Soler, V. Herrero, J. Jorge, L. Ollé, *Behavior of Leather as a Protective Heat Barrier andvFire Resistant Material*, Journal American Leather Chemists Association, 2010,vol:105, pp:51-61.
[10]. K. Donmez, W.E. Kallenberger, *Flame Resistance of Leather*, Journal- American Leather Chemists Association, 1992, vol: 87, pp:1-19.
[11]. W. Chen, C. Liu, Y. Gong, Z. Huang Z., *Influence of tanning on the flammability of leather*, Journal of The Society of Leather Technologists and Chemists, 2007, vol:91, pp:159-161.
[12]. ASTM D 2863-77, *Standard Test Method for Measuring the Minimum Oxygen Concentration to Support Candle-Like Combustion of Plastics (Oxygen Index)*, 2006.
[13]. D. H. Brainard, in: Shevell S. K. (Ed.), *Color Appearance and Color Difference Specification*, The Science of Color, 2nd ed., OSA and Elsevier, Oxford, 2003.
[14]. M.D. Fairchild, *Color Appearance Models*, 2nd ed., Wiley-IS and T Series in Imaging Science and Technology, Chichester, UK, 2005.
[15]. S.M. Acikel and A. Aslan, *Reduction of Yellowing Effect on Leathers with UV Absorber Benzophenone-4*, Journal of The Society of Leather Technologists and Chemists, 2016, vol:100(1), pp:31-38.
[16]. E. Malea, S.C. Boyatzis, M. Kehagia, *Cleaning of Tanned Leather: Testing with Infra Red Spectroscopy and SEM-EDAX*, Multidisciplinary Conservation: A Holistic View For Historic Interiors. Rome 23-26 March 2010.
[17]. L. Falcão, M.E.M Araújo, *Tannins characterization in historic leathers by complementary analytical techniques ATR-FTIR, UV-Vis and chemical tests*, Journal of Cultural Heritage, 2013, vol:14, pp:499-508.
[18]. F.S. Grasel, M.F. Ferrão, C.F. Wolf, R.A. Ligabue R.A., Characterization of Natural Tanning Extracts by FTIR and Multivariate Analysis", XXXIII IULTCS Congress November, 24-27th2015, Novo Hamburgo/Brazil.
[19]. N.M. Puica, A. Pui, F. Margareta F., *Ftir Spectroscopy for The Analysis of Vegetable Tanned Ancient Leather*, European Journal of Science and Theology, 2006, vol.2(4), pp:49-53
[20]. C. Hampton, D. Demoin D., *Vibrational Spectroscopy Tutorial: Sulfur and Phosphorus*, https://faculty.missouri.edu/~glaserr/8160f10/A03_Silver.pdf, 2010.

ICENS 4TH INTERNATIONAL CONFERENCE ON ENGINEERING AND NATURAL SCIENCE
2-6 May 2018 KIEV UKRAINE

Estimation of Flow Series using Discrete Wavelet Analysis and Artificial Neural Networks

Mehmet Cihan Aydin[1], Zafer Comert[1], Ercan Isik[1], Aydin Buyuksarac[1], Ali Emre Ulu[1]

Abstract:

In this study, considering daily average flow data for 20 years of Kotum stream in Tatvan country of Bitlis in Turkey, a model based on wavelet transform and Artificial Neural Networks (ANN) was proposed to estimate daily average flows of the stream for future. For this purpose, firstly daily average flows of the stream between 1997 and 2016 were provided from the flow measurement sta-tions of State Hydraulic Works (SHW). Then, a preprocess procedure was de-fined to estimate the lost points in the data set and to determine outliers. Discrete wavelet transform was applied to the data in order to diminish outliers and to produce more general results. In this context, Daubechies (db), Symlets (sym) and Coiflets (coif) main wavelet families were considered. ANN model consist-ing of one entry, three hidden and one output layers was trained using the daily average flows between 1997 and 2015 and seasonal notations. The data of 2016 were also used to test general performance and reliability of the model. Conse-quently, the all wavelet families and ANN combinations gave satisfactory results and the best model is coif wavelet family with $R^2 = 0.78$.

Keywords: Flow Series, Discrete Wavelet Transform, Artificial Neural Networks (ANN)

1. INTRODUCTION

Wavelet transform is one of the remarkable signal processing methods of recent periods. As an alternative to Fourier transformations, it is generally possible to use a wide range of applications such as astronomy, acoustics, data compression, signal and image processing applications, earthquake analysis, and nuclear energy because of their superior properties, such as empathizing temporal and spectral local knowledge, the ability of use for nonlinear signals and quality of multi-scale analysis [1]. In the last few years, it is clear that the wavelet transform method has been increasingly used for different purposes in the field of hydrology [2]. When the literature is examined, it has been observed that wavelet transform is used for the specific purposes such hydrologic regionalization [3], dam construction and management of hydrological effects on river systems [4], daily water level estimation [5], precipitation flow modeling [6] and hydrological regime change detection [7]. Moreover, despite its rather complex and random nature, a number of models based on wavelet transform and artificial intelligence, especially artificial neural networks (YSA) methods, are both seen as remarkable and highly promising in order to accurately and reliably plan and manage the use of water resources. [8].

In this study, a model which can estimate the flow for the coming years considering the 20-year average daily flow data and seasonal information of Kotum Deresi located in the Bitlis province of Tatvan is proposed. The model is based on discrete wavelet transform and ANN techniques. Model results gave reasonably consistent results with measured data.

[1] *Bitlis Eren University, Department of Civil Engineering ,* mcaydin@beu.edu.tr

2. MATERIALS AND METHODS

2.1. DATA SET

Daily mean flow values (m^3/s) for the Kotum Area were collected from the relevant institution for the time period between 1997 and 2016 and the data were obtained from this institution. Flow data used in the study were obtained from the State Hydraulic Works (SHW) 's current monitoring stations (CMS).

When the data set was examined, it was determined that only one data for per day was stored, and that 7305 data in total were stored with day, month and year data and that also there was a loss data of 52 days. In Figure 1, a graph of the daily average flows of Kotum Creek is plotted for the years 1997 - 2016. In addition, missing and anomalous values are emphasized on the drawing. Table 1 shows descriptive statistics including 20-year daily average flow data and standard deviation.

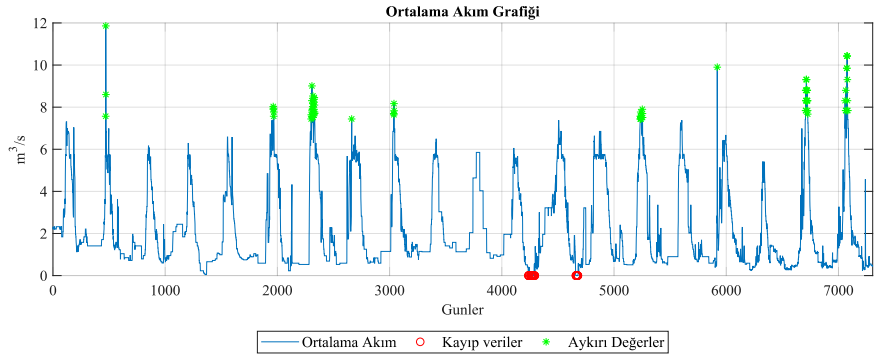

Figure 1. Average Flow Graph of Kotum Creek Between 1997 and 2016

Table 1. Monthly Average Flow Rate and Standard Deviation Values Between 1997 And 2016

Month	Average	Standard Deviation
January	1,1339	0.7575
February	1,2604	0.7979
March	2,0411	1.4169
April	4,6445	1.6434
May	5,8516	1.3365
June	4,0309	1.5408
July	2,2318	1.1025
August	1,0925	0.4652
September	0,8185	0.3799
October	0,9779	0.6110
November	0,9067	0.4096
December	0,9793	0.6162

2.2. PREPROCESSING

In the first step of the preprocessing, the missing values are detected and interpolated. The average daily flow values of the creek are defined as follows:

$$X = \{x_n, n = 1,2, \dots, N\} \; ve \; N = 7305 \tag{1}$$

Accordingly, the missing data are determined as follows.

$$\exists x_i \in X, x_i = 0 \tag{2}$$

The distribution of missing data according to the expression given in Eq. (2) is shown in Table 2.

Table 2. Distribution of Missing Data

Start Index	End Index	Days
4237	4242	6
4256	4270	15
4278	4286	9
4292	4294	3
4660	4678	19

Accordingly, a total of 52 days of data loss is recorded for August, September, October of 2008 and October of 2009. The missing data are calculated as shown in (3), taking the average of the data of the day and the month in the past years.

$$\tilde{x}_i = \frac{\sum_{n=1}^{N-1} \dot{x}_n}{N-1}, i = 1,2, \dots, 52 \; ve \; \dot{x}_n \neq 0 \tag{3}$$

Where $\tilde{x}_i$ represents the missing data with the *i*'s lost index value. And $\dot{x}_n$ represents the mean current data from the corresponding day and month outside the year in which the missing data belongs. Since 20 years of data exist, then N is 20. Since the data for the relevant year are missing, from $N-1$, the average of the corresponding days of the 19-year-old data was considered as the new value of the lost value.

In the last step of the preprocessing phase, it is ensured that anomalous values are detected. In this context, values that meet the conditions specified in (4) are considered anomalous. In Figure 1, anomalous values are highlighted with a green * value.

$$\exists x_i \in X, x_i > \left(\frac{\sum_i^n x_n}{N} + 2\sqrt{\frac{1}{N-1}\sum_{i=1}^{N}\left(x_i - \frac{\sum_i^n x_n}{N}\right)^2} + \bar{x} \right) \tag{4}$$

In the experimental study, the anomalous were accepted as the mean of the series that twice the standard deviation, and the median of the values greater than the sum of ($\bar{x}$).

2.3. DISCRETE WAVELET TRANSFORM

Signals are often shown as a function of time, and the information about the sign can also be expressed in the frequency domain. With Fourier transform, a signal can be transformed into frequency domain in the time domain and analyzed in the frequency spectrum. However, Fourier does not recognize at what time value which frequency component is existing. Naturally, although this is an advantage for time-invariant signals, the same situation cannot be the case for non-stationary signals. The time-frequency resolution of non-stationary signals can be obtained optimally with wavelet transform [9]. In other words, transformations at constant intervals (windowed) in the Fourier transform, in wavelet transform, at wide frequency interval, while in high frequencies the process is performed at small time intervals [10]. Accordingly, the wavelet transform is defined as described in (5).

$$X(\tau, a) = \frac{1}{\sqrt{|a|}} \int_{-\infty}^{\infty} x(t) \psi^* \left(\frac{t-\tau}{a} \right) dt \tag{5}$$

Where $\frac{1}{\sqrt{|a|}}\psi(\frac{t-\tau}{a})$ is a wavelet function, ψ is a complex conjugate of wavelet function, τ is a time shift parameter, and a is a scale value. In this study, the main wavelet families of Daubechies (db3), Symlets (sym3) and Coiflets (Coif3) have been taken into account, including many different wavelet functions. Figure 2 shows the main wavelets used in the experimental work.

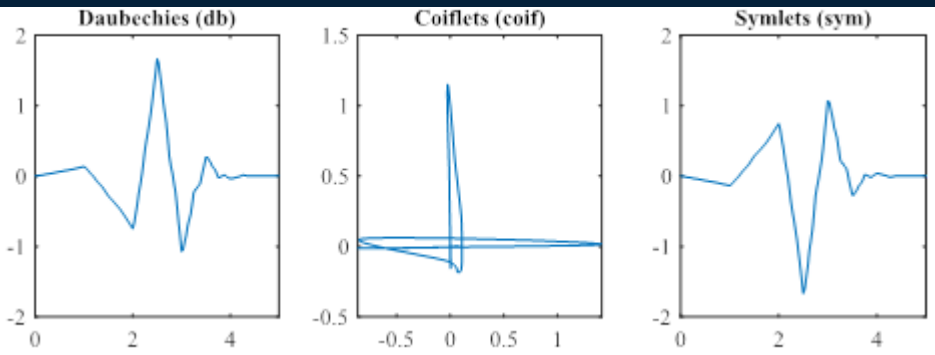

Figure 2. Main Wavelet Families

In the experimental study, discrete wavelet transform was used to eliminate outliers in the mean current values and to access a model that produces more general results. The time series of discrete wavelet transform and daily average flow rate are decomposed into convergence and detail components using a series of filters showing a similar structure to the tree structure as shown in Figure 3 [11]. Figure 3 shows the time series of x[n] discrete values, while h[n] and g[n] show high pass and low pass filters, respectively. In the experimental study, the level of separation was set at 3. Hence, a more suitable time series for modeling was obtained by choosing the convergence component (A3) and only the D3 detail components.

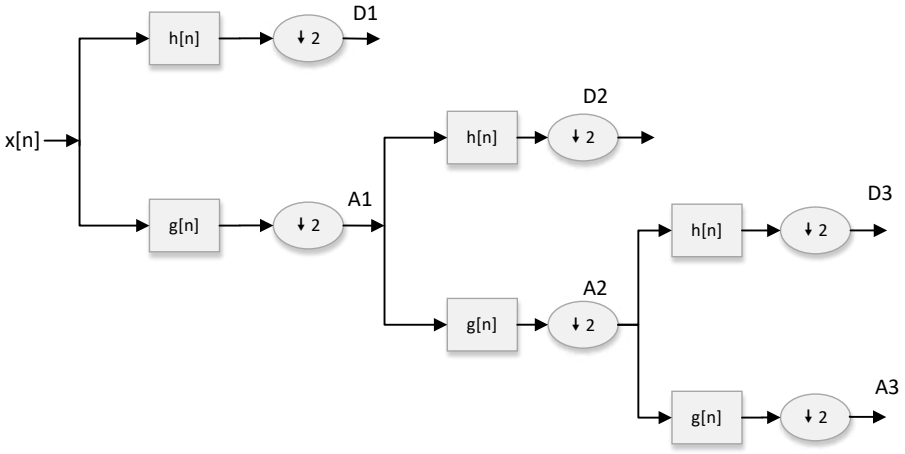

Figure 3. Subband Separation with Discrete Wavelet Transform

2.4. ARTIFICIAL NEURAL NETWORKS

Artificial neural networks (ANN) are a computational and highly flexible mathematical model that is inspired by the generalization and learning ability of the human brain [12, 13]. ANNs are a model that usually consisting of an input layer, a hidden layer (s) composed of one or more layers, and an output layer [14]. An input layer is a layer that accepts as input a set of properties that contain the characteristics of a data set that can be considered wide or large, such as a time series or an image, and has dimensions that are smaller than the whole of the data. The hidden layer is often referred to as the black box for ANN, and is a layer of elements, often referred to as a large number of neurons, to capture nonlinear construction on the data. The last layer is expressed as the output layer and usually produces a numerical value, which leads to the prediction or classification of the model [15]. Equation (6) contains the mathematical model that gives the output value of a layer of ANN.

$$o^i = \sigma\left(\sum_{j=1}^{N} w_{ij} x_j + b^i\right) \tag{6}$$

In equation (6), o^i represents the *i* th layer output, σ activation function, N is the number of nodes in the hidden layer, w_{ij} is the weight expressing the learning of the network, x_j entries and b^i are the deviation values for the *i* th layer.

3. FINDINGS

In this study, a prediction model based on discrete wavelet transform and artificial neural networks has been proposed in order to estimate the daily precipitation amount for the coming years, taking into account the 20-year average daily precipitation amount of Kotum Creek in the province of Tatvan in Bitlis province as shown in Figure 4.

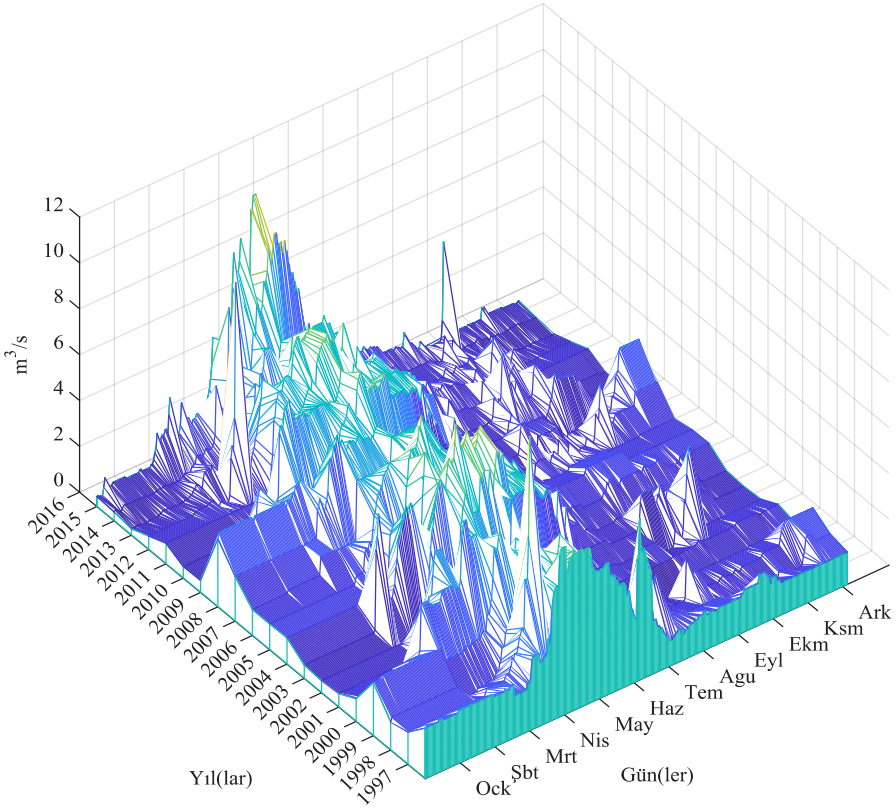

Figure 4. Bitlis Kotum Creek 20-Year Average Precipitation Discharge

For the time series expressing 20-year average precipitation, firstly interpolation of missing data is provided. For this purpose, the average of the 19-year-old data was used by using the day-month information that the lost data belonged to. Taking the time series into consideration, the next step in preparing the model for training is to eliminate the anomalous from the mark. For this purpose, discrete wavelet transform is used. With the aid of discrete wavelet transform, the time series is divided into convergence and detail components. For this purpose, it is provided to use the db3, sym3 and coif3 main wavelet families at level 3 as a result of experimental studies. At the third level decomposition, a convergence component (A3, high scaling-low frequency) and 3 detail components (D1, D2, D3, small scaling-high frequency) were obtained. Only the A3 and D3 components are used for the new marker and the D1 and D2 components are isolated from the marker to eliminate the anomalous. In Figure 5, the daily average flow series obtained using 3 different wavelet families are plotted together with the original time series. After this step, the data are ready for network training.

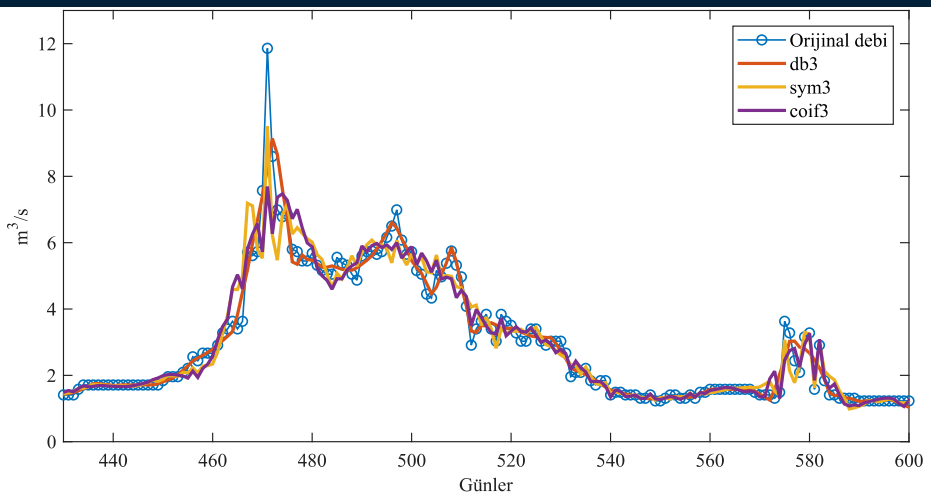

Figure 5. Average Daily Flow Series Obtained Using Different Wavelet Families

In order to realize network training, data between 1997 and 2015 were used. In order to train the network, daily, monthly and yearly information was taken into consideration along with the daily average flow rate. Three hidden layers were used to ensure that nonlinear outputs in the time series can be estimated. The number of nodes in hidden layers is set to 100, 75 and 50 respectively. For network training, "Conjugate Gradient Backpropagation with Fletcher-Reeves Restarts" training algorithm and mean square error (MSE) function are used. In conclusion, the results obtained by considering 3 wavelet families and raw data are given in Table 3. Here, R represents the regression value, and approaching 1 means that the predicted value is better.

Table 3. Applied Models and Obtained Regression Values

No	Models	Regresyon (R)
1	Raw data + YSA	0.87352
2	db3 + YSA	0.88314
3	sym3 + YSA	0.87154
4	coif3 + YSA	0.88593

According to Table 3, the best prediction results were achieved using the coif3 wavelet family. Then, the best results were obtained respectively using db3, raw data and sym3 wavelet families.

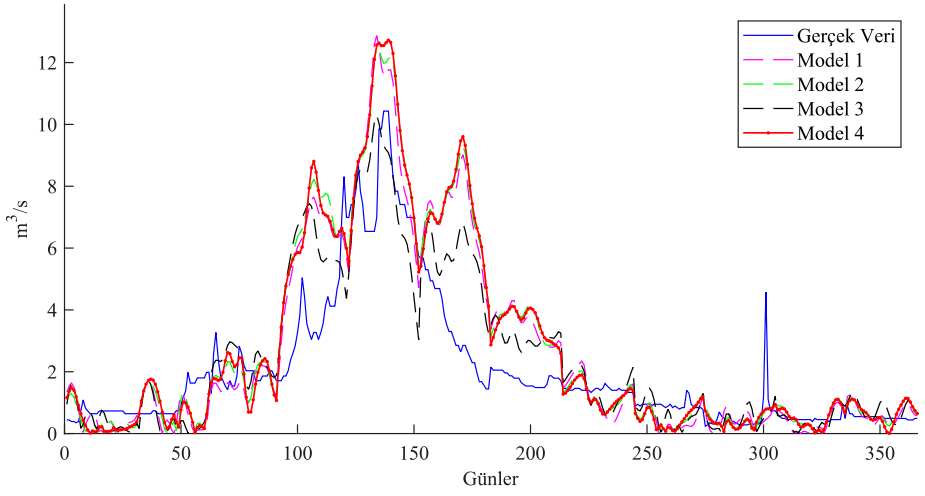

Figure 6. Model Predictions for 2016

The daily average flow values for the year 2016 are used to test the reliability of the models. Accordingly, the results produced by the four related models are illustrated in Figure 6.

4. RESULTS

In this study, a prediction model based on the discrete wavelet transform and ANN methods is proposed based on the 20-year daily average flow data of the Kotum creek located in Tatvan province, of Bitlis. In this context, a time series is obtained from the daily average flow values of the creek in the first step. In the next step, the missing values in the time series are detected and interpolated. In order to provide a model that produces more general results, anomalous in the time series have been determined and it has been aimed to reduce the effect of these values with discrete wavelet transform. For this purpose, db, sym and coif wavelet families are considered. In the experimental study, four different models were evaluated and the best results were achieved using a combination of the coif3 wavelet family and a combination of ANN (R = 0.88593).

REFERENCES

[1] Lee, D.T.L., Yamamoto, A.: Wavelet analysis: theory and applications. Hewlett Packard J. 45, 44 (1994).
[2] Nourani, V., Baghanam, A.H., Adamowski, J., Kisi, O.: Applications of hybrid wavelet–Artificial Intelligence models in hydrology: A review. J. Hydrol. 514, 358–377 (2014).
[3] Santos, C.A., Ideiao, S.M.A.: Application of the wavelet transform for analysis of precipitation and runoff time series. Predict. Ungauged Basins Promise Prog. 431 (2006).
[4] White, M.A., Schmidt, J.C., Topping, D.J.: Application of wavelet analysis for monitoring the hydrologic effects of dam operation: Glen Canyon Dam and the Colorado River at Lees Ferry, Arizona. River Res. Appl. 21, 551–565 (2005).
[5] Seo, Y., Kim, S., Kisi, O., Singh, V.P.: Daily water level forecasting using wavelet decomposition and artificial intelligence techniques. J. Hydrol. 520, 224–243 (2015).
[6] Shoaib, M., Shamseldin, A.Y., Melville, B.W.: Comparative study of different wavelet based neural network models for rainfall–runoff modeling. J. Hydrol. 515, 47–58 (2014).
[7] Labat, D., Ronchail, J., Callede, J., Guyot, J.L., De Oliveira, E., Guimaraes, W.: Wavelet analysis of Amazon hydrological regime variability. Geophys. Res. Lett. 31, (2004).
[8] Sović, A., Potočki, K., Seršić, D., Kuspilić, N.: Wavelet analysis of hydrological signals on an example of the River Sava. In: MIPRO, 2012 Proceedings of the 35th International Convention. pp. 1042–1047 (2012).
[9] Wickerhauser, M.V.: Adapted wavelet analysis from theory to software. IEEE press (1994).
[10] Heil, C.E., Walnut, D.F.: Continuous and discrete wavelet transforms. SIAM Rev. 31, 628–666 (1989).
[11] Fowler, J.E.: The redundant discrete wavelet transform and additive noise. IEEE Signal Process. Lett. 12, 629–632 (2005).
[12] Hu, Y.H., Hwang, J.-N.: Handbook of neural network signal processing. CRC press (2001).
[13] Jain, A.K., Mao, J.: Artificial Neural Network: A Tutorial. Communications. 29, 31–44 (1996).
[14] Hagan, M.T., Demuth, H.B., Beale, M.H., Jesús, O. De: Neural network design. Martin Hagan (2014).
[15] Dennis Jr, J.E., Schnabel, R.B.: Numerical methods for unconstrained optimization and nonlinear equations. SIAM (1996).

ICENS 4TH INTERNATIONAL CONFERENCE ON ENGINEERING AND NATURAL SCIENCE
2-6 May 2018 KIEV UKRAINE

Design of PID Controlled-Automatic Voltage Regulator System Based on a New Neighborhood Strategy of Simulated Annealing

Emre Celik[1], Nihat Ozturk[1], Gungor Bal[1]

Abstract

In an electric power station, automatic voltage regulator (AVR) should have good dynamic response to ensure a constant voltage for healthy operation of equipment connected with this power station. Besides, it is a system that significantly influences the power quality, grid security and grid reliability as well. Since it is, therefore, great interest to enhance the performance of an AVR system, we are motivated to deploy a new genetic algorithm-based simulated annealing (GASA) algorithm in the hope of exploring better gains of PID controller installed in an AVR. To highlight the superiority of our proposal, comparisons are made with a number of studies published in esteemed journals for the identical AVR system using transient response analysis, root locus analysis and bode analysis. Comparative analysis results demonstrate that GASA-tuned PID controller exhibits a better voltage response profile than its competitors in a sense that the system output settles to the given step reference with less settling time and very mild overshoot. Such response renders it possible to control the studied system with better stability margin.

Keywords: *automatic voltage regulator, PID controller, multi-objective optimization, simulated annealing, genetic algorithm, neighborhood, transient response analysis*

1. INTRODUCTION

As its name emphasizes, an automatic voltage regulator (AVR) is a device that is mainly used for automatically maintaining the terminal voltages of large synchronous generators at a specified voltage level in electric power grids [1]. Therefore, it holds an important role in attenuating the system voltage variation under abnormal conditions such as load fluctuation and faulty conditions which corresponds to power quality, grid security and grid reliability, being one of the main control problems for an electric power system [2]. On the other hand, ensuring the constancy of the nominal voltage level in a power station is important with regard to the performance and life span of the equipments connected to this power station since they are designed to work efficiently for a particular voltage level. Moreover, as reactive power flow is significantly affected by the bus voltages, AVR system makes it possible to suppress real line losses of transmission lines in consequence of reactive currents by controlling the system voltage level.

An uncontrolled AVR is exposed to severe transient regime presenting high oscillations and a non-negligible deviation in steady-state which are not permissible at all. In order to avoid such unwanted regimes and improve the behavior of AVR system, a suitable controller is required with its parameters tuned appropriately. Even though various control theories have been suggested in academia during the past decades, most of them usually are not suitable for the control system community because they are complex structure hard to be understood in nature and many tuning parameters sensitive to controlled plant dynamics which are rarely known. We do observe the widely popular acceptance of proportional integral (PI)- and proportional integral derivative (PID)-type controller in the industries [3, 4]. The reason of this acceptability can be attributed to its simple structure, easy implementation effort, and robust performance over a wide range of operating scenarios [5, 6]. Nonetheless, it has been fairly difficult to tune the PID controller gains suitably owing to the fact that many real world industrial plants often face problems such as time delays, high order and saturation phenomena. For these reasons, it is

[1] *Corresponding author: Gazi University, Department of Electrical Electronics Engineering, 06500, Teknikokullar/Ankara, Turkey. emrecelik@gazi.edu.tr*

encouraged to boost the capabilities of PID controllers by incorporating new features to make them cope with the above complicated situations.

When the literature is investigated, it is seen that many artificial intelligence-based optimization algorithms have been recently given much interest by the researchers in the hope of achieving high efficient PID controlled-AVR system by searching the optimal controller parameters while keeping the controller's basic characteristics. In 2009, artificial bee colony (ABC) algorithm is suggested in [2] for a self-tuning PID controller for the AVR system and its application results are compared with those based on particle swarm optimization (PSO) and differential evolution (DE) algorithm through different kinds of analysis techniques. It is shown that the ABC has a better tuning capability than the other approaches and thereby it leads to an increase in system performance. In order to improve the system performance further, an application of biogeography-based optimization (BBO) algorithm is made in [7], and the results are compared with those reported in [2]. The results of this comparison demonstrate that BBO outperforms its opponents in achieving more optimal PID parameters for the identical AVR system. Researches in the concerned field are still in progress for offering new powerful algorithms in solving the tuning problem of PID parameters in a more efficient sense. For instance, in 2016, a PID controller equipped with a first-order low pass filter in the derivative path is considered in [3] and its gains as well as the low-pass filter parameters are optimized using teaching-learning based optimization (TLBO) algorithm. According to the findings, good results are achieved in comparison with other indicated studies as far as time-domain specifications of the response are concerned. However, to the knowledge of this paper's authors, the proposed AVR system does not have a desirable stability margin. In 2018, a first attempt of applying stochastic fractal search (SFS) algorithm to the efficient design of an AVR system is performed in [1]. Using integral of time-weighted-squared-error (ITSE) formula as objective function, the controller gains are optimized and their performance are widely illustrated with the state-of-the-art techniques where the same objective function is used. At the end of the study, the AVR system tuned by SFS is found to exhibit better dynamic response profile than the existing techniques. Since the minimum value of ITSE is achieved, it is claimed in the study that the designed controller gains are made far closer to the optimal ones. However, minimizing the value of ITSE leads to improvement in the time response characteristics at the cost of possible deterioration in the frequency-domain performance of the system response. Chaotic PSO (CPSO) and global neighborhood algorithm (GNA) are applied to tuning problem of PID gains for an AVR system in [8, 9], where a comparison with standard PSO is also presented. The results based on transient response analysis show that CPSO and GNA perform better than the original PSO. A disadvantage of these studies is that they fail to establish a proper validation course for their proposals because there is no other published study used in the paper for comparison.

Simulated annealing (SA) is one of the most attractive meta-heuristic methods formally introduced by Kirkpatrick, Gelatt and Vecchi for solving combinatorial optimization problems [10]. Since then, it has been widely employed in various optimization problems. The algorithm is based upon the annealing process and iteratively applies random perturbations to the evaluation point of the objective function. In the algorithm, good solutions are accepted immediately when detected, while there is even a chance for bad solutions to be accepted depending upon the probability obtained from the Boltzman distribution [11]. The search performance of SA is significantly affected by some factors such as solution representation, neighborhood search strategy and temperature schedule [12]. Genetic algorithm (GA) is a stochastic global adaptive search optimization technique based on the mechanisms of natural selection and survival of the fittest [13]. In recent years, GA has been recognized as an effective and efficient search technique to exhibit good results in many practical problems using three essential operators: natural selection, crossover and mutation [14]. The inspiration for incorporation of GA in the neighborhood search of the SA algorithm in the hope of increasing the SA search performance has been first arose and addressed in [15]. The proposed algorithm, termed as GASA, is a hybrid algorithm based on our preliminary efforts, and its superior performance over the GA and standard SA has been validated for some benchmark functions in the given study. However, its validation from the tuning aspect of PID parameters in an AVR control application is not yet checked nor demonstrated. As a result, it is of interest and necessity to establish such validation with an aim to achieve an efficient AVR system design.

In this work, a design method which optimizes the gains of a PID controller built in a practical AVR system is suggested via the GASA algorithm. At the end of the optimization, obtained controller parameters are compared with the ones offered by the reported algorithms i.e. ABC [2], TLBO [3], and BBO [7] for the identical AVR system. For the sake of performance evaluation amongst the controllers, an investigation of the system behavior during transient-state is first realized using transient response analysis. In order to further demonstrate the effectiveness of our proposal from the stability point of view, root locus analysis and bode analysis are subsequently performed. The simulation results reveal that the presented GASA algorithm is promising and encouraging optimization tool in finding better controller parameters in the presence of AVR system because it results in better performance for the concerned control application in terms of peak overshoot, settling time and stability margin in comparison with other state-of-the-art benchmark techniques.

2. ELEMENTS OF A PID-CONTROLLED AVR SYSTEM

a. PID Controller

In spite of significant and undiminishing advances emerged in the field of control theory, the PID controller maintains its dominant position as the most acceptable feedback controller being successfully used for over 50 years in a variety range of industrial plants [3]. It has easily understandable structure and provides robust control performance regardless of uncertainties in model parameter variation and external disturbances. In addition, PID controller requires the tuning of only three parameters, thereby enabling people have relatively less degree of freedom to design PID controller. In Laplace mode, the transfer function of a PID controller is expressed by the following *s*-domain equation.

$$TF_{PID}(s) = K_P + \frac{K_I}{s} + sK_D \quad (1)$$

The three parameters of this controller in Eq. 1 are proportional gain (K_P), integral gain (K_I), and derivative gain (K_D). In order to have a PID controller with satisfactory and robust control performance against a wide range of operating conditions, its design parameters are needed to be tuned appropriately. Conventionally, such tuning process is done by trial and error method depending upon the operator prior experience and plant's behavior.

b. Mathematical Model of an AVR System

An AVR is a system that regulates the terminal voltage of a synchronous generator at a nominal constant voltage level by controlling the machine excitation current. In addition to its inherent cost advantage, excitation control of a synchronous alternator is one of the most significant factors to enhance power system stability and security as well as the quality of produced electrical power [16]. Sensor, amplifier, exciter and generator are the main components necessary in an AVR model in Fig. 1(a). By representing each component with a gain K and major time constant τ in a linearized manner, the complete transfer function block diagram of the AVR system can be given as in Fig. 1(b). Note that the transfer function of the AVR system is derived on the basis of the ratio of the incremental change in terminal voltage $\Delta V_t(s)$ to that in reference voltage input $\Delta V_{ref}(s)$ [2].

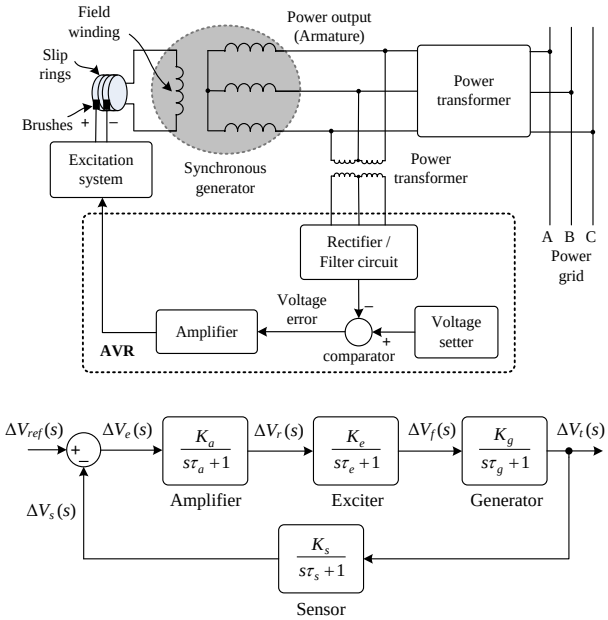

Figure 1. (a) AVR model (b) Complete transfer function block diagram of the AVR system

The typical limits of the parameters used in these transfer functions as well as their chosen values in this paper are tabulated in Table 1. The chosen parameter values are equal to those in [2, 3, 7] which are considered for comparison purposes.

Table 4. Typical limits and chosen values of the parameters used in the AVR system

Component	Parameter limits	Chosen parameter values
Amplifier	$10 \leq K_a \leq 40, \quad 0.02 \leq T_a \leq 0.1$	$K_a = 10, \quad T_a = 0.1$
Exciter	$1 \leq K_e \leq 10, \quad 0.4 \leq T_e \leq 1.0$	$K_e = 1, \quad T_e = 0.4$
Generator	$0.7 \leq K_g \leq 1.0, \quad 1.0 \leq T_g \leq 2.0$	$K_g = 1, \quad T_g = 1$
Sensor	$0.001 \leq T_s \leq 0.06$	$K_s = 1, \quad T_s = 0.01$

Thus, using the above parameters, the transfer function of the entire AVR system can be represented as,

$$\frac{\Delta V_t(s)}{\Delta V_{ref}(s)} = \frac{TF_{Amplifier}(s) \cdot TF_{exciter}(s) \cdot TF_{Generator}(s)}{1 + TF_{Amplifier}(s) \cdot TF_{exciter}(s) \cdot TF_{Generator}(s) \cdot TF_{Sensor}(s)} = \frac{0.1s+10}{0.0004s^4 + 0.0454s^3 + 0.555s^2 + 1.51s + 11} \quad (2)$$

Thanks to Eq. 2, it is now possible to obtain the unit step response of the studied uncontrolled AVR system as shown in Fig. 2.

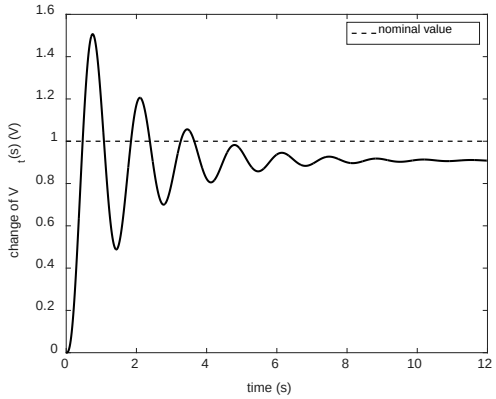

Figure 2. Unit step response of the studied AVR system without controller

From Fig. 2, it is clear that the uncontrolled system is stable, but exhibits high oscillatory behavior during transient-state and a remarkable deviation from the nominal value of 1 p.u at stead-state. In an electrical power system where operating voltages are in the range of kV, this kind of response is unacceptable and not allowed at all. As a result, a suitable controller must be installed in the closed-loop AVR system in order to improve the system performance at both transient-state and steady-state. Due to offering the aforesaid important characteristics, standard PID controller has been implemented in the studied AVR system with its parameters optimized using the GASA algorithm.

3. IMPLEMENTATION OF GASA-BASED PID CONTROLLER

Inspired from the powerful search performance of GA and keeping in mind the dependency of SA algorithm upon its neighborhood search, an idea of combining two algorithms in a proper way has been arose to enhance the search performance of the basic SA algorithm. In SA, there are many ways for generating trial solutions in a neighborhood of the current solution and conventionally the neighboring solution is generated randomly. This type of random search not based on a systematic approach for the next candidate generation mechanism is more likely to fail to find out the optimal or near-optimal solution in a reasonable time. Therefore, rather than totally randomized search for neighbor solutions, a systematic way that makes progress in increasing trial solution qualities while with good computational cost is required.

The presented GASA algorithm differs from the original SA algorithm only with regard to the neighboring solution generation strategy [15]. After a number of solutions are generated randomly around the best solution found so far, a crossover operation is performed in order between the best solution and those generated randomly previously. Then, mutation is invoked in GASA algorithm. The reason behind the crossover operation is to increase the chance of obtaining better solutions than the best solution, which is associated with the exploitation property of the algorithm. As for mutation, it is applied after invoking crossover in order to introduce random modifications in the hope of preventing being mired in local optima. Meanwhile, after new individuals are generated using crossover, the fitness of each is computed to attain the best point among all points. This best

solution is then taken as *elite* individual in order not to mutate it in the mutation phase for possible deterioration in solution quality. The following block diagram outlines the above explanation.

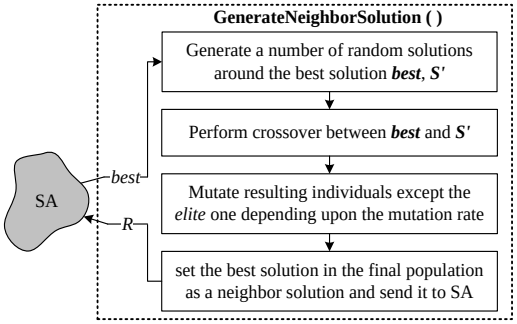

Figure 3. Block diagram of neighboring generation algorithm in GASA

As shown in Fig. 3, the best solution found at the end of the neighboring generation algorithm is sent to SA algorithm to be evaluated for the next iteration. In the present work, the use of GASA algorithm is devoted to solve the efficient design problem of a PID controller operating in an AVR system.

As we have three controller parameters K_P, K_I and K_D which have to be optimized, each set of controller parameters is made to compose an individual in the GASA algorithm by a vector $K = [K_P, K_I, K_D]$, which can also be called a GASA-PID controller. At the start of the GASA algorithm, a number of individuals are initiated at random with $K_{P,I,D}$ assigned as real numbers. Then, these individuals are fed into the AVR system model to obtain the voltage change curves by simulating the system for a certain time long enough for the responses to settle. In order to acquire a quantitative measure regarding how well each individual performs, the following cost function is defined and used in this article, which involves some time response performance parameters. Better control performance corresponds to these parameters when they are minimum following a step input perturbation.

$$J = (1 - \alpha - \beta) \int_0^{t_{sim}} t|e(t)|dt + \alpha M_P + \beta T_s \tag{3}$$

The first term on the right side of Eq. (3) is integral time of absolute error (ITAE) index based on simulation time t_{sim}, M_P and T_s are peak overshoot and settling time obtained from the transient response. Setting the value of α to 0.53 and β to 0.05 in the present work offers a good response complying with the designer requirements for a very mild overshoot and small settling time. In the study, the concerned AVR design problem has been tried to be solved by formulating it as a constrained optimization problem subject to the following constraints of PID controller gains bounds:

Minimize J
Subject to:

$$\left.\begin{aligned} K_P^{min} \le K_P^* \le K_P^{max} \\ K_I^{min} \le K_I^* \le K_I^{max} \\ K_D^{min} \le K_D^* \le K_D^{max} \end{aligned}\right\} \tag{4}$$

where the superscripts min and max stand for the minimum and maximum bounds of the respective controller parameter. In the study, in order to render a fair comparison with the indicated recent techniques in literature, all the gains are similarly assumed in the range [0.2, 2.0]. As a result, we conclude that the set of controller parameters K_P^*, K_I^* and K_D^*, which results in cost function minimization at the end of the GASA-based optimization process, is considered as optimal or near-optimal expected to yield desired level of system response.

4. SIMULATION RESULTS

In this section, three different analysis techniques are considered in order to explore the effectiveness and superiority of proposed GASA-tuned PID controller compared with those tuned by ABC [2], TLBO [3], and BBO [7] algorithms. Both the tested AVR model and GASA algorithm are developed in Matlab/M-File 8.5.0 (R2015a) program by coding in *.m file*, which is installed on a computer with an Intel core (TM) i5 processor 3.3GHz and 8GB memory. In GASA algorithm, the number of neighbor solutions and iterations are set to 30 and 100, respectively. The mutation rate in neighborhood search is 0.13. By considering an initial annealing temperature equal to 100, it is decreased slowly and geometrically by a coefficient of 0.9997 so that the algorithm may not converge too quickly.

One of the major observations of the present study for analyzing the voltage response curve is given in Fig. 4, where the incremental change of terminal voltage response of the proposed PID-controlled AVR system to the step input perturbation is shown in a superimposed manner with those yielded by the other approaches. The dashed vertical lines are for signifying settling times. It is apparent from Fig. 4 that our proposal is the pioneer in achieving better unit step response, since it leads to a response that settles to the reference faster than other existing techniques after a very mild overshoot, which suits our requirements explained before.

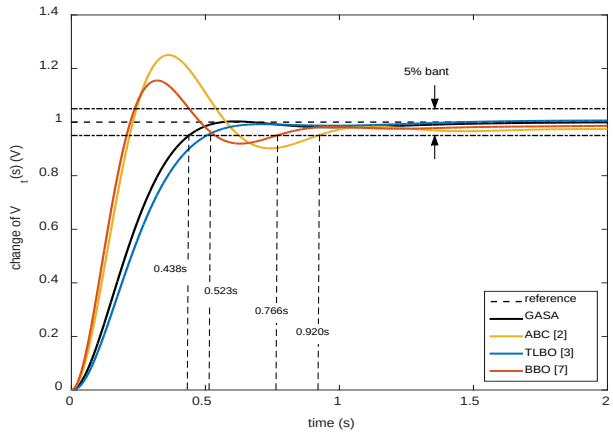

Figure 4. Comparative transient response profiles of the incremental change in terminal voltage

A comparison of the final solutions regarding the controller gains as well as their respective time domain performance characteristics such as maximum overshoot, settling time, and rise time computed from Fig. 4 is shown in Table 2 for GASA, ABC, TLBO and BBO algorithms, where the results of interests are indicated by **bold** numbers in their respective sections. From this table, it can be inferred that PID gains that are found using the GASA algorithm and cost function J are different from those offered by the other approaches. This difference results in superior transient time performance parameters with regard to minimum overshoot and less settling time as shown in Table 2, which are the two major factors for the stability concern of controlled system. It is also evident from Table 2 that the response using the TLBO-based PID controller does not have overshoot. Though such response seems desirable at first glance, it may not offer a good stability margin. When the rise time is analyzed, its best value belongs to BBO algorithm whereas TLBO algorithm has the worst.

Table 2. PID controller gains and transient performance of AVR system with different algorithms

Algorithm	K_P	K_I	K_D	Maximum overshoots	Settling times (5% bant)	Rise times
GASA	0.6093	0.4210	0.2044	**1.003**	**0.438**	0.317
ABC [2]	1.6524	0.4083	0.3654	1.250	0.920	0.156
TLBO [3]	0.5302	0.4001	0.1787	-	0.523	0.372
BBO [7]	1.2464	0.5893	0.4596	1.160	0.766	**0.149**

In order to examine the results from the perspective of stability concern, root locus analysis and bode analysis are applied to the GASA-optimized AVR system, and the results regarding root locus curve and bode diagram are given in Fig. 5.

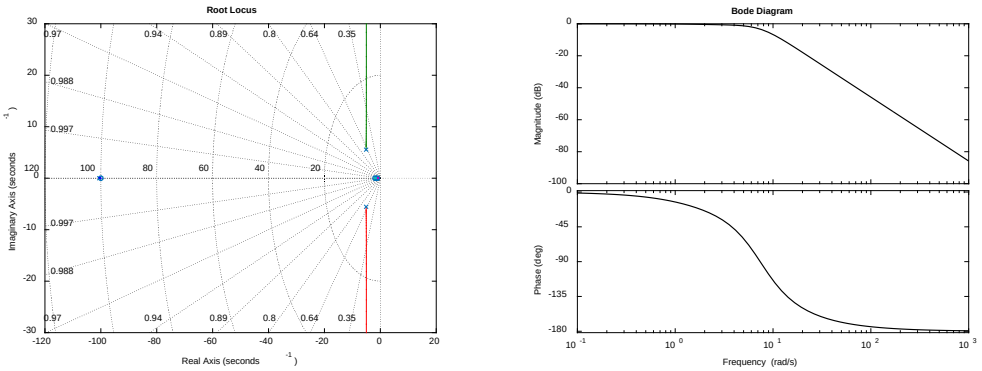

Figure 5. (a) Root locus curve of the studied system (b) Bode diagram of the studied system

The closed-loop poles and their respective damping ratios are also computed and provided in Table 3 in comparison with the results based on the reported studies. This table shows that all closed-loop poles are on the left *s*-plane, meaning that all the AVR systems under consideration are stable at different degrees depending upon the real pole number and the damping ratio magnitude of conjugate poles. In this sense, our proposal has the best stability margin with the biggest damping ratio, which followed by BBO-, ABC- and TLBO-based AVR systems.

Table 3. Comparative closed-loop poles and their damping ratios related to root locus analysis

Algorithm	Closed-loop pole	Damping ratio
GASA	−100.56	1
	−1.63	1
ABC [2]	−100.98	1
	−4.74	1
TLBO [3]	−100	1
	−1.33±0.43*i*	0.951
BBO [7]	−100.0	1
	−2.1	1

Finally, numerical results acquired from the bode plots such as peak gains, phase margins, delay margins and bandwidth are gathered in Table 4 in order to compare the stability results from another point view. Obtained results are promising for this type of stability criterion as well, such that the AVR system controlled by proposed controller has minimum peak gain, maximum phase margin and maximum delay margin, which are among the sought-after features expected from a control application to have. BBO-based system has the maximum bandwidth and the minimal one pertains to TLBO-based system.

Table 4. Comparative numerical results acquired from the bode plots for different AVR systems

Algorithm	Peak gain (db)	Phase margin (deg.)	Delay margin (s)	Bandwidth (Hz)
GASA	**0**	**180**	**Infinite**	7.04
ABC/ITSE [2]	2.87 dB (1.20 Hz)	69.4	0.111	12.87
TLBO/FOD [3]	0.01 dB (0.07 Hz)	170.2	4.392	5.20
BBO/ITSE [7]	1.56 dB (1.38 Hz)	81.6	0.122	**14.28**

5. CONCLUSION

In this research article, an application of GASA algorithm, which integrates GA into the SA neighboring generation mechanism for increased search performance, is applied to determine controller parameters of PID controller in an AVR application. To appraise the tuning performance of this algorithm, PID gains are first optimized jointly through the specific GASA phases, and their performance is subsequently compared with those offered by other state-of-the-art techniques under the identical AVR system by benefitting from various analysis techniques such as transient response, root locus and bode analysis. All the analysis results demonstrate that GASA is an effective optimizing tool for the PID-controlled AVR application. According the findings obtained from transient response analysis, it is found that settling time and peak overshoot of the incremental change of terminal voltage profile are improved. These improvements in the concerned two transient time parameters leads to an AVR system to be controlled with the increased degree of stability as approved by root locus and bode stability criteria.

Acknowledgment

This work was supported by the Infrastructure Projects of Scientific Investigation of Gazi University under Grant 07/2014-06.

REFERENCES

[1]. E. Celik, "Incorporation of stochastic fractal search algorithm into efficient design of PID controller for an automatic voltage regulator system", *Neural Comput Appl*, doi: 10.1007/s00521-017-3335-7, 2018.

[2]. H. Gozde, M.C. Taplamacioglu, "Comparative performance analysis of artificial bee colony", *J Franklin Inst*, vol. 348, pp. 1927-1946, 2012.

[3]. S. Chatterjee, V. Mukherjee, "PID controller for automatic voltage regulator using teaching–learning based optimization technique", *Int J Electr Power Energy Syst*, vol. 77, pp. 418-429, 2016.

[4]. A. Tepljakov, E.A. Gonzalez, E. Petlenkov, J. Belikov, C.A. Monje, I. Petráš, "Incorporation of fractional-order dynamics into an existing PI/PID DC motor control loop", *ISA Trans*, vol. 60, pp. 262-273, 2016.

[5]. D. Guha, P.K. Roy, S. Banerjee, "Study of differential search algorithm based automatic generation control of an interconnected thermal-thermal system with governor dead-band", *Appl Soft Comput*, vol. 52, pp. 160-175, 2017.

[6]. A. Chatterjee, V. Mukherjee, S.P. Ghoshal, "Velocity relaxed and craziness-based swarm optimized intelligent PID and PSS controlled AVR system", *Int J Electr Power Energy Syst*, vol. 31, pp. 323-333, 2009.

[7]. U. Guvenc, T. Yigit, A.H. Isik, I. Akkaya, "Performance analysis of biogeography-based optimization for automatic voltage regulator system", *Turk J Electr Eng Comput Sci*, vol. 24, pp. 1150-1162, 2016.

[8]. H. Gozde, M.C. Taplamacioglu, M. Ari, "Automatic voltage regulator (AVR) design with chaotic particle swarm optimization", *6th International Conference on Electronics, Computers and Artificial Intelligence*, pp. 23-26, Bucharest, Romania, 2014.

[9]. H. Gozde, M.C. Taplamacioglu, M. Ari, "Simulation study for global neighborhood algorithm based optimal automatic voltage regulator (AVR) system", *5th International Istanbul Smart Grids and Cities Congress and Fair*, pp. 46-50, Istanbul, 2017.

[10]. S. Kirkpatrick, C.D. Gelatt, M.P. Vecchi, "Optimization by simulated annealing", *Science*, vol. 220, pp. 671-680, 1983.

[11]. R.S. Tavares, T.C. Martins, MS.G. Tsuzuki, "Simulated annealing with adaptive neighborhood: A case study in off-line robot path planning, *Expert Syst Appl*, vol. 38, pp. 2951-2965, 2011.

[12]. S.J. Jeong, K.S. Kim, Y.H. Lee, "The efficient search method of simulated annealing using fuzzy logic controller", *Expert Syst Appl*, vol. 36, pp. 7099-7103, 2009.

[13]. E. Celik, N. Ozturk, "First application of symbiotic organisms search algorithm to off-line optimization of PI parameters for DSP-based DC motor drives," *Neural Comput Appl*, doi: 10.1007/s00521-017-3256-5, 2017.

[14]. N. Ozturk, "Speed control for dc motor drive based on fuzzy and genetic PI controller - A comparative study", *Elektron Elektrotech*, vol. 123, pp. 43-48, 2012.

[15]. E. Celik, N. Ozturk, "Genetik Algoritma Tabanli Gelistirilmis Benzetilmis Tavlama Algoritmasi", *Akilli Sistemlerde Yenilikler ve Uygulamalari Sempozyumu*, pp. 1-4, Duzce, Turkiye, 2016.

[16]. H. Shayeghi, A. Younesi, Y. Hashemi, "Optimal design of a robust discrete parallel FP + FI + FD controller for the Automatic Voltage Regulator system", *Int J Electr Power Energy Syst*, vol. 67, pp. 66-75, 2015.

ICENS 4TH INTERNATIONAL CONFERENCE ON ENGINEERING AND NATURAL SCIENCE
2-6 May 2018 KIEV UKRAINE

Two-Dimensional Flow Simulation in Spillways by Computational Fluid Dynamics (CFD)

Mehmet Cihan Aydin[1], Ali Emre Ulu[2]

Abstract:

Kopru Dam and Hydroelectric Power Plant are one of the projects of our country which are developed for energy purposes. The facility is located in the border of Adana province, on the Goksu line of the Seyhan River at the junction of Kavsak Bendi HPP. Kopru Dam and HPP have approximately 145 MW installed capacity and it is aimed to produce 381 GWh of electricity per year. When the current installed capacity is concerned, Bridge Dam and HPP is Turkey's 97th largest power plant. Nevertheless, the facility is Turkey's largest 32nd hydroelectric power plant. In this study, two-dimensional hydrodynamic behaviors of Kopru dam spillway will be investigated by using Computational Fluid Dynamics (CFD). The data obtained will be compared and interpreted with the model experiments conducted by the State Hydraulic Works (SHW).

Keywords: CFD, Spillway, Two-Dimension, Dam

1. INTRODUCTION

The dam is a structure that prevents flow by forming a reservoir and closing a river valley for accumulation of water. The dams have two important functions besides water accumulation, such as raising the water level and bringing it to the large water surface. Dams are engineering works that are expensive and long-lasting, and cause great loss of life and property if demolished. Kopru Dam and Hydroelectric Power Plant (HPP) Project was established in Goksu Brook of Seyhan River within the boundaries of Adana province. The body type of the dam is Cylinder Compressed Concrete. Height of the dam from river bed is 100 m. Some of the relevant studies in the literature are shown below.

Rodi (2017) is a comprehensive study describing the turbulence movement in almost all fluids and investigating the effects of turbulence on momentum, heat and mass transport in hydraulic fluids. It is emphasized that it is very important to anticipate the effects of turbulence, not only to understand turbulence, but to refer to the fact that turbulence movement's existence and its importance have long been studied by many scientists and engineers. In this context, the various methods used to understand and simulate turbulence in the article have been reviewed in terms of the historical development of the equations, applications and their effects on the hydraulic flows [1].

Teng and Yang (2016) pointed out that the ventilation used in the wastewater would reduce the risk of cavitation caused by the high currents generated in these areas. The characteristics of the two-phase (water-air mixed) flow were investigated and the performance of the Bergeforsen Dam ventilation system of 25 m length and 35 m width was assessed by numerical modeling. As a result, it was observed that the findings obtained from the experimental study results were very close to the obtained numerical data, and it was stated that ventilation gaps were left in the midpoints of the sluices with large discharge channels, and ventilation gaps were recommended to be used [2].

Kramer and Hager (2005) stated in their study that the air bubble rising speed in the stream is connected. It has been stated that the flow rate at high speed is dependent on the number of forces acting on the air bubble, the turbulence, the non-hydrostatic pressure gradient, the shear force, the bubble clouds and the free surface drift, and the increasing number of resulting air bubbles [3].

Pfister and Hager (2010) focus on the air transfer and flow structure located upstream of the shot aerators. In the model, chute aerators are considered divided into three flow divisions. These are the jet zone, the reconnection and sputtering zone, and the remote field zone. According to the results obtained from the experiments, it is seen

[1] *Bitlis Eren University, Department of Civil Engineering* , mcaydin@beu.edu.tr

[2] *Bitlis Eren University, Department of Civil Engineering,* aeulu@beu.edu.tr

that the aerators mainly increase the average air concentration, the lower air concentration is marginally affected, and the deflector aerators work more efficiently than the offsets in terms of air entry angle [4].

In this study, two-dimensional hydrodynamic behaviors of Kopru Dam spillway will be investigated by using Computational Fluid Dynamics (CFD) under different current and design conditions. The data obtained will be compared and interpreted with the model experiments conducted by the State Hydraulic Works (SHW).

2. METHOD

Computational Fluid Dynamics (CFD) is an advanced technique that solves the theoretical and semi-empirical dynamic equations of fluids using a variety of numerical methods and computational tools. With the advances in computer technology in recent years, even the hydrodynamics of very complex systems can be analyzed. Although physical model experiments are used as a traditional method in hydraulics, the use of CFD analysis is increasing day by day and offers great advantages in modeling and design of hydraulic systems. Numerical modeling of multi-phase fluid models and free-surface flows is rather difficult compared to other types of flow models. FLOW-3D is a general purpose computational fluid dynamics software. FLOW-3D numerically solves a set of fundamental fluid equations to determine fluid motion, like other CFD software. The basic equations of the fluid used for this purpose are given below [5].

$$V_F\frac{\partial \rho}{\partial t}+\frac{\partial}{\partial x}(\rho u A_x)+R\frac{\partial}{\partial y}(\rho v A_y)+\frac{\partial}{\partial z}(\rho w A_z)+\xi\frac{\rho u A_x}{x}=R_{\mathrm{DIF}}+R_{\mathrm{SOR}}$$

Here; V_f is the volume ratio of the fluid, ρ is the density of the fluid, R_{dif} is the turbulent diffusion term, R_{sor} is the mass flux. The momentum equation of fluid motion:

$$\frac{\partial u}{\partial t}+\frac{1}{V_F}\left\{uA_x\frac{\partial u}{\partial x}+vA_yR\frac{\partial u}{\partial y}+wA_z\frac{\partial u}{\partial z}\right\}-\xi\frac{A_y v^2}{xV_F}=-\frac{1}{\rho}\frac{\partial p}{\partial x}+G_x+f_x-b_x-\frac{R_{\mathrm{SOR}}}{\rho V_F}(u-u_w-\delta u_s)$$

$$\frac{\partial v}{\partial t}+\frac{1}{V_F}\left\{uA_x\frac{\partial v}{\partial x}+vA_yR\frac{\partial v}{\partial y}+wA_z\frac{\partial v}{\partial z}\right\}+\xi\frac{A_y uv}{xV_F}=-\frac{1}{\rho}\left(R\frac{\partial p}{\partial y}\right)+G_y+f_y-b_y-\frac{R_{\mathrm{SOR}}}{\rho V_F}(v-v_w-\delta v_s)$$

$$\frac{\partial w}{\partial t}+\frac{1}{V_F}\left\{uA_x\frac{\partial w}{\partial x}+vA_yR\frac{\partial w}{\partial y}+wA_z\frac{\partial w}{\partial z}\right\}=-\frac{1}{\rho}\frac{\partial p}{\partial z}+G_z+f_z-b_z-\frac{R_{\mathrm{SOR}}}{\rho V_F}(w-w_w-\delta w_s)$$

Where: (G_x, G_y, G_z): Mass acceleration, (f_x, f_y, f_z): Viscosity accelerations, (b_x, b_y, b_z): flow losses in porous media.

3. COMPUTATIONAL DOMAIN, MESH AND BOUNDARY CONDITION

The Dam profile produced for CFD analyzes was created using the values used in the actual project. The geometry details of the dam are given in Figure 1. In the original project, the dam's spillway width is symmetrically narrowed to be 125 m at crest and 100 m at the downstream flip bucket. In the project, at the end of the discharge channel, a submerged flip bucket was selected as the energy crushing structure. The radius of the flip bucket is 15 m. Considering turbulence effects, the RNG (Renormalized Group) turbulence model were used. In the study, two mesh blocks were used. 0.8 m for the first mesh block, and 0.5 m conform mesh block for the second mesh block were applied (Figure 2). Second mesh block conformed to the blocked volume. The values of the tail water level used in the experiments were also used in numerical simulations.

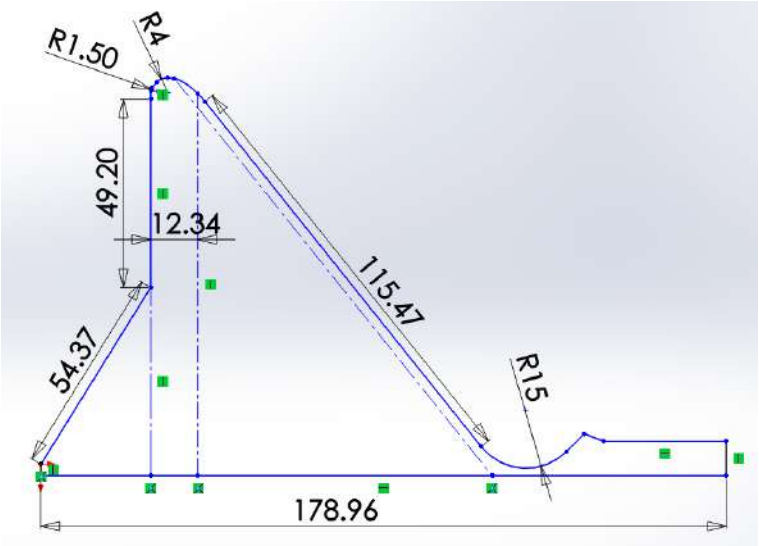

Figure 1. 2D Geometry of Kopru Dam and Flip Bucket (dimensions in meter)

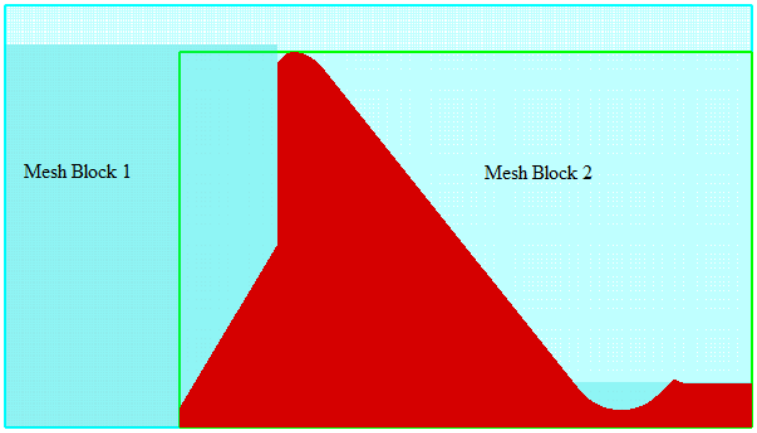

Figure 2. Mesh Blocks Applied to the Geometry

4. NUMERICAL ANALYSIS

Numerical analysis was carried out for three different flow conditions with unit flow of q = 14, 28 and 41.8 $m^3/s/m$ and Froude number of Fr = 2.31, 3.74 and 4.94 before the jump in the flip bucket. Solutions were accompanied for 60 min. Table 1 shows the scale model used in the experiment. The values read from 6 different points of the experimental work were compared with the numerical modeling values taken from the same points. These points and velocity scales illustrated in the Figure 3. The velocity values obtained from the experimental and numerical simulations and the positions of the points are given in Tables 2,3 and 4. Figure 4, 5 and 6 illustrate the flow velocity comparison between experimental and CFD data for q = 14, 28 and 41.8 $m^3/s/m$, respectively.

Table 1. Scale Rates between model and prototype of Kopru Dam

Physical Magnitude	**Unit**	**Formula**	**Scale**
Length (L)	m	$K_L=L_P/L_M$	60
Velocity (U)	m/s	$K_U=K_L^{1/2}$	7.7460

Flow Rate (Q)	m^3/s	$K_Q^{5/2}$	27885.48

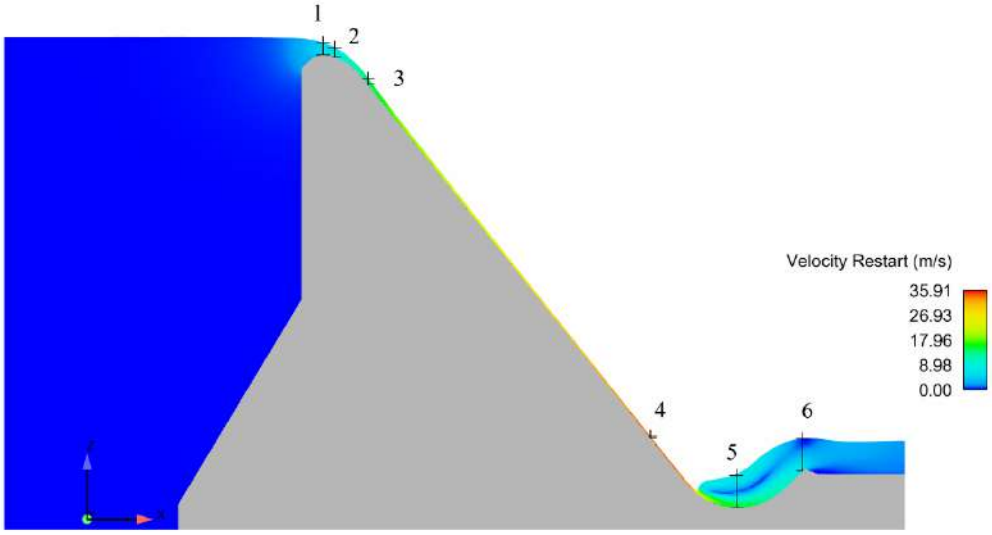

(a) q= 14 m3/s/m, Fr = 2.31

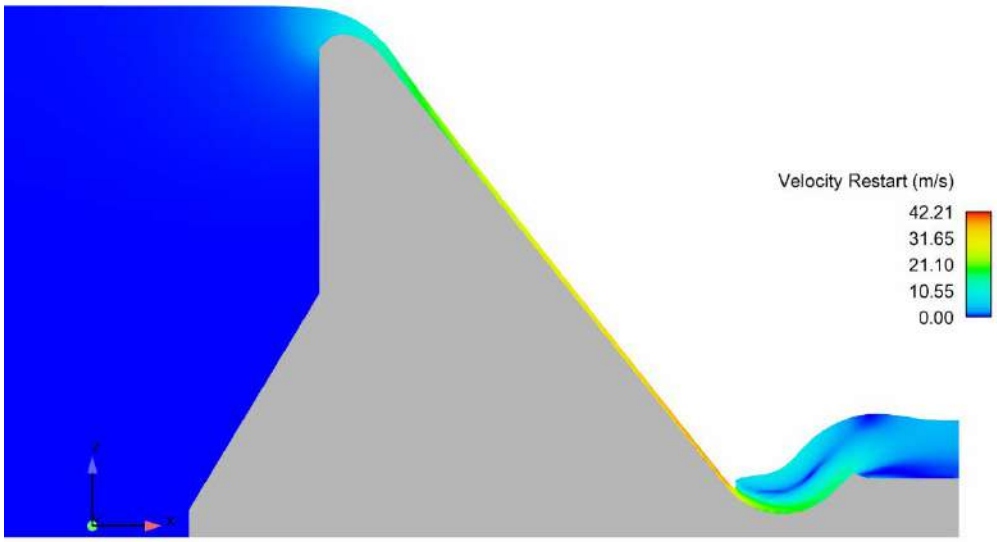

(b) q= 28 m3/s/m, Fr = 3.74

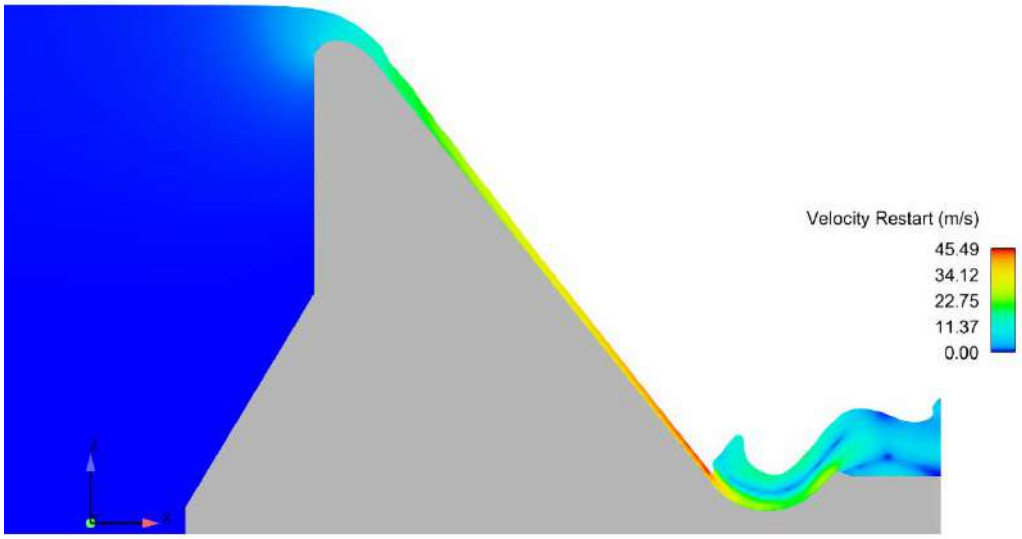

(c) q= 41.8 m3/s/m, Fr = 4.94

Figure 3. Velocity Scale of the Dam for the Unit Flow of q = 14-28-41.8 m3/s/m

Table 2. Spillway flow height and flow velocity parameters at q= 14 m^3/s/m

	Distance From Spillway Crest (m)	**Base Slope Angle, α (º)**	**Type**	**Parameter at q=14 m^3/s/m**
				Flow Velocity, *U* (m/s)
Spillway Sill Axis	0+004,56	0	Experimental	4.93
			CFD	5.82
	0+007,17	21,26	Experimental	6.44
			CFD	8.07
	0+014,60	51,34	Experimental	12.32
			CFD	14.81
	0+078,11	51,34	Experimental	46.71
			CFD	39.63
Flip Bucket Axis	0+097,47	0	Experimental	1.54
			CFD	7.75
	0+112,38	-19,65	Experimental	1.83
			CFD	3.30

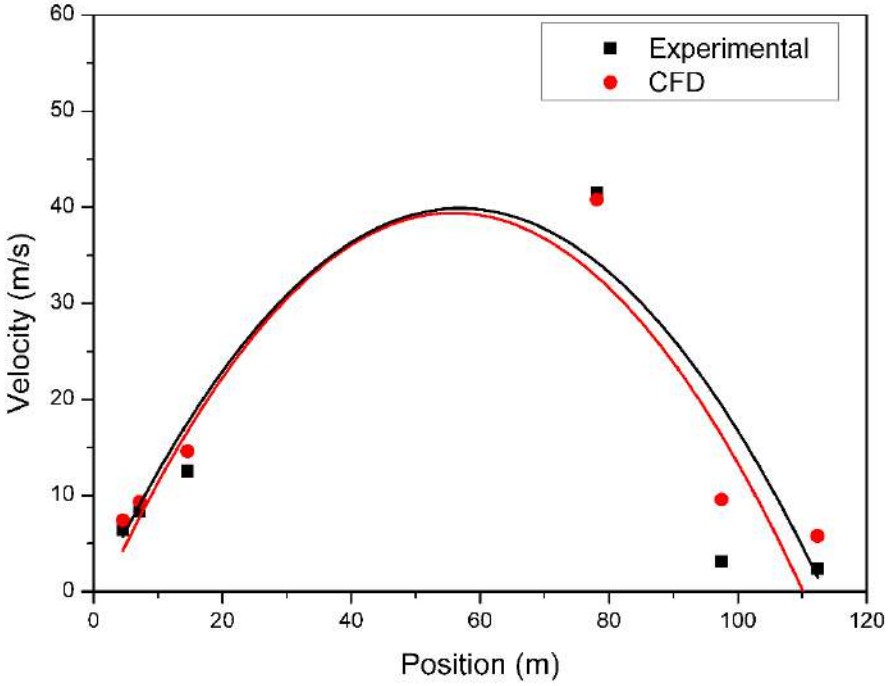

Figure 4. q=14 m^3/s/m Flow Velocity comparison between Experimental and CFD data

Table 3. Spillway flow height and flow velocity parameters at q= 28 m^3/s/m

	Distance From Spillway Crest (m)	Base Slope Angle, α (º)	Type	Parameter at q=28 m^3/s/m
				Flow Velocity, *U* (m/s)
Spillway Sill Axis	0+004,56	0	Experimental	6.45
			CFD	7.42
	0+007,17	21,26	Experimental	8.34
			CFD	9.33
	0+014,60	51,34	Experimental	12.54
			CFD	14.6
	0+078,11	51,34	Experimental	41.53
			CFD	40.78
Flip Bucket Axis	0+097,47	0	Experimental	3.14
			CFD	9.57
	0+112,38	-19,65	Experimental	2.38
			CFD	5.77

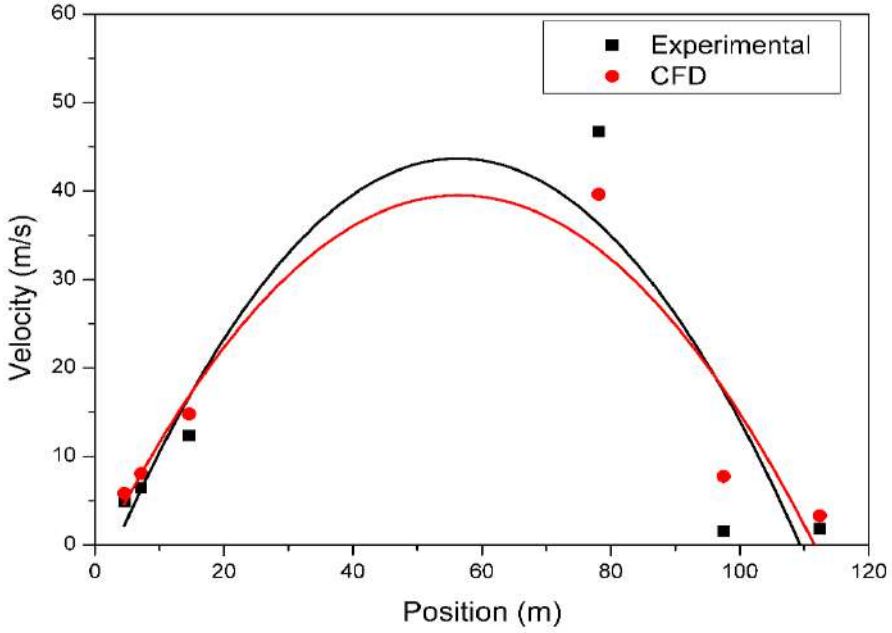

Figure 5. q=28 m³/s/m Flow Velocity comparison between Experimental and CFD data

Table 4. Spillway flow height and flow velocity parameters at q= 41.8 m³/s/m

	Distance From Spillway Crest (m)	Base Slope Angle, α (°)	Type	Parameter at q=41.8 m³/s/m
				Flow Velocity, *U* (m/s)
Spillway Sill Axis	0+004,56	0	Experimental	7.67
			CFD	8.46
	0+007,17	21,26	Experimental	9.48
			CFD	10.1
	0+014,60	51,34	Experimental	14.68
			CFD	14.96
	0+078,11	51,34	Experimental	47.79
			CFD	42.98
Flip Bucket Axis	0+097,47	0	Experimental	4.53
			CFD	15.2
	0+112,38	-19,65	Experimental	3.04
			CFD	11.4

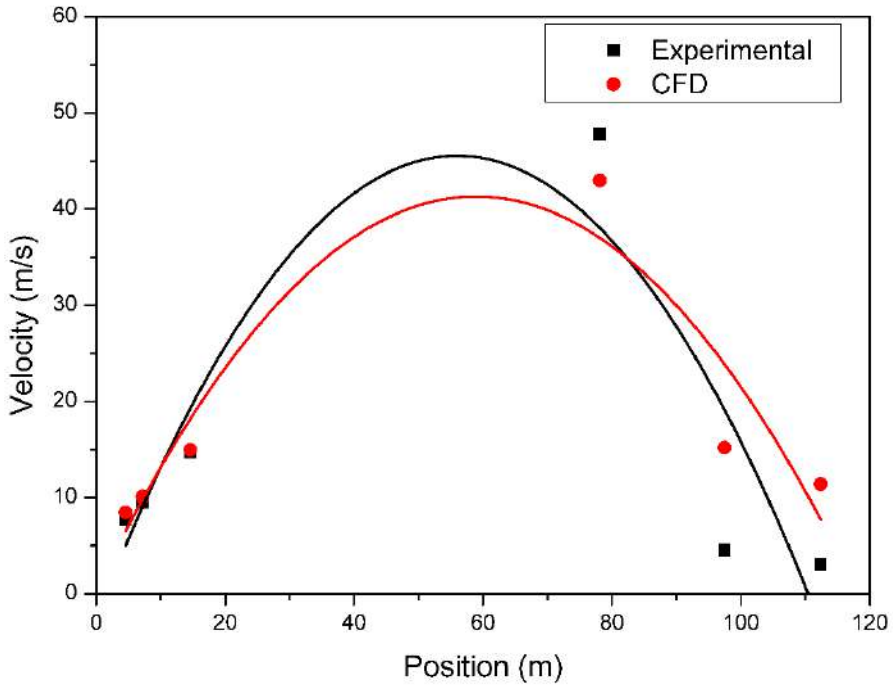

Figure 6. q=41.8 m^3/s/m Flow Velocity comparison between Experimental and CFD data

5. RESULTS

In this study, two-dimensional analysis of the Kopru Dam spillway was carried out. Flow 3D numerical simulation program was used in the study. Numerical analysis was carried out by entering the actual dimensions of the spillway. The data obtained from the numerical simulations were compared with the results of the model experiments previously carried out by the State Hydraulic Works (SHW). In the study, the velocity data measured from the dam axis are compared. In the light of the obtained results, an average difference of 10% was observed between the data obtained from the numerical modeling and the findings obtained experimentally. This difference is quite satisfactory. In the data obtained from past studies, this difference is believed to be due to the fact that the dam is studied in two dimensions and that scale effects can occur in the modeling of such large structures. It is encouraging for us that the CFD analysis will show values very close to the test results for the further study to be done in the future. In the study, it is predicted that CFD will provide accurate and reliable results in future studies, since two-dimensional analyzes are carried out so close to model experiments.

REFERENCES

[1] Rodi, W. (2017). Turbulence Modeling and Simulation in Hydraulics: A Historical Review. Journal of Hydraulic Engineering 143(5): 1-20.
[2] Teng, P., & Yang, J. (2016). CFD modeling of two-phase flow of a spillway chute aerator of large width, Journal of Applied Water Engineering and Research, 4:2, 163-177, DOI:10.1080/23249676.2015.1124030.
[3] Kramer, K., & Hager, W. H. (2005). Air transport in chute flows. International journal of multiphase flow, 31(10), 1181-1197.
[4] Pfister, M., & Hager, W. H. (2010). Chute aerators. I: Air transport characteristics. Journal of Hydraulic Engineering, 136(6), 352-359.
[5] FLOW-3D (2016), User Manual, Theory Guide.

ICENS 4TH INTERNATIONAL CONFERENCE ON ENGINEERING AND NATURAL SCIENCE
2-6 May 2018 KIEV UKRAINE

Determining Of Forearm Muscular Strengths By Using Forearm Anthropometric Measurements And Emg Signals

Cagatay Tasdemirci[1], Yasin Kisioglu[2]

Abstract

Human hand is the most important component affecting the function of the upper extremity and performing function for the continuity of daily life activities. For this reason, grip strength is considered as an objective measure in assessing upper extremity performance. Studies have shown that hand grip strength is related with forearm muscle strengths as well as general body and pulmonary muscle strength. Ratio of forearm length - circumference, hand size, age, body mass index (BMI), height are the predictive indicators of hand grip strength.In this study, the gripping forces created by forearm muscles were tried to be analyzed using anthropometric dimensions mentioned above and EMG (Electromyography) signals. To measure the muscle forces, participants including male and female having similar physical characteristics, such as BMI, height, age etc. were used. It was realized that different and additional evolution techniques should be used for male and female participants to measure the muscle forces. Therefore, it would be beneficial for female participants to use additional variables in estimation of the muscle forces other than the ratio of forearm length to circumference.

Keywords: Muscle Forces, Grip Strength, Biomechanics, EMG Signals

1. INTRODUCTION

To analyze biological systems, the engineering sciences are often use. To develop products for people with disabilities or similar disorders, to determine the causes of injuries, similarly to prevent muscles injuries, bone and articular tissue structures must be modelled by performing force analysis. For this reason Biomechanics has been born as a scientific discipline that studies the forms and functions of biological systems with engineering methods.

One of the biggest challenges in biomechanical studies is knowing the muscles forces. The relationship between muscle strength and contraction cannot be established precisely because of the difficulty of measuring muscle contractions. In order to remove this uncertainty, muscle contraction must be related to the forces applied by the muscles. In this study, EMG signals that measured from forearm muscles was tried to be related to the muscle forces during that applied during hand grip.

Muscle contractions and EMG measurements may vary in different persons and at different times of measurements. It is known that the change of hand maximum grip strength depending on the persons forearm circumference body mass index (BMI), gender, age and height. Studies have shown that hand grip strength correlates with upper extremity muscle strength, as well as general body muscle strength [1-3] and pulmonary muscle strength [4].

2. MEASUREMENT OF EMG SIGNALS

While recording the EMG signal, one of the most important factor that affecting the accuracy of the signal is noise. Noise can be defined as unwanted electrical signals in the EMG signal. The most common causes of noise

[1] *Cagatay Tasdemirci: Kocaeli University, Department of Biomedical Engineering, 41380, Izmit/Kocaeli, Turkey.* cagatay.tasdemirci@kocaeli.edu.tr

[2] *Yasin Kisioglu, Kocaeli University, Department of Biomedical Engineering, 41380, Izmit/Kocaeli, Turkey.* y.kisioglu@kocaeli.edu.tr

are electronic devices and electrical network frequency. For this reason, there must be as few electronic devices as possible in the environment during the measurements and the raw EMG signal must be filtered.

The frequency spectrum of the EMG signal is given in Figure 2.1. As it seen, the meaningful range of the EMG signal is 0-500 Hz and the range of the highest signal is 0-150 Hz.

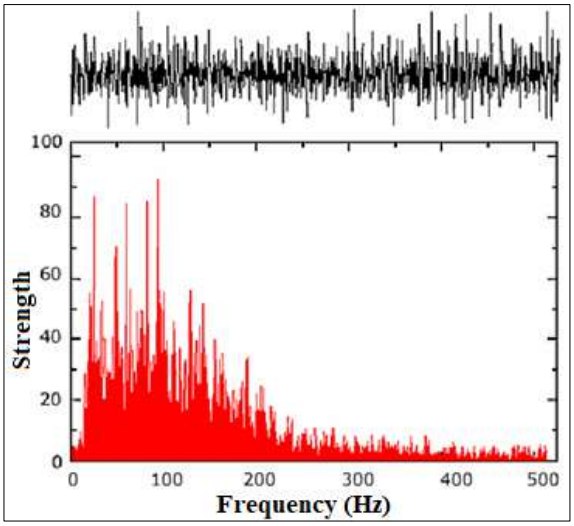

Figure 2.1 EMG Signal frequency spectrum

Other important point for EMG signal measurement is electrode locations. The electrode surfaces should be kept as small as possible and the electrodes must be placed in the center of the muscle. EMG signals in different regions of the muscle are given in Figure 2.2.

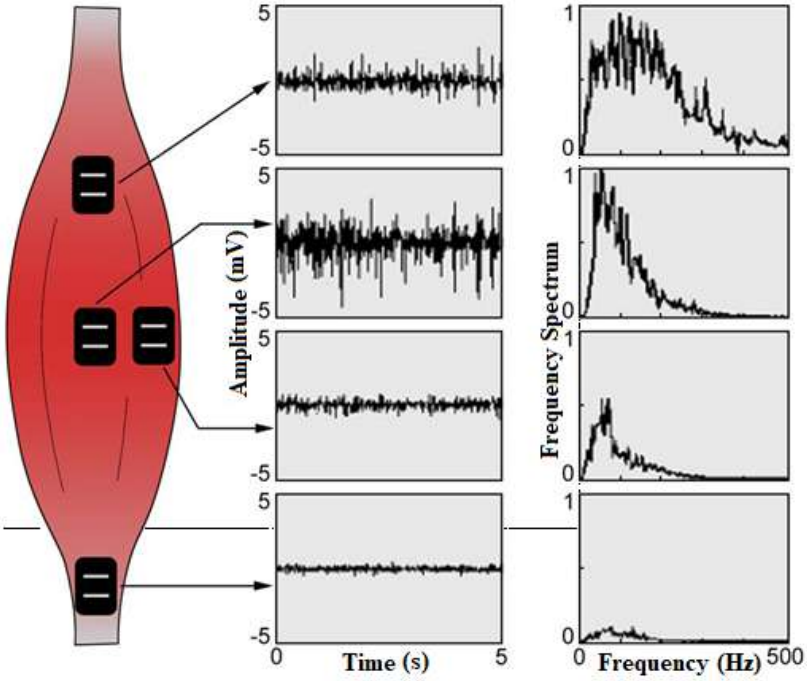

Figure 2.2 EMG Signals at different regions of the muscle

Determining muscle forces just by analyzing EMG signal is not enough, for this purpose another variable is needed. The Studies prove that anthropometric measurements such as arm circumference and arm length directly related with muscle forces [5-7].

3. MATERIALS AND METHODS

In this study, to minimize the factors that affect the EMG signal, volunteers are chosen from similar traits (25-30 years old, 1,75-1,80m for male and 1,60-1,75m for female in height and 75-80kg for male and 45-55kg for female in weight) participants, in this way height, age, weight and BMI factors were tried to be minimized. Each participant was informed before the study.

During anthropometric measurements, body was stood upright position and forearm was parallel to the ground. Recording position is given at figure 3.1. 12 records were taken from each volunteer and 10 of these records was taken for the result, in this was possible measurement errors were eliminated. EMG signals were recorded for 5 second for each different muscle loads and muscle was rested 20 second between each record.

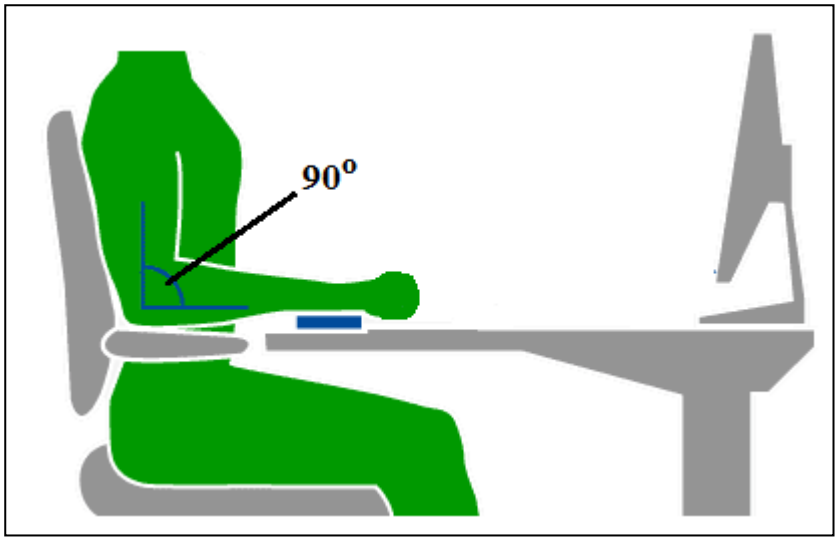

Figure 3.1 EMG signals record position

Forearm length was measured between the olecranon and the styloid while the elbow in 900 flexion. Forearm circumference was measured from 12 cm distal from olecranon when muscle was not under pressure. From forearm length and circumference measurements, forearm circumference-length ratio calculated (C-L Ratio).

4. RESULT

Determination of muscle strengths in biomechanics studies is of great importance. However, establishing the relationship between EMG signals and muscle strengths is a very difficult task because the EMG signal is influenced by many physiological, anatomical and technical factors and varies among individuals. In order to investigate this relationship, the effect of some factors should be checked and appropriate recording and signal processing methods should be used.

In this study, it was understood that the ratio of forearm length to forearm circumference would be useful in predicting muscular strength and electrical signal. Table 1 and Table 2 shows measurements of participants forearm C-L ratio, maximum EMG signal, and muscle force. For female and male participants different analysis algorithms must be use.

Table 1 Measurements of male participants

MALE	Forearm C-L Ratio	Maximum EMG Signal (mV)	Maximum Force (kgf)
1. Participant	1,1	0,56	23
2. Participant	1,06	0,6	24
3. Participant	1,04	0,67	27
4. Participant	1,01	0,75	29
5. Participant	0,95	0,83	31

Table 2 Measurements of female participants

FEMALE	Forearm C-L Ratio	Maximum EMG Signal (mV)	Maximum Force (kg)
1. Participant	1,25	0,3	18
2. Participant	1,2	0,4	20
3. Participant	1,19	0,4	21
4. Participant	1,18	0,5	22
5. Participant	1,15	0,6	24

It is hard to measure EMG signals from female participants, because amplitude of the signal is low and its hart to determine exact value. Also because of the small forearm muscle surface area and wrist circumference it is hard to place EMG electrodes.

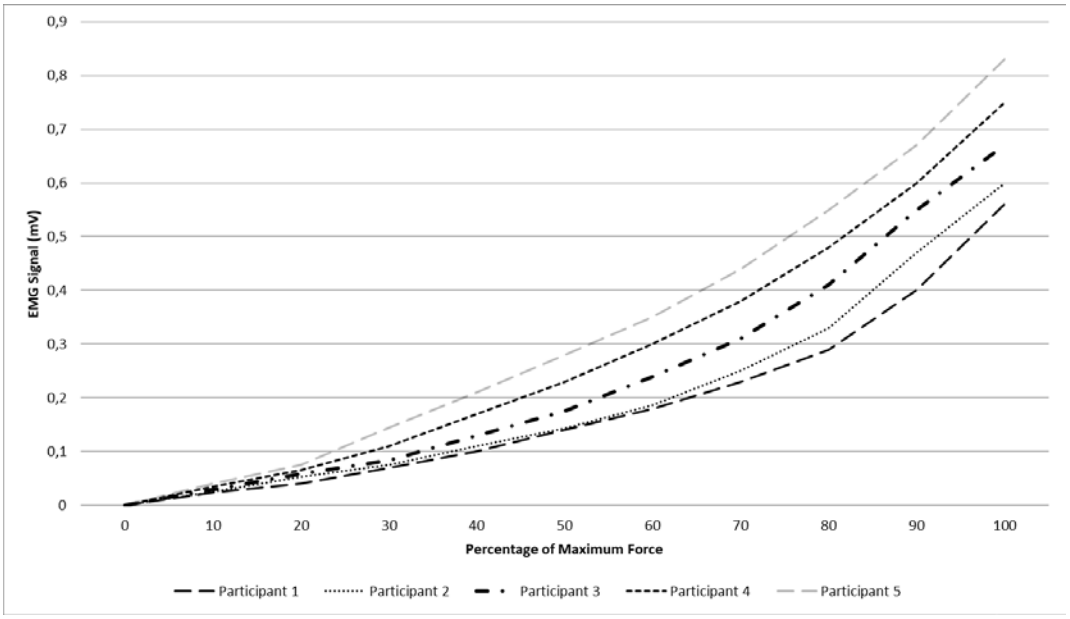

Figure 4.1 EMG signal-force graphic of male participants

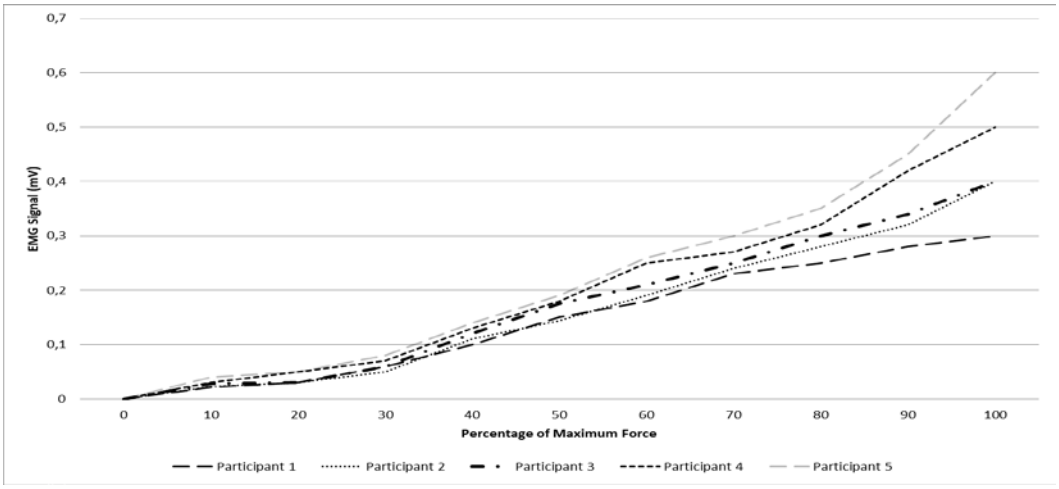

Figure 4.2 EMG signal-force graphic of female participants

It is very important to know the loads on muscles and joints especially in prosthetic design, implant selection and analysis. Since it is difficult to make these analyzes individually for individuals, making estimates with easier measurements will make it easier to work with. This study showed that the anthropometric measurements of the forearm showed a great ease in predicting the maximum amplitude of the EMG signal due to the ratio of the intact fiber. In studies done [9], it was recommended that similar anthropometric measurements of the forearm correlated with forces in the muscles were supported by EMG measurements and that the gender factor was eliminated. This study showed that when the gender factor was eliminated, the results were clearer and that measurements made with EMG signals supported the relationship between muscle force and Forearm C-L ratio.

5. CONCLUSIONS AND DISCUSSION

As seen in the study, the anthropometric measurements of the forearm showed that muscle force and Forearm C-L ratio the ratio of the cortical fiber thus greatly facilitates the estimation of the maximum amplitude and maximum muscle strength of the EMG signal, but for female participants better EMG signal measurement methods must be used, needle electrodes can be used instead of surface electrodes. Other difficulty at signal analysis is variety, because female participants have similar maximum force capacity and using just C-L ratio is not enough at that situation. Also body height and weight can be used as a variable.

REFERENCES

[1]. D. Mandalidis, M. O'Brien, "Relationship between hand grip isometric strength and isokinetic moment data of the shoulder stabilisers," *J Bodywork Mov Ther*, vol 14, pp. 19-26, Jan 2010.

[2]. J. Adams, J. Burridge, M. Mullee, A. Hammond, C Cooper, "Correlation between upper limb functional ability and structural hand impairment in an early rheumatoid population," *Clin Rehabil*, vol. 18, pp. 405-413, Jun 2004.

[3]. B. Niebuhr, R. Marion, "Voluntary control of submaximal grip strength," *Am J Phys Med Rehabil*, vol. 69, pp. 96–101, Apr 1990.

[4]. M. Sinaki, "Relationship of muscle strength of back and upper extremity with level of physical activity in healthy women," *Am J Phys Med Rehabil*, vol. 68, pp. 68, Dec 1989.

[5]. L.E. Charles, C.M Burchfiel, D. Fekedulegn, "Occupational and other risk factors for hand-grip strength: the Honolulu-Asia Aging Study," *Occup Environ Med*, vol. 63, pp. 820-827, Dec 2006.

[6]. D. Leca, "The Use of Surface Electromyography in Biomechanics," *Journal of applied biomechanics*, vol. 13, pp 135-163, May 1997.

[7]. C.W. Nicolay, A.L. Walker, "Grip strength and endurance: Influences of anthropometric variation, hand dominance and gender," *Int J Ind Ergon*, vol. 35, pp 605-618, July 2005.

[8]. R.E. Anakwe, J.S. Huntley, J.E. McEachan, "*Grip strength and forearm circumference in a healthy population," J. Hand Surg Eur Vol*, vol 32. Pp 203-209, Apr 2007.

[9]. S. Narin, I. Demirbuken, S. Ozyurek, U. Eraslan, "Dominant el kavrama ve parmak kavrama kuvvetinin onkol antropometrik olcumlerle iliskisi" *DEU Tip Fakultesi Dergisi*, vol. 23, pp. 81-85, May 2009.

BIOGRAPHY

Cagatay Tasdemirci was born in Samsun in 1989 and completed his primary school education in Kocaeli. After completing his high school education at the Anatolian High School of the Central Bank, he started university education at the Electrical Engineering Department of Kocaeli University in 2006 and graduated from university in 2011 at the end of 5 years including one year English preparatory education. Following his graduation, he started his master education in Kocaeli University Biomedical Engineering Department in 2015 after 3 years experience at companies such as Inductotherm Group and Hyundai Assan Automotive. He has been working as a Research Assistant in the same department since 2016.

ICENS 4TH INTERNATIONAL CONFERENCE ON ENGINEERING AND NATURAL SCIENCE
2-6 May 2018 KIEV UKRAINE

Buckling Analysis of Beams with Varying Flexural Rigidity on Elastic Foundation

Ali Nuri Dogruoglu[1], Sedat Komurcu[2]

Abstract

Buckling analysis of beams has become a significant requirement to constitute stable structures. Various approaches have been used to obtain robust formulations to analyze buckling of beams. In this study, buckling analysis of Bernoulli-Euler beams with varying flexural rigidity resting on elastic foundation are presented. Critical buckling loads of the beams are determined based on mixed finite element formulation via Gâteaux differential. Beams with varying flexural rigidity on Winkler and Pasternak elastic foundations are tested in this study. Single beams with increased flexural rigidities on elastic foundations are analyzed. Different boundary conditions are used with beams on elastic foundations. Fixed-free end, pinned-pinned, fixed-pinned, fixed-fixed support types are used to investigate the value of the critical buckling loads. The relationship between the critical buckling load values for beams with varying rigidity are presented separately. It is seen that the results obtained in this study are compatible with exact solutions for the buckling loads. In addition, the effects of varying rigidity provide distinct stability characteristics to beams on elastic foundations as seen the results of the comparative study. The results show that, the functionals obtained from this study are very practical for buckling analysis of beams with varying flexural rigidity on elastic foundations.

Keywords: Beam, Buckling analysis, Mixed formulation, Varying rigidity

1. INTRODUCTION

Buckling analysis of the structures is a significant issue for many engineering areas to design stable and resistant structures. Although many structures have sufficient resistance in terms satisfying strength, lack of stability usually cause to failure of the structures. Therefore, buckling analysis must be considered to construct safe structures. Especially, when the slender structures subjected to compressive loadings, the loading may cause the structure to deflect laterally. The lateral deflection is called buckling. The maximum axial load that an axially loaded member of a structure can support is called the critical buckling load. This is a failure type which is generated by exceeding the critical buckling load. The critical buckling load is only changes with the moment of inertia, height of the structure and the modulus of elasticity of a material.

Buckling is the sudden instability of structural members subjected to axial compression. There are many studies have been done about buckling analysis of beams. Theory of buckling begins with the studies by Leonhard Euler [1]. The problem of beams resting on an elastic foundation are studied by many researchers in the literature. Elastic foundations are commonly encountered structures for many engineering areas. The beam problem with the various geometries resting on the elastic foundation has become one of the most interesting topics for researchers and theorists. Significant books were written for a comprehensive analyzing of stability of structures [2], [3].

There are many studies about beams resting on the elastic foundation by various methods for buckling analyses in the literature. Buckling analysis of beams resting on an elastic foundation were studied by many researchers [4]-[6]. Varying rigidity beams have found many application areas by structural engineers. Many studies were employed for the analyzing of varying rigidity beams in literature [7]-[13].

In this study, some significant intensions are highlighted such as investigation of stability behavior of varying rigidity beams, calculation of the critical buckling load for beams via mixed finite element method, formulation

[1] *Corresponding author: Istanbul Technical University, Department of Civil Engineering, 34469, Sariyer/Istanbul, Turkey.* dogruogl@itu.edu.tr

[2] *Istanbul Technical University, Department of Civil Engineering, 34469, Sariyer/Istanbul, Turkey.* komurcus@itu.edu.tr

of a functional for buckling analyze of beams, analyzing of the interaction between the beams and elastic foundation.

2. FORMULATION

Buckling analysis of beams have become a significant requirement to constitute stable structures. Various approaches have studied to obtain reliable formulations to analyze buckling of beams. In this study, buckling analysis of Bernoulli-Euler Beams resting on elastic foundations are presented. The analyzed buckling problem is a bifurcation of the static equilibrium. Beams are considered as members resting on elastic foundation which subjected to axial compressive loads. Beams are made of homogeneous and isotropic material. The mixed finite element formulation is used to analyze of beams with varying flexural rigidity resting on elastic foundations. A schematic representation of a beam is shown in Figure 1.

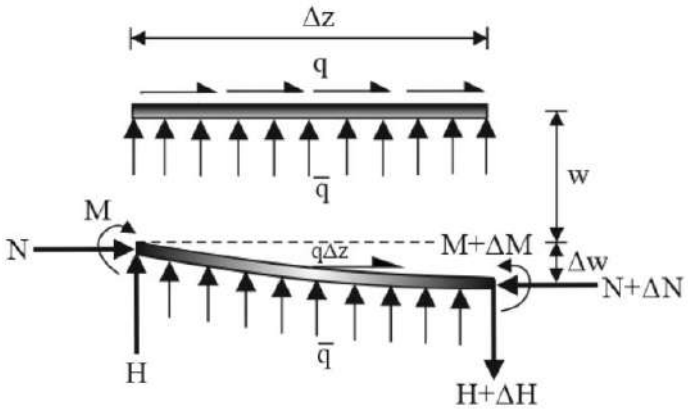

Figure 8. Schematic representation of beams on elastic foundation

Equilibrium equations are used for buckling analyses of beams as shown in Equations (1-3). In these equations N, H and M represents normal force, vertical force and moments, respectively. $\bar{q}$ represents the foundation effect and q the distributed load value on the beams. k_W and k_G are Winkler and Pasternak foundation constants, respectively.

$$\frac{dN}{dz} = q \tag{1}$$

$$\frac{dH}{dz} = \bar{q} = kw - k_G \frac{d^2w}{dz^2} \tag{2}$$

$$\frac{dM}{dz} - N\frac{dw}{dz} - H = 0 \tag{3}$$

Constitutive equation for the relation between moment M and deflection w is shown in equation (4). EI is the flexural rigidity of the beams.

$$\frac{M}{EI} = -\frac{d^2w}{dz^2} \tag{4}$$

If the Equation (3) is derived according to "z" and the Equation (2) is used, Equation (5) is obtained as follows,

$$\frac{d^2M}{dz^2} - \frac{d}{dz}\left(N\frac{dw}{dz}\right) - kw + k_G\frac{d^2w}{dz^2} = 0 \tag{5}$$

Equilibrium Equation (5) and constitutive Equation (4) and boundary conditions form the field equations. Field equations can be written in operator form as;

$$\boldsymbol{P}(\boldsymbol{u}) - \boldsymbol{f} = \boldsymbol{0} \tag{6}$$

where operator $\boldsymbol{P}$ corresponding to the field equations;

$$\begin{bmatrix} -N\frac{d^2}{dz^2}+k_G\frac{d^2}{dz^2}-k & \frac{d^2}{dz^2} & 0 & 0 \\ \frac{d^2}{dz^2} & \frac{1}{EI} & 0 & 0 \\ 0 & 0 & 1 & 0 \\ 0 & 0 & 0 & 1 \end{bmatrix} \begin{bmatrix} w \\ M \\ \varepsilon \\ \sigma \end{bmatrix} - \begin{bmatrix} 0 \\ 0 \\ \hat{\varepsilon} \\ \hat{\sigma} \end{bmatrix} = 0 \quad (7)$$

As it is known, if **P(u)** is potential, then there exists a functional I(**u**) whose gradient is the operator **P(u)**, which is given;

$$I(\boldsymbol{u}) = \int_0^1 \langle \boldsymbol{P}(\boldsymbol{u}_0 + \tau(\boldsymbol{u}-\boldsymbol{u}_0)), \boldsymbol{u}-\boldsymbol{u}_0 \rangle d\tau + \mathrm{K}_0 \quad (8)$$

Here, $K_0 = K(\boldsymbol{u}_0)$ and τ are real parameters and generally they are considered as $K_0 = 0, \boldsymbol{u}_0 = 0$. To examine whether an operator **P(u)** is potential or not, we have;

$$\langle d\boldsymbol{P}(\boldsymbol{u};\boldsymbol{\eta}), \boldsymbol{\zeta} \rangle = \langle d\boldsymbol{P}(\boldsymbol{u};\boldsymbol{\zeta}), \boldsymbol{\eta} \rangle \quad (9)$$

that is, the bilinear functional $\langle d\boldsymbol{P}(\boldsymbol{u};\boldsymbol{\eta}), \boldsymbol{\zeta} \rangle$ must be symmetric in $\boldsymbol{\eta}$ and $\boldsymbol{\zeta}$ for each **u**. This expression is a necessary and sufficient condition that **P** be potential.

In the expression above, $d\boldsymbol{P}(\boldsymbol{u};\boldsymbol{\eta})$ and $d\boldsymbol{P}(\boldsymbol{u};\boldsymbol{\zeta})$ are the Gâteaux differentials of operator **P(u)** in the direction $\boldsymbol{\eta}$ and $\boldsymbol{\zeta}$, respectively, and the Gâteaux differential of the operator $\boldsymbol{P}(\boldsymbol{u}): S \subset U \to V$ in the direction of $\boldsymbol{\eta} \in U$ at $u \in U$ is defined as;

$$d\boldsymbol{P}(\boldsymbol{u};\boldsymbol{\eta}) = \lim_{\tau \to 0} \frac{1}{\tau} [\boldsymbol{P}(\boldsymbol{u}+\tau\boldsymbol{\eta}) - \boldsymbol{P}(\boldsymbol{u})] \quad (10)$$

$\boldsymbol{\eta}$ being a fixed nonzero element of the domain [14]. Considering Equation (7) and after some mathematical operations, the functional can be obtained as follows;

$$I\left(\underset{\sim}{u}\right) = -\langle \frac{dM}{dz}, \frac{dw}{dz} \rangle + \frac{1}{2}\langle N\frac{dw}{dz}\frac{dw}{dz} \rangle - \frac{1}{2}\langle kw, w \rangle - \frac{1}{2}\langle k_G\frac{dw}{dz}, \frac{dw}{dz} \rangle + \frac{1}{2}\langle \frac{M}{EI}, M \rangle + \langle (w-\widehat{w}, \left[\frac{dM}{dz} - N\frac{dw}{dz} + k_G\frac{dw}{dz}\right] \rangle_\varepsilon + \langle \frac{d\widehat{w}}{dz}, M \rangle_\varepsilon + \langle \widehat{Q}, w \rangle_\sigma + \langle \left(M-\widehat{M}\right), \frac{dw}{dz} \rangle_\sigma \quad (11)$$

3. EXAMPLES

Numerical examples are presented to show the performance of the obtained functional for beams with varying flexural rigidity resting on elastic foundations. A code was implemented to obtain numerical results for critical buckling load. The variation of the moment of inertia is represented in Equation (12). In this equation, m values determine the varying shape of the beams. In this equation, *b* is the length of the beams, *u* is the varying length of the beams and *m* is the varying parameter which indicates the varying moment of inertia functions for the beams.

$$I = I_0\left(1-\frac{u}{b}\right)^m \quad (12)$$

Beams with varying flexural rigidity on Winkler and Pasternak elastic foundations are tested separately in this study. Fixed-free end, pinned-pinned, fixed-pinned, fixed-fixed support types are investigated for obtaining critical buckling load P_{cr}. The α values is shown in Equation (13) are obtained for varying flexural rigidity beams resting on elastic foundations. EI_0 is the initial flexural rigidity of the beams on the elastic foundation.

$$P_{cr} = \alpha\frac{EI_0}{L^2} \quad (13)$$

In this study, the m values are chosen and tested m=0, m=1/2, m=1, m=3. The α values for the beams are determined for support types fixed-free end (F-FE), pinned-pinned (P-P), fixed-pinned (F-P) and fixed-fixed (F-F). The results are shown for m=0 in Table 1. The values for obtaining k_W and k_G are equal to the zero are compatible with the exact values for beams with these support types. The values between the parentheses indicates the exact values for the analyses.

Table 5. α values for m=0

Foundation parameters		**Support Type**			
K_W	**K_G**	**F-FE**	**P-P**	**F-P**	**F-F**
0	0	2,467 (2,467)	9,870 (9,870)	20,191 (20,142)	39,479 (39,478)
	50	52,467	59,870	70,191	89,479
100	0	11,996	20,002	28,307	47,007

	50	61,996	70,002	78,307	97,007
10000	0	100,014	201,407	208,984	233,823
	50	150,014	251,407	258,984	283,823

The results are shown for m=1/2 in Table 2.

Table 2. α values for m=1/2

Foundation parameters		**Support Type**			
K_W	**K_G**	**F-FE**	**P-P**	**F-P**	**F-F**
0	0	1,959 (1,959)	6,401	12,419	21,640
	50	51,959	56,401	62,419	71,640
100	0	8,268	16,166	19,202	29,196
	50	58,268	66,166	69,202	79,196
10000	0	56,788	133,138	133,148	194,341
	50	106,788	183,138	183,148	244,341

The results are shown for m=1 in Table 3.

Table 3. α values for m=1

Foundation parameters		**Support Type**			
K_W	**K_G**	**F-FE**	**P-P**	**F-P**	**F-F**
0	0	1,446 (1,446)	3,673	6,623	12,893
	50	51,446	53,673	56,623	62,893
100	0	4,940	11,129	11,336	19,696
	50	54,940	61,129	61,336	69,696
10000	0	35,233	85,036	85,064	153,044
	50	85,233	135,036	135,064	203,044

The results are shown for m=3 in Table 4.

Table 4. α values for m=3

Foundation parameters		**Support Type**			
K_W	**K_G**	**F-FE**	**P-P**	**F-P**	**F-F**
0	0	0,038 (0,000)	0,041	0,080	0,079
	50	50,038	50,041	50,080	50,079
100	0	0,097	0,237	0,237	0,231
	50	50,097	50,237	50,237	50,231
10000	0	0,238	0,654	0,654	2,116
	50	50,238	50,654	50,654	52,116

Results were compared with the exact solutions and it was seen that the results obtained in this analytical study are compatible with exact solutions.

4. CONCLUSION

In this study, a finite element formulation is presented for buckling analysis of beams with varying flexural rigidity resting on Winkler and Pasternak elastic foundations. Mixed finite element method is used with potential energy concept. Critical buckling loads of the beams are determined based on mixed finite element formulation. A functional is obtained with using Gâteaux differential. It is seen that, the functionals obtained from this study are very robust for buckling analyze of beams resting on elastic foundations. Functionals obtained from this study are very practical for buckling analysis of beams with varying flexural rigidity on elastic foundations. Results were compared with the exact solutions and it was seen that the results obtained in this analytical study are

compatible with exact solutions. The critical load with various flexural rigidity beams are less than the critical load of a beam having constant flexural rigidity.

REFERENCES

[1]. L. Euler, "Additamentum I de curvis elasticis, methodus inveniendi lineas curvas maximi minimiui proprietate gaudentes," *Bousquent, Lausanne, in Opera Omnia I.*, vol. 24, pp. 231-297, 1744.
[2]. S.P. Timoshenko and J.M. Gere, *Theory of Elastic Stability*, 2nd ed., New York, McGraw-Hill, 1961.
[3]. J. Ratzersdorier, *Die Knickfestigkeit von Stäben und Stabwerken*, Wien, Springer-Verlag, 1936.
[4]. M. Eisenberger, J. Clastornik, "Vibrations and buckling of a beam on variable winkler elastic foundation," *J. Sound Vib.*, vol. 115(2), pp. 233-241, 1987.
[5]. W.Q. Chen, C.F. Lu, Z.G. Bian, "A mix method for bending and free vibration of beams resting on a Pasternak elastic foundation," *Appl. Math Model*, vol. 28, pp. 877-900. 2004.
[6]. A.N. Dogruoglu, M.H. Omurtag, "Stability Analysis of Composite-plate Foundation Interaction by Mixed FEM," *Journal of Engineering Mechanics, ASCE*, vol. 126(9), pp. 928-936, 2000.
[7]. Y. Huang and X.F. Li, "Buckling Analysis of Nonuniform and Axially Graded Columns with Varying Flexural Rigidity," *J. Eng. Mech.*, vol. 137(1), pp. 73-81, 2011.
[8]. M. Eisenberger, "Buckling loads for variable cross-section members with variable axial forces," *Int. J. Solids Struct.*, vol. 27, pp. 135-143, 1991.
[9]. S.M. Darbandi, R.D. Firouz-Abadi and H. Haddadpour, "Buckling of variable section columns under axial loading," *J. Eng. Mech.*, vol. 136, pp. 472–476, 2010.
[10]. W. Smith, "Analytical solutions for tapered column buckling," *Comput. Struct.*, vol. 28, pp. 677-681, 1988.
[11]. I. Elishakoff and O. Rollot, "New closed-form solution for buckling of a variable stiffness column by Mathematica," *J. Sound Vib.*, vol. 224, pp. 172-182, 1999.
[12]. Y. Zhang, Y. Liu, P. Chen, K.D. Murphy, "Buckling loads and eigen frequencies of a braced beam resting on an elastic foundation," *Acta Mechanica Solida Sinica*, vol. 24(6), Dec. 2011.
[13]. A.G. Razaqpur, "Stiffness of beam-columns on elastic foundation with exact shape functions," *Comp. Struct.*, vol. 24(5) pp. 813-819, 1986.
[14]. J.T. Oden and J.N. Reddy, *Variational Method in Theoretical Mechanics*, 2nd ed., Berlin, Springer-Verlag, 1983.

ICENS 4TH INTERNATIONAL CONFERENCE ON ENGINEERING AND NATURAL SCIENCE
2-6 May 2018 KIEV UKRAINE

Stability Analysis of Beams Subjected to Distinct Loading Types on Elastic Foundation

Ali Nuri Dogruoglu[1], Sedat Komurcu[2]

Abstract

The stability analysis of beams is a significant problem for designing structures. In this study critical buckling loads of beams subjected to different loading types on elastic foundations are determined. Bernoulli-Euler beam theory is used for investigation of beams in this study. The functionals are obtained with using mixed finite element formulation. Gâteaux differential is used for formulation of the functionals. Critical buckling loads are obtained for beams on Winkler and Pasternak foundation elastic foundation separately. For this purpose, only axial force, only uniform distributed loading and combination of axial point loading and uniform distributed loading are analyzed. Various support types are investigated to obtain critical buckling load of beams. It is seen that, there are certain distinctions between loading types in terms of support types. The relationship of the value of critical buckling load between fixed-free and pinned-pinned supports, pinned-pinned and fixed-pinned supports and fixed-pinned and fixed-fixed supports are analyzed in terms of only point load, only distributed load and combined point and distributed load separately. It is seen that, the functionals obtained from this study are robust for buckling analyze of beams subjected to distinct loading types on elastic foundations.

Keywords: Beam, Loading effect, Mixed formulation, Stability

1. INTRODUCTION

Buckling analysis of beams resting on an elastic foundation is encountered in many areas especially with various applications, construction and mechanical engineering, aircraft-space industry, gas transmission lines, nuclear power plants, railway applications. The stability behavior of beams with varying flexural rigidity on elastic foundations are analyzed. Two distinct type elastic foundations namely, Winkler and Pasternak foundations are studied for stability analysis of in plane beams with varying flexural rigidity. Winkler foundations are used where vertical displacement and contact pressure are assumed to be proportional. Pasternak foundations are two parameter foundations and they are used when the assumptions made by Winkler foundations prove to be insufficient. Finite element analysis is a robust method to investigate the behavior of structures. In this study, the analysis of beams resting on elastic foundations are analyzed via mixed finite element formulation. Thus, critical buckling loads are calculated with a functional derived via mixed finite element formulation with potential energy concept for the bifurcation type buckling problem.

Buckling is the sudden instability of structural members subjected to axial compression. There are many studies have been done about buckling analysis of beams. Theory of buckling begins with the studies by Leonhard Euler [1]. The problem of beams resting on an elastic foundation are studied by many researchers in the literature. Elastic foundations are commonly encountered structures for many engineering areas. The beam problem resting on the elastic foundation has become one of the most interesting topics for researchers and theorists. Significant books were written for a comprehensive analyzing of stability of structures [2], [3]. There are many studies about beams resting on the elastic foundation by various methods for buckling analyses are given in the literature. Buckling analysis of beams resting on an elastic foundation were studied by many researchers [4]-[13].

In this study, critical buckling load is calculated for beams via mixed finite element method with formulation of a functional. Detailed analyzing of the interaction between the beams and elastic foundation for distinct loading types are presented.

[1] *Corresponding author: Istanbul Technical University, Department of Civil Engineering, 34469, Sariyer/Istanbul, Turkey.* dogruogl@itu.edu.tr

[2] *Istanbul Technical University, Department of Civil Engineering, 34469, Sariyer/Istanbul, Turkey.* komurcus@itu.edu.tr

2. FORMULATION

Various approaches have studied to obtain reliable formulations to analyze buckling of beams. In this study, buckling analysis of Bernoulli-Euler Beams resting on elastic foundations are presented. The analyzed buckling problem is a bifurcation of the static equilibrium. Beams are considered as members resting on elastic foundation which subjected to axial compressive loads. Beams are made of homogeneous and isotropic material. The mixed finite element formulation is used to analyze of beams with distinct loadings resting on elastic foundations. Equilibrium equations for the formulation of bifurcation type buckling problem. A representation of loadings is shown in Figure 1.

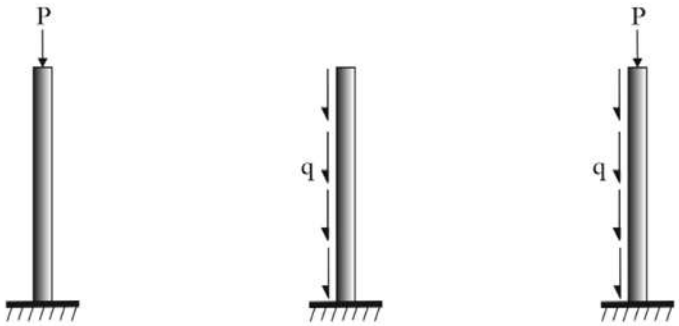

Figure 9. Loadings for stability analyzes

The normal force distributions on the beams for only axial loading, only distributed loading and the combination of axial loading and distributed loading are shown in Figure 2.

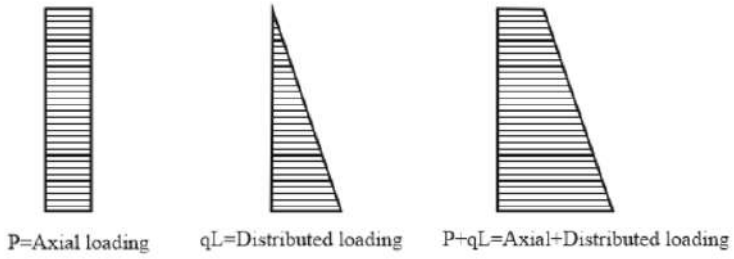

Figure 2. Normal for distributions for distinct type loadings

The mixed finite element formulation is used to analyze of beams resting on elastic foundations. A schematic representation of a beam is shown in Figure 3.

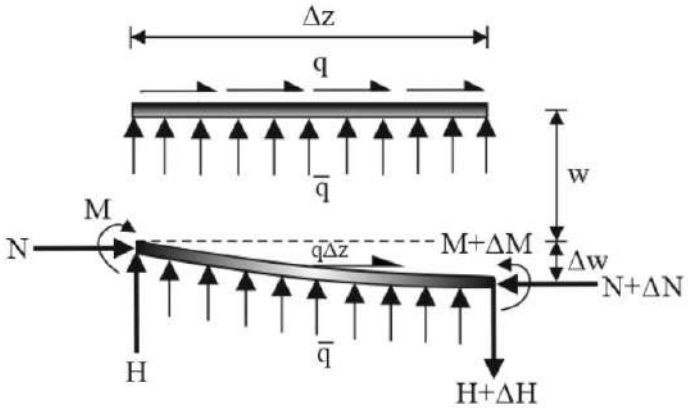

Figure 3. Schematic representation of beams on elastic foundation

Equilibrium equations are used for buckling analyses of beams as shown in Equations (1-3). In these equations N, H and M represents normal force, vertical force and moments, respectively. $\bar{q}$ represents the foundation effect

and q the distributed load value on the beams. k_W and k_G are Winkler and Pasternak foundation constants, respectively.

$$\frac{dN}{dz} = q \tag{1}$$

$$\frac{dH}{dz} = \bar{q} = kw - k_G \frac{d^2w}{dz^2} \tag{2}$$

$$\frac{dM}{dz} - N\frac{dw}{dz} - H = 0 \tag{3}$$

Constitutive equation for the relation between moment M and deflection w is shown in equation (4). EI is the flexural rigidity of the beams.

$$\frac{M}{EI} = -\frac{d^2w}{dz^2} \tag{4}$$

If the Equation (3) is derived according to "z" and the Equation (2) is used, Equation (5) is obtained as follows,

$$\frac{d^2M}{dz^2} - \frac{d}{dz}\left(N\frac{dw}{dz}\right) - kw + k_G\frac{d^2w}{dz^2} = 0 \tag{5}$$

Equilibrium Equation (5) and constitutive Equation (4) and boundary conditions form the field equations. Field equations can be written in operator form as;

$$\boldsymbol{P}(\boldsymbol{u}) - \boldsymbol{f} = \boldsymbol{0} \tag{6}$$

where operator $\boldsymbol{P}$ corresponding to the field equations;

$$\begin{bmatrix} -N\frac{d^2}{dz^2} + k_G\frac{d^2}{dz^2} - k & \frac{d^2}{dz^2} & 0 & 0 \\ \frac{d^2}{dz^2} & \frac{1}{EI} & 0 & 0 \\ 0 & 0 & 1 & 0 \\ 0 & 0 & 0 & 1 \end{bmatrix} \begin{bmatrix} w \\ M \\ \varepsilon \\ \sigma \end{bmatrix} - \begin{bmatrix} 0 \\ 0 \\ \hat{\varepsilon} \\ \hat{\sigma} \end{bmatrix} = 0 \tag{7}$$

As it is known, if **P(u)** is potential, then there exists a functional I(**u**) whose gradient is the operator **P(u)**, which is given;

$$I(\boldsymbol{u}) = \int_0^1 \langle \boldsymbol{P}(\boldsymbol{u}_0 + \tau(\boldsymbol{u} - \boldsymbol{u}_0)), \boldsymbol{u} - \boldsymbol{u}_0 \rangle d\tau + \mathrm{K}_0 \tag{8}$$

Here, $K_0 = K(\boldsymbol{u}_0)$ and τ are real parameters and generally they are considered as $K_0 = 0, \boldsymbol{u}_0 = 0$. To examine whether an operator **P(u)** is potential or not, we have

$$\langle d\boldsymbol{P}(\boldsymbol{u};\boldsymbol{\eta}), \boldsymbol{\zeta} \rangle = \langle d\boldsymbol{P}(\boldsymbol{u};\boldsymbol{\zeta}), \boldsymbol{\eta} \rangle \tag{9}$$

that is, the bilinear functional $\langle d\boldsymbol{P}(\boldsymbol{u};\boldsymbol{\eta}), \boldsymbol{\zeta} \rangle$ must be symmetric in $\boldsymbol{\eta}$ and $\boldsymbol{\zeta}$ for each **u**. This expression is a necessary and sufficient condition that **P** be potential.

In the expression above, $d\boldsymbol{P}(\boldsymbol{u};\boldsymbol{\eta})$ and $d\boldsymbol{P}(\boldsymbol{u};\boldsymbol{\zeta})$ are the Gâteaux differentials of operator **P(u)** in the direction $\boldsymbol{\eta}$ and $\boldsymbol{\zeta}$, respectively, and the Gâteaux differential of the operator $\boldsymbol{P}(\boldsymbol{u})$: $S \subset U \to V$ in the direction of $\boldsymbol{\eta} \in U$ at $u \in U$ is defined as;

$$d\boldsymbol{P}(\boldsymbol{u};\boldsymbol{\eta}) = \lim_{\tau \to 0} \frac{1}{\tau}[\boldsymbol{P}(\boldsymbol{u} + \tau\boldsymbol{\eta}) - \boldsymbol{P}(\boldsymbol{u})] \tag{10}$$

$\boldsymbol{\eta}$ being a fixed nonzero element of the domain [14]. Considering Equation (7) and after some mathematical operations, the functional can be obtained as follows;

$$I\left(\underset{\sim}{u}\right) = -\langle\frac{dM}{dz}, \frac{dw}{dz}\rangle + \frac{1}{2}\langle N\frac{dw}{dz}\frac{dw}{dz}\rangle - \frac{1}{2}\langle kw, w\rangle - \frac{1}{2}\langle k_G\frac{dw}{dz}, \frac{dw}{dz}\rangle + \frac{1}{2}\langle\frac{M}{EI}, M\rangle + \langle(w - \widehat{w}, \left[\frac{dM}{dz} - N\frac{dw}{dz} + k_G\frac{dw}{dz}\right]\rangle_\varepsilon + \langle\frac{d\widehat{w}}{dz}, M\rangle_\varepsilon + \langle\widehat{Q}, w\rangle_\sigma + \langle\left(M - \widehat{M}\right), \frac{dw}{dz}\rangle_\sigma \tag{11}$$

3. EXAMPLES

Numerical examples are presented to show the performance of the obtained functional for beams with distinct loading types on elastic foundations. A code was implemented to obtain numerical results for critical buckling load. The variation of the loadings is indicated in Equation (12), Equation (13) and Equation (14). In this equation,

Q values determine the distinct loading values. The *q* values represent the distributed load values acting on beams on elastic foundations.

$$Q_1 = \frac{q}{2L}(z-L)^2 \tag{12}$$

$$Q_2 = \frac{q}{2L}(L^2 - z^2) \tag{13}$$

$$Q_3 = 2q\left(1-\frac{z}{L}\right)z \tag{14}$$

Fixed-free end, pinned-pinned, fixed-pinned, fixed-fixed support types are investigated for obtaining critical buckling load. The α value is shown in Equation (15) is obtained for beams resting on elastic foundations. P_{cr} is the critical buckling load for beams resting on elastic foundations. *EI* and *L* presents the flexural rigidity of the beams and length of the beams respectively.

$$P_{cr} = \alpha\frac{EI}{L^2} \tag{15}$$

In this study, the loading values *P*, Q_1, Q_2, Q_3 are analysed. The α values for the beams are determined for support types fixed-free end (F-FE), pinned-pinned (P-P), fixed-pinned (F-P) and fixed-fixed (F-F). The results are shown for only point load *P* load is shown in Table 1. The values for obtaining k_W and k_G are equal to the zero are compatible with the exact values for beams with these support types. The values between the parentheses indicates the exact values for the analyses.

Table 6. α values for P loading

Foundation parameters		**Support Type**			
K_W	**K_G**	**F-FE**	**P-P**	**F-P**	**F-F**
0	0	2,467 (2,467)	9,870 (9,870)	20,191(20,142)	39,479 (39,478)
	50	52,467	59,870	70,191	89,479
100	0	11,996	20,002	28,307	47,007
	50	61,996	70,002	78,307	97,007
10000	0	100,014	201,407	208,984	233,823
	50	150,014	251,407	258,984	283,823

The results are shown for Q_1 in Table 2.

Table 2. α values for Q_1 loading

Foundation parameters		**Support Type**			
K_W	**K_G**	**F-FE**	**P-P**	**F-P**	**F-F**
0	0	2,315	8,255	18,238	33,923
	50	52,315	58,255	68,238	83,923
100	0	11,723	16,643	25,718	40,393
	50	61,723	66,643	75,718	90,393
10000	0	99,394	160,354	190,456	200,421
	50	149,394	210,354	240,456	250,421

The results are shown for Q_2 in Table 3.

Table 3. α values for Q_2 loading

Foundation parameters		**Support Type**			
K_W	**K_G**	**F-FE**	**P-P**	**F-P**	**F-F**
0	0	2,000	7,526	16,217	29,405
	50	52,000	57,526	66,217	79,405
100	0	10,449	15,188	22,845	34,963
	50	60,449	65,188	72,845	84,963
10000	0	93,408	144,263	163,324	170,753
	50	143,408	194,263	213,324	220,753

The results are shown for Q_3 in Table 4.

Table 4. α values for Q_3 loading

Foundation parameters		Support Type			
K_W	K_G	F-FE	P-P	F-P	F-F
0	0	1,849	8,000	15,827	29,016
	50	51,849	58,000	65,827	79,016
100	0	9,600	16,184	22,176	34,432
	50	59,600	66,184	72,176	84,432
10000	0	88,545	149,831	154,495	164,676
	50	138,545	199,831	204,495	214,676

Results were compared with the exact solutions and it was seen that the results obtained in this analytical study are compatible with exact solutions.

4. CONCLUSION

In this study, a finite element formulation is presented for buckling analysis of beams with distinct loading types resting on Winkler and Pasternak elastic foundations. Mixed finite element method is used with potential energy concept. Critical buckling loads of the beams are determined based on mixed finite element formulation. A functional is obtained with using Gâteaux differential. It is seen that, the functionals obtained from this study are very robust for buckling analyze of beams resting on elastic foundations. Functionals obtained from this study are very practical for buckling analysis of beams on elastic foundations. Results were compared with the exact solutions and it was seen that the results obtained in this analytical study are compatible with exact solutions. The effects of distinct loading types for beams resting on elastic foundations are analyzed.

REFERENCES

[1]. L. Euler, "Additamentum I de curvis elasticis, methodus inveniendi lineas curvas maximi minimiui proprietate gaudentes," *Bousquent, Lausanne, in Opera Omnia I.*, vol. 24, pp. 231-297, 1744.
[2]. S.P. Timoshenko and J.M. Gere, *Theory of Elastic Stability*, 2nd ed., New York, McGraw-Hill, 1961.
[3]. J. Ratzersdorier, *Die Knickfestigkeit von Stäben und Stabwerken*, Wien, Springer-Verlag, 1936.
[4]. A.D. Kerr, "Elastic and viscoelastic foundation models," *J. Appl. Mech.*, vol. 31, pp. 491-498, 1964.
[5]. B.Y. Ting, "Finite beams on elastic foundation with restraints," *J. St. Div. ASCE*, vol. 108, pp. 611-621, 1982.
[6]. M. Lentini, "Numerical solution of the beam equation with nonuniform foundation coefficient," *J. App. Mech. ASME*, vol. 46, pp. 901-904, 1979.
[7]. A.D. Rosa Maria, "Stability and dynamics of beams on winkler elastic foundations," *Earth. Eng. Struct. Dyn.*, vol. 18, pp. 377-388, 1989.
[8]. M. Eisenberger, J. Clastornik, "Vibrations and buckling of a beam on variable winkler elastic foundation," *J. Sound Vib.*, vol. 115(2), pp. 233-241, 1987.
[9]. W.Q. Chen, C.F. Lu, Z.G. Bian, "A mix method for bending and free vibration of beams resting on a Pasternak elastic foundation," *Appl. Math Model*, vol. 28, pp. 877-900. 2004.
[10]. A.N. Dogruoglu, M.H. Omurtag, "Stability Analysis of Composite-plate Foundation Interaction by Mixed FEM," *Journal of Engineering Mechanics, ASCE*, vol. 126(9), pp. 928-936, 2000.
[11]. Y. Huang and Q.Z. Luo, "A simple method to determine the critical buckling loads for axially inhomogeneous beams with elastic restraint," *Computers and Mathematics with Applications*, vol. 61, pp. 2510-2517, 2011.
[12]. C.K. Rao, L.B. Rao, "Torsional post-buckling of thin-walled open section clamped beam supported on Winkler-Pasternak foundation," *Thin-Walled Structures*, vol. 116, pp. 320-325, 2017.
[13]. H. Deng, K. Chen, W. Cheng, S. Zhao, "Vibration and buckling analysis of double-functionally graded Timoshenko beam system on Winkler-Pasternak elastic foundation," *Composite Structures*, vol. 160, pp. 152-168, 2017.
[14]. J.T. Oden and J.N. Reddy, *Variational Method in Theoretical Mechanics*, 2nd ed., Berlin, Springer-Verlag, 1983.

ICENS 4TH INTERNATIONAL CONFERENCE ON ENGINEERING AND NATURAL SCIENCE
2-6 May 2018 KIEV UKRAINE

Investigation of Optimum Longitudinal Transport Limit in Vehicles Fighting Against Snow

Metin Kaynakli[1], Dursun Bakir[2], M .Mustafa Yaylak [3],Mustafa Ulker[4] Ali Emre Ulu[5]

Abstract

There is no specific planning in the fight against snow in our country. Therefore, it is costly in areas where snow is heavy. In this study, the limit of the economic transport of the Bitlis-Rahva-Tatvan highway snow fight has been examined. According to economic limit transportation method; dozer is used between 0 and 100 meters, scraper is used between 100 to 1000 meters and trucks are used if the distance is more than 1000 meters. In this study, dozer, grader and trucks are used for the distances 0-100, 100-1000 and more than 1000, respectively. The mass distribution diagram of the vehicles used in the fight against snow is shown according to the specified distances. In the fight against the snow, the limit of transport in the longitudinal direction has been examined and it has been seen that the efforts to fight snow with minimum cost have been made.

Keywords: Transport cost; Snow load; Highway

1. INTRODUCTION

Since the terrestrial climate is dominant in our country, the efforts to fighting snow on the roads have always been a problem for us. The problem is not only the road closures, but also the transportation. The size of the event is considerable when the accidents, material damage, injuries and loss of lives considered due to snow and ice on the road. However, snow and icing which cause very big problems can be prevented by taking very small precautions. The important thing here is that while it avoids traffic problems, it also does not bring any other problems. Snow water brings a highly disturbing effect on the covered and uncovered road surfaces. When the snow is not taken in time from the coating, the melting snow waters adversely affect the adherence of the bitumen aggregate, and the deterioration that starts with the bitumen decomposition from the aggregate forms aggregate breaks and pits from the asphalt. Many basic and coating defects encountered in the bituminous coatings in the first months of spring season occur due to the fact that snow is not cleaned directly on the pavement surface in a timely and rapid manner [1].

The cleanliness of state roads and motorways in fighting against snow is very important. Since these roads that are heavily used connect cities together, first of all, it is necessary to maximize travel so that safety of life can be provided.

There is no regular planning in the snow fighting in our country. In areas where snowfall is intense, it is considered that the presence of snow mass on the road routes according to the average snow height taken from meteorological sources and the presence of economic transport limit will contribute to the economy in a great way. There are many unplanned methods to fight against the snow. In this study, snow transport and distribution conditions are examined. In this context, the optimum longitudinal transport limit has been examined in vehicles which play an active role in the struggle with the snow.

[1] *Corresponding author: Bitlis Eren University, Vocational School of Technical Sciences, 13000, Bitlis, Turkey. mkaynakli@beu.edu.tr*

[2]*Firat University, Department of Civil Engineering, dursunbakir23@gmail.com*

[3]*Bitlis Eren University, Vocational School of Technical Sciences, mmyaylak@beu.edu.tr*

[4] *Bitlis Eren University, Vocational School of Technical Sciences, 13000, Bitlis, Turkey. mulker@beu.edu.tr*

[5] *Bitlis Eren University, Department of Civil Engineering, aeulu@beu.edu.tr*

2. METHOD

In snow clearing work, the blades must work immediately when the snow accumulating on the road reaches a sufficient height so that the blades can work efficiently. When the snow height exceeds an average of 5 cm, there is a danger for the journey. The method of struggle varies according to where the snow is [2].

In the case of snowfall between 0-20 cm in the fighting snow, salting work is being done. However, since the areas with a snowfall of 20 cm are under heavy snowfall, heavy equipment such as dozers, loaders, graders are used to clean the snow covering the roads. Trucks are used as transport vehicles in the transport of snow masses. In areas under this heavy snowfall, the dozer carries the snow masses to the bank of the road. Grader removes the remaining snow accumulation on the way and cleans the path from the snow. After reaching the opening lanes, the bank is stored in a suitable area nearest to the administration by loading the accumulated stack of snow on the trucks with the loader. Cleaning the banquets is also very important. Because if a continuation of the rainfall, an area will be provided where the rainfall will be accumulated. It is very important that the snow is not left in the banquets. When the snow is left here, the water may leak from the edge of the coating to the bottom, causing the base to soften and leave the asphalt layer unsupported, causing cracks, and localized migrations.

In this study, Rahova region under heavy snowfall in the winter was taken into consideration. As a case study, the road between Bitlis and Tatvan has been examined. The length of this highway which is taken into consideration is 8,94 km. The width of the road is 16 m.

Figure 1. Calculated Distance

The amount of precipitation during the winter months of Bitlis Rahva region was evaluated according to the data obtained from the Bitlis meteorological branch office According to this, the distribution of the maximum height of snowfall according to years is examined and the average height is taken into account. (Table 1)

The results of PPCC plots tests for three different distribution model were shown in the Figures 2-4. As seen in these figures the maximum probably plot correlation coefficients (PPCC=R) of log-normal, Gumbel and Weibull distributions are estimated as 0.989, 0.986 and 0.990 respectively [3].

***Table 1**. The statistical data used in the study and the results of cumulative distribution*

17207-17208 (Bitlis Meteo.-Bitlis OMGI)					Lognormal Dist.		Gumbel Dist.		Weibull Dipt.	
i	Year	h (cm) Max. Snow Depth	ln(h)	P_i	Φ^{-1}	F(x)= CDF	$-\ln(-\ln(P_i))$	F(X)=CDF	$\ln(-\ln(1-P_i))$	F(x)=CDF
1	1999	34	3.526	0.029	3.707	0.013	-1.268	0.026	-3.541	0.046
2	1984	40	3.689	0.057	3.885	0.026	-1.052	0.039	-2.833	0.063
3	2010	45	3.807	0.086	4.001	0.043	-0.899	0.052	-2.412	0.080
4	1989	60	4.094	0.114	4.091	0.115	-0.774	0.108	-2.109	0.140
5	1998	61	4.111	0.143	4.166	0.121	-0.666	0.112	-1.870	0.144
6	1981	67	4.205	0.171	4.232	0.159	-0.567	0.142	-1.671	0.172
7	1997	70	4.248	0.200	4.290	0.179	-0.476	0.158	-1.500	0.187
8	1996	79	4.369	0.229	4.344	0.243	-0.389	0.211	-1.349	0.233
9	1990	85	4.443	0.257	4.395	0.286	-0.306	0.249	-1.213	0.265
10	2008	85	4.443	0.286	4.442	0.286	-0.225	0.249	-1.089	0.265
11	1980	86	4.454	0.314	4.487	0.293	-0.146	0.256	-0.975	0.271
12	2011	100	4.605	0.343	4.531	0.394	-0.068	0.351	-0.868	0.350
13	2007	102	4.625	0.371	4.573	0.408	0.010	0.365	-0.767	0.361
14	2009	104	4.644	0.400	4.614	0.422	0.087	0.379	-0.672	0.373
15	2001	107	4.673	0.429	4.654	0.442	0.166	0.400	-0.581	0.390
16	2002	110	4.700	0.457	4.694	0.462	0.245	0.420	-0.493	0.408
17	1995	113	4.727	0.486	4.734	0.481	0.326	0.441	-0.408	0.425
18	2005	115	4.745	0.514	4.773	0.494	0.408	0.455	-0.326	0.437
19	1986	118	4.771	0.543	4.812	0.513	0.493	0.475	-0.245	0.454
20	1994	130	4.868	0.571	4.852	0.582	0.581	0.552	-0.166	0.522
21	2004	140	4.942	0.600	4.893	0.634	0.672	0.612	-0.087	0.577
22	1991	145	4.977	0.629	4.934	0.658	0.767	0.639	-0.010	0.603
23	1988	152	5.024	0.657	4.976	0.689	0.868	0.676	0.068	0.639
24	1983	155	5.043	0.686	5.019	0.701	0.975	0.690	0.146	0.654
25	2000	161	5.081	0.714	5.064	0.725	1.089	0.718	0.225	0.682
26	2003	170	5.136	0.743	5.112	0.757	1.213	0.757	0.306	0.722
27	1985	200	5.298	0.771	5.162	0.839	1.349	0.854	0.389	0.833
28	2006	212	5.357	0.800	5.216	0.864	1.500	0.881	0.476	0.867
29	1982	217	5.380	0.829	5.275	0.873	1.671	0.892	0.567	0.880
30	1993	235	5.460	0.857	5.340	0.900	1.870	0.922	0.666	0.918
31	1987	246	5.505	0.886	5.415	0.914	2.109	0.936	0.774	0.936
32	2012	250	5.521	0.914	5.505	0.919	2.412	0.940	0.899	0.941
33	2013	250	5.521	0.943	5.622	0.919	2.833	0.940	1.052	0.941
34	1992	275	5.617	0.971	5.799	0.942	3.541	0.962	1.268	0.968

The storage area where the snow accumulates is the place where the transportation distance determined by the administration is evaluated optimally. These warehouse areas were identified as warehouse 1, warehouse 2 and warehouse 3, which are close to the work areas and which are not vulnerable to the collection of snow piles.

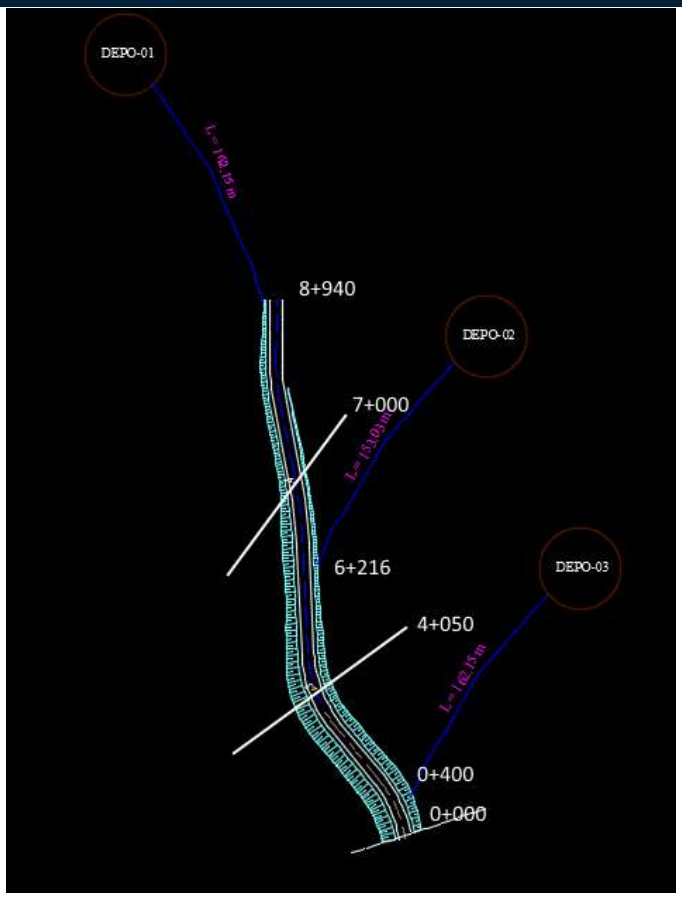

Figure 2. Warehouse locations

2.1. HEAVY EQUIPMENTS USED IN THE SNOW FIGHTING

Economical transport limits of snow transport vehicles:

- Between 0-100 m is dozer.

Figure 3. Dozer Cleans the Roads

- Between 100-1000 m is Greyder

Figure 4. Greyder Cleans the Road

- Distance over 1000m is truck.

Figure 5. Truck with Blade

2.2. DETERMINING THE OPTIMAL CONVENIENT TRANSPORT

As a result of the data obtained from the Bitlis meteorology branch office, the average profit height according to years is 1.33 m the gross mass of the road is calculated as m^3, taking the platform width as 16 m and the length as 8940 m. (Table 2)

***Table 2**. Volume of Snow Mass*

Average Snow Height (m)	Platform Width (m)	Length (m)	Accumulated Snow Volume (m^3)
1,33	16	8940	190243,2

Taşınan Kesim		Taşınan	Taşınan malzeme		Depo Serv.	Gövdede	Serv. Yol.	Toplam	Taşıma Momenti	
Başlangıç	Bitiş	Depo No		Ağ.Mrk.	Yolu Ayrımı	Taş. Mes.	Taş. Mes.	Taşıma	l ≤ 10.0000	l > 10.000
Km	Km			(Km)	(Km)	(m)	(m)	(m)	(m4)	(m4)
				(e)	(f)	(g = l e-f l)	(h)	(i = g+h)	(j = dx i)	(k=dx2/1000)
7+000,00	8+940,00	depo1	41283,2	4+470,00	8+940,00	4470,00	162,15	4632,15	191229974,9	
4+050,00	7+000,00	depo2	62776	4+470,00	6+216,00	1746,00	153,03	1899,03	119213507,3	
0+000,00	4+050,00	depo3	86184	4+470,00	0+400,00	4070,00	162,15	4232,15	364743615,6	
		Toplam malzeme	190243,2					A=	675187097,8	

$$\sqrt{L_{ort}} = \frac{675.187.097,760}{190.243,200} = 3549,07\ m$$

3. RESULTS

- In this study, if the snow accumulating on the Bitlis-Tatvan highway with heavy snowfall uses 3 depots, the average transportation distance is 3,549 km.
- As a result, it has been concluded that increasing the number of warehouses reduces the average transport distance, which in turn reduces transportation costs.
- This work is expected to contribute to the country's economy by reducing transportation costs, increasing road life and reducing costs to the minimum.

4. REFERENCES

[1]. Kigili, A.F. 2006.“ Karayollarinda Kar Ve Buz Mucadelesi Yonetiminde Yeni Bir Maliyet Hesabi Onerisi”, ITU Dergisi, Mimarlik Planlama Tasarim, Cilt:6, Sayi2, s.23-46.

[2] Karayollari Bakim El Kitabi, (1998), Karayollari Genel Mudurlugu, 284-296.

[3] Aydin, M.C., Isik, E., “ The Statistical Evaluation Of Ground Snow Loads In Regions Subjected To Heavy Snowfall ”

ICENS 4TH INTERNATIONAL CONFERENCE ON ENGINEERING AND NATURAL SCIENCE
2-6 May 2018 KIEV UKRAINE

Determination of the Optimum Number of the Heavy Equipment Used Regions with Heavy Snowfall

Metin Kaynakli[1], Dursun Bakir[2], M .Mustafa Yaylak [3],Mustafa Ulker[4] Ali Emre Ulu[5]

Abstract

In this study, the type and the custom of the heavy equipment to be used were determined in areas with heavy snowfall according to the average annual snowfall data from the meteorology. In the fight against snow, heavy equipment such as dozer, grader and trucks are generally used. It was aimed to determine the number of vehicles used in advance and to prevent the problems to be experienced in the future by making a plan against the snow according to the number of vehicles detected. By specifying the number and type of vehicles to be used during periods of heavy snowfall, the minimum number of vehicles and the types and the maximum efficiency in the fight against snow are targeted.

Keywords: Fight Against Snow; Heavy Equipment; Snowfall.

1. INTRODUCTION

Since the terrestrial climate is dominant in our country, the efforts to fight snow on the roads have always been a problem for us. The problem is not only the road closures, but also the transportation. The size of the event is considerable when the accidents, material damage, injuries and loss of lives considered due to snow and ice on the road. Snow cleared on the highway is accumulated in the bank of the road. Over time, these accumulations are damaging the road. When snow is not taken in time, snowing waters adversely affect the adherence of bitumen aggregate, and the deterioration that starts with bitumen decomposition from aggregate occurs as aggregate breaks and pits from asphalt. The sooner the snow is removed from the road surface, the faster the surface dries, the more obstacles mentioned above will be avoided. Due to these reasons, it is necessary to clean these snow accumulations as soon as possible and in a planned manner [1].

Snow water brings a highly disturbing effect on the covered and uncovered road surfaces. When the snow is not taken in time from the coating, the melting snow waters adversely affect the adherence of the bitumen aggregate, and the deterioration that starts with the bitumen decomposition from the aggregate forms aggregate breaks and pits from the asphalt.

[1] *Corresponding author: Bitlis Eren University, Vocational School of Technical Sciences, 13000, Bitlis, Turkey. mkaynakli@beu.edu.tr*

[2] *Firat University, Department of Civil Engineering, dursunbakir23@gmail.com*

[3] *Bitlis Eren University, Vocational School of Technical Sciences, mmyaylak@beu.edu.tr*

[4] *Bitlis Eren University, Vocational School of Technical Sciences, 13000, Bitlis, Turkey. mulker@beu.edu.tr*

[5] *Bitlis Eren University, Department of Civil Engineering, aeulu@beu.edu.tr*

2. METHOD

In snow clearing work, the blades must work immediately when the snow accumulating on the road reaches a sufficient height so that the blades can work efficiently. When the snow height exceeds an average of 5 cm, there is a danger for the journey. The method of struggle varies according to where the snow is [2].

Heavy equipment such as dozers, loaders, graders are used to clean the snow that covers the roads in areas where snow is heavy. Trucks are used as transport vehicles in the transport of snow masses. In areas under this heavy snowfall, the dozer carries the snow masses to the bank of the road. Grader removes the remaining snow accumulation on the way and cleans the path from the snow. After reaching the opening lanes, the bank is stored in a suitable area nearest to the administration by loading the accumulated stack of snow on the trucks with the loader. It is very important to clean the shoulders because the cumulative snowfall reduces the visibility of the vehicles over time and causes various accidents such as traffic accidents and road erosion.

In this study, the number of vehicles to transport the snow load accumulated on the Bitlis-Tatvan highway as soon as possible to the warehouse specified by the administration was determined. It is planned to use trucks and loaders to transport snow deposits. The length of this highway which is taken into consideration is 2,26 km. The width of the road is 16 m.

The amount of precipitation during the winter months of Bitlis Rahova region was evaluated according to the data obtained from the Bitlis meteorology branch. According to this, the distribution of the max imum height of snowfall according to years is examined and the average height is taken into account. (Table 1)

Table 1. The statistical data used in the study and the results of cumulative distribution

17207-17208 (Bitlis Meteo.-Bitlis OMGI)					Lognormal Dist.		Gumbel Dist.		Weibull Dipt.	
i	Year	h (cm) Max. Snow Depth	ln(h)	P_i	Φ^{-1}	F(x)= CDF	-ln(-ln(P_i))	F(X)=CDF	ln(-ln(1-P_i))	F(x)=CDF
1	1999	34	3.526	0.029	3.707	0.013	-1.268	0.026	-3.541	0.046
2	1984	40	3.689	0.057	3.885	0.026	-1.052	0.039	-2.833	0.063
3	2010	45	3.807	0.086	4.001	0.043	-0.899	0.052	-2.412	0.080
4	1989	60	4.094	0.114	4.091	0.115	-0.774	0.108	-2.109	0.140
5	1998	61	4.111	0.143	4.166	0.121	-0.666	0.112	-1.870	0.144
6	1981	67	4.205	0.171	4.232	0.159	-0.567	0.142	-1.671	0.172
7	1997	70	4.248	0.200	4.290	0.179	-0.476	0.158	-1.500	0.187
8	1996	79	4.369	0.229	4.344	0.243	-0.389	0.211	-1.349	0.233
9	1990	85	4.443	0.257	4.395	0.286	-0.306	0.249	-1.213	0.265
10	2008	85	4.443	0.286	4.442	0.286	-0.225	0.249	-1.089	0.265
11	1980	86	4.454	0.314	4.487	0.293	-0.146	0.256	-0.975	0.271
12	2011	100	4.605	0.343	4.531	0.394	-0.068	0.351	-0.868	0.350
13	2007	102	4.625	0.371	4.573	0.408	0.010	0.365	-0.767	0.361
14	2009	104	4.644	0.400	4.614	0.422	0.087	0.379	-0.672	0.373
15	2001	107	4.673	0.429	4.654	0.442	0.166	0.400	-0.581	0.390
16	2002	110	4.700	0.457	4.694	0.462	0.245	0.420	-0.493	0.408
17	1995	113	4.727	0.486	4.734	0.481	0.326	0.441	-0.408	0.425
18	2005	115	4.745	0.514	4.773	0.494	0.408	0.455	-0.326	0.437
19	1986	118	4.771	0.543	4.812	0.513	0.493	0.475	-0.245	0.454
20	1994	130	4.868	0.571	4.852	0.582	0.581	0.552	-0.166	0.522
21	2004	140	4.942	0.600	4.893	0.634	0.672	0.612	-0.087	0.577
22	1991	145	4.977	0.629	4.934	0.658	0.767	0.639	-0.010	0.603
23	1988	152	5.024	0.657	4.976	0.689	0.868	0.676	0.068	0.639
24	1983	155	5.043	0.686	5.019	0.701	0.975	0.690	0.146	0.654
25	2000	161	5.081	0.714	5.064	0.725	1.089	0.718	0.225	0.682
26	2003	170	5.136	0.743	5.112	0.757	1.213	0.757	0.306	0.722
27	1985	200	5.298	0.771	5.162	0.839	1.349	0.854	0.389	0.833
28	2006	212	5.357	0.800	5.216	0.864	1.500	0.881	0.476	0.867
29	1982	217	5.380	0.829	5.275	0.873	1.671	0.892	0.567	0.880
30	1993	235	5.460	0.857	5.340	0.900	1.870	0.922	0.666	0.918
31	1987	246	5.505	0.886	5.415	0.914	2.109	0.936	0.774	0.936
32	2012	250	5.521	0.914	5.505	0.919	2.412	0.940	0.899	0.941
33	2013	250	5.521	0.943	5.622	0.919	2.833	0.940	1.052	0.941
34	1992	275	5.617	0.971	5.799	0.942	3.541	0.962	1.268	0.968

The results of PPCC plots tests for three different distribution model were shown in the Figures 2-4. As seen in these figures the maximum probably plot correlation coefficients (PPCC=R) of log-normal, Gumbel and Weibull distributions are estimated as 0.989, 0.986 and 0.990 respectively [3].

Figure 1. Place of the Warehouse

The warehouse area where the snow accumulations are collected is the optimum location of the transportation distance determined by the administration. This warehouse area is defined as the area that is close to the work areas and is available for the collection of snow piles.

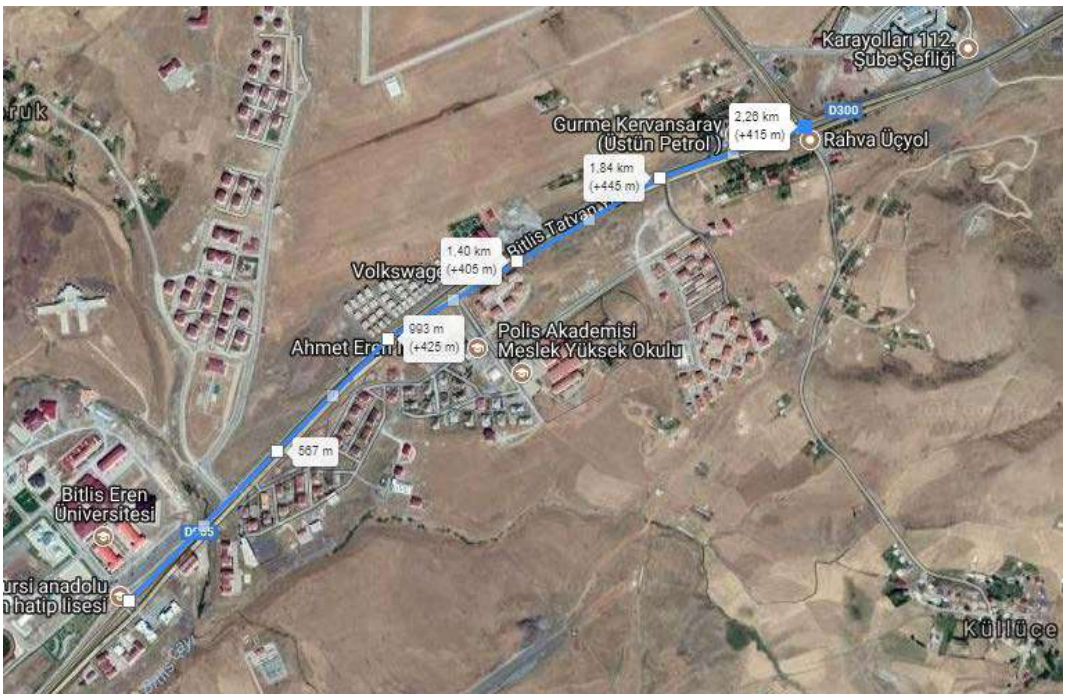

Figure 2. Distance from the Warehouse

The warehouse is 150 m away from the main road. The snow that accumulates on the side of the road is taken to the storage area through the loader and truck from the bank.

2.1. HEAVY MACHINES USED IN THE SNOW FIGHT

- Charactersistics of Loder

Cycle Time = δ = Excavete + Load (sn)

Figure 3. Snow loading work

Hourly Job Efficiency:

$$D = \frac{d}{1+Q_g} * \frac{360 - n * \tau}{\delta} * K$$

d: Spoon Capacity (m^3)

n: Displacement Number

τ : A displacement time

$K = k_r * k_l * k_g$

k_r : Coverage Factor (between 0,87-1,20)

k_l : Excavation Orbit Coefficient

k_g : Rotation Coefficient (between 0,77-1,32)

- Truck Features

Along with the snow load that a truck can carry, the total weight is explained by the following formula:

$$G_{yük} = H * \gamma_g = \frac{H}{1+Q_g} * \gamma_0$$

γ_g : Temporarily Swelling Unit Volume Weight

H : Box Volume

Q_g : Swelling Ratio

G : Truck Weight

During the loading and unloading of a truck:

$$\delta_{tvr} = t_g + t_d + t_{oy} + t_{ob} + t_y$$

t_g : Delay time

t_d : Loading time

t_{oy} : Time elapsed at the loading point

t_{ob} : Time elapsed at the unloading site

t_y : Loading time

2.2. DETERMINING THE OPTIMAL CONVENIENT TRANSPORT

The following values were found by using the formulas given above for the number of days determined in the transport of a snow load in a certain area and the number of scraped excavator and truck for transporting snow load in the result of daily working time.

On the road taken as an example, the estimated cumulative snow mass was calculated as 48.092,80 m^3. The calculations of the number of trucks and trucks planned to be used in a warehouse area of 2,41 km and snow mass to be transported in 12 working hours and 8 hours of working time per day;

- Natural ground unit weight : 1.0 t/m^3 (Frosted Snow)
- Temporary swelling number (Q_g): %16
- Worksite yield (p) : %85
- Loder spoon volume (d): 1,25 m^3
- Rotation time (t): 25 sn
- Number of displacement (n): 10 times/hour
- Time passed for one displacement (τ): 2 min
- Number of Loder improvements: $K = k_1 * k_g * k_r = 1.3$
- Volume of truck chassis (H) : 8 m^3
- Truck tare (G) : 6 ton
- Engine power (Nm): 250 BG
- Loading and Unloading preparation time (t_0): 7 min
- Specific resistance of the road (W_o): 0,12

- Slope (S): %4 (Downhill slope)

$$D_{lod} = \frac{1,25}{1+0,16} * \frac{3600-10*120}{25} *1,3*0,85*8$$

$$D_{lod} : 914,48\, m^3/day$$

$$12*914,48 = 10973,79 \text{ m}^3 \text{ / 12 day}$$

Loder number:

$$\frac{48092,80}{10973,79} : 4,38 \cong 5$$

Kamyon yukleme suresi:

$$t_y : \frac{8}{1+0,16}\frac{8}{1+0,16}/154,3 : 0,147 hour$$

$$t_y : 2,7 \text{ min}$$

Truck Load:

$$G_{load} : \frac{8}{1+0,16} *1,0 : 6,89 ton$$

$$G : 6,89 + 6 : 12,89 ton$$

$$V_{going} : \frac{0,243*250}{12,89(0,12-0,04)}$$

$$V_{going} : 58,92\, km/hour$$

$$t_g : \frac{20}{58,92}$$

$$t_g : 0,34 hour = 20,36 \text{ min}$$

$$V_{return} : \frac{0,243*250}{6(0,12+0,04)}$$

$$V_{returnş} : 63,28\, km/hour$$

Note: : It is legal for the trucks to run at 60 km / h.

$V_d : 60\,km/hour$

$$t_d : \frac{20}{60} = 0{,}333 hour = 20\,\text{min}$$

$$\delta_{lap} : 20{,}36 + 20 + 2{,}7 + 7$$

$$\delta_{lap} : 50{,}06\,\text{min}$$

Yield of the truck:

$$D_{truck} : \frac{8}{1+0{,}16} * \frac{60}{50{,}06} * 0{,}85 * 10 = 70{,}26 m^3 / day$$

Truck Number : Excavator daily yield / Daily yield of a truck

$$N : \frac{914{,}48 m^3}{70{,}26 m^3}$$

$N : 13{,}02 \cong 14$ Truck

3. RESULTS

- With this study, the number of vehicles to transport the snowload accumulated on the Bitlis-Tatvan highway as soon as possible to the warehouse specified by the administration was found.
- It is predicted that unnecessary vehicle usage or less vehicle usage will be prevented by means of planning in the fight with the snow.
- As a result of the plans made in the snow fighting, it is considered that work and time losses should be minimized and that the vehicles to be used should work in minimum number and maximum efficiency.

4. REFERENCES

[1] Ahmet Fethi Kigili“ Karayollarinda Kar Ve Buz Mucadelesi Yonetiminde Yeni Bir Maliyet Hesabi Onerisi”, ITU Dergisi, Mimarlik Planlama Tasarim, Cilt:6, Sayi2, s.23-46, Eylul 2006
[2] Karayollari Bakim El Kitabi, (1998), Karayollari Genel Mudurlugu, 284-296
[3] Mehmet Cihan AYDIN, Ercan ISIK “ The Statistical Evaluation of Ground Snow Loads in Regions Subjected to Heavy Snowfall ”

ICENS 4TH INTERNATIONAL CONFERENCE ON ENGINEERING AND NATURAL SCIENCE
2-6 May 2018 KIEV UKRAINE

The Abrasion Resistance of Mortars Containing Natural Zeolite Analcime

Yasemin Akgun[1], Omer Fatih Yazicioglu[2]

Abstract

It is always an expectation that to minimize of damage caused by abrasion as a result of increase of abrasion resistance of construction materials. Therefore, the influence of analcime on the abrasion resistance of cement mortars was investigated in this study. Analcime is a natural pozzolan and is one of the valuable minerals of zeolite group. The cement mortars were produced by using blended cements containing analcime. The abrasion losses by friction at the end of 28 days of the mortar mixtures were determined by Bohme surface abrasion tests in accordance with TS 2824 EN 1338. The abrasion tests were carried out to cement mortar mixtures produced with different cement replacement ratio (0%, 10%, 30% and 50%). The results obtained from test series were compared with each other. The test results showed that, abrasion losses of mortars containing analcime were lower than portland cement mortars as 25% approximately. It is believed that this positive effect of natural zeolite in the development of abrasion resistance is due to pozzolanic reactions.

Keywords: Abrasion, Analcime, Mortar, Natural Zeolite.

1. INTRODUCTION

Natural zeolites have recently become widely used as additive material in blended cement productions. Because, natural zeolites are pozzolanic materials containing abundant amounts of silica and alumina. When zeolite is replaced with clinker at optimum ratio, they form additional binder components by reacts with Ca $(OH)_2$ which is a result of cement hydration. These additional binders improve strength and durability of mortar/concrete. It is obtained advantages such as reducing of CO_2 emissions, energy saving and economy according as reducing of clinker consumption in blended cement applications containing zeolite. Also, natural zeolites are preferred to synthetic zeolites because of their reserve and economic status. The natural zeolites formed by the alteration of the vitric pyroclastic deposits are more reactive materials than the fly ash and furnace slags between mineral additives [1]. Natural zeolites have reserve declared as hundred billions tons in the world [2]. The using of these zeolite reserves will be possible with investigation performed on different zeolite minerals. Analcime is a natural pozzolan and is one of the valuable minerals of zeolite group. Analcime is a feldspathite mineral with a very large amount of hydrated sodium aluminosilicate ($Na\ (AlSi_2O_6)\ .H_2O$) in its structure.

Abrasion is a physical and mechanical event that is slowly occurred. The reduction in size and mass occurred by friction of abrasive materials on surfaces of objects that make contact with each other and move relative to each other is defined as abrasion loss. Generally, the amount of abrasion depends on type of material, state of abrasion surface, friction conditions and chemical effects of environment.

As a result of optimizations carried out on all of mortar/concrete components, it is known that the abrasion resistance can be increased to desired level. Therefore, it can be possible to minimize damages caused from abrasion with increasing properly of abrasion resistance of mortar/concrete in some cases such as pavement, concrete roads, factory floor surfaces, water structures, chimneys etc.

In literature, the study made with analcime is very limited [3, 4, 5]. Furthermore, there is no study to examine abrasion resistance on mortar or concrete samples containing analcime. It is always an expectation that to minimize of damage caused by abrasion as a result of increase of abrasion resistance of construction materials. Therefore, the influence of analcime on the abrasion resistance of cement mortars was investigated in this study. The abrasion tests were carried out on mortar mixtures produced with different cement replacement ratio (0%,

[1] *Corresponding author: Ordu University, Department of Renewable Energy, Ordu, Turkey. yakgun@odu.edu.tr*

[2] *Ondokuz Mayis University, Department of Civil Engineering, Samsun, Turkey. omerfatihyazicioglu@gmail.com*

10%, 30% and 50%). And, pozzolanic activity of analcime were determined. The results are compared with each other.

2. MATERIALS AND METHODS

The cement used in tests is CEM I 42.5 R type of Portland cement (PC) produced in accordance with TS EN 197-1 [6]. The analcime were used as replaced material by cement. The analcime (A) that is type of natural zeolite were obtained from Ordu/Persembe regions of Turkey. The analcime samples were finely grinded in a ball mill. The amount of analcime used in mixtures were 0%, 10%, 30% and 50% of cement weight. So, the mixtures were produced with the labels PC, A10, A30 and A50.

The CEN (The European Committee for Standardization) standard sand in accordance with EN 196-1 [7] was used in mortar mixtures. The sand-to-cement ratio is constantly 3 and water-to-cement ratio is constantly 0.5. It was used superplasticizer (at 1%, 1.5% and %2 ratios) complying with TS EN 934-2 [8] by adding to mixture water to recover of adverse effect on mortar consistency of natural zeolites in mixtures. In the production of all samples, water that does not contain organic substances and mineral salts that may be harmful is used. The flow values of mortar mixtures are about 150 ± 20 mm.

All mortar mixtures were prepared by applying the standard mixing, molding and curing procedures stated in TS 196-1. Samples was prepared in laboratory environment where temperatures are 20±2ºC and relative humidity is 60±5%. The samples taken from molds after 24 hours from their productions were kept in the curing tank at a temperature of 21 ± 1ºC until the test days.

X-Rays Fluorescence Spectrometer (XRF) analysis was performed to determine chemical composition of analcime. X-Ray Diffraction (XRD) analysis was performed to determine mineralogical composition of analcime. Some views were also obtained using a Scanning Electron Microscope (SEM).

2.1 Test of Pozzolanic Activity

Pozzolanic activity can be defined as the ability to react with $Ca(OH)_2$ of active silica which is in the pozzolan. At the end of this reaction the amount of portlandite ($Ca(OH)_2$) is reduced, calcium silicate hydrate (CSH) is increased.

The pozzolanic activity tests were performed on 40x40x160mm prismatic samples. In TS 25 [9], the pozzolanic activity test is defined as a characteristic determined in terms compressive strength of the mortar obtained by mixing natural pozzolan which is grinded at a certain fineness with water, standard sand and calcium hydroxide ($CaOH_2$). The amounts of materials required to prepare three test samples for tests on pozzolanic activity are given in Table 1.

Table 1. The amounts of materials for tests on pozzolanic activity

Materials	**TS 25**	**The amounts for tests**
Slaked lime ($CaOH_2$)	150gr	150gr
Pozzolan	2x150x(density of pozzolan /density of $CaOH_2$) (gr)	2x150x(2.28/2.15) = 318.14gr
Standard sand	1350gr	1350gr
Water	0.5x (150+pozzolan) (gr)	0.5x(150+318.14) = 234.07gr

The moulds of the prepared samples were covered with a glass plate to prevent evaporation. The samples were allowed to stand at room temperature for 24 hours (23 ± 2)ºC. And then, they were left for 6 days in an drying oven at 55 ± 2°C without removing the moulds. The samples removed from the oven were left to cool until the room temperature reached. Finally, the compressive strengths of samples were performed in accordance with TS EN 196-1.

2.2 Test of Abrasion Resistance

Three cube moulds of 70.7 mm were used for each mixture in abrasion tests. The mortars were produced by using blended cements containing analcime. The abrasion losses by friction at the end of 28 days of the mortar samples were determined by Bohme surface abrasion tests in accordance with TS 2824 EN 1338 [10] (Fig. 1).

Before tests, initial volumes and initial weights of samples were determined. The abrasive force of 294 N was applied to samples placed on rotary disk of Bohme apparatus.

The samples were subjected to abrasive effect of 20 g corundum powder poured on friction path together with operation of device. Total of 16 periods that each of them is 22 cycles were applied to samples. At the end of the test (at the end of the 352 cycles), volumetric abrasion losses (ΔV) in samples were determined.

In calculations, it was used formula at (1) which denote ΔV ($cm^3/50\ cm^2$); volumetric abrasion loss, Δm (gr); weight loss at end of 16 cycles, ρ (g/cm^3); density.

$$\Delta V = \Delta m / \rho \quad (1)$$

Figure 1. Bohme abrasion test device

3. RESULTS AND DISCUSSION

a. Some properties of portland cement, analcime and blended cements

Some properties of portland cement (PC), analcime (A), blended cements (A10, A30 and A50) are presented in Tables 2, 3 and 4. Densities of analcime is 26.92% lower than PC. Specific surface area of analcime is 48.91% higher than PC. This situation depends on mineral structure, porosity and fragilement properties of zeolite. Cumulative passing (%) of 45 μm sieve for Portland cement and analcime are 67.11% and 70.80%, respectively. Densities of blended cements have decreased with increasing of zeolite ratios. Fineness of blended cements containing zeolite has increased with increasing of zeolite ratios.

Table 2. Properties of portland cement (PC).

Chemical composition	**(wt.%)**	**Physical and mechanical properties of portland cement**			
SiO_2	19.53	Density, (g/cm^3)	3.12		
Al_2O_3	5.33	Initial set, (h)	2.50		
Fe_2O_3	3.56	Final set, (h)	4.15		
CaO	62.26	Volume expansion, mm	2.00		
MgO	0.99	Specific surface (Blaine) (cm^2/g)	3210		
SO_3	3.02	The compressive strengths	2 days	7 days	28 days
Loss of ignition	3.06	(MPa)	32.30	44.60	53.00

Over sieve	45µm	90 µm	200 µm
(%)	32.89	12.15	2.73

Table 3. Properties of analcime

Chemical composition	**Analcime (wt.%)**	**Physical properties**	
SiO_2	46.71		Analcime
Al_2O_3	17.24	Density, (g/cm^3)	2.28
Fe_2O_3	9.21	Blaine fineness (cm^2/g)	4780
CaO	3.03		
MgO	5.29	Over sieve (%)	
Na_2O	4.84	45µm	29.20
K_2O	4.08	90 µm	9.80
Loss of ignition	7.00	200 µm	2.15

Table 4. Properties of blended cements

Physical properties	**PC**	**A10**	**A30**	**A50**
Specific surface (cm^2/g) (Blaine fineness)	3210	3752	3918	4449
Density, (gr/cm^3)	3.12	2.79	2.75	2.71

3.2 Pozzolanic Activity of Analcime

Pozzolanic activity of analcime are given in Table 5. According to Table 5. In TS 25, one of the conformity criterias for pozzolans is the 7 day compressive strength of samples prepared with lime-natural pozzolan mixture. The limit value of the compressive strength is at least 4 MPa. In test study performed for analcime, the average compressive strength value for the lime-zeolite (pozzolan) mixture samples was determined as 6.30MPa. It has also been emphasized that the sum of SiO_2 + Al_2O_3 + Fe_2O_3 in TS 25 should be at least 70% by mass. The value of this total was found to be 73.16% for analcime. At the same time, the specific surfaces of the pozzolans should be greater than 3000 cm^2/gr. The specific surface of pozzolan which is used in this study were found to be 4780 cm^2/gr for analcime (Table 3). In pozzolanic activity tests. Because of the specific surface of natural zeolite were below of portland cement fineness, the reaction which is between pozzolan and lime was increased. It is thought that, this situation was lead to an increment at value of pozzolanic activity. These value show that the zeolite used in study have an usability potential as a pozzolan.

Table 5. Pozzolanic activity of analcime

TS 25 limit values	**Analcime**
Lime-pozzolan mixture 7 days compressive strength > 4MPa	6.30MPa
SiO_2+Al_2O_3+Fe_2O_3 wt. content >%70	%73.16
Specific surface area > 3000cm^2/gr	4780 cm^2/gr

3.3 Mineralogical Composition of Analcime

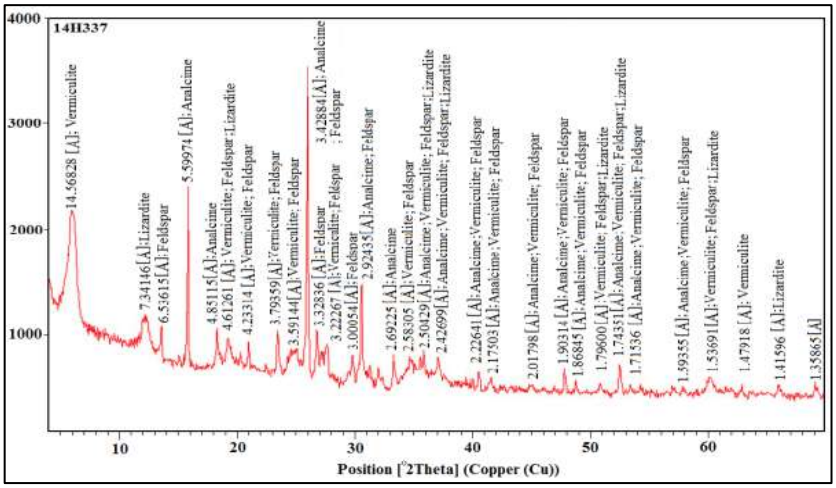

Figure 2. XRD diffraction patterns of analcime

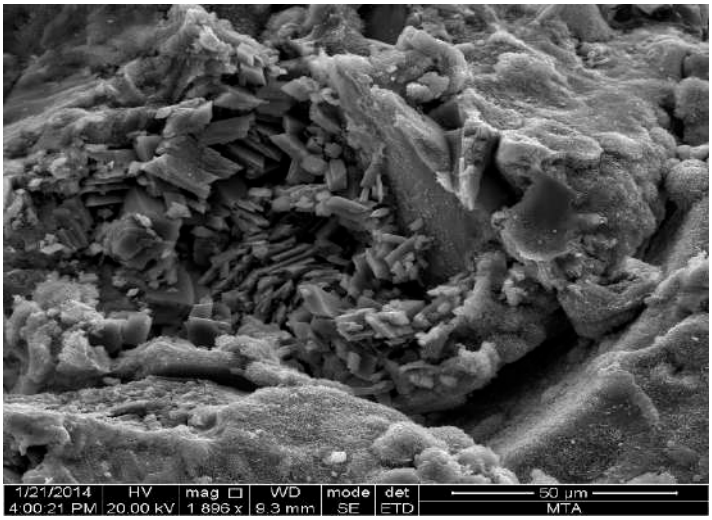

Figure 3. SEM view of analcime

XRD diffraction patterns and SEM views are presented in Figs. 2 and 3. According to the mineral modal ratios at the mineralogical composition results determined by the X-ray diffraction analysis (XRD) of analcime sample, the analcime rock is a vitric tuff and consists of glass splinters and crystal components. Glass splinters are converted to zeolite and chlorite, which are heavily altered. The analcime samples confirm the requirements of national and international standards for zeolite applications.

3.4 Abrasion Resistance of Mortars

Abrasion losses ΔV ($cm^3/50cm^2$) are given in Table 6. Abrasion losses variations for mortars are presented in Fig. 4.

Table 6. Volumetric abrasion losses and densities of mortar

Mortars	PC	A10	A30	A50
Density (gr/cm^3)	2.42	2.16	2.13	2.10
ΔV (cm^3/50cm^2)	11.84	8.97	9.17	10.23

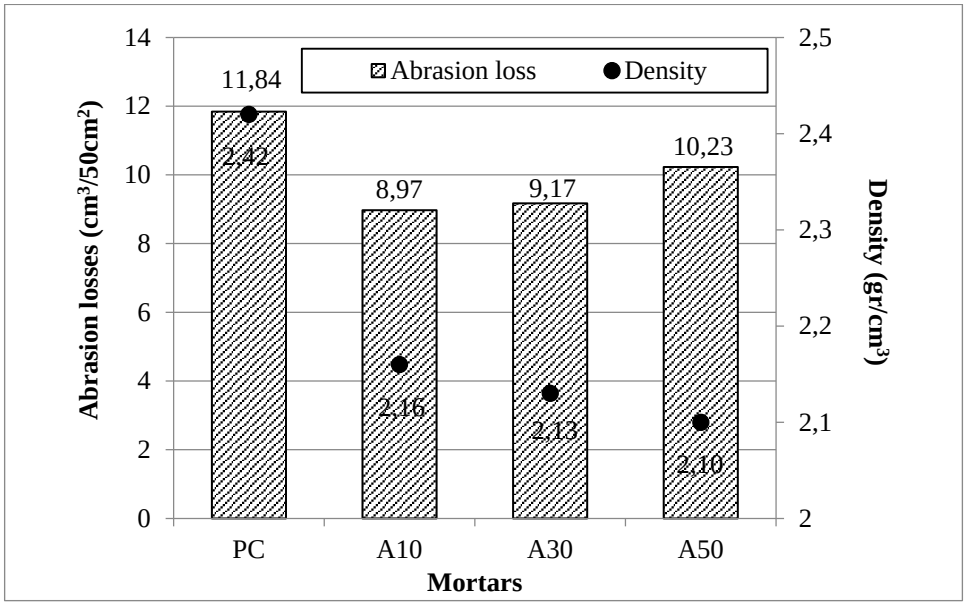

Figure 4. Abrasion loss and density variation for mortar

The volumetric abrasion losses for mortars with blended cements containing analcime (A10, A30 and A50) were 25%, 23% and 14% less than mortars with PC, respectively. In other words, it has been found that the abrasion losses of mortars with blended cement are less than mortars with PC for all replacement ratios. This positive effect in abrasion resistance is probably performance increasing occurred at aggregate-cement paste interface and cement paste due to pozzolanic reactions of zeolite. Also, as analcime replacement ratio increases, the densities of mortars decrease.

4. CONCLUSIONS

1. Since the density of analcime is lower than that of Portland cement, the densities of mortars produced by blended cement containing analcime are less than that of mortars produced by Portland cement.
2. The properties of natural zeolite analcime investigated in this study such as pozzolanic activity, mineralogical structure, high silica-alumina content, high specific surface, low density are sufficient for sustainable blended cement productions.
3. The abrasion losses of mortars containing analcime were lower than that of mortars containing portland cement for all replacement ratios. In other words, abrasion resistances of mortars containing analcime has increased up to 30% replacement ratio. It is believed that this positive effect of natural zeolite in the development of abrasion resistance is due to pozzolanic reactions.
4. A larger number of studies should be carried out on zeolites named analcime obtained from different regions to reduce amount of cement and to improve of cement performance.

ACKNOWLEDGMENT

This study was funded by the Scientific Research Project Unit of Ordu University under Project No: TF-1521. Also, we would like to thanks to General Directorate Of Mineral Research And Explorations, Votorantim

Cimentos, Mineralogy Laboratory of Blacksea Technical University, Gordes Zeolite Company for their support and assistance.

REFERENCES

[1]. Chan, SYN. and Ji, X. Comparative study of the initial surface absorption and chloride diffusion of high performance zeolite, silica fume and PFA concretes. Cem. Concr. Compos. 1999, 21:293–300.
[2]. Ozen, S., Goncuoglu, M. C., Liguori, B., Gennaro, B., Cappelletti, P., Gatt, G. D., Iucolano, F., and Colella, C., A comprehensive evaluation of sedimentary zeolites from Turkey as pozzolanic addition of cement- and lime- based binders", Construction and Building Materials, 2016, Vol: 105, 46-61.
[3]. Bilim, C., Zeolit Katkisinin Harclarin Asinma Direncine Etkisi, 6th International Advanced Technologies Symposium (IATS'11), 2011, Elazig, Turkey.
[4]. Gabriel C., Rajwant S. B., Yushan Y., and Junlan W., Zeolite as a wear-resistant coating, Microporous and Mesoporous Materials, 2012, vol: 151, 346–351.
[5]. Akgun, Y., and Yazicioglu, O. F., Iki Farkli Dogal Zeolit Katkisinin Cimento Harc Asinma Dayanimina Etkisi, Ordu Univ. Bil. Tek. Derg., Cilt:6, Sayi:1, 2016,94-104.
[6]. TS EN 197–1, (2002), Cimento - Bolum 1: Genel Cimentolar- Bilesim, Ozellikler ve Uygunluk Kriterleri. Ankara: Turk Standartlari Enstitusu.
[7]. TS EN 196–1, (2009) Cimento Deney Metotlari - Bolum 1: Dayanim Tayini. Ankara: Turk Standartlari Enstitusu.
[8]. TS EN 934-2, (2013), Kimyasal Katkilar - Beton, Harc ve Serbet icin - Bolum 2: Beton Kimyasal Katkilari - Tarifler, Gerekler, Uygunluk, Isaretleme ve Etiketleme, Ankara: Turk Standartlari Enstitusu.
[9]. TS 25, (2008), Dogal Puzolan (Tras)-Cimento ve Betonda Kullanilan-Tarifler, Gerekler ve Uygunluk Kriterleri. Ankara: Turk Standartlari Enstitusu.
[10]. TS 2824 EN 1338, (2005), Zemin Dosemesi icin Beton Kaplama Bloklari-Gerekli Sartlar ve Deney Metotlari. Ankara: Turk Standartlari Enstitusu.

ICENS 4TH INTERNATIONAL CONFERENCE ON ENGINEERING AND NATURAL SCIENCE
2 - 6 May 2018 KIEV UKRAINE

Consideration of Urbanization Impact for Sustainable Modeling of Kagithane River Floods in Istanbul

Tuba Bostan[1], Mohsen Mahmoody Vanolya[1], Kemal Baltaci[1]

Abstract

Increase of floods peaks in urban area, because of structural measures can be reduced by adding some ecologic and biologic elements in river training plan that lead to sustainable management of the river floods. In this paper, impact of sustainable alternatives for Kagithane River floods in Istanbul metropole are presented. The aim of this study is to compare impact of detention ponds and grassed river training measures instead of existing concrete floodwalls to show their impact on flood peak reduction. For this purpose, first, hydrologic and hydraulic model of the river is developed by using HEC-HMS and HEC-RAS Models (USACE) which are used for rainfall-runoff and water surface profiles computation. First, the models were used for existing condition with exist floodwalls, then by embedding urbanization and land use change the increase in floods peak are shown. For long-term and sustainable flood management some possible alternatives related to ecologic and social characteristic of countryside of Istanbul, are proposed and are modeled in some scenarios. Finally, the flood hydrographs are calculated for the Kagithane River by the models. Afterwards, results of sustainable scenarios are compared with exist condition that show reduction of floods peaks significantly. Moreover, the society and ecologic dimension of alternative increase creation area for Istanbul people that can be consider an important social and tourism factor.

Keywords: Kagithane floods, hydrologic model, detention ponds, grassed waterways

1. INTRODUCTION

Urban rivers water flow and quality are affected by changing of physical geometry of its ambient. In previous decades, their restriction in width and changing their bed slope, have converted them as a useless element in cities figurine, so that they were left as storm water drainer with trash and wastewater pollution. However, in recent years, the sustainability concept is considered their restoration by using ecologic, environmental and economic aspects, but destruction of natural land cover and river geometry is continuing [1]. Land cover degradants upstream watershed of urban river by replacing impervious streets, roofs and buildings which increase the water volume and flood risks in downstream reach. In addition, restriction of streams and main rivers by canalizing them in a limited width with concreate and smooth materials lead to decreasing the hydraulic roughness and finally increase in water velocity and floods peaks in extreme rainfalls [2]. Toward sustainable development in urban rivers projects, the aspects of green and blue infrastructures are considered for recreation and perspective protection as well as conservation of ecologic and the projects economy. Green infrastructure implies vegetation use in river training and restoration and blue infrastructure imply use of water as a component in urban design and development [3]. In this study, the effect of exist river training and sustainable management of Kagithane river in Istanbul metropole is investigated. Impact of small detention ponds and the flood control walls on its flood peak and volume is studied and then some measures adapted to Indigenous practices are proposed for this river. For study the impact of different measures, hydrologic and hydraulic model of the river is provided for exist condition(baseline) and two different sustainable scenarios and then the result of peak and volume of an extreme flood are compared for those sustainable measures.

2. MATERIALS AND METHODS

a. Study Area

Kagithane river is one of important small rivers of European part of Turkey in Istanbul metropole as shown in Figure 1. Its main river stats from forested area near to new airport (Istanbul third airport) with North-West to

[1] *Yildiz Technical University, Department of Civil Engineering, 34220, Esenler/Istanbul, Turkey. bostan@yildiz.edu.tr*

South-East direction and flow to Istanbul dense urban area and then leads to Golden Horn. Its basin area is about 170 square kilometers with domain forest and pasture land use. Urban area is developing in south part (Istanbul Kagithane district) and middle (Gokturk city) of the river basin. River channel was trained in urban area and its plan will be extended to whole of river in next years. The main problem of the river is restriction of river channel in local accesses such as bridges and culverts and the training canal with limited capacity. Extreme rainfall in this region and generated floods had been damaged the ambient buildings and infrastructures in previous years, particularly the September flood of 2009 had significant damage with three deaths in downstream of the river. Table 1 presents the analyzed rainfall of region for different return periods. In addition, rainfall of September 2009 is available and its hydrograph illustrates in Figure 2. The recent rainfall used in this study as index of this river basin floods.

Figure 1. Location of Kagithane river basin in Turkey and Istanbul

Table 1. Extreme analyzed Rainfall of the region

Tr(Year)	One hour	12 Hours	One Day
5	31.41	60.67	81.91
10	38.84	72.39	98.05
25	48.24	87.20	118.45
50	55.21	98.19	133.59
100	62.13	109.10	148.61
200	69.03	119.96	163.58
500	78.12	134.30	183.33

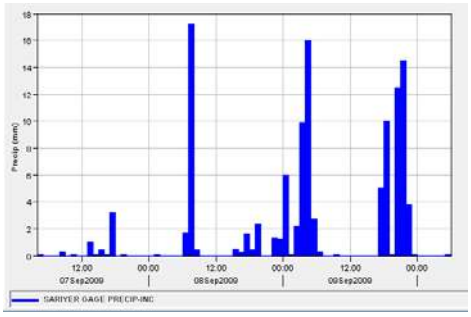

Figure 2. Rainfall of September 2009 in the region

b. Hydrologic modeling

For flood simulation, provided the hydrologic model of river basin and its rout to outlet of Golden Horn. Rainfall-Runoff models are the general methods for flood simulation and routing in river studies [4]. In this study the river basin was simulated by using Watershed Modeling System (WMS) and Hydrologic Modeling System (HMS). Land Use Map provides from the European Copernicus program (CLC 2012) and presents in Figure 3 for river basin. In addition, soil properties and type extracts from European Soil Data Centre (ESDAC, 2005) and presents in Table 2 [4]. Furthermore, for basin geometry, terrain Digital Elevation Model (DEM) of the river basin with 30×30 meters size was used to separation of the river network and submains by using WMS preprocesses as shown in Figure 4 and then transferred to HMS environment as shown in Figure 5 [5]. The combination of the data was used to determination of sub-basins area, percent of impervious area, Curve Number, retention storage, initial loss and, lag time. The amount of excess runoff computes by retention and rainfall relation in each step time using curve number of sub basins as following [6,7,8]:

$$P_e = \frac{(P - I_a)^2}{(P + s - I_a)}$$

Where P: is rainfall amount in time step

$S = \frac{25400}{CN} - 254$ is retention storage and,

$Ia = 0.2S$ is initial loss and finally, the amount of loss for each step time equal to $P - P_e$.

Table 2. Soil properties of the river Basin (ESDAC 2005)

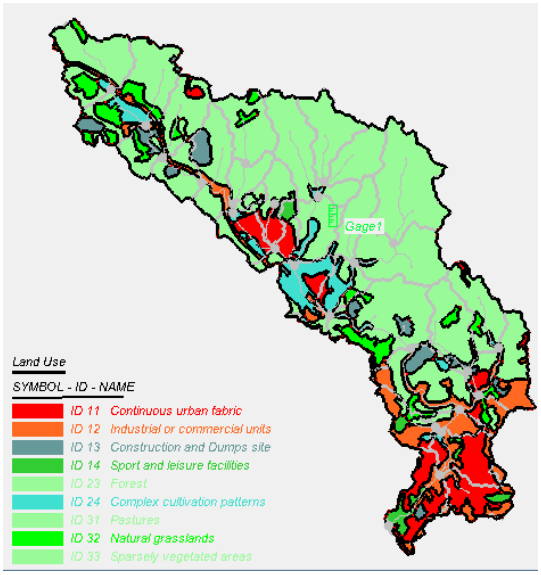

Figure 3. River basin land use (CLC 2012)

Parameter	Symbol	Unit	Amount
Total Porosity/Saturation	θ_s	(cm^3/cm^3)	0.463
Effective Porosity/Saturation	θ_e	(cm^3/cm^3)	0.434
Field Capacity Saturation	θ_f	(cm^3/cm^3)	0.27
Wilting Point Saturation	θ_{wp}	(cm^3/cm^3)	0.117
Residual Saturation	θ_r	(m^3/cm^3)	0.027
Bubbling Pressure Geometric Mean	b	(cm)	11.15
Pore Size Distribution Arithmetic Mean	λ	(cm/cm)	0.252
Saturated Hydraulic Conductivity (multiply by 0.5 for GA methods)	K_s	(cm/h)	1.32
Wetting Front Suction Head (Capillary Head)	f	(cm)	8.89

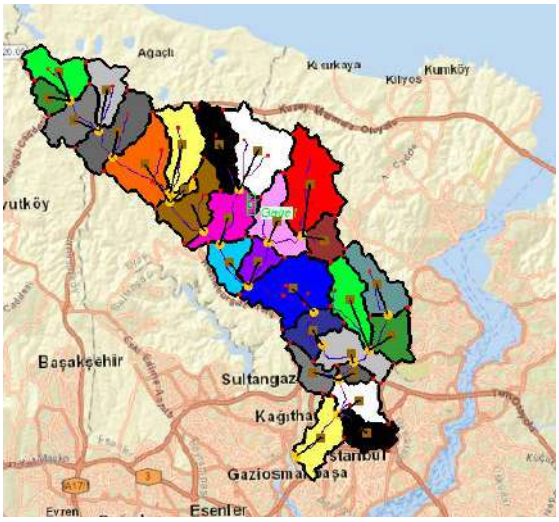

Figure 4. Separated sub basins and river network in WMS

Figure 5. Kagithane sub-basins and river network in HMS

For basin lag time from different methods, the Denver method selected that use following equation for calculation of hydrograph lag time [7]:

$$T_l = Ct(LLca/\sqrt{S_0})^{0.48}$$

Where Ct: is coefficient of peak time that calculates by $Ct = -0.00371\, I_m + 0.167$

I_m: percent of impervious area (%)

L: watershed length (m)

Lca: Length of watershed centroid (m)

S_0: weighted average along main stream in sub-basin

Unit hydrograph was calculated by SCS method in the model that uses physical characteristics and lag time for finding peak of flow and time for each sub-basin as $U_p = C\frac{A}{T_p}$ and $T_p = \frac{\Delta t}{2} + T_l$. Then by using a dimensionless empirical hydrograph, is established the unit hydrograph for time interval Δt [8].

Finally, the sequence component of the hydrograph for each sub-basin computes by discrete convolution equation as follow:

$$Q_n = \sum_{m=1}^{n<=M} P_m \, U_{n-m+1}$$

For routing of each sub basin flood hydrograph to downstream points, the lag method is used as the simplest methods that computes by using length of the reach over average velocity of the flood wave in the channel. The velocity of channel computes using river hydraulics model in next section for reaches [8].

For existing condition and two different scenarios the Kagithane hydrologic model are run that will be presented in next sections [9].

c. River Hydraulics

In this study, river hydraulics is investigated for determination of flood wave velocity in reaches and for surveying of river training by flood walls respectively. River hydraulics refer to computation of water surface profile and hydraulic routing of flood wave. First, in a proper river topography, the main channel and flood plains are specified and then by using convenient cross sections along the river and in situation of hydraulic crossing structures, computes the water surface by compatible governing equations such as steady state or unsteady flow. In Figure 6 presents the situation of river sections along Kagithane main river. For extraction the sections combination of different maps with scale of 1:5000 and DEM 30×30 were used. In addition, the training plan used to section of constructed channel as shown of its sample in Figure 7. In the end of river and near to confluence to Golden Horn, the river section and water surface assumed fixed water surface as shown in Figure 8.

Figure 6. Sections along Kagithane main river for hydraulic modeling

Figure 7. Trained cross section of the river

Figure 8. Fixed water surface in Golden Horn

In this study the river hydraulics was simulated by using River Analysis System (RAS), however data and cross sections prepared in the Watershed Modeling System (WMS). The RAS model solves Saint-Venant Equation for sequence cross section in a river reach. The governing equation is as following [10]:

$$\begin{cases} \dfrac{\partial A_T}{\partial t} + \dfrac{\partial Q}{\partial x} - q_l = 0 \\ \dfrac{\partial Q}{\partial t} + \dfrac{\partial QV}{\partial x} + gA\left(\dfrac{\partial z}{\partial x} + S_f\right) = 0 \end{cases}$$

Where A_T: is water flow cross section area (m2)

Q: river flow between the sequence cross sections (m3/sec)

q_l: lateral inflow between two cross sections (m2/sec)

x, t: are distance and time character for hydrograph and between the sequence cross sections(m)

V: river flow velocity between the sequence cross sections (m/sec)

S_f: friction slope along river flow between sequence cross sections

z: datum elevation

In practice, the dynamic model reduces to solve of steady state by energy equation between two cross sections as following [10]:

$$Z_2 + Y_2 + \frac{\alpha_2 V_2}{2g} = Z_1 + Y_1 + \frac{\alpha_1 V_1}{2g} + h_e$$

Where $Z_{1,2}$: are datum elevation in section 1 and 2

$Y_{1,2}$: water depths in cross sections 1 and 2 (m)

$V_{1,2}$: river flow velocity in cross section 1 and 2 (m/sec)

h_e: friction head between sequence cross sections 1 and 2.

Detail of the Saint-Venant and energy equations solution presented in hydraulic reference manual respectively [10]. By solving the equations for sequence sections, the result of water surface profile and velocity in various situation of river reach are obtained. In addition, the run can be repeated for geometry modification for training condition by using HEC-RAS program capabilities [11].

d. Scenarios of Sustainability

As mentioned in introduction, for sustainable management urban river, the blue infrastructure implies use of water as a component in design and development and the green infrastructure implies vegetation use in river training and restoration. In this study, adapted to previous experiences and practices in the region, two elements were used for reduction of floods peak in Kagithane urban river; detention pond and grassed waterway. There are two detention ponds (Gokturk and Erikli) with high performance of social, environment and economic benefits in Kagithane urban river, where another three of them are proposed in this study. The location of exist and proposed detention ponds presents in Figure 5 and their properties presented in Table 3. Furthermore, grassed water way proposed for whole of the main river after training and river hydraulics calculation shows that for grassed water way channel with natural section the flow velocity is near half of the river training condition as shown in Figure 9. The results of river hydraulics show that the lag time of routing in grassed water way for main river is two times of training by concrete flood walls.

Table 3. Exist and Proposed Detention Ponds reservoirs volume (1000 m3)

Pond name	Volume	Description
GOKTURK	765	Exist
ERIKLI	510	Exist
RES1	680	Proposed
RES2	224	Proposed
RES3	486	Proposed

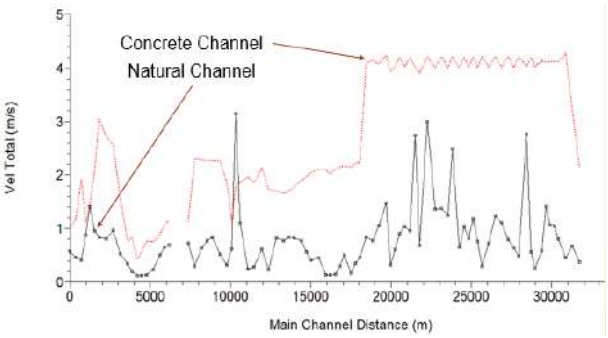

Figure 9. River Training and Natural grassed waterways velocity along Kagithane main river(m/sec)

3. RESULTS AND DISCUSSION

The prepared hydrologic model (HMS) for Kagithane river basin were run to exist condition and two sustainable scenarios respectively. The rainfall data of the September 2009 flood is used for calibration and as an extreme flood in this simulation. The result of simulations presented and compared in Figure 10 and Table 4. Figure 10 shows a little reduction of peak flow by detention basin (about 6.7 %), however, grassed waterway alternative has crucial impact on flood peak reduction (about 27 %). Reduction of floods volume only related to detention ponds storage and for each two alternatives have about 24% reduction in flood volume. The water is stored during floods in the exist and proposed detention ponds could be used for recreation and other demands in river basin. The proposed detention ponds located in upstream of the river basin and could have good role in this part of river, however, important part of the river floods generates by impervious urban area in middle and downstream of the river with dense building in the left branch of the river, thus the detention ponds cannot function significantly in this part and whole of basin for flood control. The performance of detention basin will be storage of floods in upstream. Grassed waterway shows an important impact on floods peak and as a sustainable river restoration and flood control should be considered in the Kagithane urban river. Previous studies on grassed waterway also show significant impact of this alternative for flood control in urban rivers [12].

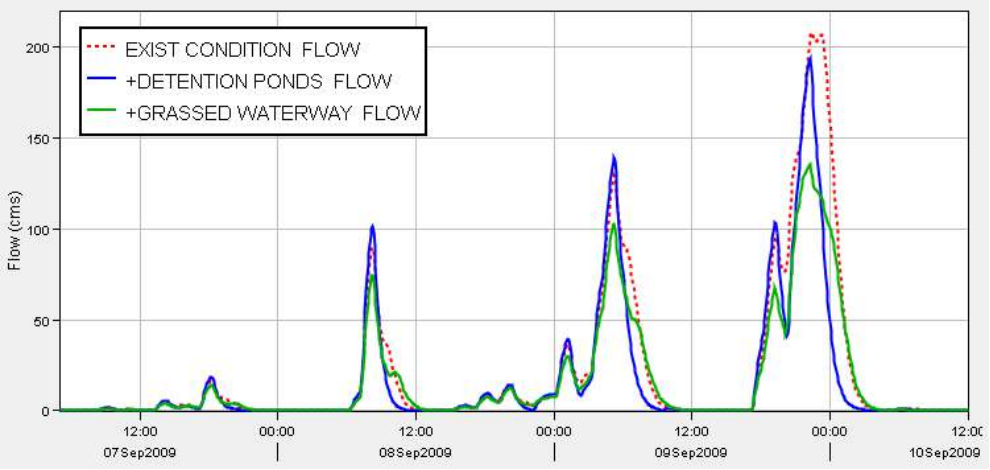

Figure 10. Impact of detention ponds grassed waterway on flood peak and volume reduction in Kagithane urban river

Scenario	Peak Flow (m3/sec)	% of Flood Peak Decreasing	Flood Volume (MCM)	% of Flood Volume Decreasing
Exist Condition	207.8	0	6.036	0
+3 Detention Ponds	193.8	6.7	4.584	24.0
+ Grassed Waterway	135.4	34.9	4.583	24.1

Table 4. Comparison Exist Condition with two sustainable modeling of flood control in Kagithane urban river

4. CONCLUSIONS

In this study two sustainable and practical alternatives (detention ponds and grassed waterway) were proposed for Kagithane urban river in Istanbul. Extreme storms in Istanbul, particularly in this river, generates flash floods that have potential of damage to infrastructure in middle and downstream urbanized area. The hydrologic model of the river basin prepared and simulated exist condition and two alternatives. The results show significant impact of grassed waterways on floods peak, however, small ponds in forestry region of the river basin could not reduce peak of the flood, but they could have significant role on flood storage and recreation in Istanbul metropole. These investigation shows grassed waterway impotency on flood control of urban river. Therefore, changing of small river channel from natural condition to lined channel needs to revise of exist plan of the river training as well. In final, for sustainable conservation and restoration of the urban river, channel with flexible grassed cover could reduce risk of floods damage more and effective than rigid concrete floodwalls.

REFERENCES

[1]. Braham, Andrew, “Fundamentals of sustainability in civil engineering”, CRC Press, ISBN 978-1-4987-7512-0, 2017
[2]. UNESCO, “River Restoration; A strategic approach to planning and management “, ISBN 978-92-3-100165-9, 2016
[3]. Perini, Katia and Paola Sabbion, “Urban Sustainability and River Restoration Green and Blue Infrastructure”, John Wiley & Sons Ltd, ISBN: 9781119244967 ,2017
[4]. United States Department of Agriculture (USDA), “National Engineering Handbook, Part 630 Hydrology, chapter 7 Hydrologic Soil Groups”, (210–VI–NEH, May 2007)
[5]. AQUAVEO, “Watershed Modeling System (WMS)”, Online User Manual, 2017
[6]. Chow, Ven Te, David Maidment and, Larry Mays, “APPLIED HYDROLOGY”, McGraw-Hill, Inc., ISBN 0-07-010810-2, 1988
[7]. Bedient, P.B., W.C. Huber, and B.E. Vieux., “Hydrology and floodplain analysis”, 4th ed., Prentice-Hall, Inc., 2008
[8]. Hydrologic Engineering Center, “HEC-HMS, Hydrologic Modeling System”, CPD-74B, Technical Reference Manual, U.S. Army Corps of Engineers, Davis, CA., 2000
[9]. Hydrologic Engineering Center, “HEC-HMS, Hydrologic Modeling System”, CPD-74C, Application Guide, U.S. Army Corps of Engineers, Davis, CA., 2015
[10]. Hydrologic Engineering Center, “HEC-RAS, River Analysis System”, CPD-69, Hydraulic Reference Manual, Version 5: U.S. Army Corps of Engineers, Davis, CA., 2016
[11]. Hydrologic Engineering Center, “HEC-RAS, River Analysis System”, CPD-68, User’s Manual, Version 5: U.S. Army Corps of Engineers, Davis, CA., 2016
[12]. Lawrence A. Baschak and Robert D. Brown, “An ecological framework for the planning, design and management of urban river greenways”, Elsevier, Journal of Landscape and Urban Planning, page 211-225, 1995

ICENS 4TH INTERNATIONAL CONFERENCE ON ENGINEERING AND NATURAL SCIENCE
2 - 6 May 2018 KIEV UKRAINE

Evaluation of Wastewater and Produced Leather Quality of Simulated Vegetable Leather Tannery Using Myrobalan Tannin

Cem Celik[1], Safiye Meric Acikel[2], Sureyya Meric[3]

Abstract

The leather tanning industry is characterized by the production of different kinds of effluents, generated in each step of leather processing. These effluents have various chemical compounds which may cause toxicity and endocrine disruption and are thus known as endocrine disrupting chemicals (EDC).Tanning stabilizes the protein structure of the hide and imparts heat stability, enhanced tensile properties, and resistance to microbial degradation. Currently most high quality leather is "chrome-tanned," produced by treatment of the hide with salts of the mineral chromium. In this study, the wastewater characteristics before and after tanning and retanning processes using myrobalan tannin are assessed. Vegetable leather production procedure was followed using one dose myrobalan tannin. Leather quality was evaluated according to standard methods. Wastewater characteristics showed that myrobalan contributed high organic content to the wastewater. The preliminary results also showed that leather quality tests failed or at minimum level to comply with the standard values indicating that there is still a need to optimize the procedure including myrobalan dose.

Keywords: Vegetable Tannery, Myrobalan Tannin, Wastewater Characterization, leather quality, polyphenols

1. INTRODUCTION

The leather tanning industry is characterized by the production of different kinds of effluents, generated in each step of leather processing. These effluents have various chemical compounds which may cause toxicity and endocrine disruption and are thus known as endocrine disrupting chemicals (EDC) [1]. Tanning stabilizes the protein structure of the hide and imparts heat stability, enhanced tensile properties, and resistance to microbial degradation. Currently most high quality leather is "chrome-tanned," produced by treatment of the hide with salts of the mineral chromium [2]. Because of environmental considerations, and customer preference, there is interest in developing new chrome-free tannages [3,4]. Thus, alternative tanning chemicals to the chromium tanning process have been evaluated during recent years to produce eco-leather [5]. The most important one among these methods is the vegetable tanning which is performed with vegetable tannins [6]. However, environmental effects of tannins should be addressed well [7,8,9] since During processing, only 40–50% of the applied tannins have been taken up, and the remaining 50–60% has been released as unspent along with the wastewater. The presence of unspent tannins poses challenge to the wastewater treatment processes, due to their recalcitrant nature. In addition, the biological treatments are less effective in degrading the tannins, due to reduced organic content and xenobiotic nature [10]. Myrobalan is a plant that grows in India and Ceylon and it is very rich in terms of tanning agent. The kernel of myrobalan do not contain any tannin. Myrobalan tree fruit without kernel, contains 34% of tannin, while 50% is in the Myrobalan tree with kernel. The amount of non-tanning substance is 17.5%. Myrobalan tree fruit is easy to extract and gives light colored tanning solution and myrobalan forms mud and precipitates. Myrobalan tree fruit gives stained and spongy leather when used alone as a tanning agent in leather process. [11]

This study was designed to produce eco-friendly leather using myrobalan in tanning and retanning processes. Leather quality and process during leather production was assessed according to standard methods.

[1] *Istanbul University, Leather Research and Application Center, Avcilar, Turkey, celik44@gmail.com*
[2] *Istanbul University, Leather Technology Program, Vocational School, Avcilar, Turkey, safiye.acikel@istanbul.edu.tr*
[3] *Namik Kemal University, Corlu Engineering Faculty, Environmental Engineering Department, Corlu 59860, Tekirdag, Turkey, E-Mail: smeric@nku.edu.tr*

2. MATERIAL AND METHODS

a. Material

Lime Splitting Cattle Leathers were supplied from Tuzla Leather Industrial Area. Myrobalan tannin was used as BASF company product and its chemical properties was given in Table 1.

Table 1. Myrobalan Tanning Chemical Properties

Tannin	Tannin (%)	Non-Tannin Matter	Non Solubility Matters	Moisture	Ash	pH	Molecular Structure
Myrobalan (Powder)	70	18	2.0	8	3.0	3.0	Hydrolyzed

b. Leather Processing

Raw leather was provided from a leather provider factory to process it with the required chemicals according to standardized procedures [12]. The processes applied on pelts are given in Table 2.

Table 2. Water and chemicals use during leather processing in this study (leather sample weight: 6.202 gr).

Process/Time	Water Consumption (v/w leather)	Chemicals	Consumption (v/w leather)	pH
Deliming (60 min)	100%	Deliming Chemicals	3.30%	8.2
Bating (40 min)	100%	Enzyme	0.50%	8.2
Washing	100%			
Pickling (180 min)	80%	Formic acid	1.60%	3.4
		Sulphiric Acid	0.20%	
Vegetable Tanning (120 min)	**80%**	**Myrobalan tannin**	**15%**	**3.8**
Retanning				
Bleaching (80 min)	200%	EDTA	0.50%	
Washing	100%			
Neutralization (70 min)	150%	Sodium Formate	2%	5.5
Washing	100%			
Vegetable retanning (150 min)	**250%**	**Myrobalan tanninn**	**8%**	
Fatliquaring (170 min)	100%	Natural and Synthetic oils	14%	

Leather samples were taken according to TS EN ISO 2418 (2006) method as detailed in Fig.1. Accordingly, the finished leather was submitted to leather quality evaluation tests following standard methods as explained elsewhere [13]. The details of preparation of leather for leather quality testing and samples taken from vertical and parallel to the back bone.

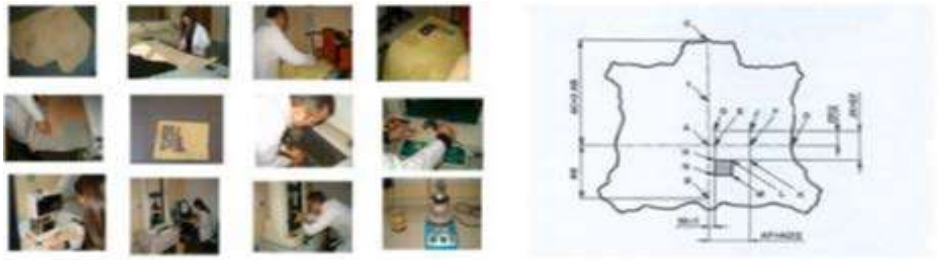

Figure 1. Vegetable Tanning and Retanning Steps

c. Wastewater Analysis

The wastewater samples originated from pickling, tanning and retanning procedures were analyzed for their COD, TOC (Schimadzu, TOC-LCPH/CPN),TSS, nitrogen (TKN and ammonia, Gerhardt, Vapodes VAP 20s) parameters according to Standard Methods (1998) as well as for absorbance (Schimadzu Lambda 1800), electroconductivity, pH, settling properties which are typical parameters and indicators for leather tannery wastewater. Furthermore, polyphenol contents (arbutrine and gallic acids) of the samples were scanned by HPLC (Prominence Modular LC20A) following the method given by Lopez-Velez et al. [14].

3. RESULTS AND DISCUSSION

a. Water consumption

As seen in Table 2, the ratio between tanning used in tannin and retanning processes is 15/8=1,87 while the ratio of water consumption between two process is 80/250=0.32. This result indicates that tanning process effluents should be more concentrated than retanning process.

b. Wastewater characteristics

Table 3 shows the characteristics of samples tested in this work. COD and TOC values increased in tanning and retanning effluent samples conforming the contribution of unspent organic chemicals [15]. As seen in Table 2, the water consumption was higher while the amount of chemicals used in retanning process were higher than tanning process. Accordingly, the ratio between amount of chemicals used and water consumption in tanning and retanning processes is assess to be more than 2. The results of waste water analysis showed that 15250 mg/L TSS, 19424 mg/L TOC, 175,84 mg/L TKN, 45,36 mg/L NH3 and 12240 mg/L COD in the myrobalan tanning effluent while 1228 mg/L TSS, 2475 mg/L TOC, 50,26 mg/L TKN, 7,87 mg/L NH3 and 5880 mg/L COD in the myrobalan retanning effluent. Drastic decrease in TOC in the retanning effluent indicates the organic content contribution of higher myrobalan tannin use in the tanning process. This drastic decrease in TKN concentration was also observed in retanning effluent. The presence of organics was followed by UV profiles as shown in Figure 2. No absorbance peaks were observed (200-300 nm) in pickling wastewater indicating that no organics were present in the effluent. As explained above, the organics were lesser in retanning process effluent than tanning process since lesser amount of water and chemicals were used in retanning process. Myrobalan which is a vegetable tanning with a low pH value and in the group of hydrolyzed tannins. This lower pH value of the tannin causes penetration problems in tanning process, and; most part of the tannin can remain in the wastewater. The waste water results of tanning process in Table 3 has higher values because of this.

Table 3. Characteristics of Myrobalan Vegetable Tanning Process Wastewaters

Sample Names	**COD (mg/L)**	**TSS (mg/L)**	**TOC (mg/L)**	**TKN (mg/L)**	**Ammonia (mg/L)**	**UV $_{254}$ (nm)[1]**	**UV $_{280}$ (nm)[1]**
Pickled		407	3044	25,76	25,76	0,001	0,008
Tanning	12240	15250	19424	175,84	45,36	>4	>4

Retanning	5880	1228	2475	50,26	7,87	2,15	2,389
	pH	**Cconductivity (ms/cm)**	**T (ºC)**	**Settling 30min (mL/L)**	**Settling 60min (mL/L)**		
Tanning	3,52	49,8	9	145	140		
Retanning	3,65	4,42	6,6	19	19		

c. Polyphenols

No arbutin was detected in both pickling and tanning processes effluents while Gallic acid (GA) was detected significantly higher in both wastewaters samples than pickling effluents as seen in Figure 3. High GA concentration (Fig.3) was found to be parallel to higher COD and TOC results (Table 2) and UV absorbance (Table 2, Figure 3) in tanning and retanning effluent samples. As seen in Table 2, UV254 and UV280 values that indicate aromatic structure and double bound in the organic content, decreased in parallel to COD and TOC parameters. The amount of gallic acid in the measurements was higher because the vegetable tanning materials of myrobalan (*Prunus cerasifera)* were included in the class of hydrolysable tannins.

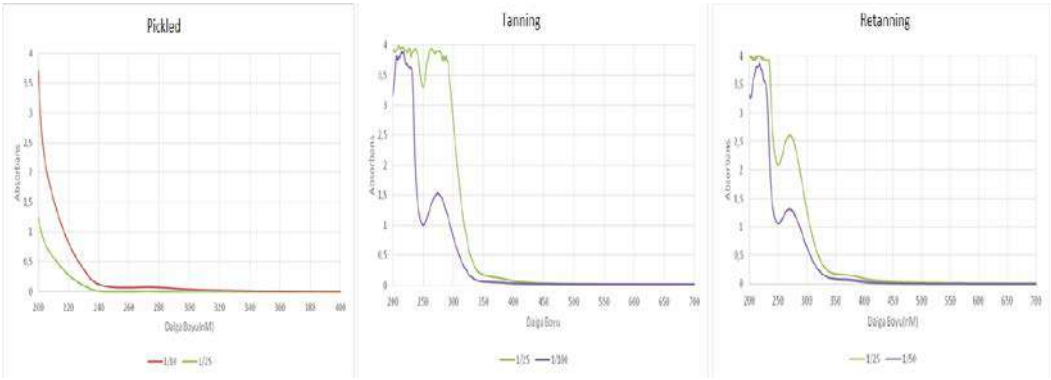

Figure 2. UV Profiles of The Myrobalan Effluent Samples

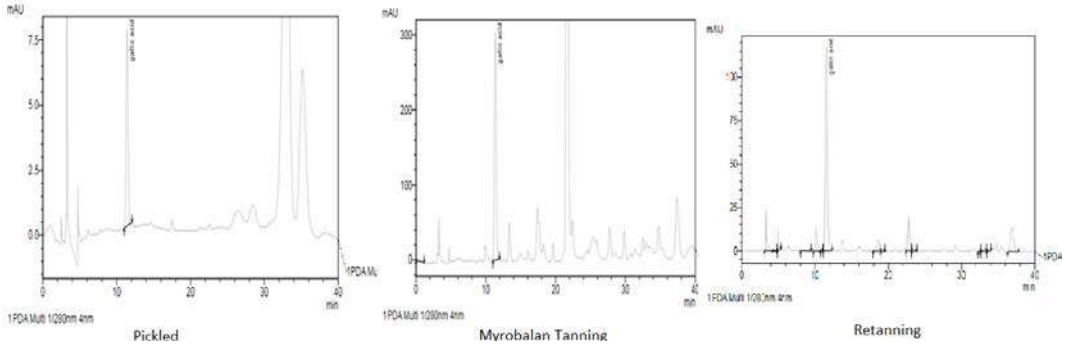

Figure 3. Gallic Acid Evolution and HPLC Profiles in the Myrobalan Effluent Samples

d. Leather Quality

Table 3 shows the leather quality tests results. Leather quality by means of the resistance coefficient for pulling was obtained significantly higher than standard values. Whereas strengthness and stretching resistance were below the standard values indicating that there is still need to improve the tanning and retanning procedures

including the amount of myrobalan to be used. Other tests regarding curving resistance measured by flexometer method, or stretching temperature definition tests were in accordance with the standard requirements.

Table 3. Physical Fastness Results of Myrobalan Tanned Leather

Tensile Strength (N/mm^2)		**Elongation at Break (%)**		**Tearing Load (N/mm)**		**Flexing Resistance (8000 Flexing)**		**Shrinkage Temperature (ºC)**	
Vertical	Parallel	Vertical	Parallel	Vertical	Parallel	Vertical	Parallel	Vertical	Parallel
15,53	27,68	110,9	67,9	114,0	73,2	No effect observed	No effect observed	75	75
EN ISO 3376:2011(EN)				EN ISO 3377-2:2005		EN ISO 5402:2005		EN ISO 3380:2005	
>25 N/mm2		>40%		>100 N/mm					

4. CONCLUSIONS

All over the abovementioned results vegetable tanning agents can be used for producing ecological high quality leather by means of leather quality tests and chromium free wastewater. On the other hand the adverse effect of myrobalan tannin of which the amount is still to be optimized for strengther leather product and higher biodegradable wastewater content, is to be better evaluated for safer effluents to protect environment.

ACKNOWLEDGMENT

This study has been performed by the support of Namik Kemal University, Scientific Research Projects Fund (NKUBAP.00.17.YL.13.06). The authors would like to thank Guclu Leather LTD. for providing leather, Ozsen Leather Factory for processing leather sample before tanning process, Stahl Company for providing tannin and other chemicals, and TASEV laboratory for supporting leather quality tests.

REFERENCES

[1]. V. Kumara, C. Majumdar, P. Roya, “Effects of endocrine disrupting chemicals from leather industry effluents on male reproductive system”, Journal of Steroid Biochemistry & Molecular Biology, vol. 111, pp. 208–216, 2008.
[2]. S. M. Mavlyanov, Sh. Yu. Islambekov, A. I. Ismailov, D. N. Dalimov, and N. G. Abdulladzhanova, “Vegetable tanning agents”, Chemistry of Natural Compounds, vol. 37, no. 1,2001.
[3]. E. De Nicola, S. Meric¸ C. Della Rocca, M. Gallo, M. Iaccarino, P. Manini, D. Petruzzelli, V. Belgiorno, M. Cheggour, A. Di Gennaro, A. Moukrim, O. Tunay, G. Pagano.“Wastewater Toxicity of Tannin-Versus Chromium-Based Leather Tanneries in Marrakesh,Morocco”,. Arch Environ Contam Toxicol, vol.53, pp. 321–328, 2007a.
[4]. S. R. Tariq, M. H. Shah, N. Shaheen, “Comparative statistical analysis of chrome and vegetable tanning effluents and their effects on related soil”, Journal of Hazardous Materials, vol. 169, pp.285–290, 2009.
[5]. S. Saravanabhavan, P. Thanikaivelan, J. Raghava Rao, B. Unni Air, T. Riramasami, “Natural Leathers from Natural Materials: Progressing toward a New Arena in Leather Processing”, Environ. Sci. Technol., vol. 38, pp. 871-879, 2004.
[6]. R. Marín-Martinez, R. Veloz-García, R. Veloz-Rodríguez, S.H. Guzmán-Maldonado, G. Loarca-Pina, A. Cardador-Martinez, L.Guevara-Olvera, R. Miranda-López b, I. Torres-Pacheco, C. Pérez Pérez, G. Herrera-Hernández, F. Villaseñor-Ortega, M. González-Chavira, R.G. Guevara-Gonzalez, “Antimutagenic and antioxidant activities of quebracho phenolics (Schinopsis balansae)recovered from tannery wastewaters”, Bioresource Technology, vol.100, pp.434–439, 2009.
[7]. E. De Nicola, M. Gallo, M. Iaccarino, S. Meric¸, R. Oral, T. Russo, T. Sorrentino, O. Tunay, E. Vuttariello, M. Warnau, G. Pagano, “Hormetic Versus Toxic Effects of Vegetable Tannin in a Multitest Study”, Arch. Environ. Contam. Toxicol., vol.46, pp.336–344, 2004.
[8]. E. De Nicola, S. Meric, M. Gallo, M. Iaccarino, C. Della Rocca, G. Lofrano, “Vegetable and synthetic tannins induce hormesis/toxicity in sea urchin early development and in algal growth”, Environ Pollut, vol. 146, pp. 46–54, 2007b.
[9]. G. Libralato, F. Avezzù, A. Volpi Ghirardini, “Lignin and tannin toxicity to Phaeodactylum tricornutum (Bohlin)”, Journal of Hazardous Materials, vol. 194, pp. 435-439, 2011.
[10]. G. Lofrano, S. Meric, G.E. Zengin, D. Orhon, “Chemical and Biological treatment technologies for leather tannery chemicals and wastewaters: A review”, Science of the Total Environment, vol. *461*, pp. 265-281, 2013.
[11]. Covington A.D. 2009, “Tanning Chemistry: The Science of Leather”, Cambridge, UK, p.384.
[12]. C. Celik, “*Vegetable Tannin Leather Processing Technology and Environmental Effects Research*”, Master Thesis, NKU, Applied Sciences Institute, 2014.

[13]. M. López-Vélez, J.A. Delgado-Prado, E. Gómez-García, F. Martínez-Martínez, "HPLC-Analysis of Polyphenolic Compounds in Spanish Red Wines and etermination of Their Antioxidant Activity by Radical Scavenging Assay". Food Onnova, Spain 2010.

[14]. International Organization for Standardisation Water Quality: Determination of the Inhibition of the Mobility of *Daphnia magna* Straus (Cladocera, Crustacea)-Acute Toxicity Test, ISO 6341 (2012) Geneva, Switzerland.

[15]. G. Lofrano, E. Aydin, F. Russo, M. Guida, V. Belgiorno, S. Meric, "Characterization, fluxes and toxicity of leather tanning bath chemicals in a large tanning district area (IT)", Water,Air, & Soil Pollution: Focus, vol. *8*(5-6), pp. 529-542, 2008.

ICENS 4TH INTERNATIONAL CONFERENCE ON ENGINEERING AND NATURAL SCIENCE
2 - 6 May 2018 KIEV UKRAINE

Usability of Alkaline Protease Enzyme in Pretreatment of Polyamide Fabrics

M. Ibrahim Bahtiyari[1], Huseyin Benli[2]

Abstract

In this study, it was planned to investigate the usability of a commercial alkaline protease enzyme in pretreatment of polyamide fabrics. For this aim different recipes, containing alkaline protease enzyme, were tested on polyamide fabrics. These pretreated polyamide fabrics were then dyed with two different acid dyes which were differed from each other in terms of molecular weight and application pH. After the dyeing processes, the dyed samples' colors were measured with a spectrophotometer and the color efficiencies were analyzed. It was found that the use of tested enzyme prior to the dyeing of polyamide fabrics with acid dyes could influence the color efficiencies of the dyed samples and most generally a limited increase could be observed.

Keywords: Enzyme, biotechnology, dyeing, acid dyes, polyamide fabrics

1. INTRODUCTION

Polyamide fibers accounted for 7% of the total synthetic fiber produced worldwide in 2014 [1]. Synthetic fibers generally do not contain naturally occurring impurities like natural fibers i.e. cotton and wool. The process sequence for nylon knitted fabric can be in this order; Desizing and Scouring, Bleaching, Fluorescent Whitening, Presetting [2]. In this study it is aimed to show the usability of alkaline protease enzyme in pretreatment of polyamide 6.6 fabrics. Nylon 6.6 is commercially synthesized by polycondensation from hexamethylene diamine and adipic acid [3].

In our previous work, polyamide fabrics were modified with two different protease enzyme "pepsin" and "trypsin" then the effect of this modification on the physical and chemical properties and on the dyeability with natural dye sources "pomegranate peels" and "walnut barks" have been examined [4]. Like that study, different studies were available on usability of protease enzymes. Proteolytic enzymes also referred to as peptidases, proteases and proteinases, hydrolyze peptide bonds in proteins [5]. They constitute one of the most important groups of industrial enzymes [6] and find use in detergents, leather industry, food industry, pharmaceutical industry and bioremediation processes [7].

2. MATERIALS AND METHODS

In scope of the study, the knitted and prewashed polyamide 6.6 fabrics were used. The fabrics were pretreated with Savinase 16 L Type EX (Novozymes) as alkaline protease enzyme. For pretreatment of polyamide fabrics, different recipes (Table 1) were carried out. The tested recipes were also conducted without use of enzyme and this process was called as blank processes. So for each recipe, 2 samples were available one was pretreated with enzyme (Savinase 16 L Type EX) and the other was treated with the same condition except using enzyme.

[1] *Corresponding author: M. Ibrahim Bahtiyari, Erciyes University, Department of Textile Engineering, 38039, Kayseri, Turkey. ibahtiyari@yahoo.com*

[2] *Huseyin Benli, Erciyes University, Mustafa Cikrikcioglu Vocational School, 38039, Kayseri, Turkey. hbenli@erciyes.edu.tr*

Table 7. Recipes used for the pretreatment of the polyamide fabrics

Recipe 1: 1 ml/l Protease Enzyme 1 g/l nonionic wetting agent pH 9-9,5 Liquor Ratio=1:30	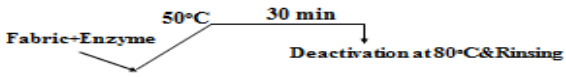
Recipe 2: 3 ml/l Protease Enzyme 1 g/l nonionic wetting agent pH 9-9,5 Liquor Ratio=1:30	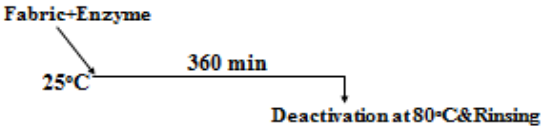
Recipe 3: 3 ml/l Protease Enzyme 1 g/l nonionic wetting agent pH 9-9,5 Liquor Ratio=1:30	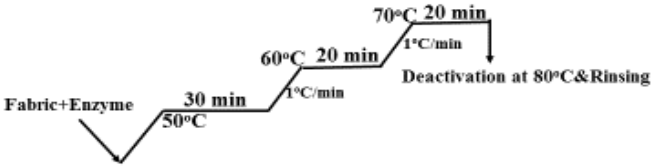
Recipe 4: 2 ml/l Protease Enzyme 1 g/l nonionic wetting agent pH 8-8.5 Liquor Ratio=1:30	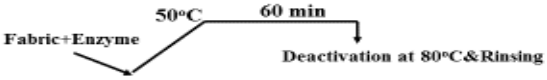
Recipe 5: 3 ml/l Protease Enzyme 1 g/l nonionic wetting agent pH 8-8.5 Liquor Ratio=1:30	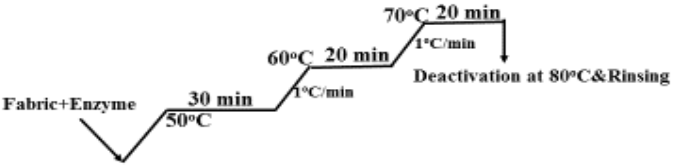

Both two samples (one was pretreated with the enzyme and the other one was pretreated with the same condition except using enzyme) for each recipe were taken to the dyeing process with two different acid dye Supracen Blue BN (dyeing pH:4) and Supranol Fast Cyanine GR (dyeing pH:6) at a dye concentration of 2%. Dyeing was conducted at a liquor ratio of 1:30. During the dyeing; after the pH adjustment, the fabrics (pretreated with the same recipe in presence and absence of protease enzyme) and the dyestuff were added to the bath and bath was heated to 40˚C. At this temperature the dyeing was conducted for 10 minutes and then the temperature was raised to 98˚C and at this temperature dyeing was carried out for 30 minutes. Afterwards, the bath was cooled and samples were taken out and washed/rinsed.

The dyed fabrics were then tested in terms of color efficiencies (K/S) with the help of Konica Minolta 3600d spectrophotometer. The increase in color efficiencies (%) caused by enzyme was calculated for each tested recipe with comparing the color efficiencies of the samples pretreated with an alkaline protease enzyme and processed with a blank process (same recipe but except using protease enzyme).

3. RESULTS AND DISCUSSION

Pretreatment of polyamide fabrics with alkaline protease enzyme was managed with the use of the different recipes. With the use of different recipes it was planned to increase the efficiency of enzymes and efficiency of processing polyamide fabrics. As seen from the table 1 recipe were differed from each other in terms of temperature, duration and the pH. After the pretreatment of the polyamide fabrics with these recipes, the samples were dyed and the change of color efficiencies (%) caused by enzymes was calculated according to the blank process of the same recipe and collected in table 2.

From the table 2 it was observed that depending on the process conditions the change in the color efficiency according to the blank process can vary. Because, recipes used in pretreatment of polyamide were differed from each other. Also, the changes in color efficiencies were varied depending on the acid dye used in dyeings after the pretreatment of polyamide fabrics as well.

Table 2. The increase in color efficiencies (%) caused by using enzyme

Recipes	Increase in color efficiency (%) in dyeings with Supracen Blue BN	Increase in color efficiency (%) in dyeings with Supranol Fast Cyanin GR
Recipe 1	0.5%	3.4%
Recipe 2	4%	2%
Recipe 3	1%	0.7%
Recipe 4	3.8%	7.2%
Recipe 5	5.4%	1.8%

It was observed that depending on the process conditions the change in the color efficiency according to the blank process can vary. By using Recipe 1, it was found that the polyamide fiber was modified to a very limited extent by the enzymatic treatment. But by using Recipe 2, in which experiments were carried out at room temperature for 6 hours at an enzyme concentration of 3 ml/l, it was determined that there was an increase in color efficiency about 4% for Supracen Blue BN and 2% for Supranol Fast Cyanin GR. Different from Recipe 2, in Recipe 3 the pretreatment of polyamide was performed stepwise. However, the modification made with this recipe did not cause any significant change when compared with the blank one.

The only unchanged factor for the tested enzyme was pH in the Recipes 1-3, and so for the next recipes (Recipes 4-5) the enzyme based pretreatment pH was adjusted to the pH 8-8.5. As a result of the pretreatment made at pH 8-8.5 and 50ºC for 1 hour (Recipe 4), it was determined that the increase in color efficiencies in dyeing with Supracen Blue BN was 3.8% and that of in dyeing with Supranol Fast Cyanin GR was 7.2 %. In Recipe 5, a gradual enzymatic hydrolysis is targeted as in recipe 3 and the aim is to relax the polyamide tight crystal structure by going to high temperatures at pH 8-8.5. It was observed that the color efficiency increase in dyeings with acid dyes was about 1.8% for Supranol Fast Cyanin GR and 5.4% for Supracen Blue BN.

4. CONCLUSION

Pretreatment is an important stage in textile finishing processes and depending on the textile material (fiber type, construction, demanded end use, etc.) the chemicals and processes can be varied. Different chemicals can be used in pretreatment stage of textile materials and in this respect enzymes can be found the area of use. Here in the study polyamide fabrics were processed with an alkaline protease enzyme and then dyed with two different acid dyes. During this process, different recipes were performed and it was found that alkaline protease enzyme can increase the dyeability of the polyamide fabrics with acid dyes. But this increase was found limited and can vary depending on the recipe and the used acid dye.

ACKNOWLEDGMENT

This work was supported by the Research Fund of Erciyes University. Project Number: FBA-11-3777.

REFERENCES

[1]. J. Wesołowski, K. Płachta, "The Polyamide Market", *Fibres & Textiles in Eastern Europe*, vol. 24, pp. 12-18, November/December 2016.
[2]. S. R. Karmakar, *Chemical Technology in the Pre-Treatment Processes of Textiles.* In: Textile science and technology series, vol 12. Amsderdam, The Netherlands: Elsevier Science B.V., 1999.
[3]. H. H.Yang, *Polyamide Fibers*, In: M. Lewin (Ed.), *Handbook of Fiber Chemistry*, 3rd ed., Boca Raton, USA: CRC Press, Taylor & Francis Group, 2007.
[4]. M. I. Bahtiyari, and H. Benli, "Dyeing of enzymatically modified polyamide fabrics with natural dyes", *Industria Textila*, vol. 67, no. 2, pp.114-120, 2016.
[5]. J. A. Mótyán, F. Tóth, J. Tőzsér, "Research Applications of Proteolytic Enzymes in Molecular Biology", *Biomolecules* vol. 3, pp. 923-942, Dec. 2013.
[6]. P. Wilson, and Z. Remigio, "Production and characterisation of protease enzyme produced by a novel moderate thermophilic bacterium (EP1001) isolated from an alkaline hot spring, Zimbabwe", *African Journal of Microbiology Research*, vol. 6(27), pp. 5542-5551, July 2012.
[7]. K. S. Naidu, "Characterization and Purification of Protease Enzyme", *Journal of Applied Pharmaceutical Science*, vol. 1, pp. 107-112, May 2011.

ICENS 4TH INTERNATIONAL CONFERENCE ON ENGINEERING AND NATURAL SCIENCE
2 - 6 May 2018 KIEV UKRAINE

Testing the *Equisetum Arvense* L. Plant for Coloration of Cotton Fibers

Huseyin Benli[1], M. Ibrahim Bahtiyari[2]

Abstract

Equisetum Arvense L. (horsetail) plant, which is now used for different aims, was used for coloring of cotton fibers in this study. Two different cotton based materials "cotton yarns" and "cotton fabrics" were colored with Equisetum Arvense L. in presence of five different metal salts (mordanting agents). These metal salts were designated as $CuSO_4.5H_2O$, $FeSO_4.7H_2O$, $KAl(SO_4)_2.12H_2O$, $ZnSO_4$ and $K_2Cr_2O_7$. By the use of these mordanting agents, it was planned to increase the color efficiency of the dyed samples and to obtain different shades. For the coloration of cotton materials, the dyeing process was conducted at boiling temperature and subsequently the process was completed by washing and drying of cotton textile materials. The dyed samples were then evaluated in terms of K/S and CIE L, a*, b*, c* and h° values. Consequently, it has been found that Equisetum Arvense L. plant can dye cotton fabrics and yarns.*

Keywords: Equisetum Arvense L., Color, Mordanting agent, Cotton, Natural dye

1. INTRODUCTION

Synthetic dyes are extensively used in many fields of upto-date technology including various branches of the textile industry [1]. Water pollution due to effluents from textile dyeing industry is a cause of serious concern [2]. On the other hand, natural dyes are generally supposed to be cheap, non-toxic, renewable and sustainable resource with minimal environmental impact [3]. So, many scientists have started to investigate natural dyes. This work is intended to provide a new source of natural colors. For this aim, *E. arvense* L. plant was tested for coloring of cotton fibers.

Equisetum arvense commonly known as field horsetail is a plant with wide prospectus. In folk medicine, it has been used for different aims [4]. In a study it was shown that the essential oil of *E. arvense* L. has strong anti-microbial activity [5]. In another study, antinociceptive and anti-inflammatory effects of hydroalcoholic extract of stem from Equisetum arvense were investigated [6]. The antioxidant activity and phenolic composition of horsetail (Equisetum arvense L.) in different extracts were studied as well [7]. Differently, a very different characteristic of this plant, as a dyestuff for textile materials, has been researched in this study.

2. MATERIALS AND METHODS

2.1. Materials

Two different cotton based textile material has been used during the study. One is the cotton fabric and the other one is the cotton yarn. Both of them were in pretreated form so they were ready for dyeing. The natural dye source "Equisetum arvense L." was obtained from local markets in the dried form and this plant was grinded before using in dyeing process. In dyeing processes five different mordanting agents "$CuSO_4.5H_2O$, $FeSO_4.7H_2O$, $KAl(SO_4)_2.12H_2O$, $ZnSO_4$, and $K_2Cr_2O_7$" were used.

[1] *Corresponding author: Erciyes University, Mustafa Cikrikcioglu Vocational School, 38039, Kayseri, Turkey.* *hbenli@erciyes.edu.tr*

[2] *M. Ibrahim Bahtiyari, Erciyes University, Department of Textile Engineering, 38039, Kayseri, Turkey.* *ibahtiyari@yahoo.com*

Figure 1. The dried plant Equisetum arvense L.

2.2. Methods

In the all experiments, mordanting agents; 3% iron (II) sulfate, copper (II) sulfate, potassium dichromate, zinc sulfate or 20% (w/w) alum were used. The weight of the natural dye source used to the textile material weight was adjusted to 1:1. The dyeing with the natural dye source and mordanting has been managed simultaneously so together mordanting method has been used and the liquor ratio was adjusted to 1:100. For all experiments, a dyeing/mordanting process shown in Figure 2 has been used.

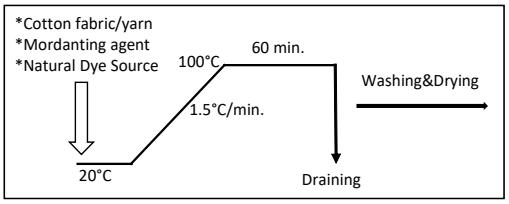

Figure 2. Dyeing diagram for cotton fabrics and yarns.

For the evaluation of the dyeings, all the dyed cotton fabrics and yarns were tested in terms of color efficiencies (*K/S*) and color values (CIE *L*a*b**) with the help of spectrophotometer (Konica Minolta 3600d). The photos of samples were also collected too.

2. RESULTS AND DISCUSSION

In scope of the study cotton yarns and fabrics were dyed with Equisetum arvense L. in presence of different mordanting agents.

*Table 1. Scanned photos and CIE L*a*b* values of dyed samples.*

Mordant agent	Cotton yarn	CIE *L*a*b**	Cotton fabric	CIE *L*a*b**
$CuSO_4.5H_2O$		***K/S*** 3.73 **L*** 59.34 **a*** 5.3 **b*** 27.32 **C*** 27.83 ***h°*** 79.01		***K/S*** 4.33 ***L**** 55.63 ***a**** 5.64 ***b**** 25.14 ***C**** 25.76 ***h°*** 77.35
$FeSO_4.7H_2O$		***K/S*** 2.42 **L*** 57,83 **a*** -0,62 **b*** 8,7 **C*** 8,72 ***h°*** 94,05		***K/S*** 1.99 ***L**** 60.94 ***a**** 0.27 ***b**** 9.59 ***C**** 9.59 ***h°*** 88.4
$KAl(SO_4)_2.12H_2O$		*K/S* 2.62 ***L**** 82,26 ***a**** -2,17 ***b**** 39,11 ***C**** 39,17 ***h°*** 93,18		***K/S*** 4.99 ***L**** 75.97 ***a**** -2.66 ***b**** 41.03 ***C**** 41.11 ***h°*** 93.71
$ZnSO_4$		*K/S* 1.19 ***L**** 80,32 ***a**** 0,82 ***b**** 21,82 ***C**** 21,84 ***h°*** 87,84		***K/S*** 1.81 ***L**** 70.52 ***a**** 0.98 ***b**** 19.19 ***C**** 19.22 ***h°*** 87.09

$K_2Cr_2O_7$		*K/S*	0.92		***K/S***	1.23
		L*	78,08		***L****	73.99
		a*	3,98		***a****	1.55
		b*	18,3		***b****	19.59
		C*	18,73		***C****	19.65
		h^o	77,72		h^o	85.49

As seen from the Table 1, *E. arvense* L. plant can dye both cotton yarns and cotton woven fabrics and it can be easily told that there is no significant differences in color shades between cotton yarns and woven fabrics dyed by using same mordanting agents. However, with the change of the mordanting agents, the colors of the samples differed from each other dramatically. It was observed that by using copper sulfate brown colors can be obtained. Moreover it was found that gray colors by using iron sulfate, yellow by using alum, beige by using zinc sulfate, and cream shades by using potassium dichromate could be obtained.

These findings from the photos of the samples were confirmed from the spectral measurements. For example, dyeing of the cotton fabrics in presence of alum caused L* value: 75.97; a* value: -2.66 and b* value: 41.11; this result represents yellow colors and the hue angle is 93.71 in that case. In case of using copper sulfate as mordanting agent in dyeing of cotton fabrics; L* value: 55.63; a* value: 5.64 and b* value: 25.14 and meanwhile a 4.33 value of color efficiency has been observed. In general the color efficiencies have varied by using different mordanting agents and the lowest color efficiencies was obtained if potassium dichromate mordant has been used during the dyeing.

3. CONCLUSIONS

The coloring of textile materials is an important stage for responding the demands of the consumers. Today, the coloring of textile materials is usually achieved by using different synthetic dyes. On the other hand, it is also seen that different natural resources have begun to be tested again as a dye source. In this context, research on different plant sources has also begun to gain importance.

In this study, Equisetum Arvense L. (horsetail) plant, which is now used for different aims were used for coloring of cotton fibers. As a result of the study, it was determined that Equisetum arvense L. plant could be used in dyeing of cotton textile materials and it was observed that mordanting agents were obviously very important in terms of the obtained colors and shades and interestingly a vivid yellow was obtained by using alum mordant.

REFERENCES

[1]. E. Forgacs, T. Cserháti, and G. Oros, “Removal of synthetic dyes from wastewaters: a review,” *Environment International*, vol. 30, issue 7, pp. 953-971, Sep. 2004.

[2]. Ratna, B.S. Padhi, “Pollution due to synthetic dyes toxicity & carcinogenicity studies and remediation”, *International Journal of Environmental Sciences*, vol. 3, no.3, pp. 940-955, Nov. 2012.

[3]. M. Shahid, S. Islam, F. Mohammad, “Recent advancements in natural dye applications: a review.” *Journal of Cleaner Production*, vol. 53, pp. 310-331, 2013.

[4]. N. S. Sandhu, S. Kaur, and D. Chopra, “Equietum Arvense: Pharmacology and Phytochemistry-A Review,” *Asian Journal of Pharmaceutical and Clinical Research*, vol. 3, issue 3, pp. 146-150, July-Sep. 2010.

[5]. N. Radulović, G. Stojanović and R. Palić, “Composition and Antimicrobial Activity of Equisetum arvense L. Essential Oil”, *Phytotherapy Research*, vol. 20, pp. 85-88, Jan. 2006.

[6]. F. H. M. Do Monte, J. G. dos Santos Jr., M. Russi, V. M. N. B. Lanziotti, L. K. A. M. Leal, and G. M. A. Cunha, “Antinociceptive and anti-inflammatory properties of the hydroalcoholic extract of stems from Equisetum arvense L. in mice,” *Pharmacological Research*, vol. 49, issue 3, pp. 239-243, March, 2004.

[7]. N. Mimica-Dukic, N. Simin, J. Cvejic, E. Jovin, D. Orcic, and B. Bozin, “Phenolic Compounds in Field Horsetail (Equisetum arvense L.) as Natural Antioxidants”, *Molecules*, vol. 13, issue 7, pp. 1455-1464, July 2008.

ICENS 4TH INTERNATIONAL CONFERENCE ON ENGINEERING AND NATURAL SCIENCE
2 - 6 May 2018 KIEV UKRAINE

Selection of Optimal Fiducial Point Locations on Faces with Genetic Algorithm for Down Syndrome Identification

Necmi Taspinar[1], Safak Saraydemir[2], Selami Parmaksizoglu[3], Osman Erogul[4], Hulya Kayserili[5]

Abstract

Down syndrome is one of the most commonly encountered dysmorphic syndromes. There are some salient facial features in patients with Down syndrome and those features contain discriminative information. This information can be implemented to diagnose the syndrome in a computarized face-based diagnostic system. But it is a time consuming process to analyze whole face images in the computer environment. We chose to carry out the diagnosis of Down syndrome by finding the most valuable and informative fiducial points on face images instead of using whole face images. Thus, useful classification results were obtained to provide for a fast pre-diagnose. Genetic Algorithm (GA) which is a successful heuristic method was used to determine the optimal fiducial points. Feature extraction was performed with Gabor Wavelet Transform (GWT). Classification process is implemented with k-nearest neighbor (kNN) and support vector machines (SVM) methods. We analyzed the classification accuracy results according to the SVM kernel type and kNN distance metric. SVM classifier with radial basis function (RBF) kernel type has obtained the best results. Experimental results confirm the advantage of the proposed approach in terms of high accuracy and significantly reduced dimensionality according to the other studies which uses local feature based techniques.

Keywords: Down syndrome, Gabor Wavelet Transform, Face Recognition, Genetic Algorithm.

1. INTRODUCTION

Dysmorphology is the subspecialty of clinical genetics focusing on the identification of syndromes, and their etiopathogenesis. Review articles and databases (LMD & POSSUM) [1] or defined syndrome descriptions are used by clinical geneticists when they do not have enough experience on the syndromes.

Several investigations, cytogenetic, molecular, and biochemical tests are needed for reaching the definite diagnosis when no clinical diagnosis is available. Performing multiple tests without a firm clinical diagnosis is expensive and time consuming. Clinical geneticists struggle in finalizing these tests even in developed western countries. Furthermore the number of clinical geneticists to evaluate all the cases with dysmorphic features is insufficient. In order to solve such problems, alternative ways to achieve clinical diagnosis, such as computer aided face recognition techniques, are underway.

Computer aided face recognition techniques are used successfully in many areas of daily life such as information security, defence, access control [2]. There are also many applications of these techniques in the field of medicine [3-4]

[1]*Corresponding author: Erciyes University, Department of Electrical and Electronics Engineering, 38039, Kayseri, Turkey, taspinar@erciyes.edu.tr*
[2]*National Defence University, Turkish Military Academy, Department of Electronics Engineering,06150 Ankara, Turkey, ssaraydemir@kho.edu.tr*
[3]*Technology Transfer Office, Antalya Bilim University, 07190 Antalya Turkey,selami.parmaksizoglu@antalya.edu.tr*
[4]*Department of Biomedical Engineering, TOBB University, 06560 Ankara, Turkey, erogul@etu.edu.tr*
[5]*Department of Medical Genetics, School of Medicine, Koc University, 34450 Istanbul, Turkey, hkayserili@ku.edu.tr*

Down syndrome is one of the most common dysmorphic syndromes. It has well defined characteristic facial features. Some of them are epicanthic folds, depressed nasal root, upward slanted palpebral fissures, short/small nose, midfacial hypoplasia, small mouth with protruding tongue and small ears. These facial features help diagnose the syndrome, when analyzed them with computer aided face recognition methods.

There are two main approaches for face recognition, holistic and local feature-based. In the holistic approach, whole face is analyzed and statistical methods are used to extract features from faces. However, local feature-based methods require the localization of fiducial points for extracting them. There are also hybrid approaches that combine information from both [2].

In this study, we utilized the local feature-based method to distinguish individuals with Down syndrome from healthy ones. We identified the salient local points instead of prediction. Local image descriptions around these points are extracted. 2D Gabor kernels used since they are robust against translation, rotation, and scaling as local descriptors [5-6]. 2D Gabor kernels can select the different orientations and spatial frequencies. When we used the 2D Gabor wavelets to extract features, dimensionality increased. We need to analyze the contribution of spatial location of the Gabor kernels to the recognition task in order to reduce Gabor features' dimension and eliminate redundant features. For high dimensional problems of 2D Gabor wavelets, there are several alternative fast sub-optimal algorithms such as sequential forward selection, sequential backward selection, plus-L-minus-R and floating search methods [7]. As it is demonstrated in [8] those sub-optimal algorithms above are inferior to GA [9]. GA searches for solutions spaces by simultaneously and can obtain optimal or near-optimal solutions on large spaces of possible solutions. It is used to optimize face recognition performance [10-11]. We used GA to find the most informative and valuable fiducial point locations on face image. We tried also lattice based sampling [8] in order to show the contribution of GA to the classification success. kNN and SVM methods used as statistical classifiers. The best results are achieved with SVM type classifier which uses RBF kernel.

2. MATERIALS AND METHODS

2.1 Image Acquisition and Selection

The photos of individuals with Down syndrome were obtained from Friendly Life Down Syndrome Foundation and the photos of healthy individuals from a day-care nursery. We informed the individuals and their parents about the study design and obtained written informed consents.

We standardized the equipment and illumination parameters. A soft illumination was obtained using two different lighting sources and thus shadows on faces were reduced. A homogeneous background was utilized. The images were obtained with a digital camera (Nikon Coolpix S2500). Our face database contains frontal face images of 80 individuals (40 individuals with Down syndrome and 40 healthy individuals).

The ages of the individuals ranged from 1 to 14. We collected images from 22 girls and 18 boys in the Down syndrome group and from 19 girls and 21 boys in the healthy group.

2.2 Image Preparation

Resolution of images set to 80x60. Image preprocessing procedures implemented on MATLAB. Conversion into gray scale of color images, histogram equalization and resizing were performed respectively. Resolution of images set to 80x60 to reduce the size of the search space on the fiducial point selection by GA. The face database is divided into four datasets. Three of these datasets were used for training and one of them was implemented for testing. This process was repeated for four times to use each dataset in training and test.

2.3 Selection of Gabor Filter Locations for Feature Extraction

In order to determine the most valuable and informative fiducial points on face images, we should place Gabor filters carefully over the face. Determining the fiducial point locations is formulated as a feature subset selection problem. Aim is to select a subset from a given set to maximize success [12]. A chromosome represents a subset in GA. Discrimination performance of the subset is fitness function. Each gene in a chromosome represents the position of a Gabor filter. We define the dimensionality of the selected subset as 25; so, each chromosome consists of 25 genes. The detailed flow chart is shown in Figure 1.

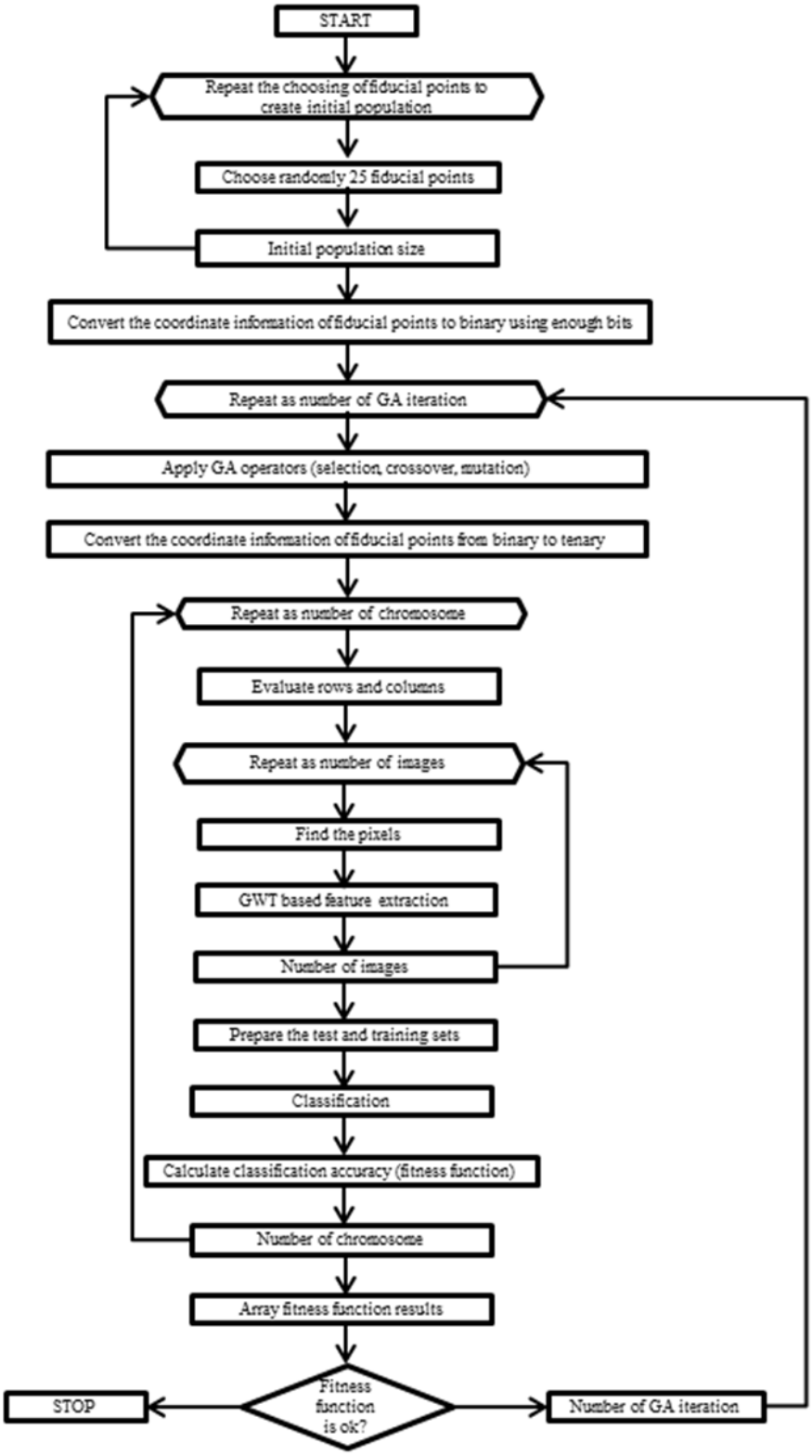

Figure 1. The detailed flow chart of GA based Down syndrome identification system.

In the lattice based method, sparse sampling of Gabor kernels at several points was performed. A rectangular lattice of size 5x5 was placed over the central part of the face region as shown in Figure 2.

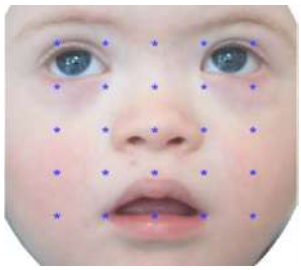

Figure 2. The rectangular lattice placed over the central part of the face region.

At each point for GA and lattice methods, 40 different Gabor kernels were used to extract feature vector. The size of each feature vector becomes 1000x1. The resolution of Gabor kernels was set to 15x15 in order to decrease the overlap. The overall diagram is shown in Figure 3.

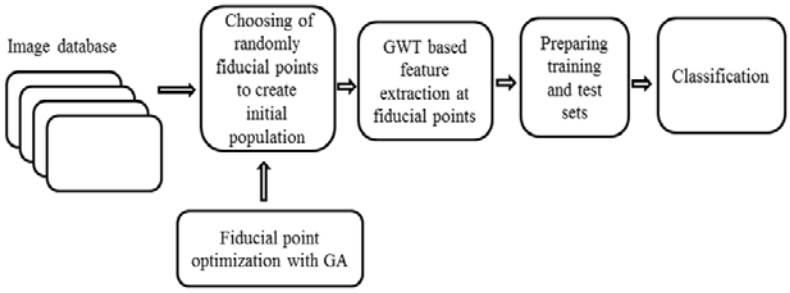

Figure 3.The overall diagram of the proposed approach.

2.4. Classification Methods

SVM and kNN statistical classification methods [13-15] were applied in determining the classification accuracy. SVM is used in classification and regression analysis problems. It has been working as supervised learning and helps us for analyzing datasets and recognizing patterns. When an input data is given to the SVM, two possible classes which form the output are predicted. The separation of two datasets with maximum distance is aimed. Linear, polynomial, quadratic and RBF kernel types were used. kNN classifies patterns according to the closest training examples in the feature space. Taking into account majority vote of neighbor of a pattern, we can assign it to the most common class between its k nearest neighbours. Euclidean and cityblock distances were used in kNN. The k value was selected as 1,3,5,7 respectively. We found similar results due to the low variance between classes. We chose to represent the results according to the 3 for kNN considering this similarity. The equations of distance metrics are formulated below. Consider that X and Y patterns with dimension N will be compared. xi and yi denotes the ith elements of X and Y patterns, respectively.

$$Euclidian\ distance = D_e(X,Y) = \sqrt{\sum_{i=1}^{N}(x_i - y_i)^2} \quad (1)$$

$$Cityblock\ distance = D_c(X,Y) = \sum_{i=1}^{N}|x_i - y_i| \quad (2)$$

The classification accuracy is obtained with proportion of true matching results to all results. Here, true matching implies the individuals correctly identified with Down syndrome or as healthy.

3.EXPERIMENTAL RESULTS

3.1.Selection Results of Gabor Filter Locations

GA was used to analyze the contribution of the most valuable and informative 25 fiducial points. The classification results were evaulated using parallel computers because of the large search space.

Single-point crossover was applied to produce new chromosomes. The uniform mutation operator was implemented to improve the fitness values at the each iteration. For quick convergence, roulette wheel selection function was used. GA was implemented with initial population size of 50. GA was terminated when we could not obtain an improvement on the fitness values for a specified time interval.

The concentration regions of the points were obtained by maximizing classification results. When we analyzed those concentration regions, it was clear that many points were localized on the nose, eyes and eyebrow regions since they contain high frequency information. Some other parts of faces like cheeks and forehead include few points since they contain low frequency information. Some of the point sets obtained with GA are shown in Figure 4.

Figure 4. Sample point sets obtained with GA based method.

In lattice approach, we positioned a rectangular 5x5 lattice over the central part of the face. 25 points equally spaced five points in the rows and columns were used to extract features with GWT as in GA approach..

Despite the use of an equal number of points in each method, when we compared Table 1 and Table 2, we obtained better classification success with GA based method according to the lattice based sampling.

Table 8.The average rates of classification results.

	ClassifierType					
	kNN (euc)	**kNN (city)**	**SVM (lin)**	**SVM (quad)**	**SVM (poly)**	**SVM (rbf)**
AverageRates	0,605	0,63	0,666	0,695	0,74	0,771

Table 2.The lattice based sampling results.

	Classifier Type					
	kNN (euc)	**kNN (city)**	**SVM (lin)**	**SVM (quad)**	**SVM (poly)**	**SVM (rbf)**
Classification Results	0,463	0,475	0,513	0,538	0,588	0,588

3.2.Classification Results

In GA based approach, the classification process was repeated 10 times in order to differentiate the initial population for each repetition. The average rates of classification results are presented in Table 1.The lattice based sampling results are shown in Table 2.

During SVM classification, the best results were attained with order of 3 in polynomial kernel and scaling factor of 1 in RBF. We used the cityblock and euclidean distances as a distance metric in kNN classifier. The results were given according to the 3NN.

In tables, lin, poly, quad and rbf stand for linear kernel, polynomial kernel, quadratic kernel and RBF kernel for SVM, respectively. city, euc abbreviations symbolize cityblock and euclidean distance metrics for kNN classifier.

Considering the average of classification accuracy rates for the GA based approach, the best results achieved were 77,1% and 74% with SVM-rbf and SVM-poly classifiers, respectively. The lowest classification level was 46,25% which was obtained with kNN-euc classifier in lattice based sampling.

SVM-rbf classifier type has showed better results than the others as seen from the tables. Considering the average of classification accuracy rates, we obtained better results with SVM based classification methods than kNN based for both testing strategies.

There is a local feature-based Down syndrome recognition study in literature which uses a combination of elastic bunch graph matching (EBGM) and artificial neural network (ANN) [16]. This is the first study in literature which uses local feature-based method combined with GA. Table 3 shows the results in comparison. Better classification rates with SVM-rbf, SVM-poly and SVM-quad were achieved.

Table 3.The comparison table.

Method	**ClassifierType**	**Number of Images (Downsyndrome / healthy)**	**ClassificationResults**
EBGM [16]	ANN	36 (18 / 18)	0,687
GWT+GA	Statistical	80 (40 / 40)	kNN-euc: 0,605 kNN-city: 0,630 SVM-lin: 0,666 SVM-quad: 0,695 SVM-poly: 0,740 SVM-rbf: 0,771

4. DISCUSSION AND CONCLUSION

For the identification of dysmorphic syndromes by novice clinical geneticists, a quick and reliable guide is necessary for everyday practice in most countries. If they achieve the clinical diagnosis at a short time span by the aid of computer based diagnostic systems, they can ask for definite/conclusive laboratory testing, inform the family on the disorder, its etiopathogenesis, prognosis, management, recurrence risk and for reproductive options with accuracy. This will lead to a reduction in health budget since laboratory testing will be pinpointed and the time gained will be offered for better clinical care of the patient and counselling of the family members.

In this study, priority was given to Down syndrome because it is a common syndrome. We utilized from GWT to extract features, GA to search points, SVM and kNN to classify results. When the classification results were analyzed, it revealed that points which were identified by GA are more informative and valuable than the points used in lattice based sampling for Down syndrome discrimination.

In analysis of points for GA based approach, it is clear that many are placed on the nose, eyes and eyebrow regions since they contain high frequency information. Some other parts of the face like cheeks and forehead include distinctive points at low rate as they contain low frequency information. In lattice based method, the syndrome discrimination success was obtained inferior to GA based method. If enough images can be obtained

for other dysmorphic syndromes, it is evaluated that successful results can be obtained in the classification of them by the same algorithm.

ACKNOWLEDGMENT

The photographs of individuals with Down syndrome were obtained at Friendly Life Down Syndrome Foundation. The authors wish to thank foundation staff for their assistance to contact the families and are also grateful to the parents of individuals with Down syndrome and healthy individuals for their cooperation and participation in the study.

REFERENCES

[1]. J. Pelz, V. Arendt, andJ. Kunze, "Computer assisted diagnosis of malformation syndromes: an evaluation of three databases (LDDB, POSSUM, and SYNDROC),"*American Journal of Medical Genetics*, vol. 63, pp. 257-267, 1996.
[2]. W. Zhao, R. Chellappa, P.J. Phillips, and A. Rosenfeld, "Face recognition: a literature survey," *ACM Computing Surveys*, vol. 35, pp. 399-458, 2003.
[3]. B. Balliu, R.P. Wurtz, B. Horsthemke, D. Wieczorek, and S. Bohringer, " Classification and visualization based on derived image features: application to genetic syndromes,". *PLoS ONE*, vol. 9(11), e109033, 2014.
[4]. P. Hammond, and M. Suttie, " Large-scale objective phenotyping of 3D facial morphology," *Human Mutationol.*, vol.33, pp. 817-825, 2012.
[5]. L. Shen, and L. Bai, " A review on Gabor wavelets for face recognition," *Pattern Analysis and Applications*, vol 9, pp. 273-292, 2006.
[6]. A. Serrano, I.M. de Diego, C. Conde, and E. Cabello, "Recent advances in face biometrics with Gabor wavelets: A review," *Pattern Recognition Letters*, vol. 31, pp. 372-381, 2010.
[7]. P. Somol, P. Pudil, J. Novovicova, and P. Paclik, "Adaptive floating search methods in feature selection," *Pattern Recognition Letters*, vol. 20, pp. 1157-1163, 1999.
[8]. B. Gokberk, M.O. Irfanoglu, L. Akarun, and E. Alpaydin, "Optimal Gabor kernel location selection for face recognition," in *Proc. International Conference on Image Processing (ICIP)*, pp. 677–680, 2003.
[9]. H.K. Ekenel, and B. Sankur, "Feature selection in the independent component subspace for face recognition," *Pattern Recognition Letters*, vol. 25, pp. 1377-1388, 2004.
[10]. P. Sukhija, S. Behal, and P. Singh, "Face recognition system using genetic algorithm," *Procedia Computer Science*, vol. 85, pp. 410-417, 2016.
[11]. W.H. Al-Arashi, H. Ibrahim, and S.A. Suandi, "Optimizing principal component analysis performance for face recognition using genetic algorithm," *Neurocomputing*, vol. 128, pp. 415-420, 2014.
[12]. A. Jain, R.P.W. Duin, and J. Mao, "Statistical pattern recognition: a review," *IEEE Transactions on Pattern Analysis and Machine Intelligence*, vol. 22, pp. 4-37, 2000.
[13]. J. Wei, Z. Jian-qi, and Z. Xiang, "Face recognition method based on support vector machine and particle swarm optimization," *Expert Systems with Applications*, vol. 38, pp. 4390-4393, 2011.
[14]. E. Gumus, N. Kilic, A. Sertbas, and O.N. Ucan, " Evaluation of face recognition techniques using PCA, wavelets and SVM," *Expert Systems with Applications*, vol. 37, pp. 6404-6408, 2010.
[15]. A. Glowacz, and Z. Glowacz, "Recognition of images of finger skin with application of histogram, image filtration and K-NN classifier," *Biocybernetics and Biomedical Engineering*, vol. 36, pp. 95-101, 2016.
[16]. O. Erogul, M.E. Sipahi, Y. Tunca, and S. Vurucu, "Recognition of Down syndromes using image analysis," in *Proc. 14th National Biomedical Engineering Meeting*, pp.289-292, 2009.

Biography of the presenting author

Necmi Taspinar received the B.S. degree in Electronic Engineering from the Erciyes University, Kayseri, Turkey in 1983, the M.S. degree in Electronic and Telecommunications Engineering from the Technical University of Istanbul, Istanbul, Turkey in 1988, and the Ph.D. degree in Electronic Engineering from the Erciyes University, Kayseri, Turkey in 1991. He has been Full Professor in the Department of Electrical and Electronic Engineering, Engineering Faculty, Erciyes University, Kayseri, Turkey since 2002. His research interests include theory and applications of error-control coding, multi-user detection, channel estimation, PAPR reduction methods, CDMA systems, MC-CDMA systems, OFDM systems, MIMO systems, IDMA systems and applications of neural networks, fuzzy logic, adaptive neuro-fuzzy inference system and intelligent optimization techniques to communications problems.

ICENS 4TH INTERNATIONAL CONFERENCE ON ENGINEERING AND NATURAL SCIENCE
2-6 May 2018 KIEV UKRAINE

Rocks Having High Potentially Toxic Elements Contents and Interaction With Environment

Kenan Kilic[1], Kadir Saltali[2], Alper Durak[3]

Abstract

The aim of this study was to determine the effect of main materials on the heavy metals content of soil and water. While the heavy metals content of the soil in the study field was higher than the limit values, only the copper, manganese, nickel and chrome contents of the water samples were found higher than the limit values. Higher heavy metals content in the soil and water can be toxic to vegetable, fruit and other cultivated plants grown in the study field and can be passed on to humans via food chains if taken by the plants to be grown. Large amounts of heavy metals in the soil and water in the study field can be a major problem for the environment and human health.

1. INTRODUCTION

Factors controlling total and biologically viable concentrations of heavy metals in soil are very important for human toxicology and agricultural production (Alloway, 1995). The amount and distribution of heavy metals in soil depends on the nature of the main soil material from which the soil develops, weathering processes, biocycle, additions originating from the atmosphere and deposits originating from natural resources (Cortizas et al., 2003). The effect of each of these factors on the heavy metals content depends on the developmental stage of soil and the mobility of the specific element in the soil system. The weathering of minerals in rocks is one of the natural sources of heavy metals in the soil system, and the metal concentrations in soil can be estimated from the amount of elements in the main material (Palumbo et al., 2000).

Composition and stratigraphy of the main material, organic matter content, degree of development of soil, climatic conditions and human activity are influential on the element distribution in soil (Cortizas et al., 2003). Heavy metals are distributed in the soil profile by events such as eluviation and accumulation, and are driven by mechanisms such as weathering, changes in soil formation factors and bio-geochemical processes. In some studies on the long-term behavior of heavy metals in soil, it has been determined that the weathering rate and the distribution of elements in the soil profile increase (Sjostrom and Qvarfort ,1992; Bain et al. 1994). Koons et al. (1990) have shown that heavy metals (Co, Cr) form compounds with Fe-oxide minerals during the formation of saprolite from the weathering of granite. Kasimov et al. (1996) determined that heavy metals (Cr, Cu, Ni, Pb, Zn) in Russian soil changed depending on soil types and horizons. These studies show that the distribution and transportation of heavy metals in soil profiles vary depending on (1) soil type, (2) horizons, (3) weathering and age, (4) Fe-oxide minerals, and (5) climatic conditions.

An environment containing heavy metals is the most important risk factor for cancer. Turkdogan et al. (2002) found that soil, vegetables and fruits contained 2–340 times more carcinogenic heavy metals (Co, Cd, Pb, Zn, Mn, Ni, and Cu) than the limit values on volcanic soils and in heavy metals content of vegetables and fruits grown on these soils. They pointed out that the “upper gastrointestinal cancer” cases, which are

[1] Department of Environmental Engineering, Faculty of Engineering, University of Nigde, 51240 Nigde, Turkey, kenan_kilic@hotmail.com

[2] Department of Soil Science, Faculty of Agriculture, University of Kahramanmaras Sutcu Imam, Kahramanmaras, Turkey, kadirs@ksu.edu.tr

[3] Department of Horticulture Science, Faculty of Agriculture, University of Inonu, Malatya, Turkey, alper.durak@inonu.edu.tr

very common in the Van region, may be due to high carcinogenic metals in soil, vegetables and fruits. Epidemiological studies have shown that cancer cases are caused by the pollution of the environment by heavy metals, radioactive elements and their products (Hayes, 1997).

2. MATERIAL AND METHODS

2.1. Study Field

The study area was located between 37°25' and 38°58' north latitudes and 33°10' and 35°25' east longitude. The average annual precipitation and average annual temperature were 338 mm and 10.8 °C, respectively.

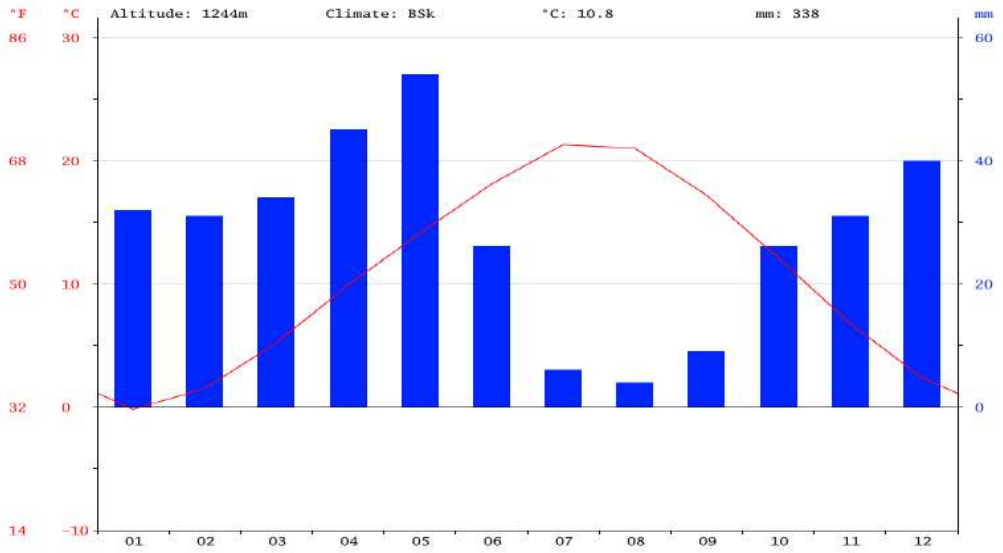

Figure 1. Average precipitation and temperature values of the study area

The study field was under different types of land use. These types of land use consisted of meadow/pasture, field, garden, dry farming and irrigated farming areas. Traditional tillage methods (plowing at a depth of about 20 cm, plowing with a cultivator at a depth of 15 cm, and plowing with a disc harrow at a depth of 10 cm) and, at the same time, diammonium phosphate, ammonium nitrate, urea and potassium sulphate fertilizers — with varying amounts depending on the product grown — were applied in the cultivated agricultural areas. Observations made during the study indicated that the soil profile thickness was usually very shallow (0–20 cm).

The main materials of the soil were metamorphic rocks such as gneisses, amphibolites, quartzite and marble (Anonymous, 2012c). The predominant minerals of these rocks were quartz, feldspar, hornblende and calcite.

2.2. Soil sampling

A total of 26 soil samples were taken from 0–20 cm depth. Air dried soil samples were sieved (<2 mm) and used for laboratory analyses. Soil samples were taken according to the random sampling method, and their GPS coordinates were recorded.

Sand, silt and clay fractions were determined using the pipette method (Gee and Bauder, 1986). The pH and electrical conductivity (EC) of the soil were determined in pure water (1:2.5 soil:water) (Blakemore et al., 1987). The soil organic matter content was determined by the wet ashing method (Walkley-Black, 1985), the cation exchange capacity by the ammonium acetate method (Thomas, 1982).

Table 1. *Limit values in soil and water of some potentially toxic elements (Rose at al., 1981)*

	Cd	Co	Cr	Cu	Mn	Ni	Pb	Zn
Soil (ppm)	0.06	8	16	20	850	40	10	50

Water (ppm)	0.01	0.02	0.05	1.5	0.05	0.02	0.05	15

The heavy metals content of soil samples was extracted in aqua regia (3 volumes of HCl acid + 1 volume of HNO_3 mixture) and measured by using ICP (ISO/CDT, 1995). Water samples from surface and drinking water were adjusted to pH 2 using nitric acid, and their heavy metals content was determined using ICP.

3. RESULTS AND DISCUSSION

3.1. The physical, chemical properties and potentially toxic elements of the soil

According to the EC values, the soil was salt-free (50.7–229 μmhos/cm) and strongly alkali (7.85–8.88), with medium pH. The soil had a silty, clayey sand texture. Organic matter contents were found to be at medium and high levels (1.94–6.11%).

Spatial distribution maps showed that the cadmium values in the research field changed between 783 ppm at the lowest and 7015 ppm at the highest. Generally, cadmium values were found high in the northern, middle northern and north eastern parts of the study field. Cobalt values varied between 11 ppm at the lowest and 83 ppm at the highest. In general, the middle, northeast and north of the study field contained more cobalt than the other parts. The chrome values ranged from 18 ppm at the lowest to 609 ppm at the highest and were found to be high in the northwestern, middle, and northeastern parts of the study field. The copper values were between 28 ppm at the lowest and 94 ppm at the highest, and the north, southeast, middle and south of the study field contained more copper than the other parts. Manganese values were found to vary between 483 ppm at the lowest and 2715 ppm at the highest. In general, the manganese values were found high in the middle, northwestern and northeastern parts of the study field. Nickel values ranged from the lowest of 333 ppm to the highest of 5198 ppm. In general, the northwestern, southwestern and southeastern parts of the study field contained more nickel than the other parts. Lead values were found to vary between 6.2 ppm at the lowest and 71.5 ppm at the highest. The lead values are generally high in the northern and southeastern parts of the study field. Zinc values varied between 302 ppm at the lowest and 1843 ppm at the highest. In general, the middle parts of the study field contained more cobalt than the other parts.

Sample number	Silt (%)	Clay (%)	Sand (%)	Organic Mat. (%)	pH	EC (µS/cm)

1	8	6,72	85,28	2,37	8,60	200,04
2	14	8,72	77,28	1,94	8,88	162,0
3	20	8,72	71,28	2,37	8,78	170,8
4	12	12,72	75,28	3,67	8,36	147,0
5	16	10,72	73,28	3,24	8,72	162,2
6	12	8,72	79,28	3,45	8,80	131,3
7	14	8,72	77,28	3,89	8,48	90,0
8	8	4,72	87,28	3,89	8,32	50,7
9	8	2,72	89,28	4,04	8,36	41,2
10	10	4,72	85,28	2,76	8,16	123,6
11	16	4,72	85,28	5,83	7,85	113,8
12	20	4,72	75,28	3,30	8,73	104,3
13	14	6,72	79,23	2,37	8,21	90,8
14	16	10,72	73,28	2,87	8,15	134,7
15	10	6,72	83,28	3,28	8,03	191,4
16	12	8,72	79,28	5,98	8,03	208,8
17	10	2,72	87,28	6,11	7,96	193,3
18	10	4,72	85,28	5,83	8,02	87,3
19	8	4,72	87,28	5,61	8,21	219,5
20	14	6,72	79,28	4,86	8,28	168,5
21	10	6,72	93,28	5,83	8,49	184,6
22	10	10,72	79,28	5,98	7,94	229,0
23	14	12,72	73,28	3,24	8,54	192,2
24	12	8,72	79,28	3,09	8,03	149,4
25	12	4,72	83,28	3,71	8,32	67,6
26	12	4,72	83,28	3,82	8,81	103,1

Table 2. Some physical and chemical properties of the soil

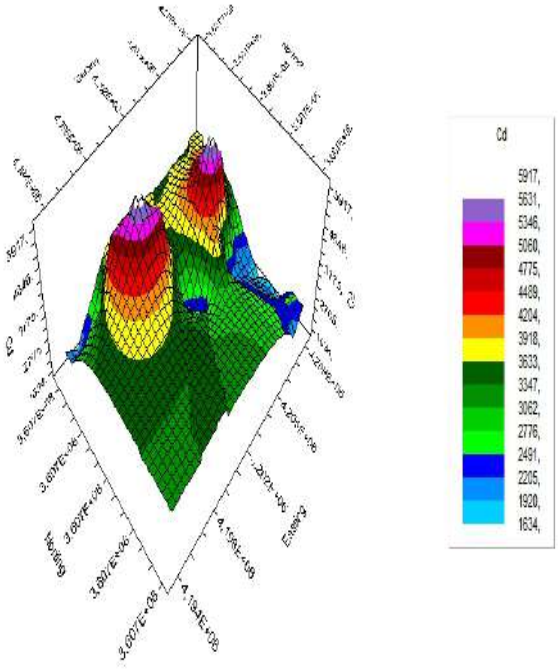
Cd
5917,
5631,
5346,
5060,
4775,
4489,
4204,
3918,
3633,
3347,
3062,
2776,
2491,
2205,
1920,
1634,

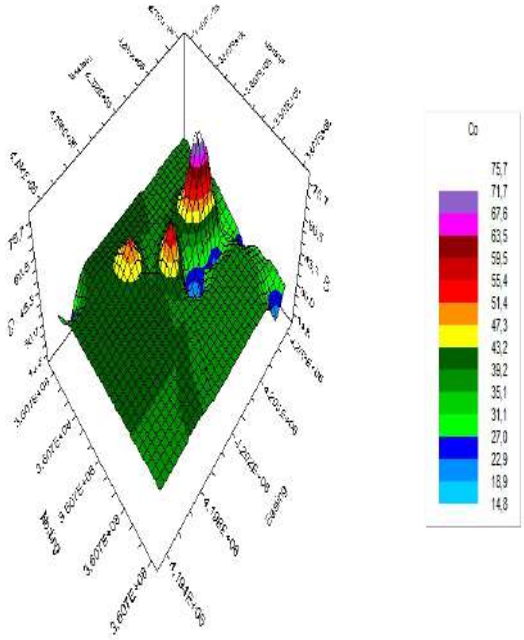
Cd
75,7
71,7
67,6
63,5
59,5
55,4
51,4
47,3
43,2
39,2
35,1
31,1
27,0
22,9
18,9
14,8

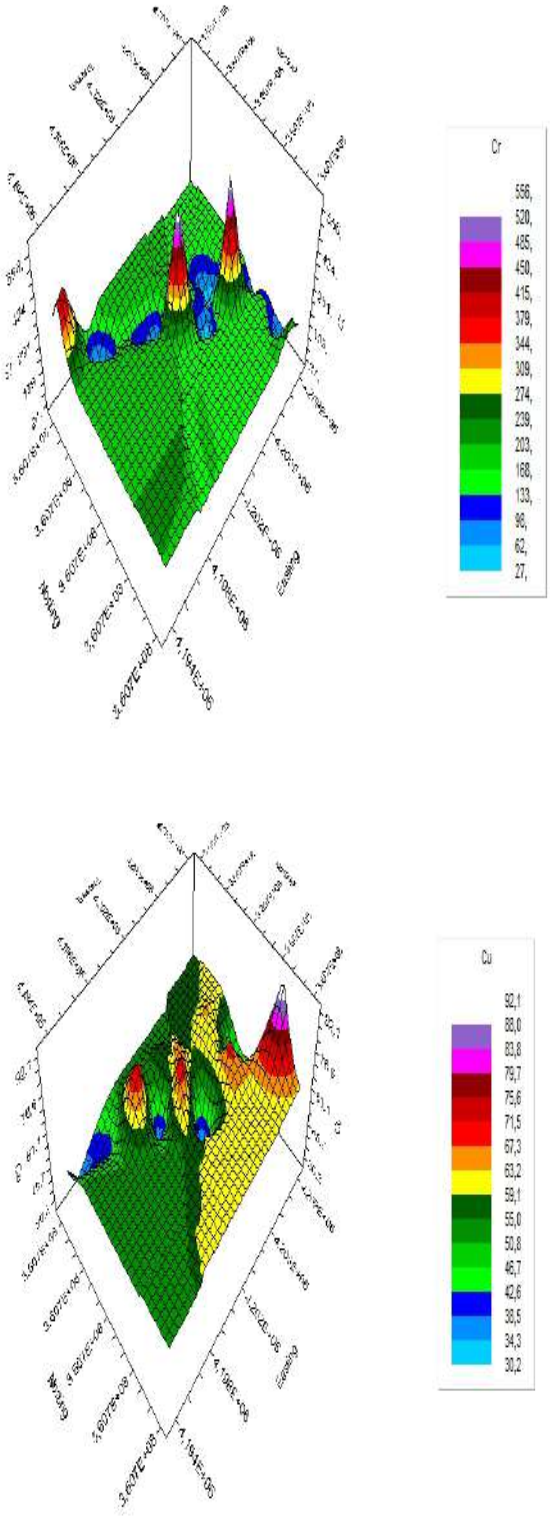

Figure 2. Spatial variability of the potentially toxic elements

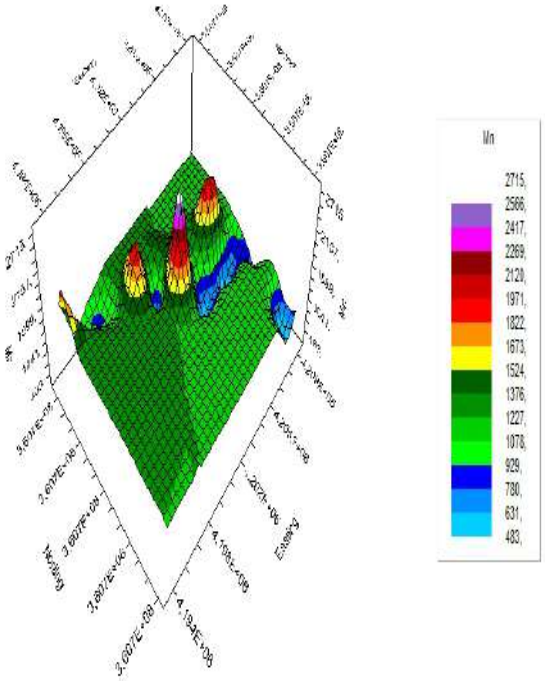
Mn
2715,
2566,
2417,
2269,
2120,
1971,
1822,
1673,
1524,
1376,
1227,
1078,
929,
780,
631,
483,

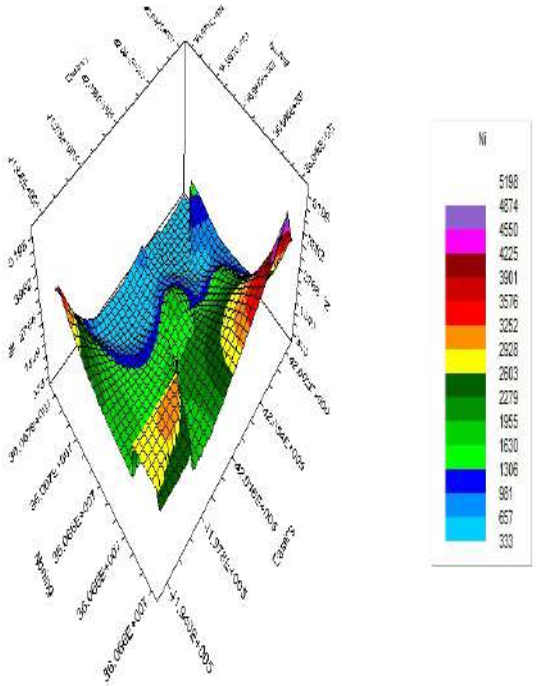
Ni
5198
4874
4550
4225
3901
3576
3252
2928
2603
2279
1955
1630
1306
981
657
333

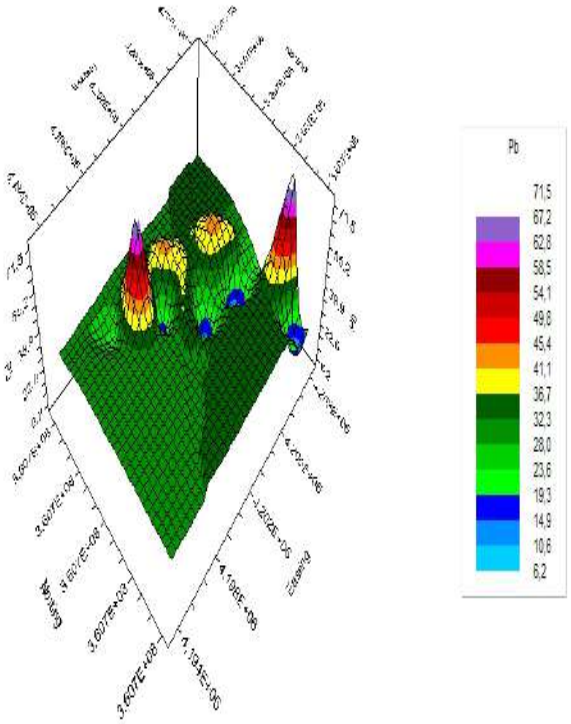

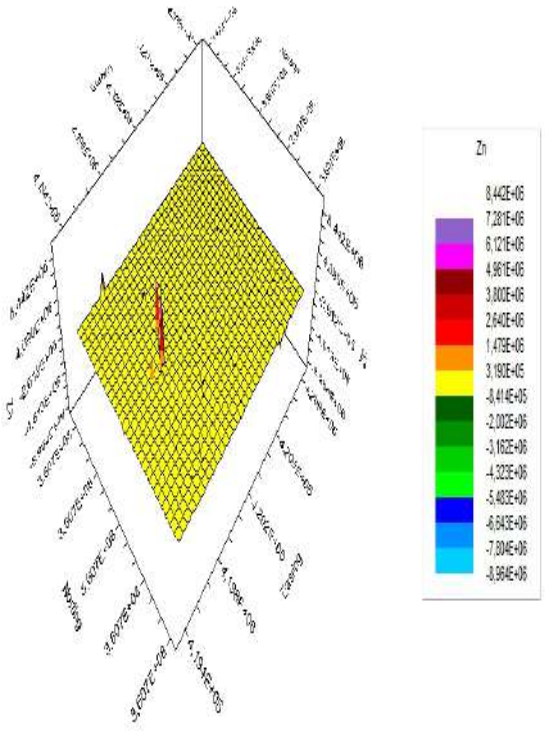

Figure 2. Continued.

3.2. Heavy Metal Contents of the Water Samples

Copper contents of the water samples were found to be between 0.77 and 4.04 ppm. The highest copper values were determined in the eastern, northeastern, northwestern and western parts. Manganese values ranged from 2.5 to 10.1 ppm, with the highest values being found in the middle northern and eastern parts. Nickel values ranged from 0.04 to 0.63 ppm, with the highest values being found in the southeastern parts. Zinc values ranged from 0.34 to 0.67 ppm, with high values in the middle northwestern and western parts. Cobalt values ranged from 0.03 to 0.20 ppm, with high values in the north-south direction. Chrome values ranged from 0.02 to 1.22 ppm, and the highest value was found in the north and northeast-southwest direction. Lead values were between 0.07 and 0.17 ppm and reached the highest values in the western and northwestern parts. In general, copper, manganese, zinc, cobalt, chrome, lead and cadmium were high in the water in the northern, northeastern, northwestern and western parts of the study field, while nickel values were found high in its southeastern parts.

4. CONCLUSIONS

The heavy metals content of the soil consisting of rocks in the study field were higher than the limit values. Copper, manganese, nickel and chrome contents of the water samples taken from the study field were higher than the limit values. High levels of heavy metal content in the soil and water can be toxic to vegetable, fruit and other cultivated plants grown in the study field and can also be passed on to humans via food chains if taken by the grown plants in high amounts. The fact that the soil and water samples contained large quantities of heavy metals can be a major problem for human and environmental health.

Acknowledgement

This study was supported by the Research Funding Chair of Nigde Omer Halisdemir University (Project number: FEB 2012/17).

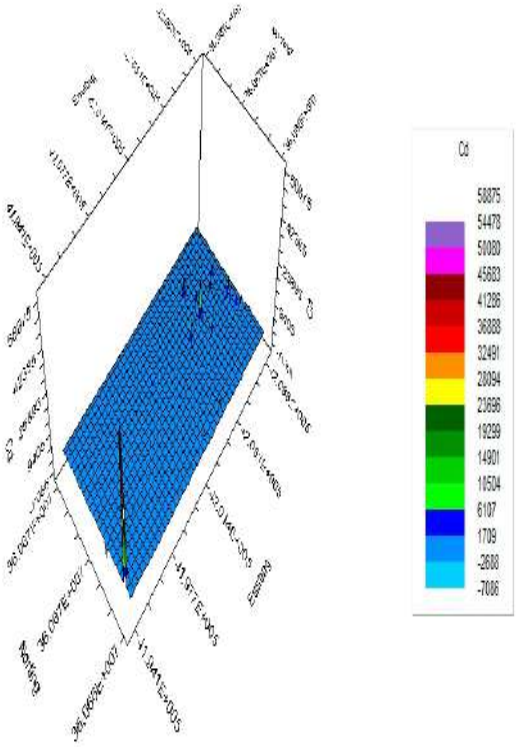
Cd
58875
54478
50080
45683
41286
36888
32491
28094
23696
19299
14901
11504
6107
1709
-2688
-7086

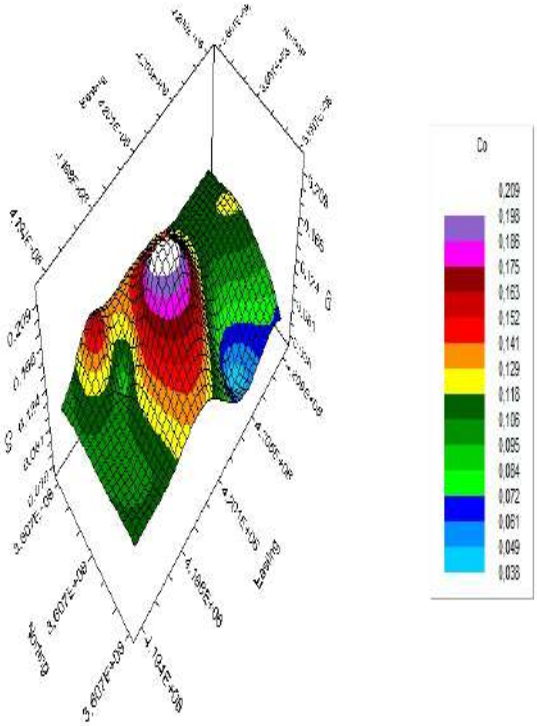
Co
0.209
0.198
0.186
0.175
0.163
0.152
0.141
0.129
0.118
0.106
0.095
0.084
0.072
0.061
0.049
0.038

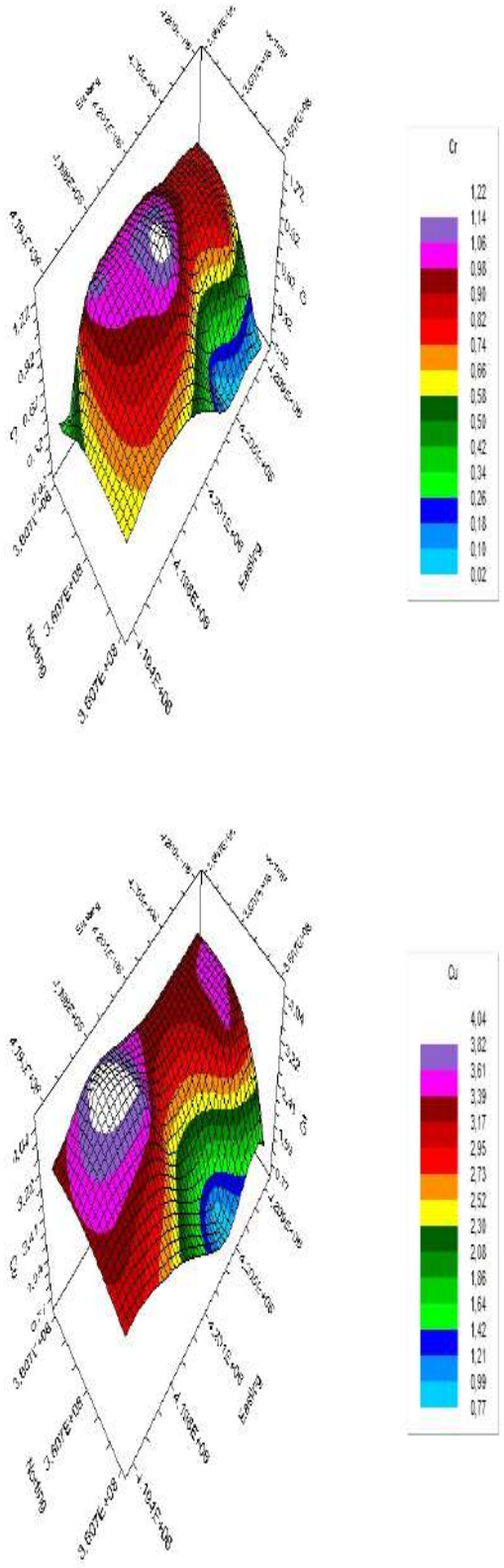

Figure 3. Spatial variability of the waters

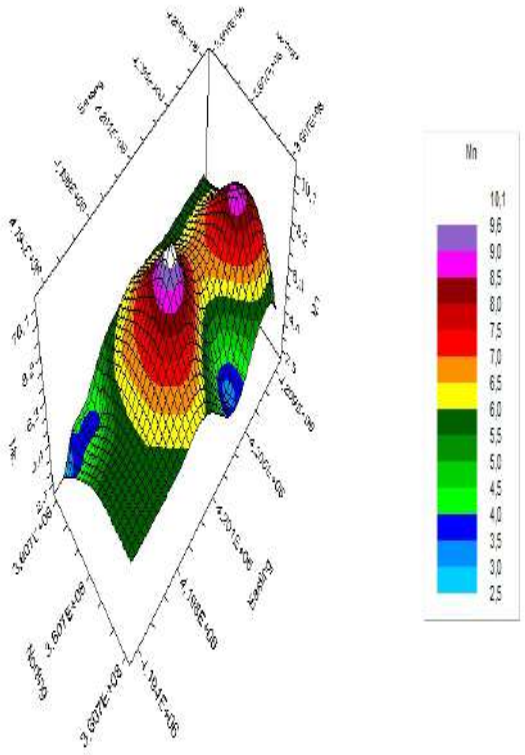
Mn
10,1
9,6
9,0
8,5
8,0
7,5
7,0
6,5
6,0
5,5
5,0
4,5
4,0
3,5
3,0
2,5

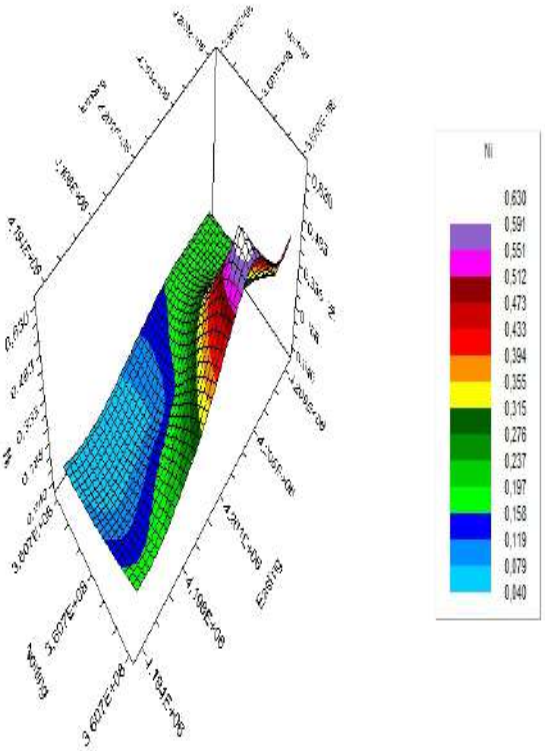
Ni
0,630
0,591
0,551
0,512
0,473
0,433
0,394
0,355
0,315
0,276
0,237
0,197
0,158
0,119
0,079
0,040

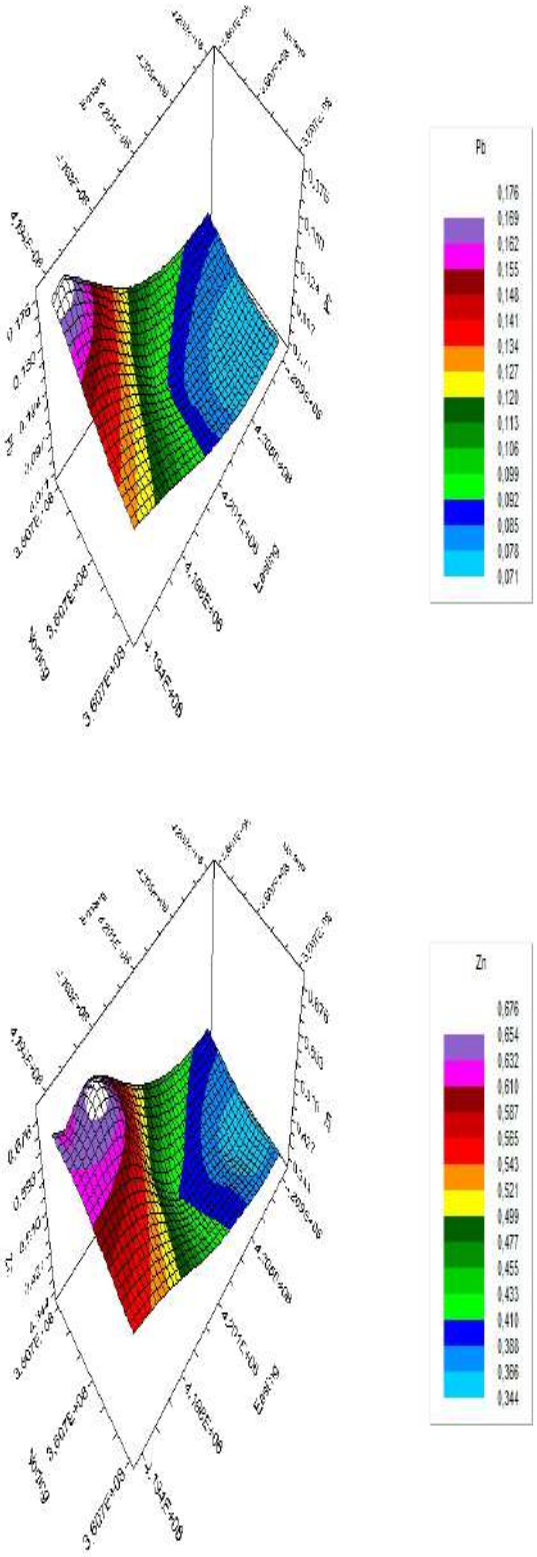

Figure 3. Continued.

LITERATURE

[1] Alloway, B.J., 1995. Heavy metals in soils, Glasgow, Scotland Blackie Academic and Professional Publishers, Pp: 22–151,
[2] Anonim,2012c.http://www.mta.gov.tr/v2.0/bolgeler/konya/index.php?id=nigde_bolgesel_jeoloji
[3] Bain I., 1994. Agriculturel Reform in Taiwan. Chinese Univ. Pr. Businessδ Economics.
[4] Blakemore, L.C., Searle, P.L., Daly, B.K., 1987. Methods for chemical analysis of soils. New Zealand Soil Bureau Scientific Report No. 80, Lower Hutt.
[5] Cortizas, M.A., 2003. García-Rodeja Gayoso E., Nóova Muñoz J.C., Pontevedra Pombal X.,
[6] Burman P., Terribile F., Distribution of some selected major and trace elements in four Italian soils developed from the deposits of the Gauro and Vico volcanoes. Geoderma, 117, 215–224.
[7] Gee, G.W., J.W,Bauder., 1986. Particle-size analysis A. Klute (Ed.), Methods of Soil Analysis. Part I. Physical and Mineralogical Methods. Agronomy Monograph 9, Soil Science Society of America, Madison , pp. 383–412
[8] Hayes R.B., 1997. The Carcinogenicity Of Metals In Humans. Cancer Causes Control 8, (3), 371–375.
[9] Koons, P.O., 1990. The two-sided wedge in orogeny; erosion and collision from the sand box to the Southern Alps, New Zealand: Geology, v. 18, pp. 679–682
[10] Palumbo, G., 2000. A look at data integration and analysis using GIS. In gradoc: Graphic documentation systems in mural paintings conservation Rome: ICCROM, 114–124.
[11] Sjostrom J., Qvarfort U., 1992. Soil Science SOSCAK, Long Term Changes of Soil Chemistry in Central Sweden.
[12] Turkdogan M.K., Kilicel, F., Kara, K., Tuncer I., Uygan I., 2002. Heavy metals soil, vegetables and fruits in the endemic upper gastrointestinal cancer region of Turkey. Environmental Toxicology and Pharmacology, 13, 175–179.
[13] Thomas, G.W., 1982. Exchangeable cations. In: Page, A.L., Miller, R.H., Keeney, D.R. (Eds.), Methods of Soil Analysis. Part 2: Chemical and Biological Properties. ASA, SSSA, Madison, pp. 159-165.
[14] Walkley-Black., 1985. A critical examination of a rapid method for determining organic carbon in soil-effect of variation in digestions and of inorganic soil constituents. Soil Sci., 63: 251-263.

ICENS 4TH INTERNATIONAL CONFERENCE ON ENGINEERING AND NATURAL SCIENCE
2 - 6 May 2018 KIEV UKRAINE

Designing and Evaluating Map Symbols for Elementary School Students

Ilkay Bugdayci[1], Huseyin Zahit Selvi[2]

Abstract

Maps can be used effectively when designed with different features and needs of the users. Especially, maps used by students in basic education need to be carefully designed. In this context, cartographers have important duties and responsibilities in the designing maps suitable for cognitive development levels of children. For this purpose, for the first stage of training namely "Turkey Atlas for Elementary School" atlas design and production was carried out by the authors. Atlas prepared in accordance with the level of the elementary school students, contains different thematic maps about Turkey (Political, Physical, Regional, Tourism and Economy Maps etc). For torism and economy maps of Turkey, 66 symbols representing the most important values of our country, were designed. In this study, the identification of the symbols and the testing of the perceptibility of these symbols will be explained. The perceptibility of these symbols was tested with 100 elementary school students (9-10 age). Symbols with a perception rate of less than 50% were redesigned. In this context 18 symbols, redesigned and with new symbols atlas completed.

Keywords: Cartographic design, Children maps, Symbolization

1. INTRODUCTION

With the use of maps in different areas, a large user has been created that varies in purpose, needs, level of education and etc. Maps can be used effectively when designed with different features and needs of the users. One of the most effective user group is children also. Maps used by students in basic education need to be carefully designed. In order to reduce learning difficulties, the process of deciding how objects should be designed in terms of the purpose and scale of the map is an important step in children's maps. For this reason, generalization and symbolization in the design of educational maps where more or less small-scale thematic maps are involved must be done carefully and carefully. Maps should be designed with signs that children can easily perceive, avoiding unnecessary detail that will create perceptual difficulties in children and difficult to read the map. In addition to this atlases are one of the most significant auxiliary materials used in the teaching of social sciences, history and geography. For this reason, it is clear that the intensive use of atlases in the primary and secondary school education will affect the use of maps in a positive or negative way.

There are many studies that indicate that maps and atlases used in the field of education should be designed in accordance with both the education system and the age of the children of the system and the perceived level of perception [1, 2, 3, 4, 5, 6]. In addition to this in many countries, it is seen that cartographers, students and educators produce quality atlases as educational materials [7, 8, 9]. There are also many studies to contribute to the development of maps for children and to test and develop the map skills of children users [10, 11, 12, 13, 14, 15, 16].

It is seen that there are problems especially in generalization and symbolization in maps and atlas which exist in our country. One of the most important problems is that the symbols that represent information on the map are not appropriately identified for children. The aim of the study is to test the effectiveness of the symbols which designed for atlas project of writers, if easily read and perceive or not by children.

[1] *Corresponding author: Necmettin Erbakan University, Department of Engineering and Architecture, 42090, Meram/Konya, Turkey. ibugdayci@konya.edu.tr*

[2] *Necmettin Erbakan University, Department of Engineering and Architecture, 42090, Meram/Konya, Turkey. hzselvi@konya.edu.tr*

2. MATERIAL AND METHOD

Current maps on atlases and textbooks have been analyzing for a while by the authors. Unfortunately, many deficiencies have determined on these maps. There are a lot of problems on maps, about printing, color, labeling, generalization, symbolization, geographical location and etc. Up to now geographers and graphic designers have designed maps for education in Turkey. Cartographers have important responsibilities in the field of map use in education too. Because of need to map for different purposes and for different users, the development of cartographic design requires. In this context, the design of symbols, font, color, graphical representation, legend must be appropriate for the children age depends on the perception and level of education. An atlas project developped for elementary school students with a project. The aims of this project are, designing and producing maps and atlases according to age groups and levels of perception of these students and measuring the contribution of maps to map use ability of children in this age group. When the atlas maps were designed, both cartographic design principles were complied with and the contents were designed according to the age and level of the students. Cartographic design should be evaluated with generalization, symbolization and production components. In order to reduce learning difficulties, generalization and symbolization are the most important parts in map design. Within the scope of generalization in the design of the maps, it was simplified by the opinions of the educators, which made it difficult for children to perceive the difficulty and to avoid unnecessary detail which would make the map difficult to read.

Firstly, the prominent values and historical places of Turkey in terms of tourism and economy, in order to design symbols, has determined. Care was taken to ensure that the content of all the atlas maps was consistent with the elementary school curriculum. It was decided to design a total of 66 symbols for tourism and economy maps. Symbols were designed with the help of the graphic designer. Symbols were assessed by asking 100 (3rd and 4th grade) students what each symbol means. A single test were used for this evaluation given in Figure 1.

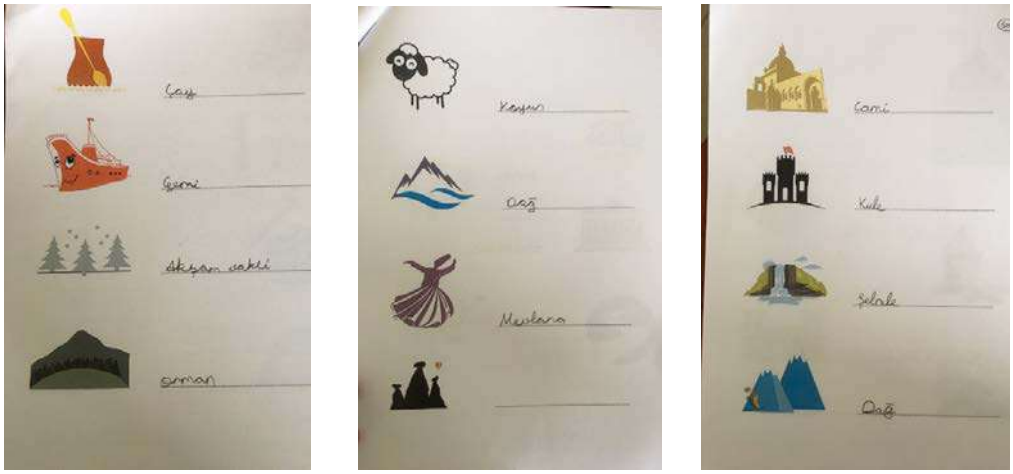

Figure 1.*The test that performed to students*

As a result of the evaluation, 18 symbols that were less than 50% detection rate were redesign. Figure 2 shows the first form of some symbols and the redesigned form after the evaluation with children.

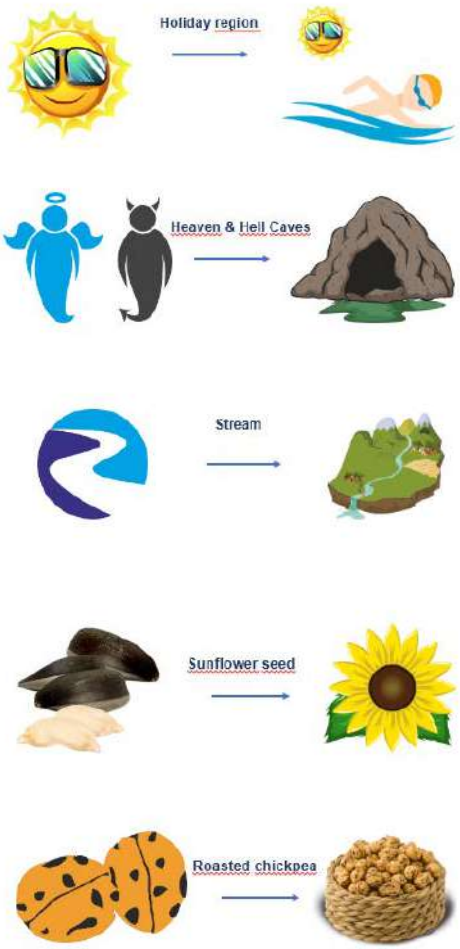

Figure 2. *First form and redesigned form of some symbols*

Easily perceived symbols by students is shown in Figure 3. The use of pictorial symbols is often suggested in terms of ease of perception in the design of children maps [2, 7, 17].

Figure 3. *Some symbols that easily perceived by the students*

The economy and tourism map of Turkey (Figure 4) and for all regions of Turkey (Figure 5) was designed with new symbols. With all designed maps atlas project has completed and published with the name of "Turkey atlas for Elementary School".

Figure 4. *The economy and tourism map of Turkey with new designed symbols.*

Figure 5. *The economy and tourism maps of some regions of Turkey with redesigned symbols*

3. CONCLUSIONS

It is the first atlas designed by cartographers and published in geomatics engineering fields in Turkey. Qualify maps with cartographic design, teachers training and interest, students and education system are the most important parts of map use in education as a whole. To designed the most suitable and effective map for each user is the most important and hard work.

In this study totally 66 symbol was designed with evaluating readability and perceptibility of symbols. A single test was prepared and asked what each symbol means to 100 elementary school students (9 and 10 age). After the assessment, less understood 18 symbols were identified. Then these symbols was redesigned. Symbolizing to be done using pictorial symbols that may be fun for children is thought to be more memorable and easier to perceive.

Improving the map use ability of children, with different studies, will provide significant contributions to the spread of map use.

ACKNOWLEDGMENT

This study was funded by Scientific Research Projects Grant of Necmettin Erbakan University.

REFERENCES

[1]. Kristien O., Philippe De M., Lien D., Nina V.D. V., Nico V. D. W., Stephanie V., "Education In Cartography: What Is The Status Of Young People's Map-Reading Skills?, Cartography And Geographic Information Science", 43:2,134-153, Doi: 10.1080/15230406.2015.1021713, 2016.
[2]. Wiegand, P., "Learning And Teaching With Maps", Taylor & Francis, London: Routledge, 2006.
[3]. Myridis, M., Christodoulou, A., Kalyva, E., Karanikolas, N., Lafazani, P., "Cartography And Children: Designing A Multimedia Educational Tool", 23. International Cartographic Conference, Moscow, Russia, 2007.
[4]. Uzumcu, N. O., "Ilkogretim 6. Sinif Sosyal Bilgiler Dersinde Harita Okuma Becerisinin Aktif Ogrenme Yontemiyle Kazandirilmasi", Yuksek Lisans Tezi, Gazi Universitesi Egitim Bilimleri Enstitusu, Ankara, 2007.
[5]. Ertugrul, Z., "Ilkogretim 6. Sinif Ogrencilerinin Harita Ve Kure Kullanim Becerilerinin Tespiti", Yuksek Lisans Tezi, Gazi Universitesi, Egitim Bilimleri Enstitusu, Ankara, 2008.
[6]. Bugdayci, I., "Ilkogretimde Harita Kullanimi Uzerine Bir Inceleme", Selcuk Universitesi, Fen Bilimleri Enstitusu, Doktora Tezi, 2012.
[7]. Bandrova, T., Deleva A., "Contemporary Cartography For Children In Bulgaria", Joint Seminar On Maps For Special Users, Wroclaw, Polonya, 1998.
[8]. Claudio, J. B. S., Herben, K. A. R., Wagner, F. B., "The Making Of School Atlas Targeted To Children In The First Grades Of Fundamental Learning In The Schools Of Brazil", 22. International Cartographic Conference, A Coruna Spain, 2005.
[9]. Bandrova, T., Dinev C., "The New Cartographic Products In Bulgaria -Modern School Atlases", Poster Presentation, 22. International Cartographic Conference, Cd, A Coruna, Spain, 2005.
[10]. Yildiz, L., "Ilkogretim 7. Sinif Sosyal Bilgiler Derslerindeki Harita, Grafik Ve Sekillerin Kavranma Duzeyi (Aksaray Ili Ornegi)", Yuksek Lisans Tezi, Gazi Universitesi, Egitim Bilimleri Enstitusu, Ankara, 2006.
[11]. Ertugrul, Z., "Ilkogretim 6. Sinif Ogrencilerinin Harita Ve Kure Kullanim Becerilerinin Tespiti", Yuksek Lisans Tezi, Gazi Universitesi, Egitim Bilimleri Enstitusu, Ankara, 2008.
[12]. Akar, B., "Ilkogretim 6. Sinif Ogrencilerinin Harita Kullanma Duzeylerinin Ve Harita Kullanimina Iliskin Ogretmen Goruslerinin Degerlendirilmesi", Mustafa Kemal Universitesi, Sosyal Bilimler Enstitusu, Yuksek Lisans Tezi, 2008.
[13]. Duman, H., "Sosyal Bilgiler Egitiminde Harita Kullanimi Ve Harita Kullanimi Konusunda Ogretmen Gorusleri", Uludag Universitesi Egitim Bilimleri Enstitusu, Yuksek Lisans Tezi, 2011.
[14]. Gunes, G., "Sosyal Bilgiler Ogretmen Adaylarinin Cografya Konularinda Harita Ve Harita Sembollerini Kullanabilme Becerileri", Ahi Evran Universitesi, Sosyal Bilimler Enstitusu, Sosyal Bilgiler Egitimi Bilim Dali, Yuksek Lisans Tezi, 2016
[15]. Koc, H., Karatekin, K., "Sosyal Bilgiler Ogretmen Adaylarinin Harita Okuryazarlik Duzeylerinin Cesitli Degiskenler Acisindan Incelenmesi", Abant Izzet Baysal Universitesi Egitim Fakultesi Dergisi, Cilt 16, (Usbes Ozel Sayi Ii), 1522-1542, 2016.
[16]. Akengin, H., Tuncel, G., Cendek, M.E., "Ogrencilerde Harita Okuryazarliginin Gelistirilmesine Iliskin Sosyal Bilgiler Ogretmenlerinin Gorusleri", Marmara Cografya Dergisi, Yil: Temmuz 2016, Sayi: 34, Ss: 61-69, Issn: 1303-2429, E-Issn: 2147-7825, 2016.
[17]. Bugdayci, I., "Ilkogretimde Harita Kullanimi Uzerine Bir Inceleme", Selcuk Universitesi, Fen Bilimleri Enstitusu, Doktora Tezi, 2012.

ICENS 4TH INTERNATIONAL CONFERENCE ON ENGINEERING AND NATURAL SCIENCE
2 - 6 May 2018 KIEV UKRAINE

Protection and Improvement of Wild Sheeps with Photogrammetry Techniques

Fatma Mutlu[1], Ilkay Bugdayci[2], Abdullah Varlik[3]

Abstract

Today, with the development of remote sensing and photogrammetry techniques of the rapid, precision and detailed maps produced, user needs and scope of map use have been increased. Documentation of archeology and cultural heritage, large-scale map making, agricultural activities and increasing agricultural productivity, disaster management and ecosystem analysis are some of these. In recent years, ecological systems that have arisen with the mutual relations of living things in a certain region and the inanimate environments that surround them, have also been explored by remote sensing techniques in recent years. Remote sensing (UAV, LIDAR, Satellite imaging), GNSS, Camera Traps techniques contribute to improvement, conservation and control of wild life and also support the detection of the old habitats of species that must be protected and biodiversity. Wildlife include various researches such as wild mammals, birds, reptiles, wild plants, forests and marine life. In this study, researches on conservation, development, control and tracking of wildlife using photogrammetry techniques in our country and other countries were examined and contribution of photogrammetry techniques to wildlife was researched. In this context a project is developed by the authors, to detect, classify and tracking wild sheeps in open spaces with UAV. Furthermore, this project is the first research will be done in the field of geomatics engineering inTurkey. In this paper, details of the techniques to be used within the scope of the project and the initial stages of the project will be shared

Keywords: Remote sensing, UAV, Wildlife

1. INTRODUCTION

Today, with the development of remote sensing and photogrammetry techniques of the rapid, precision and detailed maps produced, user needs and scope of map use have been increased. Documentation of archeology and cultural heritage, large-scale map making, agricultural activities and increasing agricultural productivity, disaster management and ecosystem analysis are some of these. In recent years, ecological systems that have arisen with the mutual relations of living things in a certain region and the inanimate environments that surround them, have also been explored by remote sensing techniques in recent years. Remote sensing (UAV, LIDAR, Satellite imaging), GNSS, Camera Traps techniques contribute to improvement, conservation and control of wild life and also support the detection of the old habitats of species that must be protected and biodiversity. Wildlife sciences generally include wild mammals, birds, reptiles, wild plants, forests, amphibians and sea creatures. It is not only limited to this, but also includes the management, examination and management of living environments of these living things [1]. The conservation of natural ecosystems requires effective monitoring of the ecosystem for continuation of biological diversity as well as regular surveys of wildlife abundance [2]. Much of the challenge tracking wild animals involves the distribution of species in geographical areas, their low population densities, their incapable habitat, their sensitive to difficult behavior and discomfort [3].

In studies related to wildlife, many different techniques have been used to protect and develop wildlife and control and detection processes. Detection of wild animals by air counting is a method that has been carried out for many years. The monitoring of the species is usually carried out from the air in the presence of human

[1] *Necmettin Erbakan University, Department of Engineering and Architecture, 42090, Meram/Konya, Turkey. ftma5008@gmail.com*

[2] *Corresponding author: Necmettin Erbakan University, Department of Engineering and Architecture, 42090, Meram/Konya, Turkey. ibugdayci@konya.edu.tr*

[3] *Necmettin Erbakan University, Department of Engineering and Architecture, 42090, Meram/Konya, Turkey. avarlik@konya.edu.tr*

aircraft and from the distance and from the ground using satellites more recently. Many methods have been used in the studies, and as technology has improved, the efficiency of the methods has also increased. Techniques used to date from past to present have contributed to wildlife science.

Recently, unmanned aerial vehicles (UAV), the most widely used remote sensing technique, have begun to be used ([4], [5], [6], [7], [8], [9], [10]).For example; Sumatran orangutans are the great ape species endangered by changes in the nature and external factors. In order to evaluate the distribution of the Sumatran orangutan and its usefulness in determining the intensity, UAV was used. ([11], [12], [13], [14]) (Dugong dugon, Physeter macrocephalus, killer whale (Orcinus orca), and Greenland whale (Balaena mysticetus) have been successfully investigated with UAV ([15], [16], [17]). In addition to counting marine mammals, useful information about body condition, age and sex could be obtained. For example, By NOAA scientists were equipped with digital cameras to identify killer whales, and photographed and then multiple scanners were used to measure body size and diagnose pregnancies [18].

It has been extensively used in other techniques to protect and improve wildlife. For example, to demonstrate how the California owl (Strix occidentalis occidentalis) can improve the characteristics of the nesting habitat, LIDAR data was used in the air. The LIDAR data were then used to measure the number, density, and pattern of residual trees (≥ 90 cm dbh) and to estimate the shaded canopy within 200 m of the four nests [19]. [20]conducted a study on a terrestrial animal tracking system in Barro Colorado Island in Panama. In this study, wild-temporal movements of terrestrial birds and mammals on the earth were observed and protected data were obtained with the camera network. A study was conducted to prove the effectiveness of the GNSS-based animal monitoring method. The study area is located in the northern part of Morton National Park, about 120 km southwest of Sydney. The indirect monitoring approach has been used to estimate the number of drop dwellers living in this area. To map a specific region, the location and timing of the drop beacon attacks has been determined.

Turkey is rich with natural and delicate balance and biodiversity aspects. Industrialization and agriculture becoming machine-based have become a threat to the stability and sustainability of ecosystems. In addition to these rapid changes, the need for more nutrients has been felt due to the rapid increase in the population, necessitating more agricultural land. Wildlife is restricted for the formation of agricultural land. Moreover, the excessiveness of used agricultural chemicals and fertilizers and the rapid increase in unconscious hunting have also affected the ecosystem in a negative way. As a result of these adverse effects, many species have disappeared or have been threatened with the depletion of many species [21].

Many studies have been done on wildlife, in the field of geomatics engineering in the world, and effective results have been obtained. Work on wildlife in our country continues, but it has not reached adequate level. There are target types identified for wildlife conservation and development sites. Effective work can be put forth to protect the diversity of target species with the methods and techniques and with the support of veterinary and biologists. In this paper, the use of geomatics engineering techniques in wildlife conservation, development, follow-up and control has been examined.

2. STUDY AREA

Wildlife Development Area in Konya Bozdag has been determined as the study area. The area is located within the borders of Karatay, Selcuk and Altinekin provinces and 59.296.5 ha area was declared as Wildlife Development Area with the Decision of the Council of Ministers No.2005/9453 on 07.09.2005. Terrestrial climate is dominant in the region and there is no other protection status in the area.Besides Anatolian wild sheep other animals such as wolves, foxes, rabbits, badgers, ferrets, eagles, partridges etc. live in Wildlife Development Area.

3. MATERIAL AND METHODS

3.1 Remote Sensing Techniques

Images that contain many information of the earth can be obtained by remote sensing technique. This information is gathered by recording the electromagnetic energy reflected from earth on the various bands by being perceived by the receivers of the satellites. The reflection values of the properties of which the band is sensitive are found in each band. Multiple bands can form a composite image, as well as images consisting of a single band [22].

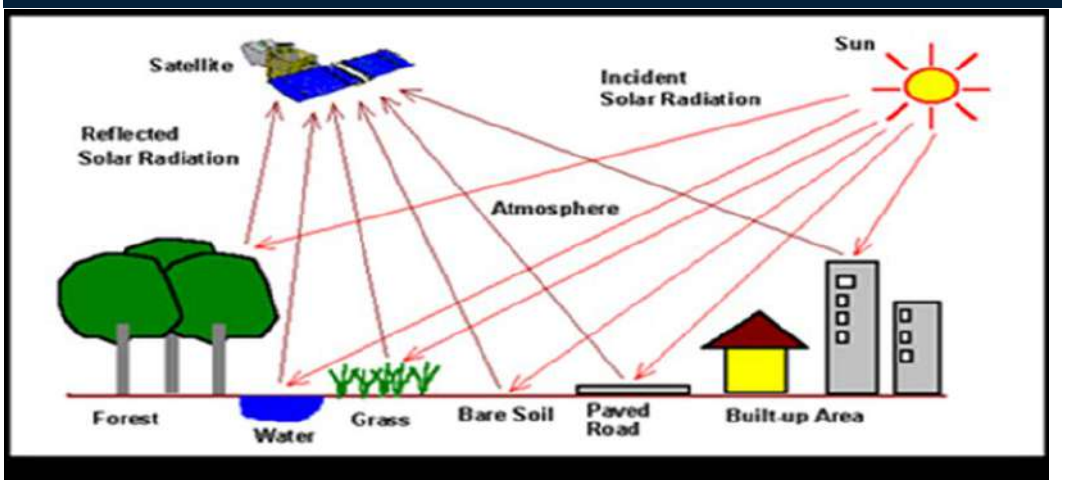

Figure 3.1. Remote sensing system

Remote sensing is a powerful and accurate tool for collecting data for wildlife management, especially for large areas with difficult access and sensitive ecosystems.

3.1.1 Unmanned Aerial Vehicles (UAV)

UAV which is similar to basic flight methods and has no pilotage on it. The air platform together with the aircraft and communication systems weighs approximately 6 kg [23], (Fig. 3.2). The maximum recommended weight for take-off is 8 kg, with 2 kg sensor load allowed. The UAVs consist of four main subsystems. These; body, power and drive subsystem, navigation subsystem and communications subsystem. During UAV flight operations, four subsystems we have been integrated to provide navigation and power [3].

The applications of AV technology consist of sampling airborne microbes, finding wildlife residents, and providing data on marine living behavior and body condition (Christie et al., 2016). Moreover, the studies assess species in a variety of habitats, from more open savannas to dense tropical rain forests. In recent years, the use of rapidly evolving UAVs in ecology has provided advantages such as a cheap, portable and low degradation platform for airborne airborne surveillance ([24], [5], [25]).

Figure 3.2. Unmanned Aerial Vehicles (UAV)

3.1.1.1. Thermal Image Cameras

The feeling that we perceive as infrared energy, that is, temperature, is evaluated as including in the electro-magnetic spectrum. Because of the length of the wave, infrared light is the invisible light that the human eye can not detect. All objects in the world are heat-retaining as well as heat-reflecting. If objects have a temperature above absolute zero, they are releasing heat [26].

Multi-criteria object-based image analysis using very high spatial resolution visual and thermal infrared images obtained with an UAV is an effective approach for simultaneous detection of many subjects. This method also showed the potential to perform population censuses of targeted species using their specific threshold values. However, further research is needed to increase the detection rate of each succession. For example, the use of multiple spectral band combinations should be investigated. These results lead to the development of a reproducible and adaptable approach to other species [27].

3.1.1.2. Multicopter type UAV

They are a multi-rotor UAV mounted on top of a thermal imager and a photo-machine capable of detecting colors in the visible range. On day and night flights, it provides automatic flight, which can be programmed manually and pre-flighted on points or routes. It has a horizontal and vertical movement feature that can be fixed in air. It has the ability to stay in the air for a minimum of 20-25 minutes and has a carrying capacity of up to 800 grams.

Draganfly X4-P mini is a suitable standard for the UAV class. The multispectral camera uses green, red edge, and near infrared wave bands to capture visible and invisible images of remote sensing imaging technology, vegetation, and vegetation cover [4].

3.1.2. LIDAR

LIDAR systems are active remote sensing systems. In these systems, laser beam pulses are used to define land. LIDAR systems, such as passive microwave systems, are also operated in either a profile or a scanning mode. A LIDAR system; laser scanner and cooler, GPS and INS (Inertial Navigation System) devices.

The LIDAR systems used in forestry operations are basically divided into two categories as intermittent rotation and full wave form. In a full-wave system, a full profile of the rotating signal is extracted at specific time intervals while the first and last or 3-5 rotations are recorded in the intermittent rotation system. Although intermittent rotation data is widely used in estimating the properties of the stands, it is reported that the full-wave system, which is more complicated in terms of data processing, is more useful than evaluating the stand structure [28]).

A laser altimeter or LIDAR (light sensing and measuring) is a remote distance measurement system that directly measures the three-dimensional distribution of plant species within wildlife, accurately predicts vegetation structural features and promises to increase both the accuracy of biophysical measurements and spatial analysis to the third (z) detection technology. LIDAR sensors directly measure the three-dimensional distribution of plant canopies and topography, resulting in high-resolution topographic maps and highly accurate predictions for plant height, cover and canopy structure [28]. LIDAR is not only limited to studies on forest wildlife habitat, but it is also used in studies on wild animals.

3.2. Camera Traps

In general modern camera traps are digital cameras with heat and / or motion sensors (Figure 3.3). Some models have a screen to view captured pictures or videos, depending on the type, the cameras must be flash or infrared illuminated. Motion-sensitive camera traps provide a visual sensor to record the presence of species that have been spread over a wide area providing specific information about motion and behavior. On the video side, modern camera traps brings new analytical opportunities as well as new data management challenges [29].

Figure 3.3. Camera traps

3.3. GNSS

The emergence of Global Navigation Satellite System (GNSS) technology has revolutionized the way 3D positions are defined on Earth's surface. GNSS based positioning has become a vital tool for a wide range of applications in areas such as measurement, mapping and asset management, precision agriculture, engineering and construction, aerial imaging and sensors and public service management. GNSS technology is one of the least used methods in animal studies.

This GNSS technique uses GPS schemes. Satellite animals are caught alive and mobile phones are attached to the leash and are left to their natural environment in a healthy way. Detailed information on living areas and behavior in the region is obtained by following the satellite. This information is used for protection and monitoring of illegal hunting.

4. RESULTS AND DISCUSSION

In studies related to wildlife, many different techniques have been used to protect and develop wildlife and control and detection processes. Detection of wild animals by air counting is a method that has been carried out for many years. The monitoring of the species is usually carried out from the air in the presence of human aircraft and from the distance and from the ground using satellites more recently. Various methods have been developed for the analysis of wildlife data obtained from terrestrial and airborne surveys.

Since the beginning of the century, rapidly evolving UAV technology has progressively entered the field of wildlife exploration and management. It is particularly suitable for collecting data at an intermediate spatial scale. Wild animals and habitats have proven to be suitable for areas that are inaccessible or difficult to navigate, and for sensitive or aggressive species. With the progress of technology, UAV is increasingly taking the place of human fixed-wing aircraft and helicopters, popular tools for measuring for research, protection and management for animals and plants. For this reason; to be effective in covering large areas, to be expensive for human aircraft, to disturb wildlife, and to have work-related deaths among biologists.

Thermal sensing cameras are particularly successful in detection of wild animals living in forests. The success rate of the data obtained by using the thermal sensor camera in the study area is affected by the topographic structure, vegetation coverings

The multispectral aerial image is more useful for detecting species because the information is continuously recorded and can be analyzed repeatedly after the census. Moreover, the use of UAV for image acquisition is much easier than for other access platforms (satellite, aircraft, helicopter, etc.). Multispectral images provide very high spatial resolution, high-level details allowing discrimination of characteristic differences between species.

Given the low noise production and its ability to reach remote, hazardous areas, the UAV can be particularly useful in exploring marine wildlife in transport areas and breeding colonies.

5. CONCLUSIONS

It is aimed to determine the most accurate method by examining the studies done on wildlife. The techniques used according to the field of study to be done and the work to be done can be changed, but the thermal imaging camera system and the multispectral camera are the most beneficial of the techniques used for wildlife. Directly measuring the three-dimensional distribution of plant species in the forest ecosystem, it has been anticipated to use the LIDAR data in the detection of vegetation cover.

REFERENCES

[1]. Chabot D, Carignan V, Bird DM., Measuring habitat quality for least bitterns in a created wetland with use of a small unmanned aircraft. Wetlands. 34(3): 527-533, 2014.
[2]. Jachmann H., Estimating Abundance of African Wildlife: An Aid to Adaptive Management. Kluwer Academic Publications, Boston, Massachusetts, USA, 2001.
[3]. Gonzalez, F., Montes, A., Puig, E., Johnson, S., Mengersen, K. And Gaston, K., Unmanned Aerial Vehicles (UAVs) and Artificial Intelligence Revolutionizing Wildlife Monitoring and Conservation, Australia, 2016.
[4]. Watts AC., Ambrosia VG., Hinkley EA., Unmanned aircraft systems in remote sensing and scientific research: classification and considerations of use. Remote Sensing 4:1671–1692, 2012.
[5]. Anderson, K., & Gaston, K.J., Lightweight unmanned aerial vehicles will revolutionize spatial ecology. Frontiers in Ecology and the Environment, 11, 138-146, 2013.
[6]. Colomina I., Molina P., Unmanned aerial systems for photogrammetry and remote sensing: A review, ISPRS J. Photogramm. Remote Sens. 92: 79-97 Crossref, 2014.
[7]. Shahbazi M., Theau J., Menard P., Recent applications of unmanned aerial imagery in natural resource manageent. GISci. Remote Sens. 51(4): 339-365 Crossref, 2014.
[8]. Whitehead K., Hugenholtz CH., Brown OW., Barchyn TE., Moorman BJ., LeClair A., Riddell K., Hamilton T., Geomorphological mapping with a small, 2013.
[9]. Pajares G., Overview and current status of remote sensing applications based on unmanned aerial vehicles (UAVs) Photogramm. Eng. Remote Sens. 81(4): 281-329 Crossref, 2015
[10]. Chabot, D. & Bird, D.M., Wildlife research and management methods in the 21st century: Where do unmanned aircraft fit in?. Journal of Unmanned Vehicle Systems, 3, 137-155, 2015.
[11]. Van Schaik, C.P., Monk, K.A. & Robertson, J.M.Y., Dramatic decline in orangutan numbers in the Leuser Ecosystem, Northern Sumatra. Oryx, 35, 14-25, 2001.
[12]. Wich, S.A., Distribution and conservation status of the orang-utan (Pongo spp.) on Borneo and Sumatra: how many remain? Oryx: 329-339, 2008.
[13]. Wich, S.A., Riswan, J., Refisch, J. & Nellemann, C., Orangutans and the economics of sustainable forest management in Sumatra. United Nations Environment Programme, 2011.
[14]. Wich, S., Fredriksson, G., Usher, G., Peters, H., Priatna, D., Basalamah, F., Susanto, W. & Kuhl, H., Hunting of Sumatran orang-utans and its importance in determining distribution and density. Biological Conservation, 146, 163-169, 2012.
[15]. Hodgson, A., Kelly, N., Peel, D., Unmanned aerial vehicles (UAVs) for surveying marine fauna: A dugong case study, 2013.
[16]. (2014) The NOAA website. [Online]. (National Oceanic and Atmospheric Administration), Spying on sperm whales. www.nmfs.noaa.gov/stories/2013/03/3_07_13sperm_whales.html. Available, 12 Jan 2018.
[17]. Durban, J.W., Fearnbach, H., Barrett-Lennard, L.G., Perryman, W.L., and Leroi, D.J, Photogrammetry of killer whales using a small hexacopter launched at sea. J. Unmanned Veh. Syst. 3(3): 131–135, 2015.
[18]. Christie, K.S., Gilbert, S.L., Brown, C.L., Hatfield, M. & Hanson, L., Unmanned aircraft systems in wildlife research: current and future applications of a transformative technology. Frontiers in Ecology and the Environment, 14, 241-251, 2016.
[19]. North, M.P., Kanec, J.T., Kane V.R., Asner, G.P., Berigane W., Churchill J.D., Conway, S., Gutiérreze, R.J., Jeronimo, S., Keane, J., Koltunovf, A., Mark, T., Moskal, M., Muntoni, T., Peery, Z., Ramirez, C., Sollmann, R., Whitea, A., Whitmore, S., Cover of tall trees best predicts California spotted owl habitat, Forest Ecology and Management 405 (2017) 166–178, USA, 2017
[20]. Kays, R., Tilake, S., Kranstauberc, B., Jansenb, P., Carboned, C., Rowcliffed, M., Fountaine, T. ve Hef, E., Monitoring wild animal communities with arrays of motion sensitive camera traps, USA, 2010.
[21]. <www.milliparklar.gov.tr/kitap/77>, Viewed 14 January 2018, Ankara.
[22]. Celik M., Saygin O., Suer, Kinaci O., Gunay E., Cactas E. and Dal F., Geographic Information Systems and Remote Sensing Studies in Urban Planning. Turkey 3. Geographical Information Systems Informatics Days Declaration, Fatih University, Istanbul, 6-9 October 2004.
[23]. Akgul, M., Yurtseven, H., Demir, M., Akay, A.E., Gulci, S., Ozturk, T., Usage opportunities of generating digital elevation model with unmanned aerial vehicles on forestry. Journal of the Faculty of Forestry Istanbul University 66(1): 104-118, 2016.
[24]. Watts, A.C., Perry, J.H., Smith, S.E., Burgess, M.A., Wilkinson, B.E., Szantoi, Z., Ifju, P.G. & Percival, H.F., Small unmanned aircraft systems for low-altitude aerial surveys. Journal of Wildlife Management, 74, 1614-1619, 2010.
[25]. Vermeulen C., Lejeune P., Lisein J., Sawadogo P., Bouché P., Unmanned aerial survey of elephants. PLoS ONE 8: e54700, 2013.

[26]. Corsi, C., Infrared: A key technology for security systems. Advances in Optical Technologies Article ID 838752, 15 p, doi: 10.1155/2012/838752, 2012.
[27]. Chrétien, L.P., Théau, J. and Ménard, P., Visible and thermal infrared remote sensing for the detection and count of white-tailed deer (Odocoileus virginianus) using an unmanned aerial vehicle, Wildlife Society Bulletin (in revision), 2015.
[28]. Lefsky, M.A., Cohen, W.B., D.J. Harding, G.G., Parker, S.A., Acker, and GOWER, S.T., LiDAR remote sending of aboveground biomass in three biomes. Glob. Ecol. Biogeogr. 11:393–399, 2002.
[29]. Hansen, M.C., Potapov, P.V., Moore, R., Hancher, M., Turubanova, S.A., Tyukavina, A., Thau, D., Stehman, S.V., Goetz, S.J., Loveland, T.R., Kommareddy, A., Egorov, A., Chini, L., Justice, C.O. & Townshend, J.R.G., High-Resolution Global Maps of 21st-Century Forest Cover Change. Science, 342, 850-853, 2013.

ICENS 4TH INTERNATIONAL CONFERENCE ON ENGINEERING AND NATURAL SCIENCE
2 - 6 May 2018 KIEV UKRAINE

Investigation of The Effect Ratios of Cutting Parameters on The Surface Roughness

Hakan Dilipak[1], Omer Asal[1], Berkhan Canlar[1], Hakan Gurun[1]

Abstract

Surface roughness is effective on the fatigue strength, corrosion resistance and friction life of the workpieces. In this experimental study, in the turning operation, parameters affecting the surface roughness of the AISI 4140 alloy were investigated. The cutting parameters; to be cutting speed (100, 150 and 200 m/min), the feed rate (0.125, 0.250 and 0.375 mm/rev) and the cutting depth (1, 2 and 3 mm) 27 cutting tests were performed. In the experiments, coated tools with a tip radius of 1.2 from Walter Company were used. A separate cutting tool was used for each experiment. The surface roughness values were measured with the MAHR-Perthometer M1 device. The effect level of the control factors on the surface roughness was determined using variance analysis (ANOVA). The model was created with the performed regression analysis. It has been determined that the most important parameter in terms of surface roughness is the feed rate.

Keywords: AISI 4140 Steel, Surface roughness, Turning, ANOVA, Regression

1. INTRODUCTION

Today's technologies require the manufacture of parts with high surface qualities. Although CNC machines are very sensitive, if suitable cutting parameters and cutting tools are not selected for the part to be manufactured, surface quality problems can be encountered even on these machines [1]. There are many studies in the literature investigating of machinability, cutting parameters and surface roughness [2-8]. The studies are concentrated to obtain the desired surface roughness and to determine the cutting parameters that will minimize the manufacturing cost. Sarikaya and friends [9] have been optimized the effects on surface roughness and tool life of cutting parameters by during cutting and have made optimization of the cutting parameters by Taguchi method.

Machinability performances of 1.4140 steel which has high toughness and hardening performance were investigated statistically in the turning operation using a channel tool. From the analyzes made, it was found that the cutting tool tip radius has the most significant effect on the roughness, followed by the chip breaker type and tip radius interaction [10-11]. Similarly, in the turning of AISI 6061T6 Aluminum, the effects of surface roughness and cutting force on machining parameters were investigated. According to the experimental results, it was determined that the most effective parameter on the surface roughness is the feedrate with the effect ratio of 98.06% [12]. Hanafi et al. (2012), optimized cutting parameters in machining of PEEK-CF30 using TiN tools under dry conditions, to achieve minimum power consumption and the best surface quality. Taguchi optimization and grey relational theory were used in the optimization process [13].

The aim of the work reported by Lee and Tarng [14], was to develop a turning machining model constructed based on a polynomial network that learned relationships between cutting parameters (cutting speed, feed rate and depth of cut) and cutting performance (surface roughness, cutting force and tool life). The material turned was S45C (AISI 1045) steel bars. In the other work, Fratila and Caizar [15] the Taguchi optimization methodology was applied to optimize the cutting parameters (depth of cut, feed rate and cutting speed) in face

milling when machining AlMg3 with high speed steel (HSS) tool under semifinishing conditions in order to achieve the best surface roughness and the minimum cutting power. Asilturk and Neseli, was generate to model the surface roughness in turning of AISI 304 austenitic stainless steel under dry conditions, using the Response

[1] *Gazi University, Department of Manufacturing Engineering, 06500, Yenimahalle /ANKARA, Turkey. hdilipak@gazi.edu.tr*

Surface Methodology [16]. An orthogonal array was applied to study the influence of cutting parameters (cutting speed, feed rate and depth of cut) on the surface roughness.

In this study, the effect ratios of the parameters affecting the surface roughness in the turning of the AISI 4140 steel were investigated. The effects of the cutting parameters on the surface roughness were determined by applying ANOVA to the obtained experimental data. Besides, a surface roughness model based on cutting parameters was generated by performing a regression analysis on the obtained experimental data.

2. MATERIAL AND METHOD

a. Workpiece Material

The AISI 4140 steel is suitable for hardening in terms of amount of carbon and chemical composition. At the same time, it is an alloy structure steel which shows high toughness properties under certain loads when subjected to tempering treatment. The chemical composition of the AISI 4140 treatment steel is given in Table 1. The experimental specimens were prepared in the size of Ø80x300 mm from AISI 4140 steel. To prepare the workpiece for the experiments, the both forehead face were turned and the spotting holes were opened.

Table 1. The Chemical composition of AISI 4140 reclamation steel

C	Si	Mn	Cr	Mo	Ni	Cu	Al	Fe
0,42	0,26	0,8	1,08	0,16	0,07	0,08	0,042	97,088

The hardness measurements were made on workpiece specimens. Firstly, the hardness measuring device given in Figure 1 has been calibrated. Then, the hardness was measured from the 6 points on the workpiece. The average of these 6 values was recorded as 90.7 HB.

Figure 1. The hardness tester

b. Experiments and Surface Roughness Measurements

The machinability experiments were carried out under dry cutting conditions at the CNC lathe at Gazi University Faculty of Technology Manufacturing Engineering laboratory. In the experiments, "Johnford TC-35" industrial CNC lathe with FANUC control unit was used. The experiments were performed at three different cutting speeds, three different feed rates and three different cutting depths. A new cutting tool was used in each

experiment. The coated carbide cutting tools were used as the cutting tool and a total of 27 experiments were carried out. The experimental parameters are given in Table 2.

Table 2. The cutting parameters

The cutting depths, a (mm)	The cutting speed, V (m/min)	The cutting rate, f (mm/rev)
1	100	0.125
2	150	0.25
3	200	0.375

The geometric properties of the insert and tool holder used in the experiments are given in Figure 2.

The tool holder | The Insert

Figure 2. The geometric features of insert and tool holder

c. The Surface Roughness Measurement

The MAHR-Perthometer M1 was used to measure surface roughness values. After each new experiment, the measurements made on surfaces where longitudinal turning operations are performed, the surface roughness measurements were made on the surfaces where the longitudinal turning operations were carried out. The Roughness measurements were made by taking 3 measurement values on each surface, with the workpiece being parallel to the workpiece and by rotating the workpiece about 120 ° around its axis. For measurements of the surface roughness values formed during machining on the workpiece, the cutting length was chosen as 0.8 mm and the measuring ranges as 5.6 mm. The surface roughness measuring device is shown in Figure 3.

Figure 3. The surface roughness measuring device

3. EXPERIMENTAL RESULTS AND DISCUSSION

In the study, the untreated AISI 4140 material was machined on the CNC lathe machine to and the cutting parameters were investigated effects on the surface roughness. The surface roughness values obtained in the result of the experiments are given in Table 3.

Table 3. The Experimental results

The Cutting depth, a, mm	The Cutting Speed, V, m/min	The Feed rate (f), mm/rev	The surface roughness, Ra, µm
1	100	0.125	1.695
		0.250	2.031
		0.375	3.729
	150	0.125	0.422
		0.250	2.051
		0.375	3.869
	200	0.125	0.808
		0.250	2.119
		0.375	4.089
2	200	0.125	2.519
		0.250	1.808
		0.375	3.926
	150	0.125	1.193
		0.250	1.859
		0.375	4.182
	100	0.125	0.622
		0.250	1.635
		0.375	3.868
3	200	0.125	1.073
		0.250	1.818
		0.375	3.894
	150	0.125	0.875
		0.250	2.016
		0.375	4.028
	100	0.125	1.210
		0.250	1.892
		0.375	3.718

For a better understanding of the effects of the cutting parameters on the surface roughness, the experimental data are transformed into the graphs shown in Figure 4 - Figure 6.

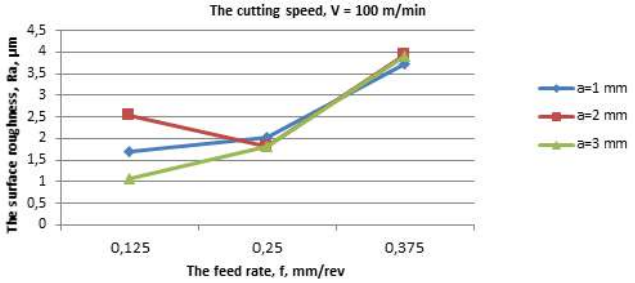

Figure 4. At the cutting speed of 100 m / min, the value graph of the mean surface roughness due to the change in the feed rate of the cutting depth

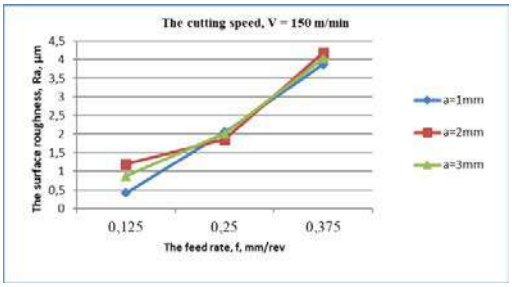

Figure 5. At the cutting speed of 150 m / min, the value graph of the mean surface roughness due to the change in the feed rate of the cutting depth

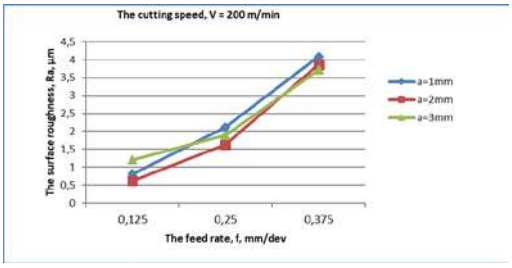

Figure 6. At the cutting speed of 200 m / min, the value graph of the mean surface roughness due to the change in the feed rate of the cutting depth

In the examining the graphics given in Figure 4, Figure 5 and Figure 6. It is observed that the surface roughness value increases with the increase of the feed rate. Conversely, it is understood that the change in cutting depth does not significantly affect the surface roughness. The maximum surface roughness value was obtained as 4,182 µm at the cutting depth of 2 mm, the cutting speed of 150 m/min and the feed rate of 0.375 mm/rev. The lowest surface roughness value was also obtained as 0.422 µm at the cutting depth of 1 mm and the cutting speed of 150 m/min and the feed rate of 0.125 mm/rev.

a. Analysis of Variance (ANOVA)

The variance analysis was performed on the experimental results to examine the influence on the surface roughness (Ra) response variable of the factors which are the cutting depth (a), the cutting speed (V), and the feed rate (f). Table 4 shows the ANOVA table determining the effects of the factors a, V and f on the response variable Ra.

Table 4. The results of the analysis of variance

Source	DF	Adj SS	Adj MS	F	P	PD (%)
a	2	0,0706	0,0353	0,23	0,798	0,18
V	2	0,3959	0,1979	1,28	0,3	0,98
F	2	36,755	18,3775	118,73	0	91,16
Error	20	3,0958	0,1548			7,68
Total	26	40,3173				100

S = 0.393433 R-Sq = 92,32 R-Sq(adj) = 90,02%

DF: Degree of Freedom, SS: Sum of squares, P:Meaningfulness<0.05, PD: Percent distribution

According to the ANOVA table in Table 4, at the 95% confidence interval, it is understood that the most effective parameter on surface roughness is the feed rate. Again according to this table, the cutting speed and the cutting depth appear to have no effect on surface roughness.

The effect ratios of the cutting parameters in forming the surface roughness are given below.

- The effect of the feed rate 91.16 %,
- The effect of the cutting depth 0.18 %,
- The effect of the cutting speed 0.98 %.

Figure 7 shows the normal effect graph and the main effect graph obtained as a result of the variance analysis.

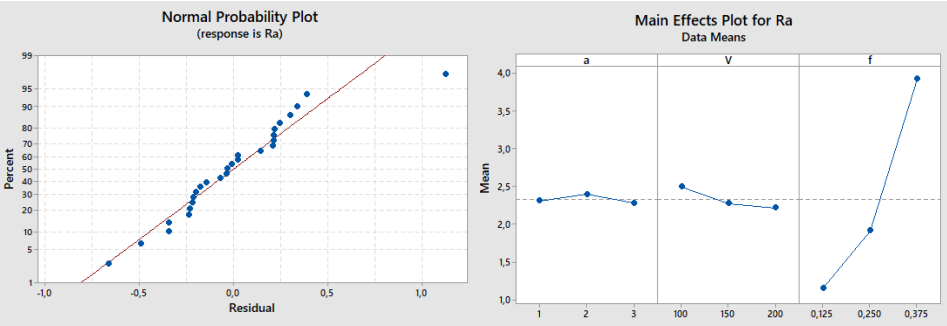

Figure 7. The graphs of normal probability and main effect

As seen in the main effect graph, the cutting depths and the cutting speeds are not effective in the formation of surface roughness. However, the increase in the value of the feed rate significantly increases the surface roughness value.

b. Regression Analysis

The statistical model constants and coefficient values of the variables obtained from the regression analysis for the surface roughness are shown in Table 5.

Table 5. Regression analysis coefficient table

Coefficients				
Term	Coef	SE Coef	T	P
Constant	0,02	0,487	0,04	0,967
a	-0,016	0,116	-0,14	0,891
V	-0,00281	0,00232	-1,21	0,237
f	11,06	1	11,94	0

When the effects of factors were examined, as a parallel to the results of variance analysis, the greatest effect on surface roughness has been shown to have the feed rate from the independent variables. The following mathematical formula has been developed considering the effects of the independent variables (a, f, V) on the surface roughness (Ra).

Ra = 0,020 - 0,016 a - 0,00281 V + 11,060 f

4. CONCLUSIONS

In the study, the parameters affecting the surface roughness were determined. Then the mathematical model was obtained for the estimation of the surface roughness. The obtained model was found to be usable at the 95% confidence level.

It has been determined that the feed rate on the surface roughness is a very effective parameter.

It has been found that the value of the feed rate increases the surface roughness values.

The cutting speed and the cutting depth appear to have no effect on the formation of the surface roughness.

REFERENCES

[1]. Dilipak, H., Guldas, A., Gezgin, A., “Investigation of the effect of number of insert on machining time and metal removal rate when milling AISI D3 steel at high cutting speeds”, Journal of Mechanical Engineering, Strojniski Vestnik-Journal of Mechanical Engineering 55 (7-8) : 438-443 Jul-Aug, 2009.

[2]. Davim, J. P., Figueira, L., “Machinability evaluation in hard turning of cold work tool steel (D2) with ceramic tools using statistical techniques”, Materials and Design, 2006.

[3]. Lima, J.G., Avila, R.F., Abrao, A. M., Faustino, M., Davim J. P., “Hard turning: AISI 4340 high strength low alloy steel and AISI D2 cold work tool steel”, Journal of Materials Processing Technology, 169: 388–395, 2005.

[4]. Sai, W. B., Salah, N. B., Lebrun, J. L., “Influence of machining by finishing milling on surface characteristics”, International Journal of Machine Tools & Manufacture, 41: 443.

[5]. Gullu, A., Karabulut, S., Guldas, A., “Inconel 718 Super Alasimlarin Islenmesinde Talas Kirilma Problemleri ve Talas Kirici Tasarimi”, Gazi Universitesi Muhendislik-Mimarlik Fakultesi Dergisi, Cilt 23, Sayi 1, 157-164, 2008.

[6]. Mustafa Goktas, Abdulmecit Guldas, Hakan Dilipak, “Tool Path Generation for Pocket Machining Operations with Island”, Gazi University Journal of Science, 30 (3), 79-88, 2017.

[7]. Gokkaya, H., Sur, G., Dilipak, H., “PVD ve CVD Kaplamali Sementit Karbur Kesici Takimlarin Isleme Parametrelerine Bagli Olarak Yuzey Puruzlulugune Etkisinin Deneysel Olarak Incelenmesi”. Z.K.U. Karabuk Teknik Egitim Fakultesi, Teknoloji Dergisi, 7(3), 473-478, 2004.

[8]. Zeyveli, M., Demir, H., “AISI 01 Soguk Is Takim Celiginin Islenebilirliginin Kesme Kuvvetleri ve Yuzey Puruzlulugu Acisindan Arastirilmasi”, ISSN:1306-3111 e-Journal of New World Sciences Academy, 4 (3), Article Number: 1A0031, 2009.

[9]. Sarikaya, M., Dilipak, H., Akin, G., “Optimization of the process parameters for surface roughness and tool life in face milling using the Taguchi analysis”. Material in Technologies: Materials and Technologies, 49(1), 139-148, 2015.

[10]. Ozlu, B., Demir, H., Nas, E., “CNC Tornalama Isleminde Yuzey Puruzlulugu ve Kesme Kuvvetlerine Etki eden Parametrelerin Matematiksel Olarak Modellenmesi”, Ileri Teknoloji Bilimleri Dergisi Cilt 3, Sayi 2, 75-86, 2014.

[11]. Pinar, A.M., Firat, K., "AISI 4140 Celigin Cok Yonlu Takimla Tornalanmasinda Yuzey Puruzluluk Performansinin Optimizasyonu", Politeknik Dergisi, 19 (4) : 491-498, 2016.
[12]. Camposeco-Negrete, C.,"Optimization of cutting parameters for minimizing energy consumption in turning of AISI 6061 T6 using Taguchi methodology and ANOVA", Journal of Cleaner Production, 53, 195-203, 2013.
[13]. Hanafi, I., Khamlichi, A., Mata Cabrera, F., Almansa, E., Jabbouri, A., "Optimization f cutting conditions for sustainable machining of PEEK-CF30 using TiN tools". Journal of Cleaner Production 33, 1e9, 2012.
[14]. Lee, B.Y., Tarng, Y.S., "Cutting-parameter selection for maximizing production rate or minimizing production cost in multistage turning operations", Journal of Materials Processing Technology 105, 61-66, 2000.
[15]. Fratila, D., Caizar, C., "Application of Taguchi method to selection of optimal lubrication and cutting conditions in face milling of AlMg3", Journal of Cleaner Production 19, 640-645, 2011.
[16]. Asilturk, I., Neseli, S., "Multi response optimization of CNC turning parameters via Taguchi method-based response surface analysis". Measurement 45, 785-794, 2011.

ICENS 4TH INTERNATIONAL CONFERENCE ON ENGINEERING AND NATURAL SCIENCE
2 - 6 May 2018 KIEV UKRAINE

Experimental Investigation of The Cutting Forces In The Machining of AISI 4140 Steel By Using The CNC Turning Machine

Omer Asal[1], Hakan Dilipak[1], Berkhan Canlar[1], Abdulmecit Guldas[1]

Abstract

Cutting force realizes in turning operation is a significant influence on tool wear, surface roughness, dimensional accuracy of parts and heat generation. In this study, the cutting speed, the feedrate and the effects on the cutting force of the cutting depth in the turning process were experimentally investigated. A total of 27 experiments were performed using three different cutting speeds, three different feed rates and three different cutting depths. Kistler 9257 type B dynamometer was used for measuring cutting forces. The Kistler 9257 B type dynamometer was used to measure the cutting forces. After the experiments, variance analysis was carried out to determine the impact rates of the cutting parameters on the cutting force. Relations between dependent and independent variables were determined by the model obtained from the regression analysis. When the obtained experimental and statistical results are evaluated, it has been determined that the most effective parameter on the cutting forces is the federate.

Keywords: AISI 4140 Steel, Cutting force, ANOVA, Regression, Cutting parameters

1. INTRODUCTION

Cutting forces are one of the most important topics in machining, as they have a direct influence on tool wear, energy consumption and heat generation. It is desirable that the cutting forces have minimum values in order to obtain good machinability and increase product quality.

AISI 4140 steel is an alloyed structural steel suitable for hardening in terms of carbon content and exhibiting high toughness after the heat treatment. Therefore, it is more difficult to machining than alloy steels. The optimization of the cutting forces is time consuming and expensive. Therefore, data obtained during the machining by many researchers are analyzed using statistical methods such as ANOVA (variance analysis) and regression analysis [1-2].

There are lots of studies in this field in the literature. Kara et al. investigated the performance of cutting parameters in the turning of AISI 4140 (30-32 HRc) tempering steel and determined the optimum machining conditions. Using the Taguchi method, the control factors that give optimum surface roughness and vibration amplitude values were identified. Four different cutting speeds (100, 150, 200, 250 m / min), feedrate (0.05, 0.1, 0.15, 0.20 mm / sec) and, cutting depth (0.25, 0.50, 0.75, 1 mm) were selected as control factors. They used variance analysis (ANOVA) using experimental results to determine the effect of cutting parameters on surface roughness and vibration amplitude. As a result, they have observed that optimization has been successfully applied [3]. Tekaslan et al. experimentally investigated and compared the theoretical results with the cutting forces of AISI 304 austenitic stainless steels during turning by titanium carbide coated cutting tools. According to the experimental results, it is found that the cutting forces calculated theoretically at the end of the study do not give a complete result due to various factors with an average difference of 25% [4].

Asilturk and Akkus were subjected to a turning process to the AISI 4140 steel with a hardness of 56-57 HRc under dry cutting conditions. They statistically modeled the tool wear by using the regression method in the turning process [5]. Korkut et al. investigated the effects of cutting parameters on the cutting forces.

[1] *Gazi University, Department of Manufacturing Engineering, 06500, Yenimahalle/ANKARA, Turkey. omerasal@gazi.edu.tr*

They measured the cutting forces generated in the milling of C1020 and C1040 materials in three dimensions. A strain gage based dynamometer was used to measure the cutting forces. As a result, it was observed that the cutting forces increased with increasing of the cutting parameters at a certain period [6]. Tasliyan et al. investigated the effects of feedrate, cutting speed and cutting depth upon the main cutting force. In this study, Inconel 718 superalloy was machined by a CNC lathe using a ceramic cutting tool [7].

Pugazhenthi et al. [8] investigated the effects of cutting speed and particle reinforcement on surface roughness and cutting force during machining of aluminum matrix composites (AMCs). According to this study, as the cutting speed increases, the amount of cutting forces and built up edge (BUE) decreases due to thermal softening [8]. In other studies on the machinability of AMCs, Anandakrishnan and Mahamani [9] reported the influence of turning parameters on flank wear, cutting force and surface roughness of AA6061 AMCs. They observed increased tool wear at higher cutting speeds. Shobaet al. [10] investigated the effect of turning parameters and volume of reinforcements on cutting forces of hybrid AMCs. They mentioned that the cutting force decreased with the increase in the percentage of the reinforcement. Joardar et al. [11] studied that the effect of turning parameters using by surface methodology in turning of AMCs. It is found that the low cutting forces were related the highest level of cutting speed and the lowest level of depth of cut. Yalcin and Ozileri [12] investigated the effects of turning of magnesium alloy using carbide tool. This study showed that feed rate and depth of cut have the major significant factors on the cutting force more than the cutting speed. Buldum et al. [13] founded that the multi-response optimization in oblique turning of magnesium alloy to obtain lowest cutting force and surface roughness with highest material removal rate by Taguchi - grey relational analysis.

In this study, the cutting force occurred turning of the AISI 4140 tempering steel was investigated. Besides, the effects of feedrate, cutting speed and cutting depth on cutting force were investigated.

2. MATERIAL AND METHOD

a. Workpiece Material

In the experiments, the AISI 4140 (42CrMo4) steel which is used in the automobile and aircraft industries has been chosen as the test material. The workpiece material was machined to the dimensions of Ø80x300 mm for experiments and a spot hole was opened.

Table 3. Chemical composition of the test material

C	Si	Mn	Cr	Mo	Ni	Cu	Al	Fe
0,42	0,26	0,8	1,08	0,16	0,07	0,08	0,042	97,088

b. Cutting Tool and Tool Holder

In the experiments, Walter brand (DSBNR2525M12) tool holder was supplied and used. The geometric properties and measurements of the cutting tool holder are given in Figure1.

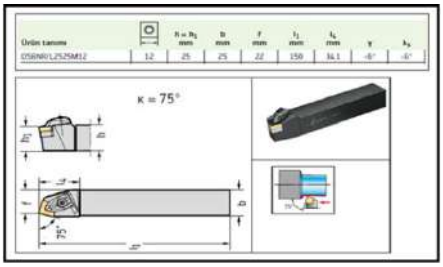

Figure 1. Geometric properties and measurements of the cutting tool holder

In the experiments, Walter brand tools (SNMG120412-NM4 WSM10) coated by physical vapor deposition (PVD) method were used. The geometrical properties of the cutting tools are shown in Figure 2.

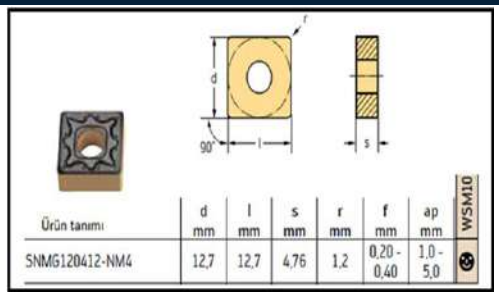

Ürün tanımı	d mm	l mm	s mm	r mm	f mm	ap mm
SNMG120412-NM4	12,7	12,7	4,76	1,2	0,20 - 0,40	1,0 - 5,0

Figure 2. The geometrical properties of the cutting tools

c. Machine and Measuring of Cutting Forces

The experiments were carried out under dry cutting conditions on a JOHNFORD brand CNC lathe. The used machine is given in Figure 3.

Figure 3. CNC machine used in experiments

A 9257B type piezoelectric dynamometer measuring three force components (Fz, Fx, and Fy) was used during machining. This dynamometer was connected to an Amplifier and cutting forces were sent to the computer to obtain graphs. The experimental setup is shown in Figure 4.

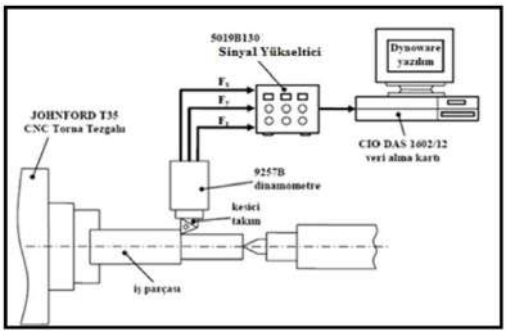

Figure 4. Experimental setup

d. Cutting Parameters and Experiments

The cutting parameters used in the experiments are stated to cover three different cutting speeds (V = 100, 150, 200 m / min), three different feedrates (f = 0.125, 0.25, 0.375 mm /rev) and three different cutting depth (a= 1, 2, 3 mm). A new cutting tool was used for each experiment and total of 27 experiments were performed.

3. EXPERIMENTAL RESULTS

In the study carried out, the AISI 4140 material was machined on a lathe to investigate the effects of the cutting parameters on the surface roughness.

a. Evaluation of Main Cutting Force

Table 2 below shows the cutting parameters and cutting forces obtained from the experiments.

Table 4. The main cutting force results depending from the cutting parameters

Cutting Depth, a, (mm)	Cutting Speed, V, (m/min)	Feedrate, f, (mm/rev)	Avarage Cutting Force, Fort, N
1	100	0.125	401
		0.25	356
		0.375	384
	150	0.125	598
		0.25	581
		0.375	571
	200	0.125	980
		0.25	783
		0.375	1080
2	100	0.125	707
		0.25	629
		0.375	618
	150	0.125	1108
		0.25	590
		0.375	1038
2	200	0.125	1537
		0.25	1526
		0.375	1533
3	100	0.125	2160
		0.25	973
		0.375	918
	150	0.125	871
		0.25	1130
		0.375	1200
	200	0.125	1500
		0.25	2010
		0.375	1712

The averages cutting force values were obtained from the DynoWare program and tabulated in Excel.

For cutting speeds V = 100, 150 and 200 m / min, the effect of the cutting depth on the main cutting force depending on the feedrate are shown in Figure 5, Figure 6 and Figure 7 respectively.

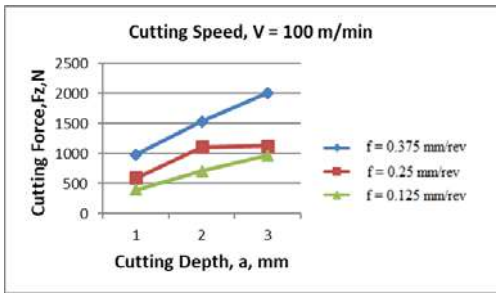

Figure 5. The effect of cutting depth on the main cutting force for cutting speed V = 100 m / min

Figure 5 shows that the cutting force values increase with increasing cutting depth. It is also understood that the increase in the feedrate in the same way increases the cutting forces.

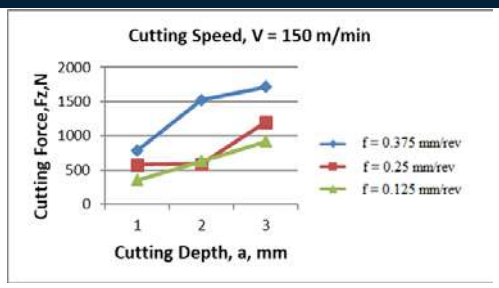

Figure 6. The effect of cutting depth on the main cutting force for cutting speed V = 150 m / min

The cutting force graph shown in Figure 6 also shows that the feedrate and cutting depth increase the cutting force. The lowest cutting force values obtained from all experiments were measured as 356 N at 150 m / min cutting speed, 1 mm cutting depth, and 0.125 mm / rev feedrate.

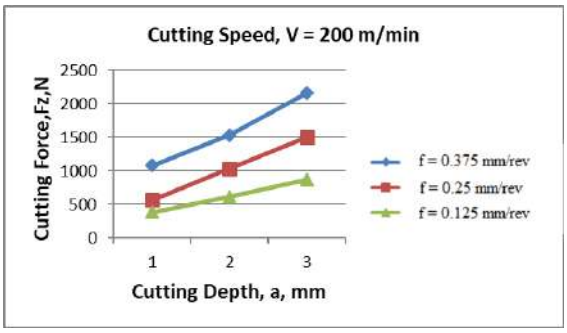

Figure 7. The effect of cutting depth on the main cutting force for cutting speed V = 200 m / min

As can be understood from the graphs given in the figures, parallel to the basic knowledge in the literature, cutting force values increased with increasing cutting depth and feedrate.

b. Statistical Analysis ANOVA

A variance analysis was performed to determine the impact ratios of cutting parameters on the cutting force.

When the P values are examined for the main cutting forces in the Anova table; the cutting speed and the feedrate values are statistically significant because they satisfy the condition P<0.05.

Table 5. Anova analysis results

Source	DF	Adj SS	Adj MS	F	P	YD (%)
a	2	2526209	1263105	56,18	0	39,96
V	2	131427	65713	2,92	0,077	2,08
f	2	3215111	1607556	71,5	0	50,85
Error	20	449697	22485			7,11
Total	26	6322444				100
S = 149,949 R-Sq = 92,89% R-Sq(adj) = 90,75%						
DF: Degree of Freedoom, SS: Sum of squares, P: Significance <0.05, PD: Percent distribution						

When the Anova Table was examined, it was determined that the a and f variables with a significance value of P lower than 0.05 were meaningful on the Fc dependent variable but the V independent variable was insignificant. It was determined that the effect of feedrate is 50.85%, the effect of cutting depth is 39.96%, and the effect of cutting speed is 2.08%.

The normal probability and the main effect plots obtained as a result of the variance analysis are shown in Figure 8 and Figure 9 respectively.

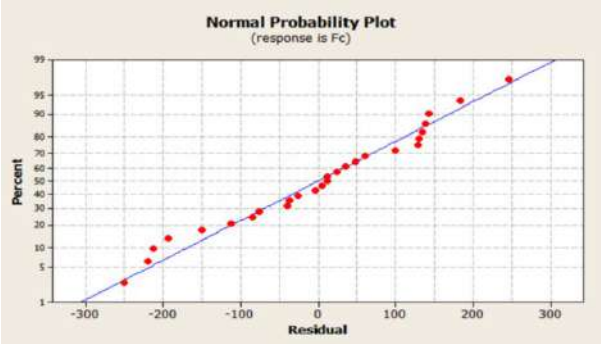

Figure 8. Normal probability plot

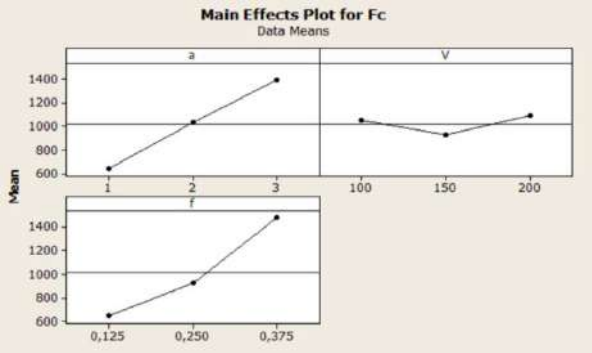

Figure 9. Main effects plot

As can be seen in the main effects graph in Figure 9, it is understood that V has no effect on Fc, while the variables a and f are effective on Fc.

c. Multiple Regression Model

Multiple regression is a statistical technique that allows dependent variables to be explained by one or more independent variables. It is used for various purposes such as analysis, ranking or categorization of experiments. For this reason, it can be considered as a technique that can be used when estimating the cutting force values and surface roughness.

The results of this study were evaluated by the multiple linear regression model using the MINITAB package program. In the regression models, the dependent variable was determined as the main cutting force (Fc), independent variables were cutting speed (V), feedrate (f), and cutting depth (a).

In the main cutting force model, it is seen that the feedrate has the greatest influence because the greatest T value is the feedrate. In Table 4, coefficients of first degree regression equations obtained for the principal shear force are given.

Table 6. First degree regression equetion coefficients for Fc

Coefficients				
Term	Coef	SE Coef	T	P
Constant	-61176	172.616	-35.441	0.002
a	374.44	41.068	91.177	0.000
V	0.35	0.821	0.4207	0.678
f	3317.33	328.544	100.971	0.000

As a result, the mathematical model of the cutting force (Fc) is;

Fc = -611,759 + 374,444 a + 0,345556 V + 3317,33 f

4. CONCLUSIONS

In this study, the variance and regression analyzes of the cutting force were performed depending on the independent variables (cutting speed, feedrate and cutting depth).

As the result of ANOVA tests, for the main cutting force; the feedrate and cutting speed parameters are significant but the cutting depth is not significant.

- According to the determined cutting parameters, the main cutting forces are explained at 90.75%.
- The cutting force values increased depending to the increase in the feedrate.
- The effect of the feedrate on the formation of the main cutting force was determined to be 50.85%.
- Cutting force values increased with increasing cutting depth.
- It is seen that the effect of cutting depth is 39.96% in the formation of the main cutting force.
- It has been determined that cutting speed is not an effective parameter on cutting force.

REFERENCES

[1]. Gurbuz, H., "Statistical Analysis and Investigation of Main Cutting Forces Resulting from Turning of AISI 1050 Steel with Coated and Uncoated Cutting Tools in Different Cutting Parameters", Batman University, Journal of Life Sciences; Volume 5 Number 2, 2015.
[2]. Cakmak, S., Saridemir, S., "The Effect of Insert Geometry On Chip Breaking and Surface Roughness in Machining of AISI 4140 Steel", Duzce University, Journal of Science and Technology, 4, 765-771, 2016.
[3]. Kara, F., Ozbek, O., Kam, M., Saruhan, H., "Optimization by Taguchi Method of Surface Roughness and Vibration in Turning of AISI 4140 Steel", International Academic Research Congresses, 2017.
[4]. Tekaslan, O., Gerger, N., Gunay, M., Seker, U., "Examination of The Cutting Forces of AISI 304 Austenitic Stainless Steel in The Turning Process with Titanium Carbide Coated Cutting Tools", Pamukkale University, Journal of Engineering Science; Volume 13 Number 2 135-144, 2007.
[5]. Asilturk, I., Akkus, H., "AISI 4140 Celiginin Sert Tornalama Isleminde Kesici Takim Asinmasinin Regresyon Yontemi Ile Istatistiksel Olarak Modellenmesi", 3. Ulusal Tasarim Imalat ve Analiz Kongresi Balikesir, 29-30 Kasim 2012.
[6]. Korkut, I., Donertas M.A., "The Effects of Cutting Parameters on Cutting Forces When Milling", Journal of Polytechnic, 6(1), 385-389, 2003.
[7]. Tasliyan, A., Acarer, M., Seker, U., Gokkaya, H., Demir, B., "The Effect of Cutting Parameters on Cutting Force During the Processing of Inconel 718 Super Alloy", J. Fac. Eng. Arch. Gazi Univ., 22(1), 1-5, 2007.
[8]. A. Pugazhenthi, G. Kanagaraj, I. Dinaharan, J. David Raja Selvam, "Turning characteristics of in situ formed TiB2 ceramic particulate reinforced AA7075 aluminum matrix composites using polycrystalline diamond cutting tool", Measurement, 121, 39–46, 2018.
[9]. Anandakrishnan, V., Mahamani, A., "Investigations of flank wear, cutting force, and surface roughness in the machining of Al-6061–TiB2 in situ metal matrix composites produced by flux-assisted synthesis", Int. J. Adv. Manuf. Technol. 55, 65–73, 2011.
[10]. Shoba, C., Ramanaiah, N., Rao, D.N., "Effect of reinforcement on the cutting forces while machining metal matrix composites – an experimental approach", Eng. Sci. Technol., Int. J. 18, 658–663, 2015.
[11]. Joardar, H., Das, N.S., Sutradhar, G., Singh, S., "Application of response surface methodology for determining cutting force model in turning of LM6/SiCP metal matrix composite", Measurement 47 452–464, 2014.
[12]. Yalcin, B., Ozileri, E.D., "Experimental investigation on turning of casted magnesium alloy used in manufacturing automotive parts, in: Advances in Material & Processing Technologies Conference, December 14–17, Madrid, Spain, 2015.
[13]. Buldum, B., Esme, U., Kulekci, M.K., Mersin, T., Sik, A., Kazancioglu, Y., Izmir, B., "Use of Grey-Taguchi method for the optimization of oblique turning process of AZ91D magnesium alloy", Mater. Test. 54, 11–12, 2012.

ICENS 4TH INTERNATIONAL CONFERENCE ON ENGINEERING AND NATURAL SCIENCE
2 - 6 May 2018 KIEV UKRAINE

Determination of The Effect Ratios of The Cutting Parameters on The Cutting Forces Using The Variance Analysis

Abdulmecit Guldas[1], Hakan Dilipak[1], Omer Asal[1], Emre Ay[1]

Abstract

In this study, determining of the effect ratios of cutting parameters on the cutting forces was aimed. For this purpose, the cylindrical AISI 1050 material was machined using uncoated cutting tools. A total of 27 experiments were performed using three different cutting speeds, three different feed rates and three different cutting depths. During the experiments, the cutting faces were measured by connecting the Kistler 9257 B type dynamometer to the tool holder where the cutting tool was located. Variance analyses were performed on the obtained cutting force values. Thus, the effect ratios of cutting parameters on the cutting forces were investigated. As the results of the variance analysis, it was determined that the cutting depth and the feed rate are effective on the cutting force respectively. Experimental results showed that cutting speed has no effect on the cutting force.

Keywords: AISI 1050 Steel, Cutting force, Cutting Parameters ANOVA, Regression

1. INTRODUCTION

Optimum cutting conditions must be ensured in the machining process in order to produce the parts in the desired size, tolerance and surface quality. In this process, the relationship between dependent variables such as cutting forces, surface quality, tool life, chip type, and independent variables such as workpiece material, tool material, cutting parameters (cutting depth, feed rate, cutting speed), tool geometry, and machine should be evaluated well. Numerical modeling of the cutting process is applied as an alternative method since the researches on machining are expensive and time consuming [1-2].

When the literature studies are examined, it is seen that too much study has been done on the cutting forces depending on the cutting tool. Cutting speed and cutting tool geometry are the most important parameters in terms of their effect on machinability properties [3]. If cutting parameters don't be selected well, this causes rapid wear, tool breakage, breakdown of the workpiece and low surface quality [4]. One of the most important problems encountered in machining is surface roughness. Changing the cutting conditions to obtain a good surface quality is the most effective method applied in the literature [5-9]. One of the most important parameters that increase surface roughness is tool wear [10, 11]. Beside the cutting parameters, the type of chip and chip length formed during cutting, increase the surface roughness [12]. In the literature, the effects of cutting parameters on machinability, surface roughness, cutting force, and tool life were investigated experimentally. Relationships between these parameters were determined by regression and variance analysis [13].

In this study, the effects of different cutting parameters on the main cutting forces in turning operations were investigated experimentally and statistically. Totally 27 experiments were carried out according to the

determined parameters. Variance analysis (ANOVA) was performed to determine the effect of each parameter on the results obtained. The relationship between dependent variables and independent variables is modeled by using regression analysis.

[1] *Gazi University, Department of Manufacturing Engineering, 06500, Yenimahalle/ANKARA, Turkey. aguldas@gazi.edu.tr*

2. MATERIAL AND METHOD

AISI 1050 steel was used as the workpiece in the experiments. This steel is also known as carbon steel because of the high amount of carbon it's contain. Hardenability of this steel increases in parallel with the amount of carbon but its toughness is inversely proportional to the amount of carbon.

The workpiece material was machined to the dimensions of Ø92x300 mm for experiments and a spot hole was opened. The experiments were carried out via the workpiece was connected between chuck and tail stock of the CNC machine. Experiments were carried out by connecting the workpiece between the chuck and the tail stock. The dimensions of the workpiece are given in Figure 1.

Figure 10. Dimension of the workpiece

In the experiments, Walter brand (SNMG120412-NRT WS10) cutting tools were used. The geometrical properties of the cutting tools are shown in Figure 2.

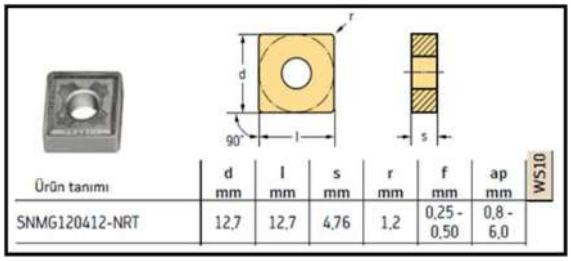

Ürün tanımı	d mm	l mm	s mm	r mm	f mm	ap mm
SNMG120412-NRT	12,7	12,7	4,76	1,2	0,25 - 0,50	0,8 - 6,0

Figure 11. The geometrical properties of the cutting tools

The geometric properties and dimensions of the Walter brand (DSBNR2525M12) tool holder used in the experiments are given in Figure 3.

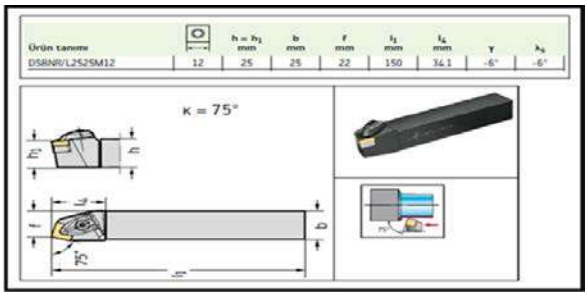

Figure 12. The geometric properties of the tool holder

The experiments were carried out at the CNC laboratory of Gazi University Technology Faculty Department of Manufacturing Engineering. JOHNFORD brand CNC lathe with FANUC control was used for the experimental studies. The experiments were performed under dry cutting conditions and a separate cutting tool was used for each experiment.

The cutting parameters used in the experiments were determined as 3 different cutting speeds, 3 different feed rates and 3 different cutting depths. The cutting parameters are given in Table 1. In the experiments, the workpiece was machined by 30 mm length. To ensure the same conditions throughout the experiments, a new

cutting tool was used in each experiment. After each experiment, the CNC machine was stopped. Totally 27 experiments were executed in which cutting speed, cutting depth and feed rate parameters were changed.

Table 9. Cutting parameters

Parameters	Value
V (m/min)	140, 170, 200
f (mm/rev)	0.15, 0.275, 0.4
a (mm)	1.5, 2.5, 3.5

A Kistler 9257B type piezoelectric dynamometer which can measure three force components (Fz, Fx, and Fy) was used during machining. This dynamometer was connected to an Amplifier and cutting forces were sent to the computer to obtain plots. The experimental setup is shown in Figure 4.

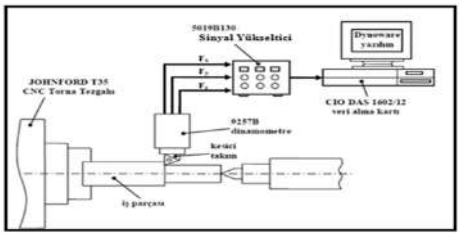

Figure 13. Experimental setup

3. EXPERIMENTAL RESULTS AND STATISTICAL ANALYSIS

a. Cutting Forces

In this study, AISI 1050 steel which has medium carbon was machined by using a CNC lathe to investigate the effects of cutting parameters on the cutting force. The data obtained from the experiments are given in Table 2.

Table 10. Experimental results

Depth of cut	**Cutting speed**	**Feed rate**	**Cutting force**
a, (mm)	V, (m/min)	f, (mm/rev)	Fc, (N)
3.5	200	0.4	2090
		0.275	1882
		0.15	1225
	170	0.4	2405
		0.275	2196
		0.15	1435
	140	0.4	3274
		0.275	2338

		0.15	2379
2.5	200	0.4	1917
		0.275	1484
		0.15	1072
	170	0.4	2277
		0.275	1563
		0.15	1036
	140	0.4	2280
		0.275	1565
		0.15	1029
1.5	200	0.4	1337
		0.275	999
		0.15	627
	170	0.4	1322
		0.275	966
		0.15	616
	140	0.4	1331
		0.275	976
		0.15	626

For cutting speed V = 140, 170, and 200 m / min, the effect of cutting depth on the average cutting force depending on the feed rate is given in Figure 5, Figure 6, and Figure 7 respectively.

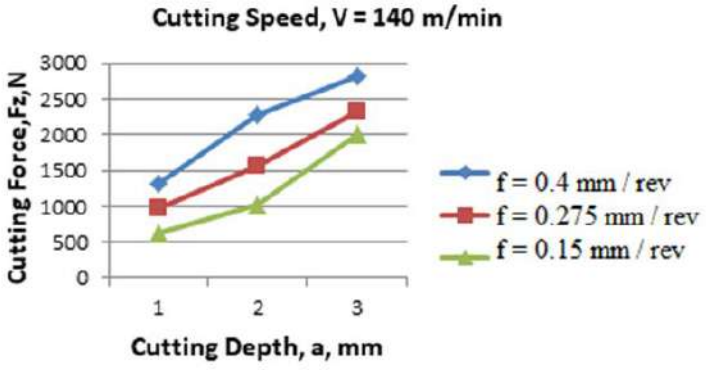

Figure 14. The effect of cutting depth on the main cutting force for cutting speed V=140 m / min

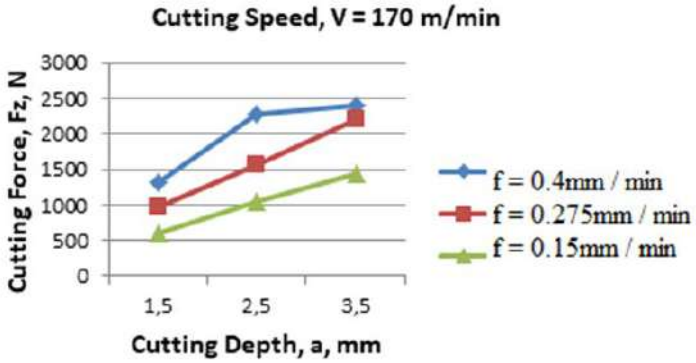

Figure 15. The effect of cutting depth on the main cutting force for cutting speed V=170 m / min

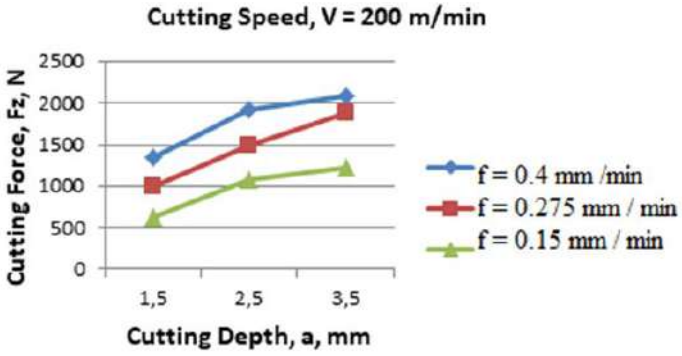

Figure 16. The effect of cutting depth on the main cutting force for cutting speed V=200 m / min

It can be seen in the graphs in Figure 5, Figure 6, and Figure 7 that the cutting force values increased with increasing cutting depth. Likewise, the increase in the feedrate value increased the cutting forces. The lowest cutting force value was obtained as 616 N at 170 m / min cutting speed, 1.5 mm cutting depth, and 0.15 mm / rev feedrate, while the maximum cutting force was realized as 2830 N at 200 m / min cutting speed, 3.5 mm cutting depth, and 0.4 mm / rev feedrate.

b. ANOVA (Variance Analysis)

The data obtained from the experiments were subjected to statistical analysis using the Minitab program and a variance analysis was done. The variance analysis is shown in Table 3. In the ANOVA table, the factors providing the P <0.05 condition are effective. Accordingly, it can be said that the all three factors are found to be effective on the main cutting forces.

Table 11. Results of the variance analysis

Source	DF	Adj SS	Adj MS	F	P	YD (%)
a	2	5170214	2585107	76,73	0	52,73
V	2	309947	154974	4,6	0,0023	3,16
F	2	3651670	1825835	54,19	0	37,24
Error	20	673820	33691			6,87
Total	26	9805651				
S = 183,551 R-Sq = 93,13% R-Sq(adj) = 91,07% **DF: Degree of Freedoom, SS: Sum of Squares, P: Significance <0.05, PD: Percent Distribution**						

The results were obtained with a reliability of 91.07%. Hence, it is understood that the all three parameters have an effect on the cutting force. The effectivities on the cutting force of the independent variables were calculated by making the necessary calculations on the Anova chart. According to these calculations, it was observed that cutting depth, feed rate, and cutting speed were effective parameters on cutting force, respectively.

Figure 8 and Figure 9 show the normal probability plot and the main effect plot respectively obtained by the variance analysis.

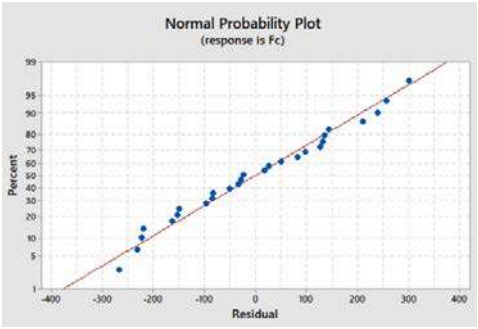

Figure 17. Normal probability plot

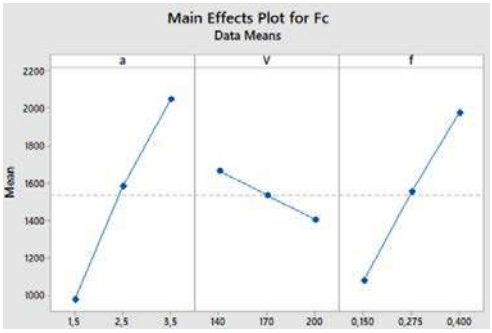

Figure 18. Main effect plot

c. Multiple Regression Model

Multiple regression is a statistical technique that allows dependent variables to be explained by one or more independent variables. It is used for various purposes such as analysis, ranking or categorization of experiments.

For this reason, it can be considered as a technique that can be used when estimating the cutting force values and surface roughness.

The results of this study were evaluated by the multiple linear regression model using the MINITAB package program. In the regression models, the dependent variable was determined as the main cutting force (Fc), independent variables were cutting speed (V), feed rate (f), and cutting depth (a).

Table 12. First degree regression equation coefficients for Fc

Coefficients				
Term	Coef	SE Coef	T	P
Constant	-48	273	-0,18	0,862
a	534,5	41,3	12,95	0,000
V	-4,37	1,38	-3,18	0,004
f	3601	330	10,9	0,000

As a result, the mathematical model of the cutting force (Fc) is;

Fc = -48 + 534,5 a - 4,37 V + 3601 f

4. CONCLUSIONS

In this study, the effects of cutting speed, feed rate and cutting depth on the cutting force in turning of AISI 1050 steel are presented. Besides, mathematical modeling of the relationship between the obtained surface roughness and machining parameters was performed. From the experiments, it was determined that the main cutting force is explained 91.07%. The results obtained from the study are summarized below:

- According to the variance analysis, it was determined that cutting depth, feed rate, and cutting speed are effective parameters on the cutting force.
- Cutting depth has the most dominant effect with a significance ratio of 52.73%.
- The effect of the feed rate on the cutting force was determined as 4%.
- The cutting speed has the least effect on the cutting force with 3.16%.

REFERENCES

[1]. Yasar, N., Sekmen, M., Korkmaz, M.E., Gunay, M., "Experimental and numerical analysis of cutting force during machining of AISI P20 steel", Gazi Un. Journal of Science, Part:C 4(1):13-19, 2016.
[2]. Tasliyan, A., Acarer, M., Seker, U., Gokkaya, H., Demir, B., "The Effect of Cutting Parameters on Cutting Force During the Processing of Inconel 718 Super Alloy", Journal of the Faculty of Engineering and Architecture of Gazi University, Cilt 22, No 1, 1-5, 2007.
[3]. Ozcatalbas, Y., "The Effects of Tool Wear and Mechanical Properties of Work Piece Material on Surface Roughness and Cutting Forces", Gazi Un. Journal of Polytechnic, Cilt 4, 47-52, 2002.
[4]. Thomas T.R., Rough Surface, Longman, New York, 1982.
[5]. Korkut, I., Donertas, M.A., "The influence of feed rate and cutting speed on the cutting forces, surface roughness and tool-chip contact length during face milling", Materials and Design, 2005.
[6]. Dilipak, H., Gezgin, A., "The Investigation of The Effects of Number of Inserts, Cutting Speed and Feed Rate on Surface Roughness in Milling of AISI D3 Steel", Gazi Un. Journal of Polytechnic, 13(1), 29-32, 2010.
[7]. Davim, J. P., Figueira, L., "Machinability evaluation in hard turning of cold work tool steel (D2) with ceramic tools using statistical techniques", Materials and Design, 2006.
[8]. Lima, J.G., Avila, R.F., Abrao, A. M., Faustino, M., Davim J. P., "Hard turning: AISI 4340 high strength low alloy steel and AISI D2 cold work tool steel", Journal of Materials Processing Technology, 169: 388–395, 2005.
[9]. Sai, W. B., Salah, N. B., Lebrun, J. L., "Influence of machining by finishing milling on surface characteristics", International Journal of Machine Tools & Manufacture, 41: 443–450, 2001.
[10]. Gokkaya, H., Sur, G., Dilipak, H., "The Experimental Investigation of The Effects of Uncoated Cementit Carbide Insert and Cutting Parameters on Surface Roughness", Pamukkale Un. Journal of Engineering Science, 12(1): 59-64, 2006
[11]. Dilipak, H., Guldas, A., Gezgin, A., "Investigation of the effect of number of insert on machining time and metal removal rate when milling AISI D3 steel at high cutting speeds", Journal of Mechanical Engineering, Strojniski Vestnik-Journal of Mechanical Engineering 55 (7-8): 438-443 Jul-Aug 2009.
[12]. Gullu, A., Karabulut, S., Guldas, A., "Chip breaking problems in machining of inconel 718 super alloy and chip breaker design", J. Fac. Eng. Arch. Gazi Univ, 23(1), 57-164, 2008.
[13]. Asal O., Dilipak, H., Mullaahmetoglu, F., "Investigation and Statistical Analysis of Surface Roughness In Turning Of Az91 Materials". III. International Conference On Engineering And Natural Science, 813-819, 2017.

ICENS 4TH INTERNATIONAL CONFERENCE ON ENGINEERING AND NATURAL SCIENCE
2 - 6 May 2018 KIEV UKRAINE

Investigation of The Effects of Cutting Parameters on The Surface Roughness in The Turning of AISI 1050 Steel

Hakan Gurun[1], Hakan Dilipak[1], Omer Asal[1], Emre Ay[1]

Abstract

AISI 1050 which is one of the unalloyed steels and it is known as carbon steels because of contains the high amount of carbon. In this study, the AISI 1050 steel was machined on the CNC turning machine and surface roughness values were recorded. After that the effects of cutting parameters on the surface roughness were investigated. Furthermore, the effect ratios of the cutting factors on the surface roughness were determined using the variance analysis. In this context, Walter Company branded SNMG120412-NRT WS10 uncoated tools were used to perform the experiments. In the experiments, cutting velocity (140, 170 and 200 m / min), feed rate (0.15, 0.275 and 0.4 mm / g) and cutting depth (1.5, 2.5 and 3 mm) were used as the cutting parameters. Surface roughnesses were measured with the Mitutoyo SJ-201 device. According to the conducted analysis results, it was determined that the most important parameter is the feed rate in terms of surface roughness. Other parameters were determined to have no effect on surface roughness.

Keywords: AISI 4140 Steel, Cutting force, ANOVA, Regression, Cutting parameters

1. INTRODUCTION

Cutting parameters such as cutting forces, feed rate, and cutting speed that occurred during machining variances change depending on type of works piece materials being machined. To know the cutting forces and to be able to predict the tool life depend on cutting forces are of great importance for a manufacturer. The bad selected machining parameters are causing economic losses such as tool wear, breakage of the cutting tools as well as loss of workpiece or poor surface quality. Determination of the appropriate cutting parameters for cutting to feed rateols allows the extension of tool life and production of the workpiece with desired surface quality. The roughness that occurs on the surface of turned products is one of the most important factors affecting the function of the product. Various operations and analyzes are carried out in order to reduce the roughness to the minimum [1-4].

Numerous studies have been carried out in the literature on machinability, cutting force, and surface roughness related to cutting parameters and optimum tool path [5-10]. Basak and et all [11] primary cutting forces and surface roughness values during turning of a medium carbon steel subjected to different spheronization heat treated have been modeled by multivariate analyses of variance (MANOVA). Gunay, used the AISI 1040 steel in the turning operation to examine the effects of the cutting tool chip angle on the surface roughness. From the experiments carried out, it was observed that the negative chip angle has a negative effect on the surface roughness [12].

Saravanakumar et all investigated investigation is to find the optimum turning parameters during machining of aluminum alloy 6063 with carbon nitride cutting tools [13]. According to this results, the responses were greatly influenced by the feed rate, followed by speed. Abhang and Hameedullah [14] employed Taguchi method to optimize the turning parameters for obtaining the minimum surface roughness. Moganapriya et all [15] investigated that the influence of cutting parameters (Coating material, cutting depth, Feedrate, and Spindle speed) on material removal rate (MRR) and surface roughness of TiAlN/WC-C, TiAlN coated tool during CNC turning of AISI 1015 mild steel. These researchers employed Taguchi optimization method for determining of effect parameters on minimization of surface roughness. It is found that cutting depth is the most influential factor (51.26%) on surface roughness, while number of layer deposited contributed significantly (30.56%) to

[1] *Gazi University, Department of Manufacturing Engineering, 06500, Yenimahalle /ANKARA, Turkey. hgurun@gazi.edu.tr*

surface roughness. The effect of process parameters in turning of AISI 4340 under MQL condition with nano fluid (Multiwalled Carbon Nano Tube) on the cutting force generated and machined surface roughness is carried out by Patole and Kulkarni [16]. From result analysis, it was found that, feed rate played a major role in producing lower surface roughness followed by cutting depth whereas cutting speed has least significance in producing lower surface roughness under MQL using nano coolant. He et all investigated to achieve a comprehensive understanding of the theoretical modeling on turned surface roughness [179. A systematic review of influencing factors and theoretical modeling methods of surface roughness in turning process. The modeling methods of surface roughness are classified into theoretical and empirical solutions is researched. Asilturk and Akkus were subjected to a turning process to the AISI 4140 steel with a hardness of 56-57 HRc under dry cutting conditions. They statistically modeled the tool wear by using the regression method in the turning process [5]. Korkut et al. investigated the effects of cutting parameters on the cutting forces.

The main purpose of this study is determining of effects of cutting parameters on surface roughness and creating a model that predicts surface roughness.

2. EXPERIMENTS AND ANALYSIS

In the experiments, the AISI 1050 medium carbon steel which is widely used in manufacturing industry was used as a test material. The workpiece material was machined to the dimensions of Ø92x300 mm for experiments and a spot hole was opened. Geometric properties of workpiece are shown in Figure 1.

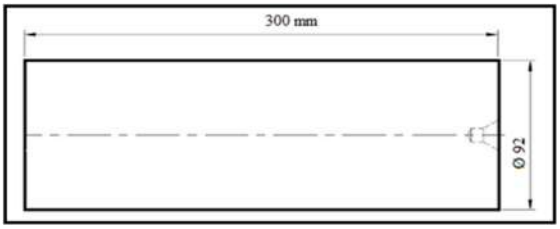

Figure 1. Geometric properties of workpiece

The experiments were carried out at the CNC laboratory of Gazi University Technology Faculty Department of Manufacturing Engineering. JOHNFORD brand CNC lathe with FANUC control was used for the experimental studies. The experiments were performed under dry cutting conditions and a separate cutting tool was used for each experiment. Geometric properties of the cutting tool are shown in Figure 2.

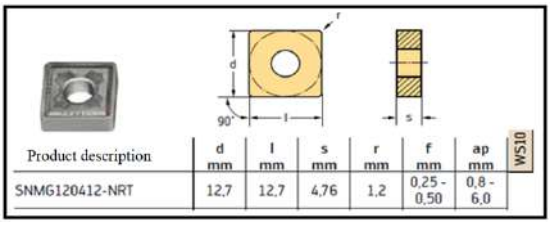

Figure 2. Geometric properties of the cutting tool

A Walter branded tool holder was used in the experiments. Geometric properties and dimensions of the tool holder are shown in Figure 3.

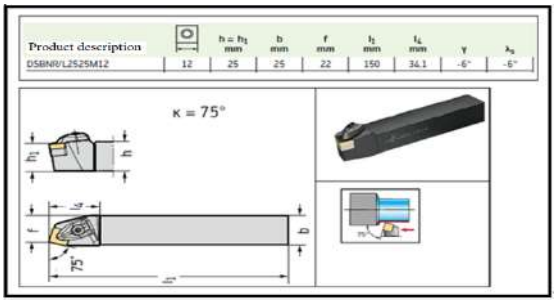

Figure 3. Geometric properties of the tool holder

Table 7. Cutting parameters

Parameter	A	B	C
Cutting Depth	1.5 mm	2.5 mm	3.5 mm
Cutting speed	140 m/min	170 m/min	200 m/min
Feed rate	0.15 mm/rev	0.275 mm/rev	0.4 mm/rev

In the experiments, the machining length was kept constant at 30 mm. A new cutting tool was used in each experiment. Totally 27 experiments were conducted. The experimental results are given in Table 2.

Table 8. The main cutting force results depending from the cutting parameters

Cutting depth (a), mm	**Cutting speed (V), m/min**	**Feed rate (F), mm/rev**	**Arithmetic mean surface roughness (Ra), µm**
1.5	140	0.15	1.27
1.5	140	0.275	3.2
1.5	140	0.4	7.67
1.5	170	0.15	1.38
1.5	170	0.275	3.01
1.5	170	0.4	7.81
1.5	200	0.15	1.14
1.5	200	0.275	3.1
1.5	200	0.4	5.26
2.5	140	0.15	1.28
2.5	140	0.275	3.34
2.5	140	0.4	7.1
2.5	170	0.15	1.4
2.5	170	0.275	2.92
2.5	170	0.4	6.34
2.5	200	0.15	1.2
2.5	200	0.275	3.99
2.5	200	0.4	7.54
3.5	140	0.15	1.26
3.5	140	0.275	2.67
3.5	140	0.4	6.23
3.5	170	0.15	1.79
3.5	170	0.275	3.8
3.5	170	0.4	6.92
3.5	200	0.15	1.47
3.5	200	0.275	3.33
3.5	200	0.4	5.73

The data obtained from the experimental results were plotted and given in Figure 4, Figure 5, and Figure 6.

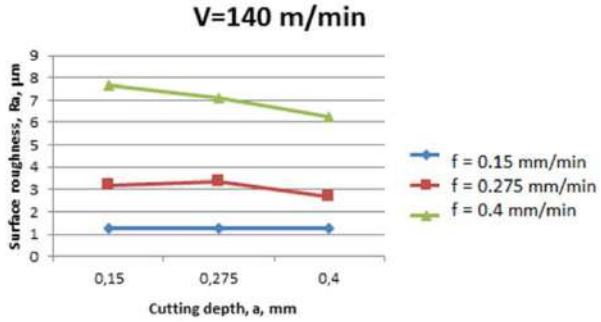

Figure 4. The effect of cutting depth on the surface roughness for cutting speed V=140 m / min

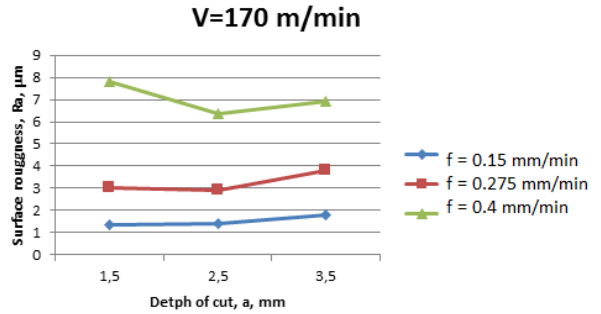

Figure 5. The effect of cutting depth on the surface roughness for cutting speed V=170 m / min

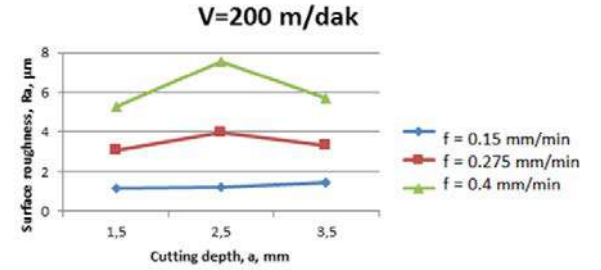

Figure 6. The effect of cutting depth on the surface roughness for cutting speed V=200 m / min

When the graphs given in Figure 4, Figure 5, and Figure 6 are examined, it is observed that the surface roughness values increase with increasing the feed rate values. The obtained experimental results were transferred to MINITAB software and variance analysis have been performed. The results of the variance analysis are shown in Table 3. In the ANOVA table, the factors providing the P <0.05 condition are effective.

Table 9. Results of the variance analysis

Source	DF	Adj SS	Adj MS	F	P	YD (%)
a	2	0.21	0.105	0.28	0.76	0.15
V	2	0.379	0.189	0.5	0.613	0.27
F	2	133.862	66.931	177.49	0	94.27
Error	20	7.542	0.377			5.31
Total	26	141.992				
S = 0.614075 R-Sq = 94.69% R-Sq(adj) = 93.10% **DF: Degree of freedom, SS: Sum of squares, P: Significance<0.05, PD: Percentage distribution**						

When the ANOVA table is examined, it can be seen that the P <0.05 condition is only provided by the variable of the feed rate. P value for cutting depth and cutting speed is also higher than 0.05. Thus, while the feed rate is an effective parameter on the surface roughness, the cutting depth and the cutting speed have no effect.

The effectivities on the cutting force of the independent variables were calculated by making the necessary calculations on the Anova chart. According to these calculations, the effects of feed rate, cutting speed, and cutting depth are 0.15%, 0.27%, and 94.27%, respectively. Normal probability plot is shown in Figure 7 and main effect plot in Figure 8.

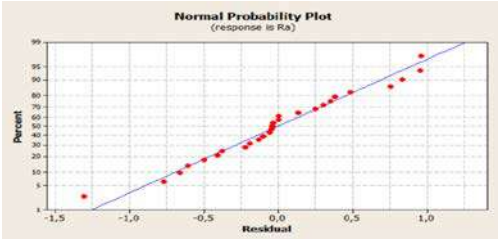

Figure 7. Normal probability plot

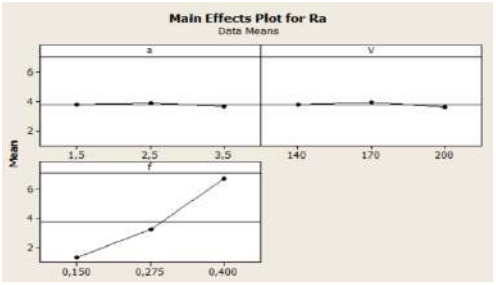

Figure 8. Main effects plot

Regression analysis was performed to estimate the surface roughness values. Regression analysis has been achieved using by MINITAP software. In the regression models, the main cutting force (Fc) has been defined as the dependent variable and independent variables have been determined as cutting speed (V), feed rate (f), and cutting depth (a).

Table 10. Result of regression analysis

Coefficients				
Term	**Coef.**	**SE Coef.**	**T**	**P**
Constant	-1.6479	1	-1.4809	0.152
a	-0.0356	0.16801	-0.2116	0.834
V	-0.0023	0.0056	-0.4167	0.681
f	21.5156	1.34404	16.0081	0

It is seen that the highest T value is the feed rate (f) in the surface roughness model. So, it is seen that feed rate has greatest effect on the surface roughness.

As a result, the mathematical model obtained from regression analysis for the surface roughness (Ra) is;

$$Ra = -1.64789 - 0.0355556\ a - 0.00233333\ V + 21.5156\ f$$

3. CONCLUSIONS

In this study, the effects of cutting parameters on the surface roughness were investigated. In this context, regression and variance analyzes were performed using values obtained from experimental studies. The results obtained from the study are summarized below:

Surface roughness is explained at the ratio of 93.10%.

According to the results of variance and regression analysis, the most effective parameter on the surface roughness was determined as the feed rate.

It has been seen that cutting speed and cutting depth have no effect on surface roughness.

It is found that feed rate in the formation of surface roughness has a great effect by 94.27 %.

REFERENCES

[1]. Manivel, D., Gandhinathan, R., "Optimization of surface roughness and tool wear in hard turning of austempered ductile iron (grade 3) using Taguchi method", Measurement, 93, 108–116, 2016.
[2]. Zhang, P., Liu, Z., "Modeling and prediction for 3D surface topography in finish turning with conventional and wiper cutting tools", Measurement 94, 37–45, 2016.
[3]. Yamanea, Y., Ryutaroa, T., Tadanori, S., Ramirez, I.M., Keiji, Y., "A new quantitative evaluation for characteristic of surface roughness in turning, Precision Engineering", 50, 20–26, 2017.
[4]. Mia,M., Dhar, N.R., "Response surface and neural network based predictive models of cutting temperature in hard turning", Journal of Advanced Research, 7, 1035–1044, 2016.
[5]. Dilipak, H., Guldas, A., Gezgin, A., "Investigation of the effect of number of cutting tools on machining time and metal removal rate in milling AISI D3 steel at high cutting speeds", Journal of Mechanical Engineering, Strojniski Vestnik-Journal of Mechanical Engineering 55 (7-8): 438-443 Jul-Aug 2009.
[6]. Mia M, Dhar NR. "Effect of high pressure coolant jet on cutting temperature, tool wear and surface finish in turning hardened (HRC 48) steel", Journal of Mech Engineering, 45(1), 1–6, 2015.
[7]. Mia M, Dhar N. "Optimization of surface roughness and cutting temperature in high-pressure coolant-assisted hard turning using Taguchi method", The International Journal of Advanced Manufacturing Technology, 88, 1-4, 739-753, 2017.
[8]. Gullu, A., Karabulut, S., Guldas, A., "Chip breaking problems in machining of inconel 718 super alloy and chip breaker design", J. Fac. Eng. Arch. Gazi Univ, 23(1), 57-164, 2008.
[9]. Lalwani, D., Mehta, N., Jain, P., "Experimental investigations of cutting parameters influence on cutting forces and surface roughness in finish hard turning of MDN250 steel", J Mater Process Technol, 206(1):167–179, 2008.
[10]. Goktas, M., Guldas, A., Dilipak H., "Tool Path Generation for Pocket Machining Operations with Island", Gazi University Journal of Science, 30 (3), 79-88, 2017.
[11]. Basak, H., Baday, S., "In processing of a spheroidized medium carbon steel, modelling with regression analysis of cutting forces and surface roughness affected by cutting parameters", Pamukkale University Journal of Engineering Sciences, 22(4), 253-258, 2016.
[12]. M. Gunay, "Investigation of the Interaction Between the Surface Quality and Rake Angle in Machining of AISI 1040 Steel", SIGMA-Journal of Engineering and Natural Sciences, 26 (2): 105-111, 2008.
[13]. Saravanakumar, A., Karthikeyan, S.C., Dhamotharan, B., Kumar, V.G., "Optimization of CNC Turning Parameters on Aluminum Alloy 6063 using Taguchi Robust Design", Materials Today: Proceedings, 5, 8290–8298, 2018.
[14]. Abhang, L.B., Hameedullah, M., "Optimization of Machining Parameters in Steel Turning Operation by Taguchi Method", Procedia Engineering, 38, 40-48, 2012.
[15]. Moganapriyaa C., Rajasekara, R., Ponappaa, K., Venkateshb, R., Jeromec, S., "Influence of Coating Material and Cutting Parameters on Surface Roughness and Material Removal Rate in Turning Process Using Taguchi Method", Materials Today: Proceedings, 5, 8532–8538, 2018.
[16]. Patole, P.B., Kulkarni, V.V., "Optimization of Process Parameters based on Surface Roughness and Cutting Force in MQL Turning of AISI 4340 using Nano Fluid", Materials Today: Proceedings, 5, 104–112, 2018.
[17]. He, C.L., Zong, W.J., Zhang, J.J., "Influencing factors and theoretical modeling methods of surface roughness in turning process: State-of-the-art", International Journal of Machine Tools and Manufacture, 129, 15–26, 2018.

ICENS 4TH INTERNATIONAL CONFERENCE ON ENGINEERING AND NATURAL SCIENCE
2 - 6 May 2018 KIEV UKRAINE

An Alternative Method for Long-Term Land Cover Change Detection: A Case Study of Hasanlar Dam

Firat Caglar Yilmaz[1], Sukran Sahin[2]

Abstract

Dams which needed to drinking and irrigation water supply, flood control etc. at first have undertaken an another task with hydroelectric power which emerged from the increasing energy demand due to population growth, technological developments and changes in consumption habits in recent years. This process has accelerated from the 1980s which was the beginning of the increasing trends in renewable energy sources due to the environmental impacts of fossil fuels. However, even though dam type hydroelectric power plant project is a renewable energy, it has some adverse effects on ecosystems. The changing flow regime with the intervention to the river generally results in destruction and fragmentation in the riparian ecosystem. This change in the land cover can lead to modification on the microclimate, thus it can change the hydrological cycle of the basin. For this reason, the monitoring of the change in the land cover at the dam and its surroundings is important for revealing the effects of the project. In this context the Hasanlar Dam in Duzce province was examined in the scope of this study. The land cover change has been determined in two temporal periods through 1:25000 scale topographic maps date on 1960, 1982 and 2013. The land cover which is consist of 4 classes was obtained by visual classification method. The amount of change was determined as the unit by grid method. It was observed that forest areas showed a decreasing tendency after the dam construction during the first temporal period but an increase was shown later. On the other hand it has been determined that non-vegetated areas are transformed into orchard predominantly. As a result, it has been seen that the proposed method can provide an effective analysis for the land cover change detection when old dated aerial photos or satellite images can not be reached.

Keywords: *Land cover change, Dam, Hydroelectric power plant, Hasanlar Dam*

1. INTRODUCTION

In our day, the development and conservation of water resources have become one of the most important parameters of their modernity beside influencing the development of countries [1]. In this context, the concept of sustainability comes to the forefront in the projects that countries implement for the utilization of water resources. Among these projects, dam projects have an important share.

It is seen that the first samples of dams were constructed for agricultural irrigation, drinking water supply and flood control. However, when it came out that the controlled water can be an energy source when released, the dams gained another function [2]. Although there are different methods that do not require a dam crest to obtain energy from the river, this discovery of humans has played a role in the increase of dam projects. This method, called hydroelectric, which works by the principle of converting the potential energy of water flowing from the highs through the turbines and generators to electric energy, is preferable as it is a cleaner and renewable resource compared to fossil fuels [3], [4]. Such that; the report by The World Commission on Dams, published in 2000, shows the extent of intervention in streams in a rational sense. In the report, it is stated that in European Union countries and United States, 60-65% of rivers were controlled, although it differs by the basin, whereas in Asia, the number of rivers taken under control by more than one large-scale dam was well below half the total number of rivers [5].

[1] *Corresponding author: Pamukkale University, Faculty of Architecture and Design, Department of Landscape Architecture, 20070, Pamukkale/Denizli, Turkey.* fcyilmaz@pau.edu.tr

[2] *Ankara University, Faculty of Agriculture, Department of Landscape Architecture, 06120, Kecioren/Ankara, Turkey.* sukran.sahin@ankara.edu.tr

Although the dam projects have an important place in development, they have some adverse effects on ecosystems. The results of studies in developed countries in the northern hemisphere show that river regulation is the most powerful and common anthropogenic impact on the riverine ecosystem [6]. These adverse effects can be seen in the short or long term and can be grouped as effects on aquatic ecosystems, fauna, and flora. Depending on the changing regime of flow; the changing habitat areas in the river due to the blocking of sediment transport [4], blocking of the transport of nutrients required for aquatic life [4], defects in some vital activities (determination of migration time etc.) of living beings due to the regime of flow [7], declining water quality resulting from eutrophication starting with transition to stagnant water [7] and changing bottom structure [8] are examples of the effects on aquatic ecosystems. In other words, the changing flow regime generally results in the destruction and fragmentation of the riverine ecosystem [9]. In terms of fauna, prevention of the passage of fish species moving between the lower and upper parts of the river seems to be an important impact value [8]. The adverse effects on the flora becomes visible in a much shorter period in the construction phase. For example; the dust created by the construction work sticks on leaves and decreases the light transmittance, thus, affects the photosynthesis and slows the growth rate of the plant [10]. In the long term, the evaporation increases together with the dam reservoir formed and therefore some climatic effects occur. The humidity in the air increases, the air movement change, and the temperature, wind, and precipitation become different. This creates a sudden change in the natural vegetation in the region, and only species that can adapt to this change can survive [7]. In the light of this information, it understood that the change in land cover is inevitable as a result of the intervention to nature through the dam projects. In fact, in the change of microclimate and land cover, there is a bi-directional setup that affects both. In other words, the change in land cover can lead to modification of the microclimate, thus, change the hydrological cycle of the basin [11]. As a result, changing land cover also affects other landscape functions. For example; the infiltration capacity of the area varies due to changing land cover, and it changes surface flow dynamics [12]. In this context, land cover change analysis can be an effective method in order to interpret long-term environmental effects of dam projects.

Nowadays, satellite images are mostly preferred as a data set in land cover change analysis. The most important reason for this preference is that the reflection values processed on the raster data can be classified by different methods in line with their closeness to each other. Since the archival images are free of charge and easy to reach, the images by Landsat satellites are frequently preferred, however, these records also do not cover the data of pre-1970s. This is the greatest constraint on the use of satellite images in long-term analyzes. For this reason, it is aimed to develop an alternative method that can be used in the analysis of land cover change, especially when there is no effective data such as the satellite image for past. In addition, the effects of the dam project and the findings obtained with this alternative method applied in Hasanlar Dam in Duzce province were interpreted.

2. MATERIAL AND METHOD

Hasanlar Dam and HEPP (Hydroelectric Power Plant) located in Duzce province were determined as study area (Figure 1). The construction of the dam on the Kucuk Melen stream, located between the Duzce and Yigilca districts, was started in 1965 [13]. The maximum water level of the dam is 271.30 m. and the crest elevation is 70.80 m. [14].

Materials used within the scope of this study are:

- Topographic maps numbered G26b1 of 1960, 1982 and 2013, provided in raster format by General Command of Mapping,
- ArcGIS 10.2, a GIS (Geographical Information System) based software used for digitizing topographic maps, storing and mapping all data, and analyzing,
- Literature review regarding the field of study and the subject,
- Interviews with officials and local people made during the area survey.

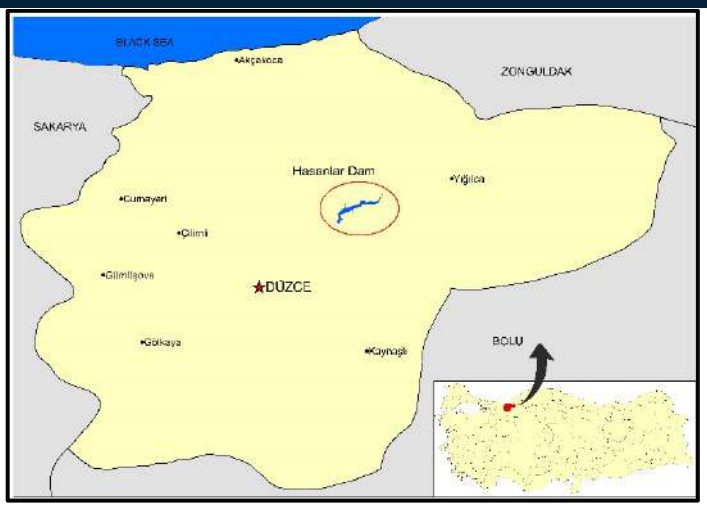

Figure 1. The location of study area

During the literature review, the largest damages and land cover changes by the dam projects were found out to be in the riverine ecosystem. For this reason, when determining the boundaries of the study area, it was meant to determine the ecological border closest to the shore line. In this context, the "direct drainage area" defined by Zielenski (2002) [15] was accepted as the boundary. The direct drainage area defines areas that are wedge-shaped on both sides of the main stream following the determination of the basin boundaries of the side streams, which has more than two branches, connected to the main stream, and which do not belong to any sub-basin boundary. These areas are not included in the sub-basin boundaries as they consist of the aspects which directly faced to the main stream. In other words, the surface flow in these areas is directed to the main stream. Zielenski argues that these areas have a sub-basin character when evaluated together. The boundaries of the study area are shown in Figure 2 starting from this point of view.

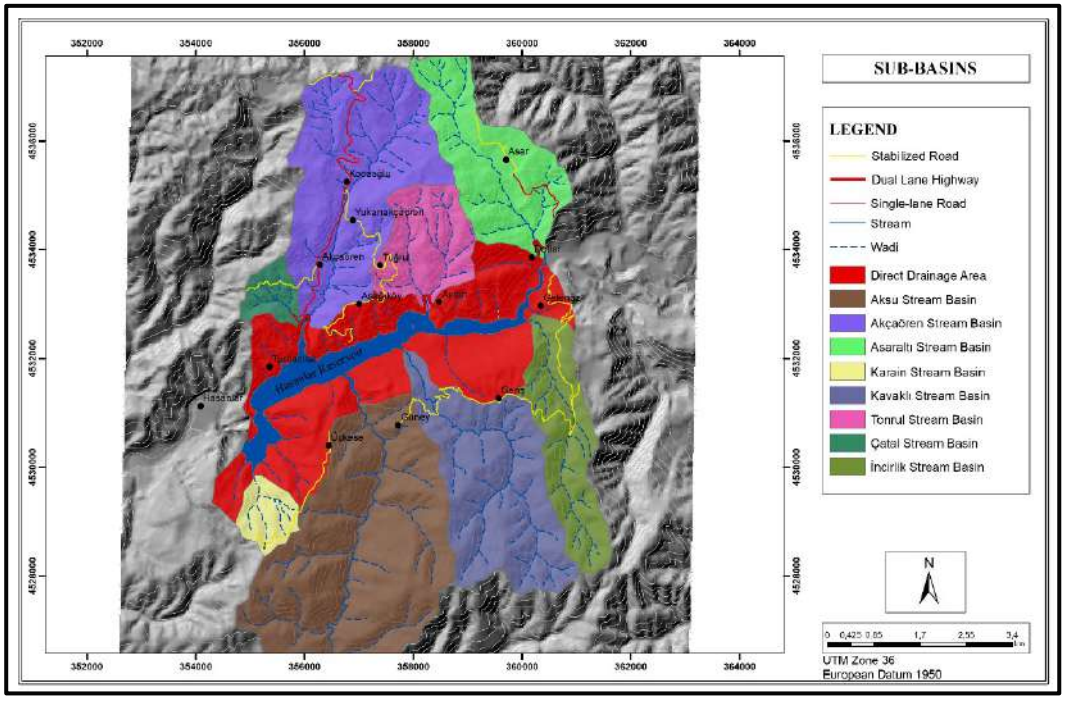

Figure 2. Direct drainage area for Hasanlar reservoir

In the mapping of the land cover for the relevant years, four classes were used in the study due to the limited information contained in the 1:25000 scale topographic maps. These are; forest, orchard, water surface, and non-vegetated area. In order to be able to perform the change analysis, the vector data required were obtained by manual on-screen digitization of the topographical maps. However, in this method, the digitization is followed by a grid method in order to eliminate the user-related differences. In this context, the area was divided into 250x250 m. flags (each square= 6.25 ha) and a land cover class was assigned for each square (Figure 3). Thus, the size of the change was not area-based but unit-based. The determination of the land cover is considered as a process consisting of two stages. In the first stage; it is aimed to determine whether the relevant square belongs only to aquatic or terrestrial ecosystems. For this purpose, the class which was bigger was assigned. Thus, the grids forming the surface of the water were identified and the only thing left was the reclassification of the terrestrial ecosystem, which contains the forests, orchards, and non-vegetated areas classes. In the second stage, this process was carried out by applying the same method. Since there were two classes in the first stage, the area that holds 50% of the overall size was looked for to make the assignment, whereas, in the second stage there were three classes, therefore the area with the largest size was assigned directly.

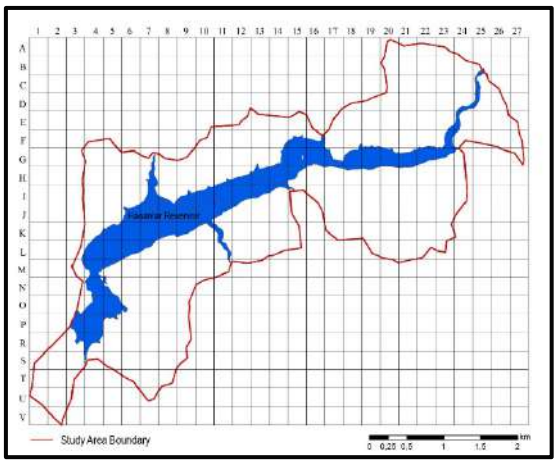

Figure 3. Applying grid method to the study area

An analysis of change in land cover was periodically examined as a 53-year process between 1960-1982 and 1982-2013, then between 1960 and 2013, which would most commonly reflect the change.

3. RESULTS

The area size distributions of the land cover structure for the related years, which were formed by applying the method, are shown in Table 1. There are only two classes that consist of forest and non-vegetated area in the 1960 land cover, which is a date before the start of the dam construction. In the 1982 land cover, even though it has a very small percentage with 2% the orchards have been seen and so four classes have presence at the area. It appears that four classes retain their existence in 2013 which is the latest land cover. On the other hand, the spatial distributions of the land cover classes are shown in Figure 4 which contains the maps by the years.

Table 13. The area size distributions of the land cover classes by the years

Land Cover Based On the Years (Unit/Percentage)	**Forest**	**Orchard**	**Non-vegetated Area**	**Water Surface**
1960	159 (%59)	-	111 (%41)	-
1982	122 (%45)	6 (%2)	101 (%38)	41 (%15)
2013	140 (%52)	67 (%25)	22 (%8)	41 (%15)

a. Land Cover Change Analysis in 1960-1982 Period

It can be seen from the matrix in the Table 2 that the reservoir observed with 41 units was formed in the year 1982 by transforming 37 units from the non-vegetated area and 4 units from the forest. Forest areas lost 37 units, despite gaining 9 units from the non-vegetated area. The losing of 28 units on the forest class is remarkable. In addition, the orchards started to be seen at the area with a small area size like 6 units by transforming 5 units from the forest and 1 unit from the non-vegetated area at the end of this temporal period. The spatial distributions of the changes in the period are shown in Figure 5.

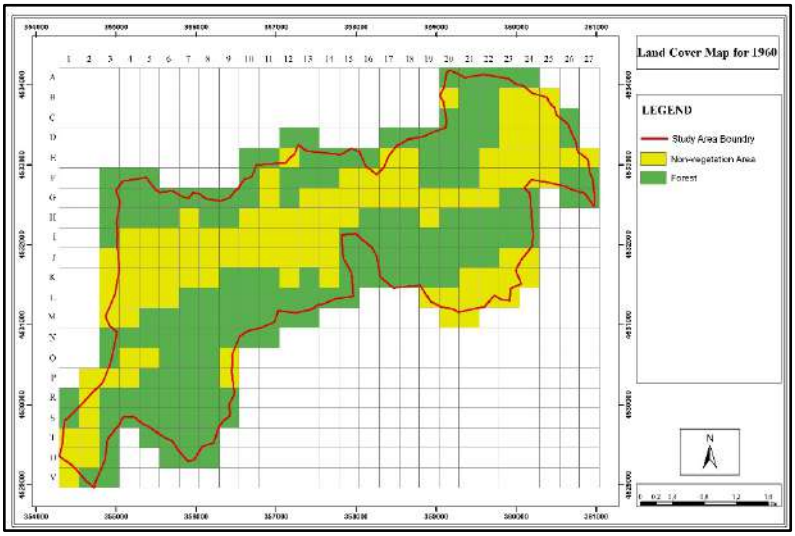

(a)

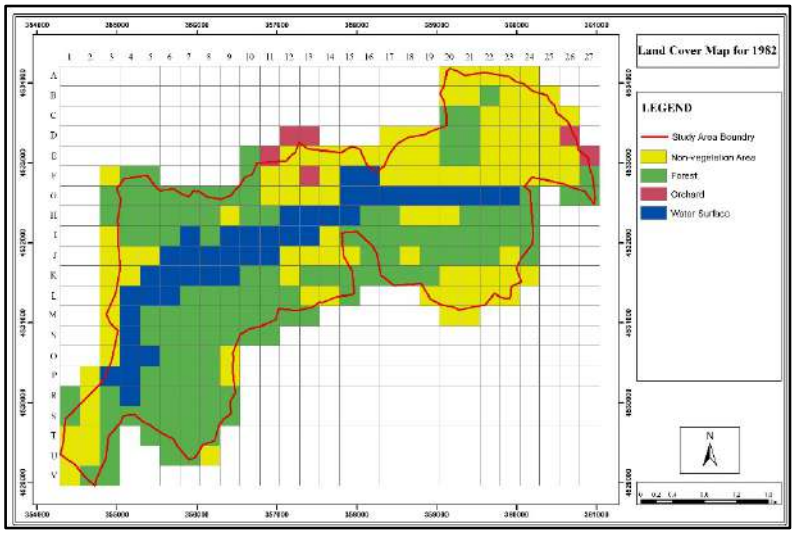

(b)

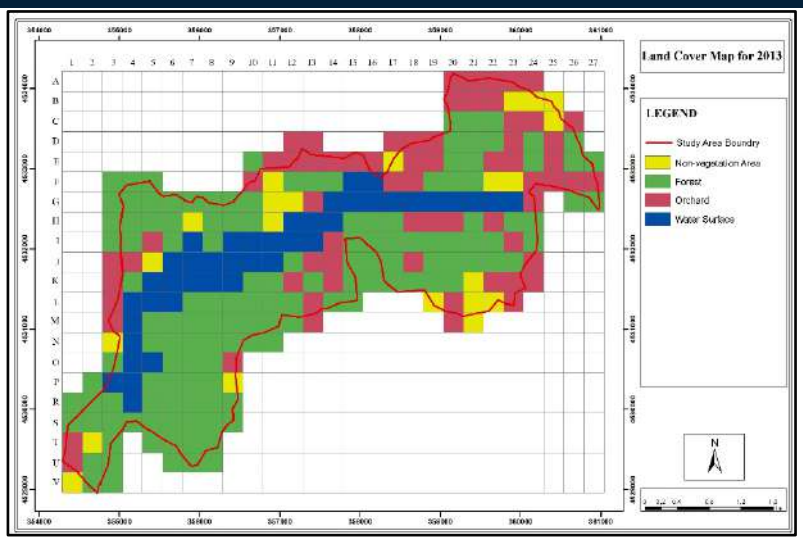

(c)

Figure 4. Land cover maps by the years a)1960, b)1982, c)2013

Table 2. The area size change of the land cover classes in 1960-1982 period

Changes in 1960-1982 (by Units)	**Forest**	**Orchard**	**Non-vegetated Area**	**Water Surface**	**The situation of 1960**
Forest	113	5	37	4	159
Orchard	-	-	-	-	-
Non-vegetated Area	9	1	64	37	111
Water Surface	-	-	-	-	-
The situation of 1982	122	6	101	41	**Total**:270

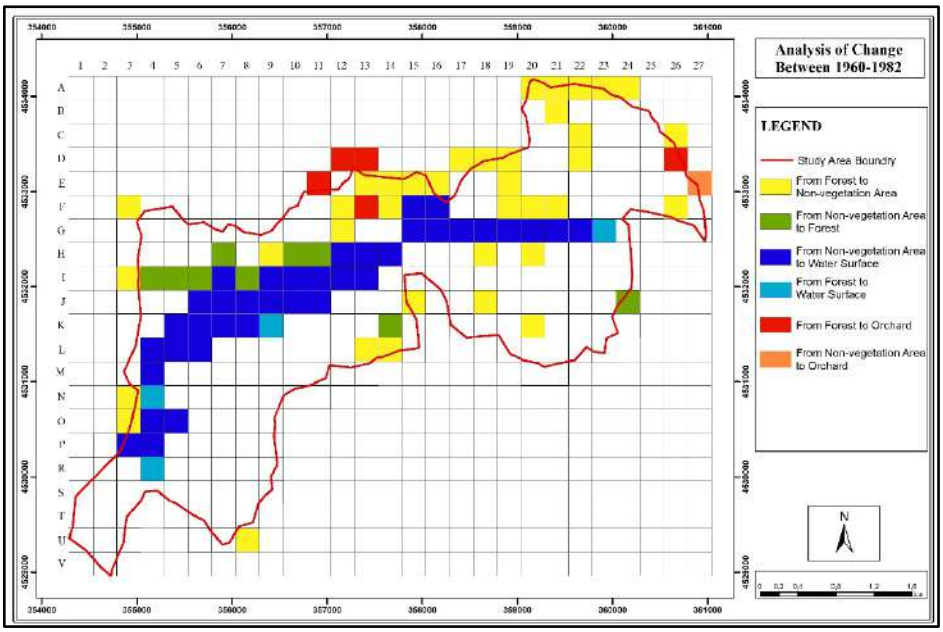

Figure 5. The units which show a change in 1960-1982 period

b. Land Cover Change Analysis in 1960-1982 Period

It has been determined that the non-vegetated areas rapidly transformed into forest and orchard areas in this temporal period. Only 22 units of non-vegetated area has been left by 2013. Besides the orchards reached 67 units by gaining 54 units from non-vegetated areas (Table 3). The spatial distributions of the changes in the period are shown in Figure 6.

Table 3. The area size change of the land cover classes in 1982-2013 period

Changes in 1982-2013 (by Units)	**Forest**	**Orchard**	**Non-vegetated Area**	**Water Surface**	**The situation of 1982**
Forest	110	10	2	-	122
Orchard	3	3	-	-	6
Non-vegetated Area	27	54	20	-	101
Water Surface	-	-	-	41	41
The situation of 2013	140	67	22	41	**Total**:270

c. Land Cover Change Analysis in 1960-2013 Period

This is the longest period analyzed in the frame of data at the study. Therefore, analyzing the period demonstrates the most general change between the land cover classes. It is almost impossible not to focus on non-vegetated areas in this analysis. 37 units of this class have been submerged, 37 units have turned into orchard and 17 units have gained forestry qualities (Table 4). The spatial distributions of the changes in the period are shown in Figure 7.

Table 4. The area size change of the land cover classes in 1960-2013 period

Changes in 1960-2013 (by Units)	**Forest**	**Orchard**	**Non-vegetated Area**	**Water Surface**	**The situation of 1960**
Forest	123	30	2	4	159
Orchard	-	-	-	-	-
Non-vegetated Area	17	37	20	37	111
Water Surface	-	-	-	-	-
The situation of 2013	140	67	22	41	**Total**:270

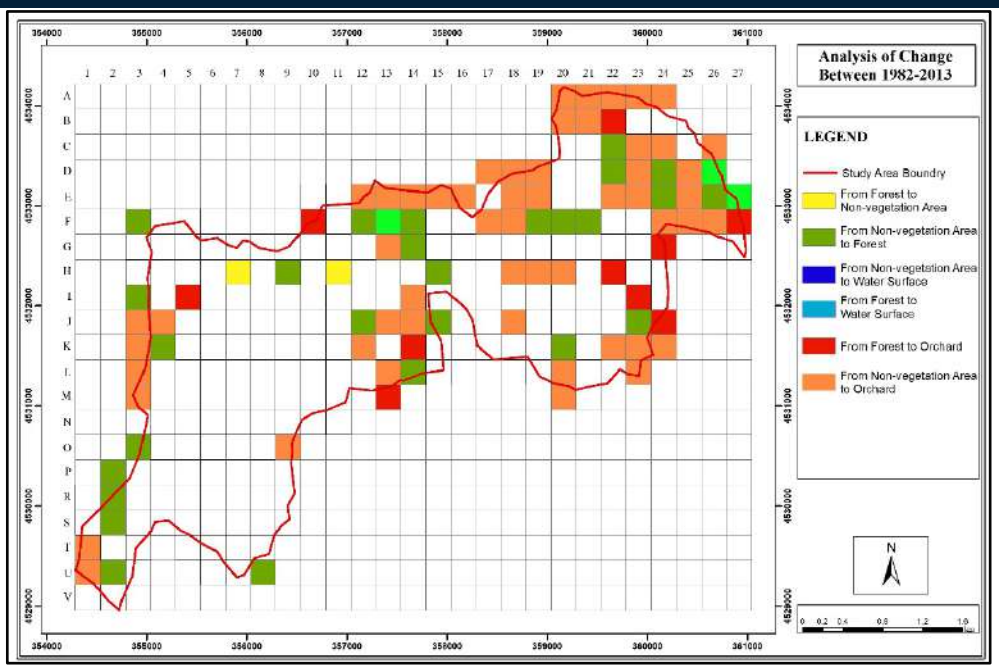

Figure 6. The units which show a change in 1982-2013 period

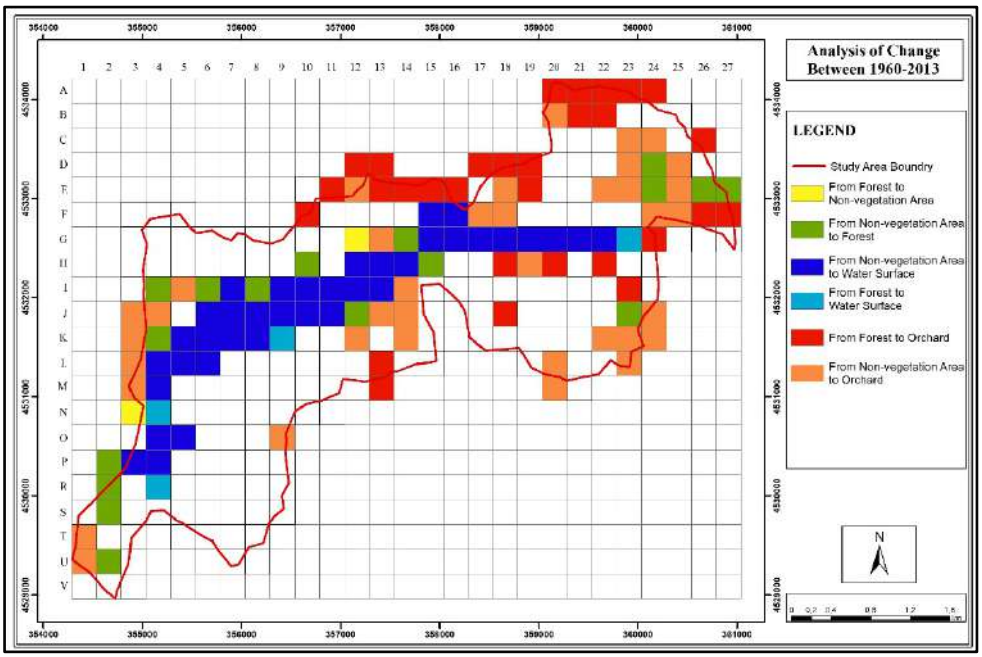

Figure 7. The units which show a change in 1960-2013 period

4. DISCUSSION AND CONCLUSION

Although it has some weaknesses, the method that been proposed in this study has an efficient use in order to monitor the temporal land cover change in general terms. As the study area expands, this efficiency increases. The method is likely to provide a good alternative when old dated aerial photos or satellite images can not be reached. The weaknesses of the method can be summarized as follows:

- Enable to create a limited number of classes
- Having low sensivity with regards to the size of changing areas

On the other hand, assessment of the environmental impacts of the Hasanlar Dam by interpreting the results is another output of the study. Interpretations in this context are as follows:

- The changes in the forest and non-vegetated area indicate the modification of microclimate in the study area with the reservoir.
- Increasing rapidly orchard areas which were not found before the dam construction, is an indirect anthropogenic effect of the dam project. Because, the changing climate conditions have become suitable for orchards and transportation to irrigation water has become easier.

ACKNOWLEDGMENT

This study is a part of master thesis of the first author. The authors would like to thank Pamukkale University Scientific Research Projects Council for their financial support with project number 2018KRM002-237 to attend the conference.

REFERENCES

[1] Ozturk, T., "Coruh havzasi su kaynaklarini gelistirme projelerinin cevresel etkileri," TMMOB Su Politikalari Kongresi, 2009, s. 220-226.
[2] Baxter R.M., "Environmental effects of dams and impoundments," Annual Review Ecological Systems, vol. 8, pp. 255-283, 1977.
[3] Kocabas, M., Bascinar, N., Kutluyer, F., Onder, A.,"HES'ler ve baliklar," Turk Bilimsel Derlemeler Dergisi, 6(1), s.128-131, 2013.
[4] Yurtseven, I., "Nehir Tipi Hidroelektrik santrallerin havzalar uzerindeki ekohidrolojik etkileri," Journal of the Faculty of Forestry, Istanbul University, 61(1), s. 55-62, 2011.
[5] "Dams and devolopment: A new framework for decision-making," The Report of the World Commission on Dams, London, Uk, Earthscan Publications, 2000.
[6] Dynesius, M. and Nilsson C., "Fragmentation and flow regulation of river systems in the northern third of the world," Science, vol. 266, pp. 753-762, Nov. 1994.
[7] Berkun, M., Aras, E. and Koc, T., "Barajlarin ve hidroelektrik santrallerin nehir ekolojisi uzerinde olusturdugu etkiler," TMH- Turkiye Muhendislik Haberleri, 6(452), pp. 41-48, 2008.
[8] Aksungur, M., Ak, O., Ozdemir, A., "Nehir tipi hidroelektrik santrallerin sucul ekosisteme etkisi: Trabzon ornegi," Journal of Fisheries Sciences, 5(1), pp. 79-92, 2011.
[9] Lovett, R.A., "As salmon stage disappearing act, dams may too," Science, vol. 284, pp. 574-575, April 1999.
[10] "10 Soruda Hidroelektrik Santraller," WWF Turkiye Yayini, 2013.
[11] Obahoundje, S., Ofosu, E.A., Akpoti, K. and Kabo-bah, A.T., "Land use and land cover changes under climate uncertainty: modelling the impacts on hydropower production in Western Africa," Hydrology, 4(2), 2017.
[12] Bewket, W. and Sterk, G., "Dynamics in land cover and its effect on stream flow in the Chemoga watershed, Blue Nile basin, Ethiopia," Hydrological Processes, vol. 19, pp. 445-458, 2005.
[13] DSI website. [Online]. Available: http://www2.dsi.gov.tr/baraj/detay.cfm?BarajID=43
[14] Hasanlar HES Proje Tanitim Dosyasi, Ankara.
[15] Zielinski, J., "Watershed Vulnerability Analysis," Center for Watershed Protection Tech. Rep., 2002.

ICENS 4TH INTERNATIONAL CONFERENCE ON ENGINEERING AND NATURAL SCIENCE
2-6 May 2018 KIEV UKRAINE

Numerical Simulation Of Thermoacoustic In A Rijke Tube And Application Of Nonlinear Analysis Tools

Fatih Selimefendigil[1]

Abstract

In this study, thermo-acoustic phenomena in a Rijke tube with different heat source characteristics were numerically examined. The numerical simulation is performed in a closed-open type resonator with a stack type heat source by using finite volume method. The pressure fluctuations in the vicinity of the heat source result in limit cycle oscillations. Recurrence plot analysis tools were utilized to investigate the short term and long term dynamics of the system. Recurrence quantification analysis measures were used to compare the dynamics of the systems with different heat source characteristics.

Keywords: Thermo-acoustic, Rijke tube, CFD, recurrence quantification

PACs: 44.05.+e, 05.45.Tp, 47.55.pb, 47.11.-j, 07.20.Pe

1. INTRODUCTION

Thermo-acoustic or combustion instabilities are a major concern in many technological applications such as in gas turbines, domestic boilers and many others. For example, the gas turbines are designed to minimize the NOx production for the environmental concerns. These systems are prone to thermo-acoustic instabilities. The coupling of the heat source with the system acoustics may result in high pressure amplitudes within this system. The occurrence of these instabilities may result in mechanical damage, fatigue and noise. Another example for the thermo-acoustic instability is the domestic boilers. The operating parameters in a domestic boiler (flame characteristics, operating power, flue length etc.) may also result in resonant coupling of the heat source with system acoustics.

In order to understand the physics behind these resonance phenomena and to develop methods to deteriorate this unfavorable coupling, a vast amount of literature is dedicated to this topic [1-4]. A simple prototype for the investigation of the thermo-acoustic instability is the Rijke tube. The type of the heat source is very important for the characteristic of the pressure oscillations in a thermo-acoustic system. In a domestic boiler, the instability is significantly affected from the flame characteristics which can be changed by varying equivalent ratio, natural gas type and burner type. The final amplitude of the pressure oscillations is determined from the nonlinear characteristics of the heat source as it has been shown in various studies [3, 5-7].

In this study, we numerically simulate a Rijke tube with stack type heat source by using finite volume method. We also used recurrence quantification analysis methods to compare the dynamics of the systems with different heat source characteristics.

2. PYSICAL PROBLEM

A schematic representation of the problem is shown in Fig.1. It consists of a resonator and a stack of parallel heated plates which are near the closed end. L, H, xf, d and b denote the length, height, heat source location, spacing between the parallel plates and length of the heat source, respectively. Along the length of the heat source linearly, quadratic and cubical spatially varying heat sources were utilized.

The form of the heat sources are given as:

[1] *Mechanical Engineering Department, Celal Bayar University, 45140, Muradiye, Manisa* fthsel@yahoo.com

Linear: $T_1+T_2(xf+b-x)/b$ (1)

Quadratic: $T_1+T_2(xf+b-x)^2/b^2$ (2)

Cubic: $T_1+T_2(xf+b-x)^3/b^3$ (3)

where T_1=300K and T_2=500K. At the ends of the heat source the temperate values are fixed and along the length of the heat source it is spatially varying. In many studies, the heat source can be considered as compact when the length of the heat source is less than that of the corresponding acoustic wavelength of the resonator, but when it is distributed or its length is not so small, then the spatial variation should be taken into account.

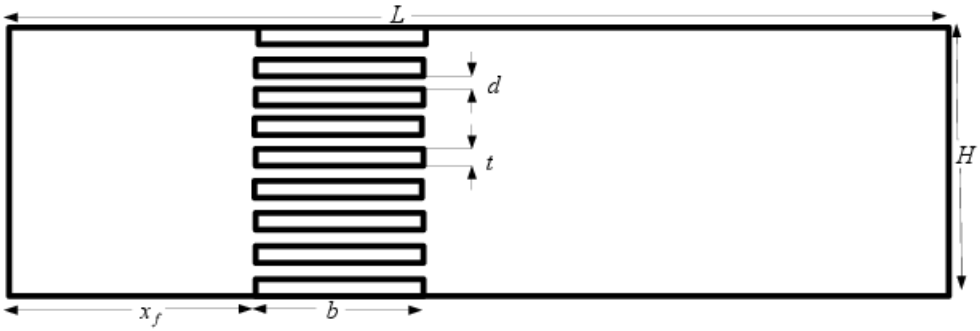

Fig.1. Sketch of the physical problem

2.1. Governing Equations and Solution Method:

The conservation equations of mass, momentum and energy equations for two dimensional laminar compressible Newtonian fluid flow are given as:

$$\frac{\partial \rho}{\partial t}+\frac{\partial(\rho u)}{\partial x}+\frac{\partial(\rho v)}{\partial y}=0 \quad (4)$$

$$\frac{\partial(\rho u)}{\partial t}+\nabla.(\rho u u)=-\nabla p+\nabla.(\tau) \quad (5)$$

$$\frac{\partial(\rho E)}{\partial t}+\nabla.(u.(\rho E+p))=-\nabla.[k\nabla T+(\tau.u)] \quad (6)$$

where ρ, u, p, τ, E denote the density, velocity, pressure, stress tensor and energy, respectively. μ and k represent the dynamic viscosity and thermal conductivity. The state equation of an ideal gas is used which is given as

$$p=\rho RT \quad (7)$$

Numerical model of thermo-acoustic system has an open end and pressure inlet to create a pressure gradient and non-zero velocity field within the computational domain. The end wall temperatures of the parallel plate heat source are 800 K and 300 K and it is spatially varying with linear, quadratic and cubic type nonlinearity as shown before. The outer wall of the system is adiabatic. Non-slip boundary condition was used for all walls. The governing equations (4-6) along with the boundary and initial conditions were solved with a finite volume based CFD code (FLUENT). Second order upwind scheme was used for spatial discretization and PISO algorithm was used for velocity-pressure coupling. For the time differencing, a second order implicit scheme was utilized. For the unsteady calculation, the pressure inlet boundary condition is replaced with an

adiabatic wall. Mesh independence of the solution was assured to get an optimal grid distribution for minimal computational time and most accurate results.

2.2. Time Series Analysis

The nonlinear time series analysis can be used to gain an understanding of the complicated nonlinear dynamical system from the time sequence of the pressure oscillation in a thermo-acoustic system which obtained from the numerical simulation. According to Takens [8], the reconstructed attractor of the original system is given by

$$U(i) = \left(u_i, u_{i+\tau}, ..., u_{i+(m-1)\tau}\right) \qquad (8)$$

with τ and m representing the embedding delay and embedding dimension, respectively. The attractor constructed using the above equation will have the same mathematical features of the original system, such as dimension, Lyapunov exponents, etc. To get an estimate for delay term τ autocorrelation function or average mutual information function can be used. To obtain an estimate for the proper embedding dimension m, the method of false nearest neighbor (FNN) can be used [9].

The recurrence plot analysis is a graphical tool used for analyzing the dynamical properties of a time series obtained from numerical simulation. A recurrence plot (RP) is obtained from the recurrence matrix $\boldsymbol{R}$ whose entries can be given as

$$R_{ij} = \theta\left(\varepsilon - \left\|y_i - y_j\right\|\right), \quad i, j = 1, ..., N \qquad (9)$$

where ||.|| represents the distance between the two state vectors, ε denotes the threshold value and θ is the Heaviside function. Depending on the value of the entries of R, either a black dot is drawn or a blank space is left in the RP. Some dynamical features of the time series obtained from the numerical simulations can be extracted from the RPs [10-12]. Abrupt changes in the dynamics, short term dynamics can be obtained with recurrence plots. The dynamics of the system can be identified using recurrence quantification analysis method. In this method, the deterministic patterns of recurrence plots based on the statics of the vertical and diagonal lines can be quantified with Recurrence Rate (RR), Determinism (DET), Entropy (ENT), Laminarity (LAM), Trapping time (TT). RR represses the fraction of recurrence points in RPs and DET denotes the fraction of recurrence points that form the diagonal lines. It gives a measure for predictability of the time series data. ENT is the Shannon entropy based the distribution of the lengths of diagonal lines. It captures the complexity of diagonal lines in RPs. For higher values of ENT, the deterministic structure is more complex. LAM is the fraction of the points which form the vertical lines and represents the occurrence of laminar states in the system. TT gives an estimate for the mean time that the system will be trapped at a specific state.

3. RESULTS AND DISCUSSION

Transient evolution of the pressure oscillation for a location in the vicinity of the heat source is seen for linear and cubically varying heat sources in Fig. 2. It is observed that the pressure oscillation starts from an initial disturbance and grows until it reaches limit cycle. In this case, the balance between the acoustic power dissipation and acoustic power generation is reached.

Fig.3 shows the limit cycle for absolute pressure oscillations when different heat sources are considered. There is a phase shift in the pressure oscillations between different heat sources. There is very slightly change in the amplitude of the pressure oscillations and the frequency of the oscillation is 624.95 Hz. This value is closer to the frequency in the first harmonic for the closed -open type pipe (quarter wave length).

Fig.4 demonstrates the effect of different heat sources on the normalized heat transfer rate from the hot plates to the air when limit cycle is reached. The amplitude of the oscillation is the lowest for the quadratic spatially varying heat sources as compared to others. There is an indication of the nonlinearity as the signal deviates from a pure sinusoid which is due to the flow reversal of the hot air particles during the part of the oscillation cycle. A phase shift when the maximum and minimum values reached occurs when varying the heat source

type. The maximum of the pressure oscillation does not coincide with the maximum of the heat transfer rate but with a phase change which is due to the thermal inertia.

Table 1. RQA parameters for various heat sources

	RR	**DET**	**ENT**	**LAM**	**TT**
Linear	0.0432	0.999	4.747	0.952	12.90
Quadratic	0.0489	0.998	4.229	0.983	10.384
Cubic	0.0395	0.997	3.857	0.979	8.244

It is possible to identify the dynamics of the system by using the recurrence quantification analysis. Table 1 shows the RQA results for the time series of the pressure oscillations when different heat sources were utilized. ENT obtains its largest value for a linear heat source which indicates higher dynamical complexity for this configuration. The predictabilities of these systems are higher since DET values are above 0.99. TT value which shows the shortest time in the laminar phase in the intermittent dynamics has its lowest value for a cubic type heat source.

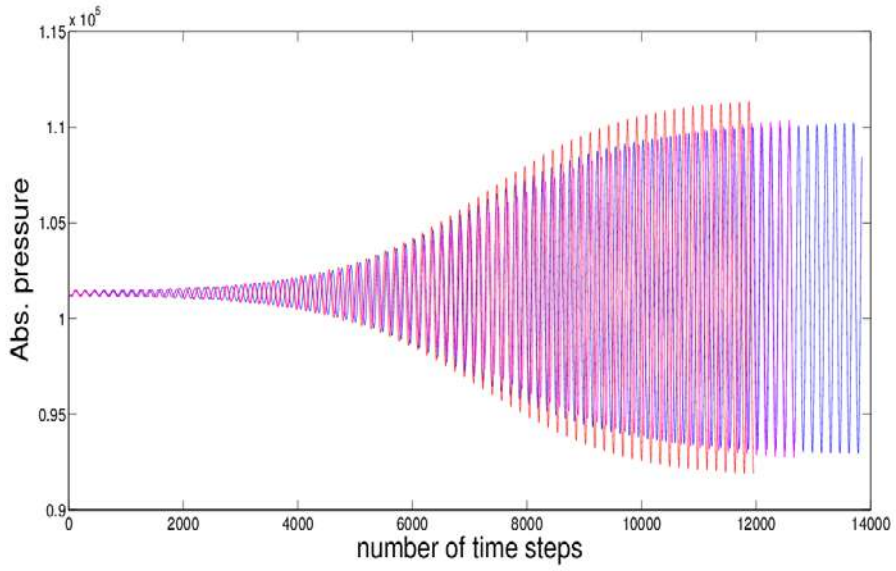

Fig.2. Transient evolution of the absolute pressure for two different heat sources

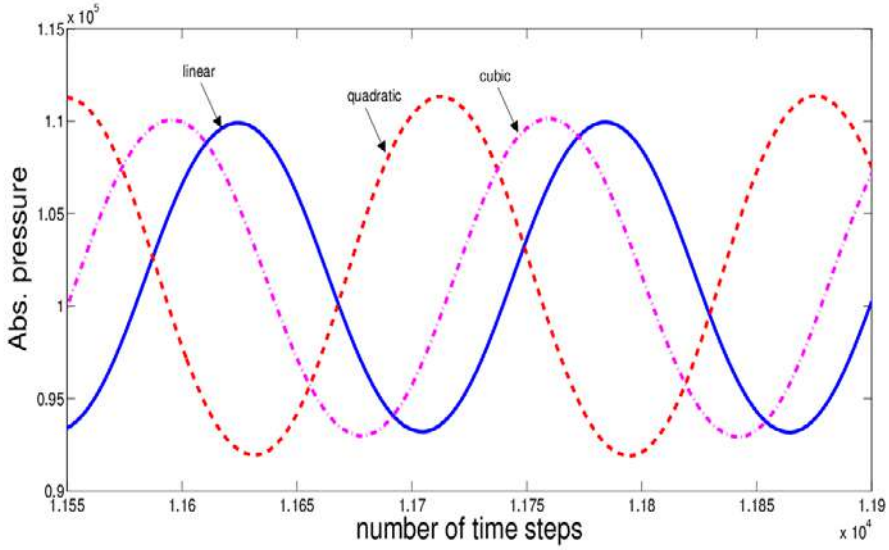

Fig.3. Pressure oscillations in the limit cycle for different heat source characteristics

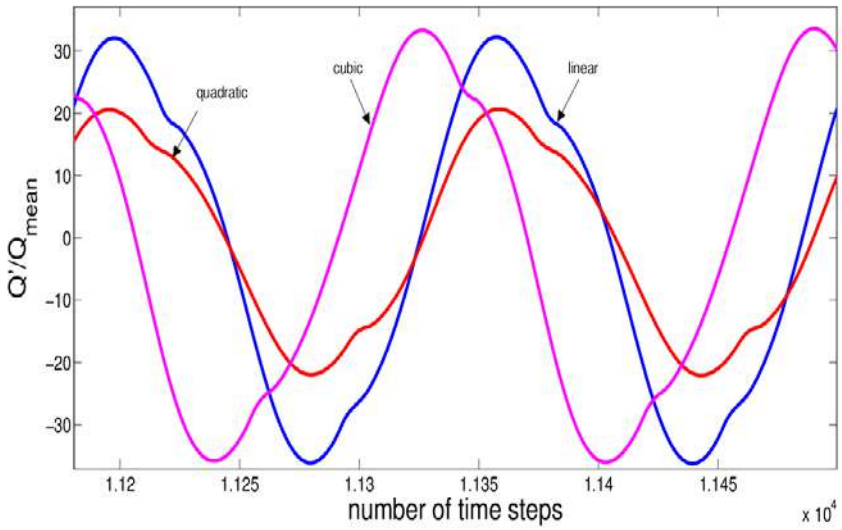

Fig.4. Heat transfer from plates to air in the limit cycle

5. CONCLUSIONS

A numerical study of thermoacoustic instability in a Rijke tube resonator with different heat source characteristics was performed. Nonlinear time series analysis tool was used to identify the dynamics of the system. Some conclusions can be listed as:

1) There is a phase shift in the pressure oscillations due to the different spatially varying heat source characteristics, but amplitude and frequency of the oscillations do not vary.
2) Heat transfer rate form the parallel plates to the air shows distortion from a pure sinusoid for different heat sources. The amplitude of the heat transfer rate oscillations change for different heat sources.
3) Recurrence quantification analysis tools show different dynamical characteristics of the systems for different heat source characteristics.

A spatially varying heat source with different nonlinear characteristics was shown to affect the pressure oscillations and dynamic characteristic of the thermo-acoustic system.

REFERENCES

[1] F. E. C. Culick. Non-linear growth and limiting amplitude of acoustic oscillations in combustion chambers, Combust. Sci. and Tech. **3**, 1-16, (1971)
[2] T. Lieuwen. Experimental investigation of limit cycle oscillations in an unstable gas turbine combustor, Journal of Propulsion and Power **18**, 61-67, (2002).
[3] N. Noiray, D. Durox, T.Schuller and S. Candel, A unified framework for nonlinear combustion instability analysis based on the flame describing function, J. of Fluid Mechanics **615**,139-167, (2008).
[4] A.P Dowling, Nonlinear self-excited oscillations of a ducted flame, J. of Fluid Mechanics **346**, 271-290, (1997)
[5] F. Selimefendigil, S. Foller and W. Polifke. Nonlinear identication of the unsteady heat transfer of a cylinder in pulsating cross flow, Computers and Fluids **53**, 1-14, (2012).
[6] F. Selimefendigil and W. Polifke. A Frequency Domain System Model with Coupled Modes for Limit Cycle Prediction of Thermoacoustic Systems, Int. Journal of Spray and Combustion Dynamics **3**,303-330, (2011).
[7] F. Selimefendigil and H. F. Oztop. POD-based Reduced Order Model of a Thermoacoustic Heat Engine, European Journal of Mechanics - B/Fluids **48**,135-142, (2014).
[8] F. Takens, Detecting strange attractors in turbulence Springer Lecture Notes in Mathematics **898**, 366–81 (1981).
[9] M. Kennel and R. B. H. Abarbanel. Determining embedding dimension for phase space reconstruction using a geometrical construction, Phys. Rev. A **45**, 3403-3411, (1992)
[10] M. Casdagli. Recurrence plots revisited, Physica D **108**, 1244, (1997)
[11] N. Marwan, N. Wessel, U. Meyerfeldt, A. Schirdewan and J. Kurths. Recurrence plot-based complexity and their application to heartrate variability data, Physical Review E **66**, 026702, (2002)
[12] N. Marwan and A. Meinke, Extended recurrence plot analysis and its application to erp data, International Journal of Bifurcation and Chaos **14**, 761-771, (2004).

ICENS 4TH INTERNATIONAL CONFERENCE ON ENGINEERING AND NATURAL SCIENCE
2-6 May 2018 KIEV UKRAINE

Cfd (Computational Fluid Dynamics) Investigation of Effect of Sloped Labyrinth Teeth on Leakage Flow

Ibrahim Zengin[1], Beytullah Erdogan[2]

Abstract

Gas turbines in turbomachinery are widely used in the energy, aviation and defense sectors. So, each element used in these machines creates a separate work area. From the past to present, prediction of leakage flow has been a great important during possible working conditions in gas turbine engine system performance.

It has been shown that the inclination of the labyrinth teeth in the direction of the incoming flow tends to reduce leakage flow with experimental data. In this study, Results were obtained via Fluent, a commercial software containing the turbulence model k-e and the wall function Enhanced Wall Treatment (flow characteristics used in Analyzes). CFD analyzes have been done for flat stator - straight labyrinth teeth and flat stator - sloped labyrinth teeth. It was determined Cr (Clearance) and Sloped Angles as Analyzes parameters. Parameters investigated for Sloped Angles include ; 90 (straight tooth), 70 and 50 degree and for Cr (Clearance) include; 0.127, 0.254, 0.508 and 1.016 mm. When the results for flat stator-straight teeth were compared with well-known analytical approaches and for flat stator-sloped teeth were also compared with experimental data, It was seen that the results were consistent with them.

Keywords: Gas turbines, Sealing Elements, Sloped Labyrinth Seal, CFD.

1. INTRODUCTION

Gas turbine and steam turbine cycles have continued to develop with an increasing operating pressure and temperature conditions. The effects of high pressure and high temperature on sealing and efficiency in the major components of the engine (compressor, combustor and turbine) have become an important issue. The internal flow system in the engine has function such as cooling for blades, blade tracks, disk, etc. and balancing for axial bearing load. However, situations encountered the higher pressure bring about the sealing problem. Therefore, many studies have been made for a long time to reduce and predict the leakage flow in sealing elements. Firstly, experimental studies have been carried out to minimize the problem of sealing from the past to the present day. Ludwing et al. conducted experiments on commonly used four different shaft sealing elements. They point out that the increase in leakage flow has boosted specific fuel consumption in an aircraft gas turbine engine. It was emphasized that the most significant losses occurred in the labyrinth seals at the turbine bed and compressor outlet, and that when all calculated losses were included, a 10% reduction in engine power and a 21% increase in SFC (Specific Fuel Consumption) were noted. [1] Stocker et al. in their work published by NASA in 1977, they worked to determine the ideal geometry for reducing the leakage flow in labyrinth seals and investigated geometric factors such as tooth clearance distance (Cr), tooth height, pitch, honeycomb cell sizes and tooth slope angle. [2] Childs et al. investigated the rotordynamic coefficients by performing experiments of these two types of geometric configurations under similar working conditions in the case where the labyrinth teeth were positioned on the rotor or stator. They found that the teeth-on-stator seal was more stable than the teeth-on-rotor seal, for inlet tangential velocity in the direction of rotation. [3]

To predict the leakage flow, many equations have been derived related to constricted flow. The Venant equation (1871) led to other equations that were developed to predict the leakage flow with orifice approach. Martin

[1] *Corresponding author: Bulent Ecevit University, Department of Mechanical Engineering, 67100, Incivez/Zonguldak, Turkey. ibrahim.zngn@hotmail.com*

[2] *Bulent Ecevit University, Department of Mechanical Engineering, 67100, Incivez/Zonguldak, Turkey, beytullaherdogan@hotmail.com*

(1908) derived a new equation including the effect of number of teeth by using thermodynamics first law and momentum law. [4] Martin derived the equation by making some assumptions. Therefore, the amount of error was observed when the analytical results were compared with the experimental data. Later, The Martin equation was used basically by different scientists to reduce the amount of error with convective and flow coefficients obtained from experimental data. [5, 6, 7] Demko et al. (1989) performed experiments with a typical labyrinth seal model with an incompressible water fluid. He then emphasized that it gives realistic results when compared with experimental data by solving the turbulent Navier Stokes equations with the finite difference method. They reported the results in relation to the dimensionless Ta and Re numbers. [8]

It is observed from the above discussion that studies in the literature are focused on numerical prediction, analytical prediction and experimental measurement of labyrinth seal leakage. The aim of this study was to investigate the changing of the leakage flow via CFD analysis by changing the tooth slope angles.

2. MATERIAL AND METHOD

a. Description of the Problem

In sealing technology, it is aimed to reduce the amount of leakage flow by minimizing the amount of clearance that the fluid gets away. However, this requires machining at very precise tolerances and additionally increases the possibility of surface wear in case of when rotor deviates from the working axis. This study aims to reduce the leakage flow by inclining the teeth to the high pressure zone, and additionally, how the clearance & tooth slope angle affects the flow by using a numerical method. As can be seen in Figure 1, air enters from the inlet to flow domain and in each tooth losses its pressure energy. After last tooth, it leave from the outlet where has static pressure.

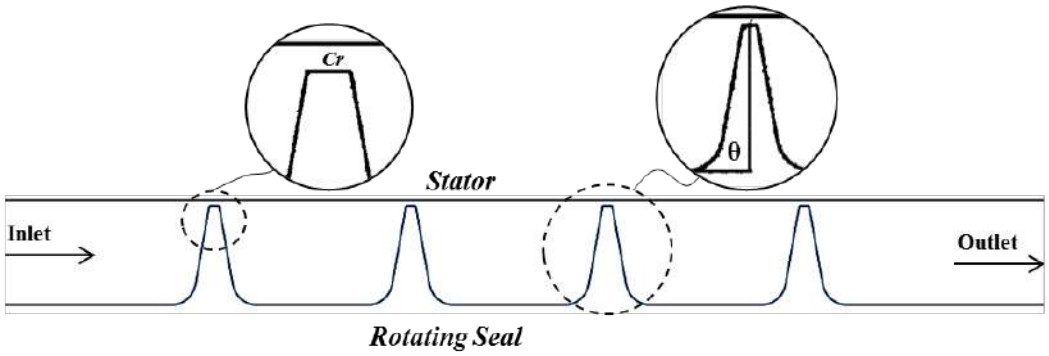

Figure 1. Schematic of the problem

The geometry of seal configuration for the present study was designed in view of dimensions commonly used in the literature and in the industry. The parameters examined in Table 1 were detailed.

Table 14. Examined Parameters

#	Parameters		Values: Min., Base, Max.
1	Slope Angles	θ[degree]	**90**; 70; 50
2	Clearance	Cr [mm]	0.127; 0.254; **0.508;** 1.016

b. Analytical Approach

As discussed in the introduction, there are many correlations commonly found in the literature to predict leakage flow. In the ESDU publication, the information about the sealing elements and the detailed correlations are briefly and understandably summarized. [9] In table 2, It can be seen selected correlations for determining the

mass flow for straight-through axial labyrinth seals. The authors selected specifically the equations for compressible flow.

Table 2. Analytical Correlations

The name of equation	**k-(carry-over factor)**	**Equation**
Martin's Equation	—	$\dot{m} = AP_{t0}\sqrt{\dfrac{1-\left(\frac{P_n}{P_{t0}}\right)^2}{RT_{t0}\left[n-\ln\left(\frac{P_n}{P_{t0}}\right)\right]}}$
Hodkinson's Equation	$k = \sqrt{\dfrac{1}{1-\frac{n-1}{n}\cdot\frac{\frac{s}{t}}{\frac{s}{t}+0{,}02}}}$	$\dot{m} = Cdk_{h}AP_{t0}\sqrt{\dfrac{1-\left(\frac{P_n}{P_{t0}}\right)^2}{RT_{t0}\left[n-\ln\left(\frac{P_n}{P_{t0}}\right)\right]}}$
Vermes' Equation	$k = \sqrt{\dfrac{1}{1-\frac{8{,}52}{\frac{s-t}{t}+7{,}23}}}$	$\dot{m} = Cdk_{v}AP_{t0}\sqrt{\dfrac{1-\left(\frac{P_n}{P_{t0}}\right)^2}{RT_{t0}\left[n-\ln\left(\frac{P_n}{P_{t0}}\right)\right]}}$
Zimmermann and Wolff's Equation	$k = \sqrt{\dfrac{\frac{n}{n-1}}{1-\frac{n-1}{n}\cdot\frac{\frac{s}{t}}{\frac{s}{t}+0{,}02}}}$	$\dot{m} = Cdk_{z}AP_{t0}\sqrt{\dfrac{1-\left(\frac{P_n}{P_{t0}}\right)^2}{RT_{t0}\left[n-\ln\left(\frac{P_n}{P_{t0}}\right)\right]}}$
Orifice Aprroach:	—	$\dot{m} = AP_{t0}\sqrt{\dfrac{2k}{RT_{t0}(k-1)}\left[\left(\frac{P_2}{P_1}\right)^{\frac{2}{k}}-\left(\frac{P_2}{P_1}\right)^{\frac{k+1}{k}}\right]}$

Table 2 shows some coefficients. One of these is the influence of carry-over factor (k). The other is discharge coefficient (Cd).

In the derivation of the ideal equations, it is assumed that all the pressure energy expands in the cavities and the next tooth entry velocity is zero. In fact, the pressure energy expands somewhat, and the rest rushes to the other tooth inlet with the speed which increases in the previous tooth. The factor that takes into account this effect is called as the carry-over factor (k).

The discharge coefficient (Cd) is used to model the effects of flow contraction in a passage. Except at very low Reynolds numbers and at situations for where compressibility is important, flow will separate from the sharp entrance edge. As a result, this separation will reduce the effective flow area. This effect can be modeled via a discharge coefficient. Zimmermann et al. reported graphics which can be determined by the Reynolds number for the k and Cd coefficients. [10]

In this study, comparisons for only straight-through axial labyrinth seals were made with CFD analyzes by using the equations and coefficients discussed above.

c. Numerical Modelling

As seen in the Equation 1-2-3, Navier-Stokes and Energy equations need to be solved numerically to model the turbulent flow in the labyrinth seal. Ansys-Fluent which has been used commonly to solve such complex flows correctly, has been selected for this study. Governing Equations are respectively that:

$$\frac{\partial \rho}{\partial t} + \nabla \cdot (\rho \vec{v}) = S_m \tag{1}$$

$$\frac{\partial (\rho \vec{v})}{\partial t} + \nabla \cdot (\rho \vec{v} \vec{v}) = -\nabla p + \rho \vec{g} + \vec{F} \tag{2}$$

$$\frac{\partial (\rho E)}{\partial t} + \nabla \cdot \left(\vec{v} (\rho E + p) \right) = -\nabla \cdot \left(\sum_j h_j J_j \right) + S_h \tag{3}$$

Figure 2 shows the representative mesh image for the flow domain. The mesh has been applied more intensely in regions where the flow is critical. Mesh independence point was determined by gradually increasing the mesh number for the 2D flow geometry. The output mass flow rate was followed to determine the independent point from the mesh. After 100k elements, the mass flow rate does not change much. This situation is repeated for geometries created in each different parameter.

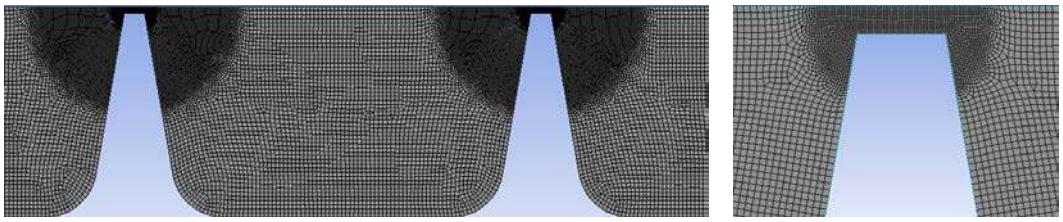

a) b)

Figure 2. (a) General mesh view, (b) Mesh view for the constricted region

For flow boundary conditions, while total pressure and total temperature (293K) is defined as at the upstream boundary, 1 atm is defined as the static pressure in the downstream boundary. Turbulent intensity are selected as 5% in the both inlet and outlet. The air properties inside the labyrinth seal are taken at the inlet temperature as ideal gas for ρ (density), $c_p = 1007 \ \frac{J}{kg.K}$ (specific heat) , $k = 0.02514 \ \frac{W}{m.K}$ (thermal conductivity), and μ= $1.825x10^{-5} \ \frac{kg}{m.s}$ (viscosity). Further information on flow characteristics is detailed in table 3.

Table 3. Flow Properties

Fluid	Air, Ideal Gas
Regime	Steady State
Flow Model	Turbulence Flow Model: k-ε/ relizable Wall Function: Enhanced Wall Treatment
Discretization method	Whole Equations: Second Order Upwind
Geometry Model	Axisymmetric, 360°

3. RESULTS AND DISCUSSION

For validation comparisons of the analyzes, both analytical equations and experimental data were used. Equations used in analytical comparisons were derived for flat-stator and straight-tooth. Analytical comparisons are therefore only valid for 90 degree tooth position. Figure 3 shows comparisons with the 6 equations selected for the compressible flow. Zimmermann and Wolff's equation was found to be very close to the CFD results by adding the Cd coefficient obtained from the experiments.

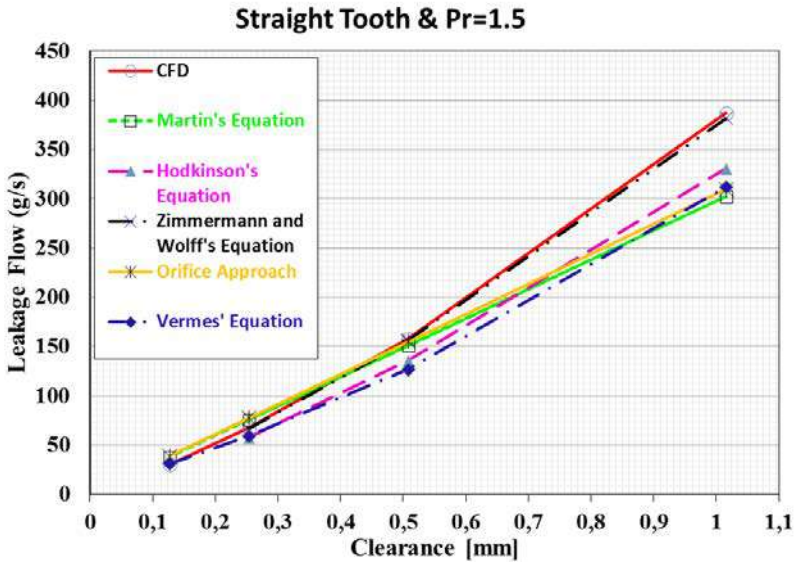

Figure 3. Analytical comparisons with CFD analyzes

Stocker's experiment data (1977) were used to compare CFD analyzes for sloped teeth. Stocker conducted experiments for 90, 70 and 50 degrees in limited clearance quantities. Although the geometry parameters and operating conditions used by Stocker were different from this study, the effect of inclination of the teeth showed a similar decrease. Table 4 shows both stocker experiment data and CFD results. In CFD studies, it was observed that the slope effect is a range of the clearance amount which is the maximum effect. The effect of slope angle and clearance amount on leakage flow drop can be seen in Fig.4. The leakage flow drop in low clearance amounts has almost the same effect in 70 and 50 degree.

Cr (Clearance) [mm]	Slope Angle [°]	CFD Leakage Drop [%]	Stocker's Exp. Leakage Drop [%]
0,127	70	~%4.18	-
	50	~%4.15	-
0,254	70	~%5.5	~%5
	50	~%6.76	~%7
0,508	70	~%6.1	~%9
	50	~%9	~%12
1,016	70	~%3.15	-
	50	~%6.55	-

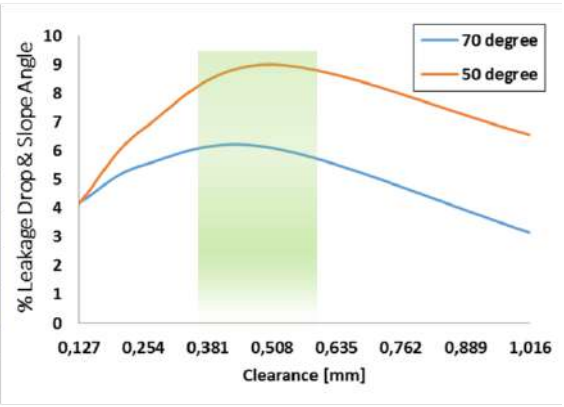

a) b)

Figure 4. (a) Stocker and CFD (present study) Leakage Flow Drop (b) CFD Leakage Drop [%]

For Cr=0.508mm & Pr=1.5, figure 5 shows the flow velocity and pressure characteristics in the labyrinth seal. The high-pressure air from upstream zone loses the pressure energy in each tooth and turns into kinetic energy as a result of the constriction. Thus, the flow reaches its maximum speed at the last tooth. As the slope angle decreases, the swirl behind the teeth gradually increases. These swirls are shown in Fig. 5, especially in velocity contours. As a result of this effect, there is a decrease in leakage flow.

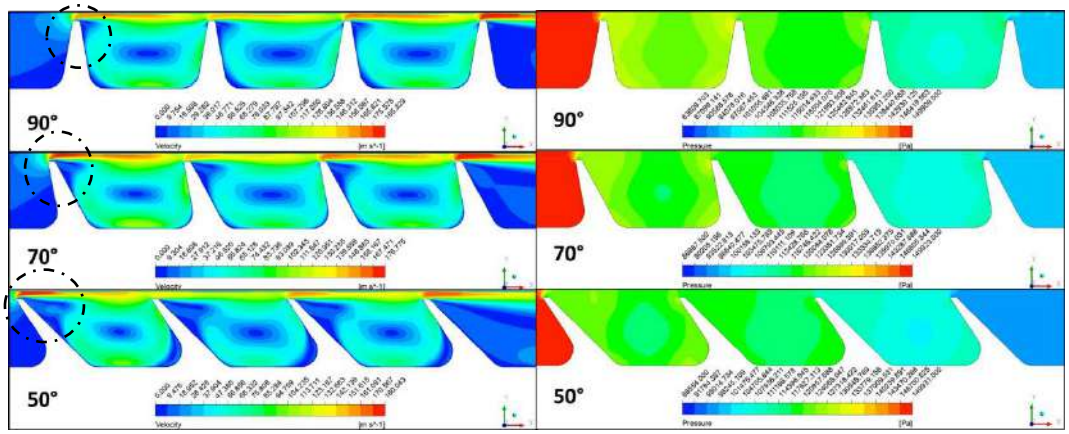

a) b)

Figure 5. (a) Velocity counters, (b) Pressure counters

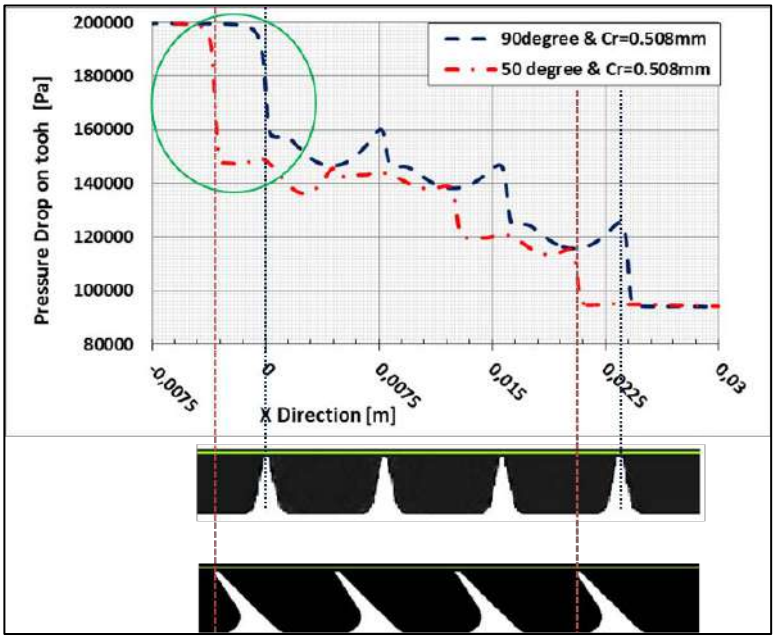

Figure 6. Pressure drop on the teeth

The result of reducing the slope angle of the teeth also affects the pressure change on the teeth. Figure 6 shows that the sloped tooth undergoes more pressure loss when compared to the straight-tooth. The increase of swirls in the labyrinth cavities and the pressure losses which happen in the teeth have a positive effect on the decrease of leakage flow.

Figure 7 was reported by the author to summarize this study. Three different slope angles were examined at 4 different Cr values. The increase in Cr value caused an increase in leakage flow due to the increase of the flow field.

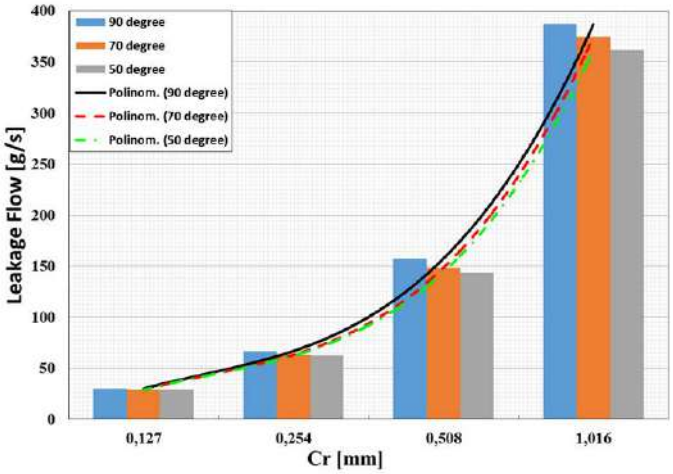

Figure 7. The effect of clearance and slope angle on leakage flow

4. CONCLUSIONS

This study describes a computational methodology developed to simulate the sloped state of teeth in labyrinth seals. The methodology was applied to a two dimensional and axisymmetric geometry The angles of inclination of the labyrinth teeth in different working parameters were examined. Analyzes were conducted through a commercial software program. The parametric study includes 0.127, 0.254, 0.508 and 1.016 of clearances, and 90, 70 and 50 degree of sloped tooth angles. As a result of analyzes it is found that :

(a) In low Cr quantities, CFD results show good agreement with both analytical and experimental data.

(b) The results of CFD for the straight tooth show best agreement with the Zimmermann's equation.

(c) It has been observed that the swirls formed behind the labyrinth teeth clearly reduce the leakage flow.

(d) Sloping the teeth towards the upstream region causes more pressure loss in the first tooth than in the straight tooth (90 degree). Therefore, it causes the leakage flow to decrease.

(e) If the labyrinth tooth is inclined by 50 degrees, the maximum fall in the leakage flow happens. However, the amount of reduction in leakage flow changes with clearance value.

REFERENCES

[1] L. P. Ludwig, R.L. Johnson, "*Sealing Tecnology for Aircraft Gas Turbine Engines*" in NASA-TM-X-71607, 1974.

[2] H. Stocker, D.M. Cox and G.F. Holle, "*Aerodynamic Performance of Conventional and Advanced Labyrinth Seals with Solid-Smooth, Abradable and Honeycomb Lands*" in NASA/CR-135307, 1977.

[3] D. Childs, J.K. Scharrer, "*Experimental Rotordynamic Coefficient Results for Teeth-on-Rotor and Teeth-on-Stator Labyrinth Gas Seals*", in ASME, vol. 108, pp. 599-604, 1986.

[4] H. Martin, "*Labyrinth Packings*" in The Engineer, pp. 35-36, Jan 10, 1908.

[5] B. Hodkinson, "*Estimation of the Leakage Through a Labyrinth Gland*" in Proceedings Inst. Mech. Eng., vol. 141, pp. 283-288, 1939.

[6] G. Vermes, "*A Fluid Mechanics Approach to the Labyrinth Seal Leakage Problem*", in Journal of Engineering for Gas Turbines and Power, vol. 83, no. 1, pp. 161-169, 1961.

[7] H. Zimmerman, K.H. Wolff, "*Comparison between Empirical and Numerical Labyrinth Flow Correlations*", in *ASME 87-GT-86*, 1987.

[8] J. Demko, G.L. Morrison, D.L. Rhode, "*The Prediction and Measurement of Incompressible Flow in a Labyrinth Seal"*, in *ASME*, vol. 111, pp. 697-702, 1989.

[9] ESDU 09004, "*Labyrinth seal flow*", The Instution of Mechanical Engineers, 2009.

[10] H. Zimmermann, K.H.Wolff, "*Air System Correlations / Part 1: Labyrinth Seals*", in *ASME*, 1998.

ICENS 4TH INTERNATIONAL CONFERENCE ON ENGINEERING AND NATURAL SCIENCE
2-6 May 2018 KIEV UKRAINE

Determination Of The Hip Stem Loosening Using Vibration Method

Talip Celik[1], Yasin Kisioglu[2]

Abstract

Aseptic loosening is a common problem in total hip replacement surgery. Routine radiological imaging techniques are used for postoperative diagnosis. An alternative technique is required to develop because of the low success rate in current diagnostic techniques. The purpose of this study is to develop a new method, vibration technique, to diagnose the aseptic loosening of the stem.

Two different experimental setups were established in this study, vibrational and cyclic loading tests. In the vibrational test, the bone-prosthetic models were vibrated from the distal femur at a certain frequency and then the vibration data were taken via accelerometer from the trochanter region of the femur. The vibration data were converted to the frequency domain for evaluations. The stability of the femur-prosthesis system was determined by evaluating the fundamental frequency change and harmonics generated at the Fast Fourier Transform analysis. In the cyclic loading test, the femur-prosthesis system was forced to fatigue at a maximum amplitude of 1700 N and frequency of 1 Hz. After every 5000 cycles in the test, the femoral prosthesis system was connected to the vibrational test and loosening of the system was considered. After 115000 cycles, the harmonic frequencies were observed and the amplitude value of the fundamental frequency was decreased. The experiments were stopped when the stem was loosened thorougly from the femur. As the degree of the loosening increased, the number of the harmonic frequencies increased and the fundamental frequency values decreased. In conclusion, the vibration method can be used as an alternative technique to determine the degree of the hip stem loosening.

Keywords: aseptic loosening, total hip prosthesis, vibration technique, cyclic loading.

1. INTRODUCTION

Orthopedic prostheses are frequently used for treatment in orthopedic surgery. The most common problem in the prostheses is aseptic loosening especially in hip prosthesis applications [1]. Because this problem causing the prostheses dislocating and become unfunctioning that require the revision surgery which is difficult and costly.

Based on literature, an average of more than 1.2 million Total hip prosthesis (THP) surgeries performed around the world per year and %10 of these surgeries need revision with the reason of the aseptic loosening [2]. The number of THP surgeries anticipated to increase with the long life expectancy through the developing technology and treatment opportunities. The radiological imaging methods are used generally to specify of the loosening, although heving very low rate of succes [3].

In this study, the vibration method was evaluated to determine the loosening degree of THP. Two different test techniques, vibration and cyclic loading tests, have been established. The bone-prosthetic models were vibrated at a certain frequency and amplitude then the response of the bone-prosthetic system was evaluated in vibration test. In the cyclic loading test, the femoral prosthesis model was forced to cyclic loading to reveal the value of the harmonic frequency and amplitude for evaluation of the loosening degree.

2. MATERIALS AND METHODS

In the tests, fourth generation composite sawbone femur model (Sawbone Europe AB, Malmo, Sweden) and pelvis model (Keklikoglu plastic Industry, Kayseri, Turkey) was used. Cementless Echelon stem and cup (stem

[1] *Corresponding author: Kocaeli University, Department of Biomedical Engineering, 41380,Izmit/Kocaeli, Turkey. talip.celik@kocaeli.edu.tr*

[2] *Kocaeli University, Department of Biomedical Engineering, 41380,Izmit/Kocaeli, Turkey, ykisioglu@kocaeli.edu.tr*

length 160 mm, cup diameter 50 mm) was implanted in the femur and pelvis models. A metal stem head with a diameter of 26 mm was used together corresponding polyethylene inlay.

a. Vibration Test Method

The femur-stem-pelvis models were placed onto a test apparatus as seen in Figure 1. The pelvis model was fixed at three locations onto the sigma-profile. Rubber dampers were placed between the junctions of the test components. Four tension springs were used to stabilize the femur and pelvis joint to represent the gluteus medius muscle and the adductors magnus and longus (Fig. 1).

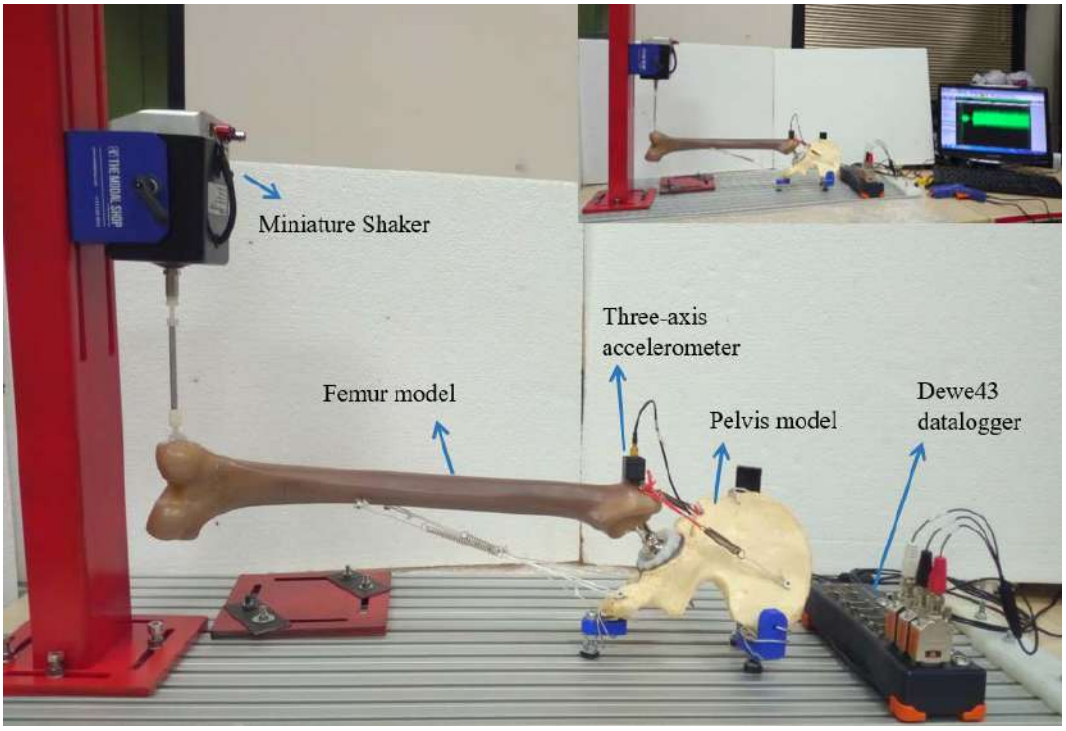

Figure 19. Vibration test setup

The femur-pelvis system were vibrated from the distal femur at the values of 200 and 250 Hz frequency via miniature shaker (The Modal Shop, Cincinnati, OH, USA). Three-axis accelerometer (Measurement Specialties, Marmatek, Turkey) was used and placed at the greater trochanter of the femur to collect the vibration data for ten seconds using DEWE43 datalogger (Dewesoft, Kumberg, Austria). In order to prevent to noises, 10 kHz low pass and 10 Hz high pass filter were used. It was also used 50 Hz block filter to prevent the electric network noise. The vibration data were evaluated by performing Fast Fourier Transform (FFT) analysis. The occurrence of the harmonic frequency in the vibration data received from the system is an indication of the deterioration of the system integrity. In addition, the changing of amplitude of the vibration were evaluated in stabilized and unstable systems.

b. Cyclic Loading Test Method

In cyclic loading test, the femoral prosthesis model was forced to cyclic loading in universal test machine as seen Fig. 2. Distal femur was fixed with the clamps. The cyclic loads between 100 N and 1700 N in 1 Hz were applied on the stem head. The purpose of this loading is to damage the contact between the femur and stem by simulating the real condition. Thus, the degree of the loosening and deterioration of the connection between the femur and stem have been determined.

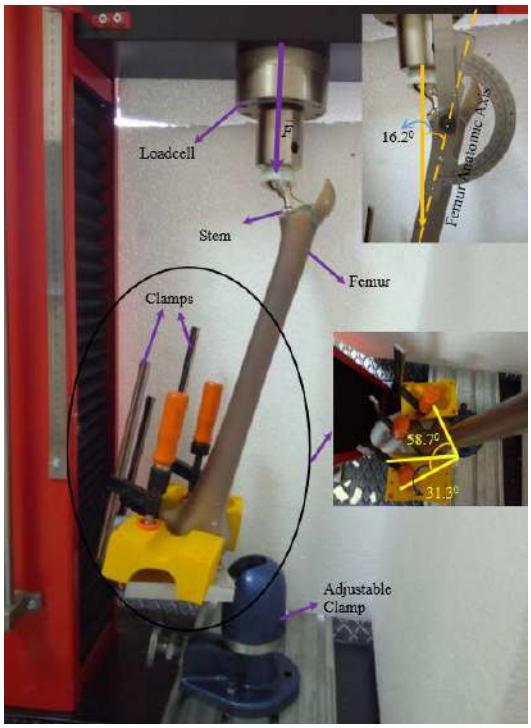

Figure 20. Cyclic loading test

3. RESULTS AND DISCUSSION

The femur-stem couple was vibrated at 200 and 250 Hz to determine the stable system data, which are taken as the reference data to examine the loosening situations obtained by cyclic tests as seen in Fig. 3. It was observed that the vibration data changed significantly at the loading cycles, 115,000, as seen in Fig 4. Based on this event, the harmonic frequencies were observed and the amplitude of main frequency was decreased. After additional applied each 5000 load cycles, the vibration tests were performed, and then it was observed clearly that the stem was loosened completely at 125,000 load cycles, as seen in Figs. 3 and 4. The loosened couple systems (stem and femur) has three harmonic frequencies, 2.3E-3, 3.2E-3 and 7.87E-4, as seen in Fig. 4. Also, the amplitude value of the main frequency, 9.3E-3, in loosened systemdecreased regarding with stable system value of 0.0112, as seen in Fig. 3 and 4.

The differences between the data given in Fig. 3 and 4 provide important information about the system stability. The number of the harmonic frequencies indicate the contact status between the femur and stem couple. As long as the integrity of the system was distorted, the number of harmonic frequencies increased. Therefore, the variation in the magnitude of the main frequency is indicating the system stability. These alterations in the main frequency values are given in Table 1. Considering the variations of the harmonics and main frequencies, it can be make a decision about the system stability.

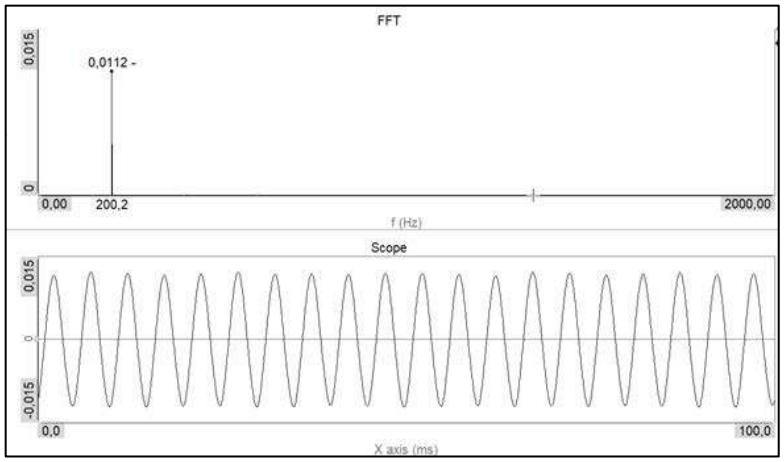

Figure 21. The amplitude-time curve and its FFT form in stable femur-stem couple vibrating in 200 Hz frequency

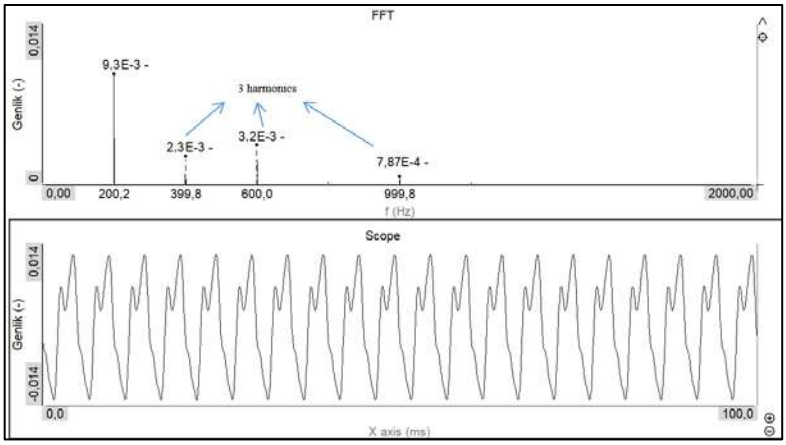

Figure 22. The amplitude-time curve and its FFT form in loosened femur-stem couple vibrating in 200 Hz frequency

Table 15. The results of the stable and loosened femur-stem systems

	The magnitude of the main frequency (10^{-3})		**The number of the harmonic frequency**	
The number of the cycli loading	200 Hz	250 Hz	200 Hz	250 Hz
Stable system	11.2	7.35	-	-
115000	11	7.25	1	2
120000	10	6.86	2	2
125000	9.3	6.39	3	3

Many studies had been studied in literature about the stability of the implants [3-5] since, aseptic loosening of the hip stem is a major problem in orthopedic application. In these studies, the degree of the stem loosening was not evaluated using vibration data, harmonic and main frequencies. In this study, however, in order to decide the stem loosening degree, the vibration data obtained using the stem and femur couple in the tests were evaluated. Therefore, it is showed that the vibrating technique can be used to determine the degree of the loosening the stem loosening degree in post-operative patient follow-up.

The vibration method has been emphasized as a reliable and minimal invasive technique in order to determine the stability of the stem system in many studies [3-6]. For this reason, the vibration method can be developed and used to determine the stem stability and aseptic loosening degree as an alternative technique to radiological imaging method currently used although low-succes rate.

Rieger et al. [5] used a method, counting peak amplitudes with resonance frequency analysis, to determine prosthesis stability. This idea provides stem loosening, but it cannot be used during postoperative patient follow-up. Because, the resonance frequency depends on the mechanical properties of the stem-femur couple. The mechanical properties or density of the human bone may change after operations so that the resonance frequency values of the stem-femur couple are changed.

4. CONCLUSIONS

One of the most important problem of the total hip replacement is tha aseptic loosening of which determination techniques used currently having low rate of succes. In this study, a vibration method is used experimentally to determine the stability and loosening degree of the hip stem system. The results obtained from the experiments showed that the loosening degree and stability of the stem-femur couple can be determined clearly. Therefore, the vibration technique can be used as an alternative method to the medical imaging technique, currently used in the low rate of succes.

ACKNOWLEDGEMENTS

This work supported by The Scientific and Technological Research Council of Turkey (TUBITAK) under project no 216M316. The corresponding author, Talip Celik, thanks TUBITAK 2211-C Scholarship program.

REFERENCES

[1]. H. Malchau, P. Herberts, T. Eisler, G. Garellick, and P. Soderman, "The Swedish Total Hip Replacement Register " *J. Bone Joint Surg. Am.*, vol. 86-A, pp. 2-20, 2002.
[2]. K. E. Dreinhofer, "Indications for total hip replacement: comparison of assessments of orthopaedic surgeons and referring physicians," *Annals of the Rheumatic Diseases*, vol. 65, pp. 1346-1350, 2006.
[3]. A. P. Georgiou and J. L. Cunningham, "Accurate diagnosis of hip prosthesis loosening using a vibrational technique," *Clinical Biomechanics*, vol. 16, pp. 315-323, 2001.
[4]. L. C. Pastrav, S. V. N. Jaecques, I. Jonkers, G. Perre, and M. Mulier, "In vivo evaluation of a vibration analysis technique for the per-operative monitoring of the fixation of hip prostheses," *Journal of Orthopaedic Surgery and Research*, vol. 4, p. 10, 2009.
[5]. J. S. Rieger, S. Jaeger, C. Schuld, J. P. Kretzer, and R. G. Bitsch, "A vibrational technique for diagnosing loosened total hip endoprostheses: An experimental sawbone study," *Medical Engineering & Physics*, vol. 35, pp. 329-337, 2013.
[6]. A. A. Alshuhri, T. P. Holsgrove, A. W. Miles, and J. L. Cunningham, "Development of a non-invasive diagnostic technique for acetabular component loosening in total hip replacements," *Medical Engineering & Physics*, vol. 37, pp. 739-745, 2015.

BIOGRAPHY

Talip Celik was born in 1987 in Kiraz, Izmir. He graduated in 2009 from Kocaeli University Mechanical Engineering Department. In 2012, he has master degree at Kocaeli University, with a master thesis titled as “Stress Distributions on Placement of Dynamic Hip Screw in Intertrochanteric Femur Fractures”. He started his doctoral thesis in Kocaeli University Department of Biomedical Engineering the thesis title as “Analysis of Mechanical Stability in Orthopedic Implants”. He is still working as a Research Assistant in Kocaeli University Department of Biomedical Engineering.

ICENS 4TH INTERNATIONAL CONFERENCE ON ENGINEERING AND NATURAL SCIENCE
2-6 May 2018 KIEV UKRAINE

Water Injection Effect on Performance of Gasoline Engine

Isilay Tasdemirci[1], Imdat Taymaz[2]

Abstract

In this study, effect on water injection is examined to understand; what extent a water injection into the cylinder can have a positive effect on engine performance. This study is aimed to develop 1-D combustion model of three-cylinder, four strokes, and spark ignited gasoline engine on various engine operating conditions. In the modeling and analyzing process of the engine; AVL Boost program has been employed. Inlet system boundary values were defined by the data coming from the dyno.

As a conclusion, at same engine operation, it has been observed that water injection has a positive effect on fuel consumption. Also, cylinder temperature has decreased. As a result of these effects, it is possible to obtain more torque with the similar inlet parameters.

Keywords: Engine Performance Parameters, Gasoline Engine, Water Injection

1. INTRODUCTION

Today and for the upcoming years passenger car transportation will primarily use fossil fuels. Even in ambitious electrification scenarios, a majority of passenger cars will still feature an internal combustion engine beyond 2025 [1].

The higher thermal efficiencies attained by an internal combustion engine could be linked to the use of higher compression ratios. However, the use of high compression ratios leads to higher combustion temperatures and creates conducive conditions for the formation of nitrogen oxide (NOx) emissions. Many studies have shown that the formation of NOx increases as the compression ratio increases [2-5]. For a gasoline engine, the increase in compression ratio, would lead to the formation of NOx emissions because of the near-stoichiometric air fuel ratio used to ensure that the conversion efficiency of the catalytic converter used for converting NOx emissions remains fairly high.

Fundamentally, water injection in the spark-ignition (SI) engine helps in controlling the temperature and pressure of the combustion process. Hence, this method is useful for controlling unwanted emissions [6].

The technical implementation of water injection is enabled by various concepts that differ significantly in terms of operating principle and effectiveness. Figure 1.1 shows four different water injection concepts which will be discussed below; Plenum injection, intake manifold/port water injection, separate water direct injection and mixture or emulsion injection.

[1] *Isilay Tasdemirci, Sakarya University, Department of Mechanical Engineering, 54050, Serdivan/Sakarya, Turkey. isilaytas@hotmail.com*

[2] *Prof.Dr.Imdat Taymaz, Sakarya University, Department of Mechanical Engineering, 54050, Serdivan/Sakarya, Turkey. taymaz@sakarya.edu.tr*

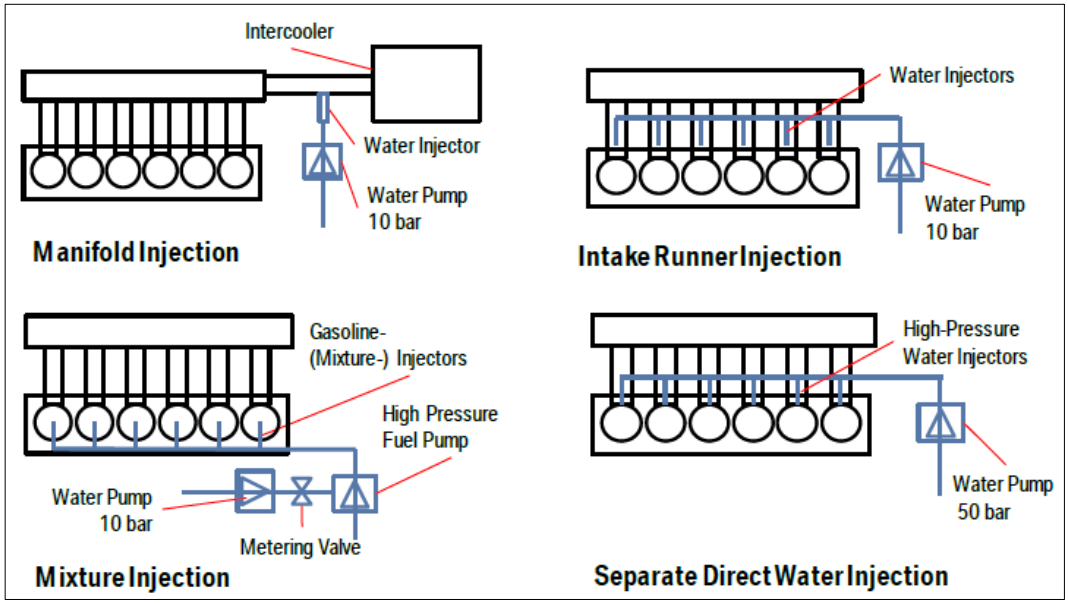

Figure 1.1. Different concepts for implementing water injection

At plenum injection, the water is injected by an injector downstream of the charge air cooler; it evaporates to a large extent in the intake manifold, thus causing cooling and, associated with that, an increase in the density of the charge air. In this way, an increase of the mass flow into the combustion chamber is achieved, and due the temperature reduction can also be consumed [7].

2. MATERIALS AND METODS

In this study, 3 cylinders (C1, C2, C3 at Figure 2.1) GTDI (gasoline turbocharger direct injection) engine is modelled by AVL-Boost in computer. The model validation for 3 operation cases (1500rpm, 2000rpm and 2500rpm) is based on full-load dyno data (throttle open %100 at full-load dyno data). The gasoline engine specification is shown in Table 2.1.

Table 2.1 the gasoline engine specification

Bore , mm	71.9
Stroke , mm	82
Compression Ratio [-]	10
Con-Rod Length , mm	137
Piston Pin Offset , mm	7.5
Effective Blow by Gap , mm	0.0008
Mean Crankcase Pressure , bar	1

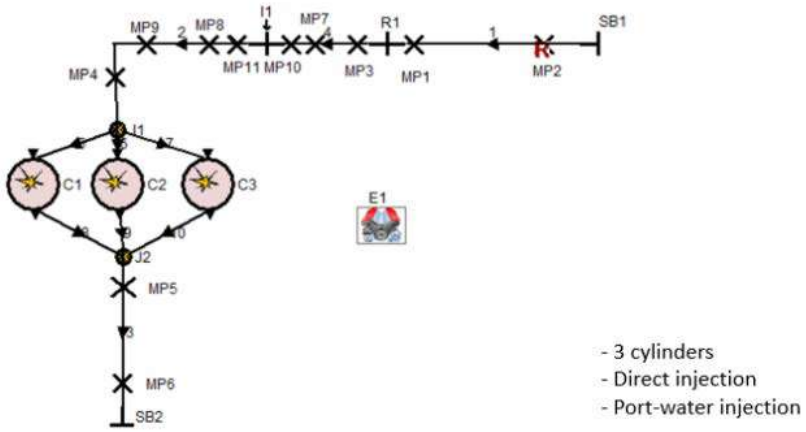

Figure 2.1. AVL-Boost model

Figure 2.1 shows the AVL-Boost model. Intercooler downstream is modeled as system boundary-1 (SB1) and turbocharger upstream is modeled as system boundary-2 (SB2). In this validated model, water (%10 of fuel) is injected (I1) to intercooler downstream by one injection. Water injection is applied to engine under the condition that 2 bar.

Figure 2.2 shows the full-load dyno data. Maximum engine torque is 172.937 Nm at 1500rpm. Maximum torque is obtained between 1500rpm and 2500rpm. So, these 3 cases is chosen to analysis.

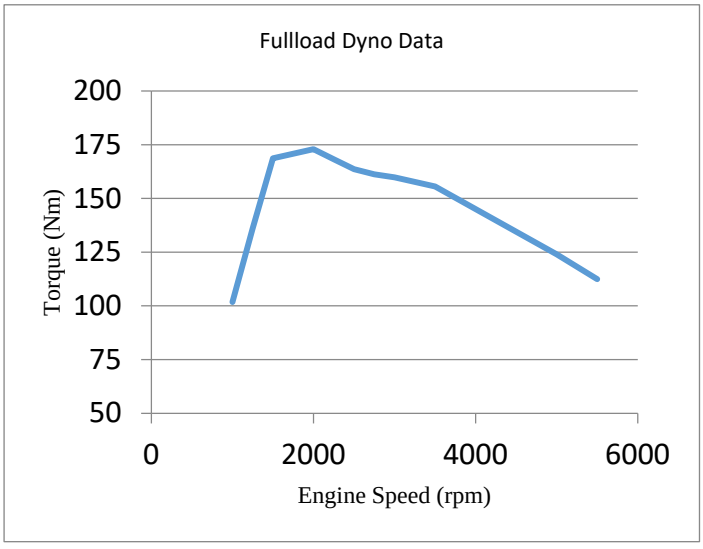

Figure 2. 2. Cylinders GTDI engine full-load dyno data

Intake and exhaust valve timing for 1500rpm are shown at figure 2.3.

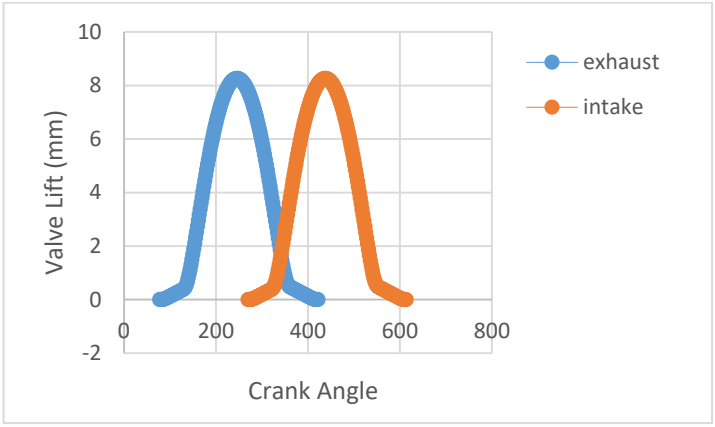

Figure 2.3. The timing data for 1500rpm

3. RESULTS AND DISCUSSION

The deviation raito between dyno data and AVL-Boost model is shown below figure 3.1. Torque deviation is %0.26497 for 1500, %0.841347 for 2000rp, %1.28318 for 2500rpm.

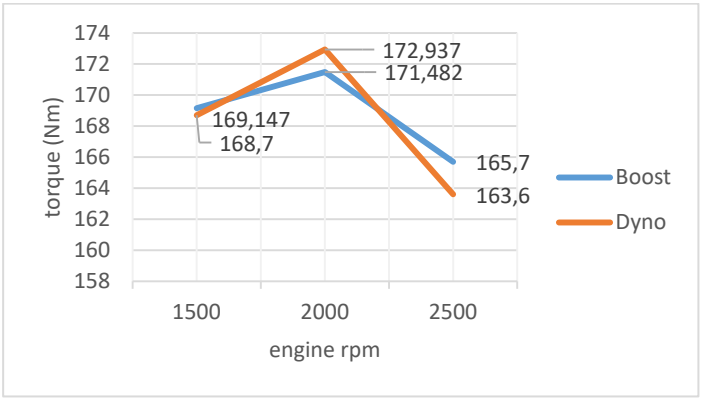

Figure 3.1. Boost model vs. Dyno data at 1500rpm, 2000rpm and 2500rpm

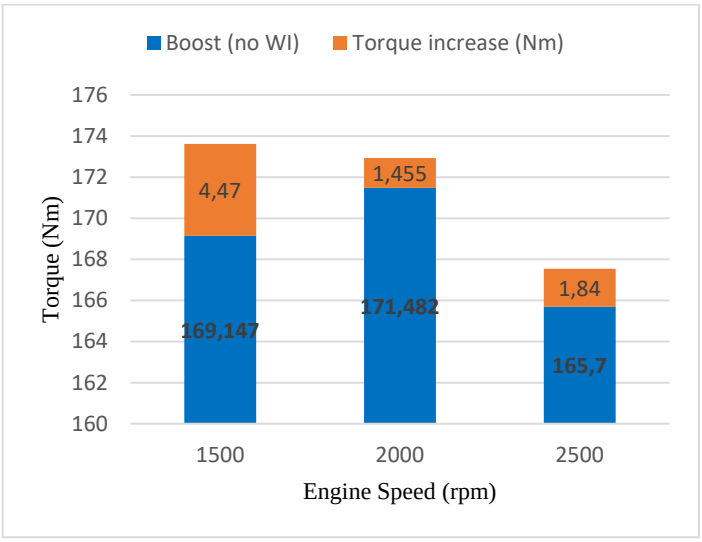

Figure 3.2. Torque increase with water injection

At validated model, water %10 of fuel is applied, correspondingly torque increase shown at figure 3.2. Torque increase is %2.642672 for 1500rpm, %0.848486 for 2000rpm, %1.110441 for 2500rpm.

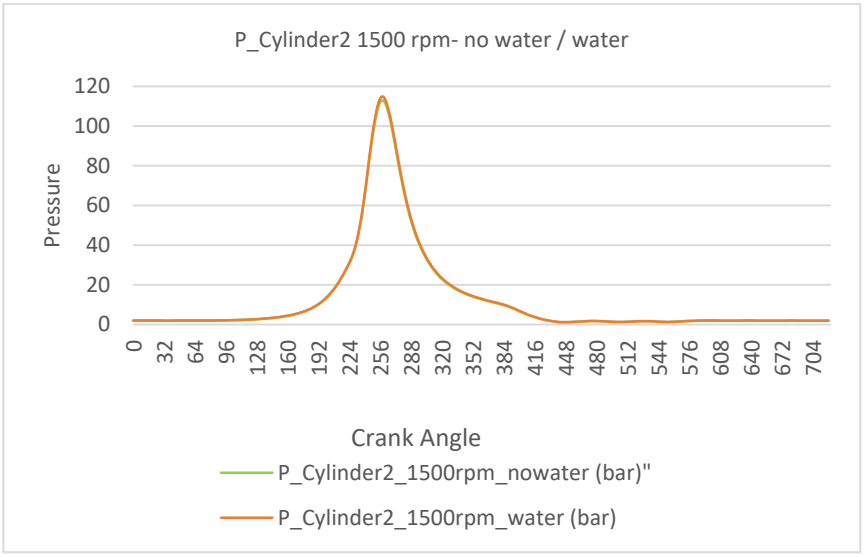

Figure 3.3. Pressure in cylinder versus crank angle for 1500 rpm

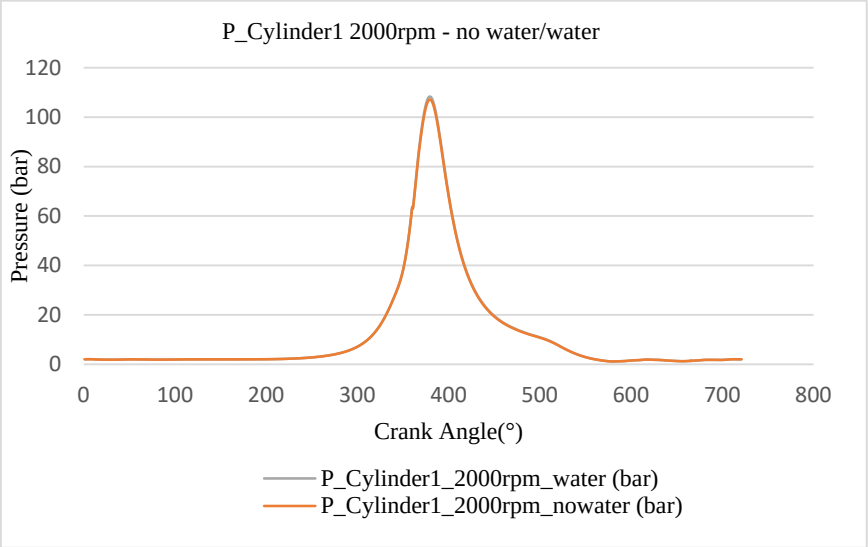

Figure 3.4. Pressure in cylinder versus crank angle for 2000 rpm

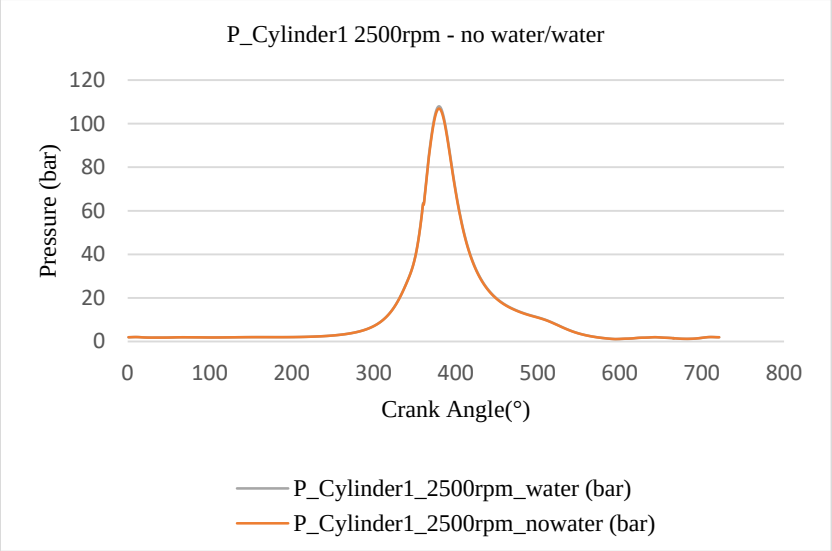

Figure 3.5. Pressure in cylinder versus crank angle for 2500 rpm

Table 3.1. Maximum pressure in cylinder for no water model and with water model for 1500rpm, 2000rpm and 2500rpm

P_Cylinder1_1500rpm_nowater (bar)	P_Cylinder1_2000rpm_nowater (bar)	P_Cylinder1_2500rpm_nowater (bar)
97,4906	107,067	106,805
P_Cylinder1_1500rpm_water (bar)	P_Cylinder1_2000rpm_water (bar)	P_Cylinder1_2500rpm_water (bar)
99,0541	108,305	107,89

Occurred maximum pressure at 1.cylinder with water injection application increase rate of %1.60374436 for 1500rpm (Figure 3.3), %1.15628532 for 2000rpm (Figure 3.4), %1.01587004 for 2500rpm (Figure 3.5). Maximum pressure values for no water cases and with water cases are shown at table 3.1 for 3 operation areas.

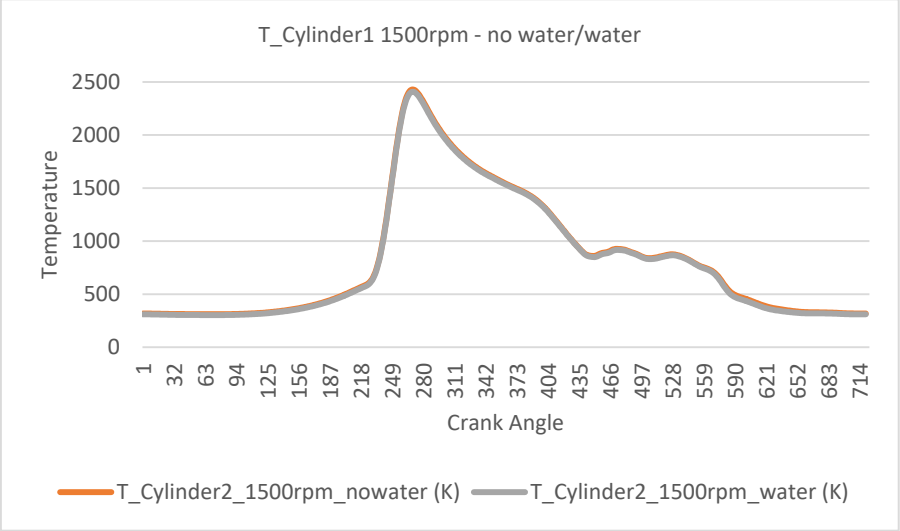

Figure 3.6. Combustion temperature versus crank angle for 1500rpm

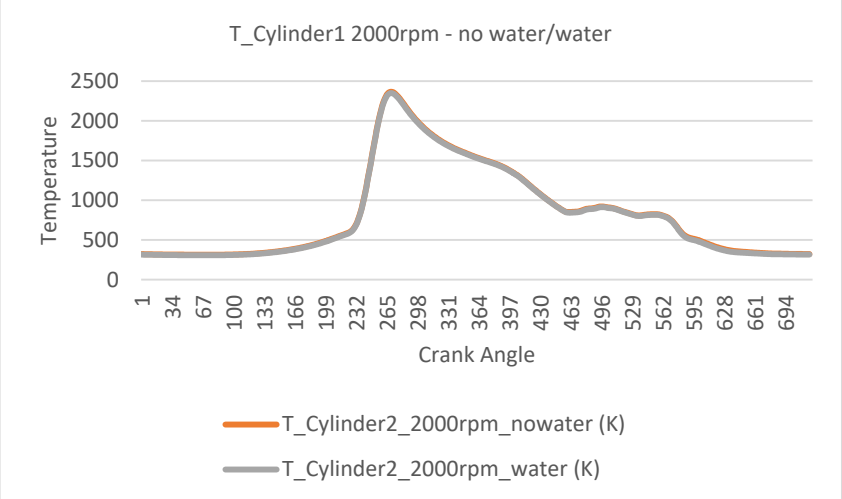

Figure 3.7. Combustion temperature versus crank angle for 2000rpm

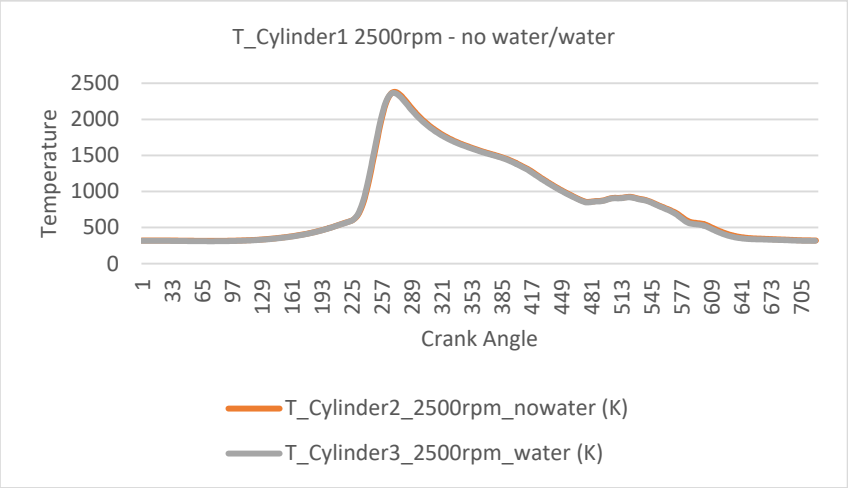

Figure 3.8. Combustion temperature versus crank angle for 2500rpm

Table 3.2 maximum temperature in cylinder for no water model and with water model for 1500rpm, 2000rpm and 2500rpm

T_Cylinder1_1500rpm_nowater (K)	T_Cylinder1_2000rpm_nowater (K)	T_Cylinder1_2500rpm_nowater (K)
2428.81	2366.97	2380.84
T_Cylinder1_1500rpm_water (K)	T_Cylinder1_2000rpm_water (K)	T_Cylinder1_2500rpm_water (K)
2407.33	2349.61	2367.03

Temperature of in cylinder with application of water decrease %0.884383711 for 1500rpm (Figure 3.6), %0.733427124 for 2000rpm (Figure 3.7) and %0.580047378 for 2500rpm (figure 3.8). Maximum temperature values for no water cases and with water cases are shown at table 3.2 for 3 operation areas.

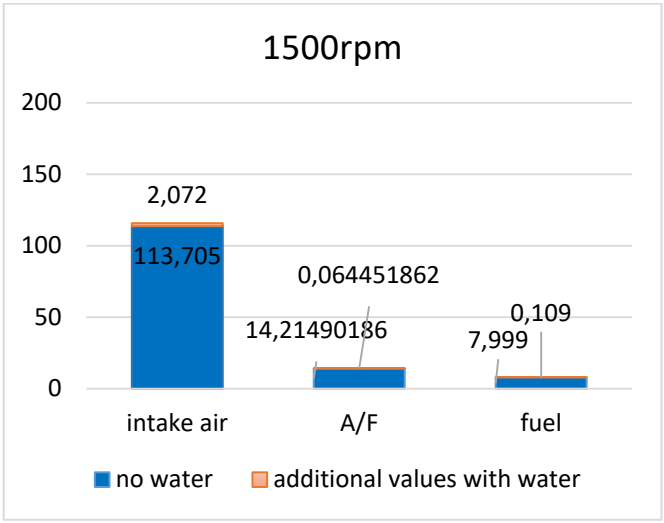

Figure 3.9. Inlet air flow (kg/h) for 1500rpm, A/F ratio and fuel consumption (kg/h)

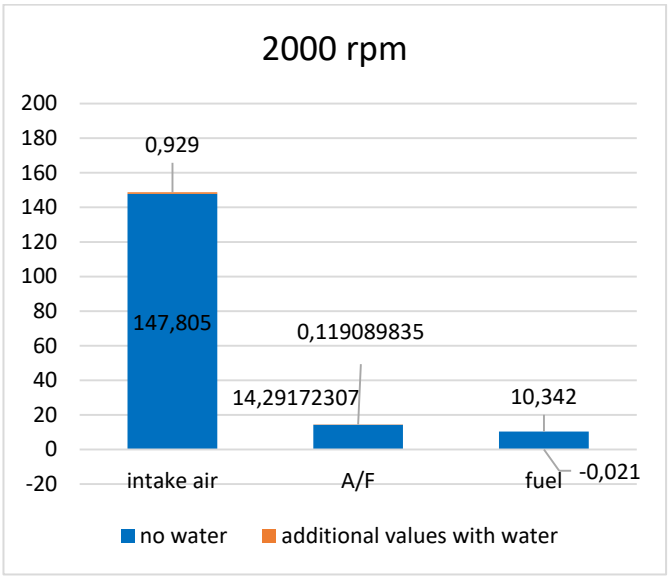

Figure 3.10. Inlet air flow (kg/h) for 2000rpm, A/F ratio and fuel consumption (kg/h)

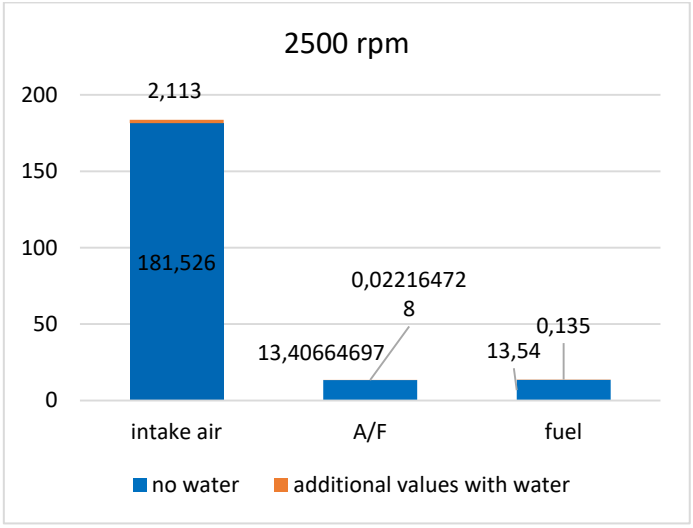

Figure 3.11 Inlet air flow (kg/h) for 2500rpm, A/F ratio and fuel consumption

Figure 3.9, 3.10 and 3.11 shown inlet air flow, A/F ratio and fuel consumption for 1500rpm, 2000rpm and 2500rpm. Intake air flow increase with water injection to port at this 3 cases and also A/F ratio increase. Fuel consumption decrease %0.2030555 with water injection for 2000rpm.

Further improvement of this direct water injection concept is expected with an optimized spray targeting for the water injector. Testing with such a spray targeting will commence soon. At the same time the trade-off between fuel and water consumption will be assessed in more detail in further simulations. Moreover, future investigations with advanced ignition systems will depict the additional benefit that can be gained from this combination of technologies [1].

4. CONCLUSIONS

In this study, 1500rpm, 2000rpm and 2500rpm cases are modeled by AVL-Boost based on dyno data of 3 cylinders gasoline engine. At this model, water is applied from one injection to intake manifold %10 of fuel. When results of water injection application analysis, it seems that torque increase for 3 cases. Most increment is for 1500rpm.. Water injection application decrease in-cylinder temperature and increase in-cylinder pressure. By means of this, intake air flow to cylinder increase. Used fuel mixture is closer to lean for 3 cases. Fuel consumption decrease %0.2030555 for 2000rpm.

REFERENCES

[1]. M. Thewes, H. Baumgarten, J. Scharf, G. Birmes, and A. Balazs, "Water injection – high power and high efficiency combined", *25th Aachen Colloquium Automobile and Engine Technology*, pp. 345-380, 2016.

[2]. R. H. Chen, L. B. Chiang, M. H. Wu, and T. H. Lin, "Gasoline displacement and nox reduction in an si engine by aqueous alcohol injection", *Fuel*, vol. 89, March, pp. 604-610, 2010.

[3]. (2002) The SAE International website. [Online]. Available: http://dx.doi.org/10.4271/2002-01-0418

[4]. (1996) The SAE International website. [Online]. Available: http://dx.doi.org/10.4271/960033

[5]. J. C. Conklin, J. and P. Szybist, "A highly efficient six-stroke internal combustion engine cycle with water injection for in-cylinder exhaust heat recovery", *Energy*, vol. 35, April, pp. 1658-1664, 2010.

[6]. W. Mingrui, N. T. Sa, R. F. Turkson, L. Jinping, and G. Guanlun, "Water injection for higher engine performance and lower emissions", *Energy*, vol. 90, April, pp. 285-299, 2017.

[7]. B. Durst, C. Landerl, J. Poggel, C. Schwarz, W. Kleczka, B. Hußmann, "BMW Water Injection: Initial Experience and Future Potentials BMW Group", *Internationales Wiener Motorensymposium*, vol. 38, April, 2017.

ICENS 4TH INTERNATIONAL CONFERENCE ON ENGINEERING AND NATURAL SCIENCE
2-6 May 2018 KIEV UKRAINE

Rock Bit Application Parameters In Geothermal Drilling Works And Cost Analysis

Sedat Toraman[1], Cem Sensogut[2]

Abstract

One of the most important parameters to make the right choice in drilling works are rock bits. The most basic rule is to choose a drill suitable for the possible formation feature. Once the drill has been selected, the drill operating characteristics are also factors that directly affect the performance of the drill as well as the drill cost. In the drilling operation, if the first basic rule is to choose the appropriate drill, the secondary basis is the drill operation conditions; the appropriate weight (WOB-weight on bit), the appropriate spinning speed (RPM-revolution per minute) and the appropriate liquid or air to get the rock pieces out of borehole.

In order to carry out the drilling process, it is essential to get the right weight on the drilling bit inside the borehole. This is achieved either by hydraulic pressure or casing pipes with certain weight. The pressure required in the geothermal drilling machines is mostly provided by the drill collar. In case of lower weight, desired breaking effect cannot be obtained, while with the case of overweight, the more wear is inevitable for the drill bits.

Rotation speed is one of the parameters that directly affect drilling bit life and drilling speed. The speed of rotation according to rock drillability is recommended to be 30-40 rev/min for the rocks with low drillability, 60-120 rev/min for the rocks with medium drillability and 70-140 rev/min for the rocks with high drillability. The rotation speed increases the drilling speed, but with it drill bit abrasion will be more. These parameters according to formation strength show variation such as high turn speed and low weight in soft formations and low turn speed and high weight in hard formations.

Their performances differ in drilling bits with the same IADC (International Association of Drilling Contractors) code from different manufacturers. For this purpose, especially in this study, the selection of the rock bits used in the drilling works, the appropriate usage parameters, the performances of the different brand rock bits and the effects on the meter cost of drilling will be given in detail.

Keywords: Drilling rock bits, Selection of rock bits, Parameters for rock bits' application, Cost analysis for rock bits, Geothermal drilling

1. INTRODUCTION

Today, geothermal energy is one of the alternative energy sources that gain importance in order to meet the increasing energy needs. Geothermal energy production is carried out by extracting the high temperature fluids in the depths of the earth's crust to the earth with similar wells to the oil-gas wells. Although equipment and standards and methods used in oil-gas wells are used in geothermal drilling work, it can be said that drilling costs are higher due to the fact that the excavated units are generally more abrasive and especially hotter than the excavated units in the case of oil-gas. The drill bits, which are related to the drilling meter costs are directly related to the amount of advancement, maneuverability, and cleaning of the boreholes from rock pieces in the long term. In order to reduce drilling costs, choosing the right drill bit is important, but not the only factor. The ability of the selected drill bit to work with optimum performance can be achieved with a combination of correct drill load and rotation speed in relation to drillability of the formation, where cracks can be removed smoothly out of the borehole.

[1] *General Directorate of Turkish Coal Board, 06560, Ankara, Turkey.* sedat.toraman@gmail.com

[2] *Corresponding author: Dumlupinar University, Department of Mining Engineering, 43270, Kutahya, Turkey.* cem.sensogut@dpu.edu.tr

2. PARAMETERS FOR ROCK BIT APPLICATION

In drilling works, the rate of penetration is primarily related to drill performance in terms of drilling costs. Drill performance depends on the coordination of some parameters at the optimum level to reduce drilling costs in the long run. The main parameters affecting the optimum performance of the drills are as follows;

- WOB (Weight on bit)- pressure
- RPM (Revolution per minute)- rotation speed
- Removing the rock pieces out of borehole

2.1. *Weight on Bit (WOB) - Pressure*

Within the basic rock mechanics principles, the force that must be applied to break any rock, that is, the load applied by the drill, must be higher than the pressure resistance of the rock. Therefore, a certain degree of weight on bit (WOB) must be applied in order for the drilling to take place. This pressing load is supplied either hydraulically or by weight pipes. If there is not enough pressure on the drill, or if it is given too much, drilling will increase the cost of drilling by reducing the life of the drill due to breakage of the tooth according to the construction of the drill. Between the load to be applied on the drill and the rock fragmentation;

- In case of minimum load on the drill; The cutting bits will be penetrating the formation very little and will only effect chipping instead of breaking.
- If less load is placed on the drill than the optimum load, it cannot perform an effective disintegration and therefore the rotation speed (ROP) remains lower.
- If more load is applied to the drill than optimum load; the cutting bits will be buried in the formation and the drilling speed will be reduced. Drill wear and therefore unit cost will increase.

It can be determined whether the appropriate load is given by monitoring the breaks during drilling. If the cracks are too small and high in dust, the drill is under optimum load while the cracks in the case of medium sized particles, then it indicates a weight close to the optimum weight. When the relationship between the optimum weight (WOB) to be applied on the drill and the speed of advancement is examined, it will not be possible to make more progress, but even more weight applied will increase the wear of the drill bit so that the drill usage time will decrease causing the time spent for changing the drill bit to increase. Factors to consider when applying pressure on the drill can be listed as follows:

- Diameter of rock bit,
- Structural features of rock bit (bearing type etc.) and
- Drillability of formation.

The maximum pressure that a bearing of a drill can receive is around 50-60 tons [1]. As the diameter of the rock bit increases, the strength of the rock bit increases as the cone bearings also grow. The maximum load that can be applied to the drill can be calculated as from Equation (1), and the appropriate drill load can be calculated as the Equation (2) [2].

Maximum drill load (lb) $=810D^2$ (1)

Appropriate drill load (lb) $Wo=Sc*D/5$ (2)

Sc = Uniaxial strength of formation (psi)
D = Diameter of rock bit (inch)

2.2. Rotation Speed (RPM)

In addition to the necessity of pressing force for squashing and crushing, rotation in the drill must be provided in order to make progress. The basic principle in rotary drilling is to bring the drill into a new disintegration position as a result of a disintegration process. Therefore, the rotation speed for the advance of the drill in the borehole is also an important parameter such as the drill load.

It is recommended that 30-40 rpm is applied in formations with low drillability while 60-120 rpm

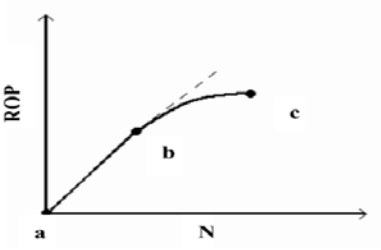

Figure 1. Relationship between rotation speed (RPM) and penetration rate (ROP)

in formations with medium drillability features, and 70-140 rpm in formations with high drillability [3]. This value can be applied as 200-250 rpm for very soft rocks [4].

When the relation between the rotation speed (RPM) and the rate of penetration (ROP) is examined, the similar result is seen to that of the weight applied on the drill (Figure 1).

2.3. Removing the Rock Pieces out of the Borehole

Removing the cut-offs from the drill bit as soon as possible is one of the important parameters affecting drill performance. It is imperative that the cut-offs be thrown away from the borehole as soon as possible and the drill should be given a new position. Proper fluidization speed and nozzle size selection are essential for the transport of small rock cracks. Drilling mud characteristics that are released to the borehole for transporting the cut-off from the borehole are one of the important parameters affecting the rate of penetration.

The density, rheological and filtration properties, solids content and size and chemical properties of the drilling mud affect the rate of penetration. The increase in drilling mud density, viscosity and solids will reduce the rate of drilling progress. (Figure 2).

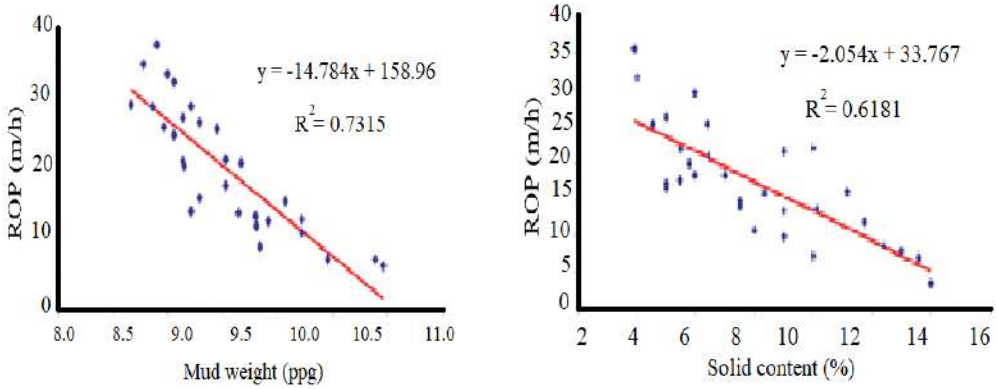

Figure 2. The effect of mud density and solid content on the rate of penetration [5]

2.4. Optimum Drilling Performance

Regardless of the parameters mentioned above, a drilling operation that focuses only on the rate of penetration cannot be carried out within economic limits. For example, in a situation where the particles are adequately moved out of the borehole, the speed of advancement may increase with any increase in pressure or rotation required for penetration, but the rock bit will wear out faster, causing a greater number of maneuvers, thereby significantly increasing drilling costs.

By using drilling fluid or air more effectively, with the correct combination of drill load and rotation speed, a faster rate of penetration can be achieved with less cost. A number of approaches have been presented for such combinations, both theoretically and on the basis of field test results. The most general approach is to select the WOB and RPM values in reverse proportion, depending on the formation (Equation 3). The general rule is to apply high pressure and low rotational speed in difficult drillable and abrasive formations and low pressure and high rotational speed in easy drillable formations [4].

$$ROP \propto \frac{(N^{\delta})(WOB^{\vartheta})}{S^{\tau}} \quad (3)$$

Here; N: Speed of rotation, S: Strength of formation, WOB: Weight on bit,

Upper indices for equation constants.
It has been found that some parameters such as depth, pressures, and hydraulics are indirectly influential on the feed rate, besides the WOB and RPM which can directly affect the rate of penetration and can be controlled, but due to the difficulties of modeling, these parameters are not considered in many models [6].

2.5. Drill-off Test in the Determination of Rock Bit Application Parameters

There are many scientific methods for determining optimum drill parameters. However, drill-off test is performed by the drilling engineer to determine the appropriate load and rotation speed of the drill after the drill selection for the formation has been performed.

Drill-off test; It is realized to determine the optimum weight (WOB) to be applied and the rotation speed (RPM) required for the maximum feed speed. In Figure 3, an example of drill-off test graph is illustrated. The drill-off test is a test that can be applied to any type of drill and can be completed in a short time. This test should be practiced in the cases of; 1) When a new drill is installed 2) When a different formation is encountered 3) When there is a decrease in the speed of progress.

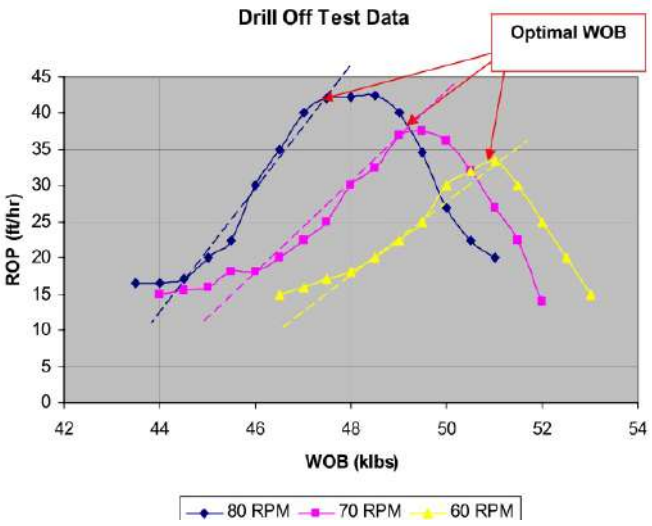

Figure 3. Drill-off Test Graph [7]

Drill -off test steps

- There is a maximum load on the drill.
- Certain weights (40,000 lbs, 45,000 lbs, etc.) are located on the drill by keeping the rotation speed constant and the duration of the drill weight drop (5,000 lbs in the determined weight) is recorded.
- This procedure is continued until the maximum weight that can be supplied is reached. Optimum WOB is the initial weight at which the weight loss is recorded as soon as possible.
- The same test can be repeated at different rotation speeds and the optimum amount of weight to be given on the drill can be determined for different rotation speeds.

3. ROCK BIT SELECTION IN GEOTHERMAL DRILLING

As the uniaxial compressive strength of the formation increases, the drillability becomes more difficult. The appropriate drill selection according to the rock uniaxial compressive strength is as shown in Figure 4 [8]. Geothermal drilling is carried out in areas where there is anomalous low-pressure and high-temperature tectonics involving very hard rocks where energy is more prevalent and volcanism is intense. The hard rocks encountered cause a very quick wear in rock bits. In addition, the fatigue and fracture due to excessive vibrations in the drilling sequence, the greater load requirement are necessitated and therefore the drills are subjected to greater loads. The high temperature damages the mechanical parts of the drills and completely destroys the rubber components. On the other hand, corrosive fluids entering the well also drastically reduce the life of the drill. Therefore, the problems that may arise in drill bits can be grouped as follows [9].

- Decrease in rock bit diameter, excessive tooth and bearing wear, due to abrasion of the formation,
- Rubber parts lose their function in short time due to high temperature,
- If the temperature is above 200^0C, the life of rock bit is shortened due to the decrease in the yield strength of carbon steels

To reduce the effect of temperature and excessive vibrations especially in geothermal drilling;

- Rock bit feature with sidewall and body protection should be chosen,
- In the drill classification with the IADC code 3, 5(sealed ball-bearing, bearing surface protection) or 7 (sealed, sliding bearing protection) will be more accurate.
- In order to reduce the effect of excessive vibrations, it may be useful to insert a "shock absorber" in the drilling set.

Uniaxial Compressive Strength of the Formation (kg/cm^2)	Look of the cutting cone	Code for IADC	Bit type & Formation Drillability	Examples of suitable formation to use
<400		First digit: 1	Steel bit Easy drillable	Clay, Anhydrite, Chalk, Gypsum, Tuff, Shale, Siltstone, Anthracite, Marl, Clayed coal, Mudstone
400-800		First digit: 2	Steel bit Normal drillable	Alluvium, Compact plastic shale, Salt, Gypsum, Loose cemented sandstone, Anhydrite, Sand, Grey sandstone, Argillaceous schist, Conglomerate, Clay, Limestone, Travertine
800-1400		First digit: 3	Steel bit Hard drillable	Dolomite, Limestone, Marble, Chalk, Schist, Mica schist, Trachyte, Porous basalt, Pegmatite, Breccia, Sandstone
<400		First digit: 4	Tungsten carbide bit Easy drillable	Sandy shale, Loose cemented sandstone, Sand, Alluvium, Rock salt, Hillside rubble, Travertine
400-800		First digit: 5	Tungsten carbide bit Normal drillable	Alluvium, Chalk, Dolomite, Siliceous shale, Anhydrite, Sandstone, Siliceous siltstone, Compact tuff, Conglomerate, Marble, Travertine
800-1700		First digit: 6	Tungsten carbide bit Hard drillable	Sandy chalk, Siliceous veined chalk, Grey sandstone, Chalkstone, Granite, Trachyte, Gneiss, Diabase, Gabbro, Diorite, Sandstone, Peridotite, Serpentine, Syenite

1700-3200		First digit: 7	Tungsten carbide bit Very hard drillable	Flintstone, Pyrite, Granite, Quartzite, Volcanic gravelly conglomerate, Andesite, Basalt, Diabase, Gabbro, Diorite, Siliceous chalkstone, Porphyry, Syenite
>3200		First digit: 8	Tungsten carbide bit Rather hard drillable	Flintstone, Pyrite, Granite, Quartzite, Andesite, Basalt, Gabbro, Chert, Radiolarite

Figure 4. Rock bit selection according to the formation's uniaxial compressive strength [8]

4. ROCK BIT APPLICATION PARAMETERS, RATE OF PENETRATION AND COST OF DRILLING

The rate of penetration as well as drill application parameters are important in drilling operations. The drill manufacturers specify the optimum weight values together with the drill application parameters. Taking into account the values determined by the drill manufacturer, drill-off test is required to determine the load to be applied and the speed of rotation. More pressure or more rotation speed does not mean faster and cheaper drilling. Optimum pressure and rotation speed together with good drilling fluid properties affect controlled drilling speed.

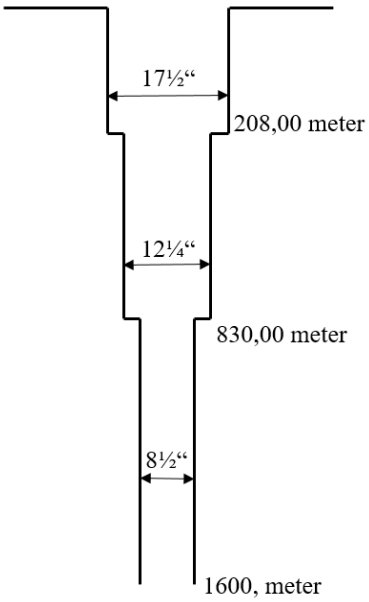

Figure 5. KSU-2 Geothermal Drilling

In Kutahya-Saphane-Karacaderbent (KSU-2) geothermal drilling, a total of 1,600 meters of wells were drilled. The drilling was performed at a diameter of 17 ½ " for 208.00 meters, a diameter of 12 ¼" for 622.00 meters and a diameter of 8 ½ " for 770 meters (Figure 5). When 8 ½ "drill application values were examined during KSU-2 drilling, it was observed that drilling speeds with 8 tons of drilling load were decreased to 1.10 m/h (Table 1).

In Aydin-Horsunlu AKH-2010/1 geothermal drilling work, a total of 1993 meters of wells were drilled. The drilling was performed at a diameter of 17 ½ " for 248.00 meters, a diameter of 12 ¼" for 340.00 meters and a diameter of 8 ½" for 1,412.00 meters. When 8 ½ "drill application values were examined, it was observed that drilling speeds with 12 tons of drilling load and 60 RPM rotation speed, 4.54 m/h of advancement rate was reached. In addition, a rate of 2,12 meters' advancement was achieved with a load value of 6 tons and 50 RPM rotation speed in the same region (Table 2).

Rock bit application parameters, drilling fluid properties and formation characteristics as well as rock bit production quality are important factors for the drilling rate. The performances of the rock bits produced by different companies with the same IADC code are also different.

If it is assumed that a total of 1,200 meters of a borehole with 8½ " diameter is completed with 2 rock bits of the brand a, it is possible to reach the same targeted length of borehole with 5.5 rock bits of the brand c. In order to complete the projected length of borehole, 1 manoeuver should be used in case of using the brand a rock bit and 5 manoeuvers by using the brand c rock bit. The maneuvering time is about 24 hours in 8½ " drilling work. In this case the lost time from rock bit change will be 1 day for the brand a rock bit and 5 days for the brand c rock bit. If the 1.200-meter progress for 8½ " borehole is planned to be realized and daily drilling cost is estimated to be about 5,000 USD;

Table 1. Kutahya-Saphane-Karacaderbent KSU-2 Geothermal Drilling Registration Form [10]

WELL NO: KSU-2	DRILLING MACHINE: WR-6		CITY: KUTAHYA		COUNTY: SAPHANE	FIELD: KARACADERBENT
Drilling rig supervisor :			Drill pipe:	4 1/2"	Mud pump-1:	Pz-8
Drilling person :			Drill PIPE:	3 1/2"	Mud pump-2:	Fm-35
Drilling person :			Drill collar:	8"		
Drilling person :			Drill collar:	6 1/2"		

No	Date of operation	Diameter (inch)	Type	Serial no	Starting depth	Ending depth	Drilling length	Total work hours	Rate of penetration	Formation
1	24.03.2007	17 1/2	Rock-Bit	Old	0.00	113.20	113.20	62.75	1.80	Alluvium, tuff, tuffite, conglomerate, marl
2	03.04.2007	17 1/2	Rock-Bit	277890	113.20	208.90	95.70	58.83	1.68	Conglomerate, claystone, marl
3	12. 04. 2007	12 1/4	Rock-Bit	683244	208.90	326.10	117.20	56.58	2.08	Basalt, tuff, tuffite
4	16.04. 2007	12 1/4	Rock-Bit	4110406	326.10	458.00	131.90	105.58	1.25	Basalt, tuff, tuffite
5	22.04. 2007	12 1/4	Rock-Bit	030479	458.00	495.60	37.60	34.83	1.80	Tuff, tuffite
6	24.04. 2007	12 1/4	Rock-Bit	030453	495.60	550.40	54.80	52.83	1.03	Tuff, tuffite
7	27.04. 2007	12 1/4	Insert	0100904	550.40	830.00	279.60	134.00	2.08	Tuff, tuffite
8	17.05. 2007	8 1/2	Insert	307	830.00	1155.15	325.15	141.08	2.30	Tuff, tuffite
9	01.06. 2007	8 1/2	Insert	300	1155.15	1394.60	239.45	128.58	1.86	Tuff, tuffite
10	13.06. 2007	8 1/2	Insert	263	1394.60	1500.00	105.40	95.75	1.10	Tuff, tuffite, conglomerate, sandstone
11	24.06. 2007	8 1/2	Insert	537	1500.00	1600.0	100.00	71.08	1.40	Tuff, tuffite, conglomerate, sandstone

Table 2. Aydin-Horsunlu Geothermal Drilling Registration Form [11]

WELL NO: AKH-2010/1	DRILLING MACHINE: MR-6000/1		CITY: AYDIN		COUNTY: KUYUCAK	FIELD: HORSUNLU
Drilling rig supervisor :			Drill pipe:	4 1/2"	Mud pump-1:	9T-800
Drilling person :			Drill collar:	8"	Mud pump-2:	9T-800
Drilling person :			Drill collar:	6 1/2"	Mud pump-3:	

No	Date of operation	Diameter (inch)	Type	Serial no	Starting depth	Ending depth	Drilling length	Total work hours	Rate of penetration	Weight on bit (ton)	Rotation (RPM)	Pressure (PSI)	Pump: No	Pump: Collar	Pump: Flowrate	Mud: Weight	Mud: Viscosity	Formation
1	11.03.2010	17 1/2	Mill-Tooth	9499	0.00	248.00	248.00	95.83	2.59	12	60	100	9T-800	6	12.5	1.06	55	Alluvium, conglomerate
2	01.04.2010	12 1/4	Insert	09677	248.00	588.00	340.00	159.00	2.14	12	60	150	9T-800	6	12.5	1.20	60	Mica-schist, granate
3	25.04.2010	8 1/2	Insert	11060	588.00	1014.30	426.30	93.83	4.54	12	60	150	9T-800	6	12.5	1.10	55	Mica-schist, gneiss
4	03.05.2010	8 1/2	Insert	11050	1014.30	1331.50	317.20	81.00	3.92	12	60	250	9T-800	6	12.5	1.10	55	Quartzite, quart-schist
5	08.05.2010	8 1/2	Insert	11054	1331.50	1413.10	81.60	29.67	2.75	14	55	300	9T-800	6	12.5	1.10	55	Phyllite, gneiss, quartzite
6	10.05.2010	8 1/2	Insert	10011	1413.10	1551.50	138.40	54.67	2.53	14	55	350	9T-800	6	12.5	1.10	55	Phyllite, gneiss, quartzite
7	14.05.2010	8 1/2	Insert	273	1551.50	1600.00	48.50	20.25	2.40	14	55	400	9T-800	6	12.5	1.10	55	Gneiss, mica-schist
8	20.05.2010	8 1/2	Insert	276	1600.00	1832.50	232.50	76.58	3.04	12	55	450	9T-800	6	12.5	1.10	55	Phyllite, gneiss, quartzite
9	04.06.2010	8 1/2	Insert	304351	1832.50	1908.00	75.50	35.58	2.12	6	50	500	9T-800	6	12.5	1.10	55	Gneiss, mica-schist
10	07.06.2010	8 1/2	Insert	279	1908.00	2000.0	92.00	40.83	2.25	6	50	500	9T-800	6	12.5	1.10	55	Phyllite, chalk-schist

Table 3. Performance of different brand rock bits

Rock bit brand	Rock bit diameter (inch)	Drilled length (m)	Working hour (h)	Rate of advancement (m/h)	Usage rate of rock bit (%)	WOB (ton)	RPM
a	8 1/2	611,2	129,5	4,71	80	14-15	50-60
b	8 1/2	371,00	78,17	4,75	80	14	65
****c***	8 1/2	217,33	68,56	3,17	80	14	65

** The brand c has been increased from 50% to 80% since it was changed after use.*

Table 4. Drill meter cost

Rock bit brand	No of rock bits consumed	Number of manoeuvres and lost days	Rock bit cost ($/unit)	Total expenses for rock bits ($)	Cost of lost days ($)	Total cost ($)	Rock bit cost for each meter drilled ($/m)
a	2	1	6.000	12.000	5.000	17.000	**14,17**
b	3,25	3	4.500	14.625	15.000	29.625	**24,68**
c	5,5	5	4.000	22.000	25.000	47.000	**39,16**

When Tables 3 and 4 are examined, the initial cost of the brand a rock bit is 25-30% more expensive than other rock bits, however the cost of each meter drilled is lower. Especially when the maneuvering time is long during the progression of 8½ "diameter boreholes, the high performance brand rock bit selection is important in minimizing the cost of the drilling meter.

5. RESULTS

✓ It is very important to select a rock bit suitable for the formation to be penetrated in order to realize the planned rate of advancement before the drilling operation is started. For this purpose, the drilling engineer should analyze the geological and geophysical studies conducted at the site before the operation begins and obtain detailed information about the possible formation characteristics to be passed. The formation properties are important parameters for both rock bit selection and drilling fluid to be used.

✓ If the first basic rule in the drilling of the borehole is to choose a rock bit suitable for the formation to be passed, the second basic rule is to use the drill with the correct parameters.

✓ Optimization of drilling work starts with rock bit optimization. The rock bit cost corresponds to 3-5% of the total drilling cost, but the impact on the total drilling cost is 50-60%.

✓ During the drilling operations, the drilling engineer will follow the parameters affecting the drilling performance such as changes in torque, rock pieces formed during drilling operation, sludge pump pressures and necessary interventions in order to reduce the cost of drilling and ensure efficient operation.

✓ Following the drill performance, the problems that can occur in the rock bit are indicated on the surface. Irregular torque occurs when the drill is overloaded or the drill bit diameter drops. In case of blockage in the drill holes, irregular pump pressure values are read. The pump pressure is regular but the change in the pump stroke number may indicate that the nozzle / drill holes are blocked again.

✓ Especially as the depth of the borehole increases, maneuvering (tooling-stroke) times for rock bit exchange will increase. Choosing quality rock bit for regular progression at 8½ "diameter will seriously affect drilling meter cost.

REFERENCES

[1]. Bilgin, N., 1991, Drills used in mines and their operating conditions and economics, Publication of Mining Faculty, Istanbul Technical University, Istanbul (in Turkish).

[2]. Praillet, R., 1990, Blast hole Drilling-Rotary Drilling and The Four Kingdoms. WME, Sept.

[3]. Bilgin, N., Eskikaya, S. & Dincer, T., 1993, Performance Analysis of Rotary Drills with Large Diameter used in Turkish Coal Board, 13. Mining Congress of Turkey (in Turkish)

[4]. Moore, P. L.,1986, Drilling Practices Manual, Second Ed., Oklahoma, USA, pp.363-399

[5]. Paiman, A.M., Al-Askari, M.K.G., Salmani, B., Al-Arazi, B.D. & Masihi, M., 2009, Effect of Drilling Fluid Properties on Rate of Penetration, NAFTA 60 (3) 129-134

[6]. **Warren, T. M., 1987,** Penetration Rate of Performance of Roller Cone Bits, SPE Drilling Engineering, March, 9-18. 8 Maurer, Journal of Petroleum Technology, December, 1433-42

[7]. Junior, D.C., 2007, Challenges and Developments Indirect Measurement of Down Hole Forces affecting Drilling Efficiency

[8]. Ister, T. & Ozdemir, A., 2005, Rock Bit Selection suitable to Formation in accordance with its Cutting Structure, 58. Geology Convention of Turkey, pp 295-296 (in Turkish)

[9]. Serpen, U. 2005, Features of Geothermal Drills and Equipments used, Geothermal Energy Seminar, Publication of Turkish Chamber of Mechanical Engineers E/2005/393-2, pp. 55-66 (in Turkish)

[10]. MTA Drill Report, 2009, General Directorate of Mineral Research & Exploration, Kutahya-Saphane-Karacaderbent KSU-2 Geothermal Drill (in Turkish)

[11]. MTA Drill Report, 2011, General Directorate of Mineral Research & Exploration, Aydin-Horsunlu AKH-2010/1 Geothermal Drill (in Turkish)

ICENS 4TH INTERNATIONAL CONFERENCE ON ENGINEERING AND NATURAL SCIENCE
2-6 May 2018 KIEV UKRAINE

The Effect of B4C Reinforcement Ratio on Mechanical Properties of Steel / Al-B4C Circular Layered Composites

Abdullah Gocer[1], Erkan Yilmaz[2], Mehmet Baki Karamis[3]

Abstract

The mechanical properties of the metal matrix materials are generally weak. That's why the composite structures must be strengthened by reinforcing with some stronger materials such as steels. In this study, the changing of mechanical properties of circular layered composites which produced in the form of steel/Al-B4C were investigated based on the B4C ceramic reinforcement ratio. In the manufacturing of these composite materials, AISI 4140, Al 2024 alloy and B4C were used as jacked, matrix and reinforcing materials respectively. Preliminary products which obtained by compression of Al2024-B4C powder mixture into steel tubes (powder in tube) were firstly subjected to sintering and then reduced to the desired diameters by circular rolling. By this process, it is aimed to increase the jacked-core interface strength. These circular composite bars were subjected to a tensile test. These tests clearly demonstrate how the tensile behavior of the material changes with the increase of the B4C reinforcement ratio in core material.

Keywords: *Bimetal rod, layered composite, tensile strength*

1. INTRODUCTION

Composite materials are referred to as materials created by merging the best properties of two or more materials in the same or different groups at a macro level in order to gather them in a single new material. In general, composite materials are the assembled state of reinforcing elements in different structures distributed in a continuous phase called matrix. Clad composites are materials in a circular structure made of different metals, both internally and externally. The purpose of using layered composite materials is to combine the properties of the inner and outer materials, while keeping the inner material with the outer materials. In addition, the inner material is called "core" and the outer material is called "sheath". In this study, it was aimed to produce a circular layered composite with a high strength / density ratio by using steel as the sheath, Al-ceramic material as the core, and the tensile strength properties of the material were investigated.

When studies on layered metal composite materials are examined, it has been found that the work is usually to produce lighter conductive materials and to increase corrosion resistance together with strength. For conductivity purposes, the intensity is on copper and aluminum pairs. In these studies, it is generally seen that the effects of production conditions on product characteristics [1], numerical modeling of production conditions [2] and examining product damage [3] are studied.

There are also studies aimed at bringing together the properties of different alloys of the same type of materials [4, 5, 6]. In this study, it was aimed to produce a circular layered composite with high strength/density ratio by using steel as a sheath and Al-ceramic material as a core, and the tensile strength properties of the material were investigated.

[1] *Corresponding author: Erciyes University, Engineering Faculty, Department of Mechanical Engineering, 38039, Melikgazi/Kayseri, Turkey. abdullahgocer@erciyes.edu.tr*

[2] *Erciyes University, Engineering Faculty, Department of Mechanical Engineering, 38039, Melikgazi/Kayseri, Turkey. erkan@erciyes.edu.tr*

[3] *Erciyes University, Engineering Faculty, Department of Mechanical Engineering, 38039, Melikgazi/Kayseri, Turkey. karamisb@erciyes.edu.tr*

2. EXPERIMENTAL STUDIES

In this study, AISI 4140 steel material is used as sheath material of layered composites and Al-B4C metal matrix composite is used as core material. The production stages of the layered composites of Steel / MMC construction produced in the scope of the study are realized in two steps.

In step 1; Al-B4C powder mixtures mixed at different ratios are pressed into the steel tube under press. Thus, preliminary products are prepared for rolling.

In step 2; these preliminary products are hot rolled by the circular rolling system; so that both the sintering of the self-material and the increase of the sheath-core interface strength are achieved.

To describe production steps in more detail;

Preparation of Steel tubes;

- Softening Annealing of steel bars: 2 hours at 720 ° C and cooling in the oven

- Tubing of bars with machining to Dout = 12 mm, Din =10,6 mm and H = 70 mm

The obtained tube is cleaned with ultrasonic cleaner with trichloroethylene. By this process, it is ensured that the oils on the inner and outer surfaces of the sheath are removed from the material.

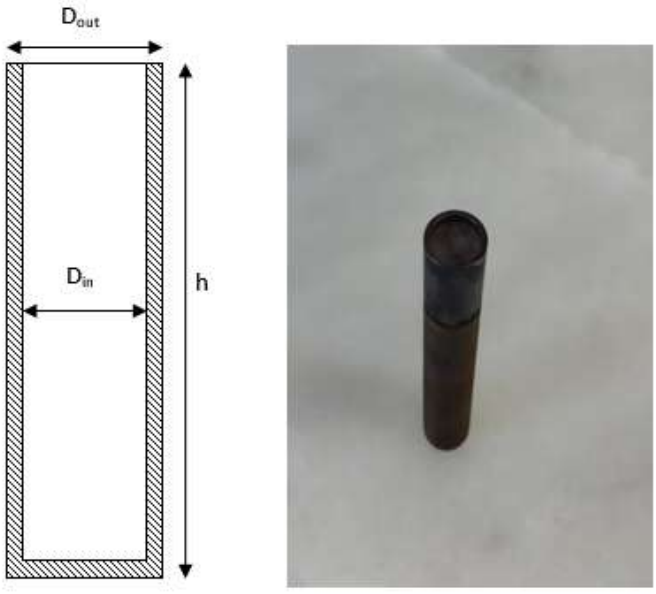

Figure 1. Dimensions of steel tube and a preliminary product

Preparation of core material;

- Volume ratios of Al 2024 and B4C powders are as follows;

ν1 = % 90 Al 2024 % 10 B4C,

ν2 = % 80 Al 2024 % 20 B4C,

ν3 = % 70 Al 2024 % 30 B4C

- Dimensions of B4C particles = 3, 17, 58 µm

The powders are mixed in a 3D mixturer for 2 hours, brought together in a closed, non-air-conditioned container.

Rolling of materials;

The rolling process was carried out step by step from diameter 12 mm to diameter of 6.4 mm. The diameter of the intermediate rolls is 11.6 mm, 11.2 mm, 10.8 mm, 10.4 mm, 10 mm, 9.6 mm, 9.2 mm, 8.8 mm, 8.4 mm, 8 mm, 7.6 mm, 7.2 mm and 6.8 mm. The process temperature was set at 500 ° C.

Figure 2. Circular rolling machine and rolled composite bars

The materials produced in the details given above are listed in the table below.

Table 1. Material components of layered composites

Sample No	Sheath	Core
1	Steel (AISI4140)	Al2024-B4C(% 10 V_f-58 µm)
2	Steel (AISI4140)	Al2024-B4C(% 20 V_f-58 µm)
3	Steel (AISI4140)	Al2024-B4C(% 30 V_f-58 µm)
4	Steel (AISI4140)	Al2024-B4C(% 20 V_f-3 µm)
5	Steel (AISI4140)	Al2024-B4C(% 10 V_f-17 µm)
6	Steel (AISI4140)	Al2024(% 100)
7	Al2024-B4C(% 20 V_f-58 µm)	

3. RESULTS AND DISCUSSION

After rolling, the hardness scan performed on composite sections. After rolling, the hardness of the sections of the composite bars was checked. The points of hardness are shown in Figure 3. The hardness distribution obtained after the hardness scan is transferred to the graphs (Fig. 4). According to the hardness values, the hardness of the core material increases with B4C reinforcement. It also increases the hardness of the core material by increasing the reinforcement ratio and the grain size. In addition, the hardness distribution on the section increases from the outside to the inside. This indicates that the deformation increases in the middle of the material.

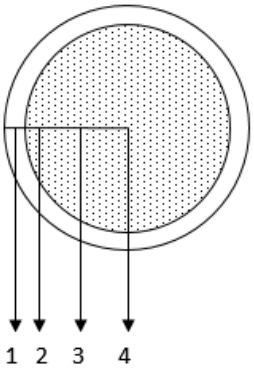

Figure 3. Hardness points on the material section

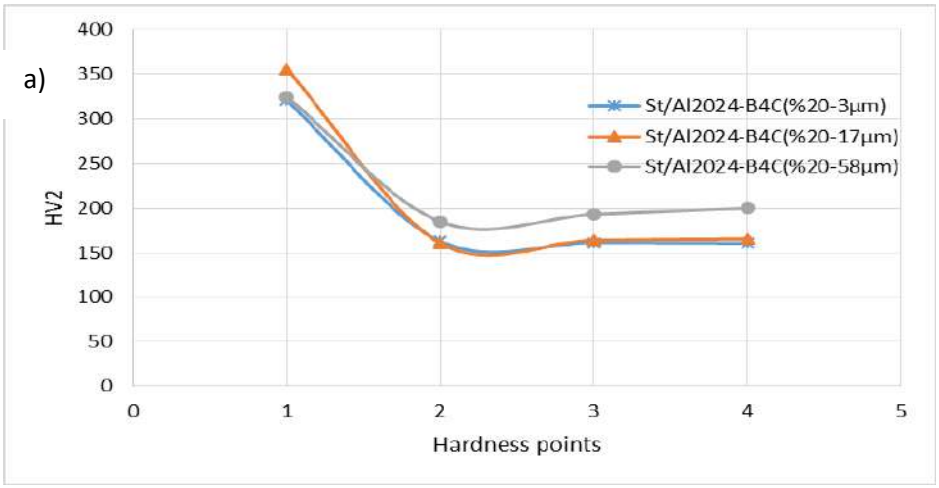

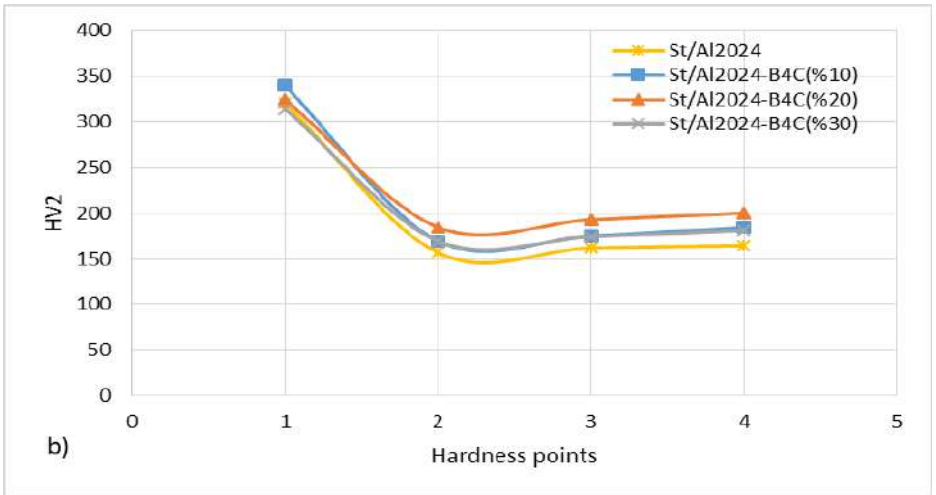

Figure 4. Hardness distributions on material sections a) Changing of hardness distribution according to B4C grain size b) Change of hardness distribution according to B4C reinforcement ratio

Tensile samples were prepared from the layered metal composites produced in the study and tensile tests were carried out. Tensile specimens are not prepared in accordance with the standards, which is why the sheath-core ratio will deteriorate when the bar is processed. The purpose of applying the tensile test to these materials is to compare the variation in tensile properties in the case of layered production of the material. In the tensile tests, the effect of the B4C volume ratio and the powder size on the tensile results was investigated in the Al 2024-B4C mixture, which is the core material.

When the effect of B4C ratio on the tensile tests was examined, it was determined that the tensile strength values of the material with B4C reinforcing material increased (Fig. 5). It is seen that the material with the highest tensile strength value (550 N / mm2) is the material containing 10% B4C. By increasing the B4C reinforcement ratio (from 10% to 30%), the deformation ability of layered composite decreases, then the tensile strength value decreases. In Fig. 5, in the tensile curve of St / Al2024 material, it is seen that the layered composite first collapses in its sheath, then the ductile Al2024 unreinforced material continues to change shape and then breaks.

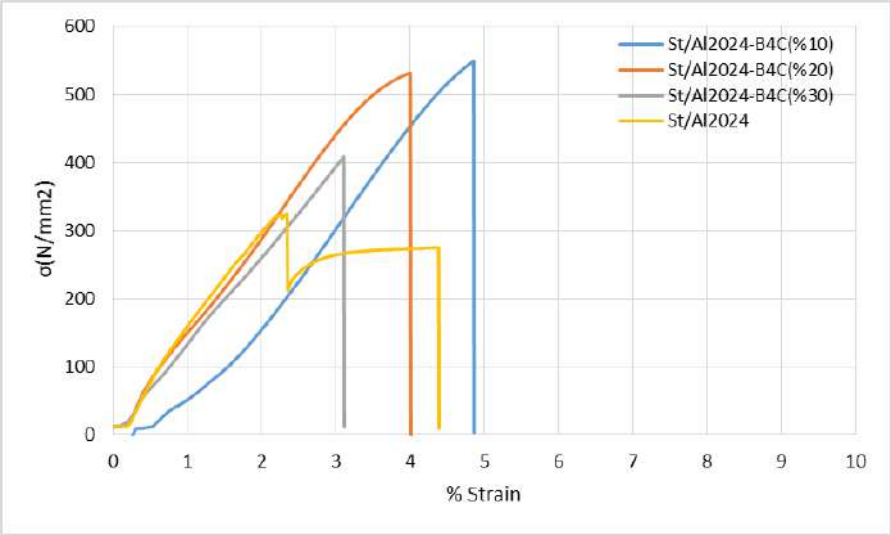

Figure 5. Variation of tensile curves with B4C volume fraction.

In Fig. 6, influence of the B4C grain size on the tensile curves is shown. In these materials the B4C reinforcement ratio was fixed at 20% and the B4C reinforcement dimensions were changed to 3, 17 and 58 μm. These curves show that the tensile values of the materials are also lowered by the decrease of the grain size. It is thought that the growth of the grain size increases the sheath-core intergrowth (Fig 7).

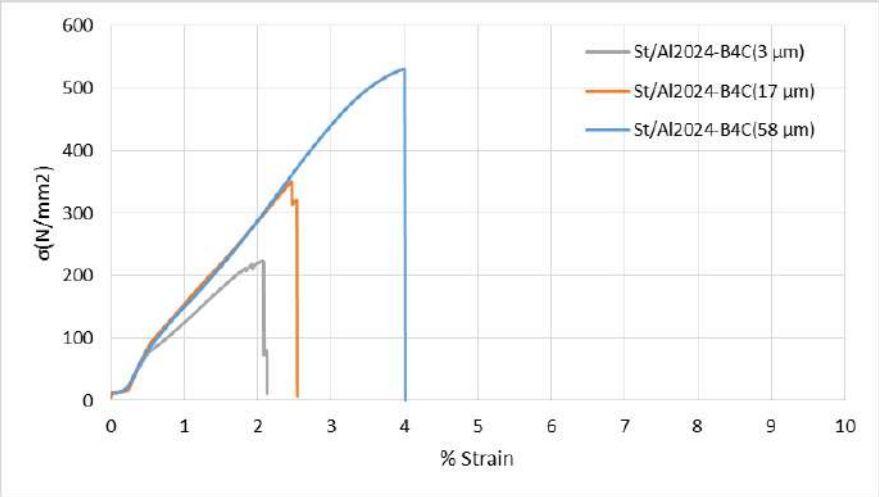

Figure 6. Variation of tensile curves with B4C grain size.

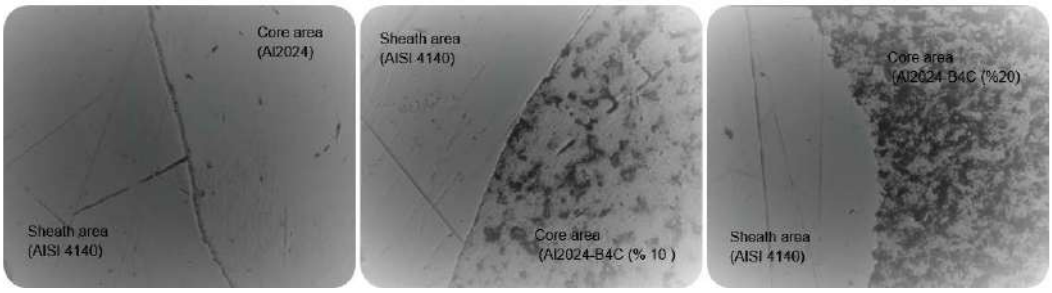

Figure 7. Variation of sheath-core boundary conditions with B4C volume fraction

In Figure 8, it is seen how to change the tensile properties of the material by forming a steel jacket outside the Al 2024-B4C composite materials. As is known, the ceramics added as aluminum reinforcement decrease the ductility with increasing the strength of the material in a certain amount of interval. As the amount of reinforcement increases, it begins to fall in strength. In this study, tensile strength of Al 2024-B4C (20%) has increased the by about two times, with the sheath formed around itself reducing the ability to deform the material.

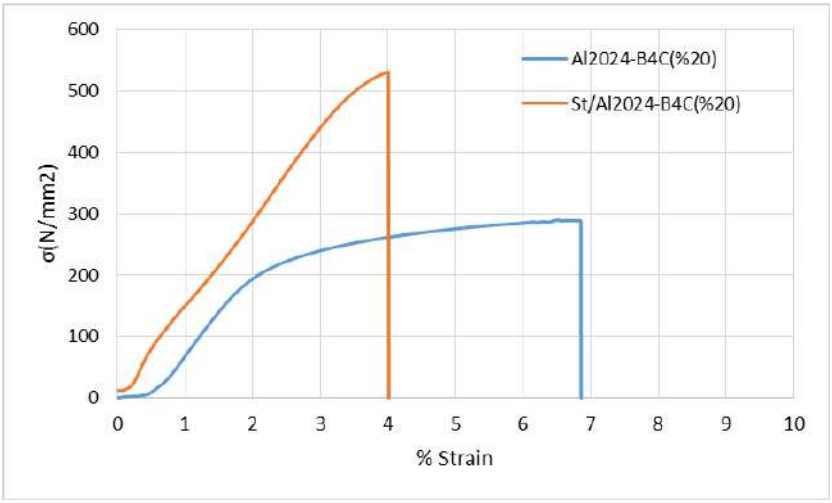

Figure 8. Variation of tensile curves with steel sheath

4. CONCLUSION

The conclusions derived from this study can be summarized as follow:

1. The steel sheath formed out of Al 2024-B4C metal matrix composites greatly increases the tensile strength of the material.

2. Because of the St / Al2024 layered composite has not a reinforcing element in its core material, the tensile curve of this material is gradual. That is, sheath and core are broken separately.

3. As the volumetric ratio of B4C reinforcement in the core material increases, the deformation ability of the material first decreases, then the strength values decrease

4. As the B4C reinforcement size in the core material decreases, the tensile strength values also decrease.

ACKNOWLEDGMENT

This project was supported by the Scientific Research Projects Unit of Erciyes University (Project number: FDK-2015-6265).

REFERENCES

[1]. H.J. Park, K.H. Na, N.S. Cho, Y.S. Lee, S.W. Kim, “A study of the hydrostatic extrusion of copper-clad aluminium tube”, Journal of Materials Processing Technology, vol. 67, pp. 24-28, 1997.
[2]. C. G. Kang, Y.J. Jung, H.C. Kwon, “Finite element simulation of die design for hot extrusion process of Al/Cu clad composite and its experimental investigation”, vol. 124, pp. 49-56, 2002.
[3]. C.G. Kang, H.C. Kwon, “Finite element analysis considering fracture strain of sheath material and die lubricant in extrusion process of Al/Cu clad composites and its experimental investigation”, International Journal of Mechanical Sciences, vol. 44, pp. 247-267, 2002
[4]. M.E. Epler, W.Z. Misiolek, “Novel billet design for co-extrusion of ferrous material tubes”, Materials Science and Engineering A, vol. 429, pp. 43-49, 2006.

[5]. I.S. Son, S.P. Lee, W.C. Kim, J.S. Moon, S. Lee, J.S. Lee, Y.B. Kim, G.A. Lee, D.S. Bae, "Effect of hydro co-extrusion on microstructure of duo-cast Al 3003/Al 4004 clad materials", Transactions of Nonferrous Metals Society of China, vol. 24, pp. 75-80, 2014.
[6]. L. Madej, H. Paul, L. Trebacz, W. Wajda, M., Pietrzyk, "Multi billet extrusion technology for manufacturing bi-layered components", CIRP Annals-Manufacturing Technology, vol. 61, pp. 235-238, 2012.

ICENS 4TH INTERNATIONAL CONFERENCE ON ENGINEERING AND NATURAL SCIENCE
2-6 May 2018 KIEV UKRAINE

Investigation of Heat Transfer from Heated Square Patterned Surfaces in a Rectangular Channel with an Air Jet Impingement

Dogan Engin Alnak[1], Koray Karabulut[2], Ferhat Koca[1]

Abstract

Heat transfer is a very important precaution for proper design and safe operation of electronic packages and systems. Impinging jets are usually used to solve thermal problems of electronic components in industry due to providing a good heat transfer performance. In this study, cooling of copper plate with five square patterned surfaces inside a rectangular channel comprising of one open and three blocked sides was numerically investigated by using a single air jet flow. The numerical computations were performed by solving a steady, three-dimensional Navier-Stokes equation and an energy equation by using Ansys-Fluent 17.0 software program with k-ε turbulance model. Air was taken as working fluid with inlet temperature of 300 K. A constant heat flux with 1000 W/m^2 was applied to square patterned surfaces while the top and side surfaces were adiabatic. The study was carried out for different Reynolds numbers (Re) of 4000, 6000, 8000 and 10000 and different jet-to-plate distances (H/D$_h$) of 4, 6, 10 and 12. The numerical results agreed well with the numerical and experimental datas of study existed in literature. The results were presented as the variations of the mean Nu numbers and temperatures for each square patterned indentation surface. The temperature and velocity distributions of jet fluid flow and mean temperature and Nu values of whole five square patterned surfaces and value of air jet outlet temperature were also researched for different Re numbers and H/D$_h$ ratios. It was seen that increasing the Re number increases the Nusselt number for all cases. Average Nusselt number increases of 59.28% from Re=4000 to Re=10000 for H/D$_h$ =4. However, Nu number was less sensitive to H/Dh ratio in the range of H/D$_h$=4-12. Average Nusselt number decreases of 9.11% from H/D$_h$=4 to H/D$_h$=12 for Re=6000. The highest average Nusselt number was attained for Re=10000 and H/D$_h$ =6.

Keywords: Impingement air jet, Patterned surface, Square channel, Numerical analysis

1. INTRODUCTION

Rapid improvement of technology leads electronic devices to have both more compact and higher processing power. The reliability of the electronic parts of a system is a primarily factor in the overall reliability of the system. Electronic components depend on transition of the electric current to implement their duties and they become potential regions for excessive heating, since the current flow through a resistance brings along heat generation. Unless properly designed and controlled, high rates of heat generation cause to high operating temperatures for electronic device, which endangers its reliability and safety. Besides, the high thermal stresses in the solder joints of the electronic equipments mounted on circuit boards resulting from temperature variations are major reasons of defects. Therefore, thermal control has become increasingly important in the design and operation of the electronic devices. For this purpose, it is needed to develop new cooling techniques instead of conventional technology. Impinging liquid and gaseous jets are used widely because of their easy application and high heat transfer coefficient. Jet impingement is employed for heating, cooling and drying in cases where coefficients of high heat transfer are aimed. Thus, it is considered that jet impingement can be used for cooling of the electronic components generating high heat and having high performance. Because high heat producing electronics evolve, it becomes proof that using air cooling alone will not provide adequate performance. Jet impingement has the ability to take away large amounts of heat from these environments with high heat flux. In the one of the earliest investigations into jet impingement flow was carried out a review of literature that included several examples [1]. In an another review study, Carlomagno and Ianiro [2] did a detailed work of

[2]*Corresponding author: Sivas Cumhuriyet University, Department of Electric and Energy, Sivas Vocational High School, 58140, Sivas, Turkey. kkarabulut@cumhuriyet.edu.tr, koray.karabulut@hotmail.com*

[1]*Sivas Cumhuriyet University, Department of Automotive Engineering, Technology Faculty, 58140, Sivas, Turkey. dealnak@cumhuriyet.edu.tr, ferhatkoca@cumhuriyet.edu.tr*

the effects of Reynolds number and jet to plate distance on the heat transfer and flow physics of the impinging jets. Argus et al. [3] researched jet flow and heat transfer by using only one jet, numerically. Popovac and Hanjalic [4] investigated cooling of a heated cubic plate using one impingement jet. Yang and Hwang [5] exhibited numerical simulations of flow properties of a turbulent slot jet impinging on convex surface with a semi-cylindrical. Mushatat [6] performed a numerical study in order to study heat transfer and turbulent flow characteristics of impinging slot jets. Zuckerman and Lior [7] numerically analyzed the effect of nozzle type on initial turbulance, pressure drop, shearing force of free jet and jet velocity profile. They also described various experimental and computational techniques from other authors.

Different from the literature, it was mainly carried out numerical investigation of heat transfer from heated square patterned surfaces, inside a rectangular channel having three closed and one open side by using an air jet with single slot in the present work. The slot jet was mounted next to closed side. Air jet geometry and channel were designed of similar to an implementation of cooling of electronic components inside various devices. The numerical computations were performed by solving a steady, three-dimensional Navier-Stokes equation and an energy equation by using Ansys-Fluent 17.0 software program with k-ε turbulance model. Air was used as working fluid with inlet temperature of 300 K. It was exerted to a constant heat flux ($\ddot{q}$) with 1000 W/m^2 on square patterned surfaces. The numerical results agreed well with the numerical and experimental datas of study existed in literature. The results were presented as the variations of the mean Nu numbers and temperatures for each square patterned indentation surface. The temperature and velocity distributions of jet fluid flow and mean temperature and Nu values of whole five square patterned surfaces and values of air jet outlet temperature were also investigated for different Re numbers and H/D_h ratios.

2. NUMERICAL METHOD

The numerical study was conducted to study the three-dimensional, steady, conjugate heat transfer of forced convection and conduction in a channel with patterned surface of fluid flow. The finite volume method (FLUENT program) was used to solve the conjugate heat transfer analysis.

The aim of finite volume method is to break down the domain of the problem into a finite number of elements to be solved to find a solution for each of these sections and then by uniting these solutions to find a general solution to the problem. This method uses a technique which is based on the control volume for transforming heat flow equations into algebraic equations which can be solved numerically. In other words, this technique is based on the principle of taking the heat flow equations integration in each control volume. This integration result provides equations which characterize each control volume which occurs. For preparing the most appropriate grid model, a fine grid should be formed in regions where the change in variables such as velocity, pressure and temperature is bigger. Therefore, the finest grid was especially used for the channel surfaces with the indentation and in other zones a sparser grid was preferred. Convergence of the computations was stopped for the continuity and the momentum equations when residues were less than 10^{-6} and for the energy equation when residues were less than 10^{-7}. A grid structure which consisted of tetrahedral was used for simulation. Also, a standard k-ε turbulance model was performed for the selected model with square patterned surfaces in the numerical investigations.

The flow and heat transfer through the geometry are governed by the partial differential equation derived from the laws of conservation of mass, momentum and energy with steady state conditions without a body force, which are expressed as follows [8].

Continuity equation

$$\frac{\partial u}{\partial x}+\frac{\partial v}{\partial y}+\frac{\partial w}{\partial z}=0 \tag{1}$$

Momentum equation

x momentum equation

$$\rho\left(u\frac{\partial u}{\partial x}+v\frac{\partial u}{\partial y}+w\frac{\partial u}{\partial z}\right)=-\frac{\partial p}{dx}+\mu\left(\frac{\partial^2 u}{\partial x^2}+\frac{\partial^2 u}{\partial y^2}+\frac{\partial^2 u}{\partial z^2}\right) \tag{2.1}$$

y momentum equation

$$\rho\left(u\frac{\partial v}{\partial x}+v\frac{\partial v}{\partial y}+w\frac{\partial v}{\partial z}\right)=-\frac{\partial p}{\partial y}+\mu\left(\frac{\partial^2 v}{\partial x^2}+\frac{\partial^2 v}{\partial y^2}+\frac{\partial^2 v}{\partial z^2}\right) \tag{2.2}$$

z momentum equation

$$\rho\left(u\frac{\partial w}{\partial x}+v\frac{\partial w}{\partial y}+w\frac{\partial w}{\partial z}\right)=-\frac{\partial p}{\partial z}+\mu\left(\frac{\partial^2 w}{\partial x^2}+\frac{\partial^2 w}{\partial y^2}+\frac{\partial^2 w}{\partial z^2}\right) \tag{2.3}$$

Energy equation

$$u\frac{\partial T}{\partial x}+v\frac{\partial T}{\partial y}+w\frac{\partial T}{\partial z}=\left(\frac{k}{\rho c_p}\right)\left(\frac{\partial^2 T}{\partial x^2}+\frac{\partial^2 T}{\partial y^2}+\frac{\partial^2 T}{\partial z^2}\right) \tag{3}$$

In the equations, ρ is density, μ dynamic viscosity, p pressure, k thermal conductivity, T temperature, c_p specific heat and u, v, w are velocities of the x, y and z direction, respectively.

In the used standard k-ε turbulance model, the turbulence kinetic energy k' and its rate of dissipation $\in$ and the viscous dissipation term ϕ are used.

Steady flow turbulence kinetic energy equation

$$\frac{\partial(\rho u k')}{\partial x}+\frac{\partial(\rho v k')}{\partial y}+\frac{\partial(\rho w k')}{\partial z}=\frac{\partial}{\partial x}\left(\frac{\mu_t}{\sigma_k}\frac{\partial k'}{\partial x}\right)+\frac{\partial}{\partial y}\left(\frac{\mu_t}{\sigma_k}\frac{\partial k'}{\partial y}\right)+\frac{\partial}{\partial z}\left(\frac{\mu_t}{\sigma_k}\frac{\partial k'}{\partial z}\right)+\mu_t\phi-\rho\varepsilon \tag{4}$$

Turbulent viscosity

$$\mu_t=C_\mu.\rho.\frac{k'^2}{\varepsilon} \tag{5}$$

Turbulence kinetic energy

$$k'=\frac{1}{2}\left(\overline{u'^2}+\overline{v'^2}+\overline{w'^2}\right) \tag{6}$$

Viscous dissipation term

$$\phi=2\mu\left[\left(\frac{\partial u}{\partial x}\right)^2+\left(\frac{\partial v}{\partial y}\right)^2\right]+\mu\left(\frac{\partial v}{\partial x}+\frac{\partial u}{\partial y}\right)^2 \tag{7}$$

Turbulence kinetic energy disappearance equation

$$\frac{\partial(\rho u\varepsilon)}{\partial x}+\frac{\partial(\rho v\varepsilon)}{\partial y}+\frac{\partial(\rho w\varepsilon)}{\partial z}=\frac{\partial}{\partial x}\left(\frac{\mu_t}{\sigma_\varepsilon}\frac{\partial\varepsilon}{\partial x}\right)+\frac{\partial}{\partial y}\left(\frac{\mu_t}{\sigma_\varepsilon}\frac{\partial\varepsilon}{\partial y}\right)+\frac{\partial}{\partial z}\left(\frac{\mu_t}{\sigma_\varepsilon}\frac{\partial\varepsilon}{\partial z}\right)+C_{1\varepsilon}\mu_t\frac{\varepsilon}{k'}\phi-C_{2\varepsilon}\rho\frac{\varepsilon^2}{k'} \tag{8}$$

The model constants C_μ, $C_{1\varepsilon}$, $C_{2\varepsilon}$, σ_k and σ_ε have typically default values for used standard k-ε turbulance model [8]. The values of these constants have been arrived at by numerous iterations of data fitting for a wide range of turbulent flows. These are as follows;

C_μ =0.09, $C_{1\varepsilon}$ = 1.44, $C_{2\varepsilon}$ = 1.92, σ_k = 1 and σ_ε = 1.3.

Reynolds number is calculated by the equation given below;

$$Re=\frac{V_\infty.D_h}{\nu} \tag{9}$$

Here, D_h is the hydraulic diameter of the jet inlet

$$D_h=\frac{4A_c}{P}=\frac{4(a.W)}{2(a+W)} \tag{10}$$

where A_c is the cross-section area of the jet inlet, P is the perimeter of the jet inlet.

The Nusselt number is evaluated as the conductive heat transfer rate of the fluid over the solid boundary equal to the convective heat rate as:

$$-k\left(\frac{dT}{dn}\right)_{surface} = h\left(T_{\infty} - T_s\right) \text{ and } Nu = \frac{h.D_h}{k} \tag{11}$$

Where h is the local heat transfer coefficient on the surface, n is the vertical direction to isotherm and the local Nusselt number is obtained as above.

3. GEOMETRIC MODEL

Perspective view of the channel having sizes was shown in Fig. 1. The boundary conditions can also be seen in this figure. The jet nozzle hydraulic diameter (D_h) was kept at 9.9 mm, the length (L) and width (W) of the channel were taken as 200 mm and 50 mm, respectively. 5.5x50 mm rectangular nozzle with an inlet velocity ranging between 6.23 and 15.58 m/s was used in the study. Uniform velocity profile for jet inlet was existed in the inlet of the rectangular nozzle. The channel height was determined at different measurements as $4xD_h$, $6xD_h$, $10xD_h$ and $12xD_h$. While space between two indentations was taken as D_h, indentation width and height were $2xD_h$ and D_h, respectively. There are five surfaces with square indentation and the constant heat flux ($\ddot{q}$) with 1000 W/m^2 was applied to only these surfaces for all simulations when the top and side surfaces were adiabatic. However, the Reynolds numbers (Re) of the jet ranged from 4000 to 10000.

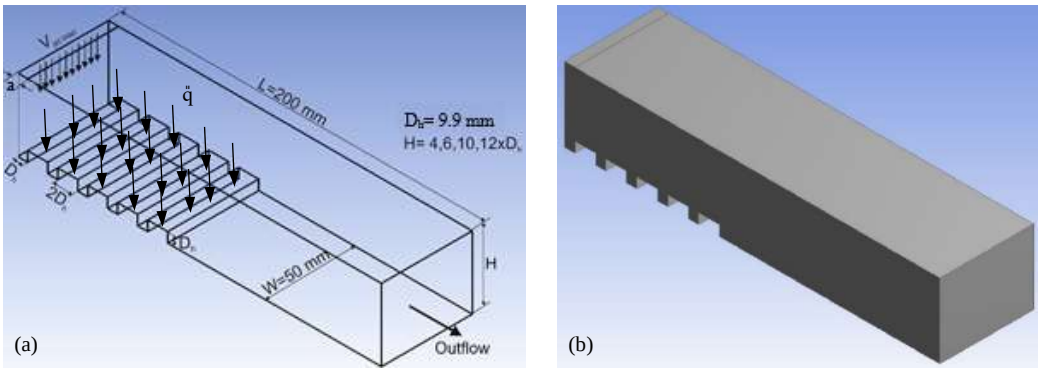

Figure. 1. Perspective view of the channel (a) Domain with boundary conditions and sizes (b) CFD simulation domain

The study was conducted under the following assumptions:

i) The flow field was assumed to be three-dimensional, steady-state and turbulent for the channel;
ii) Calculations were carried out for incompressible fluid;
iii) Air was used as working fluid for the cooling of indentation surface;
iv) Constant heat flux of 1000 W/m^2 was applied to indentation surfaces;
v) Thermal properties of the fluid were constant;
vi) There was no heat generation for both the jet fluid and the solid surfaces

4. RESULTS and DISCUSSION

Figure 2 exhibits a comparison of the effects of Re number with 6000 and 8000 on the Nu number as experimental and numerical for jet-to-plate distance (H/D_h) value of 6 between Kilic et al. [9] and the present study numerically. The comparison was performed for smooth copper plate surface that was used in [9] at Re numbers of 6000 and 8000. While the deviation of the Nu number between the experimental results of Kilic et al. [9] and the present numerical study is 3.99% at Re=6000, it is found as 1% for numerical results at the impingement region. However, difference between the experimental and numerical results increases for Re=8000 at the impingement region due to higher turbulance intensity. When the deviation of numerical results with experimental is 9.15% due to higher turbulance intensity in this region, the difference is 1.02% for the numerical results when compared the present study with Kilic et al. [9]. Therefore, it can be said that the results

of the present study are well comparable with experimental and numerical study results of the Kilic et al. [9] and the numerical study is reasonable and appropriate.

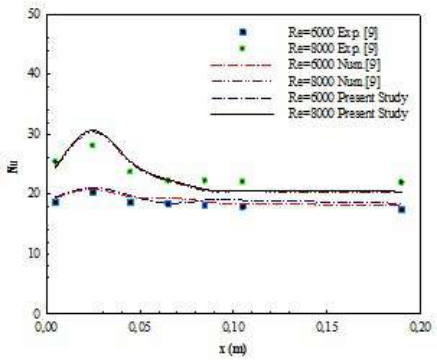

Figure 2. Comparison of the present results and those of Kilic et al. [9]

To determine the effect of the grid size on the mean Nu number and outlet temperature of jet air ($T_{out\text{-}jet}$), a grid independence test (as shown in Table 1) was carried out for H/D_h=4 and Re=4000. The test showed that 1714584 grids on a duct cross-section are adequate (< 0.01 % difference compared with 1954741 grids). Mesh structure of the channel having square patterned surfaces was also shown in Fig. 3 with zoomed image in order to clearly see the mesh shape of the square pattern.

Table 1. Grid independence test results for Nu_m and $T_{out\text{-}jet}$

Mesh Numbers	Nu_m	$T_{out\text{-}jet}$ (K)
1525412	9.7189	324.648
1714584	9.7298	324.663
1954741	9.7297	324.665

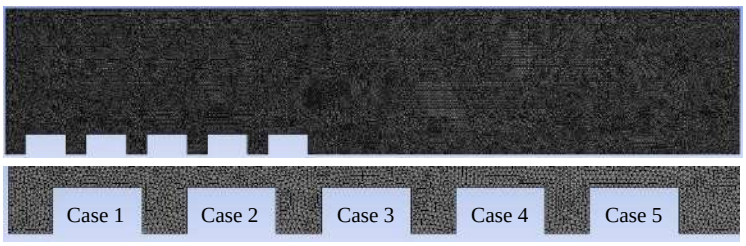

Figure 3. Mesh structure of the channel with circle patterned surface used in calculations

The effects of Reynolds number and H/D_h ratios on the Nusselt number variation for different location cases of rectangular patterned surfaces are shown in Fig. 4. Cases in the graphs indicates the location order of the rectangular surfaces beginning from the left side of the channel. Enhancement in Re number increases the Nu number on the surfaces of the rectangular patterned. Recirculations come into existence at the bottom of the left wall for all Reynolds numbers. These recirculations cause a change of direction of the jet flow. Therefore, values of the highest local Nu number were determined for the case 2 for all Re numbers. However, because the effect of recirculation increases on the location place of the highest local Nu number with increase of H/D_h ratio, the local Nu number values change according to ratio of H/D_h at the different cases from 1 to 5. Average Nusselt number increases of 59.28 % from Re=4000 to Re=10000 for H/D_h =4. Besides, Nu number was less sensitive to H/D_h ratio in the range of H/D_h=4-12. Average Nusselt number decreases of 9.11 % from H/D_h=4

to H/D_h=12 for Re=6000 because of a decline of turbulance intensity. Also, the highest average Nusselt number was attained for Re=10000 and H/D_h =6.

Fig. 5 exhibits the mean surface temperatures of the square patterned for different jet-to-plate distances (H/D_h) of 4, 6, 10 and 12 and Re numbers. Increasing of the Re number provides to reducing of the mean surface temperatures by causing to enhance the turbulence intensity and so heat transfer. However, H/D_h increment from 4 to 12 sharply affects the surface temperature of the case 1 depending on directed of the jet flow thanks to recirculations. While the lowest surface temperature value was obtained for the case of 2, the case 5 was found to have the highest surface temperature due to losing the jet effect and reduction of flow velocity toward exit of the channel for all Re numbers (Figs. 5a-d). A surface temperature increase of 1.83% was observed from the case 2 to case 5 for H/D_h=4 and Re=10000.

It can be seen in Figs. 6A and B, recirculations happen at the bottom of the left wall for analyzed Reynolds numbers. However, these occurred recirculations affect main jet flow and cause to change location of maximum heat transfer point. Besides, recirculation sizes decreases with increasing Re number from 4000 to 10000 due to prevention of expansion of recirculations by increasing jet flow velocity. When the velocity of jet flow is high at the impingement region, it reduces toward channel outlet. Therefore, surface temperatures of the square indentations increase. Because of the separation of the jet flow from the last square surface, recirculations occur. One can see that recirculations increase with increasing jet-to-plate distance H/D_h. Thus, thickness of thermal boundary layer enhances with enhancing recirculations, which causes to increase the temperature. Increasing channel height causes to decrease length of wall jet region. The reason for this is reducing of flow velocity at a longer channel height. Decreasing flow velocity, on the surface of copper indentation plate, causes an increase in temperature.

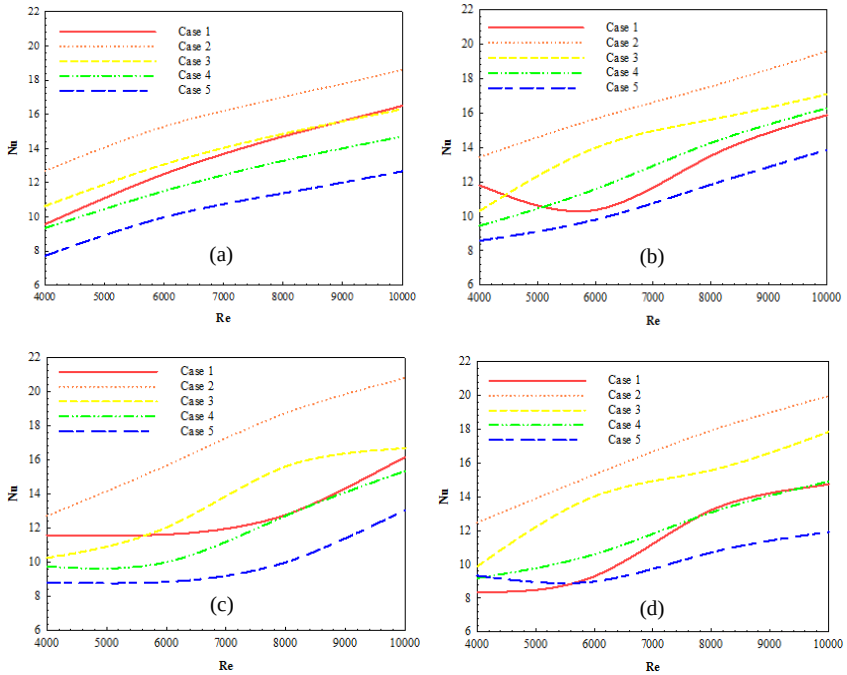

Figure. 4. Variations of mean Nu number versus different Re number for different H/D_h and cases (a) H/D_h=4 (b) H/D_h=6 (c) H/D_h=10 and (d) H/D_h=12

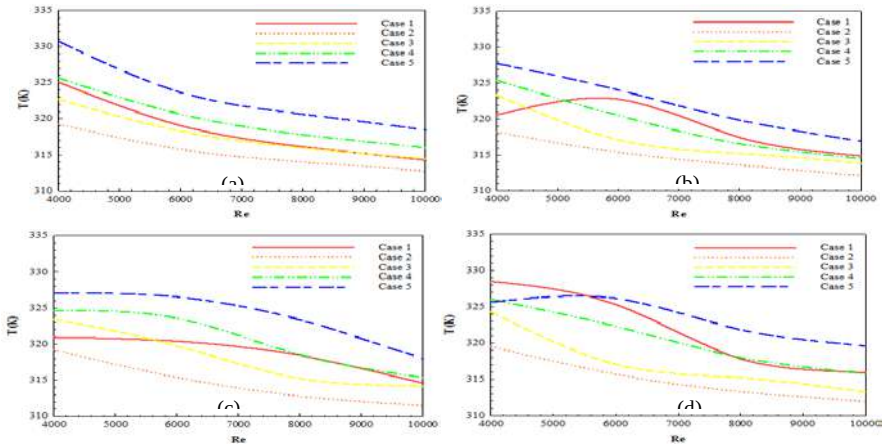

Figure. 5. Variations of mean surface temperature versus different Re number for different H/D_h and cases (a) H/D_h=4 (b) H/D_h=6 (c) H/D_h=10 and (d) H/D_h=12

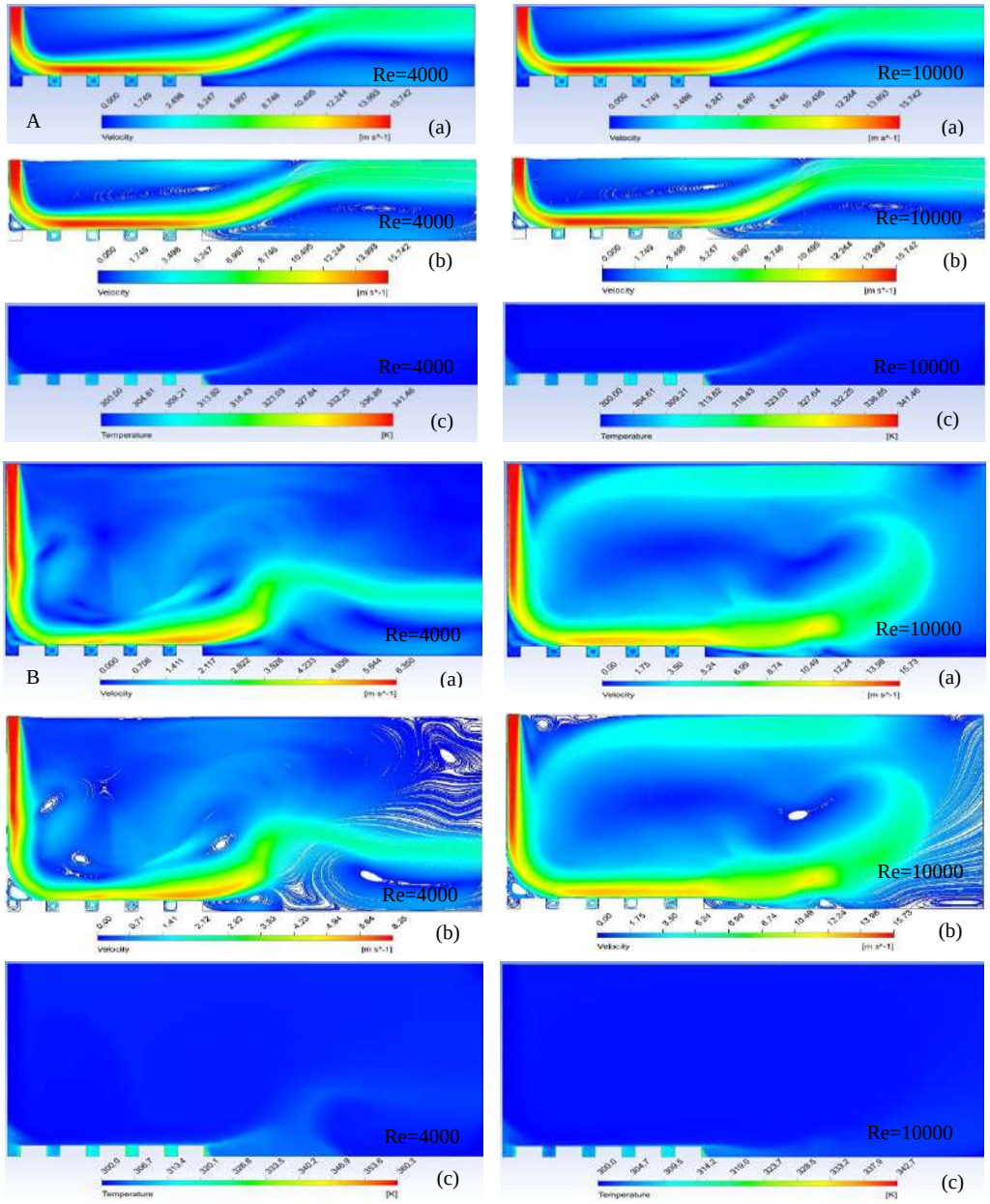

Figure. 6. A-H/D_h=4, B- H/D_h=10 a) Velocity b) Streamline c) Temperature distributions for different Re numbers

Mean Nu numbers and surface temperatures of square indentations and air jet temperature at the outlet of the channel for different Re numbers and H/D_h ratios are given in Table 2. When Nu_m increases with increasing of Re, it decreases with increasing H/D_h ratio from 4 to 12 due to reducing air jet velocity in the impingement region. However, mean surface temperatures of the square indentations enhance with enhancing jet-to-plate distance H/D_h but they decrease with increasing Re number. Besides, outlet temperature of the air jet decreases with enhancing Re number and H/D_h ratio.

Table 2. Results of Nu_m, T_{sm} and $T_{out\text{-}jet\ air}$ for different Re and H/D_h

Square Surface	Nu_m		T_{sm}		$T_{out\text{-}air\ jet}$	
	H/D_h=4	**H/D_h==12**	**H/D_h==4**	**H/D_h==12**	**H/D_h==4**	**H/D_h==12**
Re=4000	9.7298	9.6675	324.663	324.802	302.564	302.541
Re=6000	12.2246	11.1108	319.454	321.312	301.698	301.691
Re=10000	15.4981	15.3918	315.171	315.293	301.001	301.043

5. CONCLUSION

The present study was conducted into the numerical research of heat transfer from a heated square patterned copper surface, indise a rectangular channel by using a single jet flow. The numerical results were compared with the numerical and experimental datas of study existed in literature and found they were in well agreement. The results were presented as the variations of the mean Nu numbers and temperatures for each square patterned indentation surface. The temperature and velocity distributions and streamlines of jet fluid flow and mean surface temperature and Nu values of whole square surfaces and values of air jet outlet temperature were also analyzed for different Re numbers and jet-to-plate distence H/D_h ratios. The following conclusions can be drawn from the numerical results;

-Increase in Reynolds number increases the heat transfer at all jet-to-plate distances. Average Nusselt number increases of 59.28% from Re=4000 to Re=10000 for H/D_h =4. Besides, Nu number was less sensitive to H/D_h ratio in the range of H/D_h=4-12. Average Nusselt number decreases of 9.11% from H/D_h=4 to H/D_h=12 for Re=6000 because of a decline of turbulance intensity. Also, the highest average Nusselt number was attained for Re=10000 and H/D_h =6.

-Recirculations occur at the bottom of the left wall for all Reynolds numbers. These recirculations cause a change of direction of the jet flow. Thus, values of the highest local Nu number were determined for the case 2 for all Re numbers.

- Occurred recirculation sizes decrease with increasing Re number from 4000 to 10000 due to prevention of expansion of recirculations by increasing jet flow velocity.

-When the velocity of jet flow is high at the impingement region, it reduces toward channel outlet. Therefore, surface temperatures of the square indentations increase.

- Increasing the channel height causes to decrease length of wall jet region. The reason for this is reducing of flow velocity at a longer channel height. Decreasing flow velocity, on the surface of copper indentation plate, causes an increase in temperature.

-In a conclusion, the heat transfer, including local and average Nusselt numbers, are significantly affected by jet Reynolds numbers; while it is less sensitive to jet-to-plate distance. Also, it is considered that geometry of air jet and channel used in this study can be employed to cool electronic components due to resembling various electronic equipment application.

REFERENCES

[1]. B. W. Webb and C. Ma, "Single-phase liquid jet impingement heat transfer", *Adv. Heat Transf.*, vol. 26 pp. 105–117, 1995.

[2]. G. M. Carlomagno and A. Ianiro, "Thermo-fluid-dynamics of submerged jets impinging at short nozzle-to-plate distance: a review". *Exp Thermal Fluid Sci.*, vol. 58, pp. 15–35, 2014.

[3]. E. Argus, M. A. Rady and S. A. Nada, "A numerical investigation and parametric study of cooling an array of multiple protruding heat sources by a laminar slot air jet". *Int J Heat Mass Transf.*, vol. 28, pp. 787–805, 2006.

[4]. M. Popovac and K. Hanjalic K, "Large-eddy simulation of flow over a jet-impinged wall-mounted cube in a cross stream", *Int J Heat Fluid Flow*, vol. 28, pp. 1360–1378, 2007.

[5]. Y. T. Yang, C. H. Hwang, "Numerical simulations on the hydrodynamics of a turbulent slot jet on a semicylindrical convex surface", *Num Heat Transfer*, vol. 46, pp. 995–1008, 2004.

[6]. K. S. Mushatat, "Analysis of the turbulent flow and heat transfer of the impingement cooling in a channel with cross flow", *Eng Sci*, vol. 18, pp. 101–122, 2007.

[7]. N. Zuckerman and N. Lior, "Jet impingement heat transfer: physics, correlations, and numerical modeling", *Adv. Heat Transf.*, vol. 39, pp. 565–631, 2006.

[8]. FLUENT User's Guide, Fluent Inc. Lebanon, NH., 2003.

[9]. M. Kilic, T. Calisir, S. Baskaya, "Experimental and numerical study of heat transfer from a heated flat plate in a rectangular channel with an impinging air jet", *J Braz. Soc. Mech. Sci. Eng.*, vol. 39, pp. 329-344, 2017.

ACKNOWLEGMENT

The authors would like to thank Scientific Research Projects Coordination Unit of Cumhuriyet University (Sivas/Turkey) for their financial support to this research under project number TEKNO-021.

BIOGRAPHY

Koray Karabulut is an Assistant Professor in the Electric and Energy Department, Vocational High School of Sivas, Sivas Cumhuriyet University, Sivas, Turkey. He received his Ph.D. degree in Department of Energy in 2015 from the University of Cumhuriyet. His research interests include heat and mass transfer, heat insulation, conservation of energy, plate fin heat exchangers, heat transfer of nanofluids, thermodynamics, fluid mechanics and computational fluid dynamics.

ICENS 4TH INTERNATIONAL CONFERENCE ON ENGINEERING AND NATURAL SCIENCE
2 - 6 May 2018 KIEV UKRAINE

Investigation on Fatigue Behavior of B4C Powder Size in Al 6061-B4C Composites

Abdullah Gocer[1], Cihan Karatepe[2], Mehmet Baki Karamis[3]

Abstract

In this study, the size effect of the B4C reinforcement paticles was investigated in fatigue behavior of aluminum matrix materials. In the composites produced by the powder metallurgy method, three different sizes of B4C particles were used into the Al 6061 matrix material at 10% volume fraction. Al 6063-B4C powders were mixture by the 3D mixturer and mixture powders were compressed at 450 MPa to obtain circular billets, which were then extruded into composite bars. The rotational shear fatigue tests conducted with samples obtained from these bars showed that the fatigue behavior of the composite material improved with the increase of B4C size. Moreover, the graphite addition into the composite did not adversely affect the fatigue behavior of the samples. By examining the fatigue sections of the materials, it was tried to reveal the effects of grain size change on the fracture form.

Keywords: *Composite material, fatigue, powder metallurgy, sintering*

1. INTRODUCTION

Aluminum and its alloys are widely used because of their light weight and strength. Composite materials are very special materials which are formed by combining two or more materials with different physical and chemical properties. Aluminum matrix composites are composite materials that are increasingly used in the industry, because of being lightweight, having high strength and modulus values. Ceramic reinforcements such as SiC, Al2O3 and B4C in Al matrix composites are used to improve mechanical properties [1, 2, 3].

Boron carbide (B4C) is a material increasing in use as a reinforcing phase for Al matrix with high strength and low density values. Therefore, there are many studies examining the hardness, impact, creep and similar mechanical properties of B4C reinforced composites. When we look at studies of fatigue behavior of MMC, we can see that the co-existence of different Al alloys and different reinforcement elements is examined [4, 5, 6]. Studies on the fatigue behaviors of hybrid composites [7, 8] and how heat treatment affects fatigue are encountered in the literature [9, 10].

In this study, fatigue behaviors of Al-B4C composites produced by powder metallurgy under rotational bending force were investigated. In the study, the effects of B4C reinforcement size, graphite reinforcement and heat treatment on fatigue behavior of Al-B4C composites are mentioned.

[1] *Corresponding author: Erciyes University, Engineering Faculty, Department of Mechanical Engineering, 38039, Melikgazi/Kayseri, Turkey. abdullahgocer@erciyes.edu.tr*

[2] *Erciyes University, Engineering Faculty, Department of Mechanical Engineering, 38039, Melikgazi/Kayseri, Turkey. ckaratepe@outlook.com*

[3] *Erciyes University, Engineering Faculty, Department of Mechanical Engineering, 38039, Melikgazi/Kayseri, Turkey. karamisb@erciyes.edu.tr*

2. EXPERIMENTAL STUDIES

a. Manufacturing of Al-B4C Composites

The sizes and volume fractions of the components using in manufacturing of the samples, such as Al 6061, B4C and graphite powders, can be seen in Table 1.

Table 1 Volume fractions of the components used in the composite samples

	Volume fraction of samples (%)		
Sample No	Al-6061	B4C	Graphite
1	%100 (28 µm)	%0	%0
2	%90	%10 (3 µm)	%0
3	%90	%10 (17 µm)	%0
4	%90	%10 (58 µm)	%0
5	%87	%10 (3 µm)	%3 (9 µm)

By the manufacturing of the samples, Al 6061, B4C and graphite powders were mixed by 3D mixturer for 5 hours. To obtain extrusion billets, these powders were mixtured at different volume fraction and compressed at 450 Mpa pressure and then sintered at 550 °C. These billets were extruded at 450 °C with extrusion ratio of 9 (from 30 mm diameter to 10 mm) for obtaining test samples (Figure 1).

Figure 1. Billets and samples a) Billet in the extrusion cartridge b) Extruded samples

Standard test samples were produced from the obtained composites bars by machining in the dimensions shown in Fig. 2 with CNC lathe in convenient precision.

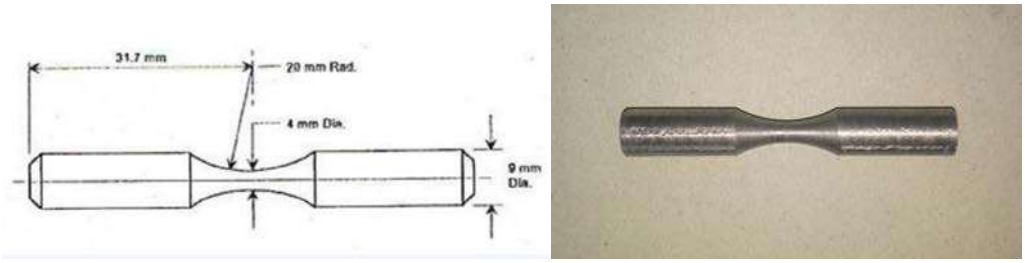

Figure 2. Fatigue test sample and dimensions

T6 heat treatment was applied to the some samples. In this process, materials were kept for 60 minutes at 540 °C. Artificial ageing was terminated by air cooling the samples that kept in oven atmosphere at 180 °C for 5 hours. Fatigue test was performed in HI-TECH rotary fatigue test equipment. The stresses applied to material in this device is shown in Fig. 3.

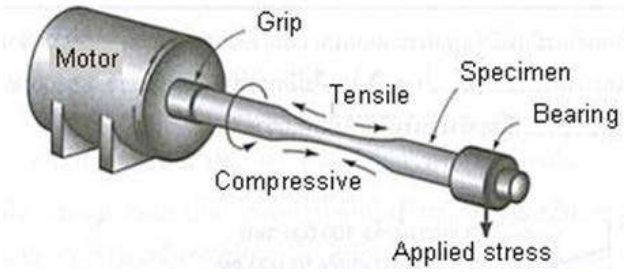

Figure 3. Stresses on rotating fatigue machine

3. RESULTS AND DISCUSSION

a. Examination of The Microstructure

After the manufacturing of the composite materials, the microstructure of the samples were examined and the microstructure images show that the particle distribution is homogeneous (Figure 4). Hardness of the samples were carried out to see how changed the mechanical properties depending on the reinforcement materials and reinforcement sizes. According to the results of the hardness test, as expected, the hardness of the composites is increased by reinforcing B4C into Al 6061 material. With increasing of B4C particle sizes from 3 µm to 58 µm, the hardness of the composite materials also increase (Figure 5). When the hardness of composite materials are examined after T6 heat treatment, it is seen that they are increased in all materials (Figure 5).

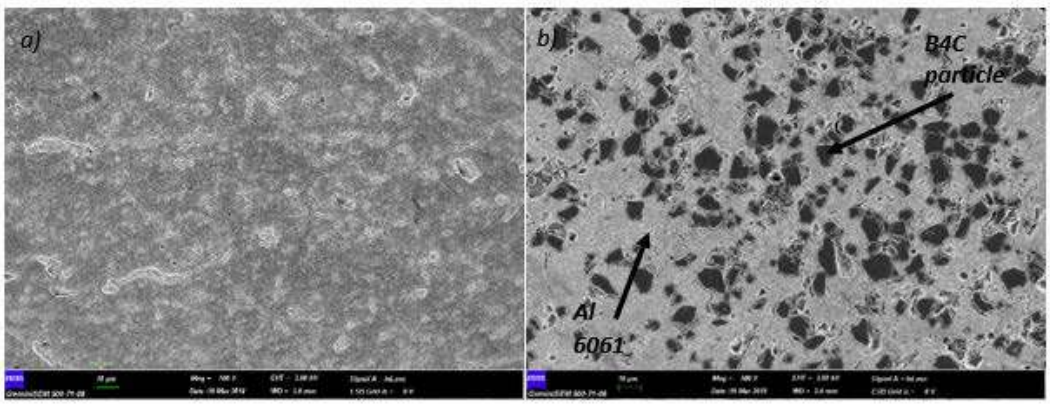

Figure 4. Microstructures of a) Al 6061 material b) Al 6061-B4C composite

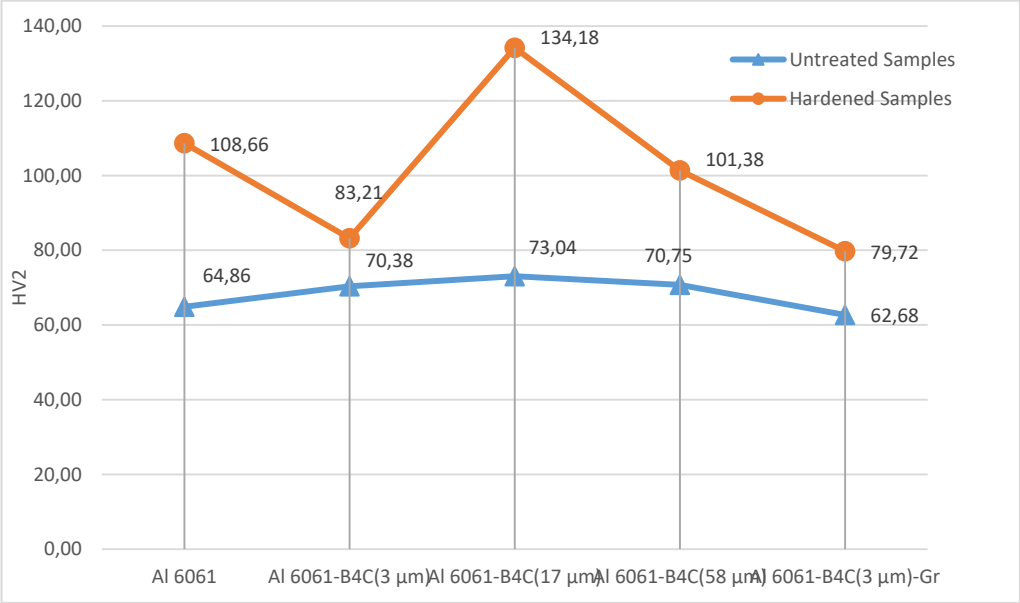

Figure 5. Hardness values of samples with and without heat treatment

b. Fatigue Results

Fatigue tests were performed under the 5 N constant load. Thus, the average stress taken place on the samples;

$$\sigma = \frac{L.P.32}{\pi.d^3}$$

L=125,7 mm)(load-section range)

d=4 mm (section of the material)

P=5 N

σ=100 N/mm^2

The mean values that obtained in three repetitive tests under average stress of 100 N/mm2 were shown graphically in Fig. 6. According to that graphic, it is surprising that, adding the B4C reinforcement into Al 6061 increases the fatigue life of material. Improvement of the fatigue life of composite materials were also observed with the increase of B4C particle size and the best fatigue life among the other was observed with an average powder size of 58 µm. These results are tally up with hardness value of materials.

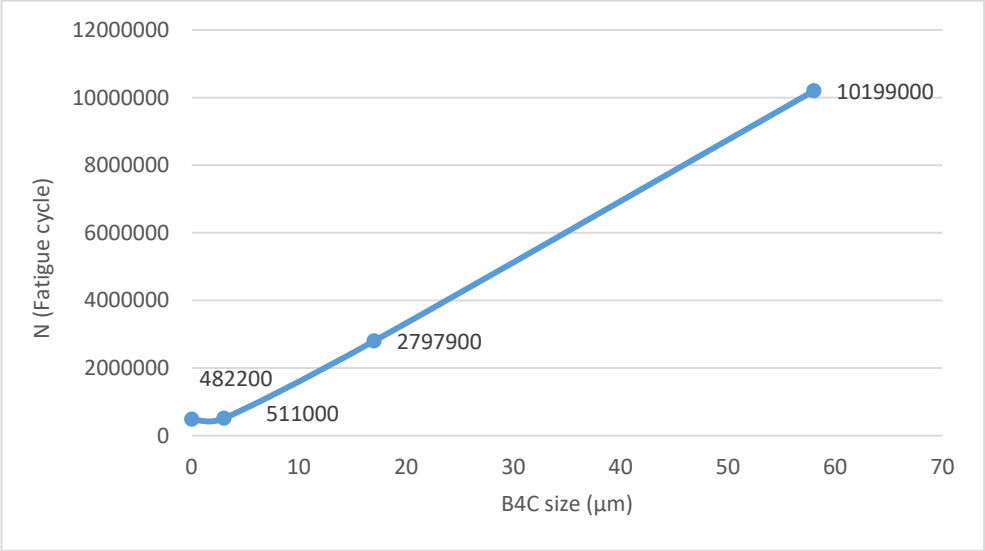

Figure 6. Variation of fatigue cycle with B4C size

There are some researches in literature about manufacturing of hybrid composite materials by reinforced aluminum matrix with ceramic in hard structure and graphite in mild structure. These hybrid structures can give high strength and good tribological properties. In these researches, composites are usually manufactured by casting method. But using of the B4C as reinforcement is also limited. In this case, when we examine the fatigue behavior of Al-B4C-Gr composites produced by powder metallurgy method, graphite reinforcement does not deteriorate the fatigue behavior of the material. Also the fatigue life increases 2 times in the corresponding stress value (Fig. 7).

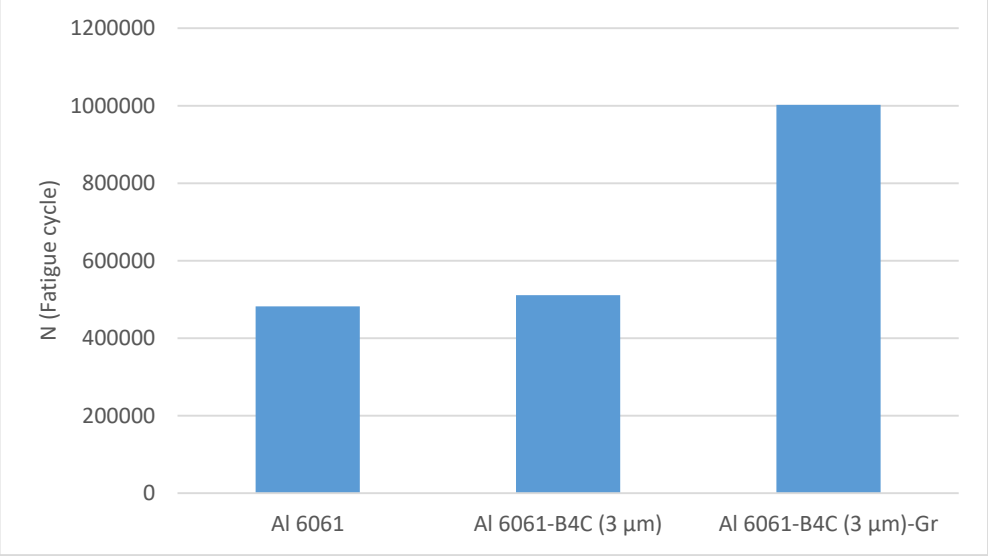

Figure 7. Variation of fatigue cycle with graphite reinforcing

T6 heat treatment is one of the most used heat treatment type used to improve the mechanical properties of Al 6061 materials. Hardness tests were carried out after heat treatment on Al-B4C composites it is obvious that

heat treatment increases the strength values of composite materials. However, increasing of the hardness has not improving on the fatigue life on every material (Fig. 8). While the fatigue lives of Al 6061 and Al 6061-B4C (3 µm) were improved by heat treatment, the other two materials which have larger particle size have shorter fatigue lives.

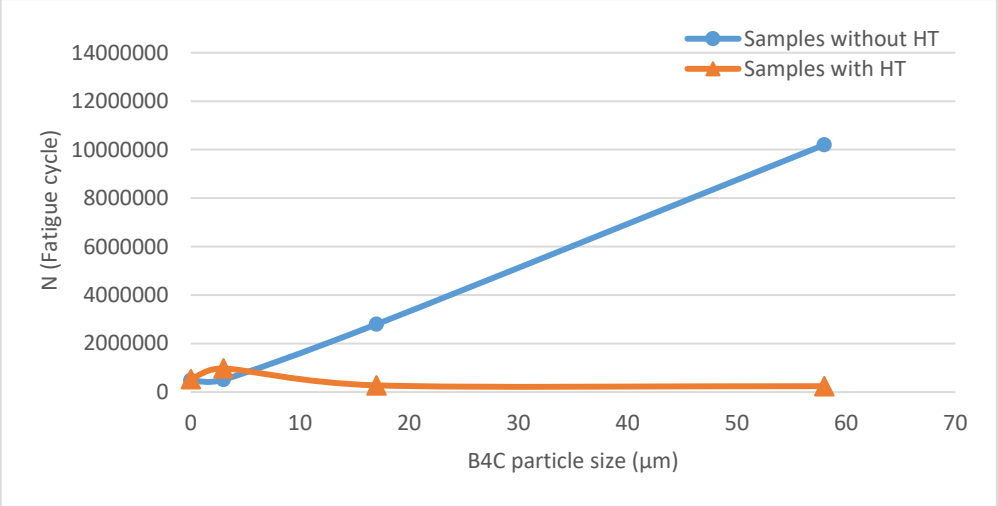

Figure 8. Fatigue cycle of heat treated composite samples

Sudden thermal changes during the heat treatment can cause cracks (in Fig. 9) around the B4C ceramic particles. Possibilities of crack formation and cracks in large size can increase with the particle size of ceramic. Thus, it is possible that the heat treatment can caused to reduce the fatigue life in composite materials.

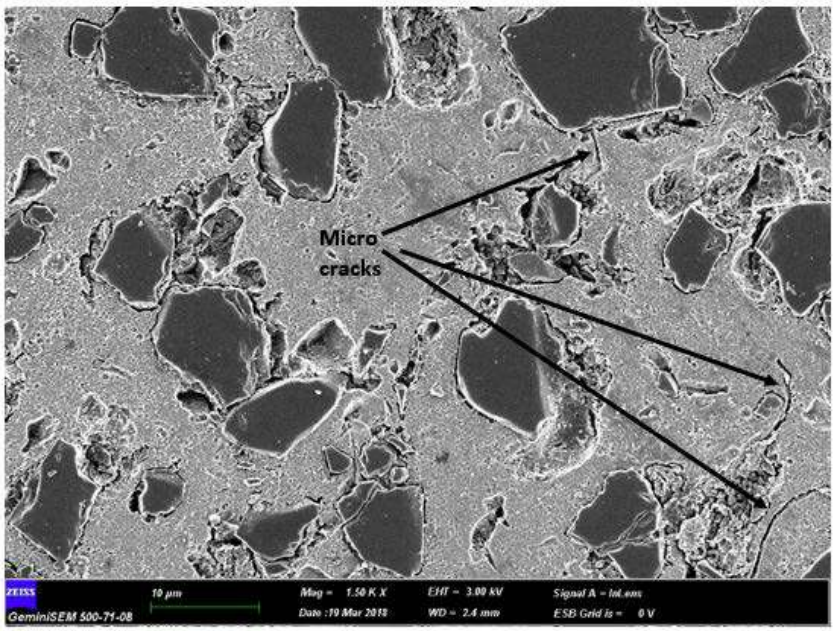

Figure 9. Micro cracks on composite material

When fracture surfaces of fatigue samples are analyzed, the fracture regions i- crack initiation, ii-fatigue crack propagation, iii-catastrophic rupture can be define by color distributions and surface roughness. However, on contrary of standard materials, beach marks are not observed clearly in crack propagation zone. In addition, fractured surface roughness was increased with increasing of B4C particle size (Fig. 10).

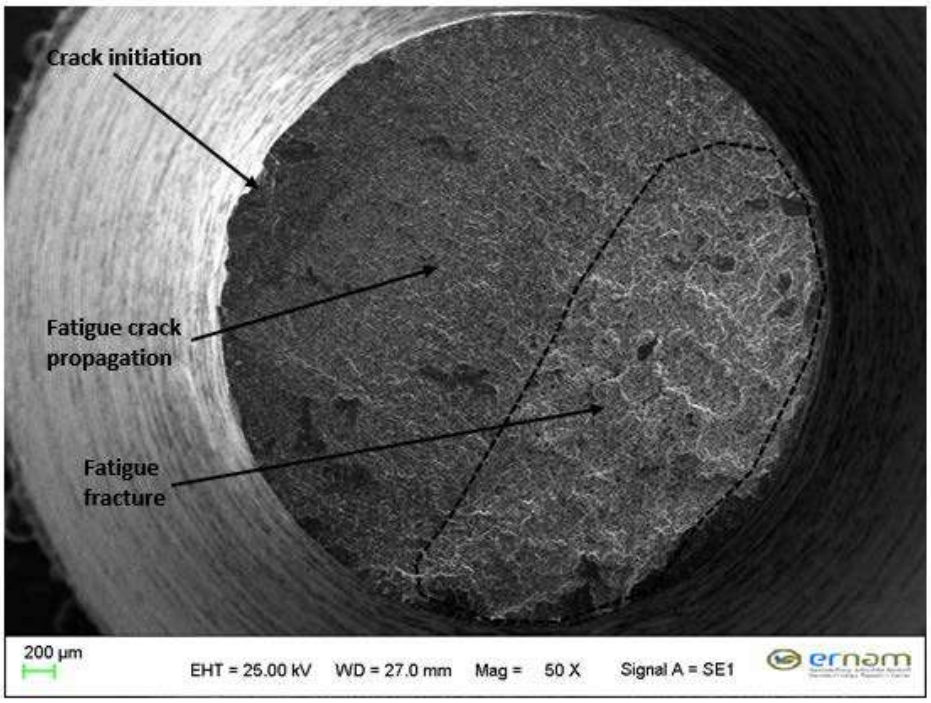

Figure 10. Fatigue crack characterization on crack surfaces.

4. CONCLUSION

The conclusions derived from this study can be summarized as follow:

1. Microstructural analysis and hardness scanning of the samples show that the B4C distribution in the composite materials can be obtained homogenously.

2. Hardness measurements indicate that the presence of B4C reinforcement in Al 6061, increases the hardness of the composite materials. The hardness of the composite materials are also increased by increasing the B4C reinforcement sizes.

3. It was determined that the fatigue life is increased with the B4C particle size by the %10 volumetric ratio. Therefore, highest fatigue life was seen in B4C reinforced material has 58 µm particle size.

4. Fatigue life of Al 6061-B4C (3 µm) composite material increased with graphite reinforcement.

5. In the heat treated materials, fatigue life increased on 3 µm B4C reinforced sample. However, fatigue life on other heat treated materials have larger reinforcement size, highly decreased.

REFERENCES

[1]. I. Topcu, H.O. Gulsoy, N. Kadioglu, A.N. Gulluoglu, "Processing and mechanical properties of B4C reinforced Al matrix composites", Journal of Alloys and Compounds, vol. 482, pp. 516-521, Ap. 2009.
[2]. R. M. Mohanty, K. Balasubramanian, S.K. Seshadri, "Boron carbide-reinforced alumnium 1100 matrix composites: Fabrication and properties", Materials Science and Engineering A, vol. 498, pp. 42-52, 2008.
[3]. K. Shirvanimoghaddam, H. Khayyam, H. Abdizadeh, M.K. Akbari, A.H. Pakseresht, E. Ghasali, M. Naebe, "Boron carbide reinforced aluminium matrix composite: Physical, mechanical characterization and mathematical modelling", Materials Science and Engineering A, vol. 658, pp. 135-149, 2016.
[4]. M.M. Sharma, C.W. Ziemian, T.J. Eden, "Fatigue behavior of SiC particulate reinforced spray-formed 7XXX series Al-alloys", Materials and Design, vol. 32, pp. 4304-4309, Ap. 2011.
[5]. A. Mkaddem, M. El Mansori, "On fatigue crack growth mechanisms of MMC: Reflection on analysis of 'multi surface initiations'", Materials and Design, vol. 30, pp. 3518-3524, 2009.
[6]. B.G. Park, A.G. Crosky, A.K. Hellier, "High cycle fatigue behaviour of microsphere Al2O3–Al particulate metal matrix composites", Composites: Part B, vol. 39, pp. 1257-1269, Feb. 2008.
[7]. M.V. Achutha, B.K. Sridhara, A. Budan, "Fatigue Life Estimation of Hybrid Aluminum Matrix Composites", International Journal on Design and Manufacturing Technologies, vol. 2, pp. 14-21, Jul. 2008.
[8]. A. Afzal, M. Naveed, "Fatigue Behavior of Heat Treated Aluminium Matrix Composites", International Journal of Science and Research, vol. 6, pp. 484-487, Feb. 2017.
[9]. R. Hedge, B.S. Ajaykumar, L.J. Kirthan, V.A. Girish, "Influence of Heat Treatment on Fatigue Behavior of Aluminum Silicon Carbide Graphite Hybrid Composite", International Journal of Applied Engineering Research, vol. 11, pp. 4179-4183, 2016.
[10]. S.L. Yang, C. Xu, Q.L. Lin, B. Ding, "Investigation on microstructure and fatigue behavior of Al-5Zn-2Mg high strength aluminum alloy with T5 heat treatment", Physics Procedia, vol. 50, pp. 19-24, 2013.

ICENS 4TH INTERNATIONAL CONFERENCE ON ENGINEERING AND NATURAL SCIENCE
2-6 May 2018 KIEV UKRAINE

Anaysis Of Recent Occupational Accidents At Seyitomer Thermal Power Plant (Turkey)

Ali Ucar[1], I.Goktay Ediz[1], Ozer Oren[1], Cem Sensogut[2]

Abstract

Occupational health and safety is one of the most important issues in work life of Turkey as all over the world. The importance given to the concepts of Occupational Health and Safety is directly related to the level of development of countries, the level of education, culture and consciousness of the individuals who constitute societies.

In this study statistical graphs were prepared by analyzing the accidents data of Seyitomer Thermal Power Plant (STPP) occupants in the past years by evaluating the accident frequency, impact level and accident rates, including the most important accident causes. Thus, it is aimed to direct the work safety studies in a good manner and to prevent work accidents by the research results obtained. In addition, the firm will be able to assess its adequacy by appropriately evaluating its occupational health and safety activities by taking advantage of the analytical approach in the study.

Keywords:

1. INTRODUCTION

Energy has become an indicator of the economic development of states. With rapidly increasing world populations, industrialization and technological developments, energy needs are also increasing rapidly and energy sources have a vital prospect for society's future. When we look at the energy sources available globally to meet this need, it is stated that the coal with the highest proven reserves is the main energy source with 9707 TWh in today's electricity generation and it is predicted that by 2040 the share of coal production will reach 15305 TWh. It is anticipated that in this framework coal electricity energy production will continue to be of importance and that within the next 23 years' coal-based electricity generation will increase by 60% [1].

The electricity production of Turkey in 2015 was 37,9% from natural gas, 29,1% from coal, 25,6% from hydraulic, 4,5% from wind, 1,3% from geothermal and 1,6% from other sources. On the other side, about 99% of the natural gas and 89% of the petroleum consumed are imported [2], [3]. In addition, about half of the coal consumed in thermal power plants is imported [4].

In order to keep external dependency at acceptable levels in terms of energy security, it is a must to give importance to domestic sources of coal, hydraulics and renewable energy and care should be taken to ensure electricity generation from these sources.

A large part of the energy needs is met by coal thermal power plants in Turkey. Thermal power plants are facilities that convert chemical energy to electricity, which is present in solid, liquid and gaseous fuels. During this conversion process, the water is converted into high-pressure steam by the heat (energy) obtained from various fossil fuels (coal, fuel oil, natural gas etc.) burned in thermal power plants. In other words, with this steam, electric generators are turned very quickly and the electric energy is generated by condensing the electric impulses produced by the effect of the magnets in the generators. There are many interdependent processes in the thermal power plants using coal as fuel such as the transportation of coal produced to the power plant,

[1] *Dumlupinar University, Department of Mining Engineering, 43270, Kutahya, Turkey. goktay.ediz@dpu.edu.tr, ozer.oren@dpu.edu.tr, ali.ucar@dpu.edu.tr*

[2] *Corresponding author Dumlupinar University, Department of Mining Engineering, 43270, Kutahya, Turkey. cem.sensogut@dpu.edu.tr*

storage, circulation in the power plant area, milling of the coal before feeding it to boilers and storing of the ash [5], [6], [7], [8].

Today, the most important issues concerning production processes, production methods, productivity, ergonomics and employees' health are also related directly with the term of occupational health and safety. Thermal power plants are the sectors where there are more dangerous works because of the fact that, compared to other businesses, there are more electric equipment and more high voltage lines.

Organizations managing well their concern of health and safety increase their profitability by minimizing the costs of occupational accidents and diseases while providing competitive advantage in the market. Enterprises with positive security cultures maximize the motivation of their employees by making significant investments in occupational health and safety and increasing workforce productivity.

Today, work accidents, occupational illnesses, incidents that occur depending on working conditions bring out big problems both economically and socially. Occupational health and safety (OHS) is a whole of laws, regulations and the examination and implementation to ensure the protection of employees. As known; the list of precautions to be taken in order to prevent workers from work accidents and to establish a safe working environment is called as safety at work.

98% of occupational accidents and 100% of occupational diseases can be prevented, however the cause or causes of the accident must be known. If they are known, it is possible to prevent and eliminate "occupational accidents" without interrupting the production.

The reasons for occupational accidents as generally accepted are classified under four main headings:

- Causes originating from the law and its implementers,
- Causes from the employer and his/her assignee,
- Reasons sourced from working environment and
- Reasons originating from employees.

The first step in pointing out and avoiding the cause of the accident should be the determination of which of the above titles is involved.

The correct outcome of this process is ensured, first and foremost, by keeping the "accident report" in a real and proper manner. In the accident report, the accident time, place, type, the equipment causing the accident, the duration of the work in the work place, the age and work title of injured occupant, the duration that the injured occupant spent at that work, the intensity of work provided, the education received, the presence of second or third person who may cause the accident, the use of appropriate personal protective equipment, and so on should take place. it is important that information is included correctly. In case of the presence of second or third person at the scene of the incident their statement should also be taken as "eyewitness" [5].

In this study, a detailed analysis of occupational accidents occurring between the years 2015 and 2017 at the Thermal Power Plant of Seyitomer was made in relation with the production values. Accident types were examined and accident frequency, accident weight and accident probability rates were determined.

2. SEYITOMER THERMAL POWER PLANT (STPP)

STPP which is one of the thermal power plants generating electricity from the heat energy formed by the burning of the coal is located in the Seyitomer District, 28 km northwest of Kutahya. 600 MW thermal power plant of Seyitomer is integrally constructed with Seyitomer Lignite Corporation as the fourth unit and represents 1.1% of the total installed capacity in Turkey.

STPP located in the north-west of Turkey with intense demand for electricity has a connection with a 27 km rail line to Eskisehir-Balikesir railway line (Figure 1).

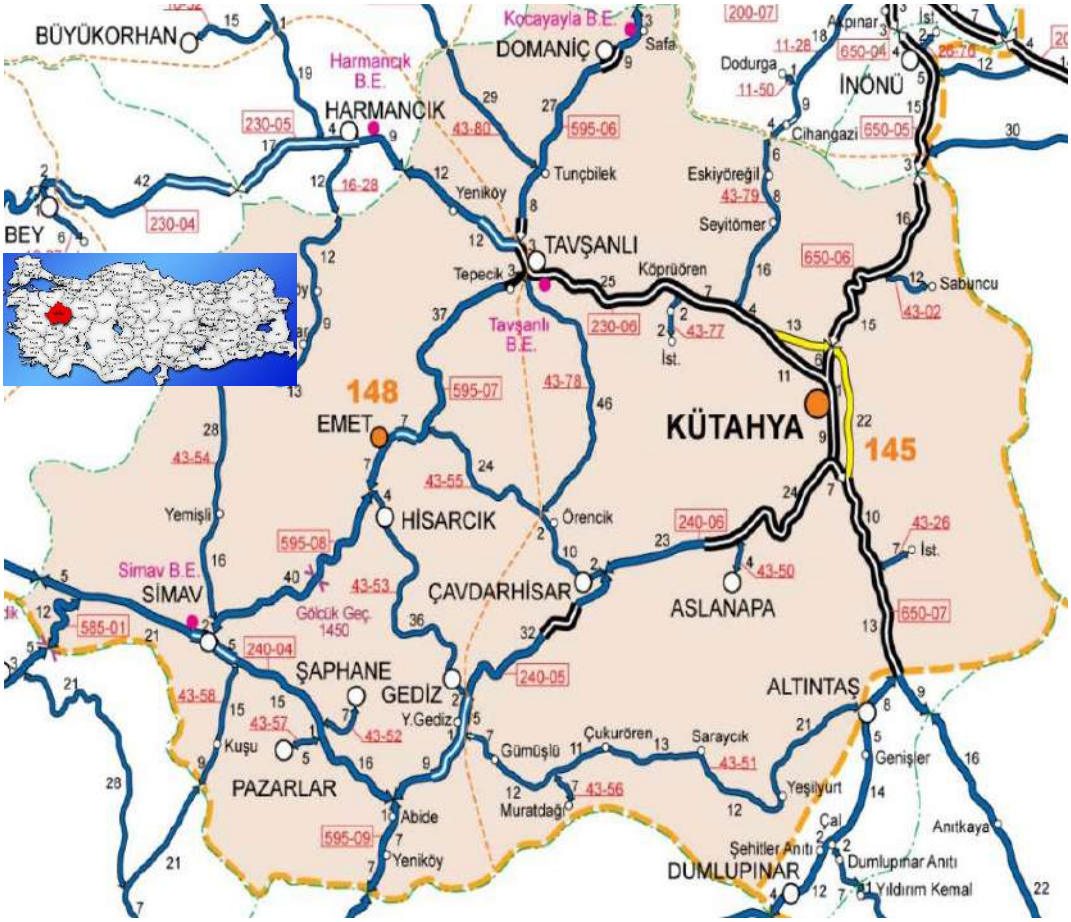

Figure 1 Map of STPP Location

The annual electricity generation capacity of the four units of the power plant consuming 5.9 to 6.6 million tons of coal per year ranges from 3.9 to 4.2 Billion kWh (Table 1). The energy produced at 1st, 2nd and 4th units with the output of 380 kV, and at 3rd unit with the output of 154 kV is supplied to the interconnected system [9].

Table 1. STPP Lignite consumption and energy production between 2015 and 2017

	2015	2016	2017
Lignite consumption (ton)	6 617 480	6 850 480	5 916 710
Energy generation (KWh)	4 131 682 700	4 257 937 090	3 968 254 140

a. Analysis of Work Accidents Between the Years 2015-2017

The work accidents that took place in STPP between 2015-2017 are given in Figure 2. A total of 148 work accidents took place between the years in concern. The types of accidents that took place during these years may be classified under the headings of maintenance, boiler operation, steam production, ash coal operation, mill maintenance, pneumatic maintenance, electrical maintenance, protection and safety, water treatment, mechanical and coil winding workshop. It is very much fortunate to see that all these accidents have not caused any loss of lives.

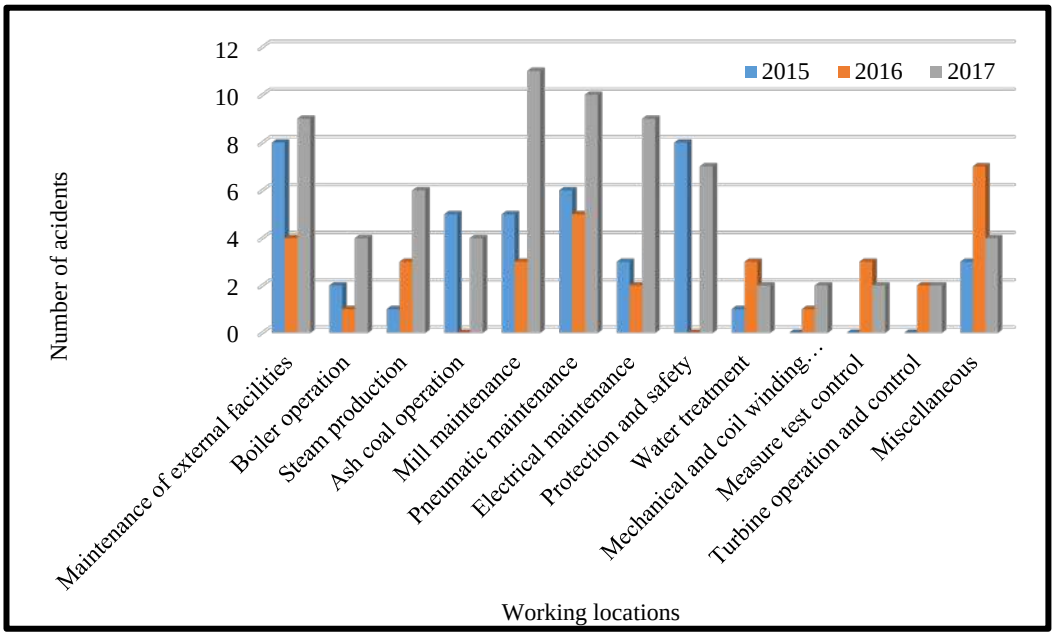

Figure 2. Number of Accidents between 2015 and 2017 by Causes of Occurrence

As seen in Figure 2, the number of accidents according to years is 42, 34 and 72, respectively, and the largest number of accidents occurred in 2017. The highest number of accidents in the year of 2017 occurred in mill maintenance (11), pneumatic maintenance (10) and maintenance of external facilities (9) (Figure 2).

In case of classification according to the causes of occurrences, it was determined that most of the accidents took place in maintenance and control works in the years of concern (Figure 3). The greatest proportion here belongs the year 2017 with a percentage of 62.5. The reason for this is that maintenance and repair work is done too much in this year and the necessary attention is not paid.

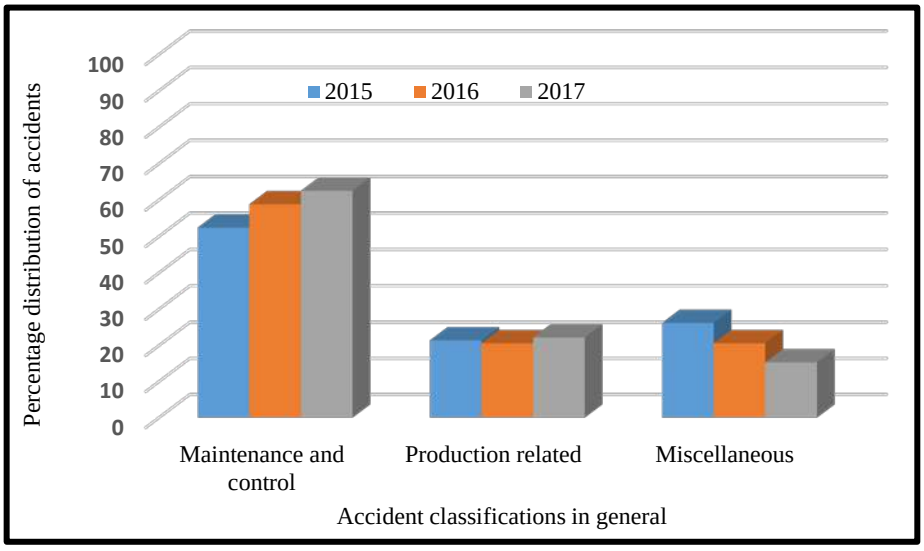

Figure 3. Percentage distribution of the accidents classified according to the occurrence location between the years 2015 and 2017

b. Ratios for Occupational Accidents

Accident frequency ratio, accident weight ratio and accident probability ratio were used in the analysis of the accidents that occurred between 2015 and 2017 at STPP. The equations used in the definition and calculations of these ratios are given below [10], [11], [12], [13]:

Accident Frequency Ratio; It is obtained by dividing the total number of mortal and immortal injuries incurred in work accidents during the year of work by the total work hours of the present year, multiplied by the coefficient of 1.106 (Equation 1). Figure 4 shows the frequency of accidents for the years in concern.

Accident Frequency Ratio = Number of Total Accident x 10^6 / (Total Work Hours) (1)

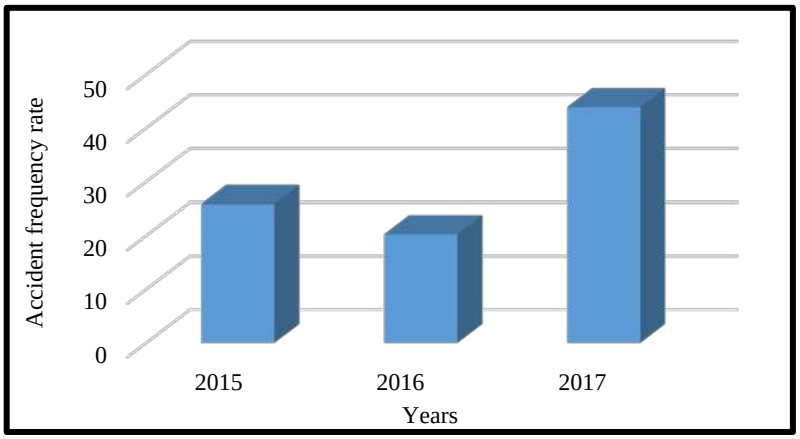

Figure 4. Accident Frequency Ratio for the Years 2015 and 2017

As can be seen in Figure 4, the accidents were most frequently observed in the year 2017 resulting in the accident frequency ratio of 43,92.

Accident Weight Ratio; It is obtained by dividing the total number of days lost due to mortal and immortal injuries occurring during a one-year work period by the total work hours of the present year, multiplied by the coefficient of 1.10^3 (Equation 2). Figure 5 shows the weight of accidents for the years in concern.

Accident Weight Ratio = Number of Lost Days x 10^3 / (Total Work Hours) (2)

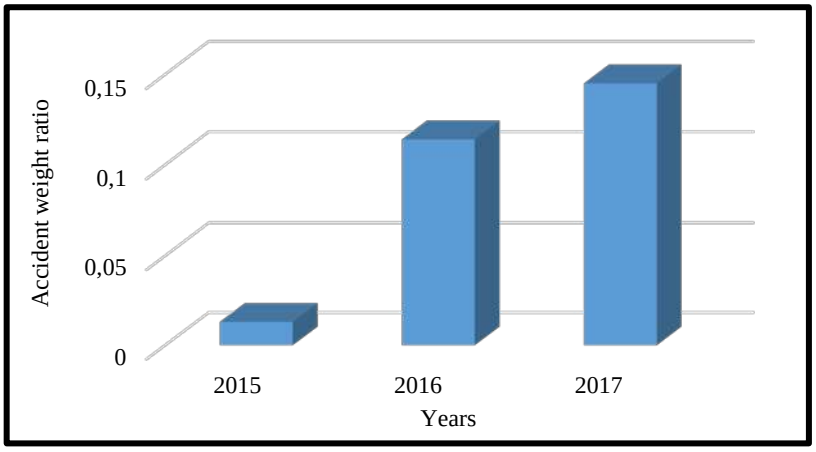

Figure 5. Accident Weight Ratio for the Years 2015 and 2017

As can be seen from Figure 5, the highest accident weight ratio was again obtained in 2017 with a value of 0,145.

Accident Probability Ratio; It is obtained by dividing the total number of mortal and immortal injuries incurred in work accidents during the year of work by the total number of workers of the present year, multiplied by the coefficient of 1.105 (Equation 3). Figure 6 shows the probability of accidents for the years in concern.

Accident Probability Ratio = Total Number of Accident x 105/Total Number of Workers (3)

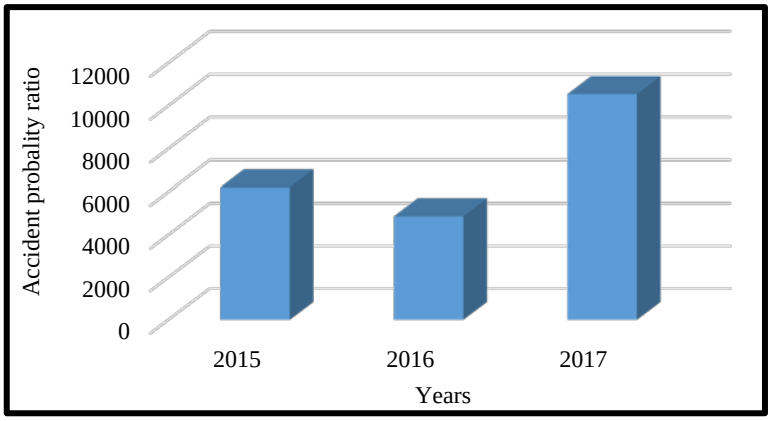

Figure 6. Accident Probability Ratio for the Years 2015 and 2017

Accident probability ratio was also the highest in 2017 with a value of 10 541.2.

The values obtained by using Equations 1, 2 and 3 are also listed in Table 3.

Table 3. Calculated Accident Ratios for the Years 2015 and 2017

	2015	2016	2017
Energy generation (MWh/year)	4 131 628,7	4 257 937,09	3 968 254,14
Coal consumption (ton/year)	6 617 480	6 850 480	5 916 710
Energy generation/accident (MWh/accident)	98 372,11	125 233,44	55 114,64
Total Number of Accident	42	34	72
Working Hours	1 624 800	1 677 600	1 639 200
Number of Workers	677	699	683
Lost Working Day Due to Accident	21	191	238
Accident Frequency Ratio	25,85	20,27	43,92
Accident Weight Ratio	0,013	0,114	0,145
Accident Probability Ratio	6 203,8	4 864,1	10 541,2

It is seen in Table 3 that the production decreases with increasing accidents at work.

3. RESULTS AND SUGGESTIONS

The concept of OHS has begun to take its place among the issues that enterprises around the world have been focusing on in the present century. There is also an increase in productivity with the production at workplaces provided by OHS.

Within the scope of the present study, the results of work accidents at the Seyitomer Thermal Power Plant between 2015 and 2017 were analyzed and the following results were obtained:

- 148 occupational accidents were recorded at STPP between the years in concern, however, none of the employees lost their lives,
- The number of accidents has reached a peak in 2017 with a value of 72,
- The highest rate of accidents in joint work areas was 62.5% in 2017 for maintenance and control work.

- Additionally, accident frequency, accident weight and accident probability ratios in 2017, were also the highest,
- Production and productivity have fallen in parallel with the increase in accidents,
- When the accidents were examined cumulatively, it was understood that most of the accidents had resulted from personal negligence of the workers.
- It is understood that the accidents are caused by human errors in large part.

Periodic maintenance and controls are important in thermal power plants counted in a very dangerous work sector. Employees in this field should be well trained and conscious of OSH aspects.

ACKNOWLEDGMENT

The authors of the paper would like to thank the authorities of the Western Lignite Corporation Directorate for their understanding and for providing necessary data during the research.

REFERENCES

[1]. IEO, International Energy Outlook 2016; U.S. Energy Information Administration, www.eia.gov.tr
[2]. MoE&U, 2012; Ministry of Environment and Urbanization, MET Guide for Large Combustion Plants using Coal (in Turkish)
[3]. BOTAS Strategy Development Department 2016, Sector Report, http://www.botas.gov.tr.
[4]. EMRBT, Energy Market Regulatory Board of Turkey, 2016; Report for Electricity Market Sector (in Turkish)
[5]. Kaynak, S. O. and Kaynak, D., 2009, A Different Look into the Occupational Accidents and Suggestions, OHS Symposium in Mines, 19-20 Nov., Adana (in Turkish).
[6]. MoE&U, 2016; Ministry of Environment and Urbanization, Sectoral Guide, Power Plants, General Directorate of Environmental Management
[7]. Basaran, M., 2017, Coal Burning Power Plants, Power Plants in Turkey, Publication No: MMO/668, ISBN: 978-605-01-1018-0 (in Turkish), Ankara.
[8]. Anar, A., 2017, Process Security at Thermal Plants, Power Plants in Turkey, Publication No: MMO/668, ISBN: 978-605-01-1018-0 (in Turkish), Ankara.
[9]. www.celiklerholding.com.tr (Access date: 25.02.2018).
[10]. Balci, B., Balci, MO., Tackin, E. & Yerden, EA., 2013, Financial Loss at Work Accidents, Journal of Social Sciences, pp72-74 (in Turkish).
[11]. Aritan, A.E. & Ataman, M., 2017, Work Accident Analysis with Accident Ratio Calculations, Afyon Kocatepe University, Journal of Science and Engineering, 17, pp239-246 (in Turkish).
[12]. Erginel, N. & Toptanci, S., 2017, Modelling of Occupational Accident Data with Probability Distributions, Journal of Engineering & Design, 5, pp201-212
[13]. Bayraktar, B., Uygucgil, H. & Konuk, A., 2017, Statistical Analysis of Work Accidents in Turkey Mining Sector, Int. Symp. on Occupational Health & Safety in Mines, 2-3 Nov., Adana-Turkey, pp147-159

ICENS 4TH INTERNATIONAL CONFERENCE ON ENGINEERING AND NATURAL SCIENCE
2-6 May 2018 KIEV UKRAINE

Evaluation Of Work Accidents Recently Occurred In Seyitomer Lignite Corporation (Turkey)

Ali Ucar[1], Cem Sensogut[2]

Abstract

Energy has presently become one of the main factors affecting the international relations and the economic, political and social development of the countries. In addition, the increase in energy consumption and the expectation of continuation of this increase cause countries to desire to reach their energy sources cheaply, uninterruptedly and reliably. The coal, which is one of these sources, will become even more important. However, it is of vital importance that the coal is presented in the most economical and safe manner for consumption. Given the fact that the highest occupational accidents are experienced in the mining business, it will be better understood.

There are many ways and means of preventing accidents. But it is also evident that it will be difficult to prevent them without analyzing the origin and cause of the accidents. For this reason, in this study, an analysis of the occupational accidents in the recent years (2015-2017) took place in the work places of Seyitomer Lignite Corporation (SLC), which has about 6 million tons of coal production per year, was carried out. Accordingly, the weight ratio, frequency ratio and probability ratios of the accidents were determined. In this study, it was determined that the accidents were caused by human error in large scale.

Keywords: Work accidents, Accident ratios, Lignite mining

1. INTRODUCTION

It is not possible to realize long-term economic growth without the contribution of fossil energy resources including coal. Coal currently accounts for more than 40% of world electricity production and is expected to continue to make a significant contribution to energy security in the future. The existing coal reserves in the world are about 985 billion tons and distributed throughout the entire continents and more than 100 countries and have a high reserve/consumption ratio (127 years) compared to other sources. This makes it secure in supply with lower cost. In Turkey, the majority of visible lignite reserves are spread across the country in a total of 16 billion tons and these reserves constitute 92% of Turkey's total coal reserves. For this reason, lignite appears to be the only domestic coal option in electricity generation. [1].

Rapid technological developments and increasing energy production serve the comfort of human beings, on the other hand putting human life and environment into danger. Mining is an industrial sector in which the coal sector is a labor-intensive and widespread employment area, where production environments are constantly changing and nature is being tackled. For this reason, it is one of the riskiest employment sector where occupational accidents are frequently encountered.

Occupational health and safety (OHS) is a globally concerned issue. But the legal safeguard mechanisms introduced in the constitution, the legislation and all the work safety legislation do not have any meaning other than the wishes on the paper if they are not adequately informed about protecting and operating these safeguards in all concerned environment and persons. For this reason, work accidents continue to increase, contrary to the decline, and they are in the foreground on the Earth. Moreover, the fact that poor occupational health and safety

[1] *Dumlupinar University, Department of Mining Engineering, 43270, Kutahya, Turkey. ali.ucar@dpu.edu.tr*

[2] *Corresponding author: Dumlupinar University, Department of Mining Engineering, 43270, Kutahya, Turkey. cem.sensogut@dpu.edu.tr*

practices account for more than 4% of countries' Gross National Product (GDP) costs, reveals how much this is necessary [2], [3].

Accidents at work cause serious burdens on workers, as well as their employers, employees' relatives, society and the country. It is also the reason for high costs, lack of continuity at work, loss of time [4]. For these reasons, it is of utmost importance to disseminate work safety culture and to ensure work safety management in order to prevent occupational accidents, to reduce the effects of these events, and to create healthier and safer working environments in the workplace [3].

Another issue is the responsibilities and legal arrangements of the parties in terms of occupational health and safety. The most important duty in this regard is in the share of the employer. The employer has responsibilities arising from private law and public law. It is possible to see the responsibility arising from private law under three main headings. It is the responsibility of the employer to protect, to provide a suitable work place and to provide adequate shelter space for the workers. Workers have started to give more importance to this issue in recent years in order to be in a healthy working environment as well as the employers to have a qualified staff, loss of time and.

By acting in a manner that is cheaper to prevent than to pay, we can reduce the potential accidents and eliminate dangerous environments if we can detect the sources of danger in the workplace and control the risks that may arise from them. The starting point of preventing the accident should determine the reasons for the accident and the precautions to eliminate them. Any precautions to be taken will also bring about monetary spending. The causes of the accidents can be examined in three parts, direct, indirect and main. The necessary work should be undertaken to address the unhealthy and dangerous working conditions that lead to the indirect causes. These studies mainly include: analysis of accident records, improvement of working conditions, development of safer working methods, training, use of appropriate equipment, effective control and maintenance. Precautions must be taken to minimize the likelihood of undesirable elements or the emergence of high energy for direct causes. In addition to first aid, there should be opportunities for rescue, medical assistance, and the transfer of the patient to the hospital. In addition, the availability of protective materials for miners and their use when necessary will have positive results [5].

Planned work control and risk analysis, proactive (preventive) and reactive (corrective) measures are used effectively and widely throughout the workplace are important issues to establish a safe workplace in avoiding possible accidents at work. The recurrence of an event cannot be avoided if its reason is precisely determined.

It is important to note that education plays an important role in solving OHS problems, and it should always be emphasized that it is as important as management and organization that employers and employees improve their job security awareness.

In this study, the occupational accidents that occurred in SLC between 2015-2017 associated with production values were analyzed by evaluating the most important causes of accidents together with accident rates. Thus, with the results of the research, it is aimed to suitably direct work safety studies and prevent work accidents. In addition, firms will be able to accurately assess their occupational health and safety activities and to measure their competencies by taking advantage of the analysis approach in the present work.

2. SEYITOMER LIGNITE CORPORATION

SLC located in the north-west of Kutahya city center has a connection with a 27 km rail line to Eskisehir-Balikesir railway line and a 11 km roadway to Kutahya-Tavsanli motorway (Figure 1).

SLI coals are low calorie, high ash and humidity lignite, and some are washed and most of them are sieved for more electricity production. However, from time to time more quality parts are domestically consumed.

SLC performs the average annual production of 6 000 000 tons of lignite which is about 10% of Turkey's lignite production. The total lignite reserves of SLC is around 200 million tons. This constitutes 1.4% of the total lignite reserve of Turkey. Lignite production is carried out by the open cast method, and the overburden is removed using dragline with shovel + truck while coal production is realized by shovel + truck system. Lignite production at SLC between 2015 and 2017 is given in Table 1 [6], [7].

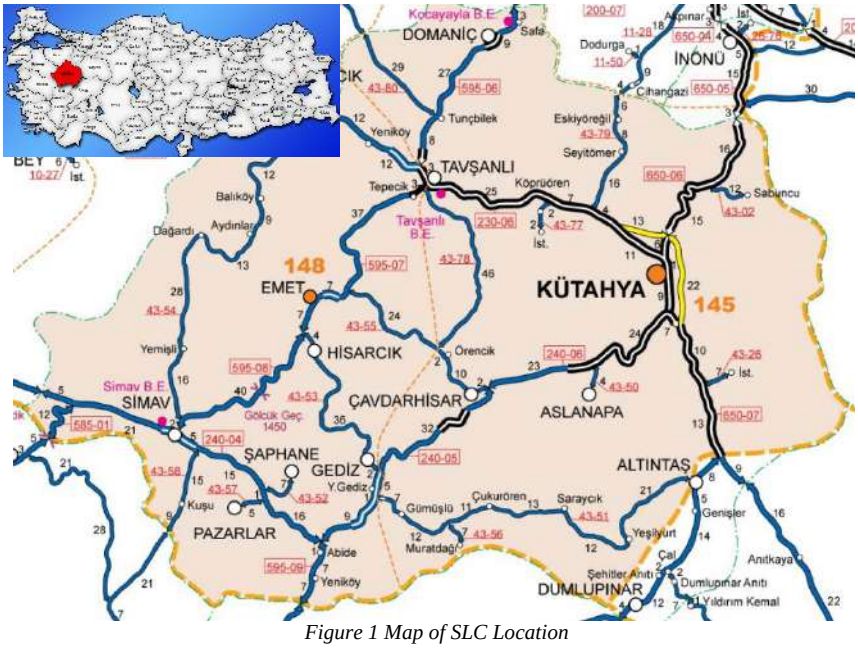

Figure 1 Map of SLC Location

Table 1. Lignite and Energy Production Values at SLC between 2015 and 2017

	2015	2016	2017
Lignite production (ton)	6 617 480	6 850 480	5 916 710
Energy production (MWh/year)	4 131 682 700	4 257 937 090	3 968 254 140

a. Analysis of Work Accidents Between the Years 2015-2017

As a result of a single accurate determination of the accidents, the way to make a total opinion is through statistics. Each workplace and firm line can find the actual cause of the accidents by using relevant reports, statistical techniques

The work accidents that took place at SLC between 2015-2017 are given in Figure 2. A total of 100 work accidents took place between the years in concern. The types of accidents that took place during these years may be classified under the headings of operation of machinery, production, facilities branch, protection and safety, coal processing plant, electrical maintenance and others. It is very much fortunate to see that all these accidents have not caused any loss of lives.

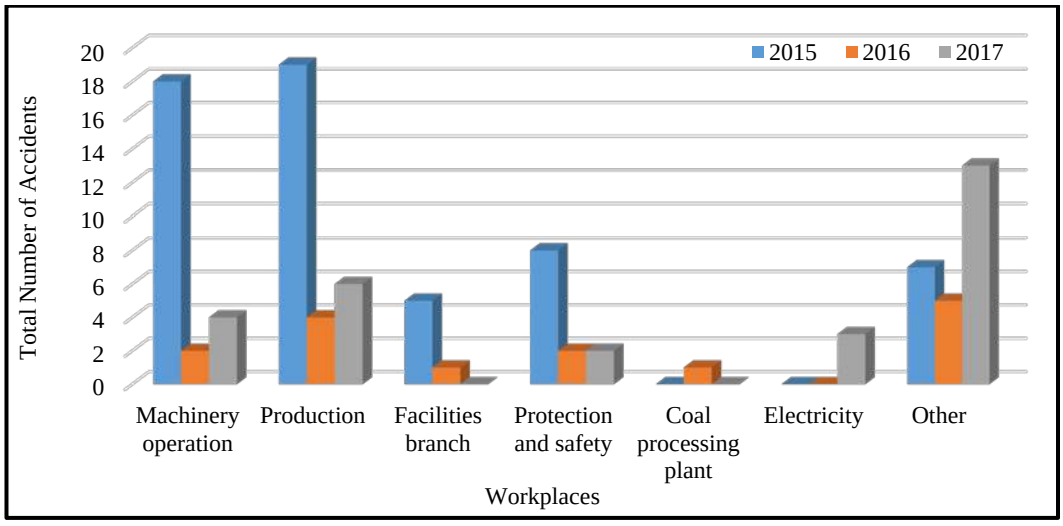

Figure 2. Number of Accidents between 2015 and 2017 by Causes of Occurrence

As can be seen from Figure 2, the number of accidents according to years in concern is 57, 15 and 28, respectively. The highest number of accidents took place in 2015 (production -19, machinery operation -18 and protection & safety -8).

In case of classification according to the occurrence of the incidents, it is determined that the accidents mostly took place in the other works in 2016 and 2017 and in maintenance and repair works in 2015 (Figure 3).

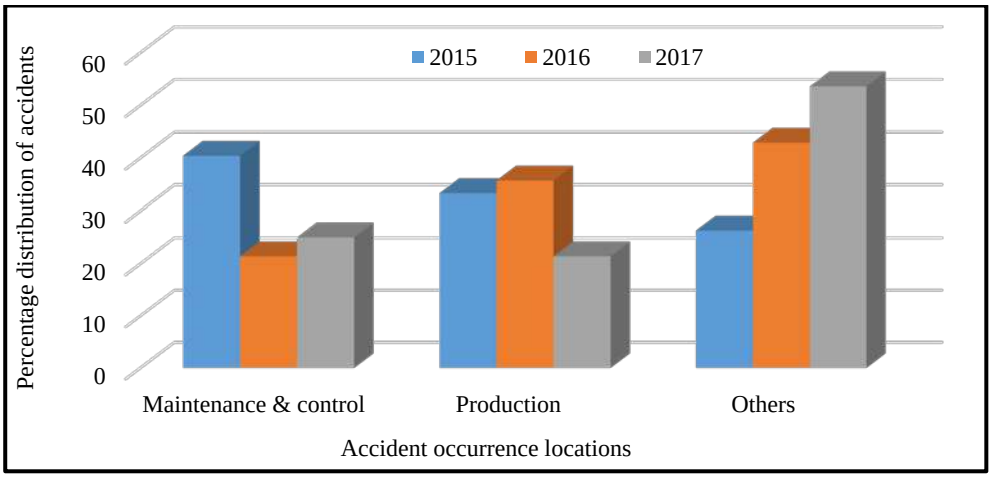

Figure 3. Percentage distribution of the accidents classified according to the occurrence location between the years 2015 and 2017

b. Ratios for Occupational Accidents

In the quantitative analysis of accident data, the frequency of accidents, accident weight ratio and probability of accident indicators are widely used for the examination of occupational accidents and comparisons related to accidents [8]. These ratios were used in the analysis of the accidents that occurred between 2015 and 2017 at SLC. The equations used in the definition and calculations of these ratios are given below [3], [4], [9], [10]:

Accident Frequency Ratio; It is obtained by dividing the total number of mortal and immortal injuries incurred in work accidents during the year of work by the total work hours of the present year, multiplied by the coefficient of 1.106 (Equation 1). Figure 4 shows the frequency of accidents for the years in concern.

$$\text{Accident Frequency Ratio} = \text{Number of Total Accident} \times 10^6 / (\text{Total Work Hours}) \quad (1)$$

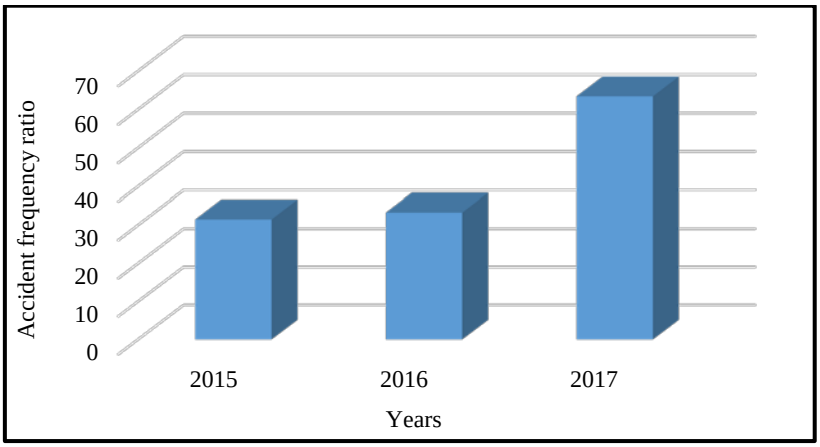

Figure 4. Accident Frequency Ratio for the Years 2015 and 2017

As can be seen in Figure 4, the accidents were most frequently observed in the year 2017 resulting in the accident frequency ratio of 63,4.

Accident Weight Ratio; It is obtained by dividing the total number of days lost due to mortal and immortal injuries occurring during a one-year work period by the total work hours of the present year, multiplied by the coefficient of 1.10^3 (Equation 2). Figure 5 shows the weight of accidents for the years in concern.

Accident Weight Ratio = Number of Lost Days x 10^3 / (Total Work Hours) (2)

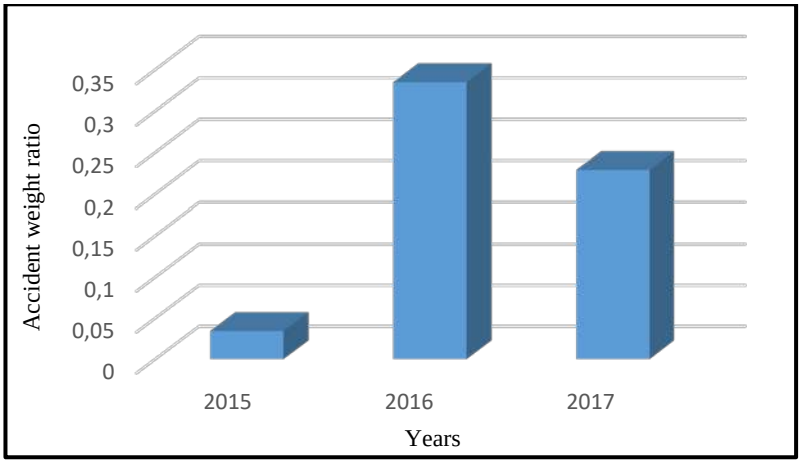

Figure 5. Accident Weight Ratio for the Years 2015 and 2017

As can be seen from Figure 5, the highest accident weight ratio was again obtained in 2016 with a value of 0,3346.

Accident Probability Ratio; It is obtained by dividing the total number of mortal and immortal injuries incurred in work accidents during the year of work by the total number of workers of the present year, multiplied by the coefficient of 1.10^5 (Equation 3). Figure 6 shows the probability of accidents for the years in concern.

Accident Probability Ratio = Total Number of Accident x 10^5/Total Number of Workers (3)

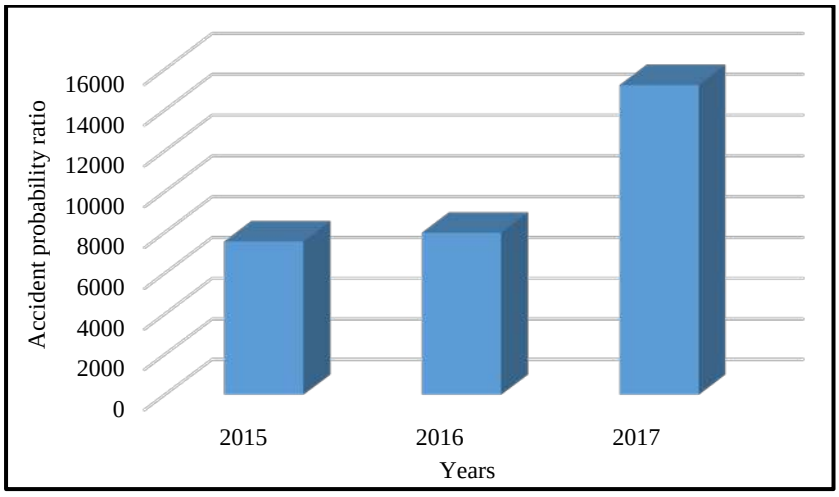

Figure 6. Accident Probability Ratio for the Years 2015 and 2017

Accident probability ratio was also the highest in 2017 with a value of 15217,4.

The values obtained by using Equations 1, 2 and 3 are also listed in Table 2.

Table 3. Calculated Accident Ratios for the Years 2015 and 2017

	2015	2016	2017
Coal production (ton/year)	6 617 480	6 850 480	5 916 710
Coal production/accident (ton/accident)	116 096	456 698	212 311
Total Number of Accident	57	15	28
Working Hours	1 812 000	451 200	441 600
Number of Workers	755	188	184
Lost Working Day Due to Accident	62	151	101
Accident Frequency Ratio	31,46	33,24	63,41
Accident Weight Ratio	0,0342	0,3347	0,2287
Accident Probability Ratio	7 549,6	7 978,7	15 217,4

3. RESULTS AND SUGGESTIONS

The concept of OHS has begun to take its place among the issues that the companies in the world have been focusing primarily on over the last century. There is also an increase in productivity with the production at workplaces where the OHS is provided appropriately.

Within the scope of the present study, the results of work accidents at Seyitomer Lignite Corporation between 2015 and 2017 were analyzed and the following results were obtained:

- 100 occupational accidents were recorded at SLC between the years in concern, however, none of the employees lost their lives,
- The number of accidents has reached a peak in 2015 with a value of 57,
- The highest rate of accidents in joint work areas was 53.5% in 2017 for other works while it was 40,4% in 2015 for maintenance and control works,
- Additionally, accident frequency and accident probability ratios were the highest in 2017. However, the ratio of accident weight was also the highest in 2016,
- The rate of production per accident is the lowest in 2015, and the year with the highest accidents is again 2015,

- Production and productivity have fallen in parallel with the increase in accidents,
- When the accidents were examined cumulatively, it was understood that most of the accidents had resulted from personal negligence of the workers.

Taking into account the results of this study, it is important that workers become more aware of the OHS issues in the area of coal production, which is very dangerous sector in particular. These accidents can mostly be counted as preventable accidents resulting from the lack of training and neglect of employees as in other sector. Most of the accidents can be considered as the result of personal behavior.

ACKNOWLEDGMENT

The authors of the paper would like to thank the authorities of the Seyitomer Lignite Corporation Directorate for their understanding and for providing necessary data during the research.

REFERENCES

[1]. CSR2016, 2017, Coal Sector Report (Lignite), Turkish Coal Board, Coordination Unit of Strategic Planning (in Turkish), p61.
[2]. Bilir, N., 2016, Occupational health and Safety Profile, International Labour Organization (ILO) Ankara Bureau.
[3]. Balci, B., Balci, MO., Tackin, E. & Yerden, EA., 2013, Financial Loss at Work Accidents, Journal of Social Sciences, pp72-74 (in Turkish).
[4]. Erginel, N. & Toptanci, S., 2017, Modelling of Occupational Accident Data with Probability Distributions, Journal of Engineering & Design, 5, pp201-212
[5]. Guyaguler, T. & Bozkurt, R., 1992, Cost of Occupational Accidents Occurred in Coal Mining, Proceedings of 8th Coal Congress of Turkey (in Turkish), pp331-343.
[6]. www.celiklerholding.com.tr (Access date: 25.02.2018).
[7]. TCB, 2016; Turkish Coal Board Activity Report 2016, Ankara, p94
[8]. SSIT, 2014; Statistics-Social Security Institute of Turkey, Ankara
[9]. Aritan, A.E. & Ataman, M., 2017, Work Accident Analysis with Accident Ratio Calculations, Afyon Kocatepe University, Journal of Science and Engineering, 17, pp239-246 (in Turkish).

ICENS 4TH INTERNATIONAL CONFERENCE ON ENGINEERING AND NATURAL SCIENCE
2-6 May 2018 KIEV UKRAINE

Evaluation of Physical and Mechanical Specifications of Natural Building Stones in Terms of Water Saturation

Cem Sensogut[1], Sunay Beyhan[2], Onder Uysal[1]

Abstract

In this study, cube samples of marble and travertine blocks obtained from 7 different parts of Turkey are used. The physical and mechanical properties of the samples such as uniaxial compressive strength, ultrasonic P wave velocity, unit volume weight, porosity, and water absorption were determined. Experimental studies were conducted on both dry and water saturated conditions. Thus, the effect of water saturation was determined in experimental works. Consideration of the effect on water saturation, strength and P-wave velocity is important in terms of usability of natural building stones.

Statistical relationships were established between the results of the experimental work. Simple regression analyzes were performed for each independent variable. The relationship representing the best correlation between water absorption, porosity, unit volume weight, uniaxial compressive strength, and P wave velocity in dry and saturated basis was determined. Accordingly, the P-wave velocity changes inversely to the porosity, in proportion to the density. Furthermore, depending on the increase in saturation, the compressive strength increases in the natural building stone where the P-wave velocity increases. The determination of such relationships is important in the sense of their use in the natural building stones.

Keywords: P-wave velocity, Saturation, Uniaxial compressive strength

1. INTRODUCTION

Sedimentary, magmatic and metamorphic rocks defined as marble, which can give blocks in sizes suitable for the standards, cut and polished or their surface can be treated and their material properties are compatible with the coating stone norms. According to this definition, sedimentary rocks such as limestone, travertine, sandstone; metamorphic rocks such as gneiss, marble, quartzite; magmatic rocks such as granite, syenite, serpentine, andesite and basalt are also called marble [1].

Natural stones have been used in various forms, mainly for building material purposes, and as a result, the marble sector has become an important branch of industry. Natural building stones are used for various objectives in the construction industry (coating, walls, pavements, flooring etc.) [2]. The physical-chemical-mineralogical properties of natural building stones are important factors in determining where these stones will be used. Therefore; resistance of natural building stones to environmental influences should be determined, their engineering and structural properties should be investigated, and by using the data obtained natural stone selection appropriate to the structure should be made [3].

Natural building stones and materials are exposed to some degradation due to various influences such as time, environment and climatic conditions. These materials are weakened by the effects of deteriorations and begin to lose their physical and mechanical properties. In order to be able to take countermeasures against degradation, it is first necessary to determine its reason [4]. Natural stones are building materials that are most damaged by various external factors such as rainfall (rain and snow), temperature difference and wind. These external factors (atmospheric and climatic conditions) cause different decomposition and degradation such as fragmentation, dispersion, spillage, loss of gloss and brittleness in natural building stones.

[1]*Dumlupinar University, Department of Mining Engineering, 43270, Kutahya, Turkey. cem.sensogut@dpu.edu.tr, onder.uysal@dpu.edu.tr*

[2]*Corresponding author: Dumlupinar University, Department of Mining Engineering, 43270, Kutahya, Turkey. sunay.beyhan@dpu.edu.tr,*

Water is an important factor in the decomposition and degradation of natural building stones. The porosity of the rock is one of the most important factors that enable the water to pass into the rock body. Rocks that have different shaped and sized porous structure are getting water to their structure depending on the porosity ratio. These pores significantly affect the unit volume weight, water absorption, permeability, durability in freezing-thawing and wetting-drying periods, compressive strength, heat and sound insulation of the rock. Water; when combined with other environmental factors such as wind and temperature difference, it accelerates the deterioration of rocks and affects the physical-mechanical properties of the rock negatively. Therefore, it is very important to know the effect of water on the building stones beforehand, in order to determine the mechanism of disintegration, especially in natural building stones.

Figure 1. Regions of marble and travertine samples used in the experiments
[1. Denizli (travertine-1), 2. Kutahya (travertine-2), 3. Bilecik (marble-1) , 4. Bursa (marble-2), 5. Mugla (marble-3), 6. Afyon (marble-4), 7. Mugla (marble-5)]

In this study, 5 marble and 2 travertine type natural stones that have different geological origin were taken from seven different regions in Turkey and examined in detail (Figure 1). The physical and mechanical properties of samples such as uniaxial compressive strength (air dry - σ_{dry}, saturated - σ_{sat}), ultrasonic wave velocity (air dry - V_{dry}, saturated - V_{sat}), unit volume weight (ρ), porosity (n) and water absorption (weight - A_w, volumetric - V_w) were determined and the relationship between them was revealed. Both dry and water saturated samples have been used in experimental studies. Thus, the effect of water saturation on the compressive strength and the ultrasonic velocity is also determined. Consideration of the effect of water saturation on strength and ultrasonic velocity is important in terms of usability of natural building stones. Knowing the physical-mechanical properties of natural stone is important in terms of choosing suitable materials for the structure.

2. EXPERIMENTAL STUDIES

a. Method

Natural stone samples were prepared in accordance with the methods recommended by ISRM [5] and TS 699 [6]. 10 samples (air dry and saturated) from each natural stone type were used in experimental studies to determine the uniaxial compressive strength of dry and water saturated specimens (Figure 2).

The dry and water saturated apparent densities of natural stone species are calculated by mass / volume ratio according to the method proposed by the standards. For dry density, samples were dried in an oven at 105 °C for 24 hours and their dry weight was determined. In the water saturated density experiment, samples were kept in water until the constant mass was reached and then weighed. In this experiment, 3 samples were used from each natural stone type.

In order to determine the effective porosity of the samples, 3 samples in sizes of 70x70x70 mm were used from each natural stone type. The high porosity of natural building stones such as marble reduces the economic efficiency of the stone as the strength property is reduced by increasing porosity [1].

For the weight and volumetric water absorption experiments, the samples were kept in pure water at 21 °C until the constant mass was reached. An ultrasonic test device was used to determine the transition time of ultrasonic sound waves through the rock (Figure 3). This device determines the transition time of the ultrasonic sound waves in the rock with the receiving and transmitting props between the two opposite surfaces of the rock sample. This transition time can take different values with the microfractures in the rock material.

Figure 2.Marble and travertine samples used in experimental work

Figure 3. View of experimental set up (water saturation of samples, uniaxial compressive strength and ultrasonic velocity test)

2.2. Test results

The results obtained within the scope of experimental studies for determining the physical and mechanical properties (σ_{sat}, σ_{dry}, V_{dry}, V_{sat}, ρ_{sat}, ρ_{dry}, n, A_w, V_w) of natural building stones are given in Table 1. According to Table 1; when the water absorption and porosity values of the experimental specimens belonging to different zones are high, the value of the strength decreases. In addition, the strength values can be different depending on the change in other physical and mechanical properties. When the ultrasonic velocities of the samples are examined according to their dry and water saturated state, by the decreasing water saturation of sample, ultrasonic velocity increases. In general, water saturation has a significant effect on physical and mechanical properties of marble and travertine type natural building stones examined in this study. This will also affect the structure that natural stones have been used. Hence, the stability of structure will be less against climate effects.

Table 1. Physical and mechanical test results of natural stone

Sample zones	Natural stone type	Physical and mechanical properties								
		σ_{sat} (MPa)	σ_{dry} (MPa)	V_{dry} (km/s)	V_{sat} (km/s)	ρ_{sat} (g/cm^3)	ρ_{dry} (g/cm^3)	Porosity (n) (%)	A_w (%)	V_w (%)
1	Travertine-1	46,03	52,01	5,253	5,646	2,37	2,35	3,634	1,470	3,512
2	Travartine-2	64,49	81,18	5,503	5,931	2,54	2,49	2,111	0,801	2,196
3	Marble-1	81,72	98,97	6,448	6,548	2,68	2,67	0,287	0,135	0,277
4	Marble-2	77,53	85,87	5,745	6,050	2,69	2,68	0,347	0,112	0,348
5	Marble-3	61,31	71,19	5,918	6,237	2,69	2,67	0,525	0,066	0,579
6	Marble-4	55,03	67,55	5,869	6,168	2,69	2,68	0,301	0,097	0,361
7	Marble-5	88,25	99,81	6,003	6,211	2,71	2,67	0,211	0,146	0,297

3. REGRESSION ANALYSES

Relations between the results of experimental studies were obtained by simple regression analysis. These relations are given in Figures 4, 5, 6, 7, 8, 9 and 10 together with the regression equations.

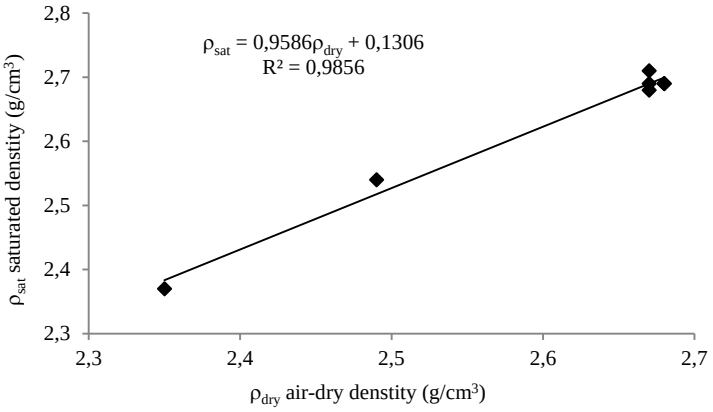

Figure 4. Relationship between the measured dry and saturated densities

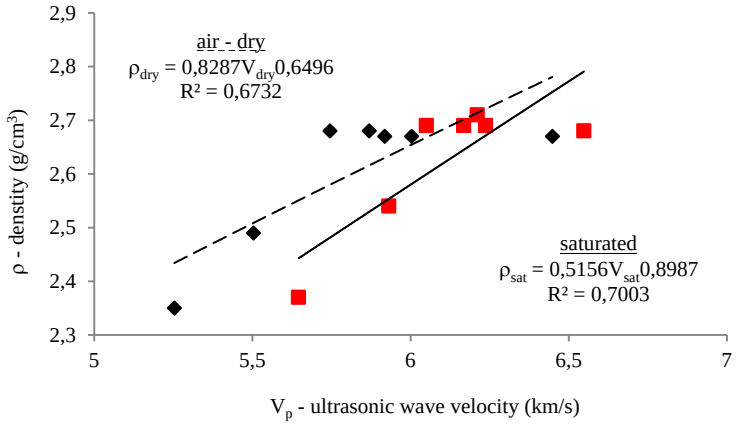

Figure 5. Ultrasonic wave velocities related to the dry and the water saturated densities

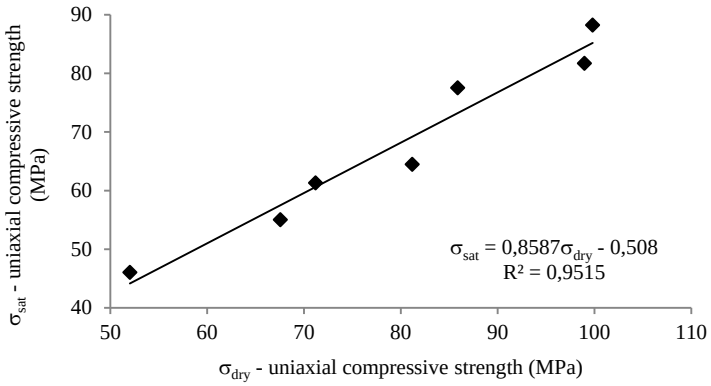

Figure 6. The uniaxial compressive strength related to dry and saturated densities

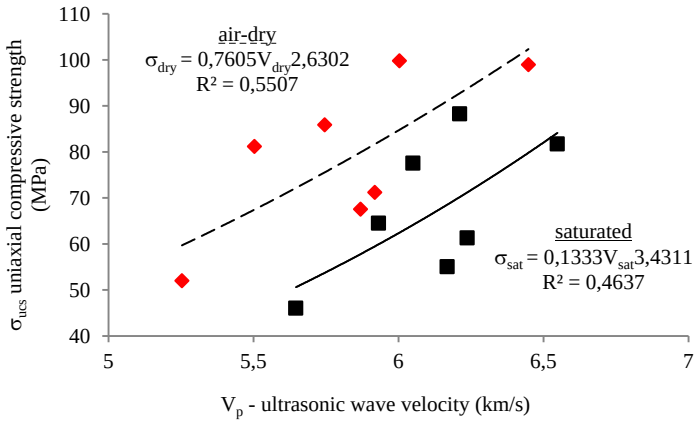

Figure 7. Relationship between the ultrasonic wave velocity and the uniaxial compressive in case of dry and saturated conditions.

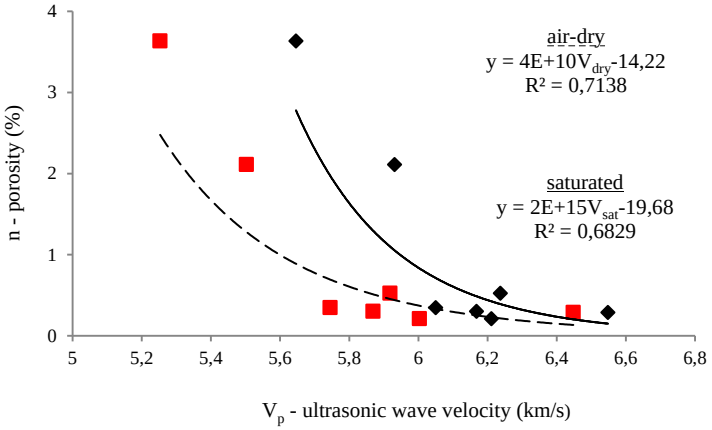

Figure 8. The porosity as function of the ultrasonic wave velocity in case of dry and saturated conditions

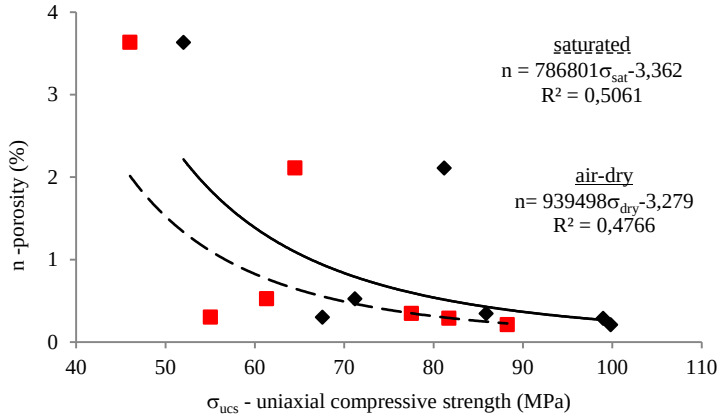

Figure 9. Relationship between the porosity and the uniaxial compressive in case of dry and saturated conditions.

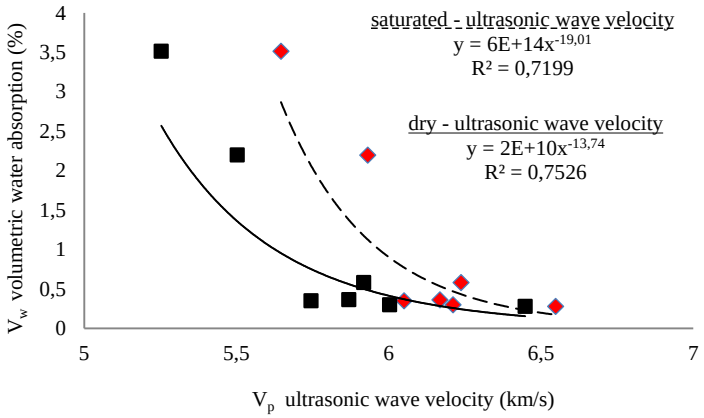

Figure 10. Relationship between the volumetric water absorption and the ultrasonic wave velocity in case of dry and saturated conditions.

4. CONCLUSIONS

In this study, the effects of rainfall (water) on the physical and mechanical properties of natural building stones were determined by experimental studies. This effect is the result of the reaction of the water through the pores of the rock. Saturated rocks fail much quicker under pressure by the influence of the water in their pores. This failure is directly proportional to the porosity of the rock.

Increasing of the porosity of the natural building stone caused the strength and the ultrasonic velocity to decrease (Figure 8, 9). According to the relationship between ultrasonic velocity and uniaxial compressive strength applied to both dry and water saturated specimens, the increase in strength caused an increase in ultrasonic velocity (Figure 7). It has been determined that the ultrasonic velocity is proportional to density and inversely proportional to porosity. According to this, the ultrasonic velocity increases while the density increases and the ultrasonic velocity decreases when the porosity increases (Figures 5, 9). In addition, when the air dry and water saturated uniaxial compressive strength test results were evaluated statistically, a high correlation was obtained between them (Figure 6). According to the results of the water saturation test of the samples (Figure 10), the decrease in water absorption value causes the ultrasonic velocity to increase.

As a result, determining the physical and mechanical properties of the natural building stones such as marble and travertine type, which will be used especially in the outdoors of the buildings, will enable us to determine the causes of the degradation that may occur due to the climatic conditions in the building. Thus, the constructions in which natural stone materials are used will preserve their original structures for many years.

REFERENCES

[1]. T. Onargan, H. Kose, A.H. Deliormanli, “Mermer”, TMMOB Maden Muhendisleri Odasi yayini, Ankara, 2005

[2]. N. Sengun, R. Altindag, C.E. Koccaz. “Isparta yoresinde bulunan bazi magmatik kokenli kayaclarin kesilebilirlik analizi”. DEU Muhendislik Fakultesi, Fen ve Muhendislik Dergisi Cilt: 11 Sayi: 31, 2009.

[3]. I. Kilic. “Kesan Bolgesi Kumtaslarinin Yapi Tasi Olarak Kullanilabilirligi” Trakya Universitesi Fen Bilimleri Enstitusu Mimarlik Anabilim Dali Edirne Doktora Tezi, 2009

[4]. M. Dal, A.D. Ocal. “Limestone used in Islamic religious architecture from Istanbul and Turkish Thrace”, METU Journal of the Faculty of Architecture, METU.JFA.2013/1 (30:1), 29-44, 2013

[5]. ISRM, “The complete ISRM suggested methods for rock characterization testing and monitoring: 1974-2006”, In: Ulusay, R. and Hudson, J.A. (Editors), Suggested Methods Prepared by the Commission on Testing Methods, International Society For Rock Mechanics (ISRM), Ankara, Turkey, 2007

[6]. TS 699, “Tabii Yapi Taslari Muayene ve Deney Metotlari”, Turk Standartlari Enstitusu, Turkiye, 1987

ICENS 4TH INTERNATIONAL CONFERENCE ON ENGINEERING AND NATURAL SCIENCE
2-6 May 2018 KIEV UKRAINE

The Effect of Freeze-Thaw Cycles on Physical-Mechanical Properties of Tuff

Sunay Beyhan[1], Cem Sensogut[2], Ahmet Ozgur[2], Sahin Yuvka[2]

Abstract

Natural stones such as tuff are widely used in areas such as interior and exterior flooring and coatings of buildings and restoration. Many types of tuffs are affected negatively by the atmospheric conditions in the outdoor use because of their porous structure. Freezing-thawing, wetting-drying, wind, moisture and acidic waters are considerably influential on the mechanical and physical properties of these stones.

In this study; the variation in the strength of tuff after the freeze-thaw cycles was examined. For this purpose; approximately 120 cubic samples were prepared from block samples in sizes of 50x50x50 mm. A total of 80 period freeze-thaw cycles were applied. To determine the effect of freezing-thawing in the laboratory environment, the strength of the solid rock samples before and after each 10 freeze-thaw cycles were recorded. In addition, the variation in the value of physical properties based on cycles is also examined. The test results were then analysed statistically. As a result, pre-test physical and mechanical properties of the tuff were affected negatively after the freeze-thaw cycles. This effect becomes more significant after the 10th period of the freeze-thaw cycles. Consequently; how the atmospheric conditions such as freezing-thawing affect the construction in buildings where the tuff is used was determined by the experimental studies in concern. Experimental results have shown that building stones such as tuffs will be affected by atmospheric events when used outdoors and this situation will affect construction negatively.

Keywords: Freeze-thaw, Natural stone, Tuff, Mechanical and physical properties

1. INTRODUCTION

Natural stones are generally used as building and covering stone inside and outside of traditional and contemporary architectural constructions. Natural stones are being influenced by time, environment, climatic conditions (freezing-thawing, wetting-drying), and their physical and mechanical properties change and deteriorate. By the effect of these deteriorations, the rocks weaken and begin to lose their physical and mechanical properties. In order to be able to take measures, it is first necessary to determine what is causing them. Various methods and experiments have been developed to determine the effects of these deterioration and changes in the rock. The freeze-thaw test is one of the index tests conducted to determine the changes of the physical and mechanical properties of natural stones used in the outdoors.

Determination of degradation of rocks after freeze-thaw cycles is important for natural building stones subjected to excessive freezing and thawing during the year. In studies to determine the change in physical and mechanical properties of rocks after freeze-thaw cycles (F-T) [1, 2, 3, 4, 5, 6], they have generally determined that the physical-mechanical properties of natural stones change with freezing-thawing.

In this study, the changes of physical and mechanical properties of the tuff (Bayburt stone-tuff) by freeze-thaw process were investigated. Approximately 120 cube samples were prepared in sizes of 50x50x50 mm to determine the changes in physical, mechanical and index properties depending on the freeze-thaw cycles (F-T). First, the physical-mechanical and index tests were performed on the original samples, and then all the samples were subjected to the F-T test and the experiments were repeated on the samples after every 10 cycles,

[1] *Corresponding author: Dumlupinar University, Department of Mining Engineering, 43100 Kutahya, Turkey.* *cem.sensogut@dpu.edu.tr*

[2] *Dumlupnar University, Department of Mining Engineering, 43100 Kutahya, Turkey*

with a total of 80 cycles. For each experiment, the amount of change from the starting value was determined as a percentage. Thus, the relation between the number of cycles and the change of the mechanical and physical parameters of the rocks determined in the laboratory is investigated.

2. MATERIAL AND METHOD

Experimental studies have been carried out in order to determine the changes in physical and mechanical properties of tuff samples that may occur over time under atmospheric influences such as freeze-thaw. The tests were carried out in accordance with the proposed methods and relevant standards ISRM [7] and TS 699 [8].

a. Physical and Mechanical Properties

The mean results of the experiments made to determine the physical properties of tuff such as unit volume weight, porosity and water absorption and the mechanical properties such as uniaxial compressive strength, bending strength and abrasion resistance are given in Table 1.

Table 1. Physical and mechanical properties of tuff before freeze-thaw

	Analysis / Test name	**Test Results**
Physical Properties	Unit volume weight (kN/m^3)	23.1
	Water absorption (mass) (%)	12.1
	Visible Porosity (%)	17.2
	Open Porosity (%)	20.9
	Solidity Ratio (%)	73.9
	Schmidt hardness (L type)	35.0
Mechanical Properties	Uniaxial compressive strength(MPa)	71.2
	Abrasion resistance (cm^3/50cm^2)	23.5
	Bending strength (MPa)	11.8

2.1.1. Freeze-Thaw Test

The freeze-thaw test was carried out in accordance with the standards. All the prepared samples were dried at 105 °C and their dry weights were determined (Figure 1). The dried samples were soaked in water until they became saturated (Figure 1). Water saturated samples were placed into the cooler which pre-cooled to -20 °C (Figure 1). The samples retained in the cooler for 12 hours were put back into the water at +20 °C again and a cycle was completed (Figure 1). From these samples, group I chosen as initial group and A, B, C, D, E, F, G, H groups were subjected to 10, 20, 30, 40, 50, 60, 70, 80 freeze-thaw cycles respectively.

Figure 1. Image of experimental work stages

b. Change of Physical and Mechanical Properties due to F-T Cycle

In order to determine the variation of the compressive strength of the tuff depending on F-T cycles, each cycle group was subjected to uniaxial compressive strength test six times (Table 2, Figure 2). As can be seen from Figure 2, there is a significant decrease in the compressive strength values due to the increase in the number of F-T cycles.

At temperatures below 0 °C, the water that has penetrated the pores of the rocks is freezing and the volume of water is increasing. If the rock is saturated, water will try to expand in the pores while becoming ice and cause thin cracks in the rock. When this situation repeats during the cold season, frozen water will cause larger cracks by enlarging fine cracks. Thus, value of the in-situ effective stress of the rock will the decrease. In addition, rock mass will become unstable because of the formation of cracks.

Table 2. Variation of compressive strength depending on number of F-T cycles.

Sample No	Number of Cycles								
	Uniaxial Compressive Strength (MPa)								
	I00	A10	B20	C30	D40	E50	F60	G70	H80
1	69.2	68.8	66.8	54.2	53.2	50.8	44.8	25.1	24.0
2	73.6	59.6	54.8	50.8	44.0	41.8	33.2	16.4	17.6
3	69.9	63.6	58.3	56.0	54.0	51.4	34.8	20.4	15.6
4	71.5	60.4	57.6	51.2	46.6	44.8	30.4	22.6	20.8
5	74.9	61.2	55.6	52.4	46.5	41.2	31.6	27.2	23.6
6	67.8	51.0	49.6	47.4	42.8	40.1	36.4	20.4	18.4
Mean Value	***71.2***	***60.8***	***57.1***	***52.0***	***47.9***	***45.0***	***35.2***	***22.0***	***20.0***
Decrease of Compressive Strength (%)		14.6	19.8	26.9	32.7	36.8	50.6	69.1	71.9

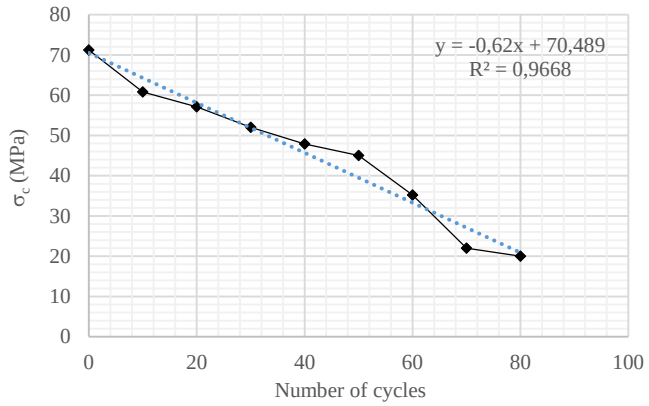

Figure 2. Change of the compressive strength according to number of F-T cycles

The change in unit volume weight and water absorption due to F-T cycles is given in Figure 3. As can be seen from Figure 3, the water absorption value is increased while the unit volume weight is decreased due to the increase in the number of F-T cycles. Due to the porous structure of the rock, the amount of water that can be

taken in the structure increases along the F-T cycles, and the unit volume weight decreases due to the physical effect of the F-T cycles on the rock.

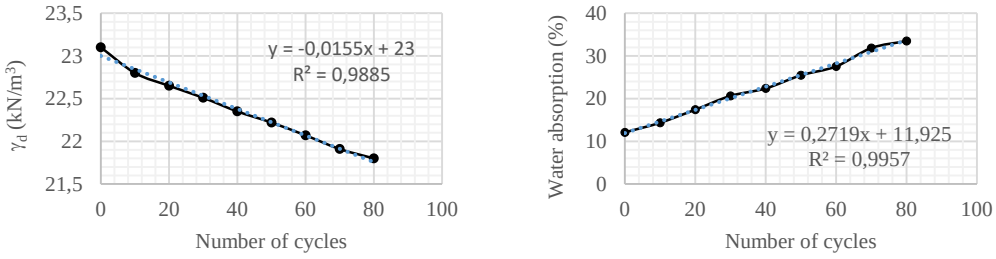

Figure 3. Change in unit volume weight and water absorption according to F-T cycles

Along F-T cycles of samples, the variation of uniaxial compressive strength according to the unit volume weight and water absorption values is given in Figure 4. According to Figure 4, an increase in the unit volume weight leads to an increase in the compressive strength, while an increase in the water absorption leads a decrease in the compressive strength.

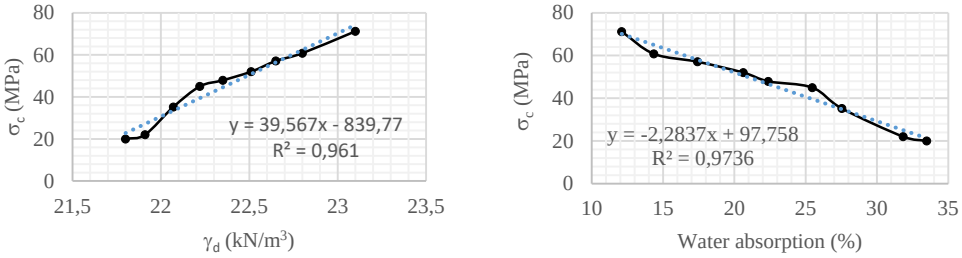

Figure 4. Variation of the uniaxial compressive strength of the rock with respect to unit volume weight and water absorption

3. DISCUSSION AND RESULT

In this study, experimental studies have been conducted to determine how natural phenomena such as freezing and thawing will affect the buildings and structures where the tuff is used. According to the results of the study, the initial physical and mechanical properties of the tuff were affected negatively after the F-T periods. Experimental results have shown that, when natural stones such as tuffs are being used in the outdoors, it will be negatively affected by atmospheric events. Besides, the deterioration type depends on the physical and chemical structure of the rock and the properties of external and internal influences. Therefore, it is important for the stability of the construction to determine which of these effects causes the rock deterioration type. Natural building stone should be selected according to the climate characteristics of the environment to be used.

REFERENCES

[1] A. Binal, K.E. Kasapoglu, C. Gokceoglu, Eskisehir-Yazilikaya Cevresinde Yuzeylenen Volkanosedimanter Kayaclarin Donma-Cozulme Etkisi Altinda Bazi Fiziksel ve Mekanik Parametrelerinin Degisimi", Hacettepe Unv. Yerbilimleri Uygulama ve Arastirma Merkezi Bulteni, Ankara, s41-51, 1997

[2]. M. Fener, I. Ince, "Effects of the freeze–thaw (F-T) cycle on the andesitic rocks (Sille-Konya/Turkey) used in construction building", Journal of African Earth Sciences vol. 109, Pages 96-106, 2015

[3]. M.V. Gokce, I. Ince, M. Fener, T. Taskiran, K. Kayabali, "The effects of freeze–thaw (F-T) cycles on the Godene travertine used in historical structures in Konya (Turkey)", Cold Regions Science and Technology, vol. 127, pp65-75, 2016

[4]. F. Bayram, "Predicting mechanical strength loss of natural stones after freeze–thaw in cold regions", Cold Regions Science and Technology, vol 83–84, pp 98-102, 2012
[5]. Z. Zhou, W. Ma, S. Zhang, Y. Mu, G. Li, "Effect of freeze-thaw cycles in mechanical behaviors of frozen loess", Cold Regions Science and Technology, vol. 146, pp 9-18, 2018
[6]. R. Altindag, S.I. Alyildiz, T. Onargan, "Mechanical Property Degradation of Ignimbrite Subjected to Recurrent Freeze-Thaw Cycles", Int. J. of Rock Mech. and Min. Sci., vol.41, pp.1023-1028, 2004
[7]. ISRM, "The complete ISRM suggested methods for rock characterization testing and monitoring: 1974-2006", In: Ulusay, R. and Hudson, J.A. (Editors), Suggested Methods Prepared by the Commission on Testing Methods, International Society For Rock Mechanics (ISRM), Ankara, Turkey, 2007
[8]. TS 699, "Tabii Yapi Taslari Muayene ve Deney Metotlari", Turk Standartlari Enstitusu, Turkey, 1987

ICENS 4TH INTERNATIONAL CONFERENCE ON ENGINEERING AND NATURAL SCIENCE
2 - 6 May 2018 KIEV UKRAINE

Analysis of Cooling of the Heated Circle Patterned Surfaces by Using an Air Jet Impingement

Koray Karabulut[1], Dogan Engin Alnak[2], Ferhat Koca[2]

Abstract

Excessive heating of electronic components may cause undesirable consequences such as increased thermal stresses in the system, which could cause mechanical failure. Impinging jets are usually used to improve thermal performances of the electronic components in industry due to providing a good heat transfer performance. In this work, cooling of copper plate with five circle patterned surfaces inside a rectangular channel composing of one open and three blocked sides was numerically investigated by using a single air jet flow. The numerical computations were implemented by solving a steady, three-dimensional Navier-Stokes equations and an energy equation by using Ansys-Fluent 17.0 program with k-ε turbulance model. Air was taken as working fluid with inlet temperature of 300 K. A constant heat flux was applied to circle surfaces as 1000 W/m^2 while the top and side surfaces were adiabatic. The study was done for different Reynolds numbers (Re) of 4000, 6000, 8000 and 10.000 and different jet-to-plate distances (H/D$_h$) of 4, 6, 10 and 12. The numerical results agreed well with the numerical and experimental datas of study found in literature. The results were presented as the variations of the mean Nu numbers and temperatures for each circle patterned indentation surface. The temperature and velocity distributions of jet fluid flow and mean temperature and Nu values of whole circle surfaces and values of air jet outlet temperature were also examined for different Re numbers and H/D$_h$ ratios. It was seen that increasing the Re number increases the Nusselt number for all cases. Mean Nusselt number increases of 64.85% from Re=4000 to Re=10000 for H/D$_h$=6. However, Nu number was less sensitive to H/D$_h$ ratio in the range of H/D$_h$=4-12. Mean Nusselt number diminishes 4.48% from H/D$_h$=6 to H/D$_h$=12 for Re=4000. The highest mean Nusselt number was achieved for Re=10000 and H/D$_h$=6.

Keywords: Cooling, Impingement air jet, Patterned surface, Numerical analysis

1. INTRODUCTION

Rapid developments in electronics have entirely surrounded the modern life and electronic devices are an inseparable part of every day life. Electronic and computer supported applications have become an intensively usable situation at heating and cooling of environment in which we live and work, defense industry, from health to education for our security and comfort in the wast area. Becoming widespread and indispensable of application areas require to work of electronic systems with confidence and high performance. Especially problems in computers used in defense, health, work and education systems will not only cause to prevent these services, but will also affect human life at a serious level. Therefore, the enhancement necessity of performances, reliabilities and working lifes of electronic equipments is inevitable. When current flows through a resistance, heat generation is a known truth. The electronic devices also generate heat while they carry out duties by means of this way. The amount of heat generated per unit volume in parallel with the downsizing of electronic devices also naturally increases. This fact makes compulsory of development in cooling systems and new researches and increases importance of thermal control at design and operating of electronic equipments, day after day. Impinging jets of liquid and gaseous are considered an excellent alternative to enhance heat transfer due to their ability to bring about turbulance and improve convective heat transfer. Heat transfer of impinging jets is an important process to many practical implementations, including coolings of extruded metals, turbine blade and, increasingly, electronic devices. Jet impingement has the ability to remove large

[1]*Corresponding author: Sivas Cumhuriyet University, Department of Electric and Energy, Sivas Vocational High School, 58140, Sivas, Turkey. kkarabulut@cumhuriyet.edu.tr, koray.karabulut@hotmail.com*

[2]*Sivas Cumhuriyet University, Department of Automotive Engineering, Technology Faculty, 58140, Sivas, Turkey. dealnak@cumhuriyet.edu.tr, ferhatkoca@cumhuriyet.edu.tr*

amounts of heat effectively from these environments having high heat flux. Therefore, systematic and regular studies on this topic are being maintained in worldwide, nowadays. Webb and Ma [1] carried out a literature review about jet impingement included several examples of their. Sezai and Mohammed [2] implemented a numerical research of laminar slot jet alignment impinging onto a flat plate. They found that the jet to jet interval had little effect on the Nusselt number. Bula et al. [3] studied jet impingement for both uniform and differently heated flat plates. They used lubricant MIL 7808 as cooling fluid in these situations, primarily due to its usage in the aeronautic industry. Because the temperature had a large effect on thermal conductivity and viscosity characteristics of the fluid, the use of a fluid with high Prandtl number required the use of varied fluid properties. Ebadian and Lewis [4] carried out a review study of high heat flux removal techniques, containing jet impingement. Sung and Mudawar [5] researched the cooling performance of defense electronics employing a slot jet. They used HFE 7100 as jet cooling fluid to cool electronic packages with a high heat flux. Liu et al. [6] exhibited experimental measurement results of heat transfer for jet impingement on grooved surfaces. Though they attained about 15% increment in local heat transfer near the groove, they determined that the overall enhancement of heat transfer was negligible.

Although the amount of available data on jet impingement in the literature is large, the effect of surface geometry researched in this work on the heat transfer have not still been analyzed. The effects of surface geometry, Reynolds number, jet-to-plate distances (H/D_h) on the steady state heating of the circle patterned surfaces being cooled by jet impingement were numerically investigeted in this study. The considered working fluid was air impinging on surfaces of circle patterned. The numerical computations were performed by solving a steady, three-dimensional Navier-Stokes equation and an energy equation by using Ansys-Fluent 17.0 program with k-ε turbulance model. While the Reynolds numbers (Re) of the jet were the range from 4000 to 10000, different channel heights were used as $4xD_h$, $6xD_h$, $10xD_h$ and $12xD_h$. A constant heat flux ($\ddot{q}$) of 1000 W/m^2 was performed on the patterned surfaces for all simulations. The numerical results were in well agreement with the numerical and experimental datas of study existed in literature. The results were presented as the variations of the mean Nu numbers and temperatures for each circle patterned indentation surface. The temperature and velocity distributions of jet fluid flow and mean temperature and Nu values of whole circle surfaces and values of air jet outlet temperature were also analyzed for different Re numbers and H/D_h ratios

2. NUMERICAL METHOD

The numerical study was conducted to study the three-dimensional, steady, conjugate heat transfer of forced convection and conduction in a channel with patterned surface of fluid flow. The finite volume method (FLUENT program) was used to solve the conjugate heat transfer analysis.

The aim of finite volume method is to break down the domain of the problem into a finite number of elements to be solved to find a solution for each of these sections and then by uniting these solutions to find a general solution to the problem. This method uses a technique which is based on the control volume for transforming heat flow equations into algebraic equations which can be solved numerically. In other words, this technique is based on the principle of taking the heat flow equations integration in each control volume. This integration result provides equations which characterize each control volume which occurs. For preparing the most appropriate grid model, a fine grid should be formed in regions where the change in variables such as velocity, pressure and temperature is bigger. Therefore, the finest grid was especially used for the channel surfaces with the indentation and in other zones a sparser grid was preferred. Convergence of the computations was stopped for the continuity and the momentum equations when residues were less than 10^{-6} and for the energy equation when residues were less than 10^{-7}. A grid structure which consisted of tetrahedral was used for simulation. Also, a standard k-ε turbulance model was performed for the selected model with circle patterned surfaces in the numerical investigations.

The flow and heat transfer through the geometry are governed by the partial differential equation derived from the laws of conservation of mass, momentum and energy with steady state conditions without a body force, which are expressed as follows [7].

Continuity equation

$$\frac{\partial u}{\partial x}+\frac{\partial v}{\partial y}+\frac{\partial w}{\partial z}=0 \qquad (1)$$

Momentum equation

x momentum equation

$$\rho\left(u\frac{\partial u}{\partial x}+v\frac{\partial u}{\partial y}+w\frac{\partial u}{\partial z}\right)=-\frac{\partial p}{dx}+\mu\left(\frac{\partial^2 u}{\partial x^2}+\frac{\partial^2 u}{\partial y^2}+\frac{\partial^2 u}{\partial z^2}\right) \tag{2.1}$$

y momentum equation

$$\rho\left(u\frac{\partial v}{\partial x}+v\frac{\partial v}{\partial y}+w\frac{\partial v}{\partial z}\right)=-\frac{\partial p}{\partial y}+\mu\left(\frac{\partial^2 v}{\partial x^2}+\frac{\partial^2 v}{\partial y^2}+\frac{\partial^2 v}{\partial z^2}\right) \tag{2.2}$$

z momentum equation

$$\rho\left(u\frac{\partial w}{\partial x}+v\frac{\partial w}{\partial y}+w\frac{\partial w}{\partial z}\right)=-\frac{\partial p}{\partial z}+\mu\left(\frac{\partial^2 w}{\partial x^2}+\frac{\partial^2 w}{\partial y^2}+\frac{\partial^2 w}{\partial z^2}\right) \tag{2.3}$$

Energy equation

$$u\frac{\partial T}{\partial x}+v\frac{\partial T}{\partial y}+w\frac{\partial T}{\partial z}=\left(\frac{k}{\rho c_p}\right)\left(\frac{\partial^2 T}{\partial x^2}+\frac{\partial^2 T}{\partial y^2}+\frac{\partial^2 T}{\partial z^2}\right) \tag{3}$$

In the equations, ρ is density, μ dynamic viscosity, p pressure, k thermal conductivity, T temperature, c_p specific heat and u, v, w are velocities of the x, y and z direction, respectively.

In the used standard k-ε turbulance model, the turbulence kinetic energy k' and its rate of dissipation $\in$ and the viscous dissipation term ϕ are used.

Steady flow turbulence kinetic energy equation

$$\frac{\partial(\rho u k')}{\partial x}+\frac{\partial(\rho v k')}{\partial y}+\frac{\partial(\rho w k')}{\partial z}=\frac{\partial}{\partial x}\left(\frac{\mu_t}{\sigma_k}\frac{\partial k'}{\partial x}\right)+\frac{\partial}{\partial y}\left(\frac{\mu_t}{\sigma_k}\frac{\partial k'}{\partial y}\right)+\frac{\partial}{\partial z}\left(\frac{\mu_t}{\sigma_k}\frac{\partial k'}{\partial z}\right)+\mu_t\phi-\rho\varepsilon \tag{4}$$

Turbulent viscosity

$$\mu_t=C_\mu.\rho.\frac{k'^2}{\varepsilon} \tag{5}$$

Turbulence kinetic energy

$$k'=\frac{1}{2}\left(\overline{u'^2}+\overline{v'^2}+\overline{w'^2}\right) \tag{6}$$

Viscous dissipation term

$$\phi=2\mu\left[\left(\frac{\partial u}{\partial x}\right)^2+\left(\frac{\partial v}{\partial y}\right)^2\right]+\mu\left(\frac{\partial v}{\partial x}+\frac{\partial u}{\partial y}\right)^2 \tag{7}$$

Turbulence kinetic energy disappearance equation

$$\frac{\partial(\rho u\varepsilon)}{\partial x}+\frac{\partial(\rho v\varepsilon)}{\partial y}+\frac{\partial(\rho w\varepsilon)}{\partial z}=\frac{\partial}{\partial x}\left(\frac{\mu_t}{\sigma_\varepsilon}\frac{\partial\varepsilon}{\partial x}\right)+\frac{\partial}{\partial y}\left(\frac{\mu_t}{\sigma_\varepsilon}\frac{\partial\varepsilon}{\partial y}\right)+\frac{\partial}{\partial z}\left(\frac{\mu_t}{\sigma_\varepsilon}\frac{\partial\varepsilon}{\partial z}\right)+C_{1\varepsilon}\mu_t\frac{\varepsilon}{k'}\phi-C_{2\varepsilon}\rho\frac{\varepsilon^2}{k'} \tag{8}$$

The model constants C_μ, $C_{1\varepsilon}$, $C_{2\varepsilon}$, σ_k and σ_ε have typically default values for used standard k-ε turbulance model [7]. The values of these constants have been arrived at by numerous iterations of data fitting for a wide range of turbulent flows. These are as follows;

C_μ =0.09, $C_{1\varepsilon}$ = 1.44, $C_{2\varepsilon}$ = 1.92, σ_k = 1 and σ_ε = 1.3.

Reynolds number is calculated by the equation given below;

$$Re = \frac{V_\infty . D_h}{\nu} \tag{9}$$

Here, D_h is the hydraulic diameter of the jet inlet

$$D_h = \frac{4A_c}{P} = \frac{4(a.W)}{2(a+W)} \tag{10}$$

where A_c is the cross-section area of the jet inlet, P is the perimeter of the jet inlet.

The Nusselt number is evaluated as the conductive heat transfer rate of the fluid over the solid boundary equal to the convective heat rate as:

$$-k\left(\frac{dT}{dn}\right)_{surface} = h\left(T_\infty - T_s\right) \text{ and } Nu = \frac{h.D_h}{k} \tag{11}$$

Where h is the local heat transfer coefficient on the surface, n is the vertical direction to isotherm and the local Nusselt number is obtained as above.

3. GEOMETRIC MODEL

Perspective view of the channel having sizes was shown in Fig. 1. The boundary conditions can also be seen in this figure. The jet nozzle hydraulic diameter (D_h) was kept at 9.9 mm, the length (L) and width (W) of the channel were taken as 200 mm and 50 mm, respectively. 5.5x50 mm rectangular nozzle with an inlet velocity ranging between 6.23 and 15.58 m/s was used in the study. Uniform velocity profile for jet inlet was existed in the inlet of the rectangular nozzle. The channel height was determined at different measurements as $4xD_h$, $6xD_h$, $10xD_h$ and $12xD_h$. While space between two indentations was taken as D_h, indentation width and height were $2xD_h$ and D_h, respectively. There are five surfaces with circle indentation and the constant heat flux ($\ddot{q}$) with 1000 W/m^2 was applied to only these surfaces for all simulations when the top and side surfaces were adiabatic. However, the Reynolds numbers (Re) of the jet ranged from 4000 to 10000.

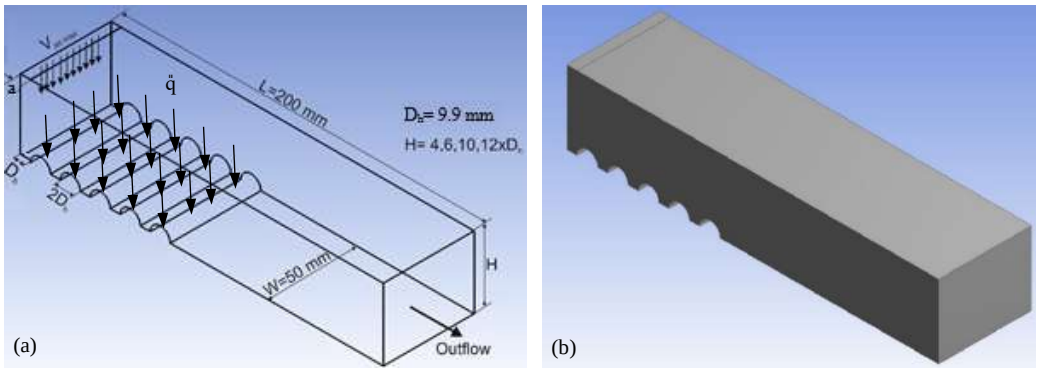

Figure 1. Perspective view of the channel (a) Domain with boundary conditions and sizes (b) CFD simulation domain

The study was conducted under the following assumptions:

i) The flow field was assumed to be three-dimensional, steady-state and turbulent for the channel;
ii) Calculations were carried out for incompressible fluid;
iii) Air was used as working fluid for the cooling of indentation surface;
iv) Constant heat flux of 1000 W/m^2 was applied to indentation surfaces;
v) Thermal properties of the fluid were constant;
vi) There was no heat generation for both the jet fluid and the solid surfaces

4. RESULTS and DISCUSSION

Figure 2 exhibits a comparison of the effects of Re number with 6000 and 8000 on the Nu number as experimental and numerical for jet-to-plate distance (H/D_h) value of 6 between Kilic et al. [8] and the present study numerically. The comparison was performed for smooth copper plate surface that was used in [8] at Re numbers of 6000 and 8000. While the deviation of the Nu number between the experimental results of Kilic et al. [8] and the present numerical study is 3.99% at Re=6000, it is found as 1 % for numerical results at the impingement region. However, difference between the experimental and numerical results increases for Re=8000 at the impingement region due to higher turbulance intensity. When the deviation of numerical results with experimental is 9.15% due to higher turbulance intensity in this region, the difference is 1.02% for the numerical results when compared the present study with Kilic et al. [8]. Therefore, it can be said that the results of the present study are in good aggreement with experimental and numerical study results of the Kilic et al. [8] and the numerical study is reasonable and appropriate.

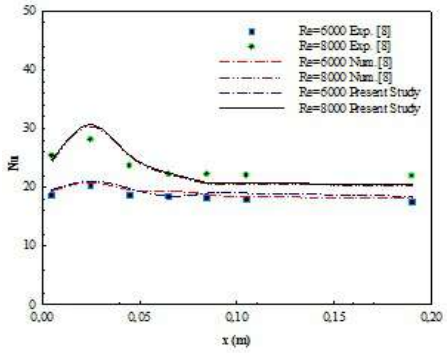

Figure 2. Comparison of the present results and those of Kilic et al. [8]

In order to obtain the number of elements in each direction for an accurate solution, a number of different grid configurations were tested for H/D_h=4 and Re=4000 as comparison of mean Nu number and outlet temperature of air jet (T_{out}). The results of these simulations were given in Table 1. The results indicated that 1704572 grid elements on the channel cross-section were adequate (<0.08 % difference compared with 18651859 grids). Mesh structure of the channel having circle patterned surfaces was also shown in Fig. 3 with zoomed image in order to clearly see the mesh shape of the circle pattern.

Table 1. Grid independence test results for Nu_m and $T_{out\text{-}jet}$

Mesh Numbers	Nu_m	$T_{out\text{-}jet}$ (K)
1480461	11.5225	320.546
1704572	11.5242	320.764
1865185	11.5241	320.765

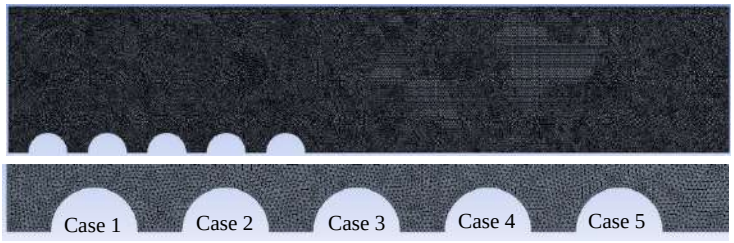

Figure 3. Mesh structure of the channel with circle patterned surface used in calculations

Figure 4a, b, c and d illustrate the variation of the Nusselt number versus Reynolds number for different H/D_h values of 4, 6, 10 and 12 and location cases of circles as cases of 1, 2, 3, 4 and 5, respectively. While case 1 indicates the first circle beginning from the left side of the channel, other circles are named as 2, 3, 4 and 5 with the same sequentially. Increase in Reynolds number increases the heat transfer on the surface of the heated circles, which enhance the Nu number. Recirculations occur at the bottom of the left wall for all Reynolds numbers. These recirculations slightly cause a change of location of maximum heat transfer point and affect main jet flow direction. As the highest local Nu number value was obtained for the case of 1 at H/D_h=4, it was attained the case for 2 with increasing in H/D_h due to resulting from recirculation. However, mean Nusselt number increased of 64.85% from Re=4000 to Re=10000 for H/D_h=6 (Figs. 4a and 4d). Besides, Nu number was less sensitive to H/D_h ratio in the range of H/D_h=4-12 (Figs. 4a-d). From H/D_h=6 to H/D_h =12 mean Nusselt number diminished 4.48% for Re=4000 due to a reduction of turbulance intensity. Furthermore, the highest mean Nusselt number was achieved for Re=10000 and H/D_h=6.

Mean surface temperature variations of the circles of different location cases depending on the Re number for different H/D_h ratios are shown in Fig. 5. As can be seen in graphs presented in Figs. 5a-d that increasing of the Re number causes to reduce surface temperatures of the circles. However, when the case of 1 has the lowest mean surface temperature for H/D_h=4, jet flow effect shifted toward circle 2 (case 2) depending on the recirculations for another investigated H/D_h ratios. This effect can be clearly seen for the cases of 1 and 2 (Figs. 5a-d). Besides, a temperature increase of 1.52% was determined from the case 1 to 5 for H/D_h=12 and Re=4000.

It is seen from Figs. 6 A and B that size of the recirculations, at the bottom of the left wall, decreases from Re=4000 to Re=10000. The reason for this is inhibition of expansion of recirculations by increasing velocity of jet fluid. As the jet velocity is high on the circle surfaces at the channel entrance which is jet region, it decreases toward the channel exit. When analyzed the temperature distributions for Reynolds number of 4000 and 10000, separated flow regions comprise along the height of the channel above the jet region. Besides, due to the separation of jet flow from the circle patterned surface, recirculations occur. Thermal boundary layer thickness also increases in that region, which causes to increase the temperature. However, increasing the jet-to-plate distance from H/D_h=4 to 10 causes a temperature increment at the impingement region due to decrement in the impingement surface area.

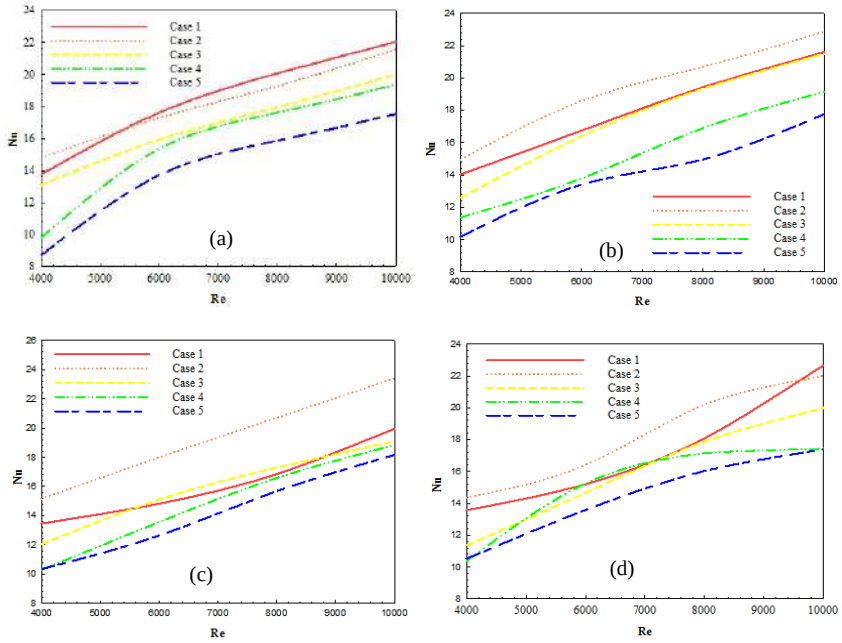

Figure. 4. Results of mean Nu number versus different Re number for different H/D_h and cases

(a) H/D_h=4(b) H/D_h=6 (c) H/D_h=10 and (d) H/D_h=12

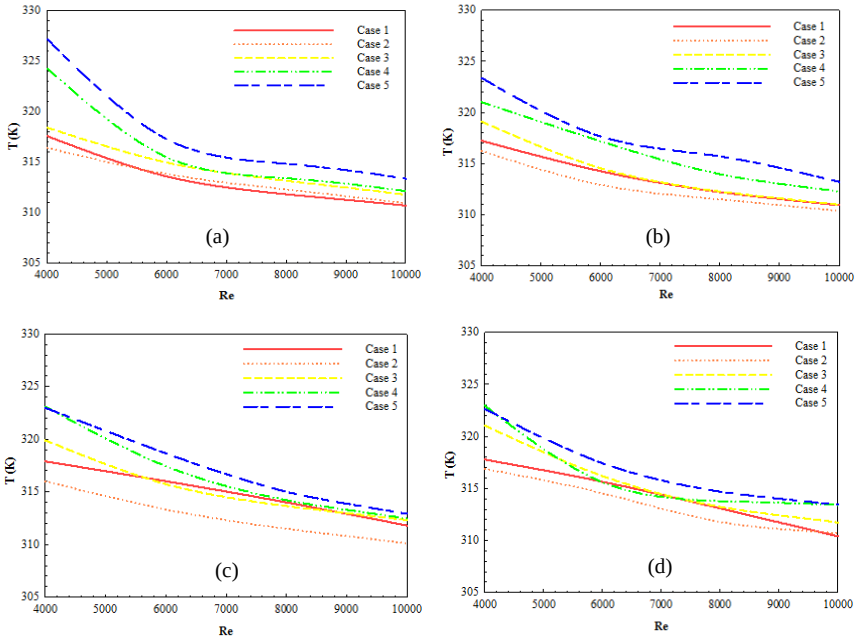

Figure. 5. Results of mean surface temperature versus different Re number for different H/D_h and cases

(a) H/D_h=4(b) H/D_h=6 (c) H/D_h=10 and (d) H/D_h=12

Table 2 shows the mean Nusselt number, surface temperatures of the circle indentations and outlet temperatures of the air jet for different H/D_h ratios and Reynolds numbers. Increasing in jet-to-plate distance from H/D_h=4 to 12 decreases mean Nu number and increases mean surface temperature of the circle indentations due to decreasing turbulance intensity. However, with increasing of Re number as Nu_m enhances, T_{sm} reduces. Besides, $T_{out\text{-}air\ jet}$ reduces with increasing Re number because of increasing conduction resistance of the surfaces.

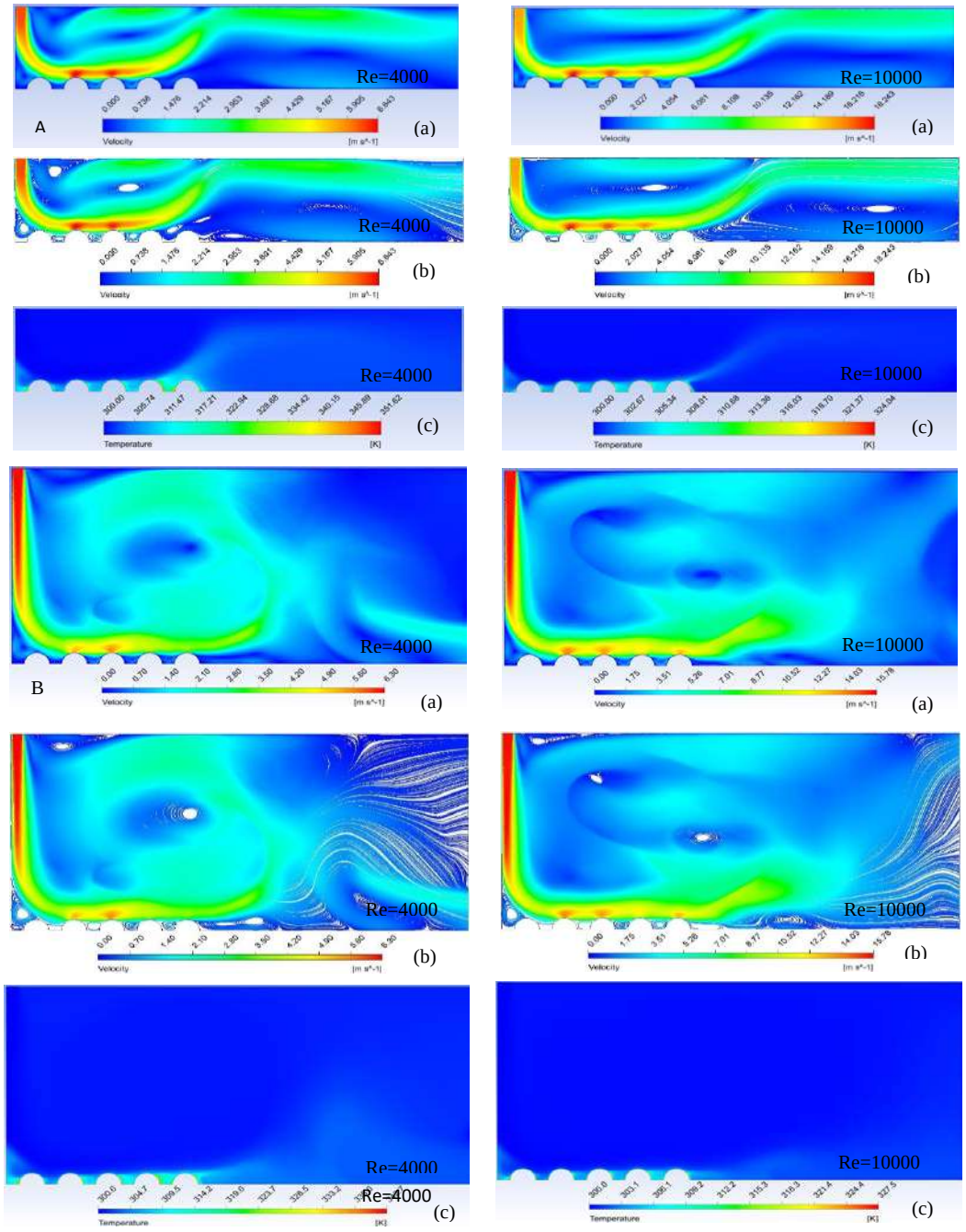

Figure. 6. A-H/D_h=4, B- H/D_h=10 (a) Velocity (b) Streamline (c) Temperature distributions for different Re numbers

Table 2. Results of Nu_m, T_{sm} and $T_{out\text{-}jet\ air}$ of the cylinder surfaces for different Re and H/D_h

Cylinder surface	Nu_m		T_{sm}		$T_{out\text{-}air\ jet}$	
	H/D_h=4	**H/D_h=12**	**H/D_h=4**	**H/D_h=12**	**H/D_h=4**	**H/D_h=12**
Re=4000	11.5242	11.8225	320.760	320.254	302.042	302.026
Re=6000	15.8538	14.9685	315.017	315.874	301.342	301.361
Re=10000	19.9690	19.6509	311.788	311.933	300.804	300.727

5. CONCLUSION

The present study focuses on the numerical research of heat transfer from a heated circle patterned copper surface, indise a rectangular channel by using a single jet flow. The numerical results were compared with the numerical and experimental datas of study existed in literature and found they were in well agreement. The results were presented as the variations of the mean Nu numbers and temperatures for each circle patterned indentation surface. The temperature and velocity distributions and streamlines of jet fluid flow and mean temperature and Nu values of whole circle surfaces and values of air jet outlet temperature were also analyzed for different Re numbers and jet-to-plate distence H/D_h ratios. The following conclusions can be drawn from the numerical results;

-Increase in Reynolds number increases the heat transfer on the surface of the heated circles, which enhance the Nu number.

- As the highest local Nu number value was obtained for the case of 1 at H/D_h=4, it was attained the case for 2 with increasing in H/D_h due to resulting from recirculation.

- Mean Nusselt number increased of 64.85% from Re=4000 to Re=10000 for H/D_h=6. However, Nu number was less sensitive to H/D_h ratio in the range of H/D_h=4-12. From H/D_h=6 to H/D_h =12 mean Nusselt number diminished 4.48% for Re=4000 due to a reduction of turbulance intensity. Besides, the highest mean Nusselt number was achieved for Re=10000 and H/D_h=6.

- When the case 1 has the lowest mean surface temperature for H/D_h=4, jet flow effect shifted toward circle 2 (case 2) depending on the recirculations for another investigated H/D_h ratios. Occurred recirculation sizes decrease with increasing Re number due to prevention of expansion of recirculations by increasing jet flow velocity.

- Because of separation of jet flow from the circle patterned surface, recirculations occur. Thermal boundary layer thickness also increases in that region, which causes to increase the temperature.

In a conclusion, the heat transfer, including local and average Nusselt numbers, are significantly affected by jet Reynolds numbers; while it is less sensitive to jet-to-plate distance, H/D_h ratio. Also, it is considered that geometry of air jet and channel used in this study can be employed to cool electronic components due to resembling various electronic equipment application.

REFERENCES

[1]. B.W. Webb, C. Ma, "Single-phase liquid jet impingement heat transfer", *Adv. Heat Transf*., vol. 26, pp. 105–217, 1995.
[2]. I. Sezai, A. A. Mohamad, "Three dimensional simulation of laminar rectangular impinging jets, flow structure, and heat transfer", *J. Heat Transf.*, vol. 121, pp. 50-56, 1999.
[3]. A. J. Bula, M. M. Rahman and J. E. Leland, "Numerical modeling of conjugate heat transfer during impingement of free liquid jet issuing from a slot nozzle", *Numer. Heat Transfer Part A: Appl*., vol. 38 (1), pp. 45-66, 2000.
[4]. M. A. Ebadian and C. X. Lewis, "A review of high-heat-flux heat removal Technologies", *J. Heat Transf.*, vol. 133, pp. 801-812, 2011.
[5]. M. K. Sung and I. Mudawar, "Correlation of critical heat flux in hybrid jet impingement/micro-channel cooling scheme", *Int. J. Heat Mass Transf*., vol. 49, pp. 2663-2672, 2006.
[6]. Y. H. Liu, S. J. Song, Y. H. Lo, "Jet impingement heat transfer on target surfaces with longitudinal and transverse grooves", *Int. J. Heat Mass Transf*., vol.58, pp. 292-299, 2013.
[7]. FLUENT User's Guide, Fluent Inc. Lebanon, NH., 2003.
[8]. M. Kilic, T. Calisir, S. Baskaya, "Experimental and numerical study of heat transfer from a heated flat plate in a rectangular channel with an impinging air jet", *J Braz. Soc. Mech. Sci. Eng.*, vol. 39, pp. 329-344, 2017.

ACKNOWLEGMENT

The authors would like to thank Scientific Research Projects Coordination Unit of Cumhuriyet University (Sivas/Turkey) for their financial support to this research under project number TEKNO-021.

BIOGRAPHY

Koray Karabulut is an Assistant Professor in the Electric and Energy Department, Vocational High School of Sivas, Sivas Cumhuriyet University, Sivas, Turkey. He received his Ph.D. degree in Department of Energy in 2015 from the University of Cumhuriyet. His research interests include heat and mass transfer, heat insulation, conservation of energy, plate fin heat exchangers, heat transfer of nanofluids, thermodynamics, fluid mechanics and computational fluid dynamics.

ICENS 4TH INTERNATIONAL CONFERENCE ON ENGINEERING AND NATURAL SCIENCE
2 - 6 May 2018 KIEV UKRAINE

Modeling the Weight and Length Changes of the Concrete Exposed to Sulfate using Artificial Neural Network

Mucteba Uysal[1], Baris Sayin[2], Veysel Akyuncu[3], Harun Tanyildizi[4], Mansur Sumer[5]

Abstract

This paper presents the modeling of an experimental investigation carried out to evaluate some mechanical and durability properties of concrete mixtures in which Turkish Class C and Class F fly ashes were partially replaced with cement. A total of 39 mixtures with different mix designs were prepared. After compressive strength testing, the mixtures containing Class F and Class C fly ashes which had similar compressive strength values to control mixtures at 28 d for each series were used for sulfate resistance tests. The degree of sulfate attack was evaluated using expansion and weight loss. The test results indicated that Class C fly ash showed higher compressive strength than Class F fly ash. Moreover, the addition of fly ash significantly increased the resistance to sulfate attack when each amount of fly ash addition regardless of fly ash types was employed. In this paper, the Artificial Neural Network (ANNs) techniques were used to model the relative change in the weight and length of the concrete exposed to sulfate. The best algorithm for length changes of concrete exposed to sulfate is BFGS quasi-Newton backpropagation algorithm while the best algorithm for weight changes of concrete exposed to sulfate is Polak-Ribiere conjugate gradient backpropagation algorithm.

Keywords: Class F fly ash, Class C fly ash, The weight change, The length change, Sulfate resistance.

1. INTRODUCTION

ANN can exhibit a surprising number of human brain characteristics [1-2]. The fundamental concept of neural networks is the structure of the information processing system [3-4]. They are consisting of a large number of simple processing elements called as neurons. A schematic diagram for an artificial neuron model is given in Fig. 1.

[1] *Corr.author: Istanbul University, Department of Civil Engineering, Istanbul, Turkey. mucteba.uysal@istanbul.edu.tr*

2 Istanbul University, Department of Civil Engineering, Istanbul, Turkey. barsayin@istanbul.edu.tr

[3] *Namik Kemal University, Department of Civil Engineering, Tekirdag, Turkey. vakyuncu@nku.edu.tr*

[4] *Firat University, Department of Civil Engineering, Elazig, Turkey. htanyildizi@firat.edu.tr*

[5] *Sakarya University, Department of Civil Engineering, Sakarya, Turkey. msumer@sakarya.edu.tr*

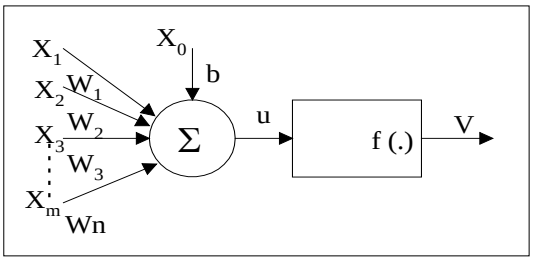

Figure 1. Artificial neuron model

Let $X=(X_1, X_2 \ldots X_n)$ represent the n input applied to the neuron. Where W_j represents the weight for input X_j and b is a bias, then the output of the neuron is given by Eq. 1. These neurons are connected with connection link. Each link has a weight that is multiplied by transmitted signal in network. Each neuron has an activation function to determine the output. There are many kinds of activation functions. Usually nonlinear activation functions such as sigmoid, step are used. ANNs are trained by experience, when an unknown input is applied to the network it can generalize from past experiences and produce a new result [5-8].

$$u = \sum_{j=0}^{m} x_j w_j - b \quad \text{and} \quad V = f(u) \tag{1}$$

Artifical neural networks are systems that are deliberately constructed to make use of some organizational principles resembling those of the human brain [5-7]. They represent the promising new generation of information processing systems.

When designing an ANN model, a number of considerations must be taken into account. At first the suitable structure of the ANN model must be chosen. Then, the activation function need to be determined. The number of layers and the number of units in each layer must be chosen. Generally desired model consists of a number of layers. The most general model assumes complete interconnections between all units. These connections can be bidirectional or unidirectional. ANN can create its own organization or representation of the information it receives during learning time [5-7]. There are many kind of ANN structure. One of these is multilayer feed forward ANN and is shown in Fig. 2.

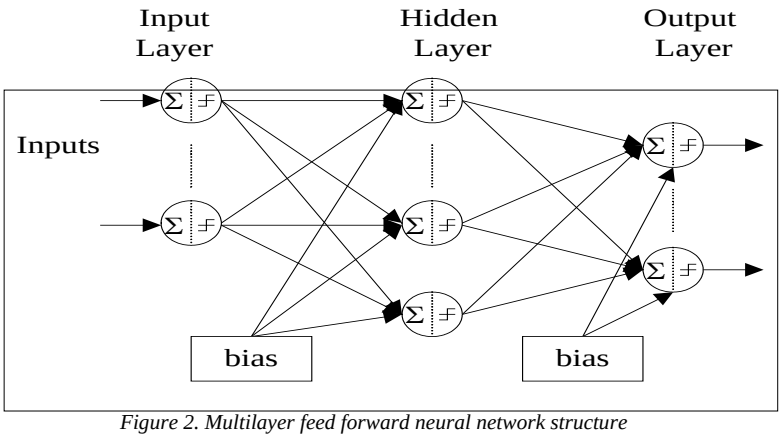

Figure 2. Multilayer feed forward neural network structure

2. METHODS

In this study, the problem is proposed to network models by means of eight inputs and two output parameters. The parameters such as amount of cement, amount of fly ash, amount of binder, amount of sand, amount of group I aggregate, amount of group II aggregate, amount of water, curing day were selected as input variables. The model output variables were the weight and length changes of the concrete exposed to sulfate. A data set including 180 data samples obtained from experimental studies were used for artificial neural networks. The data were normalized by dividing with max values. ANN architecture used for this study is given in Fig. 3.

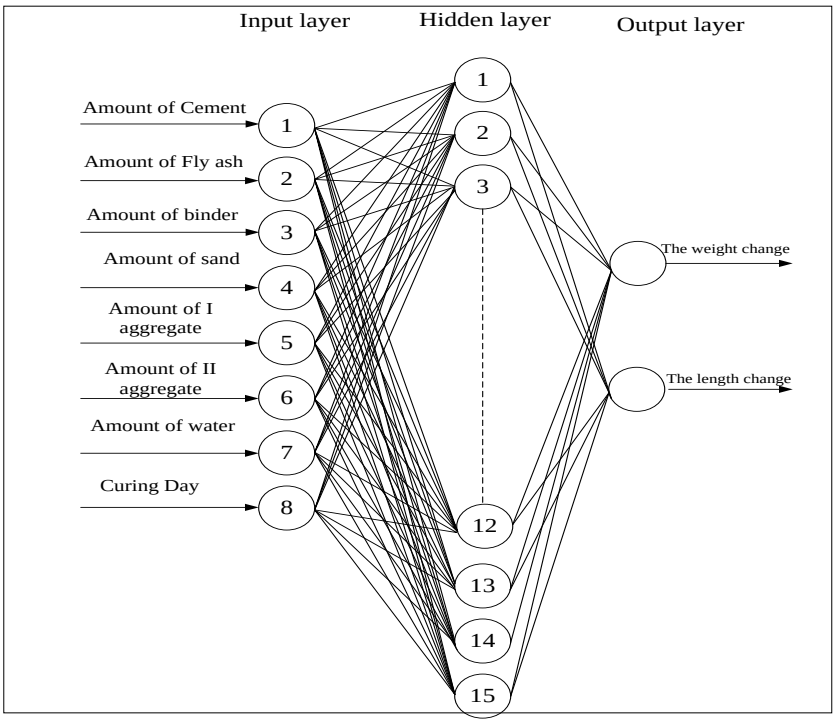

Figure 3. ANN architecture

The all algorithms of ANN were used for this study but the BFGS quasi-Newton backpropagation, Fletcher-Powell conjugate gradient backpropagation, Polak-Ribiere conjugate gradient backpropagation, Gradient descent with adaptive lr backpropagation, Gradient descent w/momentum & adaptive lr backpropagation, Levenberg-Marquardt backpropagation, One step secant backpropagation, Random order incremental training w/learning functions, Scaled conjugate gradient backpropagation were just learning. The computer program was performed under MATLAB software using the neural network toolbox. In the training, the number of neuron on the hidden layer changed to find best results. The best result for BFGS quasi-Newton backpropagation algorithm was obtained from the fifteen neurons. The best result for Fletcher-Powell conjugate gradient backpropagation was obtained from the fourteen neurons. The best result for Polak-Ribiere conjugate gradient backpropagation was obtained from the sixteen neurons. The best result for Gradient descent with adaptive lr backpropagation was obtained from the eighteen neurons. The best result for Gradient descent w/momentum & adaptive lr backpropagation was obtained from the eighteen neurons. The best result for Levenberg-Marquardt backpropagation was obtained from the six neurons. The best result for One step secant backpropagation was obtained from the sixteen neurons. The best result for Random order incremental training w/learning functions was obtained from the sixteen neurons. The best result for Scaled conjugate gradient backpropagation was obtained from the nine neurons. A data set including 180 data samples obtained from experimental studies were used for artificial neural networks. From these, 90 data patterns were used for training the network, and the remaining 90 patterns were randomly selected and used as the test data set.

Figs. 4-14 present the measured values versus predicted values by ANN model with R^2 coefficients. Fig. 4 and Fig. 14 shows that the best algorithm for length changes of concrete exposed to sulfate is BFGS quasi-Newton backpropagation algorithm with R^2 of 0.9804 while the best algorithm for weight changes of concrete exposed to sulfate is Polak-Ribiere conjugate gradient backpropagation algorithm with R^2 of 0.9708.

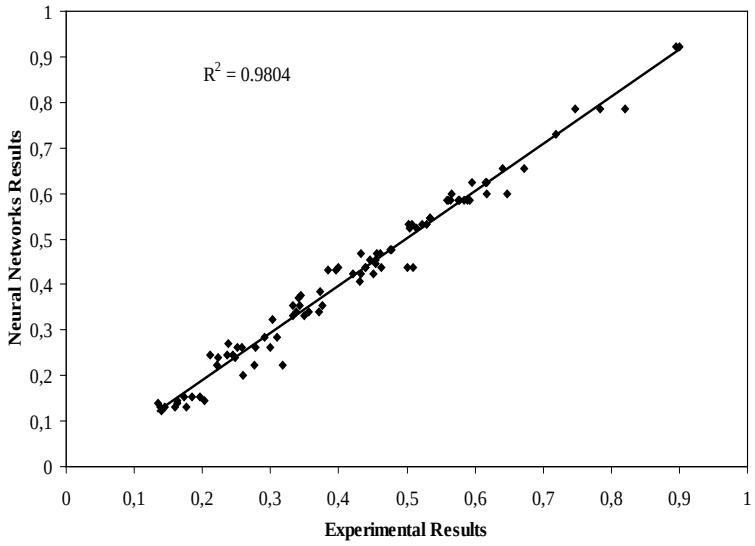

Figure 4. Linear relationship between the measured and predicted length change for the BFGS quasi-Newton B.A.

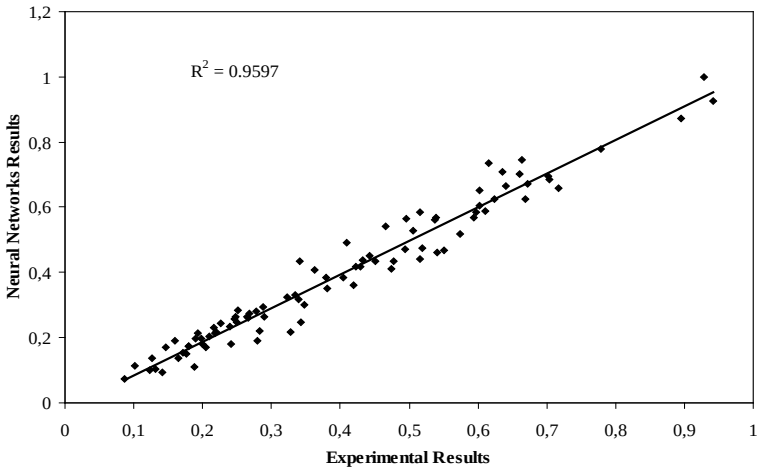

Figure 5. Linear relationship between the measured and predicted weight changes change for the BFGS quasi-Newton B.A.

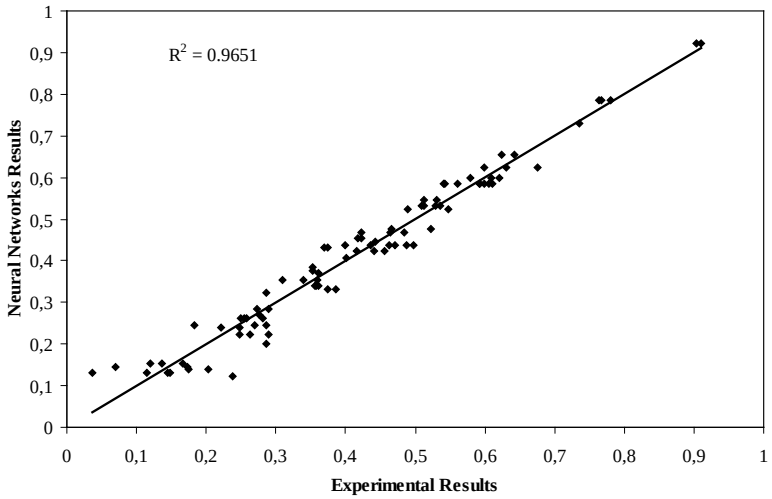

Figure 6. Linear relationship between the measured and predicted length changes for the Fletcher-Powell conjugate gradient B.A.

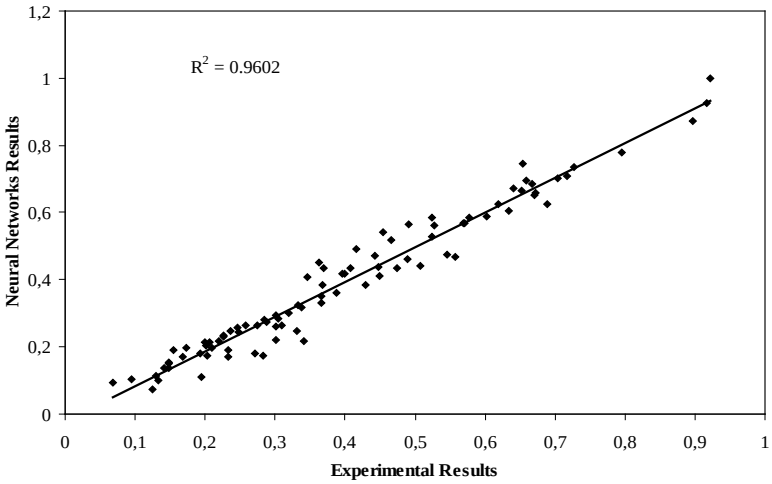

Figure 7. Linear relationship between the measured and predicted weight changes for the Fletcher-Powell conjugate gradient B.A.

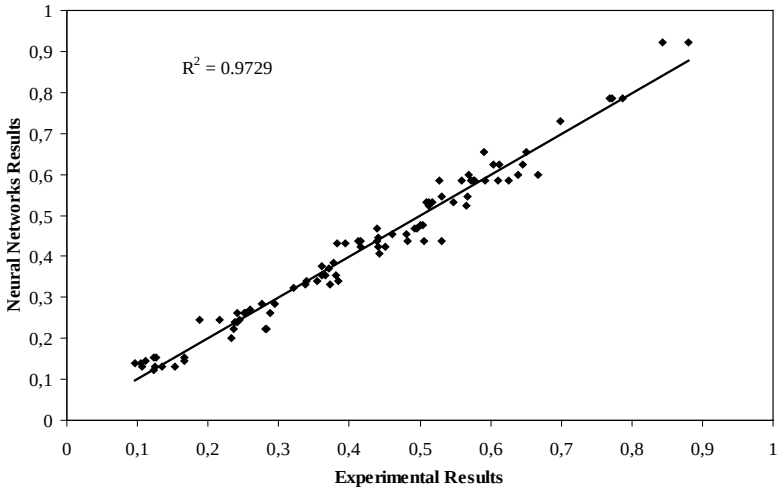

Figure 8. Linear relationship between the measured and predicted length changes for the Polak-Ribiere conjugate gradient B.A.

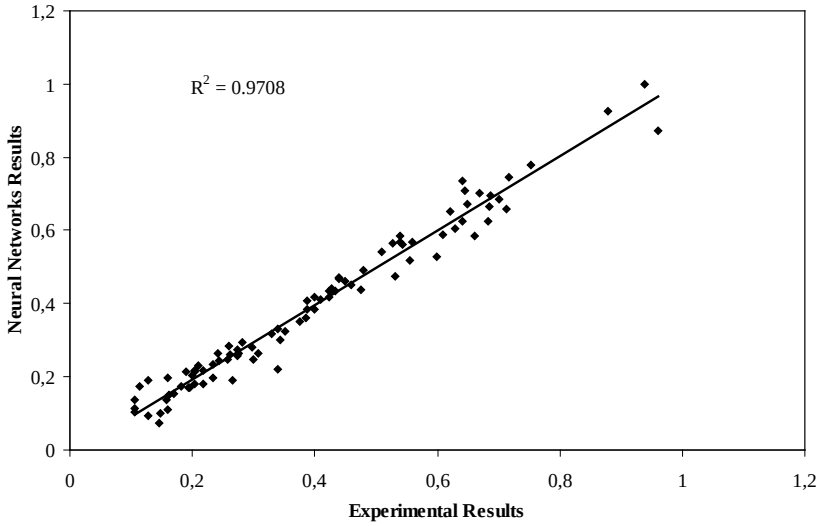

Figure 9. Linear relationship between the measured and predicted weight changes for the Polak-Ribiere conjugate gradient B.A.

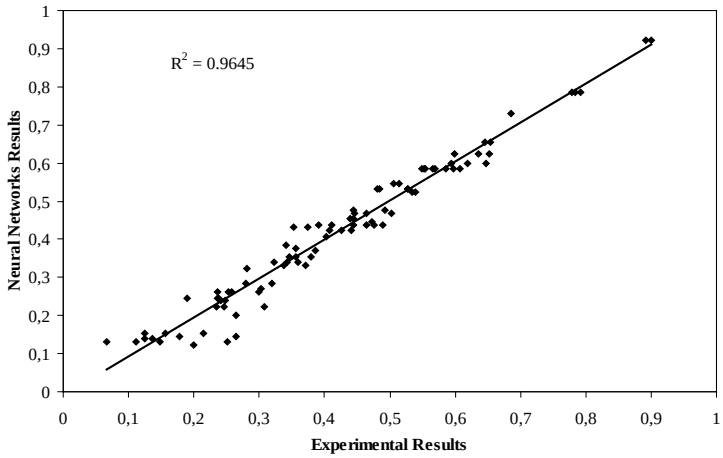

Figure 10. Linear relationship between the measured and predicted length changes for the Gradient descent with adaptive Lr B.A.

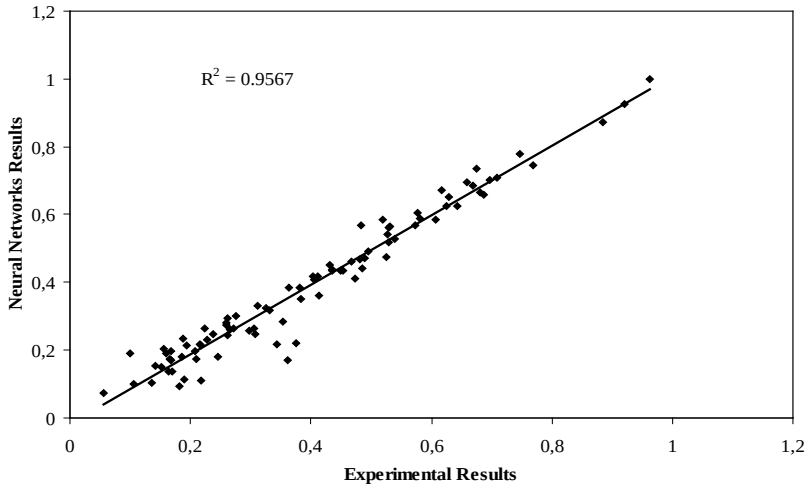

Figure 11. Linear relationship between the measured and predicted weight changes for the Gradient descent with adaptive lr B.A.

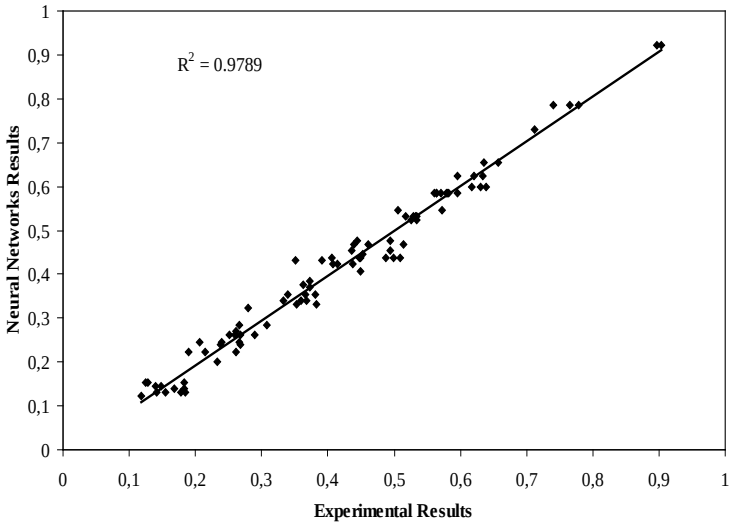

Figure 12. Linear relationship between the measured and predicted length changes for the Gradient descent w/momentum & adaptive lr backpropagation algorithm.

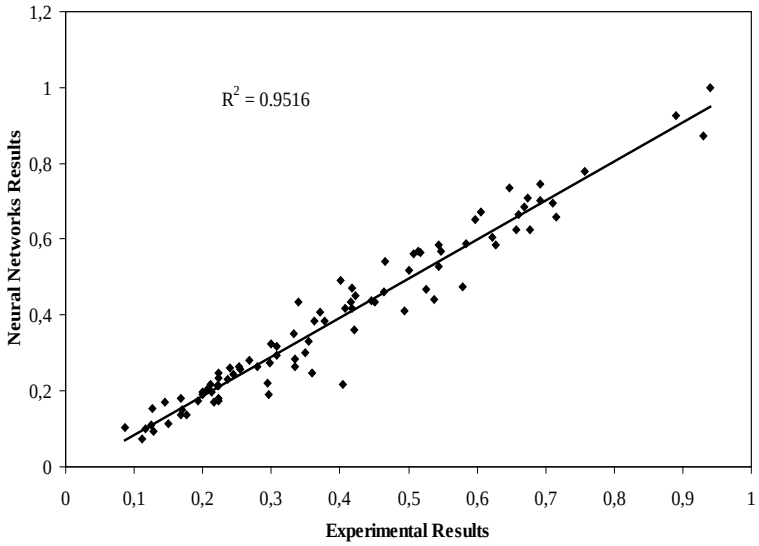

Figure 13. Linear relationship between the measured and predicted length changes for the Gradient descent w/momentum & adaptive lr backpropagation algorithm.

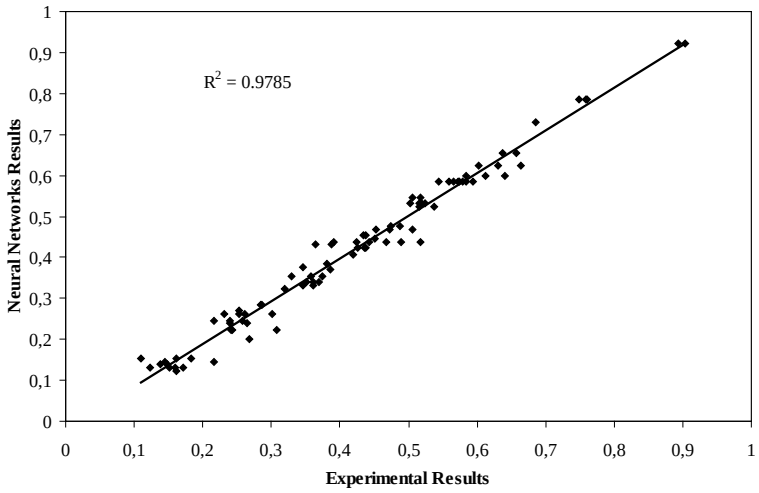

Figure 14. Linear relationship between the measured and predicted length changes for the Levenberg-Marquardt B.A.

The training performance during the training process is given in Figs. 15 and 16 where the

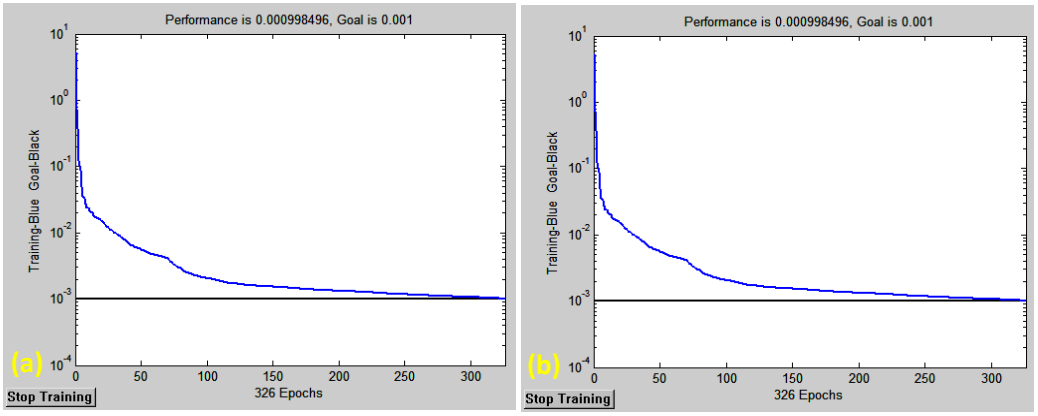

variation of mean-square error with training epochs is illustrated.

Figure 15. (a) Training performance for BFGS quasi-Newton backpropagation algorithm, (b) Training performance for Fletcher-Powell conjugate gradient backpropagation algorithm

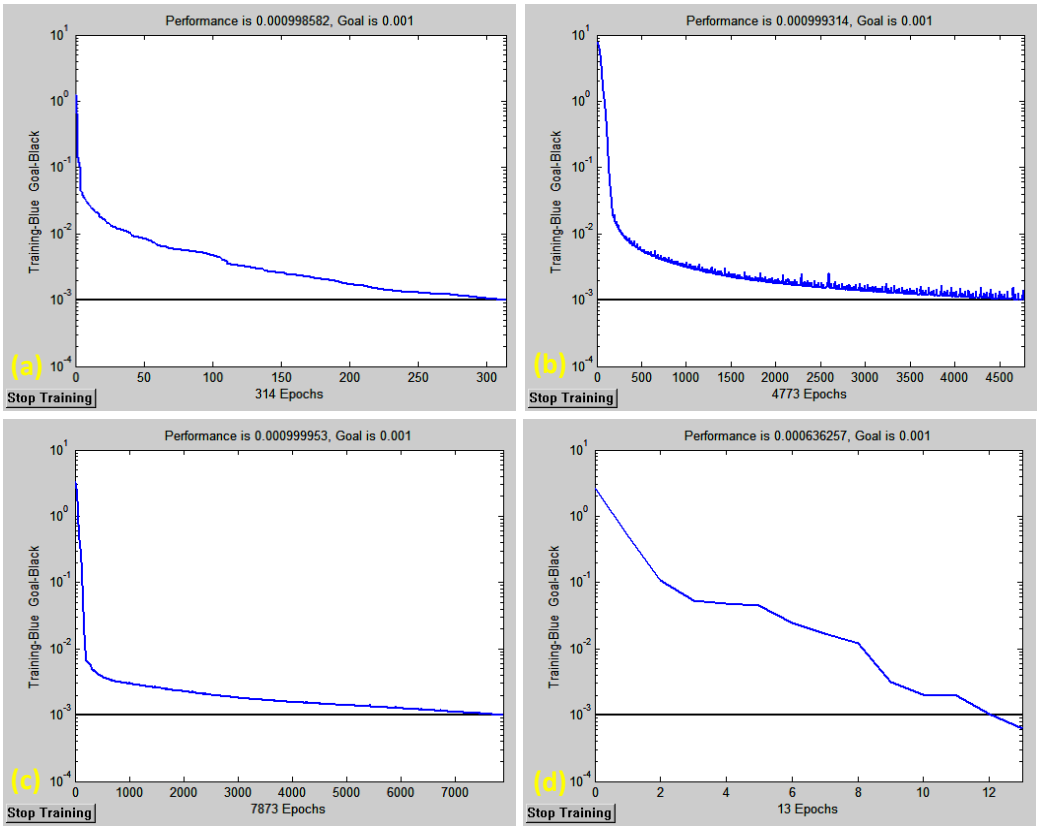

Figure 16. (a) Training performance for the Polak-Ribiere conjugate gradient backpropagation algorithm, (b) Training performance for the Gradient descent with adaptive lr backpropagation algorithm, (c) Training performance for Gradient descent w/momentum & adaptive lr backpropagation algorithm, (d) Training performance for Levenberg-Marquardt backpropagation algorithm

3. CONCLUSIONS

Laboratory tests were performed to determine the deterioration induced by the magnesium sulfate on the control and Class C and Class F type fly ashes additive concretes. Based on the experimentally obtained results, ANN has been used to for the prediction of length changes of concrete exposed to sulphate. The neural networks based model gave high prediction accuracy and correlation. The best algorithm for length changes of concrete exposed to sulfate is BFGS quasi-Newton backpropagation algorithm with R^2 of 0.9804 while the best algorithm for weight changes of concrete exposed to sulfate is Polak-Ribiere conjugate gradient backpropagation algorithm with R^2 of 0.9708. Therefore, it is possible to predict length changes of concrete exposed to sulfate using artificial neural networks.

REFERENCES

[1]. A. Oztas, M. Pala, E. Ozbay, E. Kanca, N. Caglar and M.A. Bhatti, Predicting the compressive strength and slump of high strength concrete using neural network Construction and Building Materials 2006;20:769-775.
[2]. A. Demir, I.B. Topcu and H. Kusan. Modeling of some properties of the crushed tile concretes exposed to elevated temperatures. Construction and Building Materials 2011;25: 1883-1889.
[3]. B.B. Adhikary and H. Mutsuyoshi, Artificial neural networks for the prediction of shear capacity of steel plate strengthened RC beams. Construction and Building Materials 2004;18:409-417.
[4]. M. Saridemir, Predicting the compressive strength of mortars containing metakaolin by artificial neural networks and fuzzy logic. Advances in Engineering Software 2009;40(9):920-927.

[5]. D. Hanbay, I. Turkoglu and Y. Demir, An expert system based on wavelet decomposition and neural network for modeling Chua's circuit. Expert Systems with Applications 2008;34: 2278-2283.
[6]. S. Haykin, Neural networks, a comprehensive foundation, College Publishing Comp. Inc 1994.
[7]. D. Hanbay, I. Turkoglu and Y. Demir, An expert system based on wavelet decomposition and neural network for modeling Chua's Circuit, Expert systems with applications, 2008, 34(4), 2278-2283,
[8]. C. Bilim, C.D. Atis, H. Tanyildizi and O. Karahan, Predicting the compressive strength of ground granulated blast furnace slag concrete using artificial neural network. Advances in Engineering Software 2009; 40:334-340.

ICENS 4TH INTERNATIONAL CONFERENCE ON ENGINEERING AND NATURAL SCIENCE
2 - 6 May 2018 KIEV UKRAINE

The factor of optimum angle of carbon fiber reinforced polymers

Aylin Ece Kayabekir[1], Baris Sayin[2], Gebrail Bekdas[3], Sinan Melih Nigdeli [4]

Abstract

Carbon fiber reinforced polymer (CFRP) strips can be used to increase the flexural moment or shear capacity of reinforced concrete (RC) elements. This study presents an optimization methodology in order to investigate the factor of application angle of CFRP strips. In the optimization, the spacing of the strips, the width of the strips and angle of strips are the design variables. The objective function is to minimize the area of the CFRP strips per unit meter in order to increase the shear capacity of reinforced concrete (RC) beam. ACI318- Building code requirements for structural concrete regulation is used for the development of the design constraints. Metaheuristic algorithms inspired by natural phenomena are feasible methods for the problem. The present study involves two metaheuristic algorithms, namely flower pollination algorithm (FPA) and teaching learning based optimization (TLBO). In the final, the optimum results were compared with the optimization results with constant angles (45º and 90º). Although the usage of constant 90º is practical and 45º is the angle of principle stresses, the usage of the angle as a design variable is useful in minimization of the total CFRP area.

Keywords: Carbon fiber reinforced polymer, shear capacity, Reinforced concrete, Metaheuristic algorithm, Optimization, Teaching learning based optimization, flower pollination algorithm.

1. INTRODUCTION

In reinforced concrete (RC) structures, shear reinforcements (stirrups) are used for shear forces. Because of the seismic retrofit or enlargement of existing structures, the shear capacity may be needed to increase. In order to add additional stirrups, jacketing of existing member may be needed. In that case, the RC cross section will be increased and the total weight and rigidity of the structure are effected. Thus, the retrofitted design must be also analyzed as a new project. This option is a way to increase the shear force capacity. A second option is to use carbon fiber reinforced polymer (CFRP) in the seismic retrofit. Comparing to the first option, the rigidity and weight of the structure remain the same and the shear capacity is improved by using CFRP which is easy to apply and have a linear deformation behavior with big strain capacity.

The subject of the paper is to investigate the effect of the best CFRP strip angle in order to increase the shear capacity. For that reason, two optimization methodologies are presented and these methodologies employ metaheuristic algorithms such as teaching learning based optimization (TLBO) and flower pollination algorithm (FPA). For the comparisons, the CFRP strip angles are not taken as a design variable by taking constant angles such as 45º and 90º. Then, the results are compared with the cases including the angle as a design variable.

Teaching learning based optimization (TLBO) is inspired from the education process of a class and it was developed by Rao et al. [1]. TLBO have been used in optimization of structural problems such as truss optimization [2-4], optimization of RC retaining walls [5], optimization of RC columns [6], optimization of RC beams [7] and tuning of mass damper [8-10].

[1] *Istanbul University, Department of Civil Engineering, 34320, Avcilar/Istanbul, Turkey. ecekayabekir@gmail.com*

[2] *Corresponding author: Istanbul University, Department of Civil Engineering, 34320, Avcilar/Istanbul, Turkey. barsayin@istanbul.edu.tr*

[3] *Istanbul University, Department of Civil Engineering, 34320, Avcilar/Istanbul, Turkey. bekdas@istanbul.edu.tr*

[4] *Istanbul University, Department of Civil Engineering, Istanbul, Turkey, melihnig@istanbul.edu.tr*

Yang formalized the cross and self-pollination process for a metaheuristic algorithm called flower pollination algorithm (FPA) [11]. In structural engineering, FPA has been employed in the optimization of trusses [12], tuned mass dampers [13-14] and several problems [15].

2. METHODOLOGY

The aim of the optimization is to minimize the required CFRP area per meter; A, by optimizing the design variables such as width; w_f, spacing; s_f and angle; β of CFRP in order to gain an additional shear force capacity for a RC cross section with breadth; b_w and effective depth; d. The figure of the T-shaped cross section and the figures showing the design variables are shown in Fig. 1(a for β=90 and b for general case). d_f is the depth of the RC member covered by CFRP which is formulized as

$$d_f = d - h_f \tag{1}$$

where , h_f is the height of the RC slab.

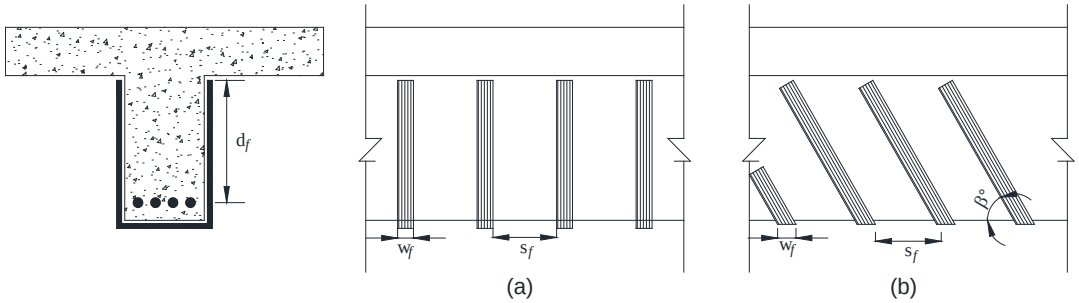

Figure 1. The design variables [16]

The objective function is given as Eq. (2).

$$A = \frac{w_f\left(\frac{2d_f}{\sin\beta} + b\right)}{s_f} x1000 \tag{2}$$

The design constraints are given as follows according to ACI 318 [17].

$$g_1(x): s_f \le d/4 \tag{3}$$

$$g_2(x): V_{additional} < 0.7R\frac{(2t_f w_f f_{fe})(\sin\beta + \cos\beta)d_f}{s_f + w_f} \tag{4}$$

$$g_3(x): \frac{(2t_f w_f f_{fe})(\sin\beta + \cos\beta)}{s_f + w_f} \le \frac{2\sqrt{f'_c}b_w d}{3} - V_s \tag{5}$$

The design constraints are presented in Table 1 with the numerical values used in the example. The ranges are also given for design variables in Table 1.

The steps of the methodology are as follows.

Step 1: Define design constants and ranges.

Step 2: Generate an initial solution matrix.

This matrix is generated by using random numbers. Discrete variables are used for practical design. β is multiples of 5˚ while w_f and s_f are multiples of 10 mm. The number of solution vectors (population) in the solution matrix is 20 in the numerical examples. For all set of solutions, design objective and constraints are calculated. For violating design constraints, the objective function is penalized with a big value such of 10^{16} mm^2 per m.

Step 3: New solutions are generated.

Table 16. The design constants

Definition	Symbol	Unit	Value
Breadth	b_w	mm	200
Height	h	mm	500
Effective depth	d	mm	450
Thickness of CFRP	t_f	mm	0.165
Reduction factor	R	-	0.5
Thickness of slab	h_f	mm	100
Comp. strength of concrete	f_c'	MPa	20
Effective tensile strength of CFRP	f_{fe}	MPa	3790
Width of CFRP	w_f	mm	10-100
Specific of CFRP	s_f	mm	0-d/4
Angle of CFRP	β	°	0-90
Additional shear force	$V_{additional}$	kN	50 (case 1) 75 (case 2) 100 (case 3) 125 (case 4) 150 (case 5)
Shear force capacity of rebar	V_s	kN	50

In TLBO, new solutions are generated by using teacher and learner phases, respectively. In FPA, global and local optimization cases are considered by using a switch probability which is taken as 0.5.

Step 4: Update the existing solutions.

In this step, all existing solutions are compared with the new ones in mean of objective function. The best one is stored.

Step 5: Iterative optimization.

The optimization (Step 3 and 4) continue until several iterations (10000 in numerical example).

3. NUMERICAL EXAMPLE

The optimization is done for several additional shear force values. The optimum results are presented in Tables 2-6. The optimization is done for 20 independent runs. Tables also contain the best (A_{best}) and mean (A_{mean}) area of CFRP with standard deviation and needed iteration values to reach to optimum results. According to the results, β values are 65˚ or 70˚ according to the different additional shear capacity cases.

Table 2. Optimum results for 50 kN additional shear capacity

	TLBO	FPA
w_f (mm)	30	30
s_f (mm)	90	90
β (˚)	65	65
A_{best} (mm^2)	243091.13	243091.13
A_{mean} (mm^2)	243091.13	243265.82
Standard deviation	$5.97x10^{-11}$	$7.81x10^{2}$
Iteration number	140	220

Table 3. Optimum results for 75 kN additional shear capacity

	TLBO	FPA
w_f (mm)	50	50
s_f (mm)	80	80
β (˚)	70	70
A_{best} (mm^2)	363432.47	363432.47
A_{mean} (mm^2)	363432.47	363432.47
Standard deviation	$5.97x10^{-11}$	$5.97x10^{-11}$
Iteration number	100	240

Table 4. Optimum results for 100 kN additional shear capacity

	TLBO	FPA
w_f (mm)	50	100
s_f (mm)	50	100
β (˚)	65	65
A_{best} (mm^2)	486182.27	486182.27
A_{mean} (mm^2)	486182.27	486182.27
Standard deviation	$1.19x10^{-10}$	$1.19x10^{10}$
Iteration number	60	40

Table 5. Optimum results for 125 kN additional shear capacity

	TLBO	FPA
w_f (mm)	80	80
s_f (mm)	50	50
β (˚)	65	65
A_{best} (mm^2)	598378.18	598378.18
A_{mean} (mm^2)	598378.18	598378.18
Standard deviation	$1.19x10^{-10}$	$1.19x10^{10}$
Iteration number	100	40

Table 6. Optimum results for 150 kN additional shear capacity

	TLBO	FPA
w_f (mm)	100	100
s_f (mm)	30	30
β (˚)	70	70
A_{best} (mm^2)	726864.95	726864.95
A_{mean} (mm^2)	726864.95	726864.95
Standard deviation	$1.19x10^{-10}$	$1.19x10^{10}$
Iteration number	60	320

4. CONCLUSIONS

The both metaheuristics are successful in finding the optimum design. Generally, the needed iteration numbers are low. In Table 4, the values for both algorithms are different, but the best results are the same. The only difference is the spacing is double for FPA and the width is also the double of TLBO. In TLBO, the design is more homogenous, but the results of FPA are more practical.

For shear deformations, 45˚ angle is the best solution according to the knowledge. It is also proved by inequality given in Eq. (4), but the application of CFRP with an angle increases the total area of CFRP strip. The optimum results are also presented for β=45˚ (Tables 7-11) and β=90˚ (Tables 12-15). Since the length of the strips will be more longer than bigger angle values, using β as 45˚ is at least 10% costly comparing to the optimum results given in Tables 2-6.

Table 7. Optimum results for 50 kN additional shear capacity (β=45˚)

	TLBO	FPA
w_f (mm)	30	30
s_f (mm)	100	100
A_{best} (mm^2)	274603.72	274603.72
Iteration number	60	40

Table 8. Optimum results for 75 kN additional shear capacity (β=45˚)

	TLBO	FPA
w_f (mm)	60	60
s_f (mm)	110	110
A_{best} (mm^2)	419982.17	419982.17
Iteration number	60	40

Table 9. Optimum results for 100 kN additional shear capacity (β=45˚)

	TLBO	FPA
w_f (mm)	60	60
s_f (mm)	70	70
A_{best} (mm^2)	549207.45	549207.45
Iteration number	60	40

Table 10. Optimum results for 125 kN additional shear capacity (β=45˚)

	TLBO	FPA
w_f (mm)	70	70
s_f (mm)	50	50
A_{best} (mm^2)	694137.20	694137.20
Iteration number	60	40

Table 11. Optimum results for 150 kN additional shear capacity (β=45˚)

	TLBO	FPA
w_f (mm)	90	90
s_f (mm)	40	40
A_{best} (mm^2)	823811.18	823811.18
Iteration number	60	40

Table 12. Optimum results for 50 kN additional shear capacity (β=90˚)

	TLBO	FPA
w_f (mm)	40	50
s_f (mm)	80	100
A_{best} (mm^2)	300000	300000
Iteration number	60	40

Table 13. Optimum results for 75 kN additional shear capacity (β=90˚)

	TLBO	FPA
w_f (mm)	40	10
s_f (mm)	40	10
A_{best} (mm^2)	450000	450000
Iteration number	60	40

Table 14. Optimum results for 100 kN additional shear capacity (β=90˚)

	TLBO	FPA
w_f (mm)	60	100
s_f (mm)	30	50
A_{best} (mm^2)	600000	600000
Iteration number	60	40

Table 15. Optimum results for 125 kN additional shear capacity (β=90˚)

	TLBO	FPA
w_f (mm)	90	90
s_f (mm)	20	20
A_{best} (mm^2)	736363.63	736363.63
Iteration number	60	40

The usage of β as 90˚ is the best design for practice, but the required shear force cannot be provided for 150 additional shear force capacity. Also, the optimum results given in Table 2-6 are nearly 20% better in the area of CFRP.

REFERENCES

[1]. Rao, R. V., Savsani, V. J., & Vakharia, D. P., (2011). Teaching–learning-Based Optimization: A Novel Method for Constrained Mechanical Design Optimization Problems. Computer-Aided Design, 43(3), 303-315.
[2]. Degertekin, S. O. and Hayalioglu, M. S. (2013), "Sizing truss structures using teaching-learning-based optimization", Computers & Structures, Vol.119, pp.177-188, DOI:10.1016/j.compstruc.2012.12.011
[3]. Camp, C. V. and Farshchin, M. (2014), "Design of space trusses using modified teaching–learning based optimization", *Engineering Structures*, Vol.62-63, pp.87-97. DOI:10.1016/j.engstruct.2014.01.020
[4]. Dede, T. and Ayvaz, Y. (2015), "Combined size and shape optimization of structures with a new meta-heuristic algorithm" Applied Soft Computing, Vol.28, pp.250-258, DOI:10.1016/j.asoc.2014.12.007
[5]. Temur, R, Bekdas, G. (2016), "Teaching learning-based optimization for design of cantilever retaining walls", Structural Engineering and Mechanics, Vol.57, No.4, pp.763-783, DOI: 10.12989/sem.2016.57.4.763
[6]. Bekdas G, Nigdeli SM. Optimum Design of Reinforced Concrete Columns Employing Teaching Learning Based Optimization. Challenge Journal of Structural Mechanics 2016; 2 (4): 216–219
[7]. Bekdas G, Nigdeli SM. Optimum Design of Reinforced Concrete Beams Using Teaching-Learning-Based Optimization. 3rd International Conference on Optimization Techniques in Engineering (OTENG '15), 7-9 November 2015, Rome, Italy
[8]. Nigdeli SM, Bekdas G. Teaching Learning Based Optimization for Parameter Estimation of Double Tuned Mass Dampers. 12th International Congress on Advances in Civil Engineering, 21-23 September 2016, Istanbul, Turkey.
[9]. Nigdeli SM, Bekdas G. Teaching-Learning-Based Optimization for Estimating Tuned Mass Damper Parameters. 3rd International Conference on Optimization Techniques in Engineering (OTENG '15), 7-9 November 2015, Rome, Italy.
[10]. Nigdeli SM, Bekdas G. Tuning of mass dampers for preventing brittle fracture by employing teaching learning based optimization. Joint Annual Meeting of GAMM and DMV, 7-11 March 2016, Braunschweig, Germany.
[11]. Yang, X. S., (2012). Flower Pollination Algorithm for Global Optimization. International Conference on Unconventional Computing and Natural Computation (pp. 240-249), Springer Berlin Heidelberg.
[12]. Bekdas G, Nigdeli SM, Yang X-S. Sizing Optimization of Truss Structures Using Flower Pollination Algorithm. Applied Soft Computing, 2015; 37: 322-331.

[13]. Nigdeli SM, Bekdas G, Yang X-S, Optimum Tuning of Mass Dampers by Using a Hybrid Method Using Harmony Search and Flower Pollination Algorithm. In: Harmony Search Algorithm. Advances in Intelligent Systems and Computing, vol 514, Del Ser J. (eds) Springer, pp. 222-231, 2017.
[14]. Nigdeli SM, Bekdas G, Yang XS. Optimum Tuning of Mass Dampers for Seismic Structures Using Flower Pollination Algorithm. 7th European Conference of Civil Engineering (ECCIE '16), 17-19 December 2016, Bern, Switzerland
[15]. Nigdeli SM, Bekdas G, Yang X-S, Application of the Flower Pollination Algorithm in Structural Engineering, In: Metaheuristics and Optimization in Civil Engineering, Yang X-S., Bekdas G., Nigdeli S.M., Eds., Springer, pp.25-43, 2016
[16]. Khalifa, Ahmed, and Antonio Nanni. "Improving shear capacity of existing RC T-section beams using CFRP composites." Cement and Concrete Composites 22.3 (2000): 165-174.
[17]. ACI 318M-05, Building code requirements for structural concrete and commentary, American Concrete Institute, 2005.

BIOGRAPHY

Aylin Ece Kayabekir, is a student of civil engineering master program of Istanbul University. She is working on structural optimization. Up to now, the authored several papers about optimization of RC retaining walls, RC shear walls, frames, carbon fiber reinforced polymers and dynamic of structures interacting with soil in conference like 7th European conference of civil engineering, International science symposium 2016, 3rd International conference on engineering and natural science and International conference on civil and environmental engineering.

Baris Sayin, Associative Professor, is currently employed by Department of Civil Engineering at Istanbul University as a Civil Engineer. Dr. Sayin graduated from Istanbul University with BS, MS and PhD in Civil Engineering. During the graduate education, he worked as a Research Assistant in the Department of Civil Engineering at the University in between 2000 and 2009. Dr. Sayin collaborated with Prof. Dr. Hamid Saadatmanesh on CFRP in RC structures as a Visiting Scholar in the Department of Civil Engineering and Engineering Mechanics at The University of Arizona for 12-months from September 2012. His research areas are fiber composites, industrial wastes and RC structures.

Gebrail Bekdas, Associative Professor, is researcher in Structural Control and Optimization at Istanbul University. He obtained his DPhil in Structural Engineering from Istanbul University with a thesis subject of design of cylindrical walls. He co-organized the 15th EU-ME Workshop: Metaheuristic and Engineering in Istanbul. In optimization, he organized several mini-symposiums or special sections in prestigious international events. He co-edited Metaheuristics and Optimization in Civil Engineering published by Springer in 2016 and he is one of the guest editors in 2017 special issue of KSCE Journal of Civil Engineering. He has authored more than 100 papers for journals and scientific events.

Sinan Melih Nigdeli, Associative Professor, is researcher in Structural Control and Optimization at Istanbul University. He obtained his DPhil in Structural Engineering from Istanbul Technical University with a thesis subject of active structural control. He co-organized the 15th EU-ME Workshop: Metaheuristic and Engineering in Istanbul. In optimization and structural control, he organized several mini-symposiums or special sections in prestigious international events. He co-edited Metaheuristics and Optimization in Civil Engineering published by Springer in 2016 and he is one of the guest editors in 2017 special issue of KSCE Journal of Civil Engineering. He has authored more than 100 papers for journals and scientific events.

ICENS 4TH INTERNATIONAL CONFERENCE ON ENGINEERING AND NATURAL SCIENCE
2-6 May 2018 KIEV UKRAINE

Designing a web based data acquisition system for battery-powered wireless sensor nodes: WiFiLab

Ismail Kirbas[1], Ayhan Dukkanci[2]

Abstract

Measurement of physical quantities such as temperature, humidity, vibration, light intensity and color by using sensors and recording the sensed data has almost become a necessity for all studies related to natural sciences. The increasing number of parameters to be measured, the necessity of using multiple sensor types, and data collection with wired devices over distant and mobile systems are difficult and laborious task. It is aimed to communicate multiple sensors to a central unit without using cables and to store the measurement data on a web based recording platform.

The proposed system WiFiLab requires no cable connection between sensor and data recording tool. The proposed data acquisition system is settled on an APACHE-based web server and MySQL database. The PHP scripting language is also preferred for coding server-side scripts. All Wi-Fi-based sensor nodes are in the client role. The data obtained from the sensor nodes is transferred to a wireless network created by the proposed system using the IEEE 802.11 communication standard and is recorded in the MySQL database via the master collection unit which is connected to the same network. After data acquisition period, the recorded data can be exported as a comma separated value file for later analysis using different analyze software.

Using the developed data collection platform, many sensors can transmit data synchronously with low latency and the transmitted values can be recorded in the web environment. It is especially seen that the developed system is extremely useful and successful in data collecting especially through moving objects when the freedom of movement is obligatory. By means of the developed system, it is now possible to collect data from hundreds of battery-powered wireless sensor node at the same time.

Keywords: Wireless data acquisition, battery-powered sensor nodes, web based data acquisition, WiFiLab, sensor signal analysis, NodeMCU.

1. INTRODUCTION

As a result of improvements in chip technology, the use of wireless sensor networks is becoming increasingly widespread. Wireless sensor networks are used in many areas, ranging from environmental monitoring to resource monitoring and industrial metering.

In accordance with the needs of the users, communication distance and frequency of signal transmission are determined and appropriate solutions are developed. Wireless sensor networks usually use ZigBee (IEEE 802.15.4), Bluetooth or Wi-Fi (IEEE 802.11) as their communication protocol.

When the literature is examined, many studies on wireless sensor networks are encountered. Arslan and Kirbas [1] proposed a wireless sensor and actuator sensor node model for Internet of Things applications. Mendez et al. [2] suggest a Wi-Fi based smart wireless sensor network for agricultural environments. Ulucinar et al. [3] offer a Wi-Fi cluster based wireless sensor network application for wildfire detection. Rawajbeh [4] suggests an object monitoring approach using wireless sensor network. Mehta [5] shows possibilities of the ESP 8266 wireless module. Kirbas and Bayilmis [6] developed a healthcare monitoring system using wireless sensor modules. Moreno et al. [7] published a paper on energy consumption of wireless sensor networks. Li et al. [8] explain applications of Wi-Fi based wireless sensor network in IoT and smart grid. Tozlu et al. [9] demonstrate

[1] *Corresponding author: Mehmet Akif Ersoy University, Department of Computer Engineering, 15100, Merkez/Burdur, Turkey. ismailkirbas@mehmetakif.edu.tr*

[2] *Mehmet Akif Ersoy University, ayhandukkanci@ogr.mehmetakif.edu.tr*

the feasibility of low-power Wi-Fi technology to enable IP connectivity of battery powered devices. Chakole et al. [10] developed an heart rate sensor using Wi-Fi module.

The designed wireless sensor network system shown in Figure 1 uses star network topology. The system can support various wireless sensor node. The basic requirement is that the sensor nodes can be connected to the network via wi-fi. The nodes connected to the network measure by means of the sensors and send the data they have obtained on the same network and whose IP address is obtained for a certain web server. The Apache Web Server software is installed on the web server to respond to incoming requests over the network. Nodes submit their own identity addresses and measurement results to a PHP page. The PHP script also saves the submitted parameters to the MySQL database along with the time information. The following figure shows the general diagram of the proposed system.

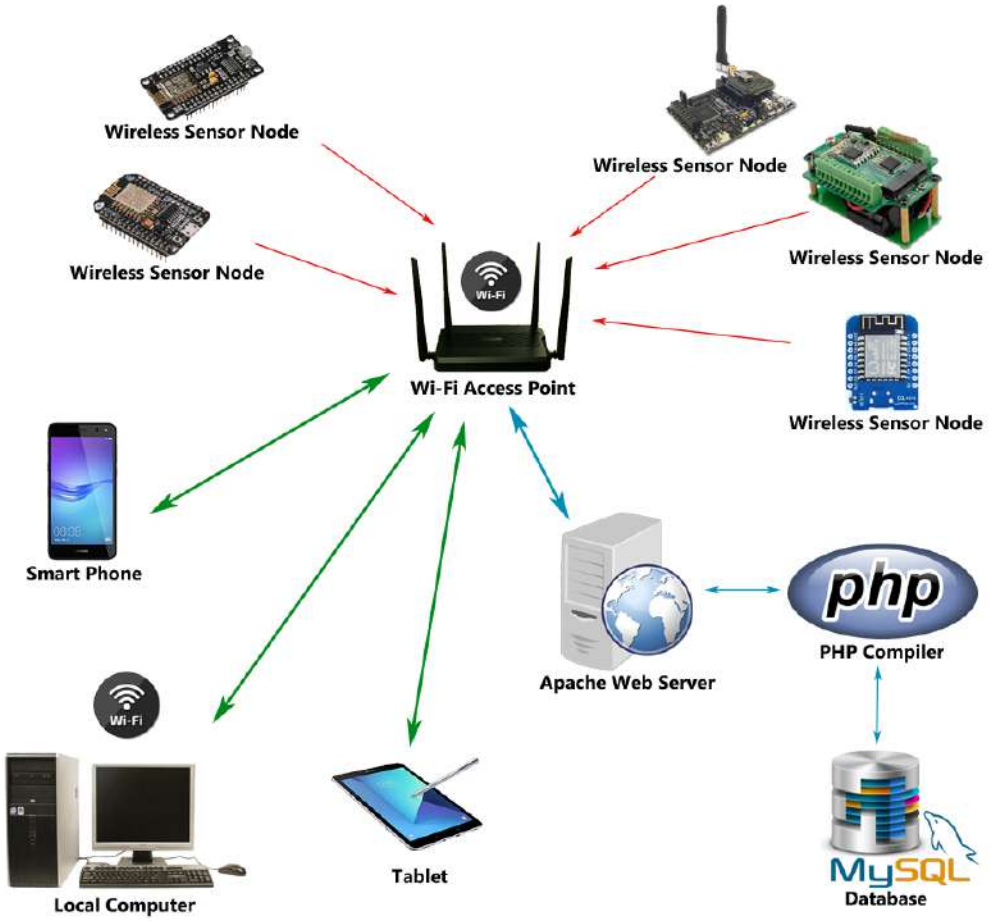

Figure 23. The proposed Wi-Fi enabled sensor network setup

Section 2 gives brief information about Wi-Fi based sensor nodes and section 3 is about ambient temperature application example. Data acquisition software is explained in fourth section. Finally, the conclusion section summarizes the main outcomes of the study.

2. WI-FI BASED SENSOR NODES

The following schematic shows the general structure of a Wi-Fi based sensor / actuator node. The central unit that forms a sensor node is a microprocessor unit with low power consumption. Microprocessor units can operate in 8-32 bit range. Low power consumption is a desirable feature in wireless sensor nodes. The energy requirement is usually eliminated from the battery in terms of portability. To achieve portability, the size of the knots must be reduced and their weight reduced. The dimensions and weights of the electronic components are less than those of the battery. It is also intended to minimize power consumption values so that smaller batteries

can be used. Voltage regulator circuits are also used to ensure that the supply voltage is stable and does not damage electronic components. A sensor / actuator node consumes the most energy when using the radio station for data reception and transmission. In order for energy efficiency to be available, the radio unit must only be switched on when it is necessary and in the closed position in other cases.

There are two units in which a sensor/actuator node is in contact with the outside world. Analog or digital sensors are used to measure physical quantities. The actuator unit is used to indicate the operating state of the knob or to control an external device. The actuator unit can output analog or digital outputs or perform a switching operation via a relay.

The radio unit is also essential for wireless communication between nodes. The obtained data is transferred to the collection point by wi-fi signals. Again, according to the commands to be taken over the collection point, the actions of the agents are provided. Figure 2 depicts essential components of a Wi-Fi based sensor node.

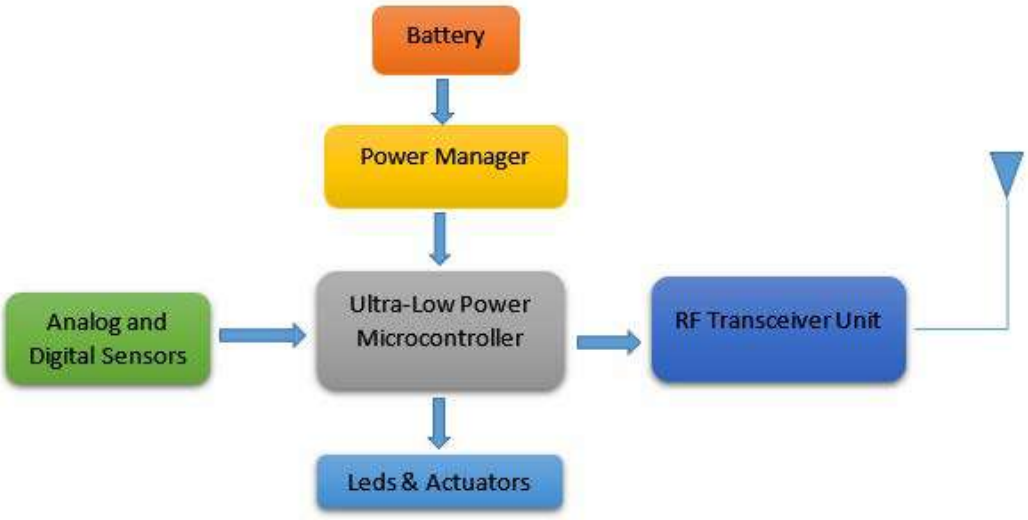

Figure 24. Wi-Fi based sensor node block diagram.

With the development of IOT based electronic components, there are many modules developed and sold by different manufacturers in the market. The NodeMCU is an open source firmware and hardware kit for easier IoT project using the ESP8266 as the base and using interactive LUA scripting language for programming. This development makes it easier for beginners as the NodeMCU community has provided many example codes and instructions.

In our application, the NodeMCU modules developed by the espressive company were used and Arduino programming software was preferred for the programming of the modules. ESP8266 Wi-Fi modules includes a CP2102 TTL to USB chip for programming and debugging, is breadboard-friendly, and can simply be powered via its micro USB port. Figure 3 shows USB supported ESP8266 based nodeMCU development board and Figure 4 depicts pinout diagram of ESP8266 Wi-Fi module.

Figure 3. ESP8266 based NodeMCU development module.

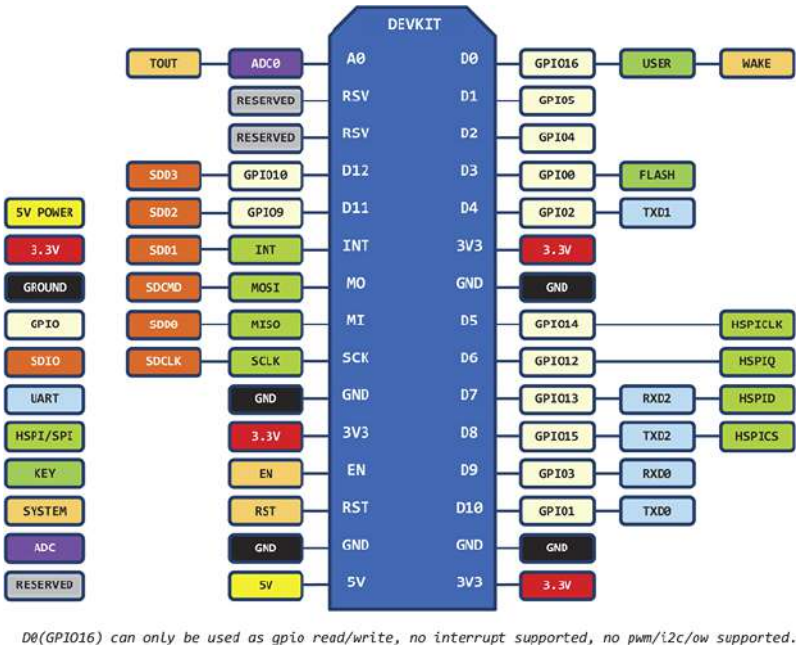

Figure 4. Pinout diagram for ESP8266 wi-fi module.

Basic technical specifications of a NodeMCU module are also listed in Table 1. The module supports multiple communication protocols and power consumption modes. Module operating voltage is between 3.0 and 3.6 volts. While average operating current is nearly 80mA, deep sleep current consumption is around 10uA.

Table 17. Technical specifications for NodeMCU wireless module.

Feature	Value
Wi-Fi Protocols	802.11 b/g/n
Frequency Range	2400Mhz-2483.5Mhz
Tx Power	802.11 b +20 dBm
Rx Sensivity	-91 dBm (11 Mbps)
Peripheral Bus	UART/SDIO/SPI/I2C/IR Remote Control
Operating Voltage	3.0 - 3.6V
Operating Current	80mA (Average)
Operating Temperature Range	-40°C - 125°C
Wi-Fi Mode	Station/SoftAP/Soft AP+station
Security	WPA/WPA2
Encryption	WEP/TKIP/AES
Network Protocols	IPv4, TCP/UDP/HTTP/FTP
Microcontroller	Tensilica L106 32 bit
CPU Clock Speed	80Mhz
RAM Size	36KB
Standby Current	0.9 mA
Deep Sleep	10 uA
Power Save Mode DTIM1	1.2 mA
Power Save Mode DTIM3	0.86 mA

The operating parameters mentioned above make it possible to use the module in battery-powered wireless solutions.

3. AMBIENT TEMPERATURE MEASUREMENT APPLICATION

Wireless nodes cannot directly measure physical quantities. Instead, physical quantities must be converted into electrical quantities using appropriate sensors and transducers. As a simple application example, a low cost NTC sensor is used to monitor the ambient temperature. For this purpose, it is necessary to find the NTC characteristic coefficients. Based on a measured resistance value of an NTC thermistor the extended Steinhart-Hart equations lets a simple calculation of the temperature [11]. The Steinhart-Hart law defines the absolute temperature T as a function of the NTC thermistor's resistance according to the equation 1 and equation 2.

$$\frac{1}{T} = a_0 + a_1.\ln r + a_2.(\ln r)^2 + a_3.(\ln r)^3 \quad (1)$$

$$t = 273.15\ ℃ + [a_0 + a_1.\ln r + a_2.(\ln r)^2 + a_3.(\ln r)^3]^{-1} \quad (2)$$

Then Equation 3 is used to calculate the resistance R at any particular temperature T. R_{T_0} is the resistance in ohms at a particular temperature T_0, β is a constant value and it is another characteristic parameter for the device.

$$R = R_{T_0}.e^{\left[\beta\left[\left(\frac{1}{T}\right)-\left(\frac{1}{T_0}\right)\right]\right]} \quad (3)$$

Then, the voltage divider circuit shown in Figure 5 can be used to obtain the resistance change in terms of voltage change on R_T. Equation 4 also used for conversion from resistance to voltage.

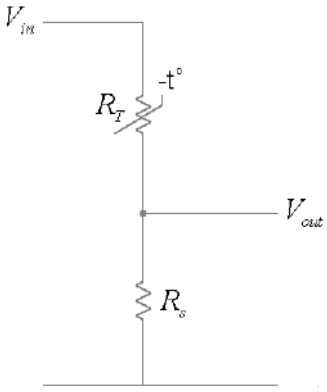

Figure 5. Voltage divider circuit for NTC thermistor.

$$V_{out} = V_{in} \cdot \frac{R_s}{R_T + R_s} \quad (4)$$

The V_{out} value can be measured by connecting to an analog input pin of the nodeMCU module. The voltage information represents the temperature value of the NTC sensor. Thus, using a simple NTC, the ambient temperature is measured in terms of voltage and all measurements are transmitted wirelessly and recorded on a remote web server system.

4. DATA ACQUISITION SOFTWARE

In proposed scheme, the Wi-Fi access point or modem acts as a Wi-Fi spot. Nodes that want to send data are first connected to the network using wireless network SSID and password. Then they post the measured data to the server IP address that were previously determined. Post requests from the sensor nodes are first met by the Apache web server and forwarded to the PHP compiler. The php scripts process the submitted information and insert the new incoming data to the predefined MySQL table.

Recorded data can be accessed remotely via data monitoring php web page published on the same server. In order to reach the collected data, users can use any network connected and browser supported device such as a computer, tablet or smart phone. In the reporting interface, the recording date and measurement number can be selected using the dropdown list. User can select desired records and track on generated charts or download the raw data in CSV format to examine later. In this way, additional data mining techniques can be applied to collected data using advanced analysis software.

To start and stop the data collecting and recording process, a php based control page has been developed. There are “start recording” and “stop recording” buttons on the page. After clicking “start recording” button the measurement Id value is automatically incremented by 1 and recording starts. All the data obtained from the

sensor nodes are stored in the MySQL table with the same measurement Id value. Figure 6 shows a screenshot of the data recording control page.

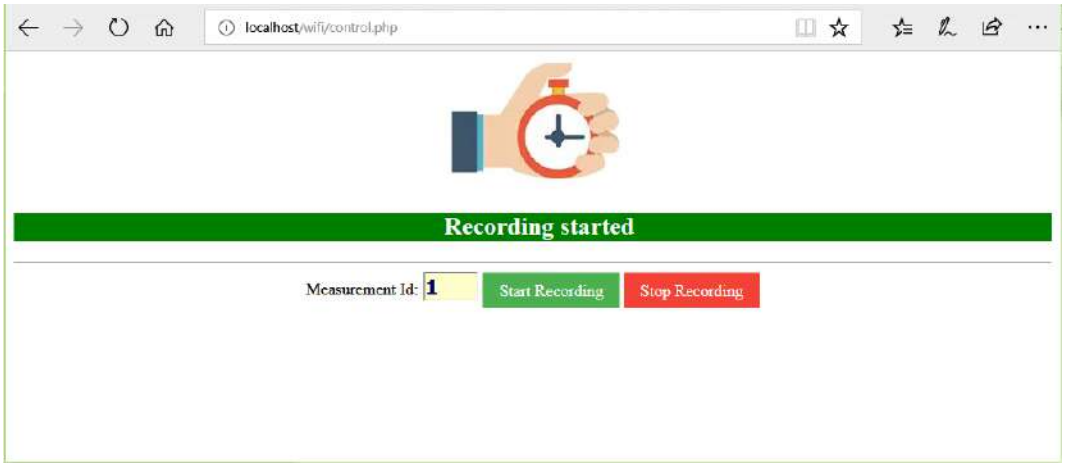

Figure 6. A screenshot of the data recording control page.

The graphical representation of the collected data is made via the "data monitor" page. There is a drop-down list element on the same page. This enables the user to choose measurement Id and measurement time in order to browse the acquired data. Along with that, raw data can be exported as a comma separated file. Figure 6 depicts a screenshot of the data monitoring page.

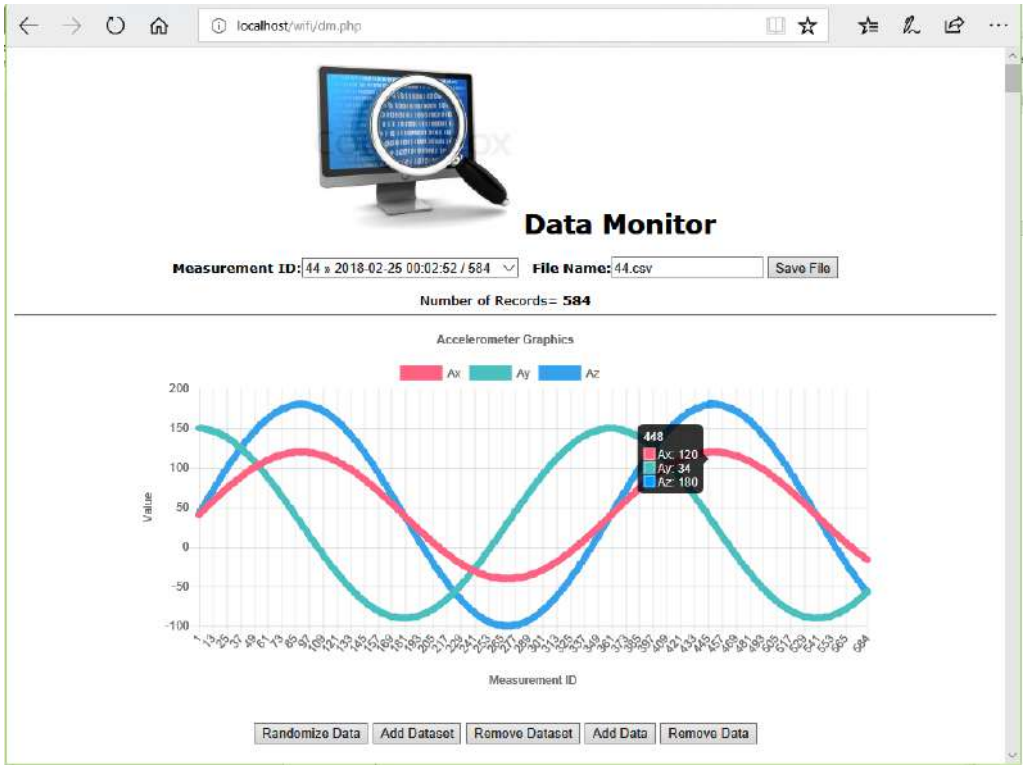

Figure 7. A screenshot of the data monitoring page.

When the cursor is moved on the graph, detailed information about the instantaneous values can be seen in a moving popup window.

5. CONCLUSION

The proposed system called WiFiLab requires no cable connection between sensor and data recording tool. The proposed data acquisition system is settled on an APACHE-based web server and MySQL database. The PHP scripting language is also preferred for coding server-side scripts. All Wi-Fi-based sensor nodes are in the client role. The data obtained from the sensor nodes is transferred to a wireless network created by the proposed system using the IEEE 802.11 communication standard and is recorded in the MySQL database via the master collection unit which is connected to the same network. After data acquisition period, the recorded data can be exported as a comma separated value file for later analysis using different analyze software.

Using the developed data collection platform, many sensors can transmit data synchronously with low latency and the transmitted values can be recorded in the web environment. It is especially seen that the developed system is extremely useful and successful in data collecting especially through moving objects when the freedom of movement is obligatory. By means of the developed system, it is now possible to collect data from hundreds of battery-powered wireless sensor node at the same time.

REFERENCES

[1] K. Arslan and I. Kirbas, "Developing Wireless Sensor/Actuator Node Prototype for Internet of Things Applications," *J. Grad. Sch. Nat. Appl. Sci. Mehmet Akif Ersoy Univ.*, vol. Special Issiue 1, no. 7, pp. 35–43, 2016.

[2] G. R. Mendez, M. A. M. Yunus, and S. C. Mukhopadhyay, "A WiFi based smart wireless sensor network for an agricultural environment," in *2011 Fifth International Conference on Sensing Technology*, 2011, pp. 405–410.

[3] A. R. Ulucinar, I. Korpeoglu, and A. E. Cetin, "A Wi-Fi Cluster Based Wireless Sensor Network Application and Deployment for Wildfire Detection," *Int. J. Distrib. Sens. Netw.*, vol. 10, no. 10, p. 651957, 2014.

[4] M. A. Rawajbeh and A. Haboush, "Advanced Object Monitoring Using Wireless Sensors Network," *Procedia Comput. Sci.*, vol. 65, pp. 17–24, 2015.

[5] M. Mehta, "ESP 8266: A Breakthrough in Wireless Sensor Networks and Internet of Things," *Int. J. Electron. Commun. Eng. Technol.*, vol. 6, no. 8, pp. 7–11, 2015.

[6] I. Kirbas and C. Bayilmis, "HealthFace: A web-based remote monitoring interface for medical healthcare systems based on a wireless body area sensor network," *TJEECS Turk. J. Electr. Eng. Comput. Sci.*, vol. 20, no. 4, pp. 629–638, 2012.

[7] C. A. Trasviña-Moreno, Á. Asensio, R. Casas, R. Blasco, and Á. Marco, "WiFi Sensor Networks: A study of energy consumption," in *2014 IEEE 11th International Multi-Conference on Systems, Signals Devices (SSD14)*, 2014, pp. 1–6.

[8] L. Li, H. Xiaoguang, C. Ke, and H. Ketai, "The applications of WiFi-based Wireless Sensor Network in Internet of Things and Smart Grid," in *2011 6th IEEE Conference on Industrial Electronics and Applications*, 2011, pp. 789–793.

[9] S. Tozlu, M. Senel, W. Mao, and A. Keshavarzian, "Wi-Fi enabled sensors for internet of things: A practical approach," *IEEE Commun. Mag.*, vol. 50, no. 6, pp. 134–143, Jun. 2012.

[10] Sonal Chakole, Ruchita R.Jibhkate, Anju V.Choudhari, Shrutika R.Gawali, and Pragati R.Tule, "A healthcare monitoring system using Wi-Fi module," *Int. Res. J. Eng. Technol.*, vol. 4, no. 3, pp. 1413–1417, Mar. 2017.

[11] I. Kirbas, "Developing and Remote Controlling a Multi-Zone Cooling Plant using Web Services and a Secure Token Mechanism," *Meas. Control*, vol. 48, no. 9, pp. 278–284, 2015.

BIOGRAPHY

Ismail KIRBAS,got his bachelors' degree in the Computer Education Department in Technical Education Faculty at Kocaeli University, Kocaeli/Turkey in 2000, his master degree in the Electronics and Computer Education at Kocaeli University in 2008, PhD degree in Electronics and Computer Education Department at Sakarya University in 2013. He is still an academic member of the Computer Engineering Department at Burdur Mehmet Akif Ersoy University. His major areas of interests are: Wireless Sensor Networks, Embedded Systems, Design of Experiments, Time Series Predictions and Mobile Programming.

Ayhan DUKKANCI, got his bachelors' degree in the Electric Education Department in Technical Education Faculty at Kocaeli University, Kocaeli/Turkey in 2000. He does master's degree in Institute of Science and

Technology, at Burdur Mehmet Akif Ersoy University. He still works as a technical teacher in Industrial Automation Technologies Department at Ataturk Technical and Vocational School, Eskisehir/Turkey. His major areas of interests are: Mobile robots, Embedded Systems, Design of Experiments.

ICENS 4TH INTERNATIONAL CONFERENCE ON ENGINEERING AND NATURAL SCIENCE
2 - 6 May 2018 KIEV UKRAINE

A Review on Low Voltage Analog Circuit Design

Sezai Alper Tekin[1], SeyfettinGurel[2], Hamdi Ercan[3], Asuman Savascihabes[4]

Abstract

Tendency in low voltage and low power analog integrated circuits has increased on several years, as system power restrictions and nanotechnologies require lower supply voltages. At the present time, a new trend towards extremely low voltage and circuits is emerging. Using lower voltage supply and decreased power consumption of integrated circuits is critical factor since it provides the device reliability, avoids overheating of the circuits and especially extends the operation time for battery powered devices. The demand for lower power dissipation in circuits such as wireless, mobile and wearable devices has motivated the value of supply voltage down to 1 V. MOSFETs (metal oxide semiconductor field effect transistors) have been considered for low voltage low power analog circuit design because their operating voltage can be made less than that of BJTs (bipolar junction transistor) known as their counterparts. In this paper, the advantages and disadvantages of each of these techniques such as bulk-driven (BD), floating-gate (FG), quasi-floating-gate (QFG)) and dynamic threshold MOS transistors (DTMOS) techniques have been elaborated. Consequently, the most crucial task for analog circuits is to maintain the performance of the circuit by designing new circuit structures ability to operate with low supply voltage.

Keywords: *Analog Circuits, Circuit Design, Design Technique, Low voltage, Low power*

1. INTRODUCTION

In recent years, the design of circuit is directly related with reducing smaller size, low power consumption and lower voltages for more efficient applications [1]. During design of these circuits, several parameters should be taken into consideration to have better design for different circuit structures. There are many ways to deal with this phenomenon. In this study, the design rules are examined for low voltage analog circuits and some ideas are put forward to get better circuit performance. The most critical parameter for a low voltage circuits is threshold voltage of MOS transistors. Threshold voltage (V_{TH}) is the parameter which is defined by Equation 1.

$$V_{TH} = V_{TH0} + \gamma \cdot \left(\sqrt{2|\varphi_F| - V_{BS}} - \sqrt{2|\varphi_F|}\right) \quad (1)$$

where V_{TH} is the threshold voltage, V_{TH0} is the zero- V_{BS} value of the threshold voltage, γ is the body effect parameter, φ_F is the surface inversion potential of silicon and V_{BS} is the bulk-source voltage. From Equation (1), it is clear that the threshold voltage decreases when the bulk-source voltage is increased. Conversely, when the bulk-source voltage diminishes, threshold voltage increases too. That is, V_{TH} can be controlled by V_{BS}.

There are also some methods for designing low voltage analog circuits bulk-driven (BD), floating-gate (FG), quasi-floating-gate (QFG), threshold voltage of the MOS transistors (MOST) and dynamic threshold MOS transistors (DTMOS) techniques. Floating Gate technique used a floating-gate transistor is very popular because it reduces circuit complication. Therefore, it can dissipate low power against with CMOS circuits [6], [7]. Quasi floating gate is another technique that increase transconductance and evolves gain bandwidth product [8]. It also offers a solution to threshold voltage limitation for MOS transistors [9]. In addition to this, DTMOS

[1] *Erciyes University, Department of Industrial Design Engineering, Kayseri, Turkey, satekin@erciyes.edu.tr*

[2] *ErciyesUniversity, Energy Systems Engineering Department, Kayseri, Turkey. sgurel@erciyes.edu.tr*

[3] *Erciyes University, Department of Avionics, Kayseri, Turkey, hamdiercan@erciyes.edu.tr*

[4] *Nuh Naci Yazgan University, Department of Electrical and Electronics Engineering, Kayseri, Turkey. ahabes@nny.edu.tr*

is also suitable method for low voltage-based circuits since it dissipates lower power than ordinary MOS based circuits [11]. This includes also some techniques and it has lower threshold voltages [12].

2. MATERIALS AND METHODS

In low voltage analog circuit design, many variables can affect the operation of the system. All these factors specify how the circuit works better. There are many parameters that affect the working of analog circuit schemes. Figure 1 shows voltage alteration for a Dynamic RAM. It is obvious that the nominal voltage falls down from 2001 to 2003. This graph can be interpreted for digital circuit with respect to gate thickness of the MOS transistor. The same comment is also valid for analog circuits. Especially, the speed and gate thickness affect the operation of low voltage analog circuit operation. To increase the total efficiency of this analogy, the gate thickness should be thinner as soon as possible. At the same time, the voltage that is required for efficient use of low voltage must be taken into consideration to stabilize suitable speed value. In other words, there is a tradeoff between these parameters. To optimize these parameters efficiently, some techniques are examined in this study.

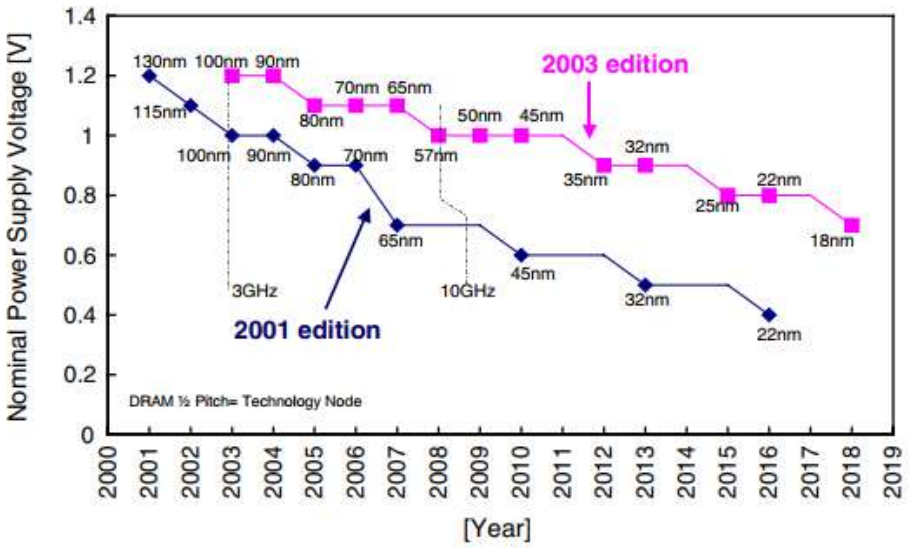

Figure 1. The Power supply voltage changes 2001 and 2003 [1].

The low voltage analog circuits are affected by undesirable effects which are power crisis, interconnection crisis and complexity crisis. Producing low power circuit design causes ever increasing power in circuit. Figure 2 illustrates the characteristics of supply voltage, power and current for per chip. On the one hand, the voltage of circuit falls over the years. On the other hand, the power consumption and V_{DD} current have increased over the years. This is the main issue that may affect the performance of circuit design.

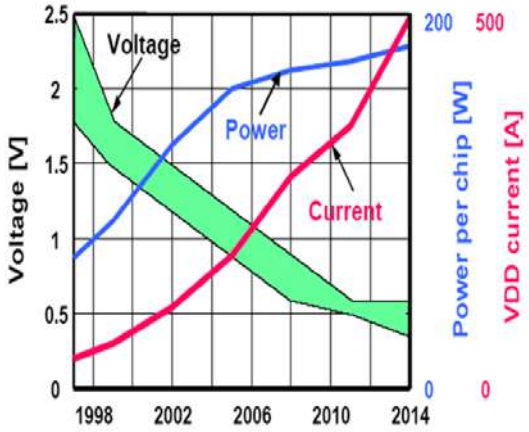

Figure 2. The characteristics of supply voltage, power and current for per chip [3].

The delay is not desirable situation for low power analog circuits since it causes delay in during operation. Figure 2 gives the relationship between power(W), supply voltage (V_{DD}) and threshold voltage (V_{TH}). The important parameter is threshold voltage (V_{TH}). This is the voltage which dominate current flow and it is formed by physical change [2]. When the threshold voltage increases, power consumption and the delay is decreases. The rise in supply voltage corresponds to increase in power. It can be controlled by threshold voltage to reduce power consumption in rising time in MOS transistor [2]. The optimum point can be specified with respect to consumed power, supply voltage and threshold voltage. When it is carefully investigated Delay- V_{DD}- V_{TH} graph, the middle point of B is the most convenient region for operating low voltage analog circuit more efficiently.

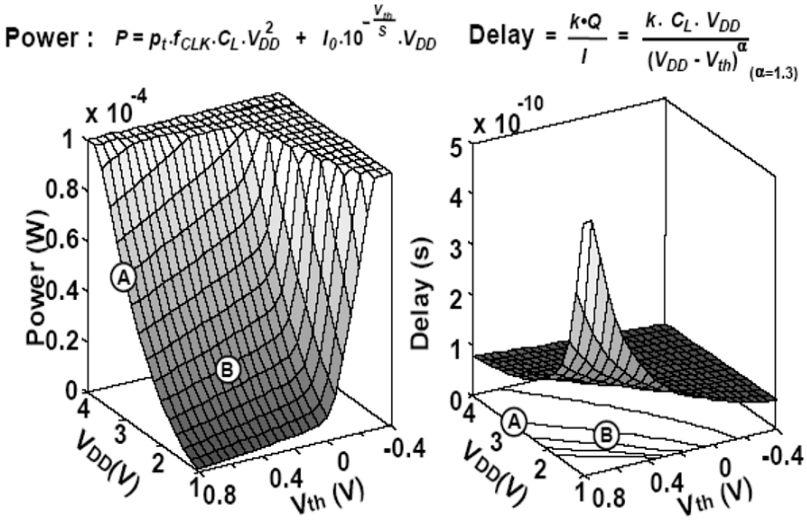

Figure 3. The relationship between power(W), supply voltage (V_{DD}) and threshold voltage (V_{TH})[3].

The idea of optimizing delay with V_{TH} may be a suitable approach for transistors. Figure 4 gives the change in leakage current over the year with threshold voltage in MOS transistors. With the given data in figure, it can be concluded that reducing with threshold voltage, the leakage current (I_{off}) increases over the years. Under the subthreshold region, the leakage current is increased int the case of reverse connection of transistor. This leads to appear some undesirable effect on a threshold voltage. Therefore, this condition makes the system disadvantageous. The solution to this phenomenon is to use adaptive resistor for finding optimized point for this system. All these effects can be surpassed with this method to have efficient system.

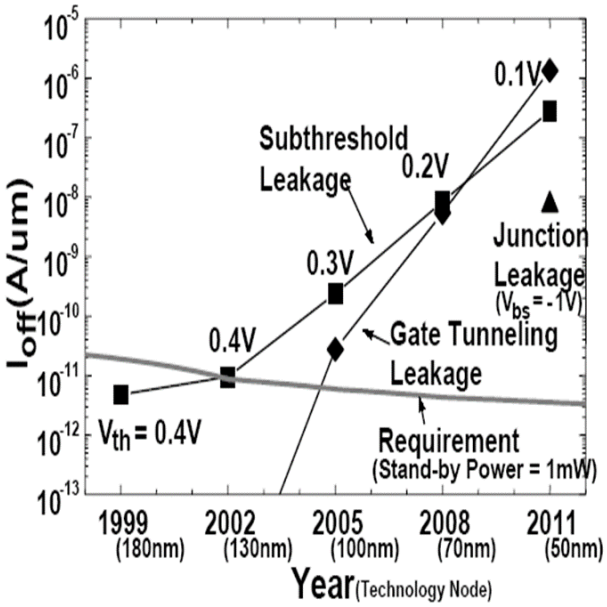

Figure 4. The change in leakage current over the year with threshold voltage in MOS transistors [4]

3. CONCLUSION

To sum up, the power consumption of low voltage analog circuits can be controlled by supply voltage (VDD) and threshold voltage (V_{TH}). However, reducing power is also causes low speed and low VTH creates high leakage in circuits. Therefore, the critical parameter is V_{DD} - V_{TH} to have more efficient circuit design. After all low power analog systems are investigated; it is offered new viewpoints to develop high efficient circuit designs. One of the ideas for reducing standby power may plug a power switch in series to logic circuits (BGMOS). The selection of power switch gate width is important variable for diminishing power consumption. A dual V_{TH} scheme and software control of V_{DD} and V_{TH} are promising for reducing active power. Here, it is important tools to support system-level low-power design with S/H co-design capability. In the future, giga-scale integration will require $V_{DD,}$ V_{TH} and $T_{OX.}$ It will also need new tools to support new technology.

REFERENCES

[1] T. Ohmi, M. Hirayama, A. Teramoto, " New era of silicon technologies due to radical reaction based semiconductor manufacturing", Journal of Physics D: Applied Physics 39 (2006) pp. R1-R17

[2] H. Ercan, S. A. Tekin, M. Alci, "Low-voltage low-power multifunction current-controlled conveyor", International Journal of Electronics, Vol. 102, No. 3, pp. 444-461.

[3] S. Gurel, S. A.Tekin, "The New Approach For Switching Performance Of Power Mosfet", **II. International Congress on Multidisciplinary Studies, Adana, Turkey.**

[4] Thomasl, Dao, " Advanced double-gate fully-depleted silicon-on-insulator (DG-FDSOI) device and device impact on circuit design and power management, International Conference on Integrated Circuit Design and Technology (IEEE Cat. No. 04EX866).

[5] Dr. R. Nakkeeran Low Power VLSI Design Lecture Notes, School of Engineering & Technology Department of Electronics Engineering Pondicherry University Pondicherry-14.

[6] R. Gupta, R. Gupta, S. Sharma, " High Performance full subtractor using floating-gate MOSFET", Microelectronic Engineering 162 (2016), pp.75-78.

[7] F. Khateb, "Bulk-driven floating gate and bulk-driven quasi-floating-gate techniques for low-voltage low-power analog circuits design", International Journal of Electronics and Communications (AEU) 88 (2014) pp. 64-72.

[8] C. Rana, N., Afzal, D. Prasad, " A high performance bulk driven quasi floating gate MOSFET based current mirror, " 7th International Conference on Communication, Computing and Virtualization", Procedia Computer Science 79 (2016) pp. 747 –754.

[9] R. Gupta, S. Sharma, "Quasi-floating gate MOSFETbased low voltage current mirror", Microelectronics Journal 43 (2012) pp. 439-443.

[10] Y. Babacan, " Ultra-low voltage-power DTMOS based full-wave rectifier", International Journal of Electronics and Communications (AEU) 91 (2018) pp. 18-23.

[11] F. Khateb, T. Kulej, M. Kumngern, "0.5 V DTMOS median filter", International Journal of Electronics and Communications (AEU) 69 (2015) pp. 1733-1736.

BIOGRAPHY

Sezai Alper Tekin was born in Kayseri, Turkey. He received the B. Engineering degree from Erciyes University, Kayseri, Turkey, in 2000, the M.S. degree from Nigde University, Nigde, Turkey, in 2005 and the Ph.D. in Electrical and Electronics Engineering from Erciyes University, Kayseri, Turkey in 2012. From 2006 to 2012 he was a member of academic staff with the Erciyes University, Engineering Faculty, Electrical and Electronics Dept., Kayseri, Turkey. Since 2012, he has been a member of academic staff with the Erciyes University, Engineering Faculty, Industrial Design Department, Kayseri, Turkey. His current research interests include free space optics, current mode circuits, current conveyors, electronic circuit design and solar cells.

Seyfettin Gurel was born in Ankara, Turkey. He received the B. Engineering degree from Atilim University, Kayseri, Turkey, in 2011, the M.S. degree from Erciyes University, Kayseri, Turkey, in 2014 in Energy Systems Engineering from Erciyes University. He is currently Ph.D. in Energy Systems Engineering from Erciyes University, Kayseri, Turkey Since 2014, he has been a member of academic staff with the Erciyes University, Engineering Faculty, Energy Systems Enginering Department., Kayseri, Turkey. His current research interests include harvesting circuits, piezoelectric systems and solar systems and its applications.

Hamdi Ercan received the B.Sc. and M.Sc. degrees from both Erciyes University, Kayseri, Turkey, in 2004 and 2007, respectively, all in Electronic Engineering. He received his Ph.D. degree in Electrical and Electronics Engineering at Erciyes University, Kayseri, Turkey in 2012. Since 2005, he has been a member of academic staff with Erciyes University, Faculty of Aeronautics and Astronautics. He has been an Associate Professor since 2018 at Erciyes University, Faculty of Aeronautics and Astronautics, Department of Avionics. His current research interests include avionics, microelectronics, current mode circuits, current conveyors and electronic circuit design.

Asuman Savascihabes, received her B.Sc. and M.Sc. degree from both Erciyes University at 2005 and 2008 respectively and received her Ph.D. degree from Gazi University all in Electrical and Electronics Engineering specializing on Signal Processing and Telecommunications. Since 2014, she serves in the faculty of Electrical and Electronics Engineering Department of Nuh Naci Yazgan University as an assistant professor. Her main research areas lie in wireless communication systems and signal processing for wireless communications issues.

ICENS 4TH INTERNATIONAL CONFERENCE ON ENGINEERING AND NATURAL SCIENCE
2-6 May 2018 KIEV UKRAINE

Quality Function Deployment Approach for Evaluation Parameters of Highway Pavement

***Dilay Uncu*[1]**

Abstract

To reach a satisfactorily performance of a highway and provide user satisfaction, several factors must be considered for safety, comfort and economical parameters in highway construction. In this study, assessment of highway engineering parameters has been made via Quality Function Deployment (QFD) method. QFD is a quality method that converts the requests of customers to measurable performance changes and major quality assurance points to be used throughout the production phase. To execute the method, firstly customer requests were determined. After technical requirements were valued, degrees of contact with each other, relationship status between them of requirements and degrees of importance of customer requests were determined. In the study flexible and rigid pavements were considered as pavement type of highway. As a result, the importance order of technical requirements was occurred according to the values obtained from the House of Quality. With regard to this importance order which pavement type providing technical requirements mostly were compared to each other.

Keywords: Flexible pavement, Highway engineering parameters, Quality function deployment, QFD, Rigid pavement

1. INTRODUCTION

Nowadays, many developments have occurred in highway engineering by the rapidly developing technology. The best and most perfect design is target in development. The pavement performance comes into prominence in design of highway engineering parameters. Highway pavement performance is appointed according to safety and driver comfort characteristics. Undoubtedly, the best highway for a driver must have the highest level of safety, comfort and economy. At this stage, satisfaction of highway driver becomes priority status.

In the scope of this study, which parameters of highway pavement the most important were determined with user requests and ideas. To do this, "Quality Function Deployment (QFD)" is one of quality techniques was applied. Quality Function Deployment technique guarantees the quality of design when products or services are at the design stage. Customer or user requests and satisfaction in the center of this technique are considered and transformed design targets which use as quality assurance points during the application.

As a result of all this, both perspective of users and technically the highest level of the desired design were achieved. As a result of the implementation of QFD methodology, changes are required in the product or service are greatly reduced and improved. Also in QFD applications, decrease was observed in pre-production and costs of initial stages. Thus, positive gains can be obtained owing to QFD technique in every respect.

2. QUALITY FUNCTION DEPLOYMENT

The original name of Quality Function Deployment was “Hinshitsu Kim Tenkai” in Japanese and the name was translated as “Quality Function Deployment” in English during the visiting to Cansas State University in 1972 of Yoji Akao who is one of the creators of this method [1]. Akao defined QFD as; “QFD is a method for developing a design quality aimed at satisfying the customer and then translating the customer’s demands into design targets and major quality assurance points to be used throughout the production phase. QFD is a way of ensuring product’s design quality at the design stage [2].”

QFD provides examining problems in a process with causes and effects. As the process continues, studies are documented. Thus, in the case of coming across same problems in the future, a real solution is provided with

[1]*Corresponding author: Manisa Celal Bayar University, Department of Civil Engineering, 45140, Muradiye/Manisa, Turkey. dilay.yildirim@cbu.edu.tr*

development similar decisions to problems. Examine the connections constituted between the data in the light of the mathematical methods [3].

a. House of Quality

QFD has many steps, all of which are interconnected to form the house of quality matrices. The house of quality is another name of the product planning stage that the product planning matrix is created. The product planning matrix is named "House of quality" because the matrix has a triangular comparison part on it [1]. House of quality provides that constituting targets of customer requirements and determining how this requirements are supplied technically. Product planning matrix in other words House of quality and its sections are as shown in the Figure 1. House of quality has a main part which satisfies customer requirements and quality properties. There is a table like a roof on this main part and comparison is made between quality properties in this part. House of quality is a kind of map that provides the realization of planning and communication between the sections [4].

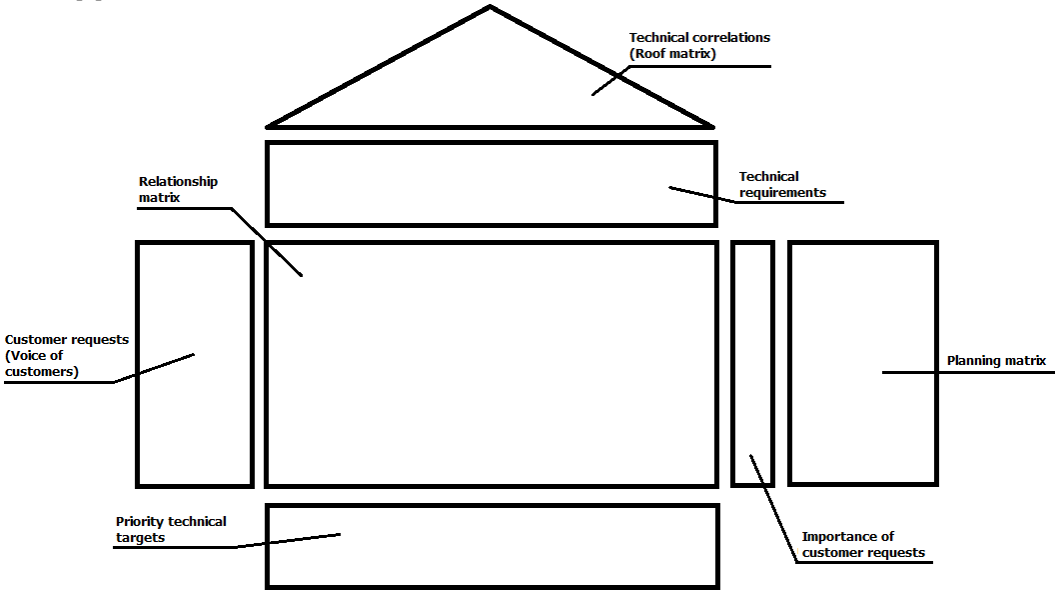

Figure 1. House of Quality

The house of quality is a large matrix consisting of the sum of seven sections. The sections of the matrix are;

- **Customer requests:** In this section, there is a requirement list which consists of information obtained from customers and this information represents the voice of the customer at the same time. This information for product design can be obtained from customers directly and also indirectly [5].

- **Technical requirements:** At this stage, technical characteristics of the existing product are determined and measurements are created for satisfying [6]. In different sources, technical responses are entitled as product properties, design requirements, enterprise expectations, engineering properties or quality properties [7]. Technical responses, at the top of the house of quality, provide to make mutual assessment with customer requirements.

- **Importance of customer requests:** It isn't sufficient to know customer requests singly. At the same time it is also important to know the importance levels of these requests. Know the importance degrees of the house of quality in this part provide to evaluate produced solutions for satisfy these requests.

- **Planning matrix:** Planning matrix helps ranking customer requests according to their priorities. In general, planning matrix consist a combination of columns of the importance degree attached to the

scores of requests from customers, targets to be achieved, operation and performance of competitors, improvement rate, absolute weight score and relative weight score.

- **Relationship matrix:** In this section, it is seen how interpreted the relationship between customer requests and technical requirements. Thanks to this section, each properties affect customer requests at which level is determined.

- **Technical correlations:** This section constitutes the roof of house of quality. This section shows the relationship level of technical requirements and how technical requirements affect each other at design stage.

- **Priority technical targets:** Calculated importance degree scores of product or service properties are in this section. Determined target values for every technical property, which desired to have new design, take part in here.

b. Data Analysis

After completion of the House of quality, the precedence order of customer requests and technical requirements are determined for design. Thus it is seen which parameter has how much importance.

$$\text{Improvement Rate}=\frac{\text{Target Quality}}{\text{Average Value}} \quad (1)$$

$$\text{Absolute weight}=\text{Importance Degree}\times\text{Importance Rate} \quad (2)$$

$$\text{Relative Importance (\%)}=\frac{\text{Absolute Importance of Each Column}}{\text{Total Absolute Importance}}\times 100 \quad (3)$$

The formulas can be symbolized as seen in Table 1.

Table 1. Planning Matrix Analysis

	Technical Requirements										
Customer Requests	1. Technical Requirement	2. Technical Requirement	3. Technical Requirement	Importance Degree	1. Option	2. Option	3. Option	Target Quality	Improvement Rate	Absolute Weight	Relative Weight (%)
1. Request	R_{11}	R_{12}	R_{13}	ID_1	A_{15}	B_{16}	C_{17}	TQ_1	IR_1	AW_1	RW_1
2. Request	R_{21}	R_{22}	R_{23}	ID_2	A_{25}	B_{26}	C_{27}	TQ_2	IR_2	AW_2	RW_2
3. Request	R_{31}	R_{32}	R_{33}	ID_3	A_{35}	B_{36}	C_{37}	TQ_3	IR_3	AW_3	RW_3
Absolute Importance	AI_1	AI_2	AI_3								
Relative Importance	RI_1	RI_2	RI_3								

$$\text{Improvement Rate:}IR_i=\prod_{i=1}^{m}\left[\frac{TQ_i}{\left(\frac{A_{i5}+B_{i6}+C_{i7}}{s}\right)}\right] \quad (6)$$

$$\text{Absolute Weight:}AW_i=\prod_{i=1}^{m}(IR_i\times ID_i) \quad (7)$$

$$\text{Relative Weight:}RW_i=\prod_{i=1}^{m}\left(\frac{AW_i}{\sum_{i=1}^{m}AW_i}\times 100\right) \quad (8)$$

$$\text{Absolute Importance: } AI_j = \prod_{j=1}^{n} \left(\sum_{i=1}^{m} I_{ij} \times AW_i \right) \quad (9)$$

$$\text{Relative Importance: } RI_j = \prod_{j=1}^{n} \left(\frac{AI_j}{\sum_{j=1}^{n} AI_j} \times 100 \right) \quad (10)$$

In the formulas; m: number of customer request, n: number of technical requirement, s: number of option, i: number of row, j: number of column.

3. QFD APPLICATION IN HIGHWAY ENGINEERING

There are lots of QFD applications in many areas of manufacturing and service industry even though there is no QFD implementation example in highway engineering. The scope of this study covers a QFD implementation in highway engineering. In the study as flexible pavement; surface treatment and asphalt concrete pavement are discussed and as rigid pavement; concrete pavement is also discussed.

The surface treatment is applied on highways at low standards. Surface treatment has a high coefficient of friction, and thus provides improved braking distances. But also, high friction coefficient increases vehicle operating costs and tire wear. Furthermore it causes wheel noise, vibration and low ride comfort.

Asphalt concrete pavement is a flexible pavement type is applied to high-standard highways, heavy traffic roads, and airports. This pavement type has high driving comfort. In flexible pavements reductions are observed in driving comfort and safety under repeated traffic loads over time with the deformation of pavement. As a result of these deformations, reduction occurs in level of service. Rehabilitation is performed to degraded pavement at the lowest acceptable service level thus the service level is removed the highest level again.

Rigid pavements as other name concrete pavements are used in roads have heavy traffic and very high traffic volume. They have higher rigidity according to the flexible pavements. Also they are less affected from strength changes of ground, temperature, humidity and such environmental conditions. However the joints made for avoid the stresses as a result of thermal changes cause wheel noise by negatively affecting driving comfort.

Considering all these features in pavements it is difficult to ensure the best level of safety, comfort and economy parameters at the same time. At this point QFD method was applied. The views of academicians, people serving in private and public sector related to transportation issues, authorized persons involved in highway businesses and civil engineers have been consulted for assessment of determined customer requests. A survey has been prepared to get opinion of the determined target audience. The data of customer requests importance were obtained as a result of the assessment of stakeholders making the survey.

4. CONSTITUTION OF THE HOUSE OF QUALITY FOR HIGHWAY ENGINEERING PARAMETERS DESIGN

Within the scope of the QFD method first it is necessary to constitute the house of quality. House of quality consists of a combination of many parts. There is “Customer Requests (Voice of Customer)” part in the vertical section of the house of quality and this part responds to the question of “What”. Similarly there is “Technical Requirements” part in the horizontal section of the house of quality and this part responds to the question of “How”. For applying the method first customer requests are constituted to contract the house of quality.

a. Customer Requests

First, the desired properties of a highway were considered for determining the customer requests. The determined customer requests are presented in Table 2.

Table 2. Customer requests section of house of quality matrix

Customer needs / Expectations

Safety & Comfort (User)	Smooth pavement surface, least wheel noise and vibration Least vehicle operating costs, least wheel and vehicle wear Short brake distance Safety driving under adverse weather conditions Easy night sight Easy daytime sight
Production & Management (Constructer)	Ready to use in a short time Easy constructability Quick constructability Lower construction cost Long service life and resistance to traffic loads Lower maintenance-repairment and rehabilitation costs Resistance to different weather conditions Resistance to chemical effects Having long term construction season Easy maintenance-repairment works

The customer requests were separated into two parts. Main topics of the customer requests were determined as “Safety & Comfort (User)” and “Production & Management (Constructer)”.

b. Technical requirements

After determining the customer requests, the technical requirements were appeared with the answers response to the question of how. Technical requirements which were defined as a result of brainstorming listed in Table 3.

Table 3. Technical requirements section of house of quality matrix

Technical requirements	
Pavement continuity	Easy obtainable material usability
Qualified workmanship	Material behavior under load
Rolling resistance	Fatigue strength
Friction coefficient	Material aging
Low friction coefficient loss	Heat, cold and moisture resistance of aggregate-binder bond
Pavement color	Resistance to chemical effects of aggregate-binder bond
Traffic opening time	Minority of periodic maintenance need
Easy construction technique	Resistance to different seasonal conditions
Minimum equipment requirement	Constructability under traffic
Featureless equipment requirement	Service road requirement
Low-cost manufacturing facilities	Maintenance-repairment time
Local material usability	

The scoring scale and the description of relations utilized within the case study are shown in Table 4.

Table 4. Scoring scale and corresponding explanation of relations

Score	**Meanings of relation**
9	Strong relationship
3	Moderate relationship
1	Weak relationship

5. FINDINGS OF THIS STUDY

According to the results obtained from house of quality, the five most important technical requirements are; ‘material aging’, ‘heat, cold and moisture resistance of aggregate-binder bond’, ‘resistance to different seasonal conditions’, ‘friction coefficient’ and finally ‘low friction coefficient loss’.

Table 5. Importance ranking of the customer requests

Customer Requests	**Absolute weight**	**Relative weight (%)**

Easy night sight	7.01	7.50
Resistance to different weather conditions	6.90	7.38
Lower maintenance-repair and rehabilitation costs	6.86	7.34
Resistance to chemical effects	6.45	6.91
Safety driving under adverse weather conditions	6.43	6.89
Long service life and resistance to traffic loads	6.43	6.89
Smooth pavement surface, least wheel noise and vibration	6.39	6.84
Least vehicle operating costs, least wheel and vehicle wear	5.81	6.22
Easy maintenance-repairment works	5.54	5.93
Having long term construction season	5.26	5.63
Short brake distance	5.21	5.58
Lower construction cost	5.21	5.58
Ready to use in a short time	5.09	5.45
Quick constructability	5.04	5.39
Easy daytime sight	4.91	5.26
Easy constructability	4.88	5.22
Total	**93.41**	**100.00**

Table 6. Technical requirements ranking according to absolute and relative importance

Technical Requirements	Absolute importance	Relative importance (%)
Material aging	323.43	10.95
Heat, cold and moisture resistance of aggregate-binder bond	256.22	8.68
Resistance to different seasonal conditions	245.80	8.32
Friction coefficient	214.57	7.27
Low friction coefficient loss	214.57	7.27
Easy construction technique	196.96	6.67
Maintenance-repairment time	153.10	5.19
Featureless equipment requirement	139.73	4.73
Traffic opening time	128.40	4.35
Fatigue strength	126.36	4.28
Minority of periodic maintenance need	115.43	3.91
Minimum equipment requirement	113.36	3.84
Pavement color	107.26	3.63
Resistance to chemical effects of aggregate-binder bond	97.91	3.32
Rolling resistance	94.72	3.21
Constructability under traffic	91.94	3.11
Easy obtainable material usability	81.11	2.75
Service road requirement	80.37	2.72
Local material usability	78.84	2.67
Qualified workmanship	76.11	2.58
Material behavior under load	75.32	2.55
Low-cost manufacturing facilities	69.27	2.35

Pavement continuity	24.98	0.85
Total	**2952.66**	**100.00**

As seen in Table 6, the assessment of the five most important technical requirements showed that rigid pavement came into prominence. “9-3-1-0” scoring scale has been used for the numerical assessment of the obtained results similar to the relationship matrix. Score values have been given to the pavement types for technical requirements. The total scores of pavement types were calculated by multiplying these values by the absolute importance values.

Rigid pavement is seen to be superior to other types of pavement according to the total scores. Flexible pavements considered in themselves, surface treatment is superior with a small difference. The reason is that the surface treatment has a simple structure and consequently the parameters for production such as easy construction technique, maintenance-repairment time, featureless equipment requirement and traffic opening time get high scores. But it should be noted that these requirements have lower importance values in the ranking of the technical requirements. If asphalt concrete and surface treatment evaluate in the scope of the structural parameters such as material aging, heat, cold and moisture resistance of aggregate-binder bond, resistance to different seasonal conditions and friction coefficient, asphalt concrete which has better values is preferred.

Table 7. Technical requirements comparison of flexible and rigid pavements

Technical Requirements	**Absolute importance**	**Flexible pavement**		**Rigid pavement**
		Surface treatment	**Asphalt concrete pavement**	**Concrete pavement**
Material aging	323.43	1	1	9
Heat, cold and moisture resistance of aggregate-binder bond	256.22	1	3	9
Resistance to different seasonal conditions	245.80	1	3	9
Friction coefficient	214.57	3	3	9
Low friction coefficient loss	214.57	1	1	9
Easy construction technique	196.96	9	3	1
Maintenance-repairment time	153.10	9	3	1
Featureless equipment requirement	139.73	9	3	1
Traffic opening time	128.40	9	9	1
Fatigue strength	126.36	1	1	9
Minority of periodic maintenance need	115.43	1	3	9
Minimum equipment requirement	113.36	9	1	1
Pavement color (night sight)	107.26	1	1	9
Pavement color (daytime sight)	107.26	9	9	1
Resistance to chemical effects of aggregate-binder bond	97.91	1	1	9
Rolling resistance	94.72	3	9	9
Constructability under traffic	91.94	9	9	1
Easy obtainable material usability	81.11	1	1	9
Service road requirement	80.37	9	9	0
Local material usability	78.84	1	1	9
Qualified workmanship	76.11	1	9	9
Material behavior under load	75.32	1	3	9

Low-cost manufacturing facilities	69.27	1	1	9
Pavement continuity	24.98	9	9	1
Total		**11895.6**	**10837.52**	**17637.1**

6. CONCLUSIONS AND SUGGESTIONS

In the QFD methodology used for the scope of this study, the assessments which are used in the roof and relationship matrix of the house of quality based on determining the degree of relationship and grading the level of the relationship. A grading can be done like this or an intelligent system method fuzzy logic can be used. Fuzzy logic theory is often used for many subjective issues not have absolute distinctions as in this study. For a more comprehensive study customer requests and technical requirements can increase in future studies. The importance must be given to the parameters and the importance ranking has been emerged within the scope of the obtained results for a pavement design. In addition, the comparison of pavement types was made. Rigid pavement is not yet widely applied in our country, is now considered as a strong option next to the surface coating and the asphalt concrete pavements.

U.S. and EU countries, using rigid pavements in a common way, see the rigid pavements as a solution to the shortages of oil and energy which will increase even more in anticipation. Rigid pavement has been gained importance with the properties being economic, safe and long-lasting especially for ground floor with weak carrying capacity and roads have high traffic volume. Also having high strength and durability supports this situation.

As a result, the prominent features of rigid pavements and easiness provided by developing technology are considered, only the flexible pavement understanding existing in our country should demolish. Rigid pavements should not be forgotten as a strong option and given importance to the construction of them.

REFERENCES

[1] Y. Akao, *QFD: Past, Present and Future,* International Symposium on QFD'97 Linkoping, 1997.
[2] Y. Akao, *Introduction to Quality Deployment (Application Manual of Quality Function Deployment 1)*, JUSE Press, 1990.
[3] D. Lyman, *The Functional Relationship Between QFD and VE*, Proceedings of the Society of American Value Engineers, Vol. 27, pp. 79-85, 1992.
[4] J. R. Hauser and D. Clausing, *The House of Quality*, Harvard Business Review, 63-73, 1988.
[5] D. H. Besterfield, C. Besterfield-Michna, G. H. Besterfield and M. Besterfield-Sacre, *Total Quality Management*, second ed. Prentice-Hall, Upper Saddle River, NJ, pp. 283-316 (Chapter 11), 1999.
[6] N. Kathiravana, S. R. Devadasanb, M. T. Bijumon and S. K. Goyald, *Total Quality Function Deployment in a Rubber Processing Company: A Sample Application Study*, Production Planning & Control, 19(1):53-66, 2008.
[7] L. Cohen, *Quality Function Deployment: How to Make QFD Work for You*, Addison-Wesley Publishing Company, Inc., Reading, Massachusetts, 1995.

BIOGRAPHY

Dilay Uncu graduated from Manisa Celal Bayar University Civil Engineering Department. She had MSc degree in Manisa Celal Bayar University Transportation division (2012) on Quality Function Deployment Approach for Determining Highway Pavement Parameters and PhD degree in Dokuz Eylul University Transportation division (2017) on Improvement of Polymer Modified Bitumen Properties by Using Nanomaterials. Dilay Uncu is a assistant professor in Department of Civil Engineering at Manisa Celal Bayar University and she has been a faculty member since 2010. Her research interests are about highway engineering, bituminous materials, modification of bitumens and nanomaterials.

ICENS 4TH INTERNATIONAL CONFERENCE ON ENGINEERING AND NATURAL SCIENCE
2-6 May 2018 KIEV UKRAINE

Determination of Mixing and Compaction Temperatures of Polymer Modified Bitumens Containing Nanoclays

Dilay Uncu[1], Ali Topal[2], M. Ozgur Seydibeyoglu[3]

Abstract

In recent years, the use of nanomaterials in different fields has become widespread with the development of nanotechnology. This development has also manifested itself in the field of modification of bituminous binders. In this study, 50/70 penetration grade bitumen was modified with Styrene-Butadiene-Styrene (SBS) polymer 3% and 5% by weight of the bitumen belongs to elastomer class, then two different nanoclays were added into the modified bitumen samples at different ratios. The workability of the obtained modified bitumens was investigated. It is important to avoid unnecessary energy consumption for the workability of bitumen and this depends on the choice of suitable mixing and compaction temperatures. For this, the viscosity values were measured at 135°C and 165°C temperature values. The viscosity values corresponding to these two temperature values were combined with a line, the temperatures corresponding to the viscosity values of 170±20 mPa.s and 280±30 mPa.s were determined as the mixing and compaction temperature values of the modified bitumens. The suitability of the obtained temperature values was examined and compared with each other.

Keywords: Polymer modified bitumen, nanoclay, viscosity, workability

1. INTRODUCTION

The usage of flexible pavement is more common as a pavement type for highways. In recent years, it is seen that the performance of flexible pavements containing base bitumen could not respond increased traffic and axle loads. As a result of the insufficient performance of flexible pavements, increase has been occurred in the formation of rutting, thermal and fatigue cracking. These deformations are shortened the service life of the highway.

It is tried to prevent or delay the formation of these deformations by mixing different additives into the base bitumen. The most common additives used for bitumen are polymers. Polymers are also divided into different classes and the most commonly used elastomer class is styrene-butadiene-styrene (SBS) block copolymer [1]. Several studies have shown that the use of SBS as a bitumen additive in hot mix asphalt improves the resistance to permanent deformation [2, 3, 4], fatigue [5] and moisture damage [6, 7].

However, the problem of separation of bitumen and polymer has been also encountered with use of polymers at high storage temperatures. In recent decedas, nanomaterials becoming a current issue have begun to be used as additives with the development of nanotechnology to remove the separation problems. Nanomaterials are described as materials which have at least one dimension between 1 and 100 nanometers. The properties of nanomaterials are more different and superior than normal sized materials thanks to their small size and high surface area [8]. Thus by addition of various nanomaterials for modification, significant improvement is achieved in thermal, mechanical and barrier properties of bitumen [9, 10]. Nanoclays are also encountered as the most used nanomaterials in the studies.

[1]*Corresponding author: Manisa Celal Bayar University, Department of Civil Engineering, 45140, Muradiye/Manisa, Turkey. dilay.yildirim@cbu.edu.tr*

[2]*Dokuz Eylul University, Department of Civil Engineering, 35390, Buca/Izmir, Turkey. ali.topal@deu.edu.tr*

[3]*Izmir Katip Celebi University, Department of Materials Science and Engineering, 35620, Cigli/Izmir, Turkey. ozgur.seydibeyoglu@ikc.edu.tr*

In this study, two different nanoclay; halloysite and sepiolite were used to modify SBS modified bitumen. The modified bitumen samples were subjected to viscosity test, mixing and compaction temperatures were determined.

2. EXPERIMENTAL

a. Materials

In this study, the base bitumen 50/70 penetration grade was obtained from Turkish Petroleum Refinery Corporation (Tupras), Aliaga/Izmir. The elastomeric type polymer SBS Kraton® D1101 was supplied from Termopol Plastic A.S. from Turkey in powder form. The properties of the SBS as presented in Table 1.

Table 1. Typical properties of Kraton® D 1101 SBS

Property	Test Method	Units	Typical Value
Elongation at break	ISO 37	%	880
Tensile strength	ISO 37	Mpa	33
Specific gravity	ISO 2781		0.94
Hardness, shore A (30 sec)	ISO 868	Hardness, Shore A (30 sec)	72
300% Modulus	ISO 37	MPa	2.9
Melt flow ratio, 200°C/5kg	ISO 1133	g/10 min.	<1
Bulk density	ASTM D 1895 method B	kg/dm^3	0.4

Two different types of nanoclay additives have been used in this study. The nanoclays are halloysite and sepiolite. They were obtained from ESAN Company to add into modified bitumen. The properties of halloysite and sepiolite are presented respectively in Table 2 and 3.

Table 2. Chemical analysis of halloysite

	AZ.(Lol)	SiO_2	Al_2O_3	Fe_2O_3	TiO_2	CaO	MgO	Na_2O	K_2O
Content (%)	16.50 ±1.00	43.00 ±1.50	37.50 ±1.50	0.70 ±0.10	0.10 ±0.05	0.10 ±0.05	0.15 ±0.05	0.05 ±0.01	0.30 ±0.05

Table 3. Chemical analysis of sepiolite

	SiO_2	Al_2O_3	Fe_2O_3	TiO_2	CaO	MgO	Na_2O	K_2O
Content (%)	18.45	0.84	0.218	0.029	21.64	22.27	0.13	0.11

The halloysite and sepiolite additives were expressed shortly as “Hal” and “Sep” respectively in the tables and figures.

b. Sample Preparation

Bitumen was heated in the oven at 160±5°C until became fluid enough and placed under the high shear mixer (Figure 1). Two types of modified bitumen samples were obtained. Modified bitumen samples contained only SBS in the first type. SBS was gradually added into the melted bitumen under high shear mixer at 2000 rpm and 180±5°C for 60 minutes. The ratios of SBS were chosen as 3% and 5% according to the commonly used ratios in the literature.

Figure 1. Modified bitumen production process with high shear mixer

In the second type of modified bitumen samples, SBS was gradually added into the melted bitumen at same ratios under high shear mixer at 2000 rpm and 180±5°C for 15 minutes. After 15 minutes nanoclays were added into the SBS modified bitumen under same mixing conditions. Halloysite and sepiolite were added into the SBS modified bitumen at two different ratios as 2% and 4% weight of the base bitumen. The mixing procedure was continued at additional 45 minutes, so the total mixing time has been 60 minutes. At the end of the mixing process modified bitumen samples were subjected to the viscosity test.

c. Rotational Viscometer (RV) Test

The rotational viscometer (RV) test is conducted to determine the high temperature fluidity characteristics of the asphalt binders. The RV test helps provide that the asphalt binder is sufficiently fluid for pumping and mixing [11]. For this purpose, Brookfield Viscometer is used according to AASHTO TP48 standard (Figure 2).

Figure 2. Brookfield viscometer

In the test, approximately 11 grams are taken from the fluidized sample and the sample is filled into the container. The sample is placed in a temperature-controlled chamber where the temperature reaches a fixed temperature value. The sample is kept at constant temperature for 15 minutes before being tested. The test is applied at 135°C and 165°C to determine the mixing and compaction temperatures. The viscosity values obtained from the test are marked in the temperature-viscosity graph and these values are combined with a straight line. The desired viscosity values are 170±20 mPa.s and 250±30 mPa.s respectively for determining the mixing and compaction temperatures [12, 13, 14]. The temperature values corresponding to these viscosity values are taken as the mixing and compaction temperature. The effect of viscosity on the workability of the asphalt binder is very important in terms of determining the suitable mixing and compaction temperatures.

3. RESULT AND DISCUSSIONS

The viscosity values of each bitumen sample were determined using rotational viscometer at 135°C and 165°C. The test results are shown in Table 4 and seen graphically in Figure 3. At the same time, the viscosity test results give information on workability.

Table 4. Rotational viscometer test results at 135°C and 165°C

Types of Bitumen	Standard	Viscosity at 135°C (cP)	Viscosity at 165°C (cP)
Base Bitumen		425	112.5
3% SBS		850	275
3% SBS + 2% Hal		912.5	312.5
3% SBS + 4% Hal		925	325
3% SBS + 2% Sep		850	362.5
3% SBS + 4% Sep	ASTM D4402	925	375
5% SBS		1563	462.5
5% SBS + 2% Hal		1638	512.5
5% SBS + 4% Hal		1700	562.5
5% SBS + 2% Sep		1638	500
5% SBS + 4% Sep		1725	525

As seen in Figure 3, the viscosity values of all bitumen samples are below the specification limit of 3000 cP. The increment in the ratio of both SBS and nanoclays increased the viscosity values.

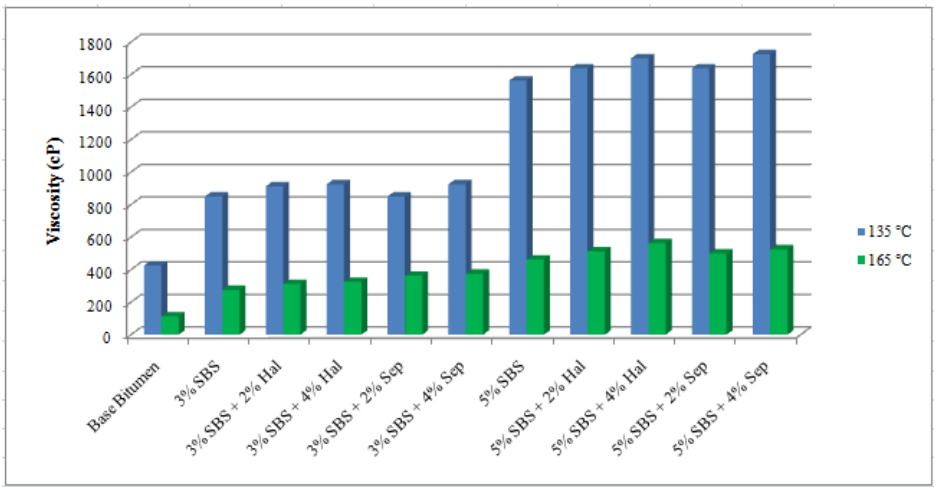

Figure 3. Change of viscosity values of bitumen samples with additives

The determined viscosity values of the bitumen samples were marked on the viscosity-temperature graph. Temperature values were determined which will provide the required viscosity values during mixing with aggregate and compaction on the field, in case of using bituminous binders in blend.

Figure 4. Viscosity-temperature relationship of base and modified bitumen samples containing halloysite

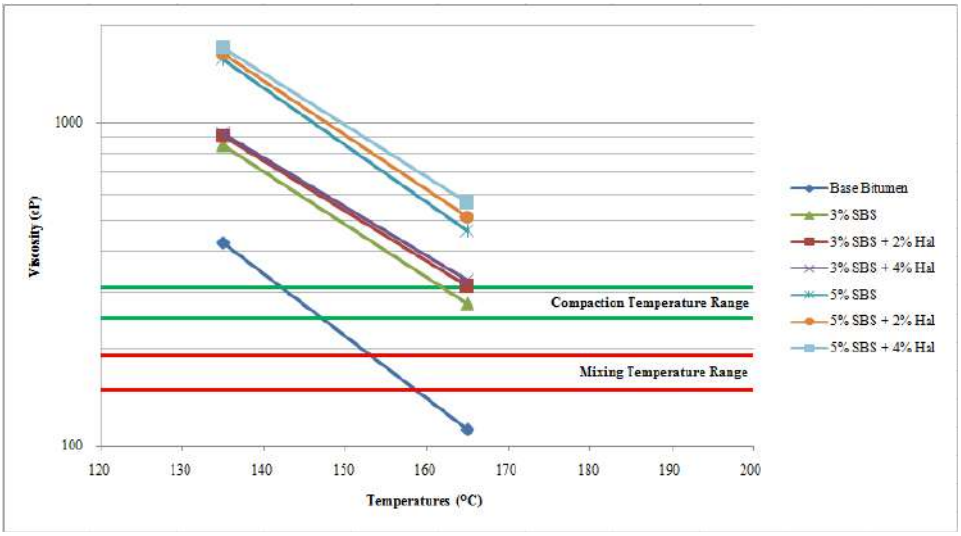

Figure 5. Viscosity-temperature relationship of base and modified bitumen samples containing Sepiolite

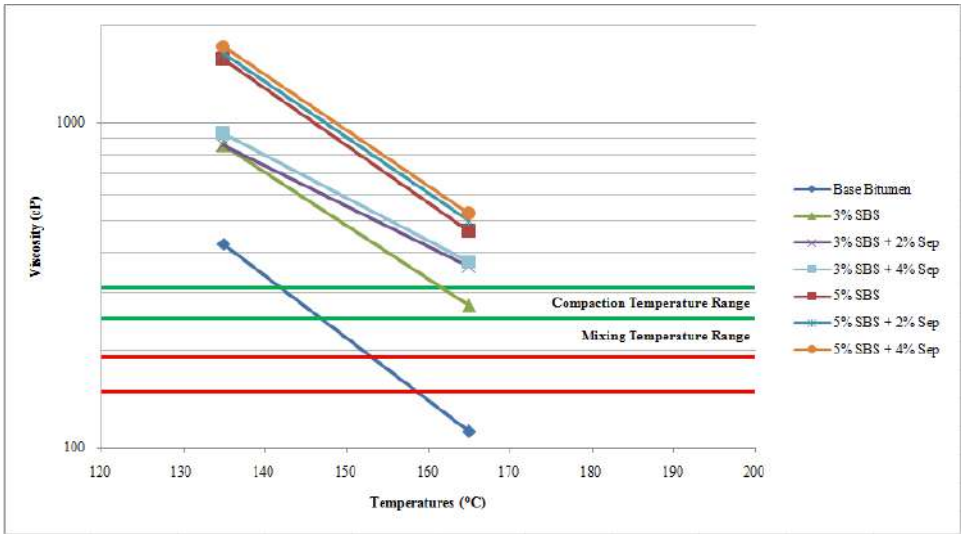

Viscosity and temperature relationship of bitumen samples are illustrated in two figures according to containing halloysite or sepiolte nanoclay in Figure 4 and 5. The temperature values corresponding to viscosity values 170±20 mPa.s and 250±30 mPa.s are listed in Table 5.

Table 5. Mixing and compaction temperatures of bitumen samples

Types of Bitumen	Mixing Temperature Range	Compaction Temperature Range
Base Bitumen	153.2-158.8	142.4-146.8
3% SBS	176.0-181.2	162.4-168.0
3% SBS + 2% Hal	178.0-185.6	164.8-170.4
3% SBS + 4% Hal	180.8-187.2	165.6-172.0
3% SBS + 2% Sep	186.8-195.2	170.0-177.6
3% SBS + 4% Sep	187.2-195.6	171.2-178.0
5% SBS	187.2-192.4	175.2-180.0
5% SBS + 2% Hal	191.2-196.4	178.0-183.2
5% SBS + 4% Hal	194.0-200.0	180.4-185.6
5% SBS + 2% Sep	189.6-195.2	177.2-182.8
5% SBS + 4% Sep	190.6-196.0	177.6-183.2

The minimum and maximum temperature values of compaction and mixing temperature range belong to bitumen samples are presented in Figure 6.

Figure 6. Mixing and compaction temperatures change of bitumen samples

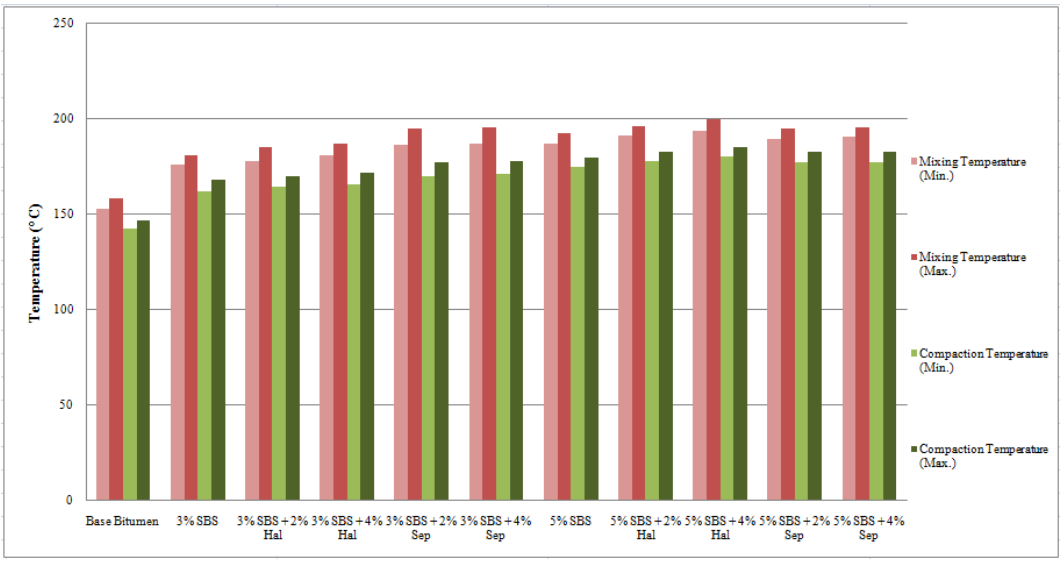

It has been observed that both mixing and compaction temperatures are increased due to the increment in viscosity values. 3% SBS modified bitumen sample has the lowest mixing and compaction temperature values and 5% SBS+4% Hal has the highest mixing and compaction temperature values between modified bitumen samples.

4. CONCLUSIONS

In this study, SBS was mixed with the base bitumen at two different mixing ratios (3% and 5%) and two different nanoclays were mixed with polymer modified bitumen at two different mixing ratios (2% and 4%). The mixing with aggregates and compaction temperatures of base and modified bitumen samples were determined by using rotational viscosity test results.

The ratio increment of SBS in the modified bitumen samples with the same combination also increased the mixing and compaction temperatures. Similarly, the addition of nanoclays into the polymer modified bitumens increased the mixing and compaction temperatures. Increasing mixing and compaction temperatures make difficult the workability and also increase energy consumption. Therefore the ratios of additives mixed with base bitumen should be very well chosen and optimized according to the test results.

ACKNOWLEDGMENT

This experimental study was supported by Scientific Research Project Office of Manisa Celal Bayar University with the project name "Investigation of Nanomaterials Effects on the Performance Enhancement of Polymer Modified Asphalt Binders".

REFERENCES

[1] B. V. Kok and M. Yilmaz, *The Effects of Using Lime and Styrene–Butadiene–Styrene on Moisture Sensitivity Resistance of Hot Mix Asphalt*, Construction and Building Materials, 23:1999-2006, 2009.

A. Khodaii and A. Mehrara, *Evaluation of Permanent Deformation of Unmodified and SBS Modified Asphalt Mixtures Using Dynamic Creep Test*, Construction and Building Materials, 23:2586-92, 2009.

[2] H. Ozen, *Rutting Evaluation of Hydrated Lime and SBS Modified Asphalt Mixtures for Laboratory and Field Compacted Samples*, Construction and Building Materials, 25:756-65, 2011.

[3] W. G. Wong, H. Han, G. He, K. C. P. Wang and W. Lu, *Rutting Response of Hot-Mix Asphalt to Generalized Dynamic Shear Moduli of Asphalt Binder*, Construction and Building Materials, 18:399-408, 2004.

[4] R. Y. Birliker, *Additives can be Added to Bituminous Mixtures and Investigation of Behaviour of This Mixtures and a Prediction Model for Fatigue Curve*, Istanbul Technical University, PhD Thesis, Istanbul, 1998.

[5] C. Gorkem and B. Sengoz, *Predicting Stripping and Moisture Induced Damage of Asphalt Concrete Prepared with Polymer Modified Bitumen and Hydrated Lime*. Construction and Building Materials, 23:2227-36, 2009

[6] M. Yilmaz and B. V. Kok, *Effects of Ferrochromium Slag with Neat and Polymer Modified Binders in Hot Bituminous Mix*, Indian Journal of Engineering Materials Science, S:16, 310-8, 2009.

[7] H. Yao, Z. You, L. Liang, S. W. Goh, C. H. Lee, Y. K. Yap and X. Shi, *Rheological properties and chemical analysis of nanoclay and carbon microfiber modified asphalt with Fourier transform infrared spectroscopy*, Construction and Building Materials, 38, 327-337, 2013.

[8] B. Golestani, F. M. Nejad and S. S. Galooyak, *Performance evaluation of linear and nonlinear nanocomposite modified asphalts*, Construction and Building Materials, *35*, 197-203, 2012.

[9] M. Jasso, D. Bakos, D. MacLeod and L. Zanzotto, *Preparation and properties of conventional asphalt modified by physical mixtures of linear SBS and montmorillonite clay*, Construction and Building Materials, *38*, 759-765, 2013.

[10] F. L. Roberts, P. S. Kandhal, E. R. Brown, D. Y. Lee, and T. W. Kennedy, *Hot mix asphalt materials, mixture design, and construction*, National Asphalt Pavement Association Education Foundation. Lanham, MD, 1996.

[11] Asphalt Institute, *Asphalt insitute manual series for asphalt concrete and other hot mix type*, Lexington: Asphalt Institute Editions, 1996.

[12] R. B. Mcgennis, S. Shuler and H. U. Bahia, *Background of Superpave Asphalt Binder Test Methods*, Report No: FHWA-SA-94-069, p:104, 1994.

[13] J. P. Zaniewski and M. E. Pumphrey, *Evaluation of Performance Graded Asphalt Binder Equipment and Testing Protocol*, Asphalt Technology Program, p:107, 2004.

BIOGRAPHY

Dilay Uncu graduated from Manisa Celal Bayar University Civil Engineering Department. She had MSc degree in Manisa Celal Bayar University Transportation division (2012) on Quality Function Deployment Approach for Determining Highway Pavement Parameters and PhD degree in Dokuz Eylul University Transportation division (2017) on Improvement of Polymer Modified Bitumen Properties by Using Nanomaterials. Dilay Uncu is a assistant professor in Department of Civil Engineering at Manisa Celal Bayar University and she has been a faculty member since 2010. Her research interests are about highway engineering, bituminous materials, modification of bitumens and nanomaterials.

ICENS 4TH INTERNATIONAL CONFERENCE ON ENGINEERING AND NATURAL SCIENCE
2-6 May 2018 KIEV UKRAINE

Turkish Construction Firms' Perceptions of Recycled Materials

Volkan Arslan[1], Serdar Ulubeyli[2], Aynur Kazaz[3]

Abstract

Waste materials are one of the most significant problems that the construction industry faces because of their harmful effects on the natural and built environment. To solve this problem, construction firms should implement a proper waste management strategy. In doing this, there are three main measures such as reducing, reusing, and recycling. In many developing countries, the first two methods are usually employed in order to deal with waste construction materials. However, the third one (that is, recycling) is skipped in general as it requires a costly and time-consuming process, environmental awareness, and technical standards. Therefore, this study aims to reveal the perspective of construction firms about recycled materials that can be used in the construction industry in a developing country, Turkey. To achieve this objective, a questionnaire survey was conducted with 66 construction companies in Turkey. The results were evaluated through a statistical analysis of questions with 5-point Likert-type scale. Consequently, Turkish construction firms' perceptions of recycled materials were determined in a detailed manner. In addition, recommendations were made given the dissemination of the use of recycled construction materials for a sustainable industry.

Keywords: construction industry, recycled materials, recycling, sustainable construction, Turkey.

1. INTRODUCTION

Construction by nature is not an environmental-friendly activity [1] and produces a significant amount of waste. Waste materials are one of the major problems that the construction industry faces because of their harmful effects on the natural and built environment. In general, the demolition waste of construction works accounts for 70% of construction and demolition waste (C&DW) [2]. Overall, C&DW amounts to more than a quarter of the municipal household waste stream and the total solid waste [3, 4]. In this respect, for sustainable built environment, this type of wastes should be treated carefully. Peng et al. [5] categorized environmental impacts of disposal options of waste into six levels, namely, reduce, reuse, recycle, compost, incinerate, and landfill. In many developing countries, the first two methods are usually employed in order to deal with waste construction materials. However, the third one (that is, recycling) is skipped in general as it requires a costly and time-consuming process, environmental awareness, and technical standards. Beside these difficulties, recycling offers three benefits: (i) reducing new resources demand, (ii) decreasing the costs of transport and energy production and (iii) creating possibility to use waste which would otherwise be landfilled [6].

C&DW including concrete, bricks and masonry, wood, and other materials such as glass, insulation, roofing, wires, pipes, rocks, and soil [7], has a significant potential to be recycled. The main advantage of recycling waste materials is that the product can be reused with economic benefits, if properly managed [8]. Recycled materials can be made to meet design specifications for regular construction materials, if properly processed [9-19]. Therefore, this study aims to reveal the perspective of construction firms about recycled materials that can be used in the construction industry in a developing country, Turkey. Moreover, the present study is the first effort to identify the approach of Turkish contractors towards recycled materials. Thus, it may fill the gap in the literature.

[1] *Corresponding author: Bulent Ecevit University, Department of Civil Engineering, 67100, Zonguldak, Turkey.* volkanarslan@beun.edu.tr

[2] *Bulent Ecevit University, Department of Civil Engineering, 67100, Zonguldak, Turkey.* ulubeyli@beun.edu.tr

[3] *Akdeniz University, Department of Civil Engineering, 07058, Antalya, Turkey,* akazaz@akdeniz.edu.tr

2. MATERIALS AND METHOD

In this study, a questionnaire survey was conducted with 66 construction professionals working in Turkey. The data gathered were evaluated through a statistical analysis of questions with 5-point Likert-type scale via SPSS 20. The obtained results were presented in two sub-sections: (i) the demographic information of respondents and (ii) Turkish construction firms' perceptions of recycled materials.

3. RESULTS AND DISCUSSION

a. Demographic information

In the first part of the questionnaire survey, participants answered questions concerning their positions in their current companies (Table 1), duration of professional experience (Table 2), companies' experience in the construction industry (Table 3), duration of experience in their current companies (Table 4), subsectors that their companies are in operation (Table 5), companies' annual average incomes (Table 6), usage of recycled materials of their companies (Table 7), type of recycled materials used before (Figure 1), reasons for using recycled materials (Table 8), and type of market where they procured recycled materials (Table 9). As shown in Table 1, 36 civil engineers, 28 company owners, and 2 architects were participated in the survey. Civil engineers who are executers of construction projects were expected to have significant knowledge about construction materials used in projects. Also, after clients, construction company owners are one of decision makers of materials that will be used in construction projects. In addition, architects have a great potential to affect the design of construction projects. From this point of view, respondents seem to be appropriate to present their decisions on the use of recycled materials in the construction industry.

Table 18. Respondents' positions in their companies

Position	Frequency	Percentage
Civil engineer	36	54.55
Company owner	28	42.42
Architect	2	3.03
Total	66	100.00

Respondents' experience can be a vital aspect for this study, since it may have a potential to influence their attitudes towards recycled materials. According to Table 2, 62.12% of respondents have experience of more than five years. As the use of recycled materials is not an old practice in the construction industry, the average experience duration of respondents seems reasonable to make a comment on these materials.

Table 19. Respondents' professional experience

Professional experience	Frequency	Percentage
0-5 years	25	37.88
6-10 years	11	16.67
11-20 years	22	33.33
> 20 years	8	12.12
Total	66	100.00

Experienced construction companies may face different problems about the material choice in their projects. Therefore, the surveyed companies' duration of experience was also investigated. Obtained results reveal that 53.03% of companies have been operating in the construction industry for more than ten years. Moreover, 25.76% have been active in the industry for less than six years, while 21.21% have had experience of six to ten years (Table 3). Thus, one can indicate that the surveyed companies have reasonable duration of experience to make a contribution to this study.

Besides these basic statistics, respondents' experience in their current companies were evaluated as well. This is because a construction professional's attitudes towards recycled materials may vary according to the policy of their companies. As indicated in Table 4 clearly, 78.79% of participants have been working in the same company for less than eleven years, while 63.64% have been working for less than six years. Therefore, it can be claimed that the effect of the company policy on respondents was limited on participants' attitudes towards recycled materials.

Table 20. Companies' experience in the construction industry

Industrial experience	**Frequency**	**Percentage**
0-5 years	17	25.76
6-10 years	14	21.21
11-20 years	12	18.18
> 20 years	23	34.85
Total	66	100.00

Table 21. Respondents' experience in their companies

Experience in company	**Frequency**	**Percentage**
0-5 years	42	63.64
6-10 years	10	15.15
11-20 years	9	13.64
> 20 years	5	7.57
Total	66	100.00

Standard Industrial Classification (SIC) system search established in the United States in 1937 classified subsectors of the construction industry as building, civil engineering, and specialty trade. The amount of recycled materials may change with subsectors of the construction industry. In this respect, these subsectors where respondents' companies operate were determined. Table 5 show that 81.82% of companies execute projects in the building subsector, while 4.54% and 1.52% operate in civil engineering and specialty trade work subsectors, respectively. Besides, there are two companies that have activities in both building and civil engineering subsectors, two companies that operate in building and specialty trade subsectors, and four companies that have projects in all three subsectors. In fact, the building subsector may be regarded as a sector which has a potential about the use of recycled materials. Therefore, the answers given may reveal a clear picture for the utilization of recycled materials in the construction industry.

Table 22. Companies' subsectors in the construction industry

Subsectors	**Frequency**	**Percentage**
Building	54	81.82
Civil engineering	3	4.54
Specialty trade	1	1.52
Building & civil engineering	2	3.03
Building & specialty trade	2	3.03
Building & civil engineering & specialty trade	4	6.06
Total	66	100.00

The annual average income of a company can be used as an indicator to classify companies in terms of size. Companies with an annual income of lower than $10 million can be considered as small, $10 million to $20 million as medium, and more than $20 million as large companies. From this point of view, 72.73% of companies are small, 24.24% are medium, and 3.03% are large companies. This may be a limitation for the study, since the number of large companies is small. However, construction companies operating in the building subsector (e.g., housing) are usually small- or medium-sized companies. Therefore, the sample may be regarded acceptable statistically.

Table 23. Annual average income of respondents' companies

Income	Frequency	Percentage
< $10 million	48	72.73
$10-20 million	16	24.24
> $20 million	2	3.03
Total	66	100.00

According to Table 7, only 31.82% of respondents have used recycled materials in construction activities. In this respect, attitudes of both experienced and unexperienced construction professionals on recycled materials were presented in the study. In addition, respondents listed the type of materials they have used in their previous projects. Results reveal that iron and steel products are commonly used recycled materials in the construction industry and that these are followed by plastic, glass, and timber. Moreover, recycled insulator, metal, concrete, ceramic, brick, gyprock, asphalt, and marble are among other recycled materials used in construction projects (Figure 1).

Table 24. The use of recycled materials

Answer	Frequency	Percentage
Yes	21	31.82
No	45	68.18
Total	66	100.00

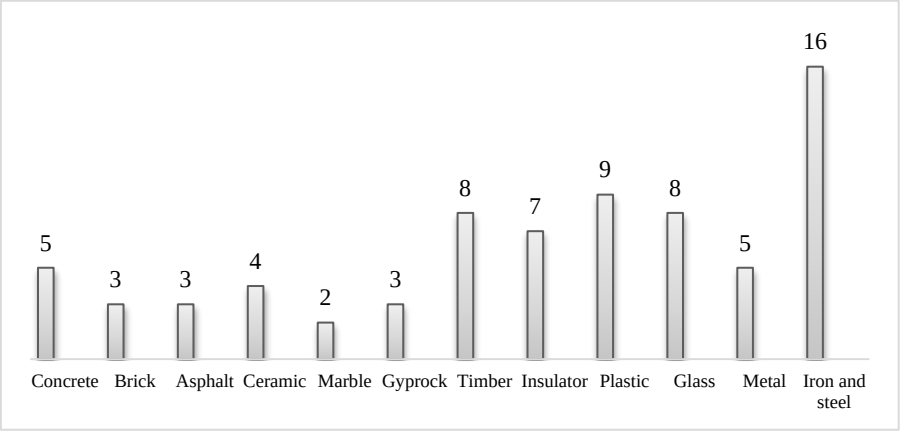

Figure 25. Frequencies of types of recycled materials used

In accordance with the answers given by respondents, there are three main reasons for using recycled materials. These are lower cost, environmental sustainability, and contractual requirements. Obtained results indicate that 59.09% of respondents utilized recycled materials in their construction activities for a better environmental sustainability performance (Table 8). In addition, 12.12% stated that the main motivation behind the use of recycled materials is their lower costs. Moreover, 25.76% expressed both environmental sustainability and lower cost as drivers for the selection of recycled materials. Lastly, 3.03% of respondents asserted that they

have used recycled materials due to contractual requirements. Consequently, the majority of participants considers environmental sustainability as a vital issue, and thus, prefers recycled materials in their construction activities.

Table 8. Reasons for using recycled materials

Answer	Frequency	Percentage
Environmental sustainability	39	59.09
Lower cost	8	12.12
Lower cost & environmental sustainability	17	25.76
Contractual requirements	2	3.03
Total	66	100.00

Participants were asked to answer if they prefer domestic or international market for the procurement of recycled materials. Results assert that 75.76% of respondents procure recycled materials from the domestic market, while 4.54% procure them from the international market. In addition, 19.70% clearly expressed that they employ both domestic and international market (Table 9). In accordance with these results, the reputation of the domestic recycled material market can be considered good for the construction industry in Turkey.

Table 925. Markets where recycled materials are procured

Answer	Frequency	Percentage
Domestic	50	75.76
International	3	4.54
Domestic and international	13	19.70
Total	66	100.00

b. Turkish Construction Firms' Perceptions of Recycled Materials

The second part of the questionnaire survey consisted of nine questions with a five-point Likert scale. These questions were prepared to determine views and attitudes of Turkish construction firms towards recycled materials. To achieve this, the survey was conducted face-to-face with 66 participants, and the results obtained were totally presented in Table 10.

There are several benefits of the utilization of recycled materials. For example, recycling has a potential to reduce the demand for the extraction and processing of new aggregate [20], to reduce the volume of waste deposited in landfills, and thereby, to extend the life of the existing landfills [21]. According to Table 10, almost all of respondents agree that using recycled materials can make a positive contribution to the national economy. In addition, 78.8% of respondents believe that their customers will be pleased if the design of their projects contains recycled materials. Therefore, it can be asserted that Turkish construction companies are aware of economic benefits of using recycled materials. However, only 18.18% agree that the use of recycled materials is encouraged in the construction industry. Moreover, 92.12% agree that there should be some incentives (e.g., tax reduction) for those who use recycled materials in their construction projects. Thus, it is clear that there is a need of government incentives for the popularization and dissemination of the use of recycled materials in the construction industry in Turkey.

Table 260. Respondents' views on recycled materials

Question	Strongly agree	Agree	Partly agree	Disagree	Strongly disagree

I believe that using recycled materials will make a positive contribution to the national economy.	72.73	21.20	4.55	1.52	-
I believe that using recycled materials will please our customers.	24.24	18.18	36.36	15.15	6.07
I believe that the use of recycled materials is encouraged in the construction industry.	12.12	6.06	24.24	31.82	25.76
I believe that there should be some incentives for those using recycled materials in the construction industry.	75.74	16.67	4.55	1.52	1.52
I believe that using recycled materials will reduce environmental pollution.	77.27	18.18	4.55	-	-
I believe that preferring suppliers who have waste reduction consciousness will be beneficial in terms of sustainable built environment.	72.72	19.70	3.03	3.03	1.52
I believe that materials which produce less waste should be used in the construction industry.	72.73	21.21	6.06	-	-
I believe that second hand or opportunities for reusing materials should be considered in the construction industry.	28.79	21.21	24.24	12.12	16.64
Recycled materials are easy to access in Turkey.	10.61	3.03	30.30	27.27	28.79

From the environmental point of view, the idea that the use of recycled materials will reduce the environmental pollution was agreed by 95.45% of respondents. Moreover, according to 92.42% of respondents, preferring suppliers who have waste reduction consciousness will be beneficial in terms of sustainable built environment. Similarly, 93.94% believe that materials which produce less waste should be used in the construction industry. Taking into account all these judgments, one can say that awareness and consciousness of Turkish construction companies about environmental sustainability are high. However, the utilization of recycled materials in construction projects is inadequate due to the lack of moral support and financial incentives. Exceptionally, according to Table 10, respondents were not enthusiastic for second hand or opportunities to reuse materials in the construction industry. This is because designers and end-users have some doubts about the quality performance of second hand materials [22].

One of the major problems of using recycled materials in the Turkish construction industry was determined as difficulties in the procurement of these materials. The obtained results indicate that only 13.64% of respondents have no problem with accessing to recycled materials in Turkey. More than half of participants asserted that it is not easy to access recycled materials in the country. Therefore, the shortage of recycled materials restricts the dissemination and extension of these materials in the construction industry in Turkey. In this respect, the existence of a well-designed and managed market of recycled materials can be considered as a vital aspect for the sake of sustainable built environment in Turkey.

4. CONCULUSION

In this study, the existing attitudes of Turkish construction companies towards recycled material were examined from the perspective of sustainable built environment. To do so, a questionnaire survey was applied to 66 construction professionals working in Turkey. The results obtained show that, from the economic point of view, Turkish construction companies are aware of the importance of recycled materials. Moreover, companies place much emphasis on the use of recycled materials in terms of environmental sustainability in the construction industry. However, the major problems of the recycled materials industry in Turkey were listed as (i) the lack of government incentives, (ii) a low performance of the quality of second hand materials, and lastly, (iii) the shortage of a recycled material market in Turkey.

Consequently, some drivers such as (i) providing government incentives for construction companies that use recycled materials, (ii) improving the second hand materials quality performance by developing related production standards, and (iii) creating a well-designed and managed recycled material industry in Turkey, may help to increase the performance of the sustainability of the Turkish construction industry.

ACKNOWLEDGMENT

The authors gratefully acknowledge the surveyed respondents for their generous collaboration and contributions. The authors also thank financial supports provided by Committees on Research Grants of Bulent Ecevit University and Akdeniz University.

REFERENCES

[1]. V. W. Y. Tam and C. M. Tam, "A review on the viable technology for construction waste recycling", Res., Conser. and Rec., vol. 47, pp. 209–22, 2006.
[2]. E. Martinez, Y. Nunez, E. Sobaberas, "End of life of buildings: three alternatives, two scenarios, a case study", Int. J. Life Cyc. Ass. vol. 18, pp. 1082–1088, 2013.
[3]. W. Lu, V.W.Y. Tam, "Construction waste management policies and their effectiveness in Hong Kong: a longitudinal review", Renew. Sust. En. Rev. vol. 23, pp. 214-223, 2013.
[4]. M. Malia, J. de Brito, M.D. Pinheiro, M. Bravo, "Construction and demolition waste indicators", Waste Manag. Res. vol .31, pp. 241–255, 2013.
[5]. C. L. Peng, D. E. Scorpio, and C. J. Kibert, "Strategies for successful construction and demolition waste recycling operations", J Construct Manag Econ, vol. 15(1), pp. 49–58, 1997.
[6]. B. Edwards, Sustainable Architecture: European Directives and Building Design. 2nd ed., Oxford: Architectural Press, 1999.
[7]. S. Coventry, C. Wolveridge, and S. Hillier, The Reclaimed and Recycled Construction Materials Handbook, Construction Industry Research and Information Association, London, 1999.
[8]. V.W.Y. Tam, D. Kotrayothar, and Y.C. Loo, On the prevailing construction waste recycling practices: a South East Queensland study
[9]. R. R. Reusser, "Recycling Portland cement concrete pavement at the contractor's option," in Proc. of the 23rd Air Transport Conference, Arlington, Virginia, 22–24 June 1994, American Society of Civil Engineers, USA, pp. 86–91.
[10]. H. Kawano, "The state of reuse of demolished concrete in Japan," in Proceedings of the International Workshop 'Rational Design of Concrete Structures under Severe Conditions' Hakodate, Japan, 7–9 August 1995, E&FN Spon, London, pp. 243–249.
[11]. H. Kawano, "Barriers for sustainable use of concrete materials," in Concrete Technology for a Sustainable Development in the 21st Century. E & FN Spon, London and New York, 2000.
[12]. H. Kawano, "The state of using by-products in concrete in Japan and outline of JIS/TR on recycled concrete using recycled aggregate," in Proceedings of the 1st FIB congress, Osaka, Japan, October 2002, Thomas Telford, USA, pp. 245–253.
[13]. K. E. Hassan, J. J. Brooks, and M. Erdman, "The use of reclaimed asphalt pavement aggregates in concrete," in Proceedings of the International Conference on the Science and Engineering of Recycling for Environmental Protection, Harrogate, England, 31May–2 June 2000, pp. 121–128.
[14]. F. Tomosawa, and Noguchi, T. "New technology for the recycling of concrete – Japanese experience," in Concrete Technology for a Sustainable Development in the 21st Century, E & FN Spon, London and New York, pp. 274–287.
[15]. C. S. Poon, S. Azhar, and S.C. Kou, "Recycled aggregates for concrete applications," in Proceedings of Materials Science and Technology in Engineering Conference: Now, New and Next, 15–17 January 2003, Professional Services Development Assistant Scheme, Hong Kong, pp. 14–16.
[16]. H. K. Cheung, "Use of recycled asphalt pavement – a practical approach to asphalt recycling," in Proceedings of Materials Science and Technology in Engineering Conference: Now, New and Next, 15–17 January 2003. Professional Services Development Assistant Scheme, Hong Kong.
[17]. Tam, W.Y.V. (2005) Recycled Aggregate from Concrete Waste for Higher Grades of Concrete Construction. PhD thesis Department of Building and Construction, City University of Hong Kong, Hong Kong, China.
[18]. W.Y.V. Tam, X. F. Gao, and C. M. Tam, "Micro-structural analysis of recycled aggregate concrete produced from two-stage mixing approach", Cem. & Con. Res., vol. 35, pp. 1195–1203, 2005.
[19]. W.Y.V. Tam, C. M. Tam, S. X. Zeng, and K. K. Chan, "Environmental performance measurement indicators in construction", Build. & Envir. , vol. 41, pp. 164–173, 2005.
[20]. A. P. Carneiro, J. C. Cassa, I. A. DeBrum, A. M. Vieira, A. D. B. Costa, T. S. Sampaio, and E. P. V. Alberte, "Construction waste characterization for production of recycled aggregate – Salvador / Brazil," in Proceedings of the International Conference on the Science and Engineering of Recycling for Environmental Protection, Harrogate, England, 31 May–2 June 2000, The International for the Environmental and Technical Implications Construction with Alternative Materials, UK, pp. 825–835.
[21]. Tech Data Sheet, Recycling Spent Sandblasting Grit and Similar Wastes as Aggregate in Asphaltic Concrete. Naval Facilities Engineering Service Center, Port Hueneme, California, 1998.
[22]. C. Aydin Ipekci, N. Coskun, T. Tikansak Karadayi, "Insaat sektorunde geri kazanilmis malzeme kullaniminin surdurulebilirlik acisindan onemi", TUBAV Bil., vol.10 (2), pp. 43-50, 2017.

BIOGRAPHY

Volkan Arslan is a Research Assistant in the Department of Civil Engineering at Bulent Ecevit University, Turkey. His areas of academic research interests include green buildings, green roofs, and sustainable built environment. He has published many papers in various scientific journals and proceedings.

ICENS 4TH INTERNATIONAL CONFERENCE ON ENGINEERING AND NATURAL SCIENCE
2-6 May 2018 KIEV UKRAINE

Construction and Demolition Waste Recycling Plants in Turkey

Serdar Ulubeyli[1], Volkan Arslan[2], Aynur Kazaz[3]

Abstract

Wastes generated in the process of construction, renovation, and demolition of buildings and structures are described as construction and demolition waste (C&DW). In many countries, C&DW is regarded as one of the major issues that threaten the environment and its embedded raw materials. In order to overcome this problem, there are three basic options such as reducing, reusing, and recycling. Considering construction projects executed in many developing countries, the first two options are usually and initially employed to reduce the amount of C&DW. However, the option "recycling" is generally neglected. This is because it needs a relatively high initial investment cost, extra sensitivity for environmental protection, and detailed regulations concerning material compositions. Therefore, the objective of the current study was to identify and examine technical features and operational capabilities of the existing C&DW recycling plants in Turkey, a developing country. For this purpose, a questionnaire survey was applied to facility managers of C&DW recycling plants operating in three different cities (i.e., Istanbul, Eskisehir, and Mugla) in Turkey. As a result, the current situation and the future perspective of C&DW recycling plants in Turkey were evaluated extensively. Moreover, the economic performance of these plants was also discussed in detail.

Keywords: C&DW, recycled materials, recycling plants, Turkey, waste management

1. INTRODUCTION

Wastes generated in the process of construction, renovation, and demolition of buildings and structures are described as construction and demolition waste (C&DW). In many countries, C&DW is regarded as one of the major issues that threaten the environment and its embedded raw materials. The European Commission considers C&DW as a priority waste stream due to large amounts generated [1]. In general, the demolition waste of construction works accounts for 70% of C&DW [2]. Overall, C&DW amounts to more than a quarter of the municipal household waste stream and the total solid waste [3, 4]. However, C&DW generation statistics are not rigorously tracked in many countries, and thus, the corresponding predictions seem to vary dramatically [5]. In order to overcome this problem, there are three basic options such as reducing, reusing, and recycling. Considering construction projects executed in many developing countries, the first two options are usually and initially employed to reduce the amount of C&DW. However, the option "recycling" is generally neglected. This is because it needs a relatively high initial investment cost, extra sensitivity for environmental protection, and detailed regulations concerning material compositions. In this respect, the recycling works of C&DW by plants should be considered as the most sustainable way to handle this serious problem in developing countries.

C&DW recycling efforts was first emerged in early 1970s. Both the shortage of landfills and the growing awareness about the pollution and resource potential of C&DW triggered actions for several plants for sorting and recycling in 1980s [6]. However, the first C&DW recycling plant in Turkey was established in 2006, and, to the best of our knowledge, this study is the first attempt to evaluate the current situation of CD&W recycling plants in Turkey.

C&D waste recycling practices have numerous advantages and these can be listed as conservation/preservation of precious land areas, extension of the lifespan of landfills, cost effectiveness of using recycled products, improvement of general environmental status in terms of energy and pollution, minimization of the resource consumption, utilization of waste which would otherwise be lost to landfill sites, and job creation [5]. However, the number of C&DW recycling plants in Turkey is small. There are only three recycling plants in three

[1] *Corresponding author: Bulent Ecevit University, Department of Civil Engineering, 67100, Zonguldak, Turkey.* *ulubeyli@beun.edu.tr*

[2] *Bulent Ecevit University, Department of Civil Engineering, 67100, Zonguldak, Turkey.* *volkanarslan@beun.edu.tr*

[3] *Akdeniz University, Department of Civil Engineering, 07058, Antalya, Turkey,* *akazaz@akdeniz.edu.tr*

different cities in Turkey. Therefore, the objective of the current study was to identify and examine technical features and operational capabilities of the existing C&DW recycling plants in Turkey, a developing country. For this purpose, a questionnaire survey was applied to facility managers of C&DW recycling plants operating in three different cities (i.e., Istanbul, Eskisehir, and Mugla) in Turkey. Consequently, it was expected to attract the particular attention of competent authorities, industrial practitioners, and society for the current situation and the future perspective of C&DW recycling plants in Turkey.

2. MATERIALS AND METHOD

In this study, three CD&W recycling plants were visited to apply a questionnaire survey to facility managers and to observe the recycling process adopted in these plants. This survey consisted of eighteen questions in four parts. In the first part, facility managers were asked to answer questions about the general information on the plants. In the second part, financial information on the plants was investigated. Then, in the third part, the type and the amount of CD&W recycled in the plants were determined. Lastly, from the perspective of facility managers, current problems of the plants were identified. Consequently, the results obtained were categorized, compared, and evaluated extensively in the context of C&DW management in the Turkish construction industry.

3. RESULTS AND DISCUSSION

a. Istanbul

Istanbul, with its population of 15 million people, is the most crowded city in Turkey. In 2006, the Environmental Protection Directorate of Istanbul Metropolitan Municipality and ISTAC Inc. developed "Istanbul C&DW Management Plan" to prevent the disposal of C&DW to forest lands, roadside, stream beds, and garbage containers and to control the potential C&DW in the future. According to this plan, CD&W shall be collected, transported, and recycled in a systematic way, considering the principals indicated in the Regulation on Control of Excavation Soil and C&DW issued by the Ministry of Forestry in 2004. In accordance with the plan, it was initially intended to build a waste collection center in each town to collect the generated C&DW and to preclude its illegal dumping. Then, the number of these centers would be increased given the amount of the collected C&DW. Finally, the C&DW collected would be recycled to be used in the construction industry again. In this context, a C&DW recycling plant with a capacity of 200 tons per hour was built in Tuzla, Istanbul. The C&DW generated due to urban transformation, renovation, and repair works in Istanbul would be recycled in this plant to be used as construction materials in infrastructure projects.

An interview was performed with the manager of Istanbul C&DW recycling plant in 2017. According to the answers given, the plant was built on an area of 12,800 square meter in 2008 as a public-private partnership (Figure 1a). It is a mobile recycling plant where trucks, excavators, stone crusher, and sieves are used during the process of recycling (Figure 1b). The initial investment cost and operation/maintenance costs were not clarified by the manager. However, it was stated that there is no entrance fee for trucks carrying C&DW to the plant. From the perspective of the manager, despite the fact that there is free entrance to the plant, the low demand for recycled materials in the construction industry and the lack of awareness on the C&DW recycling decrease the amount of C&DW recycled in the plant. This is because the financial performance of the plant is not as good as it was predicted. Considering the existing operations, the most common recycled materials in the plant are concrete, tile, ceramic, and excavation soil. Although the plant has a daily recycling capacity of 1,000 tons of inert materials and 1,400 tons of excavation soil, only 500 tons of materials go through the recycling process in the plant. Among these materials, concrete and paving stone are the most common recycled materials. The manager also stated that 90% of the incoming material can be recycled in the plant and that the remaining non-recyclable materials are stored in an area in the facility. Finally, the most significant problems determined by the manager are the improper and mixed structure of truck load and the non-recyclable characteristic of the incoming materials.

Figure 1. (a) Area of the plant in Istanbul

(b) Recycling works in the plant in Istanbul

b. Eskisehir

Eskisehir is a financially dynamic city located next to Ankara, the capital of Turkey. Considering the emerging needs, the C&DW recycling plant in Eskisehir was established in 2014 within the boundaries of the solid waste regular storage facility by the Metropolitan Municipality. It was predicted to recycle 365,000 tons of C&DW per year through this facility (Figure 2(a)). After the process of recycling, the recycled materials would be utilized in road construction works in accordance with the related regulations issued by the Metropolitan Municipality.

In this study, the C&DW plant in Eskisehir was visited in 2017 and the facility manager answered the questions about the plant. This is a public corporation and was established on an area of 34,052 square meters. In addition to a mobile recycling plant, the corporation has two loaders, three excavators, one backhoe loader, and three trucks (Figure 2 (b)). The facility manager did not declare any data about the initial investment cost, but the operation cost for 2016 was calculated €144,550. Of this amount, €84,282 is overhead and €60,268 is labor cost. Moreover, there is an entrance fee of €1.59 per ton for trucks. Since it is a public corporation, the plant is a non-profit organization which prioritizes environmental sustainability. Therefore, the manager indicated that they do not conduct any profit or loss account for the plant. Currently, except the materials such as polychlorinated biphenyls or mercury, all C&DW can be recycled in the plant. However, the most common materials processed in the plant are concrete, tiles, ceramic, and brick. The recycling capacity of the plant is 1,000 tons per day, and the plant operates in full capacity. In addition, because of the rule designed to prevent the entrance of non-recyclable materials to the plant, the plant can recycle 100% of the incoming C&DW. After the recycling process, the obtained materials are collected by the Directorate of Technical Works of Metropolitan Municipality and used in road construction works as road embankment mostly. According to the facility manager, one of the most fundamental problems of the C&DW issue is the unconsciousness of contractors and citizens about benefits of environmental sustainability and the recycling system. Another crucial problem of C&DW management is the earth-moving trucks working illegally in the city and dumping their loads in the forbidden zones.

Figure 2. (a) Recycling works in the plant in Eskisehir

(b) Equipment in the plant in Eskisehir

c. Mugla

The Mugla city is in the southwest of Turkey and its population is about 925,000. In 2015, the city council in the Metropolitan Municipality issued a tariff of the permit certificate for excavation soil and C&DW recovery facility. Then, a plant for the excavation soil and C&DW recycling was established on an area of 58,000 square meters in the Bodrum district in 2016. This plant was designed to recycle 438,000 tons of excavation soil, C&DW, and asphalt waste per year and expected to have a breakeven point in four years.

During the visit to the C&DW recycling plant in Mugla in 2017, the entire working field was observed together with the manager who gave the required information about the recycling process in the plant. Then, the questionnaire survey was applied to him in his office. The obtained answers showed that a mobile recycling plant is used in Mugla and that the employer is a public corporation owned by the Municipality. Regarding technical capabilities, the corporation conducts its operations with one excavator, one loader, one mobile impact crusher, a three-layered mobile sieve, and an electromagnetic separator on the mobile crusher (Figure 3a, 3b).

Figure 3. (a) Recycling works in the plant in Mugla

(b) Equipment in the plant in Mugla

The initial investment cost of this C&DW recycling plant is €549,792. Daily operating expenses are given in detail in Table 1. In this context, an operator earns €31.3 per day and an unskilled worker gets €20.75. The most expensive item is crusher fuel with its cost of €47.74 per hour. In total, the fuel cost of the recycling process in the plant is €100.09 per hour. In addition, it was stated that there are also maintenance and repairing costs that should be taken into account. However, there is an entrance fee of €10.37 per truck. Since the plant is a non-profit organization and the main aim of operations is to protect the environment, the financial performance of the plant has never been a significant issue for the employer. In the recycling operations, every type of C&DW is accepted in the plant, but concrete and excavation soil are the most common recycled materials. The capacity of the plant is 1,200 tons per day, and it works with full capacity. 65% of the incoming materials can be recycled, while the rest of 35% is prohibited to enter the plant. The recycled materials were usually used for public works of the Metropolitan Municipality. Consequently, the manager of the plant indicated that poor practices of segregation-at-source of C&DW is the main reason behind the low performance of the plant.

Table 27. Operating expenses

Expense item	Cost
Operator	31.13 Euro / day
Unskilled worker	20.75 Euro / day
Excavator fuel	18.16 Euro / hour
Loader fuel	18.16 Euro / hour
Sieve fuel	16.03 Euro / hour
Crusher fuel	47.74 Euro / hour

d. Comparison of three recycling plants

Comparing the three C&DW recycling plants may be considered as an advantageous method to identify and examine their technical features and operational capabilities. Therefore, the collected data through the questionnaire survey are listed in Table 2. The oldest plant was built in Istanbul while the plant in Mugla started its operations two years ago. In addition, the plant in Eskisehir was established in 2014. Although the existence of commercial C&DW recycling plants in the Netherlands and Germany [7], two of the recycling plants in Turkey are public corporations and the plant in Istanbul is the single example of public-private partnership. The main reason is the necessity of a public infusion of capital for these kind of investments in Turkey. Especially in Istanbul, due to urban transformation activities, there is a huge amount of C&DW. However, plants in Eskisehir and in Mugla were built in larger areas. From this perspective, it is clear that the plant in Istanbul should be improved and enlarged to satisfy the needs of the city in terms of the C&DW recycling. There are two types of the recycling plants: mobile and stationary. Mobile plants of which capacities are up to 100 ton/h treat smaller quantities of C&DW in temporary demolition worksites, while stationary plants of which capacities are 100-350 ton/h usually adopt higher level of technologies and are typically provided with the sorting equipment for the separation of unwanted fractions [5]. They are economically feasible from an amount of 5,000 to 6,000 ton/site [8]. According to the information gathered from managers, mobile recycling plants were preferred because of their lower costs of initial investment and the potential amount of C&DW to be recycled in the plant. Also, there are some ancillary equipment used for different purposes during the C&DW recycling process. These are truck, excavator, backhoe loader, stone crusher, sieve, and electromagnetic separator.

There were no information about initial investment costs of C&DW plants in Turkey, except the Mugla sample. It is €549,792. In addition, the operating and maintenance cost is €396.02 and €852.05 for Eskisehir and Mugla plants, respectively. Moreover, as an income item, there is an entrance fee of €1.59 per ton for trucks in Eskisehir and €10.37 per truck in Mugla. However, there is no financial information about the plant in Istanbul. Also, the managers of the plants indicated that they do not focus on the economic feasibility performance. This is because these plants were established by public authorities to provide sustainable built environment.

Table 28. Collected data for three recycling plants

	Istanbul	**Eskisehir**	**Mugla**
Date of establishment	2008	2014	2016
Type of organization	Public-private	Public	Public
Built-up area (m^2)	12,800	34,052	58,000
Type of plant	Mobile	Mobile	Mobile
Equipment	Truck, excavator, stone crusher, sieve	Loader, excavators, backhoe loader, truck	Excavator, loader, stone crusher, sieve, electromagnetic separator
Initial investment cost (Euro)	n.a.	n.a.	549,792
Operating and maintenance cost (euro per day)	n.a.	396.02	852.05
Entrance fee	none	1.59 per ton	10.37 per truck
Economic feasibility	n.a.	n.a.	n.a.
Type of recycled C&DW materials	Inert materials	Inert materials	Inert materials
Daily capacity (ton)	1,600	1,000	1,200
Current recycling operations (ton)	500	1,000	1,200
The most common material recycled daily	Concrete, tile, ceramic, excavation soil	Concrete, tiles, ceramic, brick	Concrete, excavation soil

Material recycling ratio (%)	90	100	65
Usage of recycled materials	Construction and repair works of the facility	Road embankment	Public road, pavement works
Non-recycled material procedure	Stored in a certain area in the facility	Prohibited to enter the plant	Prohibited to enter the plant
Main problems	Improper and mixed structure of truck load	Unconsciousness of contractors and citizens	Poor practices of segregation-at-source of C&DW

n.a.: not available

In general terms, C&DW is divided into two types: inert materials (i.e., sand, bricks, and concrete) and non-inert materials (i.e., plastic, glass, paper, wood, vegetation, and other organic materials). Obtained results show that the recycling plants in Turkey solely accept inert materials for recycling. The daily capacity of the plants is 1,600 tons, 1,000 tons, and 1,200 tons for Istanbul, Eskisehir, and Mugla, respectively. The plants in Eskisehir and Mugla work with full capacity, while the amount of C&DW recycled in Istanbul is 500 tons per day. In this respect, the reasons behind the low demand of C&DW in Istanbul should be examined, and precautions should be taken to increase the amount of waste to be recycled. As an expected outcome, the most common recycled C&DW materials are concrete, tile, ceramic, and excavation soil. In Istanbul and Eskisehir, the recycling ratios of these materials are between 90% and 100%. However, they are 65% in Mugla because of poor segregation-at-source practices in the construction sector in Mugla. Past studies indicated that, depending on the characteristic of the generated waste, it is possible to recycle %50 to 95% of C&DW [9, 10, 11]. Recycled materials obtained from the plant in Istanbul were usually used for construction and repair works of the facility, and non-recyclable ones are stored in an area in the facility. In recycling plants in Eskisehir and Mugla, recycled materials are collected by local public authorities to use as embankment in road works, while non-recyclable materials were prohibited to enter the plant.

Finally, the answers given by the managers show that the improper and mixed structure of truck load, unconsciousness of contractors and citizens on the C&DW issue, and poor practices of segregation-at-source of C&DW can be listed among the major problems in Turkey.

4. CONCLUSION

The construction industry will always produce a significant level of waste due to the nature of this industry. However, proper recycling practices may decrease the amount of C&DW to a minimum level. In this respect, C&DW recycling plants have a vital role to provide sustainable built environment. Therefore, this study revealed the current situation of technical features and operational capabilities of the existing C&DW recycling plants in Turkey. Consequently, it is obvious that the number of recycling plants in the country is inadequate. Moreover, the lack of consciousness and awareness on waste management results in a low demand for C&DW recycling activities. Also, the importance of government incentives for the feasibility and sustainability of C&DW recycling plants is clear. In this context, recycled material and recycling plant supportive rules of taxation, higher landfilling costs, promotions for those disposing of in the recycling centers, supporting the recycled material market by lowering taxes or recommending the use of this type of materials in public construction projects, and creating awareness on society may be beneficial economically and environmentally for sustainable built environment.

This research may have a potential to create awareness on society about the importance of C&DW management in Turkey and in other developing countries. Similarly, this study may fill the gap in the literature for the recycling plants in Turkey. From the perspective of the private sector, the results of the study reveal the current situation and needs of the Turkish C&DW recycling industry.

ACKNOWLEDGMENT

The authors gratefully acknowledge the surveyed facility managers for their generous collaboration and contributions. The authors also thank financial supports provided by Committees on Research Grants of Bulent Ecevit University and Akdeniz University.

REFERENCES

[1]. E. Dosal, B. Galan, A. Andres, and J. Viguri, "Introduction of social criteria for the optimal location of construction and demolition waste management facilities in Cantabria (Spain)", Comp. Aid. Chem. Eng., vol. 32, pp. 1027–1032, 2013.
[2]. E. Martinez, Y. Nunez, and E. Sobaberas, "End of life of buildings: three alternatives, two scenarios, a case study", Int. J. Life Cyc. Ass., vol. 18, pp. 1082–1088, 2013.
[3]. W. Lu and V.W.Y. Tam, "Construction waste management policies and their effectiveness in Hong Kong: a longitudinal review", Renew. Sust. En. Rev., vol. 23, pp. 214–223, 2013.
[4]. M. Malia, J. de Brito, M.D. Pinheiro, and M. Bravo, "Construction and demolition waste indicators", Waste Manag. Res., vol. 31, pp. 241–255, 2013.
[5]. S. Ulubeyli, A. Kazaz, and V. Arslan, "Construction and demolition waste recycling plants revisited: management issues", Proc. Eng., vol. 172, pp. 1190–1197, 2017.
[6]. P.H. Brunner and D.M. Stampfli, "Material balance of a construction waste sorting plant", Waste Manag. Res., vol. 11, pp. 27–48, 1993.
[7]. W. Zhao, R.B. Leeftink, and V.S. Rotter, "Evaluation of the economic feasibility for the recycling of construction and demolition waste in China—the case of Chongqing", Res. Cons. Rec., vol. 54, pp. 377–38 , 2010.
[8]. S.A. Kumbhar, A. Gupta, D.B. Desai, "Recycling and reuse of construction and demolition waste for sustainable development", OIDA Int. J. Sust. Dev., vol. 06, pp. 83–91, 2013.
[9]. O. Ortiz, J.C. Pasqualino, and F. Castells, "Environmental performance of construction waste: comparing three scenarios from a case study in Catalonia", Spain, Waste Manag., vol. 30, pp. 646–654, 2010.
[10]. R.A. Bohne, H. Brattebo, and H. Bergsdal, "Dynamic eco-efficiency projections for construction and demolition waste recycling strategies at the city level", J. Ind. Eco., vol. 12, pp. 52–66, 2008.
[11]. O.F. Kofoworola and S.H. Gheewala, "Estimation of construction waste generation and management in Thailand", Waste Manag., vol. 29, pp.731–738, 2009.

BIOGRAPHY

Serdar Ulubeyli is an Associate Professor in the Department of Civil Engineering at Bulent Ecevit University, Turkey. His areas of academic research interests include green buildings, green roofs, and sustainable built environment. He has published many papers in various scientific journals and proceedings.

ICENS 4TH INTERNATIONAL CONFERENCE ON ENGINEERING AND NATURAL SCIENCE
2-6 May 2018 KIEV UKRAINE

Investigation of Notch Root Strain Behaviors Under Combined Loadings

Toros Arda Aksen[1], Okan Bakbak[2],Emre Esener[3], Suphan Ercan[1], Mehmet Firat[1]

Abstract

Notches are the stress raiser regions. Along the notch section, not only the stress distrubiton becomes non-uniform, but also the stress level reaches the maximum value. These geometrical disorders can be undesirable such as casting cavity but sometimes these disorders are created deliberately for assembly process such as keyway holes or shaft steps. Because of the necessity of these notchs, This is important to understand material behavior along this region.

In this study, three different strain paths were created by the cyclic tensile and torsial loadings and strains of the notch root of a shaft which has circumferentially notch were investigated through the finite element method (FEM). MSC. Marc commercial program have been used in this study as finite element analysis software. The results have been obtained for kinematic hardening rules and compared with the experimental results obtained by Barkey. Also in this study, a subroutine file were used to calculate the Chaboche kinematic hardening parameters according to Ludwig equation.

Keywords: *Cyclic plasticity, kinematic hardening, finite element analysis, isotropic hardening*

1. INTRODUCTION

The main purpose of this study is to investigate the notch root strains for circumferentially notched bar under the combined stress situation using FEM and also examine the effect of the back stress value for kinematic hardening. MSC.Marc software were used for finite element simulations. Strain paths were created through the tensile loadings and torsial loadings together.

There is a lot of studies similar in literature. Neuber [1] examined the shear stress distribution on sharp notched material subjected to shear loading paralel to top surface. Crews Jr. [2] investigated notch root stress and strains under the cyclic loadings bu using Neuber and modified Stowell equations for different materials SAE 4130 and 2024-T3 aluminium alloy which had the same notch geometry. Barkey [3] developed a method for calculating the elasto-plastic strains at notch root under multiaxial loadings and compared the results with the finite element analysis results. Hoffman [4] realized FE analysis of a shaft which has circumferential notch under incremental axial loading, bending moments. Koettgen [5] and his co-workers used notch stress calculation method suggested by Hoffman and Seeger on a fatigue assessment of preloaded fuel injection pump and compared notch stress –strain results with elasto plastic FE analysis. Moftakhar [6] calculated notch stress – strain of filled and empty both two shafts using FE method under incremental axial loading and bending loads and he obtained better correlations. Firat [7] modeled circumferentially notched round bar and fulfilled FE analysis under combined axial and torsion loading and he compared notch root deformations with the notch root strain history. For both elastic and elastoplastic notch deformations, he obtained suitable results. In the same study Firat also examine the implementations of nonlinear kinematic hardening conservation equations on fatigue life and he obtained Al wheel rim life span using Chaboche kinematic hardening rule. He compared the results with the experimental outcomes and obtained suitable results.

[1] *Sakarya University, Department of Mechanical Engineering, 54187, Esentepe/Sakarya, Turkey.*
ardaaksen@sakarya.edu.tr, suphanercan@gmail.com, firat@sakarya.edu.tr

[2] *Yildiz Technical University, Faculty of Mechanical Engineering, 34349, Besiktas/Istanbul, Turkey.*
okanbakba81@gmail.com

[3] *Bilecik Seyh Edebali University, Department of Mechanical Engineering 11210, Gulumbe/Bilecik Turkey.*
emre.esener@bilecik.edu.tr

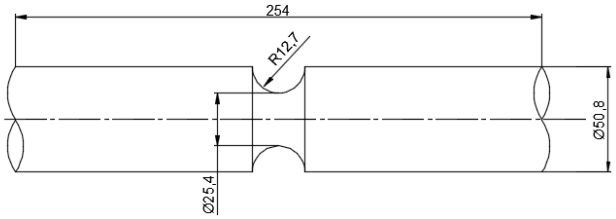

Figure 1. Circumferentially notched bar in 2D [3]

In this study, a circumferentially notched bar was modeled using Ansys and the model was transferred to Marc finite element program. The dimensions of the circumferentially notched bar can be seen in Fig 1. Materials plastic properties were calculated according to Ludwig equation and the plastic parameters of the Ludwig equation were obtained from Hollomon parameters. In order to calculate materials plastic properties, a user subroutine file was used. This subroutine file requires Ludwig parameters for isotropic hardening solutions and besides the Ludwig parameters, saturation stress and saturation strain values for kinematic hardening solutions. So as to decrease solution time, symmetric half of the model was generated. Boundary condition of the half symmetric model can be shown in Fig 2.

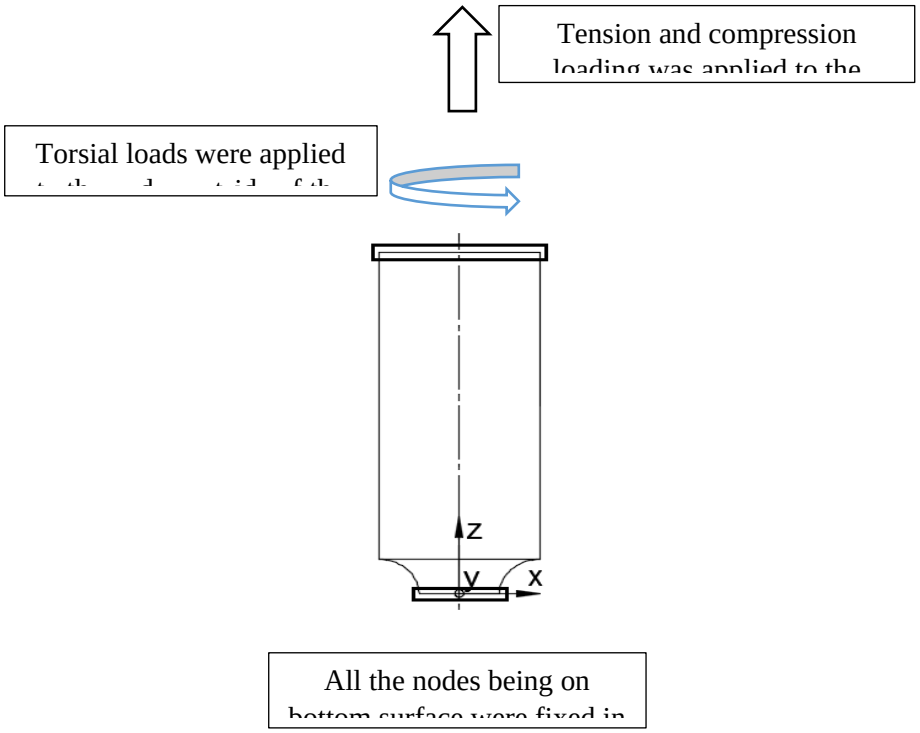

Figure 2. Boundary conditions applied on circumferentially notched bar in 2D

2. MATERIALS AND METHODS

a. Determination of Flow Curve

Material of the notched bar was determined as SAE1070 steel. The mechanical properties of SAE1070 steel were procured from the literature studies. The mechanical properties of the material are shown in Table 1.

Table 1. Mechanical properties of SAE1070 [3]

Parameter	Value
Elasticity Modulus [MPa]	210000
Poisson Ratio	0,3
Yield Stress [MPa]	250
Cyclic Strength Coefficient [MPa]	1736
Cyclic Hardening Exponent	0,199

The stress values beyond the yield stress can be calculated according to power law equation [8].

$$\sigma_{True} = K . \varepsilon_p^n \quad (1)$$

In the equation above ''K'' is the strength coefficient, ''n'' is the strain hardening exponent. Plastic strain which expressed as ''ε_p'' can be calculated by the following equation.

$$\varepsilon_p = \varepsilon_T - \frac{\sigma_{True}}{E} \quad (2)$$

In this study, materials plastic parameters were calculated according to Ludwig equation and in order to obtain Ludwigs parameters, curve fitting method was applied in Excel program. The flow curve obtained from the Hollomon power equation was matched with the Ludwig's equation. According to Ludwig's equation, true stress beyond the yield strength can be expressed by the following equation [9].

$$\sigma_{True} = C . (\varepsilon_0 + \varepsilon_p)^p \quad (3)$$

In Ludwig equation, ''C'' is the strength coefficient, ''p'' is the hardening exponent. To determine these parameters, curve fitting was applied and ''c'' parameter was obtained as 1800 MPa, ''p'' parameter was obtained as 0,215.

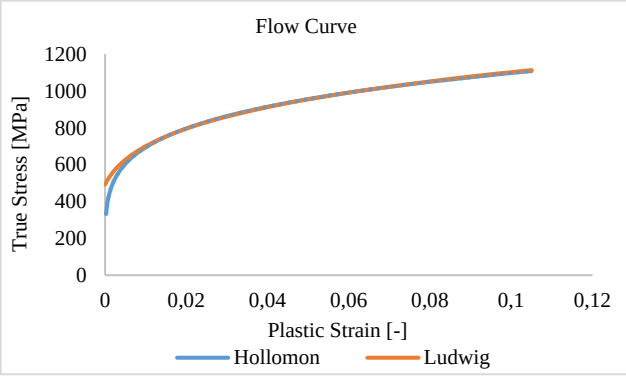

Figure 3. Curve fitting for Ludwig parameters

In order to model plastic part of the material according to kinematic hardening rule, Jiang parameters ''$c^{(i)}$'', and ''$r^{(i)}$'' should be calculated. Chaboche and Rousselier disintegrated the back stress tensor into few parts which has different hardening properties. It is assumed that 5 parts will be adequate to calculate the plastic part of the material [7], [10], [11].

$$\underline{a} = \sum_{i=1}^{n} \underline{a}^{(i)} \qquad i = 1,2,...,m \quad (4)$$

Jiang parameters can be calculated according to the following equations. [11], [12].

$$c^{(i)} = \sqrt{\frac{2}{3}} \cdot \frac{1}{\underline{\varepsilon}^{p}_{a(i)}} \qquad i = 1,2,...,m \tag{5}$$

$$r^{(i)} = \frac{2}{3} \cdot \frac{H_{(i)} - H_{(i+1)}}{c^{(i)}} \qquad i = 1,2,...,m \tag{6}$$

In the equation 6, ''H'' represents the slope between two points in sequence which belong to the stress –strain reversal curve [11]. These points have to be selected between yield stress and ultimate tensile stress. On the other hand ''i'' represents the arbitrary partition number which the back stress was divided. The back stress tensor increment can be expressed by the following equation [10].

$$d\underline{\underline{\alpha}}^{(i)} = c^{(i)} \cdot r^{(i)} \cdot [\underline{\underline{n}} - (\frac{\|\underline{\underline{\alpha}}^{(i)}\|}{r^{(i)}})^{(\chi)+1} \cdot \underline{\underline{L}}^{(i)}) \cdot dp \tag{7}$$

Here $c^{(i)}$, $r^{(i)}$ and $\chi^{(i)}$ are the scalar parameters, L, dp are the unit tensor of the back stress tensor and the equivalent plastic strain increment respectively.

b. Finite Element Method

The model was generated in Ansys software. The nodes coordinate systems were transferred from the cartesian to cylindirical coordinate system and the boundary conditions were regulated for cylindirical coordinate system in Ansys. Then the model was transferred from Ansys to Marc software. Element density at the notch root was increased toward to the specimen surface because it is assumed that the stress level will reach the maximum level on surface.

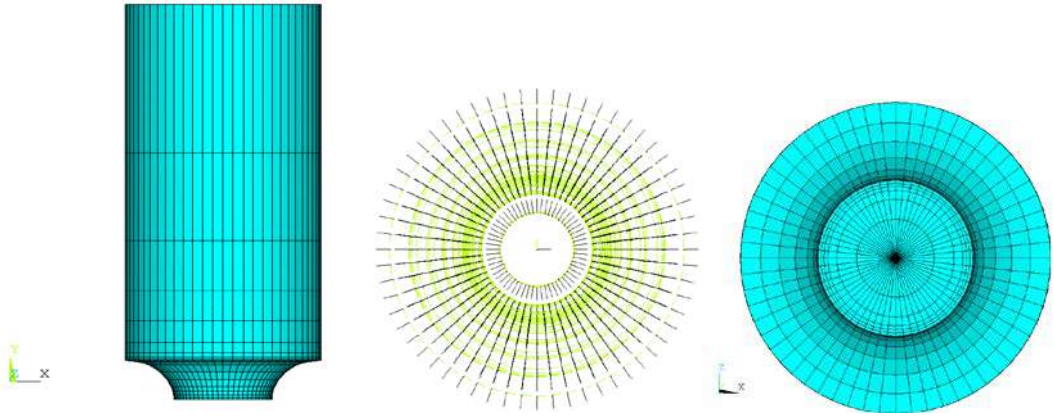

a) b) c)

Figure 4. a) Model created through Ansys software. b) Cyl. coord. sys. of the nodes. c) Bottom view of the model.

In figure 5, green line represents Θ axis which is transformed from the y axis and black line represents the r axis which is transformed from the x axis. Also there is z axis in cylindirical coordinate system which is perpendicular to the r - Θ plane. The notched bar model transferred to Marc software can be seen in Fig 5.

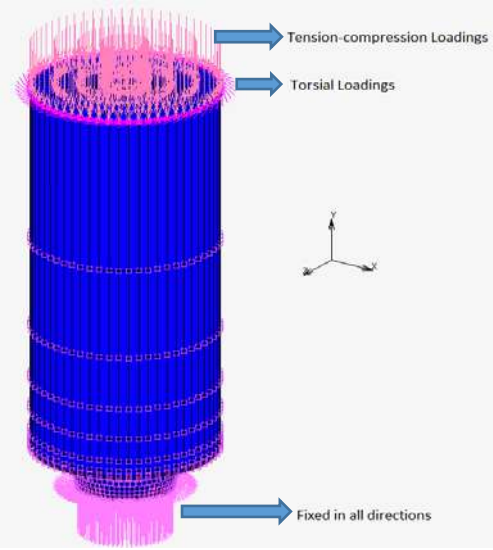

Figure 5. Model transferred to Marc software

i. Boundary Conditions

There strain paths which contain torsial and cyclic tension-compression loadings, were applied to the notched shaft. These strain paths are proportional loading, box type non-proportional loading and zig-zag type non-proportional loading, Strain paths can be shown in Fig 6.

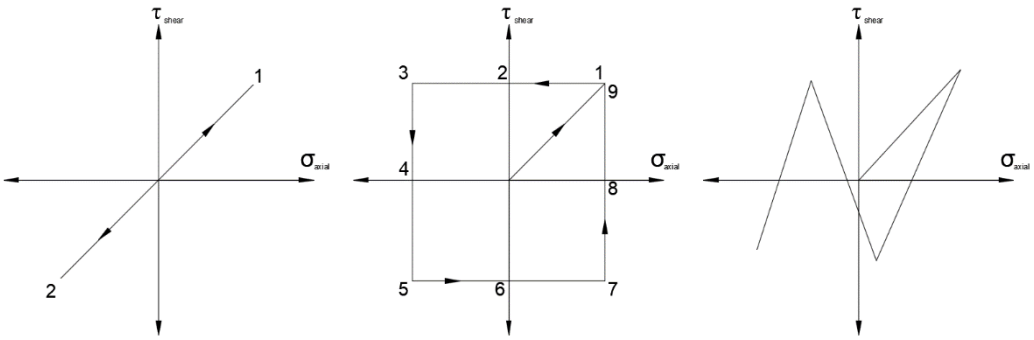

a) b) c)

Figure 6. a) Proportional loading, b) Box type non-proportional loading. c)Zig-zag type non-proportional loading [7]

The stress occurred at the notch root is determined according to the nominal stress defined by Barkey. The nominal stresses created at the notch root can be seen in following table.

Table 2. Nominal stresses created at the notch root [3]

Test Number	Nominal Axial Stress [MPa]	Nominal Shear Stress [MPa]	Loading Condition
1	296	193	Proportional Loading
2	296	193	Non-proportional Loading (Box)
3	296	193	Zig – Zag Type Loading

Because of the stress concentration at the notch root, the stress level reach the maximum level which is much more than the nominal stress. So, stress values in table 2 represent the stresses calculated at the notch root according to geometrical dimensions regardless of plastic deformation and stress concentration.

ii. Subroutine File Regulations

A subroutine file was used in this study for calculating the kinematic hardening rules parameters. In order to regulate the isotropic hardening parameters, in addition to the Young Modulus, Poisson ratio and yield stress, Ludwig parameters should be entered to the subroutine file called as Hypela2. Besides the isotropic parameters, back stress components which are saturation stress and saturation strain data were entered to this subroutine file. Analysis according to kinematic hardening rule were realized. To predict the accurate back stress parameters which are saturation stress and saturation strain, certain analysis were performed in rows. First back stress parameters are determined by offsetting the flow curve to below as yield stress and the saturation stress value determined as 855 MPa for saturation strain equal to 0,1. According to the deviations and the convergence to the experimental results, the back stress parameters were updated at every turn until the appropriate results were obtained. The first saturation stress and saturation strain values obtained from the flow curve can be shown in Fig 7.

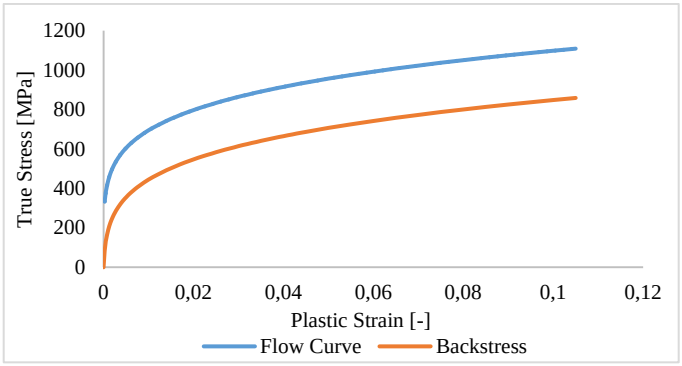

Figure 7. Saturation stress and saturation strain values obtained from the flow curve

3. RESULTS AND DISCUSSION

In order to examine strain behavior, a node which is located at the notch root, on the surface of the bar was examined. The results were compared with the experimental outcomes obtained by Barkey. The results under proportional loadings according to different saturation stresses can be shown in following Fig 8.

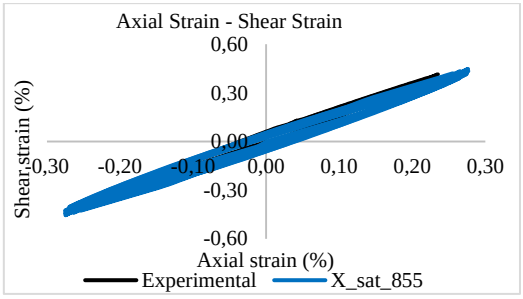

a)

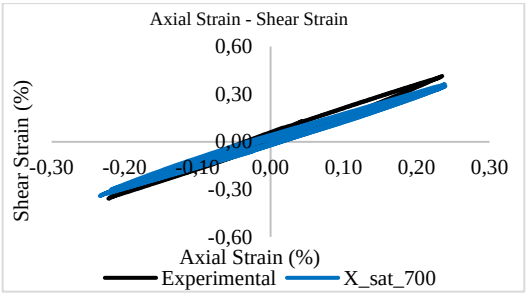

b)

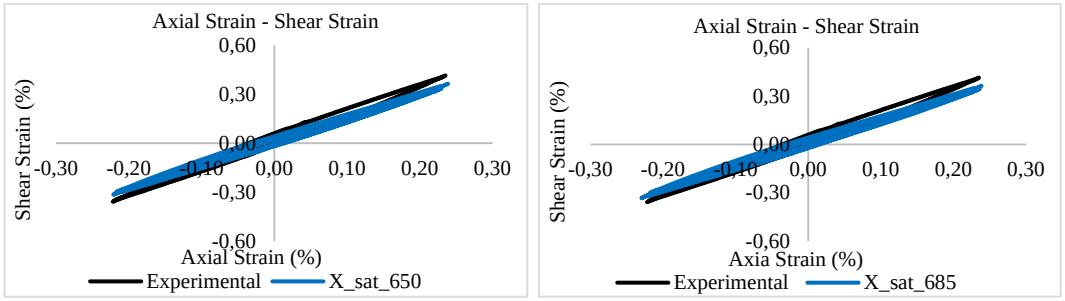

c) d)

Figure 8. Axial strain – shear strain results under proportional loadings. a) Saturation stress 855 MPa, b) Saturation stress 700 MPa, c) Saturation stress 650 MPa, d) Saturation stress 685 MPa

The results under the box type non-proportional loadings according to the different saturation stresses can be shown in Fig 9.

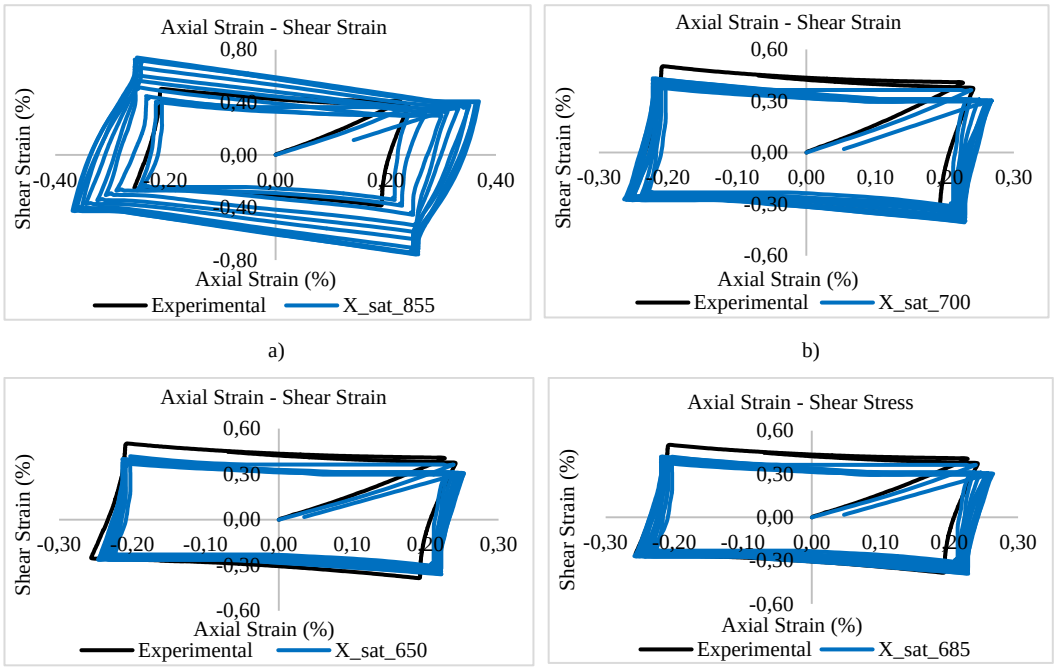

a) b)

c) d)

Figure 9. Axial strain – shear strain results under box type non-proportional loadings. a) Saturation stress 855 MPa, b) Saturation stress 700 MPa, c) Saturation stress 650 MPa, d) Saturation stress 685 MPa

The results under the zig-zag type non-proportional loadings according to the different saturation stresses can be shown in Fig 10.

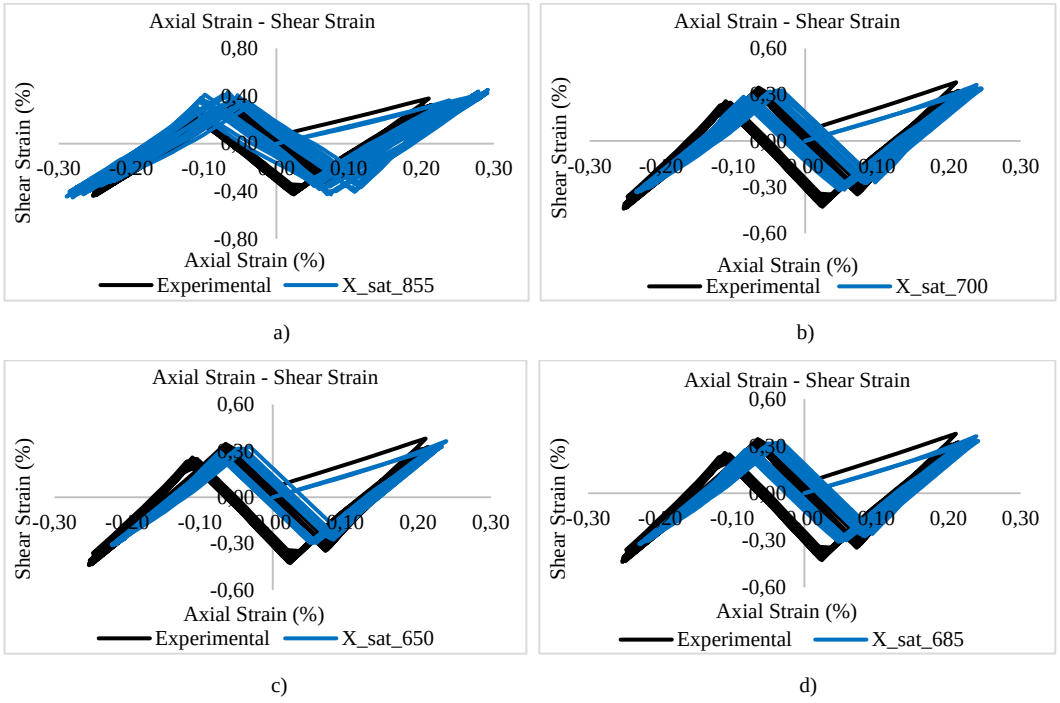

Figure 10. Axial strain – shear strain results under zig-zag type non-proportional loadings. a) Saturation stress 855 MPa, b) Saturation stress 700 MPa, c) Saturation stress 650 MPa, d) Saturation stress 685 MPa

4. CONCLUSION

In this study, under the combined loadings, notch root strain behaviors of a circumferentially notched bar were investigated. These combined loadings were proportional loading, box type non-proportional loading and zig-zag type non-proportional loading. Analysis are performed according to the kinematic hardening rule assumption. To define the kinematic hardening rule parameters, a user subroutine file was used and the plasticity calculations are realized according to Ludwig equation. Ludwig parameters were obtained from the Hollomon parameters which are procured from the literature studies. In order to calculate the back stress, saturation stress values were updated repeatedly. Then the solutions were compared with the experimental results.

It can be seen that the results were in accord with the experimental data. For all loading types this is similar that, the results obtained according to 855 MPa saturation value showed deviations in comparison with the experiments. Then the saturation stress values were updated to 700 MPa, 650 MPa and 685 MPa respectively. The results were close to each other and the deviations were fell off. For the results obtained according to the 650 MPa saturation stress, deviations were the lowest but the results diverged from the experimental results. The optimal results were obtained according to the saturation stress equal to the 685 MPa because the outcomes were in accord with the experimental results and the deviation were lower. In addition, calculating the strain behaviors at notch root according to the different back stress values is difficult and time consuming process. In this study this process accomplished readily through a user subroutine file.

REFERENCES

[1]. H. Neuber, ‘’Theory of stress concentration for shear strained prismatic bodies with arbitrary stress – strain law,’’ Journal of Applied Mechanics, vol 28, pp. 544-550, Dec. 1961.
[2]. H. J. Crews, ‘’Elastoplastic stress – strain behaviour at notch roots in sheet speciments under constant – amplitude loading,’’ Langley Research center, NASA Technical Report, D-5253, 1969.
[3]. Barkey, M., E., ‘’Calculation of notch strains under multiaxial nominal loading,’’Ph.D. thesis, University of Illinois, College of Engineering at Urbana-Champaign, Oct. 1993.

[4]. M. Hoffmann,''Ein naeherungsverfahren zur ermittlung mehrachsig elastisch-plastischer kerbbeanspruchungen'', M.Eng thesis, Darmstadt Technical University, Germany, 1985.
[5]. V.B. Koettgen, M. Schoen, and T. Seeger,''Application of multiaxial load notch strain approximitation procedure to autofrettage of pressurized components,''*American Society for Testing and Materials*, pp. 375-396, 1993.
[6]. A.A. Moftakhar,''Calculation of time – independent and time – dependent strains and stresses in notches,'' M.Eng. thesis, Univercity of Waterloo,1994.
[7]. M.Firat,''Cyclic plasticity modeling and finite element analysis of a circumferentially notched round bar under combined axial and torsion loadings'', Material and Design, vol. 34, pp 842-852, Feb. 2012.
[8]. G. E. Dieter, *Mechanical Metalurgy*, SI metric ed., United Kingdom, 1988.
[9]. Y. K. Lin, K. M. Hsu and P.K. Lee, ''The application of flow stress flow stress model to sheet metal forming simulation,'' Iron & Steel Research & Development Department, China Steel Technical Report, No 23, pp.31-35, 2010.
[10]. Y. Jiang, H. Sehitoglu,'' Modeling of cyclic ratchetting plasticity, part I: development of constitutive relations,'' Journal of Applied Mechanics, vol. 63, pp. 720-725, Sept 1996.
[11]. Y. Jiang, H. Sehitoglu,'' Modeling of cyclic ratchetting plasticity, part II: comparison of model simulations with experiments,'' Journal of Applied Mechanics, vol. 63, pp. 726-733, Sept 1996.
[12]. M. Firat, "Lineer olmayan kinematik peklesme bunye denklemlerinin yorulma omur tahmininde uygulanmasi," *M.Eng.* Thesis, Department of Mech.Engineering, Sakarya, Turkey, Mar. 2003.

ICENS 4TH INTERNATIONAL CONFERENCE ON ENGINEERING AND NATURAL SCIENCE
2-6 May 2018 KIEV UKRAINE

Numerical Simulation of Heat Exchanger for Jatropha Oil Biodiesel Fuel Preheating

Fatih Aktas[1], Salih Karaaslan[2], Nuri Yucel[3]

Abstract

Along with the increase in the number of vehicles in the world, the fuel requirement has also increased. Increasing demand for fossil-based fuels has begun to reduce fuel reserves. For this reason, the search for alternative fuels has accelerated. The most commonly used alternative fuels are biodiesel fuels because they are both less costly and less harmful to the environment than fossil fuels. In addition to the positive effects of biodiesel, it also has disadvantages such as having high viscosity and causing blockages in fuel filters.

In the work done, it is aimed to reduce the viscosity of Jatropha oil by applying preheating with the energy of exhaust gases using heat exchanger. Heat exchanger was analyzed numerically by using commercial computational fluid dynamics(CFD) code. The exit temperatures of Jatropha oil biodiesel are calculated for four different exhaust gas inlet temperatures. Flow was considered to be turbulent since the Reynolds number was greater than 2300. Realizable k-ε turbulence model and SIMPLE algorithm were used for simulations. The effects of inlet temperature of exhaust gases on the outlet temperature of the biodiesel were investigated. As a result, it has been observed that the exhaust gas entering the heat exchanger at 375 ° C heats the Jatropha oil biodiesel to approximately 140 ° C. This temperature ensures that the viscosity of Jatropha oil biodiesel decreases from 37 cSt to 2.57 cSt which is the same order of diesel fuel. The results are presented in terms of contours of temperature.

Keywords: CFD, heat exchanger, Jatropha oil biodiesel, preheating.

1. INTRODUCTION

The increase in the number of vehicles in the world has rapidly increased fuel consumption and dependence on petroleum-based fuels. This increase in petroleum-based fuel demand has accelerated the search for alternative fuels. At the top of these alternative sources of fuel are biofuels. These biofuels may be different waste oils or they may be in the form of oils obtained directly from plants.

Biofuels have many positive features such as being able to be used without being exposed to different processes, to be mixed in different ratios to fuels, low cost, low environmental damage, high flash points, and lubricating properties. However, it has disadvantages such as having high viscosity, causing blockage in the fuel filter, causing problems in cold working conditions.

There are two basic strategies to solve the problem of high viscosity; Fuel adaptation of the engine or adaptation of the fuel to the engine. Generally, the preferred method is to adapt the fuel to the engine. Biofuels have many disadvantages due to their high viscosity. These disadvantages can be eliminated by applying preheating to the biofuel by utilizing the waste heat of the exhaust gas. With increasing biofuels temperature, viscosity decreases and atomization becomes easier. Better atomization results in a better combustion, which results in both a reduction in the amount of emissions as well as a loss of power at a minimum [1]-[3].

Chauhan et al. (2010) examined the effects of the Jatropha oil additive on diesel engine emissions and performance in the medium capacity diesel engine. The Jatropha oil was pre-heated with waste heat from the exhaust gas to reduce its viscosity and improve combustion characteristics. As a result, fuel consumption decreased while brake thermal power increased with increasing Jatropha oil intake temperature. It has also been

[1] *Corresponding author: Gazi University, Department of Mechanical Engineering, 06570, Maltepe/Ankara, Turkey.* fatihaktas@gazi.edu.tr

[2] *Gazi University, Department of Mechanical Engineering, 06570, Maltepe/Ankara, Turkey.* karaaslansalih@gazi.edu.tr

[3] *Gazi University, Department of Mechanical Engineering, 06570, Maltepe/Ankara, Turkey.* nuyucel@gazi.edu.tr

observed that the amount of NO_x increases with the increase of Jatropha oil intake temperature [4].

Basinger et al. (2010) have made preheating of plant oils with the structural changes they make in a diesel engine in their work. They also demonstrated that plant oils can be used instead of diesel fuel at lower cost by performing parametric studies with the injector and valve timing. Optimization studies have been carried out to improve the emission values without affecting engine performance with the use of vegetable oils [5].

The purpose of this study is to examine the effect of exhaust gas temperature on the Jatropha oil viscosity with the use of heat exchanger under different loads. Along with the numerical study, viscosity values of Jatropha oil obtained for different exhaust gas inlet temperatures were calculated.

2. PROBLEM DEFINITION

As can be understood from the literature review, vegetable oil can be used in pure form or mixed with diesel fuels at certain ratios. However, many researchers have observed that the use of pure vegetable oil fuel brings with a lot of difficulties. These difficulties are generally related with the high viscosity of vegetable oils. Figure 1 shows the difference between the kinematic viscosities of Jatropha Oil and diesel fuel for different temperatures. As can be seen from Figure 1, there is a considerable difference between Jatropha Oil and diesel fuel viscosities. It is aimed to reduce the viscosity of pure Jatropha Oil to use with diesel fuel by preheating process.

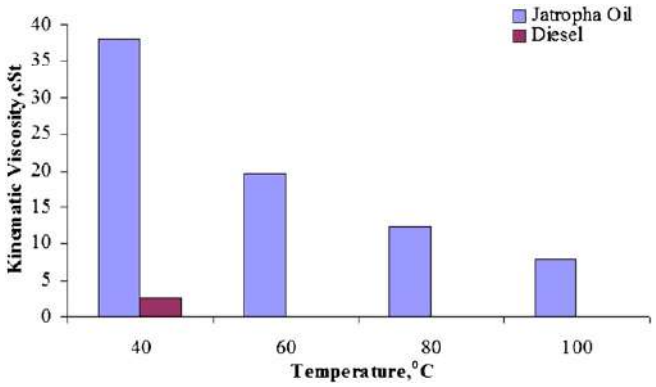

Figure 1. Kinematic viscosity of Jatropha oil at different temperatures [4]

The basic shell and tube heat exchanger model design and dimensions used in this study are given in Figure 2. The effects of the inlet temperature of the exhaust gases on the outlet temperature of the Jatropha Oil were investigated for the inlet temperatures of the different exhaust gases. 140, 220, 300 and 375℃ were used for exhaust gases inlet temperatures.

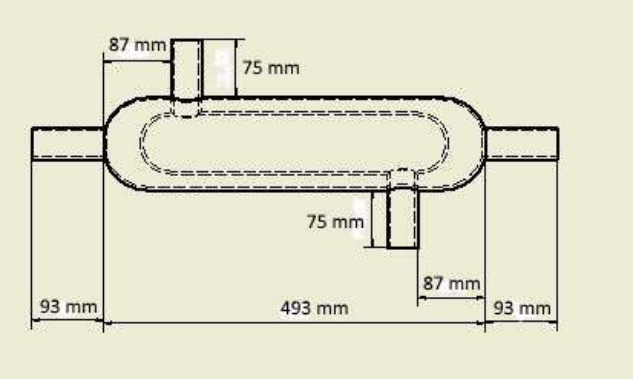

Figure 2. Heat exchanger schematic view and dimensions

3. NUMERICAL STUDY

Experimental studies can be limited by time, money, labor etc. However, from these sources savings can be achieved by using the Computational Fluid Dynamics (CFD) method. ANSYS Fluent, general purpose CFD software, was used in the study. Various algorithm and methods are used in modeling. For this study, three-dimensional continuity, momentum and energy equations were solved with steady and transient conditions.

Continuity equations;

$$\frac{\partial \rho}{\partial t}+\frac{\partial(\rho u)}{\partial x}+\frac{\partial(\rho v)}{\partial y}+\frac{\partial(\rho w)}{\partial z}=0 \quad (1)$$

Momentum equations;

X-momentum:

$$\frac{\partial(\rho u)}{\partial t}+\frac{\partial(\rho uu)}{\partial x}+\frac{\partial(\rho uv)}{\partial y}+\frac{\partial(\rho uw)}{\partial z}=-\frac{\partial p}{\partial x}+\frac{1}{Re}\left[\frac{\partial \tau_{xx}}{\partial x}+\frac{\partial \tau_{xy}}{\partial y}+\frac{\partial \tau_{xz}}{\partial z}\right] \quad (2)$$

Y-momentum:

$$\frac{\partial(\rho v)}{\partial t}+\frac{\partial(\rho vu)}{\partial x}+\frac{\partial(\rho vv)}{\partial y}+\frac{\partial(\rho vw)}{\partial z}=-\frac{\partial p}{\partial y}+\frac{1}{Re}\left[\frac{\partial \tau_{xy}}{\partial x}+\frac{\partial \tau_{yy}}{\partial y}+\frac{\partial \tau_{yz}}{\partial z}\right] \quad (3)$$

Z-momentum:

$$\frac{\partial(\rho v)}{\partial t}+\frac{\partial(\rho vu)}{\partial x}+\frac{\partial(\rho vv)}{\partial y}+\frac{\partial(\rho vw)}{\partial z}=-\frac{\partial p}{\partial y}+\frac{1}{Re}\left[\frac{\partial \tau_{xy}}{\partial x}+\frac{\partial \tau_{yy}}{\partial y}+\frac{\partial \tau_{yz}}{\partial z}\right] \quad (4)$$

To find the temperature distribution, the energy equation needs to be solved. The energy equation is as follows:

$$\frac{\partial(E_t)}{\partial t}+\frac{\partial(uE_t)}{\partial x}+\frac{\partial(vE_t)}{\partial y}+\frac{\partial(wE_t)}{\partial z}=-\frac{\partial(up)}{\partial x}-\frac{\partial(vp)}{\partial y}-\frac{\partial(wp)}{\partial z}+\frac{\partial(wE_t)}{\partial z}-\frac{1}{RePr}\left[\frac{\partial q_x}{\partial x}+\frac{\partial q_y}{\partial y}+\frac{\partial q_z}{\partial z}\right]$$
$$+\frac{1}{Re}\left[\frac{\partial}{\partial x}\left(u\tau_{xx}+v\tau_{xy}+w\tau_{xz}\right)+\frac{\partial}{\partial y}\left(u\tau_{xy}+v\tau_{yy}+w\tau_{yz}\right)+\frac{\partial}{\partial x}\left(u\tau_{xz}+v\tau_{yz}+w\tau_{zz}\right)\right] \quad (5)$$

where; x, y, z: coordinates, u, v, w : velocity components, t : time, ρ : density, p : pressure, τ : stress, Et : total energy, q : heat flux, Re : Reynolds number, Pr : Prandtl number

Independence studies were performed on the number of mesh and number of iterations in analyzes. Mesh structure and quality are shown in Figures 3 and 4, respectively. For this study, the number of the total mesh is nearly 600 000. Orthogonality and skewness values have been checked for sensitive numerical solutions.

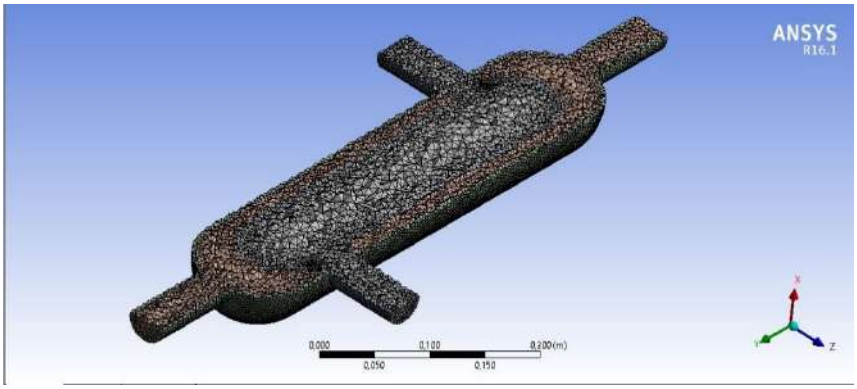

Figure 3. Mesh view

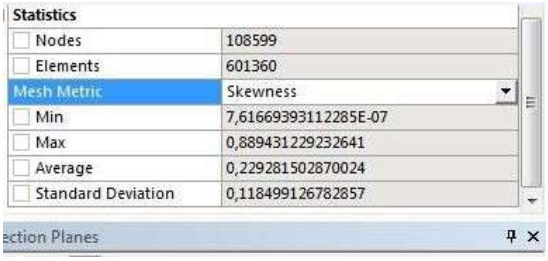

Figure 4. Mesh skewness statistics

The boundary conditions used in this study are given in Table 1. Jatropha Oil's chemical specifications are defined by user-defined functions on the Fluent with using Table 2. In this study, realizable k-ε turbulence model and second order upwind schema was used. While all calculations were solved for steady-state conditions, some calculations were solved with transient conditions. For solutions convergence all variables must show a constant decline. The solutions are requested to continue until the desired sensitivity. In this study, it is concluded that 10^{-4} residual values are obtained for continuity.

Table 1. Boundary Conditions

Flow characteristic	Turbulent
Exhaust gases inlet temperatures	140, 220, 300 and 375°C
Biodiesel inlet temperature	25°C
Mass flow rate of exhaust gases	7.35 (g/s)
Mass flow rate of biodiesel	0.35 (g/s)
Exhaust gases compositions	%2.46 CO, %8.1 CO_2, %0.293 C_3H_8, N_2 balanced.

Table 2. Physico-chemical properties of diesel and Jatropha oil[4]

Property	Diesel oil	Jatropha oil
Density (kg/m^3)	830	918
API gravity	37.15	22.81
Kinematic viscosity at 40 °C (cSt)	2.5	37
Cloud point (°C)	−12	9
Pour point (°C)	−17	4
Flash point (°C)	70	238
Calorific value (kJ/kg)	42,200	37,500
Carbon residue (%, w/w)	0.05	0.8
Ash content (%, w/w)	0.01	0.04
Carbon (%, w/w)	86.71	77.21
Hydrogen (%, w/w)	12.98	10.25
Nitrogen (ppm)	5	3
Oxygen (%, w/w)	0.31	12.52
Sulfur (ppm)	340	8

4. RESULTS AND DISCUSSION

In this study, the effects of different exhaust gas inlet temperatures on the Jatropha Oil temperature and viscosity were investigated by using a heat exchanger. The inlet and outlet positions of the exhaust gas and Jatropha Oil on the heat exchanger are shown in Figure 5. All the contours are taken from the middle point along the yz axis.

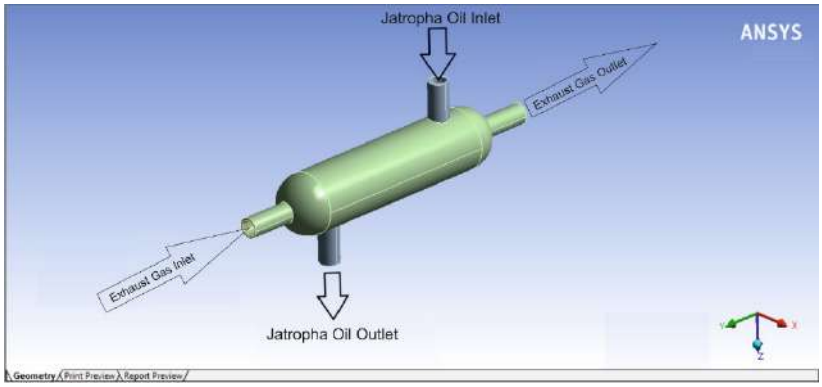

Figure 5. Heat exchanger model view on Ansys workbench with flow directions

If the exhaust gas inlet temperature is 140 °C, the output temperature from the heat exchanger of Jatropha Oil appears to be approximately 60 °C (Figure 6). For 220, 300 and 375 ° C exhaust gas inlet temperatures, the Jatropha oil outlet temperatures are 80, 100 and 140 ° C, respectively (Figure 7, 8 and 9). Figure 7, 8 and 9 are taken for steady-state conditions. For increased exhaust gas inlet temperatures, the Jatropha Oil outlet temperatures appear to increase almost linearly.

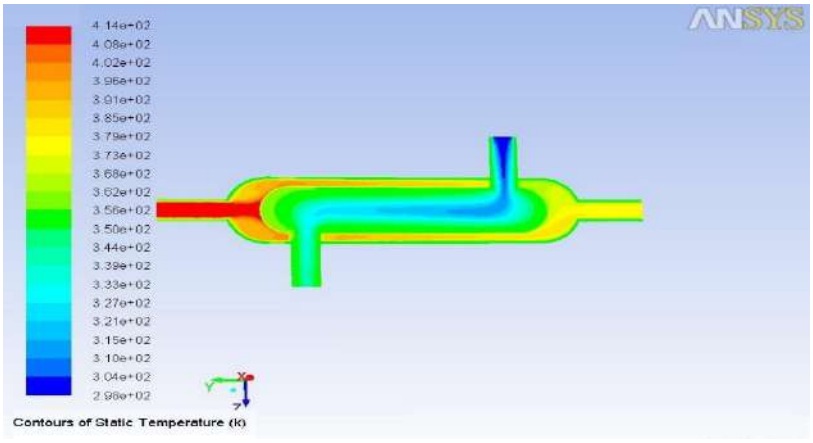

Figure 6. The temperature contours for 140℃ exhaust gases inlet (about 60℃ jatropha oil exit temperature)

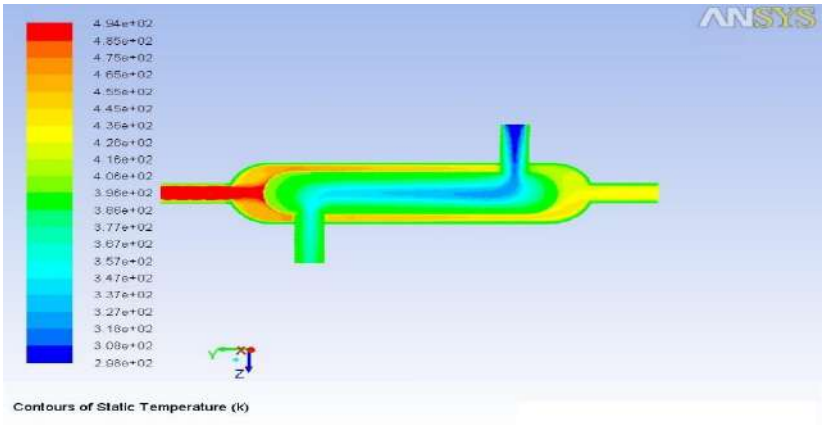

Figure 7. The temperature contours for 220℃ exhaust gases inlet (about 80℃ jatropha oil exit temperature)

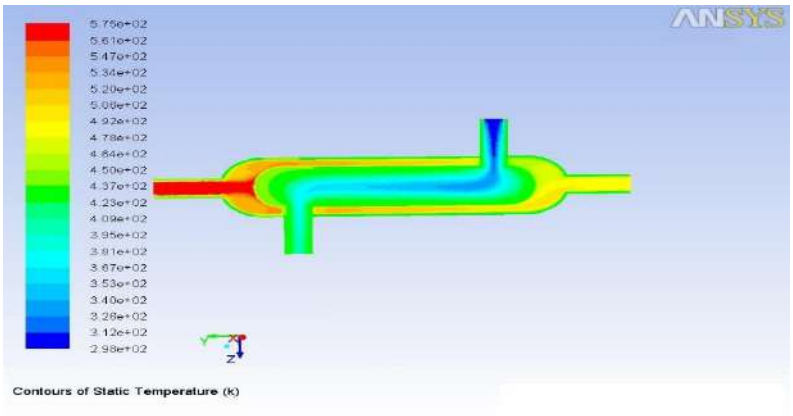

Figure 8. The temperature contours for 300℃ exhaust gases inlet (about 100℃ jatropha oil exit temperature)

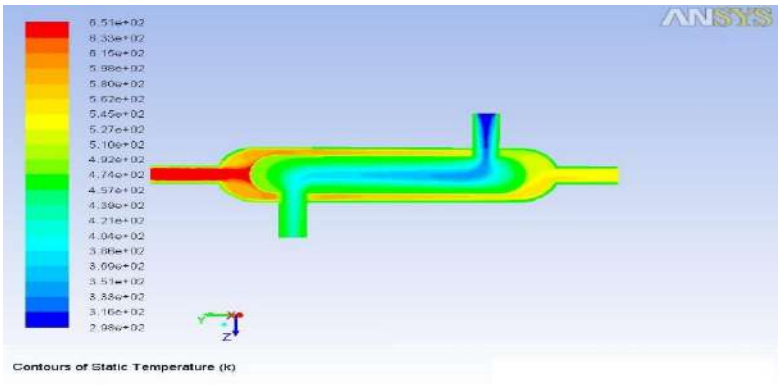

Figure 9. The temperature contours for 375℃ exhaust gases inlet (about 140℃ jatropha oil exit temperature)

When the time dependent solution is done, it is seen that the system becomes stable after 3.6 seconds. Figure 10 shows the temperature contour of the transient solution for 3.6 seconds of the preheating application. The distribution of Jatropha oil after hit the heat exchanger inner tube and the effects of exhaust gas temperature can be seen more clearly. The residual graph for transient solution is shown in Figure 11. When the residue graph is examined it is seen that there are fluctuations due to time dependent solution. However, it seems that the residuals of the solution declined first and then stabilized.

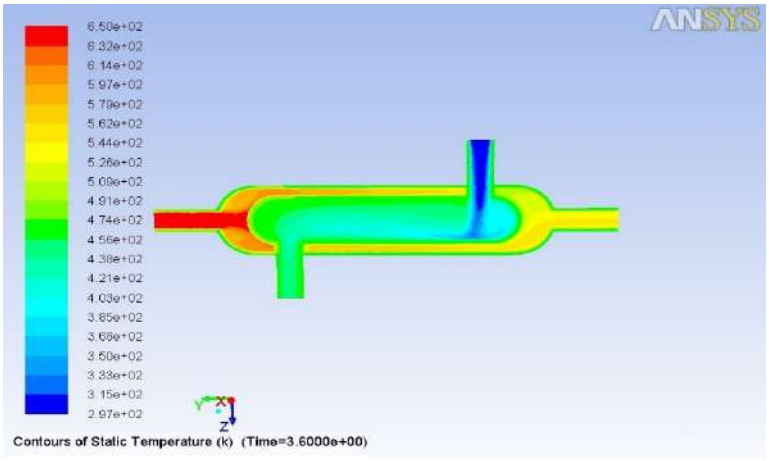

Figure 10. The temperature contours for 375 ℃ exhaust gases inlet (transient solution)

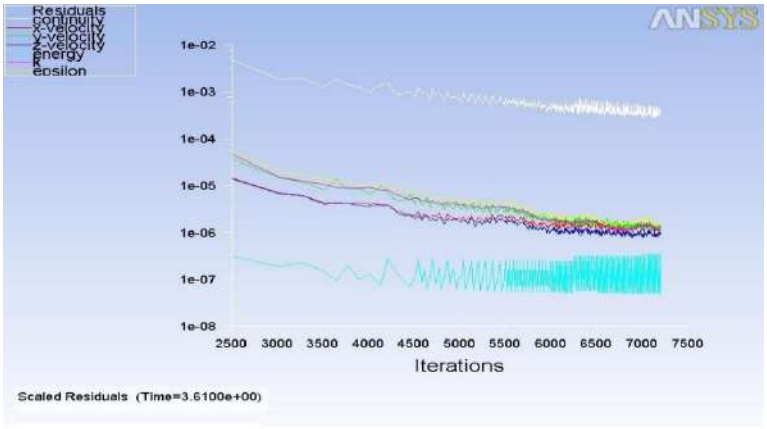

Figure 11. Residuals graph for 375°C exhaust gas inlet (transient Solution)

As a result of the obtained data, a graph of exhaust gas inlet temperature – Jatropha oil temperature output values is given below (Figure 12).

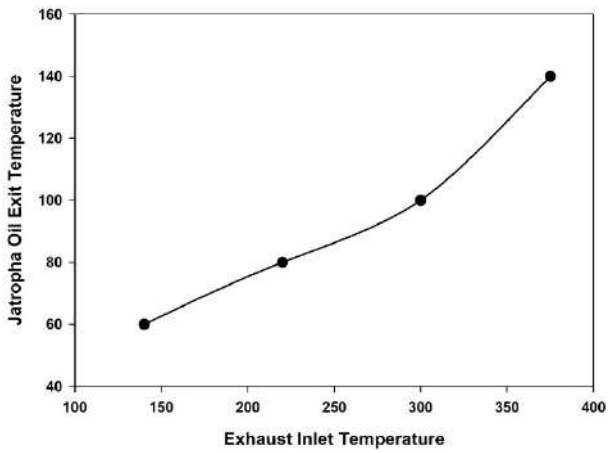

Figure 12. Exhaust gas inlet temperature – jatropha oil change

For the Jatropha oil exit temperatures obtained, the viscosity values depending on the temperature are calculated using the following equation together with the coefficients in Table 3. The viscosity values obtained are given in Figure 13 depending on the temperature.

$$\mu = A + Be^{cT}$$

Table 3: Coefficient values and temperature ranges for jatropha oil [6]

	A	B	C	Correlation coefficient	Temperature range (°C)
Soybean	1.110	109.6	−0.036	0.999	25–160
Rapeseed	5.590	141.9	−0.038	0.998	25–200
Peanut	5.768	165.9	−0.041	0.998	25–200
Palm	3.265	327.2	−0.055	0.993	25–145
Jatropha	1.607	134.1	−0.037	0.999	25–145
Soy shortening	−3.638	89.30	−0.022	0.996	50–145
Pre-WVO	1.040	146.7	−0.039	0.998	25–145
WVO	3.486	171.1	−0.040	0.997	25–160
Diesel	1.015	5.058	−0.019	0.996	25–125

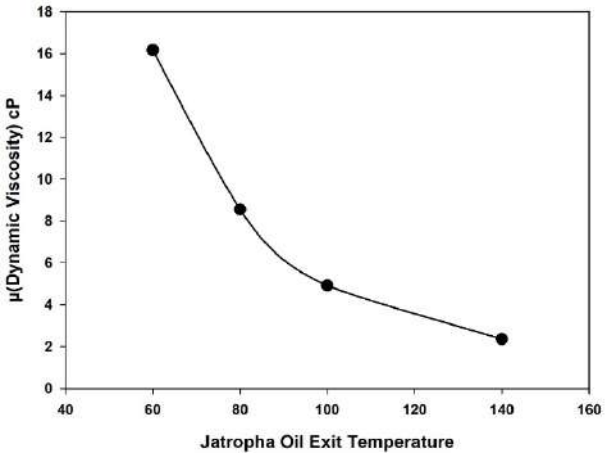

Figure 13. Jatropha oil exit temperature – viscosity change

When the exhaust gas inlet temperature is 375°C, the Jatropha oil is heated to approximately 140°C. This temperature ensures that the viscosity of Jatropha oil biodiesel decreases from 37 cSt to 2.57 cSt (2.36 cP) which is the same order of diesel fuel.

5. CONCLUSION

With the heat exchanger used in the study, different Jatropha oil exit temperatures and different viscosity values were obtained at different exhaust gas inlet temperatures. When evaluated with the obtained values, it is expected that the exhaust gas inlet temperature will be 375 ° C and the Jatropha oil temperature will be 140 ° C so that Jatropha oil can work in harmony with diesel fuel. Also, as a result of the transient resolutions, it has been seen that the system must pass about 3.6 seconds to become steady-state. When the obtained data is evaluated, it is suggested to work with diesel fuel only until the engine is warmed up and then apply the preheating by activating the heat exchanger after the necessary energy is supplied.

REFERENCES

[1]. M. Karabektas, G. Ergen, M. Hosoz, The effects of preheated cottonseed oil methyl ester on the performance and exhaust emissions of a diesel engine, Appl. Therm. Eng. 28 (2008) 2136–2143. doi:10.1016/j.applthermaleng.2007.12.016.

[2]. H. Hazar, H. Aydin, Performance and emission evaluation of a CI engine fueled with preheated raw rapeseed oil (RRO)-diesel blends, Appl. Energy. 87 (2010) 786–790. doi:10.1016/j.apenergy.2009.05.021.

[3]. S. Senthur Prabu, M.A. Asokan, S. Prathiba, S. Ahmed, G. Puthean, Effect of additives on performance, combustion and emission behavior of preheated palm oil/diesel blends in DI diesel engine, Renew. Energy. 122 (2018) 196–205. doi:10.1016/j.renene.2018.01.068.

[4]. B.S. Chauhan, N. Kumar, Y. Du Jun, K.B. Lee, Performance and emission study of preheated Jatropha oil on medium capacity diesel engine, Energy. 35 (2010) 2484–2492. doi:10.1016/j.energy.2010.02.043.

[5]. M. Basinger, T. Reding, C. Williams, K.S. Lackner, V. Modi, Compression ignition engine modifications for straight plant oil fueling in remote contexts: Modification design and short-run testing, Fuel. 89 (2010) 2925–2938. doi:10.1016/j.fuel.2010.04.028.

[6]. Compression ignition engine modifications for straight plant oil fueling in remote contexts: Modification design and short-run testing M. Basinger, T. Reding, C. Williams, K.S. Lackner, V. Modi.

ICENS 4TH INTERNATIONAL CONFERENCE ON ENGINEERING AND NATURAL SCIENCE
2-6 May 2018 KIEV UKRAINE

Analysis Of The Positioning Performance Of Beidou

Salih Alcay[1], Sermet Ogutcu[2], Yuksel Erkavas[3],

Abstract

Beidou Navigation Satellite System (BDS) is planned to provide global navigation service in 2020. Currently, as of 01.02.2018, a total of 15 BeiDou-2 satellites are operational, including 6 Geostationary Orbit (GEO, PRN: C01-C05, C17), 6 Inclined Geosynchronous Orbit (IGSO, PRN: C06-C10, C13) and 3 Medium Earth Orbit (MEO, PRN: C11, C12, C14). By the help of Beidou-3 satellites which are not operational yet, BDS can provide global coverage in the near future. In this study, positioning performance of BDS was examined using medium (~892 km) and long (~2173 km) baselines. For doing this, 10 daily datasets (10.05.2017-19.05.2017) were processed using GAMIT GLOBK scientific software and derived coordinate results were compared with the results of Global Positioning System (GPS). The results show that coordinate differences between Beidou and GPS are generally better than 1 cm for the medium baseline in both horizontal and vertical directions. However they reach larger level for the long baseline (from 2 cm to 10 cm) in all components

Keywords: Beidou, GPS, GEO, IGSO, MEO, Positioning

1. INTRODUCTION

Besides Global Positioning System (GPS) and Global Navigation Satellite System (GLONASS), which provide positioning service with full constellation status, some other countries made progress on the development of their own Navigation Satellite System including the European Global Navigation Satellite System (Galileo), the Japanese Quasi-Zenith Satellite System (QZSS), the Indian Regional Regional Navigation Satellite System (IRNSS) and Chinese Beidou Navigation Satellite System (BDS). Among them, QZSS and IRNSS provide regional navigational service [1]. In addition, although the BDS currently provides regional coverage, it is expected to provide global navigation service for worldwide users by 2020 [2]. Numerous studies have been conducted concerning the performance of Beidou satellite system [1]-[7]. Currently BDS can be used for both relative [4, 5] and Precise Point Positioning (PPP) [6, 7] methods. Besides BDS-only positioning, BDS can be used in multi constellation based positioning.

In this study, positioning performance of BDS was investigated using two baselines of different length (medium (~892 km) and long (~2173 km)). 10 daily observations were used and derived coordinate results were compared with the results of GPS.

2. BEIDOU SYSTEM OVERVIEW

BDS includes BDS-1, BDS-2 and BDS-3 modernization stages [3]. BDS-1 started operation in 2000 with GEO satellites [3]. Following BDS-1, BDS-2 started with MEO in 2007 [3]. By the help of BDS-2, this system reached regional operational status for the Asian-Pacific region. Currently BDS-2 is used (Table 1).

Table 29. Beidou constellation status (30.12.17)[8]

[1] *Corresponding author: Necmettin Erbakan University, Department of Geomatics Engineering, 42090, Meram/Konya, Turkey. salcay@konya.edu.tr*

[2] *Necmettin Erbakan University, Department of Geomatics Engineering, 42090, Meram/Konya, Turkey. sermetogutcu@konya.edu.tr*

[3] *Necmettin Erbakan University, Department of Geomatics Engineering, 42090, Meram/Konya, Turkey. yuksel.erkavas@gmail.com*

Satellite Number	No.	NORAD	Satellite Name	Type of sistem	Launch date	Outage date	Life-time (days)	Notes
---	002	34779	BDS-G2	Beidou-2	15.04.2009		---	Not in operational orbital constellation
C01	003	36287	BDS-G1	Beidou-2	16.01.2010		2902	In operation
C02	016	38953	BDS-G6	Beidou-2	25.10.2012		1892	In operation
C03	004	36590	BDS-G3	Beidou-2	02.06.2010		2768	In operation
C04	006	37210	BDS-G4	Beidou-2	31.10.2010		2616	In operation
C05	011	38091	BDS-G5	Beidou-2	24.02.2012		2135	In operation
C06	005	36828	BDS-IGSO1	Beidou-2	31.07.2010		2708	In operation
C07	007	37256	BDS-IGSO2	Beidou-2	17.12.2010		2569	In operation
C08	008	37384	BDS-IGSO3	Beidou-2	09.04.2011		2456	In operation
C09	009	37763	BDS-IGSO4	Beidou-2	26.07.2011		2348	In operation
C10	010	37948	BDS-IGSO5	Beidou-2	01.12.2011		2220	In operation
C11	012	38250	BDS-M3	Beidou-2	29.04.2012		2070	In operation
C12	013	38251	BDS-M4	Beidou-2	29.04.2012		2070	In operation
C13	014	38774	BDS-M5	Beidou-2	18.09.2012	21.10.2014	---	Not in operational orbital constellation
C13	017	41434	BDS-IGSO6	Beidou-2	29.03.2016		640	In operation
C14	015	38775	BDS-M6	Beidou-2	18.09.2012		1928	In operation
C17	018	41586	BDS-G7	Beidou-2	12.06.2016		566	In operation
C19	201	43001	BDS-3-M1	Beidou-3	05.11.2017		---	Not in operational orbital constellation
C20	202	43002	BDS-3-M2	Beidou-3	05.11.2017		---	Not in operational orbital constellation
C27	203	43107	BDS-3-M7	Beidou-3	11.01.2018		---	Not in operational orbital constellation
C28	204	43108	BDS-3-M8	Beidou-3	11.01.2018		---	Not in operational orbital constellation
C30	001	31115	BDS-M1	Beidou-2	13.04.2007		---	Not in operational orbital constellation
C31	101	40549	BDS-I1-S	Beidou-3	30.03.2015		---	Not in operational orbital constellation
C32	104	40938	BDS-I2-S	Beidou-3	29.09.2015		---	Not in operational orbital constellation
C33	102	40748	BDS-M1-S	Beidou-3	25.07.2015		---	Not in operational orbital constellation
C34	103	40749	BDS-M2-S	Beidou-3	25.07.2015		---	Not in operational orbital constellation
C35	105	41315	BDS-M3-S	Beidou-3	01.02.2016		---	Not in operational orbital constellation

Each of the BDS-2 satellites transmit navigation signals in quadrature phase-shift keying (QPSK) modulation on B1, B2 and B3 frequency bands [2].

Although the new generation Beidou-3 satellites started to launch in 2015, they are not operational yet (Table 1). BDS-3 is expected to provide global positioning service by 2020. Full constellation is aimed with a total of 35 satellites, including 5 GEO, 27 MEO and 3 IGSO satellites. For the details of the BDS-2 and BDS-3, authors refer to [2] and [3] respectively.

3. DATA COLLECTION AND RESULTS

In order to carry out assessment of BDS to get reliable results for positioning, two baselines (medium and long) were considered. For this purpose 4 IGS stations, which have capability to track Beidou satellites were used (Figure 1). Three of them (LHAZ, JFNG and HKWS) are located in China and one of them (JNAV) is located

in Vietnam. The details of the used stations including geographical locations, antenna and receiver information, are given in Table 2.

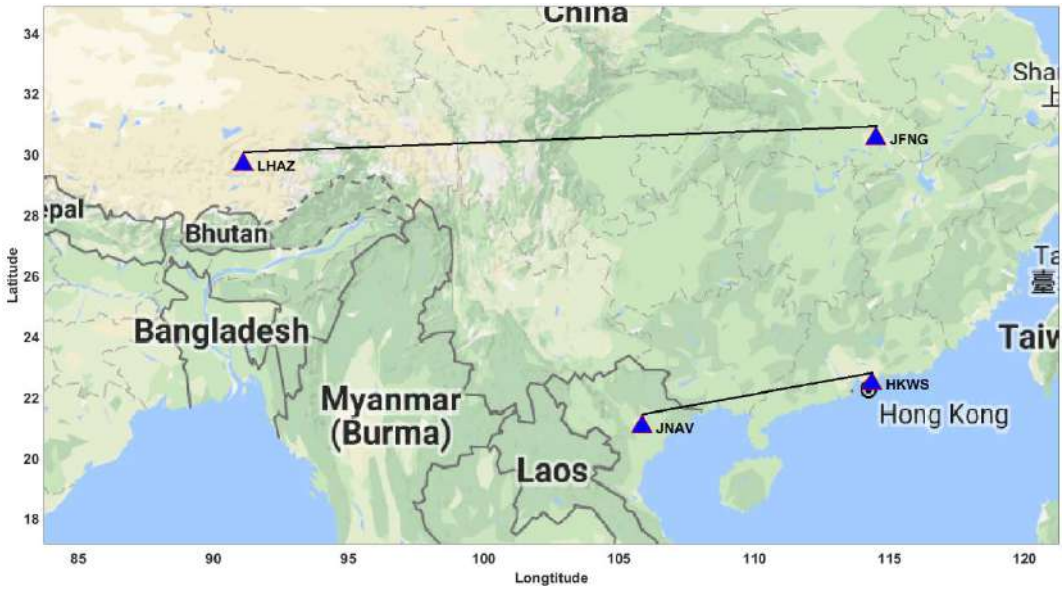

Figure 26. Locations of the used stations

Table 2. Details of used stations [9]

Site	Network(s)	City	Country	Lat	Long	Height (m)
LHAZ	IGS	Lhasa	China	29.7	91.1	3622.0
JFNG	IGS	Jiufeng	China	30.5	114.5	71.3
JNAV	IGS	Hanoi	Vietnam	21.0	105.8	34.9
HKWS	IGS	Wong Shek	China	22.4	114.3	63.8

Site	Receiver	Antenna	Radome	Satellite System
LHAZ	LEICA GR25	LEIAR25.R4	LEIT	GPS+GLO+GAL+BDS
JFNG	TRIMBLE NETR9	TRM59800.00	NONE	GPS+GLO+GAL+BDS+QZSS+SBAS
JNAV	TRIMBLE NETR9	JAVRINGANT_DM	SCIS	GPS+GLO+GAL+BDS+QZSS
HKWS	LEICA GR50	LEIAR25.R4	LEIT	GPS+GLO+GAL+BDS+QZSS+SBAS

10 daily (24 h) datasets from 10.05.2017 to 19.05.2017 were processed using GAMIT GLOBK scientific software [10]. While measurement epoch coordinates of JFNG were used as a reference and coordinates of LHAZ were estimated for the long baseline, coordinates of the JNAV were estimated based on measurement epoch coordinates of HKWS station for the medium baseline.

In order to test the reliability of the estimated BDS coordinates, same processing strategy was applied and coordinates of the stations were derived using only GPS data. Then, to observe the amount of the differences in horizontal and vertical directions, topocentric coordinates of the BDS were obtained based on GPS-only solutions for each day. Hence, the obtained “n”, “e” and “u” coordinate values illustrate the differences between Beidou only and GPS only results (Table 3).

Table 3. Coordinate values corresponding to differences between Beidou and GPS (mm)

Date	LHAZ			JNAV		
	n	**e**	**u**	n	e	u
10.05.2017	-28.9	32.3	14.0	-8.5	4.3	15.4
11.05.2017	-73.5	38.2	41.4	-9.0	6.4	15.5
12.05.2017	-32.8	27.6	17.4	3.0	5.6	2.2
13.05.2017	15.0	12.9	-12.1	-0.7	6.0	4.4
14.05.2017	-97.0	36.9	58.0	7.8	-0.6	9.2
15.05.2017	-78.4	34.1	45.0	0.0	12.2	7.4
16.05.2017	-35.6	48.7	14.8	-4.0	5.6	4.9
17.05.2017	-48.8	46.8	24.6	-8.2	8.0	17.3
18.05.2017	-56.7	47.3	29.6	-4.1	12.7	8.7
19.05.2017	-31.2	30.1	18.7	11.8	2.3	-13.7

As depicted in table 3, horizontal (n, e) and vertical (u) components of JNAV are mostly less than 1 cm corresponding to medium baseline (~892 km). In addition, while one value of "n" component (19.05.2017) is larger than 1 cm (11.80 mm) and two values of "e" components are above 1 cm (15.05.2017, 18.05.2017), four values of vertical component (u) are larger than 1 cm and reach maximum 1.73 cm level on 17.05.2017. However for the long baseline (~2173 km), horizontal and vertical components are highly large comparing to the medium baseline. Maximum "n" value is observed on 14.05.2017, reaching 9.70 cm and minimum value is 1.50 cm (13.05.2017). "e" components are between 12.90 cm and 4.87 cm. Besides, "u" components are generally less than 3 cm and reaching maximum 5.8 cm level (14.05.2017).

4. CONCLUSIONS

This study assessed the positioning performance of BDS comparing to the GPS using two baselines (medium and long). 24 h datasets of 10 days were used. The same processing strategy was applied for BDS and GPS. Results illustrated that BDS based estimated coordinates are comparable to the GPS-derived coordinates for the medium baseline which are generally below 1 cm. However differences reach above 2.5 cm for most of the horizontal and vertical components corresponding to long baseline.

ACKNOWLEDGMENT

This study was funded by the Scientific Research Projects Grant of Necmettin Erbakan University (Project No: 182518001-078). We are grateful to MIT for providing the license of GAMIT/GLOBK software. The authors would like to thank to Dr. Bob KING for his kind help in processing Beidou data.

REFERENCES

[1]. S.-S. Jan and A.-L. Tao, "Comprehensive comparisons of satellite data, signals, and measurements between the BeiDou navigation satellite system and the global positioning system," Sensors, vol. 16, no. 5, p. 689, 2016. doi: 10.3390/s16050689.

[2]. O. Montenbruck, A. Hauschild, P. Steigenberger, U. Hugentobler, P. Teunissen and S. Nakamura, "Initial assessment of the COMPASS/BeiDou-2 regional navigation satellite system", GPS Solutions, vol. 17, no. 2, pp. 211-222, 2013. doi: https://doi.org/10.1007/s10291-012-0272-x.

[3]. X. Zhang, M. Wu, W Liu, X. Li, S. Yu, C. Lu and J. Wickert, "Initial assessment of the COMPASS/BeiDou-3: new-generation navigation signals" Journal of Geodesy, vol. 91, pp. 1225–1240, 2017. doi: https://doi.org/10.1007/s00190-017-1020-3.

[4]. W. Jiang, R. Xi, H. Chen and Y. Xiao, "Accuracy analysis of continuous deformation monitoring using BeiDou Navigation Satellite System at middle and high latitudes in China" Advances in Space Research, vol.59, pp. 843–857, 2017. doi: https://doi.org/10.1016/j.asr.2016.11.010.

[5]. Y. YuanXi, L. JinLong, W. AiBing, X. JunYi, H. HaiBo, G. HaiRong, S. JunFei and D. Xian, "Preliminary assessment of the navigation and positioning performance of BeiDou regional navigation satellite system" Science China: Earth Sciences, 57, no. 1, pp. 144–152, 2014. doi: https://doi.org/10.1007/s11430-013-4769-0.

[6]. M. Li, L. Qu, Q. Zhao, J. Guo, X. Su and X. Li, "Precise Point Positioning with the BeiDou Navigation Satellite System" Sensors, vol.14, no.1 pp. 927-943, 2014. doi:10.3390/s140100927.

[7]. X. Xu, M. Li, W. Li and J. Liu, "Performance Analysis of Beidou-2/Beidou-3e Combined Solution with Emphasis on Precise Orbit Determination and Precise Point Positioning", Sensors, vol. 18, no.1 pp. 135, 2018. doi:10.3390/s18010135.
[8]. (2018) The information and analysis center for positioning, navigation and timing website. [Online]. Available: https://www.glonass-iac.ru/en/BEIDOU/index.php
[9]. (2018) The IGS website. [Online]. Available: http://www.igs.org/network
[10]. T.A. Herring, R.W. King, M.A. Floyd, S.C. McClusky (2015) Introduction to GAMIT/GLOBK release 10.6. Department of Earth, Atmospheric, and Planetary Sciences, Massachusetts Institute of Technology, Cambridge, MA

ICENS 4TH INTERNATIONAL CONFERENCE ON ENGINEERING AND NATURAL SCIENCE
2 - 6 May 2018 KIEV UKRAINE

Estimation of machining outputs in drilling of AISI 430 stainless steel by numerical analysis

Tolga Meral[1], Mehmet Erdi Korkmaz[2], Huseyin Uzun[3], Mustafa Gunay[4]

Abstract

Drilling is an inevitable process used in the manufacture of many industrial products among the machining operations, as well as a difficult cutting mechanism due to the difficulty of the chip formation. In drilling, the cutting tool-material pair characteristics in addition to the cutting parameters affect the machining efficiency depending on the machining outputs such as surface quality, cutting force, tool life, amount of energy consumed. In this context, it is possible to predict machining outputs by making cutting simulations based on the finite element method in order to contribute to sustainable manufacturing. The study presents the drillability of AISI 430 stainless steel through drilling simulations based on numerical analysis. Drilling operations were performed with uncoated carbide drill at three different cutting speeds (15, 30, 45 m/min) and feed rates (0.06, 0.08, 0.1 mm/rev). The effects of the drilling parameters on the thrust force and torque were investigated in drilling of the ferritic stainless steel. According to the results obtained by drilling simulations, it was determined that the thrust force and torque increases as feed rate increases. On the other hand, it was found that thrust force and torque decreases as cutting speed increases.

Keywords: AISI 430, finite element model (FEM), thrust force, torque

1. INTRODUCTION

Ferritic stainless steels are used in many industrial areas such as automobile chassis parts, exhaust components, hot water tanks, kitchen utensils and decorative applications. AISI 409, 430 and 439 stainless steels can be given examples of this group. The low thermal expansion, good formability and oxidation resistance are characteristic features of the AISI 430 ferritic stainless steel in this group. The machinability of AISI 430 is similar to that of unalloyed steel with a strength of approximately 500 MPa. According to the applied manufacturing technique (turning, milling and drilling), determination of the most suitable parameter values is extremely important at this point [1].

Drilling is one of the commonly used as machining process, the method makes up about 25%. In this process, the drill used as a cutting tool performs a chip formation accompanied by cutting speed and feed rate which is selected depending on the drill type, the tool material and the material being machines [2]. In recent times, new drill geometries and tool coatings have result in improved hole accuracy, longer life, self-centering action, and increased feed rate and cutting speed capabilities. For this context, the cutting tool geometry used in this process the most significant factor affecting productivity. Therefore, it is very important to investigate the estimated tool life and tool wear [3,4]. Many studies have been carried out with basic parameters such as cutting speed and feed rate in order to obtain the minimum cost and increase the productivity in drilling process. The aim of the studies is to determine the optimum parameter levels and to reduce the machining cost.

Han and Wu investigated temperature, thrust force and moment using finite element method (FEM) in drilling of AISI 1045 and Ti6Al4V materials. They found that both the feed rate and the cutting speed had a significant effect on temperature, thrust force and moment. They also stated that the margin of error between numerical and experimental study is below 20% [5]. Ahmed studied the effects of cutting speed and feed rate on thrust force and torque using FEM in the 2080 steel. It has been determined that as the feed and cutting speed

[1] *Corresponding author: Karabuk University, Department of Mechanical Engineering, 78050, Karabuk, Turkey, tolgameral54@gmail.com*

[2] *Karabuk University, Department of Mechanical Engineering, 78050, Karabuk, Turkey, merdikorkmaz@karabuk.edu.tr*

[3] *Karabuk University, Department of Mechanical Engineering, 78050, Karabuk, Turkey, huseyin.uzun55@hotmail.com*

[4] *Karabuk University, Department of Mechanical Engineering, 78050, Karabuk, Turkey, mgunay@karabuk.edu.tr*

increases, the thrust force and torque increase. It has been found that the most important parameter is feed rate [6]. Gok et al. realized drilling of AISI 1040 steel using finite element method and experimental method, with different helix angle, feed rate and cutting speed. They examined thrust force and moment. It has been found that the thrust force decreases when the cutting speed increases at each helix angle [7]. Li and Sihih examined temperature, thrust force and Von Mises stresses in drilling process of Ti6Al4V material. They found that when the cutting speed is reduced, and the feed rate is increased, the temperature decreases while Von Mises strain rises [8]. Kivak et al. investigated hole diameter, circularity and burr formation in AISI 316 stainless steel using various coatings (TiN, TiAIN, TiAIN/TiN) HSS tool. Researchers have obtained the most efficient result from TiAIN/TiN coated tools in terms of the hole diameter and circularity [9]. Caydas et al. performed drilling operations with various tools on AISI 304 austenitic stainless steel under dry conditions. The experiments were done using the Taguchi L_9 orthogonal array in experiment design. TiN-coated HSS drill has shown high performance in terms of long tool life and hole quality [10]. Siddiquee et al. investigated the optimal drilling parameters using the Taguchi experimental method to minimize the surface roughness of the AISI 321 stainless steel in the drilling process. As a result of the experiments, the optimum parameter levels were determined as 500 rpm, 0.04 mm/s and hole depth of 25 mm. According to the analysis of variance, it was seen that the considerably effect on the surface roughness was the rotation velocity [11]. Sultan et al. applied drilling operation to AISI 316L and they examined burr formation using carbide tool. At the experiments conducted, it has been determined that the low cutting speed and feed rate are optimum parameter levels desired chip formation on the austenitic stainless steel [12].

In this study, the drilling process was analyzed by the finite element method on AISI 430 ferritic stainless-steel material. Three different cutting speed and feed rate were used with the uncoated carbide tool in the simulations. Effects of the parameters on thrust force and torque were theoretically investigated in the drilling of AISI 430 stainless steel.

2. MATERIALS AND METHOD

The uncoated carbide tool and the AISI 430 ferritic stainless steel have been used in drilling simulations. The chemical and mechanical properties of the stainless steel material are shown in Table 1 and Table 2, respectively.

Table 1. Chemical properties of the material

C	Mn	P	S	Si	Cr	Ni
0.12	1.0	0.045	0.03	1.0	16.0-18.0	0.75

Table 2 Mechanical properties of the material

Density [kg/m^3]	7.89x10^3
Poission ratio	0.3
Young module	210
Yield stress [MPa]	347
Strength[MPa]	543

Firstly, the dimensions of workpiece (12 mm length, 4 mm height and 3 mm thickness) have been defined in the simulation program. Then, geometric dimensions of the tool have been entered as drill diameter of 8 mm, of helix angle of 30° and point angle of 140°. The Coulomb model was used for the interface relation between the tool and the workpiece and the coefficient of friction was selected as 0.5. The finite element model for drilling process is shown in Figure 1.

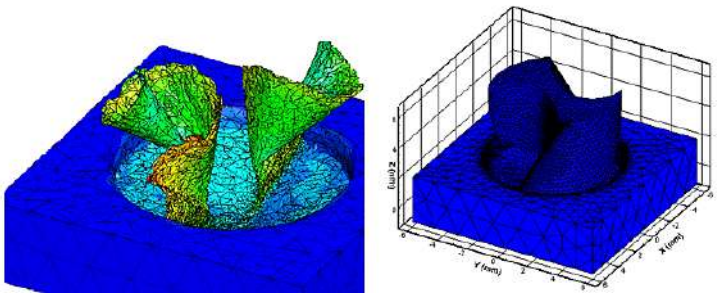

Figure 1. FEM model of cutting tool and workpiece

The process parameters are selected as the cutting speed and feed rate which are the basic cutting parameters in the drilling process. A total of 9 experiments were realized using three different values for each parameter (Table 3). The results obtained for all experiments have been interpreted.

Table 3. Experiment design

Exp. No	Cutting speed (m/min)	Feed rate (mm/rev)
1	15	0.06
2		0.08
3		0.1
4	30	0.06
5		0.08
6		0.1
7	45	0.06
8		0.08
9		0.1

3. RESULTS

The results of each experiment are examined, and it has been understood that the results are acceptable when compared with the drillability of other stainless steels in the literature [13,14]. It can be said that the obtained results could contribute to the literature in terms of the drilling of AISI 430 stainless steel. It has been found that the finite element method used in drilling is an important tool for the estimated values of the machining outputs such as thrust force and torque.

a. Thrust force

According to the cutting parameters specified in Table 3, drilling operations were performed using the finite element method. The effects of feed rate and cutting speed on thrust force have been shown.

According to graph shown in Figure 3, the lowest thrust force at a cutting speed of 45 m/min and a feed rate of 0.06 mm/rev has been measured as 909 N in drilling operation. On the other hand, the highest thrust force has been obtained as 1253 N at a cutting speed of 15 m/min and a feed rate of 0.1 mm/rev.

At constant feed rate of 0.06 mm/rev, the highest and lowest thrust force have been found 938 and 909 N, at cutting speed of 15 and 45 m/min respectively and the decrease was calculated 3.09%. At constant feed rate of 0.08 mm/rev, the maximum and minimum thrust force have been measured 1090 and 1064 N, at cutting speed of 15 and 45 m/min respectively and the decline was calculated 2.39%. At constant feed rate of 0.1 mm/rev, the highest and lowest thrust force have been determined 1253 and 1188 N, at cutting speed of 15 and 45 m/min respectively and the fall was calculated 5.29% (Figure 2).

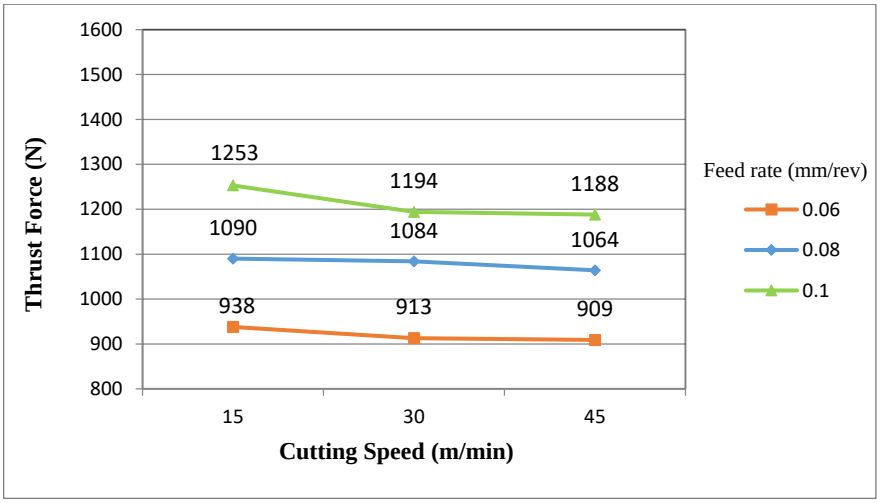

Figure 2. Variation of thrust forces versus cutting parameters

In this case, the thrust force increases as feed rate increases at the constant cutting speed, while the thrust force decreases as the cutting speed increases at the constant feed rate. This can be attributed to increasing chip cross-sectional area [15]. Decline of thrust force has been seen that at increased cutting speed. This decrease can be associated with softening of material at high cutting speed and it has been determined that the obtained results are in accordance with the literature [16]. It is also understood that the effect of feed rate is more influence than the cutting speed.

b. Torque

According to graph shown in Figure 3, the lowest torque at a cutting speed of 45 m/min and a feed rate of 0.06 mm/rev has been measured as 2,68 Nm in drilling operation. On the other side, the highest thrust force has been found as 3,92 Nm at a cutting speed of 15 m/min and a feed rate of 0.1 mm/rev.

At constant feed rate of 0.06 mm/rev, the highest and lowest torque have been obtained 2.76 and 2.68 Nm, at cutting speed of 15 and 45 m/min respectively and the decrease was calculated %2.90. At constant feed rate of 0.08 mm/rev, the maximum and minimum torque have been measured 3.34 and 3.31 Nm, at cutting speed of 15 and 45 m/min respectively and the decline was found %0.90. At constant feed rate of 0.1 mm/rev, the highest and lowest torque values have been determined 3.92 and 3.84 N, at cutting speed of 15 and 45 m/min respectively and the fall was calculated %2.05 (Figure 3).

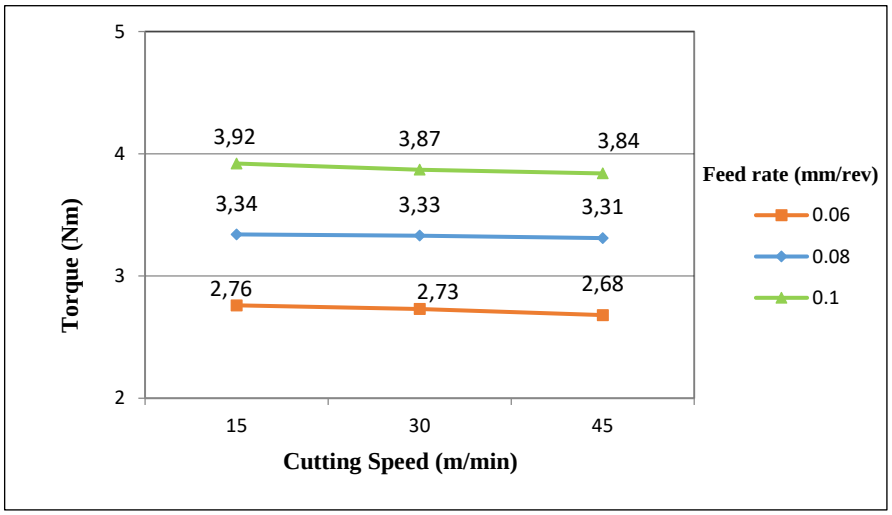

Figure 3. Variation of torque values versus cutting parameters

It has been observed that as feed rate increases the torque value increases, and as the cutting speed increases, the torque value decreases. This case is a similar relation when compared the thrust force. It has been determined that the results are consistent with the literature [14,17].

4. CONCLUSIONS

This paper presents the drilling process on AISI 430 ferritic stainless-steel material by the finite element method. Three different cutting speed and feed rate were used with the uncoated carbide tool in the simulations. Effects of the parameters on thrust force and torque were theoretically investigated in the drilling of AISI 430 stainless steel. The conclusions are specified below.

- It has been found that the thrust force decreases with increasing cutting speed in each a feed rate. At each cutting speed, the thrust force was increased by increasing feed rate. The lowest thrust force has been occurred at a feed rate of 0.06 mm/rev and a cutting speed of 45 m/min.
- It has been observed that as the cutting speed increases the torque values decreases. The lowest torque value has been obtained at a cutting speed of 45 m / min and a feed rate of 0.06 mm / rev.
- It has been determined that the feed rate has a significant impact on the thrust force and torque.
- It has been understood that the finite element method is a useful method for determining the estimated values of the machining outputs, especially, in respect of the optimization of processing parameters without the need for experimental study.

This study is supported by Scientific Research Project Unit of Karabuk University (KBÜBAP-17-YL-248) and the authors express their appreciation for this support.

REFERENCES

[1]. A. Aran ve M. A. Temel, "Paslanmaz celik yassi mamuller uretimi, kullanimi, standartlari, Acar matbaacilik A.S., Istanbul, 9, 25-29, 53-54, 86-87 2004.
[2]. J.T. Black and Ronald A. Kohser, Degarmo's Materials and Processes in Manufacturing, Prentice-Hall Inc., New Jersey, 2013.
[3]. S. Bayraktar, Y. Siyambas, ve T. Turgut, "Delik delme prosesi: bir arastirma", Sakarya Üniversitesi Fen Bilimleri Enstitusu Dergisi, 120-130 2016.
[4]. M. Nouari, G. List, F. Girot and D. Ghein "Effect of machining parameters and coating on wear mechanisms in dry drilling of aluminium alloys", International Journal of Machine Tools & Manufacture, 1436-1442, 2005
[5]. R. Han, and J. Wu, "Finite element simulation of drilling based on Thirdwave systems AdvantEdge", Key Engineering Materials, Vol. 431-432, 229-232 2010.
[6]. N. Ahmeed, "Effect of changing drilling parameters on thrust force and torque", Middle-East Journal of Scientific Research, 21 (2): 347-352 2014.

[7]. K. Gok, E. Turkes, S. Neseli, H. Saglam, and A. Gok, "The validation as experimental and numerical of the values of thrust force and torque in drilling process", Journal of Engineering Science and Technology Review, 6 (3) 93-99 (2013).
[8]. R. Li, and A. J. Shih, "Finite element modeling of high-throughput drilling of Ti6Al4V", Transactions of NAMRI/SME, Vol. 35 73-80 (2007).
[9]. T. Kivak, A. Çicek, I. Uygur ve N. A. Özbek, "AISI 316 ostenitik paslanmaz celigin delinmesinde tek katli ve cok katli kaplamalarin delik kalitesi uzerindeki etkileri", 3. Ulusal Talasli Imalat Sempozyumu 2012.
[10]. U. Çaydas, A. Hascalik, Ö. Buytoz and A. Meyveci, "Performance Evaluation of Different Twist Drills in Dry Drilling of AISI 304 Austenitic Stainless Steel", Materials and Manufacturing Processes, 26: 951–960 2011.
[11]. A. N. Siddique, Z. A. Khan, P. Goel, M. Kumar, G. Agarwal and N. Z. Khan, "Optimization of deep drilling process parameters of AISI 321 steel using Taguchi method", 3rd International Conference on Materials Processing and Characterisation, 1217-1225 2014.
[12]. A. Z. Sultan, S. Sharif and S. Kurniawan, "Chip formation when drilling aisi 316L stainless steel using carbide twist drill", 2nd International Materials, Industrial, and Manufacturing Engineering Conference, 224-229 2015.
[13]. G. Kucukturk, "Modeling and analyzing the effect of experimentally determined torque and thrust force on cutting tool according to drilling parameters", Journal of Engineering Manufacture, 227(1) 84-95 2012.
[14]. O. Balajina, and A. Vlase, "Analysis of the calculus relations of the cutting forces and moments at drilling of the stainless steel X20Cr13", Proceedings of the 6th International Conference on Manufacturing Engineering ,Quality and Production Syste, 88-93 2013.
[15]. J. S. Vas, A. Fernandes, A. D'Souza, A Rai and J. D. Quadros, "Analysis of temperature changes during dry drilling of austenitic stainless steel on twist drills having different point angles", Journal of Mechanical Engineering and Automation, 6(5A): 121-125 2016.
[16]. A. Çicek, T. Kivak, G. Samtas and Y. Çay, "Modelling of thrust force in drilling of AISI 316 stainless steel using artificial neural network and multiple regression analysis" Strojniski Vestnik – Journal of Mechanical Engineering, 492-498 2012.
[17]. M. Iliescu and A. Vlase, "New mathematical models of axial cutting force and torque in drilling 20MoCr130 stainless steel", Proceedings of the 10th WSEAS International Conference on Mathematical and Computational Methods in Science and Engineering, 210-215 2008.

ICENS 4TH INTERNATIONAL CONFERENCE ON ENGINEERING AND NATURAL SCIENCE
2 - 6 May 2018 KIEV UKRAINE

Investigation Of The Hole Quality During Fiber Laser Drilling Of Ferritic Stainless Steel

Huseyin Uzun[1], Tolga Meral[2], Nafiz Yasar[3], Mustafa Gunay[4]

Abstract

Laser drilling, which provides the manufacturing of high precision and complex parts, is one of the unconventional machining methods. In the laser drilling process, the basic parameters that are especially focal point, gas pressure and feed speed play an important role over product quality by affecting cutting process directly. These parameters significantly affect the machining efficiency as well as the machining outputs such as burr formation and hole quality. Therefore, it is important to determine the optimum parameter levels according to workpiece in terms of machining efficiency during laser drilling. In this study, the drillability of AISI 430 stainless steel with laser cutting method was investigated. Drilling operations are performed at three different focal point (0, -2, -4 mm), pressure (12, 14, 16 bar), and feed speed (1200, 1500, 1800 mm/min). In drilling of stainless steel by laser, the effects of the drilling parameters over the burr height and the deviation of diameter were analyzed. Also, analysis of variance (ANOVA) showed that the focal point and pressure are the most important parameters for the machining.

Keywords: AISI 430, laser drilling, burr height, deviation of diameters

1. INTRODUCTION

Laser drilling is known one of the improved machining processes in the manufacturing fields due to their precision, low cost, and high speed of operation. Therefore, it is used in industrial area for produce small hole such as aerospace components [1]. In this method, a laser beam is used as a heat source and provides increasing temperature rapidly to the melting. Desired hole quality with highest accuracy can be obtained by controlling the laser machining parameters [2]. At the same time, there are many basic parameters that affect this situation such as laser type and power, cutting speed, assist gas type, gas pressure and workpiece material in laser drilling [3]. For this reason, many studies were performed to understand effect of these parameters in terms of the determining optimum performance.

Pak and Moradi investigated the parameters of laser percussion drilling process of nickel-base superalloy Inconel 718 with thickness of 1 mm in the study. Laser power, laser pulse frequency and assist gas pressure has been selected as the laser drilling process parameters. They found that laser pulse frequency has a direct influence on the diameter of the entrance hole. Also, it has been understood that entrance, exit hole diameter and hole taper increases with increasing laser power [1]. Jarosz et al. studied effect of the cutting speed on heat-affected zone (HAZ) and surface roughness in laser cutting of AISI 316L stainless steel. It has been determined that cutting speed has a significant effect on surface roughness, width of the heat-affected zone and presence of macro irregularities, such as presence of dross, molten and burnt material [3]. Ozaki et al. examined cutting properties of SUS304 stainless steel by using AGF laser cutting 2. Laser power and cutting speed were varied in order to study the effect of these parameters on cutting properties. They found that when laser power was 2.0 kW, cutting speed could be increased up to 100 mm/s, and kerf width at specimen surface was 0.28 mm

[1] *Corresponding author: Karabuk University, Department of Mechanical Engineering, 78050, Karabuk, Turkey, huseyin.uzun55@gmail.com*

[2] *Karabuk University, Department of Mechanical Engineering, 78050, Karabuk, Turkey, tolgameral54@gmail.com*

[3] *Karabuk University, Department of Mechanical Engineering, 78050, Karabuk, Turkey, nafizyasar@karabuk.edu.tr*

[4] *Karabuk University, Department of Mechanical Engineering, 78050, Karabuk, Turkey, mgunay@karabuk.edu.tr*

[4]. Pocorni and Powell investigated laser drilling of 10 mm thick stainless steel by a multikilowatt fiber laser. The results show that proper laser power settings can considerably reduce both the drilling time and the required energy [5]. Wandera and Kujanpaa researched optimization of the fiber laser cutting parameters taking into account cutting speed, focal point and focal length. They indicated that dross-free cut edges with lower surface roughness and lower deviation could be obtained by decreasing cutting speed, using longer focal length, and with focal position located on the bottom workpiece surface. It has been determined that this dross-free cut edge, lower surface roughness and lower deviation were found at the 254 mm focal length, cutting speed of 1.0 m/min, and focal position located on the bottom workpiece surface [6]. Wandera et al. investigated laser power requirement for cutting mild steel and stainless steel using 5 kW, 4kW CO_2 laser. Laser power required for cutting is found to be lower for fibre laser cutting than for the CO2 laser cutting. Also, it has been found that the important process parameters are cutting speed, oxygen pressure, and nozzle diameter [7]. Petru et al. studied influence of cutting parameters on heated-affected zone after laser cutting process. It has been stated that in case of using continuous CO_2 laser, the degree of thermal influence on the workpiece does not related to only feed rate, but also other parameters. They also indicated that suitable chosen parameters are provides good results in terms of the quality of cutting surface and the size of heat-affected zone [8]. Moradi and Golchin examined effects of process parameters on Inconel 718 workpiece using finite elements method (FEM) and statistical modelling optimization in fiber laser drilling operation. At the statistical analysis conducted, it has been found that the entrance and exit hole diameters, the hole taper angel, and the weight of mass removed from the hole increase, by an increase in each of the input variables (laser pulse frequency, laser power, laser focal plane position and duty cycle). They determined that good agreement between simulation and optimization results [9]. Wang et al. investigated effect of laser power on the quality of drilled micro holes using $Cu_{50}Zr_{50}$ amorphous alloys foils as experimentally. They stated that both entrance and exit circularities diameters increase with laser power. The micro holes have been drilled with a diameter of 400 to 1200 μm successfully by laser drilling processes [10].

In this study, the effects of laser machining parameters in fiber laser drilling of the AISI 430 ferritic stainless steel was investigated as experimentally and statistically. Three different gas pressure, focal point and feed rate were used in the experiments. Effects of the parameters on burr height and deviation of diameter were evaluated with variance analysis in the laser drilling of the stainless steel.

2. MATERIAL AND METHOD

AISI 430 ferritic stainless steel has been used as workpiece material with thickness of 4 mm thickness. Nitrogen gas has been selected in order to avoid carbon dioxide and vaporization in the beam path during fiber laser drilling. The chemical properties of the AISI 430 stainless steel material are shown in Table 1.

Table 1. Chemical properties of the workpiece

C	Mn	P	S	Si	Cr	Ni
0.12	1.0	0.045	0.03	1.0	16.0-18.0	0.75

All laser drilling experiments were carried out in Nukon laser machine with 2.4 kW power. Process parameters were chosen feed rate (mm/min), gas pressure (bar) and focal point. Experiments were carried out with three different levels of machining parameters. Three sheet metals were used to analyze easily the hole quality obtained in the experiments, and 9 holes were obtained from each plate. The experiment sample designed according to the determined conditions for fiber laser drilling is given in Figure 1.

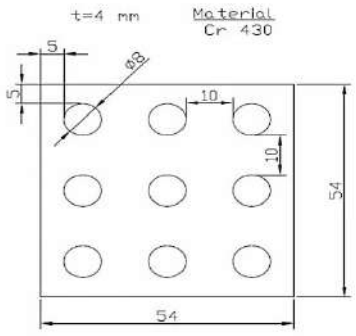

Figure 1. The experiment sample.

Design of experiments and statistical analysis have been performed using MINITAB software based on the factors and factor levels shown in the Table 1. Totally, 27 holes have been obtained in fiber laser drilling operation. Analysis of variance (ANOVA) has been realized to determine the effect of laser parameters on burr height and deviation of diameter. The experiments were repeated two times, and hole qualities were evaluated by arithmetical average of the machining outputs.

Table 1. Factors and levels of factor

Factors	Level 1	Level 2	Level 3
Feed rate [mm/min]	1200	1500	1800
Gas pressure [bar]	12	15	18
Focal point	0	-2	-4

3. RESULTS AND DISCUSSION

The influences of laser machining parameters (feed rate, gas pressure and focal point) on burr height and deviation of diameter have been assessed by means of the obtained data.

a. Burr Height

Hole drilling with laser machining were used for liquid flow applications such as turbine blade, fuel spray nozzle, tube. In this case, the flow characteristic is significantly connected with the geometry and the surface quality of holes which is negatively affected by burr formation. In addition, it is difficult to remove the burrs on the inner or outer surface by additional finishing processes as well as increases in cost. In this context, it is necessary to determine the most appropriate parameters in laser drilling, especially for stainless steels. The variations of burr height depending on the feed rate, gas pressure and focal point on are shown in Figure 2.

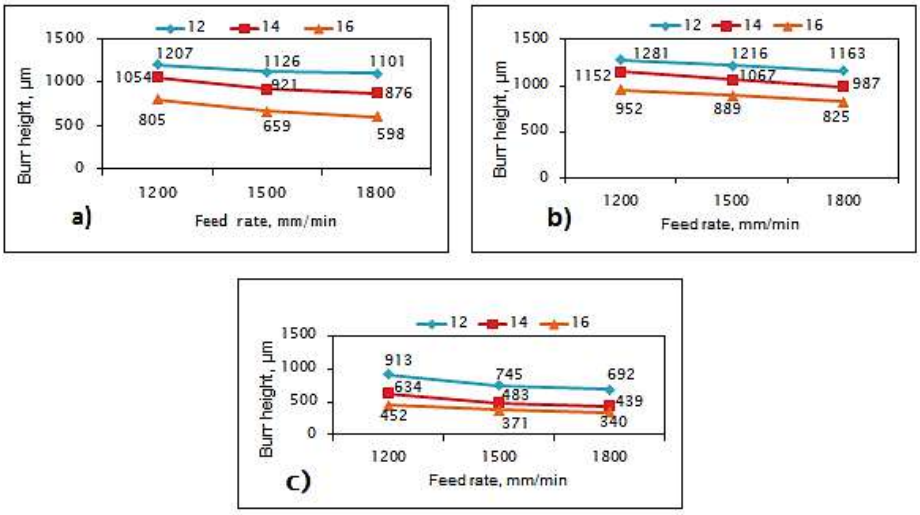

Figure 2. Burr heights versus the parameters; a) 0 focal point, b) -2 focal point, c) -4 focal point

When the Figure 2 are observed, it has been obviously seen that the burr height increases with decreasing gas pressure. It was found that burr height decreases as feed rate increases. It can be said that the burr height tends to decline as the focal point increases, as can be mentioned Ref. [11]. In the fiber laser drilling of AISI 430, the highest burr height has been obtained as 1281 µm in 12 bar, 1200 mm/min feed rate and -2 focal point while the lowest burr height has been determined as 340 µm in 16 bar, 1800 mm/min fed rate and -4 focal point.

Table 2. Variance analysis for burr height

Factors	SD	KT	KO	F	%PCR
Focal point	2	1186747	593374	788,02	58,20
Gas pressure	2	700534	350267	465,17	34,35
Feed rate	2	118261	59130	78,53	5,80
Focal point*Gas pressure	4	23409	5852	7,77	1,14
Focal point*Feed rate	4	3311	828	1,1	0,16
Gas pressure*Feed rate	4	1068	267	0,35	0,05
Error	8	6024	753		0,30
Total	26	2039354			

Analysis of variance results are shown in Table 2 in terms of the burr height. It is demonstrated that the most important factors on burr height in fiber laser drilling of AISI 430 stainless steel are the focus and gas pressure with 58.20% PCR and 34.35% PCR, respectively. According to ANOVA results, it could be seen that effect of feed rate on the burr height is 5.80%.

b. Deviation of Diameter

Stainless steel is difficult to cut by using conventional machining due to the high melting point and strength, particularly in hole drilling. Hence, it is suitable to use the laser drilling process for the such materials. The

laser drilling process is a complex process including many input parameters such as feed rate, pulse current, assisted gas, gas pressure, focal point, nozzle tip diameter, etc. Focal point, gas pressure and feed rate or cutting velocity are known to be the most effective parameter among these factors [2]. In this study, the deviation of diameter was analyzed by taken into consideration the above-mentioned three parameters in fiber laser drilling of ferritic stainless steel. The variation of deviation of diameter with respect of the laser parameters used is shown in Figure 3.

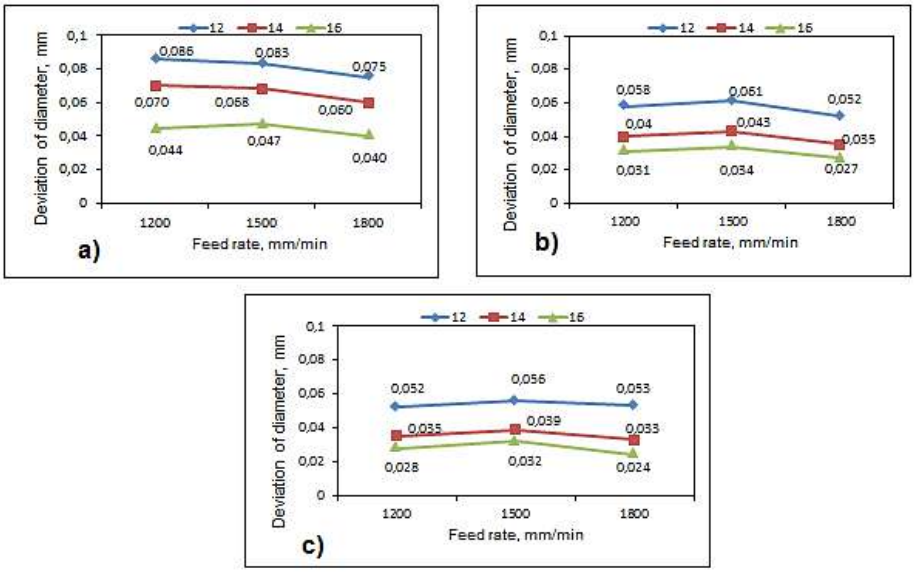

Figure 3. Deviation versus the parameters; a) 0 focal point, b) -2 focal point, c) -4 focal point

As a result of conducted experiments, it has been determined that the deviation of diameter increases with decreasing gas pressure. It has been understood that the feed rate has bidirectional effect, both reducing and increasing, on deviation of diameter in fiber laser drilling operation. In this case, it could be said that the deviation of diameter tends to fall as the feed rate increases since more of reduce effect. It was found that deviation of diameter diminishes as the focal point increases. In the fiber laser drilling of AISI 430 steel, the highest deviation of diameter was calculated as 0.086 mm in 12 bar, 1200 mm/min feed rate and 0 focal point while the lowest deviation of diameter were calculated as 0.024 mm in 16 bar, 1800 mm/min fed rate and -4 focal point.

Table 3. Variance analysis for deviation of diameter

Factors	SD	KT	KO	F	%PCR
Focal point	2	0,003205	0,001603	575,06	41,17
Gas pressure	2	0,004045	0,002023	725,75	51,97
Feed rate	2	0,00024	0,00012	43,07	3,08
Focal point*Gas pressure	4	0,000229	0,000057	20,58	2,95
Focal point*Feed rate	4	0,000037	0,000009	3,36	0,48
Gas pressure*Feed rate	4	0,000004	0,000001	0,37	0,06
Error	8	0,000022	0,000003		0,29

Total	26	0,007784

Analysis of variance results are shown in Table 3 in terms of the deviation of diameter. It has been seen that the most important factors on deviation of diameter in fiber laser drilling of AISI 430 stainless steel are the focus and gas pressure with 41.17% PCR and 51.97% PCR, respectively. Also, it can be seen from ANOVA results that effect of feed rate on the deviation of diameter is 3.08%.

4. CONCLUSIONS

In this study, effect of focal point, gas pressure and feed rate on burr height and deviation of diameter were investigated in fiber laser drilling of AISI 430 ferritic stainless steel. The results of the experimental and statistical evaluations were summarized as follows:

- According to obtained experimental results in the fiber laser drilling of AISI 430, the lowest burr height was determined as 340 µm in 16 bar, 1800 mm/min fed rate and -4 focal point.
- The highest deviation of diameter was calculated as 0.086 mm in 12 bar, 1200 mm/min feed rate and 0 focal point while the lowest deviation of diameter was calculated as 0.024 mm in 16 bar, 1800 mm/min fed rate and -4 focal point.
- According to ANOVA results, the most important factors on burr height and deviation of diameter in drilling of AISI 430 are the focal point and gas pressure with 58.20%, 34.21% PCR (for burr height), with 41.17%, 51.97% PCR (for deviation of diameter), respectively.

This study is supported by Scientific Research Project Unit of Karabuk University (KBÜBAP-17-YL-248) and the authors express their appreciation for this support.

REFERENCES

[1]. A. M. Pak and M. Moradi, “Hole geometry features analysis in fiber laser percussion drilling process”, Int’I Journal of Advances in Mechanical & Automobile Engineering, Vol. 2 18-21 2015.
[2]. B. S. Yilbas, Laser Drilling Practical Applications, Berlin, Germany: Springer, 2013.
[3]. K. Jarosz, P. Loschner and P. Nieslony, “Effect of cutting speed surface quality and heat-affected zone in laser cutting of 316L stainless steel”, International Conference on Manufacturing Engineering and Materials, 155-162 2016.
[4]. H. Ozaki, Y. Koike, H. Kawakami and J. Suzuki, “Cutting properties of austenitic stainless steel by using laser cutting process without assist gas”, Hindawi Publishing Corporation Advances in Optical Technologies, Vol. 2012 8 pages.
[5]. J. Pocorni, J. Powell, J. Frostevarg and A. F. H. Kaplan, “Investigation of the piercing process in laser cutting of stainless steel”, Journal of Laser Application, Vol.29 No 2 2017.
[6]. C. Wandera and V. Kujanpaa “Optimization of parameters for fibre laser cutting of a 10 mm stainless steel plate”, Proceedings of the Institution of Mechanical Engineers, Part B: Journal of Engineering Manufacture Vol. 225 641-649 2011.
[7]. C. Wandera, V. Kujanpaa and A. Salminen “Laser power requirement for cutting thick-section steel and effects of processing parameters on mild steel cut quality”, Proceedings of the Institution of Mechanical Engineers, Part B: Journal of Engineering Manufacture Vol. 225 651-660 2011.
[8]. J. Petru, T. Zlamal, R. Cep, K. Monkova and P. Monka “Influence of cutting parameters on heat-affected zone after laser cutting”, Tehnicki Vjesnik 20, 225-230 2013.
[9]. M. Moradi and E. Golchin, “Investigation on the effects of process parameters on laser percussion drilling using finite element methodology; statistical modelling and optimization”, Latin American Journal of Solids and Structures, 464-484 (2013)
[10]. C. J. Wang, G. Chen, D. Luan and P. Zhang “Effect of laser power on the quality of drilled micro hole using $Cu_{50}Zr_{50}$ amorphous alloys foils”, Micromachines, 1061-1068 2014.
[11]. B.Adelmanna and R. Hellmann, “Fast Laser Cutting Optimization Algorithm”, Physics Procedia 12, 591–598 2011.

ICENS 4TH INTERNATIONAL CONFERENCE ON ENGINEERING AND NATURAL SCIENCE
2-6 May 2018 KIEV UKRAINE

Influence Of Ethanol And Methanol Additives On A Diesel Engine Performance Characteristics: 1-D Modelling

Merthan Kilic[1], Fatih Aktas[2], Salih Karaaslan[3], Nuri Yucel[4]

Abstract

There are many studies in the literature about the use of alternative fuels in internal combustion engine investigations. Particularly, fuel blends mixed with alcohol content have been found to have positive effects on exhaust emission values. In addition to this positive effect, it is necessary to examine how badly the engine performance character is affected. In this study, four cylinder diesel engine was analyzed by using 1-D modelling. AVL Boost commercial software was conducted to simulate engine cycles. Pure diesel and blended fuels was used to investigate the effects of additive ratios on the engine performance characteristics. Ethanol and methanol were chosen as fuel blend additives. Ethanol and methanol additives were set to different volumetric mixtures. Engine performance characteristics such as torque, brake power, brake thermal efficiency and specific fuel consumption etc., were analyzed comparatively. In addition, in-cylinder flow and combustion process were carried out at the best performance point where the engine speed reaches the engine torque gets maximum value. Obtained results show that, engine performance reduces by using alcohol additives for whole numerical predictions. It is seen that the engine torque is about 132 Nm value at the engine speed of 2000 rpm for pure diesel usage as a fuel. Both, 5% ethanol and methanol fuel blends torque values are 130 and 129 Nm respectively at the same engine speed. It is understood that the mixture ratio of %5 ethanol and methanol additives are the nearest fuel blend to the pure diesel performance results.

Keywords: Ethanol and Methanol additive, AVL Boost, Diesel Engine, Performance characteristics.

1. INTRODUCTION

Along with the increase in population, the number of vehicles increases, which leads to an increase in the amount of harmful gas released to the environment and also to a decrease in oil resources. The increase in the amount of harmful emissions forces governments to take very strict restrictive measures. At the same time, increased fuel consumption causes an increase in the search for alternative fuels. At the beginning of these alternative fuels are ethanol, methanol, syngas and so on.

In many countries, the contribution of 5% alternative fuels is now compulsory, and most automotive companies are producing engines that support these contribution rates. Examples of some literature studies from the numerical studies made with AVL-BOOST program for different fuels in diesel engines are given below.

Voicu and Chirac [1] numerically investigated the effect of a diesel engine injection timing on engine performance and exhaust emissions values using the AVL-BOOST program for different hydrogen contribution ratios. It was observed that the addition of hydrogen caused a decrease in CO and NOx emissions, while it had a 2% decrease in thermal efficiency.

[1] *Intern Engineer, Turkish Aerospace Industries Ins. Fethiye Mahallesi, Havacilik Bulvari No:17 06980 Kahramankazan Ankara/Turkey. merthankilic@gmail.com*

[2] *Gazi University, Department of Mechanical Engineering, IC Engines Laboratory, 06570, Maltepe/Ankara, Turkey. fatihaktas@gazi.edu.tr*

[3] *Corresponding author: Gazi University, Department of Mechanical Engineering, 06570, IC Engines Laboratory, Maltepe/Ankara, Turkey. karaaslansalih@gazi.edu.tr*

[4] *Gazi University, Department of Mechanical Engineering, 06570, IC Engines Laboratory, Maltepe/Ankara, Turkey. nuyucel@gazi.edu.tr*

Wojs et al. [2] investigated the effects of a 6-cylinder diesel engine diesel-propane gas mixture on performance and emissions using the AVL-BOOST program for different injection stages. According to the obtained results, it was observed that the pressure inside the cylinder rises and the duration of combustion is prolonged.

Aldhaidhawi et al.[3] experimentally and numerically(with using AVL BOOST) investigated the effects of biodiesel and hydrogen addition on engine performance and emissions at 1400 and 2400 rpm in a 4-cylinder direct-injection diesel tractor engine. It has been observed that NOx emissions are slightly increased while CO, soot and unburned hydrocarbon emissions are reduced with the additive made.

In this study, pure diesel and blended fuels was used to investigate the effects of additive ratios on the engine performance characteristics. Ethanol and methanol were chosen as fuel blend additives. Ethanol and methanol additives were set to different volumetric mixtures. Engine performance characteristics such as torque, brake power, brake thermal efficiency and specific fuel consumption etc., were analyzed comparatively.

2. MATERIALS AND METHODS

2.1 Simulation Models and Software Theory

1-D numerical analysis programs are very important for predicting engine performance, emission values and combustion characteristics precisely. There is many commercially available software such as AVL-BOOST, Ricardo Wave, and GT-Power, which perform engine tests steady-state and transient conditions, offer near-realistic values. These programs provide realistic approaches to solving the gas dynamic equations in one dimension together with thermodynamic approaches. In this study, AVL BOOST commercial program is chosen for the numerical simulations.

2.1.1 Basic Conservation Equations for Cylinders

The calculation of the thermodynamic state of the cylinder is based on the First Law of Thermodynamics which is considering piston work, the enthalpy changes through intake and exhaust valves, heat release from combustion and the enthalpy flow due to bow-by. Figure 1 illustrates flow mentioned above. Change of the internal energy in the cylinder is calculated by the below equation:

$$\frac{d(m_c.u)}{d\alpha} = -p_c.\frac{dV}{d\alpha} + \frac{dQ_F}{d\alpha} - \sum\frac{dQ_W}{d\alpha} - h_{BB}.\frac{dm_{BB}}{d\alpha} + \sum\frac{dm_i}{d\alpha}.h_i - \sum\frac{dm_e}{d\alpha}.h - q_{ev}.f.\frac{dm_{ev}}{dt} \quad (1)$$

In Equation (1); m_c: mass in the cylinder, u: specific internal energy, p_c: cylinder pressure, V: cylinder volume, Q_F: fuel energy, Q_W: wall heat loss, α: crank angle, h_{BB}: enthalpy of blow-by, dm_i: mass element flowing into the cylinder, dm_e: mass element flowing out of the cylinder, h_i: enthalpy of the in-flowing mass, h_e: enthalpy of the mass leaving the cylinder, q_{ev}: evaporation heat of the fuel, f:fraction of evaporation heat from the cylinder charge and m_{ev}: evaporating fuel.

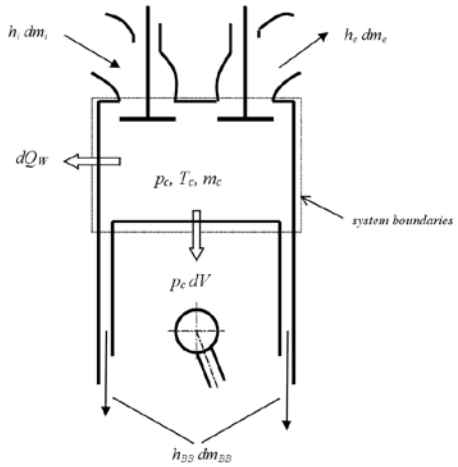

Figure 1. Energy Balance of Cylinder [4]

2.1.2 Combustion Model

In this study, Vibe Two Zone combustion model which divide combustion chamber in two zones burned and unburned was used. The rate of heat release, and thus the burned mass fraction was specified by a vibe function. The temperatures of burned and unburned charges have been calculated by applying First Law of Thermodynamics to the burned charge and unburned charge, respectively.

$$\frac{d(m_b u_b)}{d\alpha} = -p_c.\frac{dV_b}{d\alpha} + \frac{dQ_F}{d\alpha} - \sum\frac{dQ_{Wb}}{d\alpha} + h_U.\frac{dm_b}{d\alpha} - h_{BB,b}.\frac{dm_{BB,b}}{d\alpha} \quad (2)$$

$$\frac{d(m_u u_u)}{d\alpha} = -p_c.\frac{dV_u}{d\alpha} - \sum\frac{dQ_{Wu}}{d\alpha} + h_U.\frac{dm_B}{d\alpha} - h_{BB,u}.\frac{dm_{BB,u}}{d\alpha} \quad (3)$$

where index b is burned, index u is unburned, $h_U.\frac{dm_B}{d\alpha}$ is term that covers the enthalpy flow from the unburned to the burned zone due the conversion of a fresh charge to combustion products. Heat flux between two zones was neglected.

2.1.3 Engine Model and Simulation

The AVL BOOST simulation model used for this study is shown in Fig. 2, and the motor characteristics are given in Table 1. Vibe Two Zone combustion model was used to predict in-cylinder pressure traces. Woschni model was used to calculate in-cylinder heat transfer.

Table 1. Engine specifications

Parameter	Description
Engine type	Four stroke, four cylinder, water cooled, DI
Bore x Stroke	75 x 78 mm
Number of valves	2 x 4
Displacement Volume	1.378 L

Compression Ratio 21

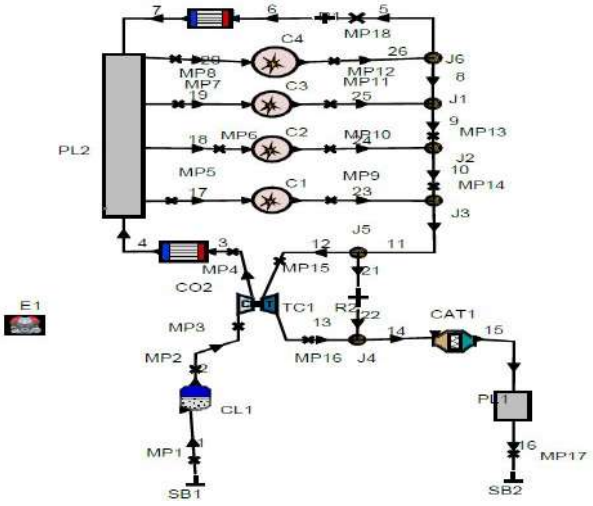

Figure 2. AVL BOOST 1-D model of the 4-cylinder engine

In Figure 2, the symbols denote E: engine, C1 to C4: cylinders, SB1 and SB2: system boundaries, MP1 to MP17: measuring points, PL1 and PL2: plenums, R1 and R2: restrictions, P1 to P26: pipes, CO1 and CO2: coolers, TC1: turbocharger, CAT1: catalyst and J1 to J6: junctions; respectively.

3. RESULTS AND DISCUSSION

The engine performance analyses were carried out at different fuel mixture ratios blended with ethanol and methanol additives of a diesel engine by using 1-D Modelling with AVL Boost. The engine was operated numerically at full load conditions. Serial analyses were conducted with increments of 500 rpm, starting from 1000 rpm to 4000 rpm by using Virtual Engine Simulation Tool AVL Boost. The variation of the engine torque as a function of engine speed for diesel fuel and blended ethanol and methanol from E5, E10, E15, M5, M10 and M15 is given in Figure 3.

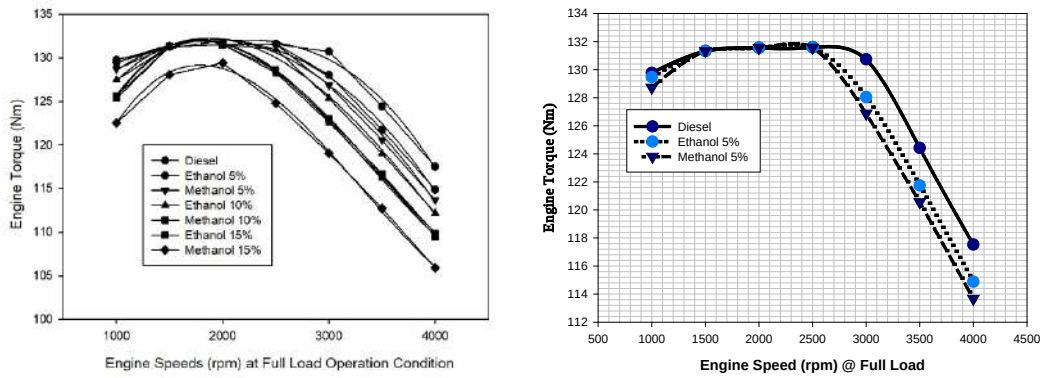

Figure 3. Engine torque as a function of engine speed for all fuel blends

It is seen that engine torques behavior are in similar trend for all fuel blends. It seems that the engine torque is quite insensitive under than 2000 rpm both E5 and M5. On the contrary, above 2000 rpm the engine torque is more sensitive. For E5 and M5 fuel mixtures, the engine torque appears to be at the same level as pure diesel at 2500 revolutions. Maximum torque value about 132 Nm was obtained at 2500 rpm both E5, M5 and diesel fuels. Under operating conditions where the engine speed is higher than 2500, it is understood that the torque values of the mixture of ethanol and methanol are reduced. The engine cylinder pressure as a function of crank angle for diesel fuel and E5-M5 blended fuels at 2500 rpm is given in Figure 4.

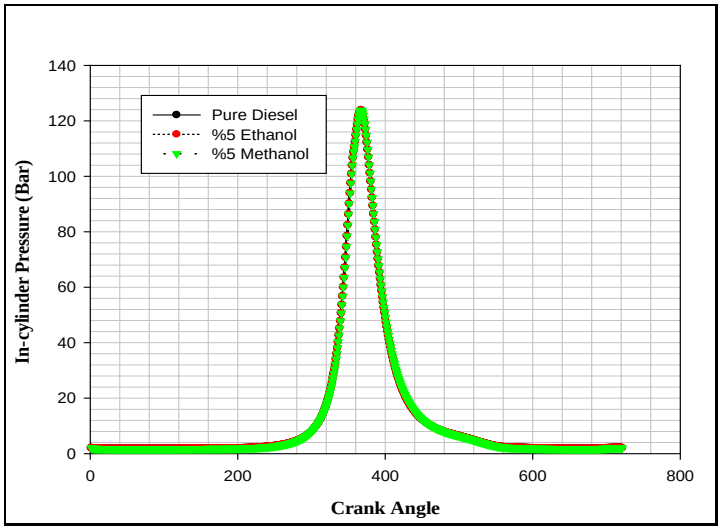

Figure 4. In cylinder pressure with respect to crank angle at 2500 rpm for E5, M5 and Diesel

It can be seen that the in-cylinder pressure for all the fuel blends is almost similar in shape. There is a small variation in the maximum pressure reached during combustion for E5, M5 and Diesel fuels at 2500 rpm. In all the cases, the maximum pressure is noted to be after the TDC. However, maximum pressure position is reached moves away little bit from TDC with the addition of ethanol and methanol contents. It is understood that the maximum torque values were obtained for pure diesel, E5 and M5 at 2500 rpm. It is seen from Fig.4, maximum in-cylinder pressure reaches about 124 bar for pure diesel. This numerical study showed that the decrease of maximum in-cylinder pressure from 124 bar to 123 bar with 5% ethanol and methanol additions to diesel fuel. The engine brake power as a function of engine speeds blended fuels is given in Figure 5.

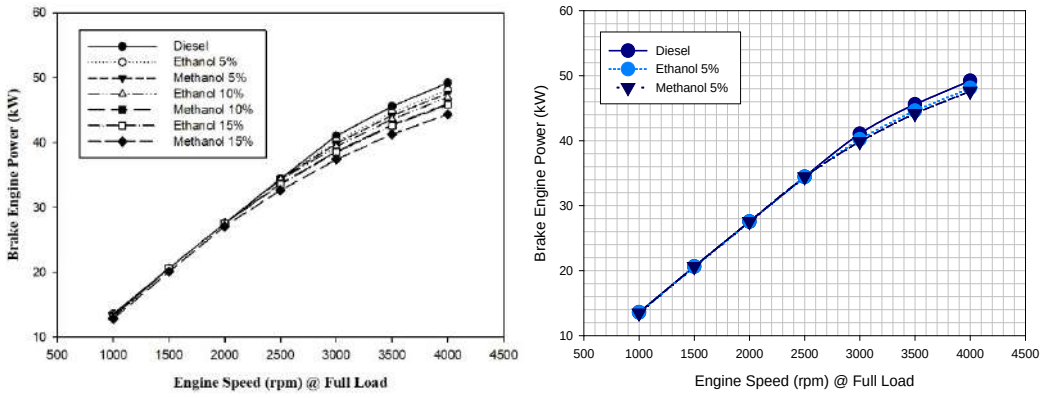

Figure 5. Engine Brake Power with recpect to engine speeds for all additive blended fuel mixtures

When the ethanol and methanol contents was increased in the blended fuel mixtures, it is seen that the engine brake power decreased for all engine speeds. The brake power of pure diesel was higher than those of E5-M5 after engine speeds reach 2500 rpm. The heating value of ethanol and methanol are lower than that of diesel and heating value of the blended fuel mixtures decreases with the increase of the ethanol and methanol contents. The heating value of the blended fuel decreases with the increase of ethanol and methanol contents. As a result of this, lower power outputs are obtained for ethanol and methanol blended fuel mixtures.

Due to the lower flame temperature and lower in-cylinder pressure rise with ethanol–methanol diesel blended fuels, the in-cylinder temperature rise is also lower for ethanol–methanol diesel blended fuels compared to pure diesel operating condition. Canakci et al. [5] also reported this type of behavior for methanol–diesel blended fuels. With the addition of methanol, the cetane number of the blends gets lowered and causes increase in ignition delay. This increase in ignition delay eventually burns more fuel in the premixed phase of combustion, thus the rate of pressure rise increases and peak pressure decreases.

Fig. 6 indicates the variations of the BSFC for ethanol and methanol diesel blended fuels under various engine speeds. As shown in this figure, the BSFC increased as the ethanol and methanol mixture percentage increased. The reason is well known: the heating value and stoichiometric air-fuel ratio are the smallest for this fuel, which means that for specific air-fuel equivalence ratio, more fuel is needed. The higher specific fuel consumptions are obtained at E15 and M15 blended fuel mixtures respectively. Also, a slight difference exists between the BSFC when using pure diesel fuel and when using ethanol and methanol gasoline blended mixture fuels E5 and M5 which are the higher performance fuel mixtures.

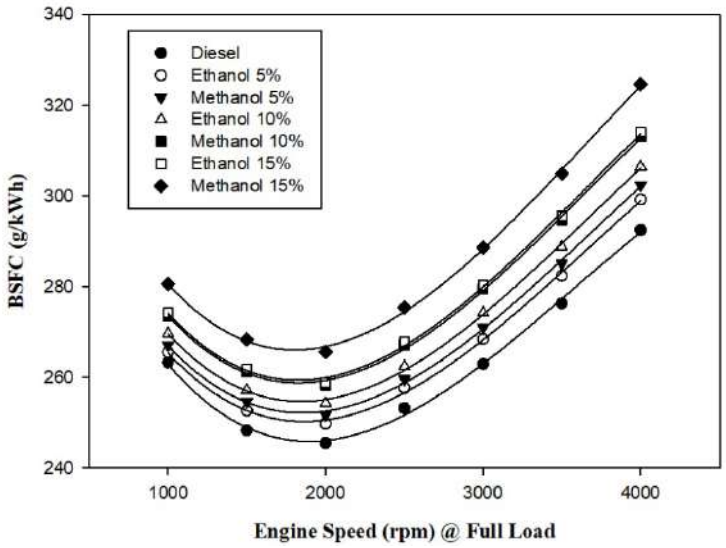

Figure 6. Brake Specific Fuel Consumption (g/kWh) with respect to engine speed

The BSFC is defined as the ratio of mass fuel consumption to the brake power. The Fig. 6 shows that the brake specific fuel consumption trend for diesel and blends are similar in nature. It is understood that increasing ethanol and methanol proportions in the fuel blend increased the BSFC. This behavior is attributed to heating value per unit mass of the ethanol and methanol, which are noticeably lower than that of the pure diesel fuel. The minimum BSFC (247 g/ kWh) was obtained for pure diesel, 251 g/kWh for E5, 254 g/kWh for M5, at 2000 rpm. Starting at the minimum BSFC point, increasing or decreasing speed increased BSFC due to reduction in the engine volumetric efficiency. Therefore, the amount of fuel introduced into the engine cylinder for a desired fuel energy input has to be greater with the ethanol and methanol blended fuel mixtures. These results agree with similar studies [6,7]. The engine exhaust gas temperature as a function of engine speeds for blended fuels is given in Figure 7.

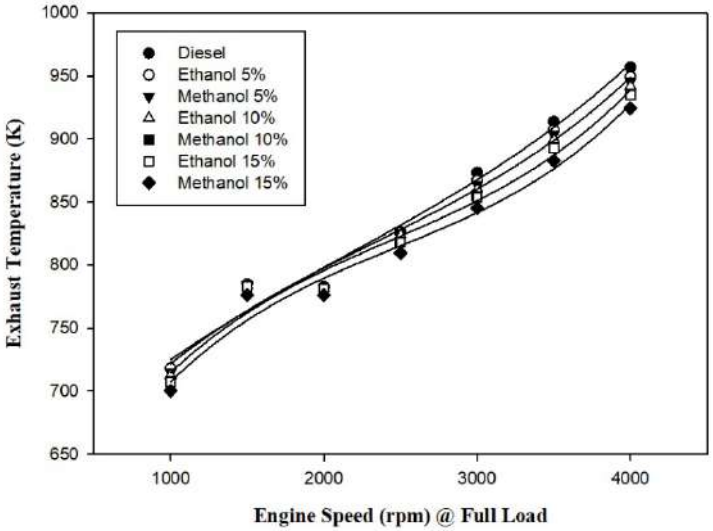

Figure 7. Exhaust gas temperature for all blended fuel mixtures with respect to engine speeds

Fig. 7 shows the variation of exhaust gas temperature for pure diesel and ethanol/methanol blended fuel mixtures. For all of the cases, it is seen that the exhaust gas temperature increases as a function of engine speed. Although there is not a significant difference between results, pure diesel fuel show slightly higher values. The higher latent heat of vaporization of ethanol and methanol compared to diesel lowers the flame temperature and thus the in-cylinder temperature decreases [6,7]. The oxygen present in ethanol and methanol blended fuels enhances the combustion efficiency and it may increase the in-cylinder temperature [8]. However, the present investigation shows that the first factor predominates and thus the temperature is lowered with alcohol blended fuels.

4. CONCLUSION

The engine performance characteristics of a diesel engine using ethanol and methanol fuel blends were investigated by using 1-D modelling. Considering the numerical results, it is possible to say the following conclusions:

Maximum torque value about 132 Nm was obtained at 2500 rpm both E5, M5 and diesel fuels. Under operating conditions where the engine speed is higher than 2500, it is understood that the torque values of the mixture of ethanol and methanol are reduced.

In-cylinder pressure values are almost similar in shape for all the fuel blends. There is a small variation in the maximum pressure reached during combustion for E5, M5 and Diesel fuels at 2500 rpm where the maximum engine torque is obtained.

The BSFC increased with the all ethanol-methanol fuel blends due to the lower LHV of methanol and ethanol. The increase in BSFC with the blend M15 was higher than that of E15. BSFC was obtained minimum values for E5 and M5 within the all ethanol-methanol blended fuel mixtures.

For all of the cases, it is seen that the exhaust gas temperature increases as a function of engine speed. Although there is not a significant difference between results, pure diesel fuel show slightly higher values.

ACKNOWLEDGMENT

The authors would like to express their gratitude to AVL LIST GmbH for Providing a AVL BOOST software under the University Partnership Program.

REFERENCES

[1] Voicu, A. I., Chiriac, R, A numerical simulation of the influence of injection characteristics on performance and emissions of a tractor diesel engine. UPB Scientific Bulletin, Series D: Mechanical Engineering, 74(3), 43–54.

[2] Wojs M.K., Orlinski P., Sar H, Combustion Process In Bi-Fuel Enginepowered By Propane And Diesel Engine. Proceedings of the institute of vehicles 2(102)/2015 2015;2:37–48.

[3] Aldhaidhawi, M., Chiriac, R., Bădescu, V., Descombes, G., Podevin, P, Investigation on the mixture formation, combustion characteristics and performance of a Diesel engine fueled with Diesel, Biodiesel B20 and hydrogen addition. International Journal of Hydrogen Energy, 42(26), 16793–16807. https://doi.org/10.1016/j.ijhydene.2017.01.222

[4] AVL BOOST 2016 Theory and Users guide documentation.

[5] M. Canakci, C. Sayin, M. Gumus, Exhaust emissions and combustion characteristics of a direct injection (DI) diesel engine fueled with methanol diesel fuel blends at different injection timings, Energ. Fuel. 22 (2008) 3709– 3723.

[6] S.H. Park, I.M. Youn, C.S. Lee, Influence of ethanol blends on the combustion performance and exhaust emission characteristics of a four-cylinder diesel engine at various engine loads and injection timings, Fuel. 90 (2011) 748– 755.

[7] R. Song, J. Liu, L. Wang, S. Liu, Performance and emissions of a diesel engine fuelled with methanol, Energ. Fuel. 22 (2008) 3883–3888.

[8] D. Li, H. Zhen, L. Xingcai, Z. Wu-gao, Y. Jian-guang, Physico-chemical properties of ethanol–diesel blend fuel and its effect on performance and emissions of diesel engines, Renew Energ. 30 (2005) 967–976.

ICENS 4TH INTERNATIONAL CONFERENCE ON ENGINEERING AND NATURAL SCIENCE
2-6 May 2018 KIEV UKRAINE

Effect of LED Position on Mass Transfer of Hazelnut (*Corylus Avellana* L.)

Mithat Akgun[1], Levent Kandemir[2]

Abstract

The most important of the main agricultural livelihoods of the Black Sea region of Turkey is hazelnut. This region accounts for about 70% of the total world hazelnut (*Corylus Avellana* L.) production. Hazelnut harvest in the region has generally been carried out in the months of August and September in which the rain and relative humidity is rather high. Average moisture content of harvested hazelnuts was around 30% which has to be lowered to 6% in order to preserve food characteristics of hazelnut kernels for a prolonged storage. Therefore, lowering moisture content of hazelnuts to 6% by sun-drying takes quite a long time and caused quality losses and deteriorations in the kernels. There has long been a need for a mechanical drying system, preserving hazelnut quality with reduced cost in a short time, that can be used both by the producers and manufacturers. An experimental study using a LED with a color temperature of 6500 K as an energy source has been carried out. A mechanical drying system with natural circulation was designed and the effect of increase in the distance between LED and hazelnut (L=5 cm, 10 cm, and 15 cm) on the mass transfer of hazelnut was investigated. The hazelnut kernels of 16-17 mm diameters were LED, sun and oven dried and the drying was terminated when the kernel moisture dropped below 6%. The time-dependent mass losses of hazelnuts in the system and temperature changes in the environment and inside of hazelnut were measured.
The LED drying of 5, 10 and 15 cm distance and sun drying took 74%, 72%, 69%, 52% shorter time, in comparison to sun drying. The internal temperature of hazelnut kernels decreased depending on the increasing distance in LED drying.

Keywords: Fruit drying, Hazelnut moisture, LED color temperature, Mass losses, Sun drying.

1. INTRODUCTION

Generally drying is to remove the water from the products such as food, medicine, textiles, timber and ceramics. The drying characteristics of a product to be dried are very important in terms of product preservation and drying cost.

Food drying is the process of lowering nourishment, which allows food to be stored for long periods of time while preserving its properties. The drying process is carried out naturally or mechanically, depending on the developing technologies. Some agricultural products (wheat, lentils, beans) can be dried naturally (by branch or by solar energy), but mechanization is needed for drying most agricultural products.

Due to the development of refrigerators, storage of foodstuffs by freezing is important in terms of preserving the appearance and taste of foodstuffs. On the other hand, keeping the product at low temperatures for a long time increases energy costs considerably. Thus, storage for the products in large quantities by drying is the oldest and the most suitable method regarding the energy cost.

Drying kinetic of a product is to determine the time-dependent moisture loss from the product, depending on the moisture amount, temperature and flow rate of the drying air. Besides these parameters, the genus, geometry, size and quantity of the product also play an important role in dryer design and optimization.

[1] Corresponding author: Ordu University, Department of Machine and Metal Technologies, 52200, Ordu, Turkey. makgun@odu.edu.tr

[2] Department of Renewable Energy, Graduate College of Science, Ordu University, Ordu/Turkey

To meet the needs of the growing world population in a short time, with the least amount of energy, very different theoretical and experimental studies have been carried out to determine the dryness of the products to dry the food, to develop the drying techniques and its mechanizations.

In the drying process, the first theoretical model for the heat and mass transfer of damp materials was proposed by Luikov in 1973 [1].

Dutta S.K. and others (1988) used the Crank-Nicholson analytical method to solve the differential equation in the case of spherical products, where the mass diffusion coefficient is variable. In that study, numerical results obtained are compared with the experimental data and the suitability of this method for general spherical products is proposed [2].

Murugesan et al. (1996) investigated the distribution of moisture and temperature in porous materials during one-dimensional finite element method in convective drying. Handerson's modified equation is used to calculate the moisture release capability of the materials. With this model, it is stated that the effect of many different parameters on drying for porous materials can be determined [3].

Hawlader et al. (1997) determined the drying characteristics of the tomato by performing experiments at various drying fluid velocities and at different atmospheric conditions. As a result of the analysis of the experiments, a correlation between the effective diffusivity and the temperature/atmospheric air pressure was developed [4].

A diffusion-based drying model has been used for model the single-layer drying of whole hazelnuts by Demirtas et al.(1998). The numerical data so obtained has been presented in the form of a series of curves which represent the drying characteristics of a whole hazelnut. Drying curve of hazelnut was determined for five different air temperature (25 °C, 30 °C, 35 °C, 40 °C, 45 °C), two different air velocity (0,2 m/s and 0,3 m/s) and relative humidity (%60). Experimental results from whole hazelnuts were correlated with the theoretical results [5].

Oztekin et al. (1999) found that the sun's rays at different wavelengths change the chemical structure of the dried product, its coloring and food hygiene [6].

Azzouz et al. (2002) found the drying kinetic of agricultural products as a function of drying conditions, and they calculated the its diffusion coefficient. They used two kinds of grapes in their work. Mathematical relations have been developed to determine the effective diffusivity [7].

Krokida et al. (2003) examined the effect of drying weather conditions (speed, temperature and humidity) and the product characteristic dimension on drying kinetic. The products selected for drying were potatoes, carrots, garlic, mushrooms, onions, leeks, corn, peas, celery, pumpkins and tomatoes. A logarithmic model was used to calculate the moisture transfer. The equilibrium moisture of the dried products was determined as 10%. The study was conducted at two different temperatures of the air (30 ºC and 70 ºC). It was found that the drying constants increased slightly by drying temperature, while the equilibrium moisture decreased with drying temperature [8].

Hussain and Dincer (2003) conducted two-dimensional analysis of heat and moisture transfer during the drying of cylindrical bodies. The end-of-difference approach is used in this analysis. The temperature and humidity distribution in damp bodies were obtained at different time periods, and these results were compared with the literature [9].

Aktas et al. (2005) modeled a hazelnut drying oven with temperature, humidity, weight control and moisture condensation (condensation). They have shown that drying speed and quality can be improved by controlling temperature, humidity and air velocity. The drying system was operated with a heat pump when it was not sunny by considering the energy efficiency [10].

Kaya et al. (2011) investigated drying kinetics, sorption isotherms and mass transfer parameters of hazelnut under various drying air conditions (temperatures at 25 ºC, 35 ºC, 45ºC and 55 ºC; velocities at 0.3, 0.6 and 0.9 m/s; relative humidity values at 20%, 40%, 60% and 80%). Sorption isotherms and drying characteristics of hazelnut are determined for various values of drying air parameters. In addition, the mass transfer parameters (Bi, moisture diffusion coefficient and hm) of hazelnut were evaluated using a correlation [11].

Ozdemir et al investigated the effect of temperature on Turkish hazelnut variety (Tombul). The hazelnut was dried at 35 ° C, 40 ° C, 45 ° C and 50 ° C air temperatures. Changes in fat content, fatty acid com position, free fatty acid content, iodine value, degree of unsaturation and rancimant value were investigated. Oil content, linoleic acid, palmitic acid and stearic acid content were not significantly effected by the drying air

temperatures. The results pointed out that drying air temperature below 45°C is necessary not to disturb stability of the major Turkish hazelnut variety, Tombul [12].

In the Black Sea region, hazelnut is harvested during August and September and because of rains and excessive amount of air moisture, it is necessary to dry hazelnut with additional energy. So, it is important to determine the drying parameters according to hazelnut and to determine technology that will enable the drying of large quantities of hazelnuts in a short time with low energy cost. Tombul Hazelnut (*Corylus Avellana* L.) were used in this experimental study.

Hazelnut is dried mostly spread on the ground and under the sun at the region. The drying time of hazelnuts is 3-7 days at sunny days whereas drying time of hazelnut is over 15 days at the rainy season. When the hazelnut is laid on the ground, aflatoxin is formed during the rainy periods and undesirable quality losses are seen in the nuts.

In this study, the traditional sun drying method of hazelnut is modeled. A LED drying system with natural convection, which is shorter time, more economic and hygienic, has been manufactured and hazelnut drying experiments have been carried out in this system. Picture of harvested fresh Tombul hazelnut was given at Figure 1.a. and picture of hazelnut at the end of drying was given on Figure 1.b.

Figure 1. (a) Fresh Tombul hazelnut

(b) Dried hazelnut (Corylus Avellana L.)

2. MATERIALS AND METHODS

Tombul hazelnut (*Corylus Avellana* L.) variety, harvested from Giresun city in Turkey, was dried. Initial moisture of hazelnut was 26-36 %. Finish moisture of hazelnut dried must be maximum 6%. To solve the problem of drying hazelnut, natural circulation drying system using 6500 K color temperature LEDs has been designed and manufactured. Schematic picture of LED drying system at natural convection is shown in Figure 2 . Photo of drying system with LED is shown in Figure 3.

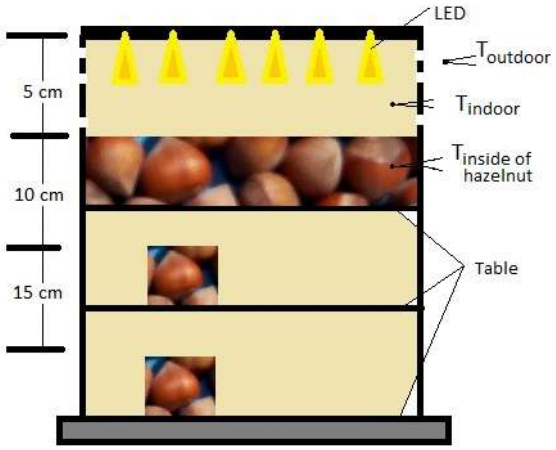

Figure 2. A LED drying system with natural convection

Tombul hazelnut (*Corylus Avellana* L.) was dried with diameter of 16-17 mm. The LED-dried hazelnut was compared to the sun and oven dried hazelnut. The distance between the LED and hazelnut was changed at three dimensions (L = 5 cm, 10 cm and 15 cm). The LED-dried hazelnut was compared to the sun and oven dried

hazelnut. During the experiments, time-dependent mass loss of hazelnut, medium temperature and inner temperature of hazelnut were measured.

Figure 3. Photo of drying system with LED.

3. RESULTS AND DISCUSSION

As a result of drying with LED color temperature, aflatoxin (B1, B2, G1, G2) values were not found in hazelnut. The bioactive compounds values of hazelnut at three different drying conditions are given in Table 1.

Table 1. Effects of drying methods on total phenolics, total flavonoids and antioxidant activity (DPPH and FRAP assay) of hazelnut

Treatments	Bioactive compounds			
	Total phenolics	Total flavonoids	Antioxidant activity (mmol TE kg^{-1} dw)	
	(g GAE kg^{-1} dw)	(g QE kg^{-1} dw)	DPPH	FRAP
Drying in sun	12.16	2.98	5.11	40.95
Drying oven	12.14	1.42	6.06	21.11
6500 K, 5 cm	13.04	1.85	6.05	30.70

Note: Total phenolics and total flavonoids values are respectively expressed as gallic acid and quercetin equivalents. DPPH and FRAP values are expressed as Trolox equivalents.

Phenolic compounds have high antioxidant activity. In the study, the highest phenolic content was determined in hazelnut fruits dried in 6500 K treatment. Also, total flavonoid and antioxidant activity (according to the FRAP assay) of 6500 K treatment was higher contents than dried fruits in oven. As a result, it revealed that LED drying technology can be used as an alternative to other drying methods without any losses in fruit quality attributes. The results of experimental studies are given Figure 4, 5, 6, 7 and 8.

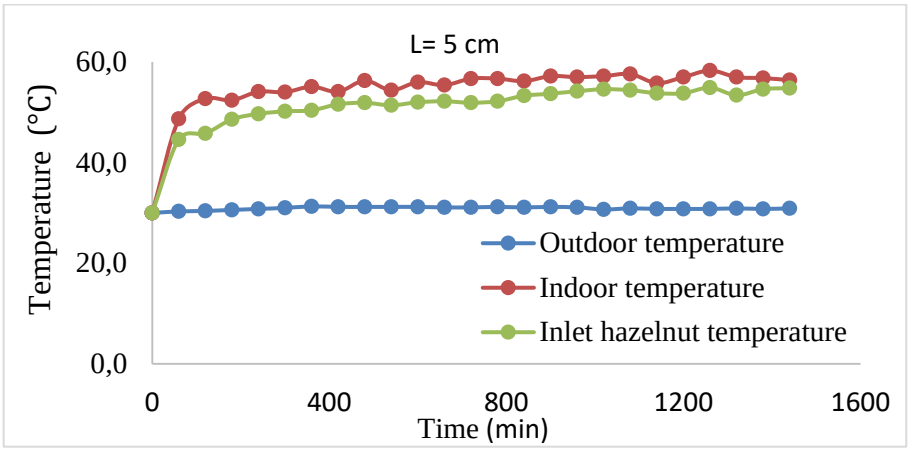

Figure 4. Time dependent change of temperature at drying system with LED (l=5 cm)

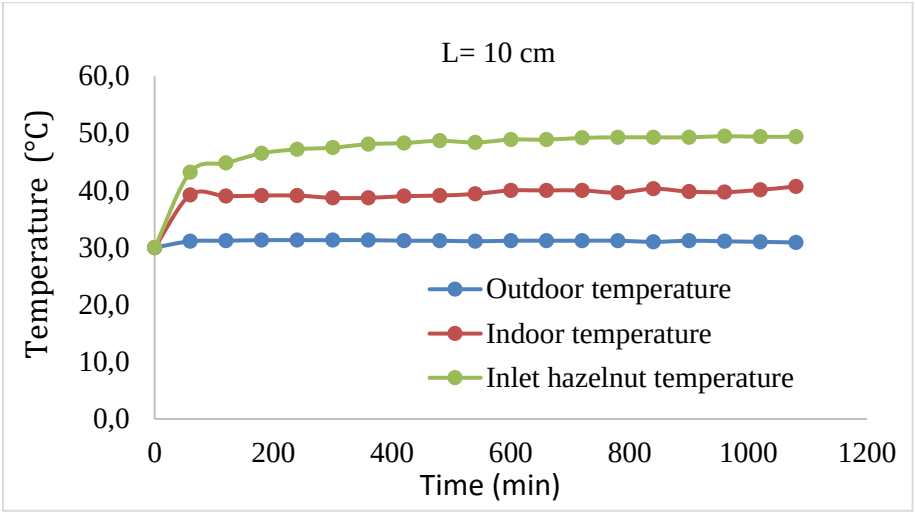

Figure 5. Time dependent change of temperature at drying system with LED (l=10 cm)

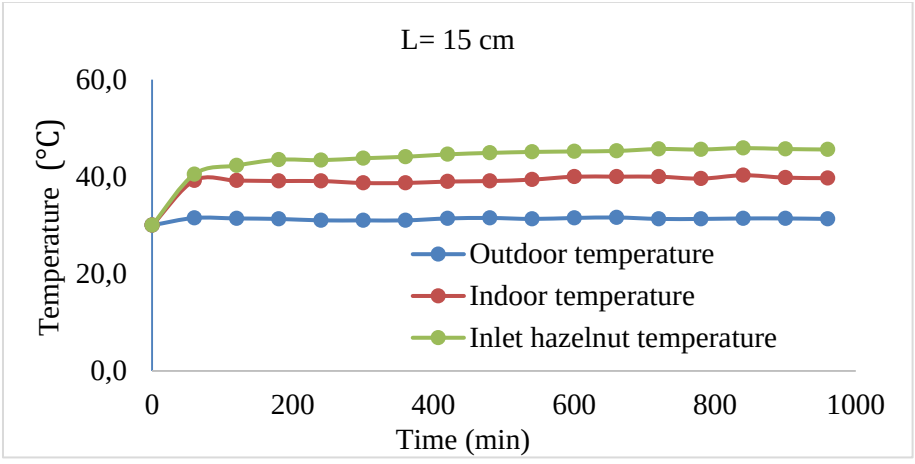

Figure 6. Time dependent change of temperature at drying system with LED (l=15 cm)

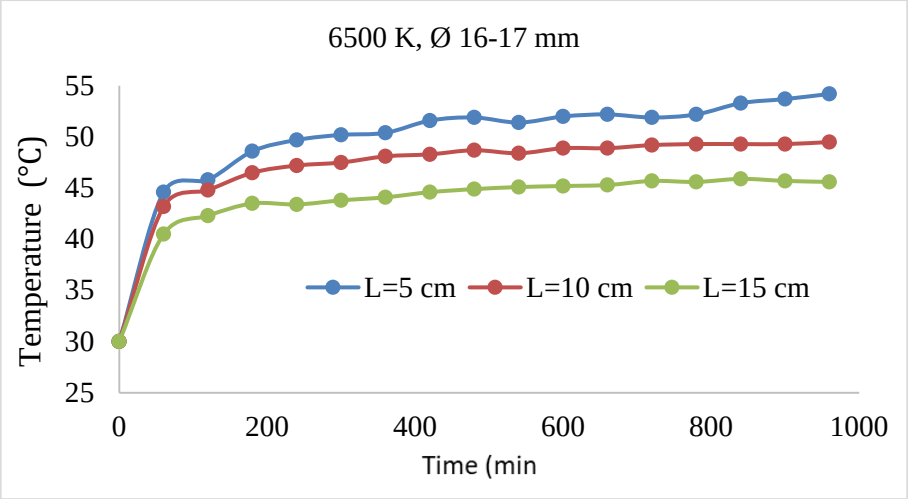

Figure 7. Time dependent change of inlet hazelnut temperature

Since the distance between LEDs and hazelnuts is small (L = 5 cm), temperature fluctuations occur in environment. The heat transfer in the drying system is also caused by transport as well as radiation. For this reason, medium temperature and inlet hazelnut temperature values are very close to each other. As the distance between hazelnut and LED increases, the internal temperature of hazelnut falls.

LED drying time with 5 cm and 10 cm distances are 72 % shorter than drying in the sun. LED drying time with 15 cm distance is 63% shorter than drying in the sun, LED drying time with 5 cm and 10 cm distances are 50% shorter than drying oven, LED drying time with 15 cm distance is 33% shorter than drying oven. Drying time at 5 cm and 10 cm distances are about 25% shorter than drying at 15 cm. Drying time at 5 cm and 10 cm distances is about the same. As expected, drying time is the shortest at a distance of 5 cm. It seems that natural transport is less effective at this distance.

4. CONCLUSION

Drying at 5 cm and 10 cm distance with 6500 K LEDs, it has been found that hazelnut is suitable for drying because it slightly changes the food characteristics of hazelnut, decreases the drying period and consequently decreases the labor and energy costs.

REFERENCES

[1] Lukov A.V., Systems of Differantial Equation of Heat and Mass Transfer in Capillary Porous, Int. Journal of Heat and Mass Transfer, 18, 1-14, 1973.

[2] Dutta S.K., Nema V.K. and Bhardwaj R.K., Drying Behaviour of Spherical Grains, Int.J. Heat Mass Transfer, Vol.31, No.4, Pp. 855-861, 1988.

[3] Murugesan K., Seetharamu K.N. and Narayana P.A.A., A One Dimensional Analysis of Convective Drying of Porous Materials, Heat And Mass Transfer, 32, 81-88, 1996

[4] Hawlader M.N.A., Chou S.K. and Chua K.J., Evelopment of Design Charts for Tunnel Dryers, Int. J. Energy Research, Vol. 21, Pp. 1023-1037, 1997.

[5] Demirtas C., Ayhan T. and Kaygusuz K., Drying behaviour of hazelnuts, J Sci Food Agric, Vol. 76, Issue 4,Pp 559-564, 1998.

[6] Oztekin S., Bastencilik A. and Soysal Y., Crop Drying Programme in Turkey, Renewable Energy, Vol. 16, Pp.789-794, 1999.

[7] Azzouz S., Guizani A., Jomaa W. and Belghith A., Moisture Diffusivity and Drying Kinetic Equation of Convective Drying of Grapes, Journal of Food Engineering, 55, 323-330, 2002.

[8] Ozdemir M., Yildiz M. and Gurcan S. T., Effect of Artificial Drying Air Temperature on Stability of the Major Turkish Hazelnut Variety, Tombul, The Journal Of Food, Vol. 27, 1, 2002.

[9] Krokida M.K., Karathanos V.T., Maroulis Z.B. and Kouris D.M., Drying Kinetics of Some Vegatables, J. Food Engineering, 59: 391-403, 2003.

[10] Hussain M.M. and Dincer I., Two-Dimensional Heat and Moisture Transfer Analysis of a Cylinder Moist Object Subjected to Drying: A Finite-Difference Approac, I. J. Heat and Mass Transfer, 46, 4033-4039, 2003.

[11] Aktas M., Ceylan I. and Dogan H., Design of Industrial Hazelnut Drying Kiln with Heat Pump, Journal of Polytechnic, Vol. 8, No. 4, Pp. 329-336, 2005.

[12] Kaya A., Aydin O. and Akgun M., Drying Kinetics and Moisture Transfer Parameters of Hazelnut, Journal of Food Processing & Preservation, Vol. 35, Issue 5, Pp 714-721, 2011.

About Authors

***Dr*. Mithat AKGUN:** He is presently working as assistant professor at the Department of Machine and Metal Technologies in Ordu University, Turkey. His studies mainly focused on food drying, heat storage and renewable energy sources.

ICENS 4TH INTERNATIONAL CONFERENCE ON ENGINEERING AND NATURAL SCIENCE
2-6 May 2018 KIEV UKRAINE

The Effect Of Different Type Of Fibers On Strength Properties Of Clay Samples

Mehmet Hakan Dogru[1], Suat Akbulut[2]

Abstract

The use of additives to improve the strength properties of soils has been become widespread gradually. Although there are many studies in the literature on materials such as cement and lime as an additive material for soil improvement, there are limited number of studies on fibers as an additive material. In this research, fibers were selected as additive materials and three different fibers (Carbon Fiber, Fiber Glass, Polyvinly Alcohol) have been used for improvement of soil. The strength properties of clay-fiber composites were conducted by a series of Unconfined Compression Test. For prepare the samples, both standard and modified proctor test were used as compaction method. In the experiments, these three fibers were prepared at four different percentages of fiber content (0.1%, 0.2%, 0.3% and 0.4% by weight of soil) at optimum moisture content. In addition to fibers, silica fume was used to increase cohesiveness between soil and fibers. The results show that unconfined compressive strength of clay samples increase with inclusion of fiber additives alone or in combination with silica fume. The highest values of UCS was obtained from 0.2% Carbon Fiber-reinforced clay, %0.3 Fiber Glass-reinforced clay and %0.2 Polyvinly Alcohol reinforced clay.

Keywords: Clay, fiber, shear strength silica fume, soil improvement

1. INTRODUCTION

Rapid population growth, urbanization and industrialization have led to a rapid decline in the site of construction in the world. For this reason, the construction of engineering structures on weak and poor soils has become compulsory. Construction of engineering structures on weak or soft soil is highly risky under normal condition since it can cause differential settlements, poor shear strength, and high compressibility [1]. In this cases, soil improvement is accepted as one of the best engineering options to solve this kind of problems. Soil improvement is defined as a technique to improve the engineering characteristics of soil in order to develop the parameters such as shear strength, compressibility, density; and hydraulic conductivity [2]. Several reinforcement methods are available for stabilizing problematic soils. Therefore, the techniques of soil reinforcement can be classified into a number of categories with different points of view [2]. Basically soil reinforcement is divided into four different categories as mechanical, hydraulic, physical and chemical reinforcement.

Using fibrous materials as a mechanical reinforcement method, is becoming widespread in recent years. Using fibrous materials is divided to 2 group as geosynthetics and randomly distributed fibers. In this research, randomly distributed fibers selected as soil improvement method and three different fiber (Carbon Fiber, Fiberglass, PVA Fiber) used as additives. These three fibers are generally used to improve properties of the concrete. Although there are many applications and studies for concrete, there is limited number of study for use in soil improvement.

In order to increase the cohesiveness between the soil and the fibers, silica fume was used as a second additive material besides fibers. Silica fume is an active pozzolana and it is also generally used to improve the physical and chemical properties of concrete such as fibers. In addition to the use of concrete, it is also becoming more popular in soil improvement. In this research, silica fume were added in low percentages in to some samples to increase the effect of fibers on the strength properties of the soil.

[1] *Corresponding author: Post Graduate Student Yildiz Technical University, Department of Civil Engineering, 34220, Esenler/Istanbul, Turkey. m.hakan.dogru@gmail.com*

[2] *Yildiz Technical University, Department of Civil Engineering, 34220, Esenler/Istanbul, Turkey. sakbulut@yildiz.edu.tr*

In the experiments, these three fibers were prepared at four different percentages of fiber content (0.1%, 0.2%, 0.3% and 0.4% by weight of soil) at optimum moisture content. The prepared mixtures were subjected to Standard Proctor and Modified Proctor Tests. Then the samples obtained from these experiments were subjected to the Unconfined Compression Test and these three fibers were compared among themselves.

1.1. Literature Review

In the literature, there are lots of study on fibers. Generally polypropylene fiber has being selected by researchers as an additive but there is a limited number of study on Carbon Fiber, Fiberglass and PVA Fibers.

Maher [3] have done extensive research on soil improvement with fibrous additives. In his study, the shear strength was generally increased by inclusion of different types of natural fibers in to the soil. Different natural fibers have improved the unconfined strength and deviatoric stress as well as the triaxial strength.

Gao, Zhou, Yu, Wu, & Mahfouz [4] has recently investigated the effect of carbon fiber on the strength properties of the clay. Their study showed that, the UCS of soil can be effectively improved by Carbon Fiber additive. In the experiment the strength increased in the beginning but then decreased with the increase of fiber content. The most significant enhanced quantity was seen when the carbon fiber content is 0.1% soil and strength enhanced proportion reached to 25.6% in this fiber content.

Asadollahi & Dabiri [5], have investigated the effects of fiberglass on the bearing capacity and shear strength of clayey soil. Their results showed that by increasing the content of fiberglass up to 0.8% in clay tends to increase the UCS and shear strength parameters.

Kalkan [6] has studied on UCS of the silica fume stabilized fine-grained soil samples. His study has showed that the maximum UCS of the stabilized fine-grained soil samples contain 30% silica fume content and it improves the Unconfined Compression Strength by 65%.

2. MATERIALS AND METHODS

a. Clay

The soil used in this experimental research was high plasticity clay that was taken from Arnavutkoy region in Istanbul. The soil properties and grain size distribution of clay were showed in Table 1, Figure 1 and Figure 2.

Table 1. Physical properties of Clay

Property	**Value**	
Liquid Limit (%)	60	
Plastic Limit (%)	21	
Plasticity Index (%)	39	
Specific Gravity (GS)	2.64	
Sand Content (%)	12.62	
Silt Content (%)	36.70	
Clay Content (%)	50.68	
Optimum Moisture Content (%)	20.4% (SP)	15.8% (MP)
Max. Dry Unit Weight (KN/m^3)	1.58	1.83
Classificiation (USCS)	CH	

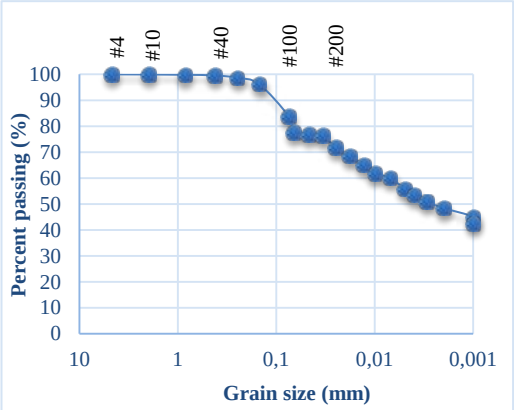

Figure 1. Grain size distribution for clay used in this study

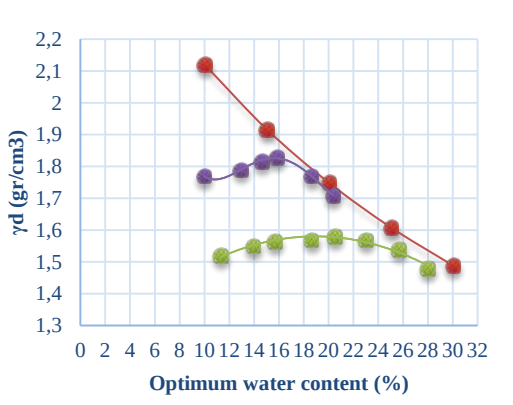

Figure 2. Standard and Modified Compaction Curves of Clay

b. Fibers

The basic physical and mechanical parameters of the Carbon Fiber, Fiberglass and PVA Fiber used in the test are shown in Table 2. The average lengths of fibers are selected as 15mm, 15mm and 6mm for Carbon Fiber, Fiberglass and PVA Fiber, respectively.

Table 2. Fiber properties

Type	Density (g/cm3)	Average Length (mm)	Tensile Strength (Mpa)	Modulus Of Elasticity (Mpa)
Carbon Fiber	1.74	15	3535	2.43*10^5
Fiberglass	2.50	15	1000-3800	0.69*10^5
PVA Fiber	1.26	6	1600	0.34*10^5

Figure 3. (a) Carbon fiber

(b) Fiberglass

(c) PVA fiber

c. *Silica Fume*

The silica fume that is used in this study was taken from Ferro-Chromite Company in Antalya. The physical and chemical properties of silica fume are shown in Table 3 and Table 4.

Table 3. Physical properties of silica fume

Table 4. Chemical properties of silica fume

Physical Properties	Value
Specific Gravity	2.2
Mean Grain Size (μm)	0.15
Specific Area cm^2/gm	150000-300000

Chemical Composition of Silica Fume (%)							
SiO_2	Al_2O	Fe_2O_3	CaO	MgO	K_2O	Na_2O	SO_3
92.26	0.80	1.97	0.49	0.96	1.31	0.42	0.33

d. *Experimental Program*

In the experimental research, experiments were performed on natural and fibers (Carbon Fiber, Fiberglass, PVA Fiber) reinforced clay samples. For observing the effect of different types and amounts of fibers on the Unconfined Compression Strength of clay soil, fibers, silica fume and clay were prepared in 17 different combinations. Then, all these mixtures were subjected to Standard Proctor test. In addition that, Modified Proctor test was also performed on the samples giving the best results in the Standard Proctor Test. Thereafter, Unconfined Compression Test were performed on a total of 75 samples obtained from Standard and Modified Proctor test.

e. *Sample Preparation*

In the process of preparing the samples firstly, the soil was prepared at optimum moisture content and then the desired amount of fiber was added and mixed into the soil. Each fibers were added to the mixtures at four different percentages of fiber content (0.1%, 0.2%, 0.3% and 0.4% by weight of soil). In addition to fibers also silica fume was added to some mixtures. After obtaining of the samples from compaction test the unconfined compression tests were performed immediately.

The experimental program showing the additive amounts of the materials and sample compositions was shown in table 5.

Table 5. Experimental Program

Mixtures	**Compaction Method**
Clay	Standard Proctor/Modified Proctor
Clay + 0,1% Carbon Fiber	Standard Proctor
Clay + 0,2% Carbon Fiber	Standard Proctor/Modified Proctor
Clay + 0,3% Carbon Fiber	Standard Proctor
Clay + 0,4% Carbon Fiber	Standard Proctor
Clay + 0,1% Fiberglass	Standard Proctor
Clay + 0,2% Fiberglass	Standard Proctor
Clay + 0,3% Fiberglass	Standard Proctor/Modified Proctor
Clay + 0,4% Fiberglass	Standard Proctor
Clay + 0,1% PVA Fiber	Standard Proctor
Clay + 0,2% PVA Fiber	Standard Proctor/Modified Proctor
Clay + 0,3% PVA Fiber	Standard Proctor
Clay + 0,4% PVA Fiber	Standard Proctor
Clay + 3% Silica Fume	Standard Proctor/Modified Proctor
Clay + 0,2% Carbon Fiber + 3% Silica	Standard Proctor/Modified Proctor
Clay + 0,3% Fiberglass + 3% Silica	Standard Proctor/Modified Proctor
Clay + 0,2% PVA Fiber + 3% Silica	Standard Proctor/Modified Proctor

3. RESULTS AND DISCUSSION

a. Unconfined Compression Test Results of Fibers Reinforced Samples

To determine the optimum fiber content, each fiber was prepared at four different percentages (0.1%, 0.2%, 0.3%, 0.4%). For Carbon Fiber and PVA Fiber, the highest values of UCS was obtained from 0.2% fiber reinforced clay. For Fiberglass, the highest values of UCS was obtained from 0.3% fiber reinforced clay. Figure 4 represents the unconfined compressive test results of samples reinforced with different percentage of fiber.

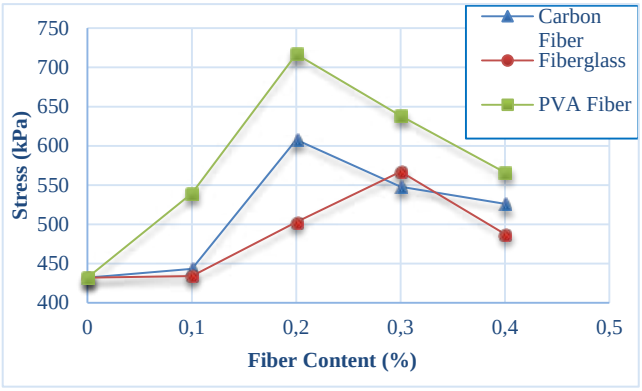

Figure 4. UCS of Carbon Fiber Reinforced Samples

b. Comparison of Unconfined Compressive Strength of Different Fibers Reinforced Samples

Table 6. shows the highest UCS values and improvement rate of each fiber reinforced clay. Results reveals that, improvement rate varies from 31% to 65% according to fiber type. Best improvement rate was obtained from 0.2% PVA fiber reinforced clay with 65%.
In addition that, Figure 5. shows the stress-strain graph of the UCS values in the table. Results show that, fiber additives increase the UCS of soil but on the other hand fiber make the soil more brittle.

Table 6. Highest UCS Values of Fiber Reinforced Clay

Property	UCS (kPa)	Percentage of Improvement (%)
Clay	432	-
0.2CF+Clay	607.80	40.69%
0.3FG+Clay	567.08	31.27%
0.2PVA+Clay	716.88	65.74%

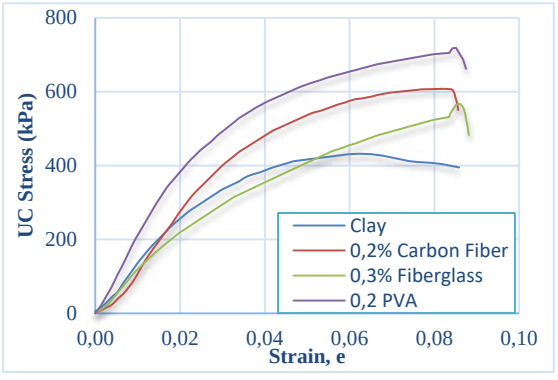

Figure 5. Stress Strain Curves of Fiber Reinforced Clay

c. *The Effect of Silica Fume on Fiber Improved Soil*

In addition to the fibers, silica fume was also used as a second additive material in order to increase the cohesiveness between the fibers and clay. To determine the optimum silica fume amount, silica fume was added to the mixtures at different percentages (from 1% to 5%). The results showed the optimum silica fume percentage as 3%.

The Table 7 represents the UCS improvement rates of fibers reinforced clay with silica fume, and results show that improvement percentages increase with the addition of silica fume.

Table 7. UCS Values of Silica Fume/Fiber Reinforced Clay

Property	UCS (kPa)	Percentage of Improvement (%)	UCS of Silica fume reinforced samples (kPa)	Percentage of Improvement (%)

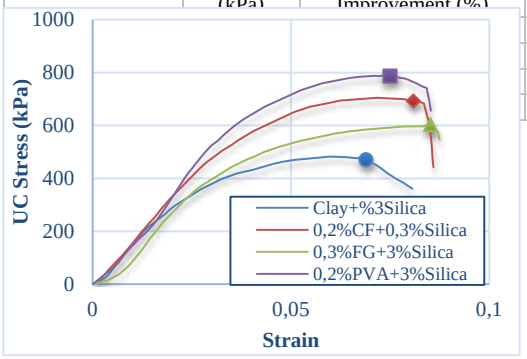

Figure 6. Stress Strain Curves of Silica Fume/Fiber Reinforced Clay

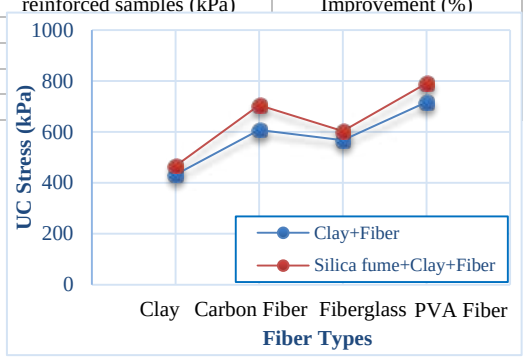

Figure 7. UCS Comparison of Fiber Reinforced Clay and Silica Fume/Fiber Reinforced Clay

d. *The Effects of Compaction Effort on Improvement Rates*

In order to determine the effect of the compaction effort on soil improvement rates, besides Standard Proctor test, Modified Proctor test was carried out.
As can be observed from Table 7 and Table 8, improvement rates decreased in Modified Proctor test compared to Standard Proctor Test. Besides, similar to the Standard Proctor Test, silica fume increased the Unconfined Compression Strength values of samples in MPT

Table 8.UCS Values of Fiber and Silica Fume Reinforced Samples Prepared by Modified Proctor Test

Property	UCS (kPa)	Percentages of Improvement (%)	UCS Silica fume reinforced samples (kPa)	Percentages of Improvement (%)
Clay	1460.40	-	1686	15.44%
0.2CF+Clay	1774	21.47%	1960.45	34.24%
0.3FG+Clay	1626.40	11.37%	1778.98	21.80%
0.2PVA+Clay	1656.30	13.41%	1975.86	35.29%

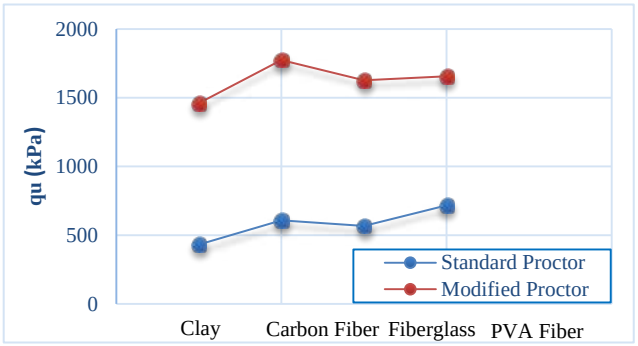

Figure 8.UCS Comparison of Fiber Reinforced Samples Prepared by Standard and Modified Proctor Test

4. CONCLUSION

- The aim of this study was evaluation of the UCS of different type and amount of fiber reinforced soil.
- The results showed that,

I. The UCS of clay can be effectively improved by Carbon Fiber, Fiberglass and PVA Fiber.

II. There is direct relationship between the UCS and weight percentage of fibers. At first, the strength was increased with increase in fiber amount but after 0.2% fiber content for Carbon Fiber and PVA fiber, 0.3 % fiber content for Fiberglass the UCS values decreased with increase in fiber amount.

III. Soil improvement rate varies with fiber type.

IV. Soil improvement rate changes according to the compaction efforts. The improvement rates of Standard Compaction Test are higher than Modified Compaction Test. The improvement rate in the Standard Proctor Test ranged from 31% to 65% for different fibers while the improvement rate in the Modified Proctor Test ranged from 11% to 21%.

V. In addition to fibers, silica fume also improves the UCS of reinforced samples.

REFERENCES

[1] Prabakar, J., & Sridhar, R. S. (2002). Effect of random inclusion of sisal fibre on strength behaviour of soil. *Construction and Building Materials*, *16*(2), 123–131.

[2] Mahdi, S., Sheikhzadeh, M., Mahdi, S., & Zadhoush, A. (2012). A simple review of soil reinforcement by using natural and synthetic fibers. *Construction and Building Materials*, *30*, 100–116.

[3] M. H. Maher and Y. C. Ho. (1994). Kaolin+Fiber Glass, *120*(8).

[4] Gao, L., Zhou, Q., Yu, X., Wu, K., & Mahfouz, A. H. (2017). Experimental study on the unconfined compressive strength of carbon fiber reinforced clay soil. *Marine Georesources & Geotechnology*, *35*(1), 143–148.

[5] Asadollahi, F., & Dabiri, R. (2018). Effects of Glass Fiber Reinforced Polymer on Geotechnical Properties of Clayey Soil Effects of Glass Fiber Reinforced Polymer on Geotechnical Properties of Clayey Soil, (January 2017).

[6] Kalkan, E. (2009). Effects of silica fume on the geotechnical properties of fine-grained soils exposed to freeze and thaw. *Cold Regions Science and Technology*, *58*(3), 130–135

BIOGRAPHY

Mehmet Hakan Dogru has been a Civil Engineer since 2015. He started the graduate study in Yildiz Technical University on Geotechnical branch in 2015 and he is still continuing the study.

ICENS 4TH INTERNATIONAL CONFERENCE ON ENGINEERING AND NATURAL SCIENCE
2-6 May 2018 KIEV UKRAINE

An Alternative Versatile Machining Process: Abrasive Waterjet Machining and Its Remarkable Applications

Cagin Bolat[1], Berkay Ergene[2]

Abstract

Abrasive waterjet machining utilizes a high speed steady flow of water and abrasive particles that can be used to machine different kinds of engineering materials. Machining and cutting with abrasive waterjet equipment has a lot of advantages over other traditional machining processes. The most significant virtue is that no heat is created in the work piece. Availability of wide range of materials and low operation forces are also important features of the process. In practice, main applications of the process are abrasive waterjet cutting(AWJC), abrasive waterjet milling(AWJM) and abrasive waterjet turning(AWJT). Recently, restricted usage of abrasive waterjet machining increases rapidly in order to get quality products for several industrial areas. In this paper, we analyze thoroughly developments in equipment, process parameters and latest applications on suitable materials. In addition to that, we try to explain differences between abrasive waterjet machining and the other conventional methods to emphasize the possibility of the future implementation of the abrasive waterjet machining.

Keywords: waterjet, abrasive particles, machining, cutting

1. INTRODUCTION

Abrasive water jet(AWJ) machining tools have become a rapid alternative of conventional machining processes during the recent years and they have been very popular abruptly in the market as they are very suitable to adapt systems working already in most of the manufacturing plants [1]. In general, high speed water jet systems consist of three main topics which are namely low/high pressure jets, continuous/discontinuous jets and water additive/abrasive water jets. Table 1.1 shows subdivision of high speed water jets in detail and it categorizes high speed jet applications in view of some perspectives [2]. Abrasive water jet machining method is a versatile and quick process that can easily be applied to several types of engineering materials such as steel, aluminum, copper, titanium and nickel alloys (e.g. [3], [4], [5], [6]). The process is also utilized for rocklike material in drilling and weakening operations [7]. Provided that all process parameters (jet pressure value, abrasive particle type and size, traverse speed, standoff distance, nozzle type and operation direction) are adjusted elaborately optimum levels, high quality products having closed tolerances are easefully obtained for targeted usage. Today, using of abrasive water jets increases rapidly in a lot of different industrial sectors like automotive, aircraft, medical, construction, nuclear and decoration [8]. Increasing quality demands and speedy manufacturing necessities of many diversified sectors also trigger new innovative developments and improvements seriously in all water jet processes. Table 1.2 demonstrates the general utilizations of abrasive water jets in today's industry and explains related material types.

[1] *Corresponding author: Istanbul Technical University, Faculty of Mechanical Engineering, 34437, Beyoglu/Istanbul, Turkey. caginbolat@gmail.com.tr*

[2] *Suleyman Demirel University, Faculty of Technology,32260,Isparta,Turkey berkay_ergene@hotmail.com.tr*

Table 30.1 Subsections of high speed water jets [2]

High Speed Water Jets		
Low/High Pressure Jets	**Continuous/Discontinuous Jets**	**Water additive/Abrasive Jets**
a-Plunger pumps up to 270 Mpa **b-Pressure intensifiers up to 400 Mpa**	Discontinuous jets a-Single impact b-Multiple impact	Abrasive water jets a- Three phase jets injection b- Two phase jets

Table 1.2 Some major sectors using AWJ and proper materials [8]

Sector	Material
Aircraft-Aviation	Titanium, aluminum, high strength steel, super alloy
Automotive	Titanium, aluminum, high strength steel
Glass Industry	Wire glass, laminated glass
Building-Construction	Light weight concrete
Composite Material	Fiber reinforced metals and ceramics
Decoration	Glass
Mining	Rocklike materials

2. AWJ PROCESS, COMPONENTS AND SIGNIFICANT VIRTUES

This process works on majorly main principle of water erosion. In the AWJ system, a high velocity well concentrated water and hard abrasive particles are used to machine work-piece material. It exploits kinetic energy of water and abrasive particles to wear and erode the work-piece at localized contact surface. A traditional abrasive water jet system normally consists of five main elements. These are an intensifier pump which is responsible for supplying high-pressure water, an abrasive particle adding module, a cutting head providing mixture for waterjet nozzles, a computer programmed head controller unit which directs the head to desired coordinates and a catcher [9]. Schematic outlook of the whole abrasive waterjet process is drawn in Figure 2.

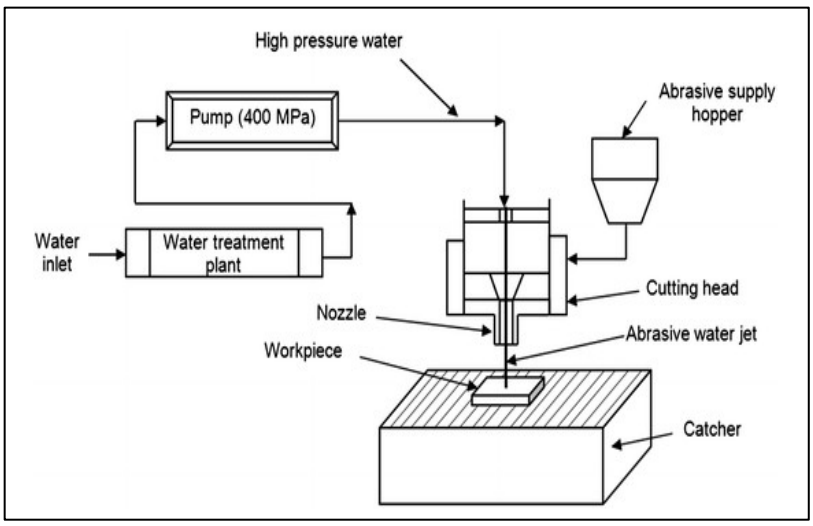

Figure 2. Schematic view of the AWJ process [9]

Most operations usually require abrasive additives to increase erosion ability of the water stream, since only water pressure is not enough to machine target material effectively. The most common abrasive material is established from garnet which is a gemstone and its hardness value and brittleness are considerably high [10]. Apart from garnet, some other abrasive materials like oxides and silicates are also added to high pressure water

[2]. Ultimately, selection of abrasive particle material type depends on the properties of the machined or cut material. In addition to that, economic and financial factors also should be taken into account by manufacturers. Compared to other conventional technics, AWJ have some significant advantages [11];

- AWJ usually automated by CNC or robots to manipulate nozzle path according to desired way. Thanks to this, closed tolerance parts and quick manufacturing properties come comfortably together.
- No heat generated on sample surface (If it is compared with laser cutting, AWJC generates less heat than laser systems on material surface and this means that possibility of any metallurgical alterations on cutting edges can be decreased notably.)
- By comparison with conventional methods, it provides minimum material loses owing to its agility of narrow cutting and sensitive material removing.
- During the process, no environmental setbacks are observed. The feature of environmental friendliness is very promising for the future implementations of the process because in today's industry tendency of clean manufacturing and sensitiveness for nature go up seriously.
- Range of the available materials is pretty wide (from steels to light alloys, composites and rocklike materials) and even in some cases (cutting of plastics, cardboard, rubber etc.) abrasives are not be inset.

3. NEW STUDIES AND INVESTIGATIONS

Super alloys are very useful and preferable engineering materials in aerospace industry and high temperature applications. A study carried out on Ni based super alloys shows that AWJM is proper method for Ni based super alloys and some operation factors affects surface quality. Water jet pressure is found as the most influencing parameter on surface morphology while traverse speed of jet nozzle and stand-off distance are checked up on [12]. Figure 3.1 indicates SEM photograph of garnet particles used in the study.

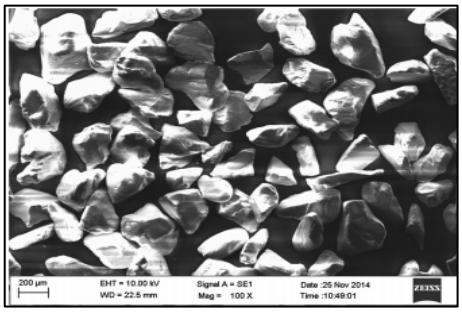

Figure 3.1. SEM micrograph of garnet particles [12]

Due to their high strength/density ratio and good corrosive resistant, titanium alloys are attractive for many engineering applications but machinability features of these materials are poor and they are difficult to machine with traditional processes. AWJM process allows to machine titanium alloys instrumentally. For instance, in a recent research Ti-6Al-4V alloy is used by researchers and the alloy is machined with abrasive jet. The researches attempted to elucidate the effect of process parameters on surface roughness and topography. It has been noticed that the abrasive flow rate and standoff distance are the most important factors [13].

Investigations of cutting of stainless steels via AWJ systems raise and get deep in technical literature. Especially, AISI 304 and 316 series of stainless steels are mentioned frequently. Finite element analysis (FEA) and experimental studies help researchers interpret feasibility of the method for stainless steels. In the light of some studies, it has been said that if cutting speed of the jet increases, surface quality decreases for 316L material and process parameters are able to be optimized by means of FEA for AISI 304 ([14], [15]).

For machining of composite materials, abrasive water jets are widely employed and very popular nowadays. In this context, some examples could be given. According to a study related to glass fiber reinforced vinyl ester matrix, standoff distance is the most effective factor on surface roughness and kerf width [16]. Another paper scrutinizing the cutting performance of hybrid glass carbon reinforced epoxy matrix states that traverse speed, water pressure, and abrasive mass flow rate are considerable parameters for minimum kerf taper and traverse

speed is the most determinant parameter for minimum surface roughness [17]. If we glance at the latest surveys, AWJM processes are also suitable for metal matrix composites like particle reinforced aluminum matrix and Figure 3.2 represents one of them ([18], [19], [20]).

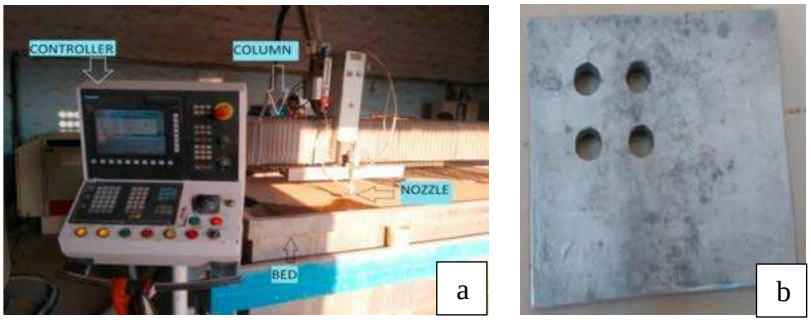

Figure 3.2. AWJM system and machined composite part [20]

Ceramics are very brittle and have low fracture toughness owing to porous structure stemming from their manufacturing stage. Although there are some difficult situations in their machining process, new developments in AWJ systems allow us to remove materials on ceramics. New studies which include ultrasonic vibration equipment into the abrasive waterjet system provide more material removal rate and facilitate the machining operation [21]. Ultrasonic vibration assisted AWJ equipment details can be seen in Figure 3.3.

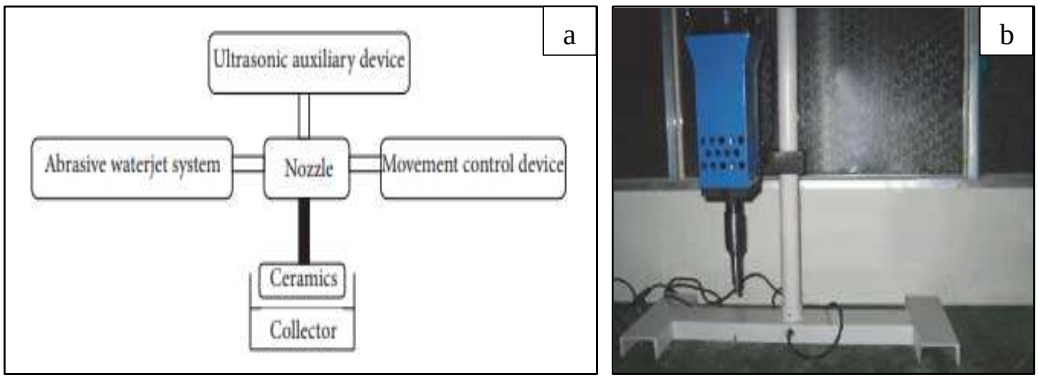

Figure 3.3. Schematic outlook of the process(a) and ultrasonic-abrasive waterjet system(b) [21]

Die design and quality die manufacturing are very sophisticated tasks requiring a lot of efforts for engineers. However, AWJC method introduces some bright solutions for cutting of die steels. One of the most common die steel in the industry is D2 steel and it is clearly true to say that D2 steel can be cut properly by the AWJC process. Experiments conducted on D2 steel indicates that impingement angles, jet pressure and abrasive mesh size influence the cutting performance. Furthermore, 225 MPa jet pressure, #100 mesh size and 70° angle are optimum values [22].

Magnesium alloys are very conspicuous materials in some industries for which strength/density ratio of the parts is vital. In order to get maximum performance from these alloys in service conditions, true surface morphology and closed tolerances must be attained. AWJC process of the magnesium alloys and parameter optimization works go up gradually in technic literature. [23].

Cross section of AWJC part surfaces is divided into three main sections comprising of initial zone, smooth zone, and rough zone. Fig 3.4 shows the zones in detail. The smooth zone has the highest surface quality. However, the rough zone has the worst surface quality since it has a lot of striations. Recent surveys claim that secondary cutting operations improve the surface quality and kerf taper properties. Opposite direction secondary cutting improves surface quality and reduces striations. Moreover, reversed positive secondary cutting contributes hugely to kerf taper properties [24].

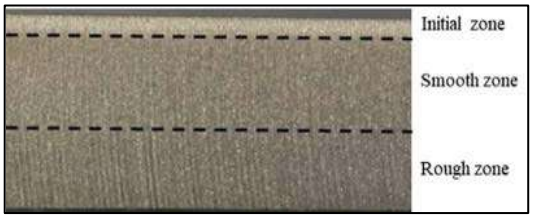

Figure 3.4. Three different zones in the cross section after AWJC

Statistical approaches and experimental design methods are pretty popular in the latest investigations about factors affecting abrasive water jet machining process. With increment of the reliability on computer based statistical design methods, researchers are prone to analyze parameters and their interactions if they are present. In spite of the fact that there are several experimental design methods, Taguchi robust design and response surface method are the most preferable methods ([25], [26], [27]). Additionally, Taguchi design offers the users two options for minimum and maximum outputs thanks to its "smaller is better" and "larger is better" modules. In terms of the type of the result parameter, proper module is selected. In Figure 3.5, effects of the three parameters (pressure, traverse speed and flow rate) on cutting depth are shown by using "larger is better" module [27].

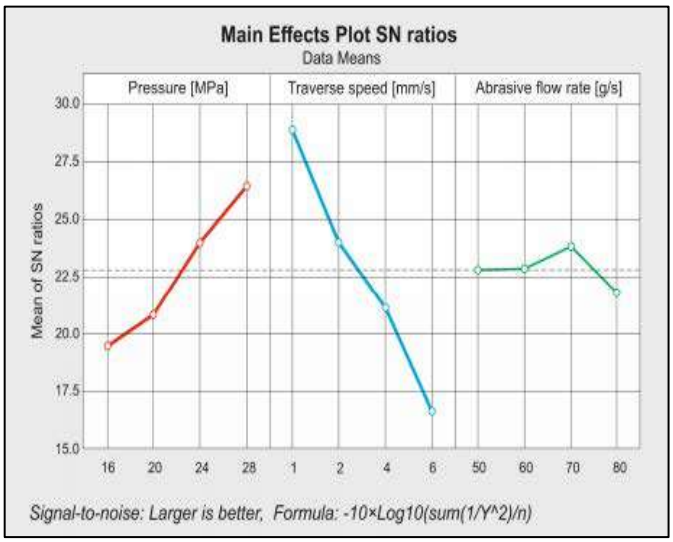

Figure 3.5. Taguchi main effects plot for cutting depth [27]

Wood plastic composites are created by the combination of the polymer matrix and wood particles or chips and chemicals such as flame retardants and binders. After the wood is inset, polymer matrix gains stiffness and strength. An investigation about availability of wood plastic composites to AWJM process finds out that AWJM is an appropriate way for these composites and owing to its low heat melting risk of polymer matrix can be prevented. Figure 3.6 depicts the composite and its #80 mesh machined circumstance clearly [28].

Figure 3.6. Wood plastic composites and AWJ machined sample [28]

Friction stir welding (FSW) is one of the solid-state welding methods which has grown fast since 1991 and has been used in a wide range of application areas (aerospace, automotive and maritime) [29]. Abrasive water jet cutting of friction stir welded parts has such a great advantage that unlike other conventional or non-traditional techniques, AWJC generates no heat affected zone after the cutting process [30].

Nowadays, using of the AWJC process in stone industry steps up discernibly. High speed hard abrasives with high pressure water can erode the materials from stone and rocklike samples. If researches being relevant to that case are probed, there is no inconveniency to say that AWJC of stone materials is possible with high dimensional accuracy. In an example study carried out last year, carrara marble is cut with AWJC and some process parameters are examined to optimize its surface quality. As a result of the study, it has found that even though stand-off distance and traverse rate indicate an opposite effect on both surface roughness and waviness, kinetic of the abrasive waterjet causes better surface quality [31]. Another study about AWJC of rocks shows that kerf taper problems after the process can be diminished by selecting of appropriate parameters, particularly traverse speed [32].

4. CONCLUSIONS

Abrasive waterjet machining process is a useful method for most of the engineering materials (from steels to rock). By means of the AWJ systems, closed tolerances and quality cut surfaces are formed easily. In this paper, we tried to create general viewpoint about abrasive waterjet system, its main components and application areas as well as familiarization of advantages of the process. In addition to this, we endeavored to touch on the newest studies and researches about AWJ process and its implementations on different engineering materials. In the light of this survey, the following results can be expressed;

- AWJ operations generate no heat on sample surfaces while laser and conventional cutting creates excessive heat around machined zone which leads to undesired metallurgical alterations. Laser or other similar methods conduct huge amount of heat on material surface to melt or boil it in the cutting operations and after that, around the cut edge some local heat effective zones causing structural changes (e.g. from soft phase to brittle phase) emerge. In sharp contrast to this, in the process of AWJC there is no excess heat on material cut surfaces.
- Material portfolio of AWJ systems is very wide in comparison with other conventional or non-conventional methods. For example; electrical discharge machining(EDM) is completely dependent on electrical conductivity of materials or agility of material removing in CNC machining is limited to hardness values of tools.
- AWJ systems are automatized and integrated to other lines for mass production. Especially, AWJC method provides swift production and high quality cut surfaces. Closed tolerances and precise dimensions are formed without any problem.
- Compared to conventional machining such as turning, milling and CNC machining, very precise dimensions are obtained in part geometry by AWJM. This advantage is hugely important for dimensional sensitive applications.

- Some materials (ceramics, marbles, rocklike objects, etc.) are considerably difficult to cut or machine owing to their extreme hardness values. AWJM and AWJC are practical option to cut or machine these materials and resolve the hardness drawbacks whereas other conventional and some advanced methods are not capable of machining those.
- In view of environmental pollution, abrasive waterjet systems are clean and have no harmful effects.
- AWJC process is combined with ultrasonic systems in order to improve cutting performance and to facilitate the cutting of hard materials.
- Technic literature and research and development activities in the industry point out that AWJ systems are very promising for the future developments from metal industry to stone sector. Parameter optimization studies and prevention of kerf taper setbacks are the main theme of the new researches.

REFERENCES

[1] Kedar M. Relekar, Ashish B. Kalase, Sachin Pralhad Dubal, "Abrasive Waterjet Machining", *International Journal of Innovations in Engineering Research and Technology*, Vol 2, pp.2394-3696, 2015.

[2] A.W.Momber, R.Kovacevic, *Principles of abrasive water jet machining*, 2012.

[3] N. Muthukrishnan, M. Naresh Babu,"Investigation on Surface Roughness in Abrasive Water-Jet Machining by the Response Surface Method", *Materials and Manufacturing Processes, Journal Materials and Manufacturing Processes* Vol. 29, Issue 11-12, 2014.

[4] M. Uthayakumar, , M. Adam Khan, S. Thirumalai Kumaran, A. Slota,"Machinability of Nickel-Based Superalloy by Abrasive Water Jet Machining", *Materials and Manufacturing Processes* ,Vol.31, Issue 13, 2014.

[5] A. Hascalik, U. Caydas, H. Gurun,"Effect of traverse speed on abrasive waterjet machining of Ti–6Al–4V alloy", *Materials & Design*, Vol. 28, Issue 6, pp.1953-1957, 2007.

[6] A. Akkurt, M.K. Kulekci, U. Seker, F. Ercan,"Effect of feed rate on surface roughness in abrasive waterjet cutting applications", *Journal of Materials Processing Technology*, Vol.147, Issue 3, pp.389-396, 2004.

[7] A.W.Momber, R.Kovacevic,"Test parameter analysis in abrasive water jet cutting of rocklike materials", *International Journal of Rock Mechanics and Mining Sciences*, Vol.34, Issue 1, pp.17-25, 1997.

[8] M.K. Kulekci, "Processes and apparatus developments in industrial waterjet applications" *International Journal of Machine Tools and Manufacture*, Vol.42, Issue 12, pp.1297-1306, 2002.

[9] M.Shukla, "Abrasive Water Jet Milling", *Nontraditional machining processes: Research advances* **,** pp.177-203, 2013.

[10] D.Austin, " Looking Inside the Waterjet Cutting Head", *Canadian Industrial Machinery*, October 2013.

[11] M. P. Groover, *Fundamentals of Modern Manufacturing*, Fourth Edition, 2010 John Wiley & Sons, Inc.

[12] M. Uthayakumar, M. Adam Khan, S. Thirumalai Kumaran, A. Slota, J. Zajac, "Machinability of Nickel-Based Superalloy by Abrasive Water Jet Machining", *Materials and Manufacturing Processes*, Vol.31, Issue 13, 2016.

[13] S.Vasanth, T.Muthuramalingam, P.Vinothkumar, T.Geethapriyan, G.Murali, "Performance Analysis of Process Parameters on Machining Titanium (Ti-6Al-4V) Alloy Using Abrasive Water Jet Machining Process", *Procedia CIRP*, Vol. 46, pp.139-142, 2016.

[14] M.Junkar, B.Jurisevic, M.Fajdiga, M.Grah, "Finite element analysis of single-particle impact in abrasive water jet machining", *International Journal of Impact Engineering*, Vol. 32, Issue 7, pp.1095-1112, 2006.

[15] P. Loschner, K. Jarosz, P. Niesłony,"Investigation of the Effect of Cutting Speed on Surface Quality in Abrasive Water Jet Cutting of 316L Stainless Steel", *Procedia Engineering*, Vol.149, pp.276-282, 2016.

[16] M. Armagan, A. Armagan Arici, "Cutting performance of glass-vinyl ester composite by abrasive water jet", *Materials and Manufacturing Processes*, Volume 32, Issue 15, 2017.

[17] R. Selvama, L. Karunamoorthy, N. Arunkumar, "Investigation on performance of abrasive water jet in machining hybrid composites", *Materials and Manufacturing Processes*, Vol. 32, NO. 6, pp.700–706, 2017.

[18] A. Gnanavelbabu, K. Rajkumar, P. Saravanan, "Investigation on the cutting quality characteristics of abrasive water jet machining of AA6061-B4C-hBN hybrid metal matrix composites", *Materials and Manufacturing Processes*, 2018.

[19] A. Nag, A. Kumar Srivastava, A. Rai Dixit, S. Chattopadhyaya, A. Mandal, D. Klichová, P. Hlaváček, M. Zeleňák, S. Hloch, "Influence of Abrasive Water Jet Turning Parameters on Variation of Diameter of Hybrid Metal Matrix Composite", *Applications of Fluid Dynamics*, pp 495-504, 2017.

[20] K. Ravi Kumar, V.S.Sreebalaji, T.Pridhar,"Characterization and optimization of Abrasive Water Jet Machining parameters of aluminium/tungsten carbide composites", *Measurement* ,Vol. 117, pp.57-66, 2018.

[21] T. Wang, R. Hou, Z. Lv, "Experimental Investigation on the Material Removal of the Ultrasonic Vibration Assisted Abrasive Water Jet Machining Ceramics", *Advances in Materials Science and Engineering*, Volume 2017, Article ID 1365786.

[22] N. Yuvaraj, M. Pradeep Kumar, "Investigation of process parameters influence in abrasive water jet cutting of D2 steel", *Materials and Manufacturing Processes*, Vol.32, Issue 2, pp.151-161, 2017.

[23] C.A. Niranjan, S.Srinivas, M.Ramachandra, "An Experimental Study on Depth of Cut of AZ91 Magnesium Alloy in Abrasive Water Jet Cutting", *Materials Today: Proceedings*, Volume 5, Issue 1, Part 3, pp.2884-2890, 2018.

[24] X. Miao, Z. Qiang, M. Wu, L. Song, F.Ye, "Research on quality improvement of the cross section cut by abrasive water jet based on secondary cutting", *The International Journal of Advanced Manufacturing* Technology, pp. 1–10, 2018.

[25] R. Shukla, D. Singh, "Experimentation investigation of abrasive water jet machining parameters using Taguchi and Evolutionary optimization techniques", *Swarm and Evolutionary Computation*, Vol.32, pp.167-183, 2017.

[26] M. Santhanakumar, R. Adalarasan, M. Rajmohan, "Experimental Modelling and Analysis in Abrasive Waterjet Cutting of Ceramic Tiles Using Grey-Based Response Surface Methodology", *Arabian Journal for Science and Engineering*, Volume 40, Issue 11, pp 3299–3311, 2015.

[27] A. Perec, "Abrasive Suspension Water Jet Cutting Optimization Using Orthogonal Array Design", *Procedia Engineering*, Vol.149, pp 366-373, 2016**.**

[28] Z. Hutyrová, J. Ščučka, S. Hloch, P. Hlaváček, M. Zeleňák, "Turning of wood plastic composites by water jet and abrasive water jet", *The International Journal of Advanced Manufacturing Technology*, Vol.84, Issue 5–8, pp 1615–1623, 2016.

[29] B.T. Gibson, D.H. Lammlein, T.J. Prater, W.R. Longhurst, C.D. Cox, M.C. Ballun, K.J. Dharmaraj, G.E. Cook, A.M. Strauss, "Friction stir welding: Process, automation, and control", *Journal of Manufacturing Processes*, Vol. 16, Issue 1, pp 56-73, 2014.

[30] R. Kumar, S. Chattopadhyaya, A. Rai Dixit, B. Bora, M. Zelenak, J. Foldyna, S. Hloch, P. Hlavacek, J. Scucka, J. Klich, L. Sitek, P. Vilaca, *The International Journal of Advanced Manufacturing Technology*, Vol.88, Issue 5–8, pp 1687–1701, 2017.

[31] M.S. Alsoufi, D.K. Suker, M.W. Alhazmi, S. Azam, "Influence of Abrasive Waterjet Machining Parameters on the Surface Texture Quality of Carrara Marble", *Journal of Surface Engineered Materials and Advanced Technology*, pp 25-37, 2017.

[32] L.M. Hlaváč, I.M. Hlaváčová, V. Geryk, "Taper of kerfs made in rocks by abrasive water jet (AWJ)", *The International Journal of Advanced Manufacturing Technology*, Vol.88, Issue 1–4, pp 443–449, 2017.

BIOGRAPHY

Res. Assistant Berkay ERGENE, who works in Mechanical and Manufacturing Department at Suleyman Demirel University (SDU) in Turkey. He is PhD student in Mechanical and Manufacturing Engineering Department at SDU. He interests in mechanical and manufacturing science and also characterization of the auxetic structures manufactured by additive manufacturing.

ICENS 4TH INTERNATIONAL CONFERENCE ON ENGINEERING AND NATURAL SCIENCE
2-6 May 2018 KIEV UKRAINE

Finite Element Analysis for Compression Behaviour of Polymer Based Honeycomb and Re-entrant Structures

Berkay Ergene[1], Bekir Yalcin[2]

Abstract

Advanced technology requires new manufacturing methods and new structures which are light, efficient and convenient in order to meet the needs of the industries. Recently, honeycomb and re-entrant (auxetic) cellular structures have been studied due to their unique properties such as energy and vibration absorbing capability, indentation resistance, homogeneous load distribution and being applicable to take a place in sandwich composite structures. Furthermore, polymer materials have been mainly used in many application because of their lighweight, excellent optical properties and to manufacture them less expensive and easily. The examined studies show that cellular structures can be manufactured by new trend additive manufacturing from various polymer materials. After doing literature surveys about honeycomb and re-entrant structures, these structures with three different rib thicknesses of 1 mm, 1.5 mm and 2 mm were designed and then polymer material was selected to use in finite element analysis (FEA). In FEA, the compression loads were applied to honeycomb and re-entrant structure under determined boundary conditions, then, and their compression behaviour was investigated. In conclusion, the obtained FEA values were compared to determine the compression behavior of polymer honeycomb and re-entrant structures. The biggest increment in σ_{vm} results were observed while rib thickness of t were changed 2 mm to 1.5 mm for all. The results exhibit that honeycomb structure expands and re-entrant structure shrinks along x axis. Furthermore, expansion values of honeycomb always higher than shrinkage values of re-entrant for all rib thickness. On the other hand, re-entrant structure has been shortening more than honeycomb structure in all rib thickness precisely.

Keywords: Cellular structure, FEA, Honeycomb, Polymer, Re-entrant (auxetic)

1. INTRODUCTION

Nowadays, cellular structures with enhancement mechanical properties like energy and sound damping, indentation resistance, higher strength with low weight and using less manufacturing materials are preferred to provide needs of industrial firms in order to move technology one step further. However, it is not so easy to design cellular structures as desired design. That's why, new manufacturing method like additive manufacturing provides a geometric design freedom unrivalled by traditional manufacturing methods such as extrusion, machining or turning, coupled with the increased accessibility of this new manufacturing technology in last years [1]. The examined studies (e.g.[2], [3], [4]) show that cellular structures can be manufactured by new trend additive manufacturing from various polymer materials. Cellular structures can be classified into two main categories as non-auxetic (honeycomb) and auxetic (re-entrant) structures. It was expressed that one advantage of cellular material over solid material can be (depending on the design of the structure and its resultant behavior) in load case [4]. When loading is applied, the structure first absorbs the energy before the actual material of the cell wall gets deformed. If impact loading is applied, this situation becomes more apparent: while a solid material gets damaged directly, most of cellular materials stretch or compress initially until the cell structure deformation is reached. In addition, Ashby [5] mentions that energy absorbing cellular materials have struts (cell walls) with a bending-dominated deformation under stress conditions, which means large strains, but low stiffness and strength. Besides, the stiffness decreases with the decreasing of density [6]. Also, cellular materials are needed to increase the stiffness and strength at low density as shown in Figure 1.1.

[1] *Corresponding author: Suleyman Demirel University, Department of Mechanical and Manufacturing Engineering, 32200, Merkez/Isparta, Turkey. berkay_ergene@hotmail.com*

[2] *Suleyman Demirel University, Department of Mechanical and Manufacturing Engineering, 32200, Merkez/Isparta, Turkey. bekiryalcin@sdu.edu.tr*

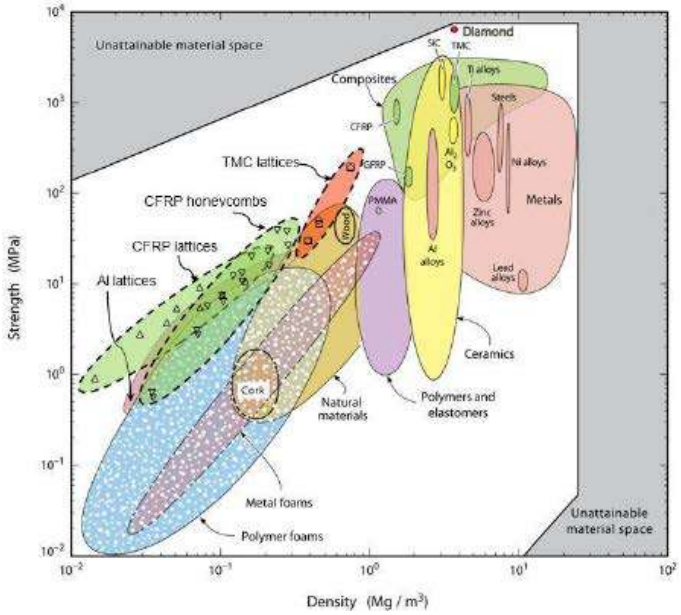

Figure 1.1. Density over strength of solid and cellular materials [7]

The "auxetic" term has been pronounced by Lakes firstly [8] and then many researches ([9], [10], [11], [12]) has been done about auxetic materials. Auxetic materials differ from other structures because of their different geometry shape. The poisson's ratio can be defined as the ratio of lateral contractile strain to the longitudinal tensile strain for a material undergoing tension in the longitudinal direction so it shows how much a material becomes thinner when it is stretched. Therefore, most of the materials have a positive ν. In case of counterintuitive behavior of auxetic material, it undergoes lateral expansion when stretched longitudinally and becomes thinner when compressed (13],[14]) In addition, auxetic structures possess appealing potential for various applications such as sandwich panel cores, energy and sound dampening structures, radome frames, aerospace filler foams, and bio-implants due to their unique shear stiffness [15], indentation resistance [16] (Figure 1.2), high fracture toughness [17], high energy dissipation ability [18] and great acoustic absorption abilities [19].

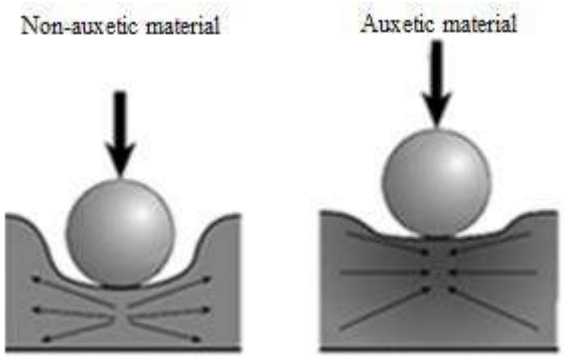

Figure 1.2. Indentation behaviour in non-auxetic and and auxetic materials [20].

In this research, a comparative study of mechanical behaviours for regular honeycomb and re-entrant (auxetic) structure is carried out by using FEA. The construction of honeycomb and re-entrant designs were evaluated with their deformation mechanism under compressive load.

2. MATERIALS AND METHODS

a. Finite Element Modelling

First of all, material of regular honeycomb and re-entrant were assigned as a solid ABS material which has elastic modulus of 2200 MPa, poisson's ratio of 0.35 and density 1.05 g/cm^3 and these material constants [2] were used in finite element program to determine material properties of regular honeycomb and re-entrant structures. After that, cell size of regular honeycomb with height (h) = length (l) = 5.2 mm, rib angle (θ)= 30^0 and cell size of re-entrant structure with h=10 mm, l=5 mm, θ=-30^0 and rib thickness (t) values vary as 1, 1.5 and 2 mm for both structures like shown in Figure 2.1(a) regular honeycomb structure and in Figure 2.1(b) re-entrant structure.

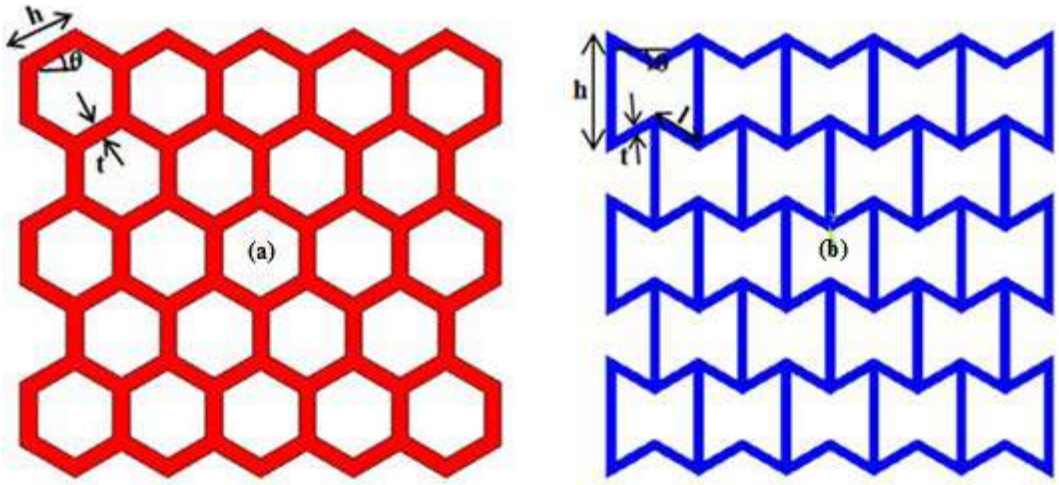

Figure 2.1 (a) The dimensional definition for regular honeycomb structure, (b) for re-entrant auxetic structure.

Afterwards, the regular honeycomb and re-entrant structure models were designed by engineering design program and then were exported to the finite element based program in order to investigate the finite element analysis (FEA) results. Furthermore, regular honeycomb and re-entrant structures from ABS material were meshed homogeneously. Moreover, both structures were fixed as ancastre from the bottom and then compression stress 0.5 MPa were applied from the top of the structures as boundary conditions which can be seen in Figure 2.2. Thus, 2D FEA were carried out for these new design structures and their mechanical behaviour such as normal stresses σ_x and σ_y von-mises stress of σ_{vm} , shear stress of τ_{xy} and displacement values along x and y axis of Δl_x and Δl_y under compression stress were obtained from analysis.

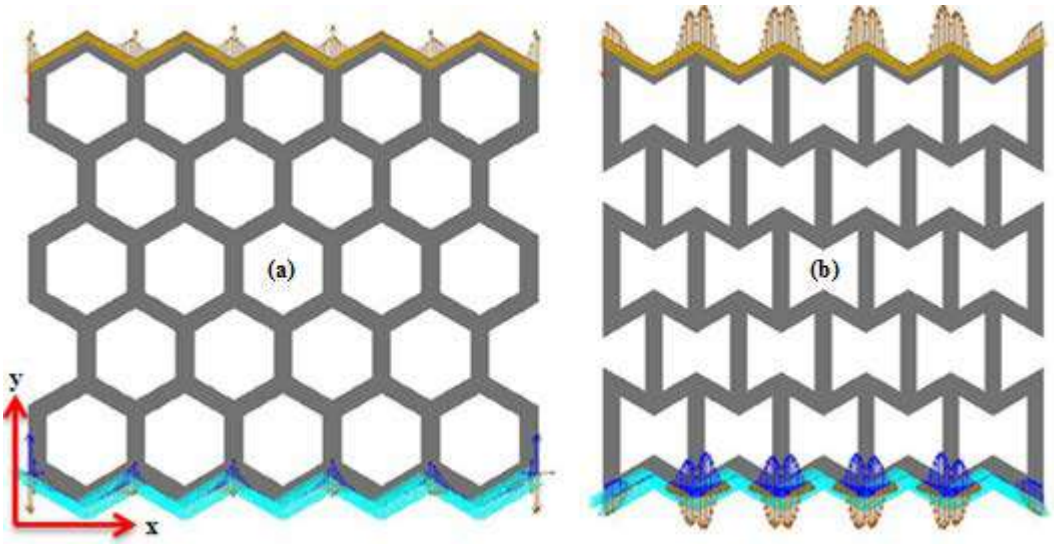

Figure 2.2 (a) boundary condition and loading status of regular honeycomb structure, (b) boundary condition and loading status of re-entrant structure.

3. RESULTS

a. Stress Results

Firstly, when the 0.5 MPa compression stress was applied to the top of the honeycomb in FEA, expansion through x axis and shortening through y axis were observed. On the other hand, shrinkage through x axis and shortening through y axis were obtained for re-entrant structure under same loading status. As a result of FEA, it can be commented that re-entrant (auxetic) structures have negative poisson's ratio although honeycomb structures have positive poisson's ratio like shown in Figure 3.1 which was formed by using FEA results. Moreover, Whitty et al. [21] emphasized about changing the rib thickness leads to a change in the poisson's ratio for honeycomb and re-entrant structures.

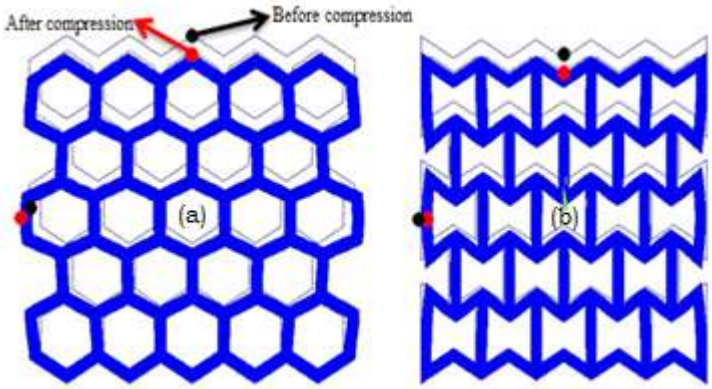

Figure 3.1. Images from FE analyses about, (a) honeycomb structure expansion, (b) the shrinkage of re-entrant structure under compression loads.

The maximum σ_{vm} for t of 2 mm for honeycomb structure was obtained around 13.795 MPa, σ_{vm} for t of 1.5 mm as 20.406 MPa and σ_{vm} for t of 1 mm as 42.723 MPa. Also, maximum σ_{vm} for t of 2 mm for re-entrant structure was obtained around 8.373 MPa, σ_{vm} for t of 1.5 mm as 14.484 MPa and σ_{vm} for t of 1 mm as 34.154 MPa. Hence, the maximum stress was observed on the smallest rib thickness of 1mm for both structures. Besides, these obtained results show that higher von-mises stress values occur on honeycomb structure than re-

entrant structure for all rib thickness values. Moreover, the biggest increment in results were observed while rib thickness of t were changed 2 mm to 1.5 mm for all.

In addition, shear stress of τ_{xy} on honeycomb structures were obtained as 5.874 MPa, 9.638 MPa and 19.493 MPa for t of 2mm, 1.5mm and 1 mm respectively. When the obtained shear stress of τ_{xy} were glanced over re-entrant structures, τ_{xy} for t of 2 mm was obtained 3.025 MPa, τ_{xy} for t of 1.5 mm as 5.447 MPa and τ_{xy} for t of 1 mm as 12.613 MPa. Same increment trend like in von-mises stress was visible for shear stress too when t decreasing. Lastly, von-mises stress results, general von-mises stress distribution on honeycomb structure, general von-mises distribution on re-entrant structure and shear stress results can be seen in Figure 3.2(a), Fig. 3.2(b), Fig. 3.2(c) and Fig.3.2(d), respectively. Furthermore, Aslam et al. [22] reported that increasing of the relative density in auxetic structures decreases stresses in structure occurred under loads.

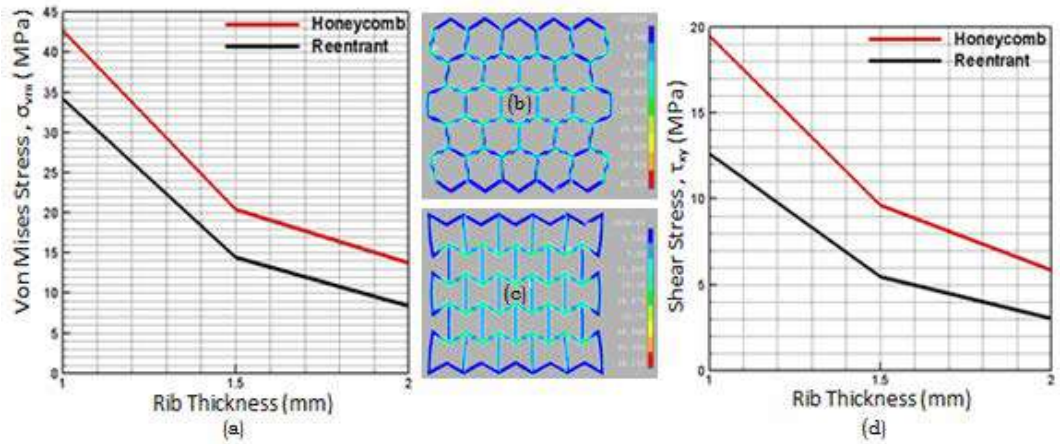

Figure 3.2. Stress results of FEA (a) von-mises stress results, (b) general von-mises stress distribution on honeycomb structure, (c) general von-mises stress distribution on re-entrant structure, (d) shear stress results.

According to the obtained FEA results, σ_x values were 12.161 MPa, 18.208 MPa and 39.007 MPa for honeycomb structure with t of 2 mm, 1.5mm and 1mm respectively and the results were obtained as 6.565 MPa for t of 2mm, 10.569 MPa for t of 1.5mm and 21.128 MPa for t of 1mm on re-entrant structures. Likewise, σ_y values were 11.619 MPa, 19.343 MPa and 43.235 MPa for honeycomb structure with t of 2 mm, 1.5mm and 1mm respectively and the results were obtained as 8.442 MPa for t of 2mm, 13.748 MPa for t of 1.5mm and 30.936 MPa for t of 1mm on re-entrant structures. The tendency of σ_x and σ_y for honeycomb and re-entrant structures were shown in Fig. 3.3(a) and Fig. 3.3(b). As a result, it can be considered that σ_x values are mostly higher than σ_y values for both structures and honeycomb structure consists of bigger normal stresses in comparison with re-entrant structures.

(a)

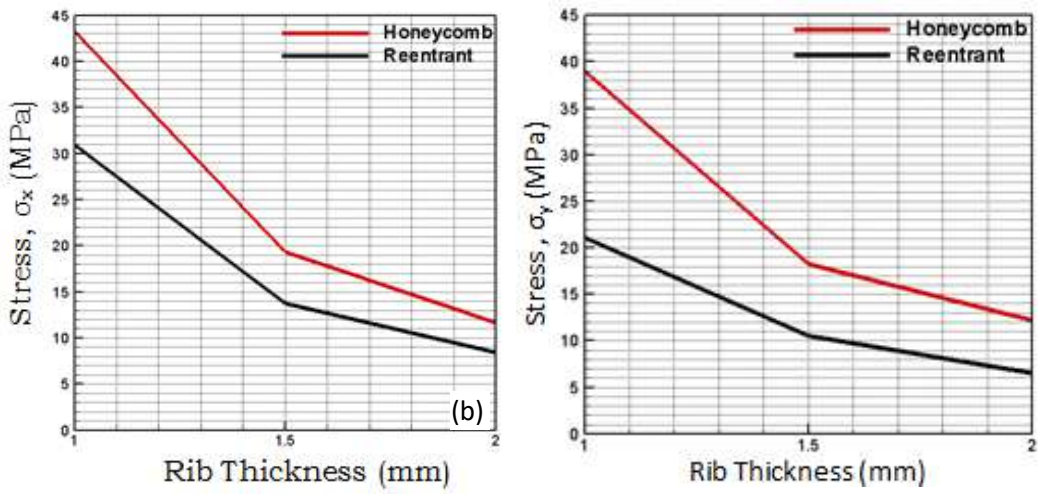

Figure 3.3. The tendency of σ_x (a) and σ_y (b) for honeycomb and re-entrant structures.

b. Displacement Results

The displacements obtained from the analyses were given in Fig. 3.4. According to Fig. 3.4(a), the displacement values (Δl_x) along x axis for honeycomb structure having t of 1 mm, 1.5 mm and 2 mm were respectively obtained as expansion of 0.8696 mm, 0.3121 mm and 0.1582 mm. Also, 0.3639mm shrinkage for t of 1mm, 0.0821mm shrinkage for t of 1.5mm and 0.0210mm shrinkage for t of 2mm were observed for re-entrant structure. In Fig. 3.4(b), the displacement values (Δl_y) along y axis for honeycomb structure having t of 1 mm, 1.5 mm and 2 mm were respectively obtained as shortening of 0.5364 mm, 0.2296 mm and 0.1380mm. Also, 0.5997mm shortening for t of 1mm, 0.2495mm shortening for t of 1.5mm and 0.1512mm shortening for t of 2mm were observed for re-entrant structure. The results exhibit that honeycomb structure expands and re-entrant structure shrinks along x axis. Furthermore, expansion values of honeycomb always higher than shrinkage values of re-entrant for all rib thickness. On the other hand, re-entrant structure has been shortening more than honeycomb structure in all rib thickness precisely and it is visible in Fig. 3.4(b).

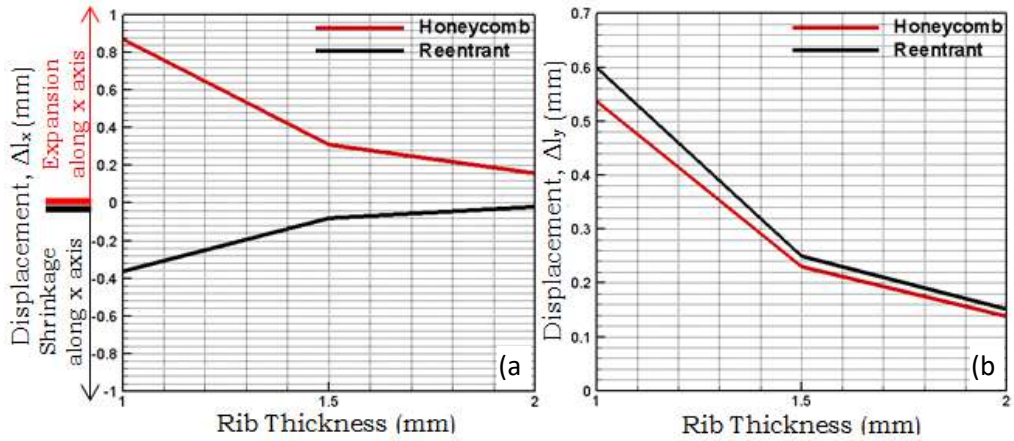

Figure 3.4. Displacement results, (a) displacement of Δl_x, (b) displacement of Δl_y

4. CONCLUSIONS

In the light of this survey, the following results can be expressed;

- ✓ It can be commented that re-entrant (auxetic) structures have negative poisson's ratio although honeycomb structures have positive poisson's ratio like shown in Fig. 3.1.
- ✓ The maximum σ_{vm} for t of 2 mm for honeycomb structure was obtained around 13.795 MPa, σ_{vm} for t of 1.5 mm as 20.406 MPa and σ_{vm} for t of 1 mm as 42.723 MPa. Also, maximum σ_{vm} for t of 2 mm for re-entrant structure was obtained around 8.373 MPa, σ_{vm} for t of 1.5 mm as 14.484 MPa and σ_{vm} for t of 1 mm as 34.154 MPa. Hence, the maximum stress was observed on the smallest rib thickness of 1mm for both structures.
- ✓ The biggest increment in σ_{vm} results were observed while rib thickness of t were changed 2 mm to 1.5 mm for all.
- ✓ Shear stress of τ_{xy} on honeycomb structures were obtained as 5.874 MPa, 9.638 MPa and 19.493 MPa for t of 2mm, 1.5mm and 1 mm respectively. When the obtained shear stress of τ_{xy} were glanced over re-entrant structures, τ_{xy} for t of 2 mm was obtained 3.025 MPa, τ_{xy} for t of 1.5 mm as 5.447 MPa and τ_{xy} for t of 1 mm as 12.613 MPa.
- ✓ σ_x values were 12.161 MPa, 18.208 MPa and 39.007 MPa for honeycomb structure with t of 2 mm, 1.5mm and 1mm respectively and the results were obtained as 6.565 MPa for t of 2mm, 10.569 MPa for t of 1.5mm and 21.128 MPa for t of 1mm on re-entrant structures. Likewise, σ_y values were 11.619 MPa, 19.343 MPa and 43.235 MPa for honeycomb structure with t of 2 mm, 1.5mm and 1mm respectively and the results were obtained as 8.442 MPa for t of 2mm, 13.748 MPa for t of 1.5mm and 30.936 MPa for t of 1mm on re-entrant structures.
- ✓ The displacement values (Δl_x) along x axis for honeycomb structure having t of 1 mm, 1.5 mm and 2 mm were respectively obtained as expansion of 0.8696 mm, 0.3121 mm and 0.1582 mm. Also, 0.3639mm shrinkage for t of 1mm, 0.0821mm shrinkage for t of 1.5mm and 0.0210mm shrinkage for t of 2mm were observed for re-entrant structure. In Fig. 3.4(b), the displacement values (Δl_y) along y axis for honeycomb structure having t of 1 mm, 1.5 mm and 2 mm were respectively obtained as shortening of 0.5364 mm, 0.2296 mm and 0.1380mm. Also, 0.5997mm shortening for t of 1mm, 0.2495mm shortening for t of 1.5mm and 0.1512mm shortening for t of 2mm were observed for re-entrant structure.
- ✓ The results exhibit that honeycomb structure expands and re-entrant structure shrinks along x axis. Furthermore, expansion values of honeycomb always higher than shrinkage values of re-entrant for all rib thickness. On the other hand, re-entrant structure has been shortening more than honeycomb structure in all rib thickness precisely.

REFERENCES

[1]. S. R.G. Bates, I. R. Farrow, R.S. Trask, "3D printed polyurethane honeycombs for repeated tailored energy absorption", *Materials and Design*, 112 (2016) 172–183.
[2]. A. Ingrole, A. Hao, R. Liang, "Design and modeling of auxetic and hybrid honeycomb structures for in-plane property enhancement", *Materials and Design*, 117 (2017) 72–83.
[3]. P. Koudelka1, O. Jirou, T. Fíla1,T. Doktor, "Compressive properties of auxetic structures produced with direct 3D printing", *Materials and technology* 50 (2016) 3, 311–317.
[4]. A. Alderson, K. L. Alderson, " Auxetic materials", *Proc. IMechE* Vol. 221 Part G: J. Aerospace Engineering, 565-575.
[5]. Ashby M. F. (2006): "The properties of foams and lattices", *Philosophical Transactions of the Royal Society A*, 364, 15-30.
[6]. X. Zheng, H. Lee, T. H. Weisgraber, M. Shusteff, J. Deotte, E. B. Duoss, J. D. Kuntz, M. M. Biener, J. A. Jackson, S.O. Kucheyev, N.X. Fang, C.M. Spadaccini, "Ultralight, ultrastiff mechanical metamaterials." *Science*, 344 (6190), 2014, 1373-1377.
[7]. http://www.virginia.edu/ms/research/wadley/celluar-materials.html Last Access: March 19, 2018
[8]. K.E. Evans, "Auxetic polymers: a new range of materials". *Endeavour*, 15 (4), 1991, 170-174.
[9]. L.Yang, O. Harrysson, H. West, D. Cormier, "Mechanical properties of 3D re-entrant honeycomb auxetic structures realized via additive manufacturing", *International Journal of Solids and Structures* 69–70 (2015) 475–490.
[10]. N. Novak, M. Vesenjak, Z. Ren, "Auxetic cellular materials - a review", *Journal of Mechanical Engineering* 62(2016)9, 485-493.
[11]. Y. Chen, M.H. Fu1, "A novel three-dimensional auxetic lattice meta-material with enhanced stiffness", *Smart Mater. Struct.* 26 (2017) 105029 (1-11).
[12]. I.I. Argatov, R.G. Diaz, F.J. Sabina, "On local indendation and impact compliance of isotropic auxetic materials from the continuum mechanics viewpoint", *Int. Journal of Engineering Science*, 54, 2012, 42-57.

[13]. K. E. Evans, A. Alderson, "Auxetic materials: functional materials and structures from lateral thinking!," *Advanced Materials*, vol. 12, no. 9, pp. 617–628, 2000.
[14]. K. E. Evans, K. L. Alderson, "Auxetic materials: the positive side of being negative," *Engineering Science and Education Journal*, vol. 9, no. 4, pp. 148–154, 2000.
[15]. F. Scarpa, G. Tomlinson, "Theoretical characteristics of the vibration of sandwich plates with in-plane negative Poisson's ratio values", *J. Sound Vib*, 2000, 230, 45–67.
[16]. K.L. Alderson, V.R. Simkins, V.L. Coenen, P.J. Davies, A. Alderson, K.E.Evans, "How to make auxetic fibre reinforced composites" *Phys. Status. Solidi (B)* , 2009, 57, 1865–1874.
[17]. M. Bianchi, F.L. Scarpa, C.W. Smith, "Stiffness and energy dissipation in polyurethane auxetic foams", *J. Mater. Sci.* ,2008, 43, 5851–5860.
[18]. A. Bezazi, F. Scarpa, "Mechanical behaviour of conventional and negative Poisson's ratio thermoplastic polyurethane foams under compressive cyclic loading" *Int. J. Fatigue*, 2007 29, 922–930.
[19]. F. Scarpa, W.A. Bullough, P. Lumley, "Trends in acoustic properties of iron particles seeded auxetic polyurethane foam", *Proc. Inst. Mech. Eng. Part C J. Mech. Eng. Sci.* , 2004, 218, 241–244.
[20]. V. H. Carneiro, J. Meireles, H. Puga," Auxetic materials – a review" , *Materials Science-Poland*, 31(4), 2013, pp. 561-571.
[21]. J.P.M. Whitty, F. Nazare, A. Alderson, "Modelling the effects of density variations on the in-plane poisson's ratios and young's moduli of periodic conventional and re-entrant honeycombs - part 1: Rib thickness variations." *Cellular Polymers*, 21 (2). pp. 69-98.
[22]. M. U. Aslam, S.M. Darwish, "Development and analysis of different density auxetic cellular structures", *Int. Journal on Recent and Innovation Trends in Computing and Communication*, 2015, 3 (1), 27-32.

BIOGRAPHY

Res. Assistant Berkay ERGENE, who works in Mechanical and Manufacturing Department at Suleyman Demirel University (SDU) in Turkey. He is PhD student in Mechanical and Manufacturing Engineering Department at SDU. He interests in mechanical and manufacturing science and also characterization of the auxetic structures manufactured by additive manufacturing.

ICENS 4TH INTERNATIONAL CONFERENCE ON ENGINEERING AND NATURAL SCIENCE
2 - 6 May 2018 KIEV UKRAINE

A Traffic Systematic Proposal for Manned and Unmanned Aerial Vehicles Encounter

Mutlu Iptec[1], Bunyamin Ciylan[2], Arif E. Sivgin[3]

Abstract

Number of unmanned aerial vehicles (UAV) in market and in usage rapidly increasing. Thanks to that rapid increase in market field applications of the UAV's also spread. This spread provides an accessible, efficient, low cost, practical transport for human being. On the other hand, it also brings out the risk of accidents in the air in case of overpopulated aerial network and nonexistence of basic traffic rules provided and controlled by a central control and observer system or systems. In this study, possible encounters of manned and unmanned aerial vehicles in a future crowded aerial network was modeled and possible difficult to solve outcomes like accidents, safety problems, integration of different types of aerial vehicles and different networks were studied. Those possible outcomes were taken as needed input for creation of the basics of the UAV network rules. At the end of the study, a prioritization triangle was designed to avoid possible negative outcomes. In this triangle the aerial vehicle which has the highest priority in the traffic keeps the top line of the triangle, and the lowest priority one vice versa. Triangle was filled with aerial vehicle types which have different characteristics in terms of their urgency situation, autonomy level, flight altitude and their central observer systems.

Keywords: Aerial Traffic, Drone, Prioritization, Rules, UAV

1. INTRODUCTION

Number of UAV (Unmanned Aerial Vehicles) is increasing day by day. According to the SESARJU (Single European Sky ATM Research Joint Undertaking) the specific category fleet size will evolve from under 10 000 drones in 2015 to nearly 400 000 drones in 2050 [1]. There is also going to be 4.3M fleet using for commercial aims at 2020 and 10% of those vehicles will be self-flying. So, a huge crowded aerial network traffic around the world is on the way [1]. The numbers show that a traffic problem is waiting for the aerial vehicles in next 10 years. Although there are different studies and applications to manage the unmanned aerial vehicles one by one or for small groups, there is such a need to create universal and easy to apply rules to prevent accidents [2]. In this article management of unmanned and manned aerial vehicles encounter during their daily life operation is taken into account and a prioritization for their 3-dimensional (3-D) route planning during encounter is studied. Prioritization in the traffic is expected to provide the main problem in a 3-D space since it creates a wider space by the time. Although there are different viewpoints to solve the traffic problem like utilizing the air traffic controller (ATC) system rules, creating different and basic rules for unmanned aerial vehicles is necessary due to their higher maneuverability. Prioritization should include both among unmanned aerial vehicles and the manned and unmanned aerial vehicles. This prioritization should also fit the current expectations of future aerial vehicle network and their classification.

In this study, it is aimed that to create a set of rules to provide a view for how to handle future aerial traffic.

2. MATERIALS AND METHODS

In this study, GUTMA (Global UTM Association) unmanned aerial vehicle traffic management architecture proposal is used as a guide for creating the possible encounters during flight [3]. In this proposal, there is a central UAS (Unmanned Aerial System) Traffic Management System to communicate all surroundings like

[1] *Gazi University, Informatics Institute, Forensics Sciences Department, Tunus Avenue No:35 Kavaklidere, Cankaya/Ankara Turkey. mutluiptec@gmail.com*

[2] *Corresponding Author: Gazi University, Department of Computer Engineering,06570 Ankara. bciylan@gazi.edu.tr*

[3] *Gazi University, Informatics Institute, Information Systems, Tunus Avenue No:35 Kavaklidere, Cankaya/Ankara Turkey. aesivgin@yahoo.com*

ATM (Air Traffic Management) Systems, UAS, UAS Registration System, conventional airspace users, situational awareness system, surveillance sensors, spatial data infrastructure, meteorological sensors etc.

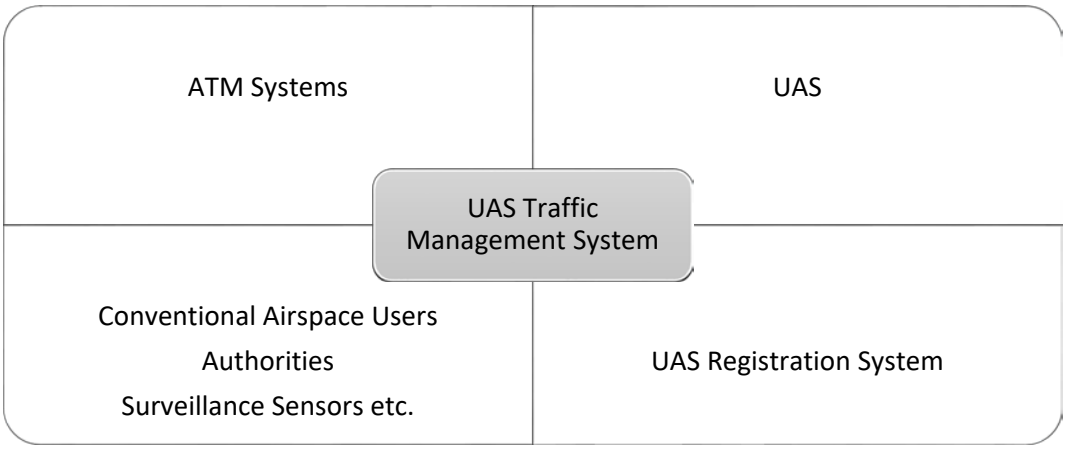

Figure 1: A view of UTM System [3]

In addition; Unmanned Aircraft Systems classification by US DOD (Department of Defense) is used to understand the complication of the air traffic in case of encounter of different levels of aerial vehicles [4]. In this classification, there are 5 different categories in terms of their operating altitudes. The most important part of this classification is that, group 3 and group 4 vehicles have the same operating altitudes, 18000 ft AGL (above ground level).

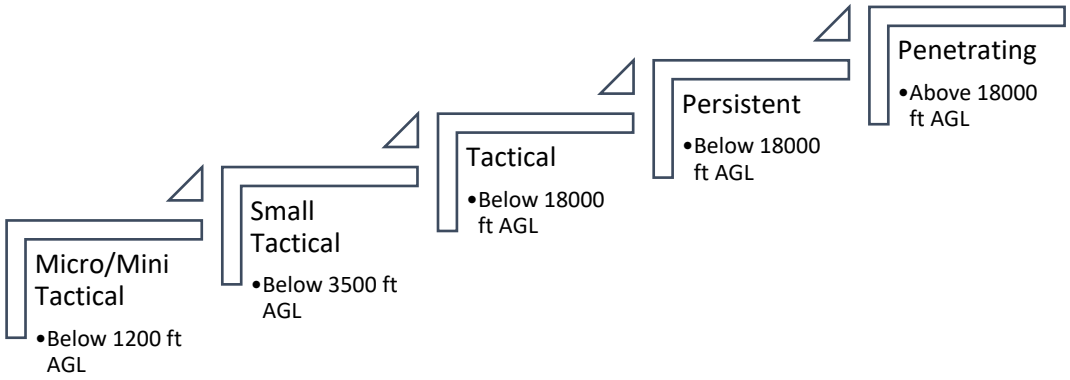

Figure 2: DOD UAS Classification [4]

Level of autonomy of the aerial vehicles is also used as an input for prioritization purpose. It is clear that higher autonomy aerial vehicles are going to have higher fitting with the aerial traffic rules to be set, so higher autonomy aerial vehicles have a higher priority in terms of possible encounter with another aerial vehicle which has same characteristics but less autonomy.

The transport type is used as another characteristics in terms of traffic prioritization. As the aerial vehicles carrying cargos have less importance in terms of public safety when compared with another aerial vehicle which has the same characteristics but carrying passengers, passenger carrying aerial vehicles do have a higher priority in the proposed solution.

During the problem solution phase, prioritization of the human safety and health is used as the main principle for proposal. Possible urgent conditions during the flight, passenger safety and the maneuverability of the vehicles are considered as key inputs for the solution. Maneuverability of the vehicles are important in terms of their side effects on the other vehicles and the traffic safety.

In the study for creation of set of rules, manned and unmanned aerial vehicles for possible encounters in a closed UAS network can be figured out by above characteristics; however, when it comes to real application on an open aerial 3-D space, there will be other outer players from the UAS network, which are ATC controlled traditional aircrafts. Since ATC controlled aircrafts are either traditional civil/military vehicles or UAV's which have very high technology that can even transport numbers of passengers from one place to another, maneuverability of those vehicles are also very low, which brings out the model.

3. RESULTS AND DISCUSSION

In the study, there is a precondition proposed to solve the probable main conflicts during encounter in a future aerial vehicles network. These preconditions are standard type segmentation, level of autonomy and the cargo types. When the segmentation, level of autonomy and the cargo type information are hold together for each aerial vehicle during their life-cycle in the GUTMA UAS Central Management System database and with their flight information in a standard form, the requirements for a healthy prioritization system are accomplished. After evaluating those information, the following prioritization pyramid is created:

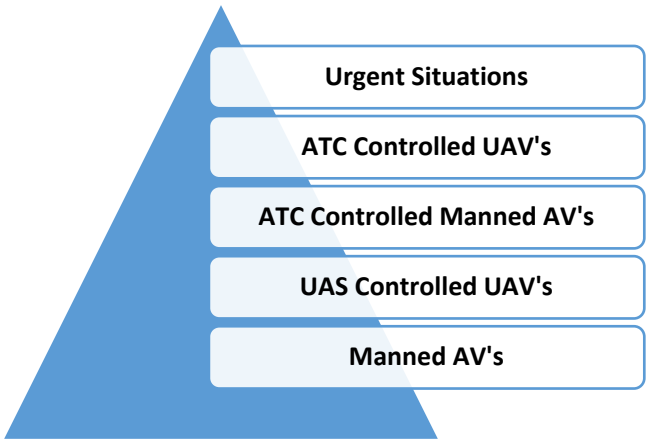

Figure 3: Prioritization Triangle

In this figure, priority gets higher when walked through top of the pyramid. It can be clearly seen that the urgent conditions do have the highest priority in the pyramid. On the other hand; ATC controlled UAV's have higher priority than the UAS controlled ones due to their transport capability and the traditional traffic rules in the air. In addition, manned aerial vehicles have the least priority since it has least autonomy level.

This prioritization can be used for take-off, landing, route planning and refueling processes of the aerial vehicles.

Although it is easy to design a solution for a predicted problem, the most important step to create safe network in terms of different types of aerial vehicles on the air and different central observer systems can be achieved by a regulation support.

4. CONCLUSIONS

In this study, the proposal of prioritization during unmanned and manned aerial vehicles' possible encounters in a future aerial vehicle network is studied. The GUTMA UAS Traffic Management System is used as the main traffic controller system for such a network. For prioritization, human health and safety is put as the main governor of the design so that the urgent conditions, passenger safety, transport type, autonomy level of the aerial vehicles and the maneuverability come into account.

In the final solution, it is proposed that; urgent situations have the highest priority and the manned aerial vehicles have the least priority due to the principle of autonomy. In addition; ATC controlled aerial vehicles have higher priority than the UAS controlled ones due to group segmentation in DOD.

REFERENCES

[1]. SESAR Joint Undertaking, *The Roadmap for Delivering High Performing Aviation for Europe - European ATM Master Plan*, Edition 2015, European Union, Eurocontrol 2015.
[2]. The Law Library of Congress, *Regulation of Drones*, Global Legal Research Center, April 2016.
[3]. Global UTM Association, UAS *Traffic Management Architecture*, April 2017.
[4]. Fred L. Templin, R. Jain, G. Sheffield, P. Taboso – Ballesteros, D. Ponchak, "Considerations for an Integrated UAS CNS Architecture,"2017 Integrated Communications Navigation and Surveillance Conference.
[5]. B. Elias, Unmanned Aircraft Operations in Domestic Airspace: U.S Policy Perspectives and the Regulatory Landscape, Congressional Research Service – R44532
[6]. T. Jiang, J. Geller, D. Ni, J. Collura, Unmanned Aircraft System Traffic Management: Concept of Operation and system architecture, "International Journal of Transportation Science and Technology", 2016, 123-135

BIOGRAPHY

Mutlu IPTEC

He is studying in Gazi University Informatics Institute. He is working on the secure traffic networks, capacity issues of the flying networks.

Bunyamin CIYLAN

He is now teaching in the Gazi University Computer Engineering and Informatics Institute. He is specifically working on the information security, secure traffic networks.

Arif Emre SIVGIN

He is studying in Gazi University Informatics Institute. He is working on the autonomous aerial vehicles applications and their optimization.

ICENS 4TH INTERNATIONAL CONFERENCE ON ENGINEERING AND NATURAL SCIENCE
2-6 May 2018 KIEV UKRAINE

Decision Mechanism for Glaucoma Disease via Classification Techniques by Employing Data Reduction

Esra Satir[1], Ekrem Baser[2], Serife Haciefendioglu[2]

Abstract

This document is a guide and sample paper for ICENS International Conference on Engineering and Natural Science. For your paper to be published in the conference proceedings, you must use this document as both an instruction set and as a template into which you can type your own text. If your paper does not conform to the required format, you will be asked to fix it. Glaucoma is one of the eye disorders caused by optic nerve damage leading to partial or complete blindness. If the significant number of nerve fibres is damaged, it creates blind spots in the field of vision. Once nerve damage, it leads to permanent vision loss and it cannot be cured completely. Unlike many other diseases, its symptoms are not immediately noticed by patients. According to World Health Organization (WHO) statistics, it is found that glaucoma is the second leading cause of vision loss globally after cataract, especially in older people. It is estimated that by 2020, there will be approximately 80 million people worldwide affected by glaucoma. Since our vision is possible by the optic nerve, early detection of this disease is essential to prevent any visual loss. The purpose of this study is the diagnosis of glaucoma with fewer attributes. In this study, the patient information which belongs to the graduate thesis of Haciefendioglu, has been employed. Number of the attributes in the dataset has been decreased from 10 to 8 by employing Principle Component Analysis (PCA). The reduced data has been classified by using k-Nearest Neighbourhood (k-NN), Support Vector Machines (SVM) and Naïve Bayes classifiers. Cross validation has been performed for performance evaluation. 80% of the employed data has been used for training while 20% of the employed data has been used for testing. Experimental results showed that the accuracy rates were significant especially after the usage of PCA.

Keywords: Glaucoma, machine learning, data reduction, classification, principal component analysis

1. INTRODUCTION

Glaucoma is an eye disease in which damage to the optic nerve of eye leads to irreversible and progressive visionloss. The optic nerve carries visual information from the retina to the brain, allowing humans to visualize the outside world. The rise in the pressure of an eye known as intraocular pressure and it is the main cause of glaucoma. This pressure is increased when the amount of fluid produced in the eye increases and as a result, block age occurs in the drain age or out flow channel of an eye. Glaucoma is detected by identifying damage to the optic nerve which starts with deteriorating of vision and finally resulting in blindness[1]. Our vision is possible by the optic nerve, which carries images from the retina to the brain. If the significant number of nerve fibers is damaged, it creates blind spots in the field of vision. Once the nerve is damaged, it leads to permanent vision loss and cannot be cured completely. Unlike many other diseases, the symptoms of glaucoma are not immediately noticed by patients. So it is a great health challenge in worldwide. According to World Health Organization (WHO) statistics, it is found that glaucoma is the second leading cause of vision loss globally after cataract, especially in older people. The signs and symptoms of this eye disorder are only experienced at its advanced stages. Accordingly, this is the main challenge of glaucoma identification. Due to this, early detection of glaucoma is more relevant in the current society [2]. The status of normal eye and the eye with glaucoma have been demonstrated in Figure 1.

[1]*Corresponding author: Duzce University, Department of Computer Engineering, Duzce, Turkey. esrasatir@duzce.edu.tr*

[2]*Duzce University, Department of Computer Engineering, Duzce, Turkey. ekrembaser@duzce.edu.tr*

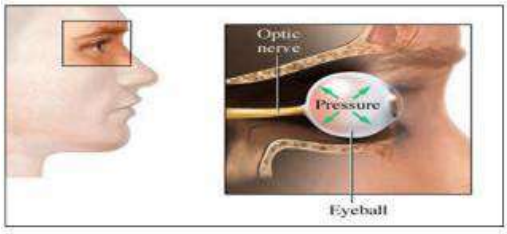

Figure 27. Normal eye and the eye with glaucoma [3]

Glaucoma can be classified into two as open angle and angle closure glaucoma (1). Open angle glaucoma: It is the most common type. Symptoms cannot be detected early and it develops progressively due to insufficient drainage of fluid out of the eye. If not detected in the early stage, it can cause gradual loss of vision. In this work, open angle glaucoma has been studied (2). Angle closure glaucoma: It is rarely found and also known as narrow angle glaucoma. This is due to the sudden blockage of drainage system of eye and results in acute pain, red eye, and immediate loss of vision [4].

Glaucoma can be characterized by eye pain, nausea, headache, blurry vision and red eye. Surgery is used to recover from glaucoma by creating a hole in the iris with the help of laser to maintain the normal flow of fluid. In general, patients with glaucoma initially have no symptoms, but with the passage of time, symptoms can be detected by the experts. Prevention of the disease depends on the type of glaucoma, which is detected by experts and accordingly the suitable treatment is given. Hence, accurate and timely detection of glaucoma can limit its progression not completely, but to a certain extent [1].
The clinical methods available for detection of glaucoma are tonometers that measures IOP, optical coherence tomography (OCT) that generates3D image of the eye tissue, scanning laser ophthalmoscope (SLO)that provides 2D scan of the optic cup, and scanning laser polarimeter (SLP)that gives information about the degradation of retinal nerve fibre (RNF). These methods are expensive, manual, time consuming and require skilled supervision. Besides, the manual methods rely, heavily on the subjective knowledge of experts. Recent advancements in signal processing techniques and high speed computing have contributed to the development of novel automated systems for glaucoma diagnosis, which are accurate, low cost, and useful for mass screening [4]. Accordingly, there is a need for improved and automated machine learning approaches for diagnosis of the disease precisely in a shorter time span. In this study, the diagnosis of glaucoma with fewer attributes has been aimed. First of all, number of the attributes in the dataset has been aimed to decrease by employing Principle Component Analysis (PCA). K-Nearest Neighbourhood (k-NN), Support Vector Machines (SVM) and Naïve Bayes classifiers have been employed for classification while cross validation has been performed for an unbiased performance evaluation. 80% of the employed data has been used for training while 20% of the employed data has been used for testing. This study has been organized as five sections. Similar studies in the literature have been mentioned in Section 2. The employed methods in the scope of this study, have been explained in section 3. The performed experiments have been expressed in Section 4 and finally, a general outcome has been reached in Section 5.

2. LITERATURE REVIEW

Since early detection of this disease is essential to prevent the permanent blindness, many efforts have been made on automatic detection of Glaucoma at an early stage.

In 2018, Kausu et al. have developed an efficient algorithm for glaucoma detection with improved accuracy rate. In order to achieve this goal, they have proposed a new feature extraction method which used some clustering based segmentation techniques and Anisotropic Dual Tree-Complex Wavelet Transform (ADT-CWT) features. Another contribution of this work is to find the minimum number of prominent features for the automatic diagnosis of glaucoma from retinal image. The proposed method showed the ability of glaucoma diagnosis with an accuracy of 97.67% using Multi-layered perceptrons (MLP) classifier [2].

In 2017, Maheshwari et al. presented a novel method for an automated diagnosis of glaucoma using digital fundus images. Variational mode decomposition (VMD) method was used in an iterative manner for image decomposition. Various features namely, Kapoor entropy, Renyi entropy, Yager entropy, and fractal dimensions were extracted from VMD components. Relief F algorithm was used to select the discriminatory features and these features were then fed to the least squares support vector machine (LS-SVM) for

classification. The proposed method achieved classification accuracies of 95.19% and 94.79% using three-fold and ten-fold cross-validation strategies, respectively. They claimed that the proposed system could aid the ophthalmologists in confirming their manual reading of classes (glaucoma or normal) using fundus images [4].

In 2016, Satir et al. proposed a study where the diagnosis of glaucoma was aimed with fewer attributes. In the study, the patient information which belongs to the graduate thesis of Haciefendioglu, has been used. Number of the attributes in the dataset has been decreased from 8 to 5 by employing Rough Sets theory. The reduced data has been classified by using Decision Trees and Artificial Neural Networks and then performance evaluation has been performed via Cross Validation method [5].

In 2015, Rao et al., proposed a study considering both structural and energy features. Then they analyzed them to classify as glaucomatous image. Energy distribution over cup to disk ration were applied to find these important texture energy features. Finally extracted energy features were applied to Multilayer Perceptron (MLP) and Back Propagation (BP) neural network for effective classification by considering normal subject's extracted energy features. They reports that Naïve Bayes classified the images in the database with the accuracy of 89.6% and MLP-BP Artificial Neural Network (ANN) algorithm classified the images in the database with the accuracy of 90.6% [6].
In 2014, Yiu proposed a study is to devise and train artificial neural network systems to recognize the peripapillary RNFL (Retinalnerve fiber layer thickness) thickness pattern associated with glaucomatous damage. The RNFL thickness profile, based on measurements from 12 clock hours, served as input variables. The performance of the artificial neural networks in diagnosing glaucoma suspect and glaucoma individuals was evaluated. They found that the area under the Receiver Operating Characteristic Curve (AROC) curve could be enlarged sufficiently by employing simple artificial neural network models. They claimed that the performed stud is the first one, using OCT measured RNFL profile as inputs to neural network systems to differentiate glaucoma and glaucoma suspect subjects [7].
In 2012, Haciefendioglu and Isik proposed a study using three important methods in machine learning classification (Support Vector Machines, Artificial Neural Networks and Decision Trees) for diagnosis of glaucoma. They used the patient data from Pamukkale University Ophthalmology Department. Besides, they determined the performance of the machine learning methods via X-validation. They reposted that the highest classification success observed with Support Vector Machines [8].
The purpose of this study is the diagnosis of glaucoma with fewer attributes by using the measured physiologic parameters of the eye, instead of employing images. In this study, the patient information which belongs to the graduate thesis of Haciefendioglu, has been employed. Number of the attributes in the dataset has been decreased by employing Principle Component Analysis (PCA) and the reduced data has then been classified by using k-Nearest Neighbourhood (k-NN), Support Vector Machines (SVM) and Naïve Bayes classifiers. Cross validation has been performed for and unbiased performance evaluation. 80% of the employed data has been used for training while 20% of the employed data has been used for testing. Experimental results showed that the accuracy rates were significant especially after the usage of PCA.

3. METHODOLOGY

In this section, the employed data set and methodologies in the scope of this study have been explained.

a. Data Set

In this study, the patient information which belongs to the graduate thesis of Haciefendioglu, has been employed. The employed data set consists of 168 samples; 84 healthy samples and 84 samples with glaucoma. Besides, 90 samples are female while 58 samples are male. The used parameters for glaucoma diagnosis and their measure intervals have been provided in Table 1.

Table 1. The used parameters for glaucoma diagnosis and their intervals

Parameter	Value
IntraocularPressure	10-21 mmHG
Central CornealThickness	545 um
DiscArea	1,63-2,43 mm^2
Cup Area	0,11-0,68 mm^2
RimArea	1,31-1,96 mm^2

C/D Linear	036-0,80 um
Mean RNFL Thickness	0,18-0,41 um
Age	<40

b. Principal Component Analysis (PCA)

Principal Component Analysis (PCA) finds a low dimensional representation of a dataset. This representation contains as much variation in the dataset as possible. The main principle here is to maximize the variance over a set of linear combinations. The basic mathematical formulation of the principal component analysis is as follows:

Let $X \in R^{n\times p}$ with rows $x_1,\ldots,x_n \in R^{n\times p}$. X is thought as n inspection dates, observations of a random vector $x_1,\ldots,x_n \in R^{n\times p}$. Since track quality indexes (TQIs) are often represented in terms of standard deviation, scaling here is not necessary. The purpose is to find a linear combination $w_1X_1+ ,\ldots,+w_2X_2$of parameters with maximum variance like a direction in R^p where X varies the most. Thus:

$$w = \underset{\|w\|_2 = 1}{argmax} \sum_{i=1}^{n}(x_i^T w)^2 \quad (1)$$

In Equation 1, w is an Eigen vector associated to the largest Eigen value (λ) of X^TX. Since $\sum_{i=1}^{n}(x_i^T w)^2$ is proportional to the sample variance of the data, each column (parameter) has a zero mean. The PCA was used for each section of track to summarize all features into 1, 2 or 3 principal components depending on the percentage of variance explained [9].

c. Support Vector Machines

Support Vector Machines are based on the concept of hyper planes that define decision boundaries. A decision plane distinguishes between a set of objects which have different class labels. In Fig. 3, let's suppose that the objects belong either to class GREEN (without defect) or RED (with at least one defect). The separating dark line defines a boundary above which all sections of a track without defects are GREEN and below which other sections with defects are RED. In Fig. 2(a), the data is separable while in Figure 2(b), shows the non separable case in which the points labelled ξ_i are on the wrong side of the margin.

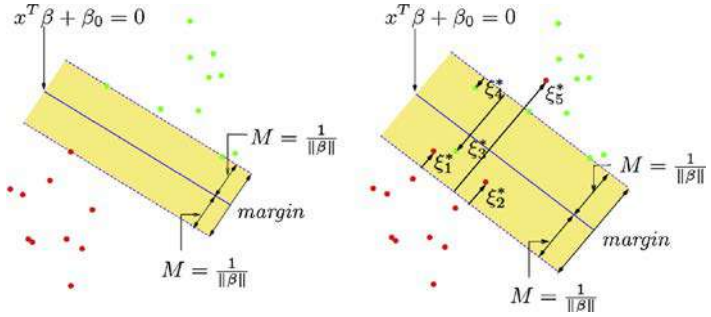

Figure 2. A simple illustration of SVM

(a) Separable data (b) Non-separable data

To maximize the margin, a total cost $\sum_{i=1}^{n}\xi_i \le c$. A simple case of an SVM formulation is as follows:

Minimize $\frac{1}{2}w^Tw + c\sum_{i=1}^{N}\xi_i$ subject to the constraints:

$y_i(w^T\phi(x_i) + b) \ge (1 - \xi_i)$
$\xi_i \ge 0$
(2)

For i=1,…,N

Here, c is the trade-off between the margin and misclassification error, w is the vector of coefficients, b is a constant, and ξ_i represents a slack parameter for handling non separable data. SVM is easy to visualize with 2 principal components only. However, a Gaussian or radial basis kernel was employed rather than the traditional linear or polynomial decision boundary. This is defined as follows in Equation 3:

$$K_{ij} = e^{-\frac{(x_i - x_j)^2}{\sigma}} \quad (3)$$

Where K_{ij} is the kernel matrix, σ or c is a positive constant and x_i, x_j are pairs of training observations. The reason for choosing a radial kernel becomes clear after the principal component analysis [9].

d. k-Nearest Neighbor Classifier (k-NN)

The *k* -Nearest Neighbor(*k*-NN) classifier is one of the well- known and simple classification algorithms. It does not make any assumptions on the input data distribution. In the *k* -NN classifier, an unknown sample is classified based on the similarity to the known, trained or labelled samples by computing the distances between the unknown sample and all labelled samples. *k* -nearest samples are then selected as the basis for classification; and the unknown sample (*x test*) is assigned to the class which has the most samples among the *k* -nearest samples. Accordingly, *k* -NN classifier depends on; (1) integer *k* (number of neighbors), (2) a set of labelled training data and (3) a distance metric. Euclidean distance is often used as the distance metric to measure the distance between two samples as denoted in Equation 4. *k* -NN classifier is analytically traceable and simple to implement, but it needs all the training samples to be in memory at runtime.

$$d(x_i, x_j) = \sum_{k=1}^{d} (x_{ik} - x_{jk})^2 \quad (4)$$

Here, d (x_i , x_j) represents the distance between the two samples x_i and x_j, (x_i, x_j) ∈ R m , $x\ i$ = { x_{i1} , x_{i2},…,x_{im}} , and m is the dimension, i.e. number of attributes, of samples [10].

e. Naïve Bayes Classifier

Naïve Bayes classifier, also called simple Bayesian classifier, is a simple but surprisingly effective classifier. Let c ϵ Ω = {1,2,…,K} andx_1, x_2,…, x_N, respectively, denote classification variable and the *N*, features. The general Bayesian classifier, in Equation 5, evaluates the posteriors of the *K* classes given the feature values and chooses the class with the highest posterior value.

$$c^* = \arg\max_{c \in \Omega} p(c|x_1, x_2, \dots, x_N) = \operatorname*{argmax}_{c \in \Omega} \frac{p(x_1, x_2, \dots, x_N|c)p(c)}{p(x_1, x_2, \dots, x_N)} \quad (5)$$

Since it is difficult to compute the joint conditional probability in Eq. (5), two assumptions are often imposed for a simple computation. One is that, all the features, i.e., x_1, x_2,…,x_N, are independent with each other given the class variable *c*. The other is that all the features are directly dependent on the class variable *c*. The two assumptions make the computation of the joint conditional probability be equivalent to the product of all the marginal conditional probabilities:

$$P(x_1, x_2, \dots, x_N|c)p(c) = p(c) \prod_{n=1}^{N} p(x_n|c) \quad (6)$$

As a result, the general Bayesian classifier given by Equation 4 can be simplified as the naïve Bayes classifier given by Equation 7:

$$c^* = \operatorname*{argmax}_{c \in \Omega} p(c) \prod_{n=1}^{N} p(x_n|c) \quad (7)$$

[11].

4. EXPERIMENTAL RESULTS

The experiments in the scope of this study have been performed via Matlab and Weka data mining with open source machine learning software. Dimension of the data set is 160×10 before PCA. After PCA, dimension of the data set has been reduced to 160×8. Namely, we have 9 inputs-1 output before PCA while we have 7 inputs-1 output after PCA.80% of the data has been used for training while 20 percent of the data has been used for testing. The data have been subjected to 700 epochs in k-NN and SVM algorithms. Cross validation, 5 fold, has been implemented for an unbiased evaluation. Results of the performed experiments both for training and testing phases have been demonstrated in Table 2.

Table 2. Experimental results for training and testing phases in terms of percent.

Method/Results	Accuracy without PCA (%)		Accuracy with PCA (%)	
	Training	Testing	Training	Testing
k-NN	42.6	40.60	81.31	77.44
SVM	43.19	41.13	81.9	78.01
Naïve Bayes	92.64	88.23	86.4	82.35

Graphical representation of the experimental results has been provided in Figure 3. Vertical axis represents the accuracy in terms of percent while horizontal axis represents the used classification algorithm. Blue columns show the training accuracies without PCA and with PCA. Red columns show the testing accuracies without PCA and with PCA. It can be claimed that PCA increased the training and testing performances extremely in k-NN and SVM classifiers although it doesn't have a significant contribution in Naïve Bayes classifier.

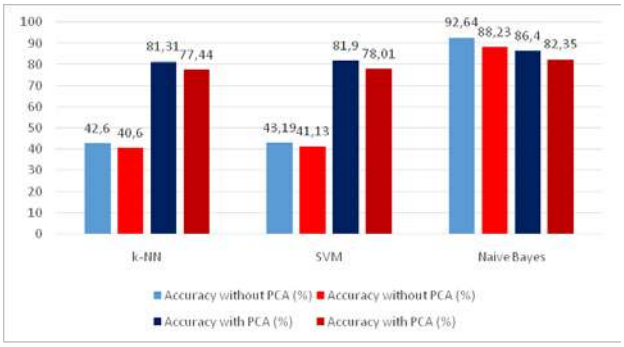

Figure 3. Graphical representation of the experimental results

5. CONCLUSION

Glaucoma is one of the eye disorders caused by optic nerve damage leading to partial or complete blindness. If the significant number of nerve fibres is damaged, it creates blind spots in the field of vision. Once nerve damage, it leads to permanent vision loss and it cannot be cured completely. Unlike many other diseases, its symptoms are not immediately noticed by patients. Since it a sly disease and the clinical methods for detection are expensive, manual, time consuming and require skilled supervision, there is aneedforimprovedandautomatedmachinelearningapproachesfordiagnosis of the disease precisely in a shorter time span. In this study, the diagnosis of glaucoma with fewer attributes has been aimed by using PCA. k-NN, SVM and Naïve Bayes classifiers have been employed for classification while cross validation has been performed for an unbiased performance evaluation. 80% of the employed data has been used for training while 20% of the employed data has been used for testing. By basing on the obtained results, we can claim that PCA increased the training and testing performances extremely in k-NN and SVM classifiers although it doesn't have a significant contribution in Naïve Bayes classifier. Accordingly, effects of the other dimension reduction techniques will be investigated in future studies.

REFERENCES

[1]. N. Thakur, M. Juneja, "Survey on segmentation and classification approaches of optic cup and optic disc for diagnosis of glaucoma", *Biomedical Signal Processing and Control*, vol. 42, pp. 162–189, 2018.

[2]. T.R. Kausu, Varun P. Gopi, Khan A. Wahid, Wangchuk Doma, and Swamidoss Issac Niwas, *"Combination of clinical and multiresolution features for glaucoma detection and its classification using fundusimages"*, Biocybernetics and Biomedical Engineering, 2018.

[3]. D. Bhowmik.,K. P. Sampath Kumar, L. Deb, S. Paswan, A.S. Dutta, *"Glaucoma -A Eye Disorder Its Causes, Risk Factor, PreventionandMedication"*,ThePharmaInnovation,vol.1(1),pp. 66-81, 2012.

[4]. S. Maheshwari, R.B. Pachori, V. Kanhangad, S.V. Bhandary, U.R. Acharya, "Iterative variational mode decomposition based automated detection of glaucoma using fundus images" Computers in biology and medicine, vol. 88, pp. 142-149, 2017.

[5]. E. Satir, F. Azboy, A. Aydin, H. Arslan, S. Haciefendioglu,*"Veri Indirgeme ve Siniflandirma Teknikleri ile Glokom Hastaligi Teshisi"*, El-CezeriJournal of Science and Engineering, vol. 3, pp. 485-497, 2016.

[6]. P.V. Rao , R. Gayathri, R. Sunitha, *"A Novel Approach for Design and Analysis of Diabetic Retinopathy Glaucoma Detection using Cup to Disk Ration and ANN"*, Procedia Materials Science, vol. 10, pp.446 – 454, 2015.

[7]. K.F. Cedric Yiu, *"Neural Network Analysis for the detection of glaucomatous"* Applied Soft Computing, vol. 20, pp. 66–69, 2014.
[8]. Haciefendioglu, "Diagnosis of Glaucoma by Machine Learning Methods", M. thesis, The Graduate School of Natural and Applied Science of Selcuk University, Konya, Turkey, 2012.
[9].A. Lasisi, N. Attoh-Okine, "Principal components analysis and track quality index: A machine learning approach", Transportation Research Part C, vol. 91, pp. 230–248, 2018.
[10]. A. Tharwat, H. Mahdi, M. Elhoseny, A. E. Hassanien, *"Recognizing human activity in mobile crowd sensing environment using optimized k -NN algorithm"*, Expert Systems With Applications, vol. 107, pp. 32–44, 2018.
[11]. L. Fan, K. L. Poh, P. Zhou, *"Partition-conditional ICA for Bayesian classification of microarray data"*, Expert Systems with Applications, vol. 37, pp. 8188–8192, 2010.

ICENS 4TH INTERNATIONAL CONFERENCE ON ENGINEERING AND NATURAL SCIENCE
2-6 May 2018 KIEV UKRAINE

Differential Diagnosis of Erythemato-Squamous Diseases via Machine Learning and Data Reduction Techniques

Esra Satir[1], Ekrem Baser[2]

Abstract

Early diagnosis and appropriate treatment is a necessary problem in health issues. The differential diagnosis of erythemato-squamous diseases is a real problem in dermatology since they all share the clinical features of erythema and scaling with very little differences. These diseases are psoriasis, seboreic dermatitis, lichen planus, pityriasisrosea, chronic dermatitis, and pityriasisrubra pilaris. Usually a biopsy is necessary for the diagnosis but unfortunately these diseases share many histopathological features as well. In this study, Machine Learning techniques have been employed for diagnosis of these dermatological diseases both on the original and reduced data set. For classification, SVM, k-Nearest Neighbourhood (k-NN) and Rough Set theory have been used. Principal Component Analysis (PCA) has been employed for data reduction. Hence, we aim to detect the disease by considering with fewer attributes. In this study, the used data have been obtained from UCI Machine Learning data set. 80% of the employed data has been used for training while 20% of the employed data has been used for testing. Experimental results showed that the accuracy rates were significant especially in spite of the usage of PCA.

Keywords: Erythemato-squamous diseases, dermatology, classification, clustering, principal component analysis

The main concept of the medical technology is an inductive engine that learns the decision characteristics of the diseases and can then be used to diagnose future patients with uncertain disease states [1].The differential diagnosis of erythemato-squamous diseases is a difficult problem in dermatology since they all share the clinical features of erythema and scaling with very few differences. The diseases in this group are psoriasis, seboreic dermatitis, lichen planus, pityriasisrosea, chronicdermatitis and pityriasisrubra pilaris [2]. For diagnosis, a biopsy is necessary; however this group of diseases shares also numerous histopathological features as well. Furthermore, at the beginning phase, the disease might exhibit the features of another disease and it may have the particular characteristics in advance [3].

Automated medical diagnosis strategies mainly rely on a Machine Learning (ML) algorithm that is trained to learn former decision characteristics of an physician about a specific disease. Then it can be used to assist human-decision makers to diagnose future patients for the same disease. Unfortunately, there is no universal ML model that can adapt itself to any kind of disease. In most cases, to develop a novel automated diagnosis system, developers uses a three-step design strategy: (i) select a specific disease dataset and prepare it no next step, (ii) if data is high dimensional, apply feature reduction strategies in accordance with the third step and finally (iii) investigate an ML strategy with highest possible accuracy [4]. High number of features in a dataset can lead to lower classification accuracy with high computational cost and risk of “overfitting”. In other words, smaller number of features might increase classification accuracy with decreased computational cost and it eliminates risk of “over-fitting”. Therefore, elimination of irrelevant features from a high dimensional dataset is a fundamental step for designing automated diagnosis systems with highaccuracy[3]. Hence, the main objective of this study is to implement some ML methods by reducing dimension of erythemato-squamous diseases dataset and to obtain high-accurate classification rates. Accordingly, k-Nearest Neighbourhood (k-NN), Rough Set theory and Support Vector Machines (SVM) have been used for classification. Principal Component Analysis (PCA) has been employed for data reduction. This study has been organised as five sections. Similar studies in the literature have been mentioned in Section 2. The employed methods in the scope

[1]*Corresponding author: Duzce University, Department of Computer Engineering, Duzce, Turkey. esrasatir@duzce.edu.tr*

[2]*Duzce University, Department of Computer Engineering, Duzce, Turkey. ekrembaser@duzce.edu.tr*

of this study, have been explained in section 3. The performed experiments have been expressed in Section 4 and finally, a general outcome has been reached in Section 5.

LITERATURE REVIEW

In 2000, Guvenir and Emeksiz proposed an expert system for differential diagnosis of erythemato-squamous diseases incorporating decisions made by nearest neighbor classifier, naive Bayesian classifier and voting feature intervals-5. The study aims to enable doctors to differentiate six types of erythemato-squamous diseases using clinical and histopathological parameters obtained from a patient. The developed in the scope of their study, also gave explanations for the classifications of each classifier. Besides, the patient records were also maintained in a database for further references [4].

In 2005, Ubeyli and Guler presented a new approach based on Adaptive Neuro Fuzzy Inference System (ANFIS) for the detection of erythemato-squamous diseases. The six ANFIS classifiers were used to detect the six erythemato-squamous diseases when 34 features defining six disease indications were used as inputs. Each of the ANFIS classifier was trained so that they are likely to be more accurate for one type of erythemato-squamous disease than the other diseases. In the performed study, the predictions of the six ANFIS classifiers were combined by the seventh ANFIS classifier. The proposed ANFIS model was then evaluated and they reported that they were able to achieve significant improvement in accuracy by applying ANFIS model when compared to the stand-alone neural networks[2].

In 2009, Ubeyli proposed a study in order to find the neural network model with high accuracy
for classification of the erythemato-squamous diseases by the usage of 34 features defining six disease indications, Combined Neural Network (CNN) and multilayer perceptron neural network (MLPNN) were implemented. A significant contribution of the presented work was training novel classifiers (CNN trained on features) for the erythemato-squamous diseases diagnosis. In order to develop CNN for the diagnosis of erythemato-squamous diseases, for the first level models, six sets of neural networks were used since there were six possible outcomes of the diagnosis of erythemato-squamous diseases (psoriasis, seboreic dermatitis, lichen planus, pityriasisrosea, chronic dermatitis and pityriasisrubra pilaris). Networks in each set were trained so that they are likely to be more accurate for one type of disease than the other diseases. The predictions of the networks in the first level were combined by a second level neural network. Significant improvement was achieved in accuracy by applying neural networks as the second level model compared to the stand-alone neural networks (MLPNN) [5].

In 2013, Ozcift and Gulten presented a new method for differential diagnosis of erythemato-squamous diseases based on Genetic Algorithm (GA) wrapped Bayesian Network (BN) Feature Selection (FS). In this GA–BN algorithm, GA made a heuristic search to find most relevant feature model that increase accuracy of BN algorithm with the use of a 10-fold cross-validation strategy. The subsets of features were sequentially used to identify six dermatological diseases via a BN fitting the corresponding data. The algorithm, in this case, produced 99.20% classification accuracy in the diagnosis of erythemato-squamous diseases. They reported that the developed model gave the classification accuracy of 99.20% [3].

Hence, the main objective of this study is to implement some ML methods by reducing dimension of erythemato-squamous diseases dataset and to obtain high-accurate classification rates. Accordingly, k-Nearest Neighbourhood (k-NN), Rough Set theory and Support Vector Machines (SVM) have been used for classification. Principal Component Analysis (PCA) has been employed for data reduction. Cross validation has been performed for and unbiased performance evaluation. 80% of the employed data has been used for training while 20% of the employed data has been used for testing. Experimental results showed that the accuracy rates were significant especially after the usage of PCA.

METHODOLOGY

In this section, the employed data set and methodologies in the scope of this study have been explained.

Data Set

In this study, a standardized dermatology data set from machine learning repository or UCI, developed by University of California, School of Information and Computer Science was used. This data set was prepared by N. Ilterfrom Gazi University and H.A. Guvenir from Bilkent University [6].The dermatology data set contains 366 samples, where there are 34 input attributes and 1 output attribute which has 6 classes for t he disease.

Principal Component Analysis (PCA)

Principal Component Analysis (PCA) finds a low dimensional representation of a dataset. This representation contains as much variation in the dataset as possible. The main principle here is to maximize the variance over a set of linear combinations. The basic mathematical formulation of the principal component analysis is as follows:

Let X ∈Rn×p with rows x1,…,xn∈Rn×p. X is thought as n inspection dates, observations of a random vector x1,…,xn∈Rn×p. Since track quality indexes (TQIs) are often represented in terms of standard deviation, scaling here is not necessary. The purpose is to find a linear combination w1X1+ ,…,+w2X2of parameters with maximum variance like a direction in Rp where X varies the most. Thus:

$$w = \underset{\|w\|_2 = 1}{argmax} \sum_{i=1}^{n} (x_i^T w)^2 \quad (1)$$

In Equation 1, w is an eigenvector associated to the largest eigen value (λ) of XTX. Since $\sum_{i=1}^{n}(x_i^T w)^2$ is proportional to the sample variance of the data, each column (parameter) has a zero mean. The PCA was used for each section of track to summarize all features into 1, 2 or 3 principal components depending on the percentage of variance explained [7].

Support Vector Machines

Support Vector Machines are based on the concept of hyper planes that define decision boundaries. A decision plane distinguishes between a set of objects which have different class labels. In Fig. 3, let's suppose that the objects belong either to class GREEN (without defect) or RED (with at least one defect). The separating dark line defines a boundary above which all sections of a track without defects are GREEN and below which other sections with defects are RED. In Fig. 2(a), the data is separable while in Figure 2(b), shows the nonseparable case in which the points labeled ξ_i are on the wrong side of the margin.

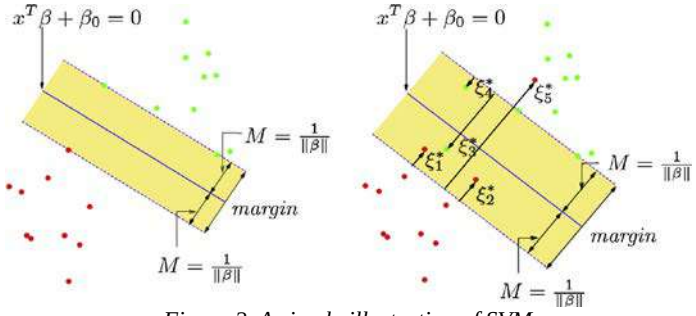

Figure 2. A simple illustration of SVM

Seperable data (b) Non-seperable data

To maximize the margin, a total cost $\sum_{i=1}^{n}\xi_i \leq c$. A simple case of an SVM formulation is as follows:

Minimize $\frac{1}{2}w^T w + c\sum_{i=1}^{N}\xi_i$ subject to the constraints:

$$y_i(w^T\phi(x_i) + b) \geq (1 - \xi_i)$$
$$\xi_i \geq 0 \quad (2)$$

For i=1,…,N

Here, c is the trade-off between the margin and misclassification error, w is the vector of coefficients, b is a constant, and ξ_i represents a slack parameter for handling non separable data. SVM is easy to visualize with 2 principal components only. However, a Gaussian or radial basis kernel was employed rather than the traditional linear or polynomial decision boundary. This is defined as follows in Equation 3:

$$K_{ij} = e^{-\frac{(x_i - x_j)^2}{\sigma}} \quad (3)$$

Where K_{ij} is the kernel matrix, σ or c is a positive constant and x_i, x_j are pairs of training observations. The reason for choosing a radial kernel becomes clear after the principal component analysis [7].

k-Nearest Neighbor Classifier (k-NN)

The k -Nearest Neighbor(k-NN) classifier is one of the well- known and simple classification algorithms. It does not make any assumptions on the input data distribution. In the k -NN classifier, an unknown sample is classified based on the similarity to the known, trained or labelled samples by computing the distances between

the unknown sample and all labelled samples. k -nearest samples are then selected as the basis for classification; and the unknown sample (x test) is assigned to the class which has the most samples among the k -nearest samples. Accordingly, k -NN classifier depends on; (1) integer k (number of neighbors), (2) a set of labelled training data and (3) a distance metric. Euclidean distance is often used as the distance metric to measure the distance between two samples as denoted in Equation 4. k -NN classifier is analytically traceable and simple to implement, but it needs all the training samples to be in memory at runtime.

$$d(x_i, x_j) = \sum_{k=1}^{d} (x_{ik} - x_{jk})^2 \quad (4)$$

Here, d (xi , xj) represents the distance between the two samples xi and xj, (xi, x j) ∈ R m , x i = { xi1 , xi2,…,xim} , and m is the dimension, i.e. number of attributes, of samples [8].

Rough Sets

In rough set theory, an information table is defined as a tuple T = (U, A) where U and A are two finite, non-empty sets, U the universe of primitive objects and A the set of attributes. Each attribute or feature a ∈ A is associated with a set Va of its value, called the domain of a. The attribute set A can be partitioned into two subsets C and D, called condition and decision attributes, respectively. Let P⊂ A be a subset of attributes. The indiscernibility relation, denoted by IND(P), is an equivalence relation defined in Equation 5:

$$IND(P) = \{(x, y) \in U \times U : \forall a \in P, a(x) = a(y)\} \quad (5)$$

Here, a(x) denotes the value of feature a of object x. If (x, y)∈IND(P), x and y are said to be indiscernible with respect to P. The family of all equivalence classes of IND(P) (Partition of U determined by P) is denoted by U/IND(P). Each element in U/IND(P) is a set of indiscernible objects with respect to P. Equivalence classes U/IND(C) and U/IND(D) are called condition and decision classes. For any concept X⊆U and attribute subset R⊆A, X could be approximated by the R-lower approximation and R-upper approximation using the knowledge of R. The lower approximation of X is the set of objects of U that are surely in X, defined in Equation 6:

$$R*(X) = [\{E \in U/IND(R) : E \subseteq X\} \quad (6)$$

The upper approximation of X is the set of objects of U that are possibly in X, defined in Equation 7:

$$R*(X) = [\{E \in U/IND(R) : E \setminus X 6 = \varphi\} \quad (7)$$

The boundary region is defined in Equation 8:

$$BNDR(X) = R*(X) - R*(X) \quad (8)$$

If the boundary region is empty, that is, R∗(X) = R∗(X), concept X is said to be R-definable. Otherwise X is a rough set with respect to R. The positive region of decision classes U/IND(D) with respect to condition attributes C is denoted by POSc(D) = $\bigcup R_*(X)$. It is a set of objects of U that can be classified with certainty to classes U/IND(D) employing attributes of C. A subset R ⊆ C is said to be a D-reduce of C if POSR(D) = POSC (D) and there is no R'⊂ R such that POS'R(D) = POSC (D). In other words, a reduce is the minimal set of attributes preserving the positive region. There may exist many reduces in an information table [9].

EXPERIMENTAL RESULTS

The experiments in the scope of this study have been performed via Matlab and Weka data mining with open source machine learning software. Dimension of the data set is 366×34 before PCA. After PCA, dimension of the data set has been reduced to 366×22. Namely, we have 34 inputs-1 output before PCA while we have 22 inputs-1 output after PCA.80% of the data has been used for training while 20 percent of the data has been used for testing. The data have been subjected to 700 epochs in k-NN and SVM algorithms. Cross validation,5 fold, has been implemented for an unbiased evaluation. Results of the performed experiments both for training and testing phases have been demonstrated in Table 1.

Table 1. Experimental Results for training and testing phases in terms of percent.

Method/Results	Accuracy without PCA (%)		Accuracy with PCA (%)	
	Training	Testing	Training	Testing
k-NN	86.41%	85.56%	97.79%	96.83%
SVM	84.6%	83.77%	97.64%	96.68%
Rough Sets	94.9	93.05%	95.4%	93.05%

Graphical representation of the experimental results has been provided in Figure 1. Vertical axis represents the accuracy in terms of percent while horizontal axis represents the used classification algorithm. Blue columns show the training accuracies without PCA and with PCA. Red columns show the testing accuracies without PCA and with PCA. It can be claimed that PCA increased the training and testing performances extremely in k-NN and SVM classifiers. The highest classification accuracy has been obtained in k-NN algorithm byte usage of PCA in both training and testing phases, 97.79% and 96.83%, respectively. However, it doesn't have a such significant contribution rough set method.

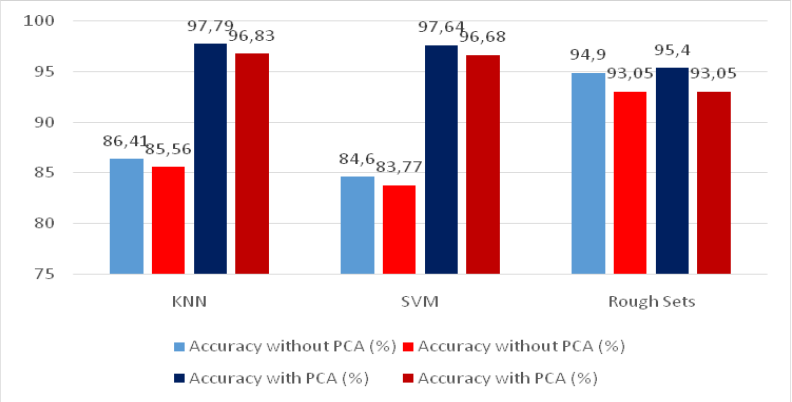

Figure 1. Graphical representation of the experimental results

CONCLUSION

Early diagnosis and appropriate treatment is a necessary problem in health issues. The differential diagnosis of erythemato-squamous diseases is a real problem in dermatology since they all share the clinical features of erythema and scaling with very little differences. These diseases are psoriasis, seboreic dermatitis, lichen planus, pityriasisrosea, cronic dermatitis, and pityriasisrubra pilaris. In this study, Machine Learning techniques have been employed for diagnosis of these dermatological diseases both on the original and reduced data set. For classification, SVM, k-Nearest Neighbourhood (k-NN) and Rough Set theory have been used. Principal Component Analysis (PCA) has been employed for data reduction. Hence, we aim to detect the disease by considering with fewer attributes. 80% of the employed data has been used for training while 20% of the employed data has been used for testing. Experimental results showed that the accuracy rates were significant especially in spite of the usage of PCA. Dimension of the data set is 366×34 before PCA. After PCA, dimension of the data set has been reduced to 366×22. Namely, we have 34 inputs-1 output before PCA while we have 22 inputs-1 output after PCA. By basing on the obtained results, we can claim that PCA increased the training and testing performances extremely in k-NN and SVM classifiers although it doesn't have a significant contribution for rough set method. Accordingly, effects of the other dimension reduction techniques will be investigated in future studies.

REFERENCES

[1].E.D. Ubeyli, *"Multiclass support vector machines for diagnosis oferythemat-squamous diseases"*, Expert Systems with Applications,vol.35, pp. 1733–1740, 2008

[2]. E.D. Ubeyli, I. Guler, *"Automatic detection of erythemato-squamous diseases using adaptive neuro-fuzzy inference systems"*, Computers in Biology and Medicine, vol. 35, pp. 421–433, 2005.

[3]. A. Ozcift, A. Gulten, *"Genetic algorithm wrapped Bayesian network feature selection applied to differential diagnosis of erythemato-squamous diseases"*, Digital Signal Processing vol. 23, pp. 230–237, 2013.

[4]. H.A. Guvenir, N. Emeksiz, *"An expert system for the differential diagnosis of erythemato-squamous diseases"*, Expert Systems with Applications, vol. 18, pp. 43–49, 2000.

[5]. E. D.Ubeyli, "Combined neural networks for diagnosis of erythemato-squamous diseases", Expert Systems with Applications, vol. 36, pp. 5107–5112, 2009.

[6]. UCI Machine Learning Repository website. [Online]. Available:https://archive.ics.uci.edu/ml/datasets/Dermatology

[7]. A. Lasisi, N. Attoh-Okine, "Principal components analysis and track quality index: A machine learning approach", Transportation Research Part C, vol. 91, pp. 230–248, 2018.

[8]. A. Tharwat, H. Mahdi, M. Elhoseny, A. E. Hassanien,*"Recognizing human activity in mobile crowdsensing environment using optimized k -NN algorithm"*, Expert Systems With Applications, vol. 107, pp. 32–44, 2018.

[9]. M. Zhang, J.T. Yao, 2004. A rough sets based approach to feature selection. *Proceedings of The 23rd International Conference of NAFIPS, 2004, paper* 434–9.

ICENS 4TH INTERNATIONAL CONFERENCE ON ENGINEERING AND NATURAL SCIENCE
2-6 May 2018 KIEV UKRAINE

The Effect of Lead-Zinc on the Strength of Clay Soil with Fly Ash

Fatih Balatan[1], Suat Akbulut[2]

Abstract

Nowadays, population growth, consumption society trends and technological innovations together with increased production in different industrial fields are required. As a result of this process, the disposal and storage of the wastes constitute serious environmental problems and academic studies are being required in this field. In this study, lead-zinc (Pb-Zn) additive material produced in Balikesir-Balya Province and high plasticity clay soils were blended in different percentages and the geotechnical properties of clay-admixtures were investigated experimentally in laboratory conditions. Then, lead-zinc additives were mixed with clay in the ratios of 0%, 10%, 20%, 30%, 40%, 50 %, 60%, 80% and 100% by weight of soil. Index, consistency, compaction and strength properties of the obtained samples were investigated. The plasticity properties of the samples showed a decrease correspondingly with the increasing percentage of the additive. Besides, the dry weight per unit volume was increased while the optimum water content decreased with increasing percentage of additive. According to the unconfined compression test results, it was observed that the highest compression strength value was obtained in 20% lead-zinc additive with clay. Afterwards, 5% fly ash ratio were added to clay-lead-zinc samples and the unconfined compression test values increased by about 200% compared to the soil without additives but decreased by adding 20% and 30% fly ash ratios. According to the results of the research, it seems that contrubiting lead-zinc or lead-zinc-flying ash additives to clay increased the strength properties of clay soils significantly compared to the soil samples without additives.

Keywords: clay, fly ash, lead-zinc, soil stabilization, unconfined compression test, wastes

1. INTRODUCTION

Soil improvement is an important part of civil engineering. In old times, Roman Empire had firstly used additives as cement and lime to enhance the road constructions. Especially, soil improvement is being improved in 20th century. Soil stabilization is the alteration of soils to enhance their physical properties. Stabilization can increase the shear strength of a soil and control the shrink-swell properties of a soil, thus improving the load bearing capacity of a sub-grade to support pavements and foundations. It aims mostly higher resistance values, reduction in plasticity, lower permeability, reduction of pavement thickness. In addition, it provides benefits economically that it extends elimination of excavation, exporting unsuitable material and importing new materials.Soil stabilization is a method of improving soil properties by blending and mixing other materials. There are plenty of additives as lime, cement, fly ash, marble powder, silica fume,fly ash and chemical additives which are being admixtured to the soils in order to improve its geotechnical properties [1]. Soil stabilization is the process of improving the shear strength parameters of soil and thus increasing the bearing capacity of soil. Soil stabilization is used to reduce permeability and compressibility of the soil mass in earth structures and to increase its shear strength. Thus to reduce the settlement of structures.

Soil stabilization involves physical, chemical and biological methods which are being improved from day to day. The ancient type of soil stabilization are mechanical in the nature. Mechanical solutions include physical changings on the property of the soil seeing that it leads soil's gradation,solidity and other characteristics. Dynamic compaction is one of the method, which uses the dynamic effect on high energy impacts,caused by

[1] *Corresponding Author: Post Graduate Student, Yildiz Technical University, Department of Civil Engineering, 34220, Esenler/Istanbul, Turkey. fatihbalatan@gmail.com*

[2] *Yildiz Technical University, Department of Civil Engineering,34220, Esenler/Istanbul, Turkey. sakbulut@yildiz.edu.tr*

dropping large steel weight weighing 15 to 40 tonnes from a height of 10-30 meters.Chemical solutions are another of the major types of soil stabilization. All of these methods rely on adding an additional material to the soil that will physically interact with it and change its properties [2].

Due to the large of quantity of industrial plants, it leads a huge amount of mine dumps. These dumps causes lots of environmental damages to the nature. Nowadays, there are lots of researches about storage for these mining dumps, which are being investigated by engineers, are mostly related with geology, environmental and geotechnical. In the scope of the research, lead-zinc (Pb-Zn) industrial waste additive which is being composed around 50 million tons in a Pb-Zn underground mine in Balikesir-Balya Region, was investigated. During investigation, two targets were aimed. Firstly, lead-zinc were admixtured to clay samples to enhance the resistance of clay. Secondly, because of the large quantity of lead-zinc waste additives, it was intented for storage in the nature safely and harmlessly.

Fly ash stabilization is gaining more importance recent times since it has wide spread availability. This method is inexpensive and takes less time than any other methods. It has a long history of use an engineering material and has been successfully employed in geotechnical applications. Fly ash is a significant waste that is released of thermal power plants and defined as very fine particles that are drifted upward with up taken by the flue gases due to the burning of used coal [3]. Studies on the country and the world of fly ash usage has increased in the last 25 years and as a result of these studies have been identified that fly ash for adsorption of heavy metals from waster water can be used as adsorbent materials [4,5]. Fly ash produced in the combustion of sub-bituminous coals exhibits self-cementing characteristics that can be adapted to a wide range of stabilization applications. Ash treatment can effectively reduce the swell potential of fat clay soils and increase subgrade support capacity of pavement subgrades. Fly ash can be used to enhance and stabilize bases, subgrades, and embankments; to enhance strength properties and to control shrink/swell properties of expansive soils. Fly ash can also be used as a drying agent to reduce soil moisture contents to permit compaction and avoid delays in construction during periods of wet weather.

2. MATERIAL AND METHODS

a. Soil

The clayey-silt soil was collected within a dept of about 3 m from the existing ground surface. From the Table.1 seen that clay has around %10 moisture content which could be acceptable as low level. Standart Compaction Test and Modified Compaction Test were experiented to define Optimum Moisture Content (OMD) of soil as %22 and %16 respectively.

Table 1. Physical properties of soil

Nature Water Content	Specific Gravity	Grain size distribution			Atterberg's Limit		
		Gravel	Sand	Silt & Clay	Liquid Limit	Plastic Limit	Plasticity Index
11,15%	2,71	0,00%	8,46%	91,54%	65,00%	23,49%	41,51%

Table 2. Engineering properties of soil

Soil Classification	Optimum Moisture Content (%)	Maximum Dry Density	Unconfined Compressive Strength (kPa)
CH	22%	1,564	228,66

b. Pb-Zn (Lead-Zinc)

Lead-Zinc is a waste additive which is being produced in mining dump, locates in Balikesir-Balya region. From the Fig.2 observed that it has %12 optimum moisture content.

Table 3. Chemical Compositions of Pb-Zn

Constituent	Percentage Range of Pb-Zn (%)
SiO2	36,19
Al2O3	8,08
Fe2O3	13,58
MgO	2,54
CaO	23,26
Na2O	0,20
K2O	2,45
TiO2	0,29
P2O5	0,08
MnO	0,38
Cr2O3	0,01

Table 4. Physical properties of Pb-Zn

Nature Water Content	Specific Gravity	Grain size distribution			Atterberg's Limit		
		Gravel	Sand	Silt & Clay	Liquid Limit	Plastic Limit	Plasticity Index
10,00%	3,14	0,00%	20,00%	80,00%	18,40%	16,78%	1,62%

Table 5. Engineering properties of Pb-Zn

Soil Classification	Optimum Moisture Content (%)	Maximum Dry Density	Unconfined Compressive Strength (kPa)
ML	12%	2,012	14,13

c. Fly Ash

Fly ash is a byproduct of coal fired electric power generation facilities; it has little cementations properties compared to lime and cement. The fly ash which is composed at the thermal power plants, locates in Turkey, are generally concerns to the class “C” (Tokyay, 1993).The availability of fly ash as a pozzolanic material depends on its physical and chemical properties. The changings which were occurred not only due to the alteration of mineral mold which turns out in fly ash, but also these changings depends on working condition of coal bunker,fineness of coal before burning and the addivites which are mixed with coad for air pollution control. These fluctuations which occurs in fly ash, affects pozzolanic activity (Joshi and Nagaraj, 1987). In this research, fly ash was provided from thermal power station “Catalagzi” which locates in Zonguldak, a city where is set at the west side of Black Sea Region of Turkey. The class of flyash which was used in this research, belongs to the class “F”.

d. Experimental Methods

In this study, high clay plasticity clay were blended with Pb-Zn (lead-zinc) in the ratios %10, %20, %30, %40, %50, %60 and %80. As a second part of the study, fly ash was added to clay-lead-zinc samples with the ratios %5, %10 and %20. The samples that were prepared with different ratios, implemented at geotechnical

experiments which named Atterberg Limit, Standart Compaction and Unconfined Compression Strength tests. The different ratios admixtures prepared by their optimum moisture content. The samples were prepared with 38.5 mm radius and 77 mm length. Then, they were waited around 24 hours in dessicator before performing unconfined compression strength tests.

3. RESULTS

a. Atterberg Limit Test

In this study, Atterberg Limit Tests [6] were done to the admixtures which includes clay, fly ash and Pb-Zn. As adding Pb-Zn (lead-zinc) and flyash, plasticity index and liquid limit showed decreasing. The liquid limit, plastic limit and plasticity index of the soil with different percentages of Pb-Zn and flyash is given Table 6.

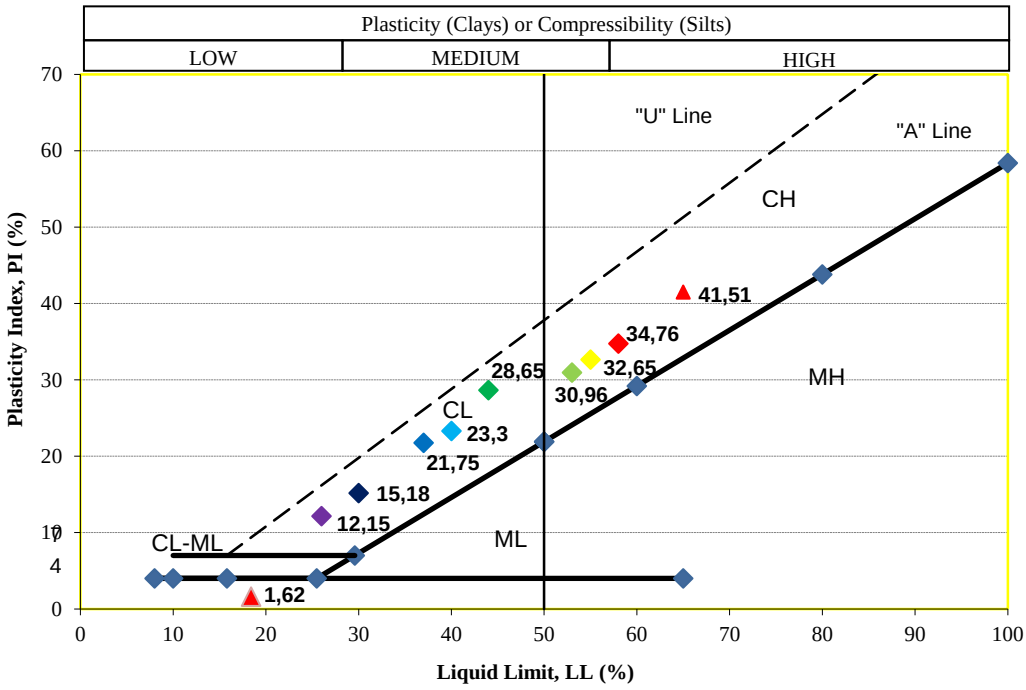

Fig 1. Plasticity Chart showing fine and Pb-Zn treated soil

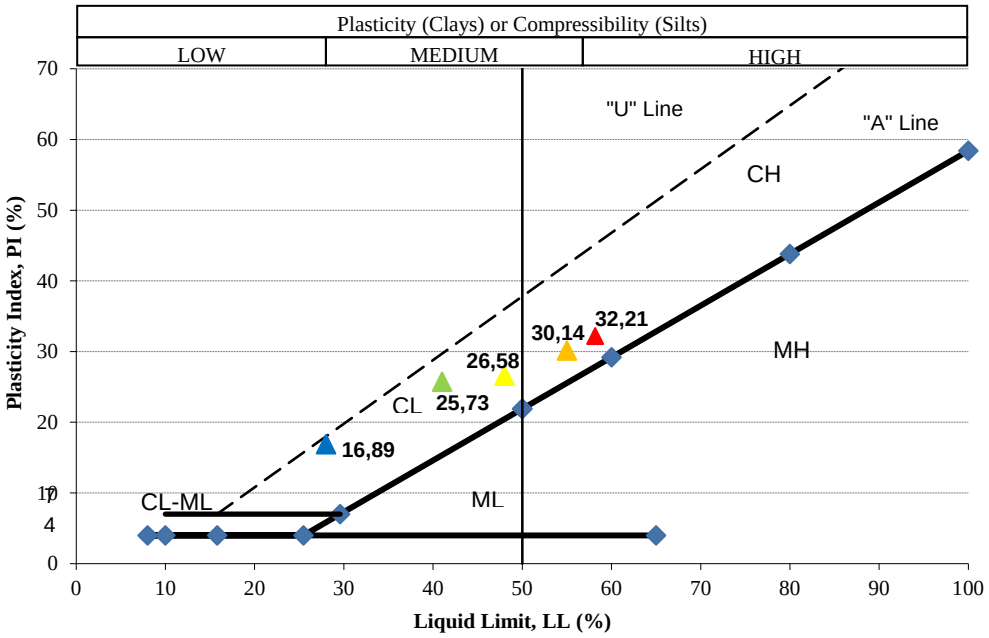

Fig 2. Plasticity Chart showing fine and Fly Ash – Pb-Zn treated soil

Table 6. The values of Atterberg Limits of Clay with Pb-Zn and Fly Ash

Fly Ash	Pb-Zn	Clay	Liquid Limit (%)	Plastic Limit (%)	Plasticity Index (%)
The Percentages of additives					
	0%	100%	65	23,49	41,51
	5%	95%	58	23,24	34,76
	10%	90%	55	22,35	32,65
	20%	80%	53	22,04	30,96
	30%	70%	44	15,35	28,65
	40%	60%	40	16,70	23,30
	50%	50%	37	15,25	21,75
	60%	40%	30	14,82	15,18
	70%	30%	26	13,85	12,15
	100%	0	18	16,78	1,220
5%	10%	85%	58	25,95	32,05
10%	10%	80%	55	24,86	30,14
10%	20%	70%	48	21,42	26,58
10%	30%	60%	42	16,37	25,63
10%	40%	50%	41	15,27	25,73
10%	50%	40%	32	12,32	19,68
10%	60%	30%	28	11,11	16,89
10%	70%	20%	22	10,85	11,15
10%	80%	10%	17	9,76	7,24

b. Proctor Compaction Test

The Proctor Compaction Test is a laboratory geotechnical testing method used to determine the soil compaction properties, specifically, to determine the optimum water content at which soil can reach its maximum dry density. In this experimental research, this method firstly was done to clay, Pb-Zn and fly ash separately. It is observed that the optimum water content is %22 for clay; %12 for Pb-Zn (lead-zinc); %23 for fly ash. Then, same method was applied to clay-Pb-Zn and Clay-Pb-Zn-Fly Ash admixtures with different percentages which their results are shown at Table 7.

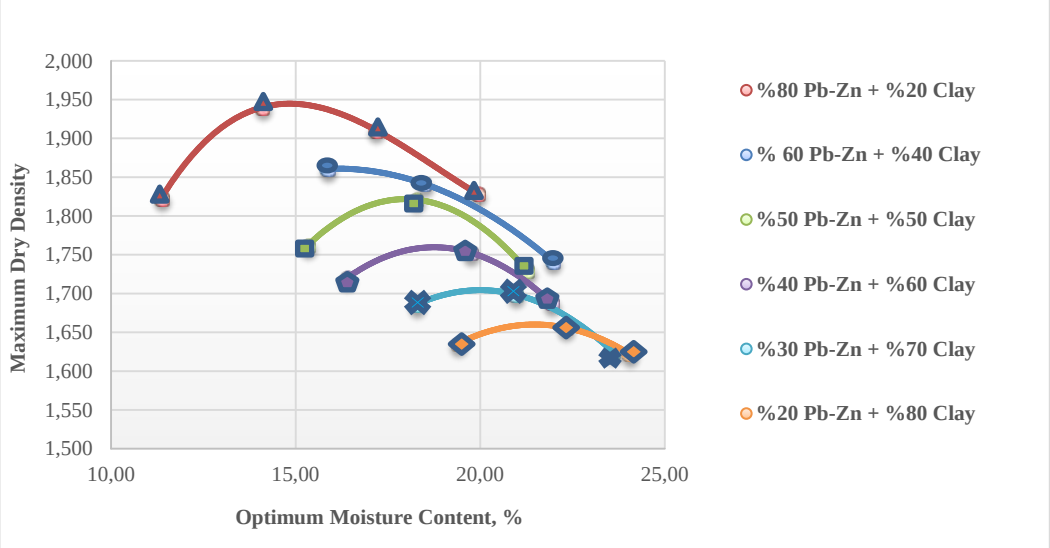

Fig 3. Optimum Water Content – Maximum Dry Density for Clay with Pb-Zn and Fly ash

Table 7. Optimum Water Content – Maximum Dry Density for Clay with Pb-Zn and Fly ash

Fly Ash	Pb-Zn	Clay	Optimum Water Content	Maximum Dry Density
	0%	100%	22,00 %	1,564
	20%	80%	21,20 %	1,664
	30%	70%	20,00 %	1,705
	40%	60%	18,75 %	1,760
	50%	50%	18,00 %	1,822
	60%	40%	16,00 %	1,860
	80%	20%	14,80 %	1,945
	100%	0%	12,00 %	2,012
100%	0%	0%	23,00 %	1,490
5%	10%	85%	22,15 %	1,634
10%	10%	80%	21,15 %	1,686
10%	20%	70%	19,90 %	1,702
10%	40%	50%	18,15 %	1,807
20%	10%	70%	20,30 %	1,641
20%	20%	60%	19,80 %	1,693
20%	40%	40%	17,40 %	1,801

c. Unconfined Compression Strength Test

Unconfined Compression Test (UCT) is a simple laboratory testing method to assess the mechanical properties of rocks and fine-grained soils. In this experimental research, high clay plasticity clay were blended with Pb-Zn (lead-zinc) in the ratios %10, %20, %30, %40, %60 and %80. As a second part, fly ash was added in the ratios %5, %10 and %20 to clay-lead-zinc admixtures. Unconfined Compression Strength Test [6] was experienced to admixtures and the results from these experiments, were shown at the Table 8 and Fig 4.

Table 8. Variation of Unconfined Strength with Pb-Zn and Flyash additives

The Percentages of Materials			Unconfined Compression Strength (kPa)	
Fly Ash	**Pb-Zn**	**Clay**	**qu**	**Cu**
	0%	**100%**	**228,66**	**114,33**
	10%	**90%**	**231,08**	**115,54**
	20%	**80%**	**258,12**	**129,06**
	30%	**70%**	**200,72**	**100,36**
	40%	**60%**	**166,05**	**83,03**
	60%	**40%**	**182,67**	**91,34**
	80%	**20%**	**82,40**	**41,20**
	100%	**0%**	**14,13**	**7,07**
5%	**10%**	**85%**	**483,78**	**241,89**
5%	**20%**	**75%**	**463,60**	**231,80**
5%	**40%**	**55%**	**214,11**	**107,06**
10%	**10%**	**80%**	**379,17**	**189,59**
10%	**20%**	**70%**	**265,44**	**132,72**
10%	**40%**	**50%**	**193,93**	**96,97**
20%	**10%**	**70%**	**358,19**	**179,10**
20%	**20%**	**60%**	**291,88**	**145,94**
20%	**40%**	**40%**	**179,65**	**89,83**

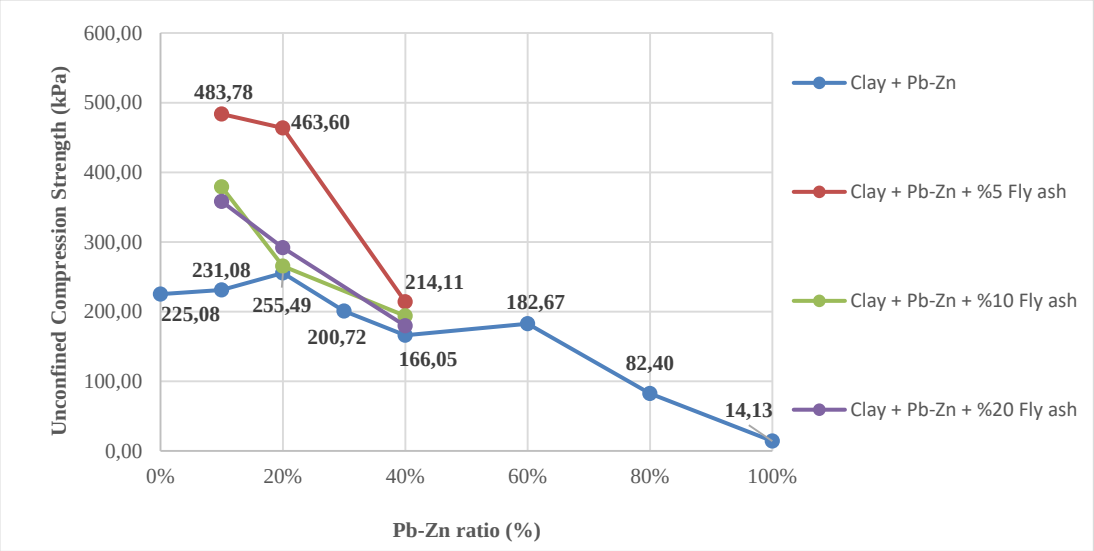

Fig 4. Influence of Pb-Zn and Fly Ash additives on UCS for Clay samples

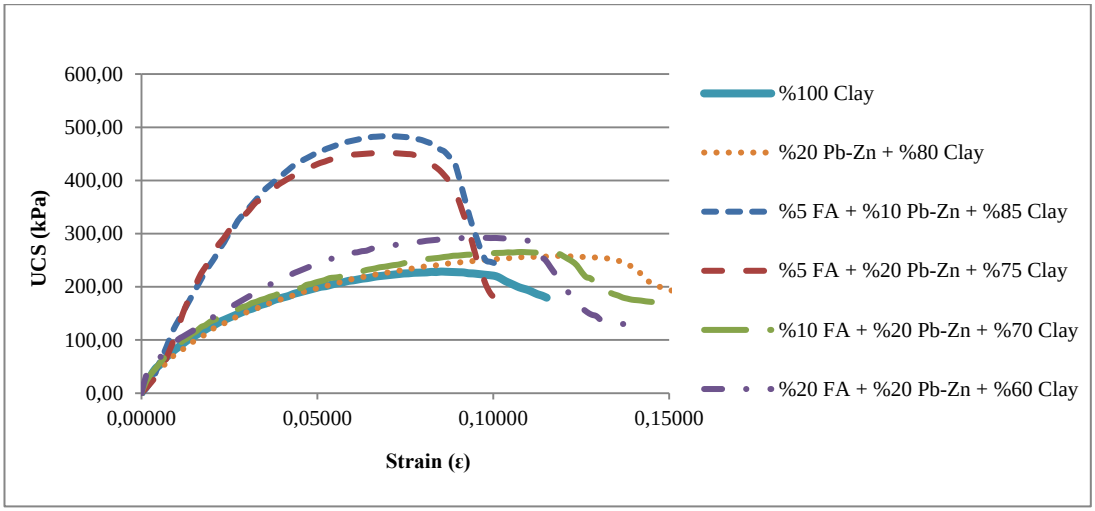

Fig 5. UC Stress strain curves of Clay and Clay-Pb-Zn-Fly ash

4. CONCLUSION

In this research, it was aimed to improve the strength of soil with industrial additives as lead-zinc and fly ash. As increasing Pb-Zn ratio with clay, the values of liquid limit (LL) and Plasticity Index (PI) showed decreasing. While increasing Pb-Zn ratio with clay, Optimum Moisture Content (OMD) showed decreasing and Max. Dry Unit Weight has increased proportionally. UCS values decreased proportionally by adding %10 and %20 Fly Ash ratio with clay-Pb-Zn samples respectively. The ratio improvement by additives was shown in Table 9.

Table 9. The ratio of improvement of clay soil with Pb-Zn and fly ash

The Percentages of Materials			Unconfined Compression Strength (kPa)		The ratio of improvement
Fly Ash	Pb-Zn	Clay	qu	Cu	%
	0%	100%	228,66	114,33	0
	20%	80%	258,12	129,06	12,88
5%	10%	85%	483,78	241,89	111,57
5%	20%	75%	463,60	231,80	102,75
10%	20%	70%	265,44	132,72	16,09
20%	20%	60%	291,88	145,94	27,65

- It was resulted that the highest compression strength value was obtained in 20% lead-zinc additive with clay. The reasonable fly ash content ratio is %5 with clay-Pb-Zn samples.
- The highest UCS value was reached at the samples which were prepared with the ratios; %5 Fly Ash + %10 Pb-Zn + %85 Clay. The soil has been improved more than %100.

Acknowledgement

The authors thank to Istanbul University, The Department of Mining Engineering, "Investigation of the use of paste technology in the underground storage of mine process wastes", Scientific Research Project Funding (TUBITAK) for their support [Project number: 116M721].

REFERENCES

[1] Ozaydin, K. 'Zemin Mekanigi', Birsen Yay.Istanbul, pp 288-289, 2011.
[2] Website According to GRT. http://www.globalroadtechnology.com/types-of-soil stabilization/
[3] A. Bilodeau and V.M. Malhotra, *High-volume fly ash system. Concrete solution for sustainable development,* ACI Mater.J., vol. 97, pp. 41-49, 2000.
[4] S. Mohan and R. Gandhimathi, *Removal of heavy metal ions from municipal solid waste leachate using coal fly ash as an adsorbent,* J Hazard Mater., vol. 169(1-3), pp. 351-359, 2009.
[5] M. Ahmaruzzaman, *Adsorption of phenolic compounds on low-costadsorbents*: A review, Colloids Surfaces Sci., vol. 143, pp. 48-67, 2008.
[6] ASTM D 2166, 2000. Standart test method for unconfined compressive strength of cohesive soils.

BIOGRAPHY

Fatih Balatan, is civil engineer who was graduated at Azerbaijan Architecture and Construction University in 2012. Having had work experience as civil engineer in Moscow/Russia between 2013-2015, started master degree (MSc.) in geotechnical engineering with thesis at Yildiz Technical University in 2015. The topic of thesis which he studies is "soil improvement with industrial additives".

ICENS 4TH INTERNATIONAL CONFERENCE ON ENGINEERING AND NATURAL SCIENCE
2 - 6 May 2018 KIEV UKRAINE

Analytical Solution and Comparison of Slip Fluid Flow in a Circular Micro-Channel with First and Second Order Boundary Conditions

***Soner Sen*[1]**

Abstract

In this study, momentum equations describing gas flow in circular micro-channels are analytically solved for first and second order slip flow boundary conditions. The results obtained are tabulated and graphically presented and compared with each other for different Knudsen numbers. The results showed that, when Knudsen number is larger than 0.5, the second order slip flow boundary condition gives a more realistic result.

Keywords: Microchannel flow, Micro-pipe, Rarefaction effect, Slip flow

1. INTRODUCTION

Micro scale electro-mechanical systems recently possess higher importance in applications such as automotive, defense industry, aviation and space systems, bio-medical and nuclear energy. Each day, transferred heat per unit area/volume in these improving systems continuously increase and serious heat and flow problems emerge due to some various factors. In order to solve these mentioned problems, the experimental investigations are not enough because of their micro scales. In addition, the slip flow phenomenon that occurs in the micro structure greatly affects the solution approaches of the problems. So that, analytical and numerical solutions have become important for these studies.

The momentum and energy transfer that occurs during the flow of fluid materials is a consequence of inter-molecular interaction. Between the two collisions that a fluid molecule made, and get an average distance is defined as the mean free path (λ). The obtained mean free path is comparable to the characteristic length (hydraulic diameter) of the system. The ratio by this comparison is called the *Knudsen* number (λ/Dh). The Knudsen number is an orgy that allows flow regimes to be characterized. Channels with dimensions of 200 μm ≥ Dh> 10 μm are called micro channels. Table 1 shows the Knudsen number-dependent flow regimes.

Table 1. Flow regimes for different Knudsen numbers [1]

Knudsen Number	Flow Regime
Kn < 0.001	Continuum flow
0.001 ≤ Kn ≤ 0.1	Slip flow
0.1 ≤ Kn ≤ 10	Transient flow
Kn > 10	Free molecular flow

We can describe the fluid motion in the slip flow regime by solving the momentum equations taking into account the slip boundary condition at the interface. This interface boundary condition can be expressed by first and second order equations respectively in equation 1 and 2.

[1] *Corresponding author: Selcuk University, Department of Airplane Airframe and Engine Maintenance, School of Civil Aviation, 42250 Selcuklu/Konya, Turkey. sensoner@selcuk.edu.tr*

$$u_s = -\frac{2-\sigma_m}{\sigma_m}\left[\lambda\frac{\partial u}{\partial r}\right]$$

(1)

$$u_s = -\frac{2-\sigma_m}{\sigma_m}\left[\lambda\frac{\partial u}{\partial r} - \frac{\lambda^2}{2}\frac{\partial^2 u}{\partial r^2}\right]$$

(2)

There are many studies in the literature investigating gas phase slip flow phenomena with micro-geometry. Some of these studies can be summarized as follows;

Luo at al. [2] extended the classic momentum transfer to account the slips of velocity and temperature between the liquid phase and the gas phase in condensing flows. This new method of moments is integrated into a numerical method and is applied to a vortex shedding problem with condensation. Due to the very strong velocity slip, a dry zone is found in the vortex core region. They said that this phenomenon was experimentally observed but not discovered by the classic moment method. Knupp et al. [3] made an integral transforms analysis is undertaken for conjugated heat transfer in circular micro-channels with laminar gaseous flow in the slip flow regime. This solution methodology is based on the Generalized Integral Transform Technique applied to a single domain formulation that models the coupled heat transfer phenomena at the fluid stream and at the channel wall. The results obtained from this study are critically compared against a dedicated finite difference numerical solution for the original multi-region problem. The magnetohydrodynamic (MHD) flow of a generalized Maxwell fluid induced by a moving plate has been investigated by Liu and Guo [4], where the second-order slip between the wall and the fluid in the wall is considered. This study results show that the velocity corresponding to flows with slip condition is lower than that for flow with non-slip conditions, and the velocity with second-slip condition is lower than that with first-order slip condition. Zhu et al. [5] investigated that the analyzes of the effects of second order velocity slip and nanoparticles migration on nanofluids between two rotating parallel plates. The showed the physical interests in Nusselt number and skin friction as well as nanoparticles migration are illustrated by graphics. Akyildiz and Siginer [6] investigated the forced convection heat transfer in fully developed gaseous laminar slip flow in transversally corrugated micro pipes for first-order slip boundary conditions on the wall. Exact results obtained in this study are compared with the recent approximate analytical solution in the literature, Sadeghi et al. [7]. Varade et al. [8] presents experimental and three-dimensional numerical study of gaseous slip flow through diverging microchannel. The measurements are performed for nitrogen gas flowing through microchannel with different divergence angles (4, 8, 12 and 16 degree), hydraulic diameters (118, 147 and 177 μm) and lengths (10, 20 and 30 mm). The obtained results on gaseous slip flow through diverging micro channels are considerably different than their continuum counterparts, and are not previously available. Hayat et al. [9] covered a study that three-dimensional flow of carbon–water nanofluid due to slendering nonlinear stretching sheet with slip effects. They showed a favorable agreement through comparison of past and present results in limiting case. Wang et al. [10] found that some slip boundary conditions for gas flow can also be applied to liquid flow, except the different way of treating accommodation coefficients. Results indicate that used boundary conditions are suitable for both linear and non-linear liquid flow. And some other studies considering the slip flow regime can be found at [11], [12] and [13].

In this study, gas flow momentum equations in a circular micro-channel is analytically solved for first and second order slip flow boundary conditions. The results obtained are tabulated and graphically presented and compared with each other for different Knudsen numbers.

2. MATHEMATICAL SOLUTION

Figure 1 shows the velocity profile of the discussed.micro-channel slip flow regime. When the figure is examined, it is seen that the velocity of the fluid in the interface region has a value that is different from the velocity of the wall, and therefore it seems that there is a slip velocity at the interface.

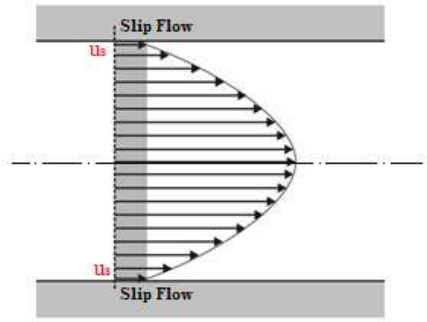

Figure 1. The schematic view of the velocity profile on slip flow regime

With assumptioning a incompressible, continuous, two dimensional, laminer and axial symmetry flow, the continuity and momentum equations become as follows;

continuity equation

$$\frac{\partial v}{\partial r}+\frac{v}{r}+\frac{\partial u}{\partial x}=0$$

(3)

x-momentum equation

$$v\frac{\partial u}{\partial r}+u\frac{\partial u}{\partial x}=-\frac{1}{\rho_f}\frac{\partial p}{\partial x}+\upsilon\left[\frac{1}{r}\frac{\partial}{\partial r}\left(r\frac{\partial u}{\partial r}\right)+\frac{\partial^2 u}{\partial x^2}\right]$$

(4)

r-momentum equation

$$v\frac{\partial v}{\partial r}+u\frac{\partial v}{\partial x}=-\frac{1}{\rho_{nf}}\frac{\partial p}{\partial r}+\upsilon\left[\frac{\partial}{\partial r}\left(\frac{1}{r}\frac{\partial(rv)}{\partial r}\right)+\frac{\partial^2 v}{\partial x^2}\right] \qquad (5)$$

For hydrodynamic fully developed flow, the following conditions can be written;

$$\frac{\partial u}{\partial x}=0$$

(6-a)

$$v = 0$$

(6-b)

$$\frac{\partial p}{\partial r} = 0 \qquad (6\text{-c})$$

If the hydrodynamic fully developed flow conditions are applied to equation 4;

$$\nu \frac{1}{r}\frac{\partial}{\partial r}\left(r\frac{\partial u}{\partial r}\right) - \frac{1}{\rho_f}\frac{\partial p}{\partial x} = 0 \qquad (7)$$

obtained and for P = P (x) at any point perpendicular to the flow, Equation (7) can be expressed as.

$$\frac{1}{r}\frac{d}{dr}\left(r\frac{du}{dr}\right) = \frac{1}{\mu}\frac{dp}{dx} \qquad (8)$$

$$\frac{dp}{dx} = const. = -\frac{\Delta P}{L}$$

Equation (8) therefore becomes:

$$\frac{1}{r}\frac{d}{dr}\left(r\frac{du}{dr}\right) = -\frac{1}{\mu}\frac{\Delta P}{L}$$

$$\frac{d}{dr}\left(r\frac{du}{dr}\right) = -\frac{r}{\mu}\frac{\Delta P}{L} \qquad (9)$$

For the equation is first integrated;

$$r\frac{du}{dr} = -\frac{r^2}{2\mu}\frac{\Delta P}{L} + c_1 \qquad (10)$$

If you divide both sides by "r"

$$\frac{du}{dr} = -\frac{r}{2\mu}\frac{\Delta P}{L} + \frac{c_1}{r}$$

and second integration, the following equation is obtained.

$$u(r) = -\frac{r^2}{4}\frac{1}{\mu}\frac{\Delta P}{L} + c_1 \ln(r) + c_2 \tag{11}$$

Boundary conditions at;

channel axis, for $r = 0$ $\frac{du}{dr} = 0$ (12-a)

the interface, for $r = r_{wi}$ (1st order) $u = u_s = -\frac{2-\sigma_m}{\sigma_m}\lambda\frac{du}{dr}\Big)_{r=r_{wi}}$ (12-b)

the interface, for $r = r_{wi}$ (2nd order) $u = u_s = -\frac{2-\sigma_m}{\sigma_m}\left(\lambda\frac{du}{dr} - \frac{\lambda^2}{2}\frac{d^2u}{dr^2}\right)\Big)_{r=r_{wi}}$ (12-c)

Momentum (σm) accommodation coefficient vary between 0.87 and 0.99 relative to the fluid and wall material type. From the analysis the accommodation coefficient is taken 1.0 to simplify the solution [1]. In this case, the 1st and 2nd order boundary conditions in the interface can be written as:

$$u = u_s = -\lambda\frac{du}{dr}\Big)_{r=r_{wi}}$$

$$u = u_s = -\lambda\frac{du}{dr} + \frac{\lambda^2}{2}\frac{d^2u}{dr^2}\Big)_{r=r_{wi}}$$

(12-a) boundary condition is applied to the equation (10);

$$-\frac{r^2}{2\mu}\frac{\Delta P}{L} + c_1 = 0$$

and get c_1 as,

$$c_1 = 0$$

(12-b) boundary condition can be write on equation (11)

$$u(r) = -\frac{r^2}{4}\frac{\Delta P}{\mu L} + c_2$$

$$u = u_s = -\lambda\left(\frac{du}{dr}\right)_{r=r_{wi}} = -\frac{r_{wi}^{\ 2}}{4}\frac{\Delta P}{\mu L} + c_2$$

$$-\lambda\left(-\frac{r}{2}\frac{\Delta P}{\mu L}\right)_{r=r_{wi}} = -\frac{r_{wi}^{\ 2}}{4}\frac{\Delta P}{\mu L} + c_2$$

$$c_2 = \lambda\frac{r_{wi}}{2}\frac{\Delta P}{\mu L} + \frac{r_{wi}^{\ 2}}{4}\frac{\Delta P}{\mu L}$$

If the constants c_1 and c_2 are written in place in Eq. (11);

$$u(r) = -\frac{r^2}{4}\frac{\Delta P}{\mu L} + \lambda\frac{r_{wi}}{2}\frac{\Delta P}{\mu L} + \frac{r_{wi}^{\ 2}}{4}\frac{\Delta P}{\mu L} \tag{13}$$

get obtained and if this statement is edited;

$$u(r) = -\frac{r^2}{4}\frac{\Delta P}{\mu L} + \frac{\lambda}{2r_{wi}}\frac{2r_{wi}^{\ 2}}{2}\frac{\Delta P}{\mu L} + \frac{r_{wi}^{\ 2}}{4}\frac{\Delta P}{\mu L}$$

$$u(r) = -\frac{r^2}{4}\frac{\Delta P}{\mu L} + Kn\frac{\Delta P}{\mu L}r_{wi}^{\ 2} + \frac{r_{wi}^{\ 2}}{4}\frac{\Delta P}{\mu L}$$

$$u(r) = \frac{1}{4\mu}\frac{\Delta P}{L}\left(r_{wi}^{\ 2} - r^2 + 4r_{wi}^{\ 2}Kn\right) \tag{14}$$

Obtained and average velocity definition;

$$u_m = \frac{\int_r^{r_{wi}} u dA}{\int_r^{r_{wi}} dA}$$

can be used and as written $dA = 2\pi r dr$;

$$u_m = \frac{\int_r^{r_{wi}} u dA}{\int_r^{r_{wi}} dA} = \frac{\int_0^{r_{wi}} \frac{1}{4\mu}\frac{\Delta P}{L}\left(r_{wi}^{\ 2} - r^2 + 4r_{wi}^{\ 2}Kn\right)2\pi r dr}{\int_0^{r_{wi}} 2\pi r dr} \tag{15}$$

$$u_m = \frac{1}{8\mu}\frac{\Delta P}{L} r_{wi}^2 \left(1 + 8Kn\right) \tag{16}$$

is obtained. Using the equations (14) and (16), the dimensionless velocity expression can be written as

$$u' = \frac{u}{u_m} = \frac{\frac{1}{4\mu}\frac{\Delta P}{L} r_{wi}^{\ 2}\left(1 - \left(\frac{r}{r_{wi}}\right)^2 + 4Kn\right)}{\frac{1}{8\mu}\frac{\Delta P}{L} r_{wi}^2 \left(1 + 8Kn\right)}$$

$$u' = \frac{u}{u_m} = \frac{2(1 - (r/r_{wi})^2) + 8Kn}{1 + 8Kn} \tag{17}$$

If a similar solution can be obtained for the second order slip boundary condition, the following dimensionless velocity profile get obtained.

$$u' = \frac{u}{u_m} = \frac{2(1 - (r/r_{wi})^2) + 8Kn - 8Kn^2}{1 + 8Kn - 8Kn^2} \tag{18}$$

3. RESULTS AND DISCUSSION

Solutions were made for seven different values of Knudsen number in order to see the differences of the first and second order boundary conditions for the slip flow regime. The handled Knudsen numbers are typical values that can be encountered in engineering problems. Table 2 gives the axial velocity values related to the first and second boundary conditions according to the radial coordinate. In addition to this, Figure 2 shows the velocity profiles in the microchannel according to the first and second order boundary conditions.

When the table is examined, it is seen that, when the Knudsen number increases, the fluid velocity at the interface begins to vary from zero, depending on the rarefaction in the fluid molecules. In addition, with the increasing Knudsen number (rarefaction effect), the maximum velocity value in the channel axis decreases. Furthermore, the difference in the first and second order boundary condition solutions on velocity values are formed after Kn≥0.025.

Table 2. Dimensionless axial velocities for different values of Kn (1st and 2nd order)

Radial Coordinate (r')	**Knudsen Number (Kn)**													
	0.000		0.001		0.005		0.010		0.025		0.050		0.100	
	Axial Velocity (u')													
	1st	2nd	1st	2nd	1st	2nd	1st	2nd	1st	2nd	1st	2nd	1st	2nd
1.00	0.000	0.000	0.008	0.008	0.038	0.038	0.074	0.073	0.167	0.163	0.286	0.275	0.444	0.419
0.95	0.195	0.195	0.201	0.201	0.226	0.226	0.255	0.254	0.329	0.326	0.425	0.417	0.553	0.532
0.90	0.380	0.380	0.385	0.385	0.404	0.404	0.426	0.426	0.483	0.481	0.557	0.551	0.656	0.640
0.85	0.555	0.555	0.559	0.559	0.572	0.572	0.588	0.588	0.629	0.628	0.682	0.678	0.753	0.741
0.80	0.720	0.720	0.722	0.722	0.731	0.731	0.741	0.741	0.767	0.766	0.800	0.797	0.844	0.837
0.75	0.875	0.875	0.876	0.876	0.880	0.880	0.884	0.884	0.896	0.895	0.911	0.909	0.931	0.927
0.70	1.020	1.020	1.020	1.020	1.019	1.019	1.019	1.019	1.017	1.017	1.014	1.014	1.011	1.012
0.65	1.155	1.155	1.154	1.154	1.149	1.149	1.144	1.144	1.129	1.130	1.111	1.112	1.086	1.090
0.60	1.280	1.280	1.278	1.278	1.269	1.269	1.259	1.259	1.233	1.234	1.200	1.203	1.156	1.163
0.55	1.395	1.395	1.392	1.392	1.380	1.380	1.366	1.366	1.329	1.331	1.282	1.286	1.219	1.230
0.50	1.500	1.500	1.496	1.496	1.481	1.481	1.463	1.463	1.417	1.418	1.357	1.362	1.278	1.291
0.45	1.595	1.595	1.590	1.590	1.572	1.572	1.551	1.551	1.496	1.498	1.425	1.431	1.331	1.346
0.40	1.680	1.680	1.675	1.675	1.654	1.654	1.630	1.630	1.567	1.569	1.486	1.493	1.378	1.395

0.35	1.755	1.755	1.749	1.749	1.726	1.726	1.699	1.700	1.629	1.632	1.539	1.547	1.419	1.439
0.30	1.820	1.820	1.813	1.813	1.788	1.789	1.759	1.760	1.683	1.686	1.586	1.594	1.456	1.477
0.25	1.875	1.875	1.868	1.868	1.841	1.842	1.810	1.811	1.729	1.732	1.625	1.634	1.486	1.509
0.20	1.920	1.920	1.913	1.913	1.885	1.885	1.852	1.852	1.767	1.770	1.657	1.667	1.511	1.535
0.15	1.955	1.955	1.947	1.947	1.918	1.918	1.884	1.885	1.796	1.799	1.682	1.692	1.531	1.555
0.10	1.980	1.980	1.972	1.972	1.942	1.942	1.907	1.908	1.817	1.820	1.700	1.710	1.544	1.570
0.05	1.995	1.995	1.987	1.987	1.957	1.957	1.921	1.922	1.829	1.833	1.711	1.721	1.553	1.578
0.00	2.000	2.000	1.992	1.992	1.962	1.962	1.926	1.927	1.833	1.837	1.714	1.725	1.556	1.581

When the Figure 2 examined, it is seen that the interface fluid velocity for a Knudsen number of 0.1 in the slip flow regime has a value of about 0.444 while the velocity in the channel center has decreased to 1.556. These two values and the sum of the interface and channel center velocity values in all other velocity profiles are always get 2.0. Also in the radial position 0.71, which intersects all the velocity profiles, local velocity value is equal to the average velocity regardless of Knudsen number.

In addition, Figure 2 shows that when the velocity profiles are evaluated in terms of the first and second order slip boundary conditions, it is more realistic to solve the momentum equation with the second order boundary condition when the Knudsen number values greater than 0.025. Whereas there is no difference between first and second order solutions up to 0.025 of Knudsen number.

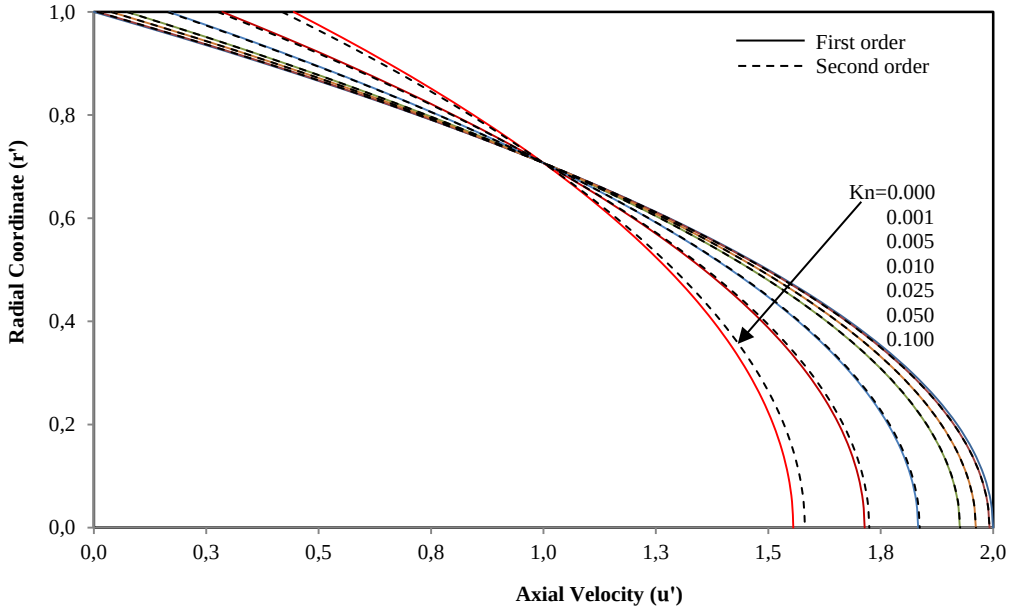

Figure 2. Dimensionless axial velocities for different values of Kn

4. CONCLUSIONS

In that work, the Knudsen number-dependent velocity profiles were obtained for first and second order interface slip boundary conditions in a slip flow regime for a circular channel with micro-geometry. The conclusions from the results can be summarized as follows;

- The increase in Knudsen number reduces the momentum transfer between the fluid molecules and the wall, and thus the fluid molecules at the interface have a different velocity than the wall. This must be taken into account in the design of electro-mechanical systems with micro-channels.
- In the case of the Knudsen number up to 0.025, the solution of the first and second boundary condition does not give different results, but the use of the second boundary condition at Knudsen numbers greater than 0.025 makes the solution more realistic.

ACKNOWLEDGMENT

The Authour is thanks to the Scientific Research Projects Coordinator ship of Selcuk University for their financial support.

REFERENCES

[1]. S.G. Kandlikar, S. Garimella, D. Li, S. Colin, M.R. King, *Heat Transfer and Fluid Flow in Minichannels and Microchannels*, Elsevier, Oxford, 2006

[2]. X. Luo, Y. Cao, F. Qin, "A phase-slip moment method for condensing flows", *International Journal of Heat and Mass Transfer*, vol. 118, pp. 1257–1263, 2018.

[3]. D. C. Knupp,, F. S. Mascoute, L. A. S. Abreu, C.P. Naveira, "Conjugated heat transfer in circular micro channels with slip flow and axial diffusion effects", *International Communications in Heat and Mass Transfer*, vol. 91, pp. 225–233, 2018.
[4]. Y. Liu, B. Guo, "Effects of second-order slip on the flow of a fractional Maxwell MHD fluid", *Journal of the Association of Arab Universities for Basic and Applied Sciences*, vol. 24, pp. 232–241, 2017.
[5]. J. Zhu, D. Yang, L. Zheng, X. Zhang, "Effects of second order velocity slip and nanoparticles migration on flow of Buongiorno nanofluid", *Applied Mathematics Letters*, vol. 52, pp. 183–191, 2016.
[6]. F. T. Akyildiz, D. A. Siginer, "Exact solution for forced convection gaseous slip flow in corrugated micro tubes", *International Journal of Heat and Mass Transfer*, vol. 112, pp. 553–558, 2017.
[7]. A. Sadeghi, H. Salarieh, M.H. Saidi, A.A. Mozafari, "Effects of corrugated roughness on gaseous slip flow forced convection in microtubes", *Journal of Thermophys. Heat Transfer*, vol. 25, pp. 262–271, 2011.
[8]. V. Varade, V. S. Duryodhan, A. Agrawal, A. M. Pradeep, A. Ebrahimi, E. Roohi, "Low Mach number slip flow through diverging microchannel", *Computers & Fluids*, vol. 111, pp. 46–61, 2015.
[9]. T. Hayat, Z. Hussain, A. Alsaedi, B. Ahmad, "Numerical study for slip flow of carbon–water nano fluids", *Comput. Methods Appl. Mech. Engrg*, vol. 319, pp. 366–378, 2017.
[10]. K. Wang, Z. Chai, G. Huo, W. Chen, S. Xu, "Slip boundary condition for lattice Boltzmann modeling of liquid flows", *Computers and Fluids*, vol. 161, pp. 60–73, 2018.
[11]. P. Rosa, T.G. Karayiannis, M.W. Collins, "Single-phase heat transfer in microchannels: the importance of scaling effects", *Applied Thermal Engineering*, vol. 29, pp. 3447–3468, 2009.
[12]. Zhu, X., and Liao, Q., "Heat transfer for laminar slip flow in a microchannel of arbitrary cross section with complex thermal boundary conditions", *Applied Thermal Engineering*, vol. 26, pp. 1246–1256, 2006.
[13]. C. Hong, Y. Asako, "Heat transfer characteristics of gaseous flows in microtube with constant heat flux", *Applied Thermal Engineering*, vol.28, pp. 1375–1385, 2008.

BIOGRAPHY

Soner SEN

He was born in 1985 in Ankara/Turkey. In 2007, he graduated from Dumlupinar University Faculty of Engineering Department of Mechanical Engineering with "Honor" degree. He gets his Master and PhD. degress in Selcuk University at 2010 and 2016 respectively. Since 2016 he has been working as a lecturer at the same university.

ICENS 4TH INTERNATIONAL CONFERENCE ON ENGINEERING AND NATURAL SCIENCE
2-6 May 2018 KIEV UKRAINE

Simulated Annealing – Based Metaheuristic Approach for Pilot Tones Design in OFDM-IDMA System

Necmi Taspinar[1], Sakir Simsir[2]

Abstract

The possibility of increasing the channel estimation performance significantly by adjusting the pilot positions for the related channel has converted the pilot design process into an important optimization problem to be considered in wireless communication systems. Therefore, in this paper, Simulated Annealing (SA) algorithm, which has been utilized to solve countless problems in various engineering fields so far, is employed for the optimization process of the pilot positions and thus, the estimation performance of the Least Squares (LS) algorithm used for channel estimation in Orthogonal Frequency Division Multiplexing – Interleave Division Multiple Access (OFDM-IDMA) system is maximized. Furthermore, the complexity of Mean Square Error (MSE) that is used as the fitness function of SA is reduced by obtaining its upper bound with the help of Gershgorin disc theorem. By using the upper bound of MSE as the fitness function of SA instead of MSE itself, the matrix inversion process which is required in the calculation of MSE is eliminated. Herewith, the computational load per the iteration of SA algorithm is decreased. In the simulations, our proposed SA-based metaheuristic approach for pilot design problem in OFDM-IDMA system is compared to the random and equispaced – based pilot placement techniques that are known as classical methods. The performance comparison of the considered pilot design techniques is carried out with respect to the Bit Error Rate (BER) and MSE criteria. According to the simulation results, our proposed method shows clearly better performance compared to the classical methods with regard to both BER and MSE criteria.

Keywords: Channel estimation, LS algorithm, OFDM-IDMA, pilot tones design, simulated annealing

1. INTRODUCTION

Orthogonal Frequency Division Multiplexing-Interleave Division Multiple Access (OFDM-IDMA) which is created for gathering the advantages of OFDM and IDMA schemes in one system is a powerful transmission technology having the potential of overcoming both Inter Symbol Interference (ISI) and Multiple Access Interference (MAI) problems, simultaneously [1]. The robustness of the OFDM-IDMA system against the ISI and MAI comes from using both multicarrier transmission technique and iterative Chip by Chip Multiuser Detection (CBC MUD) algorithm based on IDMA principle, respectively [2], [3].

In spite of the aforementioned superiorities of the OFDM-IDMA system, channel estimation which is an unavoidable process in multicarrier transmission technologies is required for eliminating the fading effects caused by the wireless channel. To this end, pilot-based channel estimation method with comb-type pilot placement strategy that is one of the most common and effective way of acquiring Channel State Information (CSI) can be utilized [4]. The strategy of comb-type pilot arrangement is based on inserting the pilot tones into each OFDM symbol in a uniformly distributed manner [5]. On the other hand, the pilot tones distribution pattern directly affects the channel estimation performance. Therefore, it is possible to increase the estimation performance significantly by optimizing the pilot positions with the help of Simulated Annealing (SA) Algorithm.

[1] *Corresponding author: Erciyes University, Department of Electrical and Electronics Engineering, 38039, Kayseri, Turkey. taspinar@erciyes.edu.tr*

[2] *Nevsehir Haci Bektas Veli University, Department of Electrical and Electronics Engineering, 50300, Nevsehir, Turkey. sakirsimsir@nevsehir.edu.tr*

Various studies in which some of the intelligent optimization-based pilot design techniques are applied to OFDM and Multiple Input Multiple Output (MIMO)-OFDM are available in the literature [6-10]. In [6], pilot design process was carried out by using Artificial Bee Colony (ABC) algorithm for MIMO-OFDM system and the ABC-based pilot design technique was compared to random, orthogonal and Particle Swarm Optimization (PSO)-based pilot placement strategies with regard to Bit Error Rate (BER) and Mean Square Error (MSE) criteria. In [7], Differential Evolution (DE) Algorithm was utilized for the optimization process of both pilot tones positions and the power of pilot tones in MIMO-OFDM system. In [8] and [9], pilot positions were optimized by using PSO algorithm. In [10], in Space-Time Block Coding (STBC)-OFDM systems, the performance of Minimum Mean Square Error (MMSE) channel equalization process was improved with the help of Genetic Algorithm (GA) and PSO.

The paper is organized as follows: In Section 2, the description about OFDM-IDMA scheme and its working principle is given. In Section 3, SA algorithm is introduced and then the implementation of the SA to the pilot design problem in OFDM-IDMA system is yielded. In Section 4, the simulation results are given and finally the paper ends with the conclusions in Section 5.

2. SYSTEM DESCRIPTION

The block diagram of the OFDM-IDMA transceiver is given in Figure 1. In the transmitter, the information bits belonging to the active users from 1 to *K* are firstly encoded by one of the existing Forward Error Correction (FEC) coding procedures. Following the encoding process, the encoded data are spread. In the spreading operation, single spreading sequence is used for each user. Each of the spread codewords are then interleaved through the user-specific interleavers generated randomly for each user. After the operations of modulation and pilot insertion, the resultant signal is applied to the Inverse Fast Fourier Transform (IFFT) block. Following the IFFT operation, the time domain signal is given to the wireless channel. At the receiver side, the received time domain signal is converted to frequency domain by the Fast Fourier Transform (FFT) operation and then, $N\times1$ signal vector $\mathbf{Y}(n)$ is achieved as follows [11], [12]:

$$\mathbf{Y}(n)=\sum_{k=1}^{K}\mathbf{X}_k^{diag}(n)\cdot\mathbf{F}\cdot\mathbf{h}(n)+\mathbf{W}(n) \tag{1}$$

where $\mathbf{W}(n)$, $\mathbf{h}(n)$, $\mathbf{F}$ and $\mathbf{X}_k(n)$ symbolizes the $N\times1$ Additive White Gaussian Noise (AWGN) vector, $N\times1$ Channel Impulse Response (CIR) vector, $N\times N$ unitary Discrete Fourier Transform (DFT) matrix and $N\times1$ transmitted symbol vector, respectively. k denotes the user number and n corresponds to the subcarrier number. Following the channel estimation process, the frequency domain signals are inputted to the Elementary Signal Estimator (ESE) and then, CBC MUD process in which the estimated channel coefficients are employed for eliminating the channel fading effects begins at the receiver side. After fulfilling the CBC MUD process, the transmitted information bits are achieved from the decoder outputs [1], [2].

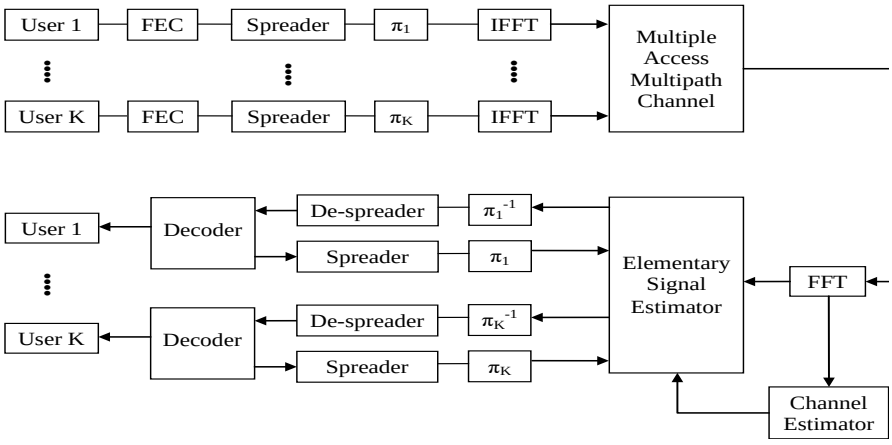

Figure 1. OFDM-IDMA transceiver with K user

The expression of MSE for LS channel estimator employed in OFDM-IDMA system is yielded below:

$$MSE = \frac{1}{N} \cdot \varepsilon \left\{ \left\| \hat{\mathbf{h}} - \mathbf{h} \right\|^2 \right\} \tag{2}$$

where $\hat{h}$ and h correspond to the estimated and real CIRs, respectively. $\varepsilon(.)$ is the expectation operator. By using the Gershgorin Circle Theorem, the fitness function of the Simulated Annealing (SA) algorithm is obtained as follows:

$$fitness\ function = \frac{R_{\max}}{P} \tag{3}$$

where R_{max} and P represents the maximum radius of the Gershgorin disc and fixed power of pilot tones, respectively. Detailed description about the way of obtaining the fitness function by utilizing the Gershgorin Circle Theorem can be found in [6-8].

3. SIMULATED ANNEALING (SA) – BASED PILOT DESIGN TECHNIQUE

The Simulated Annealing (SA) algorithm, mimicking the annealing process was introduced by Kirkpatrick and his friends in 1983 [13]. Annealing is known as a physical process in which the solid material like metal, crystal or glass is heated until exceeding its melting point, the temperature is held at that point for a while and then the related material is cooled slowly until it reaches the crystalline state with minimum defects [13-15].
The main procedure of SA algorithm is based on the acceptance conditions of the randomly generated solutions. In SA algorithm, the new solutions that improve the fitness function are always accepted. On the other hand, if the generated solution worsens the fitness function, it can still be accepted with a probability defined in Equation (4) in order to search the solution space efficiently without getting stuck in local minimums.

$$p = e^{-\Delta f / T} > r \tag{4}$$

where Δf, T and r are the amount of change in the fitness function from previous to the current iteration, the temperature decreased throughout the optimization process and random number in the range [0,1], respectively. If the probability of p which is defined by Boltzmann distribution is greater than r, the new solution that worsens the fitness function is accepted [13-15].
The cooling schedule corresponding to the procedure of decreasing the parameter T has the critical importance on the algorithm performance. In case of reducing T too fast, it is quite likely that the algorithm converges to a local minimum. On the other hand, if the parameter T is reduced too slowly, the algorithm convergence will be very slow as well. For this reason, it is crucial to determine an appropriate cooling schedule for T. In our simulations, we use the geometric decrement function suggested by Kirkpatrick as a cooling schedule [13];

$$T(t) = T_0 . \alpha^t \quad , \quad t = 1, 2, ..., t_f \tag{5}$$

where T_0, t, t_f and α denote the initial temperature, current temperature index, maximum number of temperature change, and cooling factor, respectively. The number of iterations per temperature in SA algorithm can be set by using one of the two known methods called fixed and varied. In the first method, fixed number of iteration is determined for each temperature. So, for each completion of the fixed number of iteration, the temperature is reduced periodically. In the second method, the temperature is reduced per predefined number of acceptance of the new solutions. In our simulations, we use varied number of iteration per temperature and determine the maximum acceptance number per temperature as 10.
The main steps of the SA algorithm is given below [14], [15]:

Step 1

- Generate the first solution in a random way for the fitness function $f(S)$, $S = (s_1, s_2, ..., s_D)^T$

Step 2

- Assign an initial value to T_0
- Determine the cooling schedule, cooling factor α (0<α<1) and maximum number of iterations N.
- Specify the stopping criteria.

Step 3

- Produce an adjacent solution using random walk technique; $S_{n+1} = S_n + \in$

- Calculate the difference between the fitness values of the new and previous solutions; $\Delta f = f(S_{n+1}) - f(S_n)$

Step 4

- If $\Delta f < 0$ (which means that the new solution is better than the previous solution for the minimization problems)
  - ❖ Accept the new solution S_{n+1}
- If the new solution is worse than the previous solution
  - ❖ Generate a random number r in the range [0,1]
  - ❖ If $e^{-\Delta f/T} > r$
    - o Accept the new solution S_{n+1}
  - ❖ Otherwise
    - o Don't accept the new solution S_{n+1} and keep the S_n as the current solution.

Step 5

- Reduce the temperature T with respect to the cooling schedule.

Step 6

- If the stopping criterion is provided, terminate the optimization process, otherwise, go to the Step 3.

In our study of pilot design for the OFDM-IDMA scheme, the pilot positions are represented by the dimensions of candidate solution vector $S = (s_1, s_2, ..., s_D)^T$. In the simulations, these dimensions corresponding to the position values of the pilot tones are constrained by upper and lower bounds defined for each dimension in Table 1. The subcarrier number and the number of pilot tones are determined as 256 and 16, respectively for our system. So, the number of dimension belonging to the candidate solution vector to be optimized has to be 16 as well.

Table 1. Upper and lower bounds defined for each dimension of the candidate solution vector $S = (s_1, s_2, ..., s_D)^T$

Dimensions / ***Bounds***	S_1	S_2	S_3	S_4	S_5	S_6	S_7	.....	.....	S_D
Lower Bound (Lb)	1	17	33	49	65	81	97	.....	.....	$16D-15$
Upper Bound (Ub)	16	32	48	64	80	96	112	.....	.....	$16D$

In the simulation phase, the optimization process starts with generating an initial solution with 16 dimensions each of which ensures the constriction procedure defined in Table 1 and then, the new adjacent solution is generated from the initialized solution. Later on, fitness calculation is made for both solutions with respect to the fitness function given in Equation (3) and the fitness value of the initialized solution is subtracted from the fitness value of the new solution. If the result is less than zero, the new solution is accepted. If the result is greater than zero which means that the new solution is worse than the previous solution for our pilot design problem, one random number r is generated in the range [0,1]. If the generated random number is less than $e^{-\Delta f/T}$, the new solution is accepted. Otherwise, the new solution is not accepted and the previous solution is kept as the current solution. After that, the acceptance number of new solutions is updated (when the acceptance number reaches to 10 which is the maximum number of acceptance determined for the simulations, the temperature T is reduced by using the Equation (5) and the counter indicating the acceptance number is reset). The operations carried out so far are repeated for 2000 iterations which is determined as stopping criterion for the SA algorithm. Subsequent to the termination of optimization process, the final solution vector is determined as the pilot positions vector.

4. SIMULATION RESULTS

In this study, our metaheuristic approach based on SA algorithm is applied to OFDM-IDMA scheme for pilot design process. The MSE and BER performance of the proposed technique is compared to that of the classical methods like equispaced and random-based pilot placements. The simulation parameters of the OFDM-IDMA system and the control parameters of the SA algorithm are given in Table 2 and Table 3, respectively.

In the simulations, the pilot tones are placed in three different ways:

- Random-based placement.
- Equispaced-based placement shown in Figure 2.
- SA-based optimized placement shown in Figure 3.

Table 2. Simulation parameters of the OFDM-IDMA scheme

Number of Subcarriers	256
Type of FEC Encoder	½ Convolutional Encoder
Rate of Spreading Sequence	1/16
Size of FFT	256
Number of Pilot Tones	16
Type of Modulation	QPSK
Type of Channel	COST 207 Rural Area
Sampling Frequency	250 KHz
Sampling Period (*Ts*)	4 µs
Symbol Part Duration (TFFT)	256*Ts* =1024 µs
Size of Cyclic Prefix	FFT/4 = 64
Duration of Cyclic Prefix	TFFT/4=1024/4=256 µs

Table 3. The control parameters of the Simulated Annealing algorithm

SA	
Cooling factor (α)	α = 0.95
Initial temperature (T_0)	T_0 = 1
Maximum number of accept	10
Number of Iteration	2000

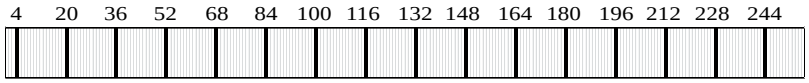

Figure 2. Equispaced-based pilot placement

Figure 3. SA-based optimized pilot placement

In Figure 4, the considered pilot design techniques are compared to each other with regard to BER criteria. The BER graph of the OFDM-IDMA system given in Figure 4 is obtained for the number of 17 users. According

to the Figure 4, our proposed SA-based pilot design technique creates a clear difference with regard to BER performance. Especially towards the higher Eb/No values, the performance superiority of our proposed technique becomes more obvious.

In Figure 5, another criteria known as MSE is utilized for making a performance analysis among the considered strategies. With the MSE graph given in Figure 5, at each Eb/No value, the estimation errors belonging to the LS channel estimator employed in the OFDM-IDMA system can be observed. Since the estimation performance of the LS estimator is directly affected by the positions of pilot tones, the effects of the considered pilot design strategies on the channel estimation performance can be investigated, separately through the MSE graph. According to the Figure 5, from the beginning to the end of the given Eb/No range, SA-based pilot design method provides less estimation errors than the random and equispaced-based pilot placement strategies.

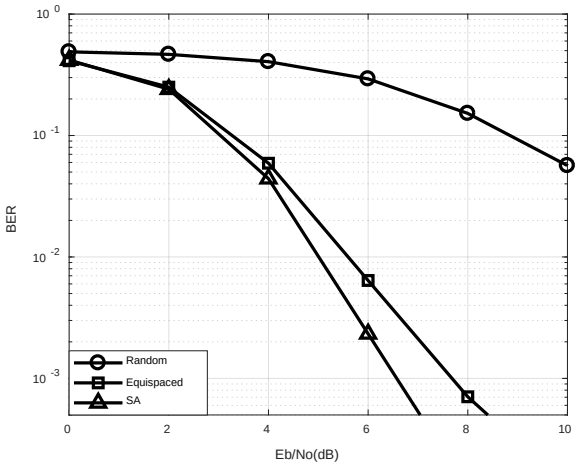

Figure 4. BER performance comparison among the considered pilot design methods

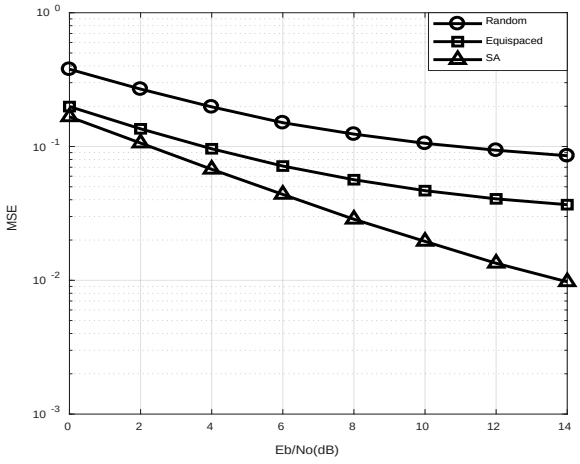

Figure 5. MSE performance comparison among the considered pilot design methods

In Figure 6, the convergence performance of the simulated annealing algorithm is demonstrated. According to the Figure 6, the MSE value of the SA starts to decline rapidly from the first iteration and the algorithm reaches its optimal solution at the end of the iterations.

In Figure 7, the OFDM-IDMA system is simulated under 15, 17, and 19 users for each pilot design method in order to make a BER performance analysis under varied user numbers. It is evident in Figure 7 that, increasing the user number causes an enhancement in the BER values for each method. For instance, in case of taking the BER performance of SA into account, when looking at the BER values at 4dB, the values of 7.7×10^{-3}, 4.4×10^{-2} and 1.4×10^{-1} will be read for 15, 17 and 19 users, respectively.

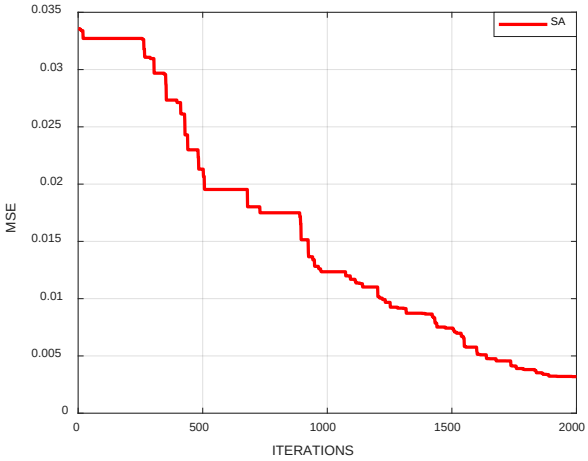

Figure 6. The convergence performance of the Simulated Annealing algorithm

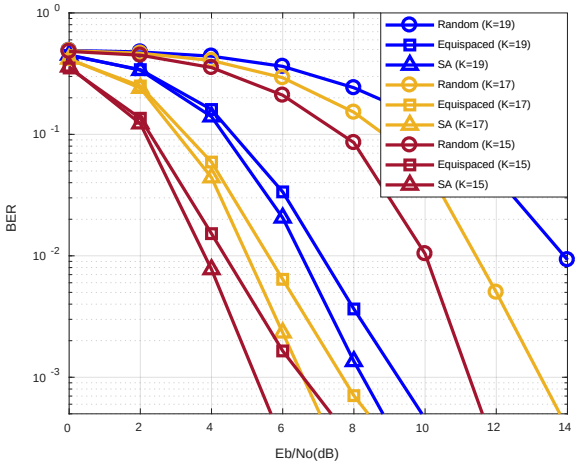

Figure 7. BER performance of the considered pilot design methods for the OFDM-IDMA system under 15, 17 and 19 users.

5. CONCLUSION

In this study, we suggest a powerful pilot design technique based on SA algorithm for the OFDM-IDMA system and compare it to the well-known conventional pilot placement strategies like Random and Equispaced. The performance comparison is made in point of both BER and MSE criteria. According to the simulation results, our proposed SA-based pilot design technique reveals its superiority over the other considered methods by ensuring a significant increase in the MSE and BER performance of the OFDM-IDMA system.

ACKNOWLEDGMENT

This work was supported by the Scientific and Technological Research Council of Turkey (TUBITAK) under Grant 115E653.

REFERENCES

[14]. L. Ping, Q. Guo, and J. Tong, "The OFDM-IDMA approach to wireless communication system," IEEE Wireless Communications, vol. 14, pp. 18-24, 2007.
[15]. L. Ping, L. Liu, K. Y. Wu, and W. K. Leung, "Interleave-division multiple-access," IEEE Transactions on Wireless Communications, vol. 5, pp. 938-947, 2006.
[16]. I. Mahafeno, C. Langlais, and C. Jego, "OFDM-IDMA versus IDMA with ISI cancellation for quasi-static Rayleigh fading multipath channels," in 4th International Symposium on Turbo Codes & Related Topics, 2006, pp. 1-6.
[17]. S. Coleri, M. Ergen, A. Puri, and A. Bahai, "Channel estimation techniques based on pilot arrangement in OFDM systems," IEEE Transactions on Broadcasting, vol. 48, pp. 223-229, 2002.
[18]. M. H. Hsieh, and C. H. Wei, "Channel estimation for OFDM systems based on comb-type pilot arrangement in frequency selective fading channels," IEEE Transactions on Consumer Electronics, vol. 44, pp. 217-225, 1998.
[19]. M. N. Seyman, and N. Taspinar, "Pilot tones optimization using artificial bee colony algorithm for MIMO-OFDM systems," Wireless Personal Communications, vol. 71, pp. 151-163, 2013.
[20]. M. N. Seyman, and N. Taspinar, "Optimization of pilot tones using differential evolution algorithm in MIMO-OFDM systems," Turkish Journal of Electrical Engineering and Computer Sciences, vol. 20, pp. 15-23, 2012.
[21]. M. N. Seyman, and N. Taspinar, "Particle swarm optimization for pilot tones design in MIMO-OFDM systems," EUROSIP Journal on Advances in Signal Processing, vol. 2011, pp. 1-11, 2011.
[22]. K. Vidhya, and K. R. Shankarkumar, "Channel estimation and optimization for pilot design in MIMO OFDM systems," International Journal of Emerging Technology and Advanced Engineering, vol. 3, pp. 175-180, 2013.
[23]. L. D'orazio, C. Sacchi, and M. Doneli, "Adaptive channel estimation for STBC-OFDM systems based on nature-inspired optimization strategies," 3rd International Workshop of Multiple Access Communication, 2010, pp. 188-198.
[24]. S. Simsir, and N. Taspinar, "Channel estimation using radial basis function neural network in OFDM-IDMA system," Wireless Personal Communications, vol. 85, pp. 1883-1893, 2015.
[25]. N. Taspinar, and S. Simsir, "Channel estimation using an adaptive neuro fuzzy inference system in the OFDM-IDMA system," *Turkish Journal of Electrical Engineering and Computer Sciences*, vol. 25, pp. 352-364, 2017.
[26]. S. Kirkpatrick, ; C. D. Gelatt, and M. P. Vecchi, "Optimization by Simulated Annealing", *Science*, vol. 220, pp. 671-680, 1983.
[27]. X. S. Yang, *Nature-Inspired Metaheuristic Algorithms*, 2nd ed., Cambridge, United Kingdom: Luniver Press, 2010.
[28]. K.L. Du and M. N. S. Swamy, Search and Optimization by Metaheuristics: Techniques and Algorithms Inspired by Nature, 1st ed., Basel, Switzerland: Birkhäuser, 2016.

Biography of the presenting author

Necmi Taspinar received the B.S. degree in Electronic Engineering from the Erciyes University, Kayseri, Turkey in 1983, the M.S. degree in Electronic and Telecommunications Engineering from the Technical University of Istanbul, Istanbul, Turkey in 1988, and the Ph.D. degree in Electronic Engineering from the Erciyes University, Kayseri, Turkey in 1991. He has been Full Professor in the Department of Electrical and Electronic Engineering, Engineering Faculty, Erciyes University, Kayseri, Turkey since 2002. His research interests include theory and applications of error-control coding, multi-user detection, channel estimation, PAPR reduction methods, CDMA systems, MC-CDMA systems, OFDM systems, MIMO systems, IDMA systems and applications of neural networks, fuzzy logic, adaptive neuro-fuzzy inference system and intelligent optimization techniques to communications problems.

ICENS 4TH INTERNATIONAL CONFERENCE ON ENGINEERING AND NATURAL SCIENCE
2-6 May 2018 KIEV UKRAINE

Low-Velocity Impact Response of Pre-Stressed GRP Tubes Reinforced with Carbon Nanotubes

Mustafa Tasyurek [1], Memduh Kara [2]

Abstract

The purpose of this work is to investigate the damage behavior of carbon nanotube (CNT) reinforced glass reinforced plastic (GRP) pipes after low speed impact. GRP pipes are produced by winding method with ± 55 ° winding angle. CNT ratios were selected as 0.5% and 1% and reinforced into the matrix by ultrasonication method. Pure, 0.5% and 1% CNT reinforced E-glass / epoxy composite specimens were pre-stressed with 32 bar internal pressure. Low-speed impact tests were applied to pre-stressed pipes at 10 Joule energy level. The contact force-time graph and the force-displacement graph were drawn according to the data of the experiments. Damages occurring in the specimen were investigated at micro-scale on the cross-sectional surface and also impact response and effects on the damage mechanism of CNT reinforcement have been evaluated.

Keywords: *Glass-reinforced plastic, carbon nanotube, low-velocity impact, damage behavior*

1. INTRODUCTION

The developments in technology and the wishes of final consumers require more extreme structures to be produced. For this reason, composite pipes which can be exposed to external factors are required to be reinforced. In layered composite structures, external impacts cause damage such as delamination, rupture, bending or fracture. In recent years, nano-sized materials have been preferred as reinforcing materials. CNT, one of them; can reduces impact damage due to the advantages such as matrix peeling, reduction of delamination, bonding between layers.

Delamination, which is one of the damages of composite materials, is a factor that reduces bending strength, tensile strength, fatigue life and impact absorption energy. These effects have been tried to be reduced by various studies. One of them is the nano material reinforcement (1-2). Laurenzi et al. (3) reported that CNT reinforcement in kevlar epoxy plate would significantly increase energy absorption capability. In another study (Cherniaev and Telichev), damage investigations were done after high speed impact (4). In the study, they pointed out that the final damage depends on the impact energy, the preloading and the degree of penetration of the filament belts into each other, So, nano materials that can be inserted between the fibers may be the factors that prevent delamination. Changliang et al. (5) have studied on the delamination prediction of low-speed impacted filament winding pipes and reported that the possible damage will occur in the inner parts of the pipe.

Some studies have reported an improvement in mechanical properties when CNT is used in epoxy materials. These developments are about tensile stress, shear stress, bending strength and elongation, fiber-matrix interface adhesion and fracture toughness (6-8). Soliman et al. (9) MWCNT reinforced woven carbon fabric tested at high energy levels. They emphasized that using 1.5% CNT increases the energy absorption capacity by 50%. Taraghi et al. (10) reported that CNTs used in kevlar-epoxy lamina increase the resistance of damage progression thanks to bridging mechanism during low-speed impact tests.

When all these studies are taken into account one can see that, studies on the improvement of damage situations of filament winding GRP tubes reinforced with CNT to increase strength, which are exposed to external impacts and also ready to be used directly in industrial applications, have not been found in the literature. The aim of

[1] *Corresponding author: Selcuk University, School of Civil Aviation, 42250, Selcuklu/Konya, Turkey.* mtasyurek@selcuk.edu.tr

[2] *Mersin University, Engineering Faculty, Yenisehir/Mersin,Turkey,* memduhkara@mersin.edu.tr

this study is to prevent or delay damage mechanisms in the event of impact damage during use of composite pipes in the industrial operation

2. MATERIALS AND METHODS

2.1 Production of GRP Composite Pipes

In this study, Vetrotex 1200 tex E glass and Ciba Geigy Bisphenol A / Hardener Epikote 828 epoxy were preferred. The matrix material is reinforced with multi-wall carbon nanotubes. The properties of CNT as follow: outer diameter <8 mm, inner diameter of 2-5 nm, aspect ratio 10-30 μm, density 2.1 g / cm3, purity 95%. The epoxy, curing agent and CNT ratio were determined to be 100: 80: 1,8 and 100: 80: 0,9.
First CNTs are mixed in epoxy by ultrasonic homogenizer to obtain homogeneous and high strength structure. Mixing time is 15 min. After the mixing process, it takes 30 minutes for the temperature to drop and for the addition of the curing agent. Curing agent was mechanically stirred. Eventually, the nanocomposite blend was prepared for filament winding (11). The final state of the produced samples is shown in Figure 1.

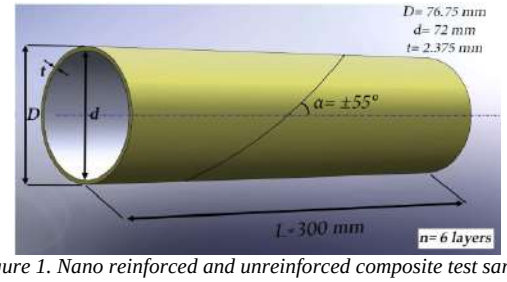

Figure 1. Nano reinforced and unreinforced composite test sample

2.2 Mechanical Experiments

Pure epoxy and CNT reinforced composite pipe samples were subjected to low speed impact test at 10 J energy level. Impact tester and internal pressure application unit were used to investigate the low speed impact behavior of the pipes under internal pressure. The impact tester and internal pressure unit are shown in Fig. 2. In the experiments, a semi-spherical tipped gun with a diameter of 24 mm and 6.35 kg was used. The test specimens were placed on the V bed to avoid external damage after applying 32 bar of internal pressure (12).

Figure 2. Low speed impact tester and internal pressure application pump (12)

3. FINDINGS AND RESULTS

3.1 Low Speed Impact Test Results

Figure 3 gives the force-time variations obtained from test result of pure, 0.5% and 1% CNT reinforced pipes. When the force-time graph is examined; it is seen that the value of the contact force decreases as the CNT reinforcement ratio. The decrease in the value of the greatest contact force with the CNT indicates a decrease in the stiffness of the specimen and an increase in ductility. In addition, oscillations in the graphs indicate that the sample is damaged as a result of the pulse effect (13).
CNTs can mechanically lock between fibers. These properties considerably reduce the physical damage of the composite. The impact is perpendicular to the fibers but parallel to the CNTs. Thus, the impact severity is less felt in the composite structure. Numerous amounts of CNTs can be mechanically locked. Thus, the layers can act like a single layer. Thus, a more robust structure has been formed. This situation also limits the area of delamination.

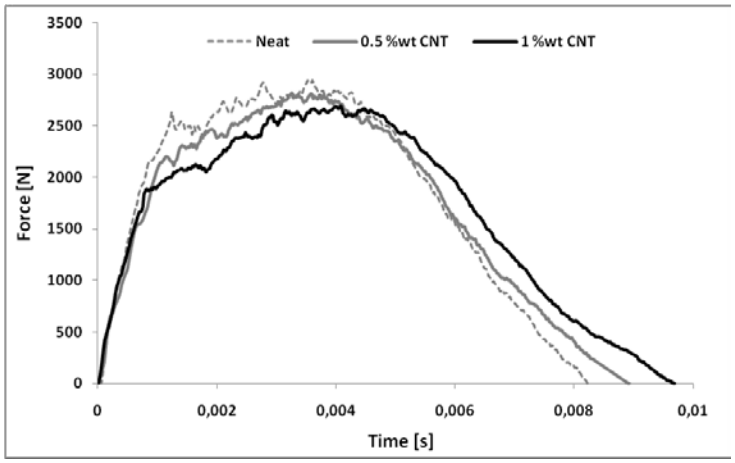

Figure 3. Contact force-time change graph for different CNT reinforcement rates

Figure 4 shows the force-displacement change graph obtained from test results of pure, 0.5% and 1% CNT reinforced pipes. When the graph is examined; It appears that there is more displacement of the CNT added samples. This is because CNT reinforcement increases the ductility of the sample as described before. According to graph; a change in the slope of the graph is observed when the force reaches a certain value while increasing rapidly. This value does not physically represent the start of damage. Because, non-critical matrix cracks and small delaminations during impact may have occurred at lower force values. Significantly changing force value in the slope line represents the initial value of the change in the stiffness characteristic of the sample (14). It is seen that CNT reinforcement reduces this value.
In the force-displacement curve, oscillations in the increasing portion of the force indicate damage to the sample. It is understood when the graphic is observed; CNT reinforced samples absorb more energy.

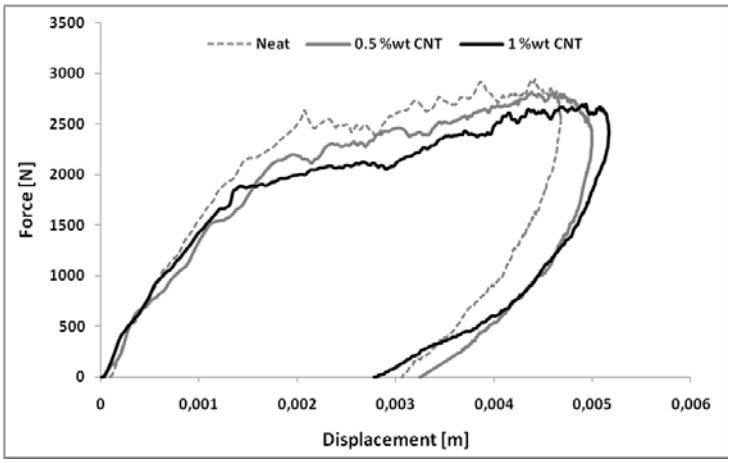

Figure 4. Contact force-collapse change for different CNT reinforcement rates

3.2 Damage Mechanics Examinations

After the impact test of the preloaded samples, the cross sections of the impact areas were examined. In order to obtain better images of the cracks in the cross-sectional area, a device with led light and foot as shown in Figure 5 is designed by the authors.

Figure 5. Led light damage display aparate

Cross-sectional damage images of pure and CNT reinforced samples subjected to low-speed impact under internal pressure at 10 J impact energy level, are given in Figures 6a, b and c, respectively. It is obvious from the figure 6, increase in the percentage of CNT reduces the damage to the samples. As a result, the tensile stresses generated by the impact load produced less delamination area. The penetration area of the shooter is visible in the center of all the samples. It also appears that there are matrix cracks in the samples. Another important cause of delamination damage during impact is the variation of bending stiffness and bending stress between layers. Increasing the amount of reinforcement allows the samples to act as a single layer due to the mechanical bond formation between the layers. For this reason, since there is less sediment in the samples the area of delamination is reduced. In addition, strength between the layers is increased due to mechanical locking.

The composite pipes used in the study are thin-walled pipes. But since they do not lean freely due to the internal pressure effect, the spread of damage has become a pine tree look. This is clearly visible when looking at the sectional views of the specimens given in Figure 6. When the damage area is examined, the damages of the pure pipe are more numerous than the others. There was a decrease in damage to the samples thanks to the CNT reinforcement.

(a)

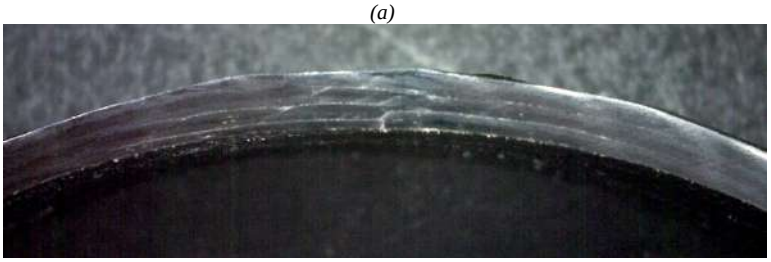

(b)

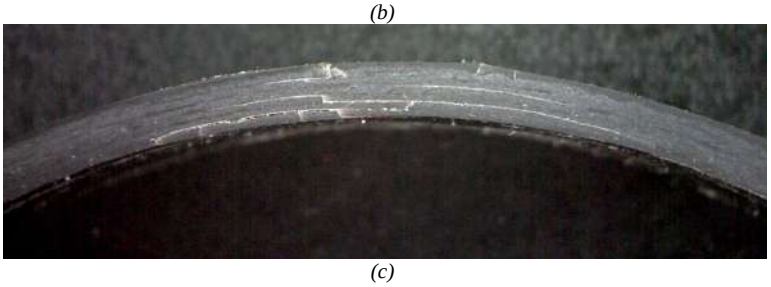

(c)

Figure 6. Cross-sectional images of impacted and reinforced specimens a) Pure GRP b) 0.5% CNT c) 1.0% CNT

4. CONCLUSION

- It has been found that the greatest contact force was reduced and the greatest displacement value is increased by the effect of CNT reinforcement. As the reinforcement ratio increased, higher contact duration and lower contact force was observed.
- It is clearly visible from the cross-section, area of impact damage is reduced as the rate of reinforcement increases. The largest delamination was obtained from pure samples.
- Impact damage is often spread around the center of the impact zone and a large portion of it is delamination.
- It can be concluded that CNT reinforcing is suitable for the increasing of the impact strength of the nanocomposite and the investigation the other mechanical properties of the epoxy matrix.

REFERENCES

[1] 1. Nano-structured sandwich composites response to low-velocity impact Antonio F. Ávila, Maria Gabriela R. Carvalho b, Eder C. Dias b, Diego T.L. da Cruz, Composite Structures 92 (2010) 745–751.
[2] 2. A study on nanostructured laminated plates behavior under low-velocity impact loadings, Antonio F. Avila, Marcelo I. Soares, Almir Silva Neto, International Journal of Impact Engineering 34 (2007) 28 – 41.
[3] 3. Experimental study of impact resistance in multi-walled carbon nanotube reinforced epoxy, S. Laurenzi ⇑ , R. Pastore, G. Giannini, M. Marchetti, Composite Structures 99 (2013) 62–68.
[4] 4. Experimental and numerical study of hypervelocity impact damage in composite materials fabricated by filament winding Aleksandr Cherniaev, Igor Telichev, International Journal of Impact Engineering 98 (2016) 19–33.

[5] 5. Delamination prediction of composite filament wound vessel with metal liner under low velocity impact Zheng Changliang, Ren Mingfa, Zhao Wei, Chen Haoran, Composite Structures 75 (2006) 387–392.
[6] 6. Qiu J, Zhang C, Wang B, Liang R. Carbon nanotube integrated multifunctional multiscale composites. Nanotechnology Nanotechnology 18 (2007) 275708.
[7] 7. Seyhan AT, Tanoglu M, Schulte K. Mode I and mode II fracture toughness of Eglass non-crimp fabric/carbon nanotube (CNT) modified polymer based composites. Eng Fract Mech 2008;75(18), 5151-5162.
[8] 8. Garcia EJ, Wardle BL, Hart AJ. Joining prepreg composite interfaces with aligned carbon nanotubes. Compos Part A 2008;39:1065-1070.
[9] 9. Low-velocity impact of thin woven carbon fabric composites incorpo rating multi-walled carbo n nanotubes Eslam M. Soliman a, Michael P. Sheyka b, Mahmoud Reda Taha, International Journal of Impact Engineering 47 (2012) 39-47.
[10] 10. Low-velocity impact response of woven Kevlar/epoxy laminated composites reinforced with multi-walled carbon nanotubes at ambient and low temperatures, Iman Taraghi, Abdolhossein Fereidoon, Fathollah Taheri-Behrooz, Materials and Design 53 (2014) 152–158.
[11] 11. Tasyurek, M., & Tarakcioglu, N. (2017). Enhanced fatigue behavior under internal pressure of CNT reinforced filament wound cracked pipes. Composites Part B: Engineering, 124, 23-30.
[12] 12. Kara, M., Uyaner, M., Avci, A., Akdemir, A., "Effect of non-penetrating impact damages of pre-stressed GRP tubes at low velocities on the burst strength", Composites: Part B, 60, 507-514 (2014)
[13] 13. Uyaner, M., Kara, M., “Dynamic response of laminated composites subjected to low-velocity impact”, Journal of Composite Materials, 41(24), 2877-2895, (2007)
[14] 14. Kara, M., & Kirici, M. (2017). Effects of the number of fatigue cycles on the impact behavior of glass fiber/epoxy composite tubes. Composites Part B: Engineering, 123, 55-63.

Biography: Mustafa Tasyurek was born in 1982, and received his PhD degree in mechanical education from Selcuk University, Turkey in 2014. From 2005 to present, he is a academician with Selcuk University. Currently, he is a Assist. Prof. Dr. at the School of Civil Aviation, Selcuk University, Turkey. His research interests are in nanomaterials, nanocomposites, mechanical properties and airplane body.

ICENS 4TH INTERNATIONAL CONFERENCE ON ENGINEERING AND NATURAL SCIENCE
2-6 May 2018 KIEV UKRAINE

Determination of Soil Moisture Content and Soil Penetration Resistance According To Different Soil Tillage

Onder Kabas[1], Ilker Unal, Salih Sozer[2], K. Cagatay Selvi[2],Huseyin Sauk[1]

Abstract

Field experiment were conducted in Antalya/Aksu between 2013-2015 to evaluate the effect of different soil tillage systems on soil penetration resistance and moisture of soil from physical soil properties under a cotton cultivation and laboratory studies were carried out in Bati Akdeniz Agricultural Research Institute in Antalya (South of Turkiye). The soil of the experimental parcel was classified as silty.The experiments were arranged in a randomized complete block design with three replications. Statistical analyses were used to compare the different soil tillage methods. In this study, four different conversation tillage systems (disc harrowing, rotarytiller and roller (S1), cultivator and scrubber (S2), rotary cultivators and scrubber (S3), rotarytiller and roller (S4) were compared in terms of their effects on some ***physical properties*** *of soil (soil penetration resistance and moisture of soil). The moisture of soil values were determined in two period (after tillage and after harvesting operation) and in three depth of soil (0-10, 10-20 and 20-30 cm) and also, penetrometer resistance values were determined in 2 period (after tillage and after harvesting operation) and in 4 in depth of soil (10, 30, 40 and 60 cm).*

Keywords: cotton, soil properties, resistance, moisture

1. INTRODUCTION

Between soil, water and plant relationship is a dynamic system that it interacts mutually. Soil plays a critical important role as a vital foundation, on which the plant can coexist comply with surrounding environments. Soil has a resilient capacity under natural conditions. Besides, soils are prone to the deteriorative processes, which have subjected to the soil formation and cultural practices [1].

There are many soil physical properties affecting to the plant growth such as texture, structure, moisture content, porosity, bulk density, thermal conductivity and soil strength. For good plant growth, it is primary that the soil must provide a sufficient physical environment for root development. Since plant root system is mostly growing in porous medium, it must therefore overcome mechanical soil resistance. Penetration resistance of soils is an important parameter that influences to the root growth and water movement. The most common method to evaluate soil strength is by using a penetrometer, which is characterized by the force required to advance a cone of specific base size into the soil [2].

The soil condition resulting from the use of different tillage systems depends on both the type of implement used and the soil condition. At present, it is not possible to sufficiently predict the resulting soil conditions from a tillage practice [3]. [1]

Studies have shown that tillage practices recast soil physical properties [4] influencing the water storage and hydraulic conductivity of soil and consequently the hydrological behavior of agricultural watersheds [5].

Soil physical properties such as moisture content and resistance to penetration were commonly assessed and evaluated to detect the influence of different tillage practices on soil and crop growth and yield. Therefore, an

[1] *Corresponding author: Akdeniz University, Vocational School of Technical Science, Department of Machinery, 07100, Antalya,Turkiye. okabas@akdeniz.edu.tr**

2 19 Mayis University, Department of Agricultural Machinery and Technologies Engineering, Samsun, Turkiye,

experiment was conducted at Antalya, Turkiye to examine the prospective effects of tillage practices on physical properties of soil in the area to cultivate second crop cotton after tillage and harvesting operation.

2. MATERIALS AND METHODS

a. Field and Soil

This study was carried out at the Bati Akdeniz Agricultural Research Institute, Antalya, Turkiye, during two summer seasons (2013 and 2015). The soil in the experiment field was a clay silty with pH of 7.4 and organic matter matter content of 1.6%. The results of soil analyses are given Table 1.

Table 1. The result of soil analyses

pH (1:2.5)	7.4
Lime (%)	18.9
Sand (%)	25
Clay (%)	30
Silty (%)	40
Organic matter (%)	1.6
P ppm	28
K ppm	225
Mg ppm	324

The average weather conditions during growing seasons such as annual temperatures and rainfall etc. are showed in Table 2.

Table 2. Average climate dates of a long-term at the site of experimentation

	May	June	July	August	September	October
Temperature (°C)	20.4	25.4	28.4	28.1	24.7	19.8
The highest Temperature (°C)	25.9	31.3	34.4	34.3	31.3	26.7
The lowest Temperature (°C)	14.8	19.4	22.5	22.4	19.1	14.9
Sunshine duration (hour)	9.5	11.4	11.5	11.3	9.5	8.0
Number of rainy days	5.0	2.4	0.7	0.5	1.7	5.4
Rainfall (kg/m^2)	29.3	7.1	3.3	1.6	11.0	74.8

The experiment, which was begun in June 2013 and finished 2015 compared four tillage systems for cotton (*Gossypium spp*.) production following a wheat-cotton rotation. The standard cultural practices recommended by Bati Akdeniz Agricultural Research Institute; other than treatments, were followed throughout the growing seasons. The experiment was established as a randomized block design with four replications. Plots were 5 m wide (four rows) and 25 m long with an inter row spacing of 0.7 m distance. After the field had been selected and before the application of the treatments, the land was free from weeds and crop residues except the no-tilled plots. The experimental procedures were the same for the both seasons.

b. Tillage Systems

Tillage systems that used in study are shown in Table 3 and Massey Ferguson 5400 (Engine Power 105 HP) tractor was used in the experiments.

Table 3. Soil tillage methods utilized in experiments

Tillage systems	**Tillage operations**
S_1	disc harrowing, rotarytiller and roller
S_2	cultivator and scrubber
S_3	rotary cultivators and scrubber
S_4	rotarytiller and roller

2.3. Investigations and data collection

Soil samples were collected from the field with four replications on each plot after tillage and harvesting operation at 0–30 cm for moisture content and penetration resistance at 0-60 cm. The determination of water content of soil (% d.b.) was carried out twice during the season. The first one was done before tillage operations and the second one was done before harvesting. Samples were transported to the laboratory and then oven dried at 105ºC for 24 hours to determine dry-basis gravimetric soil water content.

Soil resistance of penetration was determined after tillage and harvesting operations both seasons using a manually operated cone penetrometer. Four samples were randomly taken from each strip-plot using a cone with a 2.0 cm^2 area from soil depths of 0-10, 10-20, 20-30, and 30-40, 40-50, 50-60 cm, then converted to MPa.

3. RESULTS and DISCUSSION

3.1.Soil moisture

Data pertaining to soil moisture content at 0-30 cm depth before the tillage operation and after harvesting during 2013-2015 growing season the second growing period of cotton are presented in the Table 4.

Table 5. Effect of tillage methods on soil moisture content (2013-2015 growing season)

		S_1	S_2	S_3	S_4	Sign.
After tillage	**0-10**	15.09	14.72	14.83	14.57	N.S
	10-20	17.14	17.05	18.43	16.51	**
	20-30	20.08	19.65	21.71	18.88	***
After harvest	**0-10**	19.35	20.15	18.90	21.35	***
	10-20	22.16	21.56	20.63	22.90	**
	20-30	23.06	22.93	23.18	23.01	N.S

Maximum soil moisture contents were observed in soil tilled with S_3 at 20-30 cm soil depths as 23.18% followed by that in soil tilled with S_1 at 20-30 soil depths as 23.06% after harvesting operation and minimum soil moisture content were determined in soil tilled with S_4 at 10-20 cm soil depths as 14.57% followed by that in soil tilled with S_2 at 10-20 cm soil depths during both years. The analysis of variance showed that there was a significant difference between soil tillage systems for moisture content in 10-20 cm depth (p=0.05) and in 20-30 cm depths (p=0.01) after tillage operations. Also, there was a significant difference between soil tillage systems for moisture content in 0-10 cm depths (p=0.01) and in 10-20 cm depths (p=0.05)after harvest operations. These results are in agreement with those reported by Boydas and Turgut, Rashidi and Keshavarzpour ([6], [7]).

3.2.Soil penetration resistance

The result of penetration different point in the field in terms of soil penetration resistance After tillage operation and harvesting operation were explained for different tillage systems in 2013-2015 growing season in Fig 1 ve Fig 2

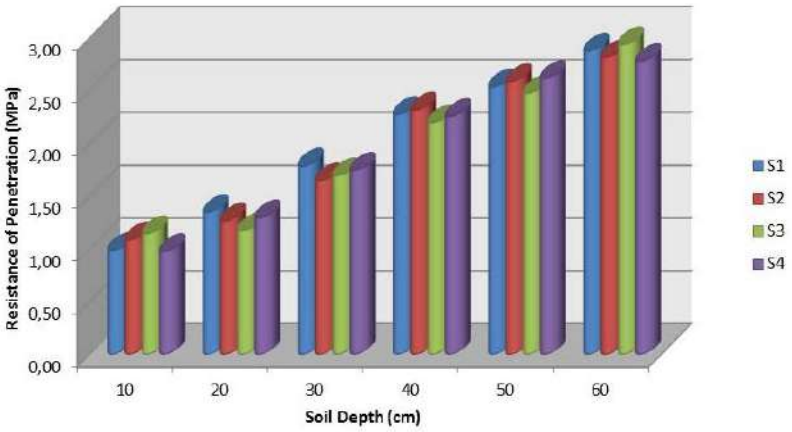

Fig 1. Soil penetration resistance (0-60 cm) before tillage

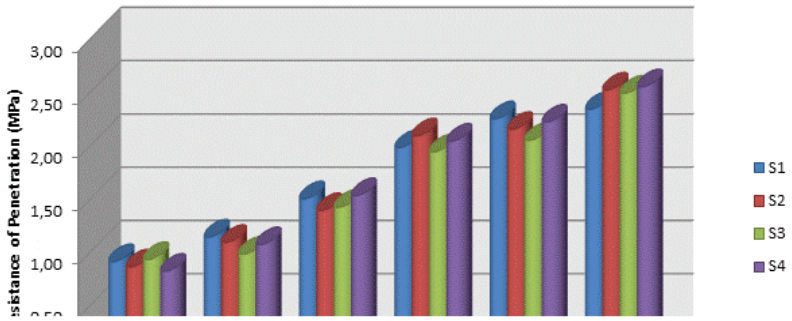

Fig 2. Soil penetration resistance (0-60 cm) after harvesting operation

Soil penetration resistance for all tillage system increase with soil depths (0-60 cm). After tillage operation, the highest soil penetration resistance (2.93 and 2.87 MPa) was recorded in soil tilled with S_3 and then S_1 at 0-60 cm soil depths, respectively. After harvesting operation, the highest soil penetration resistance (2.54 and 2.51MPa) was found in soil tilled with S_4 and then S_1 at 0-60 cm soil depths, respectively. A researcher reported that soil penetration resistance for different tillage methods increased with soil dept. For variation though conversation tillage methods, tillage methods X measuring time, tillage methods X depth and tillage methods X measuring time X depth interactions were significant statistically for four tillage systems ($p<0.001$) [8].

4.CONCLUSION

As a result of study, tillage system significantly affected soil penetration resistance and moisture content in all depths at after tillage and harvesting operation. The analysis of variance showed that there was a significant difference between soil tillage systems for moisture content in different soil depth.For variation though tillage methods, tillage methods X measuring time, tillage methods X depth and tillage methods X measuring time X depth interactions were significant statistically for four tillage systems ($p<0.001$). The no tillage system produced the highest soil penetration resistance both after tillage and harvesting operation in 0-60 cm soil depth.

REFERENCES

[1]. P.V. Quang, P. Jansson and L. V. Khoa, "Soil Penetration Resistance and Its Dependence on Soil Moisture and Age of the Raised-Beds in the Mekong Delta, Vietnam," *International Journal of Engineering Research and Development*, vol. 4, pp. 84-93, 2012

[2]. J.L. Bradford, *Methods of Soil Analysis. Part 1. Physical and Mineralogical Methods.* American Society of Agronomy/Soil Science Society of America, Madison, Wisconsin, USA, 1986.
[3]. M. Tapela and T.S.Colvin, *"Quantifying seedbed condition using soil physical properties,"* Soil and Tillage Research,vol.64, pp. 203-210, 2002.
[4]. A.R. Barzegar, M.A. Asoodar, A. Khadish, A.M. Hashemi and S.J. Herbert, *"Soil physical characteristics and chickpea yield responses to tillage treatments,"* Soil and Tillage Research, vol.71, pp.49-57, 2003.
[5]. D. Xu and A.Mermoud, *"Topsoil properties as affected by tillage practices in north China,"* Soil and Tillage Research, vol.60, pp. 11-19, 2001.
[6] M.G. Boydas and N. Turgut, *"Effect of tillage implements and operating speeds on soil physical properties and wheat emergence,"* Turk J Agric For, vol.31, pp.399-412, 2007.
[7] M. Rashidi and F. Keshavarzpour, *"Effect of different tillage methods on soil physical properties and crop yield of melon (Cucumis melo),"*American-Eurasian J. Agric. and Environ. Sci. vol.3, pp.31-36, 2008.
[8] J.A. Osunbitan, D.J. Oyedele and K.O. Adekalu, *"Tillage effects on bulk density, hydraulic conductivity and strength of a loamy sand soil in southwestern Nigeria,"* Soil Till. Res. vol.82, pp.57-64, 2005.

ICENS 4TH INTERNATIONAL CONFERENCE ON ENGINEERING AND NATURAL SCIENCE
2-6 May 2018 KIEV UKRAINE

Geochemical Characteristics of Listvenites in the Dagkuplu Ophiolite (Eskisehir, NW Turkey)

***Gokhan Buyukkahraman*[1]**

Abstract

This study indicates geochemical characteristics of the listvenites in the Dagkuplu ophiolites. The listvenites are located in the vicinity of Sakariilica thermal area in the north of Eskisehir. This area is known as a highly tectonic region due to the fact that Izmir-Ankara Suture Zone (IASZ) developed during collision between Sakarya Zone and Anatolide-Tauride Block resulting from closure of the northern branch of Neotethyan Ocean is situated here. The major, trace and rare earth element analyzes were carried out by taking samples from the listvenites formed as a result of metasomatic / hydrothermal alteration of the serpentinites in the Dagkuplu ophiolites. According to the results of geochemical analysis; the lisvenites were enriched in SiO_2, Fe_2O_3, and K_2O; depleted in MgO and CaO with respect to serpentinites. Especially the changes in SiO_2 (% 93.04) and MgO (% 93.54) are remarkable. Similarly, the lisvenites were enriched in Ba, Nb, Rb, Sr, V, W, Zr, Mo, Cu, Ni, As, Sb, Au, and Hg according to trace elements results. It is a well-known fact that some metallic elements such as Au can be found at economic ratios in the listvenitic rocks. The amount of Au in the Dagkuplu listvenites is 2.4 ppb on average and cannot be evaluated economically. On the other hand, their Cu (10.75 ppm), As (3379 ppm), Mo (29.38 ppm), and Sb (134.88 ppm) proportions are very high and this suggests that the listvenites in the Dagkuplu ophiolites are typically controlled by silica-rich hydrothermal solutions.

Keywords: Listvenite, Dagkuplu Ophiolite, Eskisehir

1. INTRODUCTION

Listvenite (also sometimes spelled listvanite, listwanite, or listwaenite) is unusual rock formed by carbonation and silicification of the serpentinites (most commonly mantle peridotites) by hydrothermal alteration [1]. Due to the fact that listvenitic rocks may contain Au and other valuable elements in economic ratios, they are very significant rocks in metallic mineral explorations.

The listvenites in the Dagkuplu ophiolites are located in the vicinity of Sakariilica thermal area in the north of Eskisehir. This region is known as a highly tectonic region because Izmir-Ankara Suture Zone (IASZ) developed during collision between Sakarya Zone and Anatolide-Tauride Block resulting from closure of the northern branch of Neotethyan Ocean is situated here (Figure 1).

The aim of this study is to determine geochemical characteristics and metallic element contents of the listvenites in the Dagkuplu ophiolites.

[1] *Corresponding author: Balikesir University, Department of Geological Engineering, 10145, Cagis/Balikesir, Turkey.*
gokhanb@balikesir.edu.tr

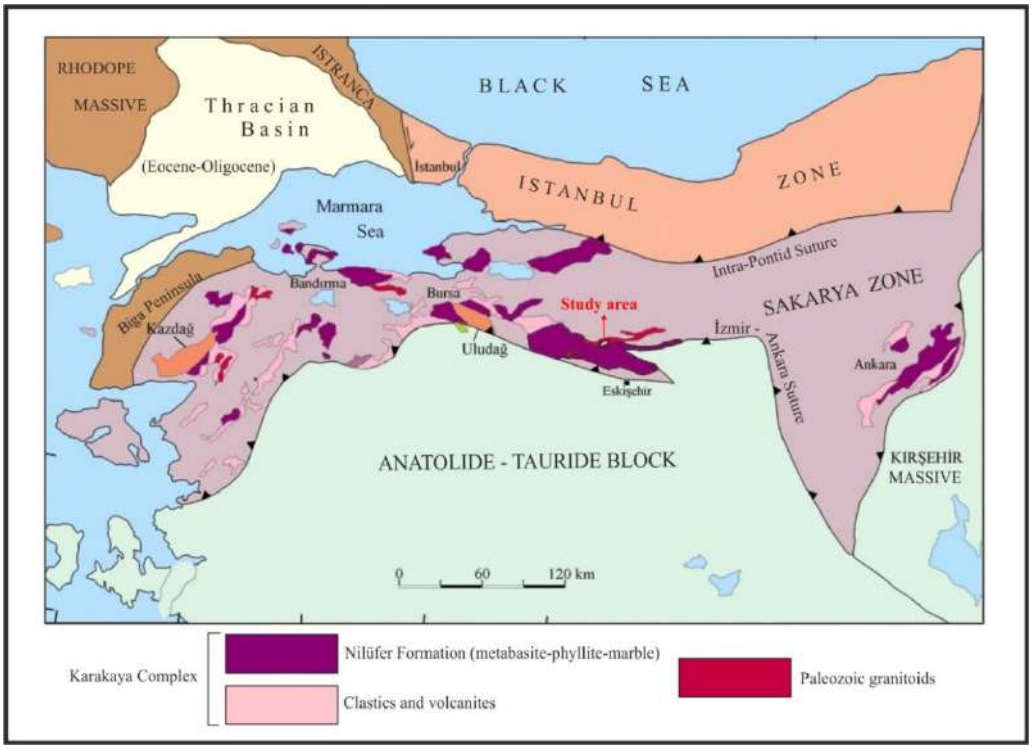

Figure 1. Simplified geological map of NW Turkey (Modified from [2]).

2. MATERIALS AND METHODS

Three main methods used in this study:

- Office studies: Previous studies were collected and reviewed.
- Drawing of geological map of the study area: 1:25000-scaled geological map of the study area was drawn.
- Geochemical analyses: Major, trace and rare earth element analyses were performed in ACME Analytical Laboratories (Canada) by using ICP-AES and ICP-MS methods.

3. RESULT AND DISCUSSION

According to the results of geochemical analysis; the lisvenites were enriched in SiO_2, Fe_2O_3, and K_2O whereas depleted in MgO and CaO with respect to serpentinites. Especially the changes in SiO_2 (% 93.04) and MgO (% 93.54) are remarkable (Table 1). The samples of NL1 to NL5 represent serpentinites which are the parent rocks of listvenites while NL6 to NL10 represent listvenitic rocks in all tables.

Similarly, the lisvenites were enriched in Ba, Nb, Rb, Sr, V, W, Zr, Mo, Cu, Ni, As, Sb, Au, and Hg according to trace elements results (Table 2). The amount of Au in the Dagkuplu listvenites is 2.4 ppb on average and cannot be evaluated economically. On the other hand, their average Cu (10.75 ppm), As (3379 ppm), Mo (29.38 ppm), and Sb (134.88 ppm) proportions are very high and this suggests that the listvenites in the Dagkuplu ophiolites are typically controlled by silica-rich hydrothermal solutions.

There is no any remarkable change in rare earth element proportions (Table 3).

Representative normalized major and trace elements depletion-enrichment diagrams were drawn in order to indicate correlations of listvenites and their parent rocks (Figure 2 and 3). According to these diagrams, there are enrichments in SiO_2 for all samples. Other relationships can also be clearly seen from the diagrams.

Table 31. Whole-rock major element (%) data for serpentinites and listvenites.

	NL1	NL2	NL3	NL4	NL5	NL6	NL7	NL8	NL9	NL10
SiO_2	24.18	38.89	24.95	42.47	13.67	58.27	62.38	85.07	59.92	49.22
Al_2O_3	3.66	0.70	0.45	0.25	0.08	0.23	7.14	2.67	0.31	0.74
Fe_2O_3	7.71	7.49	9.21	7.36	2.82	24.78	8.54	2.29	14.40	40.41
MgO	24.78	21.89	27.42	21.23	37.84	4.17	2.15	0.84	0.21	0.32
CaO	0.49	0.81	1.38	0.52	0.58	0.39	0.07	0.03	0.07	0.11
Na_2O	0.01	0.02	0.03	0.03	0.06	<0.01	0.18	0.03	0.03	<0.01
K_2O	0.02	0.02	0.03	0.02	<0.01	0.03	0.45	0.19	0.03	0.03
TiO_2	0.05	0.01	<0.01	<0.01	<0.01	<0.01	0.05	0.02	<0.01	<0.01
P_2O_5	0.01	0.02	0.02	0.07	0.01	0.02	<0.01	<0.01	0.09	0.20
MnO	0.09	0.50	0.12	0.12	0.03	0.42	<0.01	<0.01	0.06	0.03
Cr_2O_3	1.986	0.262	0.298	0.881	0.284	0.131	3.462	1.205	0.307	0.245
LOI	36.2	28.6	35.3	26.4	43.8	10.7	15.3	7.5	4.7	8.1
Sum	99.49	99.47	99.46	99.50	99.22	99.77	99.82	99.91	80.17	99.72

Table 2. Whole-rock trace element (ppm or ppb) data for serpentinites and listvenites.

	NL1	NL2	NL3	NL4	NL5	NL6	NL7	NL8	NL9	NL10
Ba	7	789	48	25	435	526	605	486	>50000	858
Be	1	<1	1	<1	3	1	<1	<1	13	19
Co	90.5	196.3	127.0	82.0	12.3	388.7	35.2	19.1	15.7	59.2
Cs	8.1	10.3	15.6	3.0	0.3	6.8	28.4	46.1	4.4	2.9
Ga	2.8	1.4	0.7	1.0	<0.5	0.7	7.2	2.3	<0.5	1.0
Hf	0.1	<0.1	<0.1	<0.1	<0.1	<0.1	<0.1	<0.1	0.1	<0.1
Nb	0.2	0.2	0.1	<0.1	0.6	1.7	<0.1	1.4	1.0	1.3
Rb	2.4	2.3	3.4	1.7	0.1	2.1	14.7	8.9	1.3	0.9
Sn	<1	<1	<1	<1	<1	<1	1	<1	<1	<1
Sr	10.3	11.6	26.9	8.4	19.0	9.8	96.9	7.5	452.6	16.6
Ta	0.6	0.8	0.1	0.3	<0.1	0.3	<0.1	0.2	0.4	0.7
Th	<0.2	<0.2	<0.2	<0.2	<0.2	<0.2	<0.2	<0.2	<0.2	<0.2
U	<0.1	<0.1	<0.1	<0.1	<0.1	0.2	<0.1	<0.1	<0.1	0.5
V	202	46	26	33	24	18	238	71	37	68

W	1.5	0.5	0.6	<0.5	9.6	0.8	2.9	1.6	24.2	7.6
Zr	2.1	1.4	1.5	1.2	1.7	0.7	2.6	2.6	2.1	2.8
Y	0.5	0.6	0.3	<0.1	1.3	1.0	<0.1	<0.1	1.9	4.0
Mo	0.9	6.9	2.5	8.0	4.6	14.8	1.2	0.6	15.0	115.3
Cu	9.8	8.9	8.8	12.0	3.4	7.9	5.1	4.1	16.2	20.4
Pb	0.2	0.3	<0.1	<0.1	<0.1	<0.1	0.1	0.1	0.2	0.2
Zn	120	384	521	1062	543	439	66	57	552	584
Ni	2248.7	2511.9	2154.1	1571.9	529.5	4851.7	389.1	240.2	356.2	2565.2
As	50.1	896.6	795.6	238.8	93.3	3206.4	1913.2	220.7	3078.1	8478.5
Cd	<0.1	<0.1	<0.1	<0.1	<0.1	<0.1	<0.1	<0.1	<0.1	<0.1

Table 2. Continued

	NL1	**NL2**	**NL3**	**NL4**	**NL5**	**NL6**	**NL7**	**NL8**	**NL9**	**NL10**
Sb	0.2	2.5	2.8	3.0	31.7	6.0	2.1	1.6	235.4	429.3
Bi	<0.1	<0.1	<0.1	<0.1	<0.1	<0.1	<0.1	<0.1	<0.1	<0.1
Ag	0.3	1.0	1.1	1.8	1.0	0.6	0.1	<0.1	1.2	0.7
Au (ppb)	1.7	<0.5	<0.5	<0.5	<0.5	2.5	2.9	<0.5	2.9	1.6
Hg	0.02	0.15	0.21	0.29	0.13	0.21	3.57	1.28	0.23	0.24
Tl	0.1	9.3	0.4	0.1	0.4	4.6	24.7	7.2	0.7	0.7
Se	<0.5	<0.5	<0.5	<0.5	<0.5	<0.5	<0.5	<0.5	<0.5	<0.5

Table 3. Whole-rock rare earth element (ppm) data for serpentinites and listvenites.

	NL1	**NL2**	**NL3**	**NL4**	**NL5**	**NL6**	**NL7**	**NL8**	**NL9**	**NL10**
La	0.5	0.2	<0.1	<0.1	0.1	0.3	<0.1	0.7	0.8	0.5
Ce	0.2	<0.1	<0.1	<0.1	<0.1	<0.1	<0.1	0.2	0.2	0.2
Pr	0.03	<0.02	<0.02	<0.02	<0.02	<0.02	<0.02	<0.02	0.02	<0.02
Nd	<0.3	<0.3	<0.3	<0.3	<0.3	<0.3	<0.3	<0.3	<0.3	<0.3
Sm	<0.05	<0.05	<0.05	<0.05	0.07	<0.05	<0.05	<0.05	<0.05	<0.05
Eu	<0.02	<0.02	<0.02	<0.02	0.04	<0.02	<0.02	<0.02	<0.02	0.03
Gd	<0.05	0.05	<0.05	<0.05	0.17	0.06	<0.05	<0.05	0.84	0.19
Tb	<0.01	<0.01	<0.01	<0.01	0.04	0.01	<0.01	<0.01	0.04	0.05
Dy	0.08	0.11	<0.05	<0.05	0.24	0.10	<0.05	<0.05	0.21	0.30

Ho	<0.02	<0.02	<0.02	<0.02	0.05	0.02	<0.02	<0.02	0.11	0.08
Er	0.05	0.07	0.04	<0.03	0.11	0.07	<0.03	<0.03	0.23	0.25
Tm	0.01	<0.01	<0.01	<0.01	0.02	<0.01	<0.01	<0.01	0.02	0.03
Yb	0.08	<0.05	<0.05	<0.05	0.09	0.07	<0.05	<0.05	0.13	0.20
Lu	0.01	<0.01	<0.01	<0.01	0.02	0.01	<0.01	<0.01	0.02	0.03

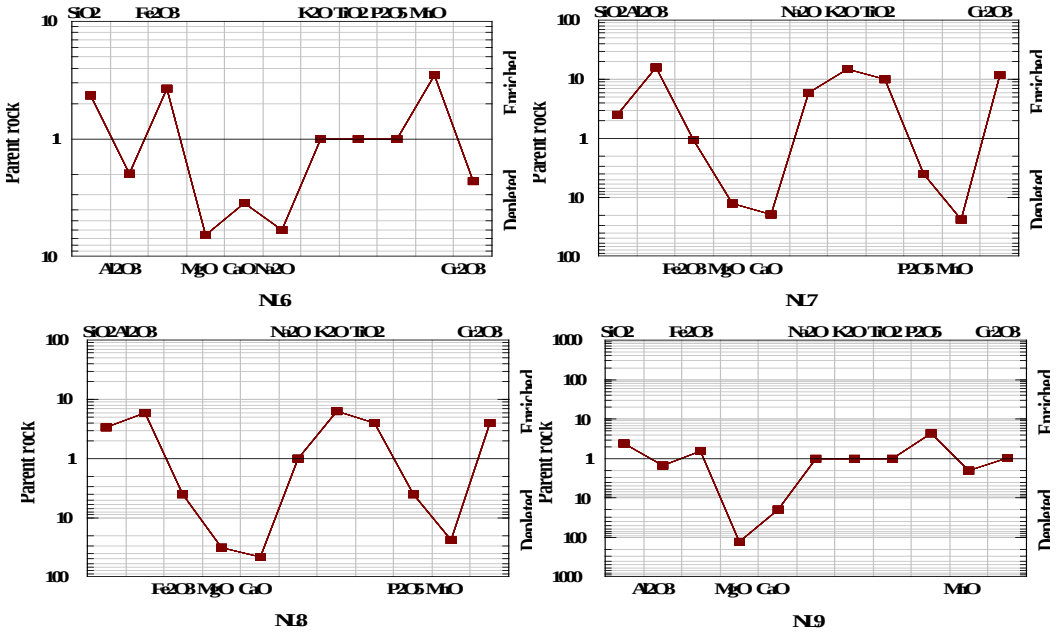

Figure 2. Normalized major elements depletion-enrichment diagram of the NL6, NL7, NL8, and NL9 listvenite samples according to parent rock (NL3 sample was selected for the parent rock).

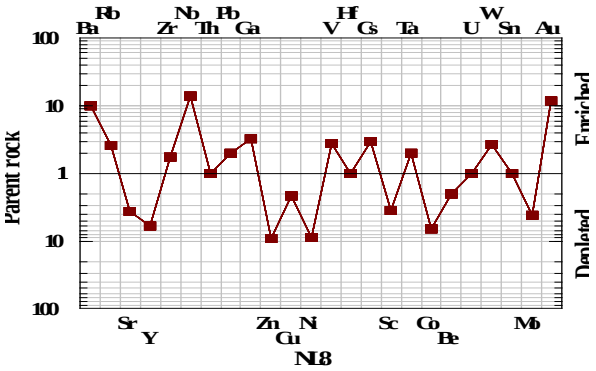

Figure 3. Normalized trace elements depletion-enrichment diagram of the NL8 listvenite sample according to parent rock (NL3 sample was selected for the parent rock).

4. CONCLUSIONS

The listvenites are located in the vicinity of Sakariilica thermal area in the north of Eskisehir. This area is known as a highly tectonic region due to the fact that Izmir-Ankara Suture Zone (IASZ) developed during collision between Sakarya Zone and Anatolide-Tauride Block resulting from closure of the northern branch of Neotethyan Ocean is situated here. According to the results of geochemical analysis; the lisvenites were enriched in SiO_2, Fe_2O_3, and K_2O; depleted in MgO and CaO with respect to serpentinites. Similarly, the lisvenites were enriched in Ba, Nb, Rb, Sr, V, W, Zr, Mo, Cu, Ni, As, Sb, Au, and Hg according to trace elements results. The amount of Au in the Dagkuplu listvenites is 2.4 ppb on average and cannot be evaluated economically. On the other hand, their Cu (10.75 ppm), As (3379 ppm), Mo (29.38 ppm), and Sb (134.88 ppm) proportions are very high and this suggests that the listvenites in the Dagkuplu ophiolites are typically controlled by silica-rich hydrothermal solutions.

ACKNOWLEDGMENT

I would like to thank Balikesir University Scientific Research Projects Unit, TUBITAK, and YOK for their financial supports. I also would like to express my gratitude to Ismail Altin and Olcay Ozbay for their great contributions during the fieldwork.

REFERENCES

[1]. Matter JM and Kelemen PB., “Permanent CO_2 storage and mineral carbonation in geologic reservoirs” Nat. Geosci. 2:837–41, 2009.

[2]. Okay AI, Monod O, Monié P, “Triassic blueschists and eclogites from northwest Turkey: vestiges of the Paleo-Tethyan subduction” Lithos, 64, 155-178, 2002.

BIOGRAPHY

Gokhan Buyukkahraman is a research assistant doctor at the Balikesir University. He studied the petrology and geodynamic evolution of volcanic rocks from NW Turkey in his doctoral dissertation in 2013. He has been studying petrology and geochemistry of different ignous rocks for 11 years.

ICENS 4TH INTERNATIONAL CONFERENCE ON ENGINEERING AND NATURAL SCIENCE
2-6 May 2018 KIEV UKRAINE

Marker-Assisted Selection in Determining of Resistant Varieties against Plant Diseases in the Breeding Process

Gulcin Akgoren Palabiyik[1], Ismail Poyraz[2]

Abstract

In recent years, the new fighting methods against plant diseases that cause important crop losses have been developed. These methods are more practical, economic and healthy.

Pesticides are widely used for fighting against the disease, but it is not an environmentally friendly method. Recently, it has been preferred to use resistant varieties in the organic farming. The purpose of resistance breeding is to detect resistance genes, transfer to cultivar plants, and clone. But the development of new varieties in classical breeding requires a long process. The using of molecular markers in the breeding process are more advantage over the other selection techniques and widely preferred today. In this study, it was investigated and compared the disease control methods used against to disease in Turkey and the World.

We aimed to reveal the advantages and disadvantages of classical and molecular-based selection techniques in the breeding studies. Marker-assisted selection (MAS) includes the molecular-based techniques and is the relatively a new approach method to solve problems of classical breeding techniques. In this review, the importance of using classical breeding and molecular techniques together has been emphasized.

Keywords: MAS, Plant breeding, Plant disease

1. INTRODUCTION

The world population is growing rapidly and hunger is a major threat. To get rid of the nutritional deficiencies, better quality and more efficient varieties should be developed which are more suitable for climate and soil conditions, resistant to diseases and insects. Breeding studies are carried out for these purposes [1].

Plant breeding contributes to agricultural production, using methods such as introduction, selection, hybridization.In human nutrition, grains are at the first place in terms of production and cultivation area. In wheat studies, the marker-assisted selection technique is used. Most of these studies are aimed at obtaining more products from the unit area. One of the most important factors that cause loss of productivity in plants is also plant diseases [2].

Today, chemical methods for combating diseases are widely used. A total of 28 million hectares of agricultural land is used in Turkey, accordingly 11200-19600 tons of pesticides are mixed into the soil each year [3].

The chemical struggle is not being suitable for organic farming and it causes significant damage in the production of organic wheat [4]. However, considering the damage the chemicals have on the environment, it is considered that different methods should be preferred [3,4]. In addition, chemicals can cause to development of host resistance.

The use of resistant varieties is an environmentally friendly alternative. Developing a resistant variety in plant breeding is very important. Developing a resistant variety is a subject of plant breeding. As well as a resistance to disease, drought and cold, there is a resistance to insects. Classical breeding methods require a long process. However, race change in pathogens can happen very quickly. This can cause disease epidemic. Therefore, it is

[1]*Corresponding author: Bilecik Seyh Edebali University, Pazaryeri Vocational School, Medicinal and Aromatic Plants 11230, Bilecik, Turkey. gulcin.akgoren@bilecik.edu.tr*

[2]*Bilecik Seyh Edebali University, Department of Molecular Biology and Genetics, 11230, Bilecik, Turkey, ismail.poyraz@bilecik.edu.tr*

needed the techniques that will expedite the breeding studies and not be restricted with growing season. Resistance resources are an important tool for breeding programs in cultivated varieties. It can be benefited from MAS in the determination of resistance sources. Resistance in the classical breeding process is assessed by selection under natural and artificial environmental conditions [5].

Conventional plant breeding is based on the phenotypic selection of superior genotypes among the progeny that is obtained as a result of hybridization and shows an expansion. However, this application is very difficult because of genotype x environment interaction. Parental selection in plant breeding may be insufficient alone. Molecular markers are emerging as a solution to the problem of selection by phenotype [6]. They provide to access information at the gene level. Molecular markers provide information at the gene level.

2. DISEASE AND DISEASE TOLERANCE IN PLANTS

The plant disease is an interaction between the host and the pathogen under environmental conditions and it is defined as the inability of the plant to fulfill all or some of its functions [7, 8].

Disease resistance can be determined by the reaction of the plant against the pathogen because the resistance is the ability of the host to inhibit the development of the pathogen [1]. A low level of infection or no infection indicates that the resistance gene in the host plant is fighting against this pathogen [9].

3. USE OF MARKER ASSISTED SELECTION INPLANT BREEDING

Selection and hybridization methods are used to develop disease-resistant varieties in plants. In the selection method, a few resistant plants are selected in the same phenotype from population Phenotype-based selection restricts plant breeding studies. Molecular markers are a convenient tool for plant breeding because they display genetic diversity at the DNA level and they are not affected by environmental conditions. The use of molecular markers in plant breeding programs increases the accuracy in selection [5].

In this method, in order to transfer the desired features to a single plant, two or more plants are selected and artificially crossed. At F_2 grade, the plants with the desired features are selected.

Molecular markers increase the effectiveness of backcrossing and pedigree methods. These markers are used for the verification of plants at F_1 grade such as hybridization, autogamy and incorrect rootstock containment. By means of molecular markers also possible to select complex features in the early generations [10,11].

a. Molecular Markers

It is utilized the marker-supported selection used in plant breeding studies in stages such as detection of resistance situation of the obtained varieties and determination of resistance sources Molecular markers are gene locus in the genome or a DNA fragment associated with that region and these are used to determine a desired gene or feature in a genotype [6].
Basic marker techniques can be classified into two categories. Non-PCR based techniques is the first category and includes RFLP (Restriction Fragment Length Polymorphism) method. The second is PCR-based techniques that includes some methods such as STS (Sequence-Tagged Sites), RAPD (Randomly Amplified Polymorphic DNA), SSR (Simple Sequence Repeat), SCAR (Sequence Characterized Amplified Regions), ISSR (Inter Simple Sequence Repeat) [12], AFLP (Amplified Fragment Length Polymorphism), RGAPs (Resistance Gene Analog Polymorphisms), SRAPs (Sequence-Related Amplified Polymorphisms), TRAPs (Target Region Amplified Polymorphisms), CAPs (Cleaved Amplified Polymorphic Sequences) and RAMPs (Random Amplified Microsatellite Polymorphism) [13, 14].

4. WHY WE ARE USING MOLECULAR MARKERS IN PLANT BREEDING

Molecular markers were first used in plant breeding to identify the diversity in the gene pool [11].
Using of molecular markers for the following purposes in plant breeding:

- in genotypic definitions for many species, especially grains,
- in distinguishing recessive characters which are difficult to identify in classical plant breeding
- at the separation of breeding lines that can not be separated by phenotype
- in determining the purity of a hybrid,
- in determining the genetic diversity and genetic origins of plant species

- in the gene transfer from wild gene sources, especially in cereals
- in the formation of gen pyramids [15]
- for early selection in backcross breeding [16-18].

Molecular markers assist in formulating a time effective breeding strategy for transferring resistance into the more adapted cultivars [19]. Therefore, they are very useful in plant breeding studies.

5. THE SELECTION APPLICATIONS SUPPORTED BY THE MOLECULAR MARKERS

Especially in the last 15 years, it has gained great importance in the development of resistance against diseases that threaten the global products resources [20]. Marker-assisted selection is not a method that can be used instead of classical breeding methods alone yet it is complementary and enhancing the success of classical breeding techniques [15].

Gene-specific markers used for identify of some resistance genes against plant diseases have been developed. These markers have been widely used in plant breeding studies. Lagudah et al. (2009) developed gene-specific markers for the wheat gene Lr34/Yr18/Pm38 which confers resistance to multiple fungal pathogens [21]. Chaithanya et al. (2011) investigated the resistance heredity against Fusarium in the F_2 generation of pigeonpea (*Cajanus cajan* L. Millsp) using SCAR markers. The sensitive/resistant assessment against this disease was performed faster by the help of SCAR markers. Chaithanya et al. (2011) suggested that SCAR markers developed from RAPD markers have the advantages of greater reliability, cost effectiveness, high reproducibility and technical simplicity than simple RAPD's which helps in monitoring disease resistance by early screening of genotypes [19]. While these specific markers are used in plant breeding today, some non-specific markers such as SSR, ISSR, and RAPD were used before. Fufa et al. (2005) used 51 SSR markers in 30 hard red wheat. They researched genetic relationships among wheat varieties and determined pre-material for the breeding studies [22]. Cota et al. (2010) tested RAPD and SSR markers for wheat resistance to *Tilletia spp*. in F_2 segregating populations [5].

Recently, some new techniques have been performed for development of new specific markers used in MAS. Bulked segregant analysis (BSA) is a useful technique for this aim. It can rapidly identify molecular markers linked to traits of interest. Many genetic markers such as restriction fragment length polymorphisms (RFLPs), amplified fragment length polymorphisms (AFLPs), simple sequence repeats (SSRs), and sequence-tagged sites (STSs) linked to disease resistance genes have been used in BSA [23]. There are many study examples about using MAS (Table 1).

Table 32.Examples of marker-assisted selection in plant diseases

Marker	Host/Resistance Source	Pathogen/Disease	References
ISSR	*Triticum aestivum*	*Tilletia* sp.	[24]
	Cicer arietinum L.	Fusarium wilt	[25]
	Mungbean	Powdery mildew (PM)	[26]
	Cicer arietinum L.	Fusarium wilt	[27]
	Cicer arietinum L.	Fusarium wilt and Ascochyta blight	[28]
RAPD	*Lens culinaris* Medik	Ascochyta blight and anthracnose	[29]
	Triticum aestivum	Leaf rust	[30]
	Oryza sativa L.	Rice blast	[31]
	Hordeum vulgare	Net Blotch	[32]
	Vigna unguiculata	Anthracnose	[33]
RFLP	Wheat	Fusarium head blight	[16]
	Rice	Blast	[34]
	Soybean	Mosaic virus	[35]
	Barley	Scald disease	[36]
STS	*Triticum aestivum*	Stripe rust	[37]
	Triticum aestivum	Powdery mildew	[38]
	Rice	Bacterial blight (BB)	[39]
	Triticum aestivum	Eyespot	[40]
	Triticum aestivum	Stem rust	[41]
SCAR	*Hordeum vulgare* ssp.	*Rhynchosporium secalis*	[42]
	Triticum aestivum	Wheat midge	[43]

	Oryza sativa L.	*Orseolia oryzae*	[44]
	Brassica oleracea	Black rot	[45]
	Capsicum annuum L.	Root-knot nematode	[46]
SSR	Apricot	Plum Pox Virus (PPV)	[47]
	Triticum aestivum	*Puccinia striiformis* f. sp. *tritici*	[48]
	Triticum aestivum	*Septoria tritici*	[49]
	Triticum aestivum	*Erysiphe graminis*	[50]
	Oryza sativa L.	Brown planthopper (BPH)	[51]

6. CONCLUSIONS

Due to climatic changes, race changes may occur in plant pathogens. These new race scan lead to the breakdown of existing resistance. Therefore, new resistance sources need to be identified and developed. The recent studies have indicated that molecular markers are useful tools for detecting variation in genetic resources.
Classical plant breeding is dependent on environmental conditions and includes difficult field works. Moreover, assessment of the disease condition in the field is limited to the growth season.The development of resistant varieties through conventional plant breeding is a long and costly process. But, it is possible to develop resistant varieties in a shorter time with marker-assisted selection. The preference of resistant varieties instead of chemical methods for combating diseases presents a more sensitive and cheaper alternative to the environment. Taking all these into consideration, it is recommended that molecular markers have to be integrated into breeding studies.

REFERENCES

[1] S. Sehirali and A. M. Ozgen, “Plant Breeding”, Ankara University Agriculture Faculty Publication, Ankara, 2010.
[2] O. A. Sonmezoglu, A. Yildirim, T. E. Gulec and N. Kandemir, “Using Marker Assisted Selection in Wheat Breeding”, Gazi Osmanpasa University, Agriculture Faculty Journal, Vol. 27 (1), pp.105-112, 2010
[3] O. Tiryaki, R. Canhilal and S. Horuz, “Usage and Risks of Pestisides”, Erciyes University Journal, Vol. 26(2), pp. 154-169, 2010
[4] F. Oncicâ, and N. Sâulescu, “Potentially New Sources of Genes for Resistance to Common Bunt (*Tilletia* spp.) in Winter Wheat (*Triticum aestivum*L.)” Proc. Rom. Acad. Series B., Vol. 1-2, pp. 97-100, 2008.
[5] L. Cota, C. Botez, D. Pamfil and M.A. Grigoras, “ Testing of RAPD and SSR markers for wheat resistance to *Tilletia* spp. in F_2 segregating populations”, Genetica, pp. 385-389, 2010.
[6] T. E. Gulec, A. Yildirim and O. A. Sonmezoglu, “MAS in Plants”, Turk Siencific Review Journal, Vol. 3(2), pp. 67-79, 2010.
[7] M. Tor, “Recent Developments In Molecular Plant-Microbe Interactions”, Turkish Journal of Biology, Vol. 22, pp. 271-285, 1998.
[8] F. Altay, “Resistance Sources to Leaf Rust and Breeding” .I. Plant Breeding Symposium Ege University Agricultural Faculty, Izmir, 2008.
[9] J. E. Van Der Plank, “Disease Resistance in Plants”, Academic Press, New York, 1968.
[10] K. Yu, S. Park and V. Poysa, “Marker-assisted selection of common beans for resistance to common bacterial blight:efficacy and economics” Plant Breed., Vol. 119, pp. 411–415, 2000.
[11] T. Akar, “MAS in Theory and Practise” Field Crops Central Research Institute Journal, 2004.
[12] M. Agarwal, N. Shrivastava and H. Padh, “Advances in molecular marker techniques and their applications
[13] in plant sciences”, Plant Cell Rep., Vol. 27, pp. 617-631, 2008.
[14] B. C. Y. Collard and D. J. Mackill, ” Marker-assisted selection: an approach forprecision plant breeding in the twenty-first century, Phil. Trans. R. Soc. B, Vol. 363, pp. 557–572, 2008.
[15] L. Zhou, Y. Cheng, X. Ye, W. Li, Z. Pu, Q. Jiang, Y. Liu, Y. Wei, M. Deng, Y. Zheng and G. Chen, “Molecular mapping of a stripe rust resistance gene in Chinese wheat landrace “Hejiangyizai” using SSR, RGAP, TRAP, and SRAP markers”, Crop Protection, Vol. 94, pp.178-184, 2017.
[16] P. O’Boyle and D.J. Kelly, “Use of Marker-assisted Selection to Breedfor Resistance to Common Bacterial Blight in Common Bean”, J. Amer. Soc. Hort. SCI., Vol. 132(3), pp. 381-386, 2007.
[17] J.A. Anderson, R.W. Stack, S. Liu, B.L., Waldron, A.D. Fjeld, C. Coyne, B. Moreno-Sevilla, J.Mitchell Fetch, Q.J. Song, P.B. Cregan and R.C. Frohberg, “DNA markers for Fusarium head blight resistance QTLs in two wheat populations”, Theor Appl Genet, Vol.102 pp.1164–1168, 2001.
[18] E. Filiz and I. Koc, “Molecular Markers in Plant Biotecnology”, GOU Agriculture Faculty Journal, Vol. 28 (2), pp. 207-214, 2011.
[19] M. Yorgancilar, E.Yakisir and M. T. Erkoyuncu, “The Usage of Molecular Markers In Plant Breeding”, Journal of Bahri Dagdas Crop Research Vol. 4 (2), pp. 1-12, 2015, ISSN: 2148-3205.
[20] B. Chaithanya, L. Prasanthi., K. Hariprasad Reddy and B.V. Bhaskara Reddy,. “Study of Inheritance of Fusarium Wilt Resistance Through Molecular Marker Analysis In Pigeonpea [*Cajanus Cajan* (L.) Millsp]”, Agricultural Research Communication Centre, Legume Res., Vol. 34 (3) pp. 212 – 216, 2011.

[21] H. S. Randhawa, M. Asif, C. Pozniak, J. M. Clarke, R. J. Graf, S. L. Fox, D. G. Humphreys, R. E. Knox, R. M. Depauw, A. K. Singh, R. D. Cuthbert, P. Hucl and D. Spaner, "Application of Molecular Markers to Wheat Breeding in Canada", PlantBreeding, Vol., 132(5), pp. 458-471 ,2013.

[22] E.S. Lagudah, S.G. Krattinger, S. Herrera-Foessel, R.P. Singh, J. Huerta-Espino, W. Spielmeyer, G. Brown-Guedira, L.L Selter and B. Keller, "Gene-specific markers for the wheat gene Lr34/Yr18/Pm38 which confers resistance to multiple fungal pathogens", Theor Appl Genet., Vol. 119, pp. 889-898, 2009.

[23] H. Fufa, P.S. Baenziger, B.S. Beecher, I. Dweikat, R.A. Graybosch and K.M. Eskridge, "Comparison of phenotypic and molecular marker-based classifications of hard red winter wheat cultivars", Euphytica, Vol, 145, pp. 133-146, 2005.

[24] Y. Wang, H. Zhang, J. Xie, B. Guo, Y. Chen, H.Zhang, P. Lu, Q. Wu, M. Li, D. Zhang, G.Guo, J. Yang, P. Zhang, Y. Zhang, Y. Zhang, X. Wang, H. Zhao, T. Cao and Z. Liu, "Mapping stripe rust resistance genes by BSR-Seq:YrMM58 and YrHY1 on chromosome 2AS in Chinesewheat lines Mengmai 58 and Huaiyang 1 are Yr17", The Crop Journal, Vol. 6, pp. 91-98, 2018.

[25] I. Poyraz and N. Gumus, "Comparison of Resistance Rates and Detection of Five Resistance Genes (Bts) in Ten Local Wheat Varieties against Common Bunt Disease", Anadolu University Science and Technology Journal, Vol. 5 (1), pp. 37-45, 2016.

[26] K. Haji-Allahverdipoor, B. Bahramnejad and J. Amini, "Selection of molecular markers associated with resistance to *Fusarium* wilt disease in chickpea (*Cicer arietinum* L.) using multivariate statistical techniques" Australian Journal of Crop Science, Vol. 5(13), pp. 1801-1809, 2011. ISSN:1835-2707

[27] O. Poolsawat, C. Kativat, K. Arsakit and P.A. Tantasawat, "Identification of quantitative trait loci associated with powdery mildew resistance in mungbean using ISSR and ISSR-RGA markers" Mol Breeding, Vol. 37, pp. 150, 2017.

[28] M.B. Ratnaparkhe, D.K.Santra, A.Tullu and F.J. Muehlbauer, "Inheritance of inter-simple-sequence-repeat polymorphisms and linkage with a fusarium wilt resistance gene in chickpea", Theor Appl. Genet., Vol. 96, pp.

[29] 348-353, 1998.

[30] H. Aggarwal, A. Rao, A. Kumar, J. Singh, J.S. Rana, P.K. Naik and V. Chhokar, "Assessment of genetic diversity among 125 cultivars of chickpea (*Cicer arietinum* L.) of Indian origin using ISSR markers", Turkish Journal of Botany, 39: 218-226, 2015.

[31] B. Tar'an, L. Buchwaldt, A. Tullu, S.Banzia, T.D. Warkentin and A. Vanderberg, "Using molecular markers to pyramid genes for resistance to ascochyta blight and anthracnose in lentil (*Lens culinaris* Medik)" Euphytica, Vol. 134, pp. 223-230, 2003.

[32] G. Schachermayr, H. Siedler, M.D. Gale, H. Winzeler, M. Winzeler and B. Keller, "Identification and localization of molecular markers linked to the *Lr9* leaf rust resistance gene of wheat", Theor Appl Genet., Vol. 88, pp. 110-115, 1994.

[33] J.Y. Zhuang, W.B. Ma, J.L. Wu, R.Y. Chai, J. Lu, Y.Y. Fan, M.Z. Jin, H. Leung and K.L. Zheng, "Mapping of leaf and neck blast resistance genes with resistance gene analog, RAPD and RFLP in rice", Euphytica, Vol. 128, pp. 363–370, 2002.

[34] S.A. Dora, M. Mansour, A.A. Aziza,. and E. Abdelwahab, "Genetic Diversity and Relationships among Some Barley Genotypes for Net Blotch Disease Resistance Using RAPD, SCOT and SSR Markers" Egypt J. Genet Cytol., Vol.46, pp. 139-165, 2017.

[35] D. Pradhan, D. Mathew, S.K. Mathew and P.A. Nazeem, "Identifying the markers and tagging a leucine-rich repeat receptor-like kinase gene for resistance to anthracnose disease in vegetable cowpea [*Vigna unguiculata* (L.) Walp.]" The Journal of Horticultural Science and Biotechnology, Vol. 93 (3), pp. 225-231, 2018.

[36] S. Hittalmani, A. Parco, T.V. Mew, R.S. Zeigler and N. Huang, "Fine mapping and DNA marker-assisted pyramiding of the three major genes for blast resistance in rice" Theor Appl Genet., Vol. 100, pp.1121–1128, 2000.

[37] S.C. Jeong and M.A. Saghai Maroof, "Detection and genotyping of SNPs tightly linked to two disease resistance loci, Rsv1 and Rsv3, of soybean", Plant Breeding, Vol. 123, pp. 305-310, 2004.

[38] D.F. Garvin, A.H.D. Brown, H. Raman, and J. Read, "Genetic mapping of the barley Rrs03 scald resistance gene with RFLP, isozyme and seed storage protein markers" Plant Breeding, Vol. 119, pp. 193-196, 2000.

[39] C. Wang, Y. Zhang, D.Han, Z.Kang, G.Li, A. Cao and P. Chen, "SSR and STS markers for wheat stripe rust resistance gene Yr26" Euphytica, 159, pp. 359-366, 2008.

[40] J. Jianhui, B. Qin, H. Wang, A. Cao, S. Wang, P. Chen, L. Zhuang, Y. Du, D. Liu and X. Wang, "STS markers for powdery mildew resistance gene Pm6 in wheat", Euphytica, Vol. 163, pp. 159-165, 2008.

[41] S.Singh, J.S.Sidhu, N.Huang, Y.Vikal, Z.LI, D.S. Brar, H.S. Dhaliwal and G.S. Khush, "Pyramiding three bacterial blight resistance genes (xa5, xa13 and Xa21) using marker-assisted selection into indica rice cultivar PR106", Theor Appl Genet., Vol. 102, pp. 1011-1015, 2000.

[42] C.D. Zanke, B. Rodemann, J.Ling, Q.H. Muqaddasi, J. Plieske, A. Polley, S. Kollers, E. Ebmeyer, V. Korzun, O. Argillier, G. Stiewe, T. Zschackel, M.W. Ganal and M.S. Roder, "Genome-wide association mapping of resistance to eyespot disease (*Pseudocercosporella herpotrichoides*) in European winter wheat (*Triticum aestivum* L.) and fine-mapping of *Pch1*" Theor Appl Genet., Vol. 130, pp. 505-514, 2017.

[43] M.A. Rashed, A.H. Atta, T.M. Shehab El-Din and A.M. Mostafa, "Development of SSR and STS molecular markers associated with stem rust resistance in bread wheat (*Triticum aestivum* L.)", Egypt. J. Genet. Cytol., Vol. 45, pp. 261-278, 2016.

[44] R.K. Genger, A.H.D. Brown, W. Knogge, K. Nesbitt and J.J. Burdon, "Development of SCAR markers linked to a scald resistance gene derived from wild barley" Euphytica, Vol. 134 pp. 149–159, 2003.

[45] J.Thomas, E.Riedel and G. Penner, "An efficient method for assigning traits to chromosomes" Z. Bedo and L. Lang (eds.), Wheat in a Global Environment, pp. 727-732, 2001.
[46] N. Sardesai, A.Kumar, R.K. Rajyashri, S. Nair and M. Mohan, " Identification and mapping of an AFLP marker linked to Gm7, a gall midge resistance gene and its conversion to a SCAR marker for its utility in marker aided selection in rice" Theor Appl Genet., Vol., 105, pp. 691-698, 2002.
[47] B.B. Sharma, P. Kalia, D. Singh and T.R. Sharma, "Introgression of Black Rot Resistance from Brassica carinata to Cauliflower (*Brassica oleracea* botrytis Group) through Embryo Rescue", Frontiers in Plant Science, Vol. 8, pp. 1255, 2017.
[48] X. Wang, A. Fazari, Y. Cao, Z. Zhang, A. Palloix, S. Mao, B.Zhang, C.Djian-Caporalino and L. Wang, "Fine mapping of the root-knot nematode resistance gene Me1 in pepper (*Capsicum annuum* L.) and development of markers tightly linked to Me1", Mol Breeding, Vol 38, pp. 39, 2018.
[49] J.M. Soriano, E.M. Vera-Ruiz, S. Vilanova, J.Martinez-Calvo, G. Llacer, M.L. Badenes, and C.Romero,. "Identification and mapping of a locus conferring plum pox virus resistance in two apricot-improved linkage maps", Tree Genetics and Genomes, Vol. 4, pp. 391-402, 2008.
[50] M. A. Furan and S. Yuce, "SSR Analysis on Some Susceptible and Resistant Wheat Varieties and Lines Against to Stripe Rust", Ege University, Agriculture Faculty Journal, Vol. 46 (1) pp. 1-8, 2009.
[51] C. Botez, D. Pamfil, D. Curticiu, L. Cota and N.N. Saulescu, "Marker Assisted Selection for *Septoria tritici* Resistance in Wheat Dihaploid Lines", Not. Bot. Hort. Agrobot. Cluj, Vol. 37 (1) pp. 253-255, 2009.
[52] X.Q. Huang, L.X. Wang, M.X. Xu and M.S. Roder, "Microsatellite mapping of the powdery mildew resistance gene Pm5e in common wheat (*Triticum aestivum* L.)", Theor Appl Genet., Vol. 106, pp. 858-865, 2003.
[53] K.K. Jena, J.U. Jeung, J.H. Lee, H.C. Choi and D.S. Brar, "High-resolution mapping of a new brown planthopper (BPH) resistance gene, Bph18(t), and marker-assisted selection for BPH resistance in rice (*Oryza sativa* L.)" Theor Appl Genet., Vol. 112, pp. 288-297, 2006.

ICENS 4TH INTERNATIONAL CONFERENCE ON ENGINEERING AND NATURAL SCIENCE
2-6 May 2018 KIEV UKRAINE

Effect of Electric Field on Inter-subband Second Order Nonlinear Transitions in Single, Double and Triple Delta-Doped GaAs Structures

***Emine Ozturk*[1]**

Abstract

In this study, the inter-subband second order nonlinear transitions in single, double and triple delta-doped GaAs structure under applied electric field have been investigate for the uniform doping distribution model. The electronic properties of the structure such as the potential profile, the subband energies, the Fermi energy, the subband concentrations and the wave functions have been calculated by solving the Schrodinger and the Poisson equations self-consistently. The results show that the position and the size of second order harmonic generation (SHG) coefficient depend on QW shapes under applied electric field. Dependence on the electric field strength of the inter-subbands second order nonlinear transitions for different delta-doped GaAs layers is more important for potential variations in photodetectors and optical modulators. In the future these structures will play an important role in the investigation of quantum electronics and photonic devices.

Keywords: *Delta-doping, electric field, second order harmonic generation coefficient, self-consistent.*

1. INTRODUCTION

A usual δ-doped semiconductor contains an impurity atomic layer in various atomic crystal layers and therefore can be described by the doping profile along the growth direction and Silicon is commonly used as an n-type additive in GaAs growth using MBE. When Si donors are localized in an atomic plane during epitaxial growth, a layer of ionized donor forms a V-shaped potential that delimits electrons in a direction perpendicular to the delta-enhanced plane and leads to the formation of quasi-two-dimensional electron gas (2DEG). The eigenstates of such a 2DEG depend on the shape of the space-charge potential. The electronic structure of the system is calculated by solving the Schrodinger and Poisson equations on its own [1]-[3].

To produce δ-doped semiconductor devices with high mobility, some authors have motivated on developing doping and material growth methods [4]. A marginal way to rise electron mobility in newly proposed δ-doped semiconductors is to form a structure with double or triple δ-sheets [5]-[7]. The rise in mobility and concentrations in these structures is partly because of the distribution of further carriers in the center of two δ-doped GaAs wells. In these constructions, the carrier transport is spatially unglued from the ionized impurity sprinkling centers, and so the electron mobility increases two to five times over a single δ-doped case [5]. Thus, double and triple layer systems open up promises for higher electron mobility than single layer structures.

The nonlinear optical properties related to the inter-subband transitions within the conduction band have attracted considerable attention due to the strong quantum-confinement effect, large values of dipole transition matrix elements and possibility of achieving resonance conditions. For the optical properties of low dimensional semiconductor systems, the linear and nonlinear inter-subband optical transitions have been drawn more attention at theoretical and experimental investigations [8]-[13]. Among various nonlinear processes, considerable attention has been paid to the second harmonic generation (SHG) [14]-[17], which requires an asymmetric quantum well (AQW).

In this study, for SDD (single δ-doped layer), DDD (double coupled δ-doped layers) and TDD (triple coupled δ-doped layers) I investigate the inter-subband second order nonlinear transitions within n-type δ -doped GaAs layer under applied electric field for the uniform doping distribution model.

[1] *Corresponding author: Cumhuriyet University, Department of Physics, 58140, Sivas, Turkey. eozturk@cumhuriyet.edu.tr*

2. MATERIAL AND METHOD

At effective-mass approximation, to find the sub-band structure (the confining potential, the density profile, the sub-band energies, the electron concentrations and the Fermi energy) I have resolved self-consistently the Schrodinger and Poisson equations for the uniform distribution. A flow chart of the self-consistent design is presented in Figure 1 and extra particulars about the calculation by solving the Schrodinger and the Poisson equations self-consistently can be found in Reference [18].

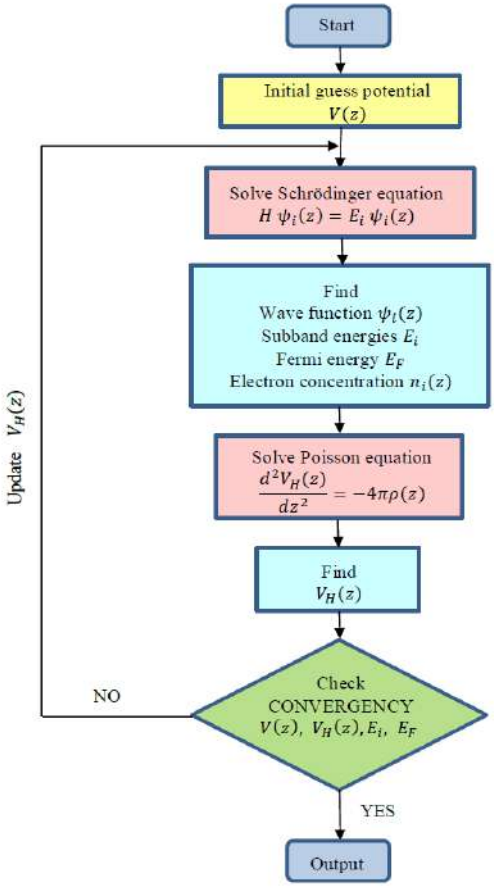

Figure 1. Flow chart of the self-consistent calculation.

The Hamiltonian in the Shrodinger equation of Figure 1 is given by

$$H = -\frac{\hbar^2}{2m^*}\frac{d^2}{dz^2} + V_H(z) + e\,F\,z \qquad (1)$$

where m^* is the electron effective mass, z is the direction perpendicular to the δ-doped layer, $V_H(z)$ is the effective Hartree potential, and F is the strength of the applied electric field.

After the effective *δ*-potential profile, the energy levels and their corresponding wave functions are obtained, the optical properties of the n-type *δ*-doped GaAs layer can be calculated by the density matrix approach.

In this study, I have interested the SHG in a three-level system, considering the filled states in SDD, DDD and TDD. By using the compact density matrix approach in Reference [16], the SHG susceptibility is derived, and it is given by

$$\chi_{2\omega}^{(2)} = \frac{e^3 \sigma_{12}\, M_{12}\, M_{23}\, M_{31}}{\varepsilon_o\, \hbar^2 (\omega - \omega_{21} - i\Gamma)(2\omega - \omega_{31} - i\Gamma/2)} \quad (2)$$

where ω is the frequency of the incident radiation, Γ is the relaxation rate for states, ε_o is the electrical permittivity of vacuum, $\omega_{ji} = E_{ji}/\hbar = (E_j - E_i)/\hbar$ and $M_{if} = < \Psi_i | z | \Psi_f >$ (i,f=1,2,3) is the dipole matrix element.

The electron density in δ-doped GaAs layer system is

$$\sigma_{12} = \frac{m^* k_B T}{L_{eff} \pi \hbar^2} \ln \left\{ \frac{1 + e^{(E_F - E_1)/k_B T}}{1 + e^{(E_F - E_2)/k_B T}} \right\} \quad (3)$$

where E_F is the Fermi energy, L_{eff} is the effective spatial extent of electrons.

3. RESULTS AND DISCUSSION

For numerical calculations, we have taken $m^* = 0.0665\, m_0$ (m_0 is the free electron mass), the separation between the adjacent two doping layers is 7 nm, thickness of the donor distribution is 3 nm, T=300 K, L_{eff} =40 nm, $\tau = 1/\Gamma$ =0.2 ps, n_r = 3.2. Total N_d^{2D} is taken as $N_d^{2D} = 24x10^{11} cm^{-2}$ (i.e. for SDD $N_d^{2D} = 24x10^{11} cm^{-2}$, for DDD $N_d^{2D} = 2x12x10^{11} cm^{-2}$ and for TDD $N_d^{2D} = 3x8x10^{11} cm^{-2}$).

For two different electric field values, Figure 2 (a, b and c) show the potential profile and the first three filled subband energies with their squared envelope wave functions for SDD, DDD and TDD structures, respectively. An increasing charge density in the δ-doped layer leads to more band bending and gives rise to the formation of a narrow and deeper potential well. Since in a SDD the donor impurities are localized in a narrower range with respect to DDD and TDD, the effective potential is narrow and deeper, the band bending is larger, and the squared wave functions of the confinement subband energies are little extended. This feature could be of use in controlling the confinement of carriers in devices using this type of doping. In the absence of an applied electric field, the effective potential has a characteristic symmetrical profile, and the square wave functions of the subband energies are symmetrical about the GaAs layers. The applied electric field tilts the potential profile and can induce a spatial separation between confined electrons and ionized dopants in the δ-doped GaAs structure. Consequently, the carriers spatially separated from the ionized donors enhance the mobility in these structures. Due to this property, in the presence of applied electric field the δ-doping can be used to enhance the mobility of free carriers in semiconductor devices.

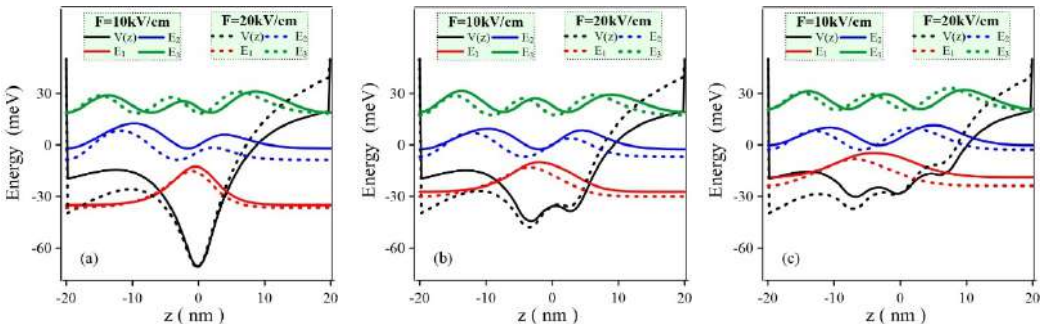

Figure 2. For two different electric field values, the potential profile and the first three filled subband energies with their squared envelope wave functions of a) SDD, b) DDD, c) TDD structures.

For SDD, DDD and TDD, the absolute SHG susceptibility as a function of incident photon energy is displayed in Figure 3 for two different electric field values. The SHG susceptibility depends on the energy difference between the electronic states and matrix elements of electric dipole moment. The former depends on the intersub-band energy levels separation and the last is determined fundamentally by the wave-function behavior. Since the dipole matrix elements (M_{31}) in Equation (2) there is no for symmetric structure, the SHG susceptibility coefficient vanishes. The asymmetry of the effective potential can be controlled by changing the applied electric field and this adjustable asymmetry is important for optimizing the SHG susceptibility.

Depending on the increase in the electric field, the potential profiles tilts and the symmetrical character is no longer present, and the (1-3) forbidden transition due to the parity for $F = 0$ are now possible. Since an increasing electric field pushes the electrons to the same side of the structures for all states, thus depending on the type of confined potential, both the energy difference between the subbands and the overlap function between these subbands change. It is displayed that an increasing electric field changes the δ-potential profiles and the separations between subbands for all structures; thus the energy differences, the Fermi energy, the dipole matrix elements, and the sub-band electron concentrations vary. For different electric field values, these variations for SDD, DDD and TDD structures are given in Table 1 and they are very sensitive to the applied electric field and the type of δ-doped GaAs layer. Changing values of the applied electric field vary both the peak sizes and the position of the SHG susceptibility. It is easily seen from Figure 3 that by increasing applied electric field, the resonant peak of SHG susceptibility of SDD and DDD layers shifts to red, whereas for TDD this peak slightly shifts to blue due to the subband energy differences. The resonance peak size of DDD structure is smaller than that of SDD and TDD, which is due to (M_{12} M_{23} M_{31}) multiplication. The results show that the position and the size of SHG coefficient depend on QW shapes under applied electric field. This behavior in the SHG susceptibility gives a new degree of freedom in regions of interest for device applications. The results open the possibility of designing some infrared optical devices.

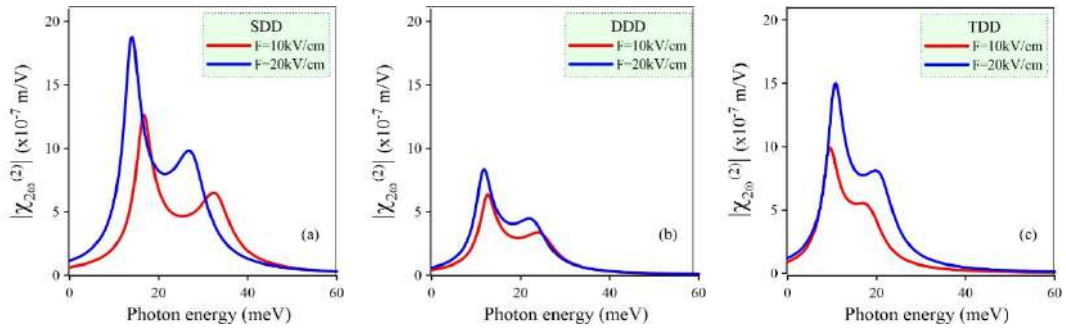

Figure 3. For two different electric field values, the SHG susceptibility as a function of incident photon energy for a) SDD, b) DDD, c) TDD structures.

Table 1. For SDD, DDD and TDD, energy differences, Fermi energy, dipole matrix elements and sub-band electron concentrations for different electric field values.

QW	F (kV/cm)	E_{21} (meV)	E_{32} (meV)	E_{31} (meV)	E_F (meV)	M_{12} (nm)	M_{23} (nm)	M_{31} (nm)	n_1 (x10^{11}cm^{-2})	n_2 (x10^{11}cm^{-2})	n_3 (x10^{11}cm^{-2})
SDD	0	35.45	17.52	52.97	23.58	-3.83	7.90	0	16.25	6.32	1.42
	1	33.05	20.801	53.86	22.53	3.81	-6.98	-0.99	16.10	6.85	1.03
	2	27.65	27.23	54.88	19.70	4.02	-5.92	-1.34	15.70	7.96	0.33
DDD	0	25.62	20.99	46.62	26.25	-4.69	-7.31	0	14.74	7.56	1.69
	1	24.84	21.73	46.67	25.10	-4.74	-7.15	0.36	14.66	7.70	1.62
	2	23.06	24.32	47.39	22.07	-4.90	-6.65	0.46	14.57	8.11	1.30
TDD	0	17.67	20.44	38.11	30.19	-5.66	-7.41	0	13.20	8.25	2.53
	1	18.58	21.18	39.77	29.26	5.48	-7.20	0.36	13.44	8.24	2.31
	2	21.04	23.23	44.27	26.59	5.07	6.70	-0.61	14.09	8.20	1.70

4. CONCLUSIONS

In this study, SHG susceptibility coefficient of SDD, DDD and TDD structure was investigated under applied electric field. The electronic structures are calculated by continuously solving the Schrodinger and Poisson equations. It has been shown that the location and magnitude of the SHG coefficient vary depending on the QW shapes for different electric fields. Based on these results, SHG susceptibility of different QW shapes can be relatively easily controlled by the electric field. These theoretical results can take place in experimental studies and provide some kind of approximate modeling for the practical application such as optoelectronics devices and optical communication.

Devices with δ-doped semiconducting structures have received a lot of attention recently due to the potential technological applications in electronic and photonic devices. For this reason, such δ-doped semiconductor structures are important for the devices such as high-power FETs and various infrared optical modulators based on the intersub-band transition of electrons.

ACKNOWLEDGMENT

This work is supported by the Scientific Research Project Fund of Cumhuriyet University under the project number F-571.

REFERENCES

[1] M. H. Degani, "Electron energy levels in a δ-doped layer in GaAs", *Phys. Rev. B*, vol. 44, pp. 5580-5584, Sep. 1991.
[2] E. Ozturk, "Optical intersubband transitions in double Si δ-doped GaAs under an applied magnetic field", *Superlatt. Microstruct.*, vol. 46, pp. 752-759, Jul. 2009.
[3] L.M. Gaggero-Sager, G.G. Naumis, M.A. Munoz-Hernandez, V. Montiel-Palma, "Self-consistent calculation of transport properties in Si δ-doped GaAs quantum wells as a function of the temperature", *Physica B*, vol. 405, pp. 4267-4270, Jul. 2010.
[4] E.F. Schubert, A. Fischer, K. Ploog, "The delta-doped field-effect transistor" *IEEE Trans. Electron Devices*, vol. 33, pp. 625-632, May 1986.
[5] X. Zheng, T.K. Carns, K.L. Wang, B. Wu, "Electron mobility enhancement from coupled wells in delta-doped GaAs", *Appl. Phys. Lett.*, vol. 62, pp. 504-506, Feb. 1993.
[6] L.-Y. Chen, S.-Y. Cheng, T.-P. Chen, K.-Y. Chu, T.-H. Tsai, Y.-C. Liu, X.-D. Liao, W.-C. Liu, "On an InGaP/InGaAs double channel pseudomorphic high electron mobility transistor with graded triple δ-doped sheets", *IEEE Trans. Electron Devices*, vol. 55, pp. 3310-3313, Nov. 2008.
[7] G.Q. Hai, N. Studart, F.M. Peeters, "Electron mobility in two coupled δ layers", *Phys. Rev. B*, vol. 52, pp. 11273-11276, Oct. 1995.
I. Karabulut, S. Baskoutas, "Linear and nonlinear optical absorption coefficients and refractive index changes in spherical quantum dots: Effects of impurities, electric field, size, and optical intensity", *J. Appl. Phys.*, vol. 103, pp. 073512-073516, Apr. 2008.
[8] E. Ozturk, Y. Ozdemir, "Linear and nonlinear intersubband optical absorption coefficient and refractive index change in n-type d-doped GaAs structure", *Opt. Commun.*,vol. 294, pp. 361-367, Jan. 2013.
[9] R.L. Restrepo, A.L. Morales, J.C. Martinez-Orozco, H.M. Baghramyan, M.G. Barseghyan, M.E. Mora-Ramos, C.A. Duque, "Impurity-related nonlinear optical properties in delta-doped quantum rings: Electric field effects", *Physica B*, vol. 453, pp. 140-145, May 2014.
[10] O. Oubram, Isaac Rodriguez-Vargas, J. C. Martinez-Orozco, "Refractive index changes in n-type delta-doped GaAs under hydrostatic pressure", *Revista Mexicana de Fisica*, vol. 60, pp. 161-167, Mar. 2014.
[11] E. Kasapoglu, U. Yesilgul, F. Ungan, I. Sokmen, H. Sari, "The effect of the intense laser field on the electronic states and optical properties of n-type double [delta]-doped GaAs quantum wells", *Optical Materials*, vol.64, pp. 82-87, Feb. 2017.
[12] E. Ozturk, "Nonlinear transitions in single, double, and triple δ-doped GaAs structures", *Romanian Journal of Physics*, vol. 62, pp. 603-612, Feb. 2017.
[13] L. Tsang, S.L. Chuang, S.M. Lee "Second-order nonlinear optical susceptibility of a quantum well with an applied electric field", *Phys. Rev. B*, vol. 41, pp. 5942-5951, Mar. 1990.
I. Karabulut, U. Atav , H. Safak , M. Tomak, "Second harmonic generation in an asymmetric rectangular quantum well under hydrostatic pressure", *Physica B*, vol. 393, pp. 133-138, Mar. 2007.
[14] J. C. Martinez-Orozco, M. E. Mora-Ramos, C. A. Duque, "Nonlinear optical rectification and second and third harmonic generation in GaAs δ -FET systems under hydrostatic pressure", *J. Lumin.*, vol. 132, pp. 449-456, Jan. 2012.
[15] J. C. Martinez-Orozco, J. G. Rojas-Briseno, K. A. Rodriguez-Magdaleno, I. Rodriguez-Vargas, M. E. Mora-Ramos, R. L. Restrepo, F. Ungan, E. Kasapoglu, C. A. Duque "Effect of the magnetic field on the nonlinear optical rectification and second and third harmonic generation in double δ-doped GaAs quantum wells", *Physica B*, vol. 525, pp. 30-35, Nov. 2017.
[16] E. Ozturk, I. Sokmen, "Intersubband transitions for single, double and triple Si δ-doped GaAs layers", *Phys. D: Appl. Phys.*, vol. 36, pp. 2457-2464, Oct. 2003.

BIOGRAPHY

Emine Ozturk was born in Sivas, Turkey, in 1966. She received her Ph.D degree in Physics from Cumhuriyet University, Sivas, Turkey in 2000. She has been working as a full professor at Cumhuriyet University, Faculty of Science, Department of Physics since 2010. Her research interests include the electronic and optical properties of the doped structures and low-dimensional systems. She has authored more than 60 papers for journals and scientific events. Also, she wrote a book entitled "Mathematical Methods in Physics and Engineering (with Resolved Examples)".

ICENS 4TH INTERNATIONAL CONFERENCE ON ENGINEERING AND NATURAL SCIENCE
2 - 6 May 2018 KIEV UKRAINE

Depending on Al and In Concentration of the Electronic Properties of Asymmetric Double GaAlAs/GaAs and GaInAs/GaAs Quantum Wells

Ozan Ozturk[1], Emine Ozturk[2], Sezai Elagoz[1]

Abstract

In this study, the electronic properties of asymmetric double $Ga_{1-x}Al_xAs/GaAs$ quantum wells (A structure) and $Ga_{1-x}In_xAs/GaAs$ quantum wells (B structure) have been investigated depending on the Al and In concentration, respectively. Using the effective mass approach, the energy levels, the wave functions and the probability densities of these system have been calculated by solving the Schrodinger equation. According to the results obtained, the main differences of A and B structure are the energy gap and the effective mass. For A structure, the barrier is GaAlAs, and the well is GaAs. Whereas for B structure, the barrier is GaAs, and the well is GaInAs. Also, the potential height and the energy levels of A structure are always lower than of B structure. We say that the Al and In concentration have a great effect on the electronic characteristics of asymmetric double quantum well (ADQW). These properties have a practical interest for the design of tunable semiconductor devices.

Keywords: *Asymmetric double GaAlAs/GaAs quantum well, asymmetric double GaInAs/GaAs quantum well, Al and In concentration, electronic properties.*

1. INTRODUCTION

The electronic features of low-dimensional systems are, to a large extent, dependent on the presence of some asymmetry of the potential profile of a semiconductor quantum well (QW). Such asymmetry in the potential prospect could provide an electric field or can rank the potential shape as a composition, and it is well known that QW structures vary considerably in electronic characteristics. We are interested in examining the structure of an asymmetric double quantum well (ADQW) shaped by two different semiconductors (e.g, GaAs/GaAlAs and InGaAs/GaAs). These systems consist of two potential wells connected by a barrier. It is a very convenient structure for observing quantum electronic transport. Since GaAlAs / GaAs QW structures are applied in modern photo-electronic and high-speed electronic devices, the pressure and external field dependence of electrical and optical properties in related systems has been extensively studied [1]-[6]. The segregation of indium atoms in the GaInAs layer has been widely studied in recent times, since the understanding of high-performance devices needs sudden hetero-interfaces [7]-[11]. It is also known that the indium atoms are strongly bound to the growth temperature and the GaInAs / GaAs hetero-structure is separated from the growth surface during MBE growth.

ADQW structures are the ideal structures for investigating the mechanisms of carrier transfer [12]-[17], as compared to single quantum wells. This study is focused on the theoretical work of the electronic properties of asymmetric Ga_{1-x} Al_x As/GaAs and Ga_{1-x} In_x As/GaAs DQW depending on the x-concentration (where x symbolizes the contribution rate of Al and In in ADQW, respectively). A structure and B structure will be named for Ga_{1-x} Al_x As/GaAs ADQW and Ga_{1-x} In_x As/GaAs ADQW, respectively. There are on the left hand side Asymmetric Inverse Semi Parabolic Quantum Well (AISPQW) and on the right hand side Asymmetric Double Semi V-shaped Quantum Well (ADSVQW). To our knowledge, this is the first work on the electronic properties of such ADQW structures as the literature. The motivation for using ADQW structures, which have various quantum wells with different shapes and height, is to construct multi wavelength optical devices.

[1] *Cumhuriyet University, Department of Nanotechnology Engineering, 58140, Sivas, Turkey.*
Corresponding author: ozanozturk@cumhuriyet.edu.tr,
[2] *Cumhuriyet University, Department of Physics, 58140, Sivas, Turkey. eozturk@cumhuriyet.edu.tr*

2. MATERIAL AND METHOD

Under an effective mass approach, the wave-functions and energy levels of electrons in QW may be acquired by resolving the Schrodinger equation with a suitable Hamiltonian.

$$\left(-\frac{\hbar^2}{2m^*}\frac{d^2}{dz^2}+V(z)\right)\Psi(z)=E\,\Psi(z) \tag{1}$$

where $V(z)$ is the potential seen by the electron along the z-direction, and E and $\Psi(z)$ are the eigen-energy and eigen-function related with the solution to the equation. The confinement potential of ADQW for the particle in z- direction, L_L and L_R being the left and right quantum well widths, respectively, b being the barrier width, are taken as,

$$V^{ADQW}(z)=V_0\begin{cases}-\left(z+\frac{b+L_L}{2}\right)^2+\frac{1}{2} & -\left(L_L+\frac{b}{2}\right)\le z\le-\left(\frac{L_L+b}{2}\right)\\ -2\left(z+\frac{b+L_L}{2}\right)^2+\frac{1}{2} & -\left(\frac{L_L+b}{2}\right)\le z\le-\left(\frac{b}{2}\right)\\ \frac{1}{L_R}\left(-z+\frac{b}{2}\right)+\frac{1}{2} & \left(\frac{b}{2}\right)\le z\le\left(\frac{L_R+b}{2}\right)\\ \frac{1}{2L_R}\left(-z+\frac{b}{2}\right)+\frac{3}{4} & \left(\frac{L_R+b}{2}\right)\le z\le\left(\frac{b}{2}+L_R\right)\\ 1 & \text{elsewhere}\end{cases} \tag{2}$$

The discontinuity in the conduction band edge and the electron effective mass of

$Ga_{1-x}Al_xAs/GaAs$ [18]-[19] and $Ga_{1-x}In_xAs/GaAs$ [18], [20] are analyzed using the following equations.

$$V_0^{GaAlAs}=\%60\left(E_g^{GaAlAs}-E_g^{GaAs}\right) \tag{3a}$$

$$V_0^{GaInAs}=\%60\left(E_g^{GaAs}-E_g^{GaInAs}\right) \tag{3b}$$

$$m^*_{GaAlAs}=(0.067+0.083\,x)m_0 \tag{4a}$$

$$m^*_{GaInAs}=(0.067-0.04\,x)m_0 \tag{4b}$$

Where $E_g^{GaAlAs}=\left(E_g^{GaAs}+1247\,x\right)$ meV, $E_g^{GaInAs}=\left(E_g^{GaAs}-1619\,x+555\,x^2\right)$ meV, $E_g^{GaAs}=1424$ meV, and m^* is the effective mass depending on the material composition.

The QW confined potential is essential for the limitation of the electrons. Therefore, the finding probability of the electron in different QWs is provided by,

$$P_i^W=\int\left|\Psi_i^W(z)\right|^2 dz \qquad (i=1,2;\quad W=L,R) \tag{5}$$

where L and R indicate the left quantum well (LQW) and the right quantum well (RQW), respectively.

3. RESULTS AND DISCUSSION

We have theoretically examined the electronic properties of A and B structures depending on the x-concentration for ADQW. In this study, all well widths are $L_L=L_R=9$ nm, $b=3$ nm, and $T=300$K.

For different x-values, Fig. 1 (A structure) and Fig. 2 (B structure) demonstrate the confinement potential, the bound energy levels and squared wave functions referred to these energy states. As seen from Eq. (3) and Eq. (4), the focal differences of A and B sample are the effective mass and the energy gap. While for A structure the well is GaAs and the barrier is GaAlAs, for B structure the well is GaInAs and the barrier is GaAs. As expected, the energy levels of A structure with lower potential height are continuously lower than the energy levels of B structure. The ground (second) state is mostly positioned in ADSVQW (AISPQW). For A structure (B structure), for $x=0.10, 0.15$, and 0.20, the number of bound energy levels is two, three and four (two, three and three), respectively. We say that the x-concentration sensitivity of A structure is greater than that of B structure.

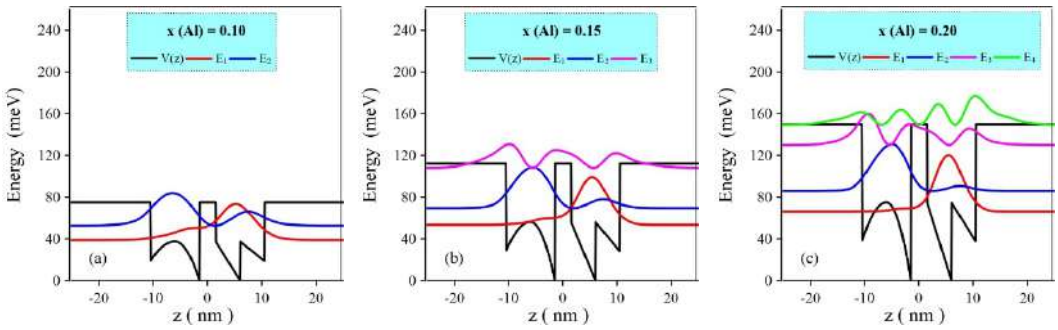

Figure 1. For ADQW (A structure), the confined potential and the bound energy levels with their squared wave functions for a) $x = 0.10$, b) $x = 0.15$, c) $x = 0.20$.

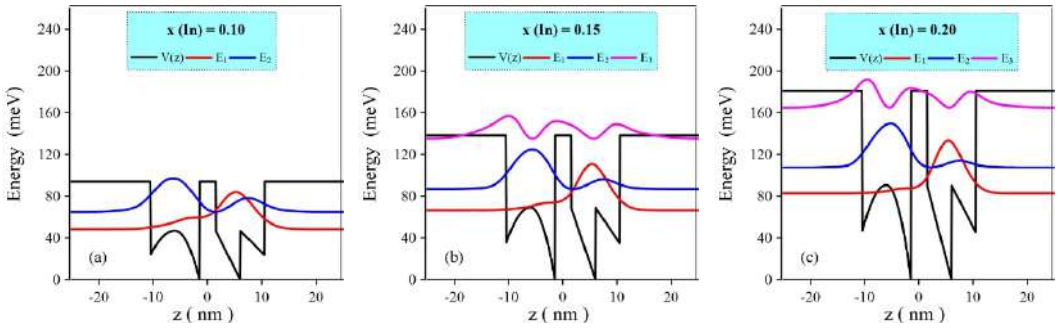

Figure 2. For ADQW (B structure), the confined potential and the bound energy levels with their squared wave functions for a) $x = 0.10$, b) $x = 0.15$, c) $x = 0.20$.

For A and B structure, the variation of potential height and bound energy levels in ADQW as a function of the x-concentration are shown in Fig. 3a and Fig. 3b, respectively. The energy levels of ADQW with different well shapes are different from each other. As expected, the potential height and all energy levels increase with increasing x-value. The energy levels of A structure are constantly lower than the energy levels of B structure. For $x = 0.10$, A and B sample has two bound state energies. There are two bonded states for $0.10 \leq x < 0.14$, and three connected states for $x \geq 0.14$. For structure A, four connected states occur for $x \geq 0.20$, whereas for B structure, four bound energy states appear for $x \geq 0.25$. Therefore, if it is desired to obtain more bound state energy levels depending on x value (for example, for $x = 0.20$), then structure A should be preferred.

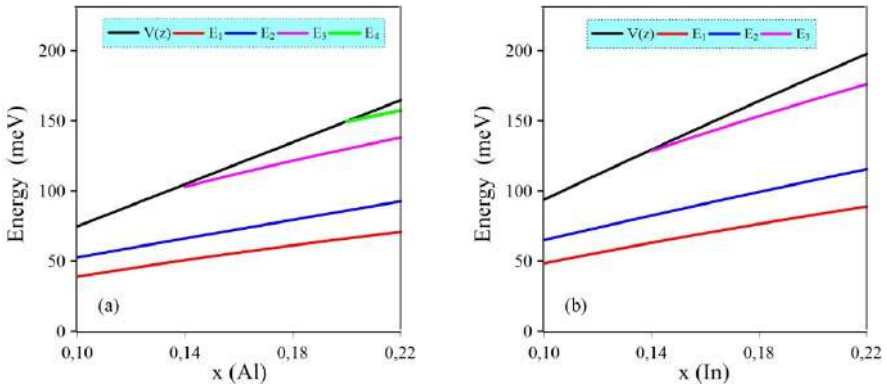

Figure 3. For ADQW the variation of potential height and bound energy levels versus the x-concentration value for a) A structure, b) B structure.

For A and B structure, the finding probability of the electron for the localized energy states in different QW are given in Fig. 4a and Fig. 4b as a function of x-parameter, respectively. The probability density of ADSVQW is slightly higher than AISPQW. The first (second) state is commonly found in the RQW (LQW), but very little in the LQW (RQW). When the x-concentration increases, the probability density in the mostly settled states increases. Whereas, the probability density of the first (second) state, which is low in the LQW (RQW), decreases even more as the x-concentration increases. The probability densities of other excited energy states increase with increasing x-value. If we compare A and B structures, the probabilities of finding electrons in different QWs for structure A change faster than structure B while increasing x-parameter.

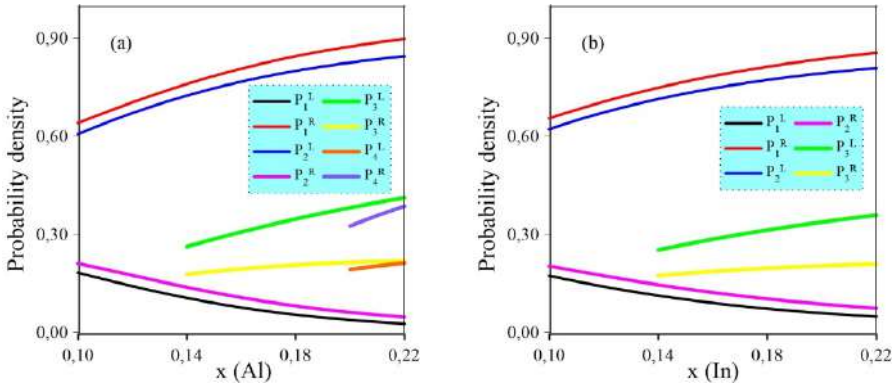

Figure 4. The probability density of the electrons for the ground state and the second state in different QW as a function of the x-concentration for a) A structure, b) B structure.

4. CONCLUSIONS

In present work, the electronic properties of asymmetric $Ga_{1-x}Al_xAs/GaAs$ and $Ga_{1-x}In_xAs/GaAs$ /GaAs DQW are examined as dependent on the x-concentration. The most important difference between these two structures is the size of energy levels. We analyzed the bound energy levels and the finding probabilities of the electrons in different QWs. We paid special attention to the calculation of the eigen-energies and the eigen-functions of these structures. It is found that depending on the x-contribution rate of the electronic properties of ADQW varies for A and B structure. These properties of ADQW may be vital in the advance of continual wave operation of DQW semiconductor devices. So, we expect that these conclusions will provide major development in multiple electro-optical semiconductor devices applications, for suitable choice of the structural parameters.

To be able to see the diversities between A and B structure more clearly, in subsequent studies, the building parameters can be changed and the external fields can be applied on these systems.

ACKNOWLEDGMENT

This work is supported by the Scientific Research Project Fund of Cumhuriyet University under the project number M-679.

REFERENCES

[1] G. J. Zhao, X. X. Liang, S. L. Ban, "Binding energies of donors in quantum wells under hydrostatic pressure", *Phys. Lett. A*, vol. 319, pp. 191-197, Oct. 2003.
[2] E. Ozturk, "Simultaneous effects of the intense laser field and the electric field on the nonlinear optical properties in GaAs/GaAlAs quantum well", *Opt. Commun.*, vol. 332, pp. 136-143, Jul. 2014.
[3] N. Raigoza, A. L. Morales, C. A. Duque, "Effects of hydrostatic pressure on donor states in symmetrical GaAs-$Ga_{0.7}Al_{0.3}As$ double quantum wells", *Physica B*, vol. 363, pp. 262-270, Mar. 2005.
A. J. Peter, K. Navaneethakrishnan, "Simultaneous effects of pressure and temperature on donors in a GaAlAs/GaAs quantum well", *Superlattice. Microst.*, vol. 43, pp. 63-71, Jan. 2008.

[4] E. Ozturk, I. Sokmen, "Nonlinear intersubband absorption and refractive index changes in square and graded quantum well modulated by temperature and hydrostatic pressure", *J. Lumin.*, vol. 134, pp. 42-48, Jan. 2013.
[5] E. Kasapoglu, C. A. Duque, M. E. Mora-Ramos, R. L. Restrepo, F. Ungan, U. Yesilgul, H. Sari, I. Sokmen, "Combined effects of intense laser field, electric and magnetic fields on the nonlinear optical properties of the step-like quantum well", *Materials Chemistry and Physics*, vol. 154, pp. 170-175, Jan. 2015.
[6] G. G. de la Cruz, A. C. Arenas, H. Herrera, "Internal electric-field and segregation effects on luminescence properties of quantum wells", *J. Appl. Phys.*, vol. 98, pp. 023501-023504, Jul. 2005.
[7] S. Martini, A. A. Quivy, T. E. Lamas, and E. C. F. da Silva, "Real-time RHEED investigation of indium segregation in InGaAs layers grown on vicinal GaAs(001) substrates", *Phys. Rev. B*, vol. 72, pp. 153304-153307, Oct. 2005.
[8] S. Wu, Z. Huang, Y. Liu, Q. Huang, W. Guo, Y. Cao, "The effects of indium segregation on the valence band structure and optical gain of GaInAs/GaAs quantum wells", *Physica E*, vol. 41, pp. 1656-1660, Jun. 2009.
[9] E. Ozturk, "Electric and intense laser field effect on the electronic properties of $Ga_{1-x}Al_xAs$/GaAs and
[10] $Ga_{1-x}In_xAs$/GaAs semi-parabolic quantum wells", *Laser Physics*, vol. 26, pp. 096102-096110, Jul 2016.
[11] P. Baser, I. Altuntas, S. Elagoz, "The hydrostatic pressure and temperature effects on hydrogenic impurity binding energies in GaAs/$In_xGa_{1-x}As$/ GaAs square quantum well", *Superlattice. Microst.*, vol. 92, pp. 210-216, Jan. 2016.
[12] N. Ohtani, Y. Hirose, T. Nishimura, T. Aida, M. Hosoda, "Formation of electric-field domains in an asymmetric double-quantum-well GaAs/AlAs superlattice", *Semicond. Sci. Technol.*, vol.19, pp. S89-S90, Mar. 2004.
[13] E. Ozturk "Linear and nonlinear optical absorption coefficients and refractive index changes in double parabolic-square quantum well as dependent on intense laser field", *Eur. Phys. J. Plus*, vol. 130, pp. 67-75, Apr. 2015.
[14] L. Silvestri, F. Bassani, G. Czajkowski, B. Davoudi, "Electromagnetically induced transparency in asymmetric double quantum wells", *Eur. Phys. J. B*, vol. 27, pp. 89-102, Jan. 2002.
[15] E. Ozturk, "Nonlinear intersubband transitions in asymmetric double quantum wells as dependent on intense laser field", Opt. Quant. Electron., vol. 48, pp. 269-282, May 2016.
[16] L. Klopotowski, M. Nawrocki, S. Mackowski, E. Janik, "Spin conserving tunneling in asymmetric double quantum well structures", Stat. Sol. B, vol. 229, pp. 769-774, Jan. 2002.
[17] E. Ozturk "Comparison of asymmetric double parabolic-inversed parabolic quantum wells for linear optical (1–2) transition", Optik, vol. 139, pp. 256-264, Apr. 2017.
[18] O. Ozturk, E. Ozturk, S. Elagoz, "The effect of barrier width on the electronic properties of double GaAlAs/GaAs and
[19] GaInAs/GaAs quantum wells", Journal of Molecular Structure, vol. 1156, pp. 726-732, Mar. 2018.
[20] E.C. Niculescu, N. Eseanu, A. Spandonide, "Laser field effects on the interband transitions in differently shaped quantum wells" U.P.B. Sci. Bull., Series A, vol. 77, pp. 281-292, Mar. 2015.
[21] T.J. Ochalski, J. Zuk, K. Reginski, M. Bugajski "Photoreflectance studies of InGaAs/GaAs/AlGaAs single quantum well laser structures", Acta *Physica Polonica A,* vol. 94, pp. 463-467, Sep. 1998.

BIOGRAPHY

Ozan Ozturk was born in Sivas, Turkey, in 1992. He completed both the Department of Electrical-Electronics Engineering and the Department of Mechanical Engineering at Cumhuriyet University, Engineering Faculty. He has been working as a Research Assistant at Cumhuriyet University, Engineering Faculty, Department of Nanotechnology Engineering since 2016, and is continuing his master's degree in the same department. His research interests include LED structures and the electronic properties of low-dimensional systems.

Emine Ozturk was born in Sivas, Turkey, in 1966. She received her Ph.D degree in Physics from Cumhuriyet University, Sivas, Turkey in 2000. She has been working as a full professor at Cumhuriyet University, Faculty of Science, Department of Physics since 2010. Her research fields include the electronic and optical properties of the doped structures and low-dimensional systems. She has authored more than 60 papers for journals and scientific events. Also, she wrote a book entitled "Mathematical Methods in Physics and Engineering".

Sezai Elagoz is a full Professor in Nanotechnology Engineering in Cumhuriyet University, where he has been a faculty member since 2003. He also acts as the director of Nanophotonic Research Center at Cumhuriyet University, the Dean of Technology Faculty at Cumhuriyet University and the chair of newly founded TRD Microelectronics Company. Elagoz completed his MSc and Ph.D. at Rackham Graduate School, Michigan University under the supervision of Roy Clarke and his undergraduate studies at Physics Department of Ankara University. His research interests lie in the area of low-dimensional structures ranging from theory to growth of such structures by using MBE and MOCVD techniques. He has collaborated actively with researchers in several other disciplines such as Nanotechnology, Physics and Electronic Engineering. He has mentored several MSc and PhD student in the related fields. His currently active projects are High Power Laser Diodes, Quantum Cascade Lasers, Short Wave Infrared Detectors, Blue LEDs and LEDs for Backplane lighting.

ICENS 4TH INTERNATIONAL CONFERENCE ON ENGINEERING AND NATURAL SCIENCE
2 - 6 May 2018 KIEV UKRAINE

Chemical Fixation of Automotive Industry Coating Sludge Containing Nickel and Zinc Using Silica Fume as an Alternative Binder to Portland Cement

Gizem Eker[1], Vedat Pinarli[1]

Abstract

The purpose of this study was to investigate the disposal of automotive industry phosphate coating sludge by stabilization/solidification technology. Silica fume (SF) was used as an alternative binder to Portland cement (PC). Silica fume, being one of the most popular pozzolans is considered to play a vital role in developing strength, durability characteristics and consuming calcium hydroxides during the hydration reaction of Portland cement. Mortar and paste samples were prepeared for laboratory tests. %5, %10 and %15 weight ratio of waste phosphate sludge (WPS) mixed with PC and the 10% of SF for preparing of mortar samples. Initial and final setting times were determined using Vicat needle. Unconfined compressive strength (UCS) values of mortars were measured following 7, 28, 56 and 90 days of water curing. Toxicity Characteristic Leaching Procedure (TCLP) was conducted for hardened mortar and paste samples after 28 curing days. Zn and Ni concetrations were measured using Inductively Coupled Plasma (ICP) Spectroscopy. WPS and SF retarded the initial and final setting times of PC. UCS values of mortar samples containing %5 WPS determined after 90 days of curing were smilar with the reference sample results. UCS values of mortar samples containing 10% and 15% WPS were lower than the reference sample. TCLP results of the mortar samples showed that heavy metals were not conformed with the EPA lanfilling limits. However, Zn concentrations of the paste samples were conformed with the EPA landfilling limits.

Keywords: ***Phosphate Sludge, Silica Fume, Portland Cement, Compressive Strength, TCLP***

1. INTRODUCTION

Pozzolans are silicaceous materials containing $Si0_2$ that react with calcium hydroxide and water to form calcium silicate hydrate or C-S-H gel. The hydration of portland cement without pozzolans produces relatively more calcium hydroxide, a weakening compound in concrete microstructure. SF, being one of the most popular pozzolans is considered to play a vital role in developing strength, durability characteristics and consuming calcium hydroxides during the hydration reaction of Portland cement [1],[2],[3] Therefore, such pozzolanic reactions may contribute to lower heat liberation, adequate early strength development, effective consumption of hydrated lime and enhancement in durability characteristics [1],[4].

Silica fume is a highly effective pozzolanic material due to its large specific surface area and high amorphous silica content [5], [6]. SF of sub-micro size is an active component which will react with $Ca(OH)_2$ to produce the C–S–H (gel) phase. The addition of SF can modify the microstructure of hydrated pastes due to the formation of denser

[1] *Uludag University Environmental Engineering Department, geker@uludag.edu.tr Corresponding author: Uludag University Environmental Engineering Department, 16059, Nilufer/Bursa, Turkey. pinarli@uludag.edu.tr*

and lower-porosity, compact C–S–H [7],[8]. Additionally, silica fume also acts as fillers due to its near-perfect spheres with diameters ranging from 20 to 500 nm [9],[10]. It is expected that silica fume exhibits good fixation efficiency of heavy metals [11],[12]. The aim of the present study was to investigate chemical fixation of automotive industry coating sludge containing Nickel and Zinc using SF as an alternative binder to PC.

2.MATERIALS AND METHODS

The waste phosphate sludge (WPS) was received from phosphate coating process of an automobile industry in Bursa.Physical and chemical compositions of WPS and binding materials were determined. Within the scope of the solidification studies, the setting times and strength values were measured. The prepared mortar and paste samples were subjected to TCLP extraction tests simulating landfilling conditions. Zn and Ni concentrations were measured in the samples after extraction. Physical characteristics of phosphate sludge were given in Table 1.

Table 1. Physical characteristics of waste phosphate sludge

Parameter	Value
pH	3,8
Specific Gravity (g/m^3)	2,6
Spesific Surface Area (cm^2/g)	3406
PO_4 (mg/l)	135
Mouisture (%)	80

Zn and Ni concentrations in the leachate were then determined using Inductively Coupled plasma (ICP) technique. The values obtained were as given in Table 2 . When Zn and Ni concentrations are > 2 mg / l and > 0.4 mg/ l, respectively, waste is classified as hazardous waste. according to Annex 11-A of the Hazardous Waste Control Regulation.

Table 2. Heavy metal concentrations of phosphate sludge

Metal	Unit	WPS	EPA Landfilling Limits
Zn	mg/l	130.22	2.0
Ni	mg/l	22.65	0.4

Reference paste sample were prepeared using only PC. Mortar (with sand) and paste (without sand) samples were prepeared with 5%, 10% and 15% weight ratio of WPS mixed with PC and 10% of SF, respectively. Initial and final setting times of paste samples were determined using Vicat needle,according to ASTM C191 standard. Square prismatic mortar molds with internal dimensions of 40*40*160 mm were used.Water-to-solid ratio was chosen as 0.5. After being removed from their molds, the mortars were cured in water. Unconfined compressive strength of mortar samples were determined using an ESEL ESL.25.001.B-015 250 kN compression machine after 3, 7, 28, 56 and 90 days of water curing. Stress-controlled loading. speed setting of 0.05 kN/s was applied for compression testing.TCLP has been used to assess the effectiveness of cement and additives in stabilization and solidification of waste. The Zn and Ni concentrations measured in the paste and mortar samples prepared by mixing the phosphate sludge with

cement and SF in different combinations were compared with the EPA lanfilling limits. Heavy metal concentrations were measured using Bausch& Lomb ARL/3520 AES inductively coupled plasma technique.

3.RESULTS AND DISCUSSION

In paste samples prepared due to the heavy metals (Zn, Ni) contained in the phosphate sludge, the initial and final setting times were prolonged (Figure 1). In a related study, Gervais and Ouki added 1% by weight of Zn to cement and they found that the initial and final setting times were extended by 20 hours [13]. Due to high SiO_2 content and finer particle size distribution of SF than cement may be the reasons for extended initial and final setting times. It was thought that chromium and MgO in the SF structure inhibit hydration reactions. Chromium inhibits cement hydration, delaying settling times [14]. Mg ions are known to slow the hydration reactions by forming impermeable layers around the cement particles [15].

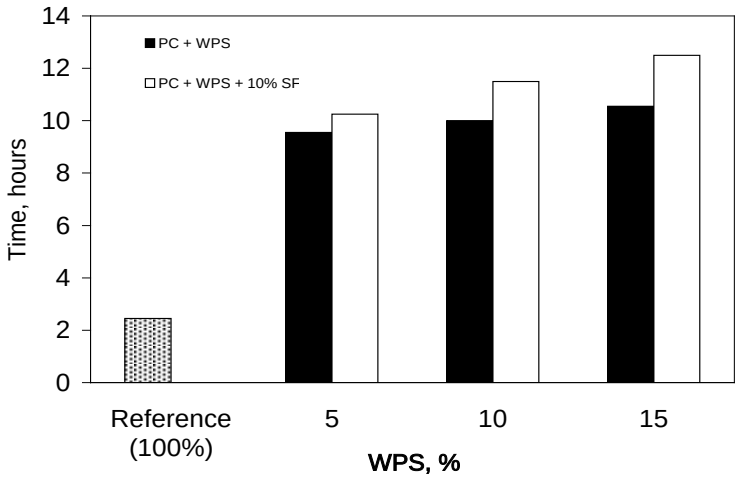

Figure 1. Initial and final setting times of paste samples containing waste phosphate sludge + cement + silica fume

3.1.Unconfined Compressive Strength (UCS) Results

Stabilization/solidification of phosphate sludge with PC and SF as an additive were determined and the UCS values of the waste forms after the curing times of 7. 28. 56 and 90 days were shown in Figure 2.

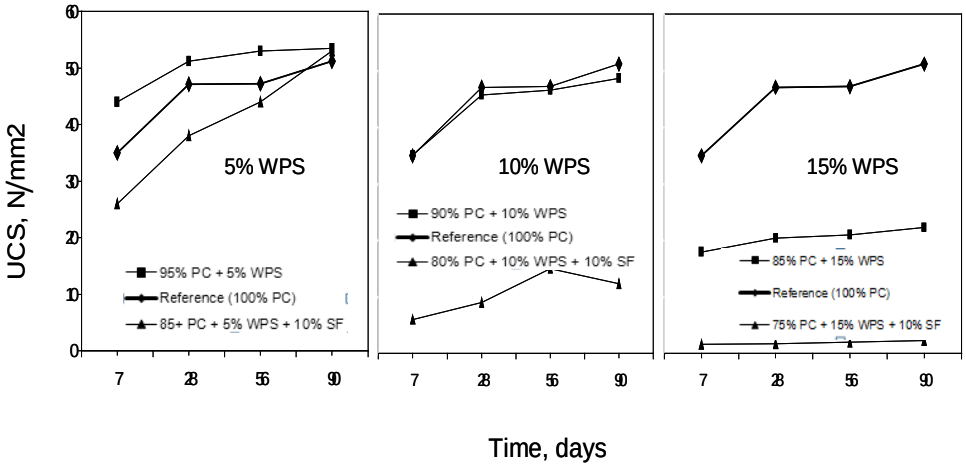

Figure 2. Unconfined compressive strength results of mortar samples containing phosphate sludge + cement + 10%sf

UCS values of mortar samples containing 5% WPS were found similar to reference sample at the end of 90 days of curing. The increase of WPS at fixed SF ratio (10%) in the prepared mortar samples affected the strength results in the negative direction. It has been concluded that the reduction in strength values is due to the inhibition effect of MgO and Cr in the composition of the SF on cement hydration. It has been noted in the studies that the MgO content caused the reduction in cement strength [15]. It has also been observed that Cr reduces the strength values as a result of the interferences during the hydration reactions.

3.2. Heavy Metal Concentrations in Leachete after TCLP Extraction in Mortar Samples

Zn and Ni concentrations in the leachates were measured using the *Inductively Coupled Plasma* (ICP) instrument and the results obtained were presented in the Figure 3.

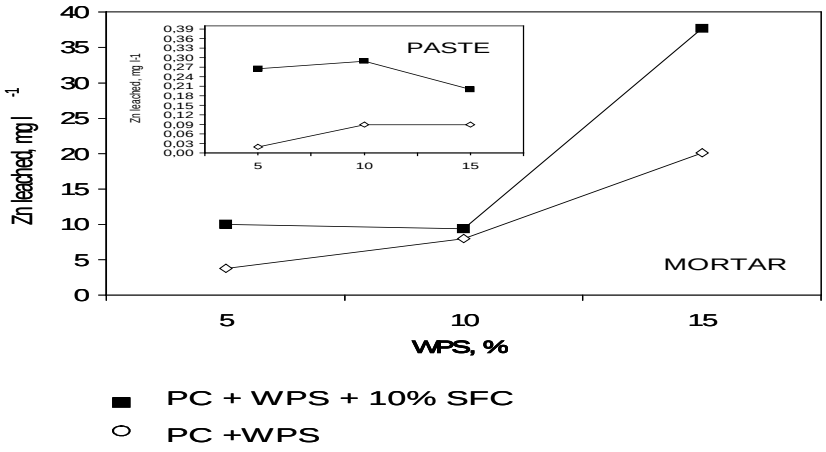

Figure 3a. Zinc concentrations of leachate (TCLP) in mortar and paste samples

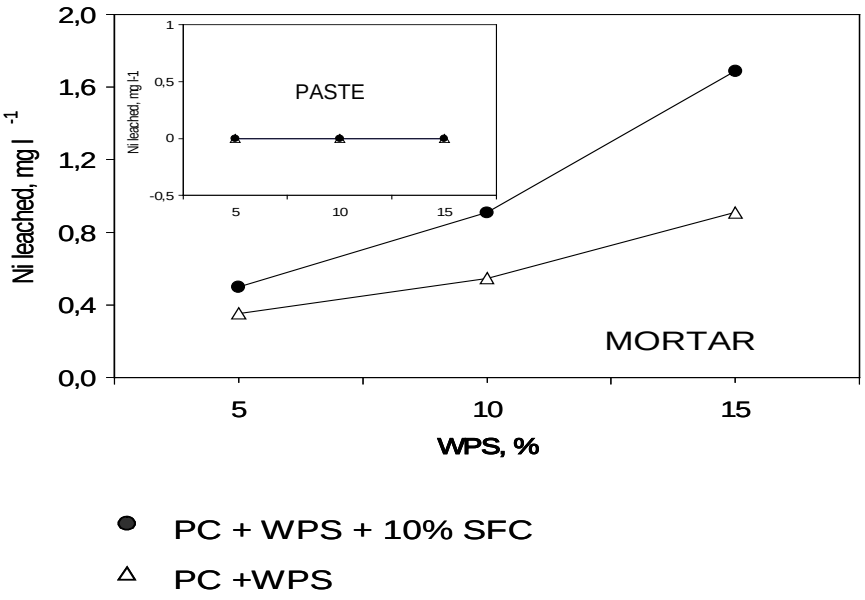

Figure 3b. Nickel concentrations of leachate (TCLP) in mortar and paste samples

It has been found that the rate of fixing of Zn in the waste form was lowered by increasing the sludge addition ratio from 5% to 15%, and the use of SF also affected the stabilization process more adversely. The use of SF as an additive has also led to the belief that the hydration of cement reduces the stability of the waste form. No significant change in the amount of Ni leached was observed by using SF as an additive in the mixture containing cement and 5% WPS. Samples containing 10% SF at 10% and 15% WPS ratios were found to have higher Ni concentrations in the leachate than Ni concentration values in SF-free samples.

Fixation of heavy metals in paste samples were achieved successfully. As seen in Figure 3a and 3b leached Zn and Ni concentrations were lower than the EPA landfilling limits. However, it has been found that the fixation of heavy metals in mortar samples has not been successfully accomplished when Zn and Ni limit values specified in EPA. In the mortar samples, the formation of intense $Ca(OH)_2$ on sand and cement paste interface was detected by Gleize [16]. $Ca(OH)_2$ develops in solution during cement hydration. Crystals of $Ca(OH)_2$ have a relatively weak and fragile structure compared to other hydration products due to their morphology. The $Ca(OH)_2$ crystals, which are concentrated in the cement-aggregate interfaces, cause sensitivity to external influences in these regions, leading to fractures such as fracture and cracking [17]. Possible deterioration at the paste-sand interfaces in the mortar samples subjected to strong acidic solutions during TCLP extraction, where landfilling conditions are simulated, caused heavy metals to migrate to solid matrix stagnant leachate. in the case of mortar samples, it was concluded that these deteriorations did not occur because of the lack of sand and that Zn and Ni did not leach from the solid matrices.

4. CONCLUSIONS

S/S of the WPS using PC and SF as cement substitute were investigated in the present study. The following conclusions can be drawn based on the experimental study:

- In paste samples prepared due to the heavy metals (Zn, Ni) contained in the phosphate sludge, the initial and final setting times were prolonged.

- UCS values of mortar samples containing 5% WPS were found similar to reference sample at the end of 90 days of curing.
- The increase of WPS at fixed SF ratio (10%) in the prepared mortar samples affected the strength results in the negative direction. It has been concluded that the reduction in strength values is due to the inhibition effect of MgO and Cr in the composition of the SF on cement hydration.
- Fixation of heavy metals in paste samples were achieved successfully. Leached Zn and Ni concentrations were lower than the EPA landfilling limits. However, it has been found that the fixation of heavy metals in mortar samples has not been successfully accomplished.

Biography: Prof. Dr. Vedat PINARLI is a graduate of Civil Engineering Faculty of Istanbul Technical University. He has carried out Post Graduate studies in Public Health Engineering at the University of Newcastle upon Tyne. He has obtained his PhD. In Industrial Chemistry at the University of West London U.K. He is currently working as a lecturer/supervisor in the Environmental Engineering Department of Uludag University, Bursa, Turkey.

REFERENCES

[1]. M. Mazloom, A.A. Ramezanianpour and J.J. Brooks,, "Effect of silica fume on mechanical properties of high-strength concrete," *Cement and Concrete Composites*, vol.26, pp.347-357, 2004.
[2]. P. Fidjestøl and M. Dåstøl., "The history of silica fume in concrete–From novelty to key ingredient in high performance concrete", *In Proceedings of the Congresso Brasileiro do Concreto.* 4th–9th Sept 2008. Salvador: El Salvador, 2008.
[3]. *A.*, Elahi, P.A.M. Basheer, S.V. Nanukuttan and , Q.U.Z Khan, "Mechanical and durability properties of high performance concretes containing supplementary cementitious materials," *Construction and Building Materials*, vol.24, pp.292-299, 2010.
[4]. C. Garg and A. Jain, "Green Concrete: efficient & eco-friendly construction materials," *International Journal of Research in Engineering and Technology*, vol.2, pp.259-264, 2014.
[5]. J., Bensted and P. Barnes, "Structure and Performance of Cements", Second ed. Spon Press, London and New York, 2008.
[6]. Khan, M.I. and Siddique, R., "Utilization of silica fume in concrete: review of durability properties," *Resources Conservation and Recycling*, vol.57, pp.30–35, 2011.
[7]. E. Sakai,, S. Miyahara, S. Ohsawa, S.H. Lee and M. Daimon, " Hydration of fly ash cement," *Cement and Concreate Resources*, vol.35, pp.1135–1140, 2005.
[8]. Z. Giergiczny and A. Krol,, "Immobilization of heavy metals (Pb, Cu, Cr, Zn, Cd, Mn) in the mineral additions containing concrete composites," *Journal of Hazardous Materials*, vol.160, pp. 247–255, 2008.
[9]. D.R.G. Mitchell, I. Hinczak and R.A. Day, "Interaction of silica fume with calcium hydroxide solutions and hydrated cement pastes" *Cement and Concrete Resources*, vol.28, pp.1571–1584, 1998.
[10]. F. Collins, J.G. Sanjayan, "Effects of ultra-fine materials on workability andstrength of concrete containing alkali-activated slag as the binder," *Cement and Concrete Resources*, vol.29, pp.459–462, 1999.
[11]. W.J. Huang and H.S. Huang, "Using fume silica as heavy metals' stabilizer for highalkali and porous MSWI baghouse ash," *Journal of Hazardous Materials*, vol.152, pp.176–182, 2008.
[12]. N. Rodella, A. Bosio, R. Dalipi, A. Zacco, L. Borgese, L.E. Depero and E. Bontempi, "Waste silica sources as heavy metal stabilizers for municipal solid waste incineration fly ash," *Arabian Journal of Chemistry*, http://dx.doi.org/10.1016/ j.arabjc.2014.04.006, 2014.
[13] C. Gervais and S.K. Ouki, "Performance study of cementitious systems containing zeolite and silica fume: effects of four metal nitrates on the setting time, strength and leaching characteristics," *Journal of Hazardous Materials*, vol.93, pp.187-200, 2002.
[14]. J. N. Diet, P. Moszkowicz, D. Sorrentino, "Behaviour of ordinary Portland cement during the stabilization/solidification of synthetic heavy metal sludge: macroscopic and microscopic aspects," Waste Management, vol.18, pp.17-24, 1998
[15]. B. Baradan, H. Yazici and H. Un, "Betonarme Yapilarda Kalicilik (Durabilite)", Dokuz Eylul Universitesi Yayinlari, Izmir, 2000.
[16]. P.J.P.Gleize, A. Muller and H.R Roman, "Microstructural investigation of silica fume-cement-lime mortar," *Cement and Concrete Composites*, vol.25, pp.171-175, 2003.
[17]. G.A. Rao, "Investigations on the performance of silica fume–Incorparated cement pastes and mortars.", *Cement and Concrete Research*, vol. 33, pp.1765-1770, 2003.

ICENS 4TH INTERNATIONAL CONFERENCE ON ENGINEERING AND NATURAL SCIENCE
2-6 May 2018 KIEV UKRAINE

Economic Analysis of Wind-Hydro Pumped Storage Power System

Cenk Kilic[1], Mehmet Kurban[2], Emrah Dokur[3]

Abstract

The use of renewable energy systems has grown continuously in recent decades and significantly in the world energy sector. Currently, the best-known renewable energy sources include solar, wind, ocean and geothermal energy. In addition, the hydroelectric power systems are important in energy conversion systems. The pumped hydro storage systems use excess electricity production, in periods of low demand, to pump water to a deposit situated at a certain height, recovering it at a later time through a turbine when it is required to cover peak load periods. Hybrid energy system has become viable alternatives to meet environmental protection requirement and electricity demands. In this paper, economic analysis of hybrid systems which are the Hydroelectric Pumped Storage System (PHES)-wind energy conversion system are presented. The hybrid system is proposed in Borcka dam, Artvin, Turkey. The detailed of project area and components of hybrid systems are determined for case study. Finally, economic analysis results for hybrid system are discussed in this paper.

Keywords: Wind Energy, Renewable Energy, Hybrid Systems, Power System.

1. INTRODUCTION

Wind energy has been the most expeditious growing renewable energy technology in the last years. In recent years along with the development of wind industry, wind turbines capacity reached approximately to 486 GW by the end of 2016. The potential of wind energy of a certain region can be determined before a wind conversion system is installed. The determination of wind energy potential depends on accurately modeling wind speed. Statistical properties of the wind speed are important to predict the output energy of a wind conversion system.

In the world the pumped hydroelectric storage (PHES) is the most established technology for utility-scale electricity storage and has been commercially deployed since the 1890s. Since the 2000s, there have been revived interests in developing PHES facilities worldwide. Because most low-carbon electricity resources (ex. wind, solar, and nuclear) cannot flexibly adjust their output to match fluctuating power demands, there is an increasing need for bulk electricity storage due to the calls to mitigate global warming. This entry introduces the PHES technology, the pros and cons, its history, and the prospect.

PHES is the only widely adopted utility-scale electricity storage technology. As of 2012, there are hundreds of PHES stations operating with total capacity of 127 GW worldwide [1]. Japan currently has the largest PHES capacity in the world.

A PHES facility is typically equipped with pumps/generators connecting an upper and a lower reservoir (Figure 1). The pumps utilize relatively cheap electricity from the power grid during off-peak hours to move water from the lower reservoir to the upper one to stored energy. During periods of high electricity demand (peak-hours), water is released from the upper reservoir to generate power at higher price.

[1] *Cenk Kilic, Anadolu University Department of Electrical Electronics Engineering, Eskisehir, Turkey.*

[2] *Mehmet KURBAN, Bilecik S.E. University, Department of Electrical Electronics Engineering, 11210, Bilecik, Turkey.*

[3] *Emrah DOKUR Corresponding author: Bilecik S.E. University, Department of Electrical Electronics Engineering, 11210, Bilecik, Turkey. emrah.dokur@bilecik.edu.tr*

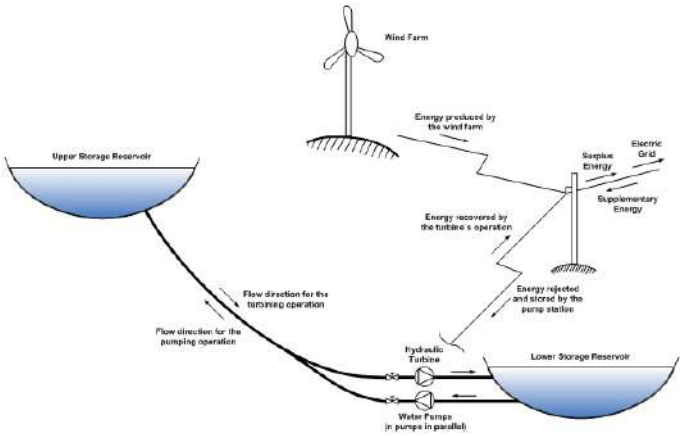

Figure 1: Hybrid wind-hydro power plant

Pure or off-stream PHES, which rely entirely on water that were previously pumped into an upper reservoir as the source of energy from wind turbine;

Combined or pump-back PHES, which use both pumped water and natural stream flow water to generate power . Off-stream PHES is sometimes also referred to as closed-loop systems. However, some may define closed-loop more strictly as entirely isolated from natural ecosystem.

The efficiency of PHES varies quite significantly due to the long history of the technology and the long life of a facility. The round-trip efficiency (electricity generated divided by the electricity used to pump water) of facilities with older designs may be lower than 60%, while a state-of-the-art PHES system may achieve over 80% efficiency.

One of the main motivations for the perusal of wind generated energy is the detrimental effects of the emissions released by fossil fuels to the environment. Climate change is generally accepted as the greatest environmental threat facing us today. As consumption, industry, and development continues to rapidly one of the main motivations for the perusal of wind generated energy is the detrimental effects of the emissions released by fossil fuels to the environment. Climate change is generally accepted as the greatest environmental threat facing us today. As consumption, industry, and development continues to rapidly increase around the globe, clean energies must begin to supplement fossil fuels or a world that may be wealthier and more productive will also be faced with more cities clouded by smog, violent weather patterns, and the inability to sustain temperature levels.

As mentioned earlier, wind energy is not without perceived environmental and aesthetic problems. Although wind energy is not a pollutant of the air, water, or soil, the turbine is often very loud, effectively making it a noise pollutant. Many arguments against wind energy also cite the disruption of farm land, grazing grounds, avian migration patterns, and open wilderness.

Similarly, although many people find the wind turbines to be elegant and sophisticated just as many people find them detrimental to the aesthetic capital of the landscape. Wind farm site analysis must take into account societal objections which are often accompanied by petitions and protests.

Wind is also hindered by limited grid infrastructure, often the regions with the most viable wind generation sites are surrounded by areas of low population and therefore low demand. Similarly, many regions have terrain that would be expensive or dangerous on which to construct a wind farm site.

This is another hindrance to the affordability and feasibility of wind on a national generating level. Hundreds if not thousands of miles of new infrastructure construction is necessary in order to transport the generated energy to areas of high demand. The expense, time, and geographic magnitude of such a feat are considerable, and a solution has yet to be reached.

From a fundamental perspective, the main disadvantage of wind energy is the intermittent nature of wind. Wind is extremely unreliable, equally likely to blow as to not blow during peak hours. Although daily and seasonal wind patterns exist, wind is still highly unstable when it comes to timing and strength. Wind storage is a way to manage this variability, allowing times of high wind speed and therefore high power generation to displace instances of low wind speed and power generation.

2. WIND ENERGY

Wind is the flow of gases on a large scale. On the surface of the Earth, wind consists of the bulk movement of air. In outer space, solar wind is the movement of gases or charged particles from the sun through space, while planetary wind is the outgassing of light chemical elements from a planet's atmosphere into space[5] . Winds are commonly classified by their spatial scale, their speed, the types of forces that cause them, the regions in which they occur, and their effect. The strongest observed winds on a planet in our solar system occur on Neptune and Saturn. Winds have various aspects, an important one being its velocity; another the density of the gas involved; another is the energy content or wind energy of a wind.

Wind turbines utilize the wind energy close to the ground. The wind conditions in this area, known as boundary layer, are influenced by the energy transferred from the undisturbed high energy stream of geostrophic wind to the layers below as well as by regional conditions.

The power of wind ; the power of an air mass that flows at speed V through an area A can be calculated this method:

$$P=\frac{1}{2}\rho AV^3(W) \quad (1)$$

The power in the wind is total available energy per unit of time. The power in the wind converted into the mechanical and rotational energy of the wind turbine rotor, which results in a reduced speed n the air mass. The power in the wind cannot be extracted completely by wind turbine, as the air mass would be stopped completely in the intercepting rotor area. Those are so many losses and the power has been lost. And we can assume the extracted power 59 percentage according to Betz. He was explain that in 1926[1] .

At wind speeds higher than the rated wind speed, the maximum power production will be limited , or , in other words, some parts of the available energy in the wind will be ‘spilled’. The power output regulation can be achieved with pitch-control or with stall control. Hence, a wind turbine produces maximum power within a certain wind interval that has its upper limit at the cut-out wind speed. The cut-out wind speed is the wind speed where the wind turbine stops production and turns out of the main wind direction. Typically , the cut-out wind speed is in the range of 20 to 25 m s^{-1} [2] .

A wind turbine is a rotary engine that extracts energy from the flow of wind. The simplest turbines have one moving part, a rotor assembly, which is a shaft with blades attached. Wind energy acts on the blades, or the blades react to wind, so that they rotate and impart energy to the rotor.

Figure 2: Wind Turbine Parts

2.2. Wind Turbine Components

1- Service Crane
2- Generator
3- Cooling System
4- Top Control Unit
5- Gearbox
6- Main Shaft
7- Rotor Lock System
8- Blade
9- Blade Hub
10- Nose cone
11- Blade Bearing
12- Bed Frame
13- Hydraulic Unit
14- Gear R. Arm
15- Yaw Ring
16- Brake
17- Tower
18- Yaw gears
19- Transmission, high speed shaft

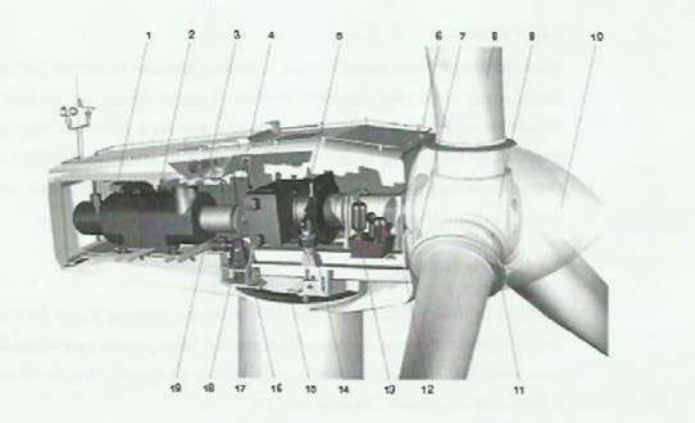

Figure 3. Wind Turbine Components

3. PUMPED HYDROELECTRIC ENERGY STORAGE

Pumped Hydroelectric Energy Storage system is one of the methods for hydroelectric power generation that stores energy in the form of potential energy of water in an upper reservoir, pumped from a second reservoir at a lower elevation. During periods of high electricity demand, the stored water is released through turbines in the same manner as a conventional hydro station. Excess energy, usually at lower cost during the night and on weekends, is used to recharge the reservoir by pumping the water back to the upper reservoir. Reversible pump/turbine and motor/generator assemblies act as both a pump and a turbine.

The first PHES on Turkey will established on Gokcekaya/ESKISEHIR [5]. PHES is a developed technologies and on Turkey we do not have enough experience for using this system. But in front year we will use this system with people that have experience about that topic.

Turkey has a great potential for this system but nowadays we can not use our potential for high price of that establishing PHES. In addition this system is great system for using peak hours.

The system will use everywhere on turkey because of our energy demand is getting greater so the system will be well known on Turkey.

The gross electricity consumption in Turkey in 2012 was 242,4 billion kWh, while this figure rose by 1,3% in 2013, reaching 245,5 billion kWh. At the same time our electricity output fell by 0,1% when compared to the previous year (239,5 billion kWh) to 239,3 billion kWh.

According to the highly probable scenario of an increase of 6,9% to 392 TWh in the base scenario, electricity consumption in the year 2020 is expected to rise by 5,5% to 357,4 TWh. In 2013, power plants containing a total of 6.985 MW additional capacity were added to the system, and our capacity has risen to around 64.044 MW.43,8% of our electricity output in 2013 came from natural gas, 24,5% from coal, 24,8% from hydraulic energy, %2 from liquid fuels, and 4% from renewable sources. As of the end of 2013, EUAS (electricity generating company) had a share of 37,1%, the generation companies 42,8%, the build and operate companies 9,5%, the auto-producers 5,4%, the build-operate-transfer plants 3,6%, and the plants whose operation rights have been transferred 1,5% of the installed capacity within Turkey. In line with the aim of liberalizing the electricity market, it has been set forth that new generation investments be carried out by the private sector, in accordance with the Legislation numbered 4628 and the new Electricity Market Legislation numbered 6446. Almost 29.474 MW of the 32.198 MW which has become operational in the last two years comes from the plants built by the private sector. In 2013, power plants containing a total of 6.985 MW additional capacity were added to the system, and of this 6.821 MW comes from the plants built by the private sector.

4. ANALYSIS OF PHES FOR BORCKA, ARTVIN

The proposed project are selected in Borcka, Artvin (Figure 4-5). Part of hybrit PHES system are given below.:

1-Water Pump

2-Upper Reservoir

3-Lower Reservoir

4-Wind Farm

5-Generator

6-Penstock

The upper reservoir of PHES is proposed at the top of Borcka. The mountain has a crest of 270 m with a suitable storage contour at 250 m. The surface has a length of 600 m and a width of 350 m. A reservoir with a dimension of length 250 m, width 150 m and depth 15 m is proposed to be constructed. This would require excavating the land surface to get a depth of 15 m. The upper reservoir will have a gross storage capacity of 0.57 million cubic meter of water. In order to prevent the loss of water from the reservoir through seepage, a lining would be required, which is an additional cost.

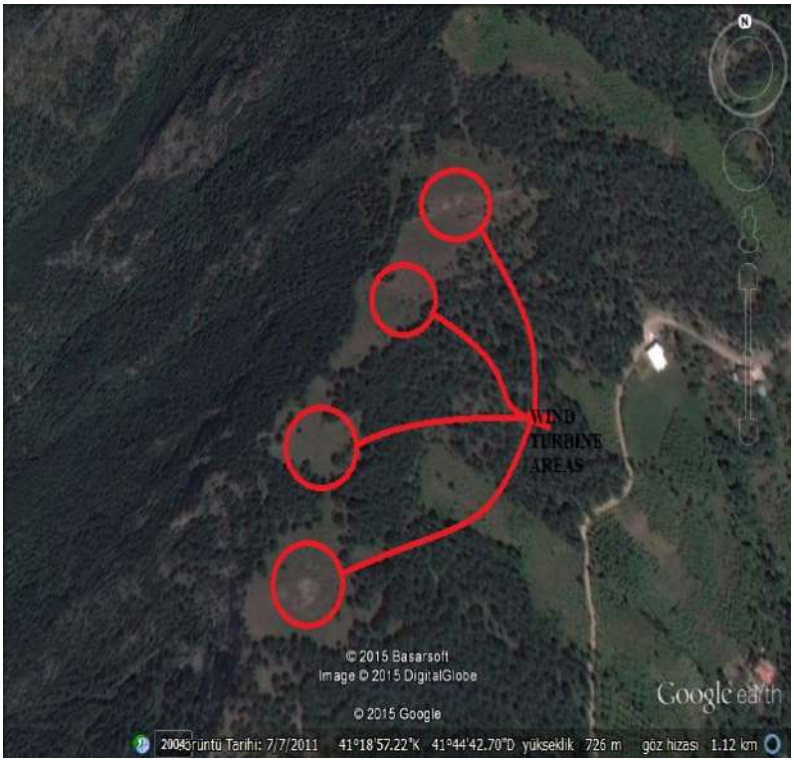

Figure 4. Location of wind farm for proposed system in Borcka

SNT 80-250 water pump is choosen for this hybrit system. Using 3 pump on our system that need 55 kW and we aim to meet this energy from the wind turbine. This proposed part of the system cost is $600,000 approximately.

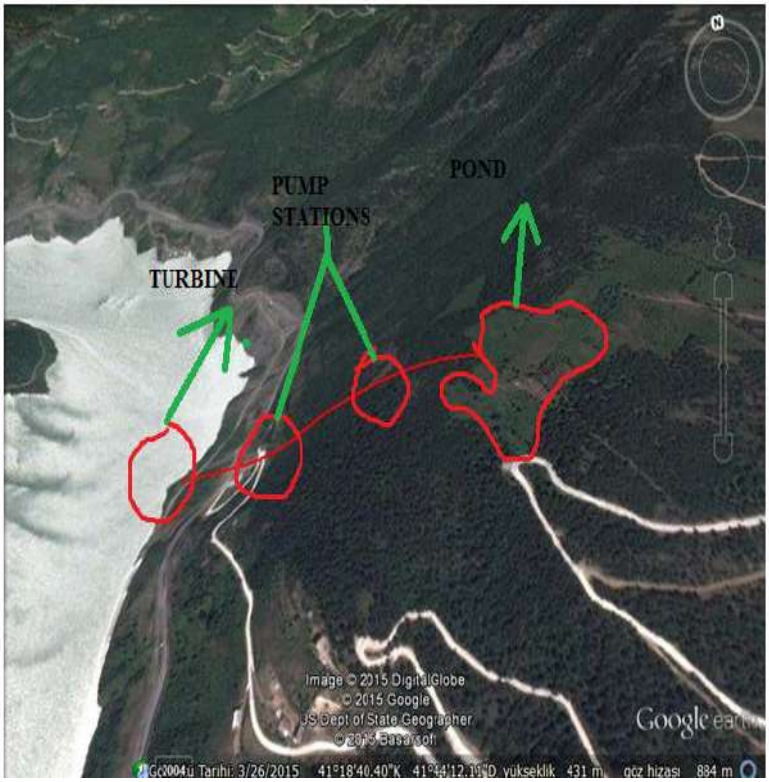

Figure 5. Location of PHES in Borcka

Francis turbine is proposed on this model because of that reasons:

A Francis turbine has a runner with fixed buckets (vanes), usually nine or more. Water is introduced just above the runner and all around it and then falls through, causing it to spin. Besides the runner, the other major components are the scroll case, wicket gates, and draft tube.

More efficiency (%90)

The difference in operating head can be extra simply controlled in francis turbine than the others.

No head failure occurs still at low discharge of water.

Penstock the elasticity modulus of 206 GPa and allowable tensile strength is at 400 MPa. The unit cost of the penstock $ 7.52 / kg, turbine closing time of 5 s and starts penstock fore bay lower end elevation is 581.25 m.

Manning roughness coefficient 0.0003 slope of the base transmission channels It was taken as 0.016. 3 and 8 of the section width of 0.5 m, a foot of water intake outlet two pieces will be used by the hood. Settling than 0.2 mm in diameter pool It is greater than the desired deposition material . Grilled entrance of the water intake structure thickness of 1.5 cm, the range is taken as 10 cm. Dimensions 4.5 m (width) and 2 m (height) with one gravel walkway will be used. The spillway crest length of 60 m. Base level in the riprap section 587.00 m, in the water intake structure input 589.40 m. The gross load of the power plant 78 m. Two Francis turbine power plant efficiency of 94% generator efficiency of 97% and 98% respectively transformer efficiency. The base of the unit and secondary energy price of $ 0.08 / kWh, while installed power unit price of $ 1,200,000 / MW. In this study, plant life of 30 years worth of interest on 10%, capital recovery factor as 12.11 it was calculated.

4. CONCLUSION

The world is witnessing a change-over from its present centralized generation to a future with greater share of distributed generation. Hybrid energy systems are inter-connected with wind power, photovoltaic power, fuel cell and micro-turbine generator to generate power to local load and connecting to grid/micro-grids that decrease the dependence on fossil fuels. The hybrid system is a better option for construction of modern

electrical grids that includes economic, environmental and social benefits. In this paper wind-PHES hybrid system is proposed for Borcka, Artvin. According to analysis results, the total cost is $2,700,000 approximately and the amortization period is calculated nearly 6 years.

REFERENCES

[1]. Ingram E. Pumped storage development activity snapshots. *Hydro Review, December* 2009, 12-25.
[2]. Wind power in power systems / edited by Thomas *Ackermann.Chichester, West Sussex, England* : J. Wiley,c2005
[3]. Connolly, David, et al. "*Practical operation strategies for pumped hydroelectric energy storage (PHES) utilising electricity price arbitrage*." Energy Policy 39.7 (2011): 4189-4196.
[4]. Elizabeth A. Ingram, "*Worldwide Pumped Storage Activity*", Hydro Review Worldwide, Pages 12-20, September 2010.
[5]. URL**,** http://www.enerji.gov.tr/enUS/Pages/Electricity, Alinti tarihi 20.04.2018

ICENS 4TH INTERNATIONAL CONFERENCE ON ENGINEERING AND NATURAL SCIENCE
2-6 May 2018 KIEV UKRAINE

Power System Analysis and Application for The Aircraft At The Different Altitudes

Hasan Karatas[1], Mehmet Kurban[2], Emrah Dokur[3]

Abstract

The electrical energy and power are important for the any modern aircraft. Because electrical energy is used by the cabin internal lightings, cabin outer lightings, displays, fuel pumps, hydraulic pumps, electrical heaters, valves and communication systems in the any modern aircraft. In this paper is presented these power generation components. Also, BPCU (Bus Power Control Unit) and BPCU (Ground Power Control Unit) are explained in detail; for purpose of protection from short circuit and overload conditions. The four engines Boeing 747 aircraft is given example for the electrical power distribution at the different aircrafts. Also the FMS (Flight Management System) is explained in detail in this paper. Especially navigation mission and flight performance mission of the FMS are explained in this study; for the purpose of emphasize that FMS adjust optimal flight profile and optimal cost in the any modern aircraft. The application; the Boeing 737-800 aircraft is handled for the purpose of determination maximum flight speeds, minimum drag speeds and consuming power values at the different altitudes values.

Keywords: *BPCU, BPCU- FMS*

1. INTRODUCTION

Ever since the first aircraft to use any kind of electric equipment was launched, the electrical loads on airplanes and other flying devices have increased. Today, modern jet airliners are equipped with scores of different electrical systems, each requiring a substan¬tial amount of electrical energy. Generators were the first means of supplying elec¬trical power for aircraft. Currently, generators or gen¬erator derivatives called alternators are found in a wide variety of sizes and output capacities. A typical alter-nator used on a large commercial aircraft can produce the equivalent of 6000 W of electrical power. On multi- engine aircraft, one generator is driven by each engine to allow for redundancy in the event of a generator failure [1]. An electrical generator can be defined as a machine which changes mechanical energy into electrical ener¬gy. On aircraft the mechanical energy is usually pro-vided by the aircraft's engines. Light aircraft use 14V or 28V DC generators. Large aircraft typically employ generators which produce an alternating current of 208V or 117 V at 400 Hz. Compared to a 28-V DC system, a higher-voltage AC system will develop several times as much power for the same weight; hence, it is a great advantage to use AC systems where heavy electrical loads are imposed.

There are two major types of alternators currently used on aircraft, the DC alternator and the AC alternator. DC alternators are most often found on light aircraft where the electrical load is relatively small. AC alternators are found on the large commercial airlines and most military aircraft. Since these aircraft require large amounts of the electrical power, the use of AC systems creates a valuable weight savings. Through the use of transformers, the transmission of the AC electrical power can be accomplished more efficiently and therefore with lighter equipment. By transmitting electrical power at relatively high voltage and low current, the power loss is kept to a minimum. The transformers are used to step up or step down AC voltage [2]. In the large aircraft, AC power is used directly to perform the majority of power functions for the operation of the control systems and electric motors for a variety of purpose. On the light aircraft, most electrical devices operate on 14V or 28V DC power. If a small amount of AC is desirable for specific application, an AC voltage. The AC voltage is then used to power only those particular items requiring AC for proper operation [1].

[1] *Hasan KARATAS, Anadolu University Department of Electrical Electronics Engineering, Eskisehir, Turkey*

[2] *Mehmet KURBAN, Bilecik S.E. University, Department of Electrical Electronics Engineering, 11210, Bilecik, Turkey.*

[3] *Emrah DOKUR Corresponding author: Bilecik S.E. University, Department of Electrical Electronics Engineering, 11210, Bilecik, Turkey. emrah.dokur@bilecik.edu.tr*

2. DC POWER GENERATION

There are two main sections of electrical energy system in the aircraft. First section is electric energy generation. Second section is electric energy distribution. Electric energy generation is occurred from the AC power generation and DC power generation in the aircraft. Electric energy distribution is occurred AC power distribution and DC power distribution in the aircraft. There are two type DC Power Generator in the modern aircraft electrical system. These are 24v Battery and Transformer Rectifier Units (TRU). DC generators are needed for many aircraft electric systems, for battery charging, and for various other applications. For this reason, an AC generator will not meet all power requirements unless a means of rectifying the alternating current is provided [13]. Electrical diagram in aircraft is shown in Figure 1.

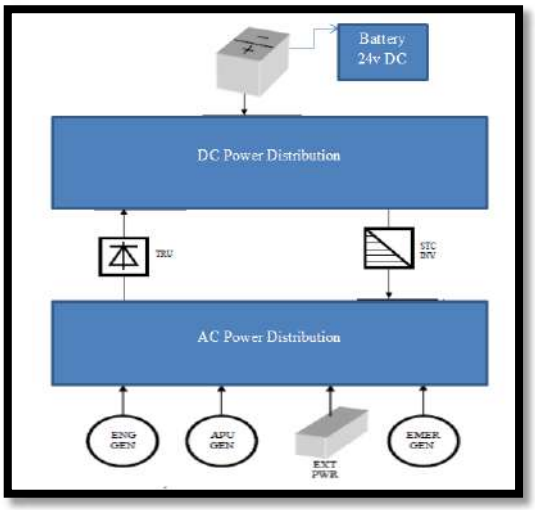

Figure 1 Electrical Diagram in Aircraft

a. Batteries

A battery is a device which converts chemical energy into electrical energy and is made up of a number of cells which, depending on battery utilization may be of the primary type or secondary type. The both types of cell operate on the same fundamental principle, i.e. the exchange of electrons due the chemical actions of an electrolyte and electrode materials [1].

A plastic lid combined with an acid proofed aluminum alloy hold down frame completely encloses the chamber. Connections are provided at each end of the chamber for coupling the pipes from the aircraft's battery compartment ventilation system [13].

The cells are assembled as two 12 volt units in mono-bloc containers made of shock-resistant polystyrene and these are, in turn housed in a polyester-bonded fiberglass outer container which also supports the main terminal box. A cover of the same material as the case is secured by four bolts on the end flanges of the case [13].

The capacity of a battery, or the total amount of energy available, depends upon the size and number of plates. More strictly it is related to the amount of material available for chemical actions. The capacity rating is measured in ampere hours and is based on the maximum current, in amps, which it will deliver for a known time period until it is discharge to a permissible minimum voltage of each cell. The time taken to discharge is called the discharge rate and the rated capacity of battery is the product of this rate and the duration of discharge in hours. Thus, a battery which discharges 7 A for 5 hours is rated at 35 ampere hours capacity [10].

b. Transformer Rectifier Unit

Transformer rectifier unit transform 115V and 3 phase AC power to 28V and 1 phase DC power, which is available when other AC power sources operate. TRU is normal DC power source in the aircraft electrical system. The DC power generated is used electronic devices in the avionics compartment. Transformer rectifier unit consist of two sections. These sections are transformer and rectifier. Transformer decrease 115 volts AC to 28 volts AC; then rectifier will convert AC to DC energy.

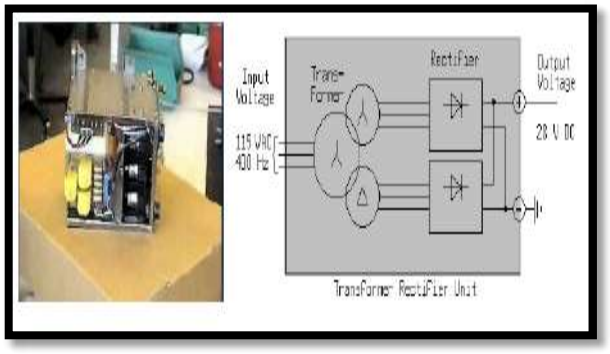

Figure 2 TR Unit Inertial Construction

3. AC POWER GENERATION

The power ratings of AC generators are generally given in kilovolt-amperes (kVA) rather than kilowatts (kW) as in the case of DC machines. The primary reason for this is due to the fact that in calculating the power, account must be taken of the difference between the true or effective power, and the apparent power. Such a difference arises from the type of circuit which the generator is to supply and the phase relationships of voltage and current, and is expressed as a ratio termed the power factor (P.F.).
If the voltage and current are in phase (as in a resistive circuit) the power factor is 100 per cent or unity, because the effective power and apparent power are equal; thus, a generator rated at 100 kVA in a circuit with a P.F. of unity will have an output 100 per cent efficient and exactly equal to 100 kW [20].
There are five AC power sources in the aircraft:
1. IDG (Integrated Drive Generator)
2. APU (Auxiliary Power Units)
3. Emergency Generator
4. Static Inverter
5. External Power Unit

a. Static Invertor

They are employed in a number of types of aircraft in some cases as a normal source of AC power, but more usually to provide only emergency AC power to certain essential systems when a failure of the normal 115-volts source has occurred. The function of an inverter used for the conversion of battery supply to single-phase 115-volts AC.

b. APU

Many of today's aircraft are designed so that if necessary, they may be independent of ground support equipment. This is achieved by the incorporation of an auxiliary power unit (A.P.U.) in the tail section which, after being started by the aircraft's battery system, provides power for engine starting, ground air conditioning and other electrical services. In some installations, the A.P.U. is also used for supplying power in flight in the event of an engine-driven generator failure and for supplementing the delivery of air to the cabin during take-off and climb [27]. Power sources location in the aircraft is shown in Figure 3.

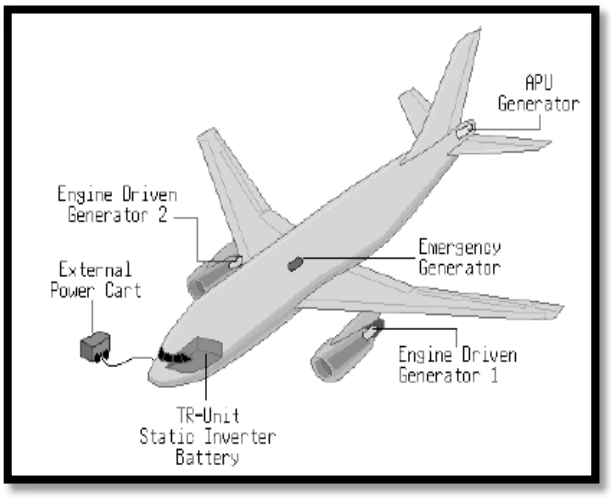

Figure 3. Power Sources Location in the Aircraft

c. External Power Unit

Electrical power is required for the starting of engines, operation of certain services during "turn-round" servicing periods at airports, e.g. lighting, and for the testing of electrical systems during routine maintenance checks. The batteries of an aircraft are, of course, a means of supplying the necessary power, and although capable of effecting engine starts their capacity does not permit widescale use on the ground and they are restricted to the supply of power under emergency conditions. It is necessary, therefore, to incorporate a separate circuit through which power from an external ground power unit may be connected to the aircraft's distribution busbar system [29].

4. LARGE AIRCRAFT ELECTRICAL SYSTEM

Large aircraft electrical systems have many similarities to those systems found on small aircraft. On large aircraft there is typically one battery and two or more AC generators (alternators) which supply power to several distribution buses (Figure 4). The AC generators are connected to the AC buses. The DC battery is connected directly to the battery or emergency bus. The AC power produced by the generators is converted to DC where needed for special applications. Essential lighting, flight control systems, and communication and navigation radios are high-priority electrical systems. Galley power, nonessential lighting, and various other comfort systems are considered low-priority electrical systems [6]. Generally, large aircraft electrical systems have four engine and we can give example that Boeing 747 aircraft. Modern large aircraft use both AC and DC electrical power. The output of a typical generator is three-phase 115-V AC; this is converted by transformer rectifier (TR) units where DC power is needed. The TR units incorporate a step-down transformer and a full-wave rectifier. Its output is 28 V DC. Most large aircraft contain two or more static inverters used for emergency situations (generator failure) [2,3].

Figure 4. Boeing 747 Aircraft with Four Engines

The static inverters supply a relatively small amount of AC power; however, their output is adequate to power all essential AC equipment. There are two basic configurations which are used to distribute electrical power, the split bus system and the parallel system [4,5].

5. FLIGHT MANAGEMENT SYSTEM

The flight management system typically consists of two units, a computer unit and a control display unit. The computer unit can be a standalone unit providing both the computing platform and various interfaces to other avionics or it can be integrated as a function on a hardware platform such as an Integrated Modular Avionics cabinet (IMA). The Control Display Unit (CDU or MCDU) provides the primary human/machine interface for data entry and information display. Since hardware and interface implementations of flight management systems can vary substantially, this discussion will focus on the functional aspects of the flight management system. The flight management system provides the primary navigation, flight planning, and optimized route determination and route guidance for the aircraft and is typically comprised of the following interrelated functions: navigation, flight planning, trajectory prediction, performance computations, and guidance [23].

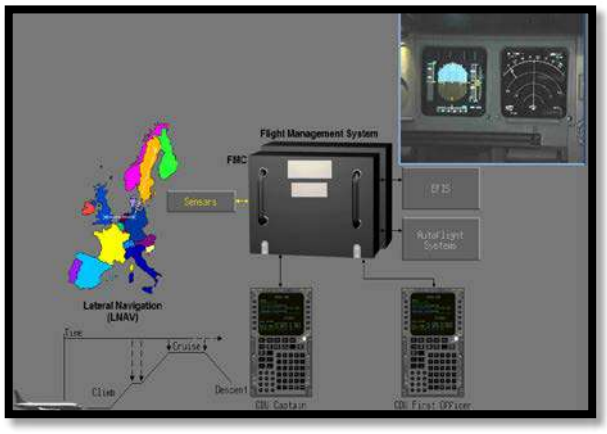

Figure 5.FMS and Subcomponent

The performance function provides the crew information to help optimize the flight or provide performance information that would otherwise have to be ascertained from the aircraft performance manual. FMSs implement a variety of these workload reduction features, only the most common functions are discussed here.

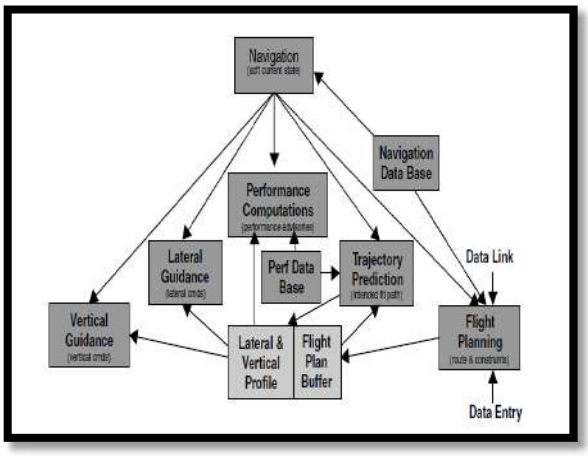

Figure 6. Flight Management Functional Block Diagram

6. APPLICATION

As the airline industry evolves, those who manage it require a good knowledge of its many facets. One important aspect is aircraft performance, which plays a vital role in the economic fortunes of airlines and aircraft designers and manufacturers.

a. Aerodynamics Terms and Calculations

F_A is resultant of the aerodynamic effecting forces on the aircraft. Equation (1) is used for determination commonly.

$$F_A = \frac{C.\rho.s.V^2}{2} \quad (1)$$

'V' is aircraft speed, 'S' is aircraft surface area, 'C' is dimensionless ratio coefficient, 'ρ' is air density. Resultant aerodynamic force is occurred parallel and perpendicular two forces. Perpendicular force is called Lift force, parallel force is called Drag force. Also C_L is dimensionless lift coefficient, C_D is dimensionless drag coefficient [36].

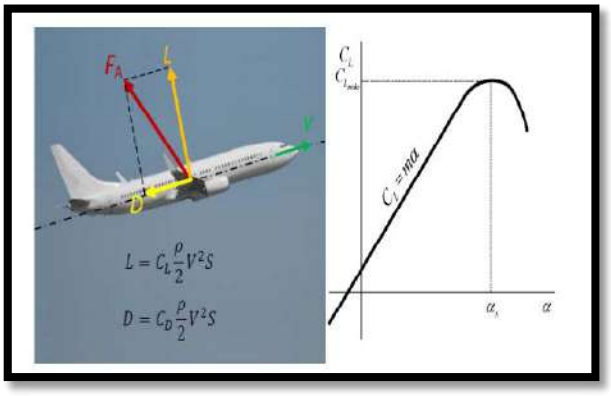

Figure 7. Aerodynamics Forces and Coefficients

$$C_D = C_{D_0} + KC_L^2 \quad (2)$$

C_{D0} is parasite drag coefficient and 'K' is induced drag coefficient.

$$K = \frac{1}{\pi . A_R . e} \tag{3}$$

A_R is aspect ratio, e is wing efficiency factor [37].

Aerodynamic fines are ratio lift to drag value on the aircraft. $E = \frac{L}{D} = \frac{C_L}{C_D}$ is showed for determination. The result of calculation maximum fines is determined

$$V_{md} = \left(\sqrt[4]{\frac{K}{C_{D_0}}} \right) . \sqrt[2]{\frac{2W}{\rho . S}} \tag{4}$$

'W' is showed that weight for determination minimum drag. So if aircraft is heavy; it has more minimum drag speed. Also we determine that, mass of aircraft does not affect the its parasite drag value. The mass of aircraft affects induced drag value [37].

$$Z = \frac{\mu^4 + 1}{2\mu^2} = \frac{F . E_{max}}{W} = \frac{F}{D_{min}}; \quad \mu = \sqrt{Z + \sqrt{Z^2 - 1}} \tag{5}$$

We accept that $Z \geq 1$ the dimensionless thrust factor for the cruise flight. Equation (5) can be write for the maximum cruise flight speed.

$$V_{C_{max}} = V_{md} . \sqrt{Z_{max} + \sqrt{z_{max}^2 - 1}} \tag{6}$$

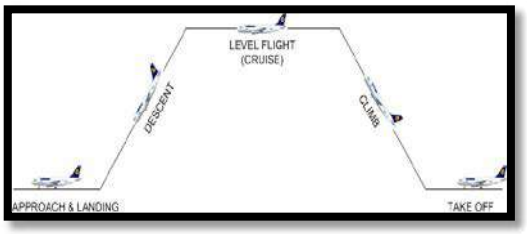

Figure 8 Flight Profiles

b. Speed Calculation of the Cruise Flight of the Boeing 737-800 Aircraft

Boeing 737-800 aircraft is used for that application, which is entered service by Boeing aerospace company in the 1998. The reason of the selection Boeing737-800 aircraft for that application is the using worldwide commonly. Also Boeing 737-800 aircraft has characteristic properties is illustrated in Table 1.

Table 11 Boeing 737-800 Aircraft Characteristic Properties

Wing Surface Area	125 m^2
Aerodynamics Drag Coefficient	C_D=0,024+0,041C_L^2
Maximum Lift Coefficient	C_{Lmax} = 1,424
Minimum Mass	41.000 kg
Maximum Take Off Mass	79.000 kg
Engine Number	2
Max. Thrust Force of the Single Engine	F=75400σ
Maximum Operation Mach Number	M_{MO} =0,82
Engine Type	CFM56-7B24

Initially maximum fines value and minimum drag value is calculated by using previously aerodynamics formulas. Then, minimum drag speed and maximum horizontal flight speed are will be calculated by using

previously aerodynamics formulas in that application on the different altitude values. It should be noted that; relative air speed (σ), air speed (ρ) and sound speed (α) are depended to the altitude values. So, if altitude value is changed; air speed, sound speed and relative air speed will be changed [36] [38].

The maximum fines are of the Boeing 737-800: $E_{max} = \frac{1}{2.\sqrt{KC_{D_0}}} = \frac{1}{2.\sqrt[2]{0,041.0,024}} = 15,94$

The minimum drag is at the maximum takeoff mass: $D_{min} = \frac{W}{E_{max}} = \frac{9,81*79000}{19,94} = 48,620\text{N}$

- Firstly, we assume that the Boeing 737-800 aircraft is flying sea level and it has ρ=1,255 kg/m^3

$$V_{md} = \left(\sqrt[4]{\frac{K}{C_{D_0}}}\right).\sqrt[2]{\frac{2W}{\rho.S}} = \sqrt[4]{\frac{0,041}{0,024}}.\sqrt[2]{\frac{2*9,81*79000}{1,225*125}} = 115\frac{m}{s} = 223,6\ kts$$

- At the 5.000 ft; σ = 0,8617, ρ = 1,0555 kg/m3, and α = 650 kts. We must determine minimum drag speed and maximum flight speed.

$$V_{md} = \sqrt[4]{\frac{0,041}{0,024}}.\sqrt[2]{\frac{2*9,81*79000}{1,0555*125}} = 124\frac{m}{s} = 241\ kts$$

The dimensionless thrust factor: $Z = \frac{F.E_{max}}{W} = \frac{F}{D_{min}} = \frac{2*75400*0,8617*15,94}{9,81*79000} = 2,673$

The dimensionless speed: $\mu = \sqrt{Z+\sqrt{Z^2-1}} = \sqrt[2]{2,673+\sqrt[2]{2,673^2-1}} = 2,27$

The maximum horizontal flight speed: V= μ .V md = 2,27*241=547 kts

The mach number: $M = \frac{V}{\alpha} = \frac{574}{650} = 0,84 > M_{MO} = 0,82$

In this case maximum horizontal flight speed is: Vmax = MMO . α = 0,82*650=533 kts. These calculations are repeated 10.000 ft, 20.000 ft, 30.000 ft and 34.000 ft altitudes values.

We must determine maximum electrical power for these altitudes values; thus we can analysis performance under the different altitude values. So we can write equation 7 for electrical power calculation two aircraft engine generator.

$$S = P + jQ = 3 * V_{P-N} * I^* = \sqrt[2]{3} * V_{P-P} * I^* \quad (7)$$

$$P = 3 * V_{p-n} * I * \cos\theta = \sqrt[2]{3} * V_{p-p} * I * \cos\theta \quad (8)$$

'S' is complex power, 'P' is active or effective power and 'Q' is reactive power. Also V p-n is voltage value between phase and neutral, V p-p is voltage value between phase and phase. We know that aircraft engine generator can produce 115 V between phase and neutral, ergo that value is equal 200 V between phase and phase. We assume; active power is 100 kW and complex power is 180 kVA for Boeing 737-800 aircraft.

So power factor is $= \frac{\text{Effective Power}}{\text{Apparent Power}} = \frac{100\text{kW}}{180\text{kVA}} = 0,55 = \cos\theta, \quad \theta = 56,25°$

$$\text{Active or effective power} = 100\text{kW} = 3 * 115 * I * \cos(56,25); \quad I = 521\ A$$

That current value is the current drawn from the aircraft electrical system. And according to flight profile by selection pilot or co-pilot, we know that which 521A value will change. hat current value is the current drawn from the aircraft electrical system.

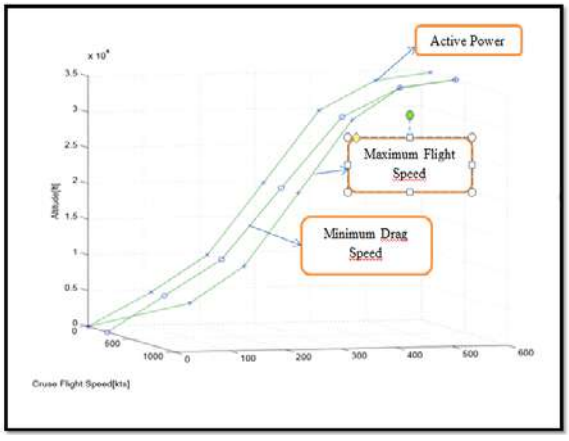

Figure 9. The 3-D results of power and speeds using MATLAB

7. CONCLUSIONS

In this paper, electrical power generation and electrical power distribution of any aircraft are examined in detail. Components of electrical power generation and distribution of the any aircraft are examined and explained in detail. These components are the engine generators, APU, emergency generator, TRUs, static inverters, external power unit and battery. Engine generators, APU, static inverters, external power unit and emergency generator are used the AC power generator in the any modern aircraft. One engine generator can produce 115 volts AC voltage between phase and neutral, which can produce 200 volts AC voltage between phase and phase in the modern aircraft. These values purport to us; one engine generator can produce 50 kW effective powers and 90 kVA apparent or complex powers in the modern aircraft approximately. The lightings, electrical heaters, electronic devices, mechanical and hydraulic devices transformer the 115 volts AC voltage to the 28 volt DC voltage value by using transformer rectifier units; for the purpose of using the DC electrical power in the any aircraft. AC buses and DC buses are used for electrical DC and AC powers distribution in the any aircraft.
The applications made in the article, for the purpose of explained consuming power at the different altitudes, different maximum flight speeds and minimum drag speeds in the Boeing 737-800 aircraft. Conclusion we can determine current drawn is 521A between lightings, electrical heaters, electronic devices, which value depend the assumption effective power. And according to flight profile by selection pilot or co-pilot, we know that which 521A value will change.
The ringed lines are illustrated the minimum drag speed, the crossed lines are illustrated maximum flight speed, and other lines are illustrated active power in the aircraft electrical system; which are illustrated the three dimensional MATLAB plot-. After the certain altitude, that can be determined; minimum drag speed will be equal the maximum flight speed theoretically. Which was determined; if altitude value change, minimum drag speed and maximum flight speed will change. And ergo, current drawn will change in the Boeing 737-800 aircraft, so active power will change.

REFERENCES

[1] Pallett, EHJ. (1987).Aircraft Electrical Systems. Third Edition. Longman Scientific&Technical
[2] Helfrick, Albert. (1984). Modern Aviation Electronics. Prentice-Hall, INC., Englewood Cliffs, New Jersey 07632
[3] Pallet, EHJ. (1981). Aircraft Instruments. Second Edition. Longman Scientific&Technical
[4] Eismin, Thomas. K., Bent, Ralph D., and McKinley, James. L.. (1990). Aircraft Electricity and Electronics. Fourth Edition. GREGG DIVISION GLENCOE Macmillan/McGraw-Hill
[5] Fozard, John W. (1978). The Jet V/STOL Harrier: an evolutionary revolution in tactical air power. Surrey, U.K: British Aerospace Aircraft Group, Kingston-Brough Division 1978.
[6] Crane, Dale. (1977). Aircraft Ignition and Electrical Power Systems. Riverton, Wyo,:Aviation Maintenance, c1977.
[7] Farokhi, Saeed. (2009). Aircraft Propulsion. Hoboken, N.J.: J, Willey, 2009.
[8] Jaw, Link C. (2009). Aircraft Engine Controls. Reston, VA: American Institute of Aeronautics and Astronautics, 2009.
[9] Barnard, R.H. (2010) Aircraft Flight: A description of the physical principles of aircraft flight. Fourth Edition. Harlow: Pearson Prentice Hall, 2010.
[10] Tooley, Michael H. (2009). Aircraft Electrical and Electronic Systems: principles, operation and maintenance. First Edition. Amsterdam: Butterworth-Heinemann, 2009.
[11] Swatton, P.J. (2008) Aircraft Performance Theory and Practice For Pilots. Second Edition. Chichester: J.Wiley, 2008.
[12] Karakoc, T.Hikmet. (2008). GTMS: gas turbine engine systems. Eskisehir: Anadolu Universitesi Sivil Havacilik Yuksekokul, 2008.
[13] R.E. Quigley Jr., More electric aircraft, in: Proc. IEEE Applied Power Electronics Conference, San Diego, 1993, pp. 906–911.
[14] L. Faleiro, Beyond the more electric aircraft, AIAA (2005).
[15] G. Gong, M. Heldwein, U. Drofenik, J. Minibock, K. Mino, J. Kolar, Comparative evaluation of three-phase high-power-factor AC–DC converter concepts for application in future more electric aircraft, IEEE Trans. Ind. Electron. 52 (June (3)) (2005) 727–737.
[16] T.L. Skvarenina, S. Pekarek, O. Wasynczuk, P.C. Krause, R.J. Thibodeaux, J. Weimer, Simulation of a switched reluctance, more electric aircraft power system using a graphical user interface, in: Proceedings of the 32nd Intersociety Energy Conversion Engineering Conference (IECEC'97), Vol. 1, July 27–August 1, 1997, pp. 580–584.
[17] T.L. Skvarenina, O. Wasynczuk, P.C. Krause, W.Z. Chen, R.J. Thibodeaux, J. Weimer, Simulation and analysis of a switched reluctance generator/more electric aircraft power system, in: Proceedings of the 31st Intersociety Energy Conversion Engineering Conference (IECEC'96), Vol. 1, 11–16 August, 1996, pp.143–147.
[18] M.L. Maldonado, N.M. Shah, K.J. Cleek, P.S.Walia, G. Korba, Powermanagement and distribution system for a more electric aircraft (MADMEL)—program status, in: Proceedings of the 31st Intersociety Energy Conversion Engineering Conference, 1996, pp. 148–153.
[19] J.A. Weimer, Power management and distribution for the more electric aircraft, in: Proceedings of the 30th Intersociety Energy Conversion Engineering Conference, 1995, pp. 273–277.
[20] Lee JJ. Can accelerate the improvement of energy efficiency in aircraft systems? Energy Conversion Management 2010;51:189e96.

[21] Brand J, Sampath S, Shum F, Bayt RL, Cohen J. Potential use of hydrogen in air propulsion. In: AIAA/ICAS international air & space symposium and exposition: the next 100 years, AIAA-2003-2879, Dayton, Ohio, USA, 14e17 July 2003 2003.
[22] Adewusi, S.A., Zubair, M., 2004. Second law based thermodynamic analysis of ammonia-water absorption system. Energy Conservation and Management 45, 2355e2369.
[23] Ahmadi, P., 2006. Exergy Analysis of Combined Cycle Power Plants: A Case Study. B.Sc. Thesis, Energy Eng. Department. Power & Water University of Technology, Tehran, Iran.
[24] Lewis III, J.H., 1976. Propulsive efficiency from an energy utilization standpoint. Journal of Aircraft 13 (4), 299e302.
[25] Perkins, C. and Hage, R., 'Airplane Performance, Stability, and Control,' Wiley, New York, 1949
[26] Wallner, L., 'Generalization of the Torbojet and Turbine-Propeller Engine Performance in Wildmilling Condition, ' NACA RM-2267, 1951
[27] Diehl, W., Engineering Aerodynamics, Ronald, New York, 1928.
[28] Raymer, D., 'Supercruise for a STOL Dogfighter, ' Aerospace America, Aug. 1985, pp. 72-75.
[29] Stinton, D., The Design of the Aeroplane, Granada, London, England, UK, 1983.
[30] Fraas, A., Aircraft Power Plants, McGraw-Hill, New York, 1943.
[31] Lan, C. and Roskan, J., Airplane Aerodynamics and Performance, Roskam Aviation and Engineering Corp., Ottawa, KS, 1980.
[32] Raymer, Daniel P. Aircraft Design: A Conceptual Approach AIAA Education Series TL671. 2.R29 1989
[33] R. Martinez-Val ve E. Perez, <<Optimum Cruise Lift Coefficient Initial Design of Jet Aircraft,>> Journal of Aircraft, Cilt 29, no.4,p. 712-714, 1991
[34] A.Cavcar, << Constant Altitude-Constant Mach Number Cruise Range of Transport Aircraft with Compressibility Effects,>> Journal of Aircraft, Cilt43, no.1, p. 125-131, 2006
[35] R.S. Shevell, Fundamentals of Flight, Prentice-Hall, 1989
[36] E. Torenbeek, Synhesis of Subsonic Airplane Design, Delft Univ. Press, 1976

ICENS 4TH INTERNATIONAL CONFERENCE ON ENGINEERING AND NATURAL SCIENCE
2-6 May 2018 KIEV UKRAINE

Measurement of Orange Size and Volume Using Microsoft Kinect Camera

Ilker Unal,[1], Onder Kabas[1], Salih Sozer[1], K.Cagatay Selvi[2], Huseyin Sauk[2]*

Abstract

In recent years, automatic vision based technology for the measurement of object sizes and volumes has become more potent and more important to many areas including agricultural fields, food industry, transportation, production, and forestry. This article presents an approach to orange size and volume measurement using Microsoft Kinect Camera. Although Microsoft Kinect Camera was developed to gather distance images for gaming environments, it can be used for real-time environmental scanning, segmentation, classifications and scene understanding. Kinect contains not only an RGB camera, but also a depth sensor based on infrared triangulation measurements to measure distance between sensor and objects. The Kinect sensor runs a series of algorithms on the captured data to give you more than an image, which tells you how far each pixel in that frame is. The depth pixel contains the distance between the Kinect device and the objects in front of the device, in millimeters. The data are represented based on the X and Y coordinates in the depth sensor view. Our approach is based on measuring distance between sensor and all image pixels from a captured depth image. In this study, the image capturing chamber which was a wooden box was designed to capture orange depth image. A Kinect camera was mounted on the top center of the image capturing chamber. And also, image processing program was designed to collect x and y coordinates and the depth value (z) of each pixel on captured orange depth image. Finally, size and volume of the orange were calculated from the depth values. This study offers suggestions evaluating the Kinect depth images to determine objects posture as digitally.

Keywords: Kinect camera, volume measurement, depth image

1. INTRODUCTION

In order to improve fruits' quality and production efficiency, reduce labor intensity, it is necessary to research non destructive automatic detection technology[1]. The size of fruits and vegetables is an essential physiological property that can be described by different parameters such as volume,weight, length, and diameter [2]. Size determination is often mandatory to the sorting of many fruits and vegetables for various reasons, such as requirements of processing machine, regulatory rules of sorting standards, and consumer preferences [3]. Size is also an important quantitative factor to evaluate for phenotyping of fruits and vegetables. Many machine vision methods have been proposed to nondestructively measure the size of various fruits and vegetables, including apple, citrus, pear, tomato,etc.. [2].

Nowadays, cameras that capture RGB images with depth information are available. Such sensing systems allow to propose new attractive solutions for robot navigation problems like 3D mapping and localization, object recognition, 3D modeling, visual odometry among others perception tasks. Recently, the release of the Kinect camera, a depth sensor based on a structured infrared-light system, has opened new possibilities for acquiring depth information [4]. The recent availability of low-cost Kinect sensor provides a valid alternative to other available sensors, namely laser-range finders and stereo-vision systems. The Kinect depth sensor brings a fast and relatively high resolution solution for depth sensing, while being considerably cheaper than the aforementioned alternatives. Nevertheless, it has some limitations, specifically, this device was designed to work indoors due to light conditions. Moreover, its range is up to 4m and can not acquire valid data at distances smaller than 0.8m [5]. Kinect camera detects comprehensive three-dimensional point cloud data (a set of vertices in a three-dimensional coordinate system). The device detects thousands of point cloud data in color at a frame rate of approximately 30 fps. RGB-depth (RGB-D) sensor provides a new prospect of active 3-D

[1]* *Corresponding author: Akdeniz University, Technical Science Vocational School, 07070, Antalya, Turkey. ilkerunal@akdeniz.edu.tr*

[2] *Ondokuz Mayis University, Faculty of Agriculture, Department of Agricultural Machinery and Technologies Engineering, 55139, Samsun, Turkey.*

machine vision techniques. As a low-cost (approximately 150 U.S. dollars) alternative for conventional laser scanners (5–10 thousands U.S. dollars or higher), the RGB-D sensor has been quickly adapted in various areas such as robotics, indoor mapping, 3-D modeling, and forensics in the past several years [6, 7]. The possibility of using the consumer-grade RGB-D sensor for the phenotyping of plant trees has been demonstrated recently by [8] and [9]. The feasibility of using a RGB-D sensor for the nondestructive measurement of the size of fruits and vegetables, however, has not been investigated.

This work aimed to measure the size of orange using nondestructive imaging methods based on the RGB-D sensor. Specific objectives of this work were to: (1) integrate a machine vision system to collect RGB-D images of orange, (2) measure the maximum equatorial diameter of orange from their color and depth images, (3) estimate the volume of orange using depth images.

2. MATERIALS AND METHODS

a. Image capturing system

An image capturing system (Figure 1) was assembled to acquire RGB-D images of orange samples. Image capturing chamber (900,900, 900 mm) was built using wood. The system used two 76 cm long cool-white fluorescent lamps (25 W, 4200 K) mounted in the upper left and the upper right part of the chamber, respectively. The inside of the image chamber box was completely painted with white.

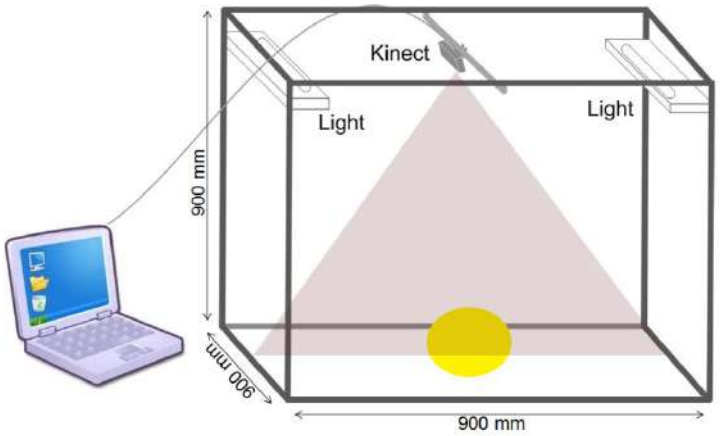

Figure 1. Schematic of the imaging system based on an Kinect camera for measuring the size of an orange

Kinect camera was mounted on the top of the image capturing chamber. The Kinect camera consists of an infrared laser emitter, an RGB (color) camera, a monochrome infrared camera, and stereo microphones [10]. The laser emitter projects the structured infrared lighting pattern for the space and the infrared camera captures the imposed pattern shined on the scene. The spatial information of the scene is calculated based on the correlation and triangulation between the captured pattern and the reference pattern stored in the sensor. In this system, the sensor was connected to a laptop via a USB cable. An image capturing and processing software was developed with C-Sharp programming language. Kinect for Windows SDK solution was used to acquire the color image (640, 480 pixels) and the depth map (640, 480 pixels), which were spatially registered to each other. The program can acquire the RGB-depth images at a speed of 30 frames per second, and save numerically 24-bit RGB image and 11-bit depth map of the scene into the array.

b. Pixel distance measurement

Figure 2 illustrates the relation between the distance of an object point k to the sensor relative to a reference plane and the measured disparity d. To express the 3D coordinates of the object points we consider a depth coordinate system with its origin at the perspective center of the infrared camera. The Z axis is orthogonal to the image plane towards the object, the X axis perpendicular to the Z axis in the direction of the baseline b

between the infrared camera center and the laser projector, and the Y axis orthogonal to X and Z making a right handed coordinate system [11].

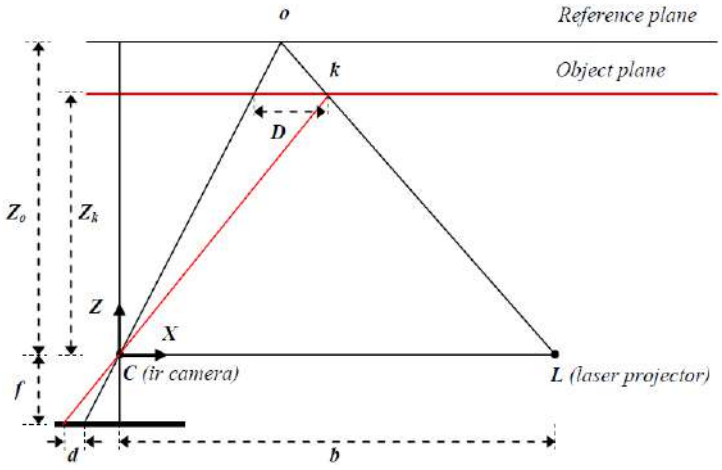

Figure 2. Relation between relative depth and measured disparity.

Each frame of the depth data stream is made up of pixels that contain the distance (in millimeters) from the camera plane to the nearest object. An application can use depth data to track an object or identify background objects to ignore. The depth data is the distance, in millimeters, to the nearest object at that particular (x, y) coordinate in the depth sensor's field of view. The depth image is available in 3 different resolutions: 640x480 (the default), 320x240, and 80x60 as specified using the DepthImageFormat Enumeration. The range setting, specified using the DepthRange Enumeration in Kinect for Windows SDK, determines the distance from the sensor for which depth values are received. In this study, All pixel's distance value between sensor and object saved to array in the software. The distance between the camera and the opposite wall was 85 cm in box. In Figure 3, we showed distance calculation and storing into array code.

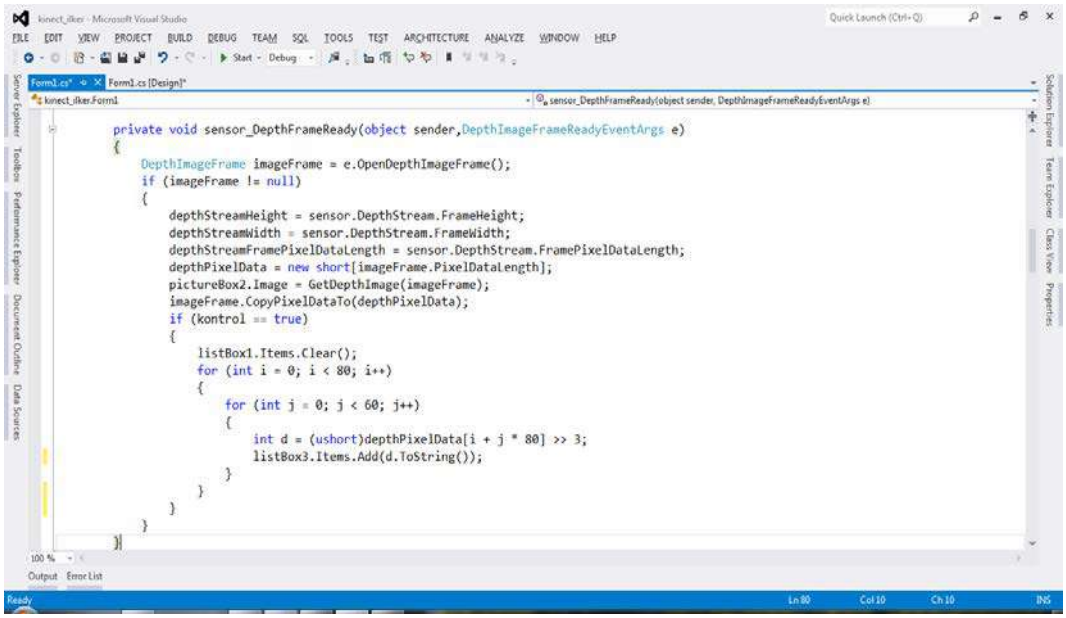

```
private void sensor_DepthFrameReady(object sender,DepthImageFrameReadyEventArgs e)
{
    DepthImageFrame imageFrame = e.OpenDepthImageFrame();
    if (imageFrame != null)
    {
        depthStreamHeight = sensor.DepthStream.FrameHeight;
        depthStreamWidth = sensor.DepthStream.FrameWidth;
        depthStreamFramePixelDataLength = sensor.DepthStream.FramePixelDataLength;
        depthPixelData = new short[imageFrame.PixelDataLength];
        pictureBox2.Image = GetDepthImage(imageFrame);
        imageFrame.CopyPixelDataTo(depthPixelData);
        if (kontrol == true)
        {
            listBox1.Items.Clear();
            for (int i = 0; i < 80; i++)
            {
                for (int j = 0; j < 60; j++)
                {
                    int d = (ushort)depthPixelData[i + j * 80] >> 3;
                    listBox3.Items.Add(d.ToString());
                }
            }
        }
    }
}
```

Figure 3. Distance calculation and storing into array code

3. RESULTS AND DISCUSSION

We stored all pixels (640x480) value(X,Y and distance) into an array. If there were no oranges in the picture, all the distances would be 85 cm. In the study, However, within the non-orange images, the pixel distances were measured as 85 cm. However, in the case of the orange images, the pixel distances were variable (Figure 4). The study was repeated for 20 different oranges.

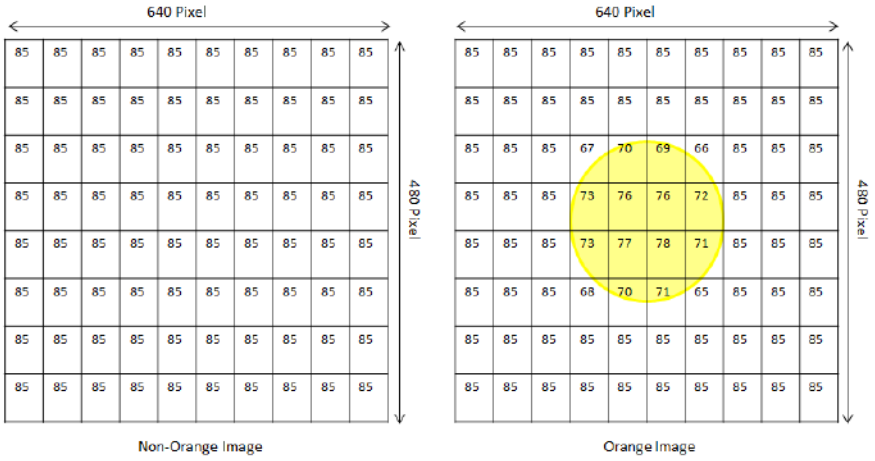

Figure 4. Distance measurement on orange pixel

In our work, we removed the 85 cm pixels in the picture from the array. The remaining data were transferred to a different array. The smallest distance in this array gave us the height of the orange. The x and y axis lengths were found by proportioning the maximum X and maximum Y values in the actual image to the dimensions of the box wall. All data (X, Y and Z values) were given in Table 1 for 20 different orange both obtained image processing method and real measurement method. In Table 2, we were given statistical analyses results.

Table 1. Real and measured values for 20 different orange

	Real size			With Kinect		
No	**X**	**Y**	**Z**	**X**	**Y**	**Z**
1	9.20	8.30	10.10	9.00	8.00	9.00
2	8.70	9.40	10.30	9.00	9.00	10.00
3	10.30	9.20	9.80	10.00	10.00	9.00
4	9.40	7.30	8.50	9.00	7.00	8.00
5	9.30	8.50	7.80	10.00	9.00	8.00
6	7.60	8.00	6.30	8.00	9.00	7.00
7	8.90	7.80	7.10	9.00	7.00	8.00
8	7.50	8.70	6.90	7.00	9.00	7.00
9	8.00	6.90	7.00	9.00	7.00	8.00
10	7.70	8.10	7.60	8.00	8.00	7.00
11	9.40	9.10	8.90	10.00	10.00	9.00
12	10.10	9.20	10.00	10.00	9.00	9.00
13	11.30	9.80	8.90	11.00	10.00	8.00
14	6.90	7.50	8.00	7.00	8.00	8.00
15	7.40	8.10	9.20	8.00	8.00	9.00
16	8.80	9.30	7.30	9.00	9.00	8.00
17	10.30	8.70	8.70	10.00	9.00	9.00

18	7.80	6.80	6.50	8.00	6.00	7.00
19	9.40	8.80	7.40	10.00	9.00	7.00
20	9.80	10.30	8.50	10.00	10.00	9.00

Table 2. Regression analyses result

	X	**Y**	**Z**
R	0.93591	0.897135	0.873495

We used regression analyses for X, Y and Z values for both real and Kinect measured values. R values were obtained very high. As a result, The differences between X, Y and Z values obtained from real measurement and Kinect measurement were statistically significant and similar for all oranges.

4. CONSLUSION

The Kinect provides an inexpensive option for acquiring 3D positional data with a time base. The device has limitations with respect to spatial and temporal resolution (data acquisition rate of 30 fps), and object size and speed need to be carefully considered when designing an experiment. Overall the Kinect has been useful to be an effective device with the potential for rapidly acquiring data in many diverse situations. The method proposed in this paper is potentially useful to improve the efficacy and efficiency of size estimation of orange sorting and grading systems. The proposed methods are easy to be integrated into existing commercial machine vision systems for several reasons. Compared to the method using the color image, the diameter estimation using the depth image was more accurate and robust to the change of the orientation of orange. The proposed method based on depth image accurately measured the volume of oranges. The size of orange estimated by the depth imaging-based method was statistically comparable to the conventional experimental approach.

5. REFERENCES

[1] H.Dang, J. Song, Q. Guo, "A Fruit Size Detecting and Grading System Based on Image Processing". Second International Conference on Intelligent Human-Machine Systems and Cybernetics, vol. 2, pp. 83-86, 2010.
[2] G. P. Moreda, J. Ortiz-Cañavate, F. J. García-Ramos, M. Ruiz-Altisent. “Nondestructive technologies for fruit and vegetable size determination – a review”. J. Food Eng. Vol. 92 (2), pp. 119–136, 2009.
[3] W. Wang, C. Li. “Size estimation of sweet onions using consumer-grade RGB-depth sensor”. Journal of Food Engineering, vol. 142, pp. 153–162, 2014.
[4] B. Dellen, I.A. Rojas. “Volume measurement with a consumer depth camera based on structured infrared light”. 16th Catalan Conference on Artificial Intelligence, poster session, 2013, Vic, Spain, pp. 1-10, ACIA.
[5] B. Q. Ferreira, M. Grine, D. Gameiro, J. P. Costeira, B. S. Santos. “VOLUMNECT–Measuring Volumes with Kinect”. Proceeding of SPIE, Vol. 9013, pp. 901304-1–901304-4, 2013.
[6] A. Canessa, M. Chessa, A. Gibaldi, S. P. Sabatini, and F. Solari, “Calibrated depth and color cameras for accurate 3D interaction in a stereoscopic augmented reality environment,” Journal of Visual Communication and Image Representation, vol. 25(1), pp. 227 – 237,2014.
[7] P. Henry, M. Krainin, E. Herbst, X. Ren, D. Fox. “RGB-D Mapping: Using Depth Cameras for Dense 3D Modeling of Indoor Environments”. In: Khatib O., Kumar V., Sukhatme G. (eds) Experimental Robotics. Springer Tracts in Advanced Robotics, vol 79. Springer, Berlin, Heidelberg, 2014
[8] Y. Chéné, D. Rousseau, P. Lucidarme, J. Bertheloot, V. Caffier, P. Morel, E. Belin, F. Chapeau-Blondeau. “On the use of depth camera for 3D phenotyping of entire plants”. Comput. Electron. Agric., vol. 82, pp. 122–127, 2012.
[9] Q.Wang, Q. Zhang. “Three-dimensional reconstruction of a dormant tree using RGB-D cameras”. In: 2013 Annual International Meeting of the American Society of Agricultural and Biological Engineers, Kansas City, Missouri, 2013.
[10] Microsoft, 2010. Kinect. http://www.xbox.com/en-us/kinect/ (accessed on 10.21.17).

[11] K. Khoshelham, S. O. Elberink. “Accuracy and resolution of Kinect depth data for indoor mapping applications”. Sensors (US), vol. 12(2), pp. 1437-1454, 2012.

ICENS 4TH INTERNATIONAL CONFERENCE ON ENGINEERING AND NATURAL SCIENCE
2-6 May 2018 KIEV UKRAINE

The Investigation and Comparison of friction stir spot welding and Electrical Resistance Spot Welding of AA2024 Aluminum Alloy Joints

Yahya Bozkurt[1], Adnan Turker[2], Serdar Salman[1,3]

Abstract

*Both Friction Stir Spot Welding (FSSW) and Electrical Resistance Spot Welding (ERSW) are contemporary techniques for joint of the thin sheet materials. But FSSW is more modern technique than RSW. FSSW is used **in** a lot of **areas** which are from marine to aerospace industries. Aluminium alloy has a lot of advantages of **over** the other materials. One of them is weight.*

*In this study, AA2024 sheets are chosen for FSSW and RSW joint. FSSW is effected with tool rotational speed, tool transverse speed, dwell time and tool plungle depth. Two sheets were joined under the tool rotational speed for 1040 rpm and dwell time for 10 **seconds**. The same samples joints with under RSW for 39 kA and dwell time for 0.5 second. These parameters are optimised for both welding techniques. Afterwards FSSW and RSW are compared about lap shear tensile test for aluminum alloy joints with plane thickness of 1.6 mm. So that FSSW is **a** more suitable joning process than ERSW. **As a results of The test** and analyses are showed that FSSW **a** is better mechanical **property** than RSW. Eventually, These results are verified by many experiments.*

Keywords: *Friction Stir Spot Welding, Electrical Resistance Spot Welding, Aluminium alloys, Mechanical properties, Welding parameters.*

1. INTRODUCTION

The ERSW method group (group of pressure welding method) has a wide range of applications in the automotive industry. This welding operation takes place in the solid phase. Especially, the ERSW used in automobile body sheet production is made by robots because this method is suitable for serial production [1]. ERSW is welding method which heat from the resistance of the materials against the electric current passing through the workpieces and at the same time applying the pressure. Apart from the heat generated by the electric current passing through the material, no heat treatment is applied to the workpieces. The heat is generated around the welded zone and pressure on this welded zone is applied through the electrodes [2]. However, the difficulties welding aluminum alloy which is a soft material with the RSW, have delayed widespread use of aluminum alloys in the automobile body sheet production [3]. A schematic presentation of the ERSW process is shown in Fig. 1 [4].

FSSW method recently advanced as an alternative to ERSW and developed from the traditional friction stir welding (FSW) method, it is one of the latest developments in joining technology [4].

In Figure 2, the steps of the FSSW technique is shown. The process is used for joined two metal plates. A non-consumable rotating tool with a specially designed pin plunges into upper plate. A support tool underneath the

[1] *Corresponding author: Marmara University, Faculty of Technology, Department of Metallurgy and Materials Engineering, 34722, Kadikoy/Istanbul, Turkey. ybozkurt@marmara.edu.tr*

[2] *National Defense University, The NCO Vocational High School, Department of Mechanical Science, Balikesir, Turkey, adnanturker2002@gmail.com*

[3] *National Defense University, Rectorate of National Defense University, Turkey, ssalman@marmara.edu.tr*

lower plate provides the force against the shoulder and pin (Fig. 2a). The tool accomplishes two important function: heat generation hereabouts weld zone, and movement of material to produce the weld (Fig 2b).The heating is served by friction between the tool and the plastic deformation of the plates (Fig 2c) [5].

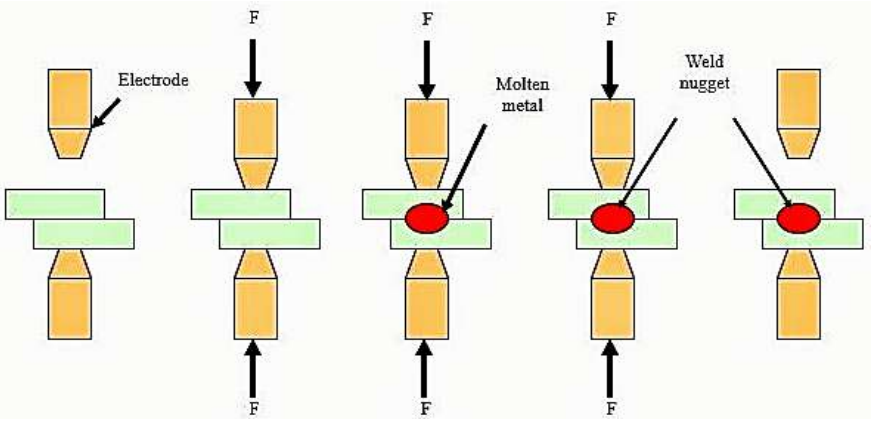

Figure 1. A schematic presentation of the ERSW process [5].

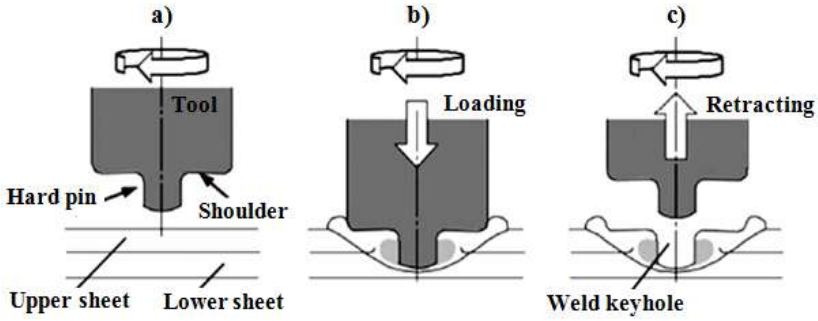

Figure. 2. A schematic presentation of the FSSW process: (a) plunging; (b) bonding; (c) drawing out [6].

After the FSSW process, the weld zone is observed as shown Figure 3. Two special segment can be identified from weld zone. The first segment is the thickness of weld nugget (X) which is an determiner of the weld (bond) section (Figure 3a and 3b). The bond section size is changed depending on nugget thickness. The second segment is thickness of the subject to shoulder operation on the upper plate (Y). The size of these segment establish the strenght of a FSSW joint [7].

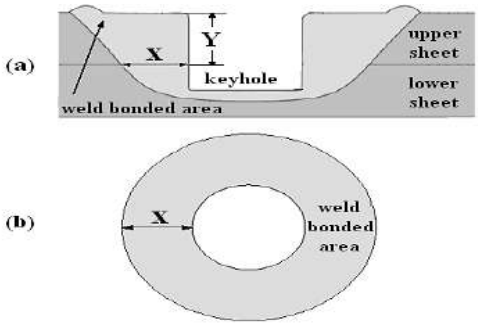

Figure. 3. (a) Schematic presentation of the cross section of a FSSW and (b) geometry of the weld bonded area; x: nugget thickness and y: the thickness of the upper sheet [7].

A new solid state welding technique, FSSW has been developed by Mazda Motor Corporation and Kawasaki Heavy Industry, as an extension of FSW for joining aluminum alloys [8-9]. Mazda reported a great reduction in energy consumption and equipment investment compared to ERSW for aluminum [10]. The only energy consumed in FSSW is the electricity needed to rotate and drive the tool. Compared to ERSW, the energy consumption has reduced by 99% for FSSW of aluminum and 80% for steel [11].

Since FSSW is a solid state welding process, no compressed air and coolant are needed, and less electricity is required than ERSW. FSSWs have higher strength, better fatigue life, lower distortion, less residual stress and better corrosion resistance. Unlike ERSW, there is no traverse movement after plunging a rotating non-consumable tool into the workpieces. Tools used for FSSW have two parts, a pin and a shoulder. The pin is projected to throw the faying surface of the workpieces, shear and transport the material around it and produce deformational and frictional heat in the thick workpieces. The tool shoulder produces a majority of frictional heat to the upper surface and lower plate zones of the workpieces. Also the shoulder constrains the flow of plasticized material and produces the downward forging action [12].

In this study, sheet materials AA2024-T3 were selected for the ERSW and FSSW methods used in the industry. These selected sheets were separately welded with RSW and FSSW. The tensile test of welded joins was carried out. In addition, these test results were examined comparatively.

2. EXPERIMENTAL STUDY

2.1. Materials

In this study, 2 mm thickness AA2024-T3 plates were used for dissimilar FSSW and ERSW. The chemical composition of these alloy sheets is shown in Table 1.

Table 1. The mechanical properties and chemical composition of the aluminum plates.

Alloy	Mechanical properties		Chemical composition (wt. %)								
	Tensile strength (MPa)	Elongation (%)	Al	Si	Fe	Cu	Mn	Mg	Zn	Ti	Cr
AA2024-T3	435	17	93.11	0.07	0.14	4.5	0.65	1.5	0.01	0.02	-

Aluminium plate dimension is 25x100 mm. The welding zone is fixed as 25x25 mm for all test specimens.

All the FSSW experiments were carried on FSW adjusted milling machine as shown in Fig 4.

Figure 4. FSSW process: a) rotating tool prior to penetration into the lap joint; b) tool shoulder makes contact with the part, making heat and the joint zone; c) retraction of the tool from the lap joint zone.

2.2 Preparation and Joint of Experimental Specimens

The FSSW tool was made of Aluminum Titanium Nitrate (AlTiN) coated, 1.2344 hot work tool steel and had a hardness of 58 HRC. FSSW tool had a shoulder diameters of 18 mm, a pin diameter of 6 mm and a pin length of 3.80 mm. Joint configuration was used to produce the FSSW joints where the rolling direction of the plates. All the welding processes were done at the room temperature. FSSW process rotating tool have a constant speed that 1040 rpm. Dwell time of the tool was determined as 10s.

During the ERSW process, the specimens were joined at the current values of 39 kA with constant welding time of 0.5s and a constant electrode force of 1710 N which is the same in each joining.

2.3 Lap Shear Tensile Test

Welded plate pairs are tested with 250 kN capacity tester at 30 mm/min. tensile speed. The test equipment's trade-mark is ZWICK Z010. The lap-shear tensile tests (LSTT) were carried out at room temperature by Zwick Z010 universal type tensile test machine at a constant crosshead speed of 5 mm/s. The load and displacement were simultaneously recorded during the test.

Figure 5. Zwick Z010 lap-shear tensile tests machine.

Three specimens were tested for each parameter from the specimens joined by ERSW and FSSW and the averages were taken. ERSW and FSSW welded specimens plates (AA2024) are shown in Figure 6a and 6b.

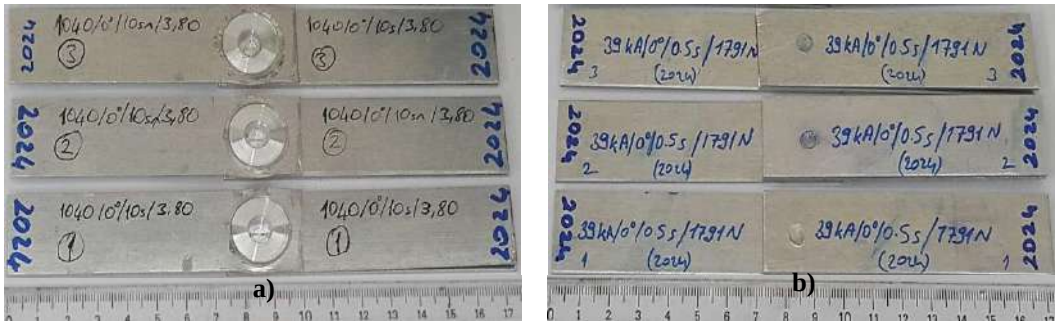

Figure 6. Lap-shear tensile tests specimens: a) Before test of FSSW specimens; b) Before test of ERSW specimens.

3. RESULTS AND DISCUSSION

3.1 Results of LSTT

The LSTT results of specimens joined with ERSW and FSSW are shown in Table 2. The results are given graphically in Figure 7. Increasing the weld current value causes inner heat rising and **as a** result of this operation nucleus grows.
Weld nucleus diameter is smaller in lower weld time and weld current values. It is also reported in other studies that heat input increases when weld current and time increased as formulated below; [13].

$Q = I^2 \cdot R \cdot t$

where Q is the generated heat (J), I the current (Ampere), R the resistance of the work (Ω) and t the time of current (s). The expansion of weld nucleus and heat affected zone with increase in heat input is an expected result [14-19]. Bonding occurred at 9kA - 40kA but bonding was not happened at 3kA - 10 kA cycles. Bonding occurred at higher heat input. Rising the weld metal size increases the tensile-shear force. As the current continues to rise, the size of the weld metal decreases due to excessive melting and splashing and therefore the tensile-shear force is also reduced [13].

Aslanlar et al. showed that in low welding currents achieved by increasing the welding time, the amount of fused metal to form a nucleus increase, so the nucleus diameter increases and the height of the nucleus nearly reaches the sheet thickness [13].

LSTT was performed to obtain information on the joint strength of AA2024 plates joined with FSSW technique and ERSW technique. Thus, the yield strength, tensile shear strength and % elongation value of the material were determined. During the tensile tests a time must be given to distribute the uniformity of the applied stress uniformly throughout the sample.

Table 2. The LSTT results.

Materials	LSTT (kN)	
	FSSW	ERSW
AA2024	4.74	2.07
	8.31	3.38
	7.3	2.72

In FSSW process, the tool plunge depth up to 3.80 mm increases of tensile-shear force and decreases after this depth. The reason for this, the tool excessively depth process on the Al-alloy plate during the FSSW that causes thinning in the weld zone on the top surface of the plate [20].

The variation in pin length and pin profiles has direct impact on material mixing, flow etc. The commonly used pin profiles are cylindrical, conical, threaded, square, octagonal etc [21]. During FSSW process, the plunge depth and dwelling time of the tool determine the flow of metal around the stirrer tip, heat generation, weld strength and geometry [22].

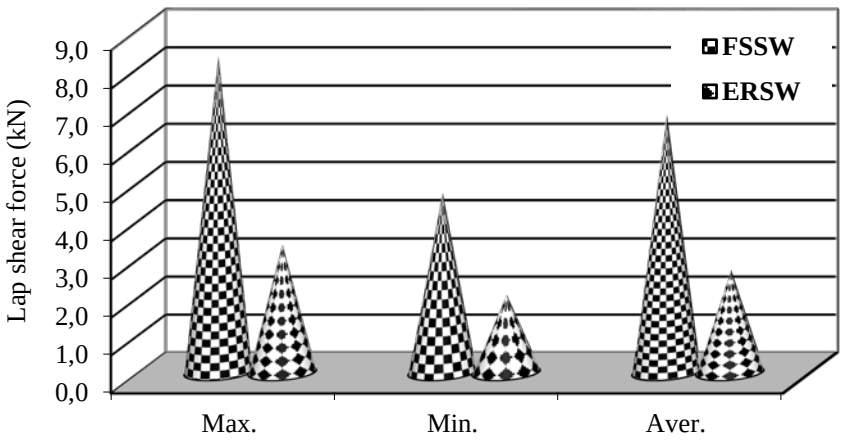

Figure 7. The lap-shear test results of specimens Joined with RSW and FSSW.

The weld metal is similar to the tool pin used in FSSW process. The shoulder of tool causes burr formation during the plunge. This situation is compatible with literature because it is formed in this way in all studies and is allowed to collapse on surface of upper material [4].

4. CONCLUSIONS

In this study, AA2024 Aluminium alloy sheets were joined with FSSW and ERSW methods. Maximum and minimum LSTT were determined. During the ERSW process, maximum LSTT force was determined to be 3.38 kN, a current value of 39 kA, a welding time (constant) of 10 s, an electrode force (constant) of 1710 N. During the FSSW process, maximum lap-shear force was determined to be 8.31 kN, a tool rotation speed of 1040 rpm, a dwelling time of tool of 10 s and a plunge depth of 3.80 mm. When these results were evaluated,

FSSW method has given better results than ERSW method. As a result of increasing the welding current, the heat input and size of weld nucleus increased.

ACKNOWLEDGMENT

This study is granted by Marmara University, BAPKO project numbers: FEN-C-YLP-150218-0059.

REFERENCES

[1]. M. H. Coskun, ‘’Otomotiv endustrisinde kullanilan AN 7114 ve Dp600 Celik Saclarin Direnc Nokta Kaynagi (RSW) ve Surtunme Karistirma Nokta Kaynagi (FSSW) Yontemleri ile Birlestirilmesi,’’ Kocaeli Unv. Fen Bil. Enst., 2009.
[2]. A.Bilal, ‘’AA 2024-T3 Aluminyum Alasiminin Surtunme Karistirma Kaynaginda Islem Parametrelerinin Mikroyapi ve Mekanik Ozelliklere Etkileri,’’ Osmangazi Unv. Fen Bil. Enst., 2006.
[3]. G. Cam, ‘’Surtunme Karistirma Kaynagi Uygulamalarinda Son Gelismeler,’’ Kaynak Tekn. VI. Kongre ve Sergisi Bildiriler Kitabi, TMMOB Makine Muhendisleri Odasi, 2007, p. 449, 42.
[4]. http://mechanicalinventions.blogspot.com.tr/2014/09/resistance-spot-welding-rsw-working-principle.html
[5]. R.S. Mishra, M.W. Mahoney, ‘’Friction Stir Spot Welding, American Society for Metals,’’ 2007, pp. 235-250.
[6]. D. A. Wang and S. C. Lee, ‘’Microstructures and failure mechanisms of friction stir spot welds of aluminum 6061-T6 sheets,’’ J. Mater. Process. Technol., 2007, 186291-297.
[7]. M. K. Bilici and A. I. Yukler, ‘’Effects of welding parameters on friction stir spot welding of high density polyethylene sheets,’’ Mater. Des., 2012, 33, 545–550.
[8]. R. Sakano, K. Murakami, K.Yamashita, T. Hyoe, M. Fujimoto, M. Inuzuka, U. Nagao, H. Kashiki, “Development of spot FSW robot system for automobile body members,’’ Proceedings of the Third Int. Symposium of Friction Stir Welding,’’ Kobe, Japan, 2001.
[9]. T. Iwashita, Method and apparatus for joining, US Patent Issued on August 5, 2003.
[10]. R. Hancock, ‘’Friction stir spot welding on similar aluminum alloys al6082 by using different shape of en19 and en 31 profile tool,’’ Welding journal, 2004, 40-43.
[11]. "Mazda Develops World's First Aluminum Joining Technology Using Friction Heat", Mazda media release, February 27, 2003.
[12]. C. B. Fuller, in: R.S. Mishra, M.W. Mahoney (Eds.), Friction Stir Welding and Processing, ASM International, Ohio, 2007, pp. 7-35.
[13]. S. Aslanlar, ‘’The Effect of Nucleus Size on Mechanical Properties in Electrical Resistance Spot Welding of Sheets Used in Automotive Industry,’’ Materials and Design, 2006, 27, pp.125-131.
[14]. P. Gupta, P.K. Ghosh, S.K. Nath and S. Ray, “Resistance spot weldability of plain carbon and low alloy dual phase steels”, Z. Metallkde., 1990, 81,7, pp. 502-508.
[15]. P. Sharma, P.K. Ghosh and S.K. Nath, “Studies on fatigue behaviour of resistance spot welded Mn-Cr-Mo dual phase steel”, Z. Metallkunde, 1993, 84, 7, pp. 513-517.
[16]. M. Vural and A.Akkus, ‘’On the resistance spot weldability of galvanized interstitial free steel sheets with austenitic stainless steel sheets,’’ J. Mater. Process. Technol., 2004, 153-1.
[17]. M.Vural, A.Akkus and B. Eryurek, ‘’Analysis of Process Parameters for Resistance Spot Welding on Cold Reduced Low Carbon Steel,’’ J. Mater. Process. Technol., 2006, 176-127.
[18]. F. Hayat, B. Demir and M. Acarer, ‘’Tensile shear stress and microstructure of low-carbon dual-phase Mn-Ni steels after spot resistance welding,’’ Sci. Heat Treat., 2007, 49 484.
[19]. P. Zhang, J. Xie, Y.X.Wang and J.Q. Chen, ‘’Effects of welding parameters on mechanical properties and microstructure of resistance spot welded DP600 joints,’’ Sci. Technol. Weld. Join., 2011, 16-567.
[20]. Y. Tozaki, Y. Uematsu, K. Tokaji, ‘’Effect of Processing Parameters on Static Strength of Dissimilar Friction Stir Spot Welds Between Different Aluminium Alloys Fatigue,’’ Fract. Engng. Mater. Struct., 2007, 30 , pp.143-148.
[21]. B.R. Singh, A handbook on Friction stir welding Research Gate, DOI/10.13140/RG.2.1.5088.6244 (2012).
[22]. Z. Zhang, X. Yang, J. Zhang, G. Zhou, X. Xu, B. Zou, ‘’Effect of Welding Parameters on Microstructure and Mechanical Properties of Friction Stir Spot Welded 5052 Aluminum Alloy,’’ Materials and Design, 2011, 32, pp.4461-4470.

ICENS 4TH INTERNATIONAL CONFERENCE ON ENGINEERING AND NATURAL SCIENCE
2-6 May 2018 KIEV UKRAINE

Optimization of Steady State Flight Parameters for a Given Trim Condition

Muharrem Selim Can[1], Hamdi Ercan[2], Sezai Alper Tekin[3]

Abstract

Aircraft control and parameter identification is challenging process. Determining parameters of control algorithm are difficult to deal with nonlinear flight dynamics and complexity. Aircraft dynamic equations of motion are highly nonlinear to control desired output states and input states. Furthermore, Trimming is very useful and important control mechanism to achieve steady flight. For a specific trim condition finding best control signals can be considered as numerical optimization problem. Evolutionary optimization algorithms are very popular to find global minimum for complex nonlinear functions. Evolutionary optimization algorithms are inspired to develop by nature. In this study, evolutionary algorithms are preferred to find optimal aircraft states. Performances of evolutionary algorithms are evaluated to find optimal states for a given trim condition. As a result, performance of algorithms shows that evolutionary algorithms are very successful for aircraft parameter optimization.

Keywords: Evolutionary algorithm, Trimming, Steady state

1. INTRODUCTION

In steady flight conditions it is critical for pilot to control the aircraft in desired direction and attitude. During the flight, the pilot sets trim to release control of the aircraft and it continues to fly under given conditions. Aircraft maintain control inputs that aren't require any control action from pilot. Forces and moments acting on aircraft are required to be zero for equilibrium. This equilibrium state occurs when axial forces, side forces, and normal forces and yawing, pitching, and rolling moments are zero respectively. At Equilibrium, it is said that approximately the lift force is equal to weight force and that thrust is equal to the drag force. Maintenance of aircraft state of equilibrium that needs to adjust six degree of freedom variables. Control surfaces, which are called elevator, rudder, and ailerons, are mounted on the aircraft. Control surfaces are used to change or maintain direction of the aircraft. In order to achieve the aircraft longitudinal and lateral stability elevator deflection angle, rudder deflection angle, deflection angles of ailerons and engine thrust parameter are chosen as inputs [1]. General aviation aircraft Navion parameters have been used to model control system [2]. Ailerons, elevator, and rudder are equipped with trim tabs which are used for adjusting trim equilibrium point. In Literature, aircraft damage and failure has been studied to avoid risks of decreasing performance during flight [3].

In this study, the aircraft trim point is determined by using numeric optimization algorithm for given trim condition. The aircraft equations of motion are highly nonlinear, so that finding the aircraft states are challenging process. The aircraft equations of motion have equality constraints for given trim condition. Optimization algorithm is desired that cope with these constraints. Numeric optimization algorithms are powerful methods for solving nonlinear problems. Particle Swarm Optimization algorithm (PSO) is population based stochastic optimization algorithm that is inspired from animal behaviors. PSO has been introduced by Kennedy in 1995. In population a member of swarm is said to be particle which has personal best solution. Global best solution is determined among each particle's personal best solution [4-7].

2. AIRCRAFT EQUATIONS AND SYSTEM DYNAMICS

Aircraft equations of motion are obtained from Newton's second law which indicates total forces acting on the aircraft equal to time rate of change of momentum of aircraft body. F is total vector forces acting on the aircraft

[2]*Corresponding author: Erciyes University, Department of Avionics, Kayseri, Turkey* hamdiercan@erciyes.edu.tr

[1]*Iskenderun Technical University, Department of Avionics, 31200, Iskenderun/Hatay, Turkey.* mselim.can@iste.edu.tr

[3]*Erciyes University, Department of Industrial Design Engineering, Kayseri, Turkey* satekin@erciyes.edu.tr

in body axis; V is the velocity vector in body axis and **Ω** angular velocity in body reference frame. **X**, **Y**, and **Z** are total forces acting on the body along x axis, y axis, and z axis respectively [2, 8, 9].

Newton's second law is defined by Equation (1), (2), (3) (4), (5) and (6).

$$\sum \boldsymbol{F} = \frac{d}{dt}(m\boldsymbol{v}) \tag{1}$$

$$\boldsymbol{F} = m\left(\frac{\partial \boldsymbol{V}}{\partial t} + \Omega x \boldsymbol{V}\right) \tag{2}$$

$$\boldsymbol{F} = [\sum \boldsymbol{X}, \sum \boldsymbol{Y}, \sum \boldsymbol{Z}] \tag{3}$$

$$\boldsymbol{V} = [u, v, w]^{\boldsymbol{T}} \tag{4}$$

$$\Omega = [p, q, r]^T \tag{5}$$

$$\frac{\partial \boldsymbol{V}}{\partial x} = \frac{1}{m}\boldsymbol{F} - \Omega \boldsymbol{x} \boldsymbol{V} \tag{6}$$

Following equations indicate angular acceleration. **M** is the vector of the moments in body axis that is total moment acting on body equals to rate of change of angular momentum. ***I*** is the inertia matrix and $\dot{\Omega}$ is the angular acceleration [2, 8, 9].

Moments and angular acceleration are defined by Equation (7), (8), (9) and (10).

$$\sum \boldsymbol{M} = \frac{d}{dt}\boldsymbol{H} \tag{7}$$

$$\boldsymbol{M} = \frac{\boldsymbol{\partial I \Omega}}{\boldsymbol{\partial t}} + \Omega \boldsymbol{x} \boldsymbol{I} \Omega \tag{8}$$

$$\boldsymbol{I}\frac{\boldsymbol{\partial \Omega}}{\boldsymbol{\partial t}} = \boldsymbol{M} - \Omega \boldsymbol{x} \boldsymbol{I} \Omega \tag{9}$$

$$\dot{\Omega} = \frac{\boldsymbol{\partial \Omega}}{\boldsymbol{\partial t}} \tag{10}$$

In order to derive aircraft equations of motion, aircraft aerodynamic equations are obtained. Aerodynamic equations are required to obtain aircraft nonlinear equations of motion. Before the aircraft aerodynamic forces are calculated that lift coefficient and drag coefficient are needed to calculate. Aerodynamic lift force and drag force are modeled following Equation (11) and (12).

$$L = \frac{1}{2}\rho V^2 S C_L \tag{11}$$

$$D = \frac{1}{2}\rho V^2 S C_D \tag{12}$$

Aerodynamic coefficients are derived by using Equations (13) and (14).

$$C_L = C_{L0} + C_{L\alpha}\alpha + C_{Leq}\frac{c}{2V}q + C_{L\delta e}\delta e \tag{13}$$

$$C_D = C_{D0} + \frac{C_L^2}{\pi e A R} \tag{14}$$

Aerodynamic moments of aircraft are given Equations (15), (16), and (17) respectively.l is rolling moment of the aircraft, $M$is pitching moment of the aircraft and N yawing moment. C_l is pitching moment coefficient, C_m is rolling moment coefficient and C_n is yawing moment coefficient that are represented by Equations (18), (19) and (20) respectively [2, 8, 9].

$$l = \frac{1}{2}V^2 \rho S b C_l \tag{15}$$

$$M = \frac{1}{2}V^2 \rho S c C_m \tag{16}$$

$$N = \frac{1}{2}V^2 \rho S b C_n \tag{17}$$

$$C_l = C_{l\beta}\beta + C_{lp}\frac{b}{2V}p + C_{lr}\frac{b}{2V}r + C_{l\delta a}\delta a + C_{l\delta r}\delta r \quad (18)$$

$$C_m = C_{m0} + c_{m\alpha}\alpha + c_{meq}\frac{c}{2V}q + c_{m\delta e}\delta e \quad (19)$$

$$C_n = C_{n\beta}\beta + C_{np}\frac{b}{2V}p + C_{nr}\frac{b}{2V}r + C_{n\delta a}\delta a + C_{n\delta r}\delta r \quad (20)$$

Translational velocity is represented by V. Angle of attack and sideslip angle are represented by α, β. Transformation from wind-axis to body-axis is obtained Equation (21), (22), and (23) respectively.

$$u = Vcos\,\alpha\cos\beta \quad (21)$$

$$v = Vsin\,\beta \quad (22)$$

$$w = Vsin\,\alpha\cos\beta \quad (23)$$

Inverse transformation from body axis to wind axis is expressed Equation (24), (25) and (26).

$$V = |V| = \sqrt{(u^2 + v^2 + w^2)} \quad (24)$$

$$\alpha = \tan^{-1}\left(\frac{w}{V}\right) \quad (25)$$

$$\beta = \sin^{-1}\left(\frac{v}{V}\right) \quad (26)$$

Translational velocities are defined in body axis and represented by u, v, w. Rate of change of translational velocity are defined by Equation (27), (28) and (29) respectively.

$$\dot{u} = \frac{X}{m} - gsin\theta + rv - qw \quad (27)$$

$$\dot{v} = \frac{Y}{m} + g\sin\varphi\,cos\theta - ur + wp \quad (28)$$

$$\dot{w} = \frac{Z}{m} - vp + up + gcos\varphi cos\theta \quad (29)$$

Rate change of angular velocities are defined by as Equation (30), (31) and (32)

$$\dot{p} = \frac{l-(I_{zz}-I_{yy})qr+I_{xz}(\dot{r}+pq)}{I_{xx}} \quad (30)$$

$$\dot{q} = \frac{m-(I_{xx}-I_{zz})pr+I_{xz}(r^2-p^2)}{I_{yy}} \quad (31)$$

$$\dot{r} = \frac{n-(I_{yy}-I_{xx})pq+I_{xz}(\dot{p}-qr)}{I_{zz}} \quad (32)$$

Rate change of pitch angle, yaw angle and roll angle are defined by as Equation (34), (35) and (36)

$$\dot{\varphi} = p + (qsin\varphi + rcos\varphi)tan\theta \quad (34)$$

$$\dot{\theta} = qcos\varphi - rsin\varphi \quad (35)$$

$$\dot{\Psi} = (qsin\varphi + rcos\varphi)sec\theta \quad (36)$$

$$\boldsymbol{x} = [u, v, w, p, q, r, \varphi, \theta, \psi, x_N, y_E, \mathrm{h}] \quad (37)$$

Following Equation (38) is called transformation matrix that is used to transform from earth coordinate system to body coordinate system [2, 8, 9].

$$R = \begin{bmatrix} cos\psi & -sin\psi & 0 \\ sin\psi & \cos\psi & 0 \\ 0 & 0 & 1 \end{bmatrix}\begin{bmatrix} cos\theta & 0 & sin\theta \\ 0 & 1 & 0 \\ -sin\theta & 0 & cos\theta \end{bmatrix}\begin{bmatrix} 1 & 0 & 0 \\ 0 & cos\varphi & -sin\varphi \\ 0 & sin\varphi & cos\varphi \end{bmatrix}$$

$$= \begin{bmatrix} cos\theta cos\Psi & cos\theta sin\Psi & -sin\theta \\ sin\varphi sin\theta cos\Psi - cos\varphi sin\Psi & sin\varphi sin\theta sin\Psi + cos\varphi cos\Psi & sin\varphi cos\theta \\ cos\varphi sin\theta cos\Psi + sin\varphi sin\Psi & cos\varphi sin\theta sin\Psi - sin\varphi cos\Psi & cos\varphi cos\theta \end{bmatrix} \quad (38)$$

V_{Body} represents body axis velocities axial velocity, side velocity and normal velocity which are defined Equation (39).

$$V_{Body} = [u, v, w]^T \quad (39)$$

V_{Earth}represents earth coordinate system velocities which is defined by Equation (40). Transformation of velocities from Earth coordinate system to body system is defined by Equation (41).

$$V_{Earth} = [V_N, V_E, V_D]^T \quad (40)$$

$$V_{Earth} = R^{-1} V_{Body} \quad (41)$$

3. CONTROL THE AIRCRAFT STEADY STATE TRIMMED EQUILIBRIUM CONDITION

Rate change of angular velocities $\dot{p}, \dot{q}, \dot{r}$, and roll angle, and sideslip angle φ, β is supposed to equal zero for providing trim condition. PSO optimization algorithm has been used to calculate trimmed equilibrium state of the aircraft. Optimization cost function is determined by using trim condition in Equation (44). Main objective of optimization is minimization of cost function which is consisting of states of the aircraft. After trimmed equilibrium state of the aircraft is optimized, the aircraft trim control has been performed by using states of the aircraft. Furthermore, nonlinear equations are linearized then state-space model is developed to control the aircraft. Linear Quadratic Regulator (LQR) control method is chosen for controlling the aircraft. The LQR method is a widely performed for controlling aerial vehicles that it gives very successful results [10]. State space representation of system is given in Equation (42). In this study, General aviation aircraft Navion's parameters are used to simulate trimmed equilibrium state of the aircraft [2]. Navion aircraft parameters are represented in Table 1 and Table 2.

$$\dot{x} = Ax + Bu \quad (42)$$

$$y = Cx + Du$$

Trimmed equilibrium point is defined by Equation (43).

$$V_0 = velocity_{trim} = 50\ m/s \quad \varphi = 0, \beta = 0, \dot{p} = 0, \dot{q} = 0, \dot{r} = 0 \quad (43)$$

J is cost of objective which is desired to converge zero.

$$J = \dot{u}^2 + \dot{v}^2 + \dot{w}^2 + \dot{p}^2 + \dot{q}^2 + \dot{r}^2 \quad (44)$$

Table 33. General Aircraft Navion Parameters (physical parameters)

Text	Text
m	1247,378 kg
I_{xx}	1420,897 kg.m^2

I_{yy}	4067,453 kg.m^2
I_{zz}	4786,037 kg.m^2
S	17.094 m^2
b	10.180 m

Table 2. General Aircraft Navion Parameters (aerodynamics parameters)

Text	**Text**
$C_{l\beta}$	-0.074
C_{lp}	-0.41
C_{lr}	0.107
$C_{l\delta a}$	0.1342
$C_{l\delta r}$	0.118
$C_{n\beta}$	0.071
C_{nr}	-0.125
$C_{L\alpha}$	4.44
C_{Lq}	3.8
$C_{L\delta e}$	0.355
$C_{D\alpha}$	0.33
$C_{Y\beta}$	-0.564
$C_{Y\delta r}$	0.157
$C_{m\alpha}$	-0.683
C_{mq}	-9.96
$C_{m\delta e}$	-0.923
C_{np}	-0.0575
$C_{n\delta a}$	-0.00346
$C_{n\delta r}$	-0.0717

Longitudinal LQR control model is shown in Figure 1.

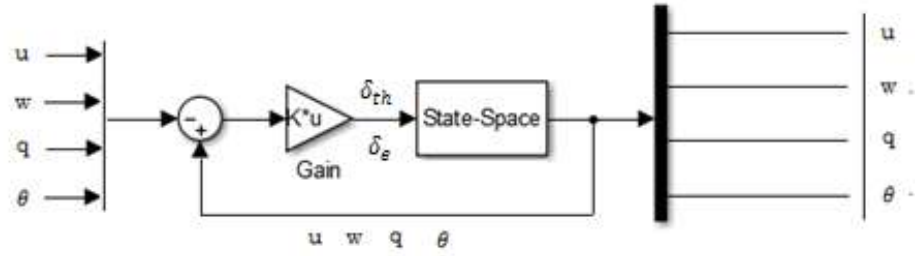

Figure 1. Longitudinal Control model

Lateral LQR control model is shown in Figure 2.

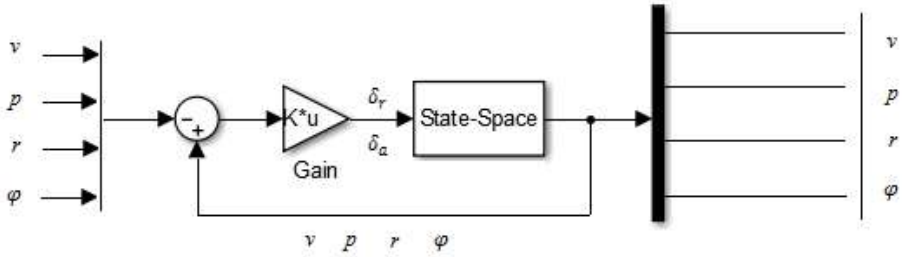

Figure 2. Lateral Control model

4. RESULTS

Matlab simulating program is used for designing and simulating the proposed controller. According to Figure 3 acceptable system response has been obtained. Side velocity has quickly reached the reference point. Roll rate response of system has been reached reference point shortly according to the Figure 4. Also, some disturbances have introduced in initial conditions. It is verified the output has behaved as desired.

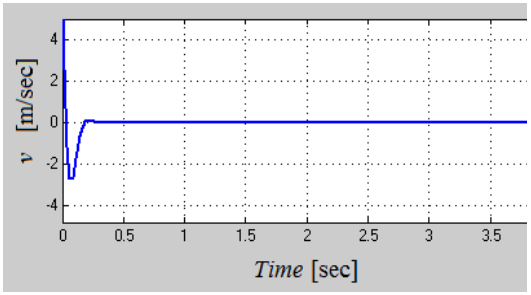

Figure 28. Response of system for side velocity

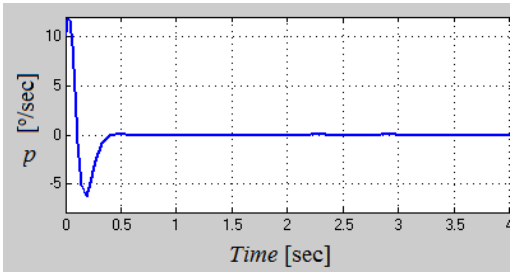

Figure 4. Response of system for roll rate

According to Figure 5, the speed of reaching the desired reference point is sufficiently successful for yaw rate system response. In Figure 6 response of system for roll angle has been reached the reference point enough quickly.

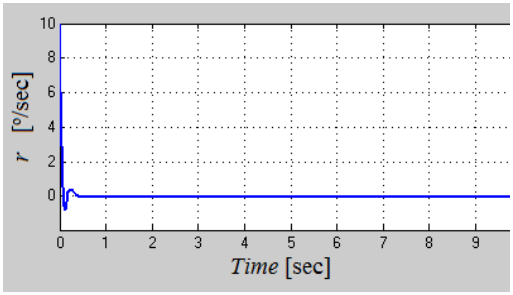

Figure 5. Response of system for yaw rate

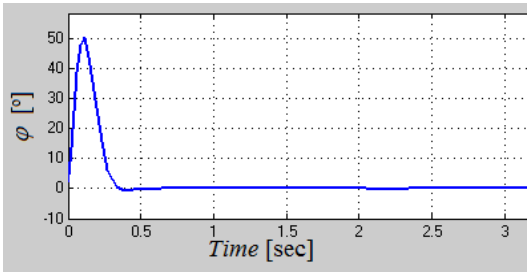

Figure 6. Response of system for roll angle

Following Figure 7 shows the response of system for axial velocity. Output reached the desired reference point immediately. Behavior of response of system for axial velocity is as desired. Figure 8 also shows the response of system for normal velocity which achieves the simulation requirements.

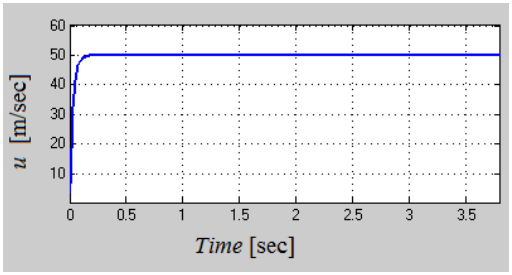

Figure 7. Response of system for axial velocity

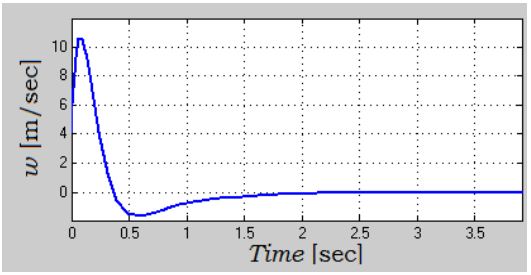

Figure 8. Response of system for normal velocity

Responses of system for pitch rate and pitch angle has shown in Figure 9 and Figure 10. Response reaches the desired reference point fast enough.

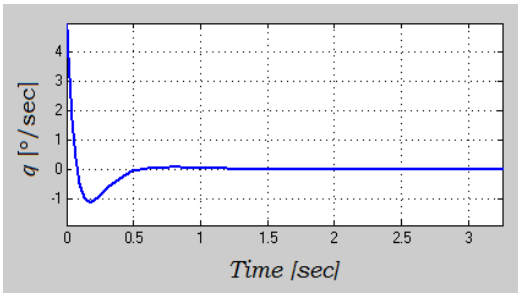

Figure 9. Response of system for pitch rate

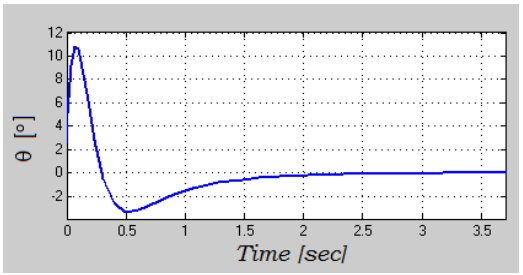

Figure 10. Response of system for pitch angle

5. CONCLUSION

In this study, trim state is optimized and the aircraft has been controlled successfully. It has been shown in this study that non-linear problems have successfully been solved by PSO. Achievement of response of system for LQR controller has been demonstrated according to the simulations. Performance of the system response has successfully been achieved. Performance of the controller has verified that response of system behaves as desired. The simulation results shows that output of the system have been verified by using system requirements.

REFERENCES

[1]. M. V, Cook., *Flight Dynamics Principles A Linear Systems Approach to Aircraft Stability and Control*, Butterworth-Heinemann, 2007.
[2]. R. Nelson, "*Flight Stability and Automatic Control*," McGraw-Hill, *1997*.
[3]. Zhong, J., Yi, G., & Wang, C.. "Adaptive flight control for extended trim state following", In Proc. of 27th Chinese Control and Decision Conference (CCDC), Qingdao, China, 2015 pp. 2265-2269.
[4]. J. C. Eberhart, J. Kennedy, "A New Optimizer using Particle Swarm Theory" in Proc. IEEE Int. Conf. in Micro Machine and Human Sciences, 1995, pp. 39-43.
[5]. R.L. Perez, K. Behdinan, "Particle Swarm Approach for Structural Design Optimization", *Computers & Structures*, vol. 85(19-20) pp.1579-1588, 2007.
[6]. M. S. Can, P. C. Besdok, "UAV Path Optimization for Minimum Fuel Consumption and CO2 Emission", 9th International Conference on Sustainable Energy Environmental Protection , Kayseri, Turkey, 2016 pp. 319-323.
[7]. M. S. CAN, P. C. Besdok, "Comparision Numerical Optimization Algorithms For Finding Less Risky And Safer 3D UAV Path", International Conference on Mathematics and Engineering , Istanbul, Turkey, 2017, pp.21.
[8]. M. Rhudy., "Analytical Determination of Trim Values for Nonlinear Fixed Wing Aircraft Models", AIAA Modeling and Simulation Technologies Conference, Washington, D.C., 2016.
[9]. D. M. Agostino, L. D. Eugene, S. B. Jon., "A General Solution to the Aircraft Trim Problem", AIAA Modeling and Simulation Technologies Conference and Exhibit South Carolina, 2007.
[10]. B. Chang, H. Kwatny, E. Ballouz, D. Hartman, "Aircraft Trim Recovery from Highly Nonlinear Upset Conditions", Proceedings of the 2016 AIAA Guidance Navigation and Control Conference pp. 1-19, 2016.

BIOGRAPY

Muharrem Selim CAN is a research assistant of Aviation Electrical and Electronics at Iskenderun Technical University in Turkey. He received his BSc degree in Electrical and Electronics Engineering from University of Pamukkale in 2010. He also received his MSc (2017) degree in Aviation Electrical and Electronics, at Institute of Natural Sciences at University of Erciyes. He is PhD student (PhD Candidate) in Aviation Electrical and Electronics from Erciyes University. His research fields are: Nonlinear Dynamical Systems and Control, Numerical Optimization, Intelligent Control, Signal Processing, Radar Systems, Microwave Circuits Design.

Hamdi Ercan received the B.Sc. and M.Sc. degrees from both Erciyes University, Kayseri, Turkey, in 2004 and 2007, respectively, all in Electronic Engineering. He received his Ph.D. degree in Electrical and Electronics Engineering at Erciyes University, Kayseri, Turkey in 2012. Since 2005, he has been a member of academic staff with Erciyes University, Faculty of Aeronautics and Astronautics. He has been an Associate Professor since 2018 at Erciyes University, Faculty of Aeronautics and Astronautics, Department of Avionics. His current research interests include avionics, microelectronics, current mode circuits, current conveyors and electronic circuit design.

Sezai Alper TEKIN was born in Kayseri, Turkey. He received the B. Engineering degree from Erciyes University, Kayseri, Turkey, in 2000, his M.S. degree from Nigde University, Nigde, Turkey, in 2005, and his Ph.D. in Electrical and Electronics Engineering at Erciyes University, Kayseri, Turkey in 2012. He is Associate Professor at Erciyes University, Faculty of Engineering, Department of Industrial Design Engineering. Since 2006, he has been a member of academic staff with Erciyes University, Engineering Faculty, Electrical and Electronics Dept., Kayseri, Turkey. His current research interests include free space optics, current mode circuits, current conveyors, electronic circuit design and solar cells.

ICENS 4TH INTERNATIONAL CONFERENCE ON ENGINEERING AND NATURAL SCIENCE
2-6 May 2018 KIEV UKRAINE

BER Performance of Precoded OSTBC MIMO System with and without Antenna Selection in Rayleigh Fading Channels

Asuman Savascihabes[1], Sezai Alper Tekin[2], Hamdi Ercan[3]

Abstract

In this paper, we address Precoded - Orthogonal Space Time Block Coding (OSTBC) in Multiple-Input Multiple- Output (MIMO) systems. Precoding transmission scheme that exploit channel state information (CSI) on the transmitter side of a MIMO system exploits channel information for increasing channel capacity, and bit – error performance with the absense of reducing hardware complexity. Whether it is impossible to have full CSI because of feedback delay at transmitter side of the communication system in practice, by using precoding technique with multipliying space-time codeword by a precoding matrix which is chosen from the codebook, and choosing an efficient codeword in order to improve the overall system performance, it is possible theoretically. Besides precoding technique, another efficient way to improve BER performance and capacity gain of the total system is antenna selection technique. By using antenna selection, a small number of RF chains, than the number of MIMO transmit antennas, are employed; and the cost related with the multiple RF modules is reduced. Besides, more diversity gain and better BER performance has been achieved without any addition RF module at the transmitter. Our simulation results demonstrate that, the behavior of precoded OSTBC outperforms the STBC without increasing any transmit power or any additional bandwidth requirement. Performing antenna selection for the STBC scheme achieves more gain in terms of BER performance over the precoding method in Rayleigh fading channels.

Keywords: *BER, CSIT, MIMO, OSTBC, Rayleigh Fading Channel, Precoding.*

1. INTRODUCTION

Compared to single-antenna systems, MIMO has benefits like higher capacity, better transmission quality in terms of bit-error-rate and outage capacity, improved user position estimation and MIMO gain which is obtained via spatial multiplexing or diversity. Besides MIMO has some well-known advantages which are defined by array gain and reduced interference due to multiple antennas at both transmitter and receiver. With the access of these advantages, in general systems a transmitter doesn't have direct access to its own channel state information and generally it is assumed that only the receiver can track the channel information. In this study we will address transmission techniques in order to obtain channel state information (CSI) at the transmitter. Exploiting this channel information it allows the increased capacity gain.

It is well-known that compared to a single antenna system, the channel capacity of a multiple antenna system with N_T tranmsit and N_R receive antennas can be improved by $\min(N_T, N_R)$ without any additional power or additional bandwidth. For fast data transmission speed in recent telecommunications, the MIMO systems are successfully deployed for networks such WiMAX [1-3].

Another important factor in communication systems besides capacity is the high-speed data transformation. MIMO has two options for this purpose: one is spatial-multiplexing and the other is diversity techniques. [4]. Transmit diversity improves the signal quality by transmitting the data through multiple antennas and receiving by single or multiple antennas. The most popular examples of transmit diversity include Alamouti code [5]. Receive diversity also used in wireless systems and within this technique the main point is all the receive antennas can achieve an independent copy of the same signal at receiver side. A block system of $N_R X N_T$ MIMO

[1] *Corresponding author: Nuh Naci Yazgan University, Department of Electrical and Electronics Engineering, Kayseri, Turkey. ahabes@nny.edu.tr*

[2] *Erciyes University, Department of Industrial Design Engineering, Kayseri, Turkey, satekin@erciyes.edu.tr*

[3] *Erciyes University, Department of Avionics, Kayseri, Turkey, hamdiercan@erciyes.edu.tr*

is shown in Figure 1 [6]. Besides, the cost related to the RF modules is reduced by means of optimum antenna selection and more diversity gain and better BER performance has been obtained with this technique.

This paper includes a brief definition of channel estimation at the transmitter in Section II, optimum antenna selection technique is defined in Section III and simulation results containing BER performances are shown in fourth Section, and finally Section V concludes the study.

2. CHANNEL AND SYSTEM MODEL

The received signal **y** can be written in a matrix form under time-invariant wireless channel **H**, for such a MIMO system as depicted in Figure 1

$$\mathbf{y} = \sqrt{\frac{E_x}{N_T}}\mathbf{H}\mathbf{x} + \mathbf{z} \qquad (1)$$

where **z** is a zero-mean circular symmetric complex Gaussian noise vector. The channel capacity (bps/Hz) when CSI is known to the transmitter is defined as:

$$C = \max_{T_r(\mathbf{R}_{XX})=N_T} \log_2 \det(I_{N_R} + \frac{E_X}{N_T \mathrm{N}_o}\mathbf{H}\mathbf{R}_{XX}\mathbf{H}^H) \qquad (2)$$

Here $\mathbf{R}_{XX}$ is auto-correlation matrix of x which is shown in (3).

$$\mathbf{R}_{XX} = E\{xx^H\} = \frac{E_X}{N_T}\mathbf{H}\mathbf{R}_{XX}\mathbf{H}^H + \mathrm{N}_o I_{N_R} \qquad (3)$$

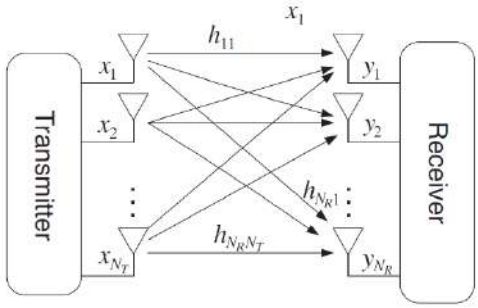

(a)

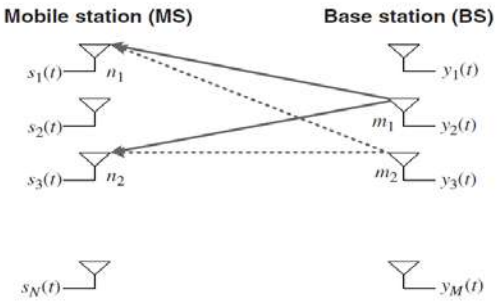

(b)

Figure 1. (a):MIMO System Block diagram [6].(b):Downlink MIMO System

a. Precoded OSTBC

For MISO system with N_T antennas the received signal $y \in C^{1XT}$ can be defined as:

$$\mathbf{y} = \sqrt{\frac{E_X}{N_T}}\mathbf{hWC} + \mathbf{z} \qquad (4)$$

Here, C denote a space-time codeword with a length of M,

$$\mathbf{C} = [\mathbf{c}_1\mathbf{c}_2 \cdots \mathbf{c}_T] \qquad (5)$$

where $\mathbf{C_k} = [\mathbf{c}_{k,1}\mathbf{c}_{k,2} \cdots \mathbf{c}_{k,M}]^T$, $k = 1,2,\cdots,T$ and $M \le N_T$. In the precoded OSTBC systems, the space-time codeword C is multiplied by a precoding matrix $\mathbf{W} \in \mathbf{C}^{N_T XM}$ choosen from codebook $\mathbf{F} = \{\mathbf{W_1}\mathbf{W_2}, \mathbf{W_3}, ..., \mathbf{W_L}\}$. The objective is to choose an appropriate codeword that improves the overall system performance such as channel capacity or error performance.

In Equation (4) the length of each vector is M, the probability of codeword error can be derived as follows: For a given channel h and precoding matrix W, we considered the pairwise codeword error probability and the upperboound of the pairwise error probability is given as in Equation (6) where ρ is the signal-to-noise ratio (SNR), given as $\rho = \frac{E_X}{N_o}$ and $\mathbf{E_{i,j}}$ is the error matrix between two codewords for a given STBC scheme.

Here in order to minimize pairwise error probability we need to maximize $\| \mathbf{hWE_{i,j}} \|_F^2$ term.

$$P_r(C_i \to C_j | \mathbf{H}) = Q\left(\sqrt{\frac{\rho \| \mathbf{hWE_{i,j}} \|_F^2}{2N_T}}\right) \le \exp\left(-\frac{\rho \| \mathbf{hWE_{i,j}} \|_F^2}{4N_T}\right) \qquad (6)$$

b. Optimum Antenna Selection

Multiple antennas and also MIMO can improve the system capacity and reliability of radio communication, howewer the multiple RF chains associated with multiple antennas are costly in terms of hardware, computational complexity and size. Antenna selection is low cost solution to reduce this problem. In this study we use optimum antenna selection in order to provide an additional performance improvement in terms of ergodic spectral efficiency for multiple communication systems:

$$\binom{N_R}{N_r}\binom{N_T}{N_t} = \frac{N_R!}{(N_R - N_r)!.N_r!} \cdot \frac{N_T!}{(N_T - N_t)!.N_t!} \qquad (7)$$

3. SIMULATION RESULTS

Monte-carlo simulations are performed in terms of Bit-Error-Rate in Rayleigh fading channel. For 2X1 Alamouti and precoded Alamouti BER vs SNR graphs is shown in Figure 2. From simulation results it is obvious that BER performance is improved with precoding for OSTBC system. Figure 3 represents ergodic spectral efficiency for antenna selection technique. By using antenna selection the higher capacity gain is available without any additional bandwidth at the receiver.

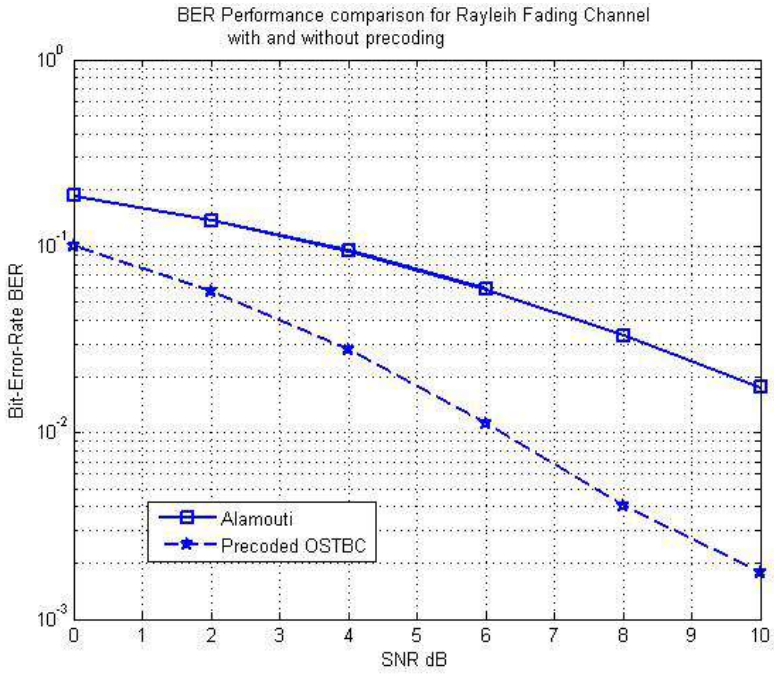

Figure 29. BER vs. SNRdB with and without precoding.

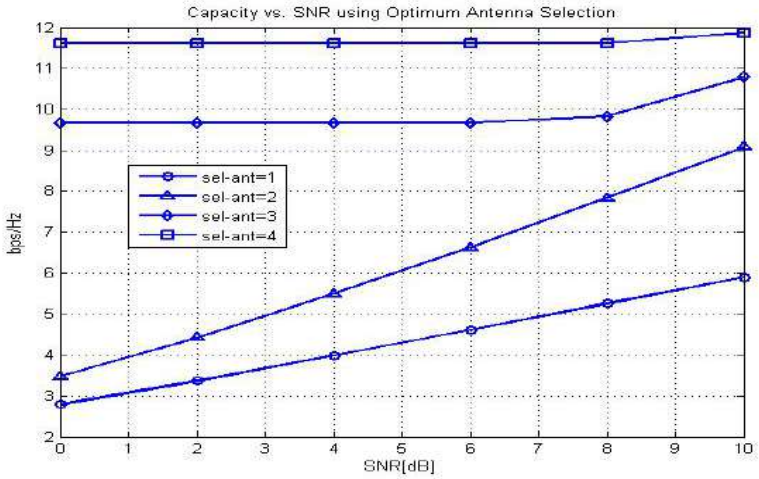

Figure 3. Spectral Efficiency vs. SNRdB using optimum antenna selection.

4. CONCLUSION

In this paper, we address Precoded - Orthogonal Space Time Block Coding (OSTBC) in Multiple-Input Multiple- Output (MIMO) systems. Precoding transmission scheme that exploit channel state information (CSI) on the transmitter side of a MIMO system exploits channel information for increasing channel capacity, and bit – error performance with the absence of reducing hardware complexity. Besides precoding technique, another efficient way to improve BER performance and capacity gain of the total system is antenna selection technique. By using antenna selection, a small number of RF chains, than the number of MIMO transmit antennas, are

employed; and the cost related with the multiple RF modules is reduced. Besides, more capacity gain has been achieved without any addition RF module at the transmitter. Our simulation results demonstrate that, the behavior of precoded OSTBC outperforms the STBC without increasing any transmit power or any additional bandwidth requirement. Performing antenna selection for the STBC scheme achieves more gain in terms of BER performance over the precoding method in Rayleigh fading channels.

REFERENCES

1. Paulraj, R. Nabar, and D. Gore, Introduction to Space-Time Wireless Communications, Cambridge University Pres, 2013.
[2] G. J. Foschini, Layered space-time architecture for wireless communication in a fading environment when using multi-element antennas, Bell Labs Tech. J.,1(2), 41-59.
[3] IEEE (2006) Std 802.16e™-2005. EEE Std 802.16™-2004/Corl-2005. Part 16: Air Interface for Fixed and Mobile Broadband Wireless Access Systems.
[4] G. D. Golden, C.J. Foschini, R. A. Valenzuela, and P.W. Wolniansky, Detection algorithm and initial laboratory result using V-BLAST space-time communication architecture, Electron. Lett., 35(1), 14-15, 1999.
[5] S.M. Alamouti, A simple diversity technique for wireless communications, IEEE Journal on Sel. Areas in Com., Vol. 16, No.8, pp.1451-1458, Oct,1998
[6] Y.S. Cho, J.Kim, W. Y. Yang, C.G. Kang, MIMO-OFDM Wireless Communications with MATLAB, Wiley-IEEE Press, 2010.

BIOGRAPHY

Asuman Savascihabes, received her B.Sc. and M.Sc. degree from both Erciyes University at 2005 and 2008 respectively and received her Ph.D. degree from Gazi University all in Electrical and Electronics Engineering specializing on Signal Processing and Telecommunications. Since 2014, she serves in the faculty of Electrical and Electronics Engineering Department of Nuh Naci Yazgan University as an assistant professor. Her main research areas lie in wireless communication systems and signal processing for wireless communications issues.

Sezai Alper Tekin was born in Kayseri, Turkey. He received the B. Engineering degree from Erciyes University, Kayseri, Turkey, in 2000, the M.S. degree from Nigde University, Nigde, Turkey, in 2005 and the Ph.D. in Electrical and Electronics Engineering from Erciyes University, Kayseri, Turkey in 2012. From 2006 to 2012 he was a member of academic staff with the Erciyes University, Engineering Faculty, Electrical and Electronics Dept., Kayseri, Turkey. Since 2012, he has been a member of academic staff with the Erciyes University, Engineering Faculty, Industrial Design Department, Kayseri, Turkey. His current research interests include free space optics, current mode circuits, current conveyors, electronic circuit design and solar cells.

Hamdi Ercan received the B.Sc. and M.Sc. degrees from both Erciyes University, Kayseri, Turkey, in 2004 and 2007, respectively, all in Electronic Engineering. He received his Ph.D. degree in Electrical and Electronics Engineering at Erciyes University, Kayseri, Turkey in 2012. Since 2005, he has been a member of academic staff with Erciyes University, Faculty of Aeronautics and Astronautics. He has been an Associate Professor since 2018 at Erciyes University, Faculty of Aeronautics and Astronautics, Department of Avionics. His current research interests include avionics, microelectronics, current mode circuits, current conveyors and electronic circuit design.

ICENS 4TH INTERNATIONAL CONFERENCE ON ENGINEERING AND NATURAL SCIENCE
2-6 May 2018 KIEV UKRAINE

Assessing Physical Properties of Denim Fabrics Including Wool/Elastane Dual-Core Yarns as Weft

Munevver Ertek Avci[1], Nida Yildirim[2], Huseyin Gazi Turksoy[3]

Abstract

Among all the textile fabrics, no other fabric has received such a wide acceptance as denim. The denim fabric has been used extensively by people of all ages, classes and genders. Denim is a hard wearing cotton twill fabric, traditionally woven with indigo dyed warp and white filling yarns. Its manufacture involves the same classical principles which have been followed since its creation, but technological advances have transformed it into a highly fashionable material. One of the technological advances in denim fabric is the using of various hybrid yarns in production stage. Hybrid yarn is a yarn structure developed to benefit from the properties of two or more different components at the same time. In this study, firstly, five different denim fabrics with different weave types and weft densities were produced by using innovative dual-core spun yarn (1st core-wool yarn, 2 nd core-elastane filament and cover fiber-cotton) as weft yarns. Then the elasticity and growth of fabric samples were measured and evaluated. The results indicated that the weft density and weaving type are significantly effective parameters for the elasticity and growth values of denim fabrics.

Keywords:, Dual-core Yarn, Wool Yarn, Elastane, Denim Fabric, Growth, Elasticity

1. INTRODUCTION

Denim is a hard wearing cotton twill fabric, traditionally woven with indigo dyed warp and white filling yarns. During the production of denim there is a variety of factors that can influence the performance of the garment, such as the containing material, yarn type, dyestuffs used and the washing treatment.

Jean consumers always demand increased comfort. Nowadays, stretchable denim fabrics are used widely in jean industries and the demand for these products is increasing day by day due to their wear comfort characteristics. Fabric stretch ability indicates the property of the fabric that facilitates the body part movements. The stretch requirements of a denim fabric can be determined from the typical values of stretch that are encountered during the actions of sitting, bending, or flexing of knees.

Various hybrid yarns which contain elastane filaments, are used in order to give elastic performance characteristics to denim fabrics [1-3]. The core-spun thread is a kind of hybrid yarns that generally manufactured at modified ring frame, by placing elastane to the center while thread is being produced out of cotton or other staple fibers. In the case of the “Dual-Core” yarns used in this study, two core threads (one of them is elastane filament) are fed into the center.

Using hybrid yarns which contain elastane in the weft, the warp or in both directions can be achieved with complete reliability. The major properties of the stretch denim depend upon the elasticity and dimensional stability. Elasticity can be defined, the ability of a fabric to return to its original length, shape, or size

[1] *Calik Denim R&D Center, Malatya, Turkey. munevver.ertekavci@calikdenim.com*
[2] *Corresponding author: Blacksea Technical University, Department of Textile, Clothing, Shoes and Leather, Trabzon,Turkey. nidayildirim@ktu.edu.tr*
[3] *Erciyes University, Department of Textile Engineering, Kayseri, Turkey.hgazi@erciyes.edu.tr*

immediately after the removal of stress/tension whereas the growth (permanent elongation) is the difference between the initial length before loading and after the relaxation period [4, 5].

This research presents a practical study of the influence of warp density and weaving type on elasticity and growth properties of denim fabric produced with dual-core spun yarn (1st core-wool yarn, 2 nd core-elastane filament and cover fiber-cotton) as weft and Ne 14 cotton yarn as warp.

2.MATERIALS AND METHODS

Five different denim fabric types with different weave types and weft density were produced by using Ne 18 dual-core spun yarn (1st core-wool yarn, 2nd core-elastane filament and cover fiber-cotton) as weft and Ne 14 cotton yarn as warp. Codes and production parameters of the denim fabric samples were summarized in Table1.

Table 1. Codes and production parameters of the denim fabric samples.

Code	Weaving Type	Weft Density (Picks/cm)
1	3/1 Z	20,5
2	3/1 Z	18,5
3	3/1 Z	22,5
4	1/1	20,5
5	2/2 Z	20,5

The elasticity and permanent elongation test of sample denim fabrics were measured according to ASTM D 3107 standard [6]. In the study, for each fabric sample, five tests were performed. The test samples were conditioned at least for 24 hours in an atmosphere of 20±2 ºC and 65±2% relative humidity in order to adjust humidity balance. Test results were also analyzed for significance in differences using one-way replicated ANOVA, and the means were compared by SNK tests at 0.05 level using the SPSS 13.0 statistical package.

3. RESULTS AND DISCUSSION

According to the ANOVA results, weft density was found to be statistically significant for the elasticity (p=0,000) and growth (p=0,000). Table 2, shows the SNK test results for elasticity and growth properties of denim fabric samples. In the interpretation of SNK results, abbreviations a, b, and c, represent factor level; factor levels that have the same letters are not different from each other at a significance level of 0.05 (Table 2). As can be seen from Table 2, the differences between weft density levels were found to be statistically significant for elasticity and growth. Also, as could be observed in Table 2, The weft density decreases cause increases in the elasticity levels as well as in the growth values. These results are supported by previous studies on denim fabric [7, 8].

Table 2. Effects of weft density and weaving type on elasticity and growth properties of denim fabrics, Student–Newman–Keuls test.

	Elasticity (%)	**Growth (2h) (%)**
Weft Density		
22,5	65,6a	8,0002a
20,5	78,1b	9,6002b
18,5	90,2c	10,4002c
Weaving Type		
1/1	28,2a	4a
2/2	64b	8b
3/1 Z	78,1c	8,3c

According to the ANOVA results, weaving type was found to be statistically significant for the elasticity (p=0,000) and growth (p=0,000). As can be seen from Table 2, the differences between weaving types were

found to be statistically significant for elasticity and growth. Denim fabric produced with 1/1 weaving type and 22,5 weft density shows the lowest elasticity and growth values.

As an additional property of denim, elasticity is used to achieve outstanding stretching performance for ultimate fit. On the other hand, while elasticity is a definitely desired property, growth is regarded as a real problem. Related with growth value of denim fabrics, dimensional stability and the preservation of stretch over the entire useful life, are the major problem of elastic denim garment.

The rate of elasticity to growth (permanent elongation) is given in Figure 1, in order to evaluate elasticity and growth together for different weft density and weave types. The best results were obtained from the 3/1 Z weaving type and 18,5 weft density in respect of Elasticty/Growth ratio.

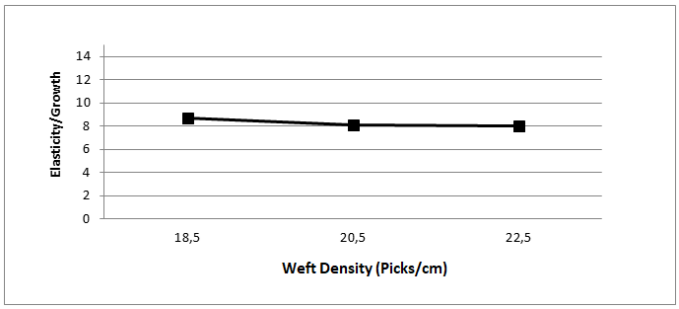

(a)

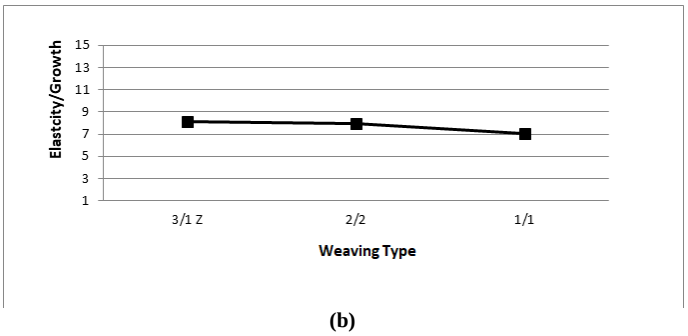

(b)

Figure 1. Weft density-Elasticity/growth (a), Weaving type-Elasticity/growth (b).

4. CONCLUSIONS

In this study, denim fabrics of different weft densities and weaving types by using dual-core yarns (containing wool and elastane cores) as weft yarn, were manufactured. The elasticity and growth properties of denim fabrics were tested and results were evaluated statistically. The elasticity and growth property of denim fabrics are affected by variation of weft density and weaving type. The weft density decreases cause increases in the elasticity levels as well as in the growth values of denim fabrics. While denim fabric produced with 1/1 weaving type shows the lowest elasticity and growth values, denim fabric produced with 18,5 weft density shows the highest elasticity and growth values. Furthermore, the best results from the point of the elasticity to growth ratio were obtained from the 3/1 Z weaving type and 18,5 weft density.

5. ACKNOWLEDGMENTS

We would like to thank the Research Center of the Erciyes University for financially supporting this research under contract FDK-2016-6700.

REFERENCES

[1] S. Kumar, K. Chatterjee, R. Padhye, R. Nayak, ‘‘Designing and development of denim fabrics: part 1 - study the effect of fabric parameters on the fabric characteristics for women’s wear’’, Journal Textile Science Engineering, vol.6,pp. 265, 2016.
[2] R. Nayak, R. Padhye, D.P. Gon, ‘‘Sewing performance of stretch denim’’, Journal of Textile and Apparel Technology and Management’’, vol. 6, pp. 1-9, 2010.
[3] B. Jaouachi, M.B. Hassen, M. Sahnoun, F. Sakli, ‘‘Evaluation of wet pneumatically spliced elastic denim yarns with fuzzy theory’’, The Journal of Textile Institute, vol. 101, pp.111-119, 2010.
[4] (2018) Textile Glossary, [Online]. Available: http://www.textileglossary.com/terms/elasticity.html.
[5] H. K. Kaynak, ‘‘Optimization of stretch and recovery properties of woven stretch fabrics’’, Textile Research Journal, vol. 87(5), pp. 582–592, 2017.
[6] Standard Test Methods for Stretch Properties of Fabrics Woven from Stretch Yarns, ASTM D3107 – 07, 2015.
1. Cataloglu, ‘‘Elasticity and permanent deformation properties of the denim fabrics with elastane mixtures’’, M. Turkish Thesis, Ege University, Institute of Sciences, 2007.
[7] O. G. Ertas, B. Zervent Unal and N. Celik, ‘‘Analyzing the effect of the elastane-containing dual-core weft yarn density on the denim fabric performance properties’’, The Journal of The Textile Institute, vol. 107, no. 1, pp. 116–126, 2016.

ICENS 4TH INTERNATIONAL CONFERENCE ON ENGINEERING AND NATURAL SCIENCE
2 - 6 May 2018 KIEV UKRAINE

Usability of Kinect Camera on Outdoor Conditions for Agricultural Mobile Robots

Ilker Unal,[1], Salih Sozer[1] Onder Kabas[1]*

Abstract

Agricultural robotics is a rapidly developing field of study and it has revolutionized many aspects of agricultural applications. In many applications, robots need to navigate through unknown environments to achieve their goals. For this reason, mobile robots require a lot of data for which to localize and navigate themselves to entering the environment. State of the art agricultural robot navigation systems uses expensive sensor systems such as laser range finders and GPS receivers for accurate perception of the environment. Nowadays, researchers are looking for cheaper solutions instead of using expensive systems for agricultural mobile robots. At this point, Microsoft Kinect, originally developed for the Xbox 360 video game console, has literally invaded the electronics market and now reaching into robotics. Combining the imaging system of the Microsoft Kinect with the sensing techniques of the human eye has led to a low-cost, high-quality 3D camera that could be used in agricultural mobile robots. Both indoor and outdoor conditions, the depth camera of Kinect can also be used to navigate environments where robots can't take advantage of GPS. This is invaluable for use in obstacle avoidance and navigation for agricultural mobile robots. This article offers an overview of a set of experiments realized in literature with a Microsoft Kinect Camera, in order to assess its potential for navigation applications of agricultural mobile robot

Keywords: Kinect camera, mobile robot, image processing, agricultural mechanization

1. INTRODUCTION

The Microsoft Kinect sensor is a peripheral device (designed for XBox and Windows PCs) that functions much like a webcam (Figure 1). However, in addition to providing an RGB image, it also provides a depth map. Meaning for every pixel seen by the sensor, the Kinect measures distance from the sensor. Recently, due to the properties of the Kinect camera, it has begun to be used extensively in image processing applications. Image processing plays more and more important role in intelligent systems such as autonomous vehicles, surveillance, and so on. Most of those image processing technologies are based on an RGB camera, which often suffers from light condition, occlusion, high computing complexity, etc. [1].

Figure 1. Kinect Camera

In November 2010 Microsoft introduced the first version of the Kinect RBG-D camera, the Kinect 1 for the Xbox 360 video game console [2]. Designed to be positioned below or above the display, it enabled the users to interact with the system through body and hand motion without holding or wearing sensors. Both the RGB and depth images created had a resolution of 640x480 pixels. The first software release to use the Kinect 1 with the computer, Kinect 1 for Windows, followed in December of the same year. This was the fist time computer vision had played such a great role in a mass-market product intended for consumer use [3]. The first generation

[1]* *Corresponding author: Akdeniz University, Technical Science Vocational School, 07070, Antalya, Turkey.*
ilkerunal@akdeniz.edu.tr

sensor was a structured light camera, but it has been replaced in 2013 by the second generation that instead works by a completely different principle, being a Time-Of-Flight (ToF) camera [4].

The commercial availability of Kinect-style RGB-D sensors have created a great excitement in robotics research due to their low cost and excellent indoor performance. Already a host of software hacks, experiments and algorithms have been reported on the uses of Kinect for robot perception, 3D mapping and human-robot interactions. Till now, most of the robotics activity centered around kinectstyle sensors is for indoor applications. For outdoor off-road type applications, it is still quite difficult to envision the use of Kinect due to its various limitations. This is especially true for applications that require agile operation and long range under varying lighting conditions. Hence, there is almost no mention of Kinect for outdoor applications. Also, since most of such applications are envisioned for high-end specialized customers such as military and automotive, the high cost of competing technologies such as laser scanners and time-of-flight cameras is not considered as a major disadvantage [5]. In this paper, the use of the new generation of the Kinect device has been investigated for outdoor navigation and offers an overview of a set of experiments realized in literature with a Microsoft Kinect Camera, in order to assess its potential for navigation applications of agricultural mobile robot.

1.1 Comparison of First- and Second-Generation Kinect Models

Figure 2 [6] tabulates the hardware specifications of the Kinect models. Note that despite the low spatial resolution that usually plagues ToF cameras, both sensors have similar spatial resolutions. The second-generation Kinect has a larger field of view, and therefore, it does not require a tilt motor. Beyond the inherent advantages of time-of-flight technology, the second-generation Kinect also boasts a higher depth resolution, though this has not yet been verified.

Comparing the Different Kinect Generations

	1st Generation Kinect	2nd Generation Kinect
Color resolution/rate	1280x960 @ 12 Hz *or* 640x480 @ 30 Hz	1920x1080 @ 30 Hz
Infrared resolution/rate	640x480 @ 30 Hz	512x424 @ 30 Hz
Depth resolution/rate	320x240 @ 30 Hz	512x424 @ 30 Hz
Depth range*	0.4 m – 3.0 m *or* 0.8 m – 4.0 m	0.5 m – 4.5 m
Depth sensing technology	Structured light	Time-of-flight
Field of view (horizontal)	58°	71°
Mic array	4 elements	4 elements
Tilt motor	±27°	none

* Reliable range; additional range possible, depending on conditions

Figure 2. Hardware specifications of the first- and second-generation Kinect models

The new Kinect uses time of flight to obtain depth. This technique is resistant to ambient light, allowing the new Kinect to be used outdoors. However, when the scene is too bright, the imaging sensor saturates and all information is lost. In outdoor experiments, the time-of-flight Kinect outperforms the old structured light Kinect.

2. LITERATURE SURVEY

Zhu and Tang [1] combined a ToF camera with an RGB camera and solve the image registration problem based on the pinhole camera model (Figure 3). Researchers have proposed a novel method to collect Kinect-comparable RGB-D outdoor image using a ToF camera and an RGB camera. They solved the image registration problem which is important to fuse two cameras based on the pin-hole camera model. A concise theory and elegant model was proposed by the researchers.

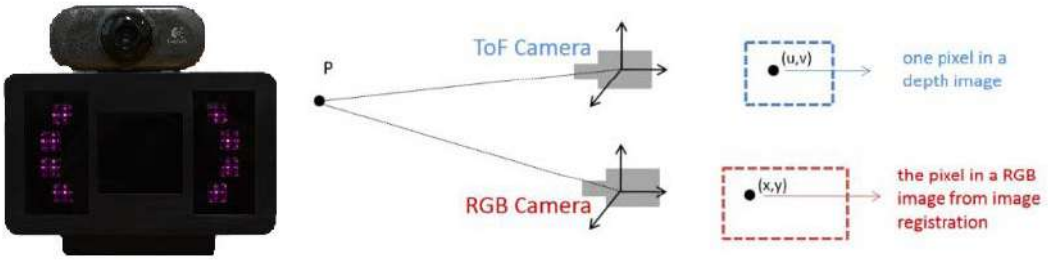

Figure 3. Combining a TOF camera with a RGB camera and the process of image registration

Francis et al. [7] has used a ToF-camera as a 3D vision sensor for autonomous mobile robotics (Figure 4). The aim of this paper was to deploy a time-of-flight (ToF) based photonic mixer device (PMD) camera on an Autonomous Ground Vehicle (AGV) whose overall target is to traverse from one point to another in hazardous and hostile environments employing obstacle avoidance without human intervention. 3D sensor was selected for their work, which is based on the photonic mixer device (PMD) technology that delivers a range and intensity data with low computational cost as frame rate. Researchers said that this camera system delivers absolute geometrical dimensions of obstacles without depending upon the object surface, distance, rotation or illumination and it is rotation-, translation- and illumination-invariant. Also, they said that RGBD cameras (e.g., Kinect, Asus Xtion, Carmine) have been widely used in object recognition and mobile robotics applications. They reported that these RGBD cameras cannot operate in outdoor environments. In this study, first generation Kinect camera was used.

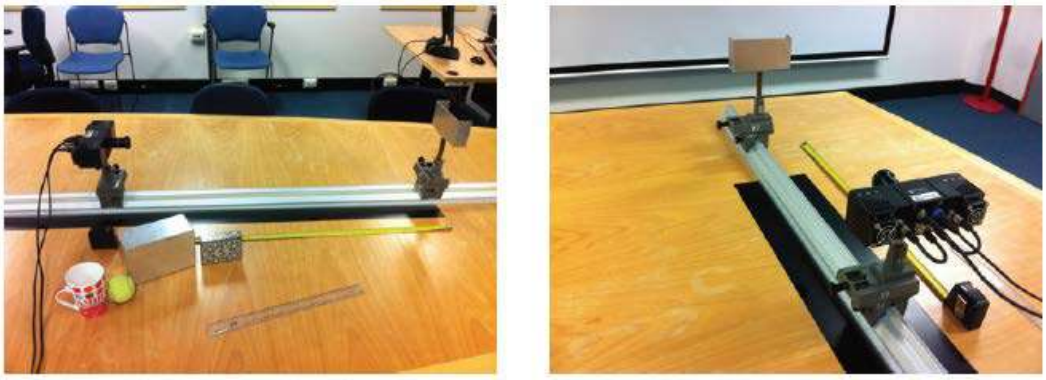

Figure 4. Experimental setup for the study

Seggers [2] explored the different available methods for the tracking of people in outdoor environments, with the aim to use this knowledge to propose a method that is optimized for this task (Figure 5). This research evaluated the performance of the HOG descriptor on both the colour and infrared images produced by the Kinect 2 for Windows in various lighting conditions. It was shown that the performance was higher in all conditions when using the infrared images. Furthermore, the algorithm was extended with a depth filter using

the depth data of the Kinect 2. This improved the algorithm significantly by reducing the number of false positives, resulting in a feasible solution for outdoor person tracking.

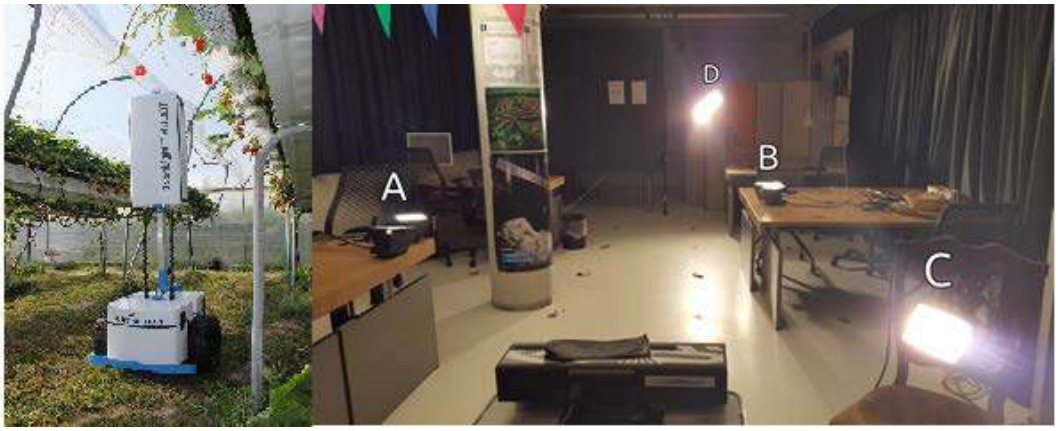

Figure 5. Hortimotion and overview of the study.

Pagliari et al.[8] has investigated the use of the new generation of the Kinect device for outdoor navigation, with the aim to create an integrated low-cost GNSS and photogrammetric navigation solution (Figure 6). The new Kinect has been advertised as capable of acquiring data even outdoor, under direct sunlight, so it is important to evaluate the expected accuracies and possible sources of error. The depth measurement accuracy of the Kinect v2 sensor has been evaluated outdoor, considering the depth response on a shaded planar surface. From the performed calibration procedure it comes out that Kinect v2 can acquire depth information with the same level of accuracy that characterizes indoor measurements.However, the data acquired outdoor are noisier. In order to evaluate the effect of the reflective properties of the emitted signal on the different surfaces a panel with square samples of 0.2 m of different materials has been realized. The point cloud generated from the Kinect has been compared with the reference scan acquired with a Leica MS60 multistation. The procedure has been repeated indoor and outdoor (in shaded conditions) obtaining in both cases differences of the order of 0.01 m, for all the considered materials. From this analysis, it comes out how the Kinect v2 can be used indifferently indoor or outdoor in shaded conditions. Of course, reflective surfaces can cause troubles in both cases. Further investigations are required when the framed object is exposed to direct sunlight radiation.

Figure 6. The cart used for the experimental test with all the instruments installed on it

Csaba et al [9] explained that the differences between Kinect and Structured Lighting Sensor in robot navigation (Figure 7). Two types of sensors were tested in the study. The Kinect sensor can sense bigger area, and the sensing is more accurate then the structured lighting sensor. Researchers said that the Kinect sensor was not suitable for outdoor using. But, First generation Kinect camera was used in this study.

Figure 7. The robot vehicle with Kinect sensor, control computer and embedded system.

Robledo et al [10] has presented the results of an experimental test that applies a low cost 3D sensor, i.e. a Kinect camera, for the perception of the terrain quality for the synthesis of a safe path. In this study, The 3D images are processed for generating a local 3D map, in front of the bicycle (Figure 8). The real time processing is based on a Piece Wise Multi-Linear (PWML) approximation of the 3D surfaces. The PWML patches are classified for inferring the traversability of the terrain. In their application the main goal of the scan matching process is for providing information for estimating the attitude of the platform, in combination with the angular velocities provided by the IMU sensor.The results have show that the approach is adequate for solving the problem and it is also applied in real-time at the expense of low processing cost.

Figure 8. Full view of the studied platform

Zhu et al. [11] were proposed a simple obstacle detection method based on fusion of depth and infrared image. They reported that a simple outdoor environment obstacle detection method based on information fusion of depth and infrared. The experiments showed that the method can identify the obstacle area accurately and it is not easy to be affected by the factors of light condition and intensity. Furthermore, better robustness is achieved. Hence, it can provide reliable data for intelligent robot. The main processes of obstacle detection in this study are as follows. Firstly, the areas to be detected are segmented by the mean-shift algorithm. Secondly, gradient calculation is carried out to highlight the edge information of the object. Finally, the obstacle can be detected by using edge detection or other methods and fusing infrared and depth information. The method proposed in the paper can solve the problems of the accuracy and robustness of obstacle detection of mobile robot and intelligent vehicle in complex environment. Blocck schema of the study was shown in Figure 9.

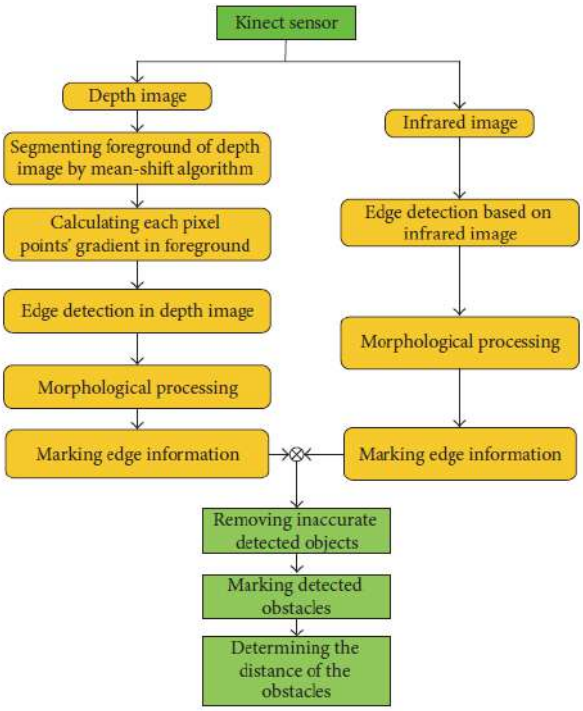

Figure 9. Block schema of the study

Benavidez and Jamshidi [12] have presented the framework for the navigation and target tracking system for a mobile robot. Navigation and target tracking were to be performed using a Microsoft Xbox Kinect sensor which provides RGB color and 3D depth imaging data to an x86 based computer onboard the robot running Ubuntu Linux. A fuzzy logic controller to be implemented on the computer was considered for control of the robot in obstacle avoidance and target following. Data collected by the computer was to be sent to a server for processing with learning-based systems utilizing neural networks for pattern recognition, object tracking, long-term path planning and process improvement. An eventual goal of this work was to create a multi-agent robot system that is able to work autonomously in an outdoor environment. Fuzzy logic control of robot in target tracking mode was shown in Figure 10.

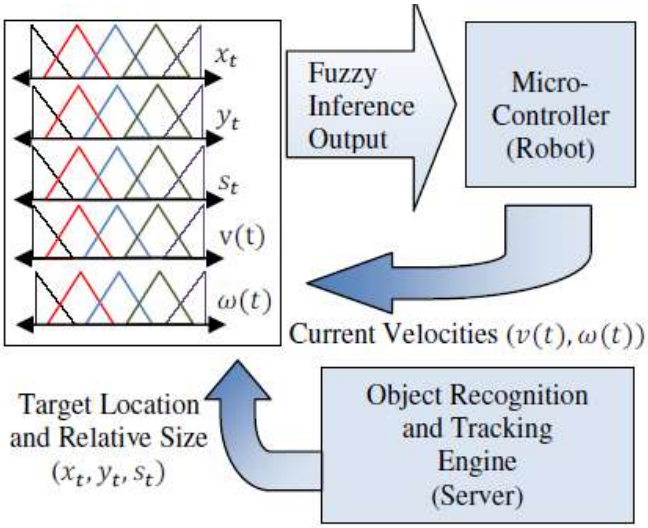

Figure 10. Fuzzy logic control of robot in target tracking mode

3. DISCUSSION and CONCLUSION

In literature, there are many Kinect Camera based image processing application. Many of them are related to the indoor applications. In literature survey section, we showed some Kinect camera based indoor and outdoor applications. Some of them was reported that Kinect camera can not use in the sunlight conditions. But these researchers were used first generation Kinect Camera in their studies. First generation Kinect Camera was not suitable for outdoor conditions. On the other hand, second generation Kinect Camera can suitable for outdoor applications. Because, second generation Kinect Camera proved to be two times more accurate in the near range and even ten times more accurate. One of the main limitations of the first generation Kinect was the total blindness in the presence of sunlight. This problem was due to the fact that the first generation Kinect estimate depth by triangulating the position of an infrared pattern of points it projects on the scene. Since sunlight also contains the infrared wavelength used in the first generation Kinect pattern, the first generation Kinect cannot recognize the pattern if some sunlight is present because the scene is filled with that infrared wavelength. The second generation Kinect is a completely different device based on the ToF technology. The basic operating principle is the one of continuous wave ToF sensors, i.e., an array of emitters sends out a modulated signal that travels to the measured point, gets reflected and is received by the CCD of the sensor. The sensor acquires a 512 × 424 depth map and a 1920 × 1080 color image at 15 to 30 fps depending on the lighting condition, since the sensor exploits an auto-exposure algorithm. For this reason, second reason second generation Kinect can suitable for outdoor robot navigation applications.

REFERENCES

[1]. X. Zhu and S. Tang. “A Novel Method To Collect Kinect-Comparable RGB-D Outdoor Image”. Global Perspectives on Artificial Intelligence (GPAI), vol. 3, pp. 19–22, 2015.
[2] S. Ruben. “People Tracking in Outdoor Environments Evaluating the Kinect 2 Performance in Different Lighting Conditions”. Bachelor thesis, University of Amsterdam, Faculty of Science, 2015.
[3] J. Ballester and C. Pheatt. “Using the Xbox Kinect sensor for positional data acquisition”. American Journal of Physics, vol:81, pp. 71–77, 2013.
[4] H. Beiping and Z. Wen. “Fast human detection using motion detection and histogram of oriented gradients”. Journal of Computers, vol. 6(8), pp. 1597-1604, 2011.
[5] S. M. Abbas and A. Muhammad, "Outdoor RGB-D SLAM Performance in Slow Mine Detection," Robotics, Proceedings of ROBOTIK 2012, 7th German Conference on, pp. 1-6, 2012.
[6] A. Kadambi., A. Bhandari, R.Raskar. *3D Depth Cameras in Vision: Benefits and Limitations of the Hardware.* In: Shao L., Han J., Kohli P., Zhang Z. (eds) Computer Vision and Machine Learning with RGB-D Sensors. Advances in Computer Vision and Pattern Recognition. Springer, Cham, 2014.
[7] S.L.X. Francis, G. S.G. Anavatti, M. Garratt, H. Shim. “A ToF-camera as a 3D Vision Sensor for Autonomous Mobile Robotics”. International Journal of Advanced Robotic Systems, vol. 12(156), pp. 1-15, 2015.

[8] D. Pagliari, L. Pinto, M. Reguzzoni, L. Rossi. “Integration of Kinect and Low-Cost Gnss for Outdoor Navigation”. The International Archives of the Photogrammetry, Remote Sensing and Spatial Information Sciences, Volume XLI-B5, 2016 XXIII ISPRS Congress, 12–19 July 2016, Prague, Czech Republic.
[9] G. Csaba, L. Somlyai, Z. Vámossy. “Differences Between Kinect and Structured Lighting Sensor in Robot Navigation”. SAMI 2012 10th IEEE Jubilee International Symposium on Applied Machine Intelligence and Informatics • January 26-28, 2012, Herlany, Slovakia.
[10] A. Robledo, S.Cossell, J. Guivant. “Outdoor Ride: Data Fusion of a 3D Kinect Camera installed in a Bicycle”. Proceedings of Australasian Conference on Robotics and Automation, 7-9 Dec 2011, Monash University, Melbourne Australia.
[11] Y.Zhu, B. Yi, T. Guo. “A Simple Outdoor Environment Obstacle Detection Method Based on Information Fusion of Depth and Infrared”. J. Robotics, vol. 1, pp. 1-10, 2016.
[12] P. Benavidez and M.Jamshidi. “Mobile Robot Navigation and Target Tracking System”. In Proceedings of 2011 6th International Conference on System of Systems Engineering: SoSE in Cloud Computing, Smart Grid, and Cyber Security, 27-30 June 2011, New Mexico, USA.

ICENS 4TH INTERNATIONAL CONFERENCE ON ENGINEERING AND NATURAL SCIENCE
2 - 6 May 2018 KIEV UKRAINE

Design of Low Power 6-Bit DACs using 180nm CMOS Technology

Selin Tastekin[1], Merve Helvaci[2], Ali Tangel[3]

Abstract

In this paper, high speed digital-to-analogue converter architectures, which are highly in demand in today's wireless communication systems, are briefly addressed. Two of the most popular DAC architectures, which are R-2R ladder network and charge scaling based are focused on and compared in this study. For this purpose, a 6-bit R-2R DAC and a 6-bit charge scaling DAC using split array are designed and simulated in TSMC 180nm CMOS process. Since the primary active element is OPAMP in designing DACs, a high performance OPAMP circuit is also designed and proposed in this work. The simulation results include DNL/INL of 0.028/-0.53 LSB, average power of 6.54mW at conversion rate of 2 GS/s for the proposed R-2R DAC implementation without opamp buffer, while DNL/INL of 0.013/-0.27 LSB, average power of 375µW at conversion rate of 10 MS/s for a conventional charge scaling DAC implementation with ±2.5V power supply voltage. Tanner Tools Pro platform is used for design and simulation. However, post layout simulations have not been completed yet but are planned as a near future work.

***Keywords*:** R-2R Ladder network, Charge Scaling DAC, DNL, INL, CMOS Data Converters, Mixed Signal VLSI

1. INTRODUCTION

High resolution analogue to digital converters (ADCs) and digital to analogue converters (DACs) with high speed are highly in demand in today's wireless communication systems due to rapid change in bandwidth especially for mobile communications [1], [2]. The performance of a digital to analogue converter depends on the circuit architecture. There are different types of DAC architectures, which are resistor string, R-2R ladder networks, charge scaling, current steering, and segmented current steering [1]. The important design parameters are conversion rate, linearity measures (INL, DNL), power consumption, layout area, resolution and spurious free dynamic range (SFDR). Most of the DAC architectures unfortunately suffer from inevitable noise and glitch problems. Also, resolution level is limited due to limited matching and linearity performance of the basic device elements such as resistors and capacitors [3]. Moreover, the speed performance can sometimes be increased by reduced feature size of the design technology. However, the trade –off between power and speed is well-known reality in VLSI design of data converters. Therefore, each DAC architecture has its own advantages and disadvantages in terms of design parameters mentioned above.

Charge scale DAC operation is based on binary dividing of the total charge applied to a capacitor array [3]. In this method, switch-induced errors can be cancelled, and offset cancelation of the OPAMP used is possible. Typical examples of DACs based on capacitor split array are presented in [3] and [4]. Different types of charge scaling techniques are addressed, and reduction of required total area of capacitor to achieve high resolution is reported in [3]. A similar design example is also presented in this study for comparison purpose. The charge scaling technique has feature of lower power consumption and glitch, but lower speed performance when compared to other architectures.

[3]*Corresponding author: Kocaeli University, Department of Electronics and Communication Engineering, 41380, Izmit/Kocaeli, Turkey. atangel@kocaeli.edu.tr*

[1] *Author: Kocaeli University, Department of Electronics and Communication Engineering, 41380, Izmit/Kocaeli, Turkey. selintastekin96@hotmail.com*

[2] *Author: Kocaeli University, Department of Electronics and Communication Engineering, 41380, Izmit/Kocaeli, Turkey. mervehelvaci95@gmail.com*

On the other hand, binary scaled converter, on which the array signal is current, may have large value resistors especially for MSB resistor. This technique is simple and very popular but more prone to resistor mismatch and especially glitch problems. The well-known suggestion is to use R-2R ladder network instead to minimize resistor mismatch effects. In this method, current ratio is reduced, but the glitch problem and lower speed are the main disadvantages of this technique. However, a low power, highly linear, low glitch effect and high performance implementation of a 6-Bit R-2R DAC implementation is realized in 180nm CMOS technology and proposed in this study.

The most preferred DAC architecture is the current steering technique. This technique is preferred for high speed applications, and no output buffer is needed to drive resistor loads due to high current drive inherent in the system. However, it requires precision current source implementations, large layout area, and more prone to errors due to switching. There are plenty of example works that can be reached in the literature such as [5]-[14]. The lowest feature size (28nm) 6-Bit DAC implementation having conversion rate of 7GS/s is reported in [5]. The fastest and the latest 6-Bit DAC implementation in the literature is [15] which has 20GS/s speed performance and 136mW power consumption in 65nm CMOS technology. This design advertises and proposes a time-interleaved DAC with full-binary Sub-DACs to achieve such a high speed performance.

The organization of this paper is as follows: Section 2 describes the proposed R-2R DAC circuit whose simulation results are also given in the same section. Similarly, Section 3 describes the design and simulation steps of the capacitor split array based charge scale DAC circuit. Section 4 compares briefly the obtained simulation results of the two designs in this study, and also compares one of them which is the proposed R-2R DAC with some other 6-bit DAC implementations published in the literature. Finally, Section 5 concludes the work and presents the future works planned in the near future.

2. DESIGN AND SIMULATIONS OF THE PROPOSED R-2R DAC

The R-2R DAC circuit proposed includes two cascaded inverters at the front end serving as input buffer circuit for the logic inputs. Therefore, the logic inputs have very high input resistance and also the inputs are isolated from the resistor ladder network as shown in Figure 1. The aspect ratios for the inverter transistors are selected as (W/L)n=2.5µm/0.18 µm while (W/L)p=7.5µm/0.18 µm. The resistor ladder network values are R=3K and 2R=6K. The buffer OPAMP schematic designed is depicted in Figure 2. This circuit has very high speed performance if no buffer OPAMP is included. However, most of the cases, an OPAMP buffer is preferred at the DAC outputs to improve the driving capability.

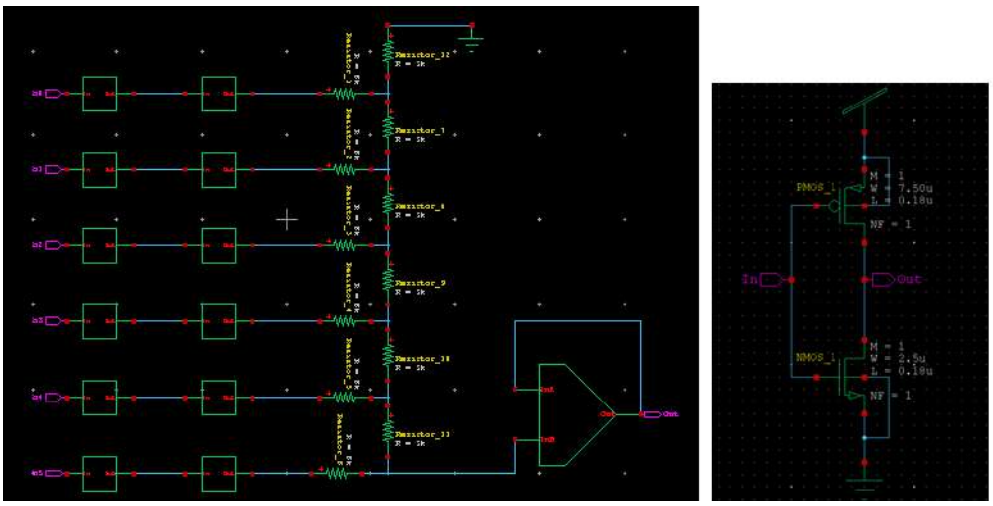

Figure 1: a) Schematic of the R-2R DAC Circuit b) The Schematic of the Inverter Block

In fact, it is difficult to design an OPAMP with a rail to rail input common mode range [4]. For the time being, a high performance OPAMP having a gain bandwidth product (GBW) of 100 MHz is designed and placed at the output although this attempt degraded the speed performance as expected. The simulation results are taken

for both cases here. During design and simulation, Tanner Tools Pro. Platform is used and the design technology is TSMC 0.18 µm CMOS process. The transient simulations shows 2GS/s conversion rate with acceptable level glitches observed as shown in Figure 3.

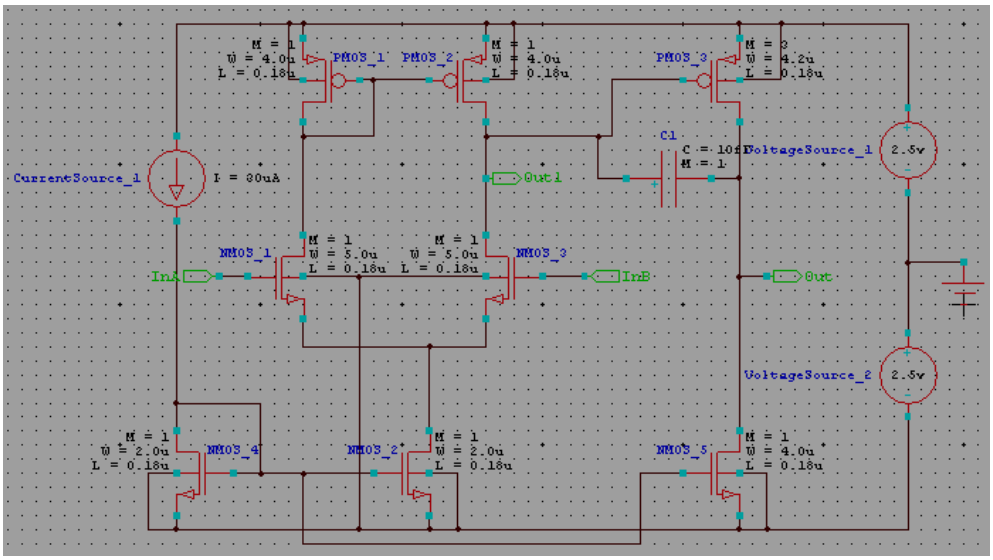

Figure 2. Schematic of the buffer opamp

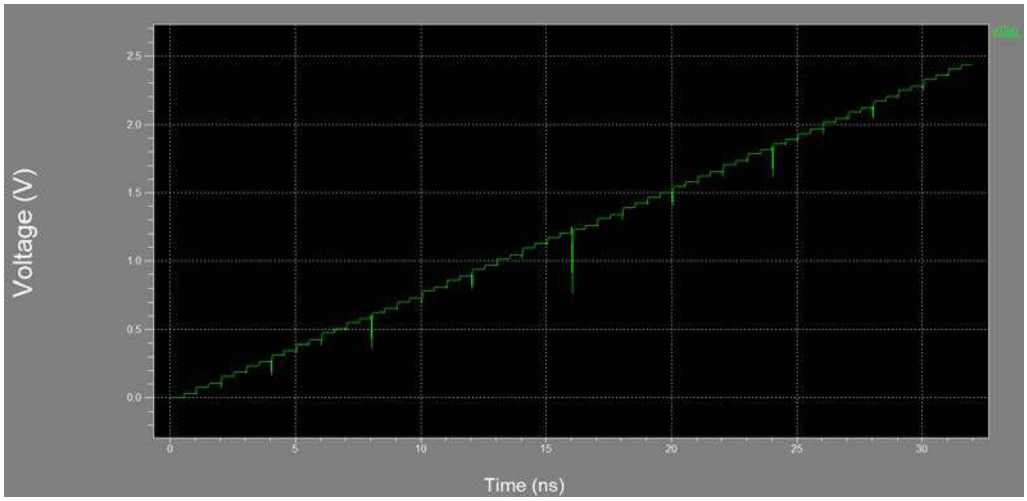

Figure 3. Transient Simulation Results of the R-2R DAC at Sampling Rate of 2 GS/s (without buffer opamp)

The conversion rate of the proposed R-2R DAC including the buffer OPAMP is only 100 MS/s currently. Therefore a higher speed buffer OPAMP design is needed as a future work. The power transient analysis is done for both cases, with and without buffer OPAMP at the output. Figure 4 shows the instantaneous power transient result at 1 GS/s conversion rate. Maximum, minimum and average power calculations are done from the transient plot and added to the figure as seen. The average power is 3.47 mW without output buffer. This average power reaches up to 6.54 mW at 2GS/s rate. An average power consumption of 1.4 mW is observed including the output buffer OPAMP at 10 MS/s rate. The linearity measures include 0.72 LSB of INL and -0.53 LSB of DNL. Therefore, the proposed DAC circuit can be considered as a highly linear converter without missing codes even at very high speeds. The linearity measures are taken at 1GS/s rate and the corresponding

linearity plots with respect to input codes are shown in Figure 5 and Figure 6. The performance summary of the proposed R-2R DAC is tabulated in Table 1.

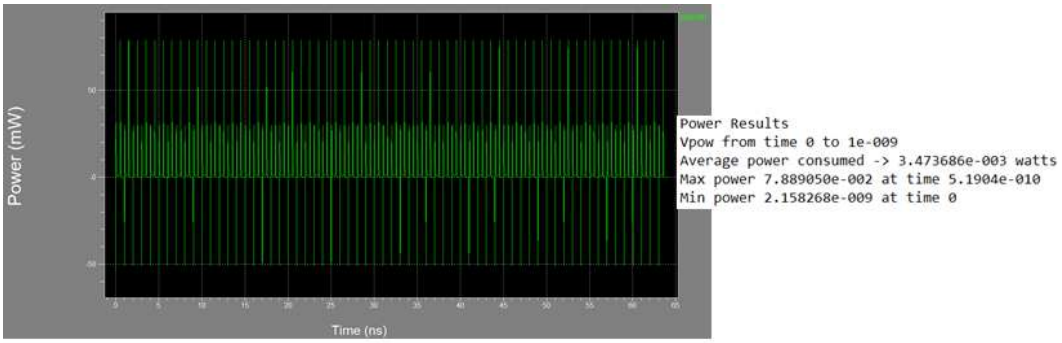

Figure 4. Power Transient Analysis Results of the R-2R DAC at 1 GS/s Sampling (without buffer opamp)

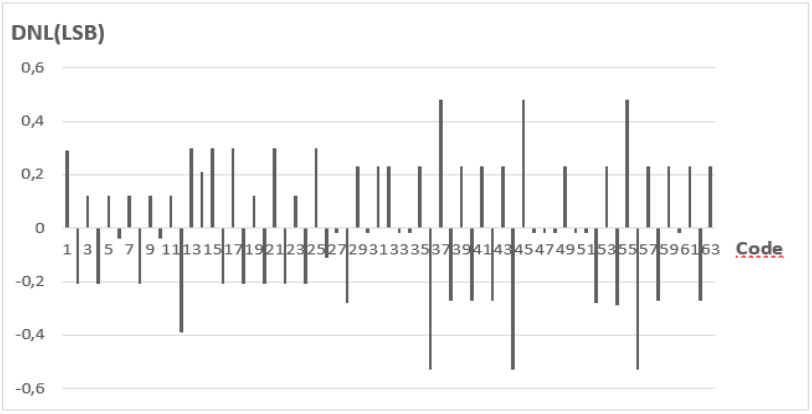

Figure 5. DNL Plot of the R-2R DAC Implementation

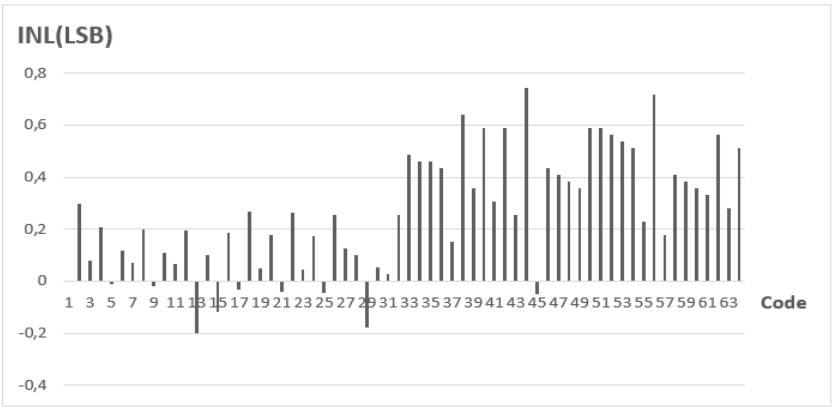

Figure 6. INL Plot of the R-2R DAC Implementation

Table 1. Performance Summary of the R-2R DAC

Process	180nm CMOS
Resolution	6-Bit
Conversion Rate	100 MS/s (with opamp buffer), 2GS/s (without buffer)
INL/DNL	0.72/-0.53 LSB
Power Supply	2.5V
Average Power	595 µW (at 1 MHz with buffer), 1.4mW (at 10 MHz with buffer), 3.47mW (at 1GS/s without opamp buffer)

3. DESIGN AND SIMULATIONS OF CHARGE SCALING DAC

As a second part of this study, a charge scaling DAC using split array technique is designed. The schematic of the circuit includes array capacitors, a buffer OPAMP at the output and analogue switches as seen in Figure 7. This circuit has a traditional type of architecture as can be found in the literature. The capacitor values and the aspect ratios of the MOSFETs used in OPAMP and switches are tried to be optimized for better performance in TSMC 180nm CMOS technology. The capacitor values are calculated using the equations described in [3]. The schematic of the analogue switch is depicted in Figure 8. The supply voltage is 2.5V. Figure 9 shows the transient analysis result taken at 1 GS/s operation. As can be seen that almost no glitch effect is observed, and a highly linear conversion is obtained. Transient power analysis includes the average power consumption of 20.8 µW only as shown in Figure 10. The DNL and INL measures are taken at 1MS/s operation as shown in Figure 11 and Figure 12 respectively. The worst case linearity measures are INL of 0.33LSB and DNL of -0.27 LSB. It seems that the only disadvantage of this technique is the slower speed except the possible capacitor mismatch problems after fabrication when compared to the R-2R DAC design above. The capacitor values in Figure 7 are decreased to fF levels for 10MS/s conversion rate by keeping the ratio between them. Almost the same quality transient output is observed at this rate as well. Table 2 shows the performance summary of this design. The main purpose of this part of study is to compare the two architectures in terms of performance parameters and to help designers at beginner level.

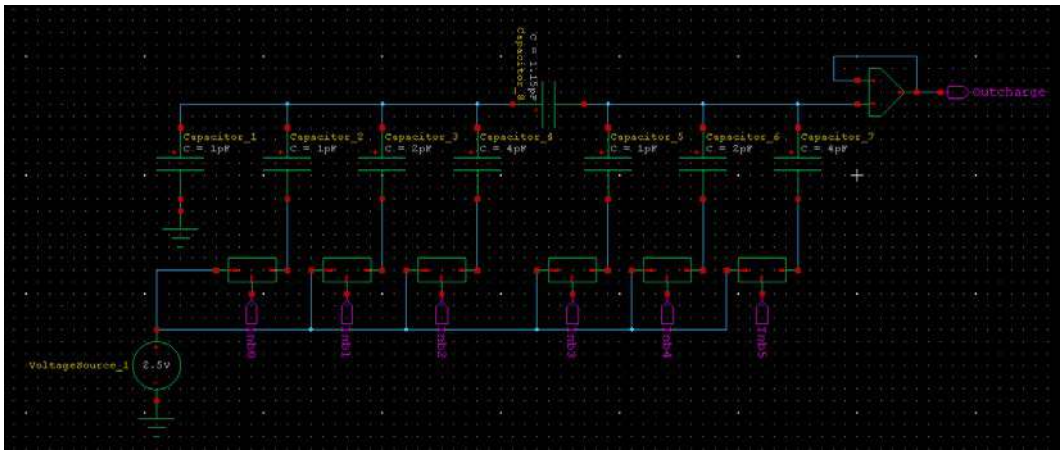

Figure 7. Schematic of the Charge Scaling DAC Circuit

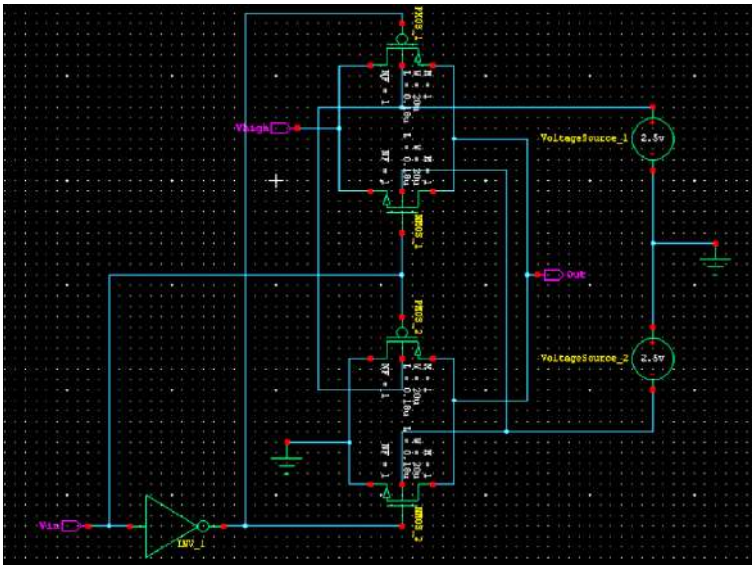

Figure 8. Schematic of the Switch Used in Charge Scaling DAC Circuit

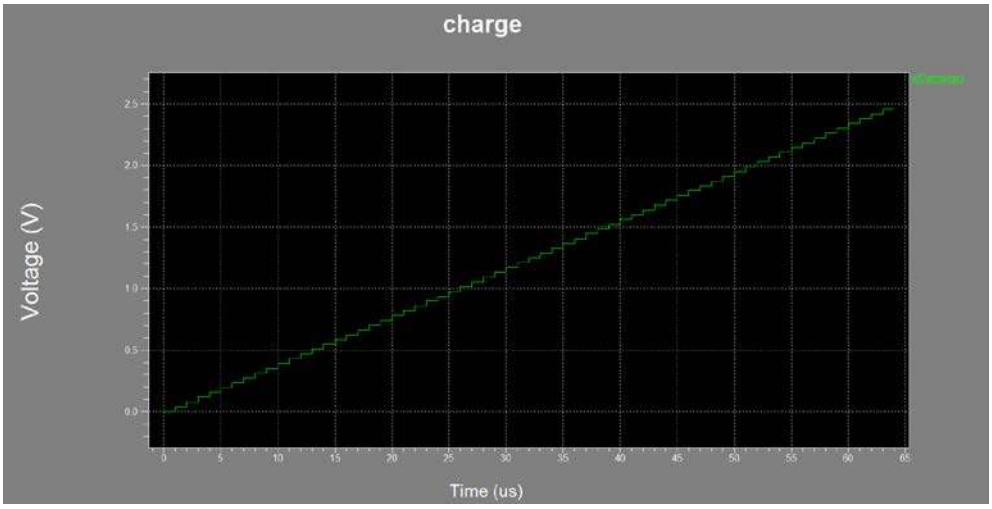

Figure 9. Transient Results of the Charge Scaling DAC at Sampling Rate of 1 MS/s

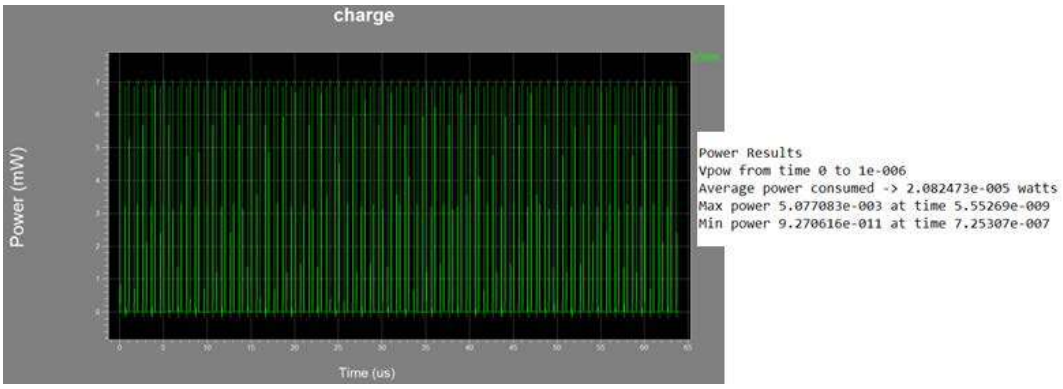

Figure 10. Power Transient Analysis Results of the Charge Scaling DAC at 1 MS/s conversion rate

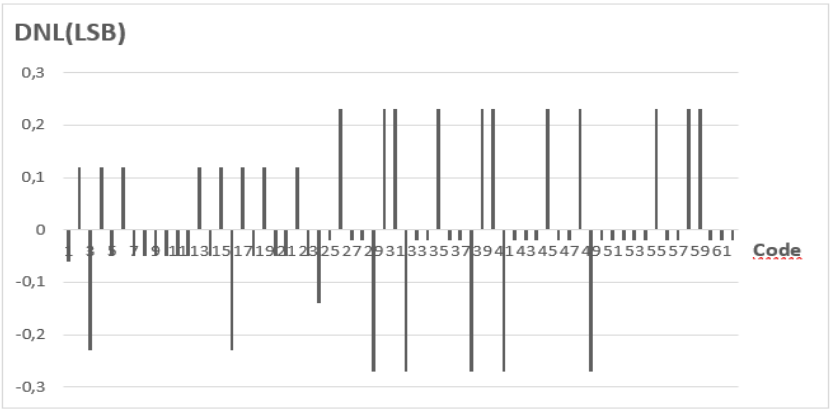

Figure 11. DNL Plot of the Charge Scaling DAC Implementation

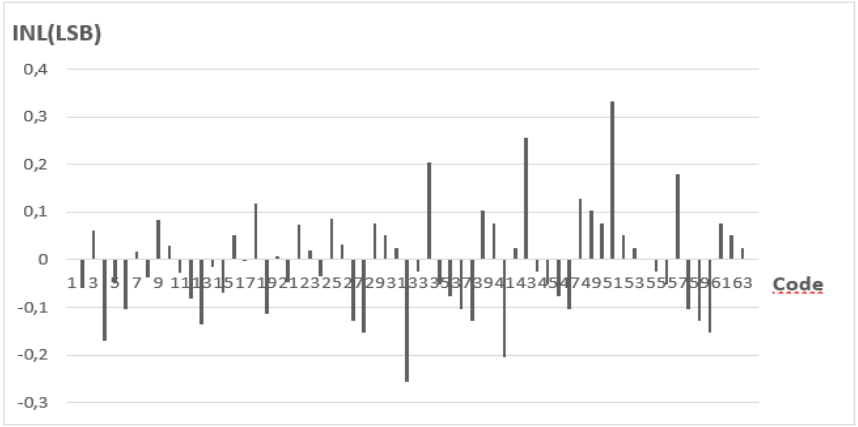

Figure 12. INL Plot of the Charge Scaling DAC Implementation

Table 2. Performance Summary of the Split Array Charge Scaling DAC

Process	180nm CMOS
Resolution	6-Bit
Conversion Rate	10 MS/s
INL/DNL	0.33/-0.27 LSB
Power Supply	2.5V
Average Power	20.8 µW (at 1 MS/s), 375 µW (at 10 MS/s)

4. COMPARISON OF THE RESULTS

The proposed R-2R DAC is compared to other 6-Bit designs published earlier as tabulated in Table 3. The 6-Bit CMOS DAC designs implemented especially using 180nm CMOS technology are taken into account for a fair comparison of this work. Since the performance parameters are more than one, the most common Figure of Merit (FOM_1) calculation is used for comparison as defined below [6]:

$$FOM_1=\frac{Power\ consumption}{2^N \cdot Sample\ rate} \quad (1)$$

Table 3. Comparison with Other 6-Bit DACs Published

	This work	[10]	[11]	[12]	[13]	[14]	[8]	[7]	[6]
Architecture	R-2R Inverter input buffered	C-S	C-S	C-S	C-S	C-S	C-S	C-S	C-S
Resolution	6-Bit	6-Bit	6-Bit	6-Bit	6-Bit	6-Bit	6-Bit	6-Bit	6-Bit
CMOS Process	180nm	180nm	180nm	180nm	350nm	180nm	65nm	40nm	130nm
Average Power(mW)	6.54	0.9446	24	6	165	2.302	14	13	29
Conversion Rate MS/s	2000	300	1000	1250	800	500	2400	4000	3000
DNL(LSB)	0.53	0.06	0.22	0.1	0.04	0.0036		0.04	NA
INL(LSB)	0.72	0.1	0.48	0.1	2.32	0.0023		0.2	0.02
Supply Voltage	2.5V	1.8V	1.8V	1.8V	3.3V	1.8V	1V	1.1V	1.2
FOM (pJ)	0.051	0.049	0.375	0.075	3.22	0.071	0.091	0.05	0.15

As can be seen from Table 3, almost all of the latest architectures are current steering (CS). Although the speed performance of some of the CS designs tabulated here ([6], [7], [8]) are faster than that of our work, they use smaller feature size of CMOS technology. Moreover, the current steering architecture requires high precision current source designs, which is not easy to implement. The FOM value of this work is 0.051 pJ, which is comparable to the values of [10] and [7], but much better than that of the rest of other works listed here. Finally, the FOM value of the charge scaling DAC implemented here is obtained as 0.585 pJ for 10MS/s conversion rate although the linearity measures are much better and almost no observed glitches at the output when compared to the R-2R DAC results.

5. CONCLUSION

In conclusion, two different DAC architectures, which are R-2R ladder network and split array capacitor based charge scaling types were designed and simulated in TSMC 180nm CMOS technology. Different types of DAC architectures were also briefly compared. The simulation results shown that the R-2R type of architecture could be proposed for high performance based on the FOM value obtained. On the other hand, designers are suggested to choose charge scaling architecture for better linearity, lower power consumption and almost no glitch on the

output signal with the cost of lower speed. Although the most common architecture preferred in the literature is current steering type, it is not the only choice for designing a high performance DAC, and it has some design difficulties that must be taken into consideration. Since the layout designs are not completed yet, the post layout simulation results and especially the area requirement of the designs realized here could not be provided for a better comparison. These works are planned as a future work. Most importantly, a higher performance buffer OPAMP having a higher GBW product and power consumption of as small as possible should be designed as a future work to be able to increase the driving capability of the proposed DAC. In fact, the FOM value obtained here will of course be degraded with some amount in this case. It is believed that this article can guide to beginner level of DAC designers before making their decisions on the architecture.

REFERENCES

[1]. K. Naga Kanya, V.S.V Prabhakar, "Design of Low Power R-2R DAC for High-Speed Communications" in *International Journal of Electrical, Electronics and Data Communication*, vol. 2, no. 12, pp. 10-14, 2004.

[2]. P. Ramakrishna, K. H. Kishore, "Design of Low Power 10GS/s 6-Bit DAC using CMOS Technology" in *International Journal of Engineering & Technology*, vol. 7, no. 1.5, pp. 226-229, 2018.

[3]. M. Kulkarni, M. Shingadi, G. H. Kulkarni, "6-Bit Charge Scaling DAC and SAR ADC" in *International Journal of Advanced Research in Electrical, Electronics and Instrumentation Engineering*, vol. 3, no. 12, pp. 13823-13832, 2014.

[4]. S. K. Akula, "8-Bit Split Array Based Charge Scaling Digital to Analog Converter with Rail to Rail Buffered Output", Theses and Dissertations, 1393, 2015, University of Arkansas, Fayetteville.

[5]. G. I. Radulov, P. J. Quinn, A. H. M. van Roermund, "A 28 nm 7-GS/s 6bit DAC with DfT clock and memory Reaching SFDR>50dB up to 1 GHz", *IEEE Transactions on Very Large Scale Integration (VLSI) Systems*, Vol. 23, No.9, pp.1941-1945, 2015.

[6]. X. Wu, P. Palmers, M. S. J. Steyaert, "A 130nm CMOS 6-Bit Full Nyquist 3 GS/s DAC", *IEEE Journal of Solid-State Circuits*, vol.43, No.11, pp. 2396-2403, 2008.

[7]. L. Zhao, J. He, Y. Cheng, "A 6-Bit 4GS/s Current Steering Digital-to-Analog Converter in 40nm CMOS with Adjustable Bias and DfT Block", *IEEE 11th International Conference on ASIC (ASICON) 2015*, pp. 1-4.

[8]. B. Kim, M. Cho, Y. Kim, J. Kwon, "A 1V 6-Bit 2.4 GS/s Nyquist CMOS DAC for UWB Systems", *IEEE MTT-S IMS-2010*, pp. 912-915.

[9]. W. Xiong, L. Nenyuan, S. Chuyang, " An 8GS/s 6-Bit Current Steering DAC in 65 nm CMOS Technology", *The 2014 International Conference on Advanced Technologies for Communications (ATC'2014)*, pp. 491-493.

[10]. M. Chakir, H. Akhamal, H. Qjidaa, " A Low power 6-Bit Current-Steering DAC in 0.18 µm CMOS process", *Intelligent Systems and Computer Vision (ISCV) 2015*, pp.1-5.

[11]. K. Farzan, D. A. Johns, "A power Efficient Architecture for High Speed D/A Converters", *Proc. 2003 Int. Symp. Circuits and Systems*, pp.1897-1890.

[12]. J. Jung, K. H. Baek, S. I. Lim, S. Kim, S. Kang,"Design of a 6 Bit 1.25 GS/s DAC for WPAN", *Proc. Int. Symp. Circuits and Systems, 2008*, pp. 2262-2265.

[13]. A. Narayanan, M. Bengtsson, R. Ragavan, Q-T Duong, "A 0.35 µm CMOS 6-Bit Current Steering DAC", *European Conference on Circuit Theory and Design (ECCTD) 2013*, pp. 1-4.

[14]. S. Khandgale, S. Sarkar, " A 6-Bit 500 MSPS Segmented Current Steering DAC with On-Chip High Precision Current Reference", *International Conference on Computing, Communication and Automation (ICCCA 2016)*, pp. 982-986.

[15]. S-N. Kim, W-C Kim, M-J. Seo, S-T. Ryu, " A 65 nm CMOS 6-Bit 20GS/s Time Interleaved DAC with Full-Binary Sub-DACs", *IEEE Transactions on Circuits and Systems II*, DOI 10.1109/TCSII.2018-2809965

ICENS 4TH INTERNATIONAL CONFERENCE ON ENGINEERING AND NATURAL SCIENCE
2-6 May 2018 KIEV UKRAINE

Magnetic Levitation System Analysis

Primož Podržaj[1]

Abstract

Magnetic levitation is a phenomenon often encountered in engineering applications ranging from high speed transportation to magnetic bearings. Depending on the setup it can be either an open loop stable or unstable system. In the latter case it therefore needs some control theory related analysis and synthesis in order for it to function properly. In this paper such a procedure is presented. First a thorough explanation about the modelling of the system is given. The system is then linearized and analyzed using the root-locus method. All the steps can be done conveniently using the Matlab software package and its toolboxes.

Keywords: Magnetic Levitation, Control Systems, Matlab/Simulink

1. INTRODUCTION

Magnetic levitation is an interesting technical problem. It is associated with a permanent magnet levitating in the air. It is shown schematically in Fig. 1.

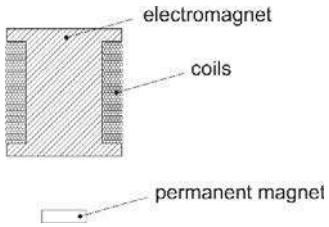

Figure 30. Schematic representation of levitation

Applications of magnetic levitation range from high speed transportation to vibration isolation systems, and magnetic bearings [1]-[3]. Depending on the setup, the system can be either open loop stable or open loop unstable. If the permanent magnet is located above the electromagnet the magnetic force has to be repulsive. As it increases when the distance between permanent magnet and electro magnet decreases, the system is open loop stable. If the permanent magnet is however located below the electro magnet (as shown in Fig. 1), the magnetic force has to be attractive. In this case the attractive force increases, when the permanent magnet is moving towards the electro magnet. As a consequence the system is open loop unstable and therefore needs an appropriate controller to be able to work at all. Magnetic levitation related control systems are an area of active research [4]-[8]. As the system is inexpensive and very easy to build it is also used for education purposes extensively [9]-[14].

In this paper an analysis of magnetic levitation system from a control point of view is made. The chosen setup is the open loop unstable system. In order to analyze the system a Matlab/Simulink software is used heavily. Possibilities of a new version of Matlab/Simulink (and its accompanying toolboxes) are discussed.

[1] *Corresponding author: University of Ljubljana, Faculty of Mechanical Engineering, 1000, Ljubljana, Slovenia.*
primoz.podrzaj@fs.uni.lj.si

2. MATHEMATICAL MODEL OF THE SYSTEM

When permanent magnet is being modelled it can be considered as an array of a microscopic magnetic dipoles as shown in Fig. 2.

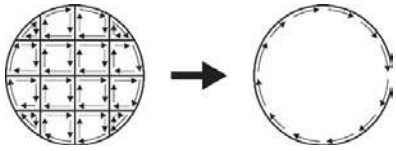

Figure 2. Physical model of a permanent magnet [15]

As the opposite currents in the neighboring inner current loops (magnetic dipoles) cancel each other, the net effect is the surface current, also called the Ampere current, as shown on the right side of Fig. 2. A situation, when such a permanent magnet is placed below an electromagnet, is shown in Fig. 3.

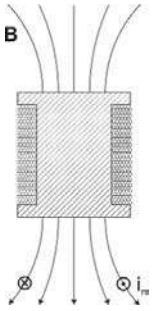

Figure 3. Permanent magnet in the field of an electromagnet

As shown in Fig. 4, force $\overrightarrow{dF}$ acting on a small piece of a conductor of the length $d\vec{l}$, thorough which the current i_m flows and is located in the magnetic field with the magnetic field density $\vec{B}$ is given by:

$$d\vec{F} = i_m \cdot d\vec{l} \times \vec{B} \tag{1}$$

It can be seen that the horizontal component of the magnetic field density $\vec{B}$ is responsible for the vertical component of the force $\vec{F}$.

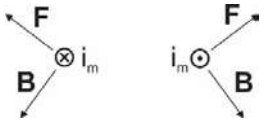

Figure 4. Force on a permanent magnet in a magnetic field

As the system is radially symmetric, the horizontal component of the force cancels. So, the system can be modelled as shown in Fig. 5.

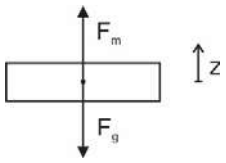

Figure 5. Forces acting on a permanent magnet in a magnetic field

The force due to magnetic field $\vec{F}_m$ is acting upwards, and the weight of the magnet $\vec{F}_g$ downwards. The equation of motion is therefore given by:

$$m \cdot \ddot{z} = F_m - F_g \Rightarrow \ddot{z} = \frac{1}{m} \cdot \left(F_m - F_g\right) \tag{2}$$

As the force $\vec{F}_m$ depends on the type of the permanent magnet (which is constant) and the magnetic field density $\vec{B}$, which in turn depends on the position of the magnet z, and the current i through the coils of the electromagnet.

$$F_m = f(i, z) \tag{3}$$

The electric current i through the coil depends on the applied voltage U and the parameters of the coil (see Fig. 6).

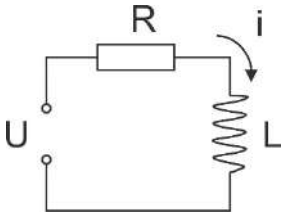

Figure 6. Circuit model of an electromagnet

The relationship between i and U is given by the following equation:

$$U = L \cdot \frac{di}{di} + R \cdot i \tag{4}$$

If we use the transfer function notation (Laplace transform), we can rewrite Eq. 4 into the following form:

$$I(s) = \frac{1}{Ls+R} \cdot U(s) \quad (5)$$

It is important to note that the time constant of this subsystem is $\tau = L/R$.

3. APPLICATION OF MATLAB/SIMULINK

Maltab/Simulink software package was used for several tasks during the analysis and design of the magnetic levitation control system.

a. The application of Curve Fitting Toolbox

The first step in the analysis of the system is the calculation of the function defined in Eq. 3, which gives the relationship between the magnetic force, the current through the coil and the position of the permanent magnet. The data must be obtained experimentally. After it is entered in the workspace with the following commands:

```
clc
clear
i=[0; 0; 0; 0; 0; 0; 0.2; 0.2; 0.2; 0.2; 0.2; 0.2; 0.4; 0.4; 0.4; 0.4; 0.4; 0.4; 0.6; 0.6 …  0.8; 0.8; 1; 1; 1; 1; 1; 1];
l=[15; 20; 25; 30; 35; 40; 15; 20; 25; 30; 35; 40; 15; 20; 25; 30; 35; 40; … 15; 20; 25; 30; 35; 40];
F=1/1000*[0; 0; 0; 0; 0; 0; 0; 51.993; 32.373; 23.544; 14.715; 9.81; 6.867; … 33.354];
cftool
```

the Curve Fitting Toolbox can be applied (see Fig. 7).

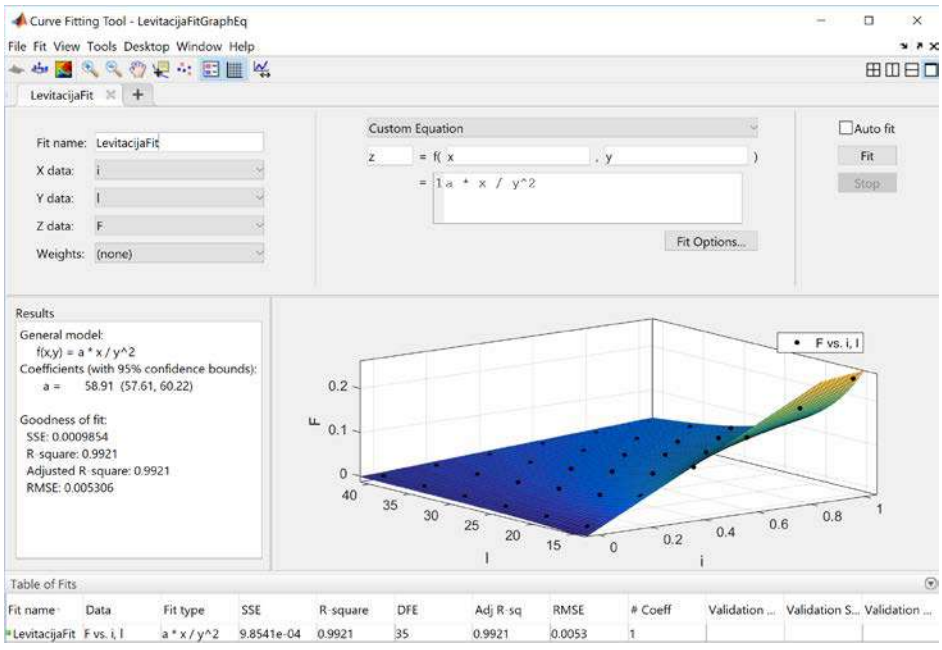

Figure 7. Curve Fitting Tool

The equation used for fitting was defined as:

$$F_m = a \cdot \frac{i}{z^2} \tag{6}$$

The coefficient a was determined to be $a = 58.91$. It should however be noted that although in the majority of references i^2 is being used, we got better fitting with i (root mean square error is 0.005306 if i is used and 0.02125 if i^2 is used.

b. Simulink model of the system

When considering the model of the whole system, it should be noted that the controller and the sensor must be included as shown in Fig. 8.

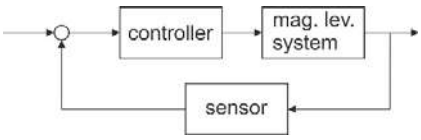

Figure 8. Schematic representation of the magnetic levitation as a control system

For the controller a PID control algorithm was chosen. The sensor was a pair of Hall sensors, which can detect the position of the magnet. The Simulink model of the system is shown in Fig. 9.

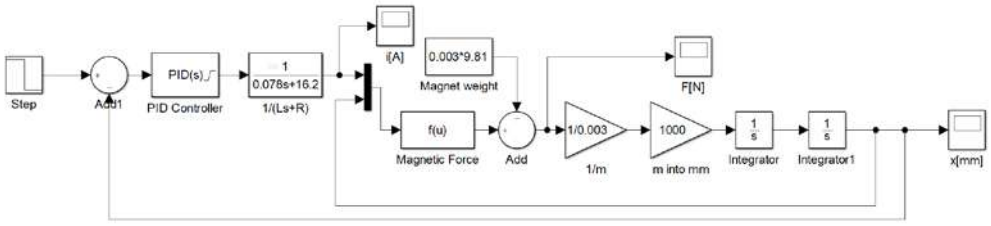

Figure 9. Simulink model of the system

The output of the PID controller is the voltage for the coil. It is modelled using the transfer function in Eq. 5. This is followed by modelling the magnetic force (Eq. 3 and 6) and the equation of motion of the permanent magnet (Eq. 2). After the model is made, we can easily check the response of the system for various reference functions. The problem is however that in order for the system to function properly the tuning of the PID controller must be made. In order that this can be done within Simulink, the system has to be linearized first.

c. Linearization using Simulink

Linearization is a process where a nonlinear model of a system is approximated by a linear one operating at a certain point. The Simulink model used for linearization of the magnetic levitation is shown in Fig. 10.

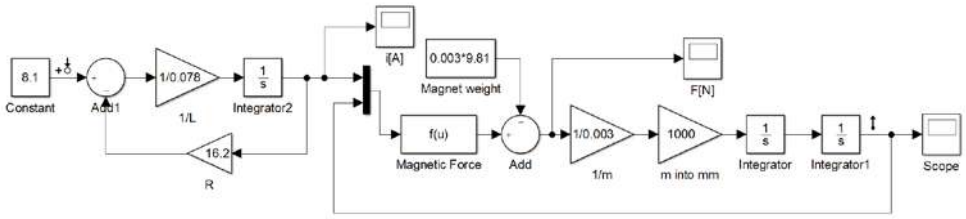

Figure 10. Simulink model for linearization

The operating point of $i = 0.5A$ and $z = -25mm$ was selected. The appropriate signals used for linearization must first be marked. In our case "Input Perturbation" and "Output measurement" were used. After that the linearization procedure can be started by Analysis → Control Design → Linear Analysis command. The results of the linearization are shown in Fig. 11.

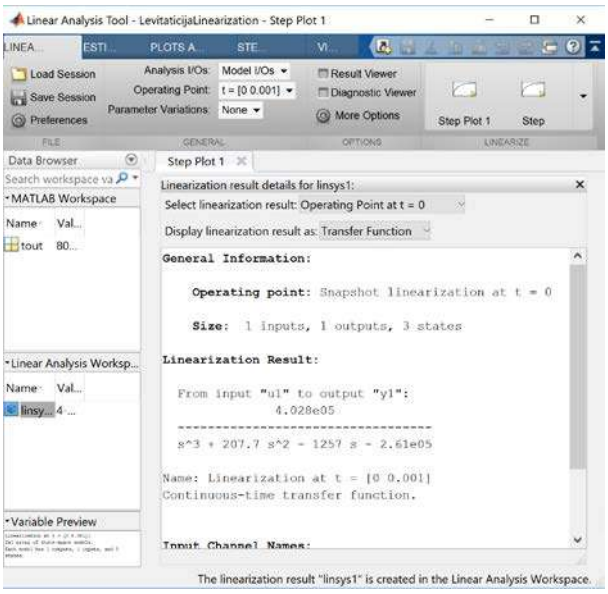

Figure 11. Simulink model for linearization

After the transfer function for the linearized model is obtained the tuning of the PID controller can be made with the application of the Control System Designer

d. The application of the Control System Designer

The control system designer can be started using the following commands:

```
s = tf('s');
object = 4.028*10^5/(s^3+207.7*s^2-1257*s-2.61*10^05);
controlSystemDesigner(object)
```

The result is shown in Fig. 12.

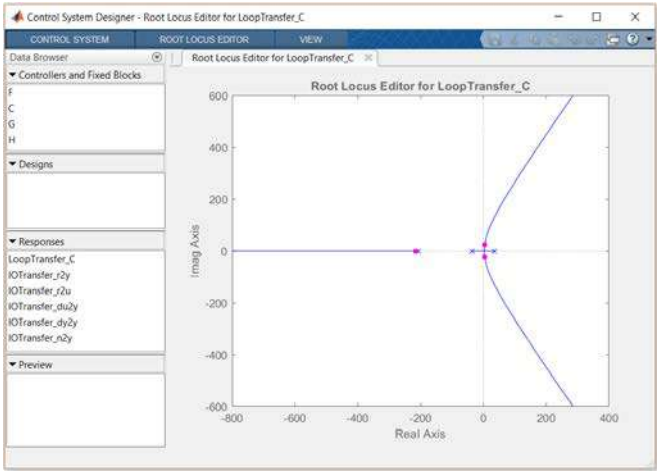

Figure 12. Simulink model for linearization

Based on the root locus it can be clearly seen that the system cannot be made stable just by gain adjustment. In order to stabilize the system a zero with a negative real part is added (PD control algorithm). Such a system can be analyzed by the following commands:

```
object1=(1+0.04*s)*object;
controlSystemDesigner(object1)
```

As shown in Fig. 13, it can be clearly seen that now the system is stable.

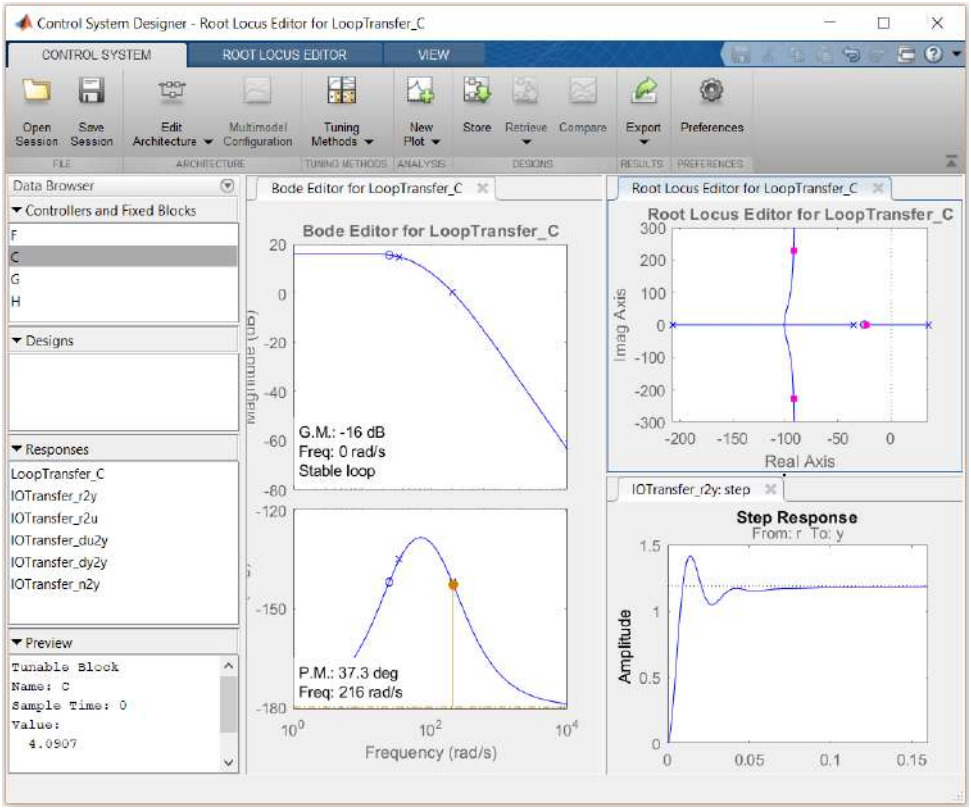

Figure 313. A sample line graph using colors which contrast well both on screen and on a black-and-white hardcopy

The Control System Designer makes it possible to interactively place the location of the close loop poles and observe the associated step response. In our case a gain of approximately 4 gives a satisfactory result.

4. CONCLUSION

It can be concluded that a nonlinear magnetic levitation system can be stabilized and therefore successfully controlled using the Matlab/Simulink software. Various toolboxes can be of great help for better visualization of the results. Especially root locus techniques seem to be very useful for the beginners, because no knowledge in frequency domain based synthesis of control systems is required.

REFERENCES

[1]. J. E. Paddison, C. Macleod, and R. M. Goodall, "State variable constraints on the performance of optimal Maglev suspension controllers," in *Proceedings of the Third IEEE Conference on Control Applications*, 1994, pp. 599-604.

[2]. K. Nagaya, and M. Ishikawa, "A noncontact permanent magnet levitation table with electromagnetic control and its vibration isolation method using direct disturbance cancellation combining optimal regulators," *IEEE Transactions on magnetics*, vol. 31, no. 1, pp. 885-896, 1995.

[3]. H. Bleuler, "A survey of magnetic levitation and magnetic bearing types," *JSME international journal, Ser. 3, Vibration, control engineering, engineering for industry*, vol. 35, no. 3, pp. 335-342, 1992.

[4]. A. El Hajjaji, and M. Ouladsine, "Modeling and nonlinear control of magnetic levitation systems," *IEEE Transactions on industrial Electronics*, vol. 48, no. 4, pp. 831-838, 2001.

[5]. C. L. Kuo, T. H. S. Li, and N. R. Guo, "Design of a novel fuzzy sliding-mode control for magnetic ball levitation system," *Journal of intelligent and Robotic Systems*, vol. 42, no. 3, pp. 295-316, 2005.

[6]. J. H. Li, and T. H. S. Li, "Multiloop control of thyristor-driven magnetic levitation system," *Mechatronics*, vol. 5, no. 5, pp. 469-481, 1995.
[7]. J. H. Li, "Fuzzy PD type control of magnetic levitation system," in *Proceedings of the 5th IEEE Conference on Industrial Electronics and Applications (ICIEA 2010)*, 2010, pp. 2052-2057.
[8]. Z. Yang, and G. Pedersen, "Automatic tuning of PID controller for a 1-D levitation system using a genetic algorithm - A real case study," in *Proceeding of the 2006 IEEE International Symposium on Intelligent Control*, 2006, pp. 3098-3103.
[9]. K. A. Lilienkamp, and K. H. Lundberg, "Low-cost magnetic levitation project kits for teaching feedback system design," in *Proceedings of the 2004 American Control Conference*, 2004, vol. 2, pp. 1308-1313.
[10]. V. A. Oliveira, E. F. Costa, and J. B. Vargas, "Digital implementation of a magnetic suspension control system for laboratory experiments," *IEEE transactions on education*, vol. 42, no. 4, pp. 315-322, 1999.
[11]. P. S. Shiakolas, and D. Piyabongkarn, "Development of a real-time digital control system with a hardware-in-the-loop magnetic levitation device for reinforcement of controls education," *IEEE Transactions on education*, vol. 46, no. 1, pp. 79-87, 2003.
[12]. P. S. Shiakolas, S. R. Van Schenck, D. Piyabongkarn, and I. Frangeskou, "Magnetic levitation hardware-in-the-loop and MATLAB-based experiments for reinforcement of neural network control concepts," *IEEE Transactions on Education*, vol. 47, no. 1, pp. 33-41, 2004.
[13]. T. H. Wong, "Design of a Magnetic Levitation Control System - An Undergraduate Project," *IEEE Transactions on Education*, vol. E-29, no. 4, pp. 196-200, 1986.
[14]. M. H. Yaseen, and H. J. Abd, "Modeling and control for a magnetic levitation system based on SIMLAB platform in real time," *Results in Physics*, vol. 8, pp. 153-159, 2018.
[15]. P. A. Tipler, and G. Mosca, *Physics for scientists and engineers*., 6th ed., New York, USA, W. H. Freeman and Company, 2008.

ICENS 4TH INTERNATIONAL CONFERENCE ON ENGINEERING AND NATURAL SCIENCE
2-6 May 2018 KIEV UKRAINE

Adapted Cooling Channels for Different Wall Thickness of Plastic Parts

Mustafa Goktas[1], Abdulmecit Guldas[2]

Abstract

A significant majority of plastic parts which is used in all areas of daily life is manufactured by plastic injection molding method. During designing these produced plastic parts, the quality and appearance of molded plastic parts are very important as well as the size, function and suitable according to the usage area. Therefore, while designing plastic parts, a lot of limitations are encountered depending on using area. In this context, one of the design constraints for producing plastic parts using injection molding method is regular thickness. In this study, a cooling system is proposed which makes it possible to design plastic parts which do not have regular thickness. For sections having different thicknesses of plastic parts, the cooling channel layout is changed to provide co-cooling for all sections of the plastic part. The distance between the cooling channels is determined by the thickness in the cooled area so that co-cooling can be achieved. Numerical analyzes have shown that thickness-matched cooling channels provide more efficient cooling.

Keywords: Injection molds, Adapted cooling channels, Uniform cooling, Different wall thickness

1. INTRODUCTION

Plastic injection molding is one of the most widely used molding methods. This method consists of some phase like melting of material, filling of the cavity, cooling, and ejection from the mold. The longest time is cooling among these phases. Because of that more effective cooling system is essential for shorter molding times and to produce high-quality plastic parts. The straight-linear cooling channel provides the typical cooling system. These channels obtained using drilling method is the most common method and suitable for simple shape plastic parts. However, plastics parts which have complex shape are not cooled properly [1]. This leads to some problems such as warpage and sink and non-uniform shrinkage on plastic parts during molding and after ejection [2,3]. Finally, because it is linear, this cooling channels cannot provide adequate cooling for the models with complex shapes [4-8].

Different cooling methods were investigated for uniform cooling of plastic parts which have complex shape [1-3,8-13]. After these research, shape adaptive cooling channel which is fit and follow part surface are developed and used. This type of cooling system is called conformal cooling. After these research, shape adaptive cooling channel which is following the surface and geometry of the part was developed and used.

Fountain method is used for cooling the mold cores, but uniform coolant temperature distribution has not been achieved [9]. The fabrication of conformal cooling system with complex connectivity must be conducted by the additive manufacturing technique such as selective laser sintering [10]. In contexts, Different methods were developed for the design of conformal cooling to achieved effective cooling [1,11-14]. The centroidal Voronoi diagram is used to help generate the cooling circuits in some recommended methods. However, the distance between channel is changing according to the surface slope, or flow rate is not controlled accurately. In addition, topological optimization studies have been achieved for reducing the cost of mold core which will be produced by additive manufacturing technique [13,14].

It was tried to prevent warpage caused by temperature differences of the coolant between inlet and exit in cooling channels used in injection molds. For this purpose, distances between cooling channel and cavity wall were gradually reduced in accordance with temperature change in the coolant. As a result of numerical

[1] *Corresponding author: Gazi University, Technical Sciences Vocational School, 06374, Yenimahalle/Ankara, Turkey.* mustafagoktas@gazi.edu.tr

[2] *Gazi University, Department of Manufacturing Engineering, 06500, Teknikokullar, Yenimahalle/Ankara, Turkey.* aguldas@gazi.edu.tr

analysis achieved a new approach conformal cooling channels for products with complex shapes, the cooling time is shortened while the amount of warpage also is decreased [15].

Purpose of this study is effective cooling of plastic parts that have a non-uniform wall thickness and complex geometry. Conformal cooling channels were used to achieve effective cooling. So, area on mold surface has different wall thickness was tried to be cooled in equal cooling rate. Thus, areas on mold surface which have different wall thickness were tried to be cooled in equal cooling rate. Warpage defects on plastic part have been tried to prevent with more uniform cooling. To verify the physical performance of cooling channels generated according to conformal cooling, analysis was performed on the injection molding simulation software-MoldFlow and then these results were compared with each other [16].

2. MATERIALS AND METHODS

a. Plastic Part and Canal Dimensions

The plastic part studied and analyzed is as shown in Figure 1 in this study. Plastic part analyzed geometry has sloping surface. It has 4 mm and 1.5 mm wall thickness, and outer dimension Is 160 x 80 x 29mm. ABS (%0 Rubber) Monsanto Kasei as a plastic material was used.

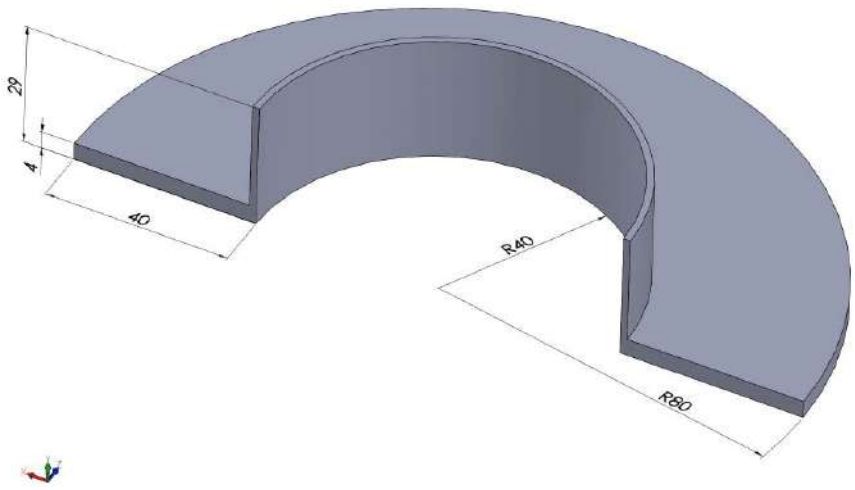

Figure 1. Plastic part dimensions

Circular section channel was preferred, and widely used diameter of channel and distance between cooling channel line and wall were used. Figure 2 shows the definition of channel sections. The diameter of channel d= 10 mm, the distance between channel axis b= 25 mm, the distance between channel axis and cavity wall a=20 mm and also plastic part thickness t=2 mm were selected.

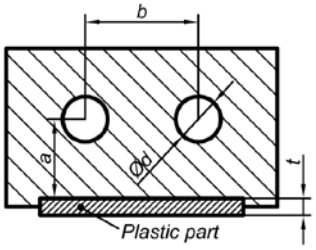

Figure 2. Cooling channel dimensions

b. Conformal Cooling Canals

A typical-straight cooling channel and conformal cooling channel were designed for cooling analysis. Cooling channel layout and dimension were as shown in Figure 3.

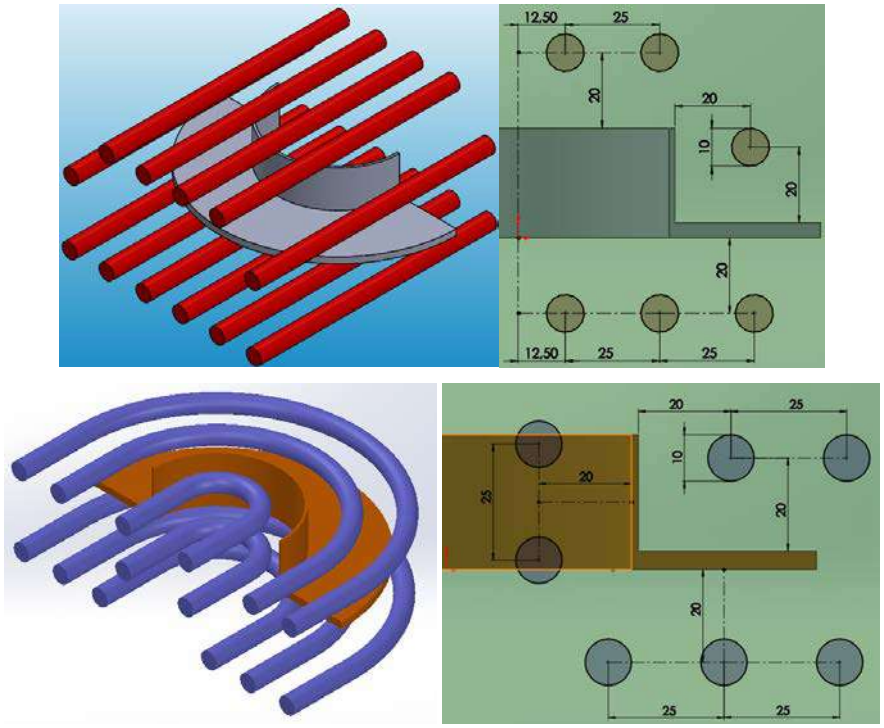

Figure 3. Straight (left) and Conformal (right) Cooling channels

3. RESULTS

Both typical cooling canal and conformal cooling canal are designed and modelled with CAD software and then cooling analysis of these canals have been performed. ABS (%0 Rubber) Monsanto Kasei are used as a plastic material to the filling of the cavity and cooling analyses. Mesh generation is produced before cooling and filling analysis. In context, 390000 mesh elements are generated for the conformal cooling canal and 414000 mesh elements are generated for the typical canal. As recommended processing parameters melt temperature 230˚C, injection temperature 88˚C, and mold temperature 50˚C are used. 5 lt/min is determined for the flow rate of cooling water. Water temperature is 25°C. Seven inlets and seven outlets are determined in a conformal cooling canal, and also six inlets and outlets are used in a typical canal. Cooling analysis results of the conformal cooling canal and typical cooling canal (straight line) are presented in Figure 4.

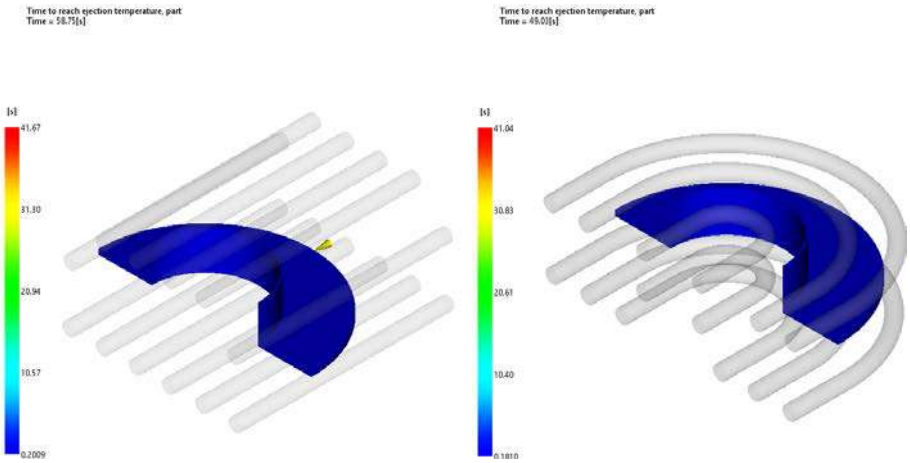

Figure 4. Time to reach ejection temperatures

In Figure 4, time to reach ejection temperature of plastic parts are shown to conformal cooling and typical cooling canal. According to the cooling analysis, it is determined that cooling time of plastic part having conformal cooling canal is less than the typical cooling canal. While cooling time using conformal cooling canal is 49.03 s, cooling time was measured as 58.75 s using the typical canal.

Amount of warpage that obtained from the result of simulation analysis using Moldflow software are shown in Figure 5. The total amount of warpage was obtained as 1.103 mm according to the result of analysis using the typical-straight cooling channel. It is determined that total amount of warpage was also as 1.188 mm according to the analysis using the conformal cooling channel.

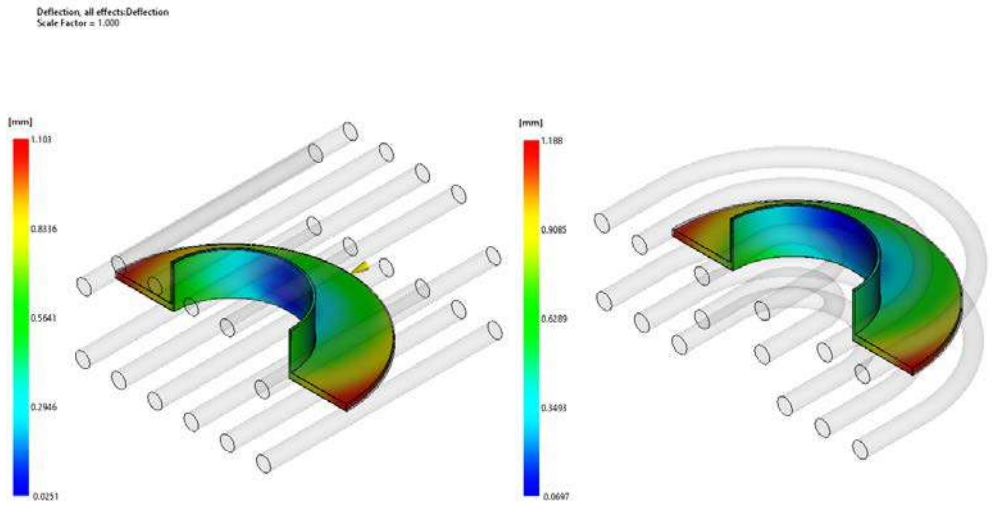

Figure 5. Warpage on the plastic parts

4. CONCLUSIONS

When plastic part with complex shapes and surface and has non-uniform wall thickness are molded, numerical analysis was carried out for more effective cooling. For this purpose, plastic part with complex shape and geometry was designed. To cooling of plastic part and mold surface, two different type cooling channel systems as typical-straight and conformal cooling channel were designed. To determine filling and cooling and, warpage rate, simulation analysis was carried out using the Moldflow software. It is concluded that according to this analysis result, cooling time using conformal cooling shorter than using the typical-

straight channel. Amount of warpage obtained from the molded plastic part using conformal cooling was also a little shorter than the typical-straight cooling channel.

REFERENCES

[1]. Sachs, E., Wylonis, E., Allen, S., Cima, M., Guo, H., Production of Injection molding tooling with conformal cooling channels using the three dimensional printing process, Polym Eng Sci, 40, 5, 1232–1247, 2000.
[2]. Sánchez, R., Aisa, J., Martinez, A., Mercado, D., On the relationship between cooling setup and warpage in injection molding, Measurement 45, 1051–1056, 2012.
[3]. Hassan, H., Regnier, N., Pujos, C., Arquis, E., Defaye, G., Modelling the effect of cooling system on the shrinkage and temperature of the polymer by injection molding, Applied Thermal Engineering, 30(13),1547-1557, 2010.
[4]. Zhang, Y., Huang, Z., Zhou, H., Li, D., A rapid BEM-based method for cooling simulation of injection molding, Engineering Analysis with Boundary Elements, 52, 110 – 119, 2015.
[5]. Wang, G., Zhao, G., Wang, X., Development and evaluation of a new rapid mold heating and cooling method for rapid heat cycle molding, International Journal of Heat and Mass Transfer 78, 99–111, 2014.
[6]. Jauregui-Becker, J., Tosello, G., Houten, F., Hansen, H., Performance evaluation of a software engineering tool for automated design of cooling systems in injection moulding, Procedia CIRP 7, 270–275, 2013.
[7]. Li, C.G., Li, C.L., Liu, Y., Huang, Y., A new C-space method to automate the layout design of injection mould cooling system, Computer-Aided Design, 44, 811–823, 2012.
[8]. Wang, G., Zhao, G., Wang, X., Heating/cooling channels design for an automotive interior part and its evaluation in rapid heat cycle molding, Materials and Design, 59, 310–322, 2014.
[9]. Eiamsa-ard, K., Wannissorn, K., Conformal bubbler cooling for molds by metal deposition process, Computer-Aided Design, 69, 126–133, 2015.
[10]. Wang, Y., Yu, K., Wang, C., Spiral and conformal cooling in plastic injection molding, Computer-Aided Design, 63, 1–11, 2015.
[11]. Xu, X., Sachs, E., Allen, S., The Design of Conformal Cooling Channels in Injection Molding Tooling, Polymer Engineering and Science, 41, No. 7, 2001.
[12]. Wu, T., Jahan, S., Kumaar, P., Tovar, A., El-Mounayri, H., Zhang, J., Acheson, D., Brand, K., Nalim, R., A Framework for Optimizing the Design of Injection Molds with Conformal Cooling for Additive Manufacturing, Procedia Manufacturing, 1, 404-415, 2015.
[13]. Agazzi, A., Sobotka, V., LeGoff, R., Jarny, Y., Optimal cooling design in injection moulding process Anew approach based on morphological surfaces, Applied Thermal Engineering 52, 170-178, 2013.
[14]. Au, K.M.,Yu, K.M., Variable Distance Adjustment for Conformal Cooling Channel Design in Rapid Tool, Journal of Manufacturing Science and engineering,136, 1-9, 2014.
[15]. Autodesk, Mold Flow Insight,2010.http://www.autodesk.com

ICENS 4TH INTERNATIONAL CONFERENCE ON ENGINEERING AND NATURAL SCIENCE
2-6 May 2018 KIEV UKRAINE

Optimal Location Determinations For Different Types Of Mandibular Fractures

Arif Ozkan[1], Murat Pusur[2], Talip Celik[1], Cagatay Tasdemirci[1]

Abstract

Mini plate surgery is one of the common fixation methods of mandibular fractures. Mini plate bone fixation prior application of the mandibular fractures. The important limitations of fixation connected with the appropriate biomaterial and geometry usage. Mini plate and fixture are required to be of a quality that corresponds to all kinds of effects, including those where the mandibula reaches maximum strength. In addition to the biocompatibility of the plates and fixators, it is expected that they will be able to meet the loads required by the region where they are applied. The plate geometry and the material to be used must be determined by pre-surgical examinations.

In this study, three dimensional mandibular models were obtained from Computerized Tomography (CT) images, and a fracture was formed in the corpus and symphysis area on this model. For both fracture models, different geometries were designed with CAD software and used three biocompatible materials (Ti6Al4V, Chromium Cobalt, and Stainless Steel) for the miniplates. ANSYS® WORKBENCH FEA program used for evaluating the load-bearing capacities are compared for each fixation models.

Keywords: Mandible, fracture, mini-plate, fixator, finite element analyses, biomechanics.

1. INTRODUCTION

The use of mini plates is one of the common intervention methods of mandible fracture healings. The force carry limit values of the biomaterials that used in mandibula fixations must be well known before to the plate fixation application. Plate and fixators responds to all influences, including maximum force of bitten cases. Plate geometry and material must be determined prior to surgery because of all these factors. Plate and fixation, including cases where the chin reaches the maximum force required to have any effect responds to the nature. Biocompatibilities fixators are applied, as well as loads of plaque and also capable of meeting the needs of the region can be expected.

The most common type of head and face injuries fracture are mandibular fractures. The causes of mandibular fractures are shown in Table 1.Mandibular fractures are divided into several zones according to their location. This classification was first made by Natvig and Dingman [2] in 1964. This classification is shown in Figure 1. Angulus fractures constitute about 20% of all mandibular fractures. Bormann et al. [3] were evaluated of rates of mandibular fractures on 364 patients with mandibular fracture. According to this study mandibular fracture classifications were take place 36% condylar, 21% corpus, 20% angulus region of mandibula.

[1] *Corresponding author: Kocaeli University, Department of Biomedical Engineering, 41380,Izmit/Kocaeli, Turkey. arif.ozkan@kocaeli.edu.tr*

[2] *Duzce University, Department of Manufacturing Engineering, 81620,Konuralp/Duzce, Turkey*

[3] *Kocaeli University, Department of Biomedical Engineering, 41380,Izmit/Kocaeli, Turkey, talip.celik@kocaeli.edu.tr*

[4] *Kocaeli University, Department of Biomedical Engineering, 41380,Izmit/Kocaeli, Turkey, cagatay.tasdemirci@kocaeli.edu.tr*

Table 34. Mandibular fracture causes [1]

Fracture Reason	Rate
Traffic accident	51%
Drop	28%
Fall	16%
Other	5%

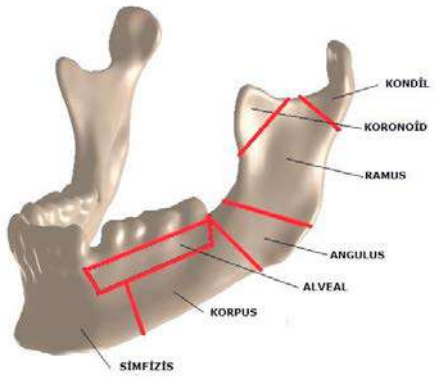

Figure 32. Classification of mandibular fractures according to locations

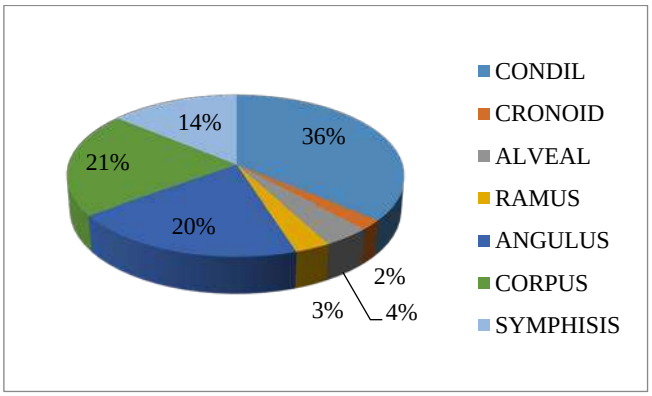

Figure 33. Distribution of fractures of mandibula according to regions

The literature works shown that the fracture on mandibula observed in angulus maximum encountered after mandibular condyle trauma type. Some authors explained twenty-year-old teeth for this reason [4]. Diagnosed mandibular fractures are treated in 3 ways [5];

- Fixation with mini plate-screw
- Brons type wire fixation
- External fixation

While mandibular fractures were formerly used with wire and intermaxillary fixation (IMF), nowadays screws and plaque systems placed in different positions are preferred [6]. Miniplates were first used by Niederdellmann et al. [7] in 1981 on 50 patients for the angulus region fractures and achieved successful results.

In this study, computed tomography (CT) images based three-dimensional models of mandible sagittal split osteotomy and fracture in angulus designed by MIMICS® software. Each broken models, and the fixator miniplate different biocompatible materials are widely used mini plates and the fixator (Titanium Alloy, Chrome Cobalt, and Stainless Steel) were designed with different geometry variations. Also they were compared. Each model and the materials used in its model were compared with the stress and deformation

capacities aided with ANSYS ® finite element software. Reverse engineering methodology was used in modeling process. Additionally, material properties of all materials were added in accordance with literature works and product market values.

2. MATERIAL AND METHODS

Obtaining the geometry of a mandibular as an individual computer-assisted process involves a number of processes. The mandibula model, which has real modeling individual geometry, is important for obtaining healthy results in experiments [8 - 9]. For the mandibular model used in this study, a healthy human computerized tomography (CT) images were used for average weight and height. CT images was obtained with a Toshiba Aquilion CT scanner device. The images are converted to DICOM (Digital Imaging and Communications in Medicine) format. The DICOM layers are used for mechanical modeling of mandibular structure as a real model. These images were processed with the MIMICS ® (Materialize's Interactive Medical Image Control System) software to create the efficient mandibular geometry (Figure- 3-a). The created geometry was saved in the point cloud format. GEOMAGIC ® (Raindrop Inc.) reverse engineering software was (Figure- 3- b) used to re design the real model by point cloud.

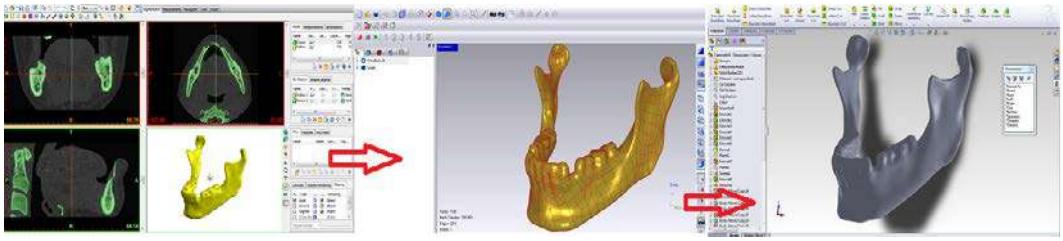

a-MIMICS b-GEOMAGIC c- SOLIDWORKS

Figure 34. Programs used in 3D modeling processes from DICOM data.

The model in the GEOMAGIC ® program was recorded in the IGS format and transferred to the SOLIDWORKS ® program (Fig. 3- c). Here, plate models were designed and fixed with screws. Manufacturer's standard dimensions for the plate and screw design reference is made to [http://www.titamed.be/ products / ABG-series / series b /]. These study steps were carried out in three different geometries (I type ,Y type , Square type)was repeated for the plate . Geometries consist of ANSYS ® for finite element analysis of individual mandibular and plaque models Design Models are transferred to the interface. Definitions of material to be used have been made. The elastic modulus and Poisson ratio of these materials are given in Table-2.

Table 35. Material properties of the materials used

	Poisson ratio (v)	*Elasticity modulus (E) GPa*
Ti-6Al-4V	*0342*	*113.8*
Mandibula	*0.3*	*14*

Mandibular models have an average of 121.839 nodes and 75.842 4-node tetrahedral elements (Figure 4a). The location and direction of fixed side were determined according to condyle zones, which is often used during occlusion. Therefore, the load is applied at the front side of mandible, and direction of the load is based on direction obtained by anatomically. Therefore, total load of 150 N was applied statically in the direction of chewing forces (a linear bite force) shown in Figure 4b. Miniplates and screws used in the finite element analysis are shown in Figure 5.

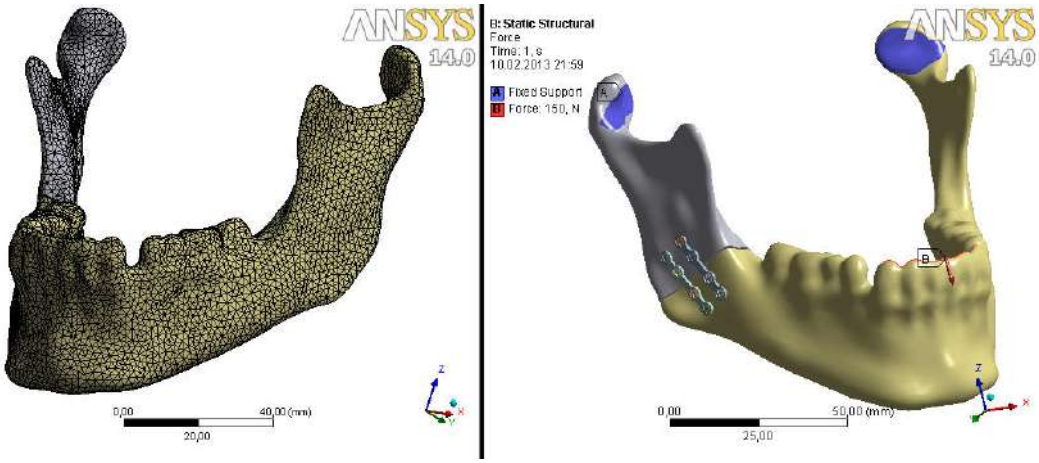

a b

Figure 35. Finite element models and loading / boundary conditions of mandibles

Figure 36. Mandibular miniplates and screw

3. RESULTS AND DISCUSSION

In this study 3 different biomaterials, which can be applied to mandibular angulus fracture, was performed separately and subjected to finite element analysis. The total amount of displacement values obtained was observed for each models. The FE models yielded significant differences in displacement and stress values among the miniplates. For assessment of stress values and displacement of a fixation models were calculated for each fixation models (Figure 6, Figure 7). Displacement values as shown in Table 3.

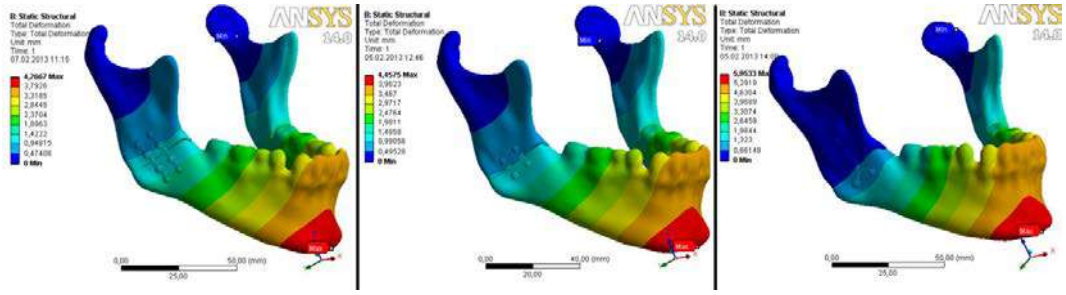

I type Square type Y type

Figure 37. FEA Deformation results of all fixation models

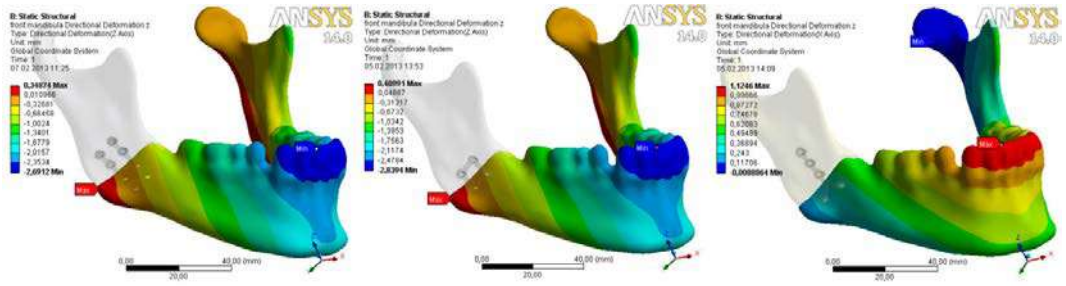

I type Square type Y type

Figure 38. Deformation on front part of mandibular fracture

Table 36. Total displacement results evaluated by FEA

		I Type	Square Type	Y Type
mandible	Max.	4.26 mm	4,45 mm	5.95 mm
	Min.	0 mm	0 mm	0 mm
Front Fracture	Max.	0.34 mm	0.4 mm	1,12 mm
	Min.	-2.69 mm	-2.83 mm	-0.01 mm
Rear Fracture	Max.	0.19 mm	0.18 mm	0.13 mm
	Min.	-0.78 mm	-0.73 mm	-0.3 mm

For each of the mandibular fractures , the displacement values appeared in the z direction; square type (max 0.4 mm , min -2.83 mm) for the frontal fracture and the I type (max . 0.19 mm , min -0.78 mm).

The maximum movement was found on the Y type miniplate with 5.95 mm and the least movement on I type miniplate with 4.26 mm. According to the results of total displacement, using I type plate will have more positive results. So that, when fixation is performed, deformation at minimum level is expected while performing mandibular chewing functions. I type mini plate was applied with two piece to the fracture of the sagittal split osteotomy for positive results than the single usage (Figure 8). Total displacement values were given in Table 4 and 5.

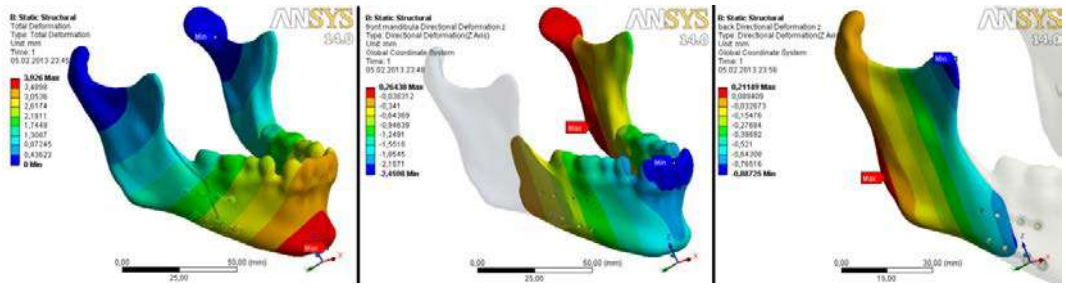

Figure 39. Sagittal split fracture fixation FEA results

Table 37. Total displacement amounts in the analysis results

		Healty mandible	Front Fracture	Rear Fracture
Displacement	Max.	3.92 mm	0.26 mm	0.21 mm
	Min.	0 mm	-2,45 mm	- 0.88 mm

Table 38. Total displacement amounts according to fracture types

		Healthy Mandibula	Angulus fracture	Sagittal split osteotomy
Displacement	Max.	3,70 mm	4.26 mm	3.92 mm
	Min.	0 mm	-2,45 mm	-0.88 mm

The first result reached was that titanium alloy would be the perfect material choice of mandibular fracture fixation. According to this, in 3 different geometries used in the mandibular angular fracture fixation; Fixation provided by the plate with I geometry allowed for less displacement than other plaques. When fractured parts were examined separately, except for the posterior part (higher values were found in the posterior fracture part), the type I plaque superiority was determined. In the study, it is shown that the proposed FE model is able to predict mechanical behaviors of mandibular fixators and mandibular fracture conditions with accuracy. In addition, the CT based 3D mandibular model can be used to evaluate structural and mechanical behaviors of mandible and different types of mandibular fractures.

4. REFERENCES

[1]. Irkoren S., Sivrioglu N., Bulut B., Sonel A., Ceylan E. Uc Yil Icerisinde Opere Edilen 63 Mandibula Frakturu Olgusunun Retrospektif Analizi. Adnan Menderes Universitesi Tip Fakultesi Dergisi, (2011), Cilt 12, Sayi 3,
[2]. Dingman R., P. Natvig. Surgery of Facial Fractures, W. Saunders Company, (1969) 142-144.
[3]. Bormann KH, Wild S, Gellrich NC, Kokemuller H, Stuhmer C, Schmelzeisen R, Schon R. Five-year retrospective study of mandibular fractures in Freiburg, Germany: incidence, etiology, treatment, and complications. J Oral Maxillofac Surg (2009); 67(6):1251-1255
[4]. Gunaydin O., Unal F., Mandibula Simfizis, Korpus Ve Angulus Kiriklari, Turkiye Klinikleri J E.N.T.-Special Topics, (2008) 1(4):81-88,

[5]. Omezli M., Dayi E., Ayranci F., Kaya G., Mandibular Condyle Fractures And Treatment Methods, Cumhuriyet Dent J., (2011) 15(1):63-70.
[6]. Sirin Y., Said M., Limani E., Soley S., The Influences Of Two Sagittal Split Osteotomy Techniques On The In Vitro Biomechanical Stability Of Titanium Plates, Istanbul Universitesi Dis Hekimligi Fakultesi Dergisi, (2011) Cilt: 45, Sayi: 3.
[7]. Niederdellmann H., Akuamoa E., Utilig G., Lag-Screw Osteosynthesis: A New Procedure For Treating Fractures Of The Mandibular Angle. J Oral Surg, (1981) 39: 93840.
[8]. Atik F., Ozkan A., and Uygur I., Insan Uyluk Kemigi Ve Kalca Protezinin Gerilme Ve Deplasman Davranisinin Kiyaslanmasi, Sakarya Universitesi Fen Bilimleri Enstitusu Dergisi, (2012), Cilt: 16 Sayi: 3, 249-253
[9]. Arat M, Rubenduz M, Koklu A, Gurbuz F. Kraniofasiyal yapinin uc boyutlu incelenmesi. Turk Ortodonti Dergisi (1995) 8(2): 223-31.

ICENS 4TH INTERNATIONAL CONFERENCE ON ENGINEERING AND NATURAL SCIENCE
2-6 May 2018 KIEV UKRAINE

Text Preprocessing for an Experiment Code on the Internet Assisted Laboratory System

Selcuk Ogutcu[1], Samet Diri[2], Mehmet Yildirim[3]

Abstract

In this study, a text preprocessing application in an engineering experiment system for the Internet assisted laboratory is proposed. Distance education has a key part in today's education system. Unlike the conventional education, students can access educational resources distantly via their computers and mobile devices. This provides students the flexibility they need allowing them to learn while continuing to their daily lives. Static and dynamic Web sites are designed to serve for this purpose replaces traditional classes and books. Natural sciences, especially the engineering programs specifically require laboratory training. Distance education solutions provided mostly based on hands-on education for a desired period, simulations mimicking real laboratory environments and online real laboratories. The educational goal is met as much as the online lab to be realized is similar to a real lab. In order to provide an online laboratory which allows students to execute engineering experiments, we have developed an Internet assisted laboratory infrastructure powered by a code preprocessing software. In this online laboratory system, the laboratory equipment is inspected and intervened as many as necessary by our software for stability, security and durability of the execution subsystem and its target hardware controlled by students' code. This task, which is essential for a flexible Internet assisted laboratory, is carried out by evaluating and manipulating the student's control code where necessary. We have successfully developed an experiment management software which monitors the students' experiment code, and an execution subsystem which runs the experiment code on a distant laboratory equipment.

Keywords: distance education, text preprocessing, distant laboratory, internet assisted laboratory

1. THE INTERNET ASSISTED LABORATORY

Laboratory works are basic and required components of education on natural and physical sciences. These laboratory works have various targets such as applications of learnt subjects, testing of proposed methods, improving hands-on experimenting experience et cetera. Excluding laboratory experiments which improve manual skills, all laboratory work can be reproduced via distant virtual laboratories. When education shifts focus towards innovation, STEM (Science Technology Engineering and Mathematics) literacy becomes relevant for all students, regardless of their intentions for further career paths[1].

Virtual laboratories can be classified under two sections: Laboratories with real hardware/equipment and software simulation based laboratories. Both laboratory models can be designed as distant laboratories which empower the distance education trend. Software simulation-based laboratories are most suitable for enriching educational subjects. Students may attend to a simulated laboratory work in an ideal environment to gather the expected results in the end in between certain limits directing them to learn a required educational goal. Working with real hardware equipment or downscaled real hardware models and acquiring realistic results is another story. In case of elearning, it becomes even more difficult because the learners are physically distant from the laboratories that they must use to get these skills[2].

The Internet Assisted Laboratory mentioned in this study provides a laboratory environment with a downscaled plant hardware. Because realistic scenarios and reports are required for an experiment like real-time PID control of a heater tube for various scenarios, the environment has been constructed with genuine hardware and hardware control equipment. The only missing part is the control method itself which is asked from the student to design for instructor-defined specific scenarios.

[1] *Corresponding author: Kocaeli University, Department of Informatics, 41380, Izmit/Kocaeli, Turkey, selcuk@kocaeli.edu.tr*

[2] *Kocaeli University, Department of Computer Engineering, 41380, Izmit/Kocaeli, Turkey. samet.diri@kocaeli.edu.tr*

[3] *Kocaeli University, Department of Information Systems Engineering, 41380, Izmit/Kocaeli, Turkey, myildirim@kocaeli.edu.tr*

2. DISTANT LABORATORY REQUIREMENTS

Distance is the very first requirement for a distant laboratory. If we assume that a laboratory experiment to be executed has a dangerous environment or one or more laboratory tasks have potential danger, the laboratory environment should be distant-enough to not only the students but also any personnel working around the environment. Therefore, in general, it is possible to say that a distant laboratory is better if it is totally managed autonomously by the laboratory hardware itself. Laboratory equipment should be able to return to pre-experiment states and condition to allow the next student to perform their task.

If it is Internet accessible as in our study, a distant laboratory should be protected against cyber threats which may lead to operating system, software and/or hardware malfunctions. For this purpose, it is also important to properly isolate all distant laboratory components where feasible in order to inflict the least damage possible when it is impossible to totally avoid a cyber threat.

Depending on the nature of an experiment, the laboratory should be monitored via video stream server(s) and real-time report screen(s). When necessary, real-time interaction should be possible.

In today's infrastructure design approach, the more components of an infrastructure are adaptive to various tasks, the better it is feasible. From an educational point of view, a distant laboratory design should satisfy a laboratory environment compatible with various programming languages and various hardware to work with. This generalization perspective will prevent an increase in number of laboratory and/or equipment requirement to fulfill educational objectives.

Ease of use is an additional key feature. While providing necessary complexity to complete a task according to educational objectives, the laboratory environment should be accessible by a student independently as much as possible from client side environment.

3. PHASES OF EXPERIMENT EXECUTION

For distant laboratory experimentation, there are necessary phases required. These phases also point to vital isolation needs for disaster recovery plans as they do in our study. As it is known that there are certain ICT (Information and Communication limitations)[3], our study targets to decrease the need for specific limitations and time needed to restore a distant laboratory in failure. This is accomplished by its isolated structure and the text preprocessor design in response to conditions which will threaten laboratory system stability.

a. Authentication

An authentication mechanism is required for a secure experimentation. It is important to confirm student IDs via a robust authentication in order to evaluate performances of students individually and genuinely. Cyber security attacks such as brute force and denial of service attacks should be considered and a cyber attack preventing mechanism should be included as a first key step of a sustainable distant laboratory design.

b. Learning

A student should learn all the essential information about what and why they are up to realize. In this phase, it is important that students are presented enough materials.

c. Code Development

Code development phase can be performed on an online page or on the student side of the wire with templates whenever needed. Basic principle is to allow students to create their codes using simple text editors where possible.

d. Upload

Codes and files which contain block and link information like Matlab/SIMULINK in this study are, in fact, plain text files. Other than specific task which require compiled files in the form of operating system-wide executable, any executable file should not be downloaded to server side, as a principle..

e. Text Preprocessing

After a successful file upload sequence, an important phase of the experimentation phase should be initiated: Text preprocessing. Since the distant laboratory platform mentioned in this study will not allow pre-compiled and/or files subject to direct execution, files downloaded to the server will be as modifiable text files.

f. Execution

Student files should be compiled or interpreted and run after a succeeded text-preprocessing phase. As we assume that code about to run has been properly modified and vital code insertions are made to ensure a safe experimentation after the text-preprocess phase of the sequence, by means of distant laboratory software and hardware, the downloaded file can be run under continuous inspection for possible run-time malfunctions.

g. Reporting

In addition to real-time monitoring information and/or video stream, a detailed final report should be provided after a distant laboratory experiment. Some files which include gathered runtime experiment information should be in generalized formats allowing third party software to process them later and further.

h. Storing

Following a successful experiment and gathering of results as expected, a report should be generated and stored in the according database table for the student and tutor(s) for further inspection and/or evaluation.

4. THE TEXT PREPROCESSING COMPONENT

A distant laboratory which supports multiple programming languages and hardware should have a critical component: A text preprocessing service. A text preprocessor should gather information of a hardware subject to experimentation, inspect and intervene to the code uploaded to the distant laboratory system by a student to ensure the system stability and durability, where necessary.

The hardware components of a laboratory have certain limits. Independently from its own protection measures, a generalized infrastructure of a distant laboratory should be liable to targeted hardware for an experiment. In our study, a certain database table and its fields are defined to hold necessary input and output limits. A code uploaded by a student may include virtually unlimited variations of harmful directives. Some codes may enforce hardware controller(s) to output damaging control signals while others may have malicious effects on software and/or operating system. Except database-defined hardware limits, operating system specific software limits and intentional task specific or laboratory condition specific limitations, students should feel free to develop their own code in their own style.

a. Error Handling

Uploaded student code won't require error handling for successful execution. On the other hand, for a complete error handling, text preprocessor frames the whole code with language-specific error handling verbs like try/catch. Even it is possible to require certain lines for a process to work correctly as in [4], our base of study is not to ask for any code restrictions or requirements from students other than their tasks, as much as possible. Of course they will need some specific code or block templates to control a specific hardware.

```
try
...
putsample(analog_output,9);              % Latch 9 volts on configured
% DAQ analog output
invalid_command(signal_in,pid_transfer_fun);
disp('this line will never be displayed');
```

```
...
catch
        putsample(analog_output,0);          % Reset analog output
error_to_report=lasterror;
% more error handling operations based on experiment hardware and report preferences
end
```

As seen in the code above, student's code is put between try and catch statements by the text preprocessor and in addition to this modification, for a condition which will force laboratory system to an unrecoverable state, lines put after catch statement will ensure that the system will return to the initial state if possible. Because various target systems require various initialization procedures, the operations which should be performed right after a critical failure are pulled from the according database table.

b. Hardware Support

The Text Preprocessor does not allow students to send values out of range to data acquisition device output(s). Before sending voltage value to the DAQ output, the output variable is checked against invalid values, again, if according policy is not set to return an error. Also, it checks absolute (directly given numerical) output values for range compatibility and does the preferred action. Based on global or task-specific hardware usage policy, it returns an error or outputs the threshold value instead:

```
if sys_out_signal>hard_max_limit
        sys_out_signal=hard_max_limit;
else
        if sys_out_signal<hard_min_limit
                sys_out_signal=hard_min_limit;
        end
end
putsample(analog_output,sys_out_signal);        % putsample detected
% Lines above putsample are inserted by text preprocessor
```

c. Time Limit

The text preprocessor detects language-specific loops and break them reporting the issue when time-limit is reached. It will also detect time variable(s) in text-based graphical representations of systems and set them to task-specific strict time limit. Default policy for the distant laboratory designed in this study is as below:

- Experiment tasks should run in a timely fashion, according to maximum time limit value set in the database
- Execution time is checked based on programming language, like tic/toc
- All language-specific loops should break if time limit set for the task is exceeded
- Text-based model files (like SIMULINK) should be configured to run for an allowed time.

d. Text Preprocessor Design

The text preprocessor used in the Internet Assisted Laboratory system is written in Hypertext Preprocessor Language (PHP). It is chosen for its powerful text manipulation functions. The programming language-specific text preprocessor codes can be included to the infrastructure whenever necessity arises.

5. THE INTERNET ASSISTED LABORATORY EXPERIMENT ENVIRONMENT

In our study, a fundamental PID experiment environment is designed and configured for general compatibility with various software development options and hardware.

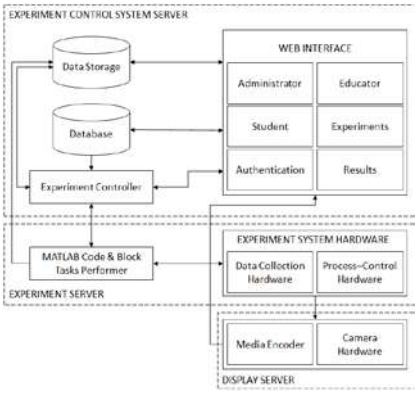

Figure 40. Internet Assisted Laboratory Scheme

The Text Preprocessor is the key component of the Experiment Controller and Task Performer shown in figure X. For ease of use and special uses in our study, Text Preprocessor is partially written in MATLAB for the "MATLAB Code & Block Tasks Performer" component.

Figure 41. A fully functional Internet assisted laboratory prototype

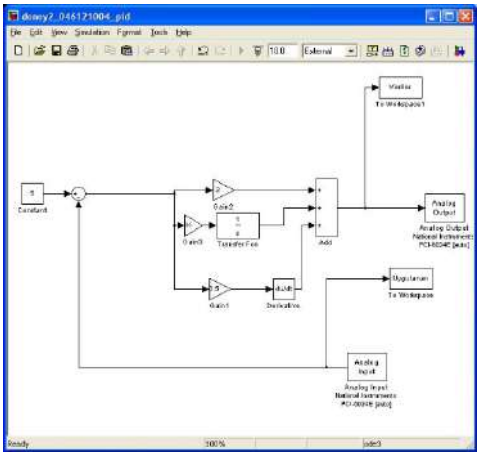

Figure 42. PID controller experiment work uploaded by a student

RESULTS AND DISCUSSION

It is seen that accessing a remote laboratory via strictly controlled infrastructure and yet which allow coding freedom to a high degree provides a second-best-to-being-there environment. It also helps tutors to present their educational material and test the educational outcome while focusing on what is important. In order to attend to ever evolving technology from a certain point, it is prominent that a remote laboratory runs as the way a real laboratory does. Experimentation by means of unrestricted operations or codes as much as possible is one of the desired features of an efficient laboratory. On the other hand, it is important to design a sustainable software and hardware infrastructure accordingly. The text preprocessor introduced in this study has a key role for this purpose since it strictly yet gently inspects and manipulates uploaded codes where necessary. Thus, it helps keeping the whole Internet assisted laboratory intact.

CONCLUSIONS

Distant and virtual laboratories designed to provide laboratory experimentation support for distance education of physical sciences require a high similarity to actual hands-on laboratories. Experiments which provide experimentation via student coding abilities require additional features, such as evaluation/interpretation of uploaded codes. The text preprocessor introduced in this paper suggests a solution to potentially malicious codes uploaded to be run in an internet assisted laboratory environment. There are plenty of programming languages in the world of software development. It is possible to develop another pseudo-code like programming language which is specific to a distant laboratory environment and its features. Although it is true that learning a programming language helps to learn another, forcing students to learn a new coding terminology despite its ease of use and similarity with programming languages which are used widely emphasizes a questionable educational method usage. This raises a need for support of programming languages currently in use by software developers. Therefore, using a database powered text preprocessor for code interpretation is one of the most flexible solutions which fit for purpose. The text preprocessor design in this study accepts a single user at a time and the Internet assisted laboratory hardware allows multiple users to view the experimentation process. Since it is shown that the distance separating the actors of a collaborative development project is no longer a problem considering the current technological means [5], it is definite that both a text preprocessor and an experiment environment controller version which support collaborative work will be needed to be developed as a future work in our ongoing study.

REFERENCES

[1]. K. Francis et al., "Forming and transforming STEM teacher education: A follow up to pioneering STEM education," 2018 IEEE Global Engineering Education Conference (EDUCON), Santa Cruz de Tenerife, Tenerife, Islas Canarias, Spain, 2018, pp. 686-693.doi: 10.1109/EDUCON.2018.8363297

[2]. I. Sanogo, S. Ouya, A. Dahirou and C. Lishou, "Proposal of cloud-based online laboratory model for practical training in the telecoms and networking fields," 2016 IEEE Global Engineering Education Conference (EDUCON), Abu Dhabi, 2016, pp. 1101-1105.doi: 10.1109/EDUCON.2016.7474691

[3]. R. Radhamani, N. Nizar, D. Kumar, B. Nair, K. Achuthan and S. Diwakar, "Low cost neuro-inspired robots for sustainable laboratory education," 2016 International Conference on Robotics and Automation for Humanitarian Applications (RAHA), Kollam, 2016, pp. 1-6.doi: 10.1109/RAHA.2016.7931870
[4]. T. O. Almeida, J. F. d. M. Netto and M. L. Rios, "Remote robotics laboratory as support to teaching programming," 2017 IEEE Frontiers in Education Conference (FIE), Indianapolis, IN, 2017, pp. 1-6. doi: 10.1109/FIE.2017.8190472
[5]. K. Gaglo, M. Seck, S. Ouya and G. Mendy, "Proposal for an online practical work platform for improving the teaching of STEM," 2018 20th International Conference on Advanced Communication Technology (ICACT), Chuncheon-si Gangwon-do, Korea (South), 2018, pp. 738-743. doi: 10.23919/ICACT.2018.8323904

BIOGRAPHY

Selcuk Ogutcu was born in Izmit in 1976. He has been graduated from Computer Technical High School in 1994. He has completed Bachelor of Science in Computer Education in 1998. Following a year of computer teaching in a high school, he has become a research assistant in 1999 in Kocaeli University. He has completed his master degree on Computer Systems in 2001. He has graduated from doctoral program on Electrics Education in 2011. He is married and is father of a daughter.

ICENS 4TH INTERNATIONAL CONFERENCE ON ENGINEERING AND NATURAL SCIENCE
2 - 6 May 2018 KIEV UKRAINE

Genetic Algorithm and Fuzzy Logic Based Auto-Test System for Distance Education

Samet Diri[1], Selcuk Ogutcu[2], Mehmet Yildirim[3]

Abstract

In this study, a genetic algorithm and a fuzzy logic based multiple choice test system is proposed. Learning is the process by which knowledge or skill creates long-term behavioral changes on individuals. Examinations are needed to measure the effectiveness of the learning process. These exams can be prepared by an instructor or automatically by means of a computer. Nowadays, with the widespread use of internet distance education has become popular, thus the necessity of creating an automatic exam through the internet has emerged. Although there are many methods for testing knowledge and skill acquired through learning, one of the most effective methods of measurement is multiple-choice test. The level of learning can be measured correctly by selecting the appropriate questions by optimizing the combination of the questions. Different attributes can be used in the selection of the questions included in the test to be created. Generally, the questions to be included in the multiple choice test are determined by the user determined difficulty, discrimination index and the frequency of the questionnaire. In the proposed system, the fitness function in the genetic algorithm consists of these attributes and is calculated using the fuzzy logic. It has been found that the system using the fuzzy logic is more successful than the system those not using the fuzzy logic when compared to each other.

Keywords: Exam evaluation, fuzzy logic, genetic algorithm, multiple choice test.

1. INTRODUCTION

With the developing technology, new methods have been developed which provide quick and easy solutions to the complex and difficult problems of the past. In particular, instead of strict optimization techniques, the use of soft computing and evolutionary algorithms is at the forefront. Genetic algorithms, one of the evolutionary approaches, have an important place in these methods. Hybrid solutions benefit from various soft computing methods with the inclusion of genetic algorithms are continuously being developed.

Genetic algorithm is a search and optimization method based on natural selection principles. The basic principles were put forward by John Holland at the University of Michigan in the 1970s [1]. After the introduction of the basic principles, many scientific studies on genetic algorithms have been published. Genetic algorithms have successful applications in fields such as optimization, scheduling, machine learning, design, cellular production, recommendation systems. Unlike traditional optimization methods, genetic algorithms use coded forms rather than whole sets of parameters. Genetic algorithms that work according to probability rules need only a well-defined objective function. Genetic algorithms scan a specific part of the solution space, not the whole. Thus, they can reach the solution in a much shorter time by searching effectively. Most of the problems require a large set of solutions to be scanned. Genetic algorithm is used to obtain an acceptable result in a short time [2].

Another important advantage of genetic algorithms is the simultaneous analysis of the population of solutions. So they should not stick to the local best solutions. Genetic algorithms have advantages over traditional artificial intelligence methods as well as traditional optimization methods. These advantages are related to the search structure of genetic algorithms. The search structure of genetic algorithms is explained by hypothesis of Subsequence Theorem and The Building Blocks [3].

[1] *Corresponding author: Kocaeli University, Department of Computer Engineering, 41380, Izmit/Kocaeli, Turkey.* samet.diri@kocaeli.edu.tr

[2] *Kocaeli University, Department of Informatics, 41380, Izmit/Kocaeli, Turkey,* selcuk@kocaeli.edu.tr

[3] *Kocaeli University, Department of Information Systems Engineering, 41380, Izmit/Kocaeli, Turkey,* myildirim@kocaeli.edu.tr

Fuzzy logic was developed in 1965 by Zadeh. According to Aristotelian logic, an object is either a member or not a member. Zadeh proposed fuzzy logic against the dual logic system in the form of Aristotelian logic [4]. Fuzzy logic is a logic system that tries to determine the proportions at which events occur in relation to events that we encounter in daily life. For example, modeling water pollution measurements in different parts of a city is a fuzzy logic problem. A model based on the degree of pollution of water rather than a model of "water is either polluted or not polluted" would be a more realistic solution [5].

The ability of the fuzzy logic theory to express gradual membership has an important place in defining uncertainties. Fuzzy logic theory provides a powerful and meaningful means of measuring uncertainty. In addition, it provides a meaningful representation of the indefinite concepts expressed by language. However, the classical logic theory based on Aristotelian logic treats all the individuals belonging to a given area as the members belonging to the family and those not belonging to it. There is a definite and indeterminate distinction between the members of the cluster and the non-members. A fuzzy set is defined by assigning a value to each element mathematically representing the degree of membership in the cluster [6].

The rapid developments demonstrated by computer and internet technologies provide high performance and convenience both in the presentation of educational material and in the management of measurement and evaluation process. As a result of these developments, distance education, e-learning and Learning Management Systems (LMS) have been developed and widely used. The use of LMS is also preferred in distance education as a space-independent education method.

Exams are necessary for measuring knowledge. Examinations are needed to measure the effectiveness of the learning process. The exams can be prepared by an instructor or automatically by means of a computer. Nowadays, with the widespread use of internet, distance education has become popular. Thus, the need of exam auto-creation via computer applications for online evaluation has emerged. Although there are many methods for testing knowledge and skill acquired through learning, one of the most effective methods of measurement is multiple-choice test. The level of learning can be measured accurately by selecting the appropriate questions by optimizing the combination of the questions based on educational goals. Different attributes can be used in the selection of the questions included in the test to be created. Generally, the questions to be included in the multiple choice tests are determined by the instructor determined difficulty, discrimination index and the frequency of the questionnaire.

In this study, a genetic algorithm and a fuzzy logic based multiple choice test system is proposed which the fitness function in the genetic algorithm consists of these attributes and is calculated using the fuzzy logic.

2. AUTO-TEST SYSTEM

The Auto-Test System (ATS) is a test process management system developed to manage pre-examination and post-examination processes. ATS performs but not limited to genetic algorithm and fuzzy logic based question selection process for exam. ATS consists of two phases. The first phase, the pre-exam process, contains the parts of the process those need to be completed before the exam. The second phase comprises of the process is to be performed after the examination. The pre-exam phase consists of the subject, questions and exam preparation procedures while the post-exam phase consists of the evaluation of the questions applied in the exam and the updating of the question values according to the results.

The web part of ATS is developed with Adobe ColdFusion 9, HTML, CSS and JavaScript. Genetic algorithm and fuzzy logic based question selection part was developed with MATLAB R2013. Questions, user information and all other data are stored in the MSSQL 2012 database.

a. Pre-Exam Process of the ATS

First of all, the user must be registered to the system. The user who completes the registration process can log on with their designated password.

Following a successful login, the user is directed to the main page with main menu, some important information and notices about the ATS, according to their credentials. At the top of the page, there is the main menu.

During the management of the examination, it is necessary to define the questions to be used in the examination and to prepare the examination booklet based on desired attributes. Definition of questions alone is not enough. Because all user-defined questions do not have to be related to the same subject or course.

Users must define their subjects in order to be able to produce an automatic test through the ATS. Questions have to be associated with the topics. Each question can only be associated with one topic. In this way, both a topic pool and a pool of questions are created. The topic referred to may be a title or a sub-topic of a course. For example, Mathematics-I course or sub-topics like "Functions" can be defined as topics. The user can define both of these fields. When creating the exam, choosing both of the topics can be an examination of both general questions about Mathematics-I and specific questions about "Functions". The user can list, edit, or delete their own topics. The user cannot delete the subjects like questions already associated.

When defining a question, the user must select the topic which the question belongs, and they must identify the question body, the correctors, and the correct answer. For using fuzzy logic based GA question selection, the user must define their prediction for difficulty and the discrimination index values. As a standard, the difficulty value is between 0 and 1. 0 represents very easy questions, 1 represents very difficult questions. This range is scaled from 1 to 5 because all users can have difficulty distinguishing between difficulty values of 0 and 1. In this scale, 1 represents very easy, 5 represents very difficult. Similarly, the discrimination index is in the range of -1 and 1. However, a problem between -1 and 0 should not be asked anyway. For this reason, the scaling is chosen as from 0 to 1 as well as difficulty between 1 and 5. In this scale, 1 represents low discriminator, 5 represents high discriminator. Difficulty factor is calculated by (1) and the discrimination index is calculated by (2) [7].

$$P_{difficulty} = \frac{d_{top}+d_{bottom}}{N} \quad (1)$$

Here, d_{top} represents the 27% student group with high scores from the exam, d_{bottom} is the 27% student group with low scores from the exam, and N is the total number of students in the upper and lower groups.

$$P_{discrimination} = \frac{d_{top}- d_{bottom}}{n} \quad (2)$$

Here, d_{top} represents the 27% student group with high scores from the exam, d_{bottom} is the 27% student group with low scores from the exam, and n is the number of students in the upper or lower groups.

The user can list, edit, or delete his or her own questions. The user cannot delete the questions for which the selection for an exam has been done.

After completing all of the subject and question definition, the user can generate an exam.

The user can list, edit, or delete his or her own exams. The user cannot delete the exam for which the evaluating for the exam has been done.

An instructor can evaluate the exam and also list all of the exam results. After evaluation, ATS updates difficulty and discrimination indexes of each questions by using (1) and (2). When the update process is completed, they can observe the number of answers given to each answer in charts and the difficulty and the discrimination index of each question.

b. Question Selection for Auto-Test System

In order to generate an exam, the name of the examination, the date, the topics to be selected, the difficulty and discriminatory values should be defined. When the questions are selected with fuzzy logic based GA, the topics, number of questions, difficulty and discrimination values are used. When the user generates an exam, ATS stores the HTML data in the database. When the form is stored, the ATS fetches the fuzzy logic calculated cost values from the database and runs the GA code. The GA code first receives the input data. Then the desired average difficulty, discriminant index and frequency values are processed by the fuzzy logic shown in figure 1.

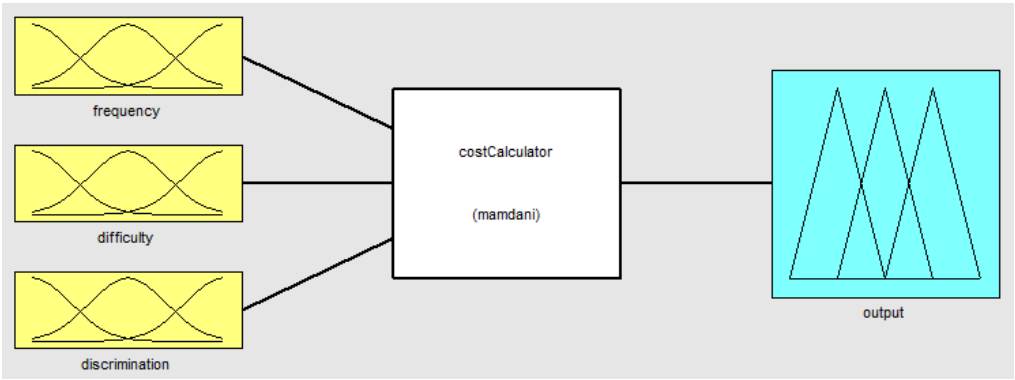

Figure 1. Fuzzy logic input parameters and output diagram

After the expected value of the test is generated with fuzzy logic, the initial population is generated. The initial population is processed in the objective function. The fitness values of the produced population can be calculated. In the objective function, the cost values are calculated with the variance of expected exam value and each genes fuzzy logic calculated values. This repeats until reaching the maximum population or when the fitness value is zero. When the GA finds the best solution, it returns the solution. If it cannot find the best solution, it returns the local best solution.

The GA uses elitism and multi-point crossover to improve the performance of the question selection process. It also uses roulette wheel for selection mechanism.

Our proposed ATS system's test parameters and trial numbers shown in Table 1.

Table 12. Comparison of the input parameters and trial number

Inputs	GA Powered by Fuzzy Logic	Traditional GA
Number of Question in the Data Set	480	480
Number of Questions in the Exam	48	48
Population Size	100	100
Max Generation	500	500
Mutation Rate	%0.2	%0.2
Elitsm	YES	YES
Selection Mechanism	Roulette Wheel	Roulette Wheel
Multi-Point Crossover	YES	YES
Diffuculty	5	5
Discrimination Index	5	5
Frequency	0	0
Number of Trials	10	10

3. RESULTS

The results obtained when traditional GA and fuzzy logic based GA codes are executed are shown in table 2. In our study, we used 480 questions as data set and we wanted 48 question to be selected by the GA. Our proposed fuzzy logic based GA is a little bit faster than traditional GA. Traditional GA runs about 6.41 seconds

but our proposed fuzzy logic based GA runs about 6.34 seconds. In addition, our proposed system's average frequency of the questionnaire is much more less than traditional GA. In traditional GA frequency of the questionnaire is about 1.41. This means most of the questions are selected at least more than one in the past. But our proposed fuzzy logic based GA's frequency of the questionnaire is about 0.86. This means some questions have been selected for the first time. Gathered results also indicate that we have enough data to select questions from the question pool precisely. Average difficulty and discrimination indexes are identical for both traditional GA and fuzzy logic based GA.

Table 13. Comparison of the results

Outputs	GA Powered by Fuzzy Logic	Traditional GA
Average Operation Time (in seconds)	6,337	6,405
Average Difficulty of the Exam	5	5
Average Discrimination Index of the Exam	5	5
Average Frequency of the Questionnaire	0,86	1,41

REFERENCES

[1]. J. H. Holland, *Adaptation in Natural and Artificial Systems*, MI: University of Michigan Press, Ann Arbor, USA, 1975.
[2]. David E. Goldberg, *Genetic Algorithms in Search, Optimization and Machine Learning*, 1st ed., Addison-Wesley Longman Publishing Co. Inc., Boston, MA, USA. 1989.
[3]. J. McCall, "Genetic Algorithms for Modelling and Optimisation", *Journal of Computational and Applied Mathematics*, vol. 184 (1), pp. 205-222, Dec. 2005.
[4]. ZADEH, L.A., "Fuzzy Sets", *Information and Control*, vol. 8 (3), pp. 338-353, 1965.
[5]. M. Sari, Y. S. Murat, M. Kirabali, "Fuzzy Logic Modelling Approach and Applications", *Dumlupinar University Journal of Institute of Sciences*, vol. 9(9), pp. 77-92, 2005.
[6]. F. Mei, Z. Man, T. Nguyen, "Fuzzy Modelling and Tracking Control of Nonlinear Systems", *Mathematical and Computer Modelling*, vol. 33 (6-7), pp. 759-770, 2001.
[7]. O. C. Adiguzel, F. Ozudogru, "Development of an Academic Achievement Test for Common Compulsory Foreign Language I Course of Universities", *Trakya University Journal of Education*, vol. 2 (3), pp. 1-11, 2013.

BIOGRAPHY

Samet Diri was born in 1988 in Bursa. He completed his primary, secondary and high school education in Bursa. He graduated from Kocaeli University Technical Education Faculty Computer Teaching Department in 2011, He is continuing his graduate education in Computer Engineering Department of Kocaeli University Institute of Science and Technology, which he started in 2011. He worked as a software developer in Kocaeli University between the years of 2012-2017. He has been working as an Instructor at Kocaeli University since 2017. He is married and father of one daughter.

ICENS 4TH INTERNATIONAL CONFERENCE ON ENGINEERING AND NATURAL SCIENCE
2 - 6 May 2018 KIEV UKRAINE

Detection of Sleep States from EEG Signals by Using Convolutional Filter Features Based on Wavelet and Short Time Fourier Image Patterns

Hasan Polat[1], Mehmet Sirac Ozerdem[2], Veysi Akpolat[3],Nezahat Akpolat[4]

Abstract

EEG based brain computer interface systems (BCIs) have become an important tool for physicians to support the diagnosis of various diseases. In clinical area, the analysis of EEG signals recorded by brain imaging methods can be faster and more stable by using these systems. The extraction of meaningful features from the EEG signals is one of the primary goals for researchers in order for BCI systems to work efficiently. It can be seen from the literature that various time-frequency transformation methods developed for non-stationary signals such as EEG are used in this context. In this study, it was aimed to determine sleep state using wavelet and short time Fourier transform based EEG image patterns. Unlike the one-dimensional time series analysis commonly used in the literature, one-dimensional time series were represented in two dimensions using different time-frequency methods in this study and the classification performances of these methods were compared. Wavelet and short time Fourier transforms were applied to obtain time-frequency images from EEG signals related to different sleep states and two-dimensional convolutional filters were applied to extract the characteristic information from the obtained the image patterns. In order to obtained characteristic features from image patterns, four different filters (blurring, edge detection, identification, Gaussian) determined in 3x3 dimensions. One-dimensional average polling operation was applied to reduce the dimension of the obtained two-dimensional feature vectors. Final feature vectors related to EEG signals obtained at the end of the average pooling process were classified by using the k-nearest neighbor algorithm (kNN). Two fold cross validation was applied to improve reliability of the classification process. The classification performances based on wavelet and short time Fourier image pattern were obtained as 97.37% and 92.37%, respectively.

Keywords: Wavelet, Short Time Fourier, Convolutional Filter, EEG

1. INTRODUCTION

The importance of sleep is still not fully expressed, but it is well known that sleep deprivation affects human health negatively [1]. it can easily be said that sleep deprivation adversely affects basic cognitive dynamics such as memorization, learning and concentration [2]. In the world, a large number of people who are experiencing sleep problems are trying to maintain their lives with these problems. Therefore, the quantity and quality of studies on sleep disorders are increasing day by day [3].

Sleep deprivation is known to seriously threaten human life. Therefore, the determination of the sleep level is very important in the clinical area. Determination of sleep levels of people on the clinical area is performed by physicians. In this context, the polysomnographic signals recorded from the persons are analyzed by the physicians. By analyzing these signals, it is tried to be determined that there is any problems while sleeping. Polysomnogram signals are consist of EEG, electrooculogram (EOG) and electromyography (EMG) [3]. it takes a considerable amount of time for these signals to be analyzed by physicians. When these signals are analyzed, there is a high probability of errors due to the long recording time. Analysis of polysomnography signals by brain computer interface systems will provide important support to physicians since human power analysis has these disadvantages.

[1]*Corresponding author:Mus Alparslan University, Department of Electrical and Electronic Engineering, 49250,Mus, Turkey. hasanpolat1989@hotmail.com*

[2]*Dicle University, Department of Electrical and Electronic Engineering,,21280, Diyarbakir, Turkey,sozerdem@dicle.edu.tr*

[3] *Dicle University, Faculty of Medicine,21280, Diyarbakir, Turkey,vakpolat@dicle.edu.tr*

[4] *Dicle University, Faculty of Medicine,21280, Diyarbakir, Turkey,nakpolat@dicle.edu.tr*

EEG signaling is a method of monitoring brain cell activities with electrical signals [4]. Since the EEG signals are cheap, easy and reliable to record, this study used the EEG signal from polysomnography signals. EEG signals are used in many areas, especially in the health area. Especially the frequency components of EEG signals contain important information related to brain dynamics [5]. It is known that different time-frequency transformation methods are used to extract meaningful information from the EEG signals.

In this study, it was aimed to determine sleep state using wavelet and short time Fourier transform based EEG image patterns. Unlike the one-dimensional time series analysis commonly used in the literature, one-dimensional time series were represented in two dimensions using different time-frequency methods in this study and the classification performances of these methods were compared. Wavelet and short time Fourier transforms were applied to obtain time-frequency images from EEG signals related to different sleep states and two-dimensional convolutional filters were applied to extract the characteristic information from the obtained the image patterns. In order to obtained characteristic features from image patterns, four different filters (blurring, edge detection, identification, Gaussian) determined in 3x3 dimensions. One-dimensional average polling operation was applied to reduce the dimension of the obtained two-dimensional feature vectors. Final feature vectors related to EEG signals obtained at the end of the average pooling process were classified by using the k-nearest neighbor algorithm (kNN). The process steps applied in this study was shown in Figure 1.

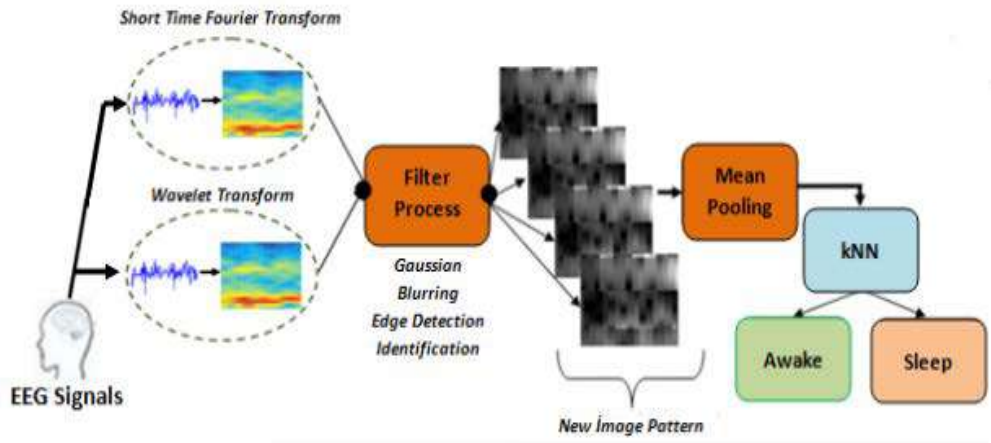

.Figure 1. The process steps applied in this study

2. MATERIAL AND METHODS

a. Datasets

The EEG records used in this study were obtained from the sleep laboratory at the Medical Faculty of the University of Dicle. EEG segments related to different sleep states have been identified with the help of a specialist physician from EEG signals. In the preprocessing step, the EEG segments were filtered with a 0-32 Hz low pass filter. Filtered EEG signals are separated by 5 second segments .EEG signals related to different sleep states were digitized with an analog digital converter with a sampling rate of 150 Hz [6].

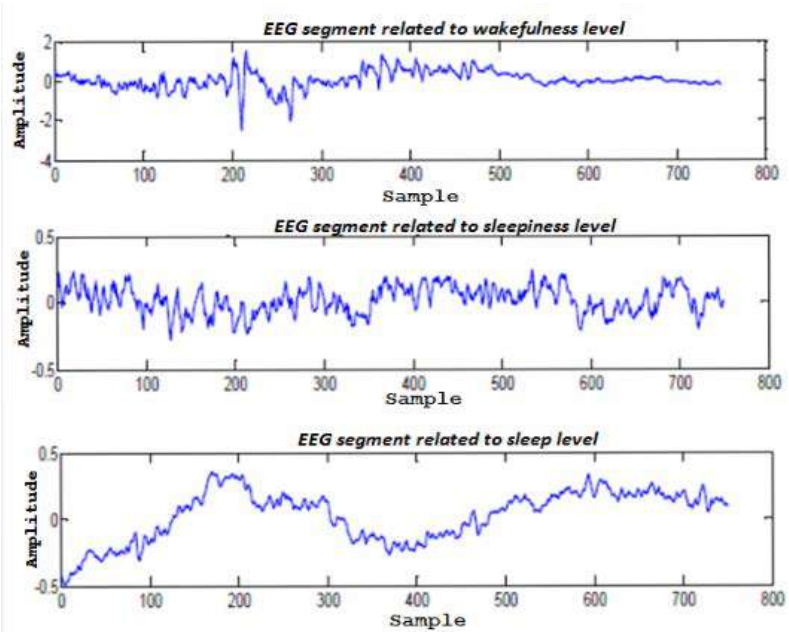

Figure 2. Examples of EEG segments related to different sleep states.

b. Representation of EEG Signals as Image Pattern

The main digital transformation methods used to represent EEG signals as images pattern are short time Fourier and wavelet transforms.

The short time Fourier transform is based on the ability to take Fourier transforms separately, dividing the signal into segments. In other words, the EEG signal can be processed using time window of different width [7]. Wavelet theory is still being developed with signal processing as a popular topic that scientists are working on. There are many applications on non-stationary signals and numerical signal processing by using wavelet analysis. For spectral analysis of non- stationary signals, wavelet transform has advantages over spectral analysis methods. The most important advantage of wavelet transform is the use of wide windows for low frequencies and narrow windows for high frequencies [8-9]. In this study, classification performances of features obtained using wavelet and short time Fourier transform were evaluated separately and compared.

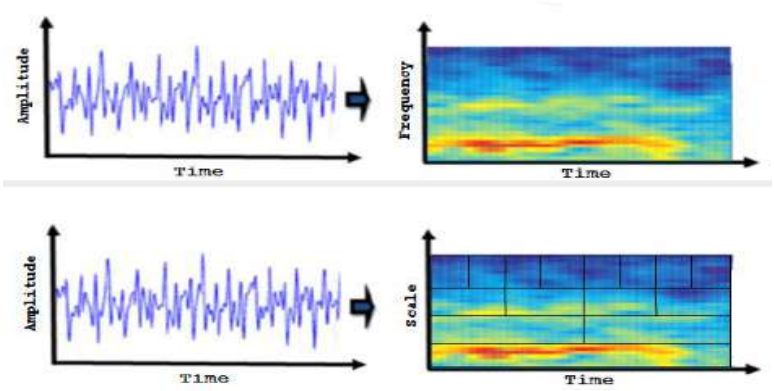

Figure 3. Short time Fourier transform ve wavelet transform

.

c. Convolution process for image pattern

Spatial filtering of a image is performed by an operation called convolution. the output value of a pixel in the convolution process is found as the weighted sum of itself and neighboring pixel values [10]. In this study, EEG signals are represented as two-dimensional image matrices using wavelet transform and short time Fourier transform. EEG signals that is one dimensional time series were processed as image patterns. Four different filters were used to extract detailed and deterministic features of the new image matrices. The same filters were applied separately for the two methods in order to compare wavelet based and short time Fourier transform based image patterns. These filters are designated as blur, gauss, sharpening, and identity filters, respectively. The filter matrix dimensions are set to 3 x 3. the average pooling process was applied to obtain the specific sub band ranges from the final filtered image patterns obtained and to reduce the feature vector dimensions.

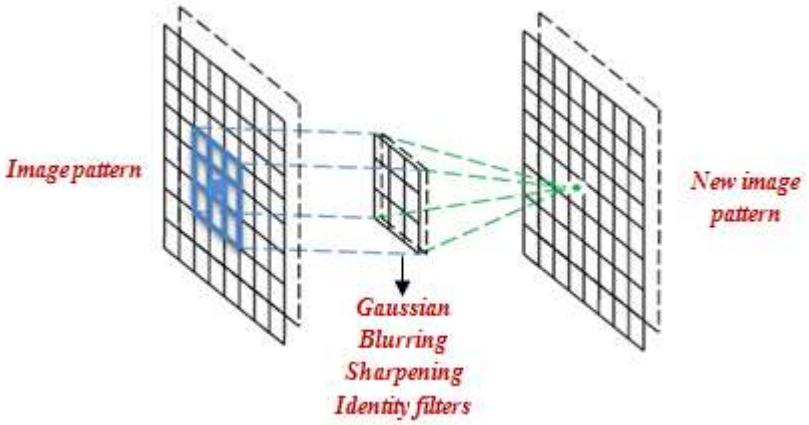

Figure 4. The convolution process

d. K-nearest neighborhood algorithm

The nearest neighbors algorithm is one of the most commonly used simple learning algorithms in the literature. Since the kNN algorithm is not a parametric method, there is no assumption about the data structure [11]. The fact that most of the data used in classification problems do not meet the theoretical assumptions makes the KNN algorithm advantageous. The classification process in the kNN algorithm begins with taking into account the features of an object of unknown class and calculating the distance of that object from its objects in the training set. In this study, the Euclidean distance measure, which is frequently used in the literature, is used in distance calculations. The mathematical expression of the Euclidean distance measure is given in Equation 1. The kNN algorithm has a user-changeable k parameter. According to the specified k parameter, an unknown object can be assigned.

$$d = \sqrt{\sum_{i=1}^{n} (x_i - y_i)^2} \qquad (1)$$

The determination distance of unknown object in kNN classifier was depicted in figure 5.

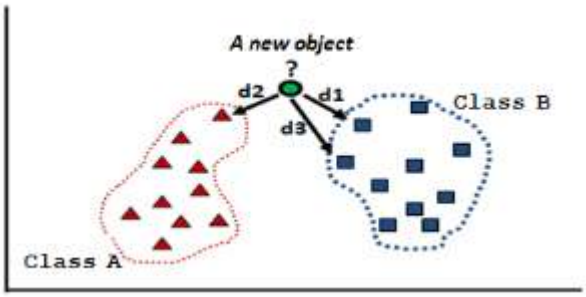

Figure 5.The classification process in kNN algorithm.

3. RESULTS AND DISCUSSION

In this study, it was aimed to determine sleep state using wavelet and short time Fourier transform based EEG image patterns. Unlike the one-dimensional time series analysis commonly used in the literature, one-

dimensional time series were represented in two dimensions using different time-frequency methods in this study and the classification performances of these methods were compared. A total of 39 EEG segments were classified, 20 awake and 19 EEG segments related to sleep states. 20 EEG segments were used for training and 19 EEG segments were used for testing. The classification performances based on wavelet and short time Fourier image pattern were obtained as 97.37% and 92.37%, respectively. Two fold cross validation were used in order to improve reliability of classification process. The confusion matrix based on short time Fourier and wavelet transform were given below, respectively in Table I and II.

Table I. Test confusion matrix related to short time Fourier transforms

	Awake	**Sleep**
Awake	**19**	**0**
Sleep	**3**	**17**

Table II. Test confusion matrix related to wavelet transform

	Awake	**Sleep**
Awake	**19**	**0**
Sleep	**1**	**19**

In this study, unlike one dimensional time series analysis commonly used the literature, one dimensional time series were represented in two dimensions.

- The high performance obtained indicates that this method can be used in different area of EEG signals.
- it can be argued that wavelet based image pattern provide more specific features in the representation of EEG signals related to sleep states.

ACKNOWLEDGMENT

The authors would like to thank to Mehmet Akin for his support in obtaining the EEG data set in this study.

REFERENCES

[1] Koley and D. Dey. (2012). An ensemble system for automatic sleep stage classification using single channel EEG signal. Computers in Biology and Medicine, no. 42, pp. 1186-1195.

[2] Ebrahimi F. Mikaeili M. Estrada E. Nazeran H. (2008). Automatic sleep stage classification based on EEG signals by using neural Networks and wavelet packet coefficients. 30th annual international IEEE EMBS conference Vancouver. August. pp. 20-24.

[3] Hassan, A. R., & Bhuiyan, M. I. H. (2017). Automated identification of sleep states from EEG signals by means of ensemble empirical mode decomposition and random under sampling boosting. Computer Methods and Programs in Biomedicine, 140, 201-210.

[4] Basar, E., Eroglu C.,Karaka,S., Schurmann, M., *Brain oscillations in perception and memory*, International Journal of Psychophysiology, 2000, 35, pp. 95-124

[5] Atagun, M.I., Guntekin, B., Ozerdem, A., Tulay, E., Basar, E., online first article. *Decrease of theta response in euthymic bipolar patients during an oddball paradigm*, Cognitive Neurodynamics, Volume 7, Issue 3, 2013, pp. 213-223.

[6] H.Acar. (2010). Uyaniklik seviyesinin kestiriminin DSP tabanli olarak gerceklestirilmesi. Dicle University, Institute of sciece.

[7] Polikar, R. 2006. The Engineer's Ultimate Guide to Wavelet Analysis. [http://person.hst.aau.dk/enk/ST8/wavelet_tutotial.pdf], Available: 05.11.2015.

[8] Subasi, A., Signal Classification Using Wavelet Feature Extraction and a Mixture of Expert Model", Expert Systems with Applications, 2007, pp. 1084–1093

[9] Subasi, A., Ercelebi, E., *Classification of EEG signals using neural network and logistic regression*, Computer Methods and Programs in Biomedicine, 2005, 78, pp. 87-99.

[10] Guo Y. Liu Y. Oerlemens A. Lao S. Wu S. Law M. S. (2015). Deep learning for visual understanding: A review. Neurocomputing. Volume 187. pp. 27-48.

[11] L. A. Berrueta,R. M. Alonso,K. Heberger, Supervised pattern recognition in food analysis. Journal of Chromatography A, 2007, 1158, 196-214

ICENS 4TH INTERNATIONAL CONFERENCE ON ENGINEERING AND NATURAL SCIENCE
2 - 6 May 2018 KIEV UKRAINE

An Investigation of Increase the Effectiveness of Ohmic Cooking of Meat by Using with Ultrasound Treatment

Anil Uzun Ozcan[1], Medeni Maskan[2], Metin Bedir[3], Huseyin Bozkurt[4]

Abstract

Cooking of meat is a very important process for providing its microbiological quality, sensory characteristics, better digestibility and nutritive value. The method of cooking is one of the major factors that affect the eating quality of beef meat. In conventional cooking methods such as grilling, frying, roasting, boiling, smoking, meat is exposed to elevated temperatures, the outside may be overcooked with the interior insufficiently cooked since low rate of heat penetration to the thermal center and this will lead to a reduction in the quality of the beef meat. Consumption of this meat product is known to cause intestinal, stomach cancer and increase risk of pancreatic cancer. For this reason, alternative cooking technologies, especially ohmic cooking that enables faster cooking, less power consumption and safer product have gained importance in recent years. However, meat has heterogeneous and compact muscle fibers structure. For this reason, in this review, increase the effectiveness of ohmic treatment for cooking meat by using with the combination of ultrasound treatment thought was searched and developed.

Keywords: Ohmic cooking, ultrasound treatment, beef meat

1. INTRODUCTION

Meat is the main constituent of our diet and it is a nutritious, protein-rich food which contains all necessary amino acids required for human body. Meat is generally cooked prior to consumption with the exception of specially dried and fermented products [1]. Cooking is always necessary to make sure that the meat is completely cooked, safe, and that all pieces of meat and areas of the meat batch have been heated to the required temperature to kill pathogens and coliforms [2]. The method of cooking is one of the major factors that affect the eating quality of meat. Nowadays, the cooking method of meat generally based on conventional cooking methods. In conventional cooking methods such as grilling, frying, roasting, boiling, smoking, meat is exposed to elevated temperatures, the outside may be overcooked with the interior insufficiently cooked since low rate of heat penetration to the thermal center and this will lead to a reduction in the quality of the beef meat. Moreover, conventional methods have long process times, high temperature application and high energy consumption. Consumption of this meat product is known to cause intestinal, stomach cancer and increase risk of pancreatic cancer. For this reason, alternative cooking technologies, especially ohmic cooking that enables faster cooking, less power consumption and safer product have gained importance in recent years.

a. Ohmic Cooking

Ohmic process also known as Joule heating is based on the passage of electrical current through a food product having electrical resistance. Heat is generated instantly inside the food, and the amount of heat is directly related to the voltage gradient and the electrical conductivity [3]. The success of ohmic heating depends on the rate of heat generation in the system, the electrical conductivity of the food, electrical field strength, residence time and the method by which the food flows through the system [4].

[1] *Corresponding author: Kilis 7 Aralik University, Engineering and Architecture Faculty, Department of Food Engineering, Kilis, Turkey. aniluzunozcan@kilis.edu.tr*

[2] *University of Gaziantep, Engineering Faculty, Food Engineering Department, Gaziantep, Turkey, maskan@gantep.edu.tr*

[3] *University of Gaziantep,Engineering Faculty, Physics Engineering Department, Gaziantep, Turkey, bedir@gantep.edu.tr*

[4] *University of Gaziantep, Food Engineering Department, Gaziantep, Turkey, hbozkurt@gantep.edu.tr*

Ohmic cooking major advantages are: continuous production without heat transfer surfaces, rapid and uniform treatment of liquid and solid phases with minimal heat damages and nutrient losses (e.g., unlike microwave heating, which has a finite penetration depth into solid materials), ideal process for shear-sensitive products because of low flow velocity, optimization of capital investment and product safety as a result of high solids loading, reduced fouling when compared to conventional heating, better and simpler process control with reduced maintenance costs, environmentally friendly system [5].

Reference [6], made a comparison between ohmic cooking and conventional cooking of beef samples having different initial fat contents (2%, 9% and 15%) in their study, Ohmic cooking was faster than the conventional cooking. Ohmically cooked samples were firmer than those conventionally cooked but yield and fat retention was similar. These results show that ohmic cooking could be a fast-alternative method for meat products. However, meat has heterogeneous and compact muscle fibers structure. So, the use of ohmic cooking alone couldn't be so effective for meat cooking. For this reason, ultrasound treatment should be applied as a pretreatment to increase the effectiveness of ohmic treatment for cooking meat.

b. Ultrasound Treatment

Ultrasound can be defined as a mechanical vibration above the audible sound spectrum (18 kHz and higher). In other words ultrasound starts when the human hearing ends. Ultrasonic waves are affected by some factors that affect sound as the density of the material/medium and they also share the same properties (wavelength, amplitude, etc.) (Gonzales, 2003). Ultrasound techniques are relatively cheap, simple and energy saving, and thus became an emerging technology for probing and modifying food products. Low power (high frequency) ultrasound is used for monitoring the composition and physicochemical properties of food components and products during processing and storage, which is crucial for controlling the food properties and improving its quality. High power (low frequency) ultrasound, on the other hand, induces mechanical, physical and chemical/biochemical changes through cavitation, which supports many food processing operations such as extraction, freezing, drying, emulsification and inactivation of pathogenic bacteria on food contact surfaces (Awad et al., 2012).

Recent years, there is a great interest in ultrasound due to the fact that industries can be provided with practical and reliable ultrasound equipment. Nowadays, its emergence as green novel technology has also attracted the attention to its role in the environment sustainability.

Ultrasound assisted cooking and can increase the water holding properties of meat and the binding strength which is responsible for increased cooking yield (Reynolds et al., 1978) Ultrasound can assist in extraction, gelation and restructuring of meat proteins. Ultrasound treatment can replace/reduce salt in restructured beef roll manufacture and results in superior colour (Vimini et al., 1983). Ultrasound assists the process by disrupting the meat myofibrils which releases a sticky exudate and this binds the meat together and leads to an increase in the strength of the reformed product (Mason et al., 1996).

In the literature, there is some information exist about the application of ohmic cooking alone, ohmic-microwave cooking, ohmic – conventional cooking and only ultrasound treatment in meat, separately. However, there is no any investigation about the combination of ultrasound - ohmic methods for cooking of meat. The use of ultrasound process as a pretreatment before ohmic cooking is believed to increase the effectiveness of ohmic cooking since ultrasound treatment has many affirmative properties on meat fiber structure. Therefore, this study will light the way for developing alternative cooking methods and optimum conditions with minimum processing to produce reliable cooked meat with different process variables. In this way, beef thickness, high power ultrasound durations, ohmic voltage values and ohmic process time should be decided by performing many experimental trials according to its indicative results of quality analyses such as moisture content, pH, texture, color, cooking yield, lipid oxidation, microbiological analyses and statistical analyses.

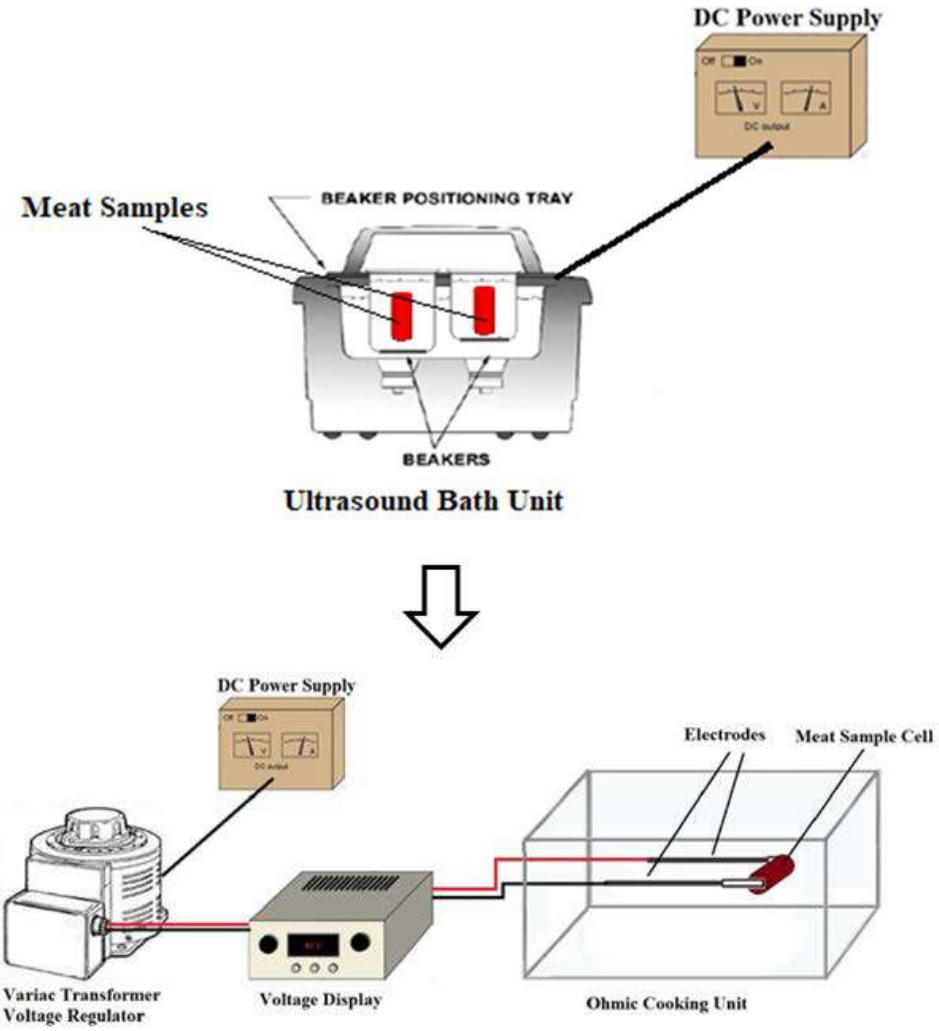

Figure 1. Experimental set-up design for the combination of ultrasound treatment with ohmic cooking

2. CONCLUSION

Consequently, the use of ultrasound process as a pretreatment before ohmic cooking is believed to increase the effectiveness of ohmic cooking. Ultrasound treatment combination with the ohmic cooking should be a reliable method to optimize quality and safety parameters for meat cooking.

ACKNOWLEDGMENT

The authors wish to thank the Scientific Research Projects Executive Council of University of Gaziantep.

REFERENCES

[1]. C. Bejerholm and M. D. Aaslyng, M. D., *Cooking of meat*, 1st ed., Encyclopedia of Meat Sciences, eBook, Academic Press, Danish Meat Research Institute, Denmark, 2004.
[2]. C. L. Knipe and R. E. Rust, Thermal processing of ready-to-eat meat products; Thermal Processing of Slurries, 1st ed., D. Horn and D. Voit, Jr., Ed. Iowa, USA: Blackwell Publishing, 2010.
[3]. Y. G. Turp, I.Y. Sengun, P. Kendirci, and F. Icier, "Effect of ohmic treatment on quality characteristic of meat: A review," Meat Sci.,vol. 93, pp. 441–448, 2013.
[4]. K. S. Varghese, M. C. Pandey, K. Radhakrishna, A. S. Bawa, "Technology, applications and modelling of ohmic heating: a review," *J. of Food Sci. and Tech*., vol. 51, pp. 2304–2317, 2014.
[5]. D. Sun, *Thermal Food Processing; New Technologies and Quality Issues*, Boca Raton, Newyork: CRC Press, 2006
[6]. H. Bozkurt, and F. Icier, "Ohmic cooking of ground beef: Effects on quality," *J. of Food Eng.*, vol. 96, pp. 481–490, 2010.
[7]. Gonzales, "Effects of power ultrasound treatments on properties of Longissimus beef muscle," Phd thesis, Iowa State University, Iowa, 2003.
[8]. T. S. Awad, H. A. Moharram, O. E. Shaltout, D. Asker, and M. M. Youssef, "Applications of ultrasound in analysis, processing and quality control of food: A review," *Food Res. Int*., vol. 48, pp. 410–427, 2012.
[9]. J. B. Reynolds, D. B. Anderson, G. R. Schmidt, D. M. Theno, and D. G. Siegel, "Effects of ultrasonic treatment on binding streangth in cured ham rolls," *J. of Food Sci*., vol. 43, pp. 866-869, 1978.
[10]. R. J. Vimini, J. D. Kemp, and J. D. Fox, "Effects of low frequency ultrasound on properties of restructued beef rolls," *J. of Food Sci*., vol. 4, pp. 1572-1573, 1983.
[11]. T. J. Mason, L. Paniwnyk, J. P. Lorimer, "The uses of ultrasound in food technology," *Ultrason. Sonochem*., vol. 3, pp. 253- 260, 1996.

ICENS 4TH INTERNATIONAL CONFERENCE ON ENGINEERING AND NATURAL SCIENCE
2-6 May 2018 KIEV UKRAINE

Effect of Ohmic Cooking Alone on Moisture Content and Total Aerobic Mesophilic Count of Beef Muscle

Anil Uzun Ozcan[1], Medeni Maskan[2], Metin Bedir[3], Huseyin Bozkurt[4]

Abstract

In this study, effects of ohmic cooking alone on moisture content and total aerobic mesophilic count of beef meat were investigated. The ohmic cooking was performed by applying three different voltage gradients which are 40, 55 and 70 V/cm for 7 minutes. The increase in voltage value caused to affect the moisture content of beef muscle insignificantly ($p > 0.05$) while affecting ($p < 0.05$) the total aerobic mesophilic count of beef significantly during the ohmic cooking process. The levels of total aerobic mesophilic count in raw meat were detected 5.7 log cfu/g. At 40 V, 55 V and 70 V total aerobic mesophilic count significantly reduced to 4.6, 4.3, 4.0 log cfu/g, but inhibition of all of the microorganisms could not be succeed. The results obtained in this study revealed that ohmic cooking process alone is not a sufficient cooking method for reaching better safety parameters of beef meat.

Keywords: Ohmic cooking, moisture content, microbiology, beef meat

1. INTRODUCTION

Meat is the main constituent of our diet and it is a nutritious, protein-rich food which is highly perishable and very much susceptible to spoilage. Cooking of meat is essential to achieve a palatable and safe product [1]. Cooking is also a preservation method which makes the meat safe to eat [2]. Meat undergoes many changes during cooking, both physical and chemical, including weight loss, modifications of water-holding capacity, texture, muscle fibre shrinkage, colour and aroma development. Quality characteristics of cooked meat products are also dependent on the composition and characteristics of the muscles, the cooking method, as well as the time/temperature evolution during cooking [3].

The method of cooking is one of the major factors that affect the eating quality of meat. The cooking method should be chosen to be appropriate for the type of meat, the amount of connective tissue and the shape and size of the meat [4]. Nowadays, the cooking method of meat generally based on conventional cooking methods. Conventional methods are the process which have long process times, high temperature application and high energy consumption. All of these problems experienced during the cooking process of meat brought on alternative cooking methods which are economic and more practical. Moreover, alternative cooking methods enables an acceptable product in terms of sensory, nutritional and microbial characteristics. Ohmic cooking method is one of the alternative methods. The advantages of ohmic cooking over conventional heating include shorter processing times, higher yields, and less power consumption while still maintaining the nutritional value of meat products [5]. Ohmic cooking is an emerging thermal process technology and describes the process when an electrical current is passed directly through a food and the resistance imposed by the food leads to the generation of heat within the product [6]. Ohmic cooking, generates heat, by direct energy application, in a volumetric fashion which reduces the long cooking times associated with conventional methods [7]. Ohmic cooking offers the potential safety for cooking faster and instantly inside the meat product. However, meat samples commonly have heterogeneous structures because of their fat content which affects the uniform distribution of heat [5]. The purpose of this study is to investigate the effect of ohmic cooking process by using

[1] *Corresponding author: Kilis 7 Aralik University, Engineering and Architecture Faculty, Department of Food Engineering, Kilis, Turkey. aniluzunozcan@kilis.edu.tr*

[2] *University of Gaziantep, Engineering Faculty, Food Engineering Department, Gaziantep, Turkey, maskan@gantep.edu.tr*

[3] *University of Gaziantep,Engineering Faculty, Physics Engineering Department, Gaziantep, Turkey, bedir@gantep.edu.tr*

[4] *University of Gaziantep, Food Engineering Department, Gaziantep, Turkey, hbozkurt@gantep.edu.tr*

three different voltage values (40, 55 and 70 Volt) on moisture content and total aerobic mesophilic count of beef meat.

2. MATERIALS AND METHODS

a. Sample Preparation and Electrode Designation

Beef meat (Longissimus dorsi) was purchased from a local market in Gaziantep. For electrode designation, a test cell that 5 cm long and 3.5 cm diameter was made which the meat could be inserted inside it. Then, 430 code number of stainless steel electrodes (3.5 cm diameter) were used to contact and cover the meat surface in whole. For this system, meat was shaped by 5 cm diameter sharp metal cutter and then located into test cell. Next, stainless steel electrodes was placed the two open gapes end of test cell and whole contact with the meat. No meat pieces were outside of the electrodes so homogeneous and uniform cooking of meat was achieved.

b. Ohmic Cooking

The designation of ohmic cooker was developed by Physical Engineering Department in Gaziantep University. For the designation of ohmic cooker, a 5 kw conductor, a 220- 24 Volt power supply, a limit switch, a 15 A fuse, a voltagemeter and an ampermeter was used. For the conduction of electric current into meat 430 code number of stainless steel metals were used as electrodes. The designed ohmic cooker was worked with the variable transformer connection in laboratory. Ohmic cooking duration was adjusted to 7 minute.

c. Moisture Content

Moisture content of the samples was determined by oven methods (AOAC, 1990) at 105°C until constant weight was reached.

d. Total aerobic meshophilic count (TAMC)

10 g of fresh beef meat, ohmic cooked meat and infrared cooked meats that were ohmically precooked and 10 volumes of sterile peptone solution (0.1 %) were added. After homogenizing the mixture a series of ten-fold dilutions was made using peptone water solution (0.1%) for analyzing microbial counts. Portions of 0.2 ml of the homogenate and each dilution were spread on duplicate plates of nutrient agar (Sisco Research, India). Total mesophillic aerobic plate counts were incubated at 37 C for 2 days. Colony numbers were determined from plates bearing 30 to 300 colonies. Data was represented in log of colony forming units (cfu) per g of beef meat.

e. Statistical Analyses

An ANOVA was performed for moisture content and total meshophilic aerobic plate count values as a function of voltage gradient for ohmic cooking to determine significant differences ($P<0.05$) using the SPSS version 21.0 (SPSS Inc., Chicago, IL, USA). Duncan's multiple range test was also carried out during the cooking period for determination of homogeneous groups. Trends were considered as significant when the means of compared parameters differed at a $P < 0.05$ significance level.

3. RESULT AND DISCUSSION

Ohmic cooking (40, 55 and 70 V, 7 min.) technique was applied to observe the moisture content and microbial quality of beef muscle in this study. Their results are given in Figure 1. and Table 1. Moisture content in cooked meats is important because it has a significant influence on taste. It also reflect the degree of cooking as insufficiently cooked patties will be moist, while over cooked patties will be hard [8]. On the other hand, it is known that total aerobic mesophilic bacteria count (TAMBC) could give an idea about the general hygiene of beef muscle that processes in these techniques. In this study, moisture content and TAMBC in raw meat was found to be 74.61% and 5.73 log cfu/g, respectively. As it is seen in the Figure 1 and Table 1, the increase of voltage value caused to decrease of moisture content insignificantly ($P>0.05$), however TAMBC was significantly decreased ($P<0.05$) below the detectable level but not to reach zero value.

Despite the different conditions (Voltage, time) used in these studies compared to our study, as a general, researchers found the reduction in microbial load by ohmic cooking as well as ours. Reference [8] studied

combined ohmic and conventional cooking of hamburger patties. Quality measurements of the meat patties cooked by the ohmic and the conventional method showed similar moisture content. Reference [9] used ohmic cooking (80 °C/13.78 min and 70 °C/31.44 – 40.36 min total holding time for inactivation of *Enterococcus faecalis*, inoculated to Bologna type sausages, and obtained a 9.06 log cfu/g reduction in the number of microorganisms. In the same way, Reference [10] studied ohmic cooking of meatballs. In their study, the initial microbial load of meatball samples by means of total aerobic mesophilic bacteria were 5.83 log cfu/g which close to ours. They investigated that, when holding time was shortened at constant temperature and voltage gradient, especially at 15 V/cm, higher reduction was achieved in total microbial counts ohmic cooking appears to be a promising and effective treatment to prevent pathogen growth in meat products. The optimum semi-cooking condition meeting these criteria was 15.26 V/cm voltage gradient and 0 s holding time at 75 °C. In this system were predicted as a 2.45 log reduction in total microbial count. All of the studies revealed that ohmic cooking is an effective method for reduction in microbial load of meat sample thus demonstrating the safety of this technique. However, ohmic cooking alone is not sufficient for obtaining safe meat. It should be combined another alternative methods. Because it is always necessary to make sure that the meat is completely cooked, safe, and that all pieces of meat and areas of the meat batch have been heated to the required temperature to kill pathogens and coliforms [11].

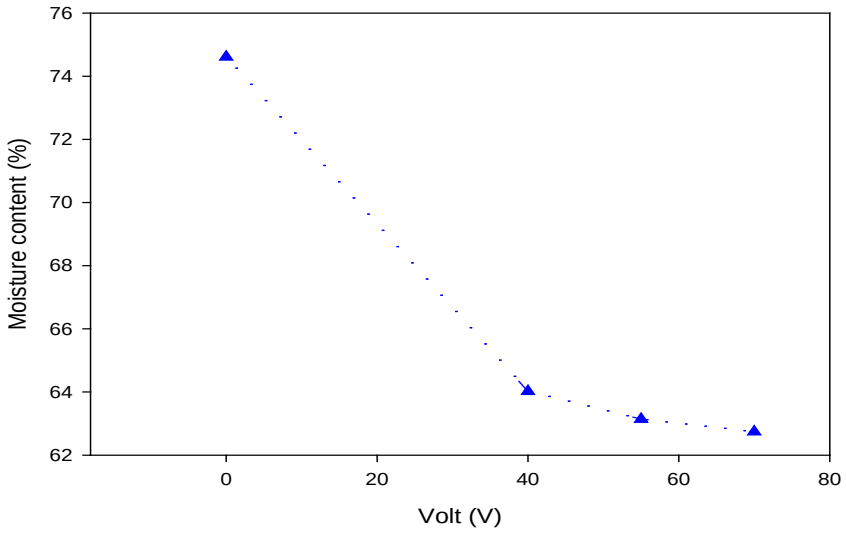

Figure 1. Effect of voltage gradient of ohmic cooking on moisture content

Table 1. Effect of ohmic cooking on moisture content and total aerobic mesophilic bacteria

Ohmic Cooking (7 min.)	**Moisture Content (%)**	**Total Count (log cfu/g)**
Raw meat	74.61[a]	5.73[a]
40 Volt	64.02[b]	4.69[b]
55 Volt	63.14[b]	4.39[c]
70 Volt	62.74[b]	4.00[d]

4. CONCLUSION

In this study, moisture content and general hygiene indicator bacteria namely total aerobic mesophilic was detected by application of ohmic cooking alone. The increase of voltage value at ohmic cooking did not cause a significant effect on moisture content however it caused a significant reduction on microbial load of beef muscle but not to reach zero value. As a consequence, the results obtained in this study revealed that ohmic cooking process alone is not a sufficient cooking method for reaching better safety parameters of beef meat. It should be combined another alternative method.

ACKNOWLEDGEMENT

The authors wish to thank the Scientific Research Projects Executive Council of University of Gaziantep.

REFERENCES

[1]. N. Gerber, M.R.L. Scheeder, and C. Wenk, "The influence of cooking and fat trimming on the actual nutrient intake from meat," *Meat Sci*., vol. 81, pp.148–154, 2009.
[2]. Uzun, "An investigation of changes in physical and chemical properties of kavurma during processing," M. Eng. thesis, University of Gaziantep, Gaziantep, Turkey, Jan. 2010.
[3]. B. Mora, E. Curti, E. Vittadini, and D. Barbanti, "Effect of different air/steam convection cooking methods on turkey breast meat: Physical characterization, water status and sensory properties," *Meat Sci*., vol. 88, pp. 489–497, 2011.
[4]. C. Bejerholm and M. D. Aaslyng, M. D., Cooking of meat, 1st ed., Encyclopedia of Meat Sciences, eBook, Academic Press, Danish Meat Research Institute, Denmark, 2004.
[5]. Y. G. Turp, I.Y. Sengun, P. Kendirci, and F. Icier, "Effect of ohmic treatment on quality characteristic of meat: A review," *Meat Sci*.,vol. 93, pp. 441–448, 2013.
[6]. J. G. Lyng, M. Zell, D. A. Cronin, and D.J. Morgan, "Ohmic cooking of whole beef muscle – Optimisation of meat preparation," *Meat Sci*., vol. 81, pp. 693–698, 2009.
[7]. J. G. Lyng, M. Zell, D.A. Cronin, and D. J. Morgan, "Ohmic cooking of whole turkey meat — Effect of rapid ohmic heating on selected product parameters," *Food Chem.*, vol. 120, pp. 724–729, 2010.
[8]. M. Farid, N. Ozkan, and I. Ho, "Combined ohmic and plate heating of hamburger patties: quality of cooked patties,"*J. of Food Eng*., vol. 63, pp. 141-145, 2004.
[9]. G. Piette, M. L. Buteau, D. De Halleux, L. Chiu, Y. Raymond, H. S. Ramaswamy, "Ohmic cooking of processed meats and its effects on product quality," *J. of Food Sci*., vol. 69, pp. 71–78, 2004.
[10]. F. Icier, I. Y. Sengun, Y. G. Turp, E. H. Arserim, "Effects of process variables on some quality properties of meatballs semi-cooked in a continuous type ohmic cooking system," *Meat Sci*., vol. 96, pp. 1345–1354, 2014.
[11]. C. L. Knipe and R. E. Rust, *Thermal processing of ready-to-eat meat products; Thermal Processing of Slurries*, 1st ed., D. Horn and D. Voit, Jr., Ed. Iowa, USA: Blackwell Publishing, 2010.

ICENS 4TH INTERNATIONAL CONFERENCE ON ENGINEERING AND NATURAL SCIENCE
2-6 May 2018 KIEV UKRAINE

Encapsulation of Synthesized Hydroxyapatite in PCL Microspheres by Using Electrospraying Method

Yahya Bozkurt[1], Necdet Mekki Ergul[2,3], Burak Ozbek[2,3], Nazmi Ekren[3,4], Serdar Salman[1,6] Faik Nuzhet Oktar[5,3], Mahir Mahirogulllari[7], Oguzhan Gunduz[1,3]

Abstract

Synthetic hydroxyapatite has been investigated for so many different applications in tissue engineering and orthopaedics. Because of their bioactivity and osteoconductivity properties, it can be used in this special applications. Polycaprolactone (PCL) are widely being used in tissue engineering operations because PCL is very cheap biodegradable polymers and also it has slow degradation rate and desirable mechanical properties. In order to create a new biodegradable and biocompatible composite scaffolds, self made synthetic hydroxyapatite mixed with PCL by electrospraying method. Hydroxyapatite powder was synthesized successfully with the different sintering temperature between 200-1000ºC by the sol-gel method. In addition to that, the synthetic hydroxyapatite powder was successfully encapsulated in biodegradable PCL microspheres by using electrospraying method.

Keywords: Synthetic hydroxyapatite, hydroxyapatite, PCL, Electrospraying, Microparticles, Biometarials

1. INTRODUCTION

New advances in bone tissue engineering new techniques are rapidly needed for invent of bone diseases, accidental damages and defects. Developments in nanotechnology and biotechnology cause to develop and use nanostructures for the aim of tissue engineering [1]. Biochemical composition and structure that supports osteogenic cell responses, appropriate kinetics of biodegradability, without any release of toxic byproducts, and a highly interconnected porous network that allows for proper tissue ingrowth and vascularization of the biomaterials are the main features that allows to use biomaterials in bone tissue treatments [2].

Hydroxyapatite (HAP: Ca10(PO4)6(OH)2) has so many attention as the replace material for deformed teeth or bones over the past years. The reason of this attention crystallographical

and chemical similarity with tissues of vertebrates. Hydroxyapatite is the main mineral that create the teeth and bones. Also it's demonstrate great biocompability with hard tissues, skins and muscle tissues. Because it can bond to bone structure easily. But Hydroxyapatite powder has low reliability with wet environments. That's why its really hard to use for heavy load bearing applications [3]. Because of all this conditions this inorganic phosphate has been investigated for medical applications, composites or coating methods. But also there are some examples and studies showed that hydroxyapatite powder can be useful in non-medical application, for example as packing media for column chromatography, gas sensors, catalysts, etc.[4]. There several various producing technique have been used to prepare hydroxyapatite powders. Some of these techniques are co-precipitation, sol-gel process, spray pyrolysis, hydrothermal synthesis, emulsion processing and mechano-chemical method. Between all these methods, Sol-gel has been most well liked method because of great inherent benefits such as homogeneous molecular mixin, low processing temperature and ability to generate nanocrystalline powders, bulk amorphous monolithic solids and thin films. With all this knowledge in this study, calcium nitrate tetrahydrate, Potassium dihydrogenphosphate and ammonia were the main ingredients to prepare hydroxyapatite particles [5].

For the creating encapsulated hydroxyapatite composite structure, many synthetic polymers were used. Such as polylactide (PLA), polyglycolide (PGA), and polycaprolactone (PCL). Among these polymers PCL is one of the common used in tissue engineering because of it has great biodegradability and biocompatibility. Slow

degradation rate is a good specialty to used in bone structure applications. And also PCL is one of the cheapest according to desired mechanical properties [6].

There are many producing techniques for forming one encapsulated composite structure from these two materials. Such as solvent extraction/evaporation, spray drying and suspension/emulsion polymerization. However these methods are not the perfect techniques for producing nano/micro particles. Electrospraying method came forward beside other techniques because of ability to produce with size controlling and near-monodisperse particles by changing parameters of process and solution concentration. Therewithal this method gives easier, faster and cheaper way to produce particles. Electrospraying working principle is dynamics of electrically charged fluids. This system is making smaller particles by charging droplets comes out from the needle tip. Electrical forces overcome the force of surface tension in the charged polymeric solution. This led to Coulomb fission of droplets which ends up with smaller jets [7,8]. With all this knowledge, synthetic hydroxyapatite and polycaprolactone as a biocompatible polymer used to make microspheres based bio composite material with electrospraying method for bone tissue engineering.

2. MATERIALS AND METHODS

a. Materials

Calcium nitrate tetrahydrate (Ca(NO3)2. 4H2O), Potassium dihydrogenphosphate (KH2PO4), Dichloromethane (DCM) and ammonia were purchased from Merck (Darmstadt, Germany). Polycaprolactone (PCL, Mw= 80.000 g/mol) were purchased from Sigma-Aldrich (Munich, Germany).

b. Synthesize of Hydroxyapatite Powder

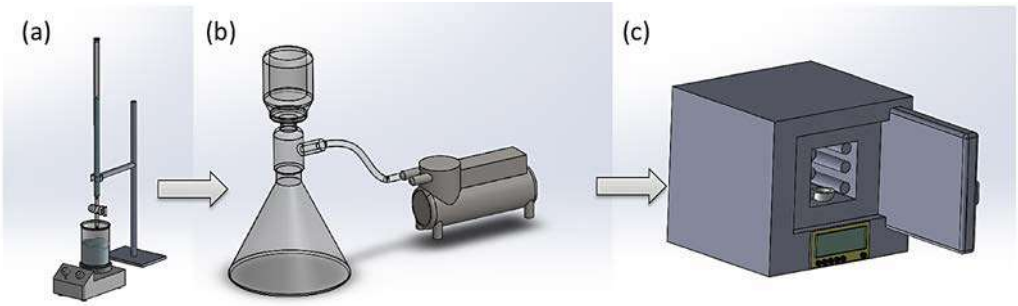

Figure 1 Hydroxyapatite synthesis process, (a) mixing process,(b) vacuuming process, (c) calcination process.

Calcium nitrate tetrahydrate (Ca(NO3)2. 4H2O) and Potassium dihydrogenphosphate (KH2PO4) were used as primary component for calcium and phosphorous. Calcium nitrate tetrahydrate and potassium dihydrogenphosphate solutions were dissolved in distilled water respectively 1M and 0.6 M (Fig. 1). Calcium nitrate tetrahydrate solution was added drop wise into potassium dihydrogenphosphate solution (Fig. 1a). Ammonia (NH_3) was added drop wise to settle pH=11 into the final solution. This precipitated solution was mixed in stirrer for 1 h and aged for a day. The precipitate were purified from solution with vacuum filter and washed with distilled water (Fig 1b). The precipitate dried in 40°C for a day in a dry oven. This dried powder separated to 9. And each sample sintered in respectively 200°, 300°, 400°, 500°, 600°, 700°, 800° ,900° and 1000° for 1 hour with electrical furnace (Fig 1c).

c. Preparation of PCL/ Synthesized Hydroxyapatite Solutions

PCL dissolved with various percentages of 1, 5 and 7 wt. % in DCM. Solutions have mixed with the magnetic stirrer at (23 ºC) for 1 hour. When PCL dissolved successfully, 0,003 gr synthesized hydroxyapatite were added separately in 1, 5 and 7 wt. % PCL solutions and mixed with magnetic stirrer for 1 hour. For the uniform mixture, final solution mixed by homogenizer for 10 min.

d. Producing of Synthesized Hydroxyapatite Loaded PCL Microspheres

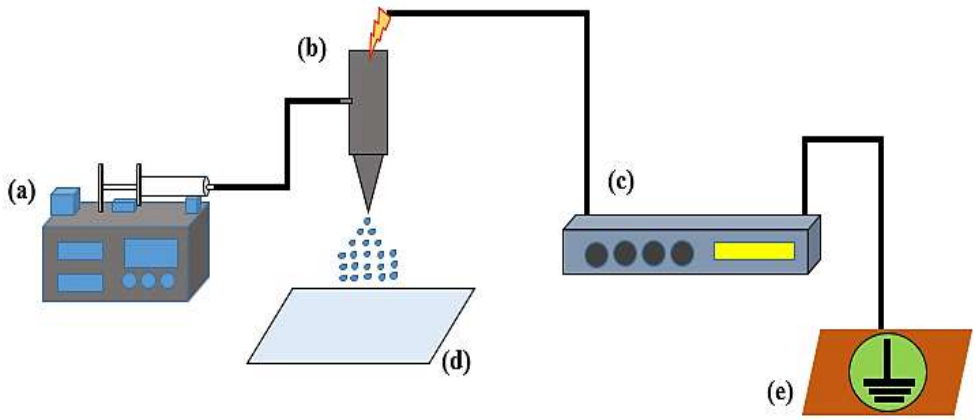

Figure 2. Schematic of electrospray set-up, (a) syringe pump,(b) needle, (c) power supply, (d) collector, (e) grounding.

Electrospraying of particles were made by using Basic System (Inovenso, Turkey) electrospraying setup (Fig. 2). First, 12 mL of prepared PCL/hydroxyapatite solution has pulled in to 20 mL plastic syringe (Fig 2a). After that process go on respectively: Flow rate applied by using syringe pump (IPS-12, Inovenso, Turkey) was 10 ml/h and solution pumped to needle which has 0.82 mm outer diameter and 0.51 mm inner diameter.(Fig 2b) Applied voltages changed between 10 to 15 kV (Fig 2c). Collector (Fig 2d) covered with baking paper adjusted at 8 cm away from the needle. Electrospraying process completed in 8 hours. Following by that, hydroxyapatite loaded PCL particles peeled from baking paper carefully for further characterization tests.

e. Scanning Electron Microscopy (SEM) and Optical Microscopy

Morphology characterization of micro particles fulfilled by using scanning electron microscope (SEM) (EVO ® LS 10, ZEISS, Germany) with an accelerating voltage of 10 kV. The surfaces of the prepared samples were coated with gold and palladium by using sputter (SC7620 Mini Sputter Coater, QUANTUM, United Kingdom) at 3 kV for 60 seconds.

f. Fourier Transform Infrared Spectroscopy (FT-IR)

Fourier transform infrared (FTIR) spectroscopy (Jasco 4700 Spectrometer, Easton, USA) used to determine any chemical interaction between the polymers. The spectra recorded in the range of 400-4000 cm^{-1} under ambient temperature (23 ºC). The system aligned before data collection. Samples with different calcination temperature hydroxyapatites and hydroxyapatite loaded PCL were prepared and collected for analysis of FT-IR.

3. RESULT AND DISCUSSION

a. Particle Morphology

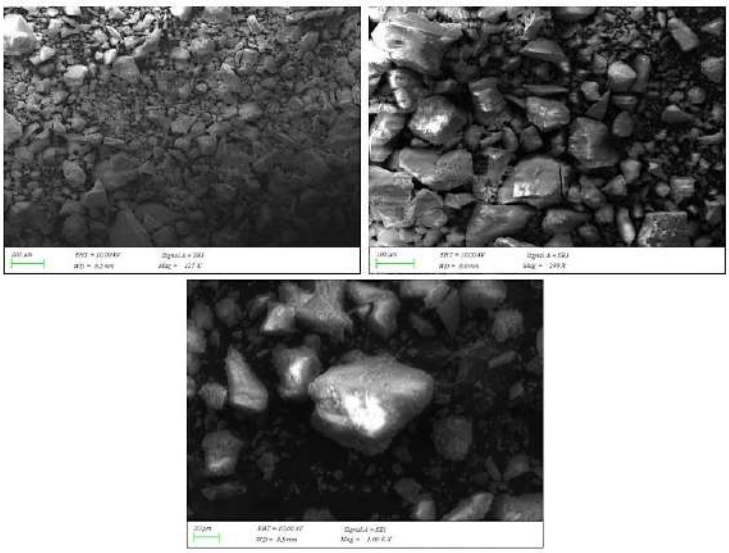

Figure 3. SEM images of Synthesized Hydroxyapatite calcinated in 600 ℃

SEM images shows hydroxyapatite synthesized successfully with sol-gel technique and heat treatment in 600 °C (Fig 3).

The powder seems like very agglomerated caused primarily by the different processes performed during the dying process. Small particles seen buried in every agglomerated cluster correspond to the calcium nitrate particles because these obtained from the recrystallization of the dissolved calcium nitrate at the drying process. The powder shows the exact morphology in (Fig 3.) after heat treatment at 600 °C. Also there are very fine particles of hydroxyapatite have been sintered during the heat treatment process. These can be seen as fracture surface of the particles [9].

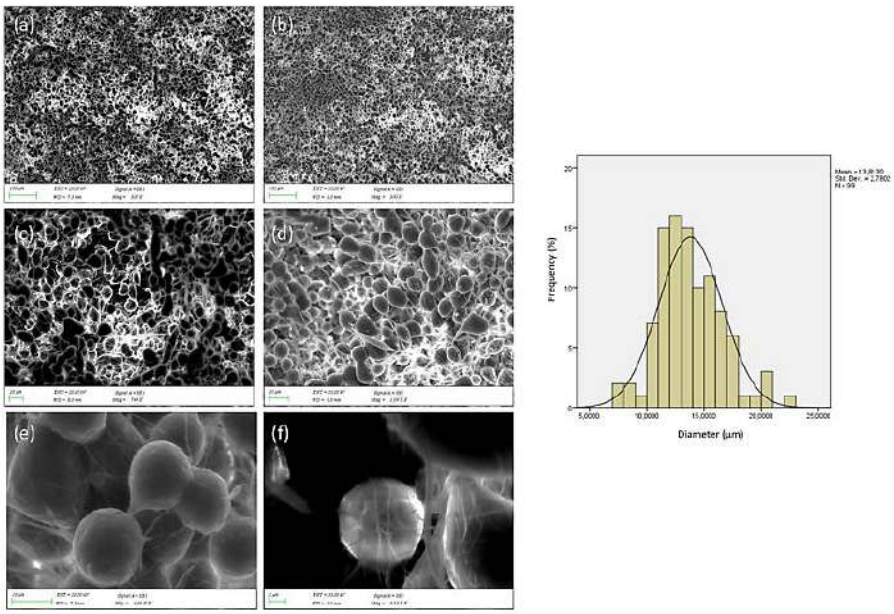

Figure 4. SEM images of the encapsulated hydroxyapatite PCL microspheres a) 300X b) 300X c)700X d) 1000X e) 4000X f) 9000X magnifications

Fig 4. is showing particle size and morphology, affected by changing polymer concentration. Particle size changed between 7.12 µm to 22.34 µm by decreasing flow rate 5 ml/h to 10 ml/h. The diameter of micro particles were between 7.12 – 22.34 µm and also depending on electrospraying solutions and parameters. PCL 3 wt. % concentration has the best spherical shape and diameter.

Aplied voltage is an other parameter that can control the morphology and size of electrosprayed particles. Common opinion is increasing the applied voltage effect to a decrease in the size of microparticles. However, there are some lower and upper voltage limits allows a stable jet in electrospraying. For the solutions with 3 wt. % PCL/HA concentrations, lower voltage applied to produce more uniform PCL/HA particles (Fig. 4) [10]

b. FTIR analysis

i. FTIR Analysis of 200-1000 ℃ Calcinated Hydroxyapatite

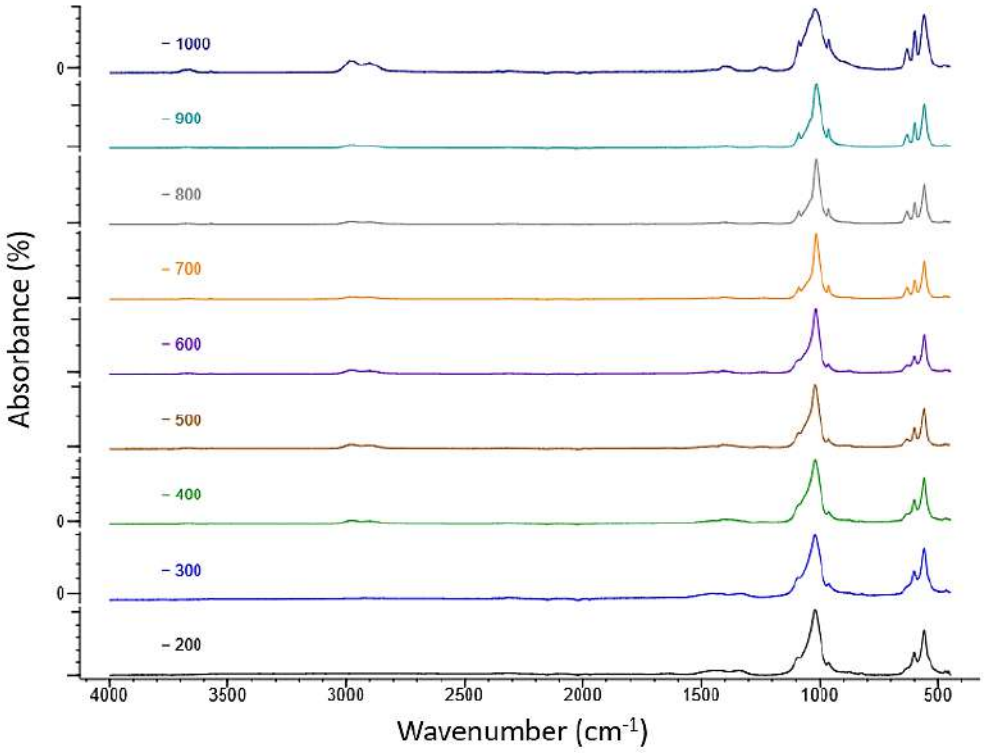

Figure 5 .FT-IR spectra of 200-1000 ℃ calcinated hydroxyapatite powders.

The FT-IR spectra of HA 200°C-1000°C are shown in (Fig 5.) In this graph between 3825 cm-1 and 2550.16 cm^{-1} shows the O-H stretching bonds. weak band of CO3-2 was shown in the region around 1567.78 cm^{-1} and the peak at 976.89 cm^{-1} corresponds to symmetric stretching mode of PO43-. Graph of each temperature shows that 560-602 cm^{-1} PO43- peaks turns 628-629cm^{-1}. But there was no change in 961 PO4-3 peaks. After 600°C sintering temperature creates PO2- peak at 1086 cm^{-1}. In 2900-3000 cm-1 H2O peaks can be seen. Also greater than 500°C temperature create OH^- peaks at 3540-3570 cm^{-1} [11].

ii. FTIR Analysis of Hydroxyapatite Loaded PCL Particles

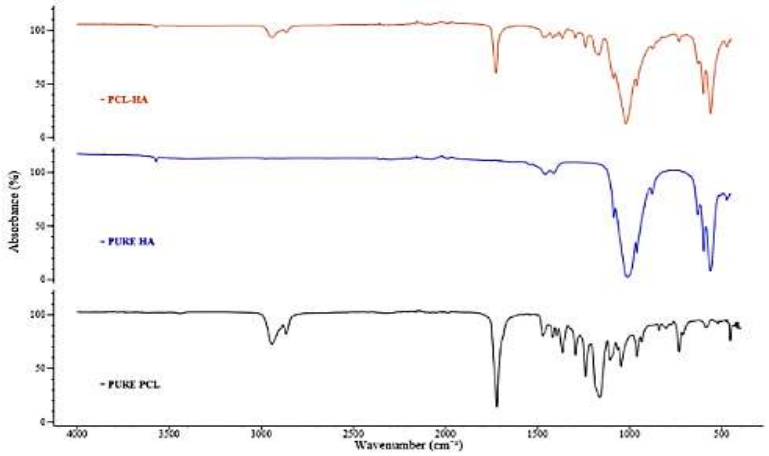

Figure 6. FT-IR spectra of Pure PCL, Pure HA and HA capsulated PCL microsphres.

In order to explore the molecular arrangement of hydroxyapatite loaded particles (fig 6.), FT-IR analysis was accomplished. Fig. proves the FT-IR spectra of the particles. There was a typical PCL related infrared band stretching was detected. The FT-IR spectra of Pure PCL, Pure HA and composite structure of PCL-HA are shown in Fig. In this graph between 3825 cm-1 and 2550.16 cm-1 shows the O-H stretching bonds. weak band of CO3-2 was shown in the region around 1567.78 cm-1 and the peak at 976.89 cm-1 corresponds to symmetric stretching mode of PO43-. This results shows that electrosprayed nanoparticles has Hydroxyapatite in their composition. And also there was typical PCL related infrared band stretching was detected. As a result asymmetric CH2 stretching peak at 2949 cm-1 , symmetric CH2 stretching peak at 2850cm -1 , carbonyl stretching peak at 1720 cm -1 , C-O and C-C stretching peak at 1285 cm -1 and asymmetric COC stretching peak at 1240 cm -1 were observed [12].

4. CONCLUSIONS

HA powder was synthesized successfully with the different sintering temperature between 200-1000°C by the sol-gel method. FT-IR graphics confirmed that all the characteristic HA bands consist of temperature between 200-600°C. The HA powders could be replaced by new bone biomaterial. In addition to that, PCL and hydroxyapatite solution able to generate micro particles from 8 cm distance by using 10mL/hr applied flow rate, 10-15 kW applied voltage. Also the synthetic hydroxyapatite powder was successfully encapsulated in biodegradable PCL microspheres by using electrospraying.

ACKNOWLEDGMENT

This project is granted by Marmara University, BAPKO project numbers: FEN-D-120418-0180

REFERENCES

[1] Gupta, D., Venugopal, J., Mitra, S., Dev, V. G., & Ramakrishna, S. (2009). Nanostructured biocomposite substrates by electrospinning and electrospraying for the mineralization of osteoblasts. Biomaterials, 30(11), 2085-2094.

[2] Phipps, M. C., Clem, W. C., Grunda, J. M., Clines, G. A., & Bellis, S. L. (2012). Increasing the pore sizes of bone-mimetic electrospun scaffolds comprised of polycaprolactone, collagen I and hydroxyapatite to enhance cell infiltration. Biomaterials, 33(2), 524-534.

[3] Mobasherpour, I., Heshajin, M. S., Kazemzadeh, A., & Zakeri, M. (2007). Synthesis of nanocrystalline hydroxyapatite by using precipitation method. Journal of Alloys and Compounds, 430(1-2), 330-333.

[4] Kim, I. S., & Kumta, P. N. (2004). Sol–gel synthesis and characterization of nanostructured hydroxyapatite powder. materials science and Engineering: B, 111(2-3), 232-236.
[5] Sanosh, K. P., Chu, M. C., Balakrishnan, A., Lee, Y. J., Kim, T. N., & Cho, S. J. (2009). Synthesis of nano hydroxyapatite powder that simulate teeth particle morphology and composition. Current Applied Physics, 9(6), 1459-1462.
[6] Wutticharoenmongkol, P., Sanchavanakit, N., Pavasant, P., & Supaphol, P. (2006). Preparation and characterization of novel bone scaffolds based on electrospun polycaprolactone fibers filled with nanoparticles. Macromolecular bioscience, 6(1), 70-77.
[7] Wu Y, Kennedy SJ, Clark RL. Polymeric particle formation through electrospraying at low atmospheric pressure. J Biomed Mater Res B Appl Biomater 2009;90(1):381-387.
[8] Chakraborty S, Liao IC, Adler A, Leong KW. Electrohydrodynamics: a facile technique to fabricate drug delivery systems. Adv Drug Deliv Rev 2009;61(12):1043-1054.
[9] Sanosh, K. P., Chu, M. C., Balakrishnan, A., Lee, Y. J., Kim, T. N., & Cho, S. J. (2009). Synthesis of nano hydroxyapatite powder that simulate teeth particle morphology and composition. Current Applied Physics, 9(6), 1459-1462.
[10] Zhou, F. L., Hubbard Cristinacce, P. L., Eichhorn, S. J., & Parker, G. J. (2016). Preparation and characterization of polycaprolactone microspheres by electrospraying. Aerosol Science and Technology, 50(11), 1201-1215.
[11] Fathi, M. H., & Hanifi, A. (2007). Evaluation and characterization of nanostructure hydroxyapatite powder prepared by simple sol–gel method. Materials letters, 61(18), 3978-3983.
[12] Polini, A., Pisignano, D., Parodi, M., Quarto, R., & Scaglione, S. (2011). Osteoinduction of human mesenchymal stem cells by bioactive composite scaffolds without supplemental osteogenic growth factors. PloS one, 6(10), e26211.

ICENS 4TH INTERNATIONAL CONFERENCE ON ENGINEERING AND NATURAL SCIENCE
2-6 May 2018 KIEV UKRAINE

Web Based Intelligent Tutorial Systems: BILZOS

Yavuz Unal[1], Yilmaz Ozturk[2], Ahmet Saglam[3], Recep Cakir[4]

Abstract

Any more, technology is used at all areas of life. The most important one of these areas is education. At education fields, Instead of classical web based systems, the use of intelligent tutorial systems is common. Intelligent Teaching Systems are education systems which aim at effective and quality education and which try to provide o good environtment between students and teachers and which include rich materials and are adapted to individual. It was started to be preferred the computer systems that determine what, to whom and how to teach and that use the techniques of artificial intelligence instead of classical web based systems. The most important one of these systems is web based adaptable Intelligent Tutorial System.

At this study, web based adaptable intelligent tutorial system was designed. The people can reach this system from everywhere because it is a web based system. In general, this software includes a lot of intelligence feature, which the contents are suitable for the students level, the student can pass the forward test according to the final test of unit, the student can see the true or false answer, the time of the students at the page is saved, the student is canalized the subject or the unit that he/she has some shortage, and the student can't pass the new unit without finishing the former subject or the unit. This web based intelligent tutorial system was designed, as it is used at the many lessons at the same time. Thanks to this feature, this platform easily can be applied at a lot of lessons. It was purposed that this system contributes to the development of the students at many lessons. The detailed and visual interface of this software was explained at the forward sections of this study.

Keywords: Intelligent tutoring system, Web based Learning System, Intelligent tutoring Software

1. INTRODUCTION

Technology, developing rapidly in its time, provides positive effects on the education field, too, as it is in every field [1]. These effects are to increase efficiency in teaching and to provide equal opportunity in education by acting independently of time and space. It is inevitable to integrate such developments in the fields of information and communication into educational programs in order to catch the modern education level [2]. Computer aided education; is a platform that allows anyone with an internet network to access the course content. Intelligent teaching systems (ITS) is a computer-based teaching system that models teaching content and instructional strategies that determine how a particular topic is taught. This term, which was first seen in 1982 in the book "Intelligent Tutoring Systems" written by Sleeman and Brown, is in the teaching systems of the future. Improvements in artificial neural networks have provided the formation of intelligent learning environments [3].

Combining computer assisted education with intelligent teaching systems (ITS) has contributed to the flexible learning environments through learning processes. As ITS uses the student system, the deficiencies are seen and can be changed by using different teaching strategies to eliminate them. ITS is an advanced education approach that imitates teacher by adapting his teaching approach to each student [4].

[1] *Corresponding author: Amasya University, Department of Computer Engineering, Amasya, Turkey.* yavuz.unal@amasya.edu.tr

[2] *Zile Dincerler Vocational and Technical Anatolian High School, Tokat, Turkey,* ylmzoztuk@gmail.com

[3] *Amasya University, Merzifon Vocational School, Amasya, Turkey.* ahmet.saglam@amasya.edu.tr

[4] *Amasya University, Faculty of Education, Amasya, Turkey.* recep.cakir@amasya.edu.tr

This rest of the paper is organized as follows. Section 2 will give an overview of the BILZOS architecture and its components. How BILZOS works and uses will be givenin Section 3. Finally, the conclusion will be given in Section 4.

a. Web-based intelligent tutoring systems

The Internet is now in almost every field of our lives. One of these field is also education. Web based education has many advantages such as being independent from time and place. The purpose of the Web based Intelligent Design and Evaluation System (WINDS) aim; is to create a computer training program and a learning environment for teaching a team. It is a European Project [4].

In this study, BILZOS is a web-based intelligent teaching system design, with this system it is possible to provide business suitability. BILZOS according to the levels of students, rests on with content. They will be able to restart the learning processes of students.

2. COMPONENTS AND ARCHITECTURE OF BILZOS

The web-based intelligent teaching system that we have developed, has five modules.

Student: Influences students to learn different things, such as knowledge, interest and talent. The students who are the target group in ITS access the course modules according to their abilities and skills through the system. Thus, this contributes each student to individual development by offering different modules according to his / her abilities and knowledge level, instead of the same educational model.

User Interface: In the user model, the student is presented an easy, clear and accessible interface. From here, users can access the content of the course they want.

Tutorial Model: Contains the use of the most appropriate and effective method transferring information to users. In this model, the feedback is provided to the user and he/she is directed to the appropriate topic [4].

Student Model: Contributes to the learning of students' learning skills and their knowledge in the light of this information.

Domain Model: This module contains course content, teaching topics and the relationships of intersubject. The information to be learned, contains the construction of information networks and the shape of a conceptual hierarchical structure [5].

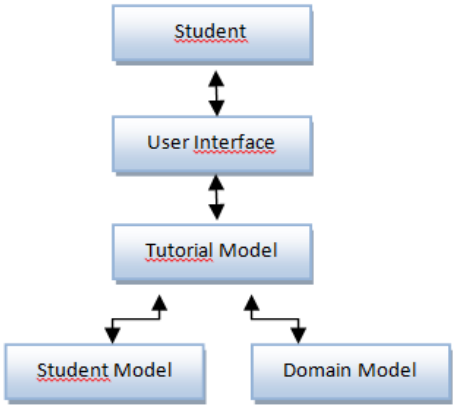

Figure 1. Architecture of ITS

3. HOW DOES WORK AND USE BILZOS?

The web-based intelligent teaching systems which have developed is available on the web address www.bilzos.com. There are separate panels for the administrator and the user. The user is filling out the form for registration. Then this membership on the admin screen and when approved by the administrator, allowed to use the system. Individuals enrolled in courses added in Bilzos, first complete the pre-tests which prepared for lessons and measure the initial levels. Users who pre-test taker has a different course content according to the successes in the pre-test. The user can select courses and access the modules of the courses he / she has selected. The system, which is prepared from the modular system, the lessons can be listened, notes can be seen and the topic end tests can be solved.

The web-based intelligent teaching system that we developed has a student final test section. The student who has not completed this final test cannot pass to the next unit. In addition, the time that the student remains in the system is recorded by the system.it is determined whether or not the learner follows the contents of the course by the period of stay in the recorded system. In addition to these, the system follows to learners modules and level of learning and redirects to the topics that are missing. The student can contact the lecturer and receive help from the lecturer in which subject are forced to learn. Along with these, the lecturer can easily see the information of each student..

a. Main Screen

After entering the system, the screen in figure 2 is displayed in front of the user who has completed the pre-test about the course.On the top left of this screen are the names of courses that are registered while On the right side there are lessons.the user has to click on the "go to tutorial (egitime git)" button to access the course content he / she wants.

Figure 43. Main Screen

b. Training Module Screen

On the training module screen, the course modules belonging to the selected course are listed. "Completion status" is seen Side of module menu In order to follow to module status and When the module name is selected, the content screen is displayed.

Figure 3.Training Module Screen

c. Content Screen

On the content page, the video prepared for the module meets the user in the system. Below it, The important information belonging to the module which has been noted. At the bottom, there are module-related tests. The user who completes these operations has completed the user mod.

Figure 4. Content Screen

4. CONCLUSION

Technology is rapidly developing and entering into every field of our lives. Web Based Intelligent Teaching Systems are used frequently in recent years. In the context of the studies conducted on students using this system, an individual learning contribution has been put forward. In this study, it is thought that BILZOS who learns how to learn and contribute to academic achievement with this result. ZOS will reduce the workload of teacher and contribute to personal learning of students by considering the individual differences among the students.

The influence of BILZOS on student success should be discussed by experiencing in the future studies. BILZOS and similar web-based intelligent teaching systems can be more developed by using artificial intelligence more effectively.

ACKNOWLEDGMENT

This work was supported by Scientific Research Projects Coordination Unit of Amasya University. Project number FMB-BAP 17-0248.

REFERENCES

[1]. Ozek, M. B., Akpolat, Z. H., and Orhan, A., "Web Tabanli Akilli Ogretim Sistemlerinde Tip-2 Bulanik Mantik Kullanarak Ogrenci Ogrenme Stili Modelleme". Firat University Journal of Engineering, 2010, vol.22(1).

[2]. Cekbas. Y., Yakar, H., Yildirim, B. and Savran, A., "Bilgisayar Destekli Egitimin Ogrenciler Uzerine Etkisi." The Turkish Online Journal of Educational Technology – TOJET October 2003 ISSN: 1303-6521 ,2003, vol.2.

[3]. Keles, A., and AyturkKELES, B. U. "Bilgisayar Destekli Ogretim ve Zeki Ogretim Sistemleri.", 2002.

[4]. Erdemir, O. G. M., and Ingec, S. K., "Fizik Egitiminde Web Tabanli Zeki Ogretim Sisteminin (Zos) Basariya Etkisi", Journal of Research in Education and Teaching, 2015, vol.3.

[5]. Yong, Z., and Zhijing, L. (2003). "A Model of web oriented intelligent tutoring system for distance education". Proceedings of the Fifth International Conference on Computational Intelligence and Multimedia Applications (ICCIMA'03), 2003.

ICENS 4TH INTERNATIONAL CONFERENCE ON ENGINEERING AND NATURAL SCIENCE
2 - 6 May 2018 KIEV UKRAINE

Usage of different machine learning algorithms in the classification of Epileptic Seizure based on EEG signals without feature extraction

Murat Arican[1], Yavuz Unal[2], Kemal Polat[3]

Abstract

Epileptic seizures occur as a result of sudden and unexpected electrical parasites of the brain. Electroencephalogram (EEG) is a valuable clinical tool used to evaluate human brain activity. Detection of epileptic seizures in EEG signals is an important part of the diagnosis of epilepsy. In this study, the epileptic seizure recognition data set from the UCI machine learning database was used. This data set contains 2300 epileptic seizures and 9200 non-epileptic EEG signals. Based on EEG data distribution, the epilepsy data set is an imbalanced dataset. The sampling frequency of the EEG signals is 173.61 Hz and the recording time is 23.6 seconds. In this study, no feature extraction algorithm was used to distinguish epilepsy from EEG signals. The raw signals are directly fed to the classification algorithm. Three different classification algorithms have been used to classify EEG signals as epilepsy and non-epilepsy. These classification algorithms are: k-NN (for k = 1), C4.5 decision tree and Naive Bayes. The classification performance values obtained with the 50-50% train-test holdout data partition method are 94.05%, 94.50% and 96.00%, with the 10-fold cross validation method are 95.05%, 94.72% and 95.75%, respectively. The obtained results show that epilepsy patients can be detected only by classification algorithms without extracting the feature from EEG signals.

Keywords: EEG signals, Epileptic seizures, classification, machine learning algorithms

1. INTRODUCTION

Electroencephalography (EEG), technique for recording and interpreting the electrical activity of the brain. EEG is used in the diagnosis and treatment of many diseases. EEG is used as a diagnostic aid in cases of head injuries, brain tumours, cerebral infections, sleep disorders, epilepsy, and various degenerative diseases of the nervous system. On the other hand it can be used to diagnose psychiatric diseases like a borderline [1].

Epilepsy is a neurological disorder that results in abnormal activity of neurons in the brain. Patients are exposed to a sudden epileptic seizure that affects the nervous system for only a few seconds. There are 50 million people worldwide with epilepsy [2, 3]. For this reason, rapid and accurate identification of the seizure is important for the intervention.

Kalbhor et al. (2016) achieved 90% accuracy in the classification study performed by wavelet transform [4]. Rajaguru et al. (2017) used the Modified Expectation Maximization Based Sparse Representation Classifier in their study and obtained 96.52% accuracy [5]. Again, Rajaguru et al. (2017) found 97.53% accuracy in their work using power density analysis and K-NN based Adaboost classifier [6]. In another study by Das et al. (2017), used Linear SVM, weighted K-NN and ensemble Bagged tree with time domain attributes and achieved accuracy of 74.78% to 91.09% [7]. Colominas et al. (2018) used the Time and Time-Frequency attributes in

[1] *Abant Izzet Baysal University, Department of Department of Electrical and Electronics Engineering, Bolu, Turkey, muratarican@gmail.com*

[2] *Corresponding author: Amasya University, Department of Computer Engineering, Amasya, Turkey, yavuz.unal@amasya.edu.tr*

[3] *Abant Izzet Baysal University, Department of Department of Electrical and Electronics Engineering, Bolu, Turkey, kpolat@ibu.edu.tr*

the study to evaluate the different regions of the brain in detecting epilepsy with the roc curve and obtained results between 0.917 and 1.000[8].

Past studies show that classifiers made by extracting attributes give good results. However, the time taken to extract the attribute increases the cost. In our study, it was aimed to detect epileptic seizures by processing EEG signals directly without extracting the feature.

2. MATERIAL AND METHOD

a. EEG Epilepsy Data Set

In this study, the epileptic seizure recognition data set from the UCI machine learning database was used[9]. The data set consists of five different files containing a hundred signals. Each signal represents one person. Recording time for each signal is 23.6 seconds. Sampling frequency is 173.61 Hz and it consists of 4097 data point. The records are divided into twenty three epochs for a second and the duration is a second. The record was labelled 1 (Recording of seizure activity), 2 (tumor area), 3 (healthy area in the brain as a tumor), 4 (eyes closed) and 5 (eyes open). Figure 1 shows signal samples for five classes. In the study, the data set has been reduced to two classes and the label number 1 has been designated as Recording of seizure activity(label 1) and the label number 2 has been designated as others (combining of non-epileptic seizure labels 2,3,4,5). Fig. 1(a) shows EEG signals of randomly selected epochs for epileptic seizure in the data set. Fig. 1(b) shows EEG signals of randomly selected epochs for other four situations in the data set.

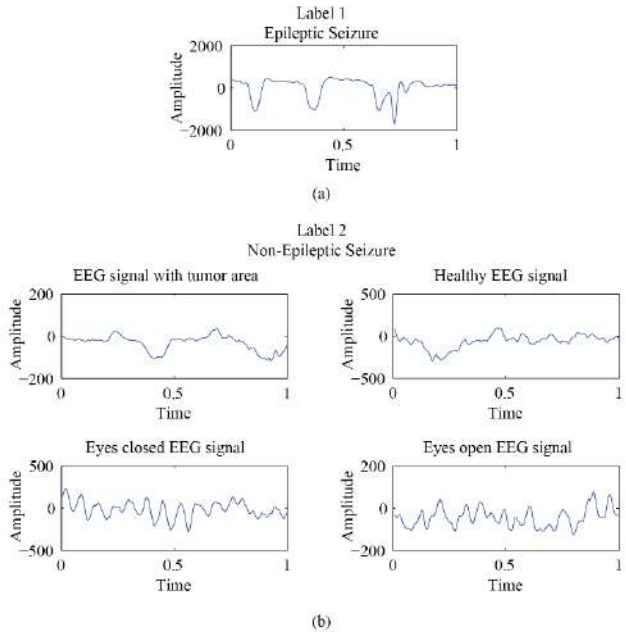

Figure 1. Sample eeg signals belonging to dataset (a) epileptic seizure (b) various non-epileptic seizure

b. Data Normalization Techniques

EEG signals were used to detect epileptic seizures. The EEG signals in the data set were assigned a classifier to be raw and normal, and no feature extraction was performed.

In the study, min-max, z-score and mad normalization were applied to the raw signal. At Equation (1), (2) and (3), X_N indicates processed data point and X_{Nn}indicates normalized data point.

- Min-max normalization[10]:

$$X_{Nn} = \frac{X_n - X_{max}}{X_{max} - X_{min}} \quad (1)$$

Where, X_{max} is the largest value of the series, and X_{min} is the smallest value of the series. While this distribution does not change the distribution of the series, it is overcome by outlier data.

- Z-Score normalization[11]:

$$X_{Nn} = \frac{X_n - \mu}{\sigma} \quad (2)$$

Where σ show standard divination of the series and μ shows mean of the series. This normalization does not give a constant value range when bringing the series to the Gaussian distribution. The sequence changes in the range [0-1] at the end of the normalization.

- Median and Median Absolute Deviation(MAD)[12]:

$$X_{Nn} = \frac{X_n - median}{MAD} \quad (3)$$

Mad is a normalization method that provides immunity for outlier values.

Where;

$$MAD = median(|X_n - median|) \quad (4)$$

c. Classification Algorithm

In the study, k-Nearest Neighbourhood (k-NN), C4.5 Decision Tree and Naive Bayes were used in supervised classification algorithms.

k-NN is an algorithm that operates on an attribute space such as $\mathbb{R}^n$. This method can be used with numeric attributes however it is not suitable for verbal attributes. By the majority voting method, the closest is classified by measuring the distance between unknown values and known values[13]. The k value is selected as odd to reduce the complexity. k = 1 is a special situation and the classifier is select class of the nearest neighbour for input data[14]. Neighbourhood level (k value) was taken as 1.

In the C4.5 decision tree method, the data is divided into several steps. Entropy is used during stepping. Smallest calculated entropy value is selected. It offers a flexible usage by its structure. The classifier works for numeric and discrete value[13, 14].

Naïve Bayes is a statistical classification method and performs the classification process according to the relations of the distributions of the data[13].

3. EXPERIMENTAL RESULTS

In the study, k-NN, C4.5 and Naïve Bayes classifiers were compared with different training and test data creation techniques.

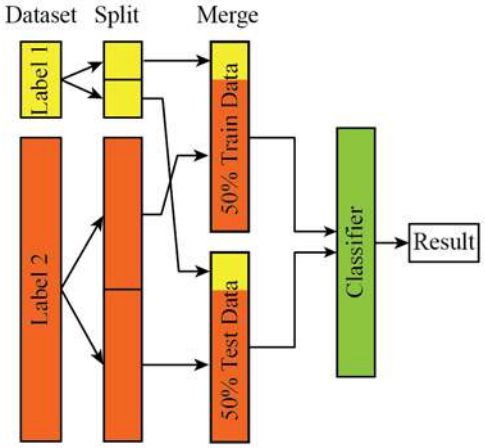

Figure 2. Hold out technique flow diagram for 50% - 50% set

Hold-out and k-fold cross validation methods are used for grouping as training and test data. In the hold out method, the data block is divided into firstly 50% training - 50% test data and secondly 60% training - 40% test data, which will cover both classes[14, 15]. Fig. 2 describes 50% hold out technique by a flow diagram.

In addition, EEG data are classified by 5 and 10 fold cross validation. In k-fold cross validation technique, each class is divided into k parts, which will cover both classes. In turn, when one of the divided groups enters to the classifier as the test, other groups become training data. At the end of the process k results are obtained. Classes are determined by majority vote from the results[14, 15]. Fig. 3 describes 5-fold cross validation technique by a flow diagram.

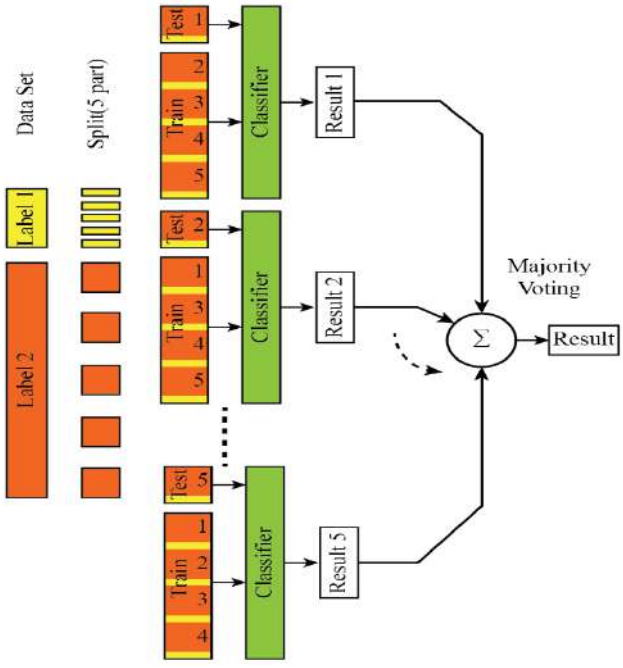

Figure 3. Flow diagram for 5-fold Cross validation technique

Table 39. k-Nearest Neighborhood (k-NN) Classification Results

	Norm.	Acc (%)	Kappa	Prec.	Recall	F-Meas	AUC
%50-%50	Raw	**94.05**	0.790	0.944	0.941	0.937	0.853
	Min-Max	86.54	0.570	0.864	0.865	0.864	0.781
	Z Score	87.76	0.609	0.876	0.878	0.877	0.609
	MAD	86.76	0.571	0.864	0.868	0.866	0.778
%60-%40	Raw	**94.37**	0.803	0.946	0.944	0.940	0.861
	Min-Max	87.80	0.607	0.876	0.878	0.877	0.797
	Z Score	88.37	0.633	0.883	0.884	0.883	0.815
	MAD	87.61	0.601	0.874	0.876	0.875	0.794
5 Fold CV	Raw	**94.83**	0.821	0.951	0.948	0.945	0.873
	Min-Max	88.64	0.640	0.885	0.886	0.886	0.816
	Z Score	89.28	0.663	0.892	0.893	0.892	0.830
	MAD	88.59	0.635	0.884	0.886	0.885	0.811
10 Fold CV	Raw	**95.05**	0.830	0.953	0.951	0.948	0.878
	Min-Max	89.09	0.655	0.890	0.891	0.890	0.824
	Z Score	89.67	0.676	0.896	0.897	0.897	0.837
	MAD	89.03	0.650	0.888	0.890	0.889	0.820

Table 2. C4.5 Decision Tree Classification Results

	Norm.	Acc (%)	Kappa	Prec.	Recall	F-Meas	AUC
%50-%50	Raw	**94.50**	0.826	0.945	0.945	0.945	0.901
	Min-Max	76.69	0.246	0.761	0.767	0.764	0.604
	Z Score	79.79	0.021	0.716	0.798	0.721	0.510
	MAD	81.09	0.217	0,777	0.811	0.774	0.716
%60-%40	Raw	**94.76**	0.833	0.947	0.948	0.947	0.892
	Min-Max	76.87	0.263	0.766	0.769	0.767	0.630
	Z Score	74.56	0.203	0.746	0.746	0.746	0.600
	MAD	80.69	0.231	0.773	0.807	0.776	0.574
5 Fold CV	Raw	**94.29**	0.819	0.942	0.943	0.943	0.893
	Min-Max	77.25	0.279	0.769	0.773	0.771	0.625
	Z Score	76.78	0.254	0.761	0.768	0.764	0.620
	MAD	81.50	0.270	0.787	0.815	0.786	0.594
10 Fold CV	Raw	**94.72**	0.833	0.947	0.947	0.947	0.834
	Min-Max	78.02	0.298	0.776	0.780	0.778	0.632
	Z Score	77.34	0.245	0.760	0.773	0.766	0.618
	MAD	80.82	0.298	0.784	0.808	0.790	0.624

Table 3. Naive Bayes Classification Results

	Norm.	Acc	Kappa	Prec.	Recall	F-Meas	AUC
%50-%50	Raw	**96.00**	0.873	0.960	0.960	0.960	0.961
	Min-Max	74.85	0.280	0.773	0.749	0.759	0.688
	Z Score	68.49	0.027	0.691	0.685	0.688	0.530
	MAD	76.89	0.282	0.772	0.769	0.770	0.672
%60-%40	Raw	**95.98**	0.873	0.960	0.960	0.960	0.960
	Min-Max	74.91	0.274	0.771	0.749	0.758	0.687
	Z Score	70.26	0.044	0.696	0.703	0.699	0.537
	MAD	77.67	0.290	0.774	0.777	0.777	0.672
5 Fold CV	Raw	**95.73**	0.866	0.957	0.957	0.957	0.959
	Min-Max	74.96	0.286	0.774	0.750	0.760	0.685
	Z Score	70.73	0.040	0.693	0.707	0.700	0.041
	MAD	77.47	0.288	0.772	0.775	0.773	0.669
10 Fold CV	Raw	**95.75**	0.867	0.957	0.957	0.957	0.959
	Min-Max	74,96	0.282	0.772	0.750	0.759	0.685
	Z Score	70.84	0.036	0.692	0.708	0.700	0.540
	MAD	77.51	0.288	0.772	0.775	0.774	0.668

Since there is an unbalanced distribution among the classes in the data set, only accuracy value will lead to misinterpretation of the results. For this reason, analysis of the results was carried out together with accuracy, kappa and AUC. Where, Acc. is accuracy, Prec. is precision, F meas. is F Measurement and AUC is area under roc curve. Kappa value is measure harmony between observations. Kappa value is change [-1 1]. As you approach Kappa value 1, harmony increases[16].

Table I shows the classification results of k-NN. The highest accuracy rate with 95.05% in raw signals is seen in 10 fold cross validation. As a result of the normalization methods, the kappa value is 0.570 - 0.676 and the AUC value is 0.609 - 0.837, although the accuracy is between 86.54 and 89.67.

Table II shows the classification results of C4.5 decision tree. The highest accuracy rate with 94.76% in raw signals is seen in 60% - 40% hold out. As a result of the normalization methods, the kappa value is 0.021 - 0.290 and the AUC value is 0.510 - 0.716, although the accuracy is between 75.56 and 81.56.

Table III shows the classification results of Naïve Bayes. The highest accuracy rate with 96% in raw signals is seen in 50% - 50% hold out. As a result of the normalization methods, the kappa value is 0.027 - 0.290 and the AUC value is 0.609 - 0.837, although the accuracy is between 86.54 and 89.67.

4. CONCLUSIONS

When the accuracy ratios obtained from the classification of raw EEG signals are examined, it is seen that there are similar or higher accuracy values in the literature than the results obtained by the feature extraction. The data obtained in the study showed that the detection of epileptic seizures could be used without any process of the raw signals.

For Naive Bayes classifier, 50% - 50% hold out method is a suitable method with 96% accuracy, 0.960 precision, 0.961 AUC and 0.873 kappa coefficient in the classification of Epileptic Seizure based on EEG signals without feature extraction.

The normalization process does not have a positive effect on the results. It also decreases its performance. In our opinion, the most important reason for this situation, amplitude difference between epileptic seizure signal, and other signals seen in fig. 1 is removed by normalization process.

REFERENCES

[1]. S. M. Metev and V. P. Veiko, *Laser Assisted Microtechnology*, 2nd ed., R. M. Osgood, Jr., Ed. Berlin, Germany: Springer-Verlag, 1998.
[2]. J. Breckling, Ed., *The Analysis of Directional Time Series: Applications to Wind Speed and Direction*, ser. Lecture Notes in Statistics. Berlin, Germany: Springer, 1989, vol. 61.
[3]. S. Zhang, C. Zhu, J. K. O. Sin, and P. K. T. Mok, "A novel ultrathin elevated channel low-temperature poly-Si TFT," *IEEE Electron Device Lett*., vol. 20, pp. 569–571, Nov. 1999.
[4]. M. Wegmuller, J. P. von der Weid, P. Oberson, and N. Gisin, "High resolution fiber distributed measurements with coherent OFDR," in *Proc. ECOC'00*, 2000, paper 11.3.4, p. 109.
[5]. R. E. Sorace, V. S. Reinhardt, and S. A. Vaughn, "High-speed digital-to-RF converter," U.S. Patent 5 668 842, Sep. 16, 1997.
[6]. (2007) The IEEE website. [Online]. Available: http://www.ieee.org/
[7]. M. Shell. (2007) IEEEtran webpage on CTAN. [Online]. Available: http://www.ctan.org/tex-archive/macros/latex/contrib/IEEEtran/
[8]. *FLEXChip Signal Processor (MC68175/D)*, Motorola, 1996.
[9]. "PDCA12-70 data sheet," Opto Speed SA, Mezzovico, Switzerland.
[10]. Karnik, "Performance of TCP congestion control with rate feedback: TCP/ABR and rate adaptive TCP/IP," M. Eng. thesis, Indian Institute of Science, Bangalore, India, Jan. 1999.
[11]. J. Padhye, V. Firoiu, and D. Towsley, "A stochastic model of TCP Reno congestion avoidance and control," Univ. of Massachusetts, Amherst, MA, CMPSCI Tech. Rep. 99-02, 1999.
[12]. *Wireless LAN Medium Access Control (MAC) and Physical Layer (PHY) Specification*, IEEE Std. 802.11, 1997.

ICENS 4TH INTERNATIONAL CONFERENCE ON ENGINEERING AND NATURAL SCIENCE
2 - 6 May 2018 KIEV UKRAINE

Optimization of Coating Parameters for Water Vapour Resistance of Denim Fabrics by Using Taguchi Method

Huseyin Gazi Turksoy[1], Sumeyye Ustuntag[2], Munevver Ertek Avci[3]

Abstract

Coating technology is an increasingly popular method for creating special designs and getting different appearance to denim fabrics. Depending on the expected properties from denim fabrics, the coating process parameters can be changed. The effect of process parameters on comfort properties of denim fabrics is important issue. The present study is focused on optimizing the various coating process parameters for the water vapour resistance properties of denim fabrics by using Taguchi method. The parameters selected for optimization are squeeze pressure, the viscosity of the coating fluid, the fabric passing speed, drying temperature and weft density. An L27(35) orthogonal design was chosen as experimental plan. In the evaluations with Taguchi Method, analyses of the signal to noise ratio (S/N) and variance (ANOVA) were used. it was found that the most effective input parameter for water vapour resistance is weft density. Also, the combination satisfying minimum water vapour resistance was determined as 20 picks/cm weft density, 140 °C drying temperature, 50 dpas viscosity, 7 bar squeeze pressure, 10 m/min fabric passing speed.

Keywords: Denim Fabric, Coating, Taguchi Method, Water Vapour Resistance

1. INTRODUCTION

Denim garments have been preferred by a wide range of consumers without limitation of age, gender and social status. Innovative approaches are needed in the production of denim fabrics to meet the constantly changing demands of consumers. Lots of developments are also taking place in the finishing process of denim fabrics which can provide aesthetic as well as functional properties. There are countless dry and wet processes in denim finishing processes to achieve fading, excellent handle and unique looks. The coating, which is one of the finishing processes of denim fabrics have further expanded the creating special designs and getting different appearance to denim fabrics [1].

Classical experimental design methods are too complex, difficult and costly in product development processes of denim fabrics. To optimize designs for quality, performance, and cost; Taguchi method presents a systematic approach that is simple and effective. The Taguchi technique is based upon the technique of matrix experiments. The experimental matrices are special orthogonal arrays, which allow the simultaneous effect of several process parameters to be studied efficiently. The purpose of conducting an orthogonal experiment is to determine the optimum level for each factor and to establish the relative significance of the individual factors in terms of their main effects on the response. Taguchi suggests signal-to-noise (S/N) ratio as the objective function for matrix experiments. The S/N ratio is used to measure the quality characteristics as well as the significant machining parameters through analysis of variance (ANOVA) [2]-[8].

Depending on the expected properties from denim fabrics, the coating process parameters can be changed. The effect of process parameters on comfort properties of denim fabrics is important issue. The present study is aimed at optimizing the various coating process parameters for the water vapour resistance properties of denim fabrics by using Taguchi method.

[1]*Erciyes University, Department of Textile Engineering, 38039, Kayseri/Turkey, hgazi@erciyes.edu.tr*

[2]*Corresponding author: Erciyes University, Department of Textile Engineering, 38039, Kayseri/Turkey, sumeyyeustuntag@erciyes.edu.tr*

[3]*Calik Denim R&D Center, Malatya/Turkey, munevver.ertekavci@calikdenim.com*

2. MATERIALS AND METHODS

Five coating parameters, namely, squeeze pressure, the viscosity of the coating fluid, the fabric passing speed and drying temperature and weft density were identified for the present investigation. Each parameter was investigated at three levels to study the non-linearity effect of the process parameters. The identified process parameters affecting the water vapour resistance of coated denim fabrics and their levels are summarized in Table 1. L27 the orthogonal array table was chosen to determine experimental plan, as seen Table 2, because it is the most suitable for the conditions being investigated; five parameters with three levels.

Table 1. Control factors and levels for the experimental design.

Code	Factors	Levels		
		1	2	3
A	Weft density (picks/cm)	14	17	20
B	Drying temperature (°C)	120	140	160
C	Viscosity (dpas)	30	50	70
D	Squeeze pressure (Bar)	3	5	7
E	Fabric passing speed (m/min)	10	20	30

After determining the control factors and their levels, three denim fabric samples were manufactured with 3/1 Z twill structure by Calik Denim A.S. Ne 8.2/1 ring yarn were used as the warp yarn with a density of 17 ends/cm for all fabric samples. The weft density of the denim fabrics was used as control parameter and Ne 10.4/1 ring core-spun yarns (%95 cotton and % 5 Elastane-70 dtex) were used as weft yarn with three different density (14, 17 and 20 picks/cm).

Depending on the Taguchi experiment design, the coating of the denim fabrics was applied by the Rotary Screen Coating Method, which is the deposition of a coating material on a substrate through a mesh screen by squeezing. A standard coating pat used in the mill was used for the coating of the denim fabrics.

Water vapour resistance was evaluated with Permetest instrument according to ISO 11092 standard [9] and the measurements were carried out under isothermal conditions (23.0 ± 0.5 °C). The schematic diagram and the actual image of the instrument has been given in Figure 1. The instrument works on the principle of heat flux sensing. When water flows into the measuring head, some amount of heat is lost. This instrument measures the heat loss from the measuring head due to the evaporation of water in bare condition and with being covered by the fabric. Then the water vapour resistance (R_{et} (m^2Pa/W)) is calculated from the following formula by a computer [10].

$$R_{et} = (p_{wsat} - p_{wo})\left(\frac{1}{q_s} - \frac{1}{q_o}\right) = C(100 - \varphi)\left(\frac{1}{q_s} - \frac{1}{q_o}\right) \quad (1)$$

q_s and q_o mean the heat flux density lost by the moist measuring head in Equation 1. p_{wat} and p_{wo} represents the water vapour saturate partial pressure valid for the temperature of air in the measuring laboratory (21.0 ± 0.5 °C), and the partial water vapour pressure in the laboratory air. The constant C is determined by the calibration procedure. For this purpose, special hydrophobic polypropylene reference fabric is delivered with the instrument [11].

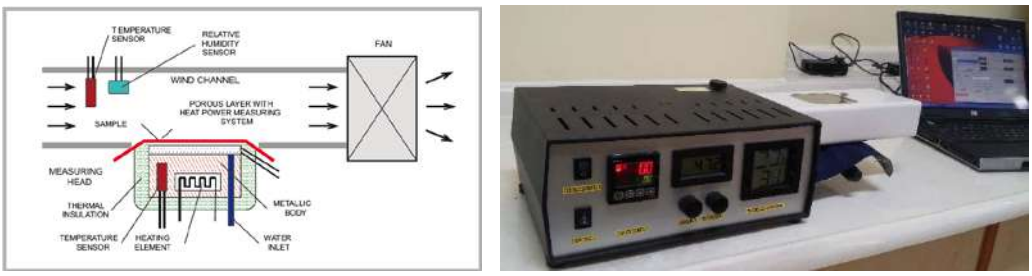

Figure 1. PERMETEST schematic diagram and actual image

3. RESULTS AND DISCUSSION

Taguchi involves the stages of system design, parameters design, and tolerance design. System design involves the application of scientific and engineering knowledge required in manufacturing a product; parameter design is employed to find optimal process values for improving the quality characteristics; and tolerance design consists of determining and analyzing tolerances in the optimal settings recommended by parameter design [2], [3]. In this study, parameter design stage of Taguchi method was used with Minitab Version 16.0 software package. The goal of parameter design is the identification of settings that minimize variation in the performance characteristic and adjust its mean to an optimal value. The Taguchi uses S/N ratio instead of the average value to interpret the trial results data into a value for the evaluation characteristic in the optimum setting analysis. The S/N ratio characteristics can be divided into three categories: nominal the better, smaller the better, and higher the better. Because the low water vapour resistance is a desirable condition for comfort, the smaller the better quality characteristic was selected. The S/N for the smaller the better quality characteristic can be described by:

$$\frac{S}{N} = -10 \log \left[\frac{1}{n} \sum_{i=1}^{n} y_i^2 \right] \tag{2}$$

where y_i denotes the data obtained from experiments; n represents the number of experiments. Regardless of category of the performance characteristics, a greater S/N value corresponds to a better performance. Therefore, the optimal level of the coating parameters is the level with the greatest S/N value. The calculated S/N ratios for all tests are given in Table 2.

Table 2. Experimental layout using an $L_{27}(3^5)$ orthogonal array table for the water vapour resistance.

Order	Parameters					R_{et} Value (m^2 Pa/W)	S/N Ratio (dB)
	A	B	C	D	E		
1	1	1	1	1	1	7.362	-17.37
2	1	1	1	1	2	5.846	-15.62
3	1	1	1	1	3	8.166	-18.43
4	1	2	2	2	1	5.416	-14.69
5	1	2	2	2	2	4.854	-13.78
6	1	2	2	2	3	6.336	-16.07
7	1	3	3	3	1	5.384	-14.63
8	1	3	3	3	2	6.826	-16.71
9	1	3	3	3	3	7.130	-17.07
10	2	1	2	3	1	6.064	-15.80
11	2	1	2	3	2	8.434	-18.54
12	2	1	2	3	3	6.004	-15.57
13	2	2	3	1	1	7.684	-17.72
14	2	2	3	1	2	8.816	-18.98
15	2	2	3	1	3	7.998	-18.07
16	2	3	1	2	1	7.890	-17.97
17	2	3	1	2	2	7.692	-17.77
18	2	3	1	2	3	8.282	-18.37
19	3	1	3	2	1	6.340	-16.05
20	3	1	3	2	2	6.172	-15.81
21	3	1	3	2	3	6.000	-15.58
22	3	2	1	3	1	5.384	-14.65
23	3	2	1	3	2	5.632	-15.03
24	3	2	1	3	3	5.938	-15.53
25	3	3	2	1	1	5.470	-14.80
26	3	3	2	1	2	7.980	-18.04
27	3	3	2	1	3	6.052	-15.65

In the Taguchi method, the average effect of each factor on the multiple quality characteristics at different levels is determined. This is equal to the sum of all S/N ratios corresponding to a factor at a particular level divided by the number of repetitions of the factor level [10]. The factor levels corresponding to the maximum average effect are selected as the optimum level. For R_{et} values of coated denim fabrics, the average factor effect is shown in Table 3, and the main effects plotted for S/N are shown in Figure 2. The delta value was calculated by subtracting the largest value from the lowest from among the values in each column. A higher delta value means that the difference at the selected level for a given factor is highly pronounced and, in turn, the level change of this factor has an impact on the water vapour resistance of coated denim fabric.

Table 3. Response table for the S/N ratio of R_{et} output

Factors	Average S/N, dB				
	Level 1	Level 2	Level 3	Delta	Rank
A	-16.04	-17.64	-15.68*	1.96	1
B	-16.53	-16.06*	-16.78	0.72	5
C	-16.75	-15.88*	-16.74	0.86	3
D	-17.19	-16.23	-15.95*	1.24	2
E	-15.97*	-16.70	-16.71	0.74	4

*: Optimum parameter level.

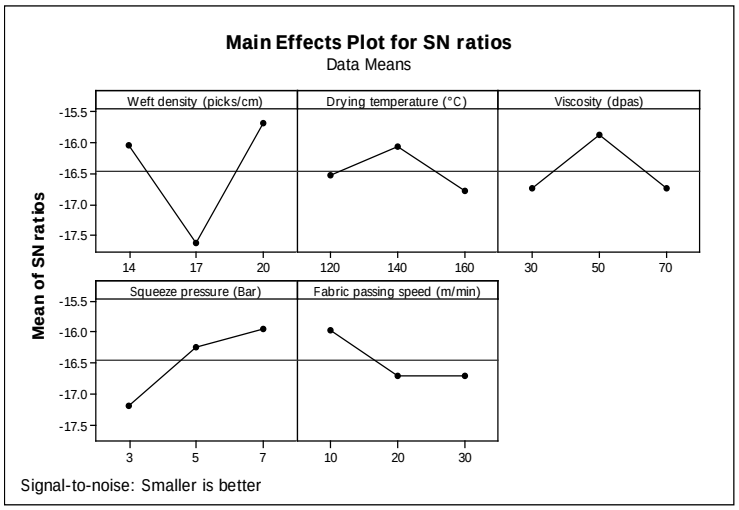

Figure 2. Main effects plot for S/N of R_{et} output

Based on the analysis of *S/N* ratio, the optimal coating parameters for the R_{et} was obtained at 20 picks/cm weft density (Level 3), 140 °C temperature (Level 2), 50 dpas viscosity (Level 2), 7 bar pressure (Level 3) and 10 m/min speed (Level 1) settings. Also, it was found that the most effective input parameter is weft density (A) and second effective input parameter is squeeze pressure (D). In Figure 2, it is shown that squeeze pressure increase negatively affects the R_{et} values of the coated denim fabrics.

Table 4. ANOVA table for S/N ratio of R_{et} output

Factor	*df*	*Sum of squares (SS)*	*Mean square (MS)*	*F-value*	*P*	*Percentage contribution (%)*
A	2	19.548	9.774	7.99	0.004	34.42
B	2	2.406	1.203	0.98	0.395	4.24
C	2	4.421	2.211	1.81	0.196	7.78
D	2	7.594	3.797	3.11	0.073	13.37
E	2	3.251	1.626	1.33	0.292	5.72
Residual	16	19.564	1.223	-	-	34.45
Total	26	56.784	-	-	-	100

The analysis of variance (ANOVA) is performed on S/N ratios to see which process parameters are statistically significant and to obtain the percentage contribution of each of the factors. The contribution ratio is calculated from the ratio of the SS of each factor to total SS value. Table 4 lists the analysis of variance for S/N ratio of R_{et} and the contribution ratio of each parameter to R_{et}. According to this analysis, the significant parameter on the R_{et} are weft density and the percent contribution of weft density on the R_{et} are 34.42%. The percent contribution of statistically insignificant B, C, D and E parameters on the R_{et} are 4.24, 7.78, 13.37 and 5.72%, respectively. Percent contribution indicates the relative power of a factor to reduce variation. So, a small variation for the weft density factor with a high percent contribution will have a great influence on the R_{et}. Further, it can be seen that the ANOVA has resulted in around 34.45% of error contribution due to interaction effect. Thus, the optimization is also affected by the interaction between the factors.

a. Confirmation tests

The confirmation experiment is the final step of the design of an experiment. The purpose of the confirmation experiment is to predict and verify the conclusions drawn during the analysis phase. The confirmation experiment is performed by conducting a test with optimal settings of the factors and levels previously evaluated [2]. The predicted value of the multiple S/N ratio at the optimum level is calculated as:

$$\eta_0 = \eta_m + \sum_{i=1}^{j} (\eta_i - \eta_m) \quad (3)$$

where, η_m is total mean of S/N ratio, j is the number of factors, and η_i are the multiple S/N ratios corresponding to optimum factor levels. The predicted S/N ratio of optimum design is found to be -13.71 dB for R_{et}. If the S/N is known and we want to learn about the result expected that will make the S/N, the procedure is to back-transform S/N to find the performance value expected [12]. When the predicted S/N was placed into Formula 2, the predicted R_{et} values of the optimum design was obtained as 4.85 m^2Pa/W.

In this study, after determining the optimum conditions and predicting the response under these conditions, a new experiment (A3B2C2D3E1) was conducted with the optimum levels of the coating parameters and four measurements were taken for verification. The average of the experimental results was determined as 5.11 m^2Pa/W and S/N ratio was calculated as -14.24 dB using Formula 2. These results are very close to that predicted by Taguchi design. Table 4 shows the comparison of the predicted R_{et} with the experimental R_{et} using the optimal coating parameters.

The confidence interval (CI) of predicted S/N value for the optimum factor level combination at 95% confidence band is calculated to determine whether the results of the confirmation experiments are reasonable or not. The CI is calculated by:

$$CI = F_{\alpha;1,DF_{MSe}} * MSe * \left(\frac{1+m}{N} + \frac{1}{n_r}\right) \quad (4)$$

In Eq. 4, F_α is the value of F table, α is the error level, DF_{Mse} is the degree of freedom of mean square error, m is the degrees of freedom of j factors, N is the number of the total experiments and n_r is the number of repetitions in the confirmation experiments. For the present study, CI was found ±1.08 and this means that the verification experiments for S/N ratio results are located in the confidence interval. Therefore, the optimal water vapour resistance can be obtained under the above-mentioned coating conditions.

Tablo 5. Results of the confirmation experiment for R_{et}

	Starting Coating Parameters	*Optimal coating parameters*	
		Prediction	Experiment
Optimal Level	A1B1C1D1E1	A3B2C2D3E1	A3B2C2D3E1
R_{et} (m^2Pa/W)	7.36	4.85	5.11
S/N ratio	-17.37	-13.71	-14.24

Finally, first trial (A1B1C1D1E1) is selected as the initial design (S/N=-17.37 dB), and the difference (d) is obtained between the S/N ratio of the selected design (S/N_i) and the predicted S/N ratio of the optimal design (S/N_0) as shown below:

$$d = \frac{S}{N_i} - \frac{S}{N_o} \quad (5)$$

$$d = -10\log L_i - (-10(\log L_o))$$

$$d = -17.37 + 13.71 = -3.66\ dB$$

$$\frac{L_o}{L_i} = 10^{\frac{d}{10}} = 10^{\frac{-3.66}{10}} = 0.43\ times$$

According to this result, the R_{et} of coated denim fabrics under optimum conditions is found to be improved 0.43 times.

4. CONCLUSIONS

This study has presented an investigation on the optimization and the effect of coating parameters on the water vapour resistance of denim fabrics. An optimum parameter combination for the minimum R_{et} was obtained by using the analysis of signal-to-noise (S/N) ratio. Based on the S/N ratio, the optimum levels of the coating parameters for Ret are 20 picks/cm weft density, 140 °C drying temperature, 50 dpas viscosity, 7 bar squeeze pressure, 10 m/min fabric passing speed. The level of importance of the coating parameters is determined by using ANOVA. According to ANOVA method, the highly effective parameters on Ret were found as weft density. Statistical results show that A, B, C, D and E affect water wapor resistance of coated denim fabrics by

34.42, 4.24, 7.78, 13.37 and 5.72%, respectively. Moreover, the confirmation tests indicated that it is possible to decrease relatively by using the proposed optimal coating conditions and confirmed the validity of the used Taguchi method for optimizing the coating parameters.

REFERENCES

[1]. Paul, R., "Denim Manufacture, Finishing and Applications", *The Textile Institute, Woodhead Publishing Series in Textiles*, Number 164, UK, 2015.
[2]. Tosun, N., Cogun, C. and Tosun, G., "A study on kerf and material removal rate in wire electrical discharge machining based on Taguchi method", *Journal of Materials Processing Technology*, 152, 316–322, 2015.
[3]. Gunes, S., Manay. E., Senyigit, E., Ozceyhan, V., "A Taguchi approach for optimization of design parameters in a tube with coiled wire inserts", *Applied Thermal Engineering*, 31, 2568-2577, 2011.
[4]. Oktem, H., Erxurumlu, T., Col, M., "A study of the Taguchi optimization method for surface roughness in finish milling of mold surfaces", *Int J Adv Manuf Technol.*, 28: 694–700, 2006.
[5]. Gaitonde, V.N., Karnik., S.R., Davim, J.P., "Taguchi multiple-performance characteristics optimization in drilling of medium density fibreboard (MDF) to minimize delamination using utility concept", *Journal of Materials Processing Technology*, 196, 73-78, 2008.
[6]. Zeydan, M., "Modelling the woven fabric strength using artificial neural network and Taguchi methodologies", *International Journal of Clothing Science and Technology*, Vol. 20 No. 2, pp. 104-109, 2008.
[7]. Mavruz, S., Ogulata, R. T., "Taguchi Approach for the Optimisation of the Bursting Strength of Knitted Fabrics", *FIBRES & TEXTILES in Eastern Europe*, Vol. 18, No. 2 (79) pp. 78-83, 2010.
[8]. Khosla, A., Kumar, S., Aggarwal, K.K, "Identification of strategy parameters for particle swarm optimizer through Taguchi method", *J Zhejiang Univ SCIENCE A*, 7(12):1989-1994, 2006.
[9]. ISO 11092 Standard "Textiles – Physiological effects - Measurement of the thermal and water vapour resistance", 1993.
[10]. Majumdar, A. and Mukhopadhyay Yadav, R., "Thermal properties of knitted fabrics made from cotton and regenerated bamboo cellulosic fibres", *International Journal of Thermal Sciences*, 49, 2042-2048, 2010.
[11]. Boguslawska-Baczek, M. and Hes, L., "Effective Water Vapour Permeability of Wet Wool Fabric and Blended Fabrics", *FIBRES & TEXTILES in Eastern Europe*, 21, 1(97): 67-71, 2013.
[12]. Mavruz, S. and Ogulata R. T., "Taguchi Approach for the Optimisation of the Bursting Strength of Knitted Fabrics", *FIBRES & TEXTILES in Eastern Europe*, Vol. 18, No. 2 (79) pp. 78-83, 2010.

ICENS 4TH INTERNATIONAL CONFERENCE ON ENGINEERING AND NATURAL SCIENCE
2-6 May 2018 KIEV UKRAINE

Static Stability Analysis of Clay Core Rockfill Dam

Muhammet Karabulut[1], Ibrahim Yigit[2], Memduh Karalar[3]

Abstract

Dams are structures that hold massive water volumes. This paper compares a Clay Core Rockfill (CCR) dam empty and full reservoir conditions for static stability assessment under hydrostatic effect. For this purpose, Duzcam CCR dam constructed in Karabuk, Turkey, is selected as an application. The Duzcam dam has 54 m height and 4430 decare irrigation area capacity annual. The unfavorable section of the dam is selected for two dimensional model. The dam model was constructed using the finite element method. The two dimensional finite element model of Duzcam CCR dam is obtained using Phase2 software. The material and soil mechanical properties were obtained from the experimental data of the dam. Base of model is fixed in horizontal and vertical directions and gravitational loading is applied. Duzcam dam was investigated to principle stresses and displacement throughout dam body height. For both cases, the stresses and displacements in the dam body were compared.

Keywords: displacement, Duzcam Clay Core Rockfill (CCR) dam, finite element method, principle stresses

1. INTRODUCTION

Water is a crucial necessity for the humanity from past to now. Dams are built for many purposes. For example, energy production, agricultural irrigation, and drinking water in major cities. The dams have very large importance especially for the countries in terms of energy production. The dam construction has a huge amount in the country's economy in terms of cost. Therefore, dams have strategic and economic importance. But, which type of dam can build must carefully investigate. Choosing the most appropriate dam type to be built is also a very important issue.

There are many important factors that affect the choice of the correct dam type. The choice of where to build the dam is as important as choosing the right dam type. The main factors which effect on choose a dam type are geo-morphological properties of the area, where the dam will build, fundamental and/or rock properties, distance from tectonic faults, cost of dam and production capacity. For instance, an arch dam building needs narrow valley side and very firm soil/rock properties. In generally, a firm soil, valley and area have to be chosen suitably for dams, but fill dams can be tolerate other soil types. Besides, fill dams are more economical than other dam types aspect cost. The fill dams can be categorized clay core rock fill dam, earth fill dam, front face concrete or asphalt-rock fill dam. It can be thought front face concrete-rock fill dams are the alternative for the clay core rock fill dams, because the material of clay core not always available [1], [2]. Nayebzadeh and Mohammadi said one of the most important dangers that treat earth dams which can lead to interior failure over a prolonged period is the hydraulic fracturing factor [3]. Because dam material sets in time period and these settlement should evaluate for dam safety. Liu et al. investigated the stress and strain numerical analysis of a clay core rock-fill dam, which is a certain building reservoir dam in Yunnan province [4]. Liu et al. modelled three-dimensional topography dam-site river valley for obtaining more realistic results.

Static analysis should be done in clay core rockfill dams firstly like other dam types. Horizontal and vertical displacements of dam body are to be calculated when reservoir is full. Geometry and material properties of dams are important factors for static durability under hydrostatic effect. The dams should be able to keep the

[1] *Corresponding author: Bulent Ecevit University, Department of Civil Engineering, 67100, Incivez/Zonguldak, Turkey. karabulut@beun.edu.tr*

[2] *Bulent Ecevit University, Department of Civil Engineering, 67100, Incivez/Zonguldak, Turkey. ibrahim.yigit@beun.edu.tr*

[3] *Bulent Ecevit University, Department of Civil Engineering, 67100, Incivez/Zonguldak, Turkey. memduhkaralar@gmail.com*

volume of water they hold in the reservoir securely. As a result of the defeats that may occur in the dam body, there is a risk of serious loss of life and property in the area where the dam is located.

Clay core-rock fill dams are modeled and designed with appropriate software (ANSYS, PHASE and FLAC etc.) for finite element and finite difference methods to better determine stress and deformation properties of the dams. Dam safety must be ensured in all conditions. The main purpose of this study is to investigate the linear static behavior of the Duzcam Dam, one of the clay core-rock fill dam due to full reservoir water level, and numerical stress and displacement analysis with statically. Numerical stress analysis is done by PHASE2 [5] program which is based on finite element analysis method as two dimensions. A typical section of the clay core rock fill dams is shown in Figure 1.

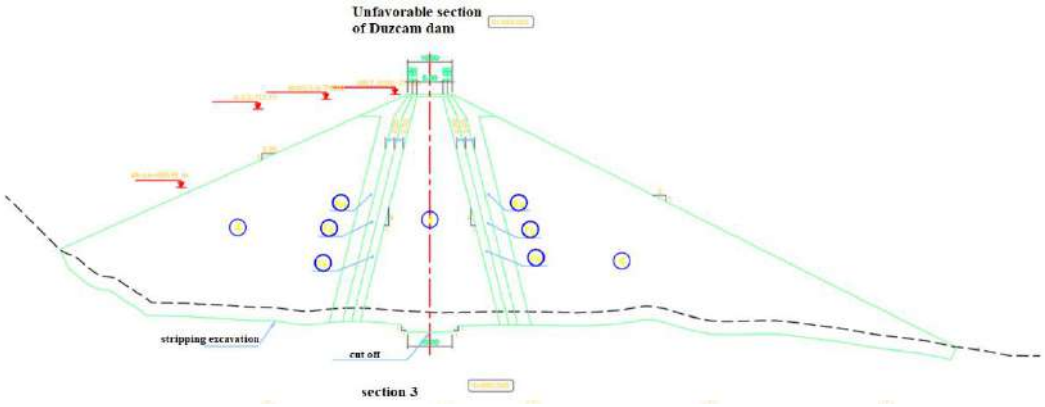

Figure 1. Unfavorable section of Duzcam Dam

2. MATERIALS AND METHOD

In the two-dimensional model, the most critical section of the dam is selected. As suggested in the finite element method, the Duzcam dam was measured at the following dimensions.

The height of the dam was accepted as "H". The dam foundation model was extended up to "H" in the downstream, "3H" in the upstream direction direction and it was extended to H in the direction of gravity. Dam and soil dimensions in the dam modeling technique are proposed in this way for finite element method. The dam ground is modeled as a fixed boundary conditions. The right and left sides of the ground in the downstream and upstream directions are modeled by moving boundary conditions.

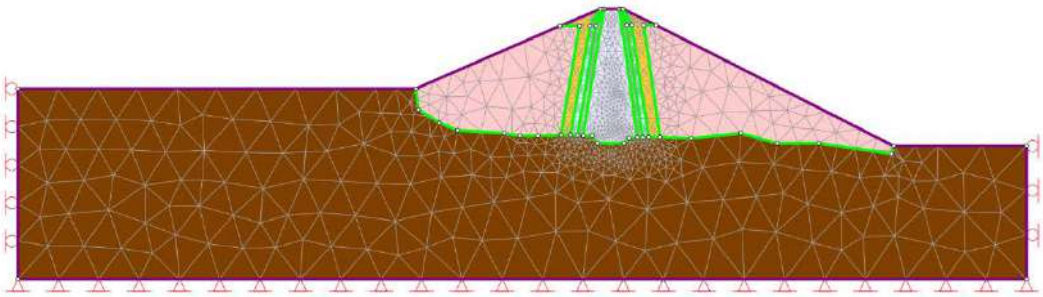

Figure 2. Empty reservoir model of unfavorable section of Duzcam dam and soil by Phase2 software

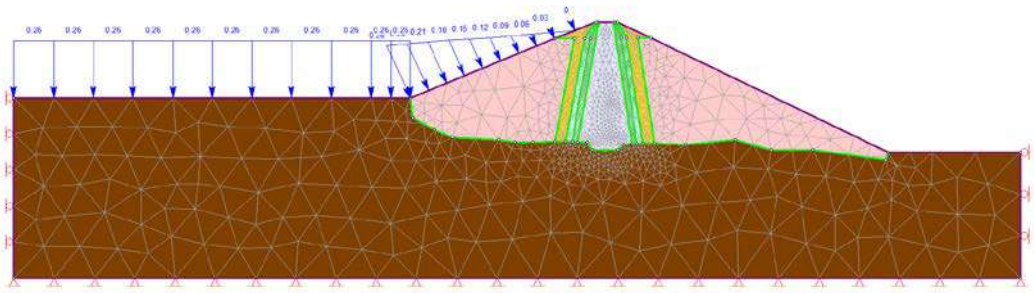

Figure 3. Full reservoir model of unfavorable section of Duzcam dam and soil by Phase2 software

Mechanical properties of the materials used in the dam body and soil are given in Table 1 below. In the static analysis, the material types were chosen as elastic. The material parameters used for the analysis were selected from the threshold values given in the RocData program.

Table1. Materials Properties of Dam Body

Materials Name	Modulus of elasticity (MPa)	Poisson ratio
Impervious fill	3686	0.35
Filter sand	6240	0.4
Filter gravel	1900	0.4
Pit-run gravel	800	0.42
Rock fill	8700	0.45
Soil	1000	0.4

3. RESULTS AND DISCUSSION

The displacements and principal stresses obtained as a result of the static analysis after entering the material mechanical properties (Young's Modulus and Poisson ratio values) are given below:

- The largest total displacement in the dam body is 7.2 cm in **Figure 4**.
- The largest vertical displacement in the dam body is 7 cm in **Figure 5**.
- The largest horizantal displacement in the dam body is 5.2 cm in **Figure 6**.
- The maximum principle stress (s1) in the dam body is 5.7 MPa in **Figure 7**.
- The maximum principle stress (s3) in the dam body is 7.6 MPa in **Figure 8.**
- The maximum Von Mises stress in the dam body is 7.6 MPa in **Figure 9.**

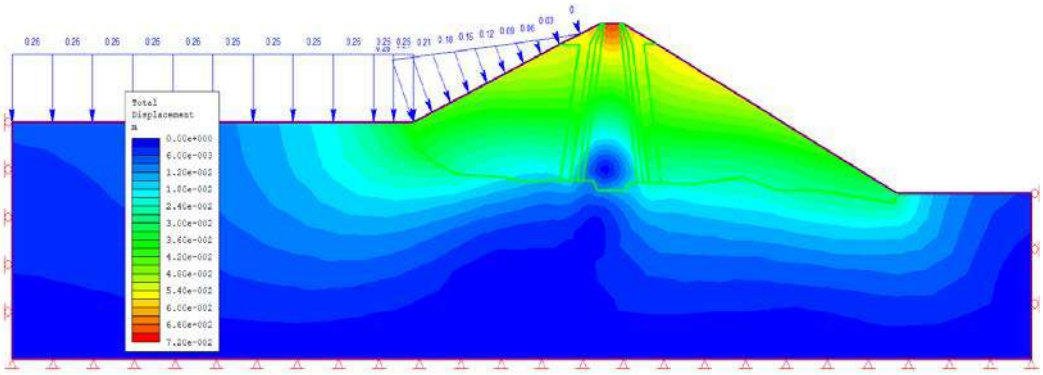

Figure 4. The total displacements in the dam body and foundation

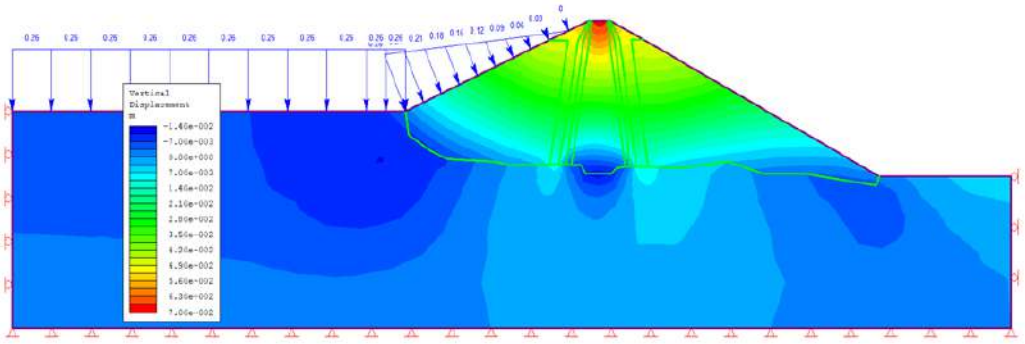

Figure 5. The vertical displacements in the dam body and foundation

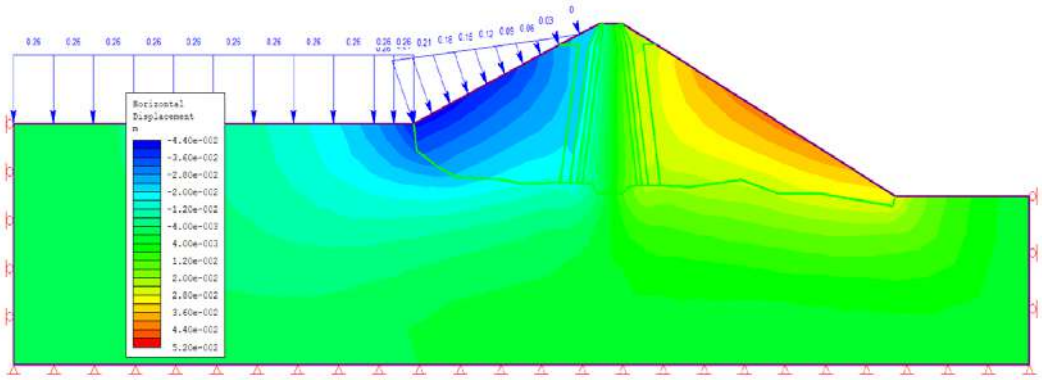

Figure 6. The horizontal displacements in the dam body and foundation

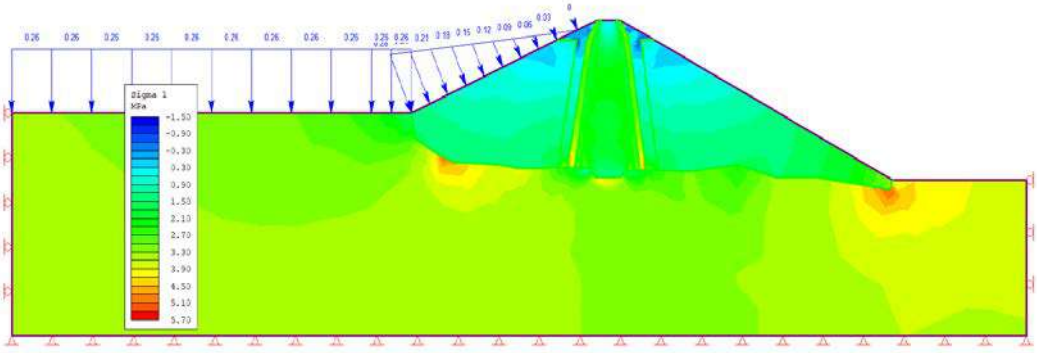

Figure 7. The principle stress (s1) in the dam body and foundation

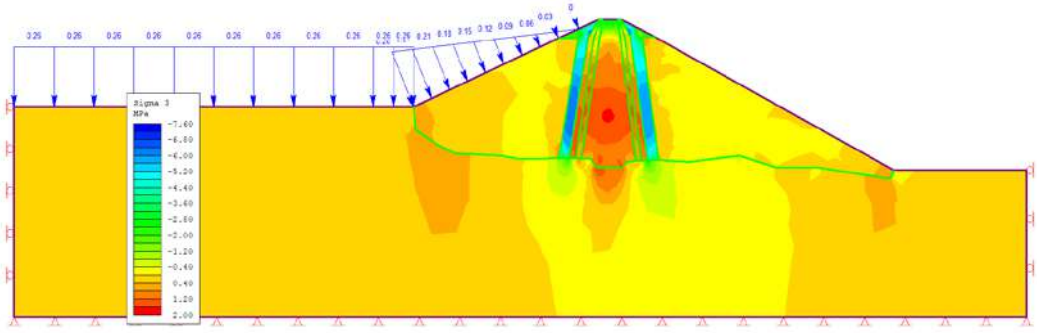

Figure 8. The principle stress (s3) in the dam body and foundation

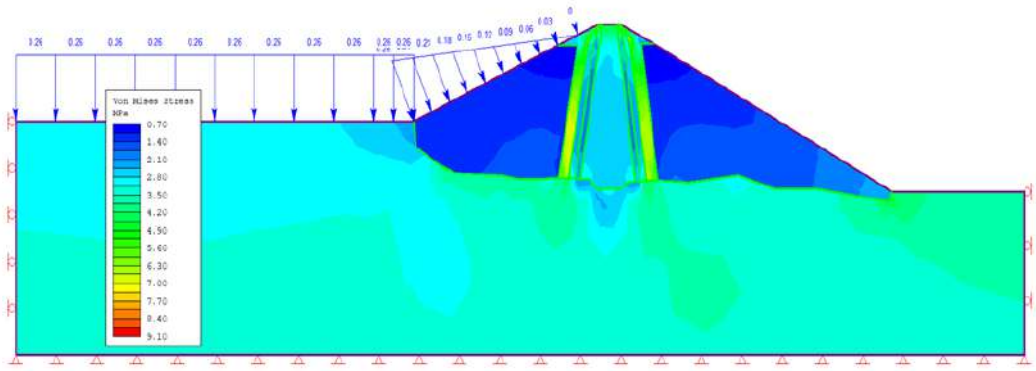

Figure 9. Von Mises stress in the dam body and foundation

4. CONCLUSIONS

The Duzcam CCR dam being constructed as a result of this study was evaluated statically. It has been observed that the maximum total displacement values obtained in the dam body are not troubled for dam safety. Considering the maximum Von Mises stress, tensile and compressive stresses in terms of dam safety, it does not appear to be a risk. These stresses and displacement values obtained this study for clay core rockfill dams are within normal limits. We can deducte from this study, static stability is safe even if the reservoir is full for Duzcam Dam.

It is necessary to determine the dam behavior in case of possible earthquakes by performing dynamic analysis. Because of the problem of seepage in clay core rockfill dams, this dam can be evaluated by seepage analysis. Analysis can be renewed for viscous or nonreflecting boundary conditions. It may result safer results for the response and performance of the dam.

REFERENCES

[1]. N. Uddin, "A Dynamic Analysis Procedure for Concrete-Faced Rockfill Dams Subjected to Strong Seismic Excitation," *Computers and Structures*, vol. 72, no. 1-3, pp. 409-421, 1999.
[2]. Wieland, M., Brenner, R.P., Seismic Performance of CFRDs, International Water Power & Dam Construction, Dam Safety, CFRD, pp. 18-21, 2007.
[3]. Nayebzadeh R. and Mohammadi M., "The Effect of Impervious Clay Core Shape on the Stability of Embankment Dams," *Geotechnical and Geological Engineering*, vol. 29, no:4, pp:627-635, 2011
[4]. Liu C., Zhang L., Bai B., Chen J. and Wang J., "Nonlinear analysis of stress and strain for a clay core rock-fill dam with FEM," *Procedia Engineering*, vol 31, pp:497-501, 2012
[5]. Rocscience. Phase2 (ver. 8), Toronto, Canada, 2007, http://www. rocscience.com/

KARABULUT is graduated from Karadeniz Technical University in 2011. He has worked as a research assistant in Bulent Ecevit University since 2013. He completed master 20 June 2016 in Bulent Ecevit University. He has been going on doctorate since 2016.

ICENS 4TH INTERNATIONAL CONFERENCE ON ENGINEERING AND NATURAL SCIENCE
2-6 May 2018 KIEV UKRAINE

Combined Heat Transfer in an Enclosure with Different Side Wall Geometry

Zerrin Sert[1], Cisil Timuralp[2], Mesut Tekkalmaz[3]

Abstract

In this study, natural convection and surface radiation heat transfer in enclosures consisting of gray walls with different side wall geometries were investigated numerically. Vertical, triangular, and circular shaped right and left walls are considered. Two cases of heat input is considered due to isothermal wall from (1) the bottom side (2) the left side wall. The hot and cold walls are isothermal. The medium is filled with air, and it is considered as non-participating medium. The simulations are done using a two-dimensional and laminar flow model, and the Boussinesq approximation is applied to simulate buoyancy. The Rayleigh number and the surface emissivity are changed between $Ra=10^4–10^7$, and $\varepsilon=0–1$, respectively. The numerical solutions are parametrically analyzed for modified side-wall geometries, different surface emissivity and Rayleigh number. The effects of the conduction-radiation parameter, the Rayleigh number, the surface emissivity and the geometry of the side-walls were examined for heat transfer and fluid flow properties.

Keywords: Different side-wall geometry, natural convection, surface radiation

1. INTRODUCTION

Natural convection in rectangular and square enclosures have been wide applications such as thermal energy storage, solar collectors and cooling processes of electronic devices. A great number of works are concerned in square, rectangular and cylindrical geometries.

Most of the numerical studies reported in the literature have considered a square or rectangular cavity with heated side walls and adiabatic top and bottom surfaces. Balaji and Venkateskan [1] showed that the surface radiation leads to reduction of the convection component. Sen and Sarkar [2] studied the effects of variable fluid properties on the interaction of laminar natural convection and surface radiation in differentially heated square cavity. Akiyama and Chong [3] studied the interaction of natural convection with thermal radiation by gray surfaces in a square enclosure. They showed that the influence of radiation on natural convection was non-negligible. Mezrhab and Bchir [4] investigated the effects of a thick partition located close to the hot wall of the cavity. They reported that the surface radiation has significant influence on the temperature distribution and flow patterns. Mahapatra et al. [5] reported a finite element solution on the interaction of surface radiation and variable property laminar natural convection in a differentially heated square cavity.

Many researchers have simulated extreme cases such as Rayleigh Bernard problem with hot bottom wall and cold top wall. Ridouane et al. [6] discussed the effects of surface radiation on convection in an air filled square cavity heated from below cooled from above using a numerical model based on finite differences. Cheickh et. al [7] conducted a numerical study of natural convection in air-filled, two-dimensional square enclosure heated with a constant source from below and cooled from above, for two different lengths of the heat source and various Rayleigh numbers. Gad et al. [8] numerically investigated two-dimensional steady Rayleigh–Bernard convection with surface radiation in cavities with different aspect ratios

A number of studies of heat transfer in non-rectangular enclosures have been performed by several authors. Kent et. al. [9] studied laminar natural convection in right triangular and quarter circular enclosures

[1] *Eskisehir Osmangazi University, Department of Mechanical Engineering, 26480, Eskisehir, Turkey. zbocu@ogu.edu.tr*

[2] *Eskisehir Osmangazi University, Department of Mechanical Engineering, 26480, Eskisehir, Turkey. cisil@ogu.edu.tr*

[3] *Corresponding author: Eskisehir Osmangazi University, Department of Mechanical Engineering, 26480, Eskisehir, Turkey. tmesut@ogu.edu.tr*

numerically. The streamlines and isotherms for all the cases and Rayleigh numbers were given in detailed and it was concluded that both aspect ratios and Rayleigh number affect the patterns. Salmun [10] re-examined a triangular geometry over the parameters of aspect ratio, Rayleigh and Prandtl numbers. Oztop et. al. [11] analyzed the laminar natural convection heat transfer inside the triangular cross-section enclosure which is applicable for roof geometry with and without eaves at different temperature for summer-day boundary condition. As a result, the heat transfer strongly depended on both aspect ratio and the length of the eave. Bhavnani and Bergles [12] experimentally examined natural convection heat transfer characteristics of sinusoidal wavy surfaces. It was concluded that the heat transfer decreased as the amplitude-to-wavelength ratio increased for constant surface area and the performance of the plate improved when the surface at the leading edge faced downward. The effect of hot wavy wall of a laminar natural convection in an inclined square cavity described numerically in the study of Adjlout et. al. [13]. The results obtained for different inclination angles and for different Rayleigh numbers show that the flow and the heat transfer are affected by the undulation of the hot wall. Rahman et. al. [14] investigated the effects of buoyancy ratio and Lewis number on heat transfer in a curvilinear triangular cavity. It was found that the Lewis number is an effective parameter on flow field and temperature distribution and heat transfer increased with positive value of buoyancy ratio and Rayleigh number. Triveni and Panua [15] solved laminar natural convection in a right-angled triangular cavity for caterpillar curve shape base hot wall. The results indicated that the rate of heat transfer was not significantly affected with the variation of the width of the curve but it was increased with the increase of Rayleigh number. Mahmud et.al. [16] carried numerical analysis of heat transfer in an enclosure with two horizontal straight walls and vertical wavy walls. They found that the heat transfer was increased with the lower surface waviness and increased with Grashof number. Das and Mahmud [17] studied hydrodynamic and thermal behaviors of fluid inside a wavy enclosure. Their results showed that amplitude-wavelength ratio affected local heat transfer rate but not influence on average heat transfer rate. Oztop et. al. [18] numerically investigated natural convection in wavy enclosure with internal heat generation. It was concluded that the wavy wall and ratio of internal Rayleigh number to external Rayleigh number affect the heat transfer and fluid flow. Sompong and Witayangkurn [19] reported the effects of Rayleigh number, Darcy number and wave amplitude on natural convection inside a trapezoidal enclosure with wavy top surface. It was noticed that compared to the influence of Ra and Da, the top wavy surface has small influence on temperature distribution. The steady natural convection of air flow in a trapezoidal room with inclined left heated wall, a vertical right cooled wall, and two insulated horizontal upper and lower walls were investigated numerically by Lasfer et al. [20]. Results are presented in terms of streamline and isotherms for local and average Nu numbers. Moukalled and Darwish [21] studied natural convection in a partitioned trapezoidal cavity with one baffle attached to the lower horizontal base. They found that heat transfer is decreased by increasing the Prandtl number and height of the baffle.

The main objective of this paper is to study combined convection and radiation heat transfer analysis for three different geometries and two different heating cases. The results are presented in terms of streamlines, isotherms and mean total Nusselt numbers.

2. MATHEMATICAL FORMULATION

In this study, the geometry of the problem is shown in Figure 1. In the problem by changing the geometry of the right and left walls of the enclosure; three different channel geometries are investigated. Also, in the first case the bottom wall is hot, the top wall is cold, and the lateral walls are adiabatic. In the second case, the left lateral wall is hot, the right lateral wall is cold, and the top and bottom walls are adiabatic. All enclosure walls are considered are gray and emissivities of walls are the same in cases considered. The enclosure is filled with air (Pr=0.71) and the medium is not participating. The flow is assumed to be laminar, incompressible and the variation of the density of the fluid is modeled by the Boussinesq approximation. Using these approximations, the governing equations used in the present study can be written as follows;

the continuity

$$\frac{\partial u}{\partial x}+\frac{\partial v}{\partial x}=0 \tag{1}$$

the momentum

$$u\frac{\partial u}{\partial x}+v\frac{\partial u}{\partial y}=-\frac{1}{\rho}\frac{\partial P}{\partial x}+\upsilon\left(\frac{\partial^2 u}{\partial x^2}+\frac{\partial^2 u}{\partial y^2}\right) \tag{2}$$

$$u\frac{\partial v}{\partial x}+v\frac{\partial v}{\partial y}=-\frac{1}{\rho}\frac{\partial P}{\partial y}+\upsilon\left(\frac{\partial^2 v}{\partial x^2}+\frac{\partial^2 v}{\partial y^2}\right)+g\beta(T-T_0) \tag{3}$$

for the energy

$$u\frac{\partial T}{\partial x}+v\frac{\partial T}{\partial y}=\alpha\left(\frac{\partial^2 T}{\partial x^2}+\frac{\partial^2 T}{\partial y^2}\right) \tag{4}$$

where T is the temperature, β is the volumetric thermal expansion coefficient, g is the gravitational acceleration, P is the pressure while α is the thermal diffusivity, υ is the kinematic viscosity and ρ is the density of air.

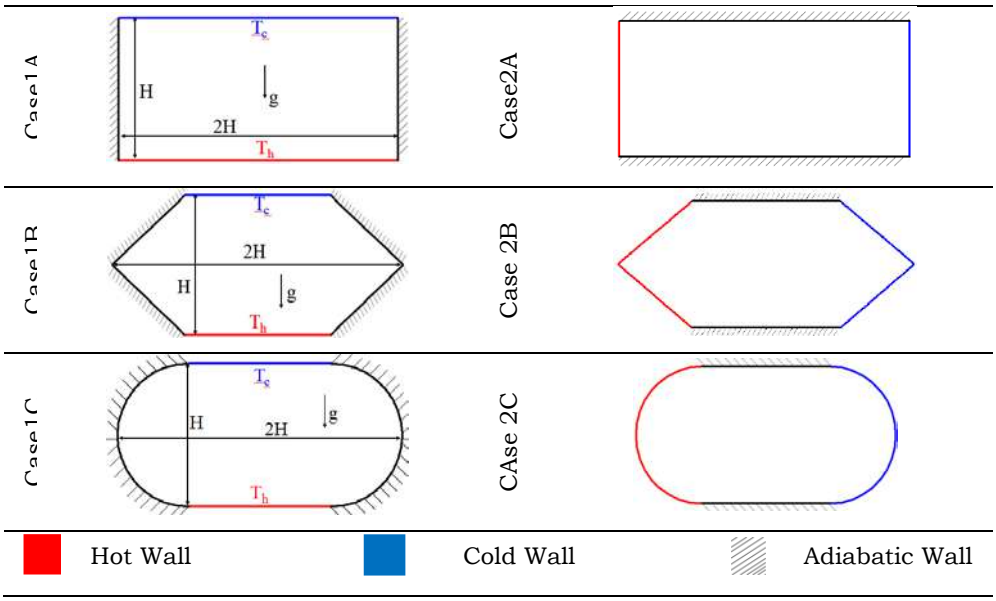

Figure 1. Schematic representation of the problem.

Boundary Conditions

in hot wall;

$$u=v=0, \quad T=T_h, \tag{5}$$

in cold wall;

$$u=v=0, \quad T=T_c, \tag{6}$$

in the adiabatic walls;

$$u=v=0, \quad q_r+q_{cv}=0 \tag{7}$$

The radiative heat transfer equation is defined by

$$\nabla\cdot(I(\mathbf{r},\mathbf{s})\mathbf{s})+(a+\sigma_s)I(\mathbf{r},\mathbf{s})=an^2\frac{\sigma T_0^4}{\pi}+\frac{\sigma_s}{4\pi}\int_0^{4\pi}I(\mathbf{r},\mathbf{s})\Phi(\mathbf{s}\cdot\mathbf{s}')d\Omega' \tag{8}$$

for a medium which is absorbing, emissing and scattering . In the preceding equation **r** represents the position vector, **s** is the direction vector, $\mathbf{s}'$ is the scattering direction vector, **s** is the path length, a is the absorbing coefficient, n is the refractive index, σ_s is the scattering coefficient, σ is the Stefan-Boltzman coefficient, I is the radiation intensity, Φ is the phase function and Ω' represents solid angle. In this study, absorbing and

scattering coefficients are zero because of the non-participating medium. In gray radiation model, the walls are opaque, diffusively and independent of wavelength.

The mean total Nusselt number for the cold wall is calculated by,

$$Nu_t = Nu_c + Nu_r = \frac{q_c + q_r}{k(T_h - T_c)/H} \quad (9)$$

q_c and q_r are the mean heat flux along the wall.

3. NUMERICAL METHOD

The governing Eqs. (1)–(4) and the radiative transfer equation are discretized using the FVM, and the resulting equations are solved in an iterative procedure using the standard implicit, second order upwind solver with velocity and pressure coupling achieved by the SIMPLE algorithm. The computations were carried out using Fluent® [22]. Segregated, implicit, 2-D, laminar steady incompressible flow solver was used for numerical study. Additionally, DO (Dicreate Ordinate Method) was used for radiation transfer equation with 4x6 angular direction selection. It has been found that the DO radiation heat transfer model performance in the Fluent® program is better than the S2S method [8]. Higher mesh resolution is used near the walls in order to be able to accurately depict the flow and temperature fields.
The numerical procedure is validated against the numerical results of Wang et al. [23], in terms of mean convection, radiation and total Nusselt numbers of differentially heated square cavity case which is heated and cooled from the lateral walls (Table 1). The numerical solutions agreed well for the range of the Rayleigh numbers considered with the maximum difference being 0.25%.

Table 1. Comparison of mean Nusselt numbers.

Ra Number	ε	H. Wang et al. [23]			Present Study		
		Nu_c	Nu_r	Nu_t	Nu_c	Nu_r	Nu_t
10^4	0.0	2.246	0.000	2.246	2.245	0.000	2.245
10^4	0.2	2.268	0.499	2.767	2.267	0.499	2.766
10^4	0.8	2.278	2.372	4.650	2.277	2.372	4.649
10^5	0.0	4.540	0.000	4.540	4.524	0.000	4.524
10^5	0.2	4.411	1.073	5.484	4.404	1.073	5.477
10^5	0.8	4.247	5.137	9.384	4.241	5.136	9.377
10^6	0.0	8.852	0.000	8.852	8.849	0.000	8.849
10^6	0.2	8.417	2.319	10.736	8.391	2.318	10.709
10^6	0.8	7.930	11.150	19.078	7.930	11.148	19.078

Table 2. Grid Sensitivity table for Case1C and $\varepsilon = 0$.

Numbers of Node	21109	83919	155170
Ra		Nu_t	
10^4	3.1663	3.1817	3.1890
10^5	5.2226	5.2427	5.2575
10^6	8.6831	8.6765	8.6947
10^7	15.0829	14.7920	14.8164

The accuracy of numerical solutions was also checked through numerous detailed tests on the effects of the grid refinement. For instance, in Table 2, the convergence of total mean Nusselt numbers for increasing Rayleigh numbers and increasing number of grids is depicted for Case1C and $\varepsilon = 0$. It is calculated that the maximum number of Nu_t changes is about 2% and 1% according to the number of nodes of 83919 of 21109 nodes and according to the number of nodes of 83919 of 155170 nodes, respectively. Therefore, in all solutions, mesh structure was used the triangular non-uniform mesh structure (83919 nodes), in which the mesh density is increased by adaptation to 0.1H from the whole wall. The mesh structure used to solve the problem is shown in Figure 2. The convergence criterion for continuity, momentum, energy and radiation heat transfer equations is accepted as 10^{-5} in all solutions.

4. RESULTS AND DISCUSSION

In this study, combined convection and radiation heat transfer analysis were performed for three different geometries and two different heating cases. The thermophysical properties of air were evaluated at the reference temperature $T_0=(T_h+T_c)/2$ =300K. The numerical simulations were performed for $10^4 \le Ra \le 10^6$ and $0 \le \varepsilon \le 1$. The results were expressed in the form of the streamlines and the isotherms plots and mean Nusselt number over the hot surface wall.

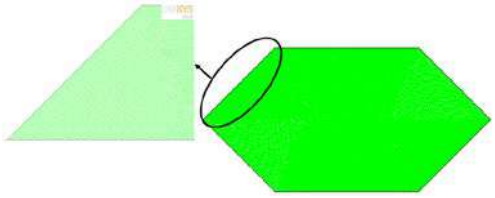

Figure 2. The mesh structure of the problem.

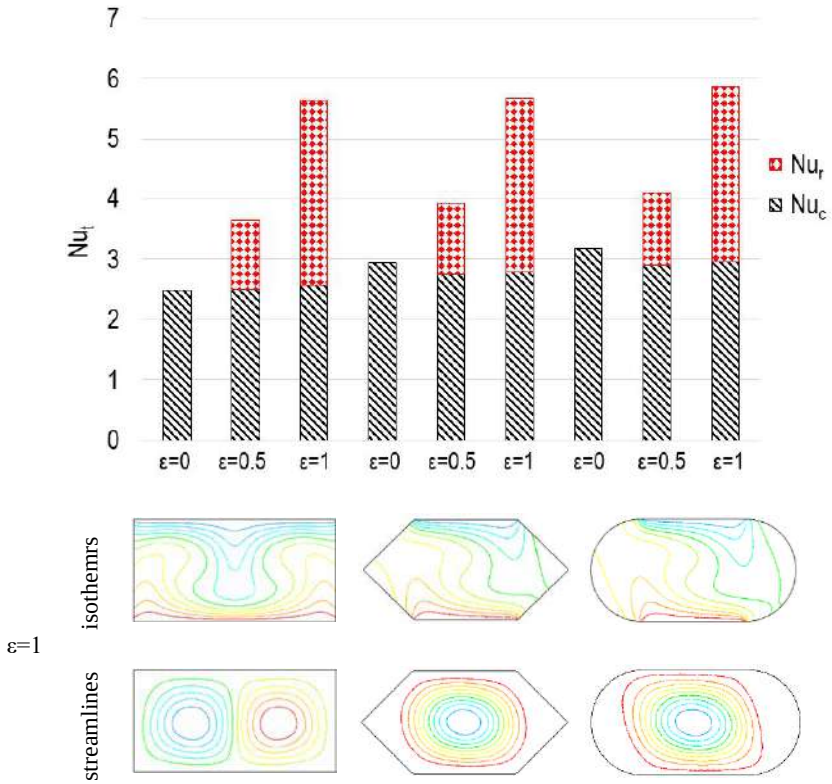

Figure 3. Variation of Nu_c and Nu_r and isotherms and streamlines for ε=1, in the case of bottom heating for $Ra=10^4$.

In Figure 3, Nu_r and Nu_c values for Ra = 10^4 and the isotherms and streamlines for ε=1 are depicted in case of bottom heating for three geometries. For ε=0, Nu_c is in ascending order Case1A, Case1B, and Case1C. In the case of radiation, Nu_c does not change almost in Case1A, while it decreases slightly in Case1B and Case1C. Nu_t is in ascending order Case1A, Case1B and Case1C. In Case1A the streamlines are two cells, whereas in case1 B and Case1 C, the streamlines are single cell. The isotherms of Case 1B and Case 1C are similar.

In Figure 4, Nu_r and Nu_c values for Ra = 10^6 and the isotherms and streamlines for ε=1 are given in case of bottom heating for three geometries For ε=0 and Ra=10^6, the mean convection Nusselt number is similar to Ra=10^4 and Nu_c is in ascending order Case1A, Case1B, and Case1C. For ε=0.5 and 1, the Nu_c value is almost unchanged in all three cases. Nu_t values are increasing rapidly as the surface emissivity values increase. Nu_t values for ε=1 are the same for three geometries. In Case1A, for Ra=10^4 the two-cell structure of streamlines was disappeared and the single-cell structure of streamlines was formed in three geometries. The streamlines are even near to the walls of geometries. Similarly, the isotherms for three geometries are similar.

In Figure 5, Nu_r and Nu_c values for Ra = 10^4 and the isotherms and streamlines for □=1 are shown in case vertical heating for three geometries. While Nu_c is similar to three geometries for Nu_t=0, decrease with surface radiation. This decreasing is more pronounced at ε=1. Nu_t is is in ascending order Case2A, Case2C and Case2B. For Nu_t=0.5, almost the same for all three geometries. As the surface emissivity increases, Nu_t rapidly changes. In three geometries, single-cell streamlines are formed and the circulation cell in the center became more flattened according to the bottom heating condition. For this case, the isotherms are similar to each other.

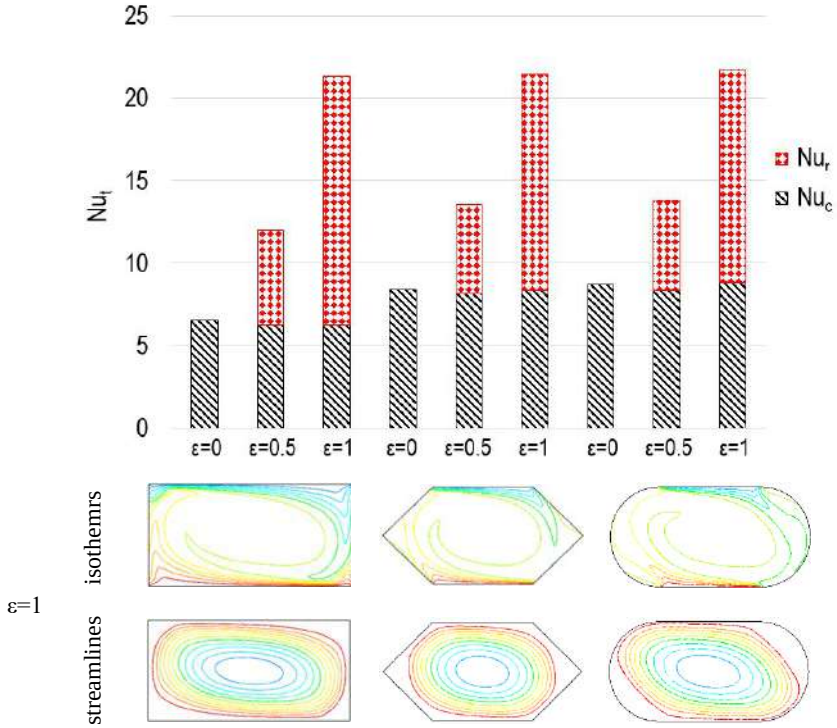

Figure 4. Variation of Nu_c and Nu_r and isotherms and streamlines for ε=1, in the case of bottom heating for Ra=10^6.

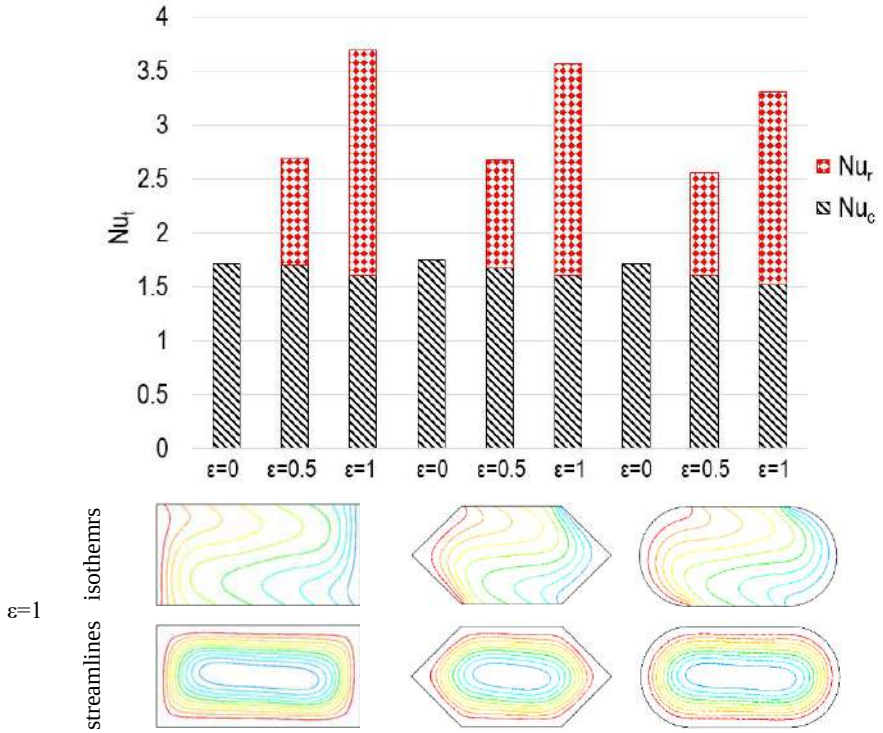

Figure 5. Variation of Nu_c and Nu_r and isotherms and streamlines for ε=1, in the case of vertical heating for $Ra=10^4$.

In Figure 6, Nu_r and Nu_c values for Ra = 10^6 and the isotherms and streamlines for ε=1 are depicted in case of vertical heating for three geometries. As the surface emissivity increases, Nu_c decreases in three geometries. This reduction is even lower in Case2C. While for ε=0.5 Nu_t is in ascending order Case2C, Case2B ve Case2A, for ε=1 Nu_t is in ascending order Case2B, Case2C ve Case2A. For Case2A and Case2C, the isotherms and the streamlines are similar to each other. In Case2B has a more irregular cell structure.

In Figure 7, the effect of different heating case in three geometries on the Nu_t is depicted for ε=0 and ε=1. In all cases, as the Rayleigh number increases, the total Nusselt number increases, because of increasing fluid flow. This trend is more pronounced since Ra = 10^6. In the case of two heating cases with pure natural convection, the Nu_t is almost equal to each other. In the case of bottom heating together with radiation, the heat transfer is significantly increased.

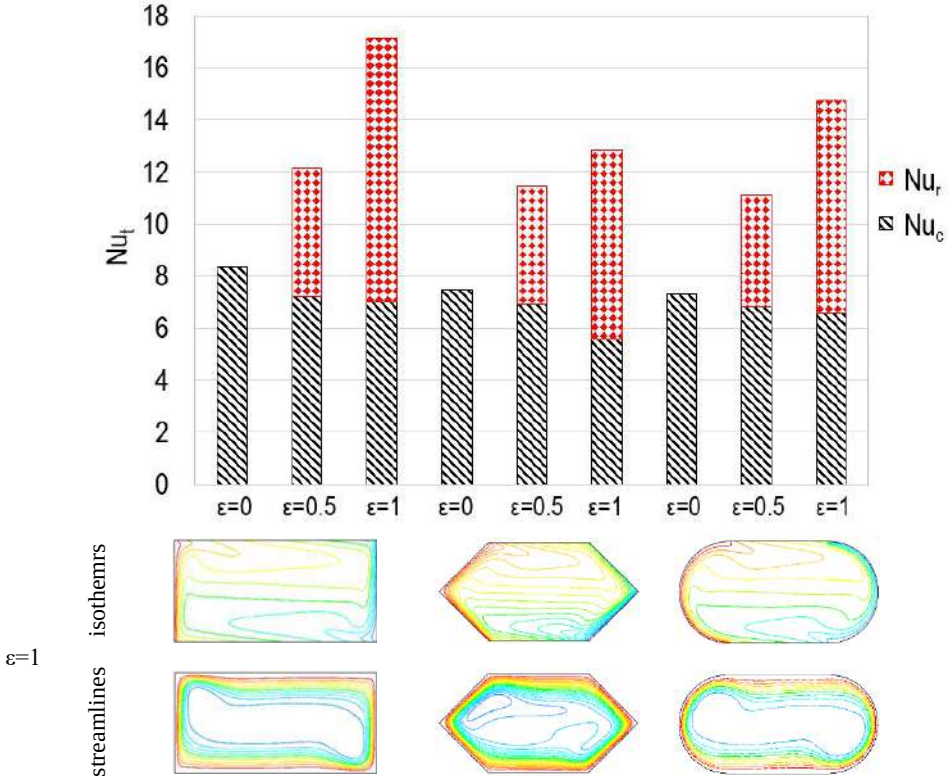

Figure 6. Variation of Nu_c and Nu_r and isotherms and streamlines for $\varepsilon=1$, in the case of vertical heating for $Ra=10^6$.

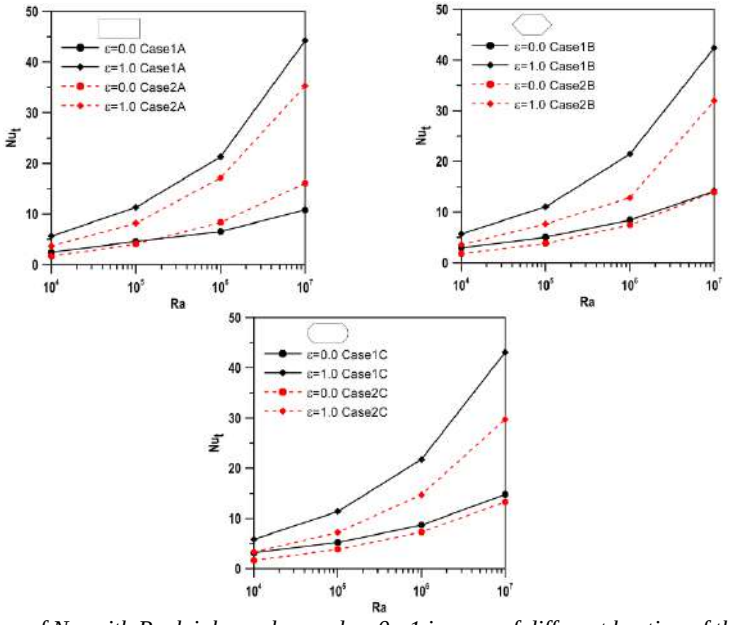

Figure 7. Variation of Nu_t with Rayleigh number and $\varepsilon=0$ –1 in case of different heating of three geometries.

4.CONCLUSIONS

Heat transfer by natural convection and thermal radiation in three different enclosures was studied numerically. Vertical, triangular, and circular shaped right and left walls were considered. Two cases of heat input is considered due to isothermal wall from (1) the bottom side (2) the left side wall. The conservation of mass, momentum and energy equations were solved using the control volume method. Based on the presented results, the following conclusions have been drawn:

a) In case of bottom heating, the heat transfer is higher than the vertical heating.
b) For Ra = 10^4 and bottom heating, two-cell flow profiles were formed in Case1A, whereas, single-cell flow profiles were formed in all other cases.
c) In case of bottom heating, Nu_t is in ascending order Case1A, Case1B ve Case1C. In case of vertical heating, for low Ra, Nu_t is in ascending order Case2C, Case2B ve Case2A. In case of vertical heating, for high Ra, Nu_t is in ascending order Case2B, Case2C ve Case2A.

REFERENCES

[1]. C. Balaji and S.P. Venkateshan, "Interaction of Surface Radiation with Free Convection in a Square Cavity", *International Journal of Heat and Fluid Flow*, vol. 14, pp. 260–267, 1993.
[2]. S. Sen and A. Sarkar, "Effects of variable property and surface radiation on laminar natural convection in a square enclosure", *International Journal of Numerical Methods for Heat and Fluid Flow*, vol. 5, pp. 615–627, 1995.
[3]. M. Akiyama and Q.P. Chong, "Numerical Analysis of Natural Convection with Surface Radiation in a Square Enclosure", *Numerical Heat Transfer Part A*, vol. 31, pp. 419–433, 1997.
[4]. A. Mezrhab and L. Bchir, "Radiation Natural Convection Interactions in Partitioned Cavities", *International Journal of Numerical Methods for Heat and Fluid Flow*, vol. 9, pp. 186–203, 1999.
[5]. S.K. Mahapatra, S. Sen and A. Sarkar, "Interaction of Surface Radiation and Variable Property Natural Convection in a Differentially Heated Square Cavity-A Finite Element Analysis", *International Journal of Numerical Methods for Heat and Fluid Flow*, vol. 9, pp. 423– 443, 1999.
[6]. E.H. Ridouane, M. Hasnaoui, A. Amahmid and A. Raji, Interaction between natural convection and radiation in a square cavity heated from below, Numerical Heat Transfer. Part A 45 (2004) 289–311
[7]. N.B. Cheikh, B.B. Beya and T. Lili, "Influence of Thermal Boundary Conditions on Natural Convection in a Square Enclosuare Partially Heated from Below", *International Communications in Heat and Mass Transfer*, vol. 34, pp. 369-379, 2007.
[8]. M.A. Gad and C. Balaji, "Effect of Surface Radiaiton on RBC in Cavities Heated from Below", *International Communications in Heat and Mass Transfer*, vol. 37, pp. 1459-1464, 2010.
[9]. E. Fuad Kent, E. Asmaz and S. Ozerbay, "Laminar natural convection in right triangular enclosures", H*eat Mass Transfer*, vol. 44, pp. 187–200, 2007.
[10]. H. Salmun, "Convection patterns in a triangular domain", International Journal Heat Mass Transfer, vol.38, pp. 351-362, 1995.
[11]. H.F. Oztop, Y. Varol and A. Koca, "Laminar natural convection heat transfer in a shed roof with or without eave for summer season", *Applied Thermal Engineering*, vol.27, pp. 2252-2265, 2007.
[12]. S.H. Bhavnani and A.E. Bergles, "Natural convection heat transfer from sinusoidal wavy surfaces", *Waerme Stoffuebertragung/Thermo Fluid Dynam*ics, vol. 26, pp. 341– 349, 1991.
[13]. L. Adjlout, O. Imine, A. Azzi and M. Belkadi, "Laminar natural convection in an inclined cavity with a wavy wall", *International Journal of Heat and Mass Transfer*, vol. 45, pp. 2141-2152, 2002.
[14]. M.M. Rahman, H.F. Oztop, A. Ahsan and J. Orfi, "Natural convection effects on heat and mass transfer in a curvilinear triangular cavity", *International J. of Heat and Mass Transfer*, vol.55, pp. 6250-6259, 2012.
[15]. M. Kr. Triveni and R. Panua, "Numerical simulation of natural convection in a triangular enclosure with caterpillar (C) curve shape hot wall", *International Journal of Heat and Mass Transfer*, vol. 96, pp. 535-547, 2016.
[16]. S. Mahmud, P. K. Das, N. Hyder and A.K.M.S. Islam, " Free convection in an enclosure with vertical wavy walls", *International Journal of Thermal Sciences*, vol. 41, pp. 440-446, 2002.
[17]. P.K. Das and S. Mahmud, "Numerical investigation of natural convection inside a wavy enclosure", *International Journal of Thermal Sciences*, vol.42, pp. 397-406, 2003.
[18]. H.F. Oztop, E. Abu-Nada, Y. Varol and A. Chamkha, "Natural convection in wavy enclosures with volumetric heat sources", *International Journal of Thermal Sciences*, vol. 50, pp. 502e514, 2011.
[19]. P. Sompong and S. Witayangkurn, "Natural Convection in a Trapezoidal Enclosure with Wavy Top Surface", *Journal of Applied Mathematics*, vol. 2013, pp. 1-7, 2013.
[20]. K. Lasfer, M. Bouzaiane and T. Lili, "Numerical Study of Laminar Natural Convection in a Side-Heated Trapezoidal Cavity at Various Inclined Heated Sidewalls", *Heat Transfer Engineering*, vol. 31[5], pp. 362-373, 2010.
[21]. F. Moukalled and M. Darwish, " Natural Convection in a Partioned Trapezoidal Cavity Heated From The Side", *Numerical Heat Transfer, Part A: Applications*, vol. 43, pp. 543-563, 2003.
[22]. Fluent, FLUENT 6.1 User's Guide, 2003, FLUENT Inc., Lebanon: NH, 2003.
[23]. H.Wang, S. Xin and P.Le Quere,"Etude numerique du couplage de la convection naturelle avec le rayonnement de surfaces en cavite caree remplie d'air", *C.R. Mecanique*, vol. 334, pp. 48-57, 2006.

ICENS 4TH INTERNATIONAL CONFERENCE ON ENGINEERING AND NATURAL SCIENCE
2-6 May 2018 KIEV UKRAINE

Tissue Engineering and Textile Materials

Asli Demir[1], Merve Turemen[1], Sukhwinder Kaur Bhullar[23],

Abstract

Textile technologies have recently attracted great attention as potential biofabrication tools for engineering tissue constructs. Using current textile technologies, fibrous structures can be designed and engineered to attain the required properties that are demanded by different tissue engineering applications. Tissue engineering is an important therapeutic strategy to be used in regenerative medicine in the present and in the future. Tissue engineering aims to improve the function of diseased or damaged organs by creating biological substitutes. To fabricate a functional tissue, the engineered construct should mimic the physiological environment including its structural, topographical, and mechanical properties.Functional biomaterials research is focused on the development and improvement of scaffolding, which can be used to repair or regenerate an organ or tissue. Scaffolds are one of the crucial factors for tissue engineering. Scaffolds consisting of natural polymers have recently been developed more quickly and have gained more popularity. For the fabrication into biomaterial scaffolds for tissue engineering, fibers are a continuous material structure that have an extremely high ratio of length to width, and particularly suitable since fibrous structures can morphologically resemble extracellular matrix components in tissues. Moreover, fibers can be collected and processed into complex fibrous networks using conventional textile techniques, such as knitting, weaving, or braiding, to create three-dimensional (3D) structures with improved structural and mechanical properties. Recently, there is a growing interest in using nanofabrication techniques to fabricate nanometer-sized fibers for tissue engineering Fiber-based methods, which include direct writing and textile techniques, have emerged as promising technologies for creating 3D structures with tunable mechanical and biological properties. Fiber-based techniques also allow a precise control over the positioning of fibers. These fibers can be used as carriers for drugs, factors, and microorganisms. In the case of microorganism-laden fibrous constructs, their high porosity facilitates the transport of nutrients and waste. The fibers can also serve as sacrificial structures to form vascular networks in cell-laden structures.

Keywords: tissue engineering,textile materials, biopolymer,biomaterial

1. INTRODUCTION

The history of fibrous biomaterials trace back to the ancient American Indians and Egyptians. These biomaterials were among the earliest materials processed in ancient times into textile structures for medical devices. The Egyptians used fibers to draw wounds together, and the American Indians used horse hair, cotton and leather. Fibrous biomaterials are fabricated into structures with different architectures have been found in usage area for medical applications during modern times. Together with the improvements in polymer and fiber processing technologies, fibrous biomaterials have used in wound healing, implantation, and tissue engineering apllications[1].

Tissue engineering is a multidisciplinary field combines the principles of cellular biology, biomaterials, and engineering to address the present demands for organ transplantation. It can be defined as preparing a living tissue construct by expanding cells in vitro and incorporating the cells into a temporary scaffold to mimic the structure and function of the native tissue[2]. Tissue engineering discipline is related with repair or replace damaged tissues by using a stem cell source seeded on a biological or artificial scaffold structure. The basic scaffolding material is gradually substituted, leaving the desired replacement tissue, as the cells proliferate and differentiate creating new tissue. Many of scaffolding materials have been researched as tissue engineering applications. Textile materials are such example that show great promise as scaffolding for tissue engineering. In this concept, different forms of fibers can be used to mimic native cellular structures, such as collagen fibres of the extracellular matrix (ECM). Electrospinning is the most common method used in the field of tissue

[1]*Corresponding author: Ege University, Department of Textile Engineering, 35100, Bornova/Izmir, Turkey.*
asli.demir@ege.edu.tr

[2] *Department of Mechanical Engineering, University of Victoria, Victoria, BC, Canada*

[3]*Department of Mechanical Engineering, Bursa Technical University, Bursa, Turkey.*

engineering. The size scale of electrospun fibres mimics that of native ECM and provides an ideal environment for cellular attachment, growth, and differentiation into the target tissue. Fabrication of large scale electrospun scaffolds is time consuming, may require harsh organic solvents, is difficult to generate sufficient 3D structures, and typically results in mechanical properties inferior to the target tissue to be replaced[3].

In general, scaffolds for tissue engineering should have mechanical properties, biocompatibility and suitable morphology to support cell growth, and have high porosity. The scaffold as artificial extracellular matrix with specific appearances and plays a crucial role in promoting cell growth and differentiation. Extracellular matrix in native tissue is a three-dimensional (3D) network whose composition and structure can interact with cells continuously to provide structural support, transfer mechanical forces and transmit chemical signals in native tissues.[2]

Fabrication of constructs with controlled mechanical properties, microstructure, and cellular distribution plays a crucial role in the engineering of functional tissues. Synthetic or natural biomaterial based scaffolds are used to provide mechanical support and 3D medium for cellular growth. Conventional methods for creating scaffolds such as freeze drying, particle leaching, and solvent casting generate porous constructs with interconnected pores that are suitable for delivery of nutrients to the cells. On the other hand, the ability of these approaches for precise control over the spatial distribution of pore size and interconnectivity, mechanical properties, and structural properties is restricted. Recently, advanced biofabrication methods such as bioprinting, stereolithography, self-assembly of microgels, and biotextiles are used to produce 3D-engineered tissues[4].

In the past few years, various biomaterials have been used to prepare scaffolds in soft tissue engineering, including collagen, gelatin and elastin,poly(E-caprolactone)(PCL), poly(glycolic acid)(PGA), poly(lactic acid)(PLA), poly(hydroxy alkenoates) (PHAs) and their copolymers. Due to their own limitations, many biomaterials are difficult to meet the mechanical properties of engineering scaffolds. When soft tissues have high mechanical activity, such as dermis, blood vessels and heart valves, the scaffold has sufficient mechanical properties that are particularly important to the effective transfer of mechanical stimuli. For example, the failure of the scaffold grafted in the blood vessel is usually due to intimal hyperplasia caused by the compliance mismatch between the graft and the host.Moreover, the mechanical properties of the scaffolds should preserve at a sufficient level during the tissue growth period[2].

2. FIBERS IN TISSUE ENGINEERING

a. Synthetic Fibers

Synthetic polymers are widely used for the fabrication of scaffolds in tissue engineering including vascular prostheses made from poly(tetrafl uoroethylene) (PTFE) seeded with bone marrow stem cells, cartilage scaffolds made from poly(glycolic acid) (PGA) yarns and seeded with porcine articular chondrocytes.They have also been used in the form of micro and nanofibers since they mimic the intricate fibrillar microstructure of the natural extracellular matrix. For creating of micro- and nanofibrillars from synthetic biomaterials, different approaches have been made. Inspired by the process of protein self-assembly, nanofibers are now being formed from oligomeric peptide, nucleotide, and nonbiological amphiphilic building blocks. Although this is a promising approach, the self-assembly process occurs under conditions that are intolerable to cells, impeding the incorporation of cells during the fabrication process.

To fabricate fibers with micron-size dimensions, other methods including melt spinning and microfluidic spinning have been utilized. Such methods enable generating grooves on the surface of the fibers, making the suitable for directing cellular alignment and growth .

Polypropylene (PP) and PTFE,PGA and PLGA can be chosen as a material in the form of monofilament or multifilament twisted or braided yarns for the biofabrication of scaffolds and biotextiles. Cells have shown to respond to the surface morphologies in nano- and microscales . The surface structure on the fabricated fibers can control the cellular orientation and alignment. It has been shown that the fabrication of monofilament fibers with microgrooves on their surface improved cellular orientation along the direction of the grooves. Multifilament yarns, with similar surface topography as threads used in textile industry, have been gathered by

commercial textile instruments for the fabrication of tissue scaffolds used in cartilage and cardiac muscle tissue engineering .

Synthetic based fibers are great candidates for creating load-bearing scaffolds for tissue engineering because of their high mechanical properties. High strength provides their assembly using textile machines. By changing the surface morphology and fiber diameter, cellular alignment and functions can be modified. One of the main challenges of synthetic fibers is weak binding sites on these fibers'surface. [4]

b. Natural fibers

Proteins and polysaccharide-based materials, as naturally derived biomaterials, have been applied in tissue engineering when compared to the synthetic materials. The first known degradable sutures were obtained by purified collagen. Nowadays, collagen threads were manufactured by different spinning methods. The fabricated fibers were used for applications in neural and bone tissue engineering.Another one is the protein-based polymer silk which can be used for tissue engineering field . The sutures made from silk have been used for a long time in surgery. Silk fibers were braided and then used as an autologous tissue engineered anterior cruciate ligament[4]

Chitosan is emerged as a promising material for different tissue engineering applications. It is deacetylated form of chitin. The physico-chemical and biological properties of chitosan would promote its usage as one of the base materials in designing and fabrication of scaffolds to obtain the enhanced effectin bone tissue repair. Chitosan has unique properties of bioactive, biodegradable, anti-bacterial and biocompatible, and it possesses hydrophilic surface, which is absent in many synthetic polymers which makes it an excellent candidate for drug delivery and wound healing applications. A role for chitosan in enhanced cell adhesion, proliferation, and osteoblast differentiation and mineralization has been reported. Chitosan can be engineered to form 3D scaffolds with varied pore structures and composites with a number of materials including ceramics and polymers, for its application in bone tissue engineering[5-6].

3. CONCLUSION

Textile fibers have a structure particularly suitable for the fabrication into biomaterial scaffolds for tissue engineering applications due to extremely high aspect ratio which are particularly suitable to be used as a controllable element to manufacture as biomaterials.

The fiber-reinforced scaffold structures have an important role to enhance biocompatibility, bioactivity, and degradation of artificial composite scaffolds in tissue repair and regeneration. Also, fiber-based biomaterials are widely used as reinforcing additives in tissue engineering to produce the desirable properties.

Current studies are being developed on fiber-reinforced scaffolds with favorable morphological structure, optical properties, and electrical properties, biological and especially adequate mechanical structures. For this purpose, textile based scaffolds will be of great significance in the future to overcome these drawbacks.

REFERENCES

[1]. Tamayol, Ali, et al. "Fiber-Based Tissue Engineering: Progress, Challenges, and Opportunities." Biotechnology Advances, vol. 31, no. 5, 2013, pp. 669–687.,
[2]. Pei, Baoqing, et al. "Fiber-Reinforced Scaffolds in Soft Tissue Engineering." Regenerative Biomaterials, vol. 4, no. 4, 2017, pp. 257–268.
[3]. Tuin, S A, et al. "Creating Tissues from Textiles: Scalable Nonwoven Manufacturing Techniques for Fabrication of Tissue Engineering Scaffolds." Biomedical Materials, vol. 11, no. 1, 2016, p. 015017.,
[4]. [4]Akbari, Mohsen, et al. "Textile Technologies and Tissue Engineering: A Path Toward Organ Weaving." Advanced Healthcare Materials, vol. 5, no. 7, 2016, pp. 751–766.,
[5]. Saravanan, S., et al. "Chitosan Based Biocomposite Scaffolds for Bone Tissue Engineering."International Journal of Biological Macromolecules, vol. 93, 2016, pp. 1354–1365.
[6]. RodrÃguez-VÃ¡zquez, Martin, et al. "Chitosan and Its Potential Use as a Scaffold for Tissue Engineering in Regenerative Medicine." BioMed Research International, vol. 2015, 2015, pp. 1–15.

ICENS 4TH INTERNATIONAL CONFERENCE ON ENGINEERING AND NATURAL SCIENCE
2-6 May 2018 KIEV UKRAINE

Using Newmark Beta Method For Quarter Car Analysis

Engin Yildirim[1], *Ismail Esen*[1]

Abstract

In this study, the interaction between quarter car model and road is presented. According to surface roughness, roads are separated into 8 groups by using ISO-8608 standard. From the least surface rough to the most, these groups are named as A, B, C, D, E, F, G, H, respectively. Quarter Car is modelled as masses, springs and dampers that have linear stiffness and damping coefficients. Vertical displacement, velocity and acceleration are simulated at different vehicle velocities for different road groups in this study. For interaction between dynamics equations of car model and the road, the Newmark Beta method that give us numerical approach is used. 3 types of road groups, namely A, B and C are used. For each group, vertical displacements, velocities and accelerations for both car body and wheel are examined. Simulations are carried out via MATLAB software. According to the result, rougher road surface has higher displacement, velocity and acceleration comparing to the less rough road surface.

Keywords: Quarter Car, Newmark Beta, Road Surface

1. INTRODUCTION

For analysis of car parameters, the interaction between car and road is important. Quarter car model gives us basic data of this parameters. Many researchers investigate this parameters aspect both handling and ride performance. Some of these focus on suspension system of quarter car model.

Quarter car model with two degree of freedom is created in Matlab Simulink and is compared with the State Space model and the Transfer function under step input signal for the handling and ride performance of a vehicle with passive suspension system [1]. For analysis effect of speed bump a step function is created as input and overshoot and settling time are analyzed with 2 DOF Quarter car model [2]. Using vibration signal parameters, evaluation of element's clearance in the Quarter Car model is studied [3]. Under a road disturbance profile, a robust control scheme is created for a Quarter Car model. Sliding mode controller is used for control of suspension system of Quarter Car [4]. Semi-active suspension systems have been designed based on variable damping coefficient limit in this study. Aspect of ride comfort system's damping coefficient limit 4000 Ns/m has best performs [5]. A new model proposes reference sliding mode control that is easy be both implemented and eliminates necessity of a road signal as well as measuring damper force [6]. For double wishbone suspension, a quarter car model prepared by using the toolbox SimMechanics and Simulink of MATLAB. PID controller used to minimize the vertical body acceleration [7]. Using Linear Quadratic Regulator (LQR) control and Proportional Derivative Integral (PID) control, performance of an active suspension of a quarter car model is investigated. PID has more good handling comparing with LQR but as for ride comfort PID is not more good from LQR [8]. Proposed an active suspension system for a quarter car model using the concept of sliding mode control. The proposed active suspension system improved the vibration isolation of the car body more than the linear active suspension system based on LQ control and passive-suspension system [9]. For improving the ride comfort of vehicle suspension system, a Grey Fuzzy Sliding Mode controller is proposed According to simulation results, the proposed controller guarantees the system robustness in presence of uncertainties [10].

2. MATHEMATICAL MODEL

Interaction between car and road has great important for the engineers. Because handling and ride comfort are among most important areas for the automotive engineers. Thus, this interaction must be created correctly. Car models can create as quarter, half or full car modeling. Full car modeling is the most complicated and detailed but quarter car modeling gives us basic parameters for car dynamics analysis. For this reason, we will analysis quarter car model in this paper. Our quarter car system model shown in figure 1. In this system;

M/4 = Mass of the car body (Sprung Mass) (Kg)

[1] *Deparment of Mechanical Engineering, Karabuk University, Karabuk 78050, Turkey*

m1 = Mass of the wheel (Unsprung Mass) (Kg)

c = Damping coefficient of the absorber (Ns/m)

cw = Damping coefficient of the wheel (Ns/m)

k = Stiffness of the car body spring (N/m)

kw = Stiffness of the wheel (N/m)

u = Actuator

z = Car body vertical displacement (m)

zw = Wheel vertical displacement (m)

zg = Road input (m)

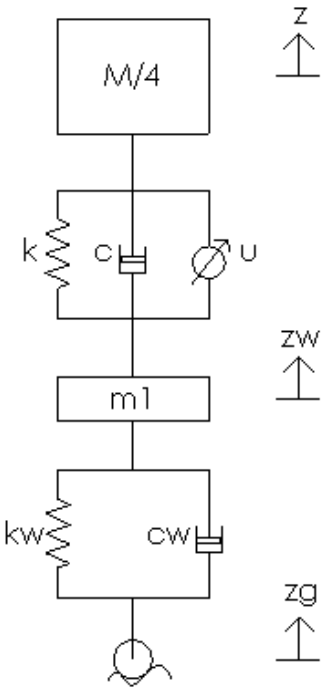

Figure 44. Quarter Car Model

This system has 2 DOF and so we can obtain 2 equations of motion. These equations are given below;

$$\frac{M}{4} * \ddot{z} + c * (\dot{z} - \dot{z}_w) + k * (z - z_w) = -f_u \quad (1)$$

$$m_1 * \ddot{z}_w - c * (\dot{z} - \dot{z}_w) - k * (z - z_w) + c_w * (\dot{z}_w - \dot{z}_g) + k_w * (z_w - z_g) = f_u \quad (2)$$

We consider passive suspension system for our system and so value of fu equals zero.

3. NEWMARK BETA METHOD

This method is a finite difference approximations and formulations given below;

$$x_{i+1} \approx x_i + h\dot{x}_i + h^2 \left[\left(\frac{1}{2} - \beta \right) \ddot{x}_i + \beta \ddot{x}_{i+1} \right] \quad (3)$$

$$\dot{x}_{i+1} \approx \dot{x}_i + h[(1-\gamma)\ddot{x}_i + \gamma\ddot{x}_{i+1}]$$
(4)

There β and γ are control parameters for equations. $\ddot{x}_i, \dot{x}_i, x_i$ are acceleration, velocity and displacement values for i th step, respectively. $\ddot{x}_{i+1}, \dot{x}_{i+1}, x_{i+1}$ are acceleration, velocity and displacement values for i+1 th step, respectively. In these formulations h represents size of the time-step. They have relation with each other as given above.

Step difference between two adjacent iteration's formulations can be written as below;

$$\delta x_i = x_{i+1} - x_i$$
(5)

$$\delta \dot{x}_i = \dot{x}_{i+1} - \dot{x}_i$$
(6)

$$\delta \ddot{x}_i = \ddot{x}_{i+1} - \ddot{x}_i$$
(7)

These formulations from equation (5) to (7) are step difference of displacement, velocity and acceleration, respectively. If formulation (5), (6), (7) put in to (3) and (4) the following equations are obtained;

$$\delta \ddot{x}_i = \frac{1}{\beta h^2}\delta x_i - \frac{1}{\beta h}\dot{x}_i - \frac{1}{2\beta}\ddot{x}_i$$
(8)

$$\delta \dot{x}_i = \frac{\gamma}{\beta h}\delta x_i - \frac{\gamma}{\beta}\dot{x}_i + h\left(1 - \frac{\gamma}{2\beta}\right)\ddot{x}_i$$
(9)

If $\beta = 1/4$ and $\gamma = 1/2$ Newmark Beta method is implicit and unconditionally stable [11]. Now using above equations we can solve our equations of motion.

4. SIMULATIONS

For solution of these equations of motion we will create MATLAB program. Firstly road inputs must be created in this program. According to ISO-8608 standards, road surface roughness related with vehicle speed using a formula that describes the interaction between the speed and displacement of the Power Structural Density (PSD). PSD displacement function of road roughness is expressed as belows;

$$G_d(n) = G_d(n_0)\left(\frac{n}{n_0}\right)^{-a} \qquad (n_0 = 0.1\ cycle/m)$$
(10)

$$G_d(n) = G_d(n_0)\left(\frac{\Omega}{\Omega_0}\right)^{-a} \qquad (\Omega_0 = 1\ rad/s)$$
(11)

Where the symbol a refers to the exponent of the PSD function. For a vehicle that has constant speed it can be 2. In above equations n_0 is the reference spatial frequency and n is the spatial frequency. $G_d(n_0)$ is found using the values given in Table 1 (a) according to ISO 8608 road class standards. If inverse Fourier transform used, road roughness function is obtained at time domain. This function that is at time domain as below;

$$r(x) = \sum_{i=1}^{N}\sqrt{4G_d(n_i)\Delta n}\cos(2\pi n_i x + \theta_i)$$
(12)

In equation (12) θ_i refers to randomly selected phase angles with normal distribution between 0 and 2π, and Δn represents frequency increase that can be calculated $\Delta n = (n_{max} - n_{min})/N$. Here N is the total number

of frequency steps. Also $n_i = n_{min} + \Delta n(i-1)$ is interpolation expression. According to ISO 2631-1 level of comfort is given Table 1 (b) [12].

Table 40. ISO 8608 (a) and ISO 2631-1 (b) values

	$G_d(n_0)$ (10^{-6} m^3)		$G_d(\Omega_0)$ (10^{-4} m^3)	
	Lower limit	Upper limit	Lower limit	Upper limit
A (Very good)	-	32	-	2
B (Good)	32	128	2	8
C (Average)	128	512	8	32
D (Poor)	512	2048	32	128
E (Very poor)	2048	8192	128	512
F	8192	32768	512	2048
G	32768	131072	2048	8192
H	131072	-	8192	-
n_o = 0.1 cycle/m			Ω_0 = 1 rad/m	

(a)

Measured Vibration (m/s^2)	Level of Comfort
Less than 0.315	Not Uncomfortable
0.315 to 0.63	A Little Comfortable
0.5 to 1	Fairly Uncomfortable
0.8 to 1.6	Uncomfortable
1.25 to 2.5	Very Uncomfortable
Greater than 2	Extremely Uncomfortable

(b)

In our study we analyzed A, B, and C class road for different vehicle velocities. Firstly we must determine road inputs for this analysis. For this reason A, B and C class roads inputs created in MATLAB program and three different vehicle speed that are 25 m/s, 40 m/s and 50 m/s applied on each class road. A, B and C class road inputs shown in figure 1, figure 2 and figure 3, respectively.

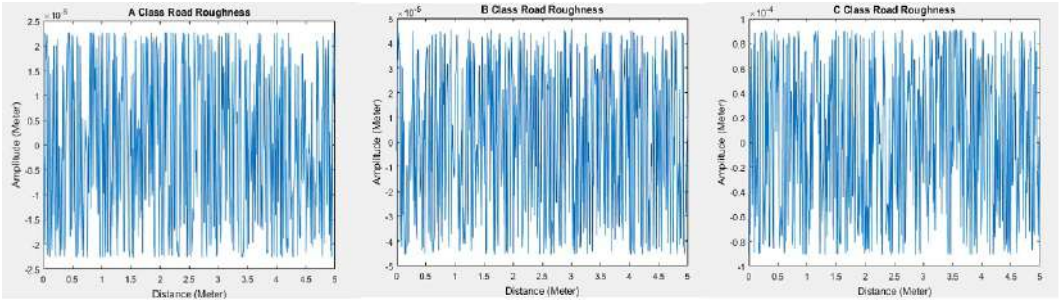

(a) *(b)* *(c)*

Figure 2. A class road input (a), B class road input (b), C class road input (c)

For this road inputs we obtained both car body's and wheel's displacements, velocities and accelerations at three different vehicle velocities. Quarter car parameters are given in Table 2.

Table 2. Quarter Car Parameters

Parameter	Value	Units
Car Body Mass (M/4)	375	kg
Wheel Mass (m1)	50	kg
Stiffness of the car body spring	30000	N/m
Stiffness of the wheel	150000	N/m
Damping coefficient of the absorber	600	Ns/m
Damping coefficient of the wheel	60	Ns/m

5. RESULTS AND DISCUSSION

Software program created in MATLAB and results graphs obtain via same software program. These results can be seen from Figure 3 to Figure 11. Both car body and wheel displacements are increase with increasing vehicle speed but these not so high values. Wheel displacements are higher than car body's. A class road has best results

compared with B and C class roads (Fig. 3-5). Car body velocities are increase with increasing vehicle speed but vehicle velocities are decrease with increasing vehicle speed (Fig. 6-8).

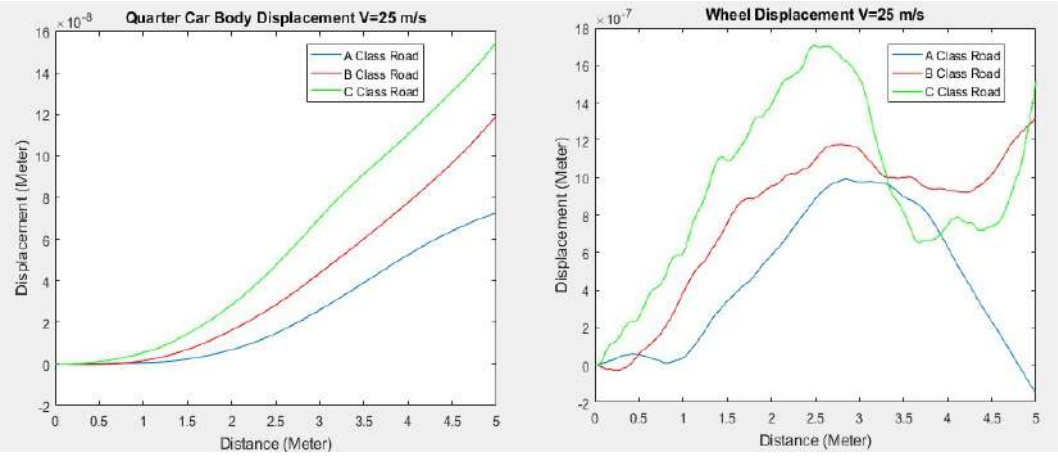

Figure 3. Displacements of Car Body and Wheel at V=25 m/s Vehicle Velocity

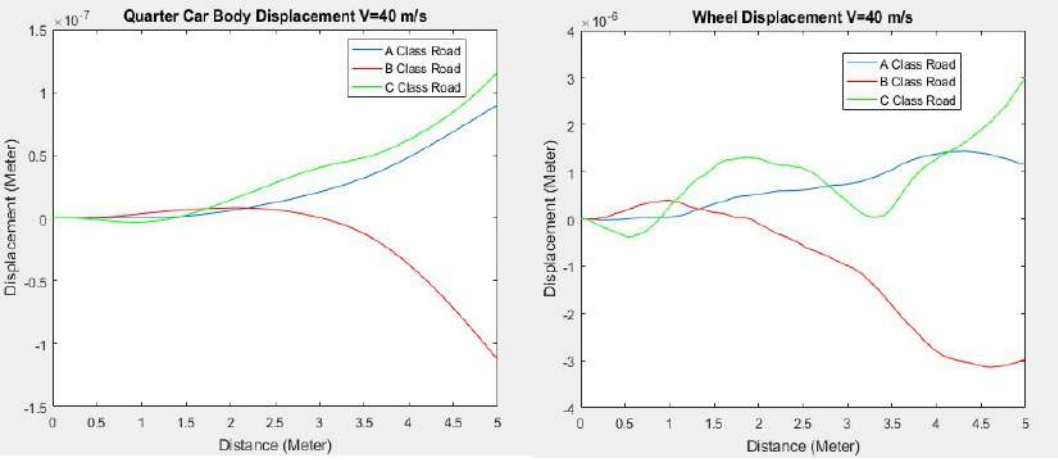

Figure 4. Displacements of Car Body and Wheel at V=40 m/s Vehicle Velocity

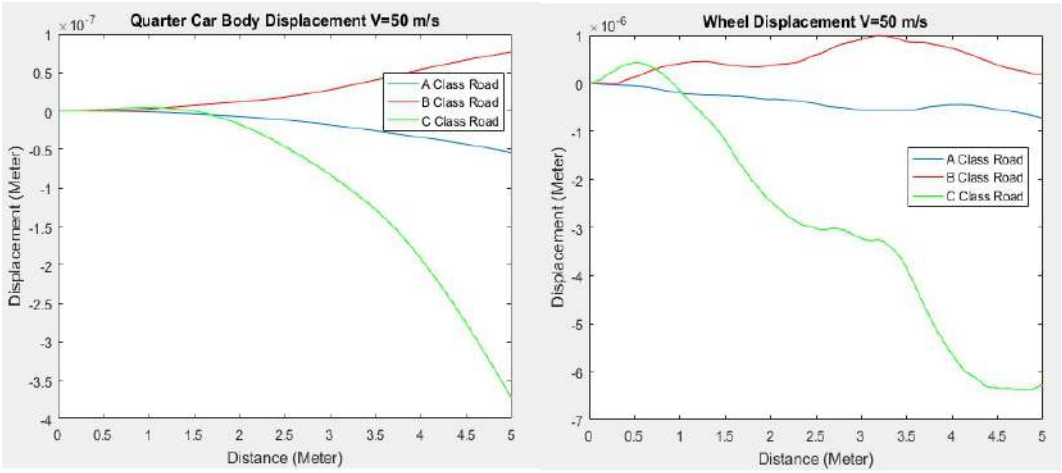

Figure 5. Displacements of Car Body and Wheel at V=50 m/s Vehicle Velocity

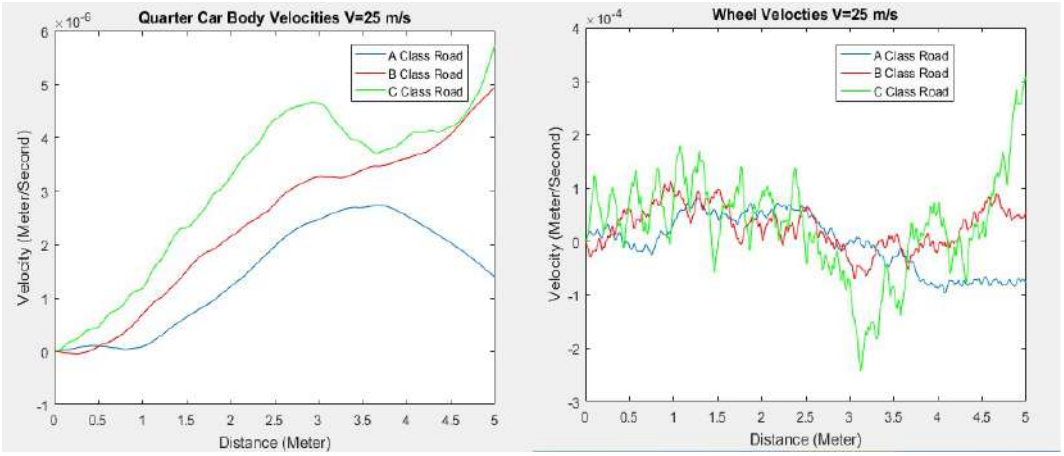

Figure 6. Velocities of Car Body and Wheel at V=25 m/s Vehicle Velocity

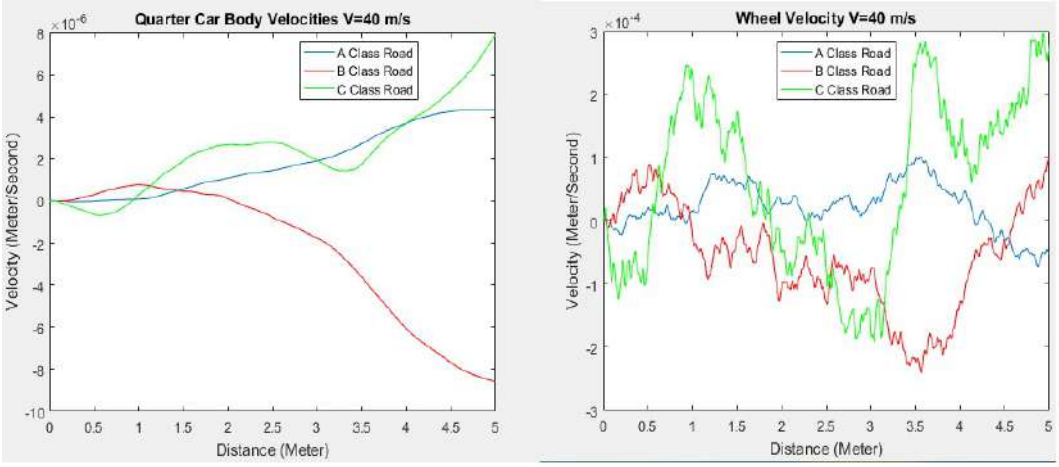

Figure 7. Velocities of Car Body and Wheel at V=40 m/s Vehicle Velocity

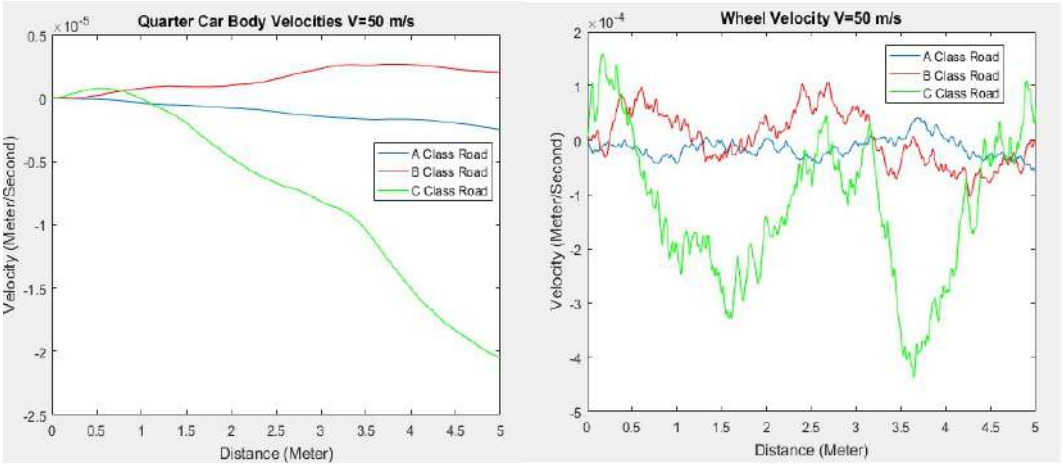

Figure 8. Velocities of Car Body and Wheel at V=50 m/s Vehicle Velocity

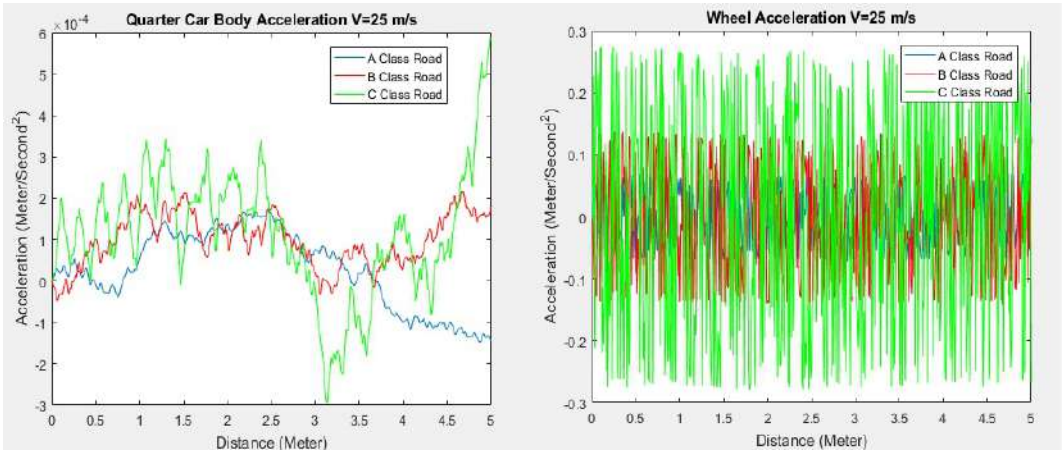

Figure 9. Accelerations of Car Body and Wheel at V=25 m/s Vehicle Velocity

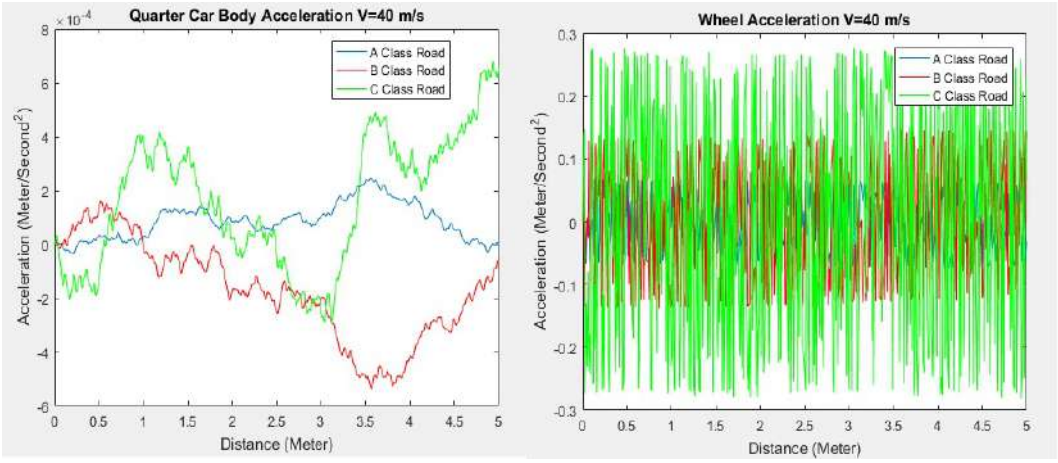

Figure 450. Accelerations of Car Body and Wheel at V=40 m/s Vehicle Velocity

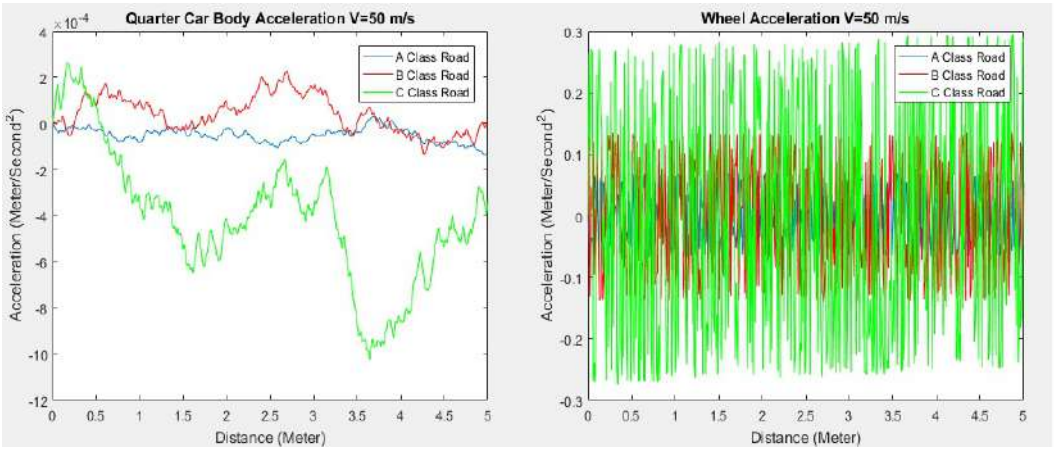

Figure 11. Accelerations of Car Body and Wheel at V=50 m/s Vehicle Velocity

Though wheel accelerations not so changing with increasing vehicle speed, car body accelerations have important changing. According to ISO 2631-1 Comfort Standard (Table 1 (b)) car body acceleration values not bigger than Not Uncomfortable value and so this vehicle parameters are suitable for ride comfort.

6. CONCLUSIONS

In this paper according to ISO standards, road roughness inputs are created as A, B and C class roads and for three different vehicle speed, displacements, velocities and accelerations of car body and wheel are obtained. Especially car body displacements are so low values and accelerations both car body and wheel are under the Not Uncomfortable value according to ISO standards. Thus, car parameters are useful for ride comfort.

Our system is passive suspension system. In future work, active suspension system can create and how results chance can be studied. Also, for other road classes broader analysis can be created.

REFERENCES

[1]. A. Florin, M. Rusu, I. Cosmin, P. Liliana, "PASSIVE SUSPENSION MODELING USING MATLAB, QUARTER CAR MODEL, INPUT SIGNL STEP TYPE" TECHNOMUS- New Technology and Products in Machine Manufacturing Technologies

[2]. P. Sharma, N. Saluja, D. Saini, P. Saini, "Analysis of Automotive Passive Suspension System with Matlab Program Generation" International Journal of Advancements in Technology, ISSN 0976-4860, Vol. 4 No. 2 (July 2013)

[3]. G. M. Szymanski, M. Josko, F. Tomaszewski, R. Filipiak, "Application of time-frequency analysis to the evaluation of the condition of car suspension" Mechanical Systems and Signal Processing 58-59 (2015) 298-307
[4]. E. A. Sanchez, "A quarter-car suspension system: car body mass estimator and sliding mode control" The 2013 Iberoamerican Conference on Electronics Engineering and Computer Science, Procedia Technology 7 (2013) 208-214
[5]. A. J. Qazi, A. Khan, M. T. Khan, S. Noor, "A Parametric Study on Performance of Semi-Active Suspension System with Variable Damping Coefficient Limit" 2013 AASRI Conference on Intelligent Systems and Control, AASRI Procedia 4 (2013) 154-159
[6]. J. L. Yao, J. G. Zheng, "Semi-active Suspension System Design for Quarter-car Model using Model Reference Sliding Mode Control" Vehicular Electronics and Safety, 2006. ICVES 2006. IEEE International Conference on
[7]. A. Tandel, A. R. Deshpande, S. P. Deshmukh, K. R. Jagtap, "Modeling, Analysis and PID Controller Implementation on Double Wishbone Suspension Using SimMechanics and Simulink" 12 th GLOBAL CONGRESS ON MANUFACTURING AND MANAGEMENT, GCMM 2014, Procedia Engineering 97 (2014) 1274-1281
[8]. *R. Darus, N. I. Enzai, "Modeling and Control Active Suspension System for a Quarter Car Model" 2010 International Conference on Science and Social Research (CSSR 2010) December 5-7 2010 Kuala Lumpur, Malaysia*
[9]. T. Yoshimura, A. Kume, M. Kurimoto, J. Hino, "CONSTRUCTION OF AN ACTIVE SUSPENSION SYSTEM OF A QUARTER CAR MODEL USING THE CONCEPT OF SLIDING MODE CONTROL" Journal of Sound and Vibration (2001) 239(2), 187-199
[10]. K. Rajeswari, S. Lavanya, P. Lakshmi, "Grey Fuzzy sliding Mode controller for Vehicle Suspension System" CEAI, Vol. 17, No. 3 pp. 12-19, 2015
[11]. H. P. Gavin, "Numerical Integration in Structural Dynamics" CEE 541. Structural Dynamics Department of Civil & Environmental Engineering Duke University Fall 2016
[12]. M. A. Koc, I. Esen, "Modelling and analysis of vehicle-structure-road coupled interaction considering structural flexibility, vehicle parameters and road roughness" Journal of Mechanical Science and Technology 31 (5) (2017) 2057-2074

BIOGRAPHY

Engin YIDIRIM graduted from from Celal Bayar University Mechanical Engineering in 2011, received the M.S. at same university in 2014. He is a Research Assistant in Mechanical Engineering, Karabuk University. He doctorate in Karabuk University in Mechanical Engineering.

Ismail ESEN graduted from ITU Mechanical Engineering in 1991, earned the M.S. in 1994 and in 2009 completed his doctorate at the same university. Between 1992 and 2009 he worked as a Professional Engineer in the industry. He has been working at Karabuk University.

ICENS 4TH INTERNATIONAL CONFERENCE ON ENGINEERING AND NATURAL SCIENCE
2-6 May 2018 KIEV UKRAINE

Earthquake Resistant Wall Material Production "Puzzle Bims"

Ercan Isik[1], Mehmet Cihan Aydin[2], Aydin Buyuksarac[3], Ibrahim Baran Karasin[4]

Abstract

The concrete briquettes that obtained from Bitlis basin which has high pumice reserves, have very low earthquake resistances. In this study, information will be given about "puzzle bims" wall material which will be produced by special production method in order to increase earthquake resistance of concrete briquettes. It is aimed to increase the earthquake safety of these wall materials produced from pumice and contribute to building performance in terms of earthquake safety. In terms of shape, the innovative Puzzle bims production is the main subject of studying. The proposes of this study are, to bring in a new generation wall element (Puzzle Bims) to construction sector, to reduce the damage of the walls due to the material properties in the earthquakes and to provide widespread use of material and in this way, contributing to the region and country's economy by expanding the usage areas of the pumice.

Keywords: *Pumice, steel fibre, puzzle bims*

1. INTRODUCTION

Worldwide detected pumice reserves are around 18 billion m^3. The main countries which have pumice reserves are U.S.A, Turkey and Italy. The pumice reserve in Turkey is around 2.8 billion m^3. According this information, Turkey's pumice reserve is 15.8% of World pumice reserve. Italy ranks in production of pumice in period of 2000-2007. Then, Turkey has settled in first rank by increasing the production during the period between 2008-2011 years. For example, in 2010, Turkey's share in world pumice production was 23% (4,000,000 m3), Italy's was 17%. These countries are followed by Greece, Iran, Syria, Chile and Saudi Arabia [1]. In Turkey, especially in some provinces in Central Anatolia and Eastern Anatolia, it is quite possible to find large pumice formation. Kayseri, Nevsehir, Nigde, Bitlis and Van have an important place among these provinces. Pumice is limitedly used in construction sector for insulation purpose, non-carrier walls and concrete production. This study was prepared in order to ensure the widespread use of pumice-produced new generation special designed pumice elements in the construction sector and in this way, contribute to the pumice's regional and national economy.

There is considerable amount of pumice reserves due to geological structure of Bitlis province. Pumice reserves formed as a result of intense volcanic activity in the region constitute important mineral reserves of the region. The pumice stones, which have formed as a consequence of volcanic events and have a hollow, spongy structure, are found in many regions of the world where volcanic activities occur. Turkey has a significant place in the World in terms of pumice reserves and their economic value. Due to the technical features of the material, it is a raw material which can be obtained economically with simple mining methods. Besides, since it is a light material, it provides a significant contribution to the reduction of seismic loads. In this context, it is clear that the widespread use of pumice in the construction sector will be beneficial in terms of economic and security principles, which are the most important principles of civil engineering. Pumice is widely used as light wall material (briquette, bims) in Bitlis province. Light masonry materials used in the nearby cities are supplied from Bitlis province. Therefore, Bitlis province serves the needs in this region. Besides the advantages of being a lightweight material, it is a disadvantage that important damage occurs after earthquakes in these walls due to it is hollow and low-strength. Scope of this study, it is suggested that these wall materials produced from

[1]*Corresponding author: Bitlis Eren University, Department of Civil Engineering, 13000, Bitlis, Turkey. eisik@beu.edu.tr*

[2]*Bitlis Eren University, Department of Civil Engineering,, absarac@beu.edu.tr*

[3]*Bitlis Eren University, Department of Civil Engineering,, mcaydin@beu.edu.tr*

[4] *Dicle University, Department of Civil Engineering, barankarasin@gmail.com*

pumice contribute to structural performance in terms of earthquake safety. Puzzle bims will be produced as steel fibre-reinforced to increase the seismic performance of the infilled walls. In this study, it is aimed to contribute to the regional economy by expanding the usage area of the pumice in order to decrease the wall damages caused by the material properties of the earthquakes by using new generation wall elements to be produced by using the pumice material. The mechanical properties of the Puzzle Bims are expected to have superior properties than the control samples. In this way, the use of pumice aggregate in the construction sector will be expanded.

2. EARTHQUAKE DAMAGES ON THE WALLS

Turkey is one of the leading country in terms of seismic risk in the World. Approximately 92% of Turkey's surface area is on the first degree seismic zone. Erzincan (1992), Dinar (1995), Adana-Ceyhan (1998), Kocaeli (1999), Bolu-Duzce (Kasim 1999), Afyon-Cay (2002) and Van (2011) earthquakes that have occurred in recent years have led to many casualties and material losses. For this reason, every precaution that can be taken to increase earthquake safety of reinforced concrete buildings has great importance.

One of the most common workmanship mistake is the overlap of vertical joints during wall construction. This prevents the distributing of vertical loads in a homogeneously, and since there is no connection between the wall materials which means, wall material is not anchoring, the walls can be opened as blocks side by side and the wall can be collapsed. Targeted clamping level of wall is that entire wall section behaves as a form of single block. Disintegration or pouring is not acceptable.

Infilled walls made for architectural purposes are not considered as structural elements in reinforced concrete buildings because they do not consider as bearing element while structural modelling. However, it is known that the infill walls, which cause significant changes in the dynamic properties of reinforced concrete frames, significantly increase the horizontal stiffness and strength of the building. Therefore, increasing the strength of the filler walls is an important factor in terms of increasing the earthquake safety of reinforced concrete buildings. For this reason, it is necessary to overcome the inadequacy in infilled walls and increase their strength. Earthquake damages that occur in non-bearing infilled walls can be classified into two groups as in-plane and out-of-plane damages in generally. The in-plane damages which occur in walls subjected to effect of earthquake load resultant X-shaped damage whereas out-of plane damages occur as outward overturning of wall (Figure 1).

Figure. 1. Wall Damages [2,3,4]

One of the most commonly used materials as wall material is concrete briquettes made of pumice. It has been observed that the hollow and low strength concrete briquettes are all fractured in the earthquake or there are horizontal shear cracks in the walls (Figure 2).

Figure 2. The damages of concrete briquette walls [5,6]

3. PUZZLE BIMS

Clamping is only provided on the side surfaces in the currently manufactured and used bims. Intermediate horizontal surfaces are tried to be clamped by using cement mortar (Figure 3).

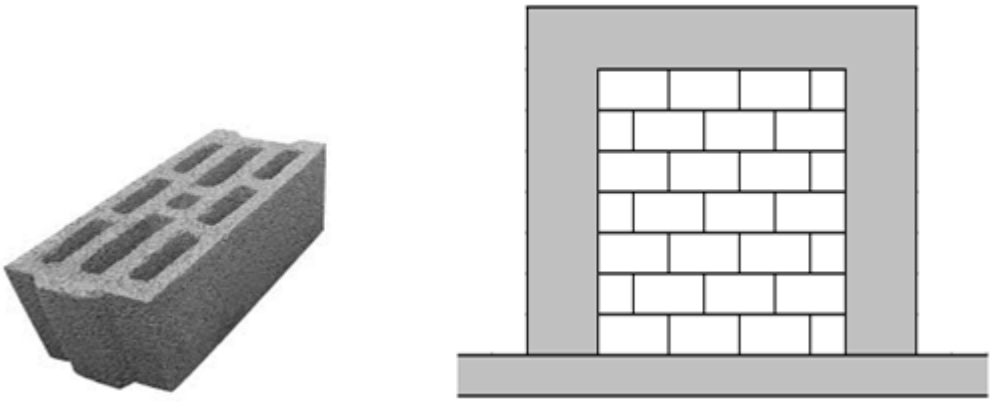

Figure 3. Traditional Concrete briquette wall and walling form

Pumice is widely used as wall material in Bitlis and its region. These materials are also widely obtained from Bitlis and its district. The earthquake behavior of such walls is weak. Within the scope of the study, it was aimed to increase earthquake safety by developing a new production way for such wall material. For this purpose, production will be carried out with different forms of production which will be further clamped. In addition, steel fiber reinforcement will be applied to the elements to increase their strength. With the use of steel fibers, these walls, which are not a carrier feature, will also be equipped with carrier features. In this study, steel fibers will be used for the first time in the production of Bims. There are no bims has been produced by using steel fibers in the literature investigations before. The innovative puzzle "bims" and its use are shown in Figure 4.

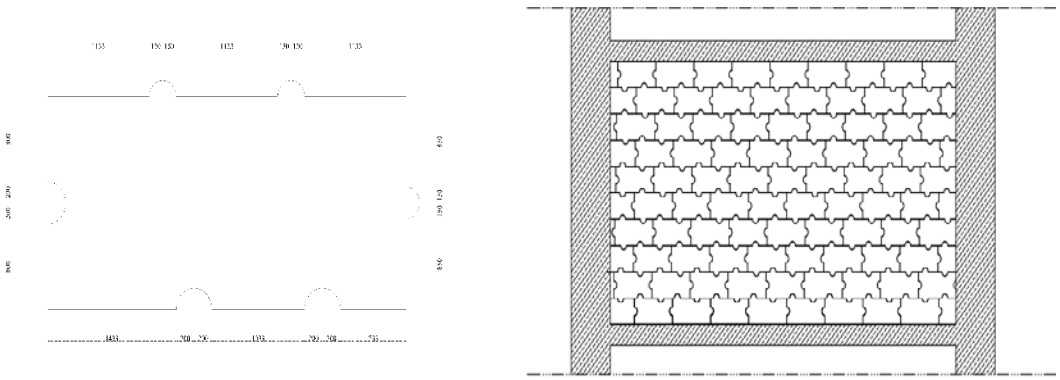

Figure 4. New generation concrete briquette and walling form

In the "puzzle bims" models which designed to prevent workmanship mistakes and increase clamping, self-compacting models have been created and required workmanship has been facilitated. Besides that, it was aimed to strengthening clamping. The puzzle pieces will be produced in different types and wall production will be realized. The front view of the puzzles in different types is shown in Figure 5.

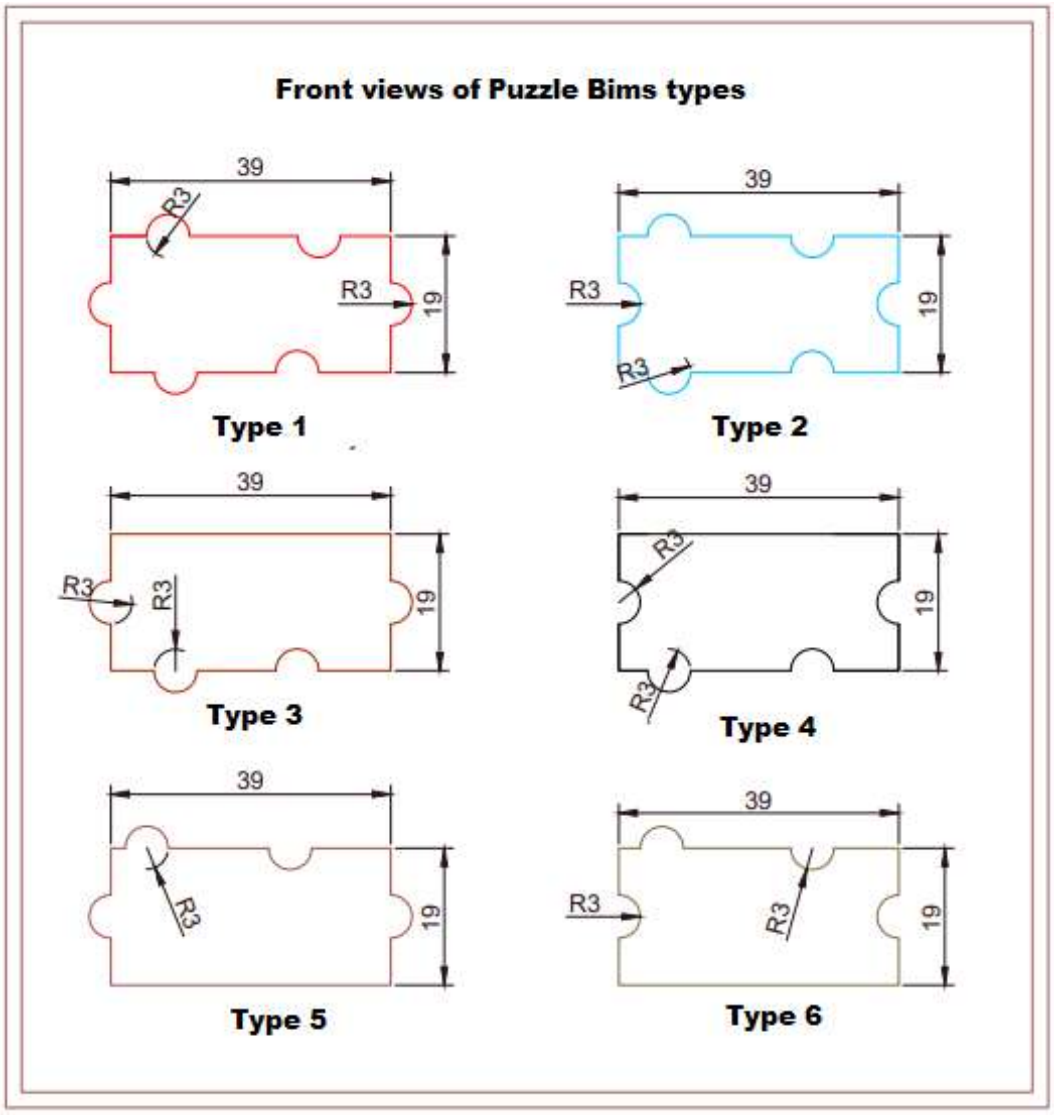

Figure 5. Front views of different puzzle bims

The front view of the wall in which puzzle bims are used in different types is shown in Figure 6.

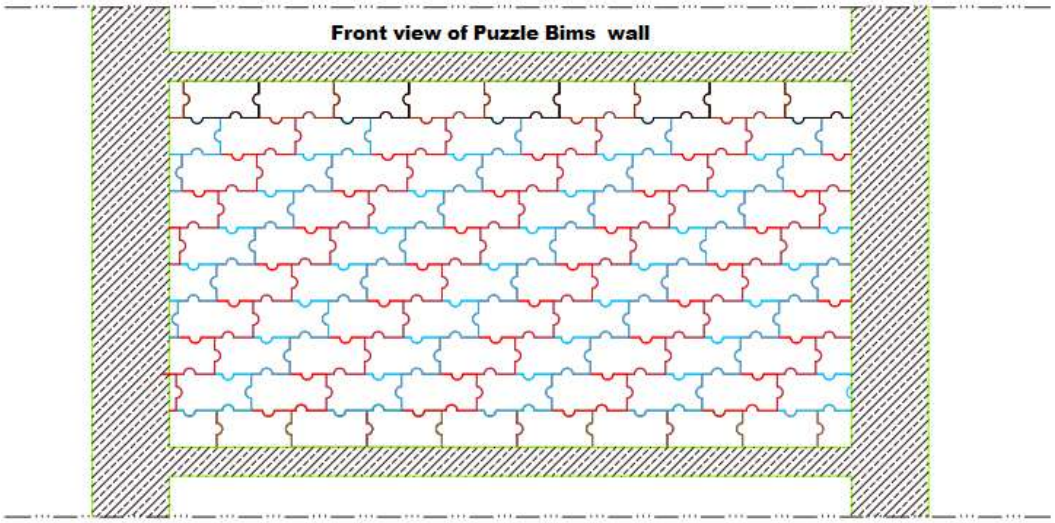

Figure 6. Front view of puzzle bims wall

4. RESULTS AND CONCLUSIONS

The level of clamping is increased at high level by giving carrier property to wall material produced from pumice by this study. Thus, partition walls that contribute to the horizontal load-carrying capacity of the buildings will be constructed. The shear cracks, which are common in the walls, will be avoided with the provided clamping. Furthermore, it is aimed to minimize the problems of clamping due to workmanship mistakes on the walls with the new generation puzzle bims that will be obtained within the scope of the project.

It is aimed to increase the clamping of infilled wall materials produced by pumice which is widespread in Bitlis province and its vicinity, with steel fiber addition and different production forms.

It is possible for the construction industry to reduce the workmanship mistakes by serial production models and their application methods. Within the scope of this aim, " puzzle bims " models were designed as self-passing models and workmanship mistakes that could be formed by facilitating needed workmanship were tried to be minimized. Besides this, it is aimed to increase of clamping level. In this application, besides horizontal clamping, it is aimed to build more strong walls by creating shear resistance in the vertical direction due to joint fillings applied in the form of Puzzle Bims.

REFERENCES

[1]. S. Coban, I. Dincer and A. Orhan, *Pomza Arastirma ve Uygulama Merkezi Fizibilite Raporu*. Nevsehir. 2015.
[2]. T.S. Koksal, O. Avsar and, N. Yilmaz, “19 Mayis 2011 Kutahya-Simav depreminde meydana gelen yapisal hasarlarin nedenleri” *1. Turkiye Deprem Muhendisligi ve Sismoloji Konferenasi*, 69, 981-1001, 2011.
[3]. M.Tapan, A, Ozvan and M.A., Sengul, “2 Temmuz 2004 Dogubeyazit depremi yer-yapi iliskisi ve yasanan kayiplar” *Deprem Sempozymu*, Izmit, 1074-1080, 2005.
[4]. A.Ergun and S. Yurtcu, “Yigma ve betonarme yapilarda deprem sonrasi olusan hasarlarin teknik analizi, *Yapi Teknolojileri Elektronik Dergisi*, 2007(1), 65-76, 2007.
[5]. E. Isik, M.H. Ozluk, E. Demir, and H. Bilici, " 23.10.2011 Van Depreminin Adilcevaz ilcesindeki etkilerinin gozleme dayali incelenmesi", *Bitlis, Eren Universitesi, Fen Bilimleri Enstitusu Dergisi*, 1(1), s.1-10, 2012
[6]. E. Isik “The effects of 23.10.2011 Van earthquake on near-field and damaged on structures”, *International Anatolia Academic Online Journal, ScientificScience*, 2(2), 10-25, 2014.

ICENS 4TH INTERNATIONAL CONFERENCE ON ENGINEERING AND NATURAL SCIENCE
2-6 May 2018 KIEV UKRAINE

Experimental Investigation of Effect of n-hexane Fuel Additive in Diesel Fuel on Engine Performance and Emissions

Mehmet Celik[1], Cihan Bayindirli[2]

Abstract

Greenhouse gas emissions from the use of fossil fuels; the most important causes of climate change. Emissions of nitrogen oxide (NOx) and particulate matter (PM) from diesel engines are a serious problem. Significant research is being conducted around the world to reduce emissions and fuel consumption based on diesel engines. Alternative methods have been tried to get low emissions and better engine performance by blending biofuels such as alcohol into diesel fuel. In this study, the experiments were performed in a single-cylinder diesel engine by addind 8% and 16% n-hexane by volume in diesel fuel (D0). As n-hexane ratio increases in diesel fuel, specific fuel consumption decreases while torque increases at all rpm. At 1400 rpm at which maximum torque is obtained, the torque of DHX16 fuel increased by 1.09% compared to D0 fuel, while the specific fuel consumption decreased by 1.53%. At 1400 rpm CO, HC and soot emissions decreased respectively 2.60%, 16.14%, 8.66% while the NOx emission increased 4.73% in the DHX16 fuel compared to D0 fuel.

Keywords: Diesel Fuel, N-Hexane, Fuel Additives, Exhaust Emissions, Engine Performance

1. INRODUCTION

In the last decade, the world's total energy consumption has increased significantly. The increased demand in the automotive industry has led to a decline in oil reserves. The diesel engine is an efficient power source. It is widely used in everyday life. In addition, emissions from the burning of petroleum-derived fuels affect both the environment and human health negatively. In order to be able to cope with this, almost every country in the world publishes increasingly stringent emission laws. Despite its popularity, the biggest disadvantage of diesel engines is the release of harmful gases such as HC, CO, NO_x and particulate matter into the atmosphere. This has to be influenced and influenced by both people and the environment to a great extent. This continues to be a major concern and requires serious attention. As a result of global warming, the average temperature of the world rises and threatens energy security. In recent years, extensive research has been conducted to control these emissions. There are a series of studies that demonstrate that the carcinogen effect is high and may cause health problems such as heart and respiratory tract from diesel engines emissions. For this reason, the research focuses on reducing harmful exhaust emissions [1-4]. In the case of tighter exhaust emission regulations, it is difficult to achieve the desired emissions standards with engine design work alone. A great deal of research is needed on environmental regulations, further development of diesel fuel quality. The use of additive materials has been the focus of research into this field in recent years. Fuel with the use of additives; performance, combustion and emission characteristics can be improved. Studies have shown that the fuel additives reduce the ignition delay time, decrease the specific fuel consumption values, and increase the thermal value of the fuel [5-6].

Nigde Omer Halisdemir Universitesi, Nigde Vocational High School, Nigde, Turkey, mehmetcelik@ohu.edu.tr

[2] Corresponding author: Nigde Omer Halisdemir Universitesi, Nigde Vocational High School, Nigde, Turkey, cbayindirli@ohu.edu.tr

2. MATERIAL AND METHOD

In this study, 8% by volume (DHX8) and 16% (DHX16) of n-hexane additive were added to diesel fuel. The features of the test fuels are given in Table 1. A single-cylinder diesel engine is used in engine tests; The specifications test engine are shown in Table 2.

Table 1. Test fuel specifications

	Cetane Number ASTM D 6751	Density (kg/m^3, 15 °C) ASTM D 1298	Viscosity (mm^2/s, 40°C) ASTM D 445	Lower Heating Value (MJ/kg) ASTM D 2015
D0 (Diesel)	52.1	0.838	2.40	41.30
DHX8	51.6	0.812	2.14	41.95
DHX16	50.7	0.788	2.03	42.80
n-hexane	44.8	0.650	0.51	---

Table 2. Test engine specifications

Model	3 LD 510
Engine type	Four stroke, Direct injection
Number of cylinders	1
Cylinder volume, cm^3	510
Diameter xStrok, mm	85x90
Compression ratio	17,5:1
Maximum engine speed, rpm	3300
Maximum engine torque, Nm	32,8
Maximum engine power, kW	9
Cooling type	Water cooled

Bosch-BEA 350 for measuring exhaust emissions and Bosch RTM 430 smoke measurement kit for smoke emission measurement were used in the tests. The Net Brake NF150 hydraulic is mounted on the dynamometer test system for engine loading. The values at the time of engine loading were read by using CAS brand SBA 200L model load cell.

Effective power is given in Eq.1.

$$P_e = \frac{\pi n M_e}{30.10^3} \text{,kW} \quad (1)$$

Effective specific fuel consumption (be) express the amount of fuel spent over an hour to obtain unit power and can be determines with using Eq. 2.

$$b_e = \frac{\dot{m}_y.3600}{P_e} \text{, g/kWh} \quad (2)$$

Here ṁy (g/s), indicates of fuel flow.

RESULTS AND DISCUSSION

Fig. 1 and Fig. 2 show the torque and power graph of the test fuels. At 1400 rpm in D0, which the maximum torque is achieved, as 35.54 Nm. According to D0 fuel, the momentum increases respectively 0.61% and 1.09%, in DHX8 and DHX16. The maximum power was 8.40 - 8.43 and 8.50 kW respectively D0 - DHX8 and DHX16 fuels. in 2800 rpm. By increasing n-hexane ratio in diesel fuel, torque and power have increased at all cycles. It is seen in Fig. 3 the specific fuel consumption graph. The decrease in specific fuel consumption in DHX8 and DHX16 fuels was 0.59% and 1.53% respectively. compared to D0 fuel was in 1400 rpm. By adding n-hexane to diesel fuel, the viscosity, density and cetane number decreased while the thermal value increased. The decrease in viscosity and density is thought to have smaller fuel droplets during the spraying of the fuel, which positively affects the atomization properties of the fuel It is thought that smaller fuel droplets have better combustion characteristics and cause specific fuel consumption reduction while increasing momentum.

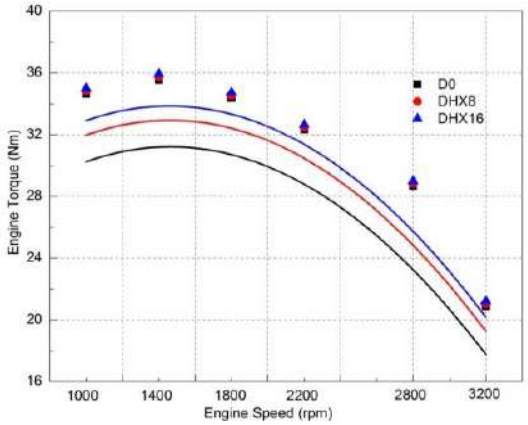

Figure 1. Moment graph of n-hexane additive fuels

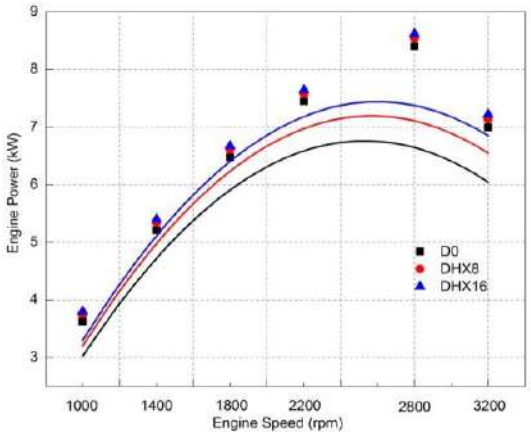

Figure 2. Engine power graph of n-hexane additive fuels

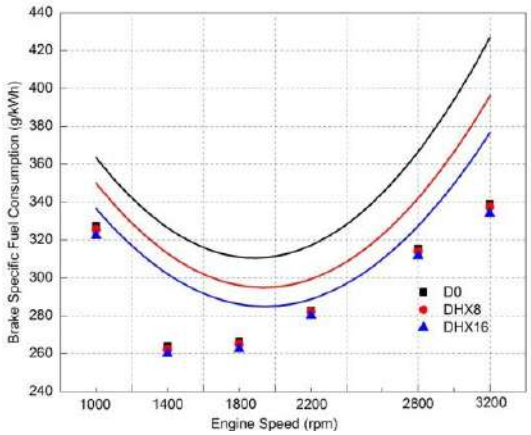

Figure 3. Specific fuel consumption graph of n-hexane additive fuels

HC and CO emissions are reduced by increasing the n-hexane ratio in the fuel. Fig. 4 and 5 show HC and CO emissions graphs. With regart to HC emissions in the 1400 rpm which maximum torque 8.21% and 16.14% a reducing is obtained in DHX8 and DHX16 fuels, respectively, compared to D0 fuel. In the case of CO emissions, respectively 1.71% and 2.60% decreasing is obtained. Density and viscosity effects to fuel atomization and combustion in the combustion chamber. The droplet diameter plays an important role in the spraying, burning and evaporation of fuel in the combustion chamber. The addition of n-hexane leads to a reduction of HC and CO emissions [7].

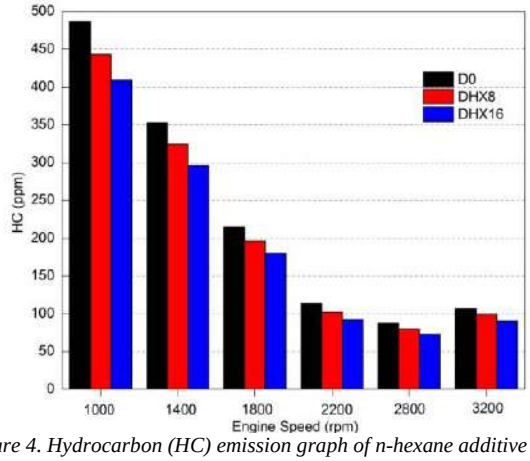

Figure 4. Hydrocarbon (HC) emission graph of n-hexane additive fuels

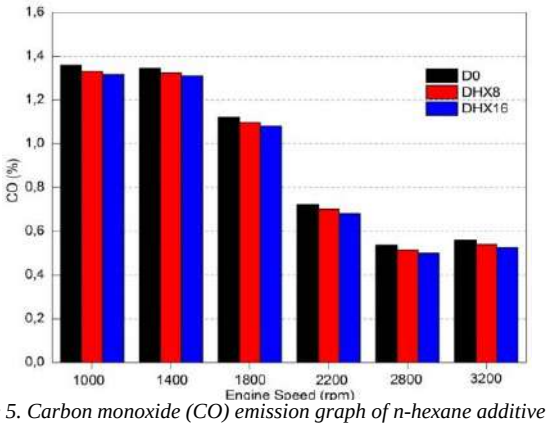

Figure 5. Carbon monoxide (CO) emission graph of n-hexane additive fuels

Fig. 6 shows a graph of NO_x emissions. The 1400 rpm which the maximum torque is obtained, NO_x emissions respectively higher 2.13% and 4.73% in DHX8 and DHX16 fuels, compared to D0 fuel. As the engine speed increases, the NO_x emissions increase due to increase of cylinder temperature. At lower rpm, the NO_x emission is lower because of lower temperature in the cylinder. NO_x emission related to the physical and chemical properties of the fuel (cetane number, iodine number, density, oxygen content, aromatic contents, etc), the pressure and temperature of the air which taken in the cylinder, the fuel injection system, the compression ratio, the percentage of residual gases in the combustion chamber. As the n-hexane ratio in the fuel increases, NO_x emissions increase [7].

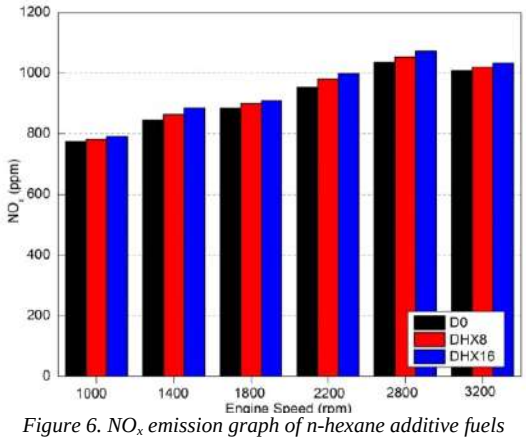

Figure 6. NO_x emission graph of n-hexane additive fuels

Fig. 7 shows a graph of soot emissions. At 1400 rpm, where maximum torque is achieved, emissions of DHX8 and DHX16 fuels are reduced by 3.96% and 8.66%, respectively, compared to D0 fuel. The decrease in the viscosity and density of the fuel affects evaporation and atomization positively. With the addition of n-hexane into the fuel, the viscosity of the fuel and the improvement of the density are seen to reduce the emission of the soot.

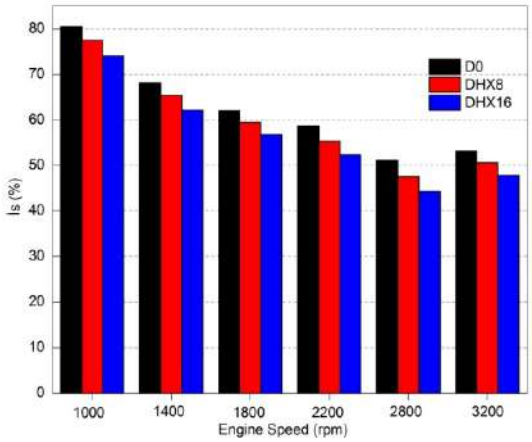

Figure 7. Smoke emission graph of n-hexane additive fuels

CONCLUSIONS

With the addition of n-hexane into the fuel, the viscosity, density and thermal value of the fuel improve while the cetane number decreases. As n-hexane ratio increases engine performance improves. The decrease in the number of cetane is expected to negatively affect engine performance and emissions, while the improvement in viscosity, density and lower thermal value of the fuel caused this neglect to disappear. Improvement in fuel properties has been positively impacting emissions. The addition of n-hexane into diesel fuel has reduced CO, HC and soot emissions, partially increased to NO_x emissions. Since the percentage of n-hexane mixture affects fuel properties, it must be kept at a certain limit in terms of fuel usebility.

References

[1] S. Mohankumar, P. Senthilkumar, “Particulate matter formation and its control methodologies for diesel engine: A comprehensive review”, Renewable and Sustainable Energy Reviews, vol. 80, pp. 1227-1238, 2017.

[2] Hamid Omidvarborna, Ashok Kumar, Dong-Shik Kim, “Variation of diesel soot characteristics by different types and blends of biodiesel in a laboratory combustion chamber”, Science of the Total Environment, vol. 544, pp. 450-459, 2016.

[3] M.S.M. Zaharin, N.R. Abdullah, G. Najafi, H. Sharudin, T. Yusaf, “Effects of physicochemical properties of biodiesel fuel blends with alcohol on diesel engine performance and exhaust emissions: A review”, Renewable and Sustainable Energy Reviews, vol. 79, pp. 475-493, 2017.

[4] J. E, M. Phama, D. Zhao, Y. Denga, D. Lea, W. Zuo, H. Zhu, T. Liu, Q. Penga, Z. Zhanga, “Effect of different technologies on combustion and emissions of the diesel engine fueled with biodiesel: A review”, Renewable and Sustainable Energy Reviews, vol. 80, pp. 620-647, 2017.

[5] M.S. Moghaddam, A.Z. Moghaddam, Performance and exhaust emission characteristics of a CI engine fueled with diesel-nitrogenated additives, Chemical Engineering Research And Design, vol. 92 (4), pp. 720-726, 2014.

[6] S.A. Basha, K.R. Gopal, A review of the effects of catalyst and additive on biodiesel production, performance, combustion and emission characteristics, Renewable And Sustainable Energy Reviews, vol. 16, pp. 711-717, 2012.

[7] M. Celik, Combustion, performance and exhaust emission characteristics of organic based manganese addition to cotton methyle ester, Applied Thermal Engineering, vol. 108, pp. 1178-1189, 2016.

ICENS 4TH INTERNATIONAL CONFERENCE ON ENGINEERING AND NATURAL SCIENCE
2-6 May 2018 KIEV UKRAINE

Alternative Natural Formaldehyde Scavenger for Leather Industry: Colloidal Amino Acid Filler in Retanning Process

Ersin Onem[1], Ali Yorgancioglu[1], Bahri Basaran[1]

Abstract

The increasing concern about the potential health problems of toxic chemicals in leather products forces many companies while producing or importing the leather articles because of the stringent stipulations. The most important technical issue concerning ecology and consumer health is the formation of free formaldehyde in the final products. In this study, colloidal amino acid filler (CAAF) was obtained from low grade by-product of gelatin manufacturing process of bovine shaving wastes with the hydrolysis reaction. 1%, 3% and 5% CAAF (concentration: 40%) was used in retanning process of phosphonium tanned leather to examine how formaldehyde content changed in the final products by comparing with the control leather samples. According to the analyses, 82.4 ppm formaldehyde content of phosphonium tanned leather as control group was reduced to 63.8 ppm with 1% CAAF, to 42.8 ppm with 3% CAAF and to 40.1 ppm with 5% CAAF. As a result, CAAF obtained from leather shavings to be used as natural formaldehyde scavenger has a good potential in achieving the benign treatment and reuse of the solid leather wastes.

Keywords: Leather, Collagen, Amino Acid, Formaldehyde, Scavenger, Shaving Wastes.

1. INTRODUCTION

Chromium, having a distinction due to its ability to produce lighter, softer, stronger and brighter leathers have gained importance in leather processing since the second half of last century and became the most important tanning agents still widely available in the world. The fact that the quicker and relatively cheaper processing has made the tanners to resort to the practice of chrome tanning has increased the adoption of the method up to 90% in the world [1]. Today; leather industry is facing with an increasingly stringent and complex environmental challenges about the tanning routines and the stricter environmental legislations which mitigate discharge of untreated chrome tanning effluents. One of the major waste categories concerning about the environmental incompatibility is chromium solid wastes such as trimmings, splittings, shavings and dusts generated from mechanical processes [2].

In the case of conventional chrome tanning processes, 45-73% (average 64%) of the raw hides and skins is shifted to by-products and solid waste [3]. The fact that around 600.000 tons of chrome tanned solid waste are being produced annually is the main sustainability problem. Hence; it should be handed down unwinded to next generations [4]. On the other hand; these wastes require to be taken some special measures since the conversion of chromium (III) to chromium (VI) poses a potential risk to human health and the environment [5]. Disposals of these wastes have many drawback carrying potentials for the landfills. In some cases, the amount of wastes generated exceed the carrying capacity of the region. This in turn leads to adverse effects on eco-systems. Solid wastes of chromium shavings are of main importance being composed of chemically treated protein, if not utilized properly, they would pose hazardous pollution problem to the environment. For this reason there necessary to manage this chrome containing shavings which is not easy.

Some authors have reported several alternatives for recovery of the chromium shavings. Due to environmental problems, many scientific studies are widely carried out all over the world for valorization of chrome containing solid wastes [6-11]. According to these methods, the use of protein and chromium after destruction with an appropriate method would possibly become preference [12-14]. This study was carried out on the chromium

shavings to hydrolyze them into amino acid colloidal solution and using as alternative natural formaldehyde scavenger for leather industry.

2. MATERIALS

In the study, commercial pickled bovine hides have been used as the leather material.

Colloidal amino acid filler (CAAF) was obtained from low grade by-product of gelatin manufacturing process of bovine shaving wastes with the hydrolysis reaction.

3. METHODS

3.1. Production Process

1%, 3% and 5% CAAF (concentration 40%) was used in retanning process of phosphonium tanned leather to examine how formaldehyde content changed in the final products by comparing with the control leather samples.

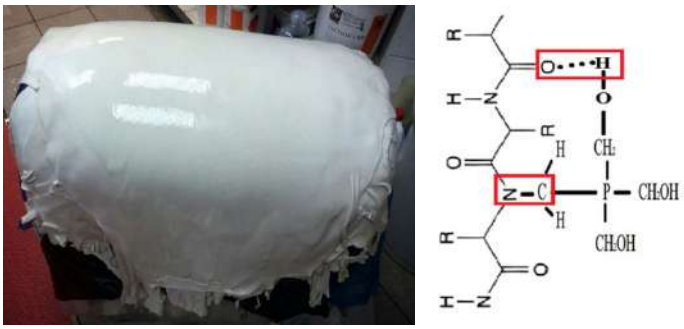

Figure 1. Phosphonium tanned leather and binding mechanism of phosphonium

Table 1. Production process

Process	%	Chemicals	Temp. (ºC)	Time (min)	Remarks
Pickle	80	Water	30		
	12	Salt		20	6 Bé
	0.5	HCOOH			pH 3.9
	1	Synthetic oils and esters		45	
Phosphonium tanning	10	THPS Tetrakis(hydroxymethyl)phosphonium sulfate		90	
	1	Synthetic oils and esters			
	1	Synthetic fatliquor		20	
	1	HCOONa		45	
	0.5	$NaHCOO_3$		60	pH 3.9, drain
Neutralization	150	Water	35		
	2	Neutral syntan		30	pH:4.8

	1	Sodium bicarbonate		30	pH:5.0, drain
Washing	200	Water	30	10	Drain
Retanning/Fatliquoring	100	Water	50		
	6	Natural fatliquoring agent			
	4	Synthetic fatliquoring agent			
	*	CAAF*(1%, 3%, 5%)		60	
	1	Formic acid		3x15+15	Drain
Horsing-Drying					

3.2. Formaldehyde Analysis

Free formaldehyde amounts on the leather were identified according to IUC 19.

Table 2. Analysis conditions

Flow rate	1,0 ml min^{-1}
Mobile phase	Acetonitrile/water, 60:40
Column	C 18
UV detection wavelength	350 nm
Injection volume	20 µl

4. RESULTS AND DISCUSSIONS

Collagen is a typical amphiphilic natural macromolecule with amino and carboxylic groups and many acidic or alkaline branches. The hydrolysis of collagen will release many hydrophilic functional groups including carboxyl, hydroxyl, amino, etc. These functional groups, especially amino group, can react with formaldehyde so that collagen-derived polypeptide can be used as natural formaldehyde scavenger.

The most important technical issue concerning ecology and consumer health is the formation of free formaldehyde in the final products. This study was carried out on the chromium shavings to hydrolyze them into amino acid colloidal solution and using as alternative natural formaldehyde scavenger for leather industry.

In this study, colloidal amino acid filler (CAAF) was obtained from low grade by-product of gelatin manufacturing process of bovine shaving wastes with the hydrolysis reaction. 1%, 3% and 5% CAAF (concentration: 40%) was used in retanning process of phosphonium tanned leather to examine how formaldehyde content changed in the final products by comparing with the control leather samples.

The results of the study on free formaldehyde amounts in control samples and the samples with CAAFs are presented in the Table 3.

Table 3. Free formaldehyde contents

	Formaldehyde content (ppm)
Control	82.4
1% CAAF	63.8
3% CAAF	42.8
5% CAAF	40.1

Figure 2 represents the reductions in formaldehyde contents of leather by the use of different CAAF proportions in retanning process.

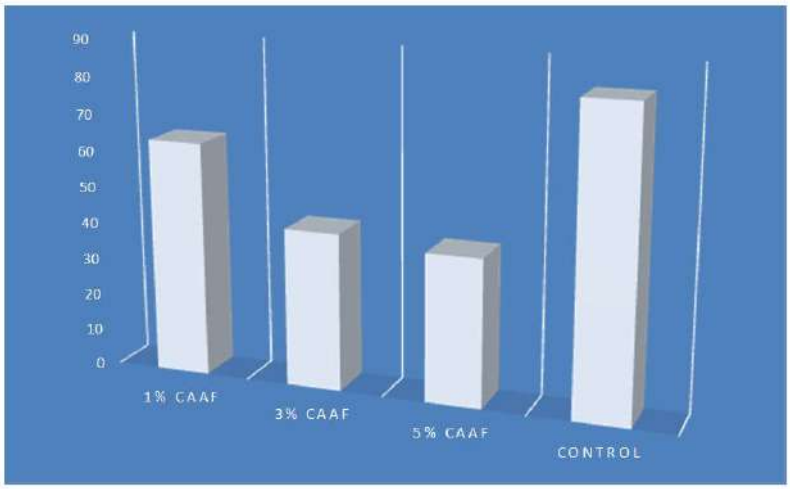

Figure 2. Reductions in free formaldehyde contents by use of CAAFs

The results showed that there was no important difference between the use of 3% and 5% CAAF. On the other hand 3% CAAF application provided the considerable elimination rather than 1% CAAF use. The control sample had 82.4 ppm free formaldehyde content. The leathers with 1% CAAF, 3% CAAF and 5% CAAF contented 63.8 ppm free formaldehyde, 42.8 ppm free formaldehyde and 40.1 ppm free formaldehyde, comparatively. When we consider about the economic value, best and optimal effect was achieved with 3% CAAF application for the formaldehyde elimination on phosphonium tanned leathers. Increased CAAF usage was not needed.

5. CONCLUSION

- In this study, during the retanning stage of leather processing, the colloidal amino acid filler has been used and the amount of free formaldehyde occurring on the leather has been decreased.
- By using colloidal amino acid filler and by increasing the ratio of CAAF used these effects may be improved further.
- The use of this filler during the retanning stage of leather processing will help resolving the formaldehyde problem, which occurs on the leather and causes serious problems.
- In retanning process, the processing of leathers with filler for 60 minutes both reduces the formaldehyde ratio significantly, and can also act like a filler.

REFERENCES

[1]. E. Heidemann, Tanning with Metal Salts, ed. Fundamentals of Leather Manufacture, 295-395, 1993.

[2]. C Shanthi, D. Shelly and B. Stennet, "Immobilization of degrative enzyme onto collagen hydrolysate films", Journal of the American Leather Chemists Association, 98, 6-12, 2003.

[3]. B. Buljan, G. Reich and J. Ludvik, "Mass balance in leather processing", World Leather, 12, 34-36, 1999.

[4]. E. Brown, M.M. Taylor and W.N. Marmer, "Production and potential uses of co-products from solid tannery waste", Journal of the American Leather Chemists Association, 10, 270-275, 1996.

[5]. A. Aslan, G. Gulumser G. and Ocak B., "Increased chromium tanning efficiency with collagen hydrolysates", Journal of the Society of Leather Technologists and Chemists, 90, 201-204, 2006.

[6]. R. Chackraborty, (2004). "Optimization of hydrolysis of chrome shavings by enzyme from P. Lilacinus", Journal of the American Leather Chemists Association, 99, 103-109, 2004.

[7]. M.M. Taylor, E.J. Diendorf and C.J. Thompson, "Extraction of value byproducts from the treatment of chromium containing collageneous leather industry waste", Journal of the Society of Leather Technologists and Chemists, 81, 5-13, 1997.

[8]. G. Manzo and G. Fedele, "Tanning action of condensates produced by chrome residues", Das Leder, 7, 142-149, 1994.

[9]. S. Danhong, L. Xieping and B. Shi, "Oxidative dechroming of leather shavings under ultrasound", Journal of the Society of Leather Technologists and Chemists, 87, 103-106, 2003.

[10]. A. Crispm, and M. Mota, "Leather shavings treatment-An enzymatic approach", Journal of the Society of Leather Technologists and Chemists, 87, 203-207, 2003.

[11]. L.F. Cabeza, M.M. Taylor and E.M. Brown, "Chemical and physical properties of protein products isolated from chromium - containing leather waste using two consecutive enzymes", Journal of the Society of Leather Technologists and Chemists, 82, 173-179, 1998.

[12]. M. Radulesu, E. Albu and P. Nicorici, New Collagen- Based Waterproofing Auxiliary Materials for Leather, IULTCS, London, 649-646, 1997.

[13]. F. Langmaier, K. Kolomaznik and M. Mladek, "Curing urea-formaldehyde adhesives with hydrolysates of chrome-tanned leather waste from leather production", International Journal of Adhesion and Adheives, 25, 101-108, 2005.

[14]. J. Cot, A. Marsal and A. Manich, Pilot-Plant Processing of Chromed Collagenic Residues. Recovery of Upgraded Bioproducts Industrially Reusable, Cape Town, 2001.

ICENS 4TH INTERNATIONAL CONFERENCE ON ENGINEERING AND NATURAL SCIENCE
2-6 May 2018 KIEV UKRAINE

Dyeing of Wool Fabrics with an Extract Mixture of Madder and Alkanet Roots

Fazlihan Yilmaz[1], M.Ibrahim Bahtiyari[2], Huseyin Benli[3]

Abstract

There is a lot of color variety in nature. People are choosing the way to make use of this color variety for different purposes. Textile dyeing also has taken its share of this color variety. In this study, extracts from madder and alkanet roots were obtained and mixed and then this mixture has been used in the coloring of wool fabrics. Meanwhile different from the previous application, a blend with alkanet roots and madder has been prepared afterwards, this blend was taken to the extraction process and this extract has been tested for coloration of wool as well. By this way, it was planned to compare two extraction processes in terms of the obtained colors and to extent the obtained colors and shades. It was observed that by the use of mix extracts, in both ways, different colors can be obtained and this method can be a way to obtain different colors and shades.

Keywords: Madder, alkanet root, color, wool, dyeing

1. INTRODUCTION

The nature gave inspiration to people as old as their presence in the world. Man used to color materials by imitating the nature [1]. Natural dyes are obtained from dye plants and dye animals in nature. They were the primary colour source of textiles until the mid to late 19th century [2]. Nowadays, most of the colors used in textile dyeing are synthetic [3]. The future demand for more sustainable processes can be seen as a driving force for new strategies which could bring a revival of natural dyes in textile dyeing [4].

In this study, alkanet roots and madder have been used by mixing the extracts in different ways. Alkanet (*Alkanna tinctoria*) belongs to the family *Borginaceae*. The roots, which are often very large in proportion to the size of the plant, yield in many of the species a red dye. The colouring matter in alkanet root is anchusin. The main pigment is alkannin, which was earlier called anchusin [5]. Madder, the root of *Rubia tinctorum* L., is one of the oldest natural dyes, which can generate colors ranging from orange to violet. The dye components are anthraquinones and the most important one is alizarin, as the main coloring substance and purpurin [6].

2. MATERIALS AND METHODS

Materials

In this study, 100% wool fabric which was for dyeing has been colored with the extracts from madder and alkanet roots. The dried form of madder and alkanet roots (figure 1a-2a) was used inscope of the study and milled (Figure 1b-2b) before extraction processes.

[1] *Corresponding author:Fazlihan YILMAZ, Erciyes University, Department of Textile Engineering, 38039, Kayseri, Turkey. fazlihanyilmaz@erciyes.edu.tr*

[2] *M. Ibrahim Bahtiyari, Erciyes University, Department of Textile Engineering, 38039, Kayseri, Turkey. ibahtiyari@yahoo.com*

[3] *Huseyin Benli, Erciyes University, Mustafa Cikrikcioglu Vocational School, 38039, Kayseri, Turkey. hbenli@erciyes.edu.tr*

Figure 1a. The dried alkanet root

Figure 1b. The milled alkanet root

Figure 2a. The dried madder

Figure 2b. The milled madder

Method

The wool fabrics used in dyeing experiments were dyed without any mordants with the extracts of madder and alkanet roots. The extractions of the sources were varied from each other.
Firstly, the extraction process was performed separately for madder and alkanet roots before dyeing experiments. In this extraction process, 12.5 gram of madder or 12.5 gram of alkanet roots were extracted separately in 1 liter of water.

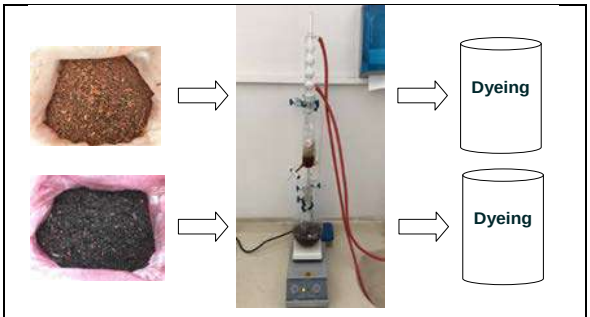

Figure 3. Extraction of madder / alkanet root separately

Also, these two natural dyestuffs were added to the extraction cycle together at the same time. The extraction experiments were carried out for plant mixture of madder (6.25) and alkanet roots (6.25) for 1 liter as well.

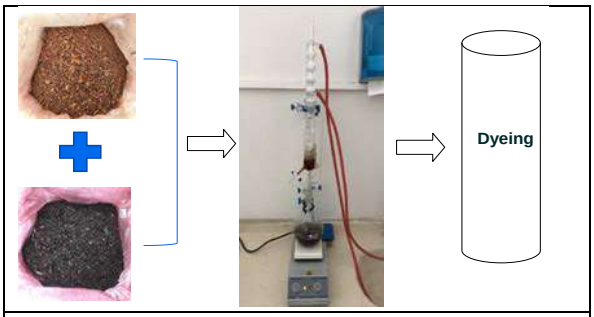

Figure 4. Extraction of alkanet root and madder mixture

By using these extracts directly as a dye bath, the dyeing of the samples was managed. The liquor ratio (Fabric to the Extract) was adjusted to 1:60.

During the dyeing process the fabrics were added to the extracts (dyeing baths) and then treated in this dye bath firstly for 5 minutes at 30°C and afterwards the bath was heated to 100°C in 35 minutes and finally at this temperature dyeing was conducted for 60 minutes and dyeing process was finished. After the dyeing processes the samples were first subjected to cold wash, followed by hot wash, and finally with rinse step, the wool fabric was allowed to dry at room temperature.

The dyed samples were prepared for various measurements; the color efficiencies (K/S) and color values (CIE L*a*b*) of samples were collected by the help of Konica Minolta 3600d spectrophotometer.

3. RESULTS AND DISCUSSION

By the study, it was planned to show the coloring effect of the extract from the mixture of dye plants so for this aim four different extract has been prepared as dye bath; extract from alkanet roots, extract from madder, mixture of the extracts from madder and alkanet roots at a ratio of 1:1 (same amount of extracts from each plant's extract has been mixed), extract from plants' mixture (firstly the mixture of the plants were arranged and then the extraction of this mixture has been prepared).

After the experiments to analyze the coloring properties of solely madder extract, solely alkanet root extract, combination extraction of them and extraction of these plants mixture, the CIE L*a*b*C*h0 values and color efficiencies of the fabrics were measured. The values are presented in table 1.

Table 1. CIELAB (L*, a*, b*, C* and h°) and K/S values of the wool samples

Dye Source		CIE L*a*b* (D65)					Colors
	K/S	L*	a*	b*	C*	h°	
Extract of Alkanet Root	2.07	61.75	4.84	13.24	14.09	69.9	
Extract of Madder	5.7	45.72	17.85	16.95	24.62	43.52	
Mixture of the Extract from Alkanet Root and Madder	3.97	50.37	15.22	15.21	21.51	44,98	

Extract from Plant Mixture (Alkanet Root and Madder)	3.96	51.06	12.75	15.12	19.78	49.85	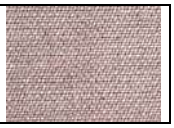

Color efficiency reached its highest value in experiments with solely madder. This value is seen as 5.7. The lowest value is observed as 2.07 and this value was obtained in dyeing which was made by using solely alkanet roots.

In the coloring process of wool fabrics made by using madder and alkanet roots; various shades of red tones, light pink and cream colour were obtained. For example; in the experiments performed with alkanet roots, a*= 4.84, b*=13.24 and h^o=69.9 were measured and the color is perceived as light brown/cream colour. When the experiments made with extract from madder, a*=17.85, b*=16.95 and h^o=43.52 were observed and thus the color is perceived as light red. In the experiments performed with mixture of the extracts from madder and alkanet root, a*=15.22, b*=15.21 and h^o=44.98 were measured and the color is perceived as light pink. Finally, the values of a*=12.75, b*=15.12 and h^o=49.95 were found by the extract from the mixture of the tested herbal sources. The color is perceived as light pink.

When the CIELAB (L*, a*, b*, C* and h°) values are checked, close results are obtained in the dyeings with the extraction of the herbal mixture and dyeings by mixing the solely extractions. But the convergence of numerical data reveals color tone differences. This suggests that these two methods may be used for obtaining same colors but in different shades.

4. CONCLUSION

In this study, extract from alkanet roots, extract from madder, mixture of the extracts from madder and alkanet root, and extract from these plants' mixture were used in dyeing of wool fabrics without any mordants. In this context, experiments were carried out at same plant concentrations. Followed by; spectral measurements of the dyed samples were performed. As a result of the obtained data, it has been observed that extract from the mixture of madder and alkanet roots can be also a way in the coloring process of wool fabrics like the other extracts.

REFERENCES

[1]. A.T. Ozguney, P. Secim, A. Demir, T. Gulumser, E. Ozdogan, "Ecological Printing of madder over various natural fibres", *Tekstil ve Konfeksiyon*, Vol. 25, No. 2, pp. 166-171, 2015.
[2]. L.M. Ozer, R. Karadag, E. Torgan, "Investigation of the Effect of Turkey Red Oil on Colour, Fastness Properties and HPLC-DAD Analysis of Silk Fabrics Dyed with Madder (Rubia tinctorium L.) and Gall Oak", *Tekstil ve Muhendis*, Vol. 23, No.103, pp. 197-204, 2016.
[3]. K.G. Gilbert, "Dyes from Plants: Past Usage, Present Understanding and Potential", *Plant Growth Regulation*, Vo.34, pp. 57-69, 2001.
[4]. T. Bechtold, R. Mussak, A. Mahmud-Ali, E. Ganglberger, S. Geissler, "Extraction of Natural Dyes for Textile Dyeing from Coloured Plant Wastes Released from the Food and Beverage Industry", *Journal of the Science of Food and Agriculture*, Vol. 86, pp. 233-242, 2006.
[5]. M. Rekaby, A. A. Salem, S. H. Nassar, "Eco-friendly Printing of Natural Fabrics Using Natural Dyes from Alkanet and Rhubarb", *The Journal of the Textile Institute*, Vol. 100, No. 6, pp. 486-495, 2009.
[6]. A. Shams-Nateri, "Reusing Wastewater of Madder Natural Dye for Wool Dyeing", *Journal of Cleaner Production*, Vol. 19, pp. 775-781, 2011.

ICENS 4TH INTERNATIONAL CONFERENCE ON ENGINEERING AND NATURAL SCIENCE
2 - 6 May 2018 KIEV UKRAINE

Experimental Investigation of Heat Transfer and Development of Shell Side Heat Transfer Correlation in a Mini-Channel Shell and Tube Heat Exchanger

Hasan Kucuk[1], Murat Unverdi[2], M. Senan Yilmaz[3]

Abstract

This study shell side convective heat transfer coefficient was investigated experimentally in a mini-channel shell and tube heat exchanger designed using Kern method. In experiments in which water was used on both sides, the shell side inlet temperature was kept constant at 40°C and Reynolds number was changed between 250 and 1,900. The tube inlet temperature was kept constant at 20°C and Reynolds number was kept constant at 5,900 where the highest convective heat transfer coefficient was obtained. The experimental convective heat transfer coefficients on the shell side were compared with Kern design, Kern-Laminar, Nitsche (Triangular and Quadratic tube arrangement), McAdam and VDI-Heat Atlas correlations. The Nusselt correlation for shell side convective heat transfer coefficient was developed to be used in the design of mini-channel shell and tube heat exchangers. It has been concluded that it is advantageous to keep the shell side Reynolds number around 800 by considering pressure drops in the mini channel shell and tube heat exchangers. While miniaturization using mini channel increases the compactness of shell and tube heat exchanger, reduces its volume, weight and amount of fluid.

Keywords: mini-channel, shell and tube heat exchanger, heat transfer, Kern method

1. INTRODUCTION

Due to gradual depletion of fossil fuels, use of different methods to reduce energy consumption is becoming widespread in industrial plants. Efforts are being made to spread techniques for enhancing heat transfer in heat exchangers used in energy conversions. Shell and tube heat exchangers (STHE) are the most widely used types of heat exchangers in practice. STHEs are preferred because of their simplicity, ease of production and maintenance, and adaptability to different operating conditions. STHEs are widely used for condensation, evaporation, heating and cooling of working fluid in power plants and industrial applications [1, 2, 3].

Industrial STHEs have a tube diameter of about 8-60 mm and an average area density of 100 m^2/m^3 [4, 5]. As the tube and shell diameter decrease in STHEs, the heat transfer area in the unit volume increases. The most important advantage of this decreasing is reduction of the heat exchanger dimensions and internal volume, in other words, increase in compactness. The increase in the compactness also reduces the heat exchanger weight and volume, as well as mass of working fluid used on both the shell and the tube sides [6].

Single-phase flow of liquids and gases through tube bundles is a significant heat transfer problem encountered in various heat exchangers. Contrary to single-phase heat transfer in the tubes, the flows on the shell side (i.e., flows on the outside of the tubes through the tube bundle bounded by baffles and shell) are very complicated due to large number of effective geometric factors and uncertainties in the flow path. The heat transfer performance of the tube side is influenced by several important variables such as arrangement of the tube bundles on the shell side, the shell diameter, the baffles, the baffle cut and orientation of baffles [7]. Only a portion of the flow on the shell side flows in ideal direction that is normal (perpendicular to the tube axes) to

[1] *Sakarya University, Faculty of Engineering, Department of Mechanical Engineering, 54050, Serdivan/Sakarya, Turkey. kucuk@sakarya.edu.tr*

[2] *Corresponding author: Sakarya University, Faculty of Engineering, Department of Mechanical Engineering, 54050, Serdivan/Sakarya, Turkey. muratunverdi@gmail.com*

[3] *Abant Izzet Baysal University, Vocational School of Gerede, 14900, Gerede/Bolu, Turkey. yilmaz_m1@ibu.edu.tr*

the axes of the tubes in the STHE with baffles. The rest of the liquid flows, through the gaps between the baffle plates and the tubes and between the baffle plates and the shell, which are defined as bypass areas. The fluid is looking for a way to flow with low resistance as much as possible, from the inlet to the outlet of the heat exchanger. Non-ideal flows can account for 40% of the total flow in a typical STHE [8].

Baffle plates are used to increase the fluid velocity by directing the shell flow perpendicular to the tube bundles to achieve higher heat transfer. The close proximity of the baffle plates increases convective heat transfer by increasing the induced turbulence. However, pressure drop is further increased due to the closer baffle plates. The cut ratio of the baffle plates is another important variable that affects the pressure drop. The cut ratios between 15% and 45% are preferred in practice. A cut ratio of 20 to 25% provides a reasonable heat transfer with a reasonable pressure drop [9].

Different tube arrangements are commonly used to form tube bundles in the STHEs. These are triangular arrangement, rotated triangular arrangement, square arrangement and rotated square arrangement. The triangular arrays are compact arrangement providing a more rigid tube sheet and a higher convective heat transfer coefficient for a given shell side flow area. However, as the heat transfer increases with this arrangement, the pressure drop also increases. With a triangular arrangement, about 15% more tubes can be placed for a given shell diameter. The distance between the tubes is small and is not preferred in situations where the mechanical cleaning of heat exchanger is required in that arrangement. When the mechanical cleaning is required, square arrangement is preferred. The square arrangement fewer heat transfer and less pressure drop are obtained than triangular arrangement [10]. The heat transfer coefficient in the flow of the tube bundle is largely determined by boundary layer separation effects and by wake interactions. The heat transfer coefficient in the tube bundles changes very low after the fourth and fifth tube rows [11].

Shell types are standardized by the Tubular Exchanger Manufacturers Association (TEMA) and are named with alphabetic letters E, F, G, J, and K in the STHEs [12]. The E-type shell is the most commonly used because of its low cost and simplicity. This shell is generally preferred for single-phase flow applications. The fluid makes only one pass through the E-type shell. However, when it is desired to increase the effective temperature difference, the two shell passes F-type is preferred. On the other hand, the pressure drop on the F-type shell is higher than on the E-type shell. The G and H-type shells, in which the fluid passing through the shell is divided into two parts, are preferred in specific applications (horizontal thermosiphon reboiler etc.). The K-type shell is a water kettle reboiler with a tube bundle covering about 60% of the shell diameter bottom the shell [7, 10]. The design methods proposed for STHEs in the literature are defined according to the geometric variables determined at the shell side. Kern (1950) and Tinker (1951) are the first researchers to make a physical description of the process for STHEs. The Delaware (1960, 1963) method proposed and republished by Bell (1986) was also used in the designs. Taborek (1983), proposed and explained a new form of this design method for single-phase shell side flows in a STHE with single segmental baffles (TEMA E-type shell) [8].

In this study, convective heat transfer coefficient of the shell side is experimentally investigated in a mini-channel shell and tube heat exchanger (MCSTHE) which is designed according to the Kern method for selected dimensions. The Kern method has been used in the MCSTHE design because of its simplicity, its reasonable results in predicting the heat transfer coefficients, its accuracy in preliminary design calculations and its easy application. More complex design methods are not preferred because of uncertainties in some additional design parameters needed in calculations, since they do not always gave results at desired accuracy. The shell side convective heat transfer coefficients were obtained experimentally for Reynolds range of 250-1900 in the heat exchanger designed according to the Kern method. The heat exchanger has TEMA E-type shell with an internal diameter of 30 mm where the tube bundle formed with rotated triangular arrangement and 4 single segmental baffles. Experimental convective heat transfer coefficients are compared with the results of other correlations proposed in the literature for the shell side.

2. SHELL SIDE HEAT TRANSFER COEFFICIENT

One shell and one tube pass heat exchanger for TEMA E-type, shell side convective heat transfer coefficient is calculated as follows. Free flow section on the shell equator A_s (m^2):

$$A_s = [(P_T - D_o)\, D_s\, l_B]/P_T \quad (1)$$

Where P_T is tube pitch, D_o is tube outside diameter (m), D_s is shell inside diameter (m) and l_B is baffle spacing (m). The term $(P_T - D_o) / P_T$ is the tube pitch ratio [13].

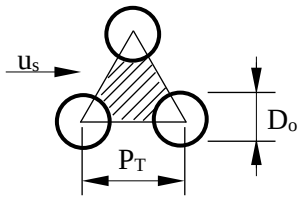

Figure 46. Equivalent diameter and rotated triangular arrangement according to Kern method

The shell side mass velocity G_s (kg/s m^2):

$$G_s = \dot{m}_s / A_s \tag{2}$$

$$u_s = G_s / \rho \tag{3}$$

Where stand for $\dot{m}_s$ fluid flow-rate on the shell-side (kg/s), ρ shell-side fluid density (kg/m^3). u_s stand for average velocity defined by the free flow cross-sectional area in the shell equator on the shell side in the Kern method. Calculate the shell side equivalent diameter or hydraulic diameter (Figure 1.), for an equilateral triangular pitch arrangement:

$$D_e = [1.1\ (P_T^2 - 0.917\ D_o^2)]/D_o \tag{4}$$

Where D_e is equivalent diameter on the shell side (m). The shell side Reynolds number (Re), given by:

$$Re = u_s D_e \rho / \mu \tag{5}$$

Heat removed by the hot fluid and absorbed by the cold fluid:

$$Q_h = \dot{m}_h\ c_{p,h}\ (T_{h,i} - T_{h,o}) \tag{6}$$

$$Q_c = \dot{m}_c\ c_{p,c}\ (T_{c,o} - T_{c,i}) \tag{7}$$

where stand for subscripts c and h cold and hot fluids, respectively, and $\dot{m}_h$ and $\dot{m}_c$ mass flow rates, $c_{p,h}$ and $c_{p,c}$, specific heats, $T_{c,o}$, $T_{h,o}$, outlet temperatures, $T_{c,i}$, $T_{c,i}$, inlet temperatures.

Thermodynamic characteristics of both fluids were calculated by using the average temperature values at the inlet and outlet of the MCSTHE. The average heat transfer values were used in the calculations due to the heat loss of both fluids. The rate of heat transfer in a heat exchanger:

$$Q_{ave.} = (Q_h + Q_c)/2 \tag{8}$$

$$Q_{ave.} = UAF\ \Delta T_{lm} \tag{9}$$

where U (W/m^2K) is the overall heat transfer coefficient, A(m^2), is the heat transfer surface area, F is the non-dimensional correction factor for logarithmic mean temperature difference and ΔT_{lm} (°C) is a logarithmic mean temperature difference. In case of TEMA E-type one shell, one tube pass and more than three or five baffles are used, the heat exchangers are regarded as counter flow, so F = 1 is taken [14]. The logarithmic mean temperature difference between hot and cold fluids in counter-flow conditions (ΔT_{lm}):

$$\Delta T_{lm} = \left(T_{h,i} - T_{c,o}\right) - (T_{h,o} - T_{c,i})/[\ln\left(T_{h,i} - T_{c,o}\right)/(T_{h,o} - T_{c,i})] \tag{10}$$

The overall heat transfer coefficient (based on the outer surface area):

$$(1/U_o) = [D_o/D_i]h_s + [(D_o/2k_t)\, In(D_o/D_i)] + [1/h_i] \tag{11}$$

The convective heat transfer coefficient h_s (W/m^2K) for the shell side is obtained using Equation (11).

a. Shell Side Heat Transfer Correlations

The heat transfer correlations obtained in the literature in relation to Reynolds number and Prandtl number for the tube bundles, which are commonly used in STHEs, are as follows:

- Kern-Laminar[15] correlation (From the Kern graphs)

$$Nu = 0.664\, Re^{0.5}\, Pr^{1/3} \qquad 100 < Re < 2000 \tag{12}$$

- Nitsche correlation[16] (for triangular arrangement)

$$Nu = 0.196\, Re^{0.6}\, Pr^{1/3} \qquad Re > 10 \tag{13}$$

- Nitsche correlation[16] (for quadratic arrangement)

$$Nu = 0.156\, Re^{0.6}\, Pr^{1/3} \qquad Re > 10 \tag{14}$$

- McAdam correlation[17] (for turbulent flow)

$$Nu = 0.36\, Re^{0.55}\, Pr^{1/3} \qquad 2 \times 10^3 < Re < 1 \times 10^6 \tag{15}$$

- The correlation obtained by curve fitting for 25% baffle cut from the Kern graphs[18]

$$Nu = j_h\, Re\, Pr^{1/3}$$
$$j_h = 0.472\, Re^{-0.477} \qquad 10 < Re < 1 \times 10^6 \tag{16}$$

- VDI-Heat Atlas correlation[19] (for rotated triangular arrangement)

$$Nu_{l,0} = 0.3 + \sqrt{Nu_{l,lam}^2 + Nu_{l,turb}^2}$$
$$Nu_{l,lam} = 0.644 \sqrt{Re_{\psi,l}}\, \sqrt[3]{Pr} \qquad 10 < Re_{\psi,l} < 1 \times 10^6 \qquad 0.6 < Pr < 1 \times 10^3 \tag{17}$$
$$Nu_{l,turb} = \frac{0.037\, Re_{\psi,l}^{0.8}\, Pr}{1 + 2.443\, Re_{\psi,l}^{-0.1} (Pr^{2/3} - 1)}$$

$$Re_{\psi,l} = (w\, l)/(\psi\, v) \qquad \psi = 1 - (\pi/4a) \quad for\ b \geq 1 \qquad a = P_T/D_o$$
$$l = (\pi/2) D_o \quad , \qquad \psi = 1 - (\pi/4ab) \quad for\ b < 1' \qquad b = P_T\sqrt{3}/2\, D_o$$

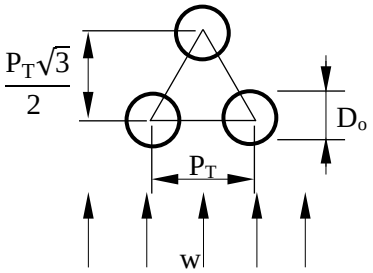

Figure 47. Triangular arrangement defined according to VDI-Heat Atlas method

The geometry and velocity w (m/s) according to VDI-Heat Atlas method for rotated triangular arranged tube bundles are given in Figure 2.

$$w = \dot{m}_s/(l_B D_s) \tag{18}$$

Where w is the average velocity defined by the flow cross-section in the shell equator without considering of the effect of tube bundle.

3. TUBE SIDE HEAT TRANSFER COEFFICIENT

The tube side convective heat transfer coefficient for the MCSTHE was obtained from an experimental study as in [20, 21]. In this study, experiments for the tube side were performed at Reynolds range of 1900-5100 (60-325 L/h) and Reynolds number of shell side was constant at 680 (180 L/h). After Reynolds 5100, convective

heat transfer coefficient of the tube side was nearly constant. In other words, heat transfer performance on the shell side was investigated by keeping the tube side Reynolds number constant at 5900 the region where the convective heat transfer coefficient is highest without increasing pressure losses on the tube side too much.

$$Nu = 0.00093\, Re^{1.183}\, Pr^{1/3}, \quad 1900 \leq Re \leq 5100, \; Pr = 6.75, \; L/D_i = 120, \; (R^2 = 0.99, \; Water) \quad (19)$$

The convective heat transfer coefficient at the tube side is calculated by the empirical correlation given in Equation (19).

4. NON-DIMENSIONAL NUMBERS

The Nusselt number, Prandtl number and Reynolds number are used in the heat transfer correlations.

$$Re = \rho u D_h / \mu \quad (20)$$

$$Pr = \mu c_p / k \quad (21)$$

$$Nu = h D_h / k \quad (22)$$

are defined as. Where stand for ρ (kg/m^3) density, μ (kg/ms) dynamic viscosity, c_p (kJ/kgK) specific heat, k (W/mK) thermal conductivity and D_h (m) hydraulic diameter.

5. EXPERIMENTAL STUDY

A mini channel shell and tube heat exchanger experimental setup and schematic representation prepared to investigate the convective heat transfer coefficient on the shell side under different flow conditions are given in Figure 3. The MCSTHE is designed according to the Kern method with E-type one shell and one tube pass. The shell internal diameter of the heat exchanger is 30 mm. The shell is made of castermid material with 4 baffles of 25% cut ratio and heat exchanger inlet-outlet connections. The total number of tubes in the bundle is

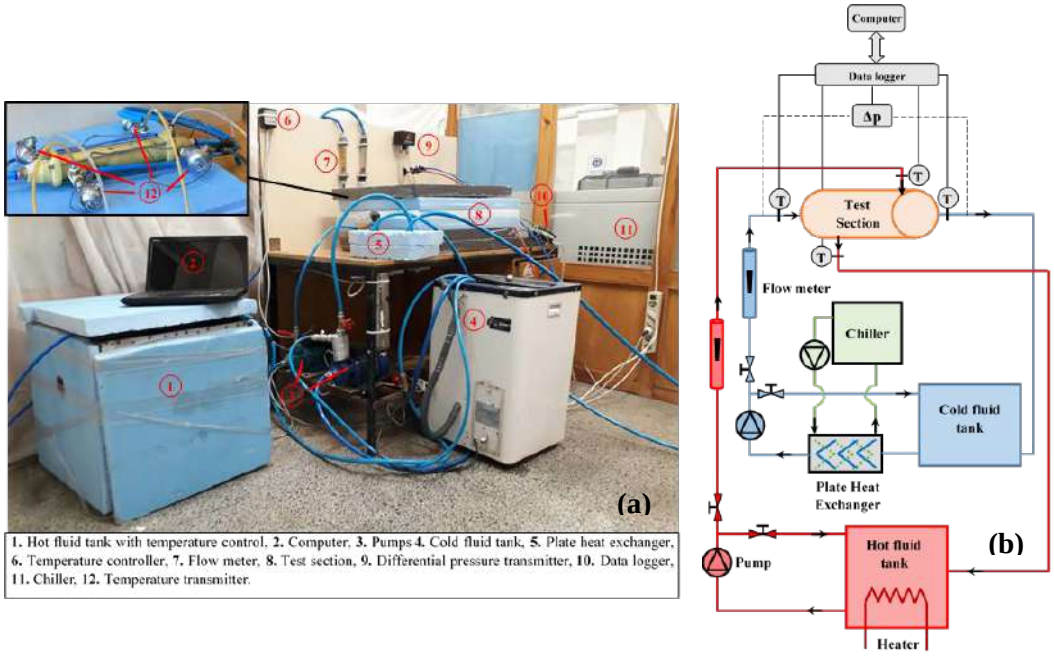

Figure 48. (a) Photo of experimental setup (b) Schematic representation of experimental setup

13. The length of the copper pipes is 240 mm, the outside diameter is 3 mm and the wall thickness is 0.5 mm. Triangular arrangement is preferred because it gives the highest heat transfer coefficient for tube bundles. There are two cycles as shown in Figure 3.b which are heat remove (hot fluid) and heat absorb (cold fluid) fluids, in the experimental setup.

The hot fluid is supplied from a 120 L capacity, insulated tank controlled by a thermostat. Cold fluid was supplied from a tank with a volume of about 30 L and a plate heat exchanger was used to keep temperature constant at the tube side inlet of the MCSTHE. The flow rates of hot and cold fluids are measured with float type rotameters. The accuracy of the measurement of the rotameters was controlled by weighted container measurement method. The inlet and outlet temperatures to the test section of the fluids are measured with K-type thermocouples. The measurement accuracy of the thermocouples was checked in an ice-water bath. The circulation of hot and cold fluid is provided by centrifugal pumps. The test section and connection pipes are insulated to reduce heat losses. Experiments were carried out at room temperature and under steady conditions. The measured temperature and flow rate are recorded in the computer. The flow rate of tube side was kept constant at 375 L/h and the cold fluid inlet temperature was kept at 20°C constant during the experiments. The hot fluid inlet temperature was kept constant at 40°C when the shell side flow rates were changed between 60 L/h and 400 L/h.

Uncertainty Analysis

Uncertainties in the measurement equipment during the experiments in the MCSTHE were calculated using Equation (23) as expressed by Kline and McClintock [22]. For a given function (R), x_1, x_2, ... x_n are independent variables, e_1, e_2, ... e_n are the error ratio of the independent variables, and e_R is the total uncertainty.

$$e_R = ([(\partial R/\partial x_1)e_1]^2 + [(\partial R/\partial x_2)e_2]^2 + \cdots [(\partial R/\partial x_n)e_n]^2)^2 \quad (23)$$

Table 41. Uncertainty results

	Average uncertainty (%)
Shell side Reynolds number	1.69
Shell side thermal power	4.33
Tube side thermal power	12.45
Overall heat transfer coefficient	7.12
Logarithmic mean temperature difference	1.86

The relative errors of the measuring equipment's in the experiment setup are 4% for the flow meter and 1% for the thermocouples. The uncertainties that occur during the experiments are calculated average uncertainty values are given in Table 1. All of the data obtained in repeated experiments have been found to be within the limits of uncertainty.

6. RESULTS AND DISCUSSION

Before calculating the shell side convective heat transfer coefficient in the experiment setup in Figure 3., hot water to cold water heat transfer test experiments were performed to evaluate the accuracy and reliability of the measurements. Although the test section was well insulated during these experiments, it was observed that there was a difference in thermal power between the hot and the cold fluid due to the heat losses to the surrounding.

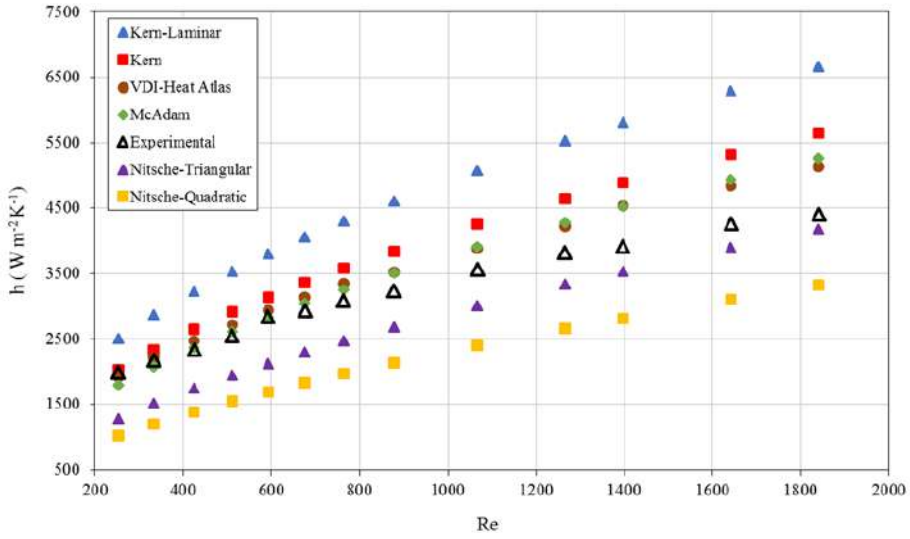

Figure 49. Experimental shell side convective heat transfer coefficient comparison with correlations

These differences are on average less than 5%. In this study, overall heat transfer coefficients and shell side convective heat transfer coefficients were obtained for the MCSTHE where the tube side flow rate was kept constant at 375 L/h (Re ≅ 5900) and the shell side Reynolds number was changed between 250 and 1900.

The shell side experimental convective heat transfer coefficients and convective heat transfer coefficients obtained from the shell side heat transfer correlations mentioned in Section 2 are compared in Figure 4 depending on the Reynolds number. Experimental convective heat transfer coefficients are in agreement with Kern, McAdam and VDI-Heat Atlas correlations in the range of 250< Re <800. Experimental heat transfer coefficients are on average 11% lower than those suggested by Kern. This difference for McAdam and VDI-Heat Atlas correlations is even lower. The results of Kern-Laminar correlation are 35% higher than the experimental results, while the results of the correlations proposed by Nitsche for Quadratic and Triangular arrangements are 41% and 26% lower than the experimental results, respectively, in that region.

The rate of increase in the heat transfer coefficient, which is high in Reynolds range 250-800, began to decrease after Reynolds>800. Experimental results in this region have away from Kern-Laminar, VDI-Heat Atlas and McAdam correlations, approaching Nitsche-Triangular correlation. The experimental heat transfer coefficients are about 12% higher than Nitsche-Triangular correlation at Reynolds 800-1900. McAdam and VDI-Heat Atlas correlations were obtained convective heat transfer coefficients an average of 13% and 12% higher than experimental results, respectively, in the same Reynolds interval. Experimental results are on average 23% and 47% lower than suggested by Kern and Kern-Laminar correlations, respectively, but on the average 30% higher than the results of the Nitsche-Quadratic correlation in this region.

Similar to the experimental results obtained for the tube side, on the shell side of the MCSTHE, the experimental convective heat transfer coefficients approaching the fully developed flow conditions at lower Reynolds numbers. In this study, increase in heat transfer coefficient on the shell side decreases after about Reynolds> 800. The final assessment for this region (Re> 800) should be made taking into account the shell side pressure losses.

$$Nu = 0.803\, Re^{0.42}\, Pr^{1/3} \quad 250 \le Re \le 1900,\ Pr = 4.56,\ L/D_o = 80,\ (R^2 = 0.99,\ Water) \tag{24}$$

The shell side heat transfer correlation given in Equation (24) is proposed for use in the design of a MCSTHEs at 250 <Re <1900 using obtained experimental results. The difference between the experimental results and the proposed correlation is less than +1%.

7. CONCLUSIONS

In this study, a MCSTHE was designed by Kern using the equations proposed for macro-pipes. E-type one shell, one pass and counter-flow MCSTHE have been manufactured according to design conditions. The experiments were carried out at Reynolds 250-1900 for shell side. The Reynolds number on the tube side is kept constant at 5900 where the highest heat transfer coefficient is obtained at the tube side. Experimental results obtained for the shell side are compared with Kern, Kern-Laminar, McAdam, VDI-Heat Atlas, and Nitsche (Triangular and Quadratic) shell side correlations used in the literature for STHE design.

- Experimental convective heat transfer coefficients were found to be in agreement with Kern, McAdam and VDI-Heat Atlas correlation at 250 <Re <800. This agreement is especially pronounced in the range of 250 <Re <500. The coherence between the results of the experimental convective heat transfer coefficient and Kern-Laminar, Nitsche-Triangular and Nitsche-Quadratic correlations was degraded in this region.
- The increase in the experimental heat transfer coefficient began to decrease after Reynolds> 800. Experiments have obtained closer results to the Nitsche-Triangular correlation after this Reynolds number.
- The Kern-Laminar, Kern, McAdam and VDI-Heat Atlas correlations in the range of 800 <Re <1900 obtained higher results than the experimental convective heat transfer coefficient.
- The shell side convective heat transfer coefficients of the mini channel heat exchanger approach fully developed flow conditions at lower Reynolds numbers than the macro tube heat exchanger, and the increase in heat transfer coefficient reduces after Reynolds> 800.
- The Reynolds and Prantl number dependent Nusselt correlation was developed using the experimental results for Reynolds 250-1900 range. The differences between the experimental results and the derived correlation are less than +1%.
- The use of mini channels in the STHEs did not increase the convective heat transfer coefficient on the shell side compared to the heat exchangers with macro tubes. Experimentally obtained shell side convective heat transfer coefficients for the MCSTHE have resulted in close to shell side correlations developed for the macro tube STHEs.

Since increasing Reynolds number more does not change the heat transfer coefficient too much, it is advantageous to keep the shell side Reynolds number around 800 in the MCSTHE in terms of limiting the pressure losses. The miniaturization of the STHE and the use of mini channels in the heat exchanger and consequent reduction in the shell diameter increase the compactness of the heat exchanger, as it reduces the volume and weight of the heat exchanger.

ACKNOWLEDGMENT

Experimental data presented in this study were obtained by using the experimental setup supported by Abant Izzet Baysal University Scientific Research Unit. Project Number: 2011.19.19.415.

REFERENCES

[1]. R. Lotfi, A.M. Rashidi, A. Amrollahi, "Experimental study on the heat transfer enhancement of MWNT-water nanofluid in a shell and tube heat exchanger," *International Communications in Heat and Mass Transfer*, 39:108–111, 2012.
[2]. R.L. Webb, N. Kim, *Principles of Enhanced Heat Transfer*, 2nd ed., Taylors & Francis Group, New York, 2005.
[3]. M. Unverdi, Y. Islamoglu, "Characteristics of heat transfer and pressure drop in a chevron-type plate heat exchanger with Al_2O_3/water nanofluids," *Thermal Science*, 21-6A, 2379-2391, 2017.
[4]. V.V. Wadekar, "Heat exchangers in process industry and mini-and microscale heat transfer," *Proceedings of Fifth International Conference on Enhanced, Compact and Ultra-Compact Heat Exchangers: Science, Engineering and Technology*, Eds. Shah RK, Ishizuka M, Rudy TM, Wadekar VV, Engineering Conferences International, Hoboken, NJ, USA, September, 2005.
[5]. B.I. Master, K.S. Chunangad, V. Pushpanathan, "Fouling mitigation using helixchanger heat exchangers," *Heat Exchanger Fouling and Cleaning: Fundamentals and Applications*, Art. 43:317-322, 2003.

[6]. M. Unverdi, H. Kucuk, M.S. Yilmaz, "Experimental investigation of heat transfer and pressure drop in a mini-channel shell and tube heat exchanger," (Under Review).
[7]. S. Kakac, H. Liu, A. Pramuanjaroenkij, *Heat Exchangers Selection, Rating, and Thermal Design*, 3nd ed., CRC Press, New York, 2012.
[8]. J. R. Thome, *Engineering Data Book III, Chapter 3-Single Phase Shell Side Flows and Heat Transfer*, Wolverine Tube, Inc., 2004-2006.
[9]. NPTEL, *Chemical Engineering, Chemical Engineering Design–II-Module#1*. [Online]. Available: http://nptel.ac.in/downloads/103103027/#
[10]. K. Thulukkanam, *Heat Exchanger Design Handbook*, Second ed., CRC Press, New York, 2013.
[11]. T. L. Bergman, A.S. Lavine, F. P. Incropera, D. P. Dewitt, *Fundamentals of Heat and Mass Transfer*, Seventh Ed., John Wiley&Sons, 2011.
[12]. Tubular exchanger manufacturer's association inc., *Standards of the tubular exchanger manufacturers association*, Ninth ed., New York, 2007.
[13]. R.K. Sinnott, *Chemical Engineering Design (Volume 6)*, fourth ed., Elsevier Butterworth-Heinemann, Oxford, 2005.
[14]. F. Kreith, *Heat and Mass Transfer*, Kreith, F., Boehm, R.F., Raithby, G.D.,…Capobianchi, M., *Handbook of Mechanical Engineering*, Second Ed..(4-1, 4-287), United State of America, CRC Press, 2005.
[15]. M. M. Martin, *Introduction Software for Chemical Engineering*, New York, CRC Press, 2015.
[16]. M. Nitsche, R.O. Gbadamosi, *Heat Exchanger Design Guide-A Practical Guide for Planning, Selecting and Designing of Shell and Tube Exchangers*, Elsevier, USA, 2016.
[17]. A.P. Fraas, *Heat Exchanger Design*, John Wiley & Sons, New York, 1989.
[18]. D.Q. Kern, *Process Heat Transfer (International Student Ed.)*, Japan, McGraw-Hill, 1950.
[19]. *VDI Heat Atlas*, Second Ed., Springer, 2010.
[20]. M.S. Yilmaz, H. Kucuk, M. Unverdi, "Experimental investigation of heat transfer and pressure drop in a minichannel shell and tube heat exchanger: Govde-borulu mini kanalli bir isi degistiricide isi gecisinin ve basinc kaybinin deneysel incelenmesi (In Turkish)," ULIBTK'17 21. Ulusal Isi Bilimi ve Teknigi Kongresi, 13-16 Eylul, Corum, Turkey, 2017, page: 284-292.
[21]. M. Unverdi, H. Kucuk, M.S. Yilmaz, N. Akcakale, "Experimental investigation of heat transfer and development of tube side heat transfer correlation in a mini-channel shell and tube heat exchanger," *2nd International Energy & Engineering Conference 12-13 October, Gaziantep, Turkey, 2017*, page: 473-485.
[22]. S. J. Kline, F.A. McClintock, Describing Uncertainties in Single-Sample Experiments, Mech. Eng., p. 3 January, 1953.

ICENS 4TH INTERNATIONAL CONFERENCE ON ENGINEERING AND NATURAL SCIENCE
2-6 May 2018 KIEV UKRAINE

Solar And Biogas Hybrid Energy Resources Used With An Example Of Hospital Building Project In Turkey

Huseyin Topal[1], Yelda Altinsoy[1], Tamer Calisir[1], Senol Baskaya[1]

Abstract

In this study, solar energy in the city of Adiyaman in Turkey and has been studied to meet the energy needs of a hospital building as a hybrid of using biomass energy. With this project, an energy production system based on renewable energy resources was designed and presented to meet the electricity and heat needs of Adiyaman Provincial Hospitals. In general, a system is planned to provide 3MW electricity generation and heating needs of 400 bed state hospitals. The conceptual design of the system components and the hybrid system is presented here.

Keywords: Biomass, Solar Energy, Hybrid System

1. INTRODUCTION

The following initial project proposal covers the supply of a Concentrating Solar Power (CSP) system with an optional by-firing biogas boiler unit. It is planned that the power plant will be located in Adiyaman province in Turkey. The size of the available land and the level of direct solar radiation found at the above mentioned site, are ideal for the deployment of the Concentrating Solar Power technology. CSP technology, unlike photovoltaic based solar systems, performs best at high levels of direct solar radiation and thus is perfectly suited for the application presented. The characteristics of the CSP system are the following; solar thermal power generator with 3 t/h steam, hybridization of the plant with a 18-20 MW biogas capacity and plant capable of operating 24/7 respectively[1].

Renewable energy sources such as solar energy are characterized by a high degree of intermittence, sometimes leading to inability to meet the demand of a power system. Hybridization with more stable renewable sources, such as biomass, represents a resourceful way of meeting energy demands uninterruptedly [2].

Facing a huge competition from other non-dispatchable renewable energy technologies (e.g. photovoltaic), hybridization presents a potential solution for forthcoming solar plants. Within the concept of fully renewable power systems, biomass is the ideal contender [3].

Brazil can develop this technology domestically, especially in its Northeast region, where most of VRE capacity is being deployed and where lies most of the CSP potential of the country. This work applies the Capacity Expansion Model REMix-CEM, which allows considering dispatch constraints of thermal power plants in long-term capacity expansion optimization. REMix-CEM calculates the optimal CSP plant configuration and its dispatch strategy from a central planning perspective [4].

Adiyaman State Hospital needs electricity, hot water and cooling energy. Generally 3MW electric power and 9 MWth heating load are available. The project was prepared to meet these needs. As it's known that; biomass is one of the most promising resources which can serve as an alternative to fossil fuels. Biomass can be considered as an environmentally friendly fuel source. There is no net increase in CO2 because of burning a biomass fuel. Forestry and agricultural waste are biomass and different conversion technologies for using of forestry and agricultural waste as energy sources such as anaerobic digestion, pyrolysis, combustion, co-combustion (with coal) and gasification.

2. POWER PLANT SETTLEMENT

The main components of a typical thermal solar system are Solar garden with parabolic groove collectors including piping, pumps and controls, Heat exchangers and thermal fluid auxiliary equipment, Power generation plant including turbine, generator, condensate system, pumps, cooling towers, water supply systems

and auxiliary plants, Biogas or natural gas incineration system hybrid system (not shown), Heat storage systems, pumps and control system (optional), and finally automatic control unit. The CSP system includes a local transformer power supply and contains a volatile thermal storage system as shown below to maximize the solar potential of the project site. In times when solar energy is not available, gaseous fuel is burned in a biogas burner and the system can generate energy throughout the day.

a. CSP Collectors

As a collector, a solar thermal plant technology is considered using the innovative medium-sized parabolic trough collector CF100. There are a number of factors, such as the exact size and layout of the solar field, the desired power output, heat storage and the need for local climatic conditions. However, the basic elements of modular design will not change. The thermal energy obtained through day-long collectors is pumped to the electricity generation system. Using solar tracking systems, collectors are programmed to take advantage of the sun from day to day and follow the sun. Thanks to the storage system it is possible to generate energy even at the end of the day. Application plants built with such large-scale parabolic solar collector systems are available all over the world (eg Andasol). The control system will also be able to automatically report all critical system parameters such as temperature and pressure to the "safe mode" of sunbathing and reporting. If the system operator exceeds the limit values of any parameter, the system installer can access the system using a modem and an appropriate remote access system if necessary. As it is known, pauses and delays can cause large costs in energy production.

b. Power System

Steam production is achieved with solar or gaseous fuel. In this system a typical steam turbine using the steam produced are used. In this application, it is planned to supply low voltage line (380V-50Hz). If desired, groups of generators working at medium voltage level can be used.

c. Cooling System

The steam turbine runs on a closed thermodynamic cycle, where cooling is required for the condenser. This cooling can be provided by a conventional cooling tower or a dry system. In the present case, a wet cooling system was selected using the lake water near the project.

d. Thermal Storage

We are integrating an effective heat storage system in our solar energy system projects with a proprietary technology consisting of a patented solid material. We can store up to 5 MW of thermal energy per module with this system, where the combined power generation and storage is possible. One of the important advantages of generating energy from solar energy using CSP technology is that the energy produced is easily stored because it is in heat form. While thermal storage can be accomplished in a variety of ways, the most suitable for this application (also known as ceramic or concrete storage) is to store heat in a solid environment. There is no specific business risk or requirement, as opposed to special maintenance needs and the storage of molten salt when the solid-state storage system is in operation.

e. Parabolic Collectors and Receiver Pipes

Parabolic collectors follow the sun throughout the day and concentrate the daylight on the receiving pipes by heat. Parabolic collectors consists of two main parts. One of is reflectors and the other is receiving pipe. In this application Flabeg F750 solar reflectors are used. The reflectors has parabolic curved mirror facets, and average reflectivity is more than 94.4 %, (ISO 9050 using ASTM G 173 direct) and a thermal oil circulates in the tubes absorbing the sun´s radiation and transforming it into heat. As a receive tube , PT-110 long of pipe 3.420 mm absorber pipe diameter 38 mm, thickness 2,0 mm glass envelope tube diameter 85 mm is used.

f. Support Structure

The steel structure supports the parabolic mirrors and the receiver tubes. Support structure consists of nine main assemblies such as CF100 support structure assembly, beam assembly, mirror attachment arm assemblies, mirror attachment brackets, torque transfer assembly, bearing housing assembly, beam support stand, Kit –

Fixation CF 100 support structure, receiver tube support arms, and all fixations and fasteners required for assembly as well.

g. Drive Unit

The hydraulic drive unit moves each row with 8 parabolic trough modules about one axis, to track the sun throughout the day. CF10 Drive unit assembly consists of drive unit support structure, crank assembly, main bearing assembly, one Hydraulic power unit, two pieces hydraulic actuators, actuator attachment pins and all fixations and fasteners required for assembly as well.

h. Control System

The control system automatically follows the sun. Solar tracking system and auxiliary systems consists of trough controllers, high accuracy inclinometers, temperature, pressure, flow rate sensors, pump control drive, master control unit including monitor, control software including SCADA interface and all power and communication cables

3. RELEVANCE

There are two basic criteria in the design of such an energy investment. One of these is direct sunlight energy level in the area where installation is required and the other is the land costs in the region. The Adiyaman region is extremely suitable for considering the year average in terms of solar structure. Land pricing is considered an economical investment when considering the municipal household waste site.

a. Available Solar Energy Level

Normal solar radiation (DNI) is required to be high so that solar thermal power plants can be installed and operated with high efficiency. DNR level in the project area in Adiyaman in Turkey 1,773 kWh/m²/year, unless otherwise determined. This is why the region is ideal for installing a solar energy system consisting of condensed collectors.

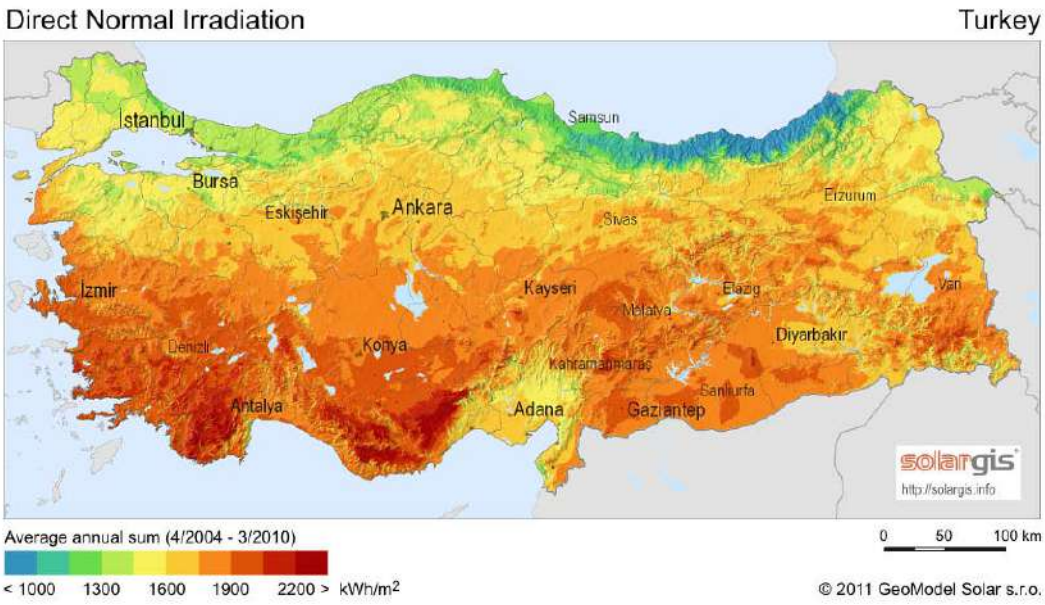

Figure 50. Turkey's annual DN values in the map

A summary of the meteorological data provided by the Meteonorm program is shown below. This data and the data provided by the Meteorology General Directorate together with the data provided by this program are more detailed and reliable.

Table 42. Sample table

Adiyaman
Location name

37.8 Latitude [°N]	38.35 Longitude [°E]
699 Altitude [m a.s.l.]	IV, 1 Climate region

Standard Radiation model	Standard Temperature model	Perez Tilt radiation model
2000–2009 Temperature period	1991–2010 Radiation period	

Additional information

Uncertainty of yearly values: Gh = 7%, Bn = 13%, Ta = 1,1 °C
Trend of Gh / decade: -
Variability of Gh / year: 3,5%
Radiation interpolation locations: Satellite data
Temperature interpolation locations: Malatya (74 km), Diyarbakir (161 km), Gaziantep (118 km), Elazig Airp. (121 km)

Month	H_Gh	H_Dh	H_Bn	Ta
	[kWh/m2]	[kWh/m2]	[kWh/m2]	[°C]
January	65	31	89	0,1
February	79	31	99	2,3
March	131	56	135	8,0
April	165	65	156	13,2
May	205	73	193	18,2
June	232	68	231	24,5
July	236	63	247	28,6
August	224	48	270	28,2
September	171	45	206	22,3
October	125	41	163	15,3
November	81	31	119	7,1
December	63	29	98	1,8
Year	1773	583	2005	14,1

H_Gh: Irradiation of global radiation horizontal
H_Dh: Irradiation of diffuse radiation horizontal
H_Bn: Irradiation of beam
Ta: Air temperature

4. RESULTS AND CONCLUSION

It is understood that there is enough space for the power plant. It is assumed that an area of approximately 16.5 hectares will be required for the CSP facility recommended for the solar energy installation. In order to maximize efficiency and increase the efficiency of the system, effective collector placement must be made. When choosing the current land, in addition to the sun areas, care facilities and avoidance from the shadows should also be considered. Establishing a shady building is not considered a problem for the planned region. However, a full assessment of shadowing effects will be made. Some constructions are needed for the construction sites required for a facility, the heat storage system and fuel storage areas needed for hybrid systems and combustion systems. It is necessary to determine detailed project works for the application of domestic waste disposal and other technical details (hospital buildings, heat exchanger, pump, etc. hot water pipes). The total cost of the CSP System and the 3MWe power generation system is estimated to be around € 10 million.

REFERENCES

[1]. Topal, H. “Adiyaman State Hospital Feasibility Report on Renewable Energy Application”, Gazi University Faculty of Engineering, ATALA Energy, 2014.
[2]. Soares J., Oliveira A. C. “Numerical simulation of a hybrid concentrated solar power/biomass mini power plant” Applied Thermal Engineering, vol. 11, pp. 1378–1386, 2017.
[3]. G.K. Singh, Solar power generation by PV (photovoltaic) technology: a review, Energy vol. 53, pp. 1-13, 2013
[4]. Fichter T., Soria R., Szklo A, Schaeffer R., Lucena A., “Assessing the potential role of concentrated solar power (CSP) for the northeast power system of Brazil using a detailed power system model,” Energy vol. 121, pp 695-715, 2017.
[5]. Coelho B., Oliveira A., Schwarzbozl P., Mendes A., “Biomass and central receiver system (CRS) hybridization: Integration of syngas/biogas on the atmospheric air volumetric CRS heat recovery steam generator duct burner,” Renewable Energy vol. 75, pp. 665-674, 2015

ICENS 4TH INTERNATIONAL CONFERENCE ON ENGINEERING AND NATURAL SCIENCE
2-6 May 2018 KIEV UKRAINE

Acoustic Improvement Design: University Conference Hall

Tarik Serhat Bozkurt[1], Ahmet Sertac Karakas[2], Cemil Akcay[3], Baris Yildizlar[4]

Abstract

Auditory comfort condition has a vital importance in daily life. Especially, the intelligibility of speech is one of the basic parameters of auditory comfort condition. This research interested in speech intelligibility in conference hall building. This study focuses on the improvement of conference hall acoustics of the building which is located in Turkey. First step of this study, acoustic evaluation of existing conference hall is performed and determined necessity of acoustic improvements. Second step of this study, acoustic improvement project is developed to generate good acoustic environment in conference hall. Acoustic improvement project is carried out based on main decisions which are changed surface sound absorption properties. Acoustic project is included not only improvement of audience visual aspect but also increased sound quality of room as well. Finally, reverberation time is controlled with acoustic project in order to provide speech intelligibility in conference hall building. Research has been shown the importance of reverberation time control and acoustic improvements decisions.

Keywords: Room Acoustic, Auditory Comfort Condition, Speech Intelligibility and Reverberation Time Analysis,

1. INTRODUCTION

Conference hall building in Sapanca Campus, used by Faculty of Fisheries, Istanbul University is located in Sakarya, Turkey. Sapanca Campus consists of dining hall building, conference hall building, education buildings, hotel building, different fish pools and wide landscape area. Acoustic improvement project was developed for the conference hall building. Before application, the building interior photos and section drawing are given in Fig.1.

[1] *Department of Architecture, Istanbul Technical University, 34743, Istanbul, Turkey, bozkurtt@itu.edu.tr*

[2] *Corresponding author: Department of Construction and Technical Affairs, Istanbul University, 34116, Istanbul, Turkey, Istanbul, Turkey, skarakas@istanbul.edu.tr*

[3] *Department of Civil Engineering, Istanbul University, 34320, Istanbul, Turkey, cakcay@istanbul.edu.tr*

[4] *Department of Civil Engineering, Istanbul University, 34320, Istanbul, Turkey, peace@istanbul.edu.tr*

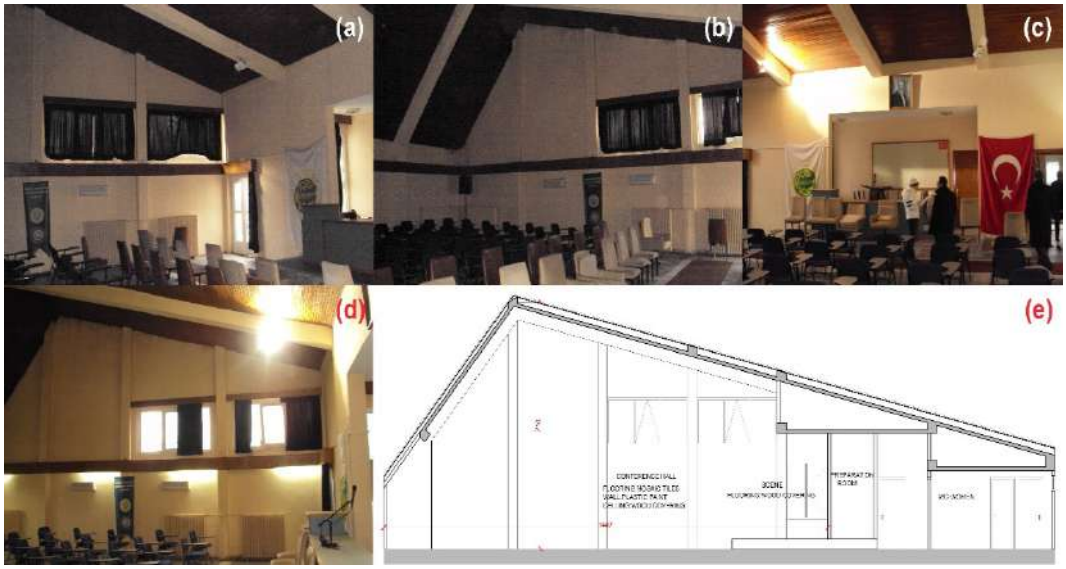

Figure 1. Conference hall building interior photos and section drawing before application (a-e)

2. METHODOLOGY

The audience seats are raised to improved audience visual and sound quality. In order to increase sound insulation level, new layers were added to exterior wall systems including aluminum composite panel, 10 cm rock wool, exist wall, 5 cm rock wool and interior claddings (Fig.2).

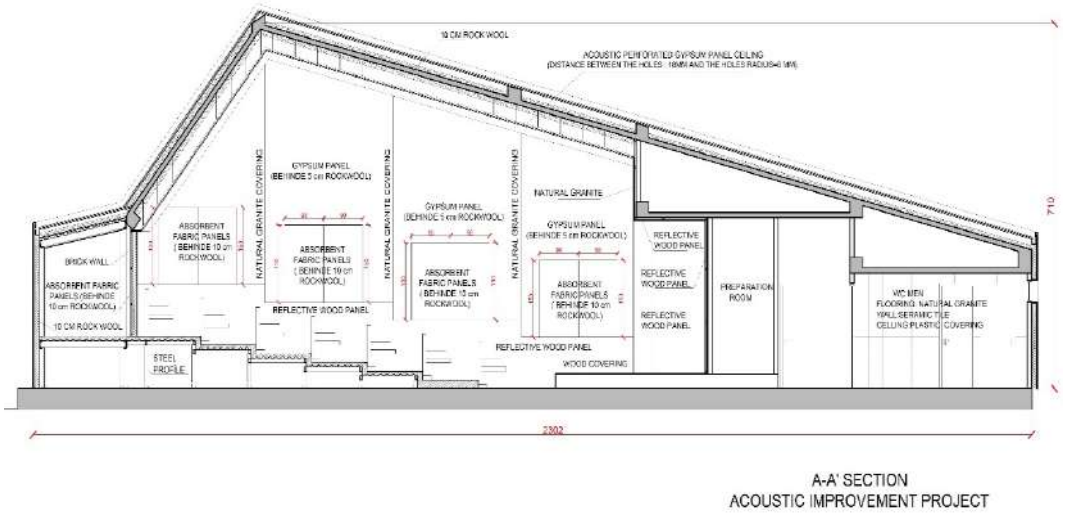

Figure 2. Conference hall acoustic improvement project (A-A' Section)

Reverberation time is an important issue for speech intelligibility. The time it takes for a signal to drop by 60 dB is the reverberation time. Reverberation time is dependent on the volume of the room and the total absorption. Reverberation time equation is defined by W.C. Sabine [1-6]. Reverberation time should be taken into account separately for the basic frequencies. Reverberation time equation is given bellow.

$$R = (0{,}161 \cdot V) / (A + x \cdot V) \quad (1)$$

In where, R: Reverberation time (sec.), A: Room absorption (m2), V: Room volume (m3), x: Air absorption. Room absorption is specified in Eq.2.

$$A = \alpha_1 \cdot S_1 + \alpha_2 \cdot S_2 + \ldots\ldots + \alpha_n \cdot S_n \qquad (2)$$

Here, α1, α2,…αn : Different absorption coefficients and S1, S2,…Sn : Different surfaces of the room. Acoustical evaluation of conference hall was performed primarily. In this regard, reverberation time of existing conference hall was calculated. It was determined that existing conference hall reverberation time was too high and existing conference hall needed acoustic improvement (Table 1).

Table 43. Reverberation time according to before acoustic improvements

ISTANBUL UNIVERSITY FACULTY OF FISHERIES CONFERENCE HALL IN SAPANCA CAMPUS THEORETICAL CALCULATION OF REVERBERATION TIME ACCORDING TO BEFORE ACOUSTIC IMPROVEMENTS													
SURFACE PROPERTIES			FREQUENCY (HZ)										
SURFACE NAME	VOLUME (m3)	AREA (m^2)	125 HZ		250 HZ		500 HZ		1000 HZ		2000 HZ		4000 HZ		MATERIALS AND DIMENTIONAL INFORMATION
			α	sxα	α	sxα	α	sxα	α	sxα	α	sxα	α	sxα	
GROUND SURFACE															
MOSAIC TILES LAYER		150,25	0,02	3,01	0,02	3,01	0,02	3,01	0,03	4,51	0,03	4,51	0,02	3,01	MOSAIC TILES LAYER
CEILING															
PLASTER		21,5	0,01	0,21	0,01	0,21	0,02	0,43	0,03	0,64	0,04	0,86	0,05	1,07	PLASTER
WOOD COVERING		149,0	0,15	22,36	0,11	16,39	0,10	14,90	0,07	10,43	0,06	8,94	0,07	10,43	WOOD COVERING
A-A' SECTION SURFACE															
PLASTER		64,92	0,01	0,65	0,01	0,65	0,02	1,30	0,03	1,95	0,04	2,60	0,05	3,25	PLASTER
DOUBLE GLAZED WINDOW		9,50	0,15	1,43	0,05	0,48	0,03	0,29	0,03	0,29	0,02	0,19	0,02	0,19	DOUBLE GLAZED WINDOW
B-B' SECTION SURFACE															
PLASTER		64,92	0,01	0,65	0,01	0,65	0,02	1,30	0,03	1,95	0,04	2,60	0,05	3,25	PLASTER
DOUBLE GLAZED WINDOW		9,50	0,15	1,43	0,05	0,48	0,03	0,29	0,03	0,29	0,02	0,19	0,02	0,19	DOUBLE GLAZED
C-C' SECTION SURFACE															
PLASTER		45,83	0,01	0,46	0,01	0,46	0,02	0,92	0,03	1,37	0,04	1,83	0,05	2,29	PLASTER
DOUBLE GLAZED WINDOW		2,50	0,15	0,38	0,05	0,13	0,03	0,08	0,03	0,08	0,02	0,05	0,02	0,05	DOUBLE GLAZED
WOOD DOOR		4,52	0,14	0,63	0,10	0,45	0,06	0,27	0,08	0,36	0,10	0,45	0,10	0,45	WOOD DOOR
D-D' SECTION SURFACE															
PLASTER		36,10	0,01	0,36	0,01	0,36	0,02	0,72	0,03	1,08	0,04	1,44	0,05	1,81	PLASTER
AIR APSORPTION															
AIR	810 m3		0,00	0,00	0,00	0,00	0,00	0,00	0,00	0,00	0,01	8,10	0,02	16,20	AIR (20º;%50 RELATIVE HUMIDITY)
ΣSa (m^2)			31,55		23,26		23,49		22,94		31,76		42,18		
REVERBERATION TIME ((1,61X VOLUME(m3))/ ΣSa (m2))			**4,13**		**5,61**		**5,55**		**5,68**		**4,11**		**3,09**		
MAXIMUM VALUE TO BE DESIRED			0,92		0,88		0,8		0,8		0,8		0,8		

Acoustical improvement project is developed in order to control reverberation time in existing conference hall. Conference hall interior surface covering was changed and conference hall absorptive surface was increased to control reverberation time (Fig.3, and Table 2).

Table 2. Reverberation time according to acoustic project proposal

ISTANBUL UNIVERSITY FACULTY OF FISHERIES CONFERENCE HALL IN SAPANCA CAMPUS

THEORETICAL CALCULATION OF REVERBERATION TIME ACCORDING TO ACOUSTIC PROJECT PROPOSAL

SURFACE PROPERTIES			FREQUENCY (HZ)												MATERIALS AND DIMENTIONAL INFORMATION
			125 HZ		250 HZ		500 HZ		1000 HZ		2000 HZ		4000 HZ		
SURFACE NAME	VOLUME (m3)	AREA (m^2)	α	sxα	α	sxα	α	sxα	α	sxα	α	sxα	α	sxα	
GROUND SURFACE															
AUDIANCE	60%	40,80	0,35	14,28	0,45	18,36	0,57	23,26	0,61	24,89	0,59	24,07	0,55	22,44	SEATS+ AUDIENCE
	40%	27,20	0,36	9,79	0,47	12,78	0,57	15,50	0,62	16,86	0,62	16,86	0,6	16,32	FIELD OF EMPTY SEATS
CORRIDOR		63,60	0,02	1,27	0,03	1,91	0,03	1,91	0,03	1,91	0,03	1,91	0,02	1,27	EPOXY FLOOR COVERING
SCENE		19,40	0,15	2,91	0,11	2,13	0,10	1,94	0,07	1,36	0,06	1,16	0,07	1,36	WOOD FLOOR COVERING
CEILING															
CELLING OF HALL		153,0	0,40	61,21	0,60	91,82	0,70	107,12	0,65	99,47	0,60	91,82	0,60	91,82	ACOUSTIC PERFORATED GYPSUM PANEL CEILING (DISTANCE BETWEEN THE HOLES: 18MM, THE HOLES RADIUS=6 MM, %11,95 PERFORATOIN RATIO)
CELLING OF SCENE		8,4	0,20	1,68	0,18	1,52	0,12	1,01	0,09	0,76	0,08	0,67	0,05	0,42	REFLECTIVE WOOD PANEL (10 MM)
A-A' SECTION SURFACE															
ABSORBENT PANELS		10,80	0,35	3,78	0,70	7,56	0,90	9,72	0,90	9,72	0,95	10,26	0,90	9,72	ABSORBENT FABRIC PANELS (BEHINDE 10 CM ROCKWOOL AND OPEN TEXTILE FABRIC)
REFLECTIVE WOOD SURFACE		17,30	0,2	3,46	0,18	3,11	0,12	2,08	0,09	1,56	0,08	1,38	0,05	0,87	REFLECTIVE WOOD PANEL (10 MM)
GYPSUM PANEL SURFACE		29,62	0,30	8,89	0,12	3,55	0,08	2,37	0,06	1,78	0,06	1,78	0,05	1,48	GYPSUM PANEL WALL (12MM -100MM GAP AND BEHIND 5cm ROCKWOOL)
GRANITE SURFACE		3,40	0,01	0,03	0,01	0,03	0,01	0,03	0,02	0,07	0,02	0,07	0,02	0,07	NATURAL GRANITE COVERING
B-B' SECTION SURFACE															
ABSORBENT PANELS		10,80	0,35	3,78	0,70	7,56	0,90	9,72	0,90	9,72	0,95	10,26	0,90	9,72	ABSORBENT FABRIC PANELS (BEHINDE 10 CM ROCKWOOL AND OPEN TEXTILE FABRIC)
REFLECTIVE WOOD SURFACE		17,30	0,2	3,46	0,18	3,11	0,12	2,08	0,09	1,56	0,08	1,38	0,05	0,87	REFLECTIVE WOOD PANEL (10 MM)
GYPSUM PANEL SURFACE		29,62	0,30	8,89	0,12	3,55	0,08	2,37	0,06	1,78	0,06	1,78	0,05	1,48	GYPSUM PANEL WALL (12MM -100MM GAP AND BEHIND 5cm ROCKWOOL)
GRANITE SURFACE		3,40	0,01	0,03	0,01	0,03	0,01	0,03	0,02	0,07	0,02	0,07	0,02	0,07	NATURAL GRANITE COVERING
C-C' SECTION SURFACE															
REFLECTIVE WOOD SURFACE		28,81	0,20	5,76	0,18	5,19	0,12	3,46	0,09	2,59	0,08	2,30	0,05	1,44	REFLECTIVE WOOD PANEL (10 MM)
GRANITE SURFACE		10,12	0,01	0,10	0,01	0,10	0,01	0,10	0,02	0,20	0,02	0,20	0,02	0,20	NATURAL GRANITE COVERING
WOOD DOOR		8,02	0,14	1,12	0,10	0,80	0,60	4,81	0,08	0,64	0,10	0,80	0,10	0,80	WOOD DOOR
D-D' SECTION SURFACE															
ABSORBENT PANELS		19,24	0,35	6,73	0,70	13,47	0,90	17,32	0,90	17,32	0,95	18,28	0,90	17,32	ABSORBENT FABRIC PANELS (BEHINDE 10 CM ROCKWOOL AND OPEN TEXTILE FABRIC)
GRANITE SURFACE		2,10	0,01	0,02	0,01	0,02	0,01	0,02	0,02	0,04	0,02	0,04	0,02	0,04	NATURAL GRANITE COVERING
OBSERVATION WINDOW		0,72	0,15	0,11	0,05	0,04	0,03	0,02	0,03	0,02	0,02	0,01	0,02	0,01	DOUBLE GLAZED WINDOW
WOOD DOOR		1,42	0,14	0,20	0,10	0,14	0,06	0,09	0,08	0,11	0,10	0,14	0,10	0,14	WOOD DOOR
AIR APSORPTION															
AIR	666 m3		0,00	0,00	0,00	0,00	0,00	0,00	0,00	0,00	0,01	6,66	0,02	13,32	AIR (20¤;%50 RELATIVE HUMIDITY)

ΣSa (m^2)	137,52	176,80	204,95	192,42	191,92	191,17
REVERBERATION TIME ((1,61X VOLUME(m3))/ ΣSa (m2))	**0,78**	**0,61**	**0,52**	**0,56**	**0,56**	**0,56**
MAXIMUM VALUE TO BE DESIRED	0,92	0,88	0,8	0,8	0,8	0,8

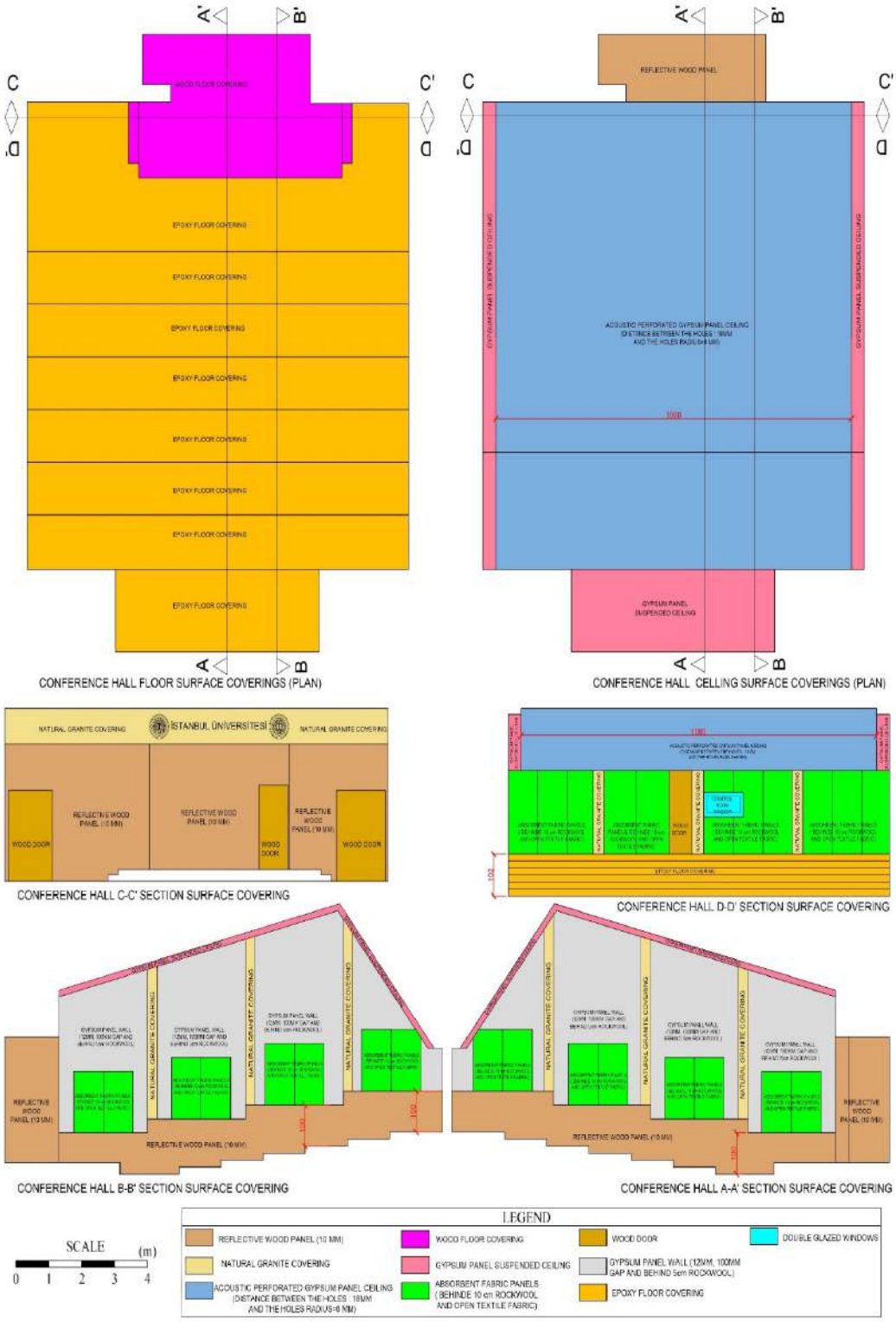

Figure 3. Conference hall acoustic improvement project – Interior surface covering

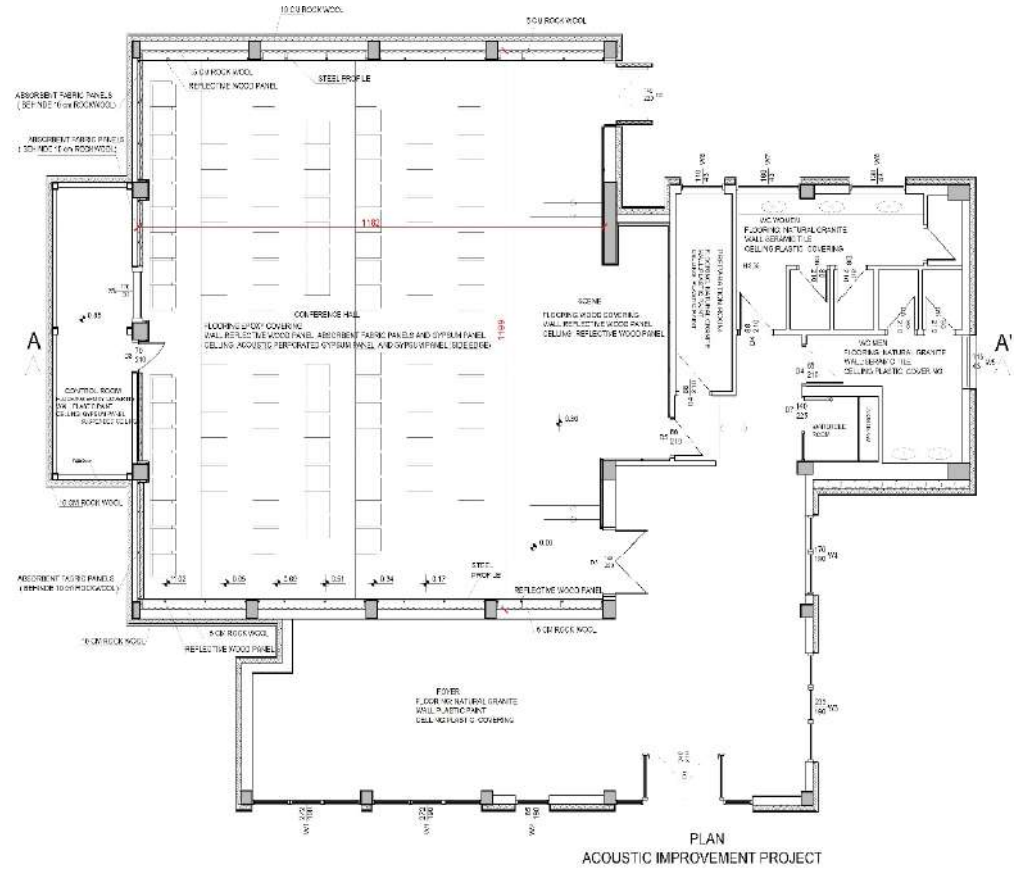

Figure 4. . Conference hall acoustic improvement project (Plan)

3. **CONCLUSIONS**

The research scopes the acoustic improvements of a conference hall. The conference hall was examined and acoustic improvement project was developed to control reverberation time (Fig.3, Fig.4 and Table 2). Thanks to conference hall acoustic improvement project, reverberation time was taken to the desired level (Fig.5). As a result, the speech intelligibility is increased by controlling reverberation time.

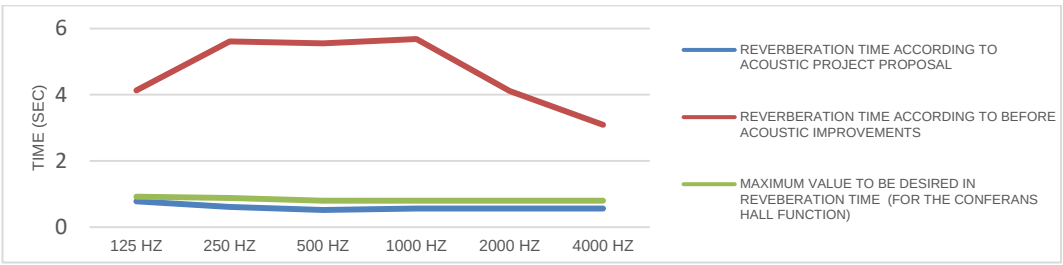

Figure 5. Comparison of reverberation time before- and after-acoustic improvements

REFERENCES

[1]. S. Y. Demirkale, Environmental and building acoustics, (Birsen publishing, Istanbul, Turkey, 2007).
[2]. M. L. Crocker, Handbook of acoustics, (John Wiley & Sons, Inc., Newyork, 1998).
[3]. M. Long, Architectural acoustics, (Elsevier Academic Press, 2006).
[4]. L. L. Beranek and I. L. Ver, Noise and vibration control engineering principles and aplications, (John Wiley & Sons, Inc., Newyork, 2006).
[5]. H. N. Ozguven, Industrial and environmental noise control, Turkish Acoustical Society, 2008.
[6]. M. Mehta, J. Johnson, and J. Rocaford, Architectural acoustics principles and design, Prentice Hall, 1999.

ICENS 4TH INTERNATIONAL CONFERENCE ON ENGINEERING AND NATURAL SCIENCE
2-6 May 2018 KIEV UKRAINE

Flood Analysis of a Part of Dicle (Tigris) River by HEC-RAS Program

Fevzi Onen[1], Selman Ogras[2]

Abstract

Floods are seen as the greatest natural disaster in the worldwide after earthquakes. Especially country like Turkey, as well as in terms of both climate and geographical features changing in a short distance, flood is the most decisive parameter in the localization planning. In this study, the floodplain analysis of Dicle (Tigris) River between Sadi Bridge located on Diyarbakir-Silvan highway and the historic ten-eyed Bridge with the symbolic value were performed. There is also the Hevsel Gardens, which was taken to the World Cultural Heritage List by UNESCO in 2015 on this route. Different cross-sections are taken from the map of the study area with AutoCAD Civil 3D program. After transfer these cross-sections to the HEC-RAS (Hydrologic Engineering Centres River Analysis System) programming, one-dimensional floodplain analysis of Dicle River is obtained. In addition to this, crossing structures (bridge) on the route were also analyzed and tried to determine the places where the flood risk was determined and their effects. According to floodplain risk analysis results water surface profiles of flow rates Q_{25}, Q_{50}, Q_{100}, Q_{500} is obtained.

Keywords: Flood, Dicle River, HEC-RAS, Hevsel Gardens

1. INTRODUCTION

Floods are among the main causes of damage caused by natural disasters in many regions around the world. Floods can be detected according to the reasons and the affected area. Therefore, the relationship between the flood characteristics of the environment exposed to the flood should be investigated. Stream floods are composed of sudden and heavy rainfall falling into the upper basin or the flow of sudden melting snow masses on the surface.

It will not be right to link the floods in our country to the irregularities of the geographical structure differences and precipitation. In addition, a negative intervention to creek beds and floodplains, improper land uses destruction of forests, untreated urbanization, and inadequate infrastructure and, of course, inappropriate activities in the basin provide serious contributions to the disaster [1]. Approximately 40% of total rainfall is observed in winter, 26% in spring, 10% in summer and 24% in autumn. In 2013, the average rainfall in Turkey was 564 mm.

In Turkey, the distribution of rainfall in time and space consisting of erratic rainfall negatively affects, sometimes total rainfall in a year is expected to be able to burn within a few days. Approximately 40% of total rainfall is observed in winter, 26% in spring, 10% in summer and 24% in autumn.

In the province of Diyarbakir, which also occurred in the city of Bismil, 14 citizens, in the city of Cinar, 3 citizens lost their lives and thousands of hectares of cultivated farmland was flooded and hundreds of houses became unusable [2], (Figure 1).

[1]*Corresponding author: Dicle University, Department of Civil Engineering, 21280, Sur/Diyarbakir, Turkey. fonen@dicle.edu.tr*

[2]*Dicle University, Department of Civil Engineering, 21280, Sur/Diyarbakir, Turkey. ugras_selman@hotmail.com*

Table 1. The floods that occurred between the years 1975-2015 in Turkey [3]

Years	Flood number	Loss of life	Underwater Area (ha)
1975	62	8	36 714
1976	29	5	22 536
1977	27	11	3 317
1978	21	0	13 850
1979	21	61	40 966
1980	44	6	83 016
1981	16	2	58 413
1982	10	0	784
1983	14	33	2 113
1984	12	0	29 140
1985	7	0	2 318
1986	8	4	679
1987	7	0	564
1988	24	17	3 910
1989	10	1	9 500
1990	26	57	7 450
1991	23	23	15 770
1992	14	1	690
1993	2	0	60
1994	9	4	1 680
1995	20	164	201 100
1996	4	1	11 000
1997	1	0	1 390
1998	2	57	7 000
1999	1	3	
2000	4	0	8 066
2001	42	8	43 297
2002	27	27	510
2003	21	7	64 200
2004	23	3	25 750
2005	25	14	13 855
2006	24	45	85 810
2007	22	11	1 050
2008	10	2	10
2009	84	59	3 250
2010	110	25	44 279
2011	56	13	202
2012	69	23	19 685
2013	38	7	17 569

2014	118	9	4 455
2015	122	9	7 985

Figure 1. Batman, Center-flood

Yarnell 1934, investigated Bridge Piers as Channel Obstructions [4]. Yurtal et al. 2003, have modeled by using the HEC-RAS package program the bubbles originating from the bridges in Seyhan River Waterfront Profiles [5]. Kara 2009, in thesis study, the study of water surface profiles with HEC-RAS packet program has been studied [6]. Tuncer 2011, In thesis study, Determination of Water Surface Profiles in Open Channels, HEC-RAS Application in the Nakkas Stream [7]. Citgez 2011, presented a Research on the Prevention of Flood and Flood Damages by giving a Duzce-Kaynasli example in his thesis [8]. Efe 2014, analyzed the flood analysis of Batman Stream using HEC-RAS program [9]. Yaylak 2016, in thesis study, conducted Flood Risk Analysis of Bitlis with Geographical Information Systems (GIS) [10].

In this study, the floodplain analysis of Dicle (Tigris) River between Sadi Bridge located on Diyarbakir-Silvan highway and the historic ten-eyed Bridge with the symbolic value were performed. There is also the Hevsel Gardens, which was taken to the World Cultural Heritage List by UNESCO in 2015 on this route.

2. MATERIALS AND METHODS

The work area is covered by the Sadi Bridge on the road of Silvan District of Diyarbakir (10 km) between the historical ten-eyed bridge. As the Tigris River flows through a wide valley with a low slope, there are settlements and fertile farmland along the river because of the nature of the plains streams. The daily maximum current distributions of the 34 annual AGI station on the Dicle River were calculated as Q_{500}=5450.71 m^3/s, Q_{100}=3871.25 m^3/s, Q_{50}=3209.47 m^3/s, Q_{25}=2598.18 m^3/s according to the Smirnov-Kolmogorov test. In this study, two different roughness coefficients (n) were calculated between the following kilometers of observations along the Tigris River (Table 2).

Table 2. Dicle River Natural state roughness coefficient calculation table

KATSAYI	0+ 000.00~ 6+ 000.00 km'ler arası	6+ 000.00~ 10+ 200.00 km'ler arası
n_0	0.028	0.028
n_1	0.005	0.020
n_2	0.000	0.005
n_3	0.000	0.000
n_4	0.040	0.045
m	1.150	1.150
$n= m(n_0+ n_1+ n_2+ n_3+ n_4)$	**0.08395**	**0.1127**

The method used in the study is as follows:

• The origin of the 1/1000 maps of the study area,

• Discharge and hydrological data of past years,

• Identification of hydraulic structures and other structures on the working route

• Creation of cross-sections along the route at 200 m intervals with the aid of the AutoCAD Civil3D package program and 2000 m wide at the right and left chambers,

• Transfer of the obtained topographic data to the HEC-RAS program,

• Hydraulic structures and hydrological parameters defined in the HEC-RAS program are used to determine flood borders by obtaining water profile profiles,

The first version of HEC-RAS was released in July 1995. Since then, the versions of this software package include: 1.1, 1.2, 2.0, 2.1, 2.2, 3.0, 3.1, 4.0, 4.1, and the latest version of 5.03. The 4.1 version was used in this study. Dicle River study route given Figure 2.

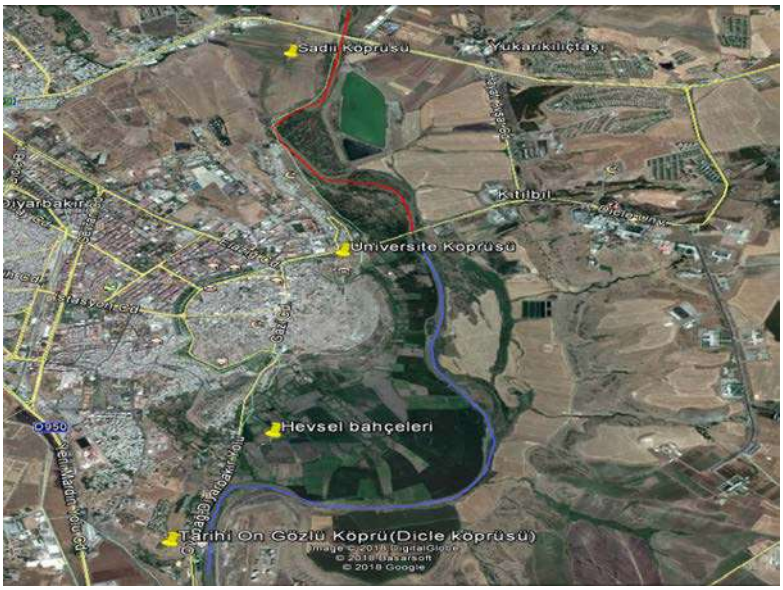

Figure 2. Dicle River study route

3. RESULTS AND DISCUSSION

From the beginning of our route, there are 3 art structures (bridges), including the Sadi Bridge (Fig 3), the University Bridge (Fig 4) and the historic ten-eyed Bridge (Fig 5).

Figure 3. Bottom view of Sadi Bridge

Figure 4. University Bridge

Figure 5. Historic ten-Eyes Bridge

The hydraulic analyses of the Dicle River were made using the 4.1 version of the HEC-RAS package program. Measurements of the existing art structures and observation data were made by entering the model and the water surface profiles obtained according to different recurrent rates were given in Figure 6-Figure 9.

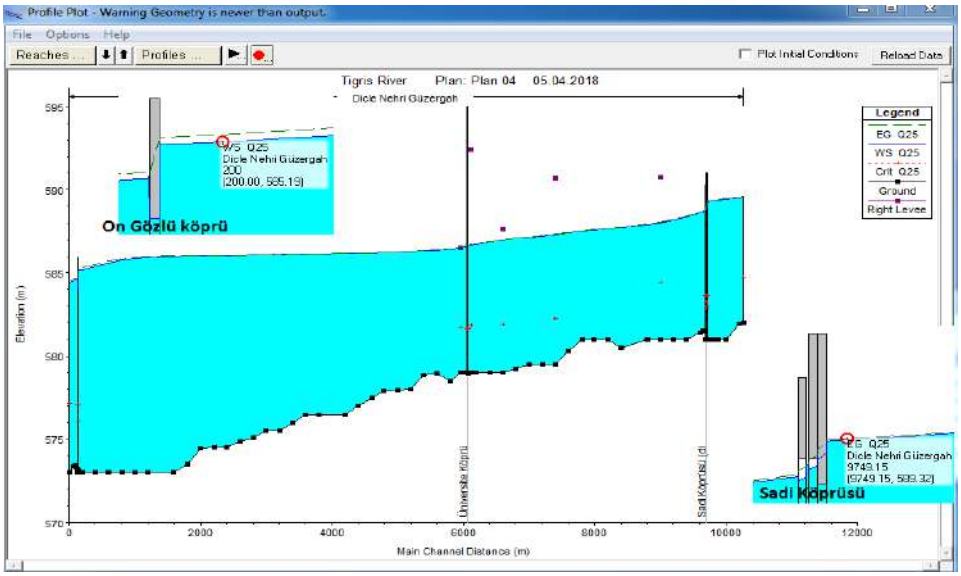

Figure 6. Q_{25}, Current Status Flow for 25-Year Recurrence

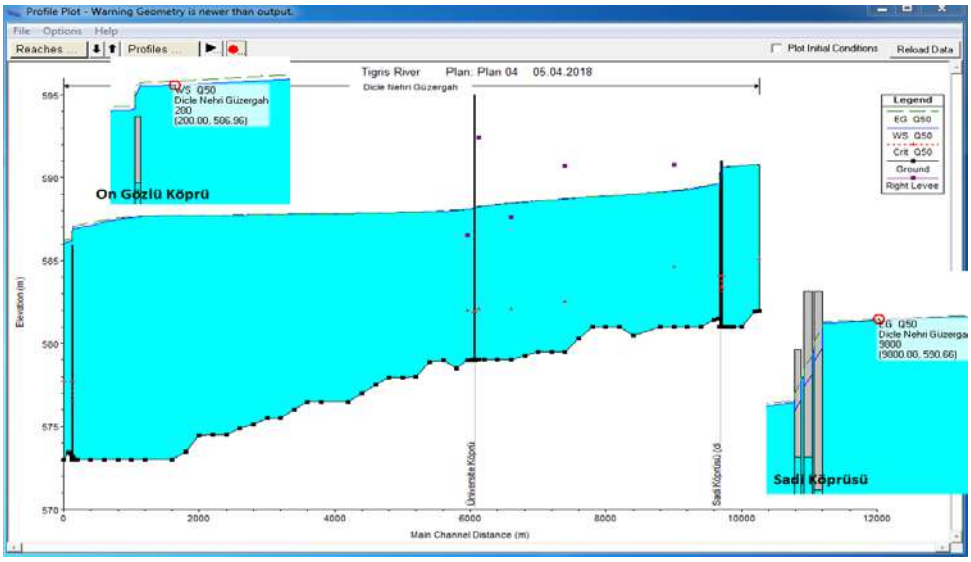

Figure 7. Q_{50} Current Status Flow for 50-Year Recurrence

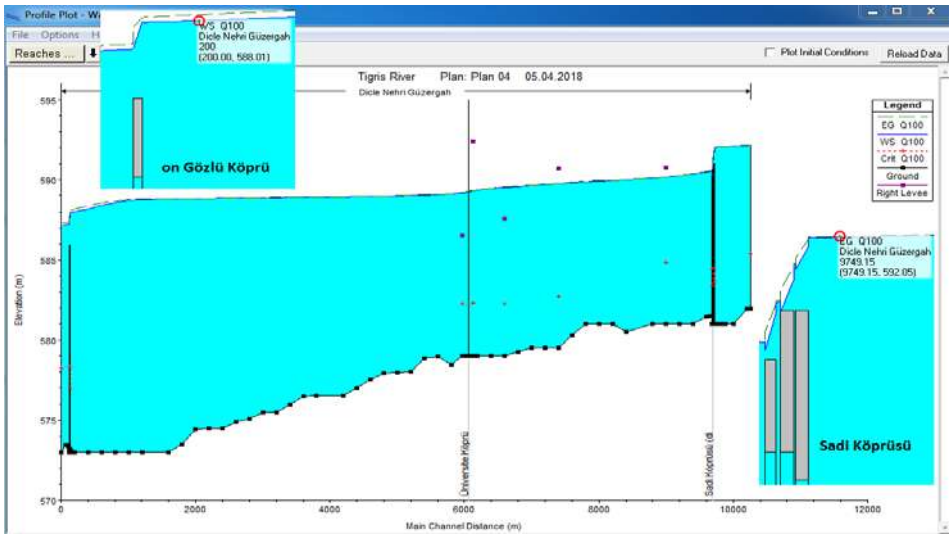

Figure 8. Q_{100} Current Status Flow for 100-Year Recurrence

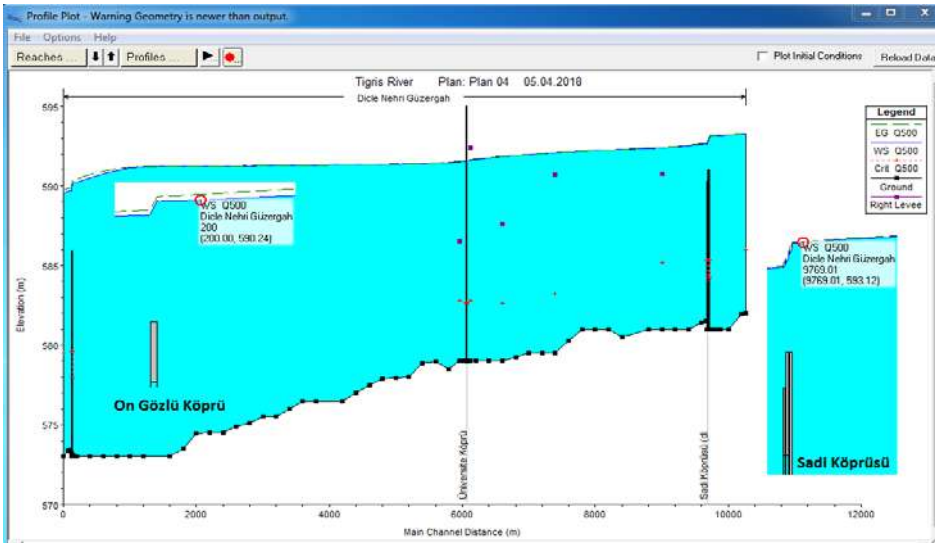

Figure 9. Q_{500} Current Status Flow for 500-Year Recurrence

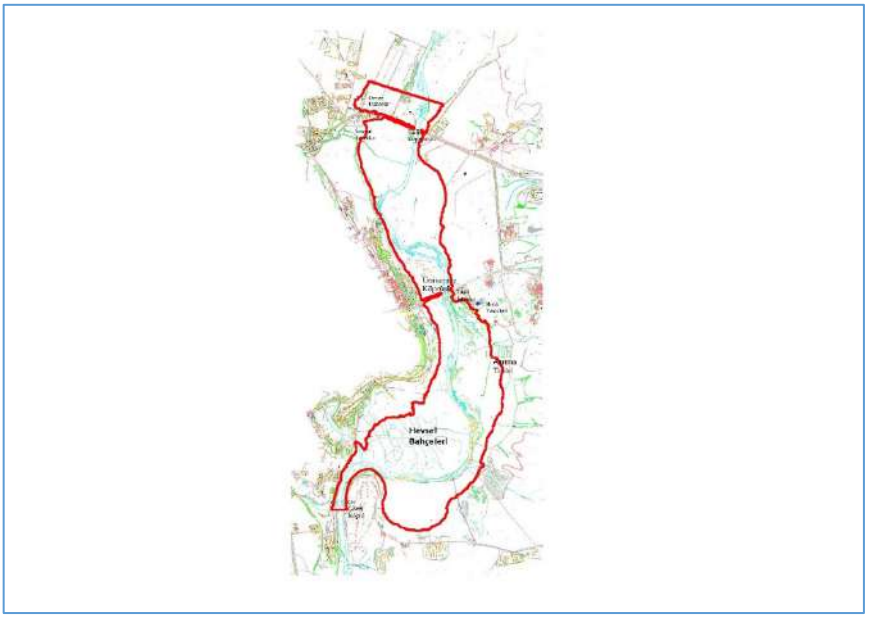

*Figure **10.** Flood Limits for Q_{25} (Dicle river)*

Given the results of this study; the capacities of Sadi and historic ten-eyed bridges are insufficient to pass the flood waters. The Hevsel Gardens, the UNESCO World Cultural Heritage List, and the settlements in the University Bridge are within flood limits.

4. CONCLUSIONS

1. There is a contraction in this part of the route due to the insufficient openness of the Sadi Bridge at the beginning of our work. Even over 25 years of recurrence, flood waters are rising due to lack of cross section.

2. It is determined that the Hevsel Gardens, which is located between the University Bridge and the Historical ten-eyed Bridge and taken to the World Cultural Heritage List by UNESCO in 2015, is also in the flood bed.

4. In addition, it has been determined that the section of the Historical Ten-Eye Bridge at the end of our study is also insufficient. In other words, bridge span is insufficient in all recurring flows.

5. In order to reduce the most possible flood damage, it is necessary to increase the openness of the Sadi Bridge.

6. The University Bridge in the same route is suitable.

7. It is essential to construct a tunnel that will overflow the flood waters since the historic ten-eyed Bridge has insufficient capacity.

ACKNOWLEDGEMENT

This study is supported by DUBAP, Muhendislik 17.016 project nuber

REFERENCES

[1] Berber, M.,Akcali,E., Erdogan,I., Kuduban,H., Erdogan,B., Kimence,S., 2016, Dogu Karadeniz Bolgesinde Taskin ve Rusubat Kontrolu Icin DSI Tarafindan Yapilan Oncu Calismalar sunumu IV. Ulusal Taskin Sempozyumu.
[2] IMO 2006, TMMOB Bolge Bilesenlerinin 31 Ekim-2 Kasim 2006 tarihleri arasinda yasanan Sel Felaketiyle Ilgili Hazirladigi On Inceleme ve Degerlendirme.
[3] Selek,B., Deniz,S., 2016, Turkiye'de Taskin Kontrolu Faaliyetlerinin Genel Degerlendirilmesi ve Yeni Calismalar sunumu 2016 IV. Ulusal Taskin Sempozyumu,
[4] Yarnell, D.L., 1934, .Bridge Piers as Channel Obstructions, Technical Bulletin 442, U.S. Department of Agriculture, Washington D.C.
[5] Yurtal, R., Seckin, G., Kaya, Đ., Atabay, S., 2003, .Seyhan Nehri Su Yuzu Profillerinde Koprulerden Kaynaklanan Kabarmalarin HEC-RAS Paket Programi Kullanilarak Modellenmesi, DMO Teknik Dergi, 14(2), 2935-2948,
[6] Kara, O.. 2009, Su Yuzu Profillerinin HEC-RAS Paket Programiyla Incelenmesi, Yuksek Lisans Tezi, Erciyes Universitesi, Fen Bilimleri Enstitusu, p. 106,
[7] Tuncer, I., 2011, Acik Kanallarda Su Yuzu Profilinin Belirlenmesi, Nakkas Dere Orneginde Bir HEC-RAS Uygulamasi. Yuksek Lisans Tezi, Gazi Universitesi, Fen Bilimleri Enstitusu, p. 160,
[8] Citgez, T., 2011, Sel ve Taskin Zararlarinin Onlenmesi Uzerine Bir Arastirma: Duzce-Kaynasli Ornegi. Yuksek Lisans Tezi, Duzce Universitesi, Fen Bilimleri Enstitusu, p. 115,
[9] Efe, H., 2014., Batman Cayi'nin Taskin Analizinin HEC-RAS Programiyla Yapilmasi, Yuksek Lisans Tezi, Dicle Universitesi, Fen Bilimleri Enstitusu, p. 96,
[10] Yaylak, M. 2016., Cografi Bilgi Sistemleri (CBS) Yardimiyla Bitlis Deresi Taskin Risk Analizi. Yuksek Lisans Tezi, Bitlis Eren Universitesi, Fen Bilimleri Enstitusu, p. 109,

ICENS 4TH INTERNATIONAL CONFERENCE ON ENGINEERING AND NATURAL SCIENCE
2-6 May 2018 KIEV UKRAINE

Development of off-shore wind energy in Turkey

Fevzi Onen[1]

Abstract

Wind energy is one of the renewable energy sources that is becoming more and more popular every day. Wind turbines are used to make use of wind energy. Wind turbines convert kinetic energy from the wind into mechanical energy first, and then convert it to electrical energy. Turkey wind power installed capacity of 51 MW in 2006, while in 2015 4718.3 MW a rose. The ratio of wind energy to total electricity demand is 4.4%. Turkey's wind energy potential of 48 000 MW. If all potential is used, 44% of the total electricity need can be met by wind power plants. For the first time in Turkey's renewable wind energy projects at sea, with maximum winds of the Aegean Sea it is among the world's regions with the potential to stand out. Usually at a depth of 20-50 meters off-shore plants established in the first example, when considering Turkey's seas "near the sea" as it is stated that the realization gained weight. As previously off-shore wind power plants yet to be done in the absence of pristine sea locations in Turkey in the ocean depths, is seen as a factor that will reduce costs. The Aegean Sea stands out among the regions with the most wind potential in the world. Turkey has a very high offshore wind potential and has a capacity of 32 thousand megawatts power plant can be established. In the Aegean region, especially the areas within the continental landscape of Bozcaada and Gokceada openings, the Canakkale region and the Black Sea coast of Saros Gulf and Trakya have serious offshore potential. At present, 13 percent of the electricity generated from wind in Europe is provided by off-shore power plants. The off-shore power plants are increasing in installed capacity and falling in costs.

Keywords: Wind Energy, Renewable Energy, Off-Shore, Turbines

1. INTRODUCTION

In terms of the potential of wind energy, the offshore wind power plants have been started to be established because the areas above the sea are richer than the land (Figure 1). On the first stage, offshore wind power plants were established in areas not more than 10 km from the coast and not more than 10 meters in depth. The first offshore wind power plant The Vindeby wind power plant, established near Denmark's Looland Island with 5 MW installed power. The world's largest offshore wind power plant is located in the UK with a capacity of 630 megawatts (175 wind turbine). With a total capacity of 6836 megawatts, the UK has the largest capacity in the off-shore wind. Britain is followed by Germany and China respectively.

The most basic characteristic features of the winds above the sea are their higher speeds compared to the land winds Figure 2. As a result of the work done, overhead wind speeds are 20-25% higher than the nearest land part. Because the roughness on the sea is lower over the land, the turbulence density of the wind flow is lower.

[1]*Corresponding author: Dicle University, Department of Civil Engineering, 21280, Sur/Diyarbakir, Turkey. fonen@dicle.edu.tr*

Figure 1. Off-shore wind power plants

Figure 2. On-shore wind power plants

There are significant differences between onshore and offshore wind power plants. These;

* Offshore regions have more stable energy and higher wind speeds, so more energy can be produced.

* The installation cost of offshore wind power plants is higher than onshore systems.

* Operation and maintenance costs are higher in offshore wind power plants.

* Various logistic problems arising from sea conditions can be encountered in offshore wind power plants.

For the first time in Turkey's renewable wind energy projects at sea, with maximum winds of the Aegean Sea it is among the world's regions with the potential to stand out. Usually at a depth of 20-50 meters off-shore plants established in the first example, when considering Turkey's seas "near the sea" as it is stated that the realization gained weight. The Aegean Sea stands out among the regions with the most wind potential in the world. Turkey has a very high off-shore wind potential and has a capacity of 32 thousand megawatts power plant can be established. In the Aegean region, especially the areas within the continental landscape of

Bozcaada and Gokceada openings, the Canakkale region and the Black Sea coast of Saros Gulf and Trakya have serious off-shore potential. At present, 13 percent of the electricity generated from wind in Europe is provided by off-shore power plants. The off-shore power plants are increasing in installed capacity and falling in costs. Work has recently accelerated for the establishment of 1000 MW of offshore wind power plants in Turkey.

Turkey's best wind resources are located particularly in the Balikesir, Izmir and Manisa provinces. As of the end of 2012, the Marmara region has the highest installed wind capacity with a total of 923.65 MW, followed by Aegean region with 857 MW and the Mediterranean region with 384.50 MW [1]. Turkey is surrounded by seas on three sides and it has 3500 km coastline. Particularly, the wind is wind is a continuous and very regular in Aegean and Marmara coastline. Nevertheless, there is no serious investment and production for offshore wind energy production [2]. Turkey's wind energy potential is primarily focused in Marmara, Aegean and Mediterranean regions from higher to lower is shown in Table 1, respectively [3].

Table 1. Technical wind energy potential regions in Turkey.

Region	Wind power potential	Percentage
Marmara	43.917	38.5
Aegean	26.150	22.9
Black Sea	14.312	12.5
Mediterranean	11.214	9.8
Central Anatolia	10.904	9.6
South-eastern Anatolia	4703	4.1
Eastern Anatolia	4974	2.6

2. ADVANTAGES AND DISADVANTAGES OF WIND ENERGY

Advantages

- It is a clean and unemission energy source, does not create greenhouse gases because of no emissions and does not contribute to global warming.
- There is no fuel cost and there are very few operating costs.
- It is a resource that is not externally dependent and creates continuous energy when environmental conditions are appropriate.
- Wind turbines are non-complex automatic machines and they work smoothly for 20-30 years of periodic maintenance.
- Commissioning and use is possible in as little as three months [4],

Disadvantages

- Energy production is dependent on the wind and energy loss occurs with the wind cutting or decreasing.
- The turbine costs can be high.
- It can cause bird deaths in its surroundings.
- The sound intensity caused by wind turbines can be reflected in the environment as noise.
- Turbines can affect the electromagnetic wave [5]

3. DISCUSSION

In order to enable offshore wind fields, it is necessary to measure the wind power potential and wind profile of these regions. Following these measurements, it will be possible to establish efficient RES with the appropriate wind turbine designs. In Offshore RES, the cost parameter, the amount of energy to be obtained, the external costs, the advantage and disadvantage of the energy source to substitute the same power is SWOT analysis logic to approach the topic.

By 2020, 20 percent of the electricity needs of the EU countries will be covered by renewable energy sources. In 2030, 10 percent of all electricity needs in the EU is targeted to be met by offshore wind turbine systems. In addition, by 2030, offshore wind turbines are planned to be installed at deeper sea points than 50 meters.

4. CONCLUSION

- By 2020, 20 percent of the electricity needs of the EU countries will be covered by renewable energy sources.
- In 2030, 10 percent of all electricity needs in the EU is targeted to be met by offshore wind turbine systems.
- In addition, by 2030, offshore wind turbines are planned to be installed at deeper sea points than 50 meters.
- Turkey, the fourth country to increase its wind power capacity in Europe in 2017, is preparing to establish its first offshore wind farm. The interest in offshore production that promises higher capacity is increasing every day.

Work has recently accelerated for the establishment of 1000 MW of offshore wind power plants in Turkey.

REFERENCES

[1] GWEC (Global Wind Energy Council), Global wind 2012 report, April, 2013.

[2] Kaplan Y.A., Overview of wind energy in the world and assessment of current wind energy policies in Turkey, Renewable and Sustainable Energy Reviews, 43, 562–568, 2015

[3] Baris K, Kucukali S., Availability of renewable energy sources in Turkey: Current situation, potential, (42). Energ Policy; 42:377–391, 2012

[4] Gabbasa M, Sopian K, Yaakob Z, Zonooz M, Fudholi A, Asim N. Review of the energy supply status for sustainable development in the Organization of Islamic Conference. Renew Sust Energ Rev; 28:18–28, 2013

[5] Maheshwari M, Chandrasekaran RS, Babu D., Optimization of electrical power using solar and wind energy systems, Proceedings of 7th international conference on intelligent systems and control (ISCO2013), 2012.

ICENS 4TH INTERNATIONAL CONFERENCE ON ENGINEERING AND NATURAL SCIENCE
2-6 May 2018 KIEV UKRAINE

Vibration Analysis of a Multiple-line Welded Aluminum Plate under Compression

Utku Uzun[1], Fatmagul Koltuk[1,] Nursah Yetmez[1]

Abstract

In this study, vibration characteristics of a multiple-line welded 2024-T351 aluminum plate is investigated numerically. Welded line effect on stress intensity factor, strain energy density and modal characteristics is examined. For this purpose, a numerical model is proposed. Results are given in graphical form.

Keywords: 2024-T351 Aluminum, Welding, Vibration, Shear Stress, Strain Energy

1. INTRODUCTION

In the recent years, welding as a damage character, investigations on welded line behavior of a multiple-line welded aluminum plate under static and dynamic loading increase in aerospace and automotive worlds [1]. Generally known that vibration based damage analysis approaches that changes in structural unity are directly related to characteristics of the measured vibration data [2-4]. For components, welded aluminum alloy plates are numerically simulated by using a general purpose finite element software and their stress field under static or dynamic loading is predicted [5]. Especially, elastic strain energy density plays an important role for understanding nonlinear behaviour of welded plates [6]. Analysis on welding of aluminum alloys obviously remains questionable according to weld fusion zone and heat-affected zone [7].

In this study, vibration characteristics of a multiple-line welded aluminum plate is investigated numerically. Gas metal arc welding process for the plate with Al2024-T351 is considered due to its high electrode efficiency.

2. MATERIALS & METHODS

Welded Al2024-T351 aluminum plate with engineering constants (ρ=2800 kg/m^3, E=70 GPa and ν=0.33) are considered. In experimental procedure, the plate is 300 mm in length. 75 mm in width and 5 mm in thickness. Aluminum filler metal electrode, namely Al5356, is used. General representation of clamped-free multiple-line welded aluminum plate is given in Figure 1. Vibration measurements are conducted such a way that an impulse hammer with a force transducer (Model No: 5800B2, Dytran Instruments, Inc., USA) is used to excite each of the composite beams through the selected point. Then, the responses are obtained by an accelerometer (Model No: 3093B, Dytran Instruments, Inc., USA). The vibration measurements are completed using a microprocessor-based data acquisition system, namely SoMat™ eDAQ-lite and nCode GlyphWorks software (HBM, Inc., USA). Experimental setup is given in Figure 2. It is assumed that the beam is considered under plane strain condition. Computations are ended up with the general-purpose finite element code MSC. Marc (v2014, MSC Software, Santa Ana, CA, USA). Finite element model possesses 24000 number of elements. Main parameters namely shear stress and strain energy density (SED) are considered.

[1] *Bulent Ecevit University, Department of Mechanical Engineering,67100, Zonguldak, Turkey.*

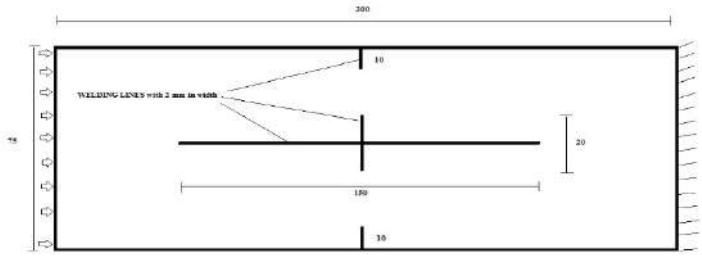

Figure 1. Representation of clamped-free multiple-line welded aluminum plate under compression

Figure 2. Representation of test configuration

3. RESULTS AND CONCLUSION

Numerical results show that (i) first natural frequency of the welded Al2024-T351 aluminum plate is 233.5 Hz (Mod 1); (ii) second natural frequency of the plate is 810.1 Hz (Mod 2); (iii) third natural frequency of the plate is 1394 Hz (Mod 3). Experimental result indicates that damping ratio of the welded Al2024-T351 aluminum plate is 0.029 for Mod 1.

Variations of shear stress and SED for free end, midpoint and fixed end of the plate are presented in Figures 3 and 4. Figure 3 points out that (i) remarkable changes of shear stress occur at Mod 2 for all three points free end, midpoint and fixed end; (ii) as expected, shear stress at free end is higher than that at midpoint; (iii) there is a fluctuating behavior of shear stress at midpoint. Figure 4 summarizes that increasing mod number increases SED nonlinearly for only free end.

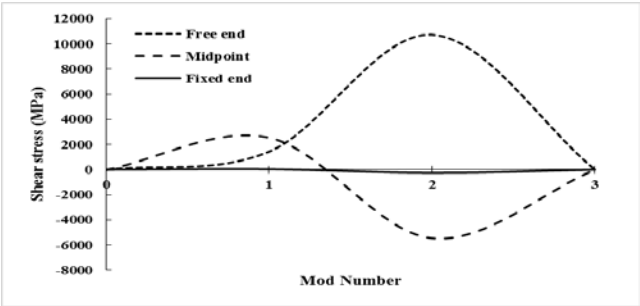

Figure 3. Variation of shear stress with mod number for free end, midpoint and fixed end of the plate

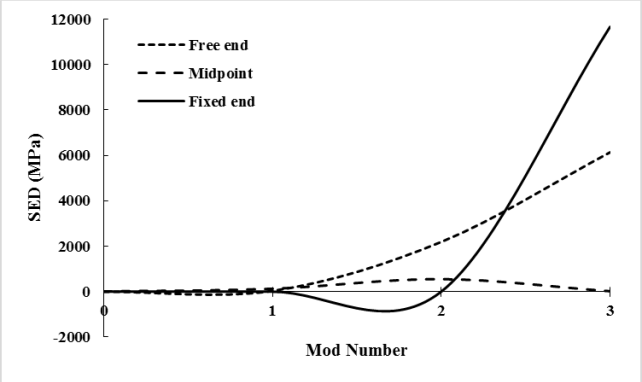

Figure 4. Variation of SED with mod number for free end, midpoint and fixed end of the plate

ACKNOWLEDGMENT

This work was supported by the Scientific Research Projects Unit (BAP) of Bulent Ecevit University (project code no: 2018-YKD-77654622-02).

REFERENCES

1. A. Perescu, L. Bereteu, D. Sinoiu, E. Nyaguly, Nondestructive method for the determination of the elastic properties of welded aluminum plates. Adv. Mater. Res. 1111 (2015) 73-78.
2. T.G. Chondros, A.D. Dimarogonas, Identification of cracks in welded joints of complex structures. J. Sound Vib. 69(4) (1980) 531-538.
3. I. Trendafilova, Vibration-based damage detection in structures using time series analysis. Proc. Inst. Mech. Eng. Part C – J. Mech. Eng. Sci. 220(3) (2006) 261-272.
4. P.S. Rao, Ch. Ratnam, Health monitoring of welded structures using statistical process control. Mech. Syst. Signal Process. 27 (2012) 683-695.
5. G. Mi, C. Li, Z. Gao, D. Zhao, J. Niu, Finite element analysis of welding residual stress of aluminum plates under different butt joint parameters. Eng. Rev. 34(3) (2014) 161-166.
6. P. Lazzarin, P. Livieri, F. Berto, M. Zappalorto, Local strain energy density and fatigue strength of welded joints under uniaxial and multiaxial loading. Eng. Frac. Mech. 75 (2008) 1875-1889.
7. A.K. Lakshminarayanan, V. Balasubramanian, K. Elangouan, Effect of welding processes on tensile propertiesof AA6061 aluminum alloy joints. Int. J. Adv. Manuf. Technol. 40 (2009) 286-296.

ICENS 4TH INTERNATIONAL CONFERENCE ON ENGINEERING AND NATURAL SCIENCE
2-6 May 2018 KIEV UKRAINE

Hardness Effect on Vibration Characteristics of a Three-Layered Composite Beam with Viscoelastic Core

Utku Uzun[1], Mehmet Yetmez[1], Buket Bilgin[2], Serdar Coban[2]

Abstract

In this study, hardness effect on vibration characteristics of a three-layered composite beam with a viscoelastic core is investigated both numerically and experimentally. For this purpose, a numerical model is proposed. Results show that (i) increasing hardness of the viscoelastic core increases first, second and third natural frequencies of the composite with a viscoelastic core, (ii) characteristic hardness behavior of second natural frequency is similar to that of third natural frequency, (iii) characteristic hardness behavior of maximum Von Mises stress at first natural frequency is similar to that in third natural frequency.

Keywords: Modal Analysis, Damping Rods, Hardness Effect, Rubber

1. INTRODUCTION

Vibration is a major design problem in structures, and often it is attempted to minimize the vibration amplitude in order to increase the fatigue resistance of the structure. Viscoelastic materials with high damping properties are combined with metallic materials and are used as a composite material in order to reduce the vibrational amplitudes in the structures. In this case, the structure can withstand the applied load, while the viscoelastic material can provide the necessary damping properties. In the first studies on this subject, the focus was on the design of composite materials. The effect of these parameters on damping is investigated by changing the geometry and boundary conditions of the sandwich composite [1]. These studies have continued with the calculation of modal parameters such as resonant frequency and modal loss factor in the cases of changing the damper and rigid material geometries and temperature values by the finite element method [2]. In addition to geometric parameters that significantly affect the dynamic character of construction, the selection and development of viscoelastic materials is also important. Under various temperature and frequency values, viscoelastic materials that provide damping according to the change of dynamic properties, the desired optimum hardness and the prescribed frequency and temperature ranges are necessary for damping unwanted vibrations in the mechanisms. In this context, studies have been carried out for the analysis and optimization of viscoelastic reinforced composite structures [3]. Experiments have been investigated for the impact behavior of sandwich panels consisting of woven carbon/epoxy interfacial layers and PVC foam core at low speed [4]. It is found that there is a need for a detailed characterization, including the effect of hardening observed on sandwich plates, which can account for the complex interactions of the loading applied to a small contact area on the sample by measuring the deformation and strain levels with the semi static test applied to the substrate exposed to the load on the sandwich plates. As an another study, analytical modeling is performed for a three-layered non-symmetrical beam system having two viscoelastic damping layers adjacent to each other, and the vibration characteristics of the structure are numerically examined. Results indicate that it is possible to achieve a structure with maximum damping without sacrificing hardness and weight requirements by modifying the physical properties of the structure and the appropriate test setup [5]. Four core materials with different modulus of elasticity (37.5 MPa, 138.6 MPa, 180 MPa and 402.6 MPa) are used between the aluminum layers. It is observed that increasing the stiffness of the core material to a certain extent increases the load carrying capacity of the sandwich panel by increasing the hardness of the core material and thus the hardness of the core material before the aluminum layers have flowed from the core material [6]. Different numerical models for linear and

[1] *Bulent Ecevit University, Department of Mechanical Engineering,67100, Zonguldak, Turkey.*

[2] *Cilas Kaucuk A.S. Devrek/Zonguldak, Turkey.*

nonlinear vibration analysis of viscoelastic sandwich panels are also analyzed using the finite element method [7]. According to linear variations along the depth of the panel core, natural frequency, loss factors and frequency and effect on time response of these variables are investigated by considering modulus of elasticity, moment of inertia and kinetic energy of core [8]. Effect of changing the material stiffness by adding silica particles to the viscoelastic structure in the sandwich panels and investigating the effect of this change on the vibration damping characteristics is tested by reinforcing spherical silica particles of 12-235 nm in size, three different polymer matrices (polyacrylate, polyamide and polypropylene) at various filler ratios (10-50% by weight) [9]. It is observed that the intense bond between the silica and the polymer matrix allows the viscoelastic layer to provide high hardness and damping. Another study finds out that shear modulus of the core material significantly affects the vibrational properties of the sandwich panel below 1000 Hz [10]. Moreover, viscoelastic core material can be calculated as elastic core material, while frequency and damping ratios are calculated in order to facilitate the numerical solution [11]. Also, a study reports that using a metal plate to form a viscoelastic layer with high high adhesion capacity and oil resistance, which can work effectively in a wide range of temperatures, reduces the amplitude and frequency values of the sandwich panel used in the work [12, 13].

Regarding the literature studies, many relationships between the mechanical properties of the resins and the vibration damping characteristics of the resins have been demonstrated through empirical and numerical approaches, but hardness-vibration characteristics have not been adequately investigated. In this study, hardness effect on vibration characteristics of a three-layered composite beam with a viscoelastic core is investigated both numerically and experimentally. For this purpose, a numerical model is proposed.

2. MATERIALS & METHODS

Damping rods having various hardness values in the range between 35 and 85 Sh (Shore hardness) are manufactured by Cilas Kaucuk A.S. Hardness of the specimens are set by changing the carbon rate in the rubber within the meaning of weight. Both increasing the carbon ratio from 6.7% to 30% and decreasing the NR (natural rubber) ratio from 68% to 40% in the specimen lead to increase in the hardness. There are also other constituents which contribute to mechanical properties of the rubber such as silica and kaolin but their effect is found to be insignificant because of their less amount.

In order to analyze the relationship between hardness and natural frequencies, experimental setup is prepared as shown in the Figure 1.

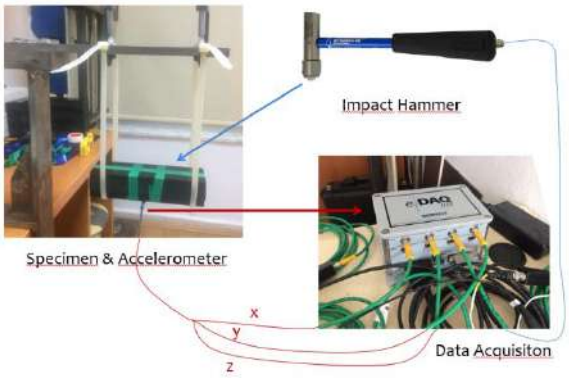

Figure 1.Experimental Setup

Specimen is hanged with two plastic robes to achieve free-free vibration boundary condition. Impact hammer with a force transducer (Model No: 5800B2, Dytran Instruments, Inc., USA) is used to excite the three-layered composite beam with a viscoelastic core through the center of the upper surface of metal. After the excitations, the responses are obtained by an accelerometer (Model No: 3093B, Dytran Instruments, Inc., USA) in order to obtain natural frequency values. The vibration measurements are completed using a microprocessor-based data acquisition system, namely SoMat ™ and eDAQ-lite. The last step of experimental process is completed by carrying out modal analysis with the help of nCode GlyphWorks software (HBM, Inc., USA)

In the numerical part, it is assumed that the beam is considered under plane strain condition. Computations are ended up with the general-purpose finite element code MSC. Marc (v2014, MSC Software, Santa Ana, CA, USA). Finite element model possesses 5000 number of elements. Main parameter namely maximum Von Mises stress is considered.

3. RESULTS

Results show that (i) increasing hardness of the viscoelastic core increases first, second and third natural frequencies of the composite with a viscoelastic core (see Figures 2-4), (ii) characteristic hardness behavior of second natural frequency is similar to that of third natural frequency (see Figures 3 and 4), (iii) characteristic hardness behavior of maximum Von Mises stress at first natural frequency is similar to that at third natural frequency (see Figure 5).

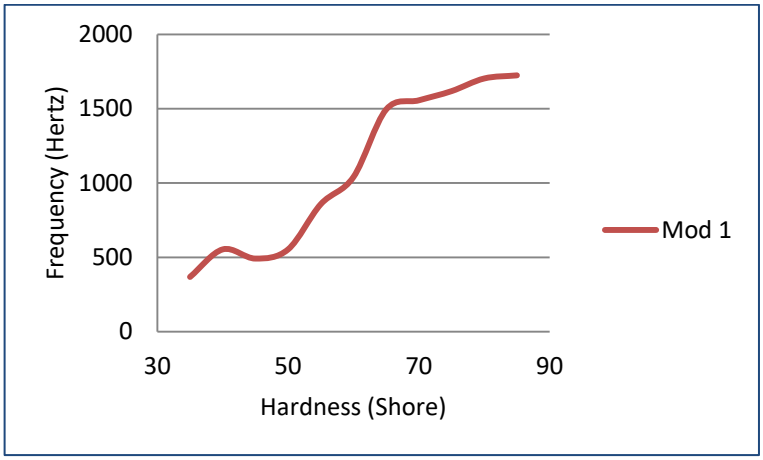

Figure 2.Variation of First Natural Frequency with Hardness

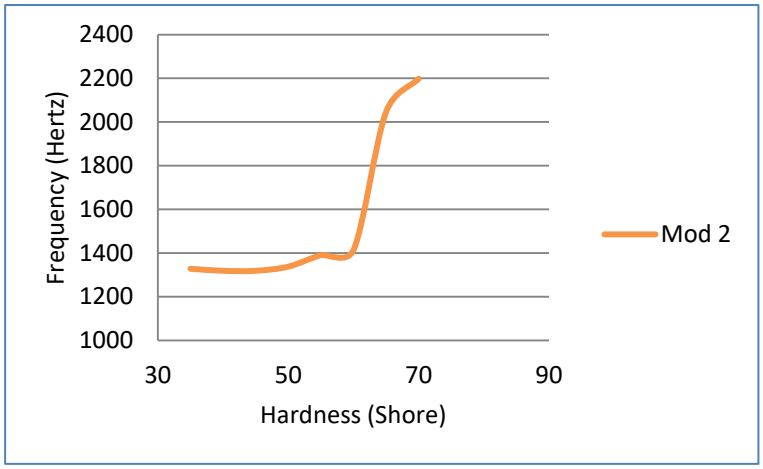

Figure 3. Variation of Second Natural Frequency with Hardness

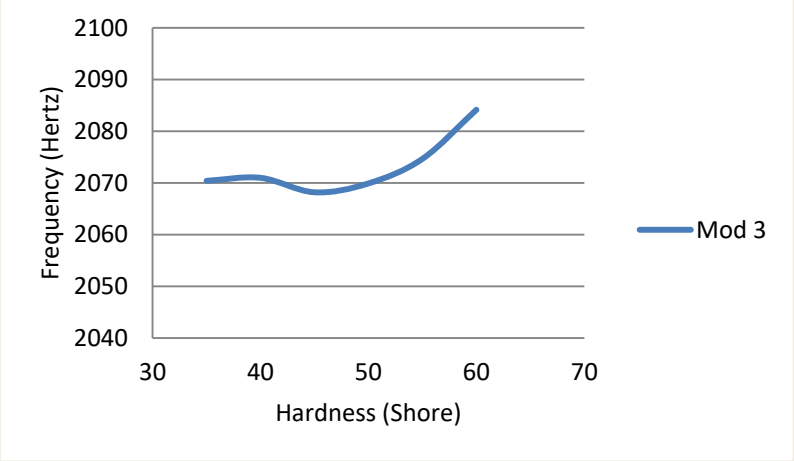

Figure 4. Variation of Third Natural Frequency with Hardness

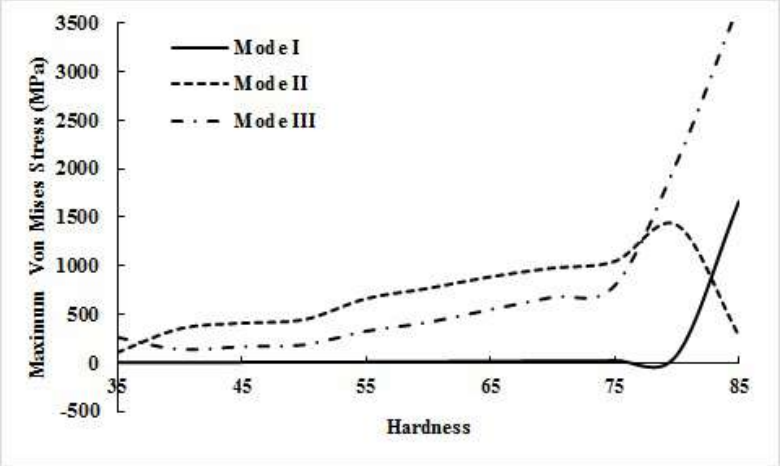

Figure 5.Variation of Maximum Von Mises Stress with Hardness for First Three Modes

ACKNOWLEDGMENT

This work was supported by the Scientific Research Projects Unit (BAP) of Bulent Ecevit University (project code no: 2018-YKD-77654622-02).

REFERENCES

[1] Lifshitz J., Leibowitz M (1987) Optimal Sandwich Beam Design for Maximum Viscoelastic Damping. Int J Solid Struct 23:1027–1034
[2] Rao MD, Echempati R, Nadella S (1997) Dynamic analysis and damping of composite structures embedded with viscoelastic layers. Compos Part B Eng 28:547–554.
[3] Nakra BC (1998) Vibration Control in Machines and Structures Using Viscoelastic Damping. J Sound Vibr 211:449–465.
[4] Schubel PM, Luo JJ, Daniel IM (2005) Low velocity impact behavior of composite sandwich panels. Compos Part A Appl Sci Manuf 36:1389–1396.

[5] Hao M, Rao MD (2005) Vibration and damping analysis of a sandwich beam containing a viscoelastic constraining layer. J Compos Mater 39:1621–1643.
[6] Akour SN, Maaitah HZ (2010) Effect of core material stiffness on sandwich panel behavior beyond the yield limit. Proc World Congr Eng 2010 Vol II WCE 2010, June 30 - July 2, 2010, London, UK II:1321–1330.
[7] Bilasse M, Daya EM, Azrar L (2010) Linear and nonlinear vibrations analysis of viscoelastic sandwich beams. J Sound Vib 329:4950–4969.
[8] Arvin H, Sadighi M, Ohadi AR (2010) A numerical study of free and forced vibration of composite sandwich beam with viscoelastic core. Compos Struct 92:996–1008.
[9] Lin JC (2010) Characterization and numerical evaluation of vibration on elastic-viscoelastic sandwich structures. Compos Struct 92:669–675.
[10] Sargianis J, Suhr J (2012) Core material effect on wave number and vibrational damping characteristics in carbon fiber sandwich composites. Compos Sci Technol 72:1493–1499.
[11] Pawlus D (2015) Dynamic behaviour of three-layered annular plates with viscoelastic core under lateral loads. J Theor Appl Mech 775.
[12] Latifi M, Kharazi M, Ovesy HR (2017) Effect of integral viscoelastic core on the nonlinear dynamic behaviour of composite sandwich beams with rectangular cross sections. Int J Mech Sci 123:141–150.
[13] Cherkasov VD, Yurkin Y V, Avdonin V V (2017) Damping Properties of Sandwich Beams with Viscoelastic Layer. IOP Conf Ser Mater Sci Eng 262:12024.

ICENS 4TH INTERNATIONAL CONFERENCE ON ENGINEERING AND NATURAL SCIENCE
2-6 May 2018 KIEV UKRAINE

Investigation on flammability and mechanical properties of polypropylene/red mud polymer composites

Munir Tasdemir[1], Ali Anil Ulu[2]

Abstract

In parallel with the continually increasing use of plastics, the issue of fire safety has come to the forefront. Flame retardancy of polymers has become essential in many application fields such as transportation, construction, and electrical industries. The burning process is comprised of five fundamental steps, which are, heating, decomposition, ignition, combustion and propagation.
In this study, polypropylene matrix contributes to ground red mud powder is handled as 0, 10, 20, 30 and 40 wt% ratio will be mixed in the extruder. Mixture obtained from the extruder to be granulated and then the granules will be obtained as appropriate standard test sample of the injection molding machine. Flammability and mechanical tests will be applied such as UL94 flammability test, limit oxygen index (LOI), wire flammability test method (glow wire), elasticity modulus, yield strength, tensile strength at break, % elongation, Izod impact strength, hardness, density. Also, SEM examination will be conducted to evaluate the microstructure of red mud particles as well as material distribution in these experiments.

Keywords: Polypropylene, red mud, UL 94, flammability, limit oxygen index, mechanical properties

1. INTRODUCTION

Being lightweight they are the most suitable materials for weight sensitive uses, but their high cost sometimes becomes the limiting factor for commercial applications. Use of low cost, easily available fillers is therefore useful to bring down the cost of components. Study of the effect of such filler addition is necessary to ensure that the mechanical properties of the composites are not affected adversely by such addition. Available references suggest a large number of materials to be used as fillers in polymers [1]. Polymer/clay nano composites have received great attention in the past three decades owing to their light weight coupled with significantly better mechanical and barrier properties than the corresponding neat polymer resins [2−5]. The mechanical and thermal properties of polymers are generally improved by the addition of inorganic fillers. The challenges in this area of high-performance organic–inorganic hybrid materials are to obtain significant improvements in the interfacial adhesion between the polymer matrix and the reinforcing material since the organic matrix is relatively incompatible with the inorganic phase. Polymer/clay nanocomposites have received great attention in the past three decades owing to their light weight coupled with significantly better mechanical and barrier properties than the corresponding neat polymer resins [3, 6-7]. Popularity of polymer composites in the present scenario is mainly due to their low density, high specific strength and wear resistance as compared to monolithic material. These are the most suitable material to be used as weight sensitive material. Polymer materials by themselves have found extensive use in noncritical products [8]. Such man made reinforcement though yield attractive mechanical properties are expensive. Hence, it has become important to explore the potential use of cheap materials like minerals ores and industrial wastes in preparing particle- reinforced polymer composites. One such inexpensive filler to fit the slot is red mud [9]. Red mud emerges as the major waste material during production of alumina from bauxite by the Bayer's process. The red mud which is derived from the bauxite by different methods is potentially applicable to use in building materials due to its strength [10-12]. Red mud has been suggested as filler for polymer

[1] Marmara University, Technology Faculty, Metallurgy and Materials Eng. Dep., Istanbul, 34722, Turkey munir@marmara.edu.tr
[2] Marmara University, Ins. for Graduate Studies in Pure and Appl. Sci., Istanbul 34722, Turkey a_anil_ulu@hotmail.com

reinforcement or as a cheap adsorbent for removal of toxic metals or an acid by several researchers. Chand and Hashmi [13], tried to improve the mechanical properties and abrasive wear properties of polymer blend filled with red mud. Pradhan et al. [14] had reported that activated red mud as a good adsorbent was used for adsorption of phosphate or chromium. In addition, the mechanical and thermal properties of polymers are generally improved by the addition of inorganic fillers. Reinforcement of polymer filled with inorganic material is largely dependent on the physical interfacial phenomenon between the filler and matrix [15-17]. In this investigation, composites of polypropylene, red mud powder were prepared. The effects of red mud powder ratio on the mechanical, physical, flammability and morphological properties of the polymer composites are presented. Red mud, in five different concentrations (0, 10, 20, 30 and 40 wt %) were added to PP to produce composites.

2. EXPERIMENTAL

2.1 Compositions and Materials

Five different polymer blends were prepared. Compositions of PP/red mud (RM) polymer composites that were formed are given in Table I.

Table I Composition of the different polymer blends formulations

Groups	PP (wt %)	Red Mud (wt %)
1	100	-
2	90	10
3	80	20
4	70	30
5	60	40

PP (Moplen EP 3307) supplied by Lyondell Basell. Its density is 0.900 g/cm^3, MFI value is 15 g/10 min (230 ^{o}C, 2,16 kg) and its head deflection temperature (0.45 MPa, unannealed) is 95.0 ^{o}C. Red Mud was supplied Guray seramic Company (Avanos-Turkey). The chemical composition of red mud is listed in the Table II.

Table II The chemical composition of the red mud (wt %)

Composition of red mud	Proportion
Fe_2O_3	30-60
Al_2O_3	5-20
SiO_2	1-20
S	0.09-0.15
Na_2O	1-10
CaO	2-8

2.2 Sample Preparation

Red mud dry grinded with Siemens simatic C7-621 control system device to obtain unsegregated powders. The size of red mud particles varied between 38–250µm. Powder preparations steps are given in Figure 1. Then, red mud was dried in a Yamato vacuum oven ADP-31 (Yamato/VWR Scientific Products, Japan) at 105 ^{o}C for 24 hours before being blended with PP. Mechanical premixing of solid compositions was done using a LB-5601 liquid-solids blender (The Patterson-Kelley Co., Inc. east Stroudsburg, PA - USA) brand batch blender for 20 min. Samples with various proportions of PP/RM polymer composites were produced between 180-210 ^{o}C at 30-35 bar pressure, and a rotation rate of 25 rpm, with a Microsan co-rotating twin-screw extruder (Microsan Instrument Inc., Turkey). Polymer composites were also dried in vacuum oven at 105 ^{o}C for 24 hours after extrusion. Subsequently, test samples were molded in injection molding machine. Extrusion and injection conditions are given in Table III.

Table III Extrusion and injection conditions of the PP/RM polymer composites

PROCESS	Extrusion	Injection
Temperature (°C)	180–210	180–210
Pressure (bar)	30-35	120–140
Waiting time in mold (s)	-	20
Screw speed (rpm)	25	25
Mould temperature (°C)	-	35

waste red mud *granulation* *red mud powder*

Figure 1 Waste red mud powder preparation steps

2.3 Characterization

For every composition, five samples were tested, and the averages of the five measurements were reported. The elasticity modulus, yield strength, tensile strength at break and % elongation of the compressed plates were measured by using a tensile testing machine (Zwick Z010, Germany) according to ASTM D638 at room temperature and crosshead speed of 50 mm/min. The hardness test was done according to the ASTM D2240 method with Zwick hardness measurement equipment. To investigate fracture behavior, Izod impact test (notched) was done at room temperature according to the ASTM D256 method with Zwick B5113 impact tester (Zwick, Germany). Determination of density was done according to ISO 2781 test standard. Limit oxygen index (LOI) testing of all the mixtures was done according to ISO 4589 standard with Devotrans LOI equipment. UL-94 flammability test was done according to the ASTM D3801 method with UL 97 test measurement equipment. Wire flammability test (glow wire) was done according to IEC 60695-2-11 method with glow wire test measurement equipment. The fractured surfaces of the composites were coated to an approximate thickness of 10 nm of a gold (Au) (80%)/palladium (Pd) (20%) alloys to prevent electrical charging by Polaron SC 7620 (Gala Instrumente GmbH, Germany). The surfaces of the prepared samples were observed by the JEOL-JSM 5910 LV (JEOL Ltd.**,** Japan) scanning electron microscopy (SEM) at an acceleration voltage of 5 kV.

3. RESULT AND DISCUSSION

3.1 Physical and mechanical properties of PP/RM composites: The relationship between the elasticity modulus and the percentage of the waste red mud powder of PP composites is shown in the Figure 2-A. With the addition of RM in PP has been a change in elasticity modulus values. The elasticity modulus of PP/RM blend decreases as the red mud concentration increases from 0 to 40 wt %. For example, the elasticity modulus of the four different samples (with 10, 20, 30, and 40 wt% of red mud) are measured as 1103, 1065, 1052 and 974 MPa respectively. The elasticity modulus of pure PP is 1134 MPa. The minimum elasticity modulus is observed at the 40 wt % RM concentration for PP. In comparison with the elasticity modulus of virgin PP, the elasticity modulus decreased by 14% for the composites with a 40 wt % RM concentration. The relationship between the yield strength and the percentage of the waste red mud powder of PP composites is shown in the Figure 2-B. With the addition of RM in PP has been a change in yield strength values. The yield strength of PP/RM blend decreases as the red mud concentration increases from 0 to 40 wt %. For example, the yield strength of the four different samples (with 10, 20, 30, and 40 wt% of red mud) are measured as 17.0, 15.4, 14.3 and 14.2 MPa respectively. The yield strength of pure PP is 29.2 MPa. The minimum yield strength is observed at the 40 wt % RM concentration for PP. In comparison with the yield strength of virgin PP, the yield strength decreased by 51% for the composites with a 40 wt % RM concentration.
The relationship between the tensile strength at break and the percentage of the waste red mud powder of PP composites is shown in the Figure 2-C. With the addition of RM in PP has been a change in tensile strength at break values. The tensile strength at break of PP/RM blend decreases as the red mud concentration increases from 0 to 40 wt %. For example, the tensile strength at break of the four different samples (with 10, 20, 30,

and 40 wt% of red mud) are measured as 15.9, 13.2, 13 and 12 MPa respectively. The tensile strength at break of pure PP is 20.1 MPa. The minimum tensile strength at break is observed at the 40 wt % RM concentration for PP. In comparison with the tensile strength at break of virgin PP, the tensile strength at break decreased by 40% for the composites with a 40 wt % RM concentration. The relationship between the %elongation and the percentage of the waste red mud powder of PP composites is shown in the Figure 2-D. With the addition of RM in PP has been a change in % elongation values. The % elongation of PP/RM blend decreases as the red mud concentration increases from 0 to 40 wt %. For example, %elongation of the four different samples (with 10, 20, 30, and 40 wt% of red mud) are measured as 3.7, 3, 2 and 1.8 % respectively. The % elongation of pure PP is 9 %. The minimum % elongation is observed at the 40 wt % RM concentration for PP. In comparison with the %elongation of virgin PP, the %elongation decreased by 80% for the composites with a 40 wt % RM concentration.

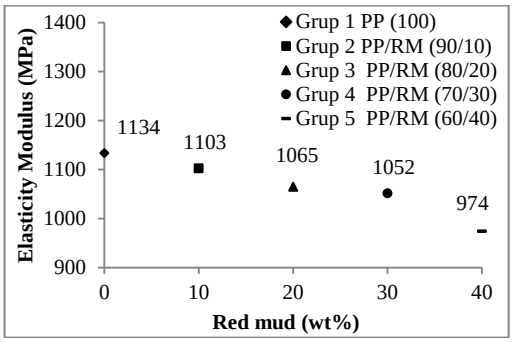

A

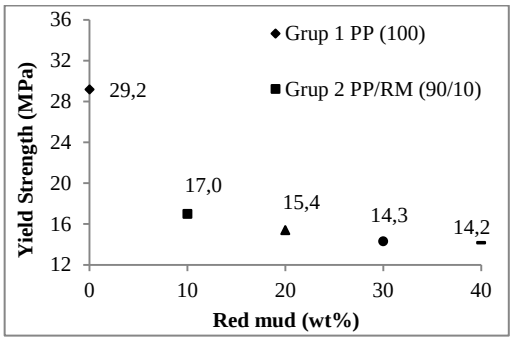

B

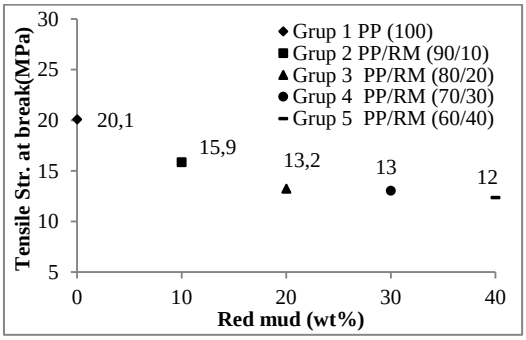

C

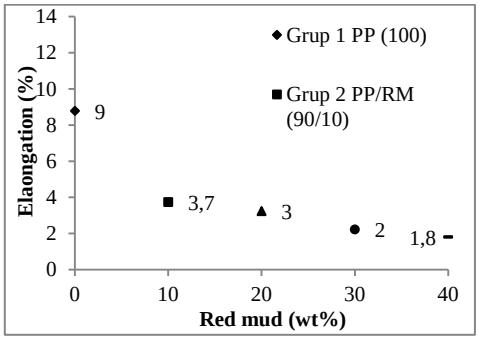

D

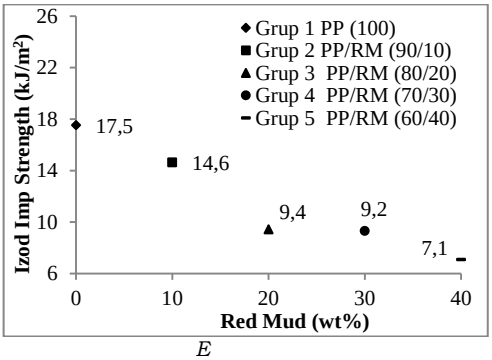

E

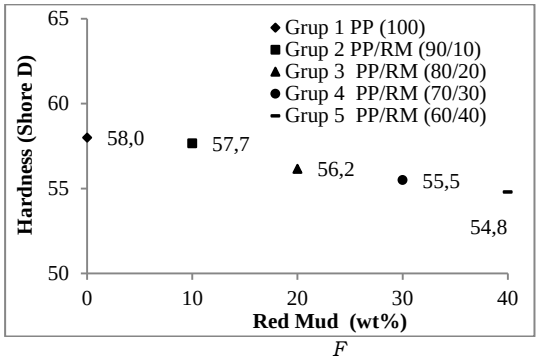

F

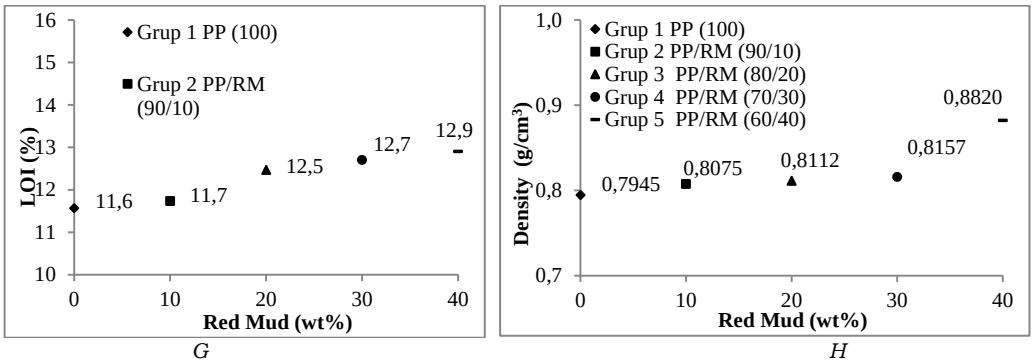

Figure 2 Physical properties of PP/RM polymer composites

The relationship between the Izod impact strength and the percentage of the waste red mud powder of PP composites is shown in the Figure 2-E. With the addition of RM in PP has been a change in Izod impact strength values. The Izod impact strength of PP/RM blend decreases as the red mud concentration increases from 0 to 40 wt %. For example, Izod impact strength of the four different samples (with 10, 20, 30, and 40 wt% of red mud) are measured as 14.6, 9.4, 9.2 and 7.1 kJ/m^2 respectively. The Izod impact strength of pure PP is 17.5 kJ/m^2. The minimum Izod impact strength is observed at the 40 wt % RM concentration for PP. In comparison with the Izod impact strength of virgin PP, the Izod impact strength decreased by 59% for the composites with a 40 wt % RM concentration. The relationship between the hardness and the percentage of the waste red mud powder of PP composites is shown in the Figure 2-F. The hardness of PP/RM blend decreases as the red mud concentration increases from 0 to 40 wt %. For example, hardness of the four different samples (with 10, 20, 30, and 40 wt% of red mud) are measured as 57.7, 56.2, 55.5 and 54.8 Shore D respectively. The hardness of pure PP is 58 Shore D. The minimum hardness is observed at the 40 wt % RM concentration for PP. In comparison with the hardness of virgin PP, the hardness decreased by 6% for the composites with a 40 wt % RM concentration. The relationship between the LOI and the percentage of the waste red mud powder of PP composites is shown in the Figure 2-G. The LOI of PP/RM blend increases as the red mud concentration increases from 0 to 40 wt %. For example, LOI of the four different samples (with 10, 20, 30, and 40 wt% of red mud) are measured as 11.7, 12.5, 12.7 and 12.9 % respectively. The LOI of pure PP is 11.6 %. The maximum LOI is observed at the 40wt % RM concentration for PP. In comparison with the LOI of virgin PP, the LOI increased by 11% for the composites with a 40 wt % RM concentration. The relationship between the density and the percentage of the waste red mud powder of PP composites is shown in the Figure 2-H. The density of PP/RM blend increases as the red mud concentration increases from 0 to 40 wt %. For example, density of the four different samples (with 10, 20, 30, and 40 wt% of red mud) are measured as 0.8075, 0.8112, 0.8157 and 0.8820 g/cm^3 respectively. The density of pure PP is 0.7945 g/cm^3. The maximum density is observed at the 40wt % RM concentration for PP. In comparison with the density of virgin PP, the density increased by 11% for the composites with a 40 wt % RM concentration.

3.2 Horizantal burn (HB) of PP/RM polymer composites: The specimen is placed horizontally and exposed to a Bunsen burner flame (h:20 mm) for 30 seconds. Any ignition or burning is noted. Burning over a 75 mm distance of less than 75 mm/min for specimens of less than 3 mm thick or less than 40 mm/min for specimen of 3 to 13 mm thick or less than 100 mm from the end of the specimen in the flame. This is the lowest (least flame retardant) UL 94 flame test rating. For every composition, six samples were tested, and the averages of the six measurements were reported. The relationship between the burning rate and the percentage of the red mud powder of PP composites is shown in the Table IV and Figure 3. With the addition of red mud in PP has been a change in burning rate values. The burning rate of PP/RM composites decreases as the red mud concentration increases from 0 to 40 wt %. For example, the burning rate of the four different samples (with 10, 20, 30 and 40 wt% of red mud) are measured as 35.0, 32.8, 31.6 and 31.2 mm/min respectively. The burning rate of pure PP is 35.3 mm/min. The minimum burning rate is observed at the 40 wt % RM concentration for PP. In comparison with the burning rate of virgin PP, the burning rate decreased by 12% for the composites with a 40 wt % RM concentration.

Table IV Horizontal burn criteria

Groups	Speciment sizes (mm) *Length x width x thickness*	Distance (mm)	Burning time (min) (75 mm zone)	Burning rate (mm/min)	Class
1	125 x 13 x 3	75	2.12	35.3	HB
2	125 x 13 x 3	75	2.14	35.0	HB
3	125 x 13 x 3	75	2.28	32.8	HB
4	125 x 13 x 3	75	2.37	31.6	HB
5	125 x 13 x 3	75	2.40	31.2	HB

Flame height: 20 mm. Flame impingement time (applied to 25 mm zone): 30 s

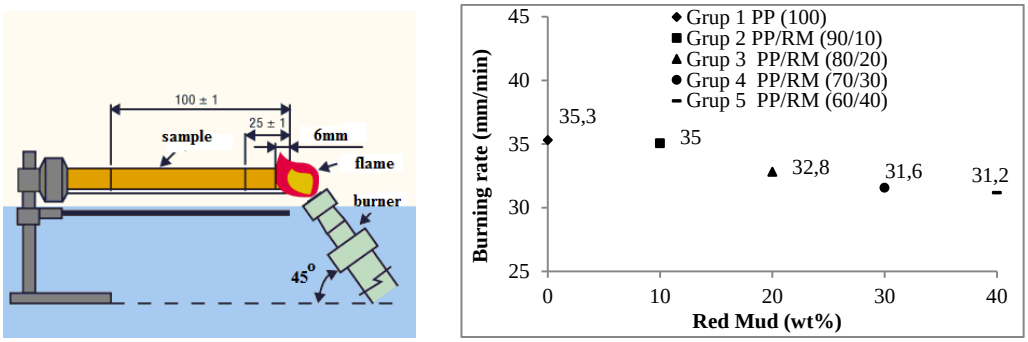

A.Horizontal burning test device [18] B. Burning rate

Figure 3 Horizontal burning test device and *burning rate of PP/RM polymer composites*

3.3 Wire flammability (glow wire) of PP/RM polymer composites: The glow wire test to IEC 60695-2-11 [19] is used to test electrical products, assemblies or individual components. The glow wire temperature is determined by the electrical equipment committee as a function of the type of risk arising when the product is used. During the test, a note is made of the burning time after an application time of 30 s, and the propping of burning or glowing particles of the specimen. The test is considered passed if a a) the specimen does not constitute an ignition risk to the environment and b)any flames or glowing on the test specimen extinguish not later than 30 seconds after removal of the ignition source. The relationship between the glow wire test criteria and the percentage of the red mud powder of PP composites is shown in the Table V. With the addition of red mud in PP has been a change in glow wire test values. The wire flammability of PP/RM composites decreases as the red mud concentration increases from 0 to 40 wt.

Table V Glow wire test criteria

(Pressing force: 1 N. Max. penetration depth:7 mm. Aplication time:30 s. Speciment sizes (mm): 70x70x10. Rate of approach and withdrawal: 10mm/ s)

Groups	Temperatures of glow wire (°C)	Flame (within 30 s)	Dropping	Dropping of burning
1	550	no	no	-
	600	no	yes	no
	650	yes	yes	no
2	550	no	no	-
	600	no	no	-
	650	no	yes	no
3	550	no	no	-
	600	no	no	-
	650	no	no	-

4	550	no	no	-
	600	no	no	-
	650	no	no	-
5	550	no	no	-
	600	no	no	-
	650	no	no	-

3.4 Morphological properties of PP/RM polymer composites: The SEM study was carried out to study the dispersion of waste red mud in the PP matrix. The boundaries and the contrast can be obviously seen between the red mud and PP matrix on the fractured surfaces of polymer matrix (Figure 4). The micrographs indicate that the all particulates are homogeneously dispersed on the fractured surfaces of polymer matrix.

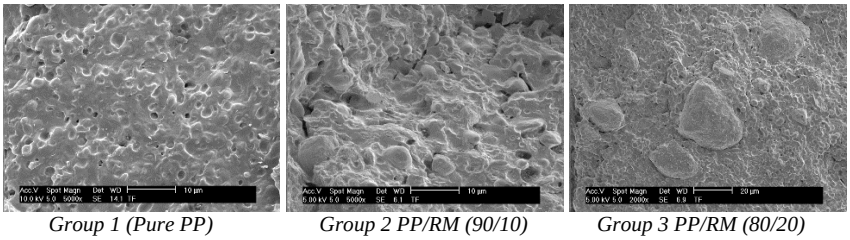

Group 1 (Pure PP) *Group 2 PP/RM (90/10)* *Group 3 PP/RM (80/20)*

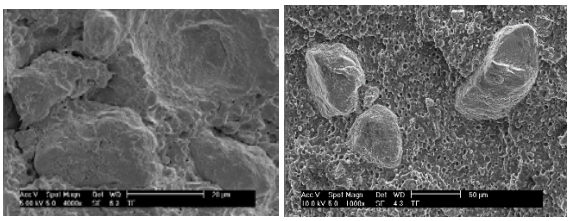

Group 4 PP/RM (70/30) *Group 5 PP/RM (60/40)*

Figure 4 SEM micrographs of the PP/RM polymer composites

4 CONCLUSIONS

Flammability and mechanical tests will be applied such as UL94 flammability test, limit oxygen index (LOI), wire flammability test method (glow wire), elasticity modulus, yield strength, tensile strength at break, % elongation, Izod impact strength, hardness, density. Also, SEM examination will be conducted to evaluate the microstructure of red mud particles as well as material distribution in these experiments. Red mud, an industrial waste, can be used as a potential filler material in polypropylene matrix composites. It has effects on the some properties of the composites. The following results were obtained:

1. The elasticity modulus, yield strength, tensile strength at break, % elongation, Izod impact strength and hardness of PP/RM composites decreased as the red mud concentration increases.
2. With the addition of red mud in PP has been a change in burning rate values. The burning rate of PP/RM composites decreases as the red mud concentration increases from 0 to 40 wt %.
3. The wire flammability of PP/RM composites decreases as the red mud concentration increases from 0 to 40 wt
4. The micrographs indicate that the RM particulates are homogeneously dispersed on the fractured surfaces of PP matrix.

References

[1] HS. Katz, and JV Mileski, 1987, *Handbook of Fillers for Plastics*, November 30, A Von Nostrand.
[2] S. Pavlidou, CD Papaspyrides, A review on polymer–layered silicate nanocomposites, *Prog. Polym. Sci*. 33, 1119−1198, 2008.
[3] YC. Chua, X. Lu, Polymorphism behavior of poly(ethylene naphthalate)/clay nanocomposites: The role of clay surface modification, *Langmuir*, 23, 1701−1710, 2007.
[4] L. Fogelstrom, E. Malmstrom, M. Johansson, A. Hult, Hard and flexible nanocomposite coatings using nanoclay filled hyperbranched polymers, *A. ACS Appl. Mater. Interfaces*, 2, 1679−1684, 2010.
[5] P.,Podsiadlo, AK. Kaushik, EM. Arruda, AM. Waas, BS. Shim, J. Xu, H. Nandivada, BG. Pumplin, J. Lahann, A. Ramamoorthy, NA. Kotov, Ultrasrtong and stiff layered polymer nanocomposites, *Science*, 318, 80−83, 2007.
[6] S. Pavlidou and C. D. Papaspyrides, *Prog. Polym. Sci*. 33, 1119, 2008.
[7] L. Fogelstrom, E. Malmstrom, M. Johansson, and A. Hult, *A. ACS Appl. Mater. Interfaces*, 2, 1679, 2010.
[8] RB. Seymour, *Engineering Polymer Source Book*, Mc-Graw Hill Pub Co., New York.1990.
[9] SAR. Hashmi and N. Chand, SEM Observation of Tensile Fractographs of Red Mud Filled Linear Low Density Polyethylene, *Journals of Material Science Letters*, 14, pp 377-379, 1995.
[10] Y. Pontikes, I. Vangelatos, D. Boufounos, D. Fafoutis, and G. Angelopoulus, "Environmental aspects on the use of bayer's process bauxite residue in the production of ceramics", *Advances in Science and Technology*, Vol. 45, 2176-2181, 2006.
[11] Y. Liu, C. Lin, and Y. Wu, "Characterization of red mud derived from a combined bayer process and bauxite calcination method", *Journal of Hazardous Materials*, Vol. 146, No. 1, 255-261, 2007.
[12] W. Pinnock, and J. Gordon, "Assessment of strength development in bayer-process residues", *Journal of Materials Science*, Vol. 27, No. 3, 692-696, 1992.
[13] N. Chand, S.A.R. Hashmi, Effect of Red Mud Addition on Abrasive Wear Rate of Isotactic Polypropylene/Low Density Polyethylene Blend under Low Stress Conditions, *J Sci Ind Res*, 58, 795, 1999.
[14] J. Pradhan, S.N., Das, R.S. Thakur, Adsorption of Hexavalent Chromium from Aqueous Solution by Usin Activated Red Mud, *J Colloid Interface Sci*, 217, 137, 1999.
[15] T. Agag, T. Koga, T. Takeichi, Studies on thermal and mechanical properties of polyimide–clay nanocomposites, *Polymer*, 42, 3399, 2001.
[16] B.Z. Jang, Control of interfacial adhesion in continuous carbon and kevlar fiber reinforced polymer composites, *Compos Sci Technol*, 44, 333, 1992.
[17] M. Tasdemir, M. Kurt, Acrylonitrile Butadiene Styrene/Red Mud Polymer Composites: Ultraviolet Annealing, *Advanced Science, Engineering and Medicine* Vol. 8, 804–809, 2016.
[18] https://www.plasticsportal.net/wa/plasticsEU~en_GB/portal/show/common/content/campaigns/fire_protection/englisch/material.html
[19] XXX IEC 60695-2-11 Fire hazard testing - Part 2-11: Glowing/hot-wire based test methods - Glow-wire flammability test method for end-products (GWEPT)

Acknowledgement: This work has been supported by the Scientific Research Project Program of Marmara University (project no: FEN-C-YLP-081117-0630).

ICENS 4TH INTERNATIONAL CONFERENCE ON ENGINEERING AND NATURAL SCIENCE
2-6 May 2018 KIEV UKRAINE

Tribological Properties of HDPE/Urea Formaldehyde Polymer Blends

***Munir Tasdemir*[1]**

Abstract

Polymer alloys and blends are of great interest academically and technologically. In many cases, a balance between the hardness and toughness is desired. The hardness of many synthesized polymers is characterized by brittleness and crack propagation upon impact. Therefore, improvement of the toughness was the subject of academic and technological investigations.
In this study, tribological properties of the high density polyethylene/urea formaldehyde polymer blends were investigated. The addition of urea formaldehyde to high density polyethylene changed the tribological properties of the blends significantly. High density polyethylene matrix contributes to ground urea formaldehyde powder is handled as 0, 5, 10, 20 and 30 % ratio will be mixed in the extruder. Mixture obtained from the extruder to be granulated and then the granules will be obtained as appropriate standard test sample of the injection molding machine. SEM examination will be conducted to evaluate the microstructure of urea formaldehyde particles as well as material distribution in these experiments.

Keywords: tribology, polyethylene, urea formaldehyde, powder, polymer blends.

1. INTRODUCTION

High density polyethylene (HDPE) is widely used as a commodity polymer with high-tonnage production due to its distinctive mechanical and physical properties. Because of its low toughness, weather resistance, and environmental stress cracking resistance as compared to engineering polymers, its application in many areas has been limited. To improve these disadvantages, HDPE has been reinforced with fillers [1-4]. The wear resistance of polymer composites is significantly decreased and increased depending upon the type of particles, particles size and size distribution, interfacial actions between polymer matrix and fillers, as well as wear test conditions, i.e., wear mode, sliding distance, applied load, test temperature, and humidity [5]. Urea-formaldehyde (UF) accounts for about 15% of the total thermoset resin production. Currently, one of its major applications is in molded products, including electrical equipment, dinner ware, buttons, cosmetic caps, and bottles. However, the same factors that make UF a good choice for many applications, namely its chemical, thermal, and mechanical stability, are also what make recycling such a big challenge [6]. Much research on the wear performance of polymer has been reported elsewhere [7-12]. However, very little has been reported on the wear performance of the HDPE/UF polymer composites. Further, research into the wear of polymers has usually investigated the effects of a single factor-such as sliding distance, sliding speed, or contact pressure on the wear performance. In this study, high density polyethylene matrix contributes to ground urea formaldehyde powder is handled as 0, 5, 10, 20 and 30 % ratio will be mixed in the extruder. Mixture obtained from the extruder to be granulated and then the granules will be obtained as appropriate standard test sample of the injection molding machine.

2. EXPERIMENTAL

2.1 Compositions and Materials

Five different polymer blends were prepared. Compositions of HDPE/waste urea formaldehyde (UF) polymer blends that were formed are given in Table I.

[1] *Marmara University, Technology Faculty, Metallurgy and Materials Eng. Dep., Istanbul, 34722, Turkey*
munir@marmara.edu.tr

Table I Composition of the different polymer blends formulations

Groups	HDPE (wt %)	Waste urea formaldehyde (wt %)
1	100	-
2	90	5
3	85	10
4	75	20
5	65	30

High-density polyethylene (HDPE) (I-668 UV) was supplied by Petkim (Izmir-Turkey). Specific gravity is 0,970 g/cm^3. Melt flow rate is 5.2 g/10 min (190ºC–2.16 kg). Yield strength is 28 MPa and notched Izod impact (23ºC) is 12 kJ/m^2.Waste urea formaldehyde was supplied Viko by Panasonic Company (Istanbul-Turkey).

2.2 Sample Preparation

UF was dried in a Yamato vacuum oven ADP-31 (Yamato/VWR Scientific Products, Japan) at 105 ºC for 24 hours before being blended with HDPE. Mechanical premixing of solid compositions was done using a LB-5601 liquid-solids blender (The Patterson-Kelley Co., Inc. east Stroudsburg, PA - USA) brand batch blender for 20 min. Samples with various proportions of HDPE/PU polymer composites were produced between 190-220 ºC at 25-35 bar pressure, and a rotation rate of 20 rpm, with a Microsan **co-rotating** twin-screw extruder (Microsan Instrument Inc. Kocaeli - Turkey). Polymer composites were also dried in vacuum oven at 105 ºC for 24 hours after extrusion. Subsequently, test samples were molded in injection molding machine. Extrusion and injection conditions are given in Table II.

Table II Extrusion and injection conditions of the HDPE/UF polymer composites

3. PROCESS	Extrusion	Injection
Temperature (º C)	190–220	190–220
Pressure (bar)	25-35	110–130
Waiting time in mold (s)	-	20
Screw speed (rpm)	20	20
Mould temperature (ºC)	-	40

Waste urea formaldehyde dry grinded with Siemens simatic C7-621 control system device to obtain unsegregated powders. The size of urea formaldehyde particles varied between 10–80µm. Powder preparations steps are given in Figure 1.

waste *granulation* *powder*

Figure 1 Waste urea formaldehyde powder preparation steps

2.3 Physical characterization

For every composition, five samples were tested, and the averages of the five measurements were reported. Heat deflection temperature (HDT) and Vicat softening point tests were done according to ISO 75 and ISO 307 standard with determined by CEAST 6521. HDT-Vicat test equipment. Flow behavior testing of all the mixtures was done according to ISO 1133 standard with Zwick 4100 MFI equipment. Moisture testing of all the mixtures was done according to ASTM D 6980 standard with Kern DBS 60-3 equipment. Limit oxygen index (LOI) testing of all the mixtures was done according to ISO 4589 standard with Devotrans LOI equipment.

2.4 Tribological Tests

Static coefficient of friction test was done according to the ISO 8295 method with Devotrans friction coefficient measurement equipment. The dimensions of the tested specimens were 80x200x4 mm and the dimensions of the sled specimens were 63x63x4 mm. Speed was selected as 100 mm/min.

Static coefficient of friction (μs): The force increases linearly to a maximum which represents the static frictional force F_S. Measurements made at a high friction drag permit the dynamic coefficient of friction to be calculated, but not the static coefficient of friction. The static coefficient of friction μs is given by the equation,

$$\mu s = F_S / F_P \quad (1)$$

Where F_S is the static frictional force, expressed in Newton, F_P is the normal force exerted by the mass of the sled, expressed in Newton [13].

Wear rate: The wear tests were done according to the DIN 53 516 method with Devotrans DA5 (Devotrans quality control test equipment Istanbul-Turkey) abrasion test equipment. The thickness of the test specimens was 7.0 mm and diameter was 15.5 mm. Cylinder rotational speed was selected as 40 rpm and normal load (F_N) of 10N was used. Total sliding distance (L) was 40 m. The mass loss of the samples (Δm) was measured after the wear process, and the specific wear rates (Ws) were calculated using the following equation:

$$Ws = (\Delta m)/\rho . F_N . L \ (mm^3/Nm) \quad (2)$$

Where Δm is the specimen's mass loss, ρ is the density of specimen, F_N is the normal load applied, and L is the total sliding distance. The friction coefficients and wear rates reported in the present study were the averages of at three measurements.

2.5 Microscopy

The fractured surfaces of the composites were coated to an approximate thickness of 10 nm of a gold (Au) (80%)/palladium (Pd) (20%) alloys to prevent electrical charging by Polaron SC 7620 (Gala Instrumente GmbH, Bad Schwalbach-Germany). The surfaces of the prepared samples were observed by the JEOL-JSM 5910 LV (**JEOL Ltd.,** Tokyo, Japan) scanning electron microscopy (SEM) at an acceleration voltage of 5-20 kV.

3. RESULT AND DISCUSSION

3.1 Physical properties of HDPE/UF blends

The relationship between the vicat softening point and the percentage of the waste urea formaldehyde powder of HDPE blend is shown in the Figure 2-A. With the addition of UF in HDPE has been a change in vicat softening point values. The Vicat softening point of HDPE/UF blend decreases as the urea formaldehyde concentration increases from 0 to 30 wt %. For example, the Vicat softening points of the fore different samples (with 5, 10, 20, and 30 wt% of urea formaldehyde) are measured as 132.2, 129.4, 128.5 and 122.2 ^oC respectively. The vicat softening point of pure HDPE is 132.5, ^oC. The minimum vicat softening point is observed at the 30 wt % UF concentration for HDPE. In comparison with the vicat softening point of virgin

HDPE, the vicat softening point decreased by 8% for the composites with a 30 wt % UF concentration. The relationship between the HDT and the percentage of the waste urea formaldehyde powder of HDPE blend is shown in the Figure 2-B. The HDT of HDPE/UF blend decreased as the urea formaldehyde concentration increases from 0 to 30 wt %. For example, the HDT of the four different samples (with 5, 10, 20, and 30 wt% of urea formaldehyde) are measured as 50.1, 49.1, 48.9 and 48.1 ºC respectively. The HDT of pure HDPE is 52.4 ºC. The minimum HDT is observed at the 30 wt % UF concentration for HDPE. In comparison with the HDT of virgin HDPE, the HDT decreased by 8% for the composites with a 30 wt % UF concentration.

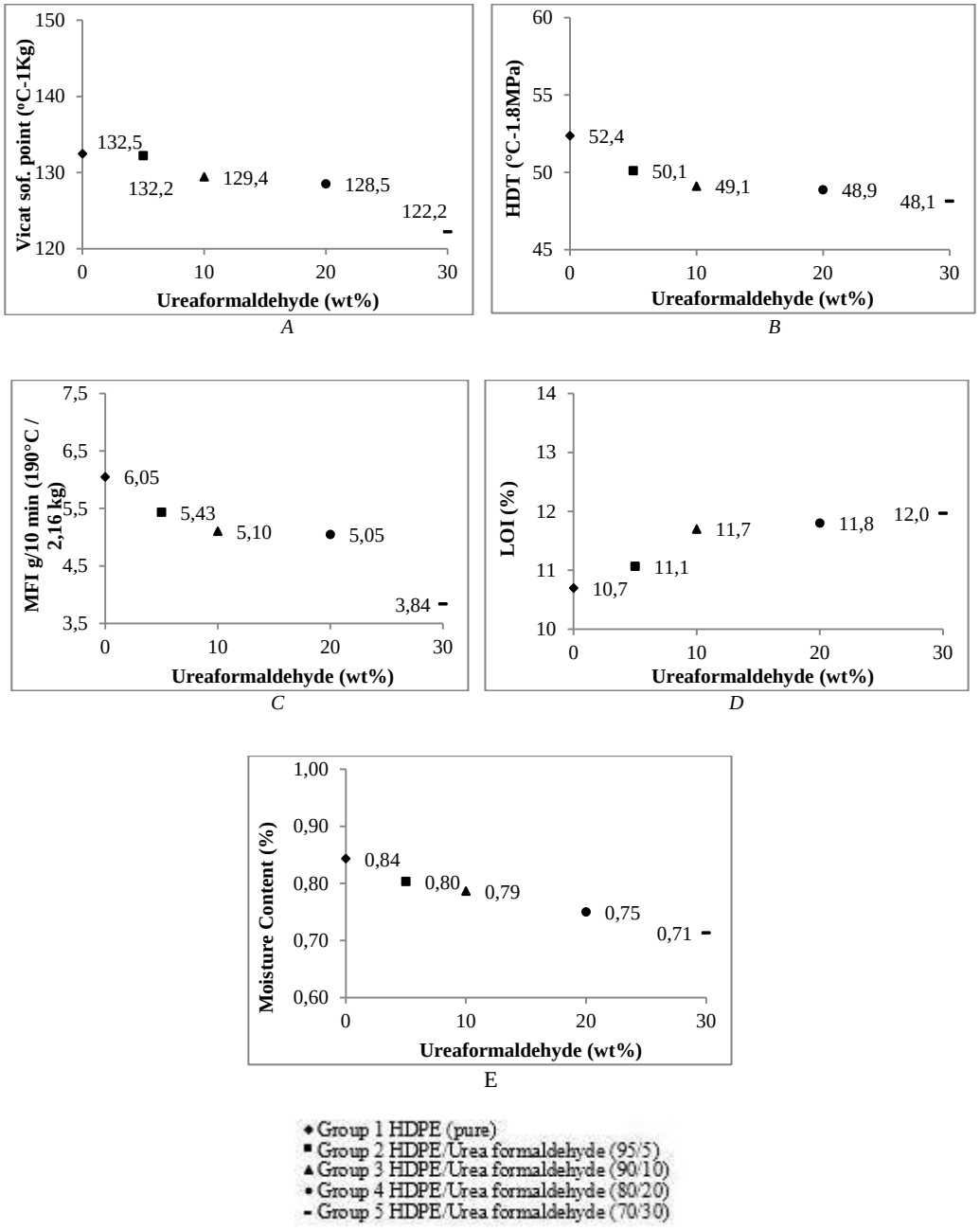

Figure 2 Physical properties of HDPE/UF polymer composites

The relationship between the MFI and the percentage of the waste urea formaldehyde powder of HDPE blend is shown in the Figure 2-C. The MFI value decreased with the addition of urea formaldehyde (from 0 to 30

wt % UF). The maximum MFI is observed at pure HDPE. In comparison with the MFI of pure HDPE, the MFI decreased by 37% for the composites with a 30 wt % UF concentration. The relationship between the LOI and the percentage of the waste urea formaldehyde powder of HDPE blend is shown in the Figure 2-D. The LOI of HDPE/UF blend increased as the urea formaldehyde concentration increases from 0 to 30 wt %. The LOI of the four different samples (with 5, 10, 20, and 30 wt% of urea formaldehyde) are measured as 11.1, 11.7, 11.8 and 12.0 % respectively. The LOI of pure PP is 10.7 %. The maximum LOI content is observed at the 30 wt % UF concentration for HDPE. In comparison with the moisture content of virgin HDPE, the moisture content increased by 12% for the composites with a 30 wt % UF concentration. The relationship between the moisture content and the percentage of the waste urea formaldehyde powder of HDPE blend is shown in the Figure 2-E. The moisture content of HDPE/UF blend decreased as the urea formaldehyde concentration increases from 0 to 30 wt %. For example, the moisture content of the four different samples (with 5, 10, 20, and 30 wt% of urea formaldehyde) are measured as 0.80, 0.79, 0.75 and 0.71 % respectively. The moisture content of pure HDPE is 0.84 %. The minimum moisture content is observed at the 30 wt % UF concentration for HDPE. In comparison with the moisture content of virgin HDPE, the moisture content decreased by 15% for the composites with a 30 wt % UF concentration.

3.2 Wear properties of HDPE/UF polymer blends

Obviously, the tribological processes involved in this investigation are complex. The effects of sliding distance and urea formaldehyde content on the tribological behaviors of HDPE composites were examined. The wear rate for various specimens sliding distance against the sand paper (#60) under 10N load and 0,32 m/s abrasion speed. It can be seen that the wear rate of composites increase with increasing urea formaldehyde content. The values of wear rate are shown in Figure 3. The wear rate of HDPE/UF composites increases as the urea formaldehyde concentration increases from 0 to 30 wt %, which could be attributed to the weakened adhesion between the urea formaldehyde and HDPE matrix in the presence of an excessive amount of urea formaldehyde particulates. The weak bond led to the urea formaldehyde particles detaching from the HDPE and the HDPE pulling out more easily, which could increase the wear rate of the composite. So, a high level of the urea formaldehyde led to the high wear rate of the composite.

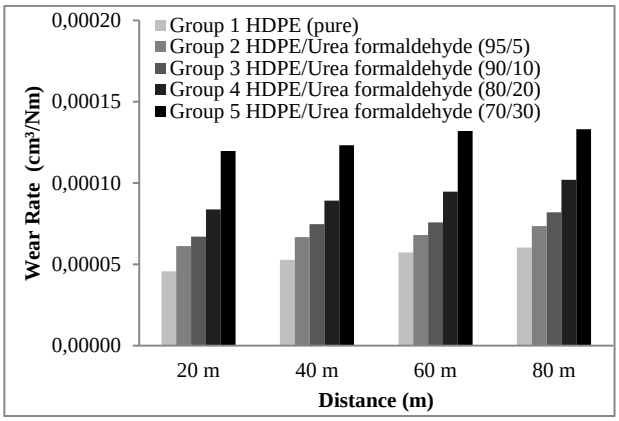

Figure 3 Wear rates of the HDPE/UF polymer composites

3.3 Static friction coefficients of the urea formaldehyde filled HDPE

Static friction performance is shown in Figure 4 when speed was 100mm/min; load separately was 1.96, 2.94, 3.92, 4.90 and 6.86 N respectively. It is seen that the UF ratio and load had a great effect on the static friction coefficient of the composite. As the UF ratio and load increases, the static friction coefficient of all kinds of composites increases.

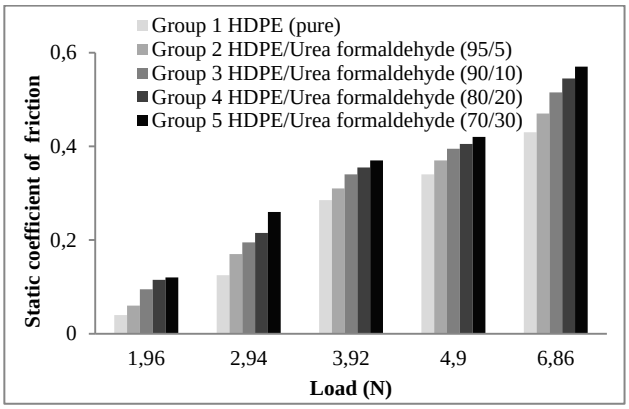

Figure 4 Static friction coefficients of the HDPE/UF polymer composites against load

3.4 Morphological properties of HDPE/UF polymer blends

The SEM study was carried out to study the dispersion of waste urea formaldehyde in the HDPE matrix. The boundaries and the contrast can be obviously seen between the urea formaldehyde and HDPE matrix on the fractured surfaces of polymer matrix (Figure 5). The micrographs indicate that the UF particulates are homogeneously dispersed on the fractured surfaces of polymer matrix.

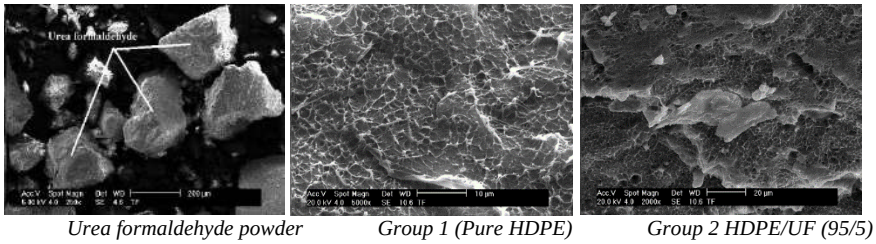

Urea formaldehyde powder *Group 1 (Pure HDPE)* *Group 2 HDPE/UF (95/5)*

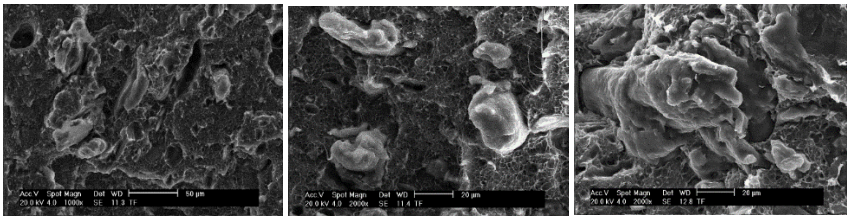

Group 3 HDPE/UF (90/10) *Group 4 HDPE/UF (80/20)* *Group 5 HDPE/UF (70/30)*

Figure 5 SEM micrographs of the HDPE/UF polymer blends

4 CONCLUSIONS

The effects of waste urea formaldehyde on the physical properties such as vicat softening point, HDT, MFI, LOI and moisture content of HDPE/UF blends were investigated. Also, the effects of waste urea formaldehyde on the tribological properties such as wear rate and static friction coefficient of HDPE/UF blends were investigated. The vicat softening point, HDT, MFI and moisture content of HDPE/UF blend decreased as the urea formaldehyde concentration increases from 0 to 30 wt %. On the other hand, the LOI of HDPE/UF blend increased as the urea formaldehyde concentration increases from 0 to 30 wt %. The wear rate of HDPE/UF composites increases as the urea formaldehyde concentration increases from 0 to 30 wt %, which could be attributed to the weakened adhesion between the urea formaldehyde and HDPE matrix in the

presence of an excessive amount of urea formaldehyde particulates. The addition of urea formaldehyde to the HDPE changed significantly the friction coefficient of the composites. Applied load and UF ratio had a great effect on the friction coefficient of composites. The micrographs indicate that the urea formaldehyde particulates are homogeneously dispersed on the fractured surfaces of HDPE matrix.

References

[1] M. Tasdemir and H. Yildirim, 'Efffect of styrene-butadiene-styrene addition on polystyrene/high-density polyethylene blends'J. Appl. Poly. Sci., Vol.83, 2967-2975, 2002.
[2] Y. Wang, J. Shi, L, Han and F, Xiang, 'Crystallization and mechanical properties of T-ZnOw/HDPE composites 'Mater Sci Eng A , 501, 220-228, 2009
[3] R.N. Rothon, Particulate-Filled Polymer Composites; Longman Scientific and Technical: Harlow, 1995.
[4] R.N. Rothon, 'Mineral Fillers in Thermoplastics: Filler Manufacture and Characterisation 'Adv Polym Sci, 139, 67-107, 1999.
[5] P. Podsiadlo, A.K. Kaushik, E.M. Arruda, A.M.Waas, B.S. Shim, J. Xu, H. Nandivada, B.G. Pumplin, J. Lahann, A. Ramamoorthy and N.A. Kotov, 'Ultrastrong and stiff layered polymer nanocomposites 'Science, 80, 318, 2007.
[6] D.B. Evelin, C.W. Chris and T.S. Montgomery, 'Mechanical properties of blends of HDPE and recycled urea-formaldehyde resin' Journal of Applied Polymer Science, 77, 3220 –3227, 2000.
[7]L. Zhenhua and L. Yunxuan,' Mechanical and tribological behavior of UHMWPE/HDPE blends reinforced with SBS' Poly. Plast. Tech. and Eng., 51, 750, 2012.
[8] K.S. Karuppiah, A.L. Bruck, S. Sundararajan, J. Wang, Z. Lin, Z.H. Xu and X. Li, 'Friction and Wear Behavior of Ultra-High Molecular Weight Polyethylene as a Function of Polymer Crystallinity' Acta Biomaterialia, 4, 1401, 2008.
[9] A.L. Bruck, K.S. Karuppiah, S. Sundararajan, J. Wang and Z. Lin, 'Friction and wear behavior of ultrahigh molecular weight polyethylene as a function of crystallinity in the presence of the phospholipid dipalmitoyl phosphatidylcholine' J Biomed Mater Res B Appl Biomater., 93(2), 351, 2010.
[10] M. Tasdemir and I. Miskioglu, 'Friction and Wear Behaviors of HIPS/SBS Polymer Blends' Int. J. of Mat. And Manufacturing, 4/2, 95-99, 2016.
[11] M. Tasdemir and S. Ersoy, 'Friction and wear performance of HDPE/talc-calcium carbonate polymer composites against sliding distance and applied load'Romanian journal of materials, 3/ 44, 257-264, 2014.
[12] M. Tasdemir and U.Yerlesen, 'Study on the friciton and wear behaviors of modified HDPE/glass spheres composites' Romanian journal of materials, 1/ 45, 59-66, 2015.
[13] ISO 8295:1995(E) test standard: Plastics-Film and sheeting-Determination of the coefficients of friction.

Acknowledgement: This work has been supported by the Scientific Research Project Program of Marmara University (project no: FEN-C-YLP-081117-0630).

ICENS 4TH INTERNATIONAL CONFERENCE ON ENGINEERING AND NATURAL SCIENCE
2-6 May 2018 KIEV UKRAINE

Input Variance Constrained Control of Morphing Tactical Unmanned Aerial Vehicles (TUAVs)

Coban Sezer [1], Oktay Tugrul[2]

Abstract

In this study, using dynamic model of passive and active morphing featured Tactical Unmanned Aerial Vehicle (TUAV) called as ZANKA III which is produced in Erciyes University, Faculty of Aeronautics and Astronautics, Model Aircraft Laboratory, under the TUBITAK ARDEB 1001 program and designing Input Constrained Variance Controller (IVC) for aircraft tracking the desired trajectory achieved with minimal vibration and minimum energy consumption. For this purpose, using MATLAB, in the simulation environment, studies have been performed and closed loop responses have been obtained. Longitudinal motion is in primary interest, desired putput is pitching angle of TUAV, and desired input is elevator angle.

Keywords: TUAVs, Flight Performance, Variance Constrained Controller.

1. INTRODUCTION

Numerous casualties have been experienced in basic military missions, such as exploration, surveillance and intelligence, especially in the enemy air. During the performance of such tasks, a higher level of performance necessity in the tasks of human life not to be put in danger and long enough for the human structure to withstand could make it necessary for unmanned aerial vehicles to be used in these missions. In this respect, the missions stated with human aircrafts are carried out by unmanned aerial vehicle systems and the above-mentioned undesirable situations are eliminated. The unmanned aerial vehicle systems are equipped with necessary equipment to perform such missions [1].

The precise UAV observed in this article is Tactical UAVs (i.e. TUAVs). TUAVs are heavier class of UAVs (range from 50 kg to 1,500 kg) that fly at higher altitudes (range from 3000 m to 12000 m) and are presently applied principally to support military applications. The classification of Tactical UAVs is listed next: EN-TUAV (long endurance TUAV), LR-TUAV (long range TUAV), SR-TUAV (short range TUAV) and CR-TUAV (close range TUAV) [2]. Our TUAV called as ZANK III is in the class of CR-TUAV.

In this conference article input variance constrained controllers for vibration control of TUAVs is first time evaluated in TUAVs in the literature.

2. TACTICAL UAV IN LITERATURE

With the Cold War era, nuclear threats have increased steadily. Therefore, unmanned aerial vehicles have begun to be used for exploration purposes. Following the designs, the designs started to develop continuously and the first Tactical Unmanned Aerial Vehicle specimens started to be formed. Camera systems were first added to tactical unmanned aerial vehicles. Then NBC field detection systems, radar, IR camera, etc. installation.

The Vietnam War emphasized the importance of unmanned aerial vehicles, and unmanned aerial vehicles were produced in the 1960s with many short, medium and long range varieties. However, although the Vietnam War made these tools more noticeable, the budgetary strains from warfare have brought many tactical unmanned aerial vehicles into production.

[1] *College of Aviation, Iskenderun Technical University, Iskenderun, Turkey, sezer.coban@iste.edu.tr*

[2] *Faculty of Aeronautics and Astronautics, Erciyes University, Kayseri, Turkey, tugruloktay52@gmail.com*

An aircraft with an altitude of 8,000 meters with a maximum take-off weight ranging from 4 to 12 hours for exploration and surveillance and ranging from 50 to 1500 kg, is now more suitable for the most accepted definition of TUAV [3].

3. OUR TACTICAL UNMANNED AERIAL VEHICLE

Some of the technical properties of our produced TUAV called as ZANKA-III are listed in Table 1. It is also illustrated in Fig 1.

Table I. Some Properties of Zanka III

Property	Magnitude
Total Take-off Weight	50 kg
Total Payload	15 kg (5 kg of fuel)
Aircraft Length and Width	4 m wing span 2.188 m longitudinal length
Engine Horse Power (HP)	18 Hp
Maximum Flight Range	2550 km
Maximum Flight Endurance	28.7 h
Speed For Maximum Flight Endurance	88. 9 km/h
Flight Ceiling Altitude	12792 m

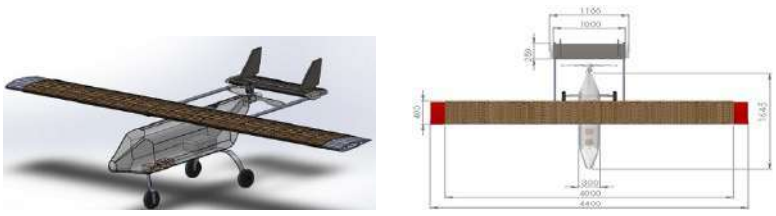

Figure 1. Drawings of ZANKA-III

In Eq. 1 the longitudinal state-space model is given and it is used for flight control system design [4] .

$$\begin{bmatrix}\Delta\dot{u}\\ \Delta\dot{w}\\ \Delta\dot{q}\\ \Delta\dot{\theta}\end{bmatrix}=\begin{bmatrix}X_u & X_w & 0 & -g\\ Z_u & Z_w & u_0 & 0\\ M_u+M_{\dot{w}}Z_w & M_w+M_{\dot{w}}Z_w & M_q+M_{\dot{w}}u_0 & 0\\ 0 & 0 & 1 & 0\end{bmatrix}\begin{bmatrix}\Delta u\\ \Delta w\\ \Delta q\\ \Delta\theta\end{bmatrix}+\begin{bmatrix}X_{\delta_T} & X_{\delta_e}\\ Z_{\delta_T} & Z_{\delta_e}\\ M_{\delta_T}+M_{\dot{w}}Z_{\delta_T} & M_{\delta_e}+M_{\dot{w}}Z_{\delta_e}\\ 0 & 0\end{bmatrix}\begin{bmatrix}\Delta\delta_T\\ \Delta\delta_e\end{bmatrix} \quad (1)$$

In Eq. 2 the lateral state-space model is given and it is used for flight control system design [4] .

$$\begin{bmatrix}\Delta\dot{v}\\ \Delta\dot{p}\\ \Delta\dot{r}\\ \Delta\dot{\Phi}\end{bmatrix}=\begin{bmatrix}Y_v & Y_p & -(u_0-Y_r) & g\cos\theta_0\\ L_v & L_p & L_r & 0\\ N_v & N_p & N_r & 0\\ 0 & 1 & 0 & 0\end{bmatrix}\begin{bmatrix}\Delta v\\ \Delta p\\ \Delta r\\ \Delta\Phi\end{bmatrix}+\begin{bmatrix}0 & Y_{\delta_r}\\ N_{\delta_a} & L_{\delta_r}\\ N_{\delta_a} & N_{\delta_r}\\ 0 & 0\end{bmatrix}\begin{bmatrix}\Delta\delta_a\\ \Delta\delta_r\end{bmatrix} \quad (2)$$

4. INPUT VARIANCE CONSTRAINED VIBRATION CONTROL

For a known continuous linear time invariant (LTI), stabilizable and detectable plant (see [5,6])

$$\dot{x}_p = A_p x_p + B_p u_p + w_p,\ y = C_p x_p,\ z = M_p x_p + v \quad (3)$$

and a positive definite input penalty matrix, $R > 0$, determine a full order dynamic controller

$$\dot{x}_c = A_c x_c + Fz,\quad u_p = G\ x_c \quad (4)$$

to answer the problem

$$\min_{A_c,F,G}\ J = E_\infty\ y^T R y \quad (5)$$

expose to variance constraints on the input or inputs

$$E_\infty\ u_i^2 \le \mu_i^2,\qquad i = 1,....,n_u \quad (6)$$

Above *y* and *z* characterize inputs of interest and sensor measurements, respectively, u_p is the control vector, w_p and *v* are zero-mean uncorrelated Gaussian white noises with intensities of *W* and *V*, respectively, *F* and *G* are state estimator and controller gain matrices, respectively, x_c is the controller state vector, μ_i^2 is the upper limit imposed on the *i*-th input variance, n_u is the number of inputs, and furthermore $E_\infty \triangleq lim_{t\to\infty}E$, and *E* is the expectation operator. Finally, ^{T} symbolizes matrix transpose operator. After the algorithm [5,6] converges and the input penalty matrix *R* is determined, IVC parameters are

$$A_c = A_p + B_p G - F M_p,\ F = X M_p^T V^{-1},\ G = -R^{-1} B_p^T K \quad (7)$$

Above, *X* and *K* are solutions of solutions of two algebraic Riccati equations:

$$0 = XA_p^T + A_p X - XM_p^T V^{-1} M_p X + W$$

(8a) $$0 = KA_p + A_p^T K - KB_p R^{-1} B_p^T K + C_p^T Q C_p$$ (8b)

5. RESULTS

In Fig. 2 closed loop responses after using soft and tight variance constraint on input are given. It can be seen that when tight input variance constrained used for aircraft elevator angle its peak values decreases. On the other hand, the peak values of aircraft pitch angle which is the output of interest increases. In both cases IVC exponentially stabilizes closed loop systems. When soft input variance constrained used for aircraft elevator angle, its peak values increases. On the other hand, the peak values of aircraft pitch angle which is the output of interest decreases.

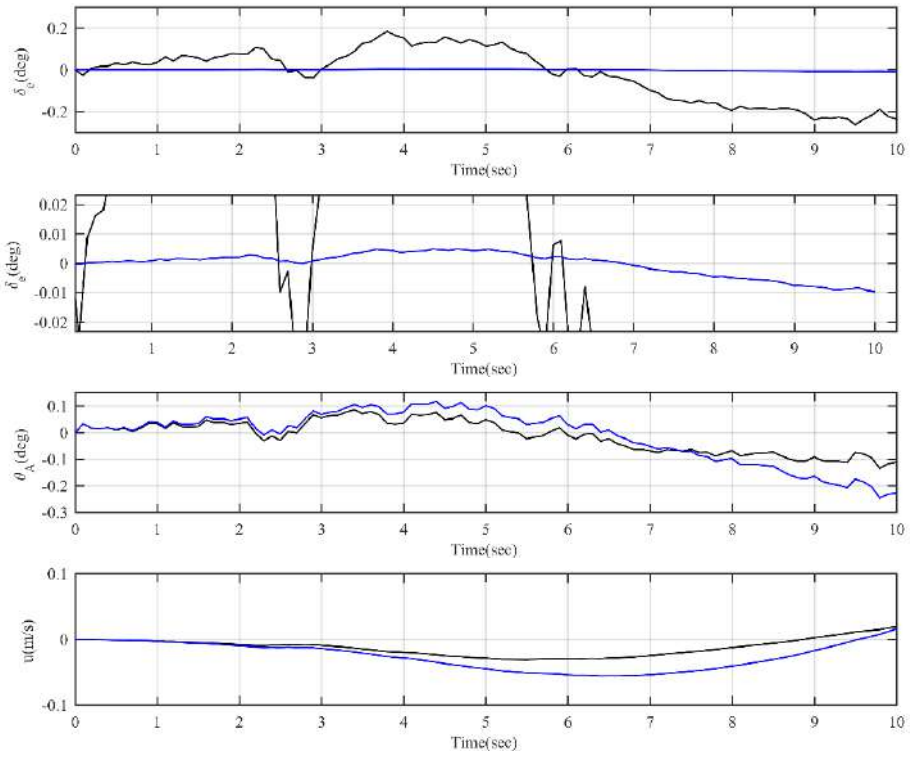

Figure 2. Longitudinal Autopilot Design and Closed Loop Responses (Blue: Tight IVC, Black: Soft IVC)

6. CONCLUSIONS

Effects of using input variance constrained control on Tactical Unmanned Aerial Vehicles are examined. For this purpose dynamic model of passive and active morphing featured Tactical Unmanned Aerial Vehicle (TUAV) called as ZANKA III which is produced in Erciyes University, Faculty of Aeronautics and Astronautics, Model Aircraft Laboratory, under the TUBITAK ARDEB 1001 program is used. It is found that when tight constrained on IVC is used, the peak values of outputs of interest increases. On the other hand, the peak values of inputs of interest decreases. For other case, opposite results are fund.

REFERENCES

[1] R. Austin, *Unmanned aircraft systems*. Wiley, 2010.
[2] MSI Monthly Defense Technologies Journal
[3] M. F. Bento, *Unmanned aerial vehicles: An Overview*. Working papers, 2008.
[4]Nelson, R. C. 2007. Flight Stability and Automatic Control. 2nd ed., McGraw-Hill, New York, chapters 2-6.
[5] Hsieh C., Skelton R. E. and Damra F. M., 1989, Minimum energy controllers with inequality constraints on input variances, Optimal Control Application and Methods, 10 (4), 347-366.
[6] Zhu G. and Skelton R E., 1991, Mixed L_2 and L_∞ problems by weight selection in quadratic optimal control. *International Journal of Quadratic Optimal Control*, 63 (5) : 1161-1176.
[7] Sadegh, P., Spall, J. C. (1998). Optimal random perturbations for multivariable stochastic approximation using a simultaneous perturbation gradient approximation, IEEE Transactions on Automatic Control, 43 (10), 1480-1484.
[8] Oktay T., Coban S. , "Variance Constrained Vibration Control of Morphing Tactical Unmanned Aerial Vehicles (TUAVs)", 2. International Defence Industry Symposium, KIRIKKALE, TURKIYE, 6-8 Nisan 2017, pp.12-16

Acknowledgement

This work was supported by Research Fund of the Erciyes University, Project no. FBA-2018-6712.

This work was also supported by Research Fund of The Scientific and Technological Research Council of Turkey (TUBITAK) under Project Number: 115M603.

ICENS 4TH INTERNATIONAL CONFERENCE ON ENGINEERING AND NATURAL SCIENCE
2-6 May 2018 KIEV UKRAINE

Unmanned Aerial Vehicles (UAVs) by Engine Type

Coban Sezer [1], Oktay Tugrul[2]

Abstract

Unmanned Aerial Vehicles (UAVs) can be classified according to their civilian and military use and performance characteristics such as weight, distance to air, wing load, range and speed. In this study, the types of engine used in unmanned aerial vehicles and the advantages, disadvantages and differences between these types of engines are mentioned. Unmanned Aerial Vehicles(UAV) are used in many different tasks and need different engine types depending on the area they are used to perform these tasks. Two-stroke, Turbofan, Turboprop, Piston engine, Electric and Propeller types are different types of engines used in Unmanned Aerial Vehicles(UAV). Piston engines and electric engines are the most commonly used types. Unmanned Aerial Vehicles(UAV) also vary in engine size and type, as well as aircraft sizes and weights, as in humans. Electric engines are generally used in light and small models, while piston engines are used in heavy and large models.

Keywords: UAVs, Engine

1. INTRODUCTION

They are, in their simplest terms, vehicles that can be manipulated by remote control, autonomously directing themselves or both, loading and unloading their useful cargo into their main body, and landing at the end of the mission. In other words, these tools are also called "drone".

In recent years, "Unmanned Aerial Vehicle Systems" have just started to be used for these new unmanned vehicles, mostly known as "unmanned aerial vehicles" in the development process. The reason is that the unmanned aerial vehicle implies only the aircraft platform and cannot meet the entire system that is flying it. But both countries and institutions seem to use different terminologies for air vehicles. For example, while Israel's official open sources are often referred to simply as "unmanned aerial vehicles", British and European Union official open sources seem to use the concept of "Remotely Piloted Aircraft Systems (RPAS)", a sub-component of unmanned aerial vehicles. Despite this, the notion of "unmanned aerial vehicle system", which is used both by the sector representatives and by the country as the most accepted concept in the literature, stands out because it expresses the whole of the system.

With the revolution in the military technology that lived in the 90s, the unmanned aerial vehicles that can be operated in any weather condition for a longer time, much more remotely controlled, have come to the point where intelligence, exploration and surveillance tasks are indispensable. From the beginning of the 2000's, the use of the armed versions started. The work of the world public to recognize and perceive these systems has also been influenced by the effects of armed versions.

The unmanned aerial vehicle system has a complex structure and can perform its function by integrating various elements. In other words, it is a system that requires coordinated and coordinated operation of multiple components as shown in Figure 1. Unlike the flying of human systems, it is a system that brings together the sub-elements and works in a synchronized manner [1].

[1] *College of Aviation, Iskenderun Technical University, Iskenderun, Turkey, sezer.coban@iste.edu.tr*

[2]*Faculty of Aeronautics and Astronautics, Erciyes University, Kayseri, Turkey, tugruloktay52@gmail.com*

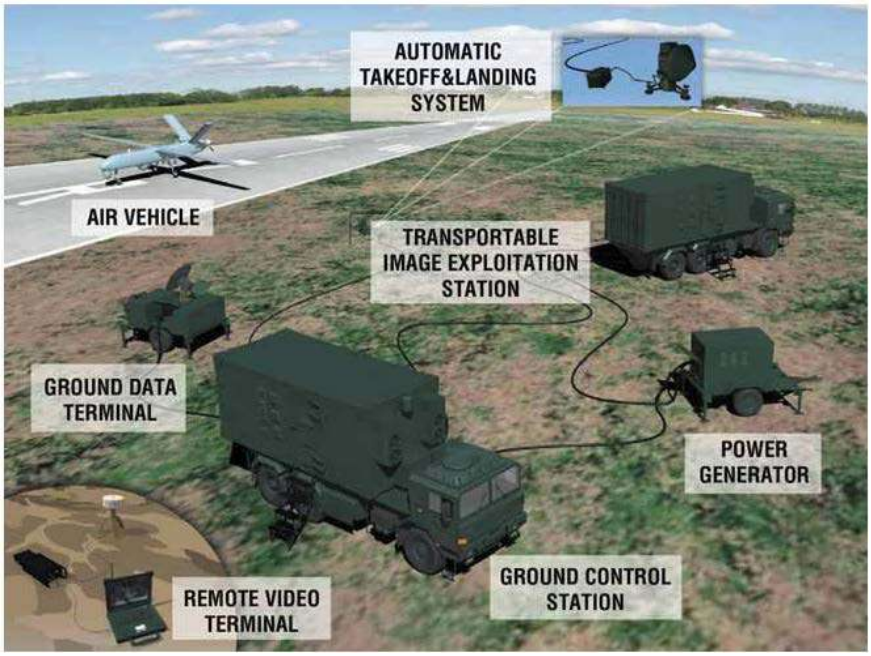

Figure 1. Unmanned Aerial Vehicle (UAV) Components [2]

2. CLASSIFICATION OF UNMANNED AIRCRAFT SYSTEM

Unmanned Aerial Vehicles (UAV) can be classified according to their civilian and military use and performance characteristics such as weight, distance to air, wing load, range and speed.

UAVs can be classified according to their performance characteristics such as weight, wing load, endurance, range, wing span, maximum height and speed at which they can take off. Classifying UAVs according to their performance characteristics is useful for UAV designers, manufacturers and customers to meet their needs.

2.1. Classification by weight

UAVs have a wide range of micro UAVs weighing several kilograms in weight, up to the Global Hawk (Tier III), which weighs 11 tons, as shown in Figure 2.1

Figure 2. Global Hawk (Tier III) [3]

Classification of UAVs was made by taking the weight ranges into consideration while classifying the weights. This classification is given in Table 1.

Table 1. Classification of UAVs weights [4]

Category	Weight Range	Sample UAVs
Too heavy	>2000 Kg	Global Hawk
Heavy	200 - 2000 Kg	A - 160
Middle	50 - 200 Kg	Raven
Light	5 - 50 Kg	RPO Midget
Micro	<5 Kg	Dragon Eye

2.2. Classification According to Duration And Range Of Air

Airborne duration and range are important factors to consider when classifying UAVs. These two parameters are usually interrelated for a long UAV operation. For UAV designers it is important to consider these two parameters when determining the UAV type. In addition, with these parameters it is possible to determine how long the UAV will be fueled regularly and how long it will remain in service.

Three types of classification are possible, long, medium and short, depending on the duration of the air and the range. Table 2 summarizes the classification of UAVs according to the duration of airborne and range.

Table 2. Classification of Uavs According To The Duration of Flight and Flight Range [4].

Category	Endurance	Range	Sample UAVs
Long	> 24 Saat	> 1500 Km	Predator B
Middle	5 - 24 Saat	100 - 400 Km	Silver Fox
Short	< 5 Saat	< 100 Km	Pointer

2.3. Classification By Altitude

When some UAVs used for military purposes are selected, UAVs are required to fly at high altitudes in order to be detected and destroyed by the enemy, while UAVs that are used for civilian purposes are required to fly at UAV low altitudes. One of the important factors in the classification of UAVs is the ease of selection of the desired elevation of the exit elevation, which the end buyers need.

The altitude at which UAVs can exit can be classified into three levels: low, normal, and high altitude. Table 3 gives the classification according to the height at which UAVs can occur.

Table 3. Classification of UAVs By Altitude [4].

Category	Maximum Altitude	Sample UAVs
Low	< 1000 m	Pointer
Middle	1000 - 10000 m	Finder
High	> 10000 m	Darkstar

2.4. Classification According to Wing Loading

Another classification method, wingletting, is one of the important factors in the classification of UAVs. For a UAV, the wing load calculation is obtained by dividing the total weight into the wing area. UAVs are classified into 3 types as shown in Table 4., considering the wing loading rates.

Table 4. Classification of UAVs According to Wing Loading [4].

Category	**Wing Loading (kg/m^2)**	**Sample UAVs**
Low	< 50	Seeker
Middle	50 - 100	X - 45
High	> 100	Global Hawk

2.5. Classification by Engine Type

UAVs are used in many different tasks and require different types of engines depending on the area they are used to perform these tasks. Table of UAVs is given according to the engine type used in Table 5.

Two-stroke, Turbofan, Turboprop, Piston, Electric, and Propeller types are the different types of engines used in IHA. Piston and electric engines are the most widely used types. UAVs also vary in size and type of engine, in proportion to aircraft size and weight, as in human aircraft. Electric engines are generally used in light and small models, piston engines are used in heavy and large models.

Table 5. **Examples of UAVs According To Engine Types** [4]

Wankel	**Turbophan**	**Turboprop**	**Piston**	**Electric**
RQ-7A Shadow 200	**Darkstar**	**Predator B**	**Neptune**	**Dragon Eye**
Sikorsky Cypher	**Global Hawk**		**Dragon Drone**	**Dragon Warrior**
	Phoenix		**Finder**	**Pointer**
	X - 45		**A 160**	**Raven**
	X - 50		**GNAT**	**Luna**
	Fire Scout		**Crecerelle**	**Javelin**
			Seeker	
			Brevel	
			Snow	
			Goose	
			Silver Fox	
			Heron	

A classification with international validity for UAVs is not available at this time. Each country has its own classification. Some classifications are made by such factors as altitude, duration of air stay and departure

weight. The classification of UAVs according to performance characteristics, such as duration of airborne occupancy, weight and altitude, is the same as in Table 6 [1].

Table 6. Classification of UAVs According to Performance Characteristics

Category	**Maximum Take-Off Weight (Kg)**	**Maxsimum Flight Altitude (Meter)**	**Endurance (Hour)**	**Sample Platform**
Micro (<2kg)	3	250	1	Blackwindow, Microstar, Microbat, Fancopter, Hornet
Mini (2-20 Kg)	3-30	150-300	1-2	Bayraktar, Malazgirt, Scan Eagle, Mikado, Raven, Robocopter
Small (20-50 Kg)	30-75	300-100	2-3	Hermes 90,yh-300sl
Tactical UAV	50-1500	3000-8000	4-12	Zanka-III, Caldiran, Karayel, Aerostar, Anka, Heron, Predator, Reaper
Medium Altitude Long Endurance (MALE)	1500-2500	3000-8000	12-24	Skyforce, Hermes 1500, Heron Tp, Predator-it, Dominator,e-hunter
High Altitude Long Endurance (HALE)	2500-5000	5000-12000	12-24	Global Hawk, Raptor, Condor, Theseus, Hellos Eurohawk, Mercator ,Global Observer
Attack/ Battle	-	8000-12000	-	X-47b, Phantom Ray

If the performance required by an Unmanned Aerial Vehicle (UAV) is similar to that of conventional aircraft, the drive system may be similar. Many unmanned aerial vehicles will fly at subsonic and supersonic speeds at altitudes of less than 1000 pounds, at altitudes below 60,000 feet, maneuver at a speed of 9 g or less, and will be protected in the same manner as existing military or commercial aircraft. These unmanned aerial vehicles will not need unique drive technology. Indeed, every new aircraft is designed to use existing engines to prevent the time and expense of developing new engines. In this section, the concepts of Unmanned Aerial Vehicles (UAVs) that need new drive technology are discussed.

A few classes of Unmanned Aerial Vehicle (UAV) require unused engine innovation, modern plans, or indeed modern essential investigate and impetus concepts. For illustration, a Tactical Unmanned Aerial Vehicle (TUAV) may require a gas turbine engine that can work at much more than the 9g powers that constrain kept

an eye on vehicles. For tall g loadings, the whole engine structure, particularly the rotor back, will have to be reevaluated. An engine able of maneuvering at 30g, for case, would require unused plan concepts that could require impressive building advancement but not modern essential inquire about. By the by, for a few UAVs, the drive framework is a basic restricting innovation. These incorporate subsonic Sound flying machine that must work over the elevation limits of current engine advances; micro aircraft vehicles; and exceptionally low-cost, high-performance vehicles.

The Gas Turbine Engine is unfathomably prevalent to elective engines in all impetus measurements. This tall level of execution reflects the inborn merits of the concept and the $50 billion to $100 billion contributed in gas turbine investigate and advancement. The power-to-weight proportion of gas turbines is three to six times that of airplane piston engines. The contrast in unwavering quality is indeed more prominent [5]

Vibration and noise, numerous moving parts, Seal and lubrication requirements, Cooling neccessities are some disadvantages of piston engines. Possibly light weight, Possibly small sizes, Supports forced-induction for high altitude use are some advantages of piston engines.

Table 7. Conceptual Decomposition of Piston Engines

Propulsion System	Conceptual Unit	Description
Reciprocating Piston Engine	Energy source	Petroleum distillates
	Energy transformer	Heat production and expanding volumes resulting from contained combustion of petroleum distillates
	Powerplant	Piston motion resulting from expanding volumes, which in turn, rotate the crankshaft
	Propulsion effecter	Propeller or fan unit driven directly or indirectly (geared) by the crankshaft
	Control effecter	Throttle, regulation of fuel flow

Table 8. Technical Issues of An Piston Engine

Technical Issue	Applicability to UAS Context
Crankshaft Weakness	For engines large enough for manned systems, this is largely covered in the CFRs. The issue here is with smaller engines, where it may be sufficient
Noise	Noise in manned aircraft interferes with in-flight communication and alerts ground personnel to engine activity. In small UAS. those issues may not apply. However, smaller engines are quieter and may not have loud enough launch personnel alerting volume. However, there is no effect on the nonexistent pilot's ability to hear in-flight communication.
Vibration	As in manned vehicles, vibration can affect long-term reliability.
Seals	Over time, seals can fail, which leads to power loss and/or potential critical failure
High Temperature	As in manned vehicles, the engine can fail or seize if heat is not removed from the engine fast enough.

The project, which was signed between TEI and the Undersecretariat of Defense Industry (SSM) on 27 December 2012, includes the development of a turbodiesel aviation engine with superior technical features in line with the needs of MALE class unmanned aerial vehicles.

Qualification and certification of civil projects expected to be completed in 2018 with Turkey MALE class will have superior national turbodiesel engine that can be used in unmanned aerial vehicles. Detailed design studies have come to the prototype production stage in the ongoing project in the process of certification processes.

EASA CS-E scope of the project on the basis of Airworthiness and Certification on the basis of EASA Part 21 Design Organization for Competency Assurance (Piston Engines) that will be a first in Turkey. The dual-stage turbocharged diesel PD170 UAV engine is shown in figure 3.

Figure 3. Dual Stage Turbocharged Diesel Aviation Engine PD170[6]

The advantages of the Operational HVAC Engine compared to the existing MALE class HVAC engines are listed below:

- More Power, Higher Power / Weight Ratio
- More Altitude Power Capability
- Lower Fuel Consumption
- More Compact Design
- Certification of Fulfillment in Compatibility with Civil Hijacking Standards and Military Standards
- Original Engine Control System Software and Hardware (Open code, enhanceable)
- Fast Technical and Logistic Support
- Potential to increase power as needed

Like piston engines, Wankel revolving engines utilize the burning of oil distillates to produce warmth and work, and the coveted yield is the pivot of a power shaft that drives whatever is left of the framework. Wankel revolving engines contrast from customary responding engines in that their volume dislodging and related inner movement happens in a rotational manner, rather than a forward and backward way. An interior triangular center with bended sides separates a chamber with an epitrochoid-formed stator into three development territories. As the center turns a capricious shaft (figure 3.), the emptied sides of the bended triangular rotor (figure 3.) pack a vaporous volume against the sides of the fenced in area. A start occasion happens, extending this volume and propagating the turn of the center and shaft and proceeding with the burning cycle, creating usable work and waste warmth [7]

Figure 4. Wankel Rotary Engine Eccentric Shaft, Bathtub Face of Wankel Rotor, Wankel Rotor and Stator [7]

Higher power yield for comparative relocation, Iron rotor in aluminum lodging decreases probability of engine seizure, Lighter weight than heritage or pressure start engines, Much calmer than responding engines, Lower vibration than responding engines are som points of interest of the Wankel rotational engine. Fluid cooled engine adds to weight and many-sided quality, disappointment modes, half higher fuel utilization than practically identical diesel engines, Higher electromagnetic and warm marks contrasted with diesel engine, Limited data concerning specialized achievement of Wankel revolving engines, Potential trouble meeting outflow guidelines are a few weaknesses of the Wankel rotational engine [10].

A gas turbine engine is an internal combustion engine operating on a highly dynamic process, investing work to process air and fuel in a way that yields high-velocity output thrust as the return on investment. A gas turbine engine comes in various forms, and the three described in particular are the jet turbine engine, turbofan engine, and turboprop engine [7].

At the point when maybe a low-determination portrayal of a stream turbine, thoughtfully, the vitality substance of the items versus the reactants (deplete) is separated to deliver movement in a controllable response. Nonetheless, the immediate fly approach has enough proficiency downsides that, in a few applications, a turbofan is more proper. A turbofan takes a shot at a comparable guideline as a stream turbine, aside from that more work is sapped from the high energy fumes gas to drive a fan component, exchanging off some immediate push for extra fandriven push . A turboprop engine works on a comparable guideline as a turbofan, with the exception of that rather than a part, the majority of the high-vitality yield is utilized to drive a turbine that is equip coupled to a propeller. A turboshaft is like the turboprop aside from that the power is provided to a pole as opposed to a propeller [8].

Gas turbine engines are field tried and demonstrated solid impetus components, but are classically exceptionally huge and overwhelming. Advanced advancements have yielded the unused concept of microturbine engines, which are gas turbine engines little sufficient to be held by a single person and create pushed yields on the arrange of tens of pounds [9]. While occurrences exist of unmanned aircraft system that actualize each already said variation of the gas turbine engine, there are no known examples of little unmanned aircraft system that utilize a micro turbine engine. Be that as it may, industry producers have acknowledged the potential of micro turbine engines for Unmanned Aircraft System applications and have responded accordingly. Examples of gas turbine engines are shown in table 9. [10].

Table 2.9. Properties of the Northrop Grumman RQ-4A Global Hawk (Gas Turbine)

UAS Characteristics		**Propulsion Characteristics**	
Vehicle Dimension	**Length 44.4 ft Wingspan 116.2 ft**	**Propulsion Class**	**Gas turbine engine**
Vehicle Gross Weight	**26,750 lb**	**Propulsion Subclass**	**Turbofan**
Payload Data	**1,950-lb capacity**	**Propulsion Unit Make**	**Rolls Royce AE- 3007H '**
Endurance RangeTime	**5,400 nm/32 hr**	**Propulsion Unit Weight**	**Engine: 1,5861b**
Ceiling	**65.000 ft**	**Power Output**	**8.290-Ib thrust**

Some advantages of turbine engines are:

High power density, Enormous thrust capacity, Not limited to sound barriers like propeller blades, Good efficiency at 30% load, Insensitive to fuel quality, Use of air bearings, auxiliary lubrication fluid or oil need [11].

Costly, Complex systems, High speed rotation, Working at high temperatures are some disadvantages of gas turbine engines.

Electric engines work as a power source to generate rotational motion from electrical energy. For electrically driven drive systems, the electric engines are used as a power source because they can be easily combined with propellers as a propulsive effect; everything needed is a constant source of electricity [12].

Table 10. Solong Electric Engine

UAS Characteristics		Propulsion Characteristics	
Vehicle Dimension	Wingspan 4.75 m	Propulsion Class	Electric Motor
Vehicle Gross Weight	12.6 kg (28 lb)	Propulsion Subclass	DC motor
Payload Data	Unavailable	Propulsion Unit Make	Kontronik Tango 4506 3-phase, brushless, ironless motor with 4.2:1 planetary gear reduction
Endurance RangeTime	48+hr	Propulsion Unit Weight	300 g
Ceiling	8000 m	Power Output	Max motor power 800W

Low maintenance cost, Safe, Electrically operated, Robust, Less trouble surrounding overheating as opposed to thermodynamic engines, High torque power, Scalability, Silent operation are some of the advantages of electric engine systems.

Some of the disadvantages of electric engine based systems are that they are sensitive to large currents, electromagnetic field, water and other conductive fluids.

3. RESULTS

For this study, Unmanned Aircraft System propulsion systems were investigated. The research results show that there are several types of drive systems with different power sources used in the Unmanned Aerial Vehicle System. Their dimensions range from fully certified turbine engines with fewer trailers used in transport category aircraft. As such new power supplies are often used to meet operational needs. In summary, many of these propulsion systems, which are unique to unmanned aerial vehicle systems, are not traditionally considered to be present at the present regulatory standards. It is largely due to the unique operational objectives of the unmanned aerial system with specific mission requirements that are significantly different from human aviation [13].

Piston engines and electric engines are the most commonly used types. Unmanned Aerial Vehicles(UAV) also vary in engine size and type, as well as aircraft sizes and weights, as in humans. Electric engines are generally used in light and small models, while piston engines are used in heavy and large models. It is anticipated that the data obtained in this way will be brought to the forefront of many driver frameworks that are required in order to implement administrative guidelines. In this archive, various technical topics related to each frame are displayed. In response to the desire for an unmanned aircraft system, it is recommended that current regulations be re-audited to understand and address the unused issues that arise with new technologies [14].

Acknowledgement

This work was supported by Research Fund of the Erciyes University, Project no. FBA-2018-6712.

REFERENCES

[1] Coban S. , Oktay T., "A Review Of Tactical Unmanned Aerial Vehicle Design Studies", The Eurasia Proceedings of Science, Technology, Engineering & Mathematics, vol.1, pp.30-35, 2017

[2] European RPAS Steering Group. (2013a). Roadmap for the integration of civil remotely piloted aircraft systems into the European aviation.

[3] www.fas.org

[4] Arlomandi,M., Classification of Unmanned Aerial Vehicles, MECH ENG 3016 course note

[5] Theiss, T.J., Conklin, J.C., Thomas, J.F., and Armstrong, T.R., “Comparison of Prime Movers Suitable For USMC Expeditionary Power Sources,” Oak Ridge National Laboratory (ORNL), 2000.

[6] https://www.tei.com.tr/detay/operatif-iha-motoru-gelistirme-proje3
[7] Griffis, C., Wilson, T., Schneider, J., & Pierpont, P. (2009). Unmanned Aircraft System Propulsion Systems Technology Survey. , (). Retrieved from http://commons.erau.edu/publication/72
[8] Mattingly, Jack D., *Elements of Gas Turbine Propulsion*, McGraw-Hill, Inc., New York, New York, 1996.
[9] Microjet UAV Limited, "Microjet UAV Limited, Turbine Technology," http://www.microjeteng.com/products.html, last visited November 12, 2006.
[10] AREN, "Mazda Wankel Rotary Engines for Aircraft Website," http://www.rotaryeng.net/, last visited November 3, 2006.
[11] Army-Technology.com, "CL289 Unmanned Aerial Vehicle," http://www.armytechnology. com/projects/cl289/, last visited February 15, 2007.
[12] Tower Hobbies, "Kontronik Tango 45-06 Brushless Engine," http://www2.towerhobbies .com/cgi-bin/wti0001p?&I=LXHEW1, last visited March 3, 2007.
[13] Reid, C., Manzo, M., and Logan, M., "Performance Characterization of a Lithium-Ion Gel Polymer Battery Power Supply System for an Unmanned Aerial Vehicle,"
NASA/TM—2004-213401 2004–01–3166, November 2004.
[14] Griffis, C., Wilson, T., Schneider, J., & Pierpont, P. (2009). Unmanned Aircraft System Propulsion Systems Technology Survey. , (). Retrieved from http://commons.erau.edu/publication/72

ICENS 4TH INTERNATIONAL CONFERENCE ON ENGINEERING AND NATURAL SCIENCE
2 - 6 May 2018 KIEV UKRAINE

Development of Ecological Biodesign Products by Bacterial Biocalcification

Tugba Keskin[1], Irem Deniz[2] Alpcan Aric[1], Burak Talha Yilmazsoy[1], Ozge Andic-Cakir[3,4],Aysegul Erdogan[4], Didem Altun[5], Ayca Tokuc[5] , Burcu Filiz Demirci[5], Aylin Sendemir-Urkmez[1], Gulden Kokturk[6], Feyzal Ozkaban[5]

Abstract

Biodesign is an interdisciplinary field in which biological processes are combined with many different fields to produce environmentally friendly and economically feasible products. Within the scope of this study, first $CaCO_3$ production potential of Sporosarcina pasteurii has been observed and optimized, and then the capability of hardening of the sand is examined. In this study the growth curve of Sporosarcina pasteurii was sketched. Also the optimum $CaCl_2$ concentration for maximized $CaCO_3$ formation was found as 50 mM. The ecological urban element was designed and its mold was produced by 3D printer at lab scale. The Sporosarcina pasteurii was mixed with sand and filled into the mold. The sand was mixed with 50 mM $CaCl_2$ solution every day until hardening is observed. At the end of one week, a sitting element from hardened sand was produced. The $CaCO_3$ formation was observed with XPS analysis. Thus, an interdisciplinary approach was used to produce ecological biodesign products.

Keywords: Biocalcification, Biodesign, Urban living elements, Sand hardening, *Sporosarcina pasteurii*

1. INTRODUCTION

With the progress of technology, great changes and developments especially in the social sense are emerging. The adverse effects of increasing technology and production capacities on nature and human health are also increasing at the same rate. The elimination of the negative environmental conditions or the reduction of the minimum environmental burden has been the focus of many researchers, along with developing bioengineering approaches. Increasing production capacities, which are the biggest reason of globalization, result in increasing harm to the human health of the emerging products [1].

On the other hand, the products related to the building sector causes the most damage to the environment in human activities. In this point of view, environmentally friendly, sustainable design products that are compatible with nature are now a developing field of study. A number of structures under the heading of sustainable architectural design are criticized by different approaches such as high material or resource consumption during the production process or afterwards, negative associations with the natural environment, and inability to integrate with the socio-cultural structure. Today, all kinds of urban furniture, architectural / structural / industrial materials / products (children playgrounds, seating elements, kiosks, exhibition stands, etc.) can be produced and used by processing natural materials (wood, stone, etc.) [2]–[4].

[1] *Bioengineering Department, Engineering Faculty, Ege University, Izmir, Turkey*
[2] *Bioengineering Department, Engineering Faculty, Manisa Celal Bayar University, Turkey*
[3] *Civil Engineering Department, Engineering Faculty, Ege University, Izmir, Turkey*
[4] *Ege University Application and Research Center for Testing and Analysis, Izmir, Turkey*
[5] *Department of Architecture, Faculty of Architecture, Dokuz Eylul University, Izmir, Turkey*
[6]*Department of Electrical and Electronics Engineering, Faculty of Engineering, Dokuz Eylul University, Izmir, Turkey*
Corresponding author: keskin.tugba@gmail.com

Biodesign is a study field, in which organisms are used as a design input, to create sustainable, functional, durable and non-health threatening products related to taking inspiration from natural processes [5]. It also investigates natural building designs and structures for human welfare. Cooperative studies between engineers and designers are needed with respect to build progressive, bio-based, natural forms using microorganisms as a factory to produce a structure that is both functional and has aesthetics. One way to produce products can be by utilization of mineralization and biocalcification processes inherent in nature.

Formation of minerals in nature is known as a very slow process that can take as long as a geological time. Many of the mineral types are evoluted by microbial activity which is very dependent on microorganism strain. Ureases are the main enzymes used in mineralization processes. Ureases are homologous and Ni-dependent enzymes which can be found in many living organisms such as plants, bacteria etc. Ureases hydrolyze urea into ammonia and CO_2. *Sporosarcina pasteurii* is a wide spread soil bacterium. It has very large capacity of urease production [6].

One of the main activities of the role of microorganisms in nature is the microbial cementation, in other words biocalcification. Biocalcification can be performed by different strains of bacteria, *Sporosarcina pasteurii*, *Sporosarcina urea, Sporolactabacillus* etc[7].

Traditionally, gram-positive, aerobic or facultative anaerobic, sporulating, rod-shaped bacteria belong to the *Bacillus* family. This causes many heterogeneities in terms of the characteristics that must be defined within the *Bacillus* family. In 1889, the microorganism identified by Miquel Chester as *Bacillus pasteurii* was defined in 2001 by Yoon et al.[8], and its name was changed to *Sporosarcina pasteurii*. The cell size of *Sporosarcina pasteurii* varies between 1.3-4 ηm and the spores size is between 0.8-1.3 ηm. They live at a maximum temperature of 30-45 ° C and a minimum temperature of 5-15 ° C. They can be isolated from soil, water and mud layers and they are non-pathogenic microorganisms with a biosafety level of 1. *Sporosarcina pasteurii* is not conventional because its living conditions can withstand high pH conditions as well as environments containing ammonium salts at high concentrations. In most studies, urea has been used instead of the ammonium salt because these organisms have the ability to break down the urine [9].

The metabolic pathway of *Sporosarcina pasteurii* is as follows.

1 mol urea is converted to 2 mol ammonia and 1 mol CO_2.

$CO(NH_2)_2+H_2O \rightarrow NH_2COOH+NH_3$

$NH_2COOH+H_2O \rightarrow NH_3+CO_2+H_2O$

The pH of the soil medium is increased and the enzymatic reaction occurs by the addition of $CaCl_2$ and $CaCO_3$ precipitates. By the $CaCO_3$ metabolism, the negative effect of atmospheric release and global warming would be prevented [10].

$CO_2+H_2O \leftrightarrow H_2CO_3 \leftrightarrow HCO_3^-+H^+ \leftrightarrow CO_3^{+2}+2H^+$

$CO_3^{-2}+Ca^{+2} \rightarrow CaCO_3$

The microbial cementing ability demonstrated by this microorganism is widely used as an innovative and promising biotechnological application such as rehabilitation and reinforcement of cement materials [11]. In recent years, the selective cementation activity with the precipitation of $CaCO_3$ by microbiologically induced calcium carbonate biocalcification, was used for filling of cracks with calcite layers[12], blending of self healing mechanism with bacterial immobilization techniques [13], [14]. Another new application area is the use of *Sporosarcina pasteurii* to reduce the hydraulic conductivity in environmental processes. Magnus Larsson proposed this solution as a solution to desertification, including soil remediation, solid phase sequestration of contaminants, and carbon sequestration technologies[15].

In summary biocalcification is a process that is used in healing cracks in reinforced concrete buildings, soil stabilization and environmental processes. Recent studies were also showed that it can be used for hardening sand[16].

This study aimed to develop an architectural design product that is in harmony with the nature and suitable to human health with partnership of bioengineering and architecture disciplines via bacterial calcification to form an architectural structure with the support of 3D printing technology of poly-lactic acid (PLA). For this purpose, *Sporosarcina pasteurii* (*Bacillus pasteurii*) was chosen to use the urea mechanism to precipitate $CaCO_3$ thus hardening sand by utilizing urea. Even though there are limited studies that make use of bacterial calcification

to harden sand, this is the first study to show a successful design element built with the help of a 3D printed mold.

2. MATERIALS AND METHODS

2.1. Inoculum Preperation

Sporosarcina pasteurii was obtained from the DSMZ culture collection and grown in Caso Agar DSM 33 medium. Growth medium content of bacterium; For 1L; 15 g peptone from meat, 5 g peptone form soymeal, 5 g NaCl, 20 g urea. For $CaCO_3$ production in broth medium 10, 30 and 50 mM $CaCl_2$ was added to the medium. For biocalcification DSM 33 medium with urea and 50 mM $CaCl_2$ was used.

2.2. Bacterial Staining and Growth Curve

The Schaeffer-Fulton method was used for bacterial staining. The growth broth and the broth with $CaCl_2$ was prepared on microscope and air dried and heat fixed. The malachite green was added for endospore staining. Then the slide was rinsed with water to remove malachite green. Then the broth on slide was stained by safranin this secondary stain was again washed with water and air dried. The bacteria were observed under 1000X (oil immersion) with total magnification. The vegetative cells were observed by pink/red color.

Using the broth medium the growth performance of *Sporosarcina pasteurii* was measured at 600 and 660 nm of optical density during 24 h.

2.3. $CaCl_2$ Concentration Optimization in Broth Media

$CaCO_3$ concentration was reacted with an optimum concentration of $CaCl_2$. 10, 30 and 50 mM $CaCl_2$ was added to broth medium to start $CaCO_3$ formation. $CaCO_3$ was separated from broth medium by filter paper (Advantec 5, USA).

2.4. Bacterial Solidification

In bacterial solidification experiments, preliminary experiments were performed on petri dishes. First bacteria were grown on petri dishes agar medium. One petri without inoculums was used as control. The two petri dishes (with and without inoculums) were added with equal amounts of sea sand so that the height would be 2-3 cm. 10 mL of 50 mM $CaCl_2$-containing growth medium was added to the sand. Inoculum was added to one of the petri dishes. The petri dishes were left open in the incubator at 30°C. The feed medium was depleted for one week as the petri dishes appeared to solidify.

2.5. Design of urban, architectural and industrial elements

If the bacterial calcification process is directed, it is thought that it is possible to produce architectural, urban and industrial design products. Today, many industrial products contain harmful and toxic substances for health. Particularly the construction sector is one of the most harmful activities for environment within human activities. The designs, produced by this method, will be organic and ecological because they are shaped like processes in nature. It will not contain harmful and toxic substances found in the urban environment, architectural structures or in many other things we use in everyday life.

Basically, here is to direct the bacteria through engineering methods, without leaving it to natural growth process, for generating creative design products. By using this method, a vase or a plate, or a seating element or a playground for the city can be produced. These biodesign products will be a healthy and ecological alternative with a completely natural, non-toxic character. The goal is to make this even more advanced, so that it can be used on larger scale, in architectural structures or production of buildings. Very different from the construction methods of today, buildings can be produced from soil or from sand, by bacteria - in the direction of architects and engineers' designs. Although there are a variety of researchers study on this method, there is no detailed research on the directing of bacteria, nor is there an architectural structure produced by this method.

2.6. $CaCO_3$ Analysis

The presence of $CaCO_3$ was revealed by XPS analysis. The measurements were performed with a Thermo Scientific Model K-Alpha XPS instrument using monochromatic Al Kα radiation (1486.7 eV). Survey spectra and high-resolution spectra were acquired using analyzer pass energies of 50 eV. The X-ray spot size was 300 µm for single point analysis. Data were analyzed using Avantage XPS software package. Peak fitting was performed using Gaussian/Lorentzian peak shapes and a Shirley/Smart type background.

3. RESULTS AND DISCUSSIONS

3.1. Bacterial Staining Results and Growth Curve of Bacteria

Determination of life cycle of microorganisms is very important for optimal process performance. The growth curve of *Sporosarcina pasteurii* was sketched by measuring the optical density of 600 and 660 nm by taking samples every 2 h during 24 h and the graph was sketched time vs OD (Optical Density). The results showed that the most active times of *Sporosarcina pasteurii* is between 6-8 h (Figure 1). According to this result the inoculation of all processes was done at 6 h.

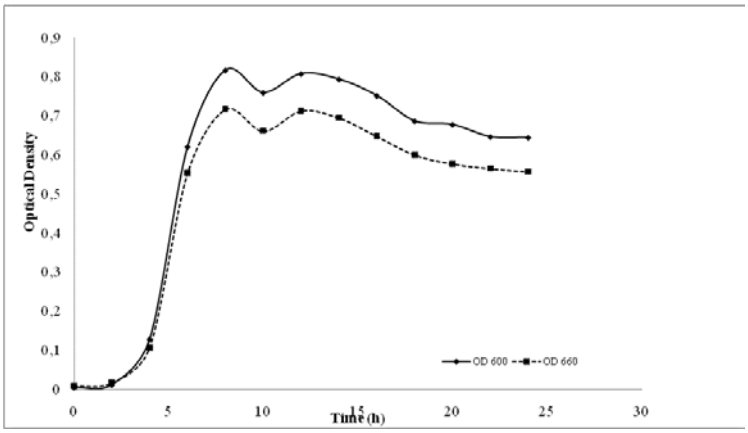

Figure 1. Growth curve of Sporosarcina pasteurii

The bacterial staining was performed according to Schaffer Fulton method. In this method red-purple colors showed the vegetative *Sporosarcina pasteurii*, which means these are active microorganisms (Figure 2 a). In this method the stains were not washed with alcohol or any other chemicals so we can observe the cluggings of $CaCO_3$ formation in the broth medium containing 50 mM $CaCl_2$ (Figure 2 b). The $CaCO_3$ formation was not enough with the broth medium containing 10 mM $CaCl_2$(Figure 2c) and 30 mM $CaCl_2$ (Figure 2 d) .

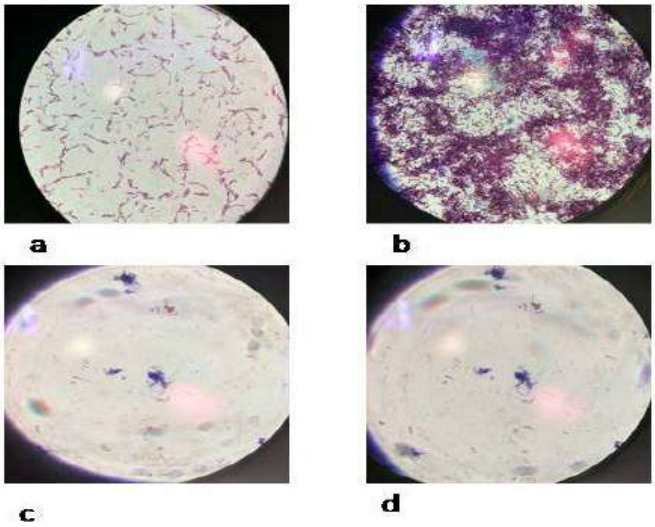

Figure 2. Staining microphotographs of the bacteria(X100; 1024dpi, olympus E 400)

3.2.$CaCl_2$ Concentration Optimization in Broth Media

$CaCO_3$ precipitates were produced by hydrolysis of urea which results in production of ammonia and carbonate. Carbonate binds calcium ions in medium and after this reaction $CaCO_3$ crystals can be formed. $CaCO_3$ (calcium carbonate) concentration is related with an optimum concentration of $CaCl_2$;10 mM, 30 mM and 50 mM $CaCl_2$ was added to broth medium to start $CaCO_3$ formation. Starting from the second hour (Figure 3a) of the process a white powder started to appear which is a mixture of $CaCl_2$ and $CaCO_3$ crystals. The concentration of the $CaCO_3$ increased by incubation at 30 ^oC during 7 days and the photos taken on day 1, day 2 and day 7, respectively. (Figure 3b, c and d)). $CaCO_3$ was separated from broth medium by filter paper and weighted. The weight of the $CaCO_3$ produced from 10 mM, 30 mM and 50 mM are 1.02 g, 1.34 g and 1.62 g respectively. In another study conducted by Dhami et al.[17]. The amount of precipitated $CaCO_3$ from different strains of B. megabacterium MTCC 1684 was between 0.84-0.076. This difference caused from the difference of bacteria and also the medium used.

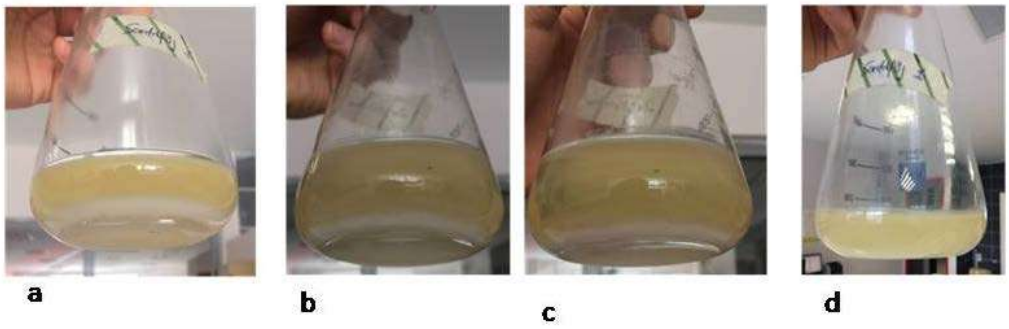

Figure 3. $CaCO_3$ formation during incubation (after; a)1 hour; b) 2 hours; c) 1 day; d) 1 week)

3.3. Bacterial Solidification

Microbially induced $CaCO_3$ is a very important product which can be used to fix cement cracks and fissures in structural formation. The most important application area for microbiologically induced $CaCO_3$ is remediation of damaged concrete. Microbiologically induced $CaCO_3$ formation reaction generally ends with high pH because of series biochemical reactions. *Sporosarcina pasteurii* is plays an important role in this process by producing urease to hydrolyze urea to ammonia and O_2. The produced ammonia will increase the pH of surroundings and calcite precipitation will start[18].

In this study, first of all, attempts were made to be sure about the solidification process is carried out by *Sporosarcina pasteurii* in petri dishes. *Sporosarcina pasteurii* is grown on agar plates and the 2-3 cm height sand as put on it. Then the medium with $CaCl_2$ was spread over sand daily until solidification completed. Another petri without inoculums was used as control. The same procedure was applied on it. It was seen that the inoculum-free sand has elasticity (Figure 4a) just because of the agar and can be easily and rapidly disintegrated while the inoculum-containing sand is hardened (Fig. 4b).

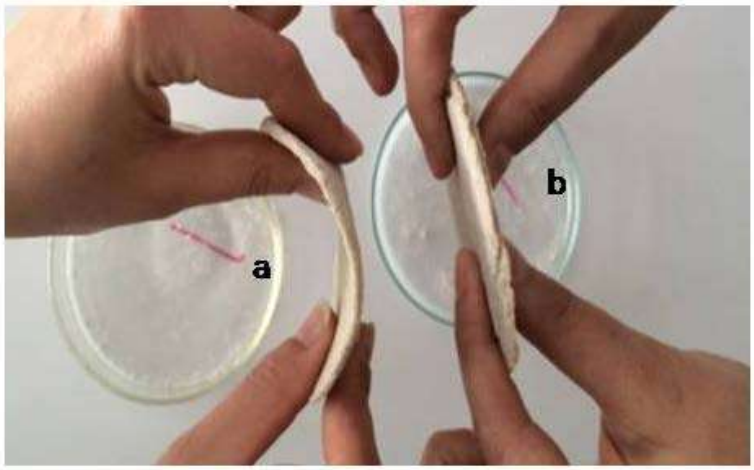

Figure 4. Solidification trials on petri dishes (a. without inoculum; b. with inoculum)

3.4. Production of Environmentally Friendly Design Elements by Bacterial Solidification

After the successful solidification process in petri dishes, a unique design element was designed and taken out from the 3-D printer. The design element that was selected for production with biodesign in this paper is a multipurpose urban furniture. It is part of a product range for parks and can be used to sit or lie on under various weather conditions including next to the sea. The product in this paper was scaled down for laboratory conditions.

First of all this structure was filled with sand. Inoculum was then added to the sand and evenly distributed throughout. The DSM 33 growth medium containing 50 mM $CaCl_2$ was evenly distributed on the sand too and incubated for 1 week in a 30°C incubator. The design unit obtained at the end of one week is shown in Fig 5.

Figure5. Environmentally friendly solidified design element

The ability of CO_2 capture by *Sporosarcina pasteurii* is was analyzed by Okwadha and Li [19] and they found that CO_2 usage by ureolytic activity can be used for microbial $CaCO_3$ formation. Another application area where *Sporosarcina pasteurii* is used is civil engineering. A study conducted by Achal et al.[20] resulted in the increase of durability of concrete and Jonkers et al.[16]showed the self healing capability of concrete by *Sporosarcina pasteurii*.

Stocks and Fisher [7] used narrow plastic columns to detect the solidification ratio and ability of sand hardening by *Sporosarcina pasteurii* was analyzed by SEM and XRD. The analysis showed the formation of calcite crystals which decreased the permeability of solid by 98%.

The sand hardening properties of the bacteria in the work done by Sarmast et al.[21] have been tested in plastic columns. It has been observed to harden for 7 days in a similar quadrant in our study. At the end of this process, the stiffened sections were taken and $CaCO_3$ crystals formation was compared and equal distribution throughout the column was observed. In our study, the possibility of taking the advantage of the sand hardening properties of bacteria to create a sophisticated architectural design elements which can be readily used in daily life.

3.5. Solidification and $CaCO_3$ Analysis Results

Ca 2p peaks have clearly spaced spin-orbit components ($\Delta_{carbonate}$ =3.5 eV). In the present study, Ca 2p region for this material (Figure 6) exhibits a well-resolved doublet with a Ca $2p_{3/2}$ component at 347.1 eV and a Ca $2p_{1/2}$ component at 350.7 eV. The Ca $2p_{1/2}$ and Ca $2p_{3/2}$ bands are separated by ~3.6 eV indicating that the structure is $CaCO_3$.

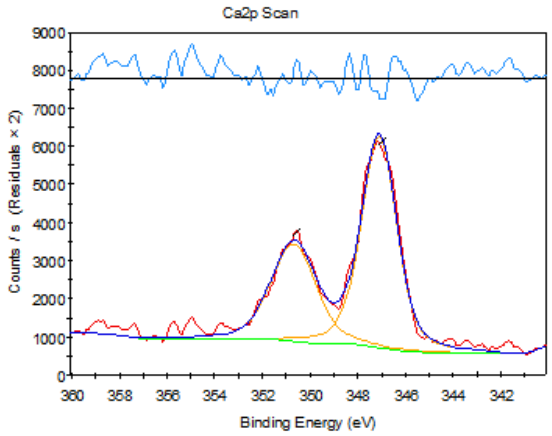

Figure 6. XPS spectrum of Ca in solidified sand

Sarmast et al. [21] used 2 bacterial species (*Sporosarcina pasteurii* is and *Sporosarcina urea*) to test the reaction times of solidifying at sandy soil columns. The results showed that $CaCO_3$ precipitation so does solidification is more favorable with *Sporosarcina pasteurii* and 12% $CaCO_3$ precipitation was observed. In our study according to XPS results 10% $CaCO_3$ precipitation was observed with 50 mM $CaCl_2$ addition.

CONCLUSION

Sporosarcina pasteurii is an environmentally friendly bacterium that can be used in hardening sand. Bacterial solidification was achieved after addition of $CaCl_2$ to the medium. In future studies, real scale designs will be manufactured via harmless environmental processes and elements made by living organisms can be produced at larger scales. The originality of this study is that the resulting products are healthier and ecological alternatives to urban constructions with detrimental health and environmental effects. Besides the novel composition and production of the design products, they aim to be totally natural, non-toxic and durable. From a social point of view, this totally natural alternative production method in the environmentally notorious construction industry gives hope to the future generations for a new way of living.

ACKNOWLEDGMENT

The authors wish to thank Prof. Dr. Nuri Azbar for the technical support by Environmental Biotechnology and Bioenergy Laboratory and Can Aysan for 3D printing support.

REFERENCES

[1] L. S. Wong, "Microbial cementation of ureolytic bacteria from the genus *Bacillus*: a review of the bacterial application on cement-based materials for cleaner production," *J. Clean. Prod.*, vol. 93, pp. 5–17, 2015.
[2] I. Fjørtoft and J. Sageie, "The natural environment as a playground for children," *Landsc. Urban Plan.*, vol. 48, pp. 83–97, 2000.
[3] I. Fjørtoft and J. Sageie, "The natural environment as a playground for children. Landscape description and analyses of a natural playscape," *Landsc. Urban Plan.*, vol. 48, no. 1–2, pp. 83–97, 2000.
[4] E. M. Campa, "Pensamientos compartidos. Aldo van eyck, el grupo cobra y el arte," *Rev. Proy. Progreso, Arquit.*, no. 11, pp. 64–75, 2014.
[5] M. Taya, "Bio-inspired design of intelligent materials," *Smart Struct. Mater.*, vol. 5051, pp. 54–65, 2003.
[6] D. Olivera-Severo, G. E. Wassermann, and C. R. Carlini, "*Bacillus pasteurii* urease shares with plant ureases the ability to induce aggregation of blood platelets," *Arch. Biochem. Biophys.*, vol. 452, no. 2, pp. 149–155, 2006.
[7] S. Stocks-Fischer, J. K. Galinat, and S. S. Bang, "Microbiological precipitation of $CaCO_3$," *Soil Biol. Biochem.*, vol. 31, no. 11, pp. 1563–1571, 1999.
[8] J. H. Yoon, K. C. Lee, N. Weiss, Y. H. Kho, K. H. Kang, and Y. H. Park, "*Sporosarcina aquimarina* sp. nov., a bacterium isolated from seawater in Korea, and transfer of *Bacillus globisporus* (larkin and stokes 1967), *Bacillus psychrophilus* (Nakamura 1984) and *Bacillus pasteurii* (Chester 1898) to the genus *Sporosarcina* as *Sporosa*," *Int. J. Syst. Evol. Microbiol.*, vol. 51, no. 3, pp. 1079–1086, 2001.
[9] W. R. Wiley and J. L. Stokes, "Requirement of an alkaline pH and ammonia for substrate oxidation by Bacillus pasteurii.," *J. Bacteriol.*, vol. 84, pp. 730–734, 1962.
[10] R. Siddique and N. K. Chahal, "Effect of ureolytic bacteria on concrete properties," *Construction and Building Materials*, vol. 25, no. 10. pp. 3791–3801, 2011.
[11] S. J. Park, Y. M. Park, W. Y. Chun, W. J. Kim, and S. Y. Ghim, "Calcite-forming bacteria for compressive strength improvement in mortar," *J. Microbiol. Biotechnol.*, vol. 20, no. 4, pp. 782–788, 2010.
[12] Q. Chunxiang, W. Jianyun, W. Ruixing, and C. Liang, "Corrosion protection of cement-based building materials by surface deposition of $CaCO_3$ by *Bacillus pasteurii*," *Mater. Sci. Eng. C*, vol. 29, no. 4, pp. 1273–1280, 2009.
[13] J. Wang, K. Van Tittelboom, N. De Belie, and W. Verstraete, "Use of silica gel or polyurethane immobilized bacteria for self-healing concrete," *Constr. Build. Mater.*, vol. 26, no. 1, pp. 532–540, 2012.
[14] H. M. Jonkers and E. Schlangen, "Crack Repair By Concrete-Immobilized Bacteria," *Civ. Eng.*, no. April, pp. 1–7, 2007.
[15] B. Mahanty, S. Kim, and C. G. Kim, "Biokinetic modeling of ureolysis in *Sporosarcina pasteurii* and its integration into a numerical chemodynamic biocalcification model," *Chem. Geol.*, vol. 383, pp. 13–25, 2014.
[16]H. M. Jonkers and M. C. M. van Loosdrecht, "BioGeoCivil Engineering," *Ecological Engineering*, vol. 36, no. 2, pp. 97–98, 2010.
[17] N. K. Dhami, M. S. Reddy, and A. Mukherjee, "Bacillus megaterium mediated mineralization of calcium carbonate as biogenic surface treatment of green building materials," *World J. Microbiol. Biotechnol.*, vol. 29, no. 12, pp. 2397–2406, 2013.
[18] S. S. Bang, J. K. Galinat, and V. Ramakrishnan, "Calcite precipitation induced by polyurethane-immobilized *Bacillus pasteurii*," *Enzyme Microb. Technol.*, vol. 28, no. 4–5, pp. 404–409, 2001.
[19] G. D. O. Okwadha and J. Li, "Optimum conditions for microbial carbonate precipitation," *Chemosphere*, vol. 81, no. 9, pp. 1143–1148, 2010.
[20] V. Achal, A. Mukherjee, and M. S. Reddy, "Microbial Concrete: Way to Enhance the Durability of Building Structures," *J. Mater. Civ. Eng.*, vol. 23, no. 6, pp. 730–734, 2011.
[21] M. Sarmast, M. H. Farpoor, M. Sarcheshmehpoor, and M. K. Eghbal, "Micromorphological and biocalcification effects of *Sporosarcina pasteurii* and *Sporosarcina ureae* in sandy soil columns," *J. Agric. Sci. Technol.*, vol. 16, no. 3, pp. 681–693, 2014.

ICENS 4TH INTERNATIONAL CONFERENCE ON ENGINEERING AND NATURAL SCIENCE
2-6 May 2018 KIEV UKRAINE

A Novel Optimization Algorithm; Fox Hunting Algorithm (Fha) And Antenna Array Pattern Synthesis Aplication

Murat Onay[1]

Abstract

An efficient and fast optimization algorithm named Fox Hunting Algorithm (FHA) is presented here. FHA is a general-purpose population-based search algorithm. FHA can be used to solve many optimization problems. There are many algorithms in the literature that mimic animal and plant behavior. But human is the most intelligent living entity in the world. The human uses the superiority of animals for hunting. The FHA algorithm mimics the fox hunting activity which is formed and improved since 16th century by the human. In this study, FHA is applied to pattern synthesis problem of linear antenna arrays with the prescribed nulls. Antenna pattern synthesis of linear antenna arrays is a well-known hard problem of electronic engineering. Antenna pattern synthesis is achieved by controlling only the amplitude of each array elements. Some numerical examples of Chebyshev pattern with nulls applied at interference directions are given to show the efficiency and flexibility of the FHA.

Keywords: Fox Hunting Algorithm, FHA, Amplitude only pattern nulling, antenna pattern synthesis, optimization

1. INTRODUCTION

In the real world, it is often encountered with multi-variable optimization problems, and classical methods often face great difficulties in solving these problems. In recent decades, population-based soft computing algorithms have been introduced to overcome up from the shortcomings of traditional mathematical techniques. Several evolutionary or meta-heuristic algorithms have been developed. These algorithms usually mimic rules and randomness of natural behaviors of the animals. These behaviors include biological evolutionary processes (e.g., the evolutionary algorithm proposed by Fogel et al. [1], De Jong [2], and Koza [3] and the genetic algorithm (GA) proposed by Holland [4] and Goldberg [5]) and animal behaviors (e.g., the Ant Colony Optimization proposed by Dorigo et al. algorithm [6] and the Particle Swarm Optimization algorithm proposed by Eberthart and Kennedy [7], the Bees Algorithm proposed by Pham [8] , Artificial Fish Swarm Algorithm proposed by Li [9] artificial bee colony (ABC) algorithm proposed by Karaboga [10]). In last years, these meta-heuristic algorithms, especially GA [4]and ABC [10] based methods have been studied by many researchers to solve various problems. That is clear meta-heuristic algorithms have great results in many engineering area.

Human beings are the cleverest living creature in the world. The proposed algorithm is a new meta-heuristic optimization algorithm which simulates the fox hunting activity of the human beings. The name is Fox Hunting Algorithm (FHA). FHA involves the tracking, chase, and sometimes killing of a fox. Trained foxhounds, other scent hounds, fell terrier or smooth fox terrier are used to chase the fox. A master of foxhounds follows the hounds on foot or on horseback. A group of unarmed followers led follow the master of foxhounds [11]. Human beings use horses to go faster. They use foxhounds for tracking. Also they use terriers to deep search in holes and hives. The FHA mimics these all behaviors.

Usual optimization algorithms have two search mechanisms. The first one is a global search mechanism and the second one is a local search mechanism. By the experience researchers knows that the local search mechanism must be modified while searching approaches to the solution. Because of that local search mechanisms are not efficient after reaching close to the solution. So there are three search mechanisms in the

[1]*Corresponding author: Erciyes University, Faculty of Aeronautics and Astronautics, Turkey, e-mail: muratonay@erciyes.edu.tr*

FHA for searching in a more efficient way. The first one is a global search mechanism; second one is a local search mechanism; and third one is the deeper local search mechanism. They are similar to the fox hunting activity in the real world. The first search with horses is like global search in the optimization process; it is fast and searches bigger areas with biggest steps in the whole search mechanism. The second one with trained foxhounds is like local search; it is slower than horses but searches the areas better. The third one with terriers is like deeper local search; it has the smallest steps but searches really deeply. So the solution can be found most closely to the global best position as fast as possible.

In this study the FHA is used to solve an antenna array synthesis problem. Antenna array synthesis problem is a hard problem to solve by traditional methods because of its huge solving dimensions. Ten elements antenna array amplitude parameters are optimized by using the FHA, to show the ability and flexibility of the FHA. In the next section FHA will explain briefly.

2. FOX HUNTING ALGORITHM (FHA)

The FHA is a fast and new optimization algorithm in the field of swarm intelligence. Writing FHA code is easy in any programming language. The FHA simulates superior behaviors of the animals in fox hunting activity in the real world (for more details please see reference [12, 13]). Swarm is made of initial population composed of individuals to search in the solution space. Swarm based algorithms usually mimics animals insect or plants. Here in FHA, we use horses and different kinds of dogs as in the real world.

Every individual has its own position composed of *D* (dimension of the problem) dimensions in FHA. A fitness value which represents the accommodation of the individual to the fitness function is calculated for every individual. The final solution would be the best position of the terriers. The FHA keeps the best solution until it reaches the end of the iterations. Figure I. shows the pseudo code for the algorithm in its simplest form. In the fox hunting, real animals are used for tracking and chase. In the FHA, artificial animals are used for tracking and chase. These animals are horses, foxhounds and terriers respectively. Horses are used to move promising areas like rough or brushy areas in the hunting area. Then, foxhounds are used to pursue the fox. At the end, the fox goes to underground and terriers are used to enter underground to flush fox hidden underground and to locate the fox. In real world, horses move faster with bigger steps than dogs. Also, foxhounds moves faster than terriers with middle steps. Finally, terriers are used, so they move with smallest steps in the swarm. Similarly in the FHA, artificial horses (AH) move faster with bigger steps than artificial foxhounds (AF), and the AF move faster than terriers (AT). This behavior makes the FHA more effective.

1. Divide the *AH* into two groups (*AH1* and *AH2*) as in the real world
2. Randomly sprinkle *AH1* into M-dimensional solution space and randomly give values, which are in-range of boundaries.
3. Calculate the fitness of the *AH1*
4. Choose better *m* members of *AH1*and their positions (mp_i) for neighborhood search
5. Calculate the promising weights of *m* members (pwm_i) by the equation (1)
6. The latest improvement obtained iteration number *(LIN)* is set to 0. Iteration number *IN* is set to 0.
7. While stopping criterion is not satisfied// Forming the new population
8. Randomly sprinkle *AH2* into M-dimensional solution space by the range of boundaries
9. Calculate the fitness of the*AH2*
10. Send the *AF* around the every mp_i according to pwm_i
11. Calculate the fitness of the *AF*
12. Find *m* best solutions between all *AF* and *AH2*
13. If any improvement is done in this iteration by*AH2* or *AF* then *LIN=IN*
14. If *LIN*<*IN*-7 then make a sub-search:
    a. Send the *AT* around the mp_1;
    b. Calculate the fitness of the *AT*;
    c. If best *AT* is better than mp_1 then hold it as mp_1;
    d. kill %5 *AF* (decrease the value of *AF* to 0.95*AF*);
    e. re-calculate pwm_i
15. Increase *IN*; End While

Figure I.Pseudo Code Of The Basic Fox Hunting Algorithm

where m is number of promising solutions that is chosen from a group of solutions. mp_i is position of the m members where $i = 1, 2, \ldots, m$. pwm_i is an array that determines how many AF members will send to every mp_i. pwm_i can be written as :

$$pwm_i = round\left(\frac{AF}{m} + \frac{AF}{10m}\left(round\left(\frac{m-2i}{2}\right)\right)\right) \quad \text{where } i = 1, 2, \ldots, m \quad (1)$$

Here in Table I typical values of the parameters can be found. These parameters can be changed by experience on the problem and algorithm.

Table I. Typical Values Of Parameters For A Search Space Between 0–20 (For Example).

Scalers:	***m***	***AH***	***AF***	***AT***	***AH*Step size**	***AF* Step size**	***AT* Step size**
Typical Values:	10	300	100	100	20	2	0,2

AH will be divided into two groups as been in the real world. First group, *AH1*, moves in the search area randomly at the beginning of the algorithm to find promising positions. Then *AH1* followed by*AF* to find the way to the solution. *AF* starts with the promising positions of *AH1*. While *AF* makes neighborhood search in the promising areas, the second group, *AH2*, moves all around the search space to find a more promising area. The search of *AH2* is like the global search in the optimization. Also search of *AF* is like the local search in the optimization. When *AF* can't find a better solution for about 7 iterations, *AF* gives his turn to *AT*. *AT* makes deeper search with smaller steps than AF (for more details please see reference [12, 13]). In the next section antenna array pattern synthesis is explained briefly and numerical results are given.

3. ANTENNA ARRAY PATTERN SYNTHESIS

The antenna array pattern synthesis is an important work to reject unwanted interference sources while receiving the desired signal from a chosen direction [14-36]. Radiation pattern nulling is needed to avoid the unwanted interference. Desired pattern can be synthesis by pattern nulling. The increased pollution of the electromagnetic environment has led to the study of array pattern nulling techniques. These techniques are very important in radar, sonar and many communication systems for minimizing degradation in signal-to-noise ratio performance.

In this study, the amplitude of the array elements are controlled to obtain the desired pattern. The amplitude-only control [16, 17, 26, 27, 32, 40] uses a set of variable attenuators to adjust the element amplitudes. If the element amplitudes possess even symmetry about the center of the array, the number of attenuators and the computational time are halved. The classical optimization techniques used for antenna array synthesis are likely to be stuck in local minima if the initial guesses are not reasonably close to the final solution. The most of the classical optimization techniques and analytical approaches also suffer from the lack of producing flexible solutions for a given antenna pattern synthesis problem. Because of the disadvantages of the classical and analytical techniques, FHA [12, 13] is firstly to calculate elements amplitudes to steer the single and multiple nulls to the directions of interference.

The next section briefly explains the formulation of the problem, calculated antenna array patters are then presented and conclusion is made.

4. FORMULATION

In this study, the element amplitudes are chosen symmetrical about the center of the linear array, the far field array factor of this array with an even number of isotropic elements (2N) can be written as

$$F(\theta) = 2\sum_{k=1}^{N} a_k \cos\left(\frac{2\pi}{\lambda} d_k \sin\theta\right) \tag{1}$$

where a_k is the amplitude of the k*th* element, θ is the angle from broadside, and d_k is the distance between position of the k*th* element and the array center. In this particular problem of null synthesizing, we restricted ourselves to find an appropriate set of a_k to place array nulls at any prescribed directions. Whence, the following cost function is minimized by using FHA.

$$C = \sum_{\theta=-90^0}^{90^0} \left[W(\theta)\left|F_o(\theta) - F_d(\theta)\right| + ESL(\theta)\right] \tag{2}$$

where $F_o(\theta)$ and $F_d(\theta)$ are, respectively, the pattern obtained by using BA and the desired pattern. $W(\theta)$ and $ESL(\theta)$ are included in the cost function to control the null depth level and maximum sidelobe level, respectively. The values of $W(\theta)$ and $ESL(\theta)$ should be selected by experience such that the cost function is capable of guiding potential solutions to obtain satisfactory array pattern performance with desired properties (for more details please see reference [37]).

5. CALCULATED ANTENNA ARRAY PATTERS

To show the flexibility and capability of the proposed FHA for steering single and multiple nulls with the imposed directions by controlling the amplitude-only, three examples of a linear array with 20 isotropic elements have been performed. A 30-dB Chebyshev pattern for 20 equal spaced elements with λ/2 inter element spacing is utilized as the initial pattern. Typical values of parameters for FHA are used to calculate the antenna array amplitude values. In the first example, the direction of interference θ_i is chosen at the peak of the second sidelobe, which occurs about 14°. In the second example, the direction of double interferences θ_i are chosen at the peak of the second and forth sidelobe, which occurs about 15° and 26°. In the third example, the direction of triple interferences θ_i are chosen at the peak of the second, fourth and fifth sidelobe, which occurs about 15°, 26° and 33°. The values of the cost function parameters given in equation (2) are selected as follows:

$$F_d(\theta) = \begin{cases} 0, & \text{for} \quad \theta = \theta_i \\ \text{Initial pattern}, & \text{elsewhere} \end{cases} \tag{3}$$

- $$W(\theta) = \begin{cases} 50, & \text{for} \quad \theta = \theta_i \\ 1, & \text{elsewhere} \end{cases} \tag{4}$$
- $$ESL(\theta) = \begin{cases} 5, & \text{if MSL} > -28\,\text{dB} \\ 0, & \text{otherwise} \end{cases} \tag{5}$$

where *MSL* given in equation (5) represents the maximum sidelobe level of achieved pattern in the sidelobe region. The resultant patterns are shown in Figure 1-3. Minimum null dept of the patterns are shown in the figures. Those are 144 dB, 120 dB and 100 dB respectively. All amplitude values of these examples are given in Table I.

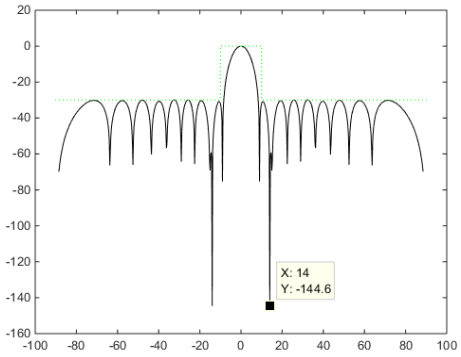

Figure 51. Radiation pattern with one imposed null at 14º.

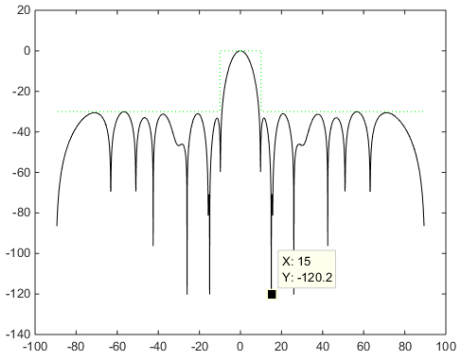

Figure 52. Radiation pattern with one imposed null at 15º and 26º.

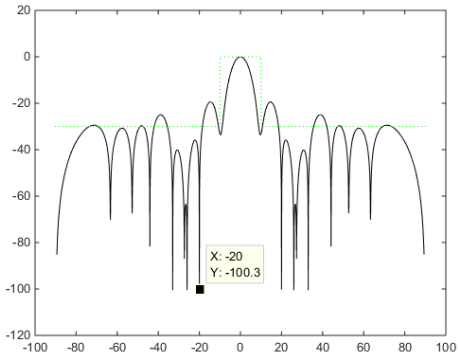

Figure 53. Radiation pattern with one imposed null at 20º, 26º and 33º.

Table2.Computed Antenna Array Amplitude Values by using FHA

k	Computed with the FHA		
	Fig. 1	Fig. 2	Fig. 3
1	0,81367	1.00000	1.00000
2	0,80317	0,94762	0,85578
3	0,76309	0,93500	0,75253
4	0,70219	0,85325	0,64821
5	0,61701	0,68498	0,46982
6	0,50425	0,51403	0,44304
7	0,37944	0,41865	0,48010
8	0,26809	0,34850	0,37899
9	0,18143	0,14130	0,21352
10	0,23498	0,17353	0,24788

6. CONCLUSION

In this paper, a new, fast, easy to write and efficient optimization algorithm is used to antenna array synthesis which is a hard work engineering problem. The algorithm mimics the fox hunting activity which is formed and improved since 16th century. In the activity some animals are used by their superior features. The algorithm simulates these animals with their superiorities to find the optimal solution. By using the algorithm amplitudes of 20 isotropic elements of the antenna array are calculated.

ACKNOWLEDGMENT

This work was supported by Research Fund of The Scientific and Technological Research Council of Turkey (TUBITAK) under Project Number: 215M042.

The author would like to thank Prof. Dr. M. Emin Yuksel, Ass. Prof. Dr. Ilke Turkmen, Ass. Prof. Dr. Tugrul Oktay, Mr. Mehmet Konar and Mr. Hasan Murat Sert for their technical supports during this study and also would like to thank Prof. Dr. Ilker YILMAZ for serving opportunities of Erciyes University, Faculty of Aeronautics and Astronautics.

REFERENCES

[1]. L.J. Fogel, A.J. Owens and M.J. Walsh, *Artificial Intelligence Through Simulated Evolution*, John Wiley, Chichester: UK, 1966.
[2]. K. De Jong, “Analysis of the behavior of a class of genetic adaptive systems”, Ph.D. Thesis, University of Michigan, Ann Arbor, MI, 1975.
[3]. J.R. Koza, *Genetic programming: a paradigm for genetically breeding populations of computer programs to solve problems*, Rep. No. STAN-CS-90-1314, Stanford University, CA, 1990.
[4]. J.H. Holland, *Adaptation in Natural and Artificial Systems*, University of Michigan Press, Ann Arbor, MI, 1975.
[5]. D.E. Goldberg, *Genetic Algorithms in Search, Optimization and Machine Learning*, Addison Wesley, Boston, MA, 1989.
[6]. M. Dorigo, V. Maniezzo, A. Colorni, “Ant system: Optimization by a colony of cooperating agents”, *IEEE Transactions on Systems, Man, and Cybernetics – part B: Cybernetics*, vol. 26, pp. 29–41, 1996.
[7]. R.C. Eberhart, and J. Kennedy, “A new optimizer using particle swarm theory”, Proceedings of the Sixth International Symposium on Micro Machine and Human Science, Nagoya, Japan,. Piscataway, NJ: IEEE Service Center, pp. 39-43, 1995.
[8]. D.T., Pham, A. Ghanbarzadeh, E. Koc, S. Otri, S. Rahim, and M. Zaidi, *The bees algorithm - a novel tool for complex optimisation problems*, Proc 2nd Int Virtual Conf on Intelligent Production Machines and Systems *(IPROMS 2006)*, Oxford, Elsevier, 2006.

[9]. X.L. Li, "A New Intelligent Optimization-Artificial Fish Swarm Algorithm", Doctor thesis, Zhejiang University of Zhejiang, China, 2003.
[10]. D. Karaboga, B. Basturk, A powerful and efficient algorithm for numerical function optimization: artificial bee colony (ABC) algorithm, Journal of global optimization 39 (3), 459-471, 2007. 3724, 2007.
[11]. Lord Burns, V. Edwards, J. Marsh, Lord M. Winter, *The Final Report of the Committee of Inquiry into Hunting with Dogs in England and Wales*, Her Majesty's Stationery Office, 2009.
[12]. M. Onay, "A New and Fast Optimization Algorithm: Fox Hunting Algorithm (FHA)," in *Proc. International Conference on Applied Mathematics, Simulation and Modelling (AMSM 2016)*, pp. 153-156, 2016.
[13]. M. Onay, "A Novel, Fast and Improved Fox Hunting Optimization Algorithm (FHA) and Blur Kernel Estimation Application", in *Proc. 3rd International Conference on Engineering and Natural Sciences (ICENS 2017)*, pp. 938-943, 2017.
[14]. Steyskal, H., R.A. Shore, and R.L. Haupt, "Methods for null control and their effects on the radiation pattern," *IEEE Trans. Antennas Propagat.*, Vol. 34, pp. 404-409, 1986.
[15]. Er, M.H., "Linear antenna array pattern synthesis with prescribed broad nulls," *IEEE Trans. Antennas Propagat.*, Vol. 38, pp. 1496-1498, 1990.
[16]. Ibrahim, H.M., "Null steering by real-weight control—a method of decoupling the weights," *IEEE Trans. Antennas Propagat.*, Vol. 39, pp. 1648-1650, 1991.
[17]. Liao, W.P. and F.L. Chu, "Array pattern synthesis with null steering using genetic algorithms by controlling only the current amplitudes," *Int. J. Electronics*, Vol. 86, pp. 445-457, 1999.
[18]. Shore, R.A., "Nulling at symmetric pattern location with phase-only weight control," *IEEE Trans. Antennas Propagat.*, Vol. 32, pp. 530-533, 1984.
[19]. Haupt, R.L., "Phase-only adaptive nulling with a genetic algorithm," *IEEE Trans. Antennas Propagat*., Vol. 45, pp. 1009-1015, 1997.
[20]. Ismail, T.H. and M.M. Dawoud, "Null steering in phased arrays by controlling the element positions," *IEEE Trans. Antennas Propagat*., Vol. 39, pp. 1561-1566, 1991.
[21]. Tennant, A., M.M. Dawoud, and A.P. Anderson, "Array pattern nulling by element position perturbations using a genetic algorithm," *Electronics Letters*, Vol. 30, pp. 174-176, 1994.
[22]. Liao, W.P. and F.L. Chu, "Array pattern nulling by phase and position perturbations with the use of the genetic algorithm," *Microwave and Optical Technology Letters*, Vol. 15, pp. 251-256, 1997.
[23]. Hejres, J.A., "Null steering in phased arrays by controlling the positions of selected elements," *IEEE Trans. Antennas Propagat*., Vol. 52, pp. 2891-2895, 2004.
[24]. Abu-Al-Nadi, D.I., T.H. Ismail, and M.J. Mismar, "Interference suppression by element position control of phased arrays using LM algorithm," *Int. J. Electronics*, Vol. 60, pp. 151-158, 2006.
[25]. Ares, F., J.A. Rodriguez, E. Villanueva, and S.R. Rengarajan, "Genetic algorithms in the design and optimization of antenna array patterns," *IEEE Trans. Antennas Propagat*., Vol. 47, pp. 506-510, 1999.
[26]. Guney, K. and A. Akdagli, "Null steering of linear antenna arrays using modified tabu search algorithm," *Progress in Electromagnetics Research*, PIER 33, pp. 167-182, 2001.
[27]. Karaboga, N., K. Guney, and A. Akdagli, "Null steering of lineer antenna arrays by using modified touring ant colony optimization algorithm," *Int. J. RF and Microwave Computer Aided Eng*., Vol. 12, pp. 375-383, 2002.
[28]. Akdagli, A., K. Guney, and D. Karaboga, "Pattern nulling of linear antenna arrays by controlling only the element positions with the use of improved touring ant colony optimization algorithm," *J. Electromagnetic Waves and Applications*, Vol. 16, pp. 1423-1441, 2002.
[29]. Karaboga, D., K. Guney, and A. Akdagli, "Antenna array pattern nulling by controlling both the amplitude and the phase using modified touring ant colony optimisation algorithm," *Int. J. Electronics*, Vol. 91, pp. 241-251, 2004.
[30]. Akdagli, A. and K. Guney, "Null steering of linear antenna arrays by phase perturbations using modified tabu search algorithm," *J. Communications Technology and Electronics*, Vol. 49, pp. 37-42, 2004.
[31]. Khodier, M.M. and C.G. Christodoulou, "Linear array geometry synthesis with minimum sidelobe level and null control using particle swarm optimization," *IEEE Trans. Antennas Propagat*., Vol. 53, pp. 2674-2679, 2005.
[32]. Yang, S., Y.B. Gan, and A. Qing, "Antenna-array pattern nulling using a differential evolution algorithm," *Int. J. Microwave RF Computer-Aided Engineering*, Vol. 14, pp. 57-63, 2004.
[33]. Chung, Y.C. and R.L. Haupt, "Amplitude and phase adaptive nulling with a genetic algorithm," *J. Electromagnetic Waves and Applications*, Vol. 14, pp. 631-649, 2000.
[34]. Mouhamadou, M., P. Vaudon, and M. Rammal, "Smart antenna array patterns synthesis: null steering and multi-user beamforming by phase control," *Progress In Electromagnetics Research*, PIER 60, pp. 95-106, 2006.
[35]. Mouhamadou, M., P. Armand, P. Vaudon, and M. Rammal, "Interference supression of the linear antenna arrays controlled by phase with use of SQP algorithm," *Progress In Electromagnetics Research*, PIER 59, pp. 251-265, 2006.
[36]. Akdagli, A. and K. Guney, "A clonal selection algorithm for null synthesizing of linear antenna arrays by amplitude control," *J. Electromagnetic Waves and Applications*, Vol. 20, pp. 1007-1020, 2006.
[37]. Guney K., Onay M., "Amplitude-only pattern nulling of linear antenna arrays with the use of bees algorithm", *Progress in Electromagnetics Research-PIER*, vol.70, pp.21-36, 2007

ICENS 4TH INTERNATIONAL CONFERENCE ON ENGINEERING AND NATURAL SCIENCE
2-6 May 2018 KIEV UKRAINE

Use Of A Vertical Take-Off And Landing (Vtol) Unmanned Aerial Vehicle (Uav) In The Control Of Highways

Murat Onay[1], Muzaffer Ozkoca[2],IlhanKurtulus Ciklaiblikci[2],Ziya Ozcelik[2], Omer Canga[2],Fazil Onur Sonmez[2]

Abstract

Unmanned Air Vehicles (UAVs) are popular and well known air vehicles. Vertical take-off and landing (VTOL) UAVs are hybrid air vehicles. Those can also take of like a helicopter and fly like an aircraft. This combines the superiority of the helicopter take-off with the efficient and fast flight of the aircraft. This paper focuses on a VTOLUAV that used in the control of highways. By using this VTOLUAV in the highways; road construction works, traffic jam, data of traffic accidents, road defects and so on could be detected. The VTOLUAV is used to take images of road constructions. The taken images are processed and discussed in this paper. The processed images are taken by the VTOLUAV while the construction process of the road. The map of differences of the taken images is calculated by the algorithm. This map is used to find the changes of the construction area. In this way, every stage of road construction works is controlled. Also the design and build phases of the VTOLUAV are presented in this paper.

Keywords: Image Processing, Unmanned Aerial Vehicle, UAV, Vertical take-off and landing, VTOL

1. INTRODUCTION

Nowadays, Unmanned Aerial Vehicle (UAV) technologies are developing rapidly day by day.UAV systems have become reasonable fields for researching in the academic and engineering area. There are usually three types of UAVs. First one is aircraft type, secondone is helicopter type and the third one is hybrid type. The aircraft type goes faster than helicopters but it can't fly without axial movement and also it needs runway for take-off and landing [1-3]. The helicopter type can fly without axial movement and also it doesn't need runway for takeoff or landing, but it is relatively slower and also spends more energy to fly [4,5]. To overcome these disadvantages, hybrid type UAVs are manufactured [6-9].Vertical Take Off and Landing Vehicles (VTOL) is one of the hybrid types which doesn't need long runways for take-off and landing. In this study a VTOLUAV is designed and built. The VTOL UAVs can easily take off and land on all types of surfaces [10]. Many civilian areas such as traffic control, natural disaster control, filming etc. are used VTOLs [11].

Today, aviation is one of the most beneficial areas of development in electronics and communication fields. In the light of these developments, the functions and usage areas of VTOL UAVs will increase also this will make human life easier. Using UAVs ensures that the needed tasks are done safely and quickly. They are usually both controlled by a pilot from a ground station and autonomously navigate on a predetermined route. The most important feature that differentiates UAVs from guided missile systems is their ability to be used again and again [12]. They can be electric and fossil fuel powered according to usage purposes. These tools can be as small as a bug or as heavy as thousands of kilograms. One of the most important elements for the UAV is an aerodynamic structure that uses a good light wind [13]. In the next section mathematical control formulations are given.

[1] *Corresponding author: Erciyes University, Faculty of Aeronautics and Astronautics, Department of Avionics, 38039, Melikgazi/Kayseri, Turkey. muratonay@erciyes.edu.tr*
[2]*Erciyes University, M.S.Candidate of Civil Aviation, M.S. student of Murat ONAY, Turkey*
e-mail: muzaffer38@gmail.com; kurtulusiplikci@yahoo.com.tr; ziyaozcelik@outlook.com; omercanga@hotmail.com; fo5sz@outlook.com (respectively)

2. VTOL FLIGHT CONTROL

In this study, an electrically driven quadrotor is used. Each engine produces a thrust and torque from the center, which, in turn, creates a drag force as opposed to the flight direction of the device. If all the engines rotate at the same angular velocity, the second and fourth engines rotate opposite directions to the first and third engines. Then the total aerodynamic torque and hence the angular acceleration, which affects the yaw axis, is zero. In other words, there is no need for an engine that stabilizes the deflection used in conventional helicopters. It is caused by the disagreement between the aerodynamic torques. The angular acceleration that affects the pitch and roll axes can be applied without affecting the yaw axis. Each propeller rotating in the same direction controls one of the pitch or roll axes, while reducing the other while increasing the thrust of an engine maintains the torque balance required for yaw stability, allowing torque to be applied to the roll or pitch axis. Thus, the fixed propellers provide each axle maneuver of the quadrotors. The displacement acceleration is provided by a non-zero pitch or roll. It's easy to give a push with four engines and roll. By increasing the speed of one of the two rotating motors in the same direction and decreasing the other, the total torque and the force applied to the yaw remain at zero [14].

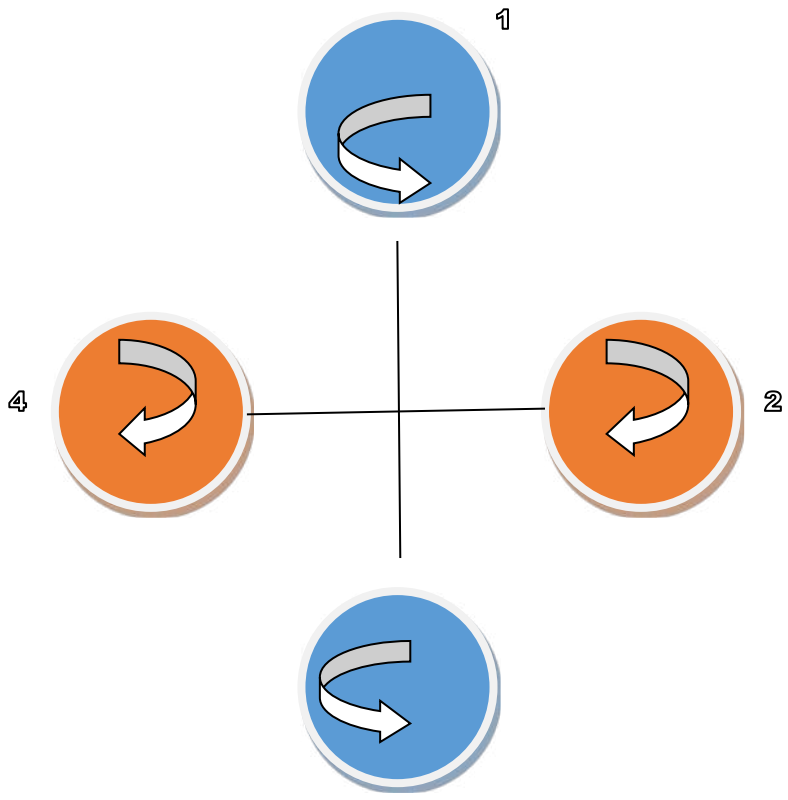

Figure.1:Direction of rotation of engines belonging to VTOL

3. QUADROTOR MATHEMATICAL MODEL

The quadrotor structure is a system of air intake that is driven by engines formed by connecting four (4) rotors to each other (+) or (x).

Due to the structure of the quadrotor, the directions of rotation of the propellers rotate in the same direction 1-3 and 2-4. When the number of revolutions is the same, it moves in the Z axis as well as in the vertical movement. The direction change of quadrotor is provided by changing the engine speeds [15,16]. The basic units of quadrotors are generally composed of 5 parts: brushless direct current engine, electronic speed control board, micro controller, communication unit and energy unit.

The position of the quadrotor propellers is shown in Figure 2.

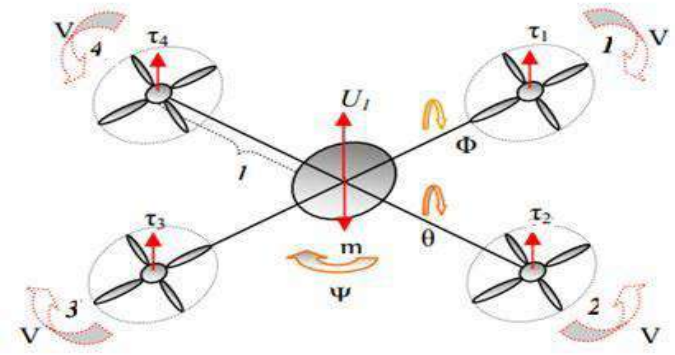

Figure 1: Position of the quadrotor propellers

By changing the propeller turns, torques and moments are created in the system. Vi is the velocity of rotation of the propeller, and τi is the velocity. Thus the total impulse effect on the system is:

U1=τ1+τ2+τ3+τ4 (1)

Turns 2 and 4 arechangedtocreatetheyaw moment in thesystem.

U2=l(τ4 – τ2) τ4 (2)

Pulsating moment is also obtained by changing the rotation of the propellers 1 and 3.

U3=l(τ3 – τ1) τ4 (3)

And in a singleyard, thedivergence moment is obtainedbyturningthedoublenumberedpropellers.

U4=(τ1 – τ2 + τ3 – τ4) (4)

Since the push is directly proportional to the square of rotation, the thrust dependence can be written as

$T_i = b\Omega^2$ *(b constant)* *(5)*

$D_i = d\Omega^2$*(d constant)* *(6)*

Thus, momentsacting on thesystem;

$U_1 = l(\Omega_4^2 - \Omega_2^2)$ *(7)*

$U_2 = l(\Omega_3^2 - \Omega_1^2)$ *(8)*

$U_3 = \Omega_1^2 - \Omega_2^2 + \Omega_3^2 - \Omega_4^2$ *(9)*

$\Omega_r = \Omega_1 - \Omega_2 + \Omega_3 - \Omega_4$ *(10)*

is written as.U^{123}control signals.

The dynamic model has been established with the Euler-Lagrange approach in accordance with the following assumptions:

• The structure is rigid.

• Structure is symmetric.

• The mass center and the body center are identical.

• Propellers are rigid.

• Impulse and drag are proportional to the turn of the turn. If we write Lagrangian's differentiated motion equation

L=T-V, $\Gamma_i = \frac{d}{dt}\left(\frac{\partial L}{\partial \dot{q}_i}\right) - \frac{\partial L}{\partial \dot{q}}$ (11)

Her $\dot{q}_\iota$ generalized coordinates and Γi are generalized forces. The equation of motion from here is as follows;

$I_{xx}\ddot{\Phi} = \dot{\theta}\dot{\Psi}\left(I_{yy} - I_{zz}\right) + J_R\dot{\theta}\Omega_r + U_1$ (12)

$I_{yy}\ddot{\theta} = \dot{\Phi}\dot{\Psi}(I_{zz} - I_{xx}) + J_R\dot{\Phi}\Omega_r + U_2$ (13)

$I_{zz}\ddot{\Psi} = \dot{\Phi}\dot{\theta}\left(I_{xx} - I_{yy}\right) + U_3$ (14)

Definitions of the symbols shown in this equation are shown in the following table.

Table 1: Equation symbols

Symbol	**Definition**
φ	Angle of roll
θ	Angle of pitch
Ψ	Angle of yaw
τ	Propulsion
Ω	Propellercycle
Ω_r	Cyclicalimbalance
m	Mass
L	Armlength
b,d	Propulsion, draggingconstant

4. METHOD

a. UAV DESIGN

First, the quadrotor structure was mounted on the carbon rods (Figure 3). The extremely important reasons for choosing carbon rods are that they are light and robust. The carbon rods are secured with the help of screws

through holes drilled for brushless DC motors. The structure obtained by adding ESC, LiPo battery, receiver and control card to the X-shaped structure is obtained.

Figure 2: Quadrotor with carbon rods

This quadrotor provides data acquisition for control, trend and orientation movements. In Figure. 3, quadrotor was routed through carbon rods in a laboratory environment.

Figure 3: Quadrotor flight in laboratory

In the obtained data beam, the equipment is placed on a rigid plastic rectangular structure as shown in Figure 4., which is next prototype. In this structure, the knowledge gained from the first design was used. In this design, UAV is one step more closed to VTOL UAV.

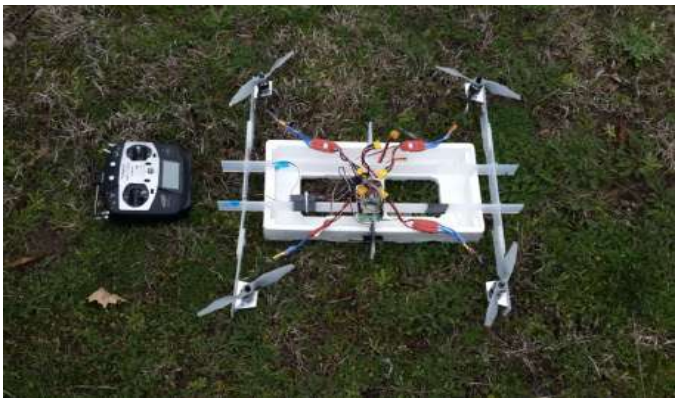

Figure 4: VTOL made with rigid plastic

Both of these designs have been studied on the VTOL structure. As a result of the tests made with the two designs, the most recent design was decided to be able to fly more steadily. Tests were completed done without

the camera, which is a useful load for the first two designs. In the third and final design, the camera structure was added to the equipment.

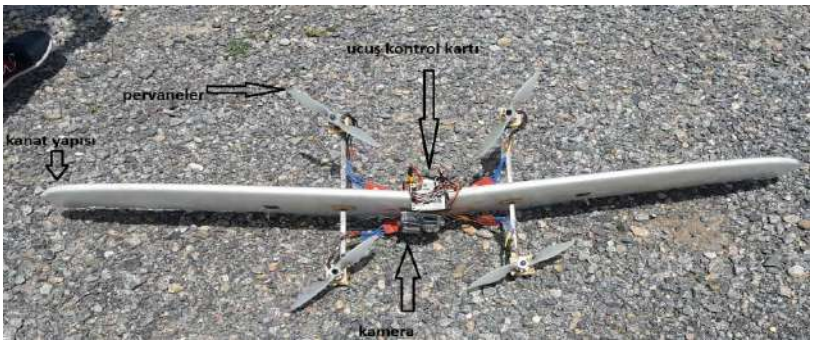

Figure 6: Final VTOL structure

5. CONSTRUCTION FIELD CONTROL WITH CONSTRUCTION

Once the design phases of the UAVs have been folded one by one, on the VTOL structure with the 3D design below is decided.

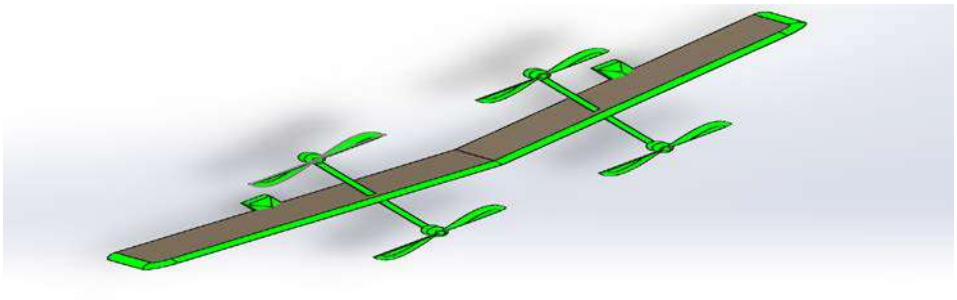

Figure 7: 3D drawing top view

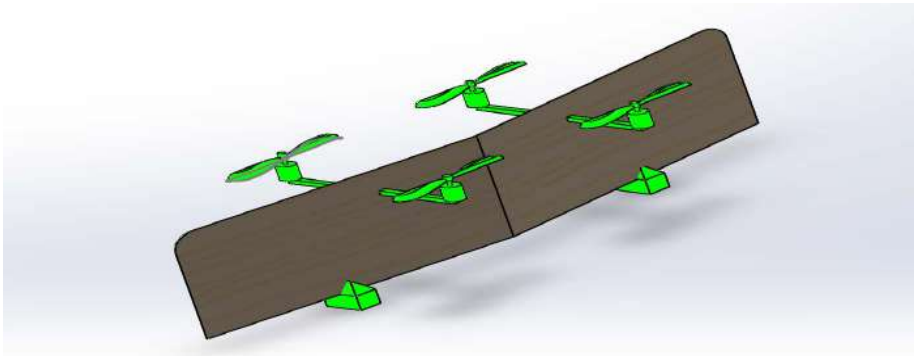

Figure 8: 3D drawing side view

It was is aimed to stay in the air for a long time while consuming minimum energy without compromising image quality both during landing-take-off and during navigation. In this direction, the design parameters of the UAV were changed in the testing process and the following design was decided as the optimum design [17] shown in Figure 9 and Figure 10.

Figure 9: VTOL top view

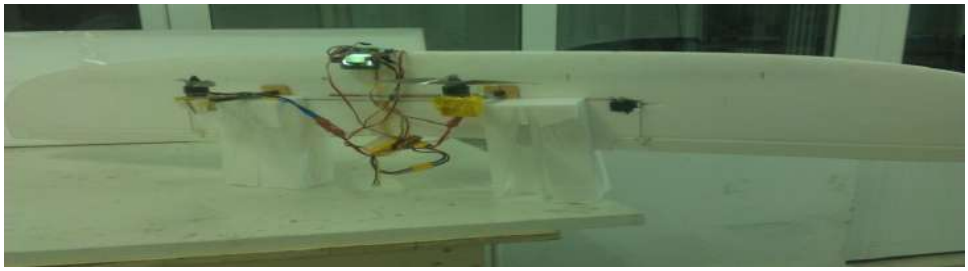

Figure 10: VTOL side view

The aerodynamics of wing have been tested in a different structure from the conventional quadrotor structure. With this aerodynamic structure, a mechanical structure that swings the wings is not needed, and the RC control is parallel to the side as shown by the perpendicular position shown in Figure 12 of the UAV's wings shown in Figure 11.

Figure 11: Perpendicularflights

Figure 12: Parallel flights

In this case, the VTOL UAV has been risen like a helicopter from the surface and has been navigating like an airplane in the air. The images obtained with the high resolution camera which takes the HD image are shown in Figure 13.

Figure 13: Aerial images

Airborne images are analyzed in the MATLAB. As a result of the analyzed images, progress of road construction is monitored.

6. IMAGE PROCESSING

Image processing is the process of grouping the color properties of images into meaningful expressions [18]. Aerial images are processed with MATLAB. There is a high resolution camera on the VTOL UAV. Images can be transferred in real time. In addition, images in memory card on the camera can be analyzed after landing [19,20].In this study, aerial images are evaluated after landing. The images obtained in the system will be presented as a report after the images have been processed. Thus, the development of the construction will be determined.

7. EXAMPLES

First of all, the UAV was positioned at the same position for every image. The UAV is constantly transmitted images. These images were observed every day for the same hour and minute and that showed how much progress has been made on the construction between the two days. There are two images of the construction site below which are shown in Figure 14 and Figure 15.

Figure 14: The first image

Figure 15: Second image

The first image is taken at the beginning of the road construction area. The second image is taken close to the end of the works. In these two images, we see before and after the construction site. In order to process images with Matlab, the first image is subtracted from the second one in Matlab so subtracted image is calculated. The subtracted image is translated into black and white image. So that map of difference is calculated.

Below, the difference between the first and second image is seen in Figure 16.d.

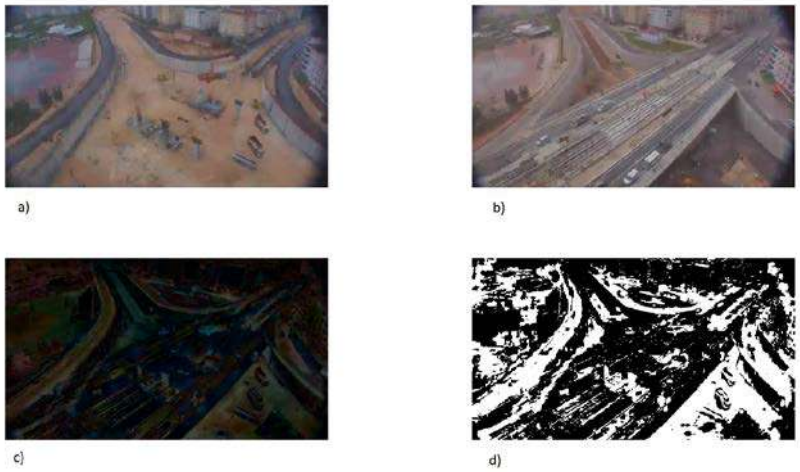

Figure 16: differencemap a)first image b) second image c) subtracted image, d) map of difference

a) The image shows the beginning of the road construction area, b) the image is close to the end of road construction.

The d) Image te thedifference between the two images is visible.As you can see, the white pixel sare the same as the first and second images. where as a black pixel shows us the difference between the two images.

Figure 17 below shows the histograms of thechanges of the images.

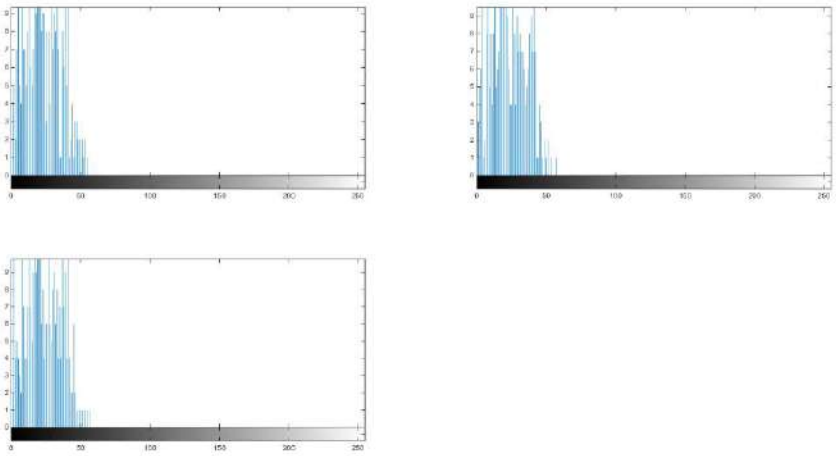

Figure 17: shows the histograms of the changes in the images

8. CONCLUSIONS

In this study, a vertical take-off landing unmanned air vehicle is introduced and used to follow was used to monitor the road construction progress. The VTOL UAV will meet the necessity of the General Directorate of Highways (GDH) in Turkey. The UAV increases speed and reduces cost of road construction control activity of GDH. Also any kind of defect or foreign object on the road can be detected by using this UAV.

ACKNOWLEDGMENT

This work was supported by Research Fund of The Scientific and Technological Research Council of Turkey (TUBITAK) under Project Number: 215M042.

The author would like to thank Prof. Dr. M. EminYuksel, Ass. Prof. Dr. Ilke Turkmen, Ass. Prof. Dr. Tugrul Oktay, Mr. Mehmet Konar and Mr. Hasan Murat Sert for their technical supports during this study and also would like to thank Prof. Dr. Ilker Yilmaz for serving opportunities of Erciyes University, Faculty of Aeronautics and Astronautics.

This work was supported by scientific research projectof Turkey (Erciyes BAP) under Project Number:FYL-2014- 4916

REFERENCES

[1]. A. Kacar, B. Tok, ,A. C. Kahvecioglu, O. Albostan, S. Kose, B. Irfanoglu, K. B. Arikan, "UcDonerkanatliveDoner-RotorluInsansizHavaAracininTasarimi-Design of the Triple Tilt-Rotor Unmanned Aerial Vehicle." *Emo BilimselDergi*, *3*(6), pp. 107-114. 2013.

[2]. A. Guclu, K. B. Arikan, D. F. Kurtulus, "HibritInsansizHavaAracininYonelimDinamiklerininHibritDenetimi" *Vi. UlusalHavacilikVeUzayKonferansi*, UHUK-2016-078, pp. 1-7, 2016.

[3]. O. Tekinalp, A. S. Onen, D. F. Kurtulus, L. Cevher, M. Senipek, T. Mutlu. , O. Gungor, I. O. Uzunlar "Modeling and Controller Design of a VTOL UAV", *Proceedings of the 2015 International Conference on Unmanned Aircraft Systems (ICUAS'15)*, Denver, CO, USA 9-12 June 2015

[4]. M. YILDIZ, A. KACAR, , K. B. ARIKAN, "Doner-Rotor MekanizmasinaSahip, IkiRotorluSiradisiUcan Robot Tasarimi, ModellenmesiVeYonelimDenetimi",*MekatronikMuhendisligiOgrenciKongresi (Memok) 2010*, 16 Haziran 2010

[5]. M. O. Efe, , M. Onkol, N. Imamoglu , A. Eresen, U. Kaynak , "Doner Kanat Tipinde BirInsansiz Hava Aracinin Anatomisi", *Otomatik Kontrol Turk Milli Komitesi Otomatik Kontrol Ulusal Toplantisi* , Ekim 13-16, Istanbul, Turkiye,2009.

[6]. G. Homan, H. Huang, C. J. Tomlin , S. L. Waslander, " Quadrotor Helicopter Flight Dynamics and Control: Theory and Experiment." *In Proceedings of the AIAA Guidance, Navigation, and Control Conference*, Hilton Head, SC, Agustos 2007.

[7]. U. Ozdemir , Y. O. Aktas , A. Vuruskan, Y. Dereli, A. F. Tarhan, K. Demirbag, G. Inalhan,"Design of a commercial hybrid VTOL UAV system". *Journal of Intelligent & Robotic Systems*, *74*(1-2), 371-393. 2014.

[8]. R. AUSTIN, *Unmanned aircraft systems: UAVS design, development and deployment*. John Wiley & Sons, 2011.

[9]. K. Muraoka , O. Noriaki, and K. Daisuke "Quad tilt wing vtoluav: Aerodynamic characteristics and prototype flight." *AIAA Infotech@ Aerospace Conference and AIAA Unmanned... Unlimited Conference*. 2009.

[10]. E. C. Suicmez, A. T. Kutay, "Dort Rotorlu Bir Insansiz Hava Aracinin Geri-Adimlama Yontemi Ile Yol Takibi Kontrolu", *Havacilik Ve Uzay Teknolojileri Dergisi Temmuz 2014 Cilt 7 Sayi 2 (1-13)* 2014.

[11]. i.C. Dikmen, A. Arisoy, ve H. Temeltas, "Dikey Inis-Kalkis Yapabilen Dort Rotorlu Hava Aracinin (Quadrotor) Ucus Kontrolu", *Havacilik ve Uzay Teknolojileri Dergisi*, sayi 3, sayfa 33-40. 2010.

[12]. A. Mevlutoglu, , Insansiz Hava Araclari Ve Ag Merkezli Muharebe Kavrami,TMMOB Makina Muhendisleri Odasi V. Ulusal Ucak, Havacilik ve Uzay Muhendisligi Kurultayi,Eskisehir, 2009.

[13]. S. Erdemir," IHA Sistemlerinde Hava Araci ve Gorev Faydali Yukleri", Aselsan, v.45, 1998.

[14]. S. Bouabdallah, , M. Pierpaolo, S. Roland "Design andcontrol of an indoor microquadrotor." *RoboticsandAutomation, 2004. Proceedings. ICRA'04. 2004 IEEE International Conference on*. Vol. 5. IEEE, 2004

[15]. W. B. Randal , Quadrotor Dynamics andControl, BrighamYoung University,2008.

[16]. C. Ballas, ModellingandLinear Control Of A Quadrotor, MsThesis, CranfieldUniversity, 2007

[17]. O. Atsushi, A. Satoko, K. Atsushi, K. Takuya, F. Tatuya, U. Masaru, 2013,Development of a Quad Rotor Tail-Sitter VTOL UAV without Control SurfacesandExperimentalVerification, 2013 IEEE International Conference on RoboticsandAutomation (ICRA) Karlsruhe, Germany, May 6-10, 2013.

[18] . R. Gonzalez (Digital) Image Processing. 2002.

[19]. C Yuan,. , L. Zhixiang, Z. Youmin "UAV-basedforest fire detectionand tracking using image processing techniques." *Unmanned Aircraft Systems (ICUAS), 2015 International Conference on*. IEEE, 2015.

[20]. K. Guney, ve M. Onay, 2004, Insansiz Hava Araclari Ve imge islemenin Vizyonu, *Kayseri V. Havacilik Sempozyumu*, Kayseri

ICENS 4TH INTERNATIONAL CONFERENCE ON ENGINEERING AND NATURAL SCIENCE
2 - 6 May 2018 KIEV UKRAINE

Analysis of Preseismic and Postseismic Deformation of Gulbahce and surroundings with Sigacik (Izmir-Turkey) Earthquake (2005)

Oya Pamukcu [1], Baris Can Malalici [2]

Abstract

One of the most important cities of Western Anatolia is Izmir. A great number of tectonic structures located in Izmir and surroundings, so there are high seismic activity. Within this study, preseicmic and postseicmic deformation analysis of the earthquake whose magnitude is Ml =5.9 occurred in Sigacik Gulf where is located in the south part of Izmir on 17/10/2005 have been carried out. Before the earthquake, preseismic deformation analysis has been carried out by evaluating the GPS velocity datas obtained from the Global Positioning System (GPS) campaign measurement held in the years 2001, 2003, and 2004 in SSPX software. It is stated that the deformation areas obtained as a result of analysis and the distribution of earthquake areas in the region are compatible to each other. In consequence of deformation calculated by evaluating the velocity datas obtained from the GPS campaign measurement conducted in the region in 2009, 2010, and 2011 after the earthquake, it is seen that high deformation areas have been moving towards to northwest. It is observed that the high deformation area has displaced to north of Gulbahce after the earthquake in Sigacik in 2005 and this deformation are is compatible with the current earthquake distributions.

Keywords: deformation,earthquake,Gulbahce, preseismic, postseicmic

1. INTRODUCTION

West Anatolia and Aegean Sea where the study area is located (Figure 1) have a complex tectonism that shows North-South oriented extension [1]-[2]. The formation occurred by North-South extension from Pliocene to present day in West Anatolia which is bounded by North Anatolian Fault Zone in the North and Helen-Cyprus Arc in the south is based upon the deformation related to the tectonic escape [3]. As a result of this tectonic escape, two big fault zones have occurred in the plate boundaries. (Right-Lateral North Anatolian Fault Zone and Left-Lateral East Anatolian Fault Zone) [3]. According to the GPS studies [4] [5]- [6], westwardly movement of West Anatolia has been rotating counter-clockwise. This rotation shows that West Anatolia changes direction towards the Helen Arc in the southwest approximately N200E directional transfer zone between Izmir and Balikesir [3]. In the study conducted by Reference [4] around West Anatolia and Izmir, directions of movement which are compatible with the general tectonic of the region have been determined. In addition, it is stated that the region located in the west of Tuzla fault has a range of high extension. Reference [5] have revealed the relation between b-value and deformation for the same study area. The Karaburun Peninsula where is in the western part of the study area is a region that has a complex tectonism and there are three main tectonic structures in the region; these are Karaburun Fault, Gulbahce Fault [7], and Karaburun Seismic Zone (KSZ) [8]. Locations and areal extent of these main tectonic structures have been defined by GPS studied by Reference [6] and depth-dependent stress changes of the region have been revealed by Reference [9].

[1] *Corresponding author: Dokuz Eylul University, Engineering Faculty, Department of Geophysical Engineering, 35160, Tinaztepe Campus, Buca, Izmir –TURKEY, oya.pamukcu@deu.edu.tr*

[2] *Dokuz Eylul University, The Graduate School of Natural and Applied Sciences, 35160, Tinaztepe Campus, Buca, Izmir – TURKEY, barismalalici@gmail.com*

Earthquakes in different magnitudes occurred in Sigacik (Izmir) and its surroundings in 17th October 2005 and successive earthquakes were being observed during the year 2005 in the region. In this study, GPS velocities obtained from 2001 to 2004 [4] before the earthquake in 17th October 2005 have been used. The SSPX software [10] have been used to analyze the deformation analysis with the help of these velocities before the earthquake. Then, the post-earthquake deformation analysis has been carried out by using the velocities obtained from the GPS observations [6] made in and around Izmir in 2009, 2010 and 2011, and information about the change of deformation after the earthquake has been given. Besides, the results of this deformation analysis have been scrutinised together with the earthquakes that occurred in the region.

Figure 1. The location of the study area (Google Earth) and the simplified tectonic structure of the region [3]-[7].

2. APPLICATIONS

In pre-seismic analysis, GPS velocities obtained from the GPS campaign measurements from 2001 to 2004 [4] have been used. Surface deformations have been obtained by using SSPX software [10] from the horizontal speeds of 24 stations (Figure 2). The distribution map of the earthquakes (M ≥2.5, [11]) in the region in 2005 have been created in order to detect the compatibility of the earthquakes and the result of deformation analysis (Figure 3).

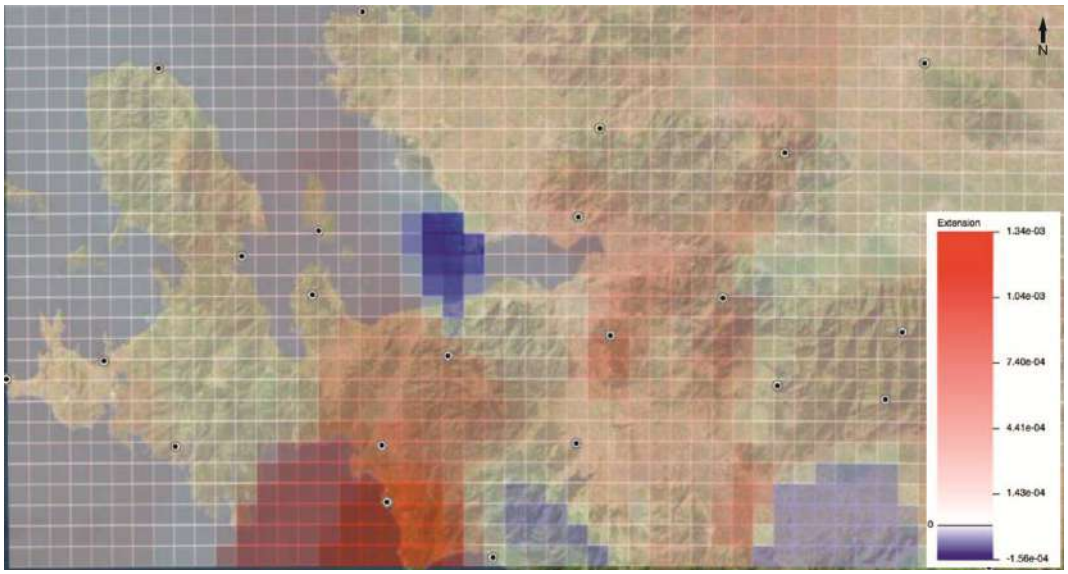

Figure 2. 2005 Sigacik earthquake pre-seismic deformation analysis (Red: Extension / Blue: Shortening).

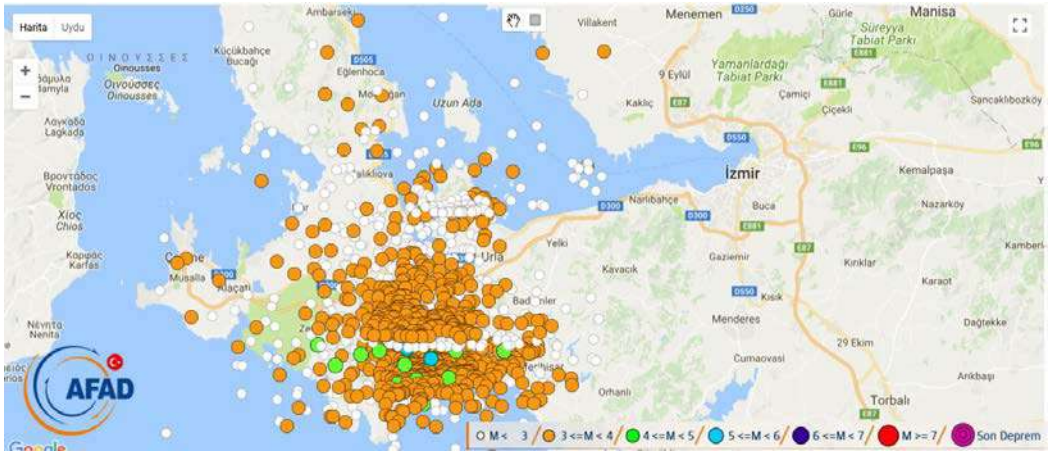

Figure 3. Earthquakes that occurred in the region between 01/01/2005 and 31/12/2005 (M ≥2.5).

Post-seismic deformation analysis has been performed by using the velocity data [6] of GPS campaign measurements (2009, 2010 and 2011) carried out in and around Izmir (Figure 4). In order to investigate the relation between this deformation analysis result and the earhtquakes, the epicentral distributions of earthquakes (M ≥ 2.5) between 2007 and 2010 were investigated (Figure 5).

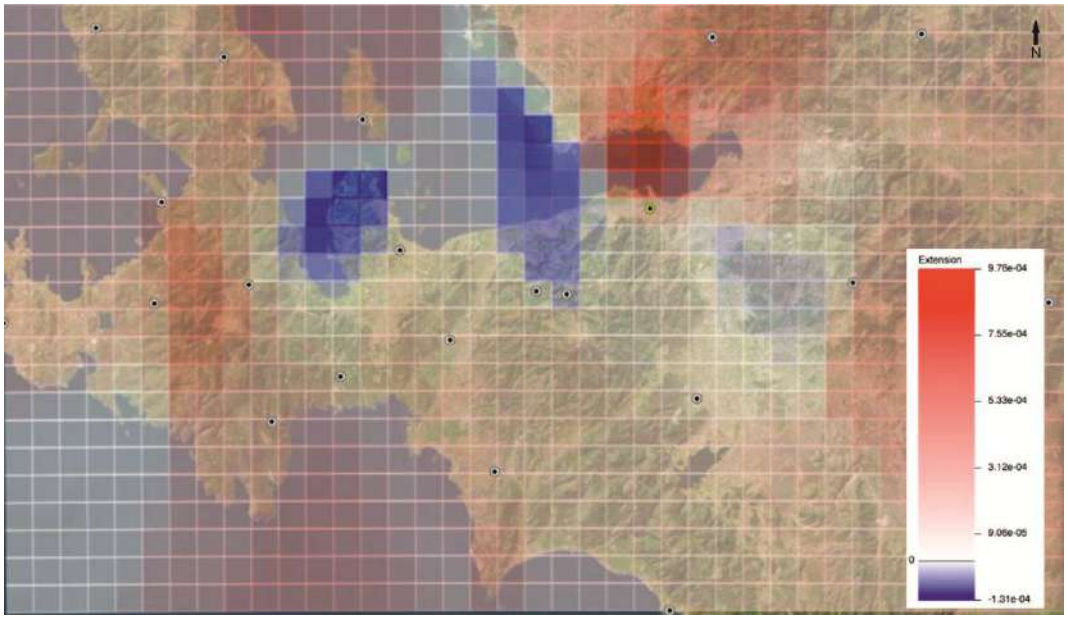

Figre 4. 2005 Sigacik earthquake post-seismic deformation analysis (Red: Extension / Blue: Shortening).

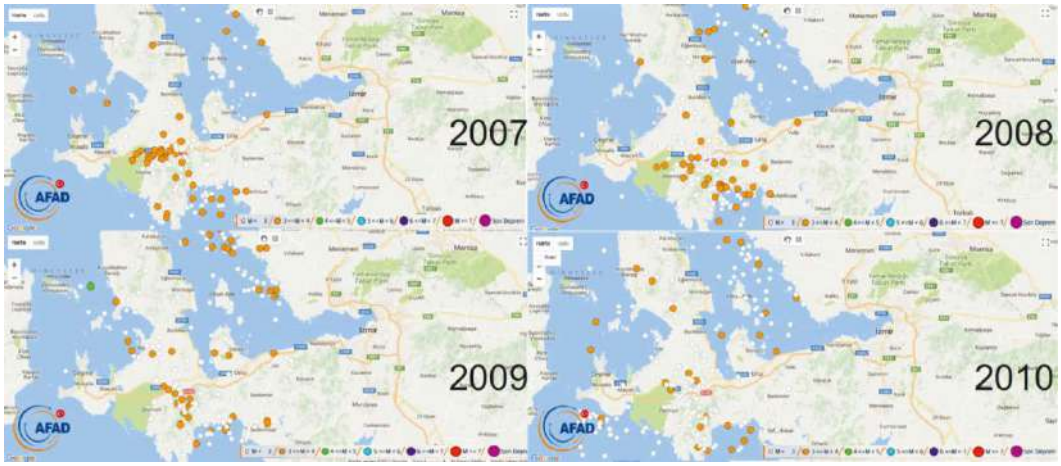

Figure 5. Distribution of earthquakes (M ≥ 2.5) in the region between 2007-2010.

3. DISCUSSİONS AND CONCLUSIONS

In consequence of pre-seismic deformation analysis determined by GPS velocities obtained from GPS observations made in the region before the earthquake [4], high extension range has been confirmed in Sigacik Gulf (Figure 2). This is a foreshadow for high seismic activity in the region. When Figure 2 and Figure 3 have been examined together, it has been seen clearly that high deformation area is compatible with the earthquakes occurred in the region in 2005. In figure 4, it has been confirmed that the surface deformations was determined by using horizontal velocities obtained from GPS observations made in the region [6] after the earthquake were changed. In pre-seismic deformation analysis (Fig. 2), high deformation area has been observed in Sigacik Gulf. As a result of post-seismic analysis, it is determined that this deformation area has moved to the region that Gulbahce Fault and Karaburun Seismic Zone are located in the western part of Sigacik Gulf (Fig. 4). Especially when the epicentral distributions of earthquakes between 2007 and 2010 are examined, it is observed that the

frequency of earthquake has decreased in Sigacik Gulf and it has increased in Gulbahce Fault and Karaburun Seismic Zone (Figure 5).

ACKNOWLEDGMENT

This study is derived from a master thesis on "Examination of geodynamic structure of gulbahce fault and its surroundings" conducted by Baris Can Malalici. We thank to Dr. Ayca CIRMIK for GPS calculations.

REFERENCES

[1]. McKenzie, D. (1972). Active tectonics of the mediterranean region. Geophysical Journal International, 30(2), 109–185.
[2]. Dewey, J. F., and Sengor, A. C. (1979). Aegean and surrounding regions: complex multiplate and continuum tectonics in a convergent zone. Geological Society of America Bulletin, 90(1), 84–92.
[3]. Uzel, B., ve Sozbilir, H. (2008). A first record of strike-slip basin in western Anatolia and its tectonic implication: the Cumaovasi basin as an example. Turkish Journal Earth Science, 17, 559–591.
[4]. Aktug, B., and Kilicoglu, A. (2006). Recent crustal deformation of Izmir, Western Anatolia and surrounding regions as deduced from repeated GPS measurements and strain field. Journal of Geodynamics, 41, 471–484.
[5]. Dogru, A., Gorgun, E., Ozener, H., and Aktug, B. (2014). Geodetic and seismological investigation of crustal deformation near Izmir (Western Anatolia). Journal of Asian Earth Sciences 82, 21–31.
[6]. Cirmik,, A., Pamukcu, O., Gonenc, T., Kahveci, M., Salk, M., and Herring, T . (2017a). Examination of the kinematic structures in Izmir (Western Anatolia) with repeated GPS observations (2009, 2010 and 2011). Journal of African Earth Sciences, 126, 1–12.
[7]. Emre, O., Ozalp, S., Dogan, A., Ozaksoy, V., Yildirim, C., Goktas¸, F. (2005). Izmir Yakin Cevresinin Diri Faylari ve Deprem Potansiyelleri [The Active Faults of the Izmir Region and Their Earthquake Potentials]. Mineral Research and Exploration Institute of Turkey (MTA) Report no. 10754 (in Turkish, unpublished).
[8]. Tan, O. (2013). The dense micro-earthquake activity at the boundary between the Anatolian and South Aegean microplates. Journal of Geodynamics, 65(2013), 199–217.
[9]. Cirmik, A., Dogru, F., Gonenc, T., and Pamukcu, O. (2017b). The Stress/Strain Analysis of Kinematic Structure at Gulbahce Fault and Uzunkuyu Intrusive (Izmir, Turkey). Pure and Applied Geophysics, 174, 1425–1440.
[10]. Cardozo, N., and Allmendinger, RW. (2009). SSPX: A program to compute strain from displacement/velocity data. Computers &Geosciences 35, 1343–1357.
[11]. AFAD webpage [Online]. Available: https://deprem.afad.gov.tr/ddakatalogu

ICENS 4TH INTERNATIONAL CONFERENCE ON ENGINEERING AND NATURAL SCIENCE
2-6 May 2018 KIEV UKRAINE

Magnetic Anomaly of The Mid-Atlantic Ridge and Its Surroundings Obtained From Swarm Constellation

Oya Pamukcu [1], Ilkin Ozsoz [2]

Abstract

The Swarm constellation was succesfully launched by ESA on 22 November 2013. Swarm constellation was comprised of three different spacecrafts, Alpha, which was used in this study, Bravo and Charlie. In this study, in order to examine current location of the Mid-Atlantic Ridge, the Swarm satellite magnetic data was used. Total magnetic field intensity and Residuals of the total magnetic field intensity was obtained from Swarm Vires services. Furthermore, the heat flow data ,which was obtained from American Association of Petroleum Geologists (AAPG), is used for comparing magnetic anomaly with heat flow. It is known that magnetic anomaly decreases at the points where Curie Temperature is exceeded. Current earthquake data was used for locating active zones at the ridge.The various data processing techniques, such as polynomial fitting, reduction to the pole, filtering was applied to the data, which was obtained from Swarm Alpha, with the aim of revealing main magnetic anomaly of the Mid-Atlantic Ridge and its surroundings. The high consistency has been observed between heat flow data, current earthquakes data and the processed magnetic data. This study demonstrates that the magnetic data, obtained from Swarm constellation mission, is available for using in crustal studies.

1. INTRODUCTION

The world is extended by mid-ocean ridges which extend nearly 65 000 km [4]. In general, mid-ocean ridges' characteristics are relatively high heat flow and shallow ocean floor and seismicity [4]. It is known that mid-ocean ridges generate oceanic lithosphere and alter its chemical and physical properties [4]. Spreading rate is associated with many features of ridges [4]. Briefly, steep irregular topography and heterogeneous lithosphere are observed at slow spreading ridges [5]. On the other hand, at fast spreading ridges, more gentle slopes are observed [5]-[9]. Mid-Atlantic Ridge has slow spreading rate, approximately 25 mm/yr [3].Furthermore, its axial rift valley width is 30-45 km and depth is 1-2 km [3]. Many normal faults are detected at Mid-Atlantic Ridge and they form crestal mountains with displacing the crust upwards [3]. Segments are occurred by discontinuities [7]. Additionally, there are many tectonomagmatic segmentations at the Mid-Atlantic Ridge [6].

There is a strong link between magnetic and heat flow data. It is known that magnetic properties associated with temperature until the Curie Temperature, which is exceeded the material lose its magnetization (remanent or induced) [8]. It is about 580 ºC for the low-Ti magnetite, the principal source of the crustal magnetization [8]. In this study, therefore, both heat flow data, higher values are expected on the ridge, and magnetic data, lower values are expected at high heat flow regions, used for testing accuracy of the magnetic data. As it was mentioned above, mid-ocean ridges are characterized by higher heat flow. Furthermore, there is a negative correlation between age and heat flow. The Swarm constellation was successfully launched by ESA on 22 November 2013. The Swarm constellation was comprised of three different spacecrafts (Figure 1), Alpha, which was used in this study, Bravo and Charlie. Alpha and Charlie are flying side-by-side roughly 450 km initial altitude and Bravo is flying approximately 530 km initial altitude [1]. Each satellites can make precise magnetic field, navigation, acceleration, plasma and electric field meaurements [2]. Swarm constellation

[1] *Corresponding author: Dokuz Eylul University, Engineering Faculty, Department of Geophysical Engineering, 35160, Tinaztepe Campus, Buca, Izmir –TURKEY, oya.pamukcu@deu.edu.tr*

[2] *Dokuz Eylul University, The Graduate School of Natural and Applied Sciences, 35160, Tinaztepe Campus, Buca, Izmir – TURKEY, ilkinozsoz@hotmail.com*

mission's essential research objectives are (1) determining core dynamics, (2) core-mantle interaction zone, (3) lithospheric magnetization and (4) 3D mantle conductivity [2]. In this study, magnetic field data was provided by Vires Services [10].

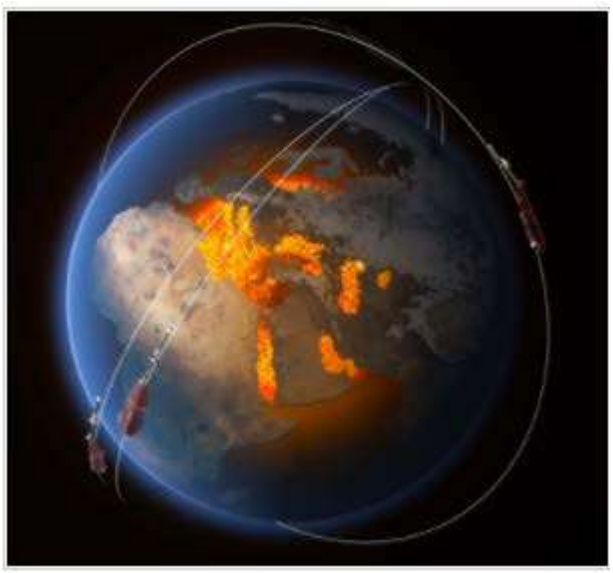

Figure 1. Swarm constellation which comprises 3 identical spacecrafts. Two satellites are flying side-by-side approximately 450 km altitude. Additionaly, Another satellite is flying about 530 km altitude [12].

2. APPLICATIONS

Total magnetic field intensity (nT) data and IGRF residuals were downloaded from Vires Services in order to obtain Mid-Atlantic Ridge magnetic anomaly. The data downloaded in parts due to more precise data processing. Neccessary corrections were performed to the data and the data was plotted (Figure 2). During plotting the data, grid size has been adjusted carefully, in order to avoid edge and plot errors. Furthermore, at data processing stage, upward continuation was applied to the data owing to the fact that eliminate the residuals.

Heat flow data [11] was used for interpretation and testing magnetic anomaly precision. Average heat flow at Atlantic Ocean is 64.2 mW/m^2 [11]. Hence, only heat flow data which is higher than 100 mW/m^2 was plotted. It can be seen that higher heat flow areas are nearly located around the ridge (Figure 3).

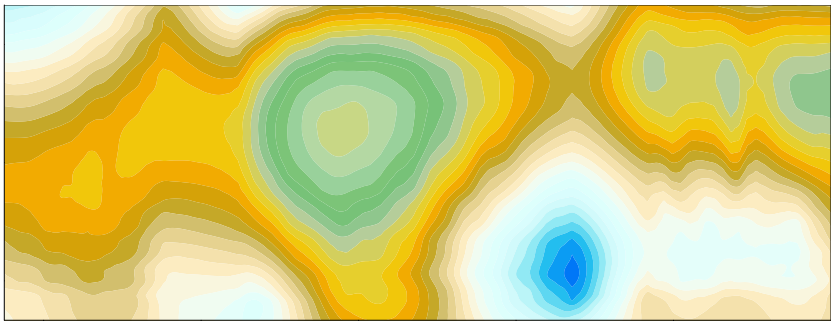

Figure 2. North part of the obtained magnetic anomaly of the Mid-Atlantic Ridge after the performed corrections and data processing.

3. DISCUSSİONS AND CONCLUSIONS

It is known that intensity of magnetic anomaly is inversely proportional to high temperature. As a consequence, in the study area, the total magnetic field intensity is approximately below 0 where the heat flow is higher than 100 mW/m^2. Consistence between the total magnetic field intensity and the heat flow is considerably high. Therefore, it can be said that the magnetic data, provided by Vires Services, completely reliable for regional surveys.

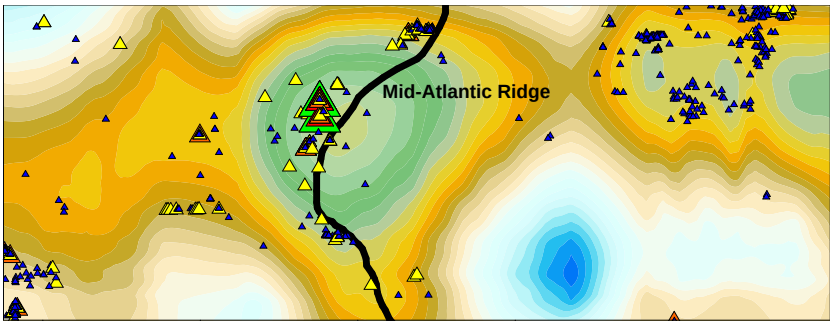

Figure 3. North part of the obtained magnetic anomaly of the Mid-Atlantic Ridge and heat flow data.

As can be seen from the Figure 3, magnitude of the total magnetic anomaly (nT) is between 1400 and -1400 nT. In addition, the highest heat flow points, from 5000 to 10000 mW/m^2, located at the lowest magnetic anomaly. From a different perspective, it can be said that there are roughly no heat flow points, above 100 mW/m^2, close to the magnetic anomaly, above approximately 200 nT.

ACKNOWLEDGMENT

This study is derived from a master thesis on "Examination of satellite magnetic data" conducted by Ilkin Ozsoz.

REFERENCES

[1]. Friis-Christensen, E., Luhr, H and Hulot, G. (2006). Swarm: A constellation to study the Earth's magnetic field. Earth, planets and space, 58(4), 351-358.

[2]. Olsen, N., Friis-Christensen, E., Floberghagen, R., Alken, P., Beggan, C. D., Chulliat, A., and Van den Ijssel, J. (2013). The Swarm satellite constellation application and research facility (SCARF) and Swarm data products. Earth, Planets and Space, 65(11), 1.

[3]. Smith, D. K. and Cann, J. R. (1993). Building the crust at the Mid-Atlantic Ridge. Nature, 365(6448), 707.

[4]. Searle, R. (2013). Mid-ocean ridges. Cambridge University Press.

[5]. NOAA Ocean Explorer. (2014). URL: http://oceanexplorer.noaa.gov/facts/mid-ocean-ridge.html.

[6]. Sharkov, E. V. (2012). Cyclic Development of Axial Parts of Slow-Spreading Ridges: Evidence from Sierra Leone Area, the Mid-Atlantic Ridge, 5-7 N. In Tectonics-Recent Advances. InTech.

[7]. Tucholke, B. E. and Lin, J. (1994). A geological model for the structure of ridge segments in slow spreading ocean crust. Journal of Geophysical Research: Solid Earth, 99(B6), 11937-11958.

[8]. Maule, C. F., Purucker, M. E., Olsen, N. and Mosegaard, K. (2005). Heat flux anomalies in Antarctica revealed by satellite magnetic data. Science, 309(5733), 464-467.

[9]. Sharkov, E. V. (2012). Cyclic Development of Axial Parts of Slow-Spreading Ridges: Evidence from Sierra Leone Area, the Mid-Atlantic Ridge, 5-7 N. In Tectonics-Recent Advances. InTech.

[10]. Vires for Swarm. URL: https://vires.services/

[11]. Jessop, A. M. (2012). The world heat flow data collection-1975.

[12]. ESA Earth Online. URL: https://earth.esa.int/web/guest/missions/esa-eo-missions/swarm/mission-overview.

ICENS 4TH INTERNATIONAL CONFERENCE ON ENGINEERING AND NATURAL SCIENCE
2-6 May 2018 KIEV UKRAINE

Accuracy Analysis of Matrakci Nasuh's Kutahya Miniature

Huseyin Zahit Selvi[1] Ilkay Bugdayci[1]

Abstract

The Ottoman Empire survived for about 600 years. At the end of the 16th century, the Ottoman Empire ruled an area of approximately 20 million km2 extending from the Caspian Sea in the east to the Atlantic Ocean in the west. The Ottoman Empire, which had a very large landscape, needed products as a guide to determine its existing borders and to learn new places. Even during the Ottoman history, it is possible to encounter many products bearing map quality. Maps produced especially in the 16th century had an important place in Ottoman cartography. In particular, the world map designed by Piri Reis is valuable in terms of quality even today. Although both lived in the same period, researchers had more interest to piri reis' maps than Matrakci Nasuh's miniatures. However, while the maps of Piri Reis in terms of marine cartography is crucial, Matrakci's miniatures are valuable in terms of landscape cartography. Over 100 miniatures designed by Matrakci during the Suleiman The Magnificent's east and west expeditions should be evaluated in terms of city planning and cartography. The aim of this study is to examine Matrakci's Kutahya miniature in terms of cartography and to detect its importance as a map and city plan by determining the geometric and topological accuracy. In this context, landmarks such as mosque, mountain, bath etc. in the miniature were compared with maps and Google Earth images obtained by today's technology. In addition, the miniature was evaluated with the MapAnalyst software used to determine the geometric accuracy of historical maps and examined in terms of geometric and topological accuracy. Results indicated that although geometrical accuracy of the miniature was poor, topological accuracy was good.

Keywords: Historical Map; Matrakci Nasuh; Geometric Accuracy; Topologic Accuracy

1. INTRODUCTION

Map production was important in Ottoman Empire. The Ottoman Empire, which had a very large landscape, needed products as a guide to determine its existing borders and to learn new places. Many products being map quality were designed during the Ottoman history. Maps produced especially in the 16th century had an important place in Ottoman cartography. In particular, the world map designed by Piri Reis is valuable in terms of quality even today. Although both lived in the same period, researchers had more interest to Piri Reis' maps than Matrakci Nasuh's miniatures [1-3]. Matrakci Nasuh, as a historian, a swordsman, a mathematician, a calligrapher and an artist, was one of the most interesting people of the 16th century. Over 100 miniatures designed by Matrakci during the east and west expeditions should be evaluated in terms of city planning and cartography. The aim of this study is to examine Matrakci's Kutahya miniature in terms of cartography and to detect its importance as a map and city plan by determining the geometric and topological accuracy. In this context, Matrakci Nasuh's Kutahya miniature was compared with the Google Earth images produced with today's possibilities. Then, the miniature was evaluated with the MapAnalyst software used to determine the geometric accuracy of historical maps and examined in terms of geometric and topological accuracy. This paper is divided into five sections. Following the Introduction, the next section provides a brief overview of Matrakci's life. Used materials and methods are explained in the third part. Then, a detailed presentation of application is given. Finally, conclusions are shared in the last section.

[1] *Corresponding author: Necmettin Erbakan University, Geomatics Engineering Department Konya/ Turkey.*
hzselvi@konya.edu.tr

2. MATRAKCI NASUH'S LIFE

Nasuh was born in Bosnia towards the end of the 15th century. It was taken to the Ottoman palace at a young age as a devshirmeh. He was educated in Enderun in the last years of Sultan II. Bayezid period (1481-1512) [4]. Matrakci Nasuh was one of the most interesting people of the 16th century as a historian, a swordsman, a mathematician, a calligrapher and an artist. Intensive military activities during the Kanuni period encouraged the writing of productive works in many disciplines. The most important work that described the expeditions of this period was Matrakci Nasuh's work titled Beyan-i Menâzil-i Sefer-i Irakayn-i Sultan Suleyman Han or Mecmû'-i Menâzil. In this book, he documented all ranges along the Kanuni's Iran expedition (1533-1536), that started from Istanbul and reached Baghdad over and again from here back to Istanbul, again over Tabriz. He gave important information about the landmarks of these regions with carefully drawn miniatures [5]. Nasuh's book, written in 1537, consists of 88 pages of text, 107 pages of miniature, 25 pages of miniature and text [4]. Miniatures such as Istanbul, Galata, Kutahya, Adana and Erzurum were included in this book.

Matrakci Nasuh has two additional works bearing the same qualities as Mecmu-i Menazil. Nasuh described important places along the Kanuni's Second Hungarian Expedition (1542-1543) with the miniatures in the book of History-i Feth-i Siklos Estergon and Istol-Belgrad. There are 32 miniatures in this book. This book was completed in 1543. Another similar work of Nasuh was the work called Tarih-i Sultan Bayezid, which told about the expeditions of the 2. Beyazit period. Miniatures of the cities of Kili, Akkerman, Inebahti, Muton and Gulek were included in this book. Distances between destinations were presented in miles [4]. It is thought that Matrakci was died in 1564 [6].

3. MATERIAL METHOD

a. Miniature

Miniature refers to painting made with watercolors to decorate handwritten books. Miniatures have their own characteristics. Some of these properties are objects do not close each other, the remaining objects are drawn on the top of the paper, and the size of the objects is determined according to their importance [7].

Paintings of landmark buildings such as mosques, tombs and palaces are very valuable in terms of the history of Turkish architecture in Matrakci's miniatures. On the other hand, the plants and animals seen in these miniatures give important information about the vegetation and lifestyle of those regions [8].

b. MapAnalyst

MapAnalyst is a software application for the accuracy analysis of old maps. Its main purpose is to compute distortion grids and other types of visualizations that illustrate the geometrical accuracy and distortion of old maps. MapAnalyst uses pairs of control points on an old map and on a new reference map. The control points are used to construct distortion grids, vectors of displacement, accuracy circles, and isoclines of local scale and rotation. MapAnalyst also computes the old map's scale, rotation and statistical indicators [9-13]. In this study, the geometrical accuracy of miniatures was investigated with MapAnalyst software.

c. Method

In this study, first of all, the Google Earth image of the studied region was returned to the viewpoint of Matrakci in order to examine Matrakci's Kutahya miniature in terms of cartography. Then, with the help of clear historical details drawn by Matrakci, the historical places in the miniature were compared with their real positions in Google Earth. After this, with the help of MapAnalyst software, the locations of the obvious historical places on the miniature were geometrically compared with the current maps in order to investigate the geometric accuracy of the miniature.

4. APPLICATION

a. Map Accuracy

Map production based on original (classical or photogrammetric methods) measurements may be possible at large scales (1: 1000, 1: 5 000) or at the bottom of medium scales (1: 25 000) as applied in Turkey. Smaller scale maps are produced with cartographic generalization techniques by using larger scale maps [14]. Cartographic generalization is the process of changing the content of a map to a new map design in terms of

geometric position, number of objects and format of representation [15]. As a result of such changes, the planimetric accuracy on the map is no longer preserved. However, in small-scale maps, it is expected that the spatial objects, especially called topological accuracy, should protect their relations with each other. A well-designed map should provide a metric and topological understanding of the objects [16].

b. Kutahya Minyaturu

Kutahya's miniature is in the book of Matrakci's Beyân-i Menâzil-i Sefer-i Irakayn-i Sultan Suleyman Han. There are 4 mosques, a castle, a bath and two river canals emerging from the castle on the miniature (Figure 1). These river canals were called Felent Stream but they were disappeared today. There is also uncertainty about the name and present place of Matrakci's bath. For these reasons, Matrakci's bath and Felent Stream were not considered as known points in this study. Kutahya Castle is shown with number 1 in miniature (Figure 1) and Google Earth (Figure 2). In the miniature (Figure 1) and the Google Earth image (Figure 2), the Kaleici Mosque is indicated as location 2, the Takvacilar Mosque is location 3, Ulu Mosque is location 4 and Saray Mosque is location 5. When the topological position and metric consistency of constructions are examined, it is seen that Ulu Mosque and Saray Mosque were drawn nearer than required. The positions of other constructions according to Google Earth are topologically harmonious.

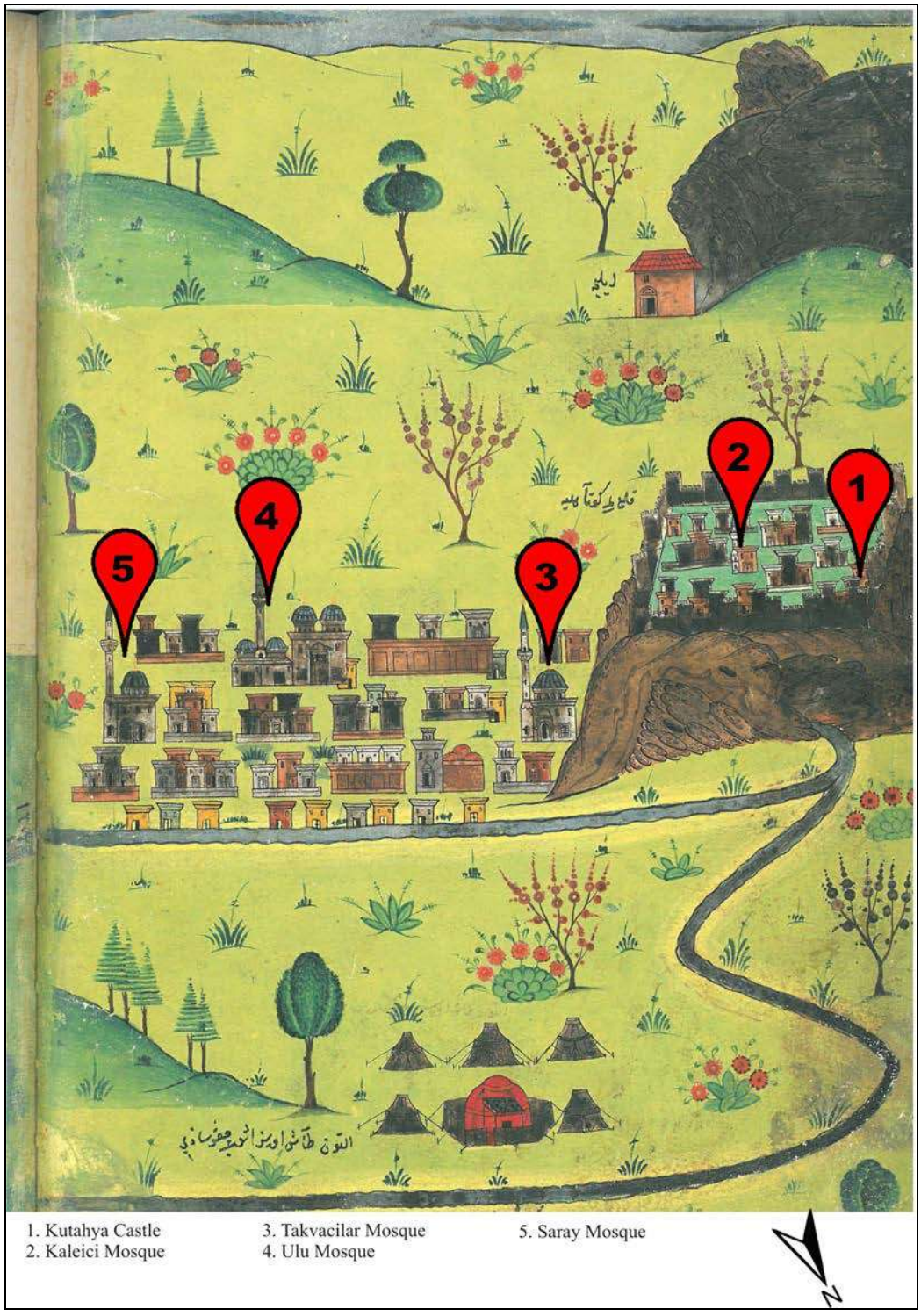

Figure 54. Matrakci Nasuh's Kutahya miniature

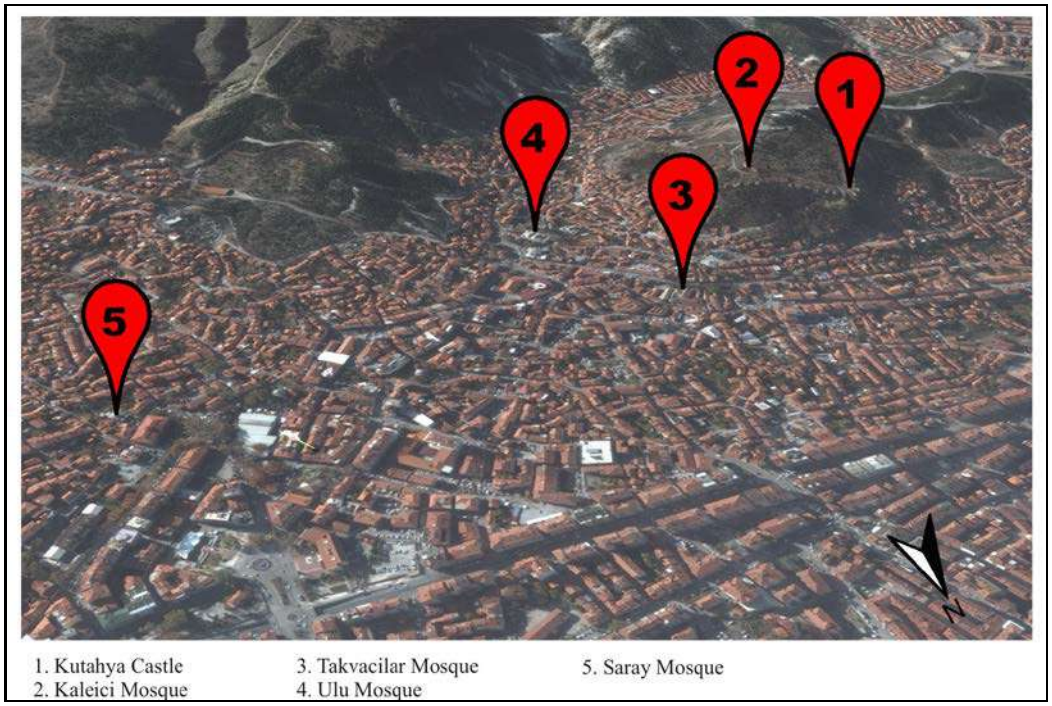

Figure 2. Kutahya in Google Earth (rotated to Matrakci's drawing angle)

i. Investigation of Kutahya Miniature in terms of Planimetric Accuracy

In order to investigate the planimetric accuracy of the Kutahya miniature with the help of MapAnayst software, 5 points (Kutahya Castle, Kaleici Mosque, Takvacilar Mosque, Ulu Mosque, Saray Mosque) which can be selected clearly on Kutahya Miniature were chosen. Then, the correspondences of these points in the current map (Open Street Map) were determined and analyzed with the transformation parameters of Affine (6 parameters). As a result of the analysis, it was determined that the mean scale of the miniature was 1:6400, the mean rotation angle was 125° (clockwise) from the north, and the average positioning error was 208 m. While considering the value of this rotation angle, it should not be forgotten that Matrakci drew a miniature from his own point of view, and he was not in the opinion of drawing north-up miniature. The residuals in the X and Y directions for each point are given in Table 1, and the true locations of the selected points according to the analysis results are shown in Figure 3.

Table 44. Residuals in the X and Y directions for selected points on the Kutahya miniature

Points	Vx (m)	Vy (m)	V (m)
1	-0.00925	-0.00527	0.01064
2	-0.02117	-0.00619	0.02205
3	0.02056	0.00897	0.02243
4	0.02589	0.00843	0.02723
5	-0.01604	-0.00595	0.0171

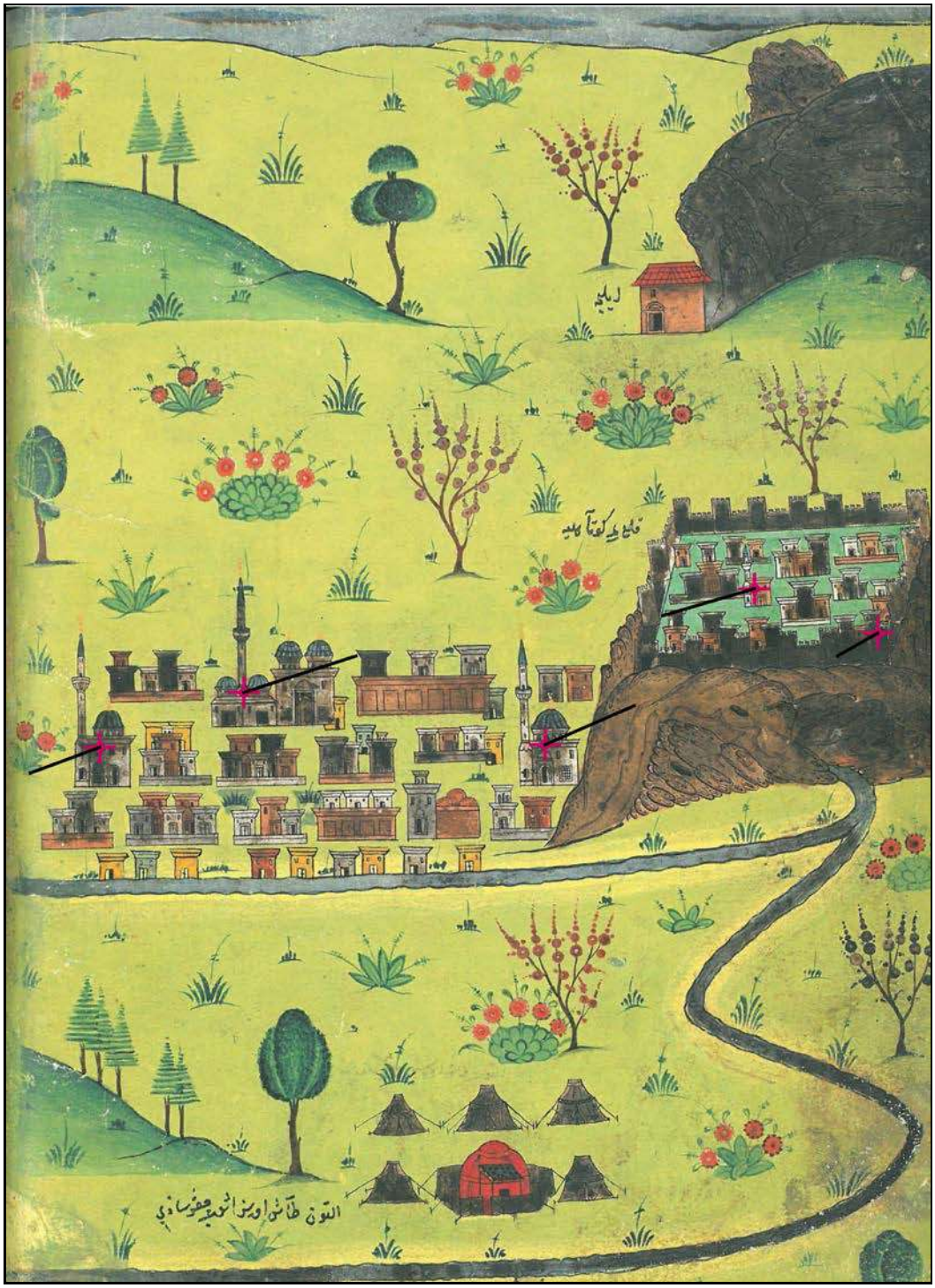

Figure 3. Investigation of Kutahya Miniature in terms of planimetric accuracy

5. CONCLUSIONS

When Matrakci's Kutahya miniature is examined in term of cartography, it is possible to detect the deficiency of the miniature in terms of map quality. Because exact scale is not specified and required information such as coordinate is not determined. However, Matrakci represents objects according to importance is very meaningful in terms of cartography. In addition the chosen objects have been drawn to reflect their shapes and colors. Planimetric accuracy of Kutahya miniature was determined as 208 m. Considering the conditions of the period in which the miniature was made, this accuracy value is also quite good. Moreover, topological accuracy is more important than planimetric accuracy when working with a scale of 5000 or smaller. From this point of view, it is seen that the topological neighborhood relations in Matrakci's miniature are very compatible.

ACKNOWLEDGEMENT

This study was funded by Scientific Research Projects Grant of Necmettin Erbakan University.

REFERENCES

[1] M. Yerci, "The accuracy of the first world map drawn by Piri Reis", *The Cartographic Journal*, 26, pp. 154–155, DOI: 10.1179/caj.1989.26.2.154, 1989.

[2] I. Yilmaz, "The Kitab-i Bahriye (Book of Navigation) of Piri Reis", *The Cartographic Journal*, 47 (3), pp. 278-283, DOI: 10.1179/000870410X12708074472152, 2010.

[3] I.Yilmaz, "Geo-information heritage contained within Kitab-i Bahriye (Book of Navigation): The Sicily Island", *Journal of Cultural Heritage*, 19, pp. 502-510, DOI: 10.1016/j.culher.2015.12.006, 2016.

[4] M. Onder, "Gecmisten Gunumuze Resimlerle Turk Haritacilik Tarihi", Ankara, 2002, [in Turkish].

[5] M. Ak, "Osmanli'nin Gezginleri", Istanbul, 2006, [in Turkish].

[6] D. Erkan, "Osmanli Arastirmalari," n. 37, Istanbul, p.185,186,2011, [in Turkish].

[7] I. Binark, "Turklerde Resim ve Minyatur Sanati," Istanbul, p.272, 1978, [in Turkish].

[8] H.G. Yurdaydin, "Beyan-i Menazil-i Sefer-i Irakeyn," Istanbul, 2014, [in Turkish].

[9] B. Jenny, "MapAnalyst – A Digital Tool for the Analysis of the Planimetric Accuracy of Historical Maps," *e-Perimetron*, 1(3), 239-245, 2016.

[10] B. Jenny, A.Weber, L. Hurni, "Visualizing the Planimetric Accuracy of Historical Maps with MapAnalyst," *Cartographica*, 42(1), 89-94, 2007.

[11] B. Jenny, "New Features in MapAnalyst," *e-Perimetron*, 5(3), 176-180, 2010.

[12] B. Jenny, L. Hurni, "Studying Cartographic Heritage: Analysis and Visualization of Geometric Distortions", *Computers & Graphics*, 35(2), 402-411, 2011.

[13] T. Gokgoz, B. Karahan, B. Kuzucu, "1878 Tarihli Davutpasa Haritasinin Planimetrik Dogruluk Analizi", 6. *Uzaktan Algilama-CBS Sempozyumu (UZAL-CBS 2016)*, 5-7 Ekim 2016, Adana, [in Turkish].

[14] D. Ucar, N. Ulugtekin, "Kartografyaya Giris ders notu", s.46, 2006, [in Turkish].

[15] K. Brassel, "Der Generalisierungsbegriff in der Kartographie und anderen Disziplinen", in Kartographisches Generalisieren, Schweizerische Gesellschaft fur Kartographie, Zurich, 3-5, 1990.

[16] W. Mackaness, D. Burghardt, C. Duchêne, "Map Generalisation: Fundamental to the Modelling and Understanding of Geographic Space", Chapter 1, *Abstracting Geographic Information in a Data Rich World* (edt. Dirk Burghardt Cécile Duchêne William Mackaness), 2014.

ICENS 4TH INTERNATIONAL CONFERENCE ON ENGINEERING AND NATURAL SCIENCE
2-6 May 2018 KIEV UKRAINE

Some New Results on Soft n-T_4 Spaces

Orhan Gocur[1]

Abstract

*Gocur and Kopuzlu [5] showed that if a soft topological space (X,τ,E) is a soft T_4 space, then (X,τ,E) may not be a soft T_2 space (also may not be a soft T_3 space). In this case, they described a new soft separation axiom which is called soft n-T_4 space. Then they indicated that if a soft topological space (X,τ,E) is a soft n-T_4 space, then (X,τ,E) is a soft T_3 space. In the present paper we showed that if a soft topological space (X,τ,E) is a soft n-T_4 space, topological space X,τ_e is a T_4 space for all $e \in E$. Then we showed that any Soft Metric space is soft n-T_4 space also. Consequently, we indicated that any Soft Metric space ⟹ Soft n-T_4 space ⟹ Soft T_3 space. ⟹ Soft T_2 space ⟹ **S**oft T_1 space ⟹ soft T_0 space.*

Keywords: soft metric space, soft separation axioms, soft set, soft closed set, soft n-T_4 space, soft topological space.

1. INTRODUCTION

None mathematical tools can successfully deal with the several kinds of uncertainties in complicated problems in engineerig, economics, environment problems, sociology, medical science, etc, so Molodtsov [12] introduced the concept of a soft set in order to solve these problems in 1999. However, there are some theories such as theory of probability, theory of fuzzy sets [16], theory of intuitionistic fuzzy sets [2], theory of vague sets [5], theory of interval mathematics [9] and the theory of rough sets [13], etc, which can be taken into account as mathematical tools for dealing with uncertainties. But these theories have their own difficulties. Maji et al. [10] introduced a few operators for soft set theory and made a more detailed theoretical study of the soft set theory. Recently, study on the soft set theory and its applications in different fields has been making progress rapidly [1], [3], [15], [18]. Shabir and Naz [14] introduced the concept of soft topological spaces which are defined over an inital universe with fixed set of parameter. They indicated that a soft topological space gives a parameterized family of topological spaces and introduced the concept of soft open sets, soft closed sets, soft interior point, soft closure and soft separation axioms. Also they gave some interesting properties about soft separation axioms, which are really valuable study in this field. They gave definitions of soft T_i spaces for $i = 0,1,2,3,4$. And they gave some relations about them. They indicated that if a soft topological space (X, τ, E) is a soft T_i space, (X, τ, E) is a soft T_{i-1} space for $i = 1,2$. And they asserted that any soft T_3 space may not be a soft T_2 space by given an example. But the example is false. In this case, Won Keun Min [11] indicated that if a soft topological space (X, τ, E) is a soft T_3 space then (X, τ, E) is a soft T_2 space. Also Shabir and Naz [14] asserted that if a soft topological space (X, τ, E) is a soft T_1 space, topological space (X, τ_e) is T_1 space for all $e \in E$. But this proposition is false. In this case, Gocur and Kopuzlu [7] showed that if a soft topological space (X, τ, E) is a soft T_1 space, topological space (X, τ_α) is a T_1 space for which $\alpha \in E$. And also they showed that if a soft topological space (X, τ, E) is a soft T_0 space, topological space (X, τ_α) is a T_0 space for which $\alpha \in E$. Shabir and Naz [14] indicated that if a soft topological space (X, τ, E) is a soft T_2 space, topological space (X, τ_e) is a T_2 space for all $e \in E$. And in this case Won Keun Min [11] indicated that if a soft topological space (X, τ, E) is a soft T_3 spaces, topological space (X, τ_e) is a T_3 space for all $e \in E$.

Shabir and Naz [14] asserted that if a soft topological space (X, τ, E) is a soft T_4 space, (X, τ, E) may not be a soft T_3 space. This proposition is true but given an example about this is false. For this, Zhang [17] gave correct example about it. After then Gocur and Kopuzlu [8] showed that if a soft topological space (X, τ, E) is a soft T_4 space, (X, τ, E) may not be a soft T_2 space (also may not be a soft T_3 space). And they indicated that any soft discrete space is soft T_2 space. Then they showed that any soft discrete space may not be soft T_3 space. After then they indicated that any soft discrete space is soft T_4 space. In this case, they described a new soft separation axiom which is called soft n-T_4 space. Then they indicated that if a soft topological space (X, τ, E) is a soft n-T_4 space, (X, τ, E) is a soft T_3 space. Consuquently they showed that any soft n-T_4 space ⇒ soft T_3

[1] *Department of Banking and Insurance, Pazaryeri Vocational Training School, Bilecik Seyh Edebali University Pazaryeri-Bilecik, Turkey.* orhangocur@gmail.com

space ⇒ Soft T_2 space ⇒ soft T_1 space ⇒ soft T_0 space. In this case, Gocur and Kopuzlu [8] showed that any soft discrete topological space may not be a soft n-T_4 space. So they introduced a new soft topological space that is called soft single point space. And they showed that any soft single point space is also soft subspace of soft discrete space. Then they indicated that any soft single point space is soft n-T_4 space. After then, Gocur O. [6] introduced soft metric space which is defined over an initial universe set with fixed set of parameter. And he gave the definition of soft open ball and soft closed ball in soft metric spaces. Also he introduced soft metrizable. And he showed that any soft discrete space is soft non-metrizable while soft single point space is soft metrizable. Finally, he indicated that any soft metrizable space is soft n-T_4 in [6].

In the present paper, we show that if a soft topological space (X, τ, E) is a soft n-T_4 space, then topological space (X, τ_e) is a T_4 space for all $e \in E$. Then we show that any Soft Metric space is soft n-T_4 space also. Consuquently, we indicate that any Soft Metric space ⇒Soft n-T_4 space ⇒ soft T_3 space. ⇒ Soft T_2 space ⇒ soft T_1 space ⇒ soft T_0 space.

2. MATERIALS AND METHODS

Definition 1. [12] Let X be an initial universe and E be a set of parameters. Let $P(X)$ denote the power set of X, where F is a mapping given by $F: E \to P(X)$. A soft set over X is a parametrized family of subsets of the universe X. For $e \in E$, $F(e)$ may be considered as the set of e-approximate elements of the soft set (F, E).

Definition 2. [10] For two soft sets (F, E) and (G, E) over X, (F, E) is a soft subset of (G,E), denoted by $(F, E) \,\widetilde{\subseteq}\, (G, E)$, $F(e) \subseteq G(e)$, for all $e \in E$. (F, E) is said to be a soft superset of (G, E), if (G, E) is a soft subset of (F, E), $(F, E) \,\widetilde{\supseteq}\, (G, E)$.

Definition 3. [10] Two soft sets (F, E) and (G, E) over X are said to be soft equal if (F, E) is a soft subset of (G, E) and (G, E) is a soft subset of (F, E).

Definition 4. [10] A soft set (F, E) over X is said to be an empty soft set denoted by $\widetilde{\emptyset}$ if for all $e \in E$, $F(e) = \emptyset$.

Definition 5. [10] The union (H, E) of two soft sets (F, E) and (G, E) over X, denoted by $(F, E) \,\widetilde{\cup}\, (G, E)$, is defined as $H(e) = F(e) \cup G(e)$ for all $e \in E$.

Definition 6. [4] The intersection (H,E) of two soft sets (F,E) and (G,E) over X, denoted $(F, E) \,\widetilde{\cap}\, (G, E)$, is defined as $H(e) = F(e) \cap G(e)$ for all $e \in E$.

Definition 7. [14] The difference (H, E) of two soft sets (F, E) and (G, E) over X, denoted by $(F, E)\,\widetilde{\setminus}\,(G, E)$, is defined as $H(e) = F(e) \setminus G(e)$ for all $e \in E$.

Definition 8. [14] Let (F, E) be a soft set over X and $x \in X$. We say that $x \in (F, E)$ read as x belongs to the soft set (F, E) whenever $x \in F(e)$ for all $e \in E$. Note that for any $x \in X$, $x \notin (F, E)$, if $x \notin F(\alpha)$ for some $\alpha \in E$.

Definition 9. [14] Let Y be a non-empty subset of X, then Y denotes the soft set (Y, E) over X for which $Y(e) = Y$, for all $e \in E$. In particular, (X, E) will be denoted by $\tilde{X}$.

Definition 10. [14] Let $x \in X$, then (x, E) denotes the soft set over X for which $x(e) = \{x\}$, for all $e \in E$.

Definition 11. [14] The relative complement of a soft set (F, E) is denoted by $(F, E)'$ and is defined by $(F, E)' = (F', E)$ where $F': E \to P(X)$ is a mapping given by $F'(e) = X - F(e)$ for all $e \in E$.

Definition 12. [14] Let τ be the collection of soft sets over X, then τ is said to be a soft topology on X if

1. $\widetilde{\emptyset}$, $\widetilde{X}$ belong to τ
2. the union of any number of soft sets in τ belongs to τ
3. the intersection of any two soft sets in τ belongs to τ .

The triplet (X,τ,E) is called a soft topological space over X.

Definition 13. [14] Let (X, τ, E) be a soft space over X, then the members of τ are said to be soft open sets in X.

Definition 14. [14] Let (X, τ, E) be a soft space over X. A soft set (F, E) over X is said to be a soft closed set in X, if its relative complement $(F, E)'$ belongs to τ.

Proposition 1. [14] Let (X, τ, E) be a soft space over X. Then the collection $\tau_e = \{F(e) | (F, E) \in \tau\}$ for each $e \in E$, defines a topology on X.

Proposition 2. [3] Let (X, τ, E) be a soft topological space over X and (F, E) be a soft closed set over X. Then $F(e)$ is closed set in (X, τ_e) for all $e \in E$.

Definition 15. [14] Let (X, τ, E) be a soft topological space over X and $x, y \in X$ such that $x \neq y$. If there exist soft open sets (F, E) and (G, E) such that $x \in (F, E), y \notin (F, E)$ or $y \in (G, E), x \notin (G, E)$, then (X, τ, E) is called a soft T_0 space.

Remark 1. [7] Let (X, τ, E) be a soft T_0 space. Then there exist soft open sets (F, E) and (G, E) such that $x \in (F, E), y \notin (F, E)$ or $y \in (G, E), x \notin (G, E)$ from Definition 15. Also we know that for each $e \in E$, (X, τ_e) is a topological space from Proposition 1. Then we can see that clearly, since $x \in (F, E)$, there exists open set $F(e)$ in τ_e such that $x \in F(e)$ for all $e \in E$; and since $y \notin (F, E)$, there exists open set F(e_i) in τ_{e_i} such that $y \notin F(e_i)$ for $e_i \in E$, $i \in I$. Or similarly since $y \in (G, E)$, there exists open set $G(e)$ in τ_e such that $y \in G(e)$ for all $e \in E$; and since $x \notin (G, E)$, there exist open sets G(e_j) in τ_{e_j} such that $x \notin G(e_j)$ for $e_j \in E, j \in I$.

Theorem 1. [7] Let (X, τ, E) be a soft topological space over X and $x, y \in X$ such that $x \neq y$ and let $i, j \in I$ such that mentioned in Remark 1, $e \in E$. If (X, τ, E) is a soft T_0 space, then at least one of (X, τ_{e_i}) and (X, τ_{e_j}) are T_0 spaces.

Definition 16. [14] Let (X, τ, E) be a soft topological space over X and $x, y \in X$ such that $x \neq y$. If there exist soft open sets (F, E) and (G, E) such that $x \in (F, E)$, $y \notin (F, E)$ and $y \in (G, E), x \notin (G, E)$, then (X, τ, E) is called a soft T_1 space.

Remark 2. [7] Let (X, τ, E) be a soft T_1 space, then there exist soft open sets (F, E) and (G, E) such that $x \in (F, E), y \notin (F, E)$ and $y \in (G, E), x \notin (G, E)$ from Definition 16. Also we know that for each $e \in E$, (X, τ_e) is a topological space from Proposition 1. Then we can see that clearly, since $x \in (F, E)$, there exists open set $F(e)$ in τ_e such that $x \in F(e)$ for all $e \in E$; and since $y \notin (F, E)$, there exists open set F(e_i) in τ_{e_i} such that $y \notin F(e_i)$ for $e_i \in E$, $i \in I$ And similarly since $y \in (G, E)$, there exists open set $G(e)$ in τ_e such that $y \in G(e)$ for all $e \in E$; and since $x \notin (G, E)$, there exist open sets G(e_j) in τ_{e_j} such that $x \notin G(e_j)$ for $e_j \in E, j \in I$.

Theorem 2. [7] Let (X, τ, E) be a soft topological space over X and $x, y \in X$ such that $x \neq y$ and let $i, j \in I$ such that mentioned in Remark 2, $e \in E$. Let $k, l \in I$ such that $e_{i_k} = e_{j_l}$. If (X, τ, E) is a soft T_1 space, then $(X, \tau_{e_{i_k}})$ are T_1 spaces.

Example 1. [7] Let $X = \{x, y\}, E = \{e_1, e_2\}$ and $\tau = \{\emptyset, X, (F_1, E), (F_2, E), (F_3, E)\}$ where

$$F_1(e_1) = \{x, y\}, \quad F_1(e_2) = \{x\},$$
$$F_2(e_1) = \{y\}, \quad F_2(e_2) = \{y\},$$
$$F_3(e_1) = \{y\}, \quad F_3(e_2) = \emptyset.$$

We note that (X, τ, E) is a soft T_1 space because there exist soft open sets (F_1, E) and (F_2, E) such that $x \in (F_1, E), y \notin (F_1, E)$ and $y \in (F_2, E), x \notin (F_2, E)$.

We can see that (X, τ_{e_1}) is not T_1 space because of $\tau_{e_1} = \{\emptyset, X, \{y\}\}$. Also we can see that, τ_{e_2} is a T_1 space because of $\tau_{e_2} = \{\emptyset, X, \{x\}, \{y\}\}$.

Definition 17. [14] Let (X, τ, E) be a soft topological space over X and $x, y \in X$ such that $x \neq y$. If there exist soft open sets (F, E) and (G, E) such that $x \in (F, E), y \in (G, E)$ and $(F, E) \widetilde{\cap} (G, E) = \widetilde{\emptyset}$, then (X, τ, E) is called a soft T_2 space.

Proposition 3. [14] Let (X, τ, E) be a soft topological space over X. If (X, τ, E) is a soft T_2 space, then (X, τ_e) is a T_2 space for each $e \in E$.

Definition 18. [14] Let (X,τ,E) be a soft toplogical space over X, (G,E) be a soft closed set in X and $x \in X$ such that $x \notin (G,E)$. If there exist soft open sets (F_1,E) and (F_2,E) such that $x \in (F_1,E), (G,E) \,\widetilde{\subseteq}\, (F_2,E)$ and $(F_1,E)\,\widetilde{\cap}\,(F_2,E) = \widetilde{\emptyset}$, then (X,τ,E) is called a soft regular space.

Definition 19. [14] Let (X,τ,E) be a soft topological space over X. Then (X,τ,E) is said to be a soft T_3 space if it is soft regular and soft T_1 space.

Remark 3. [11] If (X,τ,E) is a soft T_3 space, then (X,τ_e) is a T_3 space for each parameter $e \in E$.

Definition 20. [8] Let (X,τ,E) be a soft topological space over X and $x,y \in X$. Let (F,E) and (G,E) soft closed sets such that $x \in (F,E)$ and $(F,E)\,\widetilde{\cap}\,(G,E) = \widetilde{\emptyset}$. If there exist soft open sets (F_1,E) and (F_2,E) such that $y \in (F_2,E), (F,E) \,\widetilde{\subseteq}\, (F_1,E), (G,E) \,\widetilde{\subseteq}\, (F_2,E)$ and $(F_1,E)\,\widetilde{\cap}\,(F_2,E) = \widetilde{\emptyset}$, then (X,τ,E) is a soft n-normal space.

Definition 21. [8] Let (X,τ,E) be a soft topological space over X. If (X,τ,E) is a soft n-normal space and soft T_1 space, then (X,τ,E) is a soft n-T_4 space.

Theorem 3. [8] Soft n-T_4 space is soft T_3 space.

Corollary 1. [8] Soft n-T_4 space ⇒ soft T_3 space. ⇒ Soft T_2 space ⇒ soft T_1 space ⇒ soft T_0 space.

Definition 22. [6] Let X be an initial universe set and E be the non-empty set of parameters. Let $\tilde{X}$ be the absolute soft set i.e., $F(e) = X$, for all $e \in E$, where $(F,E) = \tilde{X}$. Let $\widetilde{\mathbb{R}}$ denote the set of all soft real numbers. We use notations $\tilde{r}$ to denote soft real numbers such that $F(e) = r$, for all $e \in E$, where $(F,E) = \tilde{r}$ For instance, $\tilde{0}$ is the soft real number where $F(e) = 0$, for all $e \in E$ where $(F,E) = (0,E)$ for $0 \in \mathbb{R}$. Also for shortly, we use $\tilde{x}, \tilde{y}, \tilde{z}, \tilde{a}, \tilde{b}$ instead of $(x,E), (y,E), (z,E), (a,E), (b,E)$ respectively for all $x,y,z,a,b \in X$ and for all $e \in E$.

A mapping $d: \tilde{X} \times \tilde{X} \to \widetilde{\mathbb{R}}$ is said to be a soft metric on the soft set X if d satisfies the following conditions:

1. $d(\tilde{x}, \tilde{y}) \geq \tilde{0}$, for all $x,y \in X$.
2. $d(\tilde{x},\tilde{y}) = \tilde{0}$ if and only if $x = y$, for $x,y \in X$
3. $d(\tilde{x},\tilde{y}) = d(\tilde{y},\tilde{x})$ for all $x,y \in X$.
4. $d(\tilde{x},\tilde{z}) \leq d(\tilde{x},\tilde{y}) + d(\tilde{y},\tilde{z})$, for all $x,y,z \in X$.

The soft set $\tilde{X}$ with a soft metric d on $\tilde{X}$ is called a soft metric space and denoted by $(\tilde{X},d,E)$.

Definition 23. [6] Let $(\tilde{X},d,E)$ be a soft metric space and $\tilde{r}$ be a non-negative soft real number. For any $a \in X$, by a soft open ball with centre $\tilde{a}$ and radius $\tilde{r}$ satisfy $d(\tilde{x},\tilde{a}) < \tilde{r}$. Thus the soft open ball with centre $\tilde{a}$ and radius $\tilde{r}$ is denoted by $B(\tilde{a},\tilde{r})$. Hence $B(\tilde{a},\tilde{r}) = \{x \in X; d(\tilde{x},\tilde{a}) < \tilde{r}\}$

Definition 24. [6] Let $(\tilde{X},d,E)$ be a soft metric space and $\tilde{r}$ be a non-negative soft real number. For any $a \in X$, by a soft closed ball with centre $\tilde{a}$ and radius $\tilde{r}$ satisfy $d(\tilde{x},\tilde{a}) \leq \tilde{r}$. Thus the soft closed ball with centre $\tilde{a}$ and radius $\tilde{r}$ is denoted by $B[\tilde{a},\tilde{r}]$. Hence $B[\tilde{a},\tilde{r}] = \{x \in X; d(\tilde{x},\tilde{a}) \leq \tilde{r}\}$.

3. RESULTS AND DISCUSSION

Theorem 4. Let (X,τ,E) be a soft topological space over X. If (X,τ,E) is a soft n-normal space, then (X,τ_e) is a normal space for all $e \in E$.

Proof Let (X,τ,E) be a soft n-normal space and $x,y \in X$. And let (F,E) and (G,E) be soft closed sets such that $x \in (F,E)$ and $(F,E)\,\widetilde{\cap}\,(G,E) = \widetilde{\emptyset}$. Then, there exist soft open sets (F_1,E) and (F_2,E) such that $y \in (F_2,E), (F,E) \,\widetilde{\subseteq}\, (F_1,E), (G,E) \,\widetilde{\subseteq}\, (F_2,E)$ and $(F_1,E)\,\widetilde{\cap}\,(F_2,E) = \widetilde{\emptyset}$ from Definition 20. Here, because (F,E) and (G,E) be soft closed sets such that $x \in (F,E)$ and $(F,E)\,\widetilde{\cap}\,(G,E) = \widetilde{\emptyset}$, there exist closed sets F(e) and G(e) in (X,τ_e) such that $F(e) \cap G(e) = \emptyset$, for all $e \in E$ from Proposition 2 and Definition 4. And then there exist open sets F_1(e) and F_2(e) in (X,τ_e) such that $F(e) \subset F_1(e)$, $G(e) \subset F_2(e)$ and $F_1(e) \cap F_2(e) = \emptyset$, for all $e \in E$ from Definition 2, Proposition 1 and Definition 4. Hence (X,τ_e) is a normal space for all $e \in E$.

Theorem 5. Let (X,τ,E) be a soft topological space over X. If (X,τ,E) is a soft n-T_4 space, then (X,τ_e) is a T_4 space for all $e \in E$.

Proof Let (X,τ,E) be a soft n-T_4 space. Then (X,τ,E) is both soft n-normal space and soft T_1 space from Definition 21. Because (X,τ_e) is normal space for all $e \in E$ from Theorem 4 and (X,τ_e) is T_1 space for all $e \in E$ from Corollary 1, Proposition 3 and we know that any T_2 space is also T_1 space from classical topology, then (X,τ_e) is T_4 space, for all $e \in E$.

Example 2. Let $X=\{x,y,z\}, E=\{e_1,e_2\}$ and $\tau=\{\emptyset, X, (F_1,E),(F_2,E),(F_3,E),(F_4,E),(F_5,E),(F_6,E)\}$ where

$$F_1(e_1)=\{x\}, \quad F_1(e_2)=\{x\},$$
$$F_2(e_1)=\{y\}, \quad F_2(e_2)=\{y\},$$
$$F_3(e_1)=\{z\}, \quad F_3(e_2)=\{z\}.$$
$$F_4(e_1)=\{x,y\}, \quad F_4(e_2)=\{x,y\}$$
$$F_5(e_1)=\{x,z\}, \quad F_5(e_2)=\{x,z\}$$
$$F_6(e_1)=\{y,z\}, \quad F_6(e_2)=\{y,z\}$$

Then (X,τ,E) is a soft topological space over X. Here, we can see clearly that (X,τ,E) is soft n-T_4 space and so (X,τ_{e_1}) and (X,τ_{e_2}) are T_4 space.

Theorem 6. Any soft metric space is soft T_1.

Proof Let $(\tilde{X},d,E)$ be a soft metric space; $a,b \in X$ and let $\tilde{\varepsilon}$ be a non-negative soft real number such that $d(\tilde{a},\tilde{b})=\tilde{\varepsilon}$. Then there exist soft open ball $B(\tilde{a},\widetilde{\varepsilon/3})$ such that $b \notin B(\tilde{a},\widetilde{\varepsilon/3})$. And similarly, there exist soft open ball $B(\tilde{b},\widetilde{\varepsilon/3})$ such that $a \notin B(\tilde{a},\widetilde{\varepsilon/3})$. Hence $\tilde{X}$ is soft T_1.

Theorem 7. Any soft metric space is soft n-normal.

Proof Let $(\tilde{X},d,E)$ be a soft metric space. Let (A,E) and (B,E) be disjoint soft closed soft subsets of $\tilde{X}$. For each $a \in (A,E)$, choose $\widetilde{\varepsilon_a}$, which is non-negative soft real number, so that the soft ball $B(\tilde{a},\widetilde{\varepsilon_a})$ does not intersect (B,E). Similarly, for each $b \in (B,E)$, choose $\widetilde{\varepsilon_b}$, which is non-negative soft real number, so that the soft ball $B(\tilde{b},\widetilde{\varepsilon_b})$ does not intersect (A,E). Define

$$(U,E)=\bigcup_{a\in(A,E)}\widetilde{B(\tilde{a},\widetilde{\varepsilon_a/3})}$$

and

$$(V,E)=\bigcup_{b\in(B,E)}\widetilde{B(\tilde{b},\widetilde{\varepsilon_b/3})}$$

Then (U,E) and (V,E) are soft open sets containing (A,E) and (B,E) respectively. Also $b \in (V,E)$. We assert they are disjoint. For if $z \in (U,E)\ \widetilde{\cap}\ (V,E)$, then

$$z \in B(\tilde{a},\widetilde{\varepsilon_a/3}) \cap B(\tilde{b},\widetilde{\varepsilon_b/3})$$

for some $a \in (A,E)$ and $b \in (B,E)$ the triangle inequality applies to show that $d(\tilde{a},\tilde{b}) < (\widetilde{\varepsilon_a}+\widetilde{\varepsilon_b})/3$. If $\widetilde{\varepsilon_a} \leq \widetilde{\varepsilon_b}$, then $d(\tilde{a},\tilde{b}) < \widetilde{\varepsilon_b}$, so that the soft ball $B(\tilde{b},\widetilde{\varepsilon_b})$ contains a. If $\widetilde{\varepsilon_b} \leq \widetilde{\varepsilon_a}$, then $d(\tilde{a},\tilde{b}) < \widetilde{\varepsilon_a}$, so that the soft ball B$(\tilde{a},\widetilde{\varepsilon_a})$ contains $\tilde{b}$. Neighter situation is possible.

Theorem 8. Any soft metric space is soft n-T_4.

Proof It is obvious that Definition 21, Theorem 6 and Theorem 7.

Corollary 2. Soft Metric Space ⇒ Soft n-T_4 space ⇒ soft T_3 space. ⇒ Soft T_2 space ⇒ soft T_1 space ⇒ soft T_0 space.

Proof It is obvious that Theorem 8 and Corollary 1.

4. CONCLUSIONS

In the present paper, we showed that if a soft topological space (X, τ, E) is a soft n-T_4 space, then topological space (X, τ_e) is a T_4 space for all $e \in E$. Then we showed that any Soft Metric space is soft n-T_4 space also. Consuquently, we indicated that any Soft Metric space ⇒Soft n-T_4 space ⇒ soft T_3 space. ⇒ Soft T_2 space ⇒ soft T_1 space ⇒ soft T_0 space.

In this study, our purpose is completing as much as possible that soft separation axioms defined over an initial universe with fixed set of parameter. And we hope that researchers investigate soft metric, soft compactness, soft connectedness, soft sequences etc., defined over an initial universe with fixed set of parameter by using this study.

ACKNOWLEDGEMENT

The author is highly grateful to the anonymous reviewers and satisfied attending ICENS and being in Kiev.

REFERENCES

[1]. A. M. Abd El-Latif, Soft extra strongly semi star generalized closed sets, gujs, 30(4) (2017) 421-430.
[2]. K. Atanassov, Intuitionistic fuzzy sets, Fuzzy Sets and Systems, 20 (1986) 87- 96.
[3]. Evanzalin Ebenanjar P, Thangavelu P, On quasi soft sets in soft topology, GJPAM, 13(12) (2017) 8343-8359.
[4]. F. Feng, Y.B. Jun and X.Z. Zhao, Soft semirings, Comput. Math. Appl. 56 (2008) 2621- 2628.
[5]. W. L. Gau and D. J. Buehrer, Vague sets, IEEE Trans. System Man Cybernet 23(2) (1993) 610- 614.
[6]. O.Gocur, Soft single point space and soft metrizable, Ann. Fuzzy Math. Inform. 13(4) (2017) 499-507.
[7]. O. Gocur, A. Kopuzlu, On soft separation axioms, Ann. Fuzzy Math. Inform. 9(5) (2015) 817-822.
[8]. O. Gocur, A. Kopuzlu, Some new properties on soft separation axioms, Ann. Fuzzy Math. Inform. 9(3) (2015) 421-429.
[9]. M. B. Gorzalzany, A method of inference in approximate reasoning based on interval valued fuzzy sets, Fuzzy Sets and Systems 21 (1987) 1- 17.
[10]. P.K. Maji, R. Biswas, R. Roy, Soft set theory, Comput. Math. Appl. 45 (2003) 555- 562.
[11]. W. K. Min, A note on soft topological spaces,Comput. Math. Appl. 62 (2011) 3524- 3528.
[12]. D. Molodtsov, Soft set theory first results, Comput. Math. Appl. 37 (1999) 19- 31.
[13]. Z. Pawlak, Rough sets, Int. J. Comp. Inf. Sci. 11 (1982) 341- 356.
[14]. M. Shabir, M. Naz, On soft topological spaces, Comput. Math. Appl. 61 (2011) 1786- 1799.
[15]. R. Thakur, S.K. Samantha, A study on some fundamental properties of continuity and differentiability of functions of soft real numbers, Advances in fuzzy Systems, doi: 10.1155/2018/6429572
[16]. L.A. Zadeh, Fuzzy sets, Information and Control 8 (1965) 338--353.
[17]. Zhang, X., Further Study on Soft Separation Axioms, Computer Engineering and Applications, 49(5) (2013) 48-50.
[18]. A.M. Khattak, G.A. Khan, M. Ishfaq, F. Jamal, characterization of soft α- separation axioms and β- seperation axioms in soft single point spaces and in ordinary spaces, Journal of New Theory, 19 (2017) 63-81.

BIOGRAPHY: *ORHAN GOCUR, DR.*

Department of Banking and Insurance, Pazaryeri Vocational Training School, Bilecik Seyh Edebali University Pazaryeri Bilecik, Turkey.
orhangocur@gmail.com
Topology, Soft topology, Generalized Metric spaces

ICENS 4TH INTERNATIONAL CONFERENCE ON ENGINEERING AND NATURAL SCIENCE
2-6 May 2018 KIEV UKRAINE

Structural Analysis of Historic Houses of Bitlis

Ercan Isik[1], Mehmet Cihan Aydin[2], Aydin Buyuksarac[3], Ali Emre Ulu[4]

Abstract:

The historical Silk Road, involves commercial through road networks used especially for economic targets between Asia and Europe. Bitlis is a trade and production city on Silk Road which is in the important period of rich Anatolian history. Historical artefacts are priceless cultural assets which connect strongly the past and the future. In order to convey our historical heritage to the posterity, the involvements to be applied historical structures to know the properties of constructions together forms the first step of the involvements to protect the historical structures. In the historical urban texture of Bitlis, traditional Bitlis Houses which are sample of vernacular architecture, occupies a large area. Natural disasters in the historic Bitlis houses have been damaged due to environmental impacts such as wearing and tearing over time. Structural analyzes of such structures have an important place in order to transfer historical and cultural heritage to the next generations. With this study, the structural analyzes of selected buildings as examples for the historical Bitlis houses have been carried out. Information about both these houses and the damages has been given and solution suggestions have been presented.

Keywords: Historic Bitlis Houses, Structural Analysis

1. INTRODUCTION

Preservation of cultural heritage and transferring it to the future with confidence are at the forefront of important architectural and engineering research and practice issues of the 21st century. Since this important issue has a common stake in the fields of science such as engineering, architecture, art history and archeology, the interdisciplinary working groups which have gained considerable attention in recent years attract attention. [1].

Studies on historical buildings have an important place today in order to transfer our historical heritage to the next generations. Also, the place of historical buildings is very important in order not to ruin the historical texture of our country. From this point of view, the characteristics of these types of structures are important for the protection of historical and cultural heritage. Considering the number of historical houses in the province of Bitlis, it is possible to say that such structures constitute a large part of this heritage. Hence, it is possible to transfer the construction stages of such houses and the structural analyzes to be carried out by knowing the properties of the materials used in construction in a way that protects the next generation. The preservation of these structures will serve as a bridge between the past and the future in order to prevent the historic houses from disappearing in the process.

Van Lake basin has been home to many civilizations in the historical process. Because the basin is a very old settlement area, it has carried the historical buildings and cultural values left behind by many civilizations to daylight. There are many historic buildings in the basin, which were built in ancient times and which are still being used with renovation works. Bitlis is one of the host of many civilizations in this basin. [2].

It can be seen that traditional Bitlis houses dating back to the 16th century point to an organic texture formed by the use of local materials under the compelling effects of climate and topography, and according to the physical and socio-economic needs of local people. The changes in the socio-demographic and economic structure of the 20th and the century after it have brought out examples of new/modern architecture, which

[1] *Corresponding author: Bitlis Eren University, Department of Civil Engineering, 13000, Bitlis, Turkey.eisik@beu.edu.tr*
[2] *Bitlis Eren University, Department of Civil Engineering ,* mcaydin@beu.edu.tr
[3] *Bitlis Eren University, Department of Civil Engineering,* absarac@beu.edu.tr
[4] *Bitlis Eren University, Department of Civil Engineering,* aeulu@beu.edu.tr

have begun to separate from the traditional architecture by using natural materials and construction techniques with mass production techniques [3].

In the past, cities came forward with their identities. With the rapid changes of the last century and the effects of globalization, cities have started to lose their identities and began resemble to each other and devalue as they lose their identities. Today, cities that are urban consciousness formed have been trying to stop this trend, and on the other hand they are developing models that can be integrated with the world while protecting their identity. Bitlis has not yet lost this powerful identity that both its geography and historical heritage have provided. Bitlis is a trade and production city on the Silk Road, which has existed in significant periods of Anatolia's rich history. The creativity of the Seljuk Renaissance and the monuments and medrescents institutionalized by Ottoman Empire are also evidence that the city is as much a center of art and education as commerce. Historical Bitlis houses are one of these evidence as well [3,4,5].

With this study, it is aimed to make suggestions by carrying out the structural analysis of the historical Bitlis Houses in order to bring the future potentials of the Bitlis's heritage and geographical aspects, by transforming them into innovative, economic and social structures that will give it a global power. The study describes the construction techniques in the traditional Bitlis houses and informs about the damages that have occurred, and suggests a solution to the problem by recording the facts.

2. BITLIS HOUSES

It is observed that the traditional Bitlis Houses have cubic form, plain facade arrangements, earthy roofs, masonry constructions, flexible and sparing area usage in interior space organization. Same of the room analysis suitable for large families are to meet the requirements for creating sun-intensive rooms called "beroj", vertical circulation arrangements (vertical access to the barn or storage section from any room) in which the needs are met from inside to reach provisions in winter conditions, lack of accession, and existence of direct connection of house and road with roof and gargoyle analyzes show the influence of the climate factor. Considering this situation, it can be said that in order to protect the Bitlis Houses, it is a necessity to provide insulation and comfort which protects the building by reducing the climate effects. However, while thermal and water insulation applications are being made in historical buildings, solutions should be produced that do not deteriorate the natural appearance and can provide maximum comfort. This study presents a light, economical and rational solution proposal that does not place much burden on the structure. It has been tried to combine the natural materials used in the roofs and the materials and techniques that today's technology makes easily accessible with mass production [3,4,5].

Traditional Bitlis Houses have their own structure. Under present conditions, it is important that the historic Bitlis houses that have reached to the day are protected and transferred to the future with confidence. The houses are generally constructed from local stones obtained from stone quarries in Bitlis province. It is used after being subjected to the cutting process in local stone quarries. Fine grout mortars are used among the local stones. In general, roofs are made of flat earth dams built from local materials. Generally, local craftsmen and workers are involved in the construction process (Figure 1).

Figure 1. Historical Bitlis Houses [6]

Mortars were used between the cutted stones obtained from stone quarries in Bitlis. Wooden ceilings are used in all the houses. Soil are used as roofs. Generally, when these dams are being built, wooden beams are used firstly. In terms of aesthetics, their top surfaces are covered with wood veneers. On top of that, the soil that will form the roof is laid, and a mixture of seh and salt is laid on it to provide insulation. Water channels called 'coratan' are used to provide water drainage in soil dams. Stones called 'sal' are placed around the roof for an aesthetic appearance. Due to wearing and tearing of the material during certain periods, the roof can be partially or completely replaced. Section of these roofs shown in Figure 2.

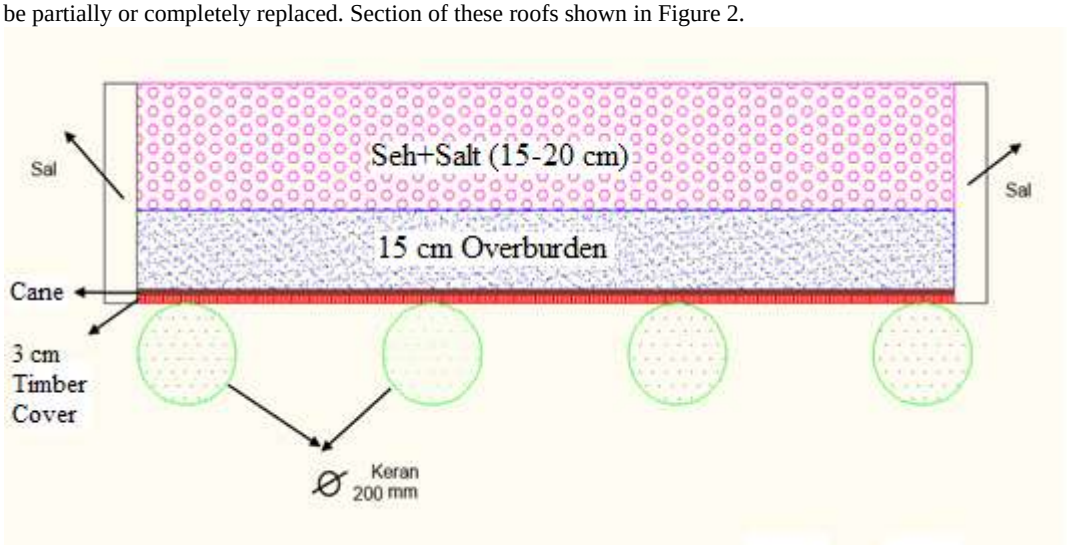

Figure 2. Historical Soil Roof Section of Bitlis Houses [3]

Carrier walls is used as load-bearing system. The thickness of these walls varies between 1-1.5 m. During the planning stage, the experience of the craftsmen and the wishes of the building owner are taken into account. In general, the plans are similar. The main reason for this is that such houses are built by the same craftsmen or by trained staff by these craftsmen. As part of the foundation excavation, the walls of the house plan are subjected to excavation. The foundation is built under each wall. In the excavated part, first of all 1 m high plinth part is being built and it is transferred to the superstructure part by leaving the girder on it. It can be

said that basic design has been realized in accordance with today's understanding of masonry construction. All the houses are designed as masonry construction. However, due to the widespread use of reinforced concrete materials today, such houses are now confronted as a besieged masonry structure. At certain points of the walls, structures surrounded by columns built from concrete. None of these structures have received engineering services. Despite their lack of engineering services, however, there are many structures that can come in a sturdy way until today. Such intervention in historic houses has been challenged by a long and difficult formal process. The windows used on the exterior walls are flat arched, double and triple. The fact that they are made in groups, (not being made in one piece) is due to the fact that the climatic conditions are very severe. On inner walls, the space left on the walls are used as storage areas (Figure 3).

Figure 3. The Part Used as a Storage Area on the Inner Walls of the Historic Bitlis Houses

3. DAMAGES OBSERVED IN HISTORIC BITLIS HOUSES

Due to heavy snowfall in Bitlis, avalanche, snowflakes, especially snow accumulation in flat and land roofs and stalagmites in the settlement units due to the formation of stalactite ice are adversely affected lives of people living in both rural areas and the city center. The snowfall also causes serious transportation problems, fatal traffic accidents, damages to roofs and destruction of energy lines. Snowfall generally starts in the first week of November and continues until the middle of spring. In the last week of April, the precipitation leaves its place to the melting process of the accumulated snow. The fact that the snowfall period is so long during the year increases the risk duration of damages in structures in Bitlis [7,8,9]. It is known that due to the soft spongy nature of the local Bitlis Stone, the erosion and destruction are excessive, this is caused by temperature differences and frost humid environments, causing fragmentation and rupture. It is necessary to prevent water movement (groundwater and rainwater) seen on the ground level by making installation with drainage. Moisture-induced deterioration is seen in the areas of the stone exposed the water. The damage and causes observed in the Historic Bitlis houses can be listed as follows:

- Over time, people want to use reinforced concrete new buildings in terms of comfort and to let these houses decay, and as a result the buildings are partially or wholly demolished.
- Due to the difficult formal processes and procedures, this type of construction cannot be intervened over time, resulting in increased damage.
- Deformation of soil roofs over time due to excessive snowfall and high temperature differences.
- Partial or complete collapses due to natural disasters, environmental factors and heavy snowfall on exterior walls.
- The timber beams on the walls of the building begin to decay over time.
- The fact that the joint material between the walls is drained from time due to environmental reasons, and the result is to move in the stones that bring the wall to the square.

- Local Bitlis stone is worn out due to climate and environmental factors.
- Breaking cracks in the walls due to different settlement.
- In such houses, stoves are generally used as the heating system. Due to the heavy winter conditions people prefer calorific buildings as heating system, consequently, these houses are abandoned in time. The smallest damage that occurs due to the lack of use of construction causes the building to become completely unusable over time.
- The rain and snow waters that leak from the soil drips due to heavy rainfall decay the wooden ceiling cover and wooden beams.
- Leaked waters cause humidity and moisture in the building.
- Dispersement of lichen formations over time in facade walls and soil roofs.

Figure 4. Observed Damage Historic in Bitlis Houses

4. CONCLUSIONS AND RECOMMENDATIONS

It is aimed to contribute the Bitlis' natural, historical and cultural heritage to the self-preserving Developing Cities Strategy that will be introduced to the world with the internal and external tourism industry to be established with an innovative planning concept. It will be possible for old buildings and new living spaces in the city center and districts to exist in integrity, without destroying each other, and to meet the comfort standards of the future while preserving the past.

In Bitlis province, both natural disasters and environmental factors have resulted in various damages resulting in wearing and tearing. In this study, the construction techniques of the historic Bitlis houses are expressed and the causes and consequences of the damages that occurred in these structures are revealed. Suggestions were made according to the observed damages.

One of the most important problems in the historic Bitlis houses is the difficult and lengthy formal repair processes. The duration of this process increases the amount of damage. Methods to be carried out by experts, which will make this process fast and feasible, should be presented. The fact that this process is fast and feasible will increase the sense of ownership of those who already use these homes. With the increase in ownership, the functionality of these houses will be made sustainable.

Determining the houses that can be used in the tourism sector and starting to use them especially in the style of boutique hotels will contribute to the economic growth of the province as well as creating employment.

In general, the fact that houses are not used over time is noteworthy when considering the damages of houses. Due to various reasons, those who use these houses before are starting not to use these houses over time. Over time, the abandoned structures wear out and become damaged.

Particularly, solution proposals should be produced for soil roofs where the biggest damages occur. This solution recommendation should bring into action as soon. In the houses which are abandoned due to heavy winter conditions in Bitlis province, people should be prevented from leaving these houses due to warming reasons by using natural gas heating system.

Damage that may occur in these structures can be reduced to a minimum by allowing the use of today's developing construction technologies and building materials to protect old buildings.

The meaning of historical masonry structures in the sense of not ruining the historical texture of Bitlis is very important. In this respect, it is important to take necessary measures for the masonry structures and to protect the historical and cultural heritage.

REFERENCES

[1]. MF Isik, E. Isik, MA Bulbul and IB Karasin "QR code application for location and geometric information of historical structures," *International Conference and Advanced Engineering* Technologies, Bayburt, Turkey, 2017.
[2]. I.B. Karasin, E. Isik and B.Eren, "Structural analysis of Bitlis Grand Mosque", *International Conference on Natural Science and Engineering (ICNAS*A-2016),Kilis, 2016.
[3]. VS Bicen, E., Isik, MH Ozluk and M. Ulker "Solution for existing soil housetops of traditional Bitlis houses", *International Engineering, Science and Education Conference (INESEC - 2016), Diyarbakir Turkey, 2016.*
[4]. G. Bas, "Gelenek ve gelecek arasinda sikisan tarihi bir kent : Bitlis" *International Journal of History* ISSN: 1309 4173 (Online) Volume2 / 2. 2010.
[5]. GO Payasli and IB, AKSULU, "Geleneksel Bitlis evleri: koruma sorunlari ve oneriler." *Megaron* Journal,11 (1), 63-77, 2016.
[6]. E. Isik "Evaluation of the masonry building stock in Bitlis province with street screening method *"Bitlis Eren University, Journal of the Institute of Science*, 2 (1), 22-30, 2013.
[7]. E. Isik and MH Ozluk" Natural disasters analysis of Bitlis province and suggestions ", *3rd International Science Technology and Engineering Conference (ISTA -C 2012)*, Dubai, Unites Arab Emirates, 2012.
[8]. E. Isik, MC, Aydin, MH Ozluk, E. Demir and VS Bicen, "Economic analysis and suggestions for roof damages in the region was subjected to heavy snowfalls," *5thinternational Science Technology and Engineering Conference (ISA-C 2014)*, Qatar, in 2014
[9]. MC Aydin and E. Isik "Evaluation of ground snow loads at the micro-climate regions", *Russian Meteorology and* Hydrology,40 (11), 741-748, 2015.

ICENS 4TH INTERNATIONAL CONFERENCE ON ENGINEERING AND NATURAL SCIENCE
2 - 6 May 2018 KIEV UKRAINE

The Determination of the Effect of Wheels and Fender Gap on Drag Force on a Bus Model by Computational Fluid Dynamics (CFD) Method

Cihan Bayindirli[1], Mehmet Celik[2]

Abstract

The aerodynamic drag forces significantly affect the vehicle's performance, fuel consumption, acceleration properties, handling characteristics, environmental pollution, noise and comfort. The drag force is increased proportionally with the square of the speed. Because of buses perform cruising at high speed in intercity a bus model was chosen to investigate of aerodynamic force in this study. The flow structure around a 1/64 scaled bus model is investigated using computational fluids dynamics method. The effect of the wheels and the fender gap on the total drag force is determined. Flow analysis and determination of the drag force were carried out in the Fluent® program at 4 different free flow speeds. CFD analyzes were made at the range of 173 000 - 346 000 Reynolds numbers. To ensure geometric similarity 1/64 scaled licensed model bus is used. For the kinematic similarity blockage rate was % 4,75. In studies Reynolds number independence is used to ensure dynamic similarity. As a result of the flow analyzes 3.91% of the drag force results from the wheels and fender gap.

Keywords: *Aerodynamic drag coefficient (C_D), drag force, Fluent®, bus model, CFD*

1. INRODUCTION

CFD means “Computational Fluid Dynamics.” Which is useful to solve basic equations that model of flow? These equations do not have analytical solution hence we resort to numerical analysis with CFD. Computational Fluid Dynamics theory and is applied for solves different fluid flow which related problems like flow velocity, density, temperature, and chemical concentrations for any area where flow is present. It’s a numerical method for calculation for nonlinear differential equations describing/relating to fluid flow. According to Mohamed-Kassim and Filippone (2010), the fuel consumption can be improved from 1% to 17% using passive flow control parts on truck trailers. By improving the spoiler design 9-17%, aerodynamic improvement can be achieved, 4-6% with trailer skirts, and 0-4 % with closing the air gaps [1]. Nisugi et al. (2004), the reduction of the aerodynamic drag force for a vehicle was investigated by using feedback flow control. As a result, it was stated that 21% of power saving was achieved with this study [2]. According to Ji-qiang et al. (2017), the change in turbulence intensity does not change the pressure distribution on the model [3].The aim of this study is to examine the aerodynamics structure of the a bus model determine of flow structures around of its and determination of the effect of whelles and fender gaps to total drag force by numerically.

[1] *Corresponding author: Nigde Omer Halisdemir University, Nigde Vocational School of Technical Sciences, 51100, Merkez/Nigde, Turkey.* cbayindirli@ohu.edu.tr

[2] *Nigde Omer Halisdemir University, Nigde Vocational School of Technical Sciences, 51100, Merkez/Nigde, Turkey.* mehmetcelik@ohu.edu.tr

2. MATERIAL AND METHOD

The bus model which is examined in this study is 1/64 scale licensed model. The measurement of the bus model was precisely carried out and was created by computer-aided drawing method.

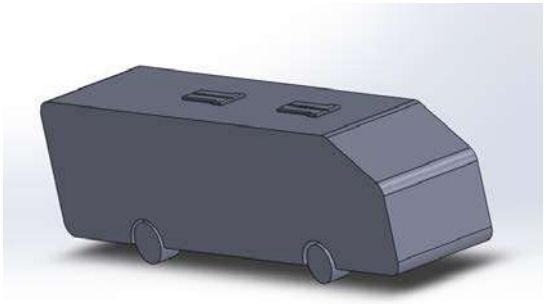

Fig. 1. Solid Works drawing of 1/64 scaled model bus with whells and fender gap[9]

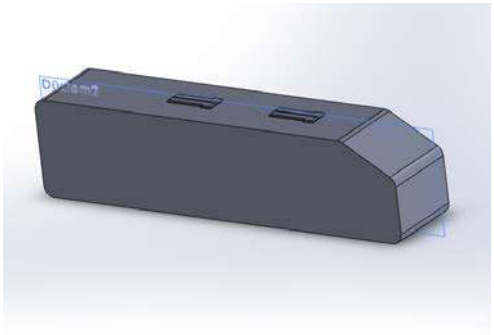

Fig. 2. Solid Works drawing of 1/64 scaled model bus without whells and fender gap

The aerodynamic drag coefficient which is obtained in this study originates from from pressure and friction and their distribution is also determined.

2.1. Similarity conditions

In studies on vehicle aerodynamics, three different similarity conditions must be provided between prototype and model car. These are geometric, kinematic and dynamic similarity conditions. To provide geometric similarity, the licensed model bus has been used and faults that may occur due to surface roughness, very small parts are ignored. In kinematic similarity the rate of blockage is determinat factor. The front surface area of model bus is 0.00542 m^2; front surface area of test area is 0.16 m^2 and a blockage rate is 3.39%. Cengel Y.A. (2008) recommends that blocking rate should be lower than 7,5% . Reynolds number independence was used to provide dynamic similarity in the study [4].

2.2. CFD Setup

The Fluent program used in flow analysis solves general integral equations for continuity, momentum, energy, turbulence based on the finite volume method.When these equations come into equilibrium at every point in the solution area, convergence occurs in the solution found with the Fluent program. The convergence and C_D exchange graph is shown in Fig 4. For each fluid variant, residuals indicate the severity of the error in the solution. In this study, convergence criteria is taken as 1.0×10^5 for continuity, x-velocity, y-velocity and z-

velocity. The intensity of turbulence is also taken as 1%. The air density is taken as 1 kg / m^3 and the dynamic viscosity is $1{,}56x10^{-5}$. The front surface area of the vehicle is calculated as 0.00542 m^2 from the reports-projected area. The analysis were made as standard initialization using standard wall functions and Simple Least Squared Cell Based k-ε RNG turbulence model. The numeric flow analysis were carrieded out in the Fluent® program using Workstation computer which has Intel® Xeon® CPU E3-1270 V5 3.60 GHz processor and 32 Gb Ram.

2.3. RNG k-ε Turbulence Model Selection

The basic aim of turbulence models is to improve the calculation methods. The RNG k-ε model provides a different analytical equation for drag effects, which is used to calculate the effects of low Reynolds numbers.

Using of this feature makes the near-wall approach reliable [5]. The k-ε model is used the most model in practice and is the model that yields reliable results when compared with experimental data. RNG k-ε model is used as the turbulence model in this study because it is accepted in the literature, it is compatible with the experimental results and the analysis time is shorter.

2.4. General Equations

The Fluent program solves the general integral equations for continuity, momentum, energy, turbulence using the finite volume method. Continuity and momentum equations are used in solving the finite volumes with computational flow dynamics (CFD). In practice, it is difficult to solve these equations analytically. Therefore, these equations are solved numerically using packet programs.

Continuity equation

The continuity equation is expressed as the mass balance in the control volume in a flow.

$$\frac{\partial u}{\partial x}+\frac{\partial v}{\partial y}+\frac{\partial w}{\partial z}=0 \tag{1}$$

Momentum equation

According to Newton's second law, the rate of change of the momentum of a fluid fraction is equal to the total of the forces acting on that fluid fraction. The momentum increase rate in the x, y and z directions of the unit volume of a fluid fraction is respectively expressed in terms of $\rho\frac{Du}{Dt}$, $\rho\frac{Dv}{Dt}$ $\rho\frac{Dw}{Dt}$ [6].

The x-component of the momentum equation;

$$\rho\frac{Du}{Dt}=\frac{\partial(-p+\tau_{xx})}{\partial x}+\frac{\partial\tau_{yx}}{\partial y}+\frac{\partial\tau_{zx}}{\partial z}+S_{M_x} \tag{2}$$

The y-component of the momentum equation;

$$\rho\frac{Dv}{Dt}=\frac{\partial\tau_{xy}}{\partial x}+\frac{\partial(-p+\tau_{yy})}{\partial y}+\frac{\partial\tau_{zy}}{\partial z}+S_{My} \tag{3}$$

The z-component of the momentum equation;

$$\rho\frac{Dw}{Dt}=\frac{\partial\tau_{xz}}{\partial x}+\frac{\partial\tau_{yz}}{\partial y}+\frac{\partial(-p+\tau_{zz})}{\partial z}+S_{M_z} \tag{4}$$

Navier – Stokes equations

Navier - Stokes and continuity equations are also referred to as differential motion equations. When these equations are solved, some assumptions are taken and pressure and three components of velocity (x, y, z) are calculated.

The most useful way to develop the finite volume method of Navier - Stokes equations;

$$\rho\frac{Du}{Dt} = -\frac{\partial p}{\partial x} + div(\mu\, grad\, u) + S_{M_x} \quad (5)$$

$$\rho\frac{Dv}{Dt} = -\frac{\partial p}{\partial y} + div(\mu\, grad\, v) + S_{My} \quad (6)$$

$$\rho\frac{Dw}{Dt} = -\frac{\partial p}{\partial z} + div(\mu\, grad\, w) + S_{Mz} \quad (7)$$

The sizes of the test area are 20x 20x 100cm. In this section as seen in Figure 3, the mold cavity of the model vehicle is formed, the drawing data are defined and transferred to the meshing section.

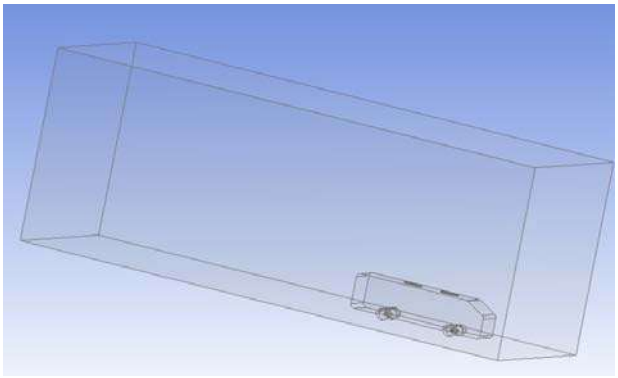

Fig.3. The interface view of truck in design modeler and mold cavity[9]

As seen in Figure 4a,b. the mesh structure is formed more frequently in the regions which affects the aerodynamic structure of the model bus significantly, the boundary definitions are made and the mesh file is transferred to the setup section. For the model bus, 1702305 triangular volumes cell structure (tedrahedrons) was created. The boundary conditions in the solution area are defined as inlet, outlet, wall and bus model *[9]*.

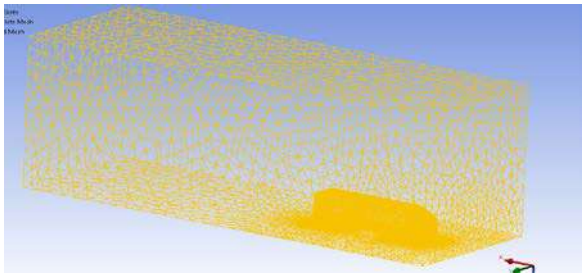

Fig.4a. Mesh distrubion on bus model[9]

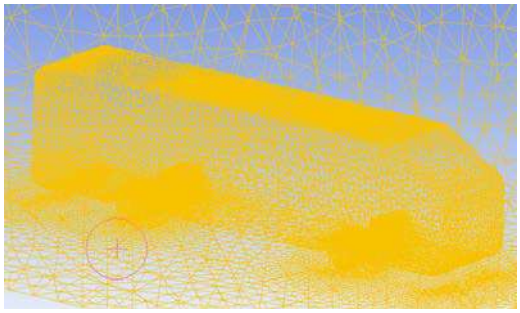

Fig.4b. Mesh distrubion on bus model[9]

As a results of the flow analysis, the drag force which acted on the model bus was obtained as 1000 iteration results and the C_D coefficient was determined. The aerodynamic resistance coefficient C_D is the function of the drag force F_D, density ρ, free flow velocity V and front view area and it is given in Equation 8.

$$C_D = \frac{F_D}{\frac{1}{2}\rho V^2 A} \quad (8)$$

2.5. Mesh Independent In CFD Analysis

It is very important to establish a smooth and high quality mesh in the numerical analysis about the finite volumes in terms of the correctness of the results. Therefore, mesh quality is sought in numerical studies.

However, as the complexity of the analyzed geometries increases, it becomes more difficult to obtain this mesh quality. The bus and passive flow control bar have small, curved parts. In this case, the mesh quality could not be obtained at the desired level. In order to achieve desired mesh quality, it will be necessary to further simplify the drawing data, draw flat parts instead of arcuate parts, or to close small parts and create alarger number of mesh structures. In this case, the drawing data will move away from the geometric similarity. In this study, the average element quality was 0.82. It is not recommended that this value be higher than 0.5. One of the methods to verify numerical studies is the independence test from the mesh. If the result does not change after a certain value despite the increase in the number of mesh in the numerical solution, independence in the solution from the mesh is obtained. In this study, as shown in Table 1. mesh independence tests were carried out for 10 different triangular volumes (tetrahedrons) mesh structure at 15 m / s free flow rate for model bus. The mesh independent analyzes were carried out by changing the minimum and maximum dimensions of the triangular mesh in the mesh configurations of the bus and the desired mesh number structures were created at different skewness rates and the same turbulence models.

Table1 Mesh independence test results at 15 m / s

Reynolds Number	Mesh Number	Drag Force (N)	C_D
288 463	350 306	0,22	0,360
288 463	554 520	0,320	0,524
288 463	760 210	0,346	0,567

288 463	950 651	0,287	0,470
288 463	1 095 765	0,287	0,470
288 463	1 347 211	0,286	0,469
288 463	1 622 354	0,287	0,470
288 463	2 169 195	0,287	0,470
288 463	2 765 968	0,287	0,470
288 463	3 011 460	0,286	0,469

The independence tests from the mesh were conducted on 10 different mesh numbers. As seen in Figure 5, the C_D coefficient was obtained at approximate values after 950 651 mesh numbers. In this study, the number of mesh was determined as 1702305. These mesh number is in the region where the mesh independence is obtained. Therefore, it has been accepted that flow analyzes are performed independently from the mesh. The faults which were caused mesh number and quality in numerical results were ignored *[9]*.

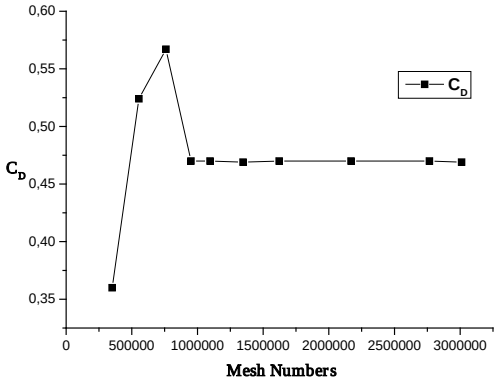

Fig. 5. The grapg of mesh independent[9]

3.RESULTS AND DISCUSSIONS

3.1.Drag coefficient of model bus

The C_D coefficient of the model bus was determined as 0.657on the basis of the drag force obtained after the 1000 iterations at 4 different free flow velocity. It was determined that 86.42 % of the total drag force was caused by pressure induced and 13,38% by friction induced.

The C_D values which were obtained after the analysis are given in Table 2, according to Reynolds number, C_D graph is in Fig. 6, and the flow images are in Figures 7a,b and 8.

Table 2. Aerodynamic drag coefficients of model bus[9]

Reynolds Number	Free Flow Velocity (m/s)	C_D
173076	15	0,673
230769	20	0,655
288461	25	0,640

346153	30	0,663

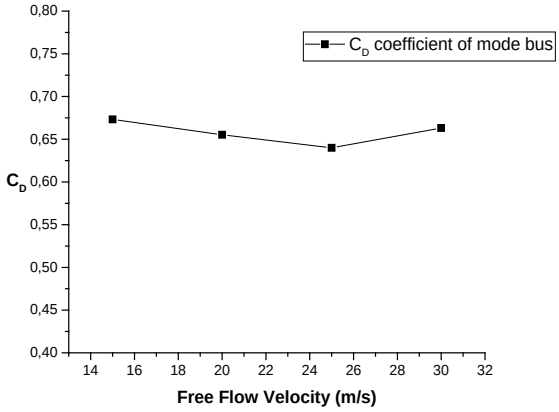

Fig. 6. Aerodynamic drag coefficient graph (C_D) of model bus[9]

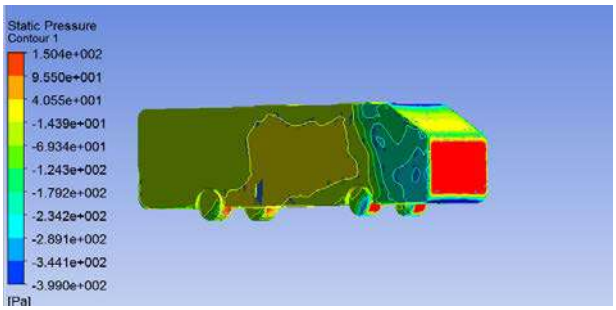

Fig. 7a. The pressure distribution on the model bus 30 m/s velocity[9]

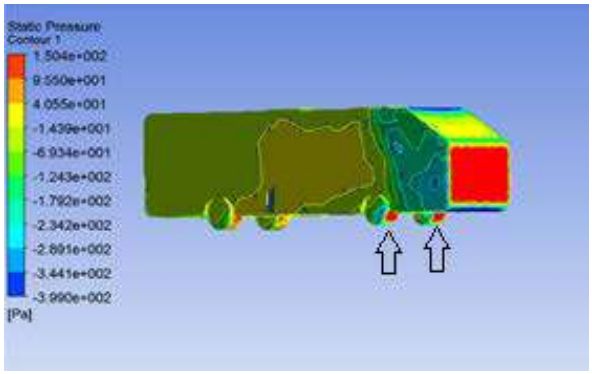

Fig. 7b. The pressure distribution on the model bus 30 m/s velocity[9]

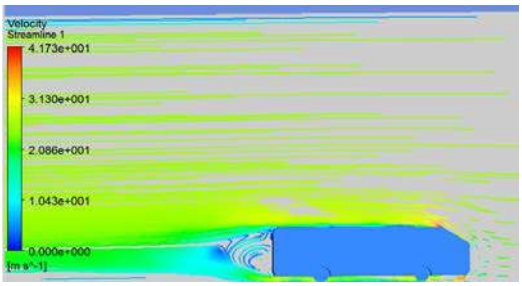

Fig.8. The streamline image of the wind speed around the bus model at 30 m/s velocity[9]

3.2.Drag coefficient of model 1 bus (without fender gap and whells)

The C_D coefficient of the model bus 1 was determined in same flow speed and Reynolds number as 0.632. This value is %3.91 lower than model bus which have fender gap and wehells. In that case the total %3.91 of drag force of a bus model originated from fender gaps and whells .The C_D values which were obtained after the analysis are given in Table 3, according to Reynolds number, C_D graph is in Fig. 9, and the flow images are in Figures 10, 11and 12.

Table 3. Aerodynamic drag coefficients of model 1 bus

Reynolds Number	Free Flow Velocity (m/s)	C_D
173076	15	0,646
230769	20	0,634
288461	25	0,620
346153	30	0,629

As a result of the analysis which were carried out at 4 different speeds, average C_D coefficient of model 1 bus was calculated as 0.632 and which is seed in Fig. 15.

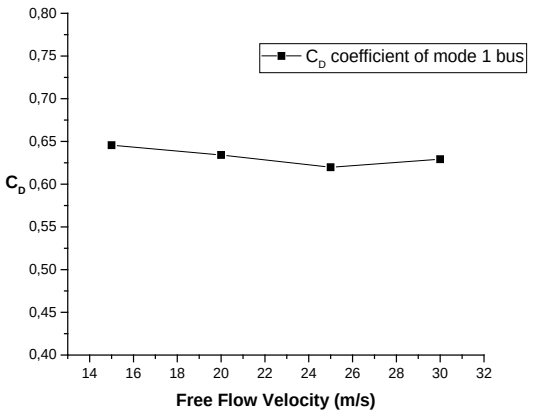

Fig. 9. The drag coefficient (C_D) of model bus model 1 buses

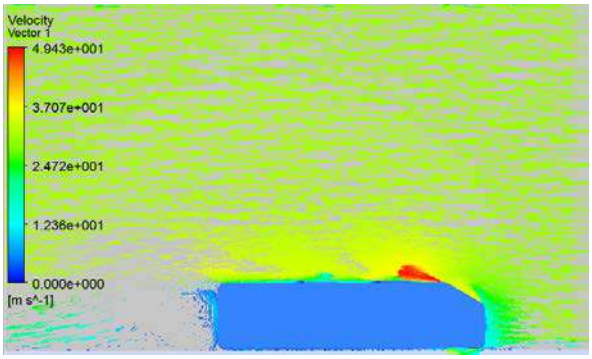

Fig. 10. The vector image of the effecting wind speed to model 1 at 30 m/s velocity

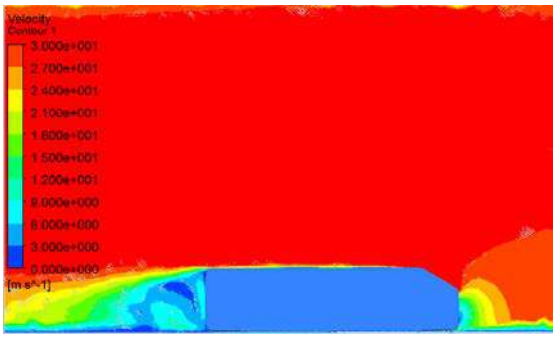

Fig. 11. The pressure distribution on the model 1 at 30 m/s velocity

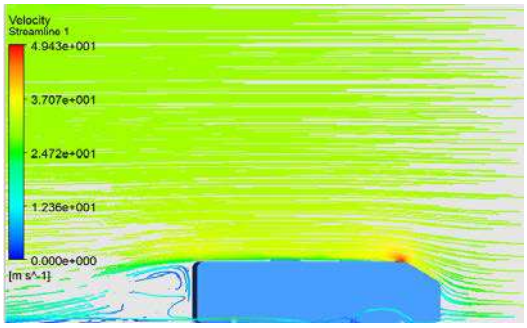

Fig. 12. The streamline image of the wind speed around the bus model at 30 m/s velocity

4. CONCLUSIONS

Fuel consumption is reduced by 1% when the aerodynamic drag coefficient of vehicles is reduced by 2% at high speeds (over 96 km / h) [7]. Fuel consumption of these vehicles a significant concern for consumers. Because a significant part of the transportation costs are related to fuel consumption.In this study, the current aerodynamic structure of a bus model is examined and the effect of fender gaps and whelles to total drag force is determinated by CFD method.

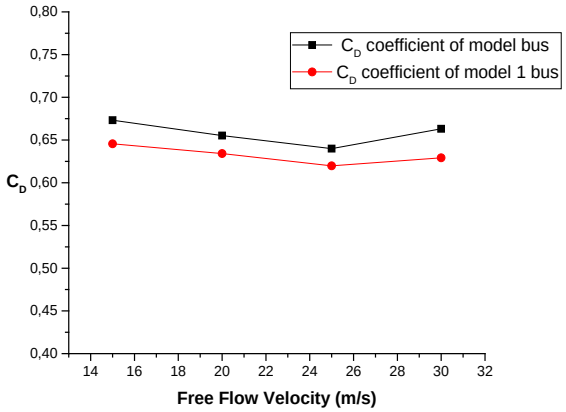

Fig. 13. Comparison graph of drag coefficient of model bus, model 1 buses

- ✓ The aerodynamic drag coefficient of the model bus is measured as 0.657, which is coherent with the literature values.
- ✓ The aerodynamic drag coefficient of the model 1 bus which has not got any fender gaps and whells is measured as 0.632.
- ✓ I that case for this bus model, %3.91 of ttal drag originates from whells and fender gaps.
- ✓ Bayindirli et al. (2015) found in their numerical study, 5.8% of total drag force was friction induces and, 94.2% was pressure induced for a truck trailer model [8].
- ✓ In this study, 86,42% of total drag force of model bus is pressure induced and 13,38% is friction induced.
- ✓ It has been seen that there is an important potential for reducing friction induced resistance on the bus model.

THANKS

This study was supported by Nigde Omer Halisdemir University Scientific Research Projects Coordination Unit with ref. FEB 2016/24 BAGEP. The author would like to thank to Nigde Omer Halisdemir University Scientific Research Projects Coordination Unit for their support.

REFERENCES

[1] Mohamed-Kassim, Z. Filippone, A. (2010), "Fuel savings on a heavy vehicle via aerodynamic drag reduction", Transportation Research Part D 15, 275–284, 2010.
[2] Nisugi, K. Hayase, T. and Shirai, A. (2004), "Fundamental Study of Aerodynamic Drag Reduction for Vehicle with Feedback Flow Control", JSME International Journal, Ser. B, Vol. 47, No. 3, pp. 584-592.
[3] Ji-qiang, N. Dan, Z. Xi-feng, L.(2017), "Experimental research on the aerodynamic characteristics of a high-speed train under different turbulence conditions" Experimental Thermal and Fluid Science 80,117–125.
[4] Cengel Y A and Cimbala J M. Akiskanlar Mekanigi Temelleri ve Uygulamalari Guven Bilimsel Yayinlari 2008, pp 562-599.
[5] Kocyigit N and Unal M F. Calculation of aerodynamic coefficient of helicopter body on pancake and forward using Fluent. Havacilik ve Uzay Teknolojileri Dergisi 2005; 2- 1: 57-64.
[6] Ince I T. Aerodynamic Analysis of GTD Model Administrative Service Vehicle, PhD Thesis, Gazi Universty Ankara, 2010.
[7] Wood R M and Bauer S X S. Simple and low cost aerodynamic drag reduction devices for tractor-trailer Trucks. SAE Technical Paper 2003; 01–3377: 1-18.
[8] Bayindirli C, Akansu Y E, Salman M S, and Colak D. The Numerical Investigation of Aerodynamic Structures of Truck and Trailer Combinations. International Journal of Automotive Engineering and Technologies 2015; 4 -3: 139-145.
[9] Bayindirli C., Celik M., Demiralp M.Bir Otobus Modeli Etrafindaki Akis Yapisinin CFD Yontemi Ile Incelenmesi ve Surukleme Kuvvetinin Pasif Akis Kontrol Yontemi Ile Iyilestirilmesi. Journal of Politeknik 2018, Early appearance format (DOI: 10.2339/politeknik.403993)

ICENS 4TH INTERNATIONAL CONFERENCE ON ENGINEERING AND NATURAL SCIENCE
2-6 May 2018 KIEV UKRAINE

Design Of A Robotic Pneumatic Pruner For Robotic Apple Harvesting

Erhan Kahya[1], Selcuk Arin[2]

Abstract

The robotic systems firstly developed in industrial production domain. But, in countries, in which the number of agricultural workers is limited and the costs are high, there is a tendency towards robotic technology in agricultural production. For this reason, the robotic system implementations started to seem in many agricultural activities. In the present study, the robotic system was discussed in terms of harvesting that is one of the agricultural activities. The robotic harvesting system consists of image processor, robotic arm, and gripper, which performs the final action. In this study, the position of fruit was determined in real-time by using the image processing. The X- and Y-coordinates sent to robotic arm directed the movement of it. Z-axis, which is the third axis and provides the forwards movement, was controlled using distance sensor. The designed pneumatic pruner system was mounted at the tip of robotic arm. The experiments were carried out on 100 Golden apples at different locations on the branch. Based on the coordinates of fruit, 85% positioning accuracy and 73% success rate were obtained in cutting the fruit from branch. The cutting success was statistically analyzed. At the end of study, the position of fruit stem corresponding to the tip of pruner, the position of pruner corresponding to the body of fruit, the fruit, or the beginning of stem rather than the stem itself, and the position of pruner on the shoot of stem were observed to cause failure during cutting procedure. According to the results obtained from experiments, it was concluded that the system to be used in such systems is the pneumatic pruner system.

Keywords: robotic,harvesting,apple

1. INTRODUCTION

Mechanization technology field in the agriculture is in the important development in both our country and all around the world because of some reasons such as obtaining quality product and decreasing the labor force. Traditional production techniques have given its place to agricultural mechanization applications. For that reason, mechanization applications have became widespread in some fields such as planting, spraying, harvesting in different production areas. These kind of computer-aided systems have been used in the agriculture with the advancement of technology and the introduction of the computer technology. In particular, all workings are automatically maintained in combine harvesters. Such systems provide us the transition to the robotics agriculture. Robotics agriculture, hydraulic and pneumatic systems are the agricultural systems that include both computer control systems and image processing technologies.

[1]*Corresponding author: Control and Automation Technology Department, Technical Sciences Vocational School, Namik Kemal University, Tekirdağ , Turkey(E-mail:ekahya@nku.edu.tr)*

[2]*Department of Agriculture Machine, Faculty of Agriculture, Namik Kemal University, Tekirdağ, Turkey, sarin@nku.edu.tr*

Even if produced systems are intelligent systems, all encodings must be performed by people. The system must be encoded with the help of the control parameters according to the process can be applied. It is expected that the machine must act in the way that it encoded by the people by understanding of the complexity of the workings. This act is called as robotics system action.

Robotics system action depends on the human factor entirely. Sensibility in the defining of the parameters which belong to workings affects the robotics system action. If the parameters are not suitable for the working expected result will not be proper. Environmental impacts, product features, the structure of the field, weather conditions are the factors that determine the robotics system action.

All input and output results must be well-analyzed for the expected action. The codes and expected results must be encoded exactly. Other additional equipments which will be used in robotics agriculture must be chosen correctly. Which system is needed, which controllers will control these systems and the selection of them are the factors that affect the functioning of the system. If these descriptions are inadequate and incomplete wrong harvesting, wrong seed planting, incorrect operation of automatic irrigation or incorrect amount of water can occur.

Kataoka et al. (2001) conducted a study for an automatic discovery system in detecting the location of apples for robotic apple harvesting. Decisions involving embalming. They stated that the fruit is the most important criterion to decide the harvest time. The Munsell color system is pre-primed, colored and separated in XYZ color units. According to this color, the time of harvest was found according to apple color.

Bulanon et al. (2004) conducted a research on the development of a real-time machine vision system for the apple harvesting robot. In this research, the red Fuji apple harvester has developed a real-time machine vision system for robot manipulator guidance. They took images from apple garden with CCD camera. The acquired images were transferred to the PC and the locations of the appliances were determined by image processing method. Under different light conditions, it is possible to recognize the fruits and determine their location. The red and green coefficients are used to identify the fruit. As a result of the research, they defined the fruit with an accuracy of 80% and an error margin of less than 3%.

Mao et al. (2009) conducted a study on the determination of the location of apples for robotic apple harvesting. They used two high-resolution digital cameras at the location of the fruit. They determined the selection of the fruit using color and shape analysis. The software they use for image processing is Microsoft C ++ based RelCtrl. RelCtrl for C ++ 'in vfw32.lib, JpegLib.lib, PRSDK.lib, and CDSDK.lib. They used their libraries. They are based on the following algorithm for the program. They determined 9.4% error rate in the process.

The important point for the above-mentioned systems is to obtain the data and information about the product to be harvested. Robotics system actions are provided at the end of the collected data and information. In the collected data; the robot is moved over this coordination by finding the coordination of the systems and lands.

Robotics agriculture systems use many technologies. It is an environmental approach that has a tight bond with the development of many technologic fields. Drug utilization, fertilization, irrigation and harvesting can be made more sensible. Robotics agriculture provides more sensitive agriculture. Energy consumption is maximum expense in the agriculture. It is required to provide the energy consumption less than before. Applications are applied only specific areas so, the lower energy consumption can be provided.

It can be achieved that more production will be done with less power and more efficient in the agriculture as a result of all this studies. Sensitive agriculture can provide that there can be less pollution in the world.

2. MATERIAL AND METHODS

2.1. MATERIAL

Figure 1 shows the locations of the values entered into the calculations for the pneumatic shear system. Table 1 shows the characteristics of the parallel holder used.

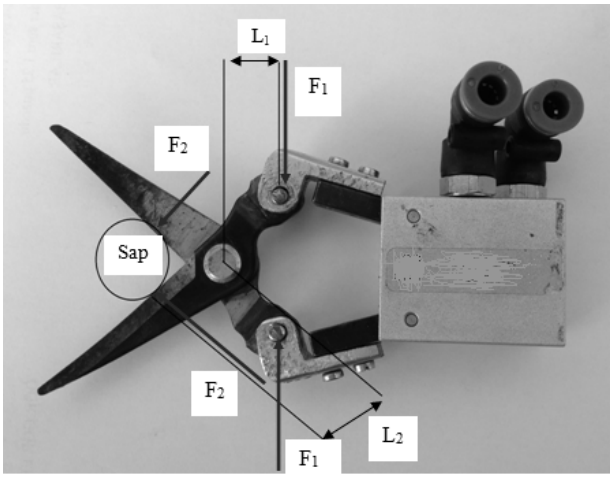

Figure 1. Values for pneumatic system

Calculation of the machine cutting force:

Cutting Strain(D. Dursun 2001) :

$$\tau = \frac{F}{A} \quad (1)$$

τ =Cutting Strain(N mm $^{2\text{-}1}$)

A= Cross-section area (mm^2) (D. Dursun 2001)

F=Force(N)

$$A = \frac{\pi * d^2}{4} \quad (2)$$

d=Stem Diameter(mm)

Cutting Force(D. Dursun 2001) :

$$F_1 * L_1 = F_2 * L_2 \quad (3)$$

L_1=Steam length(mm)

L_2=Cutting Length(mm)

F_1= Force applied to the arm(N)

F_2=Cutting Force(N)

Pneumatic pressure (D. Dursun 2001):

$$P = \frac{F}{A} \quad (4)$$

P=Pressure(Pascal)

F=Force(N)

A= Cross-section area (mm^2)

The system in Figure 1 is attached to the robotic system for cutting the fruit over the handle. Formulas 1, 2, 3 and 4 are used for the cutting stress applied during the cutting of the fruit. During formulas calculations, stem thicknesses were measured with calipers and values were recorded.

For L_1 and L_2 lengths,the measured values of pneumatic hose inner diameter with caliper are given below.
L_1=20 mm

L_2=25 mm

The inner diameter of the hose is 4 mm.
Hose Area (A) = 12,56 mm^2 .

Table 1 Parallel the holder properties

	Parallel the holder
Movement Type	Double act
Pipe Type (mm)	16
Port Size	M5x0.8
Working environment	Air
Average pressure ratio (kgf cm^{2-1})	1.5~ 7 (0.15~0.7 MPa)
Operating temperature (C^o)	-5 ~ +60
Max. Frequency (Devir d^{-1})	180
Max. Arm length (mm)	30
Free Devergence Angle	-10^o ~ 30^o
Technical moment(kgf cm^{-1})	Close 0.4 x P /Open 0.5 x P.
Clamp Force (F) (kgf)	F=M / L x 0.85
Sensor key	RCE , RCE1
Weight (gr.)	53

Table 2. Pneumatic cutting system

	Pressure Ratings (Bar)			
	5	6	7	8
F_1(N)	6.28	7.53	8.79	10.04
F_2(N)	5.02	6.03	7.03	8.04

2.2. METHODS

The most important variable is to know the space coordinate axes of the fruits in order to harvest the fruit with robotics system. Image processing technique has been applied in order to find the coordinate axes. 2D camera model has been used for image processing. Both horizontal axis (x) and vertical axis (y) have been found in the space coordinate axis of the fruits with this camera. Ultrasonic sensor has been used for the distance (z) which is the third coordinate axis. The code has been written in C# for the use of this sensor and the robot has been prevented when it reaches a certain distance. Necessary smooth and kinematic calculations have been written in C# which is necessary for image processing. These calculations and the program have been installed to the processor in the robotics system control card with USB port. The communication between the writing of the program and 2D camera has been provided. Coordinate axes to be obtained as a result of image processing and 2D camera coding have been found. Obtained results have been identified by using 2D camera interface and it has been recorded. It has been provided that robotics arm stops and cut when it is 10cm in front of the fruit according to the value from the ultrasonic sensor via written program.

The most important point in the system is to introduce the fruit shape to the camera with the program in the camera. Shape recognition screen is shown in Figure 2.

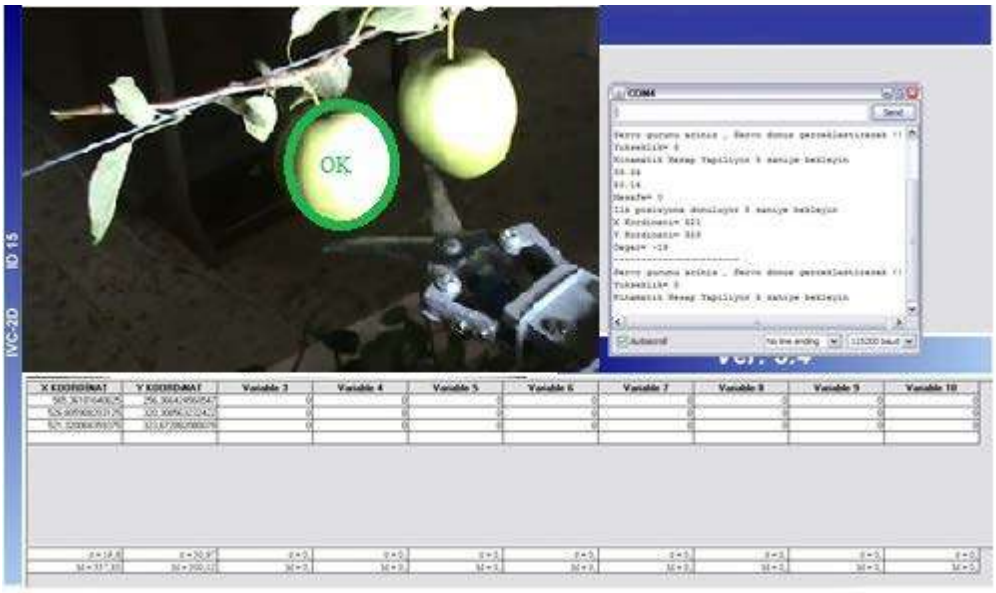

Figure 2.Shape Recognition Screen

Robot arm's movement has been provided after the calculation according to the coordinate from the camera in the Robotics Control card. Coordinate values from camera to processor are shown in Figure 3.

Index	DB Value	Value	Description
994	0	0	
995	0	0	
996	0	0	
997	0	0	
998	0	0	
999	0	0	
1000	160,402...	160,40225...	X KOORDİNAT
1001	76,8049...	76,804977...	Y KOORDiNAT
1002	0	0	
1003	0	0	
1004	0	0	
1005	0	0	
1006	0	0	
1007	0	0	
1008	0	0	

Figure 3. Coordinate values from camera to processor

The positioning of the robot arm has been conducted for both kiwi and apples. Fruits have been cut with the help of pneumatic cutting. Cutting action for apple is shown in Figure 4.

Figure 4. Cutting for apple

3.RESULTS AND DISCUSSION

The pressure value of the compressor which enables the operation of the pneumatic system varies between 5 - 8 bar.The force (F1) applied to the arm is calculated by the formula (4), the cut force (F2) by the formula (3).In Table 2, values F1 and F2 are shown.

The force (F1) and the cut stretching (F2) applied to the arm calculated by using formulas 3 and 4 are substituted into formula 1 and the cut stretching (τ) is calculated.For each type of fruit, 100 calculations were statistically analyzed.Statistical analysis was calculated according to the cutting conditions of the fruits. The results are summarized in Table 3.

Table 3. Exchanges cutting force for Apple

		Sum of Squares	df	Mean of Squares	F	Sig.
a*	Between Groups	95.118	73	1.865	4.111E32	.000
	In-Group	.000	27	.000		
	Total	95.118	100			
b*	Between Groups	137.609	73	2.698	8.753E32	.000
	In-Group	,000	27	.000		
	Total	137.609	100			
c*	Between Groups	186.847	73	3,664	1.188E33	.000
	In-Group	.000	27	.000		
	Total	186.847	100			
d*	Between Groups	244.169	73	4.788	6.351E32	.000
	In-Group	.000	27	.000		
	Total	244.169	100			

*a=5 bar, b=6 bar, c=7 bar, d=8 bar

At the end of the experiments, the wrong value of the robot arm has been determined as 15% for apples. The reason for this is that the camera chooses the fruit randomly during finding the coordinate in the fruits that stand side by side or back to back in the experiments. It has been determined that the most suitable fruit coordinates have been given. It is required to choose color camera which processes three-dimensional image in order to prevent this.

The cut rate for the fruit is 73%.It has been found that the cause of the difference between finding and cutting is the location of the fruit on the scissors.As a result of the constructed T-test, it has been determined that not only the x-axis but also the y-axis are important for breaking the fruit over the branch.It has been found that during positioning of the scissors, the y-axis scissors are positioned on the stalk of the fruit.When the stalk of the fruit is on the tip of the scissors, when the scissors touches the fruit, when both fruit and the stalk of the fruit come to the initial point, they can cause errors for breaking process.According to the Anova test, pressure values ranging from 5 to 8 bar applied by the compressor were found to be significant for the cutting force.It is understood that the compressor pressure operating the pneumatic system provides

sufficient pressure for the cutting operation.The change in pressure between 5 and 8 bar was found to have sufficient pressure values for the shear force.It has been determined that the pressure change in the compressor will not affect the cutting force.

4.CONCLUSION

It is understood that the system to be used in the gripper for the robotic system fruit harevesting is the pneumatic system.It has been determined that the applied pressure values are sufficient for cutting.It has been shown that the fruit must be pulled inward from the point of the scissors and held constant to increase the success rate in the cutting process.It was understood that the cutting performance would be increased by the vacuum system attached to the scissors system.It is considered that the special design of the fruit of the vacuum pad at the end of the vacuum generator used for pulling the fruit into the fruit will increase the success of holding the fruit constantly.It is understood that with this research the most important factor in the robot design is the gripper which provides the latest movement.As a result of the study, it has been seen that pneumatic cutting is the factor that will affect the system success besides all the parts and software of the robotic system.

REFERENCES

[1]Kataoka T, Okamoto H, Hata S (2001). Automatic Detecting System Of Apple Harvest Season For Robotic Apple Harvesting. 2001 ASAE Annual International Meeting. Sacramento Convention Center Sacramento, Paper Number: 01-3132, California, USA.

[2]Bulanon D.M, Kataoka T , Ota Y, Hiroma T (2004). Estimation Of Apple Fruit Location Using Machinehine Vision System For Apple Harvesting Robot. Internatioan Commision of Agricultural and Biosysmes Engineering the CIGR Journal of Scientific Research and Development,Volume 3,1-6.

[3]Mao W, Ji B, Zhan J, Zhang X, Hu X (2009). Apple Location Method For the Apple Harvesting Robot. Image and Signal Processing, CISP '09. ,2nd International Congress on, ISBN:978-1-4244-4229-7,Chine.

[4] D. Dursun,2001. *Cisimlerin Dayanimi Temel Ders Kitabi*.Milli Egitim Basimevi, ISBN 975-11-1913-8, Ankara

ICENS 4TH INTERNATIONAL CONFERENCE ON ENGINEERING AND NATURAL SCIENCE
2 - 6 May 2018 KIEV UKRAINE

Diffusion Welding of Nodular Cast Iron to Copper

Ibrahim Çelikyurek[1], Osman Torun[2], Bedri Baksan[1]

Abstract

GGG60 grade nodular cast iron and pure copper was welded using a vacuum diffusion welding process. The cylindrical samples having a diameter of 8 mm and 8 mm in length were used. The flat surfaces of both samples were ground, and finally polished using 1 μm diamond paste. The prepared surfaces of samples were matched together. A vacuum furnace was used for diffusion welding process. For the diffusion, forging pressure and temperature were 4 MPa and 950 °C respectively. The diffusion welding of samples was carried out at 30, 60, and 90 minute durations. Before heating, the furnace was evacuated to 10^{-1} millibar for all welding processes. After welding the microstructure of welding interfaces were examined with optical microscopy on the perpendicular sections of the welds. The micro hardness deviation from one matrix to another was measured. The mechanical properties of welding interfaces were determined using a specially designed shear test apparatus. The optical microscopy investigations were revealed that the welding interfaces of diffusion welded nodular cast iron and pure copper have a smooth morphology without any crack or pore. The micro hardness measurements of welding interfaces showed that the hardness values differ slightly from one matrix to another one. It means a diffusion zone is occurred at the interface. The shear test results showed that the shear strength of welding interface is increased with increasing diffusion time at 950 °C diffusion process.

Keywords: Welding, diffusion, Nodular cast iron, Copper, Interlayer, Hardness, Strength

1. INTRODUCTION

Nodular cast Iron, also called ductile Iron or spheroidal graphite cast Iron is widely used some applications in which the impact loads exist and damping the vibration is required. Whereas, pure Copper is widely used for its high electrical and thermal conductivity.

The ductile cast Iron has been used in different industries due to its good mechanical properties, corrosion resistance and machinability [1]. The welding of the ductile cast Iron has some problems because of high Carbon content which causes to formation hard and brittle carbides in melting zone and martenzite in both melting and heat-affected zones [1]. Most of the welding techniques can be used for bonding or repairing ductile cast Iron [2-6].

Joining of dissimilar materials is generally more difficult than that of similar metals due to different chemical and metallurgical properties. The solid state welding processes such as explosion, friction, friction stir, diffusion and cold roll welding are being developed for joining dissimilar materials [6].

For the welding of pure Copper, using of traditional welding processes like brazing, there are some difficulties because of high thermal diffusivity of Copper [7]. On the other hand, with the solid state welding techniques, most of them might be avoided since the base materials not melted [8-12].

Diffusion welding process is a solid state welding technique which has some advantages due to lack of melting contrary to other fusion welding techniques and can be used on the joining of a variety of dissimilar materials. The advantages of this technique can be summarized as smaller heat affected zone or lack of this zone, eliminating the reactivity of materials, ability to join dissimilar materials and less equipment is required.

[1] *Corresponding author: Eskisehir Osmangazi University, Department of Metallurgical and Materials Engineering, 26480, Odunpazari/Eskisehir, Turkey. cibrahim@ogu.edu.tr*

[2] *Afyon Kocatepe University, Department of Mechatronics Engineering, Afyonkarahisar, Turkey, otorun@aku.edu.tr*

In this study, a nodular cast Iron and pure Copper were joined using diffusion welding process. The effect of the diffusion duration on the microstructural evaluation and mechanical properties of the welding interface was revealed.

2. MATERIALS AND METHODS

A GGG60 grade nodular cast Iron and a commercially pure Copper were bonded using diffusion welding process. A specially designed vacuum furnace was used for welding as shown in Figure 1. The flat surfaces of the samples in diameter of 8 mm were polished and matched immediately. The matched samples were put on the lower support perpendicularly. The load was applied trough upper support using weights. The applied forging pressure was 4 MPa for each samples. The furnace was evacuated to 0.1 mb to prevent oxidation and heated to 950 ^{o}C . The diffusion durations were 30, 60 and 90 minutes. At the end of these durations the samples were cooled in the furnace under the temperature of 200 ^{o}C slowly. For each diffusion welding condition 3 samples were prepared. One of them was used for metallographic examination and the others were used in shear tests.

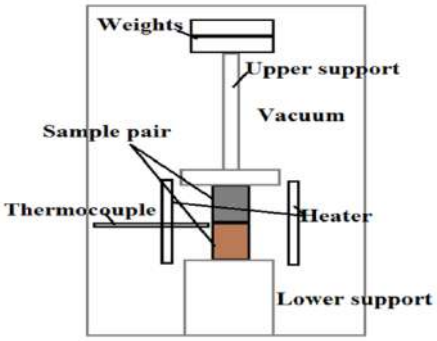

Figure 1. A schematic illustration of diffusion welding furnace.

After welding, the samples were cut perpendicularly. The cross section of the samples was ground up to 1000 mesh paper and finally polished using 1μm diamond paste. The microstructure of the welding interfaces of the samples were examined before and after etching using an optic microscope.

The micro hardness deviation from one matrix to another one was measured to reveal the diffusion zone. The strength of the welding interfaces was determined using a specially designed shear test apparatus (Figure 2) by means of compression test. The shear strength is determined by dividing the ultimate load to the cross section area of the sample. The loading speed was 10 mmmin^{-1} for all samples.

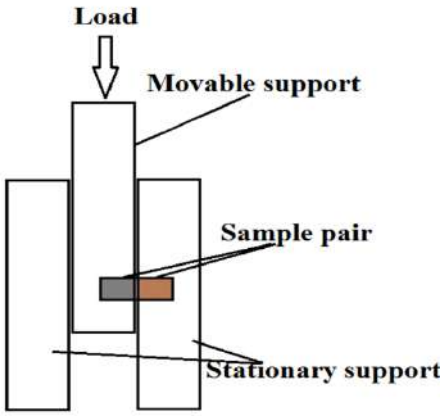

Figure 2. A schematic illustration of shear test apparatus.

3. RESULT AND DISCUSSION

According to Iron-Copper binary phase diagram (Figure 3) both Iron and Copper has only a limited solubility in each other and there is no other chemical compound. Iron can dissolve 2%wt. Copper at 857 ° C, whereas Copper dissolve 3.4%wt. Iron at 1094 ° C.

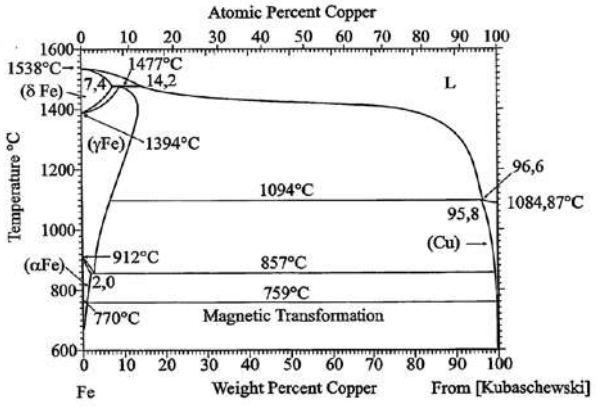

Figure 3. Fe- Cu binary phase diagram.

The un-etched microstructure of the cross sections of the samples are shown in figure 4. As seen from un-etched micrographs, the samples have a smooth morphology at the welding interface for all welding durations.

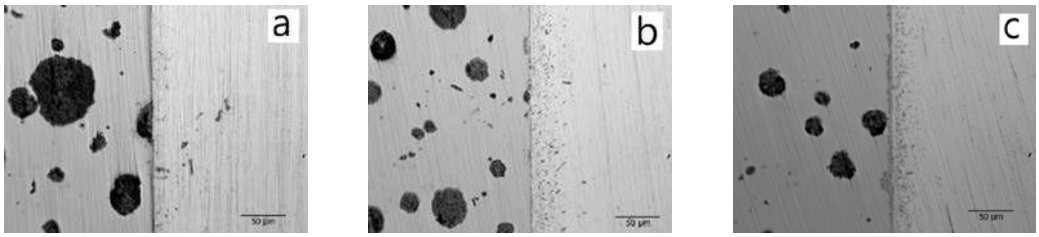

Figure 4. The un-etched cross section micrographs of the welded samples. a)30 min. b) 60 min. c) 90 min.

On the other hand, the etched microstructures were exhibited in figure 5. Each side of the samples were etched one by one. The left side is GGG60 and right side is pure Copper in all figures. As seen from the figures GGG60 nodular cast Iron has a ferrite-pearlite matrix with spherical graphite and Copper has a single grain structure.

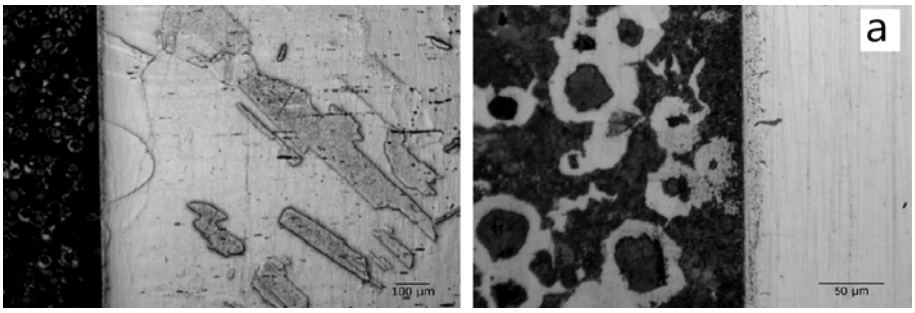

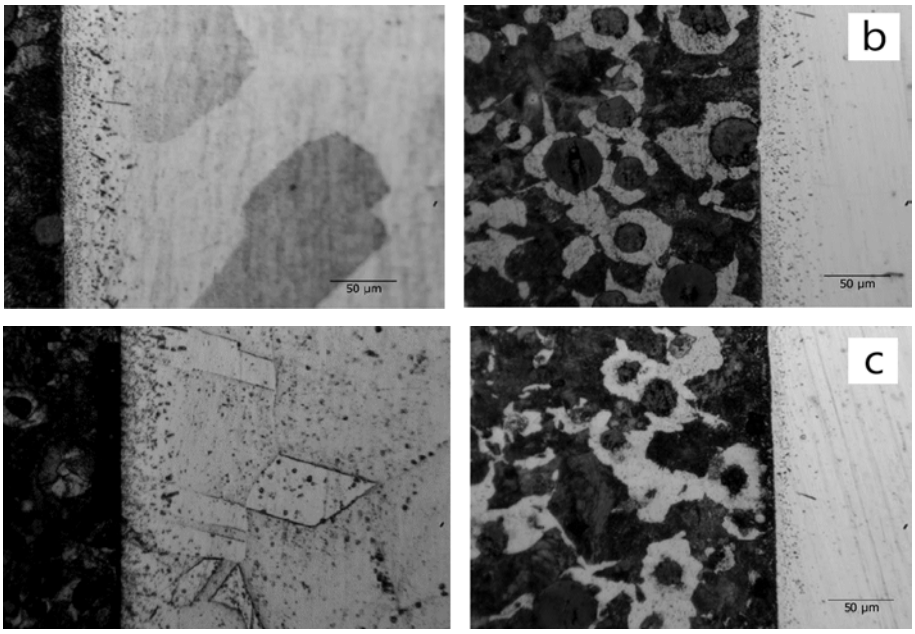

Figure 5. The etched cross section micrographs of the welded samples. a)30 min. b) 60 min. c) 90 min.

The micro hardness deviation from one matrix to another one is given in figure 6. On the graph right side belong to cast Iron and left side belong to Copper. The hardness values differ slightly from one matrix to another one. It means a diffusion zone is occurred at the interface. The micro hardness values of 30 and 60 min. are high near the welding interface of the cast Iron side whereas for the 90 min. the hardness value is lower. On the other hand, the hardness values on the Copper side are similar.

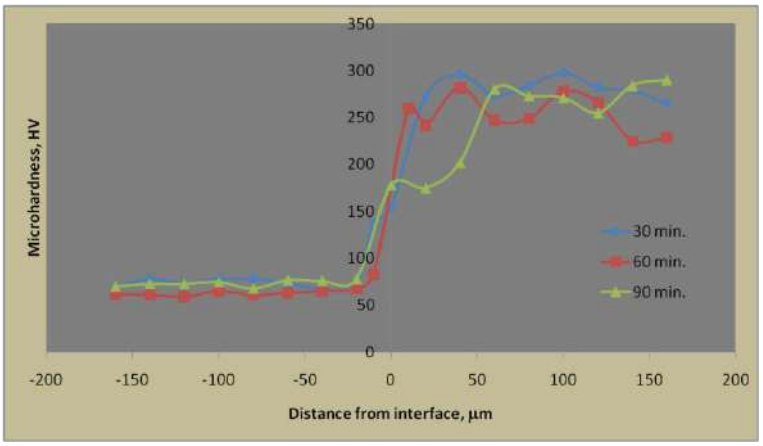

Figure 6. The micro hardness deviations of the welding interfaces.

Figure 7 shows the shear test results. According to these results, the strength of the welding interface tends to increase with increase in welding duration. But, the sample welded for 90 min. has a lover strength than others. This results are matching with hardness measurements. But all of them have a lower shear strength then both copper and cast iron. The new phases formed on the interface have a lower strength. Nevertheless, the sample welded for 60 min. have a strength of 35 % of copper.

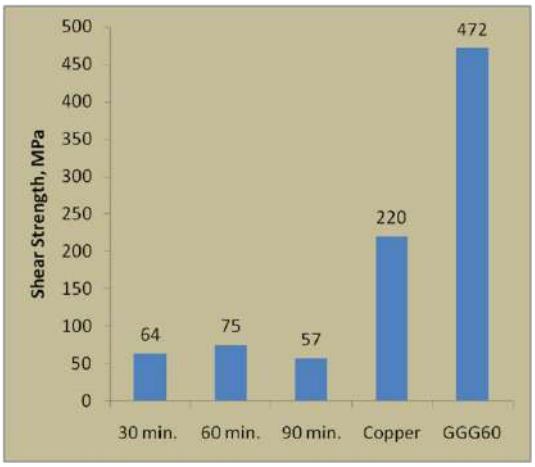

Figure 7. The shear strengths of the welding interfaces.

The fractured surface microstructures of the sample pieces are given in figure 8. These micrographs show that fractured surfaces include both copper and cast iron on each sides. The fracture was occurred on the welding interface.

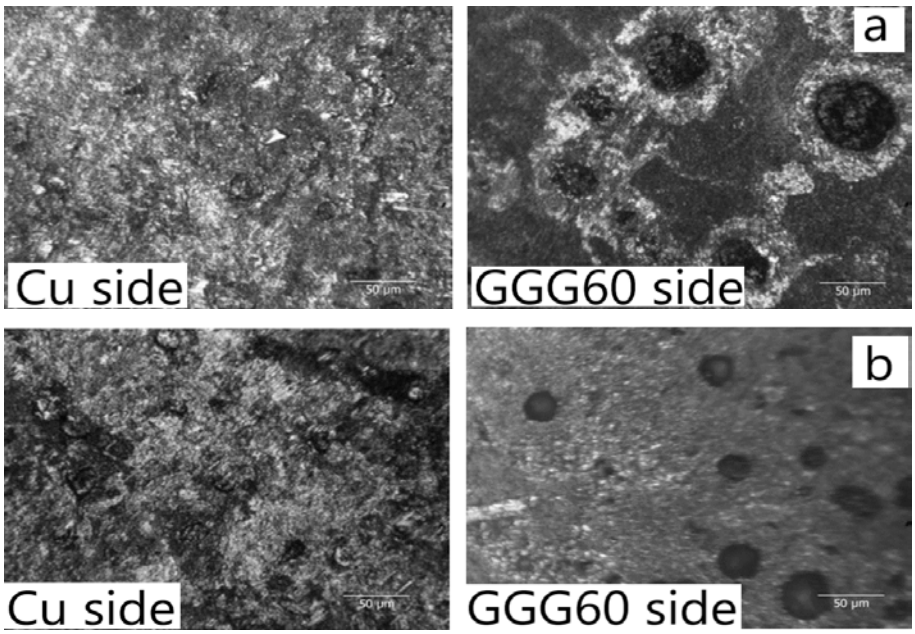

Figure 8. The fractured surfaces of the samples. A) 30 min. and b) 90 min.

4.CONCLUSIONS

The GGG60 cast Iron and commercially pure copper can be welded using diffusion welding process. Although Fe and Cu has only a limited solubility in each other, they can be joined using diffusion welding process. The welding interfaces of diffusion bonded nodular cast Iron and pure Copper have a smooth morphology without any crack or pore. The hardness values differ slightly from one matrix to another one. It means a diffusion zone is occurred at the interface. The shear strength of welding interface is increased with increasing diffusion time. But very long time is resulted with reduction of strength due to formed phases which have a lower strength.

REFERENCES

[1]. M. A. Paykani, M. Shayan and M. Shamanian, "Weldability of Ferritic Ductile Cast Iron Using Full Factorial Design of Experiment", Journal of Iron and Steel Research International, vol. 21, pp. 252-263, 2014.
[2]. F. Malek Ghaini, M. Ebrahimnia, S. Gholizade, "Characteristics of cracks in heat affected zone of ductile cast iron in powder welding process.", vol. 18, pp. 47-51, 2011.
[3]. M. Hatatea, T. Shiotaa, N. Abeb, M. Amanoc, T. Tanaka, "Bonding characteristics of spheroidal graphite cast iron and mild steel using electron beam welding process", Vacuum, vol. 73, pp. 667-671, 2004.
[4]. R. Winiczenko and M. Kaczorowski, "Friction welding of ductile cast iron using interlayers.", Materials and Design, vol. 34, pp. 444-451, 2012.
[5]. S. M.Mirhedayatian, S. E.Vahdat, M. J. Jelodar and R. F. Saen, "Welding process selection for repairing nodular cast iron engine block by integrated fuzzy data envelopment analysis and TOPSIS approaches.", Materials and Design, vol. 43, pp. 272-282, 2013.
[6]. SONG Yu-lai, LIU Yao-hui, ZHU Xian-yong, YU Si-rong, ZHANG Ying-bo, "Strength distribution at interface of rotary-friction-welded aluminum to nodular cast iron.", Trans. Nonferroous Met. Sos. China, vol. 18, pp. 14-18, 2008.
[7]. JW. Lina, HC. Changa, MH. Wub, "Comparison of mechanical properties of pure copper welded using friction stir welding and tungsten inert gas welding.", Journal of Manufacturing Processes, vol. 16, pp. 296-304, 2014.
[8]. L. Pana, P. Lia, X. Haoa, J. Zhoub, H. Donga, "Inhomogeneity of microstructure and mechanical properties in radial direction of aluminum/copper friction welded joints.", Journal of Materials Processing Tech. vol. 255, pp. 308-318, 2018.
[9]. G. Carvalho, R. Mendes, R.M. Leal, I. Galvão and A. Loureiro, "Effect of the flyer material on the interface phenomena in aluminium and copper explosive welds.", Materials and Design, vol. 122, pp. 172-183, 2017.
[10]. I. Galvão, C. Leitão, A. Loureiro and D.M. Rodrigues, "Study of the welding conditions during similar and dissimilar aluminium and copper welding based on torque sensitivity analysis.", Materials and Design, vol. 42, pp. 259-264, 2012.
[11]. P. Nagabharam, D. Srikanth Rao, J. Manoj Kumar and N. Gopikrishna, "Investigation of Mechanical Properties of Friction Stir Welded pure Copper Plates.", Materials Today: Proceedings, vol. 5, pp. 1264-1270, 2018.
[12]. J. Hea, D. Sirois, S. Li, M. Sullivanb, C. Wikle, Bryan A. Chinb, "Ballistic impact welding of copper to low carbon steel.", Journal of Materials Processing Technology, vol. 232, pp. 165-174, 2016.

Biography: Bachelor degree: Istanbul Technical University (1992-1996), Master's degree: Osmangazi University (1997-2000), Phd degree: Eskisehir Osmangazi University (2000-2006) Affilation: Asist Prof. Dr. in Eskisehir Osmangazi University Department of Metallurgical and Materials Engineering.

ICENS 4TH INTERNATIONAL CONFERENCE ON ENGINEERING AND NATURAL SCIENCE
2 - 6 May 2018 KIEV UKRAINE

Determination of Parameters Affecting Hardness of AA7075 Aluminum Alloy by Response Surface Method

Bedri Baksan[1], Ibrahim Celikyurek[2], Adem Tasdemir[3], Osman Torun[4]

Abstract

In this study, one of the important alloys group of AA7075 was held to obtain the optimum aging heat treatment conditions by response surface method. AA7075 alloy is an important alloy especially for aerospace applications, for its higher specific strength respect to other engineering materials.

In this study, three cold working rates of 0%, 20%, and 40%, and three aging temperatures 150 ˚C, 200°C, and 250 °C, and three aging treatment times of 2 hours, 4hours, and 6 hours were applied to AA7075 aluminum alloy to investigate the effect of these parameters on its Vickers hardness. Experiments, which were planned according to a three parameters and three levels Box-Behnken design, which is a type of response surface method, were carried out in predetermined conditions.

According to the design of experiments results, first and second order of temperature has the most significant parameter on the hardness of AA7075 alloy. The first order of time parameter was found statistically significant at 92% confidence level. Only the interaction between temperature and time parameter was determined significant at 85% significance level. The rest of parameters were determined insignificant.

A second order and statistically significant mathematical model with 0.9565 determination coefficient, predicting hardness of AA7075 alloy at 95% significance level, was obtained. Lack of fit was insignificant and it is predicted versus actual harness values are very good agreement. According to the optimization, evaluation revealed that optimum hardness values of 145.18 can be obtained when the sample should be treated at 182 °C temperature for 2 hours and 0% aging procedure.

Keywords: Response surface method, Box-Behnken Design, AA7075 Alloy, Aging, Vickers Hardness

1. INTRODUCTION

The 7xxx series of aluminum alloys are commonly used in aerospace industry in structural applications due to their low density, high strength, ductility, toughness and fatigue resistance [1-3].

AA7075 aluminum alloys, one of the commercial forged aluminum alloys containing zinc, copper and magnesium-based alloys having very high mechanical properties such as 505 MPa yield strength and 11% elongation.

Since AA7075 aluminum has many excellent properties such as low density, good corrosion resistance, machinability and electrical conductivity besides its high mechanical properties, it is preferred in places where high strength is required such as aircraft bodies and wings (places where strength is required), machine parts, automotive industry and military fields [2-4] .

Aging is the most important heat treatment used for hardening in non-ferrous metals, primarily aluminum, and in high-strength stainless steels. Aluminum used in various industries such as aviation is strengthened by aging

[1] *Corresponding author: Eskisehir Osmangazi University, Department of Metallurgical, and Materials Engineering, 26480, Odunpazari/Eskisehir, Turkey. baksan@ogu.edu.tr*
2 Eskisehir Osmangazi University, Department of Metallurgical, and Materials Engineering, 26480, Odunpazari/Eskisehir, Turkey. cibrahim@ogu.edu.tr
3 Eskisehir Osmangazi University, Department of Mining Engineering, 26480, Odunpazari/Eskisehir, Turkey. atasdem@ogu.edu.tr
4 Afyon Kocatepe University, Department of Mechatronics Engineering, 03200, Afyonkarahisar, Turkey. otorun@aku.edu.tr

process. The purpose of the aging hardening process, also known as the precipitation hardening process, is to precipitate the second phase, which has a hard structure, finely dispersed in the matrix phase [4,5].

Box-Behnken method is a very useful method for experimental design. In many engineering applications By this method important time, money, workforce reduction can be obtained. The experimental and calculated results from Box-Behnken method were compared, and a very good agreement of calculated model results experimental results were found.

2.EXPERIMENTAL

In this study AA7075 Aluminum alloy aging process was applied. AA7075 aluminum sample was first homogenized at 540 ° C for 72 hours. Firstly, at 200 ° C, the solutionizing treatment was applied to the samples. Three levels of deformation rates 0, 20, and 40% respectively were applied to these samples.

Aging heat treatment was also conducted at three different temperatures 150, 200, and 250° C for three different aging times of 2, 4, and 6 hours, under argon atmosphere in custom made atmosphere controlled heat treatment furnace.

The mechanical strength values were obtained from microvickers hardness testing instrument. At least average of three measurement values were taken into consideration to observe the effect of heat treatment to aluminum samples.

The collected data was compared with the values obtained by Box-Behnken method. The Box-Behnken method was based on the three independent parameters; deformation rate 0, 20, and 40%, aging temperature 150, 200, and 250° C, and aging times of 2, 4, and 6 hours. Table 1 is showing the methodology of Box-Behnken design values. In Table.2 the limit values for experimental design values were given. Three factors with three levels values were calculated and a mathematical model equation generated from these parameters. The analyses of the variables were done by Analysis of Variables (ANOVA) study.

Table 55. The Box-Behnken design parameter methodology for AA7075 aging optimization

Independent parameters	**Symbol**	**Code levels**		
		-1	0	+1
Temperature (ºC)	A	150	200	250
Time (hour)	B	2	4	6
Deformation(%)	C	0	20	40

The predicted model and the real measured values were plotted on the same diagram to see the reliability of the calculated model. The main effects of variables were also plotted by Box-Behnken method using the predicted values. As well as interactions of parameters were observed to distinguish which parameters were effective on aging. Finally the optimization of aging procedure was calculated to obtain the maximum hardness which represents the maximum strength of the samples.

Table 2. The required number of experiments due to the three levels with three factors.

Experiment No	A-Temperature (°C)	B-Time (hour)	C-Deformation (%)
1	-1	-1	0
2	1	-1	0
3	-1	1	0
4	1	1	0
5	-1	0	-1
6	1	0	-1
7	-1	0	1
8	1	0	1
9	0	-1	-1
10	0	1	-1
11	0	-1	1
12	0	1	1
13	0	0	0
14	0	0	0
15	0	0	0

4. RESULTS AND DISCUSSION

The model according to three factors with three levels was based on the values given on Figure 1 and Figure 2. The predicted model was found to be appropriately as in equation (1).

$$Y = b_0 + b_1A + b_2B + b_3C + b_{12}AB + b_{13}AC + b_{23}BC + b_{11}A^2 + b_{22}B^2 + b_{33}C^2 \quad (1)$$

The hardness values were calculated from Box-Behnken method is given in Table 3.

Table 3. The mathematical model and ANOVA results

Source	Sum of Squares	df	Mean Square	F Value	p-value Prob > F	Significance
Model	7007.80	9	778.64	14.66	0.0020	significant
A-Temperature	4593.61	1	4593.61	86.50	< 0.0001	
B-Time	230.05	1	230.05	4.33	0.0826	**
C-Deformation	5.44	1	5.44	0.10	0.7597	
AB	144.00	1	144.00	2.71	0.1507	***
AC	16.40	1	16.40	0.31	0.5985	
BC	17.22	1	17.22	0.32	0.5897	
A^2	1920.63	1	1920.63	36.17	0.0010	*
B^2	26.78	1	26.78	0.50	0.5043	
C^2	53.66	1	53.66	1.01	0.3536	
Residual	318.63	6	53.10			
Lack of Fit	269.06	3	89.69	5.43	0.0992	not significant
Pure Error	49.57	3	16.52			
Cor Total	7326.43	15				

: Significant at 95% confidence level, **: Significant at 90% confidence level, *: Significant at 85% confidence level*

The second order mathematical model for predicting the hardness values from Table.3 can be expressed as below equation

$$\textbf{Hardness (HV)} = 129.43 - 23.96A - 5.36B + 0.83C - 6AB - 2.03AC + 2.07BC - 21.91A^2 + 2.59B^2 + 3.66C^2 \quad (2)$$

If the model compared with experimental data, the reliability was found as R^2=0.9565. The normal plot of residuals were shown on Figure.1, the fitting of experimental data on calculated curves were given on Figure.2.

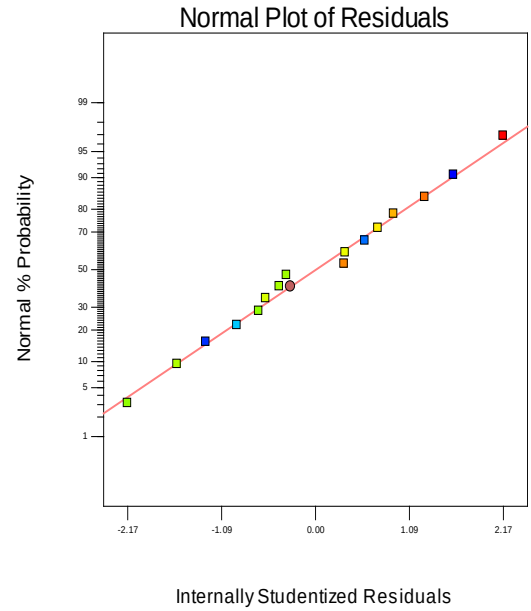

Figure.1 Normal plot of residuals

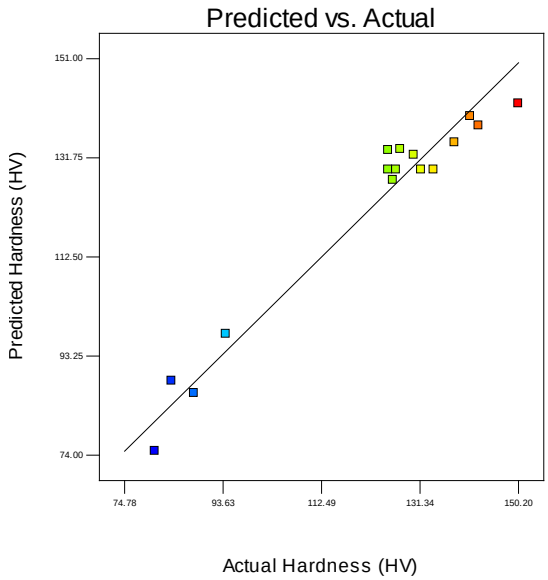

Figure.2 Predicted versus actual hardness plot

Main effects of variables against hardness were given on Figure.3 (a), (b), and (c). From these plots hardness highly effected by temperature, We can obtain highest hardness value at 182 °C (Fig.3(a)), increasing the aging time have a deleterious effect on hardness (Fig.3 (b)), increasing the amount of cold deformation to 20% the hardness have the lowest value, but increasing the amount of cold work has a favorable effect to hardness. All of these findings are quite fitting with experimental results. The highest hardness value of 150.2 Hv was obtained experimentally at 200° C, 2 hours of aging time, and a cold work rate of 0%. Increasing the amount

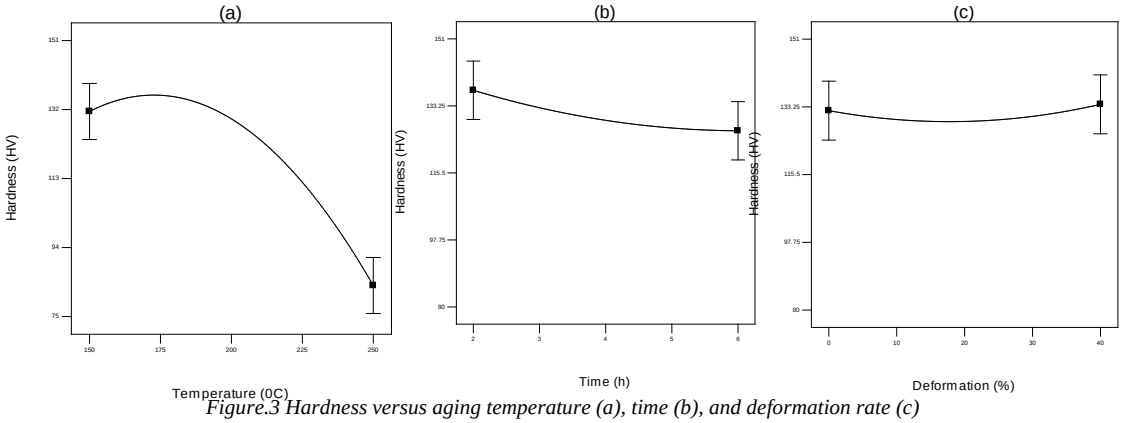

Figure.3 Hardness versus aging temperature (a), time (b), and deformation rate (c)

of cold work have no significant effect on hardness, the calculated model gives the temperature of 182 °C, 2 hours of aging time and no cold work necessary. Increasing the time and temperature have deleterious effect of aging. Increase in the hardness value occurs as the result of the second phase precipitations that occur during the process of aging performed on the AA7075 Al-Zn-Mg alloys. The sequential structure that occurs during the aging heat treatments is as follows; super saturated solid solution → GP zones → η'(MgZn2) → η(MgZn2) [6,7]. The Guinier-Preston (GP) zones that have low interfacial energies and therefore can be produced at lower temperatures are compatible with the matrix and they are round-shaped. It is indicated in some of the previous studies that the material obtain higher strengths because of the heat treatment [8-10].

The interactions of time, and deformation on temperature for 20% deformed samples were given on Figure.4 (a), (b), and (c)

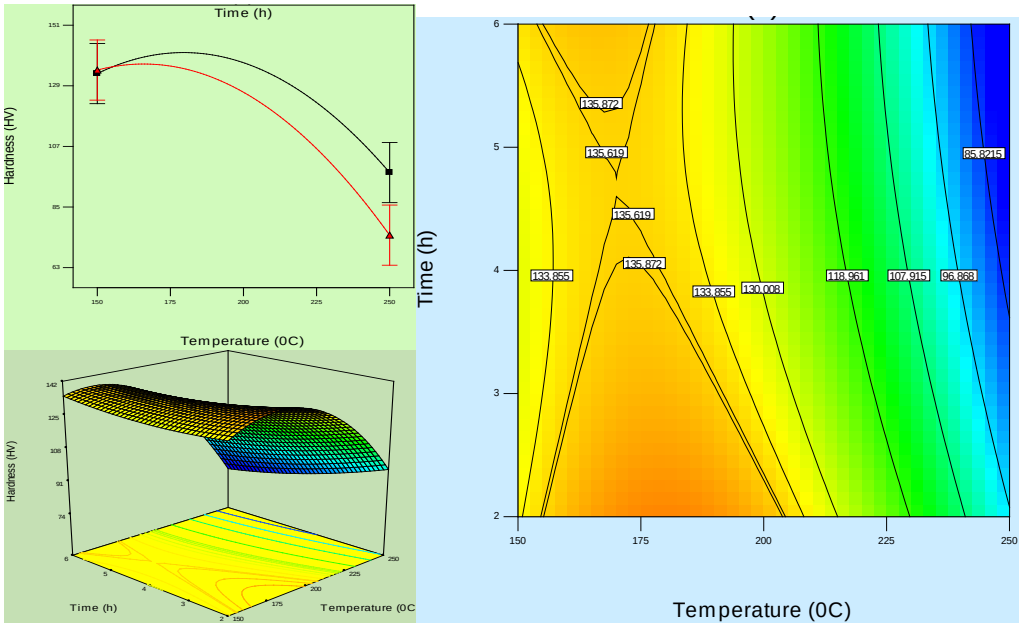

Figure 4. The surface response plot for the interactions of aging time and temperature hardness vs temperature (a), 3D surface plot of hardness, time and temperature (b), isopleth of time and temperature (c)

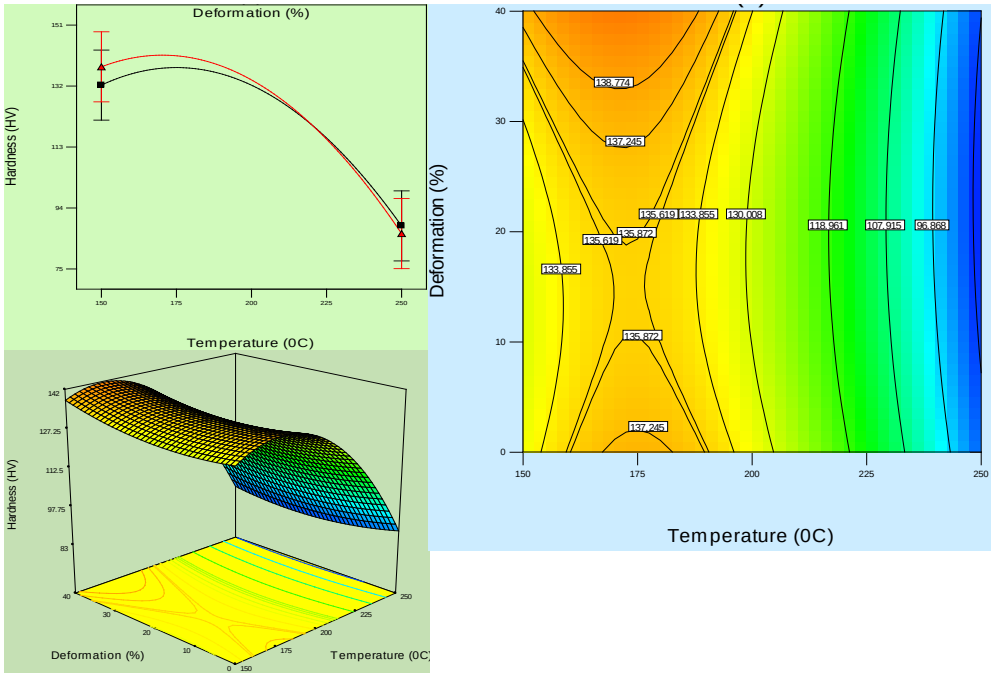

Figure 5. The surface response plot for the interactions of aging time and temperature hardness vs temperature (a), 3D surface plot of hardness, time and temperature (b), isopleth of deformation and temperature (c)

The optimization results found by Box-Behnken method were given in Table.4 and 5

Table 4. Optimization Goals for Optimization

Name	Goal	Lower Limit	Upper Limit
Temperature (^{0}C)	is in range	150	250
Time (hour)	is in range	2	6
Deformation (%)	is in range	0	40
Harndess (HV)	maximize	80.6	150.2
Name	Goal	Lower Limit	Upper Limit

Table 5. Optimization Results found by Box-Behnken Method

Optimization No	Temperature (^{0}C)	Time (hour)	Deformation (%)	Hardness (HV)	Desirability
1	**182**	**2**	**0**	**145.185**	**0.928**
2	182	2	0	145.183	0.928
3	181	2	0	145.182	0.928
4	181	2	0	145.169	0.928
5	180	2	0	145.155	0.928
6	179	2	0	145.117	0.927
7	181	2	1	144.923	0.924
8	163	6	40	144.886	0.924
9	167	6	40	144.804	0.922
10	164	6	40	144.653	0.920
11	177	2	40	144.345	0.916
12	177	2	40	144.343	0.916
13	176	2	40	144.331	0.916
14	177	2	40	144.221	0.914
15	188	2	40	143.348	0.902
16	168	5	40	143.271	0.900
17	183	2	14	141.388	0.873
18	189	2	33	141.282	0.872
19	168	6	0	136.317	0.801

5. CONCLUSIONS

From the Box Behnken Design and ANOVA studies optimum hardness value found to be 145 Hv This value can be obtained by without any cold work, but we need a temperature of 182 ºC, and an aging time of 2 hours.

In our study 200 ºC, and 2 hours of aging time revealed hardness value of 150.2 Hv.

The optimization problem solution was found to be within 95.65% reliability, thus it can be said that the design of experiment and reliability analysis is reliable and applicable.

REFERENCES

[1] Alan G. Leacock, Conrad Howe, Desmond Brown, Odd-Geir Lademo, and Alan Deering, Evolution of mechanical properties in a 7075 Al-alloy subject to natural ageing, J.of Materials and Design 49 (2013) 160–167,

[2] LI Jin-feng, PENG Zhuo-wei, LI Chao-xing, JIA Zhi-qiang, CHEN Wen-jing, and ZHENG Zi-qiao, Mechanical properties, corrosion behaviors and microstructures of 7075 aluminium alloy with various aging treatments, Trans. Nonferrous Met. Soc. China, Vol.18, (2008), 755-762

[3] Sushanta Kumar Panigrahi, and R. Jayaganthan, Effect of ageing on microstructure and mechanical properties of bulk, cryorolled, and room temperature rolled Al 7075 alloy, Journal of Alloys and Compounds 509 (2011) 9609– 9616

[4] S.B.Pankade, D.S.Khedekar, and C.L.Gogte, Procedia Manufacturing 20 (2018) 53–58

[5] Xiu-liang ZOU, Hong YAN, and Xiao-hui CHEN, Evolution of second phases and mechanical properties of 7075 Al alloy processed by solution heat treatment, Trans. Nonferrous Met. Soc. China 27(2017) 2146−2155

[6] A.Somoza, and A.Dupasquier, Positron studies of solute aggregation in age-hardenable aluminum alloys. J. Mater. Process Tech.,Vol.135(2003) 83-90.

[7] G.Waterloo G, V.Hansen, J.Gjonnes, and SR Skjervold, Effect of predeformation and preaging at room temperature in Al-Zn-Mg-(Cu,Zr) alloys. Mat. Sci. Eng. A., Vol.303(2001): 226-233

[8] J.Gjonnes, C.J.Simensen, An electron microscope investigation of the microstructure in an aluminium–zinc-magnesium alloy. Acta Metall. Sin., Vol.18 (1970): 881-890

[9] K. Chen K, L.Huang,Effect of high-temperature pre-precipitation on microstructure and properties of 7055 aluminum alloy. T. Nonferr.Metal Soc. J., Vol.13(4)(2003): 750-754.

[10] L.Huang, K.Chen, S.Li, M.Song, Influence of high-temperature pre-precipitation on local corrosion behaviors of Al-Zn-Mg alloy. Scripta Mater., Vol.56(4)(2007): 305-308.

ICENS 4TH INTERNATIONAL CONFERENCE ON ENGINEERING AND NATURAL SCIENCE
2-6 May 2018 KIEV UKRAINE

Resistance Spot Welding Of Fe3Al Alloy

Osman Torun[1], Alptug Senses[2], Ibrahim Çelikyurek[2]

Abstract

In this study, the alloy Fe-28Al was prepared with vacuum arc melting under an argon atmosphere from iron and aluminum with 99.99 wt.% and 99.7 wt.% purity, respectively. The samples were heated to 700 ◦C and rolled. Rolled samples were prepared 10 mm in width and 30 mm in length. The resistance spot welding experiments were carried out by a resistance spot welding machine at different welding times under a welding current of 3 kA. After welding, the microstructures of welding interfaces of the welded samples were examined with optical microscopy. The optical microscopy investigations were revealed that the welding interfaces of the welded samples have smooth morphology without any crack or pore. Tension test of the welded samples was performed out in the universal tension-compression testing machine to determine weld strength. The hardness values were measured from the center of the welding interface to both sides.

Keywords: Resistance spot welding, Fe_3Al, Tension test

1. INTRODUCTION

Electrical resistance spot welding is a modern welding method commonly used in industry. It is one of the earliest electric welding methods in use by industry. The weld is made by a combination of heat, pressure, and time. It is the resistance of the material to be welded to current flow that causes a localized heating in the part. The pressure is applied by the tongs and tips. In resistance spot welding; current flow time, materials thickness, the ration of current, cross-sectional area, and contact surfaces of the welding tips are important factors affecting the quality of weld joint [1,2]. Spot welding is one form of resistance welding, which is a method of welding two or more metal sheets together without using any filler material by applying pressure and heat to the area to be welded. The process is used for joining sheet materials and uses copper alloy electrodes to apply pressure and convey the electrical current through the work pieces. In all forms of resistance welding, the parts are locally heated. In automotive industry, weight reduction is strongly demanded for energy and natural resource savings. Resistance spot welding is a widely used and important welding process in automotive body construction because of its low cost, easy automation, minimum skill requirements, and robustness to part tolerance variations [3]. Electrical resistance spot welding is widely used in iron, steel, aluminum alloys, magnesium alloys, titanium alloys, and aluminum-iron [4-6]. Fe_3Al and FeAl-based alloys are excellent candidates for use at high temperatures as structural materials due to oxidation and sulfurization resistance at low temperatures, low cost and low density [7-9].

Previous works on welding of these alloys have focused on TIG welding and beam welding methods. In these studies, crack sensitivity was observed due to the alloy composition of the Fe3Al alloy. It has been found that good weldability is observed in Cr, Nb, and C alloyed alloys, while B and Zr addition cause hot cracking [10, 11]. Recently, Ma and colleagues examined the influence of the B2 / DO3 transformation on the weldability and performance of the Fe3Al alloy. Kratochvil et al. observed the weldability of the hardened Fe3Al alloys. Torun and colleagues have investigated the weldability of Fe_3Al alloys with diffusion welding and friction welding and have achieved successful results [12-16].

[1] *Corresponding author: Afyon Kocatepe University, Department of Mechatronics Engineering, Afyonkarahisar, Turkey.* otorun@aku.edu.tr

[2] *Eskisehir Osmangazi Üniversity, Department of Metallurgical and Materials, Eskisehir*

2. EXPERIMENTAL STUDIES

The Fe-28 Al alloy was produced under an Ar gas atmosphere in a vacuum arc furnace using 99.97% and 99.9% pure iron and aluminum, respectively. The materials prepared according to the composition of the alloy were melted in a water-cooled copper crucible and poured into sand mold. The samples were homogenized at 1100 C for 96 h and cooled in furnace. The samples rolled at 650 C. And then Fe_3Al samples for welding were prepared in dimensions of 30x10x1 mm. During the welding process, a mold is prepared to prevent the overlapped plates from slipping off the axis. Welding operations were carried out in a water-cooled and pneumatically controlled point resistance welding machine. The samples were welded for 10, 20, 30 cycles at 3 kA welding current. Four welding operations were performed for each parameter. In the middle of a core for metallographic investigation cut and baked. The surfaces of the welded samples were ground with 1200 grinding paper and polished 1 mm diamond paste then the samples were etched with a mixture of H2O (30 ml) , HNO3 (30 ml), HCl (20 ml) and HF (20 ml). The microstructures of the samples were examined with optical microscope. Microhardness values of the welded samples were measured by means of Vickers indenter with a load of 100 g. Pull-Shear tests were performed to determine the strength of the weld interface using an electromechanical universal test machine (Shimadzu AG-IS-250) at room temperature (Figure 1).

Figure 1. Illustration of pull shear test

3. RESULT AND DISCUSSION

The micrographs of the samples for three different times are shown in fig 2. It was obvious that there was a nugget zone for all the welding times. New grains formed at the interface of the welded samples, these regions were very different from the original microstructure and the grains to the heat center right direction. The heat input increased with the increase of the welded time, which increased the nugget zone size.

The hardness tests were applied to all of the welded samples to determine the change in hardness. The hardness scans in the welded specimens were measured parallel direction to the nugget zone. The effect of welding time

on hardness of welded joints was examined. significant change in the hardness values measured from the welded samples was no observed.

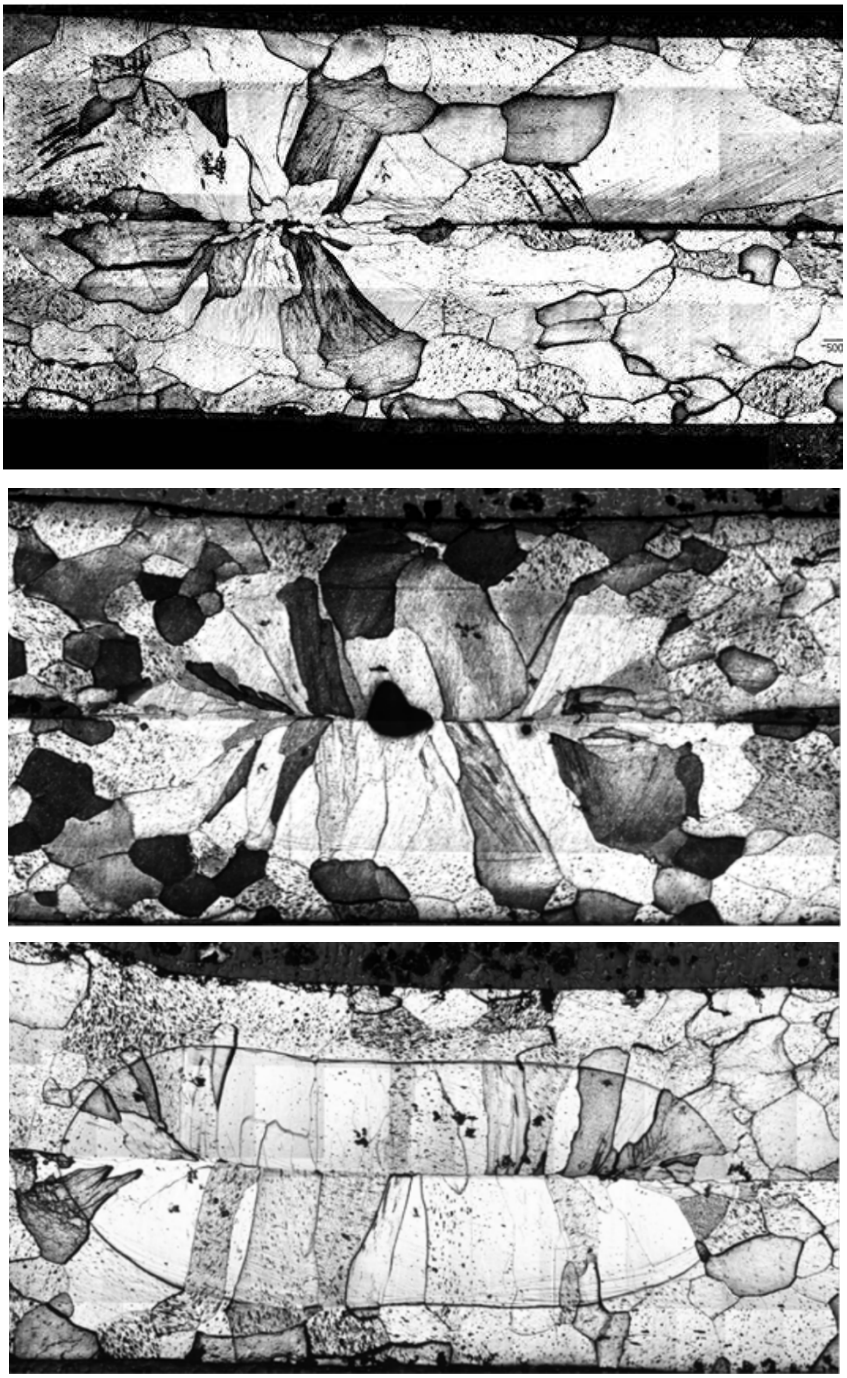

Figure 2. Welded samples a) 10 cycle b) 20 cycle c) 30 cycle

The shear forces of the welds are shown in fig. 3. Test results demonstrate that the shear strength values of the welds are increased with increasing welding time. This observation indicates that the increase in the shear strength is related to the magnitude of the accumulated heat input, which depends on the friction time. The magnitude of the accumulated heat input is increased with increasing welding time and the larger nugget zone formed. This leads to better bonding.

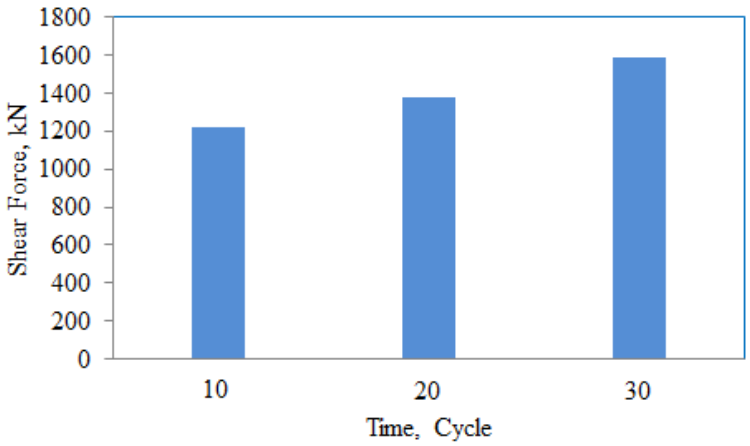

Figure 3. The shear forces of the welds

4. CONCLUSIONS

In this study, the resistance spot welding of the Fe3Al alloy were carried out successively. The micrographs clearly indicate a sound welding at the weld region which is free from crack. Microstructure studies revealed that the nugget zone formed and the nugget zone is greater increasing with welding time. The shear forces of the welds are dependent of the process time. The shear strength values of the welds are increased with increasing welding time. The highest shear force was found as 1586 kN at welded sample for 30 cycle.

ACKNOWLEDGMENT

This study is supported by TUBITAK with project no 117M831

REFERENCES

[1]. Safety and health fact sheet no. 21, American Welding Society, 1999
[2]. S. Aslanlar, "The Effect of Nucleus Size on Mechanical Properties in Electrical Resistance Spot Welding of Sheets Used in Automotive Industry", *Mater. Des.*, vol 27, p 125–131, 2006.
[3]. R. Qiu, H. Shi, H. Yu, K. Zhang, Y. Tu, and S. Satonaka, "Effects of Electrode Force on the Characteristic of Magnesium Alloy Joint Welded by Resistance Spot Welding with Cover Plates", *Mater. Manuf. Process.*, vol 25(11), p 1304–1308, 2010.
[4]. R. Qiu, C. Iwamoto, S. Satonaka, "Interfacial microstructure and strength of steel/ aluminum alloy joints welded by resistance spot welding with cover plate". *J Mater Process Technol.*, vol 209, p 4186–4193, 2009.
[5]. N. Kahraman, "The influence of welding parameters on the joint strength of resistance spot-welded titanium sheets". *Mater Des.* vol 28, p 420–427, 2007.
[6]. L. Han, M. Thornton, M. Shergold, "A comparison of the mechanical behavior of self-piercing riveted and resistance spot welded aluminum sheets for the automotive industry". *Mater Des*., vol 31, 1457–1467, 2010.
[7]. CT. Liu, J. Stringer, JN. Mundy, LL. Horton, P. Angelini, **"**Ordered intermetallic alloys: an assessment" *Intermetallics*, vol 5, p 579-596, 1997.
[8]. SC. Deevi, RW. Swindeman, "Yielding, hardening and creep behavior of iron aluminides" *Mater Sci Eng.*, vol A258, p 203-210, 1998.

[9]. N.S. Stoloff, C.T. Liu, SC. Deevi, "Emerging applications of Intermetallics", *Intermetallics*, vol 16, p 1313-1320. 2000.
[10]. ML. Santella In: SC. Deeevi, VS. Sikka, PJ. Maziasz, RW Cahn, editors. Proceedings of materialsWeek'96 on nickel and iron aluminides: processing, properties, and applications, Ohio, 7-9 October. USA: ASM International; p 321-323. 1997.
[11]. SA. David, T. Zacharia, "Weldability of Fe3AI-Type Aluminide" *Weld J.*, vol 72, p 201-207. 1993.
[12]. H. Ma, Y. Li, SA. Gerasimov, J.Wang, W Sun, "Investigation of transformation models of B2 → DO_3 ordered structures for Fe_3Al intermetallic under welding condition" *Mater Lett*., vol 62, p 1953-1956, 2008.
[13]. P. Kratochvil, H. Neumann, "Welds of Fe_3Al-type alloy with hardened structure". *Intermetallics*, vol 17, p 378-380, 2009.
[14]. O. Torun, R. Gurler, I. Çelikyurek, B. Baksan, "Diffusion bonding of iron aluminide Fe72Al28 using a pure iron" *Intermetallics*, vol 13, p 801–804, 2005.
[15]. O. Torun I., Çelikyurek, R.Gurler, "Diffusion bonding of iron aluminide Fe72Al28 using a copper interlayer" *Materials Characterizations*, vol 59, p 852-856, 2008.
[16]. O. Torun I., Çelikyurek, B. Baksan, "Microstructure and strength of friction-welded Fe–28Al and 316 L stainless steel" *Materials Science and Engineering A* , vol 528, p 8530– 8536, 2011.

ICENS 4TH INTERNATIONAL CONFERENCE ON ENGINEERING AND NATURAL SCIENCE
2-6 May 2018 KIEV UKRAINE

Lateral and Longitudinal Dynamics Control of a Fixed Wing UAV by using PID Controller

Saban Ulus[1], Ikbal Eski[2]

Abstract

Unmanned aerial vehicles (UAV) are taking more attention in both civilian and army applications in the world. One of the most important thing in UAV applications is to make an autonomous, fast and stable control of a UAV. In this study, one of the fixed wing UAV model (Ultrastick -25e) is analyzed and aerodynamic parameter coefficients of the UAV model which needed for dynamic equations are acquired from literature. For that reason, firstly, as a classical control techniques of a fixed wing UAV, PID controller is applied and transfer functions of different state variables are derived by using state-space model. PID gains of state variables according to different control inputs are obtained by using Matlab tuning and Ziegler-Nichols methods. Optimum PID gains, rise time, settling time, peak overshoots of the roll, pitch and yaw dynamics are obtained. Future studies will give a chance to compare classical PID controller results and modern control techniques in terms of altitude, roll and heading angle controller of the UAV model.

Keywords: Fixed wing, PID controller, unmanned aerial vehicle, Ziegler-Nichols.

1. INTRODUCTION

UAVs are commonly known as drone or remote-control aircraft and they have been very popular for both academic and practical applications during past few decades because of their mobility, cost and application areas. UAVs are especially used in army applications such as reconnaissance and surveillance and armed UAV applications and also they have a safe and low cost operation in terms of pilot needs [1], [2]. In addition to that, UAVs have different types and sizes according to their subtask such as mapping, crop monitoring and spraying pesticide in agriculture, photography, cargo transport etc.

According to their mission and capacity, different types of UAVs can be used, and UAVs are classified in to two groups like fixed-wing and multi-rotor applications. They have different advantages and some disadvantages according to their subtask. Fixed-wing UAVs are mostly chosen for high speed and heavy payload applications but not capable to stay in a position while rotary wings have capability to stay in a stationary position. Multi-rotor aircrafts are not suited to lift heavy payload. Many studies are investigated in this part to understand UAV types and missions [3], [4], [5].

The main objective of this research is to design an optimum PID controller and compare PID parameter setting techniques for UAV which will be used in real time applications. The UAV is a fixed-wing aircraft and it will be used in agricultural areas such as crop monitoring, spraying etc. To achieve an effective flight, it is needed to develop an autonomous system to process multiple functions at the same time, in an effective and stable manner [6], [7], [8]. In addition, it is necessary to develop stable and fast system under different conditions and even when there is no connection between UAV and ground station [9]. In UAV applications, autopilots need PID controller by implementing proportional, integral and derivative (P, I, D) terms. To have a stability of the flight, PID parameters must be chosen well suited to the system dynamics. [10].

In this study, it is chosen a UAV model which is called “Ultra-stick 25e” from the previous studies in Minnesota University UAV research group. All system parameters and sizes are obtained according to chosen UAV model. The UAV model has a rudder, aileron, elevator control surfaces and an electric motor to drive propeller.

[1] *Corresponding author: Erciyes University, Mechatronics Engineering Department, 38039, Melikgazi/KAYSERI, TURKEY.* sabanulus@erciyes.edu.tr

[2] *Erciyes University, Mechatronics Engineering Department, 38039, Melikgazi/KAYSERI, TURKEY.* ikbal@erciyes.edu.tr

2. SPECIFICATONS OF THE UAV MODEL

The Ultrastick-25e UAV model is chosen to design a PID controller and its' aerodynamic characteristics and specifications are used in this study. The UAV model has fixed wing and its wingspan is 1.2 m and its weight is 1.9 kg. Table 1 represents some properties of the given UAV model and Figure 1 shows the aircraft axis and control surfaces [11].

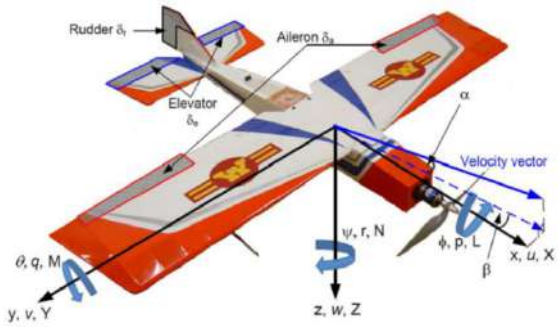

Figure 1. Ultrastick 25e UAV platform [11]

Table 1. Specifications of the given UAV model

Parameter	Definition	Value
S	Wing reference area	0.32 m^2
b	Wing span	1.27 m
$\bar{c}$	Wing Chord	0.25 m
m	Gross weight	1.9 kg
I_x	Roll moment of inertia	0.0894 $kg.m^2$
I_y	Pitch moment of inertia	0.144 $kg.m^2$
I_z	Yaw moment of inertia	0.162 $kg.m^2$
I_{xz}	Product of inertia	0.014 $kg.m^2$

- ***Longitudinal and Lateral Aircraft Equations of Motions***

The main purpose of obtaining aircraft equations of motion is to define and model system dynamics which reflect the real time applications. Aircraft equations are based on Newton laws and obtained from Nelson [12]. Equations in (1) determine the aircraft equations of motion. The subscripts a, g, c, p, d in eq. (1) mean as aerodynamics, gravitational, control surfaces, thrust and atmospheric disturbance effects respectively.

$$m.(\overset{g}{u}+qw-rv)=X_a+X_g+X_c+X_p+X_d$$

$$m.(\overset{g}{v}+ru-pw)=Y_a+Y_g+Y_c+Y_p+Y_d$$

$$m.(\overset{g}{w}-qu+pv)=Z_a+Z_g+Z_c+Z_p+Z_d$$

$$L=I_x.\overset{g}{p}-(I_y-I_z)qr-I_{xz}(pq+\overset{g}{r})=L_a+L_g+L_c+L_p+L_d \quad (1)$$

$$M=I_y.\overset{g}{q}+(I_x-I_z)pr+I_{xz}(p^2-r^2)=M_a+M_g+M_c+M_p+M_d$$

$$N=I_z.\overset{g}{r}+(I_x-I_z)pq+I_{xz}(qr-\overset{g}{p})=N_a+N_g+N_c+N_p+N_d$$

X, Y, Z indicate force equations and L, M, N define the roll, pitch and yaw moments respectively. I is the inertial moment in the x, y, z axis and m is the gross weight of the UAV. Velocity components are u, a, v in the x, y, z axis.

- ***State Space Representations of the UAV Model***

In this part, longitudinal and lateral state space (ss) models are obtained according to given aircraft equations of motion in 1 and UAV motion is analyzed by separating equations of motion in to two parts as longitudinal and lateral state space model. State space models are needed to develop transfer functions of each state variables and control inputs. By using state space models all transfer functions are obtained under different conditions such as different velocities (40 km/h, 60km/h etc.). In this study, 40 km/h airspeed is investigated. In equation (2), longitudinal state space model equation is given. Gust disturbance is not considered for state space model in this study.

$$\begin{bmatrix}\Delta\dot{u}\\ \Delta\dot{w}\\ \Delta\dot{q}\\ \Delta\dot{\theta}\\ \Delta\dot{h}\end{bmatrix}=\begin{bmatrix}X_u & X_w & 0 & -g & 0\\ Z_u & Z_w & u_0 & 0 & 0\\ M_u+M_wZ_u & M_w+M_wZ_w & M_q+M_wu_0 & 0 & 0\\ 0 & 0 & 1 & 0 & 0\\ -\sin(\Theta_0) & -\cos(\Theta_0) & 0 & -u0*\cos(\Theta_0) & 0\end{bmatrix}\begin{bmatrix}\Delta u\\ \Delta w\\ \Delta q\\ \Delta\theta\\ \Delta h\end{bmatrix}+\begin{bmatrix}X_\delta & X_{\delta_T}\\ Z_\delta & Z_{\delta_T}\\ M_\delta+M_wZ_\delta & M_{\delta_T}+M_wZ_{\delta_T}\\ 0 & 0\\ 0 & 0\end{bmatrix}\begin{bmatrix}\Delta\delta_e\\ \Delta\delta_T\end{bmatrix} \quad (2)$$

Equation (3) defines the lateral state space model of a UAV. The variables in the matrix frames can be derived from different resources and detailed formulas are obtained from Nelson [13].

$$\begin{bmatrix}\Delta\dot{v}\\ \Delta\dot{p}\\ \Delta\dot{r}\\ \Delta\dot{\phi}\\ \Delta\dot{\psi}\end{bmatrix}=\begin{bmatrix}Y_v & Y_p & -(u_0-Y_r) & -g.\cos\theta_0 & 0\\ L_v & L_p & L_r & 0 & 0\\ N_v & N_p & N_r & 0 & 0\\ 0 & 0 & 1 & 0 & 0\\ 0 & 0 & \sec(\Theta_0) & 0 & 0\end{bmatrix}\begin{bmatrix}\Delta v\\ \Delta p\\ \Delta r\\ \Delta\phi\\ \Delta\psi\end{bmatrix}+\begin{bmatrix}0 & Y_{\delta_r}\\ L_{\delta_a} & L_{\delta_r}\\ N_{\delta_a} & N_{\delta_r}\\ 0 & 0\\ 0 & 0\end{bmatrix}\begin{bmatrix}\Delta\delta_a\\ \Delta\delta_r\end{bmatrix} \quad (3)$$

According to given eqs. above, for 40 km/h flight speed, calculated state space models for both longitudinal and lateral dynamics are obtained and shown in Fig. 2. A_long indicates longitudinal state variables while A_lat indicates lateral state variables. B matrix defines control input matrix in Fig. 2.

A_long =

-0.1492	0.1490	0	-9.81	0
-0.5272	-5.2988	11.1100	0	0
2.6669	-3.3818	-32.9054	0	0
0	0	1.0	0	0
-0.0523	-0.9986	0	-11.0948	0

B_long =

8.4872	0
0	-1.6553
0.2546	-49.7923
0	0
0	0

A_lat =

-0.9512	0	-1.0000	0.8830	0
-12.0240	-7.4665	5.8687	0	0
5.0421	-1.9428	-6.6032	0	0
0	1.0	0	0	0
0	0	1.0	0	0

B_lat =

0	0.2189
21.6477	4.4873
-0.2506	-5.7111
0	0
0	0

Figure 2. Longitudinal and Lateral State Space Values

All the transfer functions are extracted by using MATLAB toolbox from given ss models. Some of the transfer functions are listed below according to different control inputs such as throttle, elevator, aileron and rudder. It is obtained totally 20 transfer functions from each state variables and control inputs for longitudinal and lateral motion but just a few of the transfer functions are presented below. Subscripts t, e, a, r indicates throttle, elevator, aileron and rudder respectively.

3.PID CONTROLLER DESIGN

PID controller structure consists of proportional, integral, derivative (P, I, D) respectively. PID structure has a general use in UAV applications to achieve autonomous and stable flight by using feedback control algorithm. To achieve a stable and fast response at the flight conditions, PID parameters must be set very well and appropriate to system dynamics conditions. For that reason, in this study, MATLAB tune algorithm and Ziegler-Nichols (ZN) methods are applied to set up the optimum PID parameters. Both methods are compared and analyzed.

3.1.PID Controller Structure

The general PID feedback controller structure of the UAV is shown in Fig. 3. In this study, PI, PD, PID algorithms are evaluated to compare results and it is checked which control algorithm was more suitable for each transfer functions.

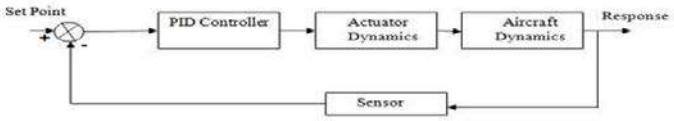

Figure 3. PID feedback controller structure of the UAV

Optimum PID results are investigated according to ZN setting and MATLAB tune methods. Ideal MATLAB tuning structure is depicted in Fig. 4. ZN method can also be called as continuous cycling method or ultimate gain tuning method. The gain is gradually reduced or increased until the system response oscillates continuously. A main design criteria is the decay of oscillation to 1/4 of its initial value.

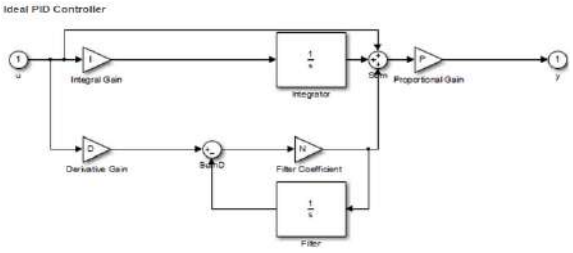

Figure 4. Ideal PID controller structure for Matlab Tuning

4.RESULTS

In this section, MATLAB Tuning and ZN setting results for PID controller structure are presented. First, all transfer functions are evaluated in terms of MATLAB tuning algorithm. Step input is applied to each control inputs of throttle, elevator, aileron and rudder. After obtaining tuning results, ZN method is applied to PI, PD, PID controller structure to compare and choose best results for transfer functions. Results are presented in figures below and PID responses of the two methods are given in Table 2 and 3. Some of the longitudinal PID results for elevator deflection is given in Fig. 5-6-7-8.

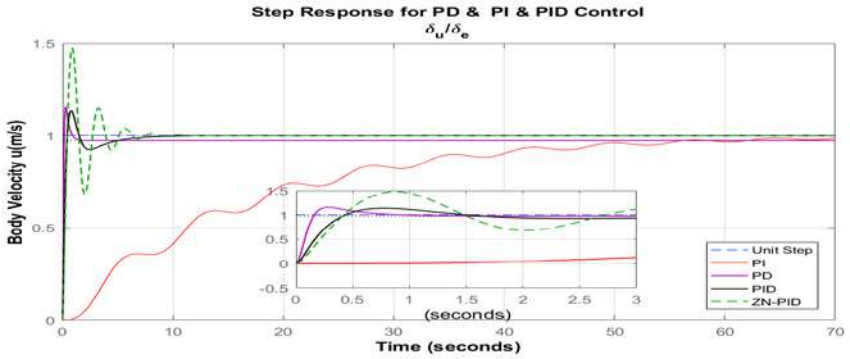

Figure 5. "Matlab Tune – ZN PID" step response for elevator control input and airspeed output

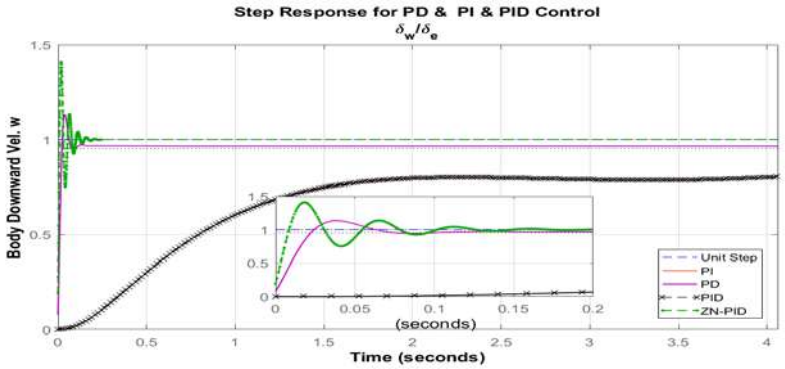

Figure 6. "Matlab Tune – ZN PID" step response for elevator control input and downward speed output

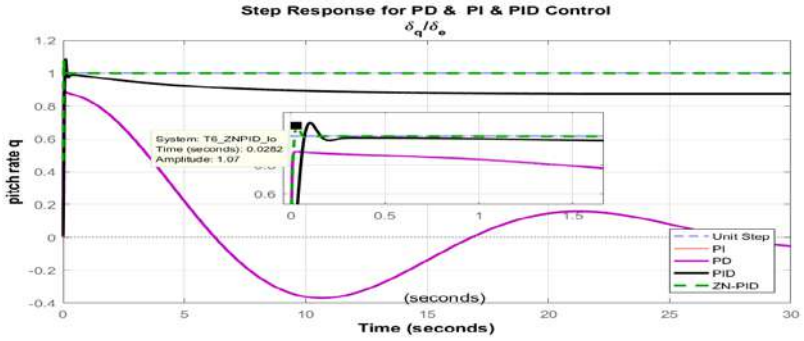

Figure 7. "Matlab Tune – ZN PID" step response for elevator control input and pitch rate output

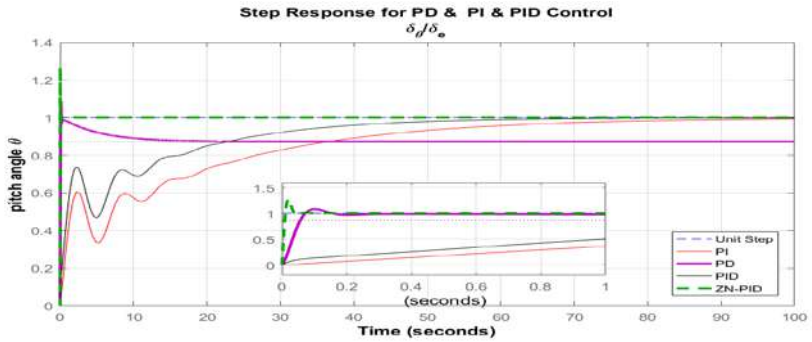

Figure 8. "Matlab Tune – ZN PID" step response for elevator control input and pitch angle output

Figures between 9-12, show some of the lateral PID controller results for both Matlab tuning and ZN setting results.

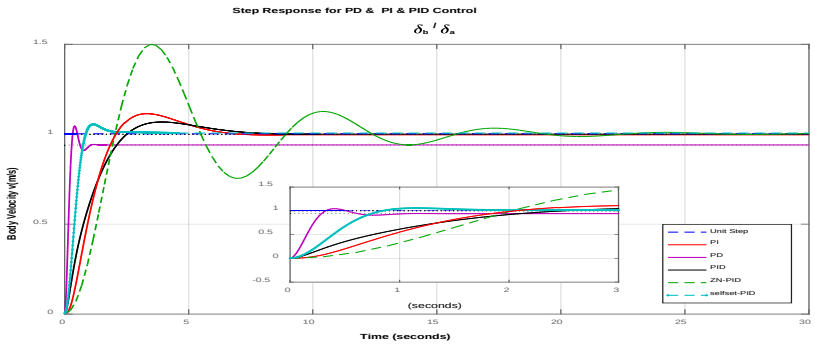

Figure 9. "Matlab Tune – ZN PID" step response for aileron control input and body velocity output

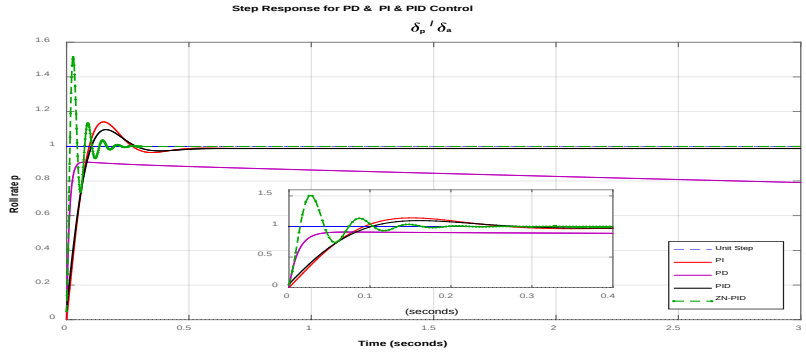

Figure 10. "Matlab Tune – ZN PID" step response for aileron control input and roll rate output

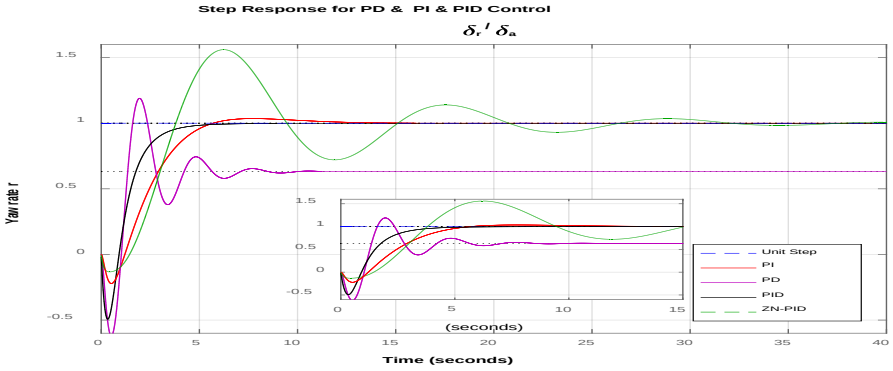

Figure 11. "Matlab Tune – ZN PID" step response for aileron control input and yaw rate output

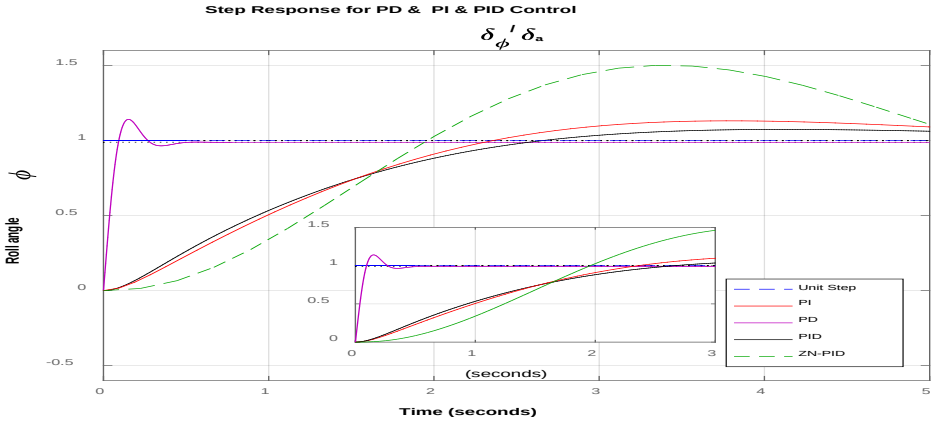

Figure 12. "Matlab Tune – ZN PID" step response for aileron control input and roll angle output

In Table 2, step responses of the longitudinal transfer functions for both Matlab tuning and ZN methods are given. Only elevator (de) control surface is shown as a control input in Table 2.

Table 2. Step Response Results of the Matlab Tune and ZN Settings for Longitudinal Motion

Matlab TUNE	Rise Time	Peak Time (s)	Peak Value	Overshoot (%)	Settling Time	Ziegler Nichols	Rise Time	Peak Time	Peak Value	Overshoot (%)	Settling Time (s)
du/de	0,106	0,285	1,155	18,742	0,748	**du/de PD**	0,298	0,825	1,260	38,014	2,348
du/de	0,304	0,756	1,135	13,541	3,684	**du/de PID**	0,310	0,875	1,475	47,500	4,794
dw/de	5,009	7,969	1,081	8,052	9,208	**dw/de PI**	0,006	0,017	1,770	77,039	0,342
dw/de	0,017	0,038	1,134	19,006	0,064	**dw/de PD**	0,008	0,019	1,147	16,329	0,034
dw/de	5,020	7,987	1,080	8,037	9,211	**dw/de PID**	0,007	0,018	1,409	40,894	0,114
dq/de PI	0,042	0,100	1,088	24,753	5,734	**dq/de PI**	0,008	0,020	1,092	10,603	0,035
dq/de	0,000	0,026	0,892	inf	34,805	**dq/de PD**	1,678	0,052	0,834	inf	36,292

dq/de	0,042	0,101	1,090	24,851	5,764	**dq/de PID**	0,013	0,032	1,075	8,808	0,055
dΘ/de	41,418	123,745	0,998	0,000	56,580	**dΘ/de PI**	0,008	0,023	1,758	75,834	0,230
dΘ/de	0,042	0,100	1,088	24,753	5,734	**dΘ/de PD**	0,008	0,019	1,235	24,613	0,033
dΘ/de	26,215	86,445	0,998	0,000	36,756	**dΘ/de PID**	0,008	0,020	1,266	26,570	0,034

Table 3 represents step responses of the lateral transfer functions. Aileron input (da) is given in Table 3 for both Matlab Tuning and ZN methods.

Table 3. Step Response Results of the Matlab Tune and ZN Settings for Lateral Motion

Matlab TUNE	**Rise Time**	**Peak Time (s)**	**Peak Value**	**Overshoot (%)**	**Settling Time (s)**		**Ziegler Nichols**	**Rise Time**	**Peak Time**	**Peak Value**	**Overshoot (%)**	**Settling Time (s)**
db/da PI	1,375	3,313	1,114	11,401	5,070		**db/da PI**	1,302	3,417	1,503	50,284	14,505
db/da PD	0,195	0,408	1,044	11,072	0,535		**db/da PD**	0,000	0,000	0,000	0,000	0,000
db/da PID	1,730	3,912	1,066	6,629	5,031		**db/da PID**	1,336	3,438	1,496	49,621	14,579
dp/da PI	0,069	0,153	1,141	15,414	0,238		**dp/da PI**	0,045	0,104	1,174	18,114	0,172
dp/da PD	0,000	0,074	0,909	inf	68,463		**dp/da PD**	0,000	0,000	0,000	0,000	0,000
dp/da PID	0,074	0,161	1,096	10,992	0,242		**dp/da PID**	0,054	0,121	1,154	16,057	0,199
dr/da PI	2,965	7,725	1,035	3,515	4,767		**dr/da PI**	1,697	6,158	1,591	59,067	24,172
dr/da PD	0,257	1,950	1,190	88,652	5,300		**dr/da PD**	3,118	9,582	0,234	0,000	4,533
dr/da PID	1,958	8,939	0,998	0,000	3,252		**dr/da PID**	1,824	6,235	1,560	56,038	24,331
dϕ/da PI	1,695	3,769	1,131	13,087	5,782		**dϕ/da PI**	1,278	3,339	1,501	50,074	14,168
dϕ/da PD	0,069	0,153	1,141	15,414	0,238		**dϕ/da PD**	0,000	0,000	0,000	0,000	0,000
dϕ/da PID	1,834	4,108	1,074	7,367	5,485		**dϕ/da PID**	1,279	3,341	1,501	50,059	14,170

4.CONCLUSIONS

In this study, “Ultra-stick 25e” fixed-wing UAV model is chosen to design PID controller structure. The UAV model and its aerodynamic parameters obtained from previous studies to build state space model. 40 km/h airspeed is analyzed for a cruise flight condition and all transfer functions are obtained according to 40 km/h airspeed.

Two different PID parameter setting algorithms like Matlab Tuning and ZN methods are applied to compare results and chose optimum ones. Results show that Matlab Tuning was not capable to reach step response very quickly at some transfer functions. ZN results have less settling time in general even if it has more overshoot.

PID structure has less steady state error even if, PD has a quick response in some cases. It is obvious that both methods have some advantages and disadvantages. ZN methods need more time to catch optimum P, I, D parameters while Matlab Tuning choose parameters automatically. It is seen that for some transfer functions, parameters can be set by using ZN methods even if MATLAB tuning was not successful.

REFERENCES

[1]. Zhang C., Kovacs J.M., “The application of small unmanned aerial systems for precision agriculture: a review”, *Precision Agriculture*, Vol 13.6, pp. 693-712, 2012.

[2]. Psirofonia P., Samaritakis V., Eliopoulos P., Potamitis I., "Use of unmanned aerial vehicles for agricultural applications with emphasis on crop protection: Three novel case-studies" *International Journal of Agricultural Science and Technology*, Vol 5, No.1, pp. 30-39, 2017.
[3]. Zeng Y., Zhang R., Lim T. J., "Wireless Communications with unmanned aerial vehicles: Opportunities and challenges" IEEE Communications Magazine, pp:36-42, 2016.
[4]. Vogeltanz T., "A survey of free software for the design, analysis, modelling and simulation of an unmanned aerial vehicles" *Arch. Computat Methods Eng*., Vol 23, pp. 449-514, 2016.
[5]. Marinello F., Pezzuolo A. Chiumenti A., Sartori L., "Technical analysis of an unmanned aerial vehicles (drones) for agricultural applications" in *Engineering for Rural Development*, Jelgava, pp 870-875, 25-27 May 2016.
[6]. Aliyu B.K., Petinrin A.A., Adewumi J.A., "PID control design of sideslip angle for a fixed-wing mini-UAV" *Advances in Research*, Vol 6(3), pp. 1-14, 2016.
[7]. De Filipps L., Guglieri G., Quagliotti F.B., "A novel approach for trajectory tracking of UAVs", *Aircraft Engineering and Aerospace Technology: An International Journal*, Vol. 86(3), pp.198-206, 2014.
[8]. Fiuzy M., Haddadnia J., Mashhadi S.K.M, "Designing an optimal PID controller for control the plan's height, based on control of autopilot by using evolutionary algorithms", Journal of Mathematics and Computer Science, Vol. 6, pp. 260-271, 2013.
[9]. Ding Y.R., Liu Y.C, Hsiao F.B, "The application of extended Kalman filtering to autonomous formation of small UAV system", Vol. 1(2), pp. 154-186, 2013
[10]. Kada B., Ghazzawi Y., "Robust PID controller design for an UAV flight control system" in Proceedings of the World Congress on Engineering and Computer Science, Vol. 2, WCECS, San Francisco, October 19-21, 2011.
[11]. Paw Y. C., "Synthesis and validation of Flight control for UAV", Doctor of Philosophy, University of Minnesota, December 2009.
[12]. Nelson R. C., *Flight Stability and Automatic Control*, 2nd ed., Mc. Graw Hill International Editions Aerospace Sciences and Tech. series, Singapore, 1998.

ICENS 4TH INTERNATIONAL CONFERENCE ON ENGINEERING AND NATURAL SCIENCE
2-6 May 2018 KIEV UKRAINE

Geosynthetic Material Applications Used In Mining Sector – A Case Of Emet Boron Works

Cem Sensogut[1] , Ali Ucar[2]

Abstract

A large quantity of waste is produced as a result of mineral enrichment processes. Proper storage/disposal of plant wastes are high of importance in control of environmental problems occurring chemically and mineralogically due to heavy metal pollution (HMP) and acid mine drainage (AMD). The resulting residue from mining activities should be stored in specific areas according to their properties. The structures used for this purpose are named as "Waste Dam", "Waste Storage Area" etc. Especially following the mineral preparation processes, the process of ensuring that contaminated waters coming from mine field and rain water leaking into the facility area and the solid and liquid (water, various heavy liquids, chemicals) isolation should be provided in order to prevent their effect to the environment.

For the preparation of the waste dam base, the following considerations should be taken into consideration:

a) preventing possible leakages to groundwater,

b) reducing the pressure at the bottom of the dam and

c) recycling of the wastewater.

It is imperative that a fully secure core dam, which is impervious to all directions and free of leakage from slope, stream bed and body of dam, is required prior to the start of storage. Geosynthetic materials provide better containment performance than or equal to significantly thicker soil-only base or barrier layers. In this work, the application of geosynthetic works took place in the Boron Plant of Emet, Turkey was addressed in detail.

Keywords: Mining, Waste storage dam, Geosynthetics material, Geomembrane

1. INTRODUCTION

Geomembranes are preferred because of their impermeable structure for the storage of waste, especially in mining sector for a long time. Under very difficult environmental conditions, sometimes they are expected to last forever. However, this is not possible due to many reasons such as chemical and ultra violet degradation, re-polymerization under pressure, etc. As with all other materials, it should be mentioned that geomembranes have also a period of life for resistance and planning should be done with this in mind [1].

Geomembranes and geosynthetic clay lining, which have replaced the application of compressed clay lining used in the past, are currently utilized for many purposes in the mining industry. At the beginning of these used areas, land reclamation of open pits, lining of waste dams and restoration of old open pits with completed production etc. may be listed [2].

[1] *Corresponding author: Dumlupinar University, Department of Mining Engineering, 43270, Kutahya, Turkey, cem.sensogut@dpu.edu.tr*

[2] *Dumlupinar University, Department of Mining Engineering, 43270, Kutahya, Turkey, ali.ucar@dpu.edu.tr*

As opposed to many other industries, environmental protection measures in mining must be easy to apply, durable and sustainable [3]. It can be stated that geomembranes have more acceptable properties among others exposed to normal and shear stress under large loads.

Waste dams should be designed considering the characteristics of waste in mines. It is absolutely necessary to ensure the highest degree of impermeability in order to minimize the environmental damage of the chemicals used during the production and the processing of the ore. In terms of application of the impermeability, the composition of the waste, particularly the ground geology and the groundwater resources where the waste is stored should be carefully analyzed [4]. Impermeability is mainly realized by

a) Compressed clay used classically on the base,
b) Geomembrane and
c) Geosynthetic clay liners [5].

Known geomembrane lining materials generally consist of "linear low density polyethylene (LLDPE)", "high density polyethylene (HDPE)", "polyvinyl chloride (PVC)" and "polypropylene (PP)" [6]. Geomembrane lining design usually contains single or double composite systems (Figs 1 and 2).

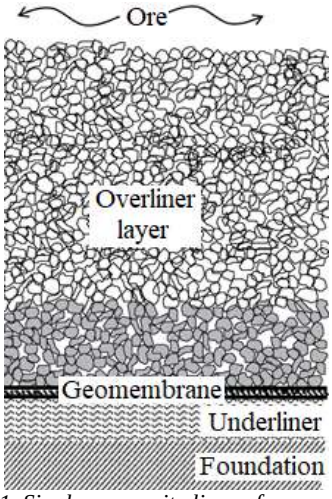

Figure 1. Single composite liner of geomembrane

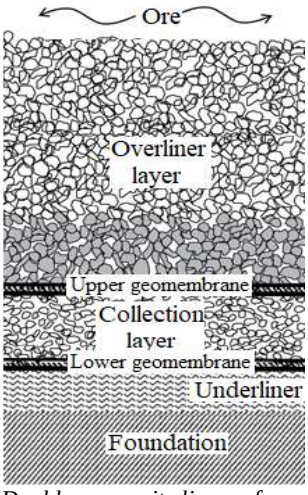

Figure 2. Double composite liners of geomembrane

The use of geosynthetics in mining is summarized in Table 1 [7].

Table 1. Geosynthetics used in mining

Geosynthetics	Field of Use
Geomembrane	Process solution pond liners Heap leach facility liner systems Tailings impoundment liner system Encapsulation of waste rock to mitigate acid mine drainage
Geosynthetic Clay Layer	Encapsulation of waste rock to mitigate acid mine drainage Barrier layer below geomembrane liner
Geotextile	Filter layer for underdrains and collection pipes Cushion layers over geomembrane liners Ground stabilization Erosion control
Geogrid	Ground stabilization Remediation of mine workings
Plastic Pipe	Process solution collection and conveyance Solution recovery Leak detection and monitoring

2. EMET BORON WORKS

The Emet Boron Works (EBW) is located in the town of Emet, southwest and 100 km away from the city center of Kutahya. The Hisarcik open pit and concentrator unit, which are the parts of EBW continues its production at the Hisarcik district, 12 km south of the Directorate of EBW (Figure 3). Espey open pit and concentrator unit continues its activities 4 km north of Emet district. Boric acid plants I, II and the multipurpose boric acid plant are located on the 6th km of Emet-Kutahya highway. The data of the facilities are summarized in Table 1. The capacity of the impervious dam to store the wastes to be generated between 2015 and 2030, which is required by the company together with the last installations, is increased to 4000000 m^3 in Espey.

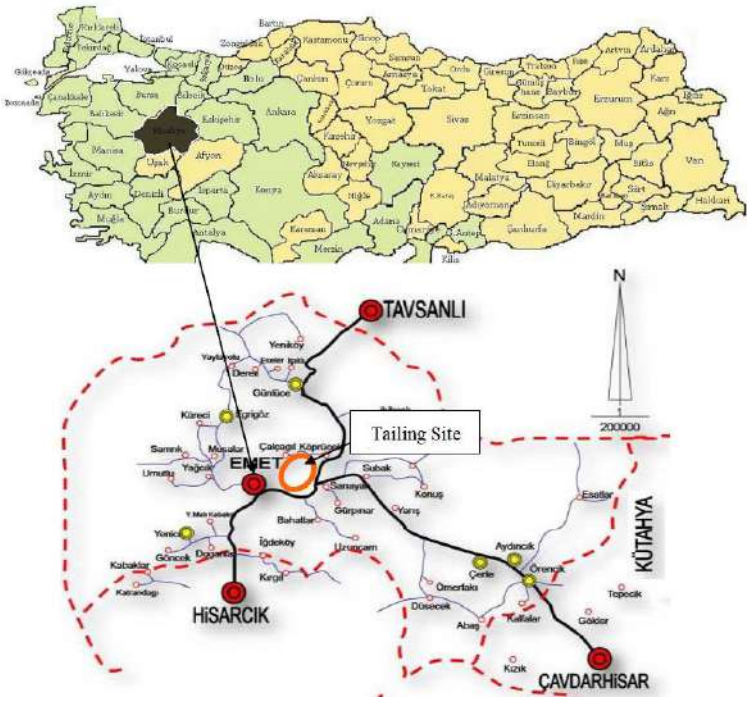

Figure 3 Location Map of Emet Boron Works

Table 1. Emet Boron Facilities

	Espey Concentrator	Hisarcik Concentrator	I. Boric Acid Plant	II.Boric Acid Plant	Multipurpose Boric Acid Plant
Foundation year	1997	1973	2003	2011	2015
Production capacity (ton/year)	300.000	547.500	120.000	120.000	50.00-100.000
Products	Colemanite concentrate	Colemanite concentrate	Boric acid	Boric acid	Boric acid

3. GEOSYNTHETIC APPLICATIONS IN THE TAILING PONDS OF EBW

The followings are the operations performed by the Directorate of the EBW for waste dams that are built for the purpose of storing the wastes released during production without damage to the environment.

In the construction of the impermeable layer formed at the bottom and side surfaces of the storage dams of the mineral wastes, the clay group with a minimum of 50 cm thickness and a maximum permeability of 10^{-9} cm/sec, is laid with at least two layers and moistened under suitable conditions. These layers were reinforced with the use of high density polyethylene (HDPE) geomembrane with a minimum thickness of 1.5 mm and a

permeability of 10^{-10} cm/sec. A geosynthetic clay was also applied to protect the geomembrane. If it is technically difficult to reduce slope inclination due to topographical conditions on the side surfaces and if it is possible to provide stability in steep slopes, instead of clay, geosynthetic clay layer is applied together with high density polyethylene (HDPE) geomembrane. The membrane is protected with a gravel-paved filter cover of 20 cm thickness and a soil-rock filling material is placed on top of it. The elongation on the membrane are determined according to DIN 16726.

Waste areas are illustrated in Figure 4.

Figure 4. Waste areas of Emet Boron Works

4. RESULS AN DISCUSSIONS

The mining industry can cause environmental problems due to its nature. Unless environmental concerns are taken into account both during underground and open pit mining and during the enrichment of produced ores, undesirable consequences can be caused. As a result of underground productions, collapses are formed on earth, large excavation spaces and spoil piles resulting from open pit production will lead to both visual and economic problems. At the same time, the enrichment of the extracted ore will result in serious waste disposal and storage problems. Making scheduled planning of prospective problems and proactive measures to be taken will result in both more economical and environmental approaches.

In the light of the above explanations, the characteristics of the dams where solid and liquid wastes are stored by the processing plants of the Emet Boron Works, one of the major boron production centers in Turkey were mentioned. It can be emphasized that the dams made for the storage of the wastes that will come out for the next 15 years without causing environmental problems are in line with the desired national and international standards.

REFERENCES

[1]. Oboni, F., Oboni, C. & Caldwell, J., 2014, Geosynthetics risk-based design in mining, Proceedings of Geosynthetics Mining Solution, Sept. 8-11, Canada, pp1-13
[2]. Davies, N., 2012, Geosyntethic Clay Liners in Mining Applications, International Mine Water Association 2012 (reproduced from IMWA Proceedings 1999), pp631-635
[3]. Renken, K., Mcchaina, D.M. & Yanful, E.K., 2005, Geosynthetics Research and Applications in the Mining and Mineral Processing Environment, NAGS 2005/GRI 19 Conference, 20p.
[4]. Avci, C.B., Guler, E. & Ozhan, H., 2008, Evaluation of the use of geosynthetic clay layers in mine tailings dams, 3. National Geosynthetics Conference, 13-14 Nov 2008, Bogazici University, Istanbul, pp71-79. (in Turkish)
[5]. US EPA, Office of Solid Waste, 1997, The feasibility of lining ponds.
[6]. Lupo, J.F. & Morrison, K.F., 2007, Geosynthetic Design and Construction Approaches in the Mining Industry, Geotextiles and Geomembranes, Vol. 25, Issue 2, April 2007, pp96-108
[7]. Caldwell, J & Kavazanjian, Ed., 2012, http://technology.informine.com/reviews/geosynthetics/welcome.asp?view=full

ICENS 4TH INTERNATIONAL CONFERENCE ON ENGINEERING AND NATURAL SCIENCE
2-6 May 2018 KIEV UKRAINE

Rock Bit Application Parameters In Geothermal Drilling Works And Cost Analysis

Sedat Toraman[1], Cem Sensogut[2]

Abstract

One of the most important parameters to make the right choice in drilling works are rock bits. The most basic rule is to choose a drill suitable for the possible formation feature. Once the drill has been selected, the drill operating characteristics are also factors that directly affect the performance of the drill as well as the drill cost. In the drilling operation, if the first basic rule is to choose the appropriate drill, the secondary basis is the drill operation conditions; the appropriate weight (WOB-weight on bit), the appropriate spinning speed (RPM-revolution per minute) and the appropriate liquid or air to get the rock pieces out of borehole.

In order to carry out the drilling process, it is essential to get the right weight on the drilling bit inside the borehole. This is achieved either by hydraulic pressure or casing pipes with certain weight. The pressure required in the geothermal drilling machines is mostly provided by the drill collar. In case of lower weight, desired breaking effect cannot be obtained, while with the case of overweight, the more wear is inevitable for the drill bits. Rotation speed is one of the parameters that directly affect drilling bit life and drilling speed. The speed of rotation according to rock drillability is recommended to be 30-40 rev/min for the rocks with low drillability, 60-120 rev/min for the rocks with medium drillability and 70-140 rev/min for the rocks with high drillability. The rotation speed increases the drilling speed, but with it drill bit abrasion will be more. These parameters according to formation strength show variation such as high turn speed and low weight in soft formations and low turn speed and high weight in hard formations.

Their performances differ in drilling bits with the same IADC (International Association of Drilling Contractors) code from different manufacturers. For this purpose, especially in this study, the selection of the rock bits used in the drilling works, the appropriate usage parameters, the performances of the different brand rock bits and the effects on the meter cost of drilling will be given in detail.

Keywords: Drilling rock bits, Selection of rock bits, Parameters for rock bits' application, Cost analysis for rock bits, Geothermal drilling

1. INTRODUCTION

Today, geothermal energy is one of the alternative energy sources that gain importance in order to meet the increasing energy needs. Geothermal energy production is carried out by extracting the high temperature fluids in the depths of the earth's crust to the earth with similar wells to the oil-gas wells. Although equipment and standards and methods used in oil-gas wells are used in geothermal drilling work, it can be said that drilling costs are higher due to the fact that the excavated units are generally more abrasive and especially hotter than the excavated units in the case of oil-gas. The drill bits, which are related to the drilling meter costs are directly related to the amount of advancement, maneuverability, and cleaning of the boreholes from rock pieces in the long term. In order to reduce drilling costs, choosing the right drill bit is important, but not the only factor. The ability of the selected drill bit to work with optimum performance can be achieved with a combination of correct drill load and rotation speed in relation to drillability of the formation, where cracks can be removed smoothly out of the borehole.

[1] *General Directorate of Turkish Coal Board, 06560, Ankara, Turkey.* sedat.toraman@gmail.com

[2] *Corresponding author: Dumlupinar University, Department of Mining Engineering, 43270, Kutahya, Turkey.* cem.sensogut@dpu.edu.tr

2. PARAMETERS FOR ROCK BIT APPLICATION

In drilling works, the rate of penetration is primarily related to drill performance in terms of drilling costs. Drill performance depends on the coordination of some parameters at the optimum level to reduce drilling costs in the long run. The main parameters affecting the optimum performance of the drills are as follows;

- WOB (Weight on bit)- pressure
- RPM (Revolution per minute)- rotation speed
- Removing the rock pieces out of borehole

2.1. *Weight on Bit (WOB) - Pressure*

Within the basic rock mechanics principles, the force that must be applied to break any rock, that is, the load applied by the drill, must be higher than the pressure resistance of the rock. Therefore, a certain degree of weight on bit (WOB) must be applied in order for the drilling to take place. This pressing load is supplied either hydraulically or by weight pipes. If there is not enough pressure on the drill, or if it is given too much, drilling will increase the cost of drilling by reducing the life of the drill due to breakage of the tooth according to the construction of the drill. Between the load to be applied on the drill and the rock fragmentation;

- In case of minimum load on the drill; The cutting bits will be penetrating the formation very little and will only effect chipping instead of breaking.
- If less load is placed on the drill than the optimum load, it cannot perform an effective disintegration and therefore the rotation speed (ROP) remains lower.
- If more load is applied to the drill than optimum load; the cutting bits will be buried in the formation and the drilling speed will be reduced. Drill wear and therefore unit cost will increase.

It can be determined whether the appropriate load is given by monitoring the breaks during drilling. If the cracks are too small and high in dust, the drill is under optimum load while the cracks in the case of medium sized particles, then it indicates a weight close to the optimum weight. When the relationship between the optimum weight (WOB) to be applied on the drill and the speed of advancement is examined, it will not be possible to make more progress, but even more weight applied will increase the wear of the drill bit so that the drill usage time will decrease causing the time spent for changing the drill bit to increase. Factors to consider when applying pressure on the drill can be listed as follows:

- Diameter of rock bit,
- Structural features of rock bit (bearing type etc.) and
- Drillability of formation.

The maximum pressure that a bearing of a drill can receive is around 50-60 tons [1]. As the diameter of the rock bit increases, the strength of the rock bit increases as the cone bearings also grow. The maximum load that can be applied to the drill can be calculated as from Equation (1), and the appropriate drill load can be calculated as the Equation (2) [2].

Maximum drill load (lb) $=810D^2$ (1)

Appropriate drill load (lb) $Wo=Sc*D/5$ (2)

Sc = Uniaxial strength of formation (psi)
D = Diameter of rock bit (inch)

2.2. Rotation Speed (RPM)

In addition to the necessity of pressing force for squashing and crushing, rotation in the drill must be provided in order to make progress. The basic principle in rotary drilling is to bring the drill into a new disintegration position as a result of a disintegration process. Therefore, the rotation speed for the advance of the drill in the borehole is also an important parameter such as the drill load.

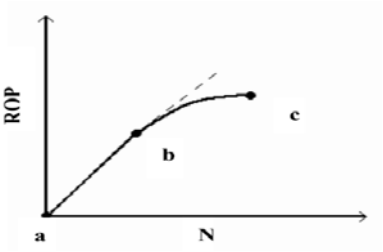

Figure 1. Relationship between rotation speed (RPM) and penetration rate (ROP)

It is recommended that 30-40 rpm is applied in formations with low drillability while 60-120 rpm in formations with medium drillability features, and 70-140 rpm in formations with high drillability [3]. This value can be applied as 200-250 rpm for very soft rocks [4].

When the relation between the rotation speed (RPM) and the rate of penetration (ROP) is examined, the similar result is seen to that of the weight applied on the drill (Figure 1).

2.3. Removing the Rock Pieces out of the Borehole

Removing the cut-offs from the drill bit as soon as possible is one of the important parameters affecting drill performance. It is imperative that the cut-offs be thrown away from the borehole as soon as possible and the drill should be given a new position. Proper fluidization speed and nozzle size selection are essential for the transport of small rock cracks. Drilling mud characteristics that are released to the borehole for transporting the cut-off from the borehole are one of the important parameters affecting the rate of penetration.

The density, rheological and filtration properties, solids content and size and chemical properties of the drilling mud affect the rate of penetration. The increase in drilling mud density, viscosity and solids will reduce the rate of drilling progress. (Figure 2).

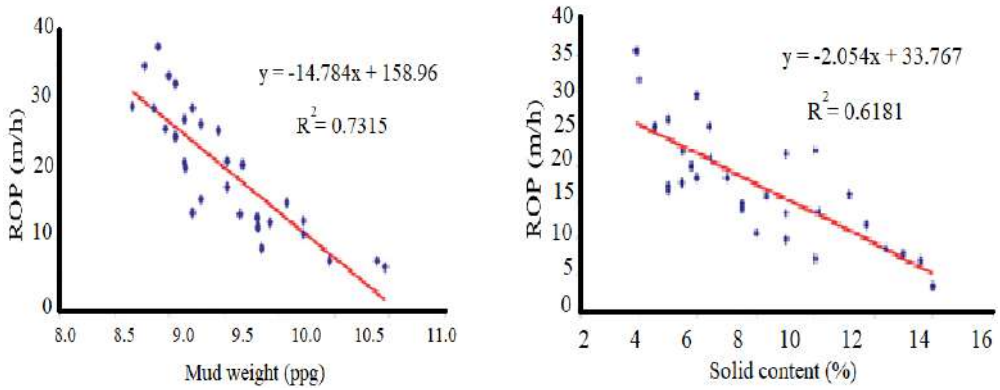

Figure 2. The effect of mud density and solid content on the rate of penetration [5]

2.4. Optimum Drilling Performance

Regardless of the parameters mentioned above, a drilling operation that focuses only on the rate of penetration cannot be carried out within economic limits. For example, in a situation where the particles are adequately moved out of the borehole, the speed of advancement may increase with any increase in pressure or rotation required for penetration, but the rock bit will wear out faster, causing a greater number of maneuvers, thereby significantly increasing drilling costs.

By using drilling fluid or air more effectively, with the correct combination of drill load and rotation speed, a faster rate of penetration can be achieved with less cost. A number of approaches have been presented for such combinations, both theoretically and on the basis of field test results. The most general approach is to select the WOB and RPM values in reverse proportion, depending on the formation (Equation 3). The general rule is to apply high pressure and low rotational speed in difficult drillable and abrasive formations and low pressure and high rotational speed in easy drillable formations [4].

(3)

Here; N: Speed of rotation, S: Strength of formation, WOB: Weight on bit,
Upper indices for equation constants.
It has been found that some parameters such as depth, pressures, and hydraulics are indirectly influential on the feed rate, besides the WOB and RPM which can directly affect the rate of penetration and can be controlled, but due to the difficulties of modeling, these parameters are not considered in many models [6].

2.5. Drill-off Test in the Determination of Rock Bit Application Parameters

There are many scientific methods for determining optimum drill parameters. However, drill-off test is performed by the drilling engineer to determine the appropriate load and rotation speed of the drill after the drill selection for the formation has been performed.

Drill-off test; It is realized to determine the optimum weight (WOB) to be applied and the rotation speed (RPM) required for the maximum feed speed. In Figure 3, an example of drill-off test graph is illustrated. The drill-off test is a test that can be applied to any type of drill and can be completed in a short time. This test should be practiced in the cases of; 1) When a new drill is installed 2) When a different formation is encountered 3) When there is a decrease in the speed of progress.

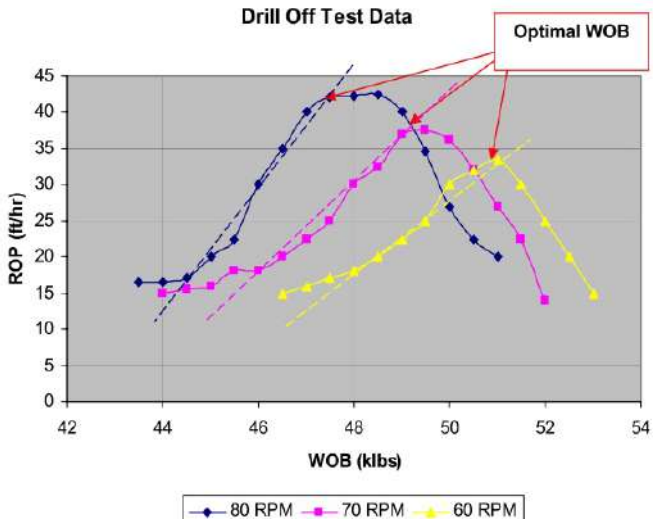

Figure 3. Drill-off Test Graph [7]

Drill -off test steps

- There is a maximum load on the drill.
- Certain weights (40,000 lbs, 45,000 lbs, etc.) are located on the drill by keeping the rotation speed constant and the duration of the drill weight drop (5,000 lbs in the determined weight) is recorded.
- This procedure is continued until the maximum weight that can be supplied is reached. Optimum WOB is the initial weight at which the weight loss is recorded as soon as possible.
- The same test can be repeated at different rotation speeds and the optimum amount of weight to be given on the drill can be determined for different rotation speeds.

3. ROCK BIT SELECTION IN GEOTHERMAL DRILLING

As the uniaxial compressive strength of the formation increases, the drillability becomes more difficult. The appropriate drill selection according to the rock uniaxial compressive strength is as shown in Figure 4 [8]. Geothermal drilling is carried out in areas where there is anomalous low-pressure and high-temperature tectonics involving very hard rocks where energy is more prevalent and volcanism is intense. The hard rocks encountered cause a very quick wear in rock bits. In addition, the fatigue and fracture due to excessive vibrations in the drilling sequence, the greater load requirement are necessitated and therefore the drills are subjected to greater loads. The high temperature damages the mechanical parts of the drills and completely destroys the rubber components. On the other hand, corrosive fluids entering the well also drastically reduce the life of the drill. Therefore, the problems that may arise in drill bits can be grouped as follows [9].

- Decrease in rock bit diameter, excessive tooth and bearing wear, due to abrasion of the formation,
- Rubber parts lose their function in short time due to high temperature,
- If the temperature is above 200^0C, the life of rock bit is shortened due to the decrease in the yield strength of carbon steels

To reduce the effect of temperature and excessive vibrations especially in geothermal drilling;

- Rock bit feature with sidewall and body protection should be chosen,
- In the drill classification with the IADC code 3, 5(sealed ball-bearing, bearing surface protection) or 7 (sealed, sliding bearing protection) will be more accurate.
- In order to reduce the effect of excessive vibrations, it may be useful to insert a "shock absorber" in the drilling set.

Uniaxial Compressive Strength of the Formation (kg/cm^2)	Look of the cutting cone	Code for IADC	Bit type & Formation Drillability	Examples of suitable formation to use
<400		First digit: 1	Steel bit Easy drillable	Clay, Anhydrite, Chalk, Gypsum, Tuff, Shale, Siltstone, Anthracite, Marl, Clayed coal, Mudstone
400-800		First digit: 2	Steel bit Normal drillable	Alluvium, Compact plastic shale, Salt, Gypsum, Loose cemented sandstone, Anhydrite, Sand, Grey sandstone, Argillaceous schist, Conglomerate, Clay, Limestone, Travertine
800-1400		First digit: 3	Steel bit Hard drillable	Dolomite, Limestone, Marble, Chalk, Schist, Mica schist, Trachyte, Porous basalt, Pegmatite, Breccia, Sandstone
<400		First digit: 4	Tungsten carbide bit Easy drillable	Sandy shale, Loose cemented sandstone, Sand, Alluvium, Rock salt, Hillside rubble, Travertine
400-800		First digit: 5	Tungsten carbide bit Normal drillable	Alluvium, Chalk, Dolomite, Siliceous shale, Anhydrite, Sandstone, Siliceous siltstone, Compact tuff, Conglomerate, Marble, Travertine
800-1700		First digit: 6	Tungsten carbide bit Hard drillable	Sandy chalk, Siliceous veined chalk, Grey sandstone, Chalkstone, Granite, Trachyte, Gneiss, Diabase, Gabbro, Diorite, Sandstone, Peridotite, Serpentine, Syenite

1700-3200		First digit: 7	Tungsten carbide bit Very hard drillable	Flintstone, Pyrite, Granite, Quartzite, Volcanic gravelly conglomerate, Andesite, Basalt, Diabase, Gabbro, Diorite, Siliceous chalkstone, Porphyry, Syenite
>3200		First digit: 8	Tungsten carbide bit Rather hard drillable	Flintstone, Pyrite, Granite, Quartzite, Andesite, Basalt, Gabbro, Chert, Radiolarite

Figure 4. Rock bit selection according to the formation's uniaxial compressive strength [8]

4.ROCK BIT APPLICATION PARAMETERS, RATE OF PENETRATION AND COST OF DRILLING

The rate of penetration as well as drill application parameters are important in drilling operations. The drill manufacturers specify the optimum weight values together with the drill application parameters. Taking into account the values determined by the drill manufacturer, drill-off test is required to determine the load to be applied and the speed of rotation. More pressure or more rotation speed does not mean faster and cheaper drilling. Optimum pressure and rotation speed together with good drilling fluid properties affect controlled drilling speed.

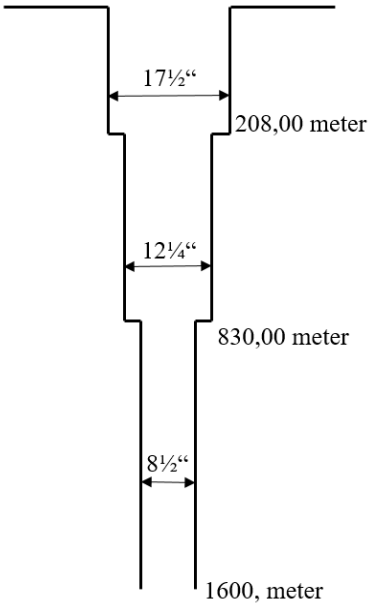

Figure 5. KSU-2 Geothermal Drilling

In Kutahya-Saphane-Karacaderbent (KSU-2) geothermal drilling, a total of 1,600 meters of wells were drilled. The drilling was performed at a diameter of 17 ½ " for 208.00 meters, a diameter of 12 ¼" for 622.00 meters and a diameter of 8 ½ " for 770 meters (Figure 5). When 8 ½ "drill application values were examined during KSÜ-2 drilling, it was observed that drilling speeds with 8 tons of drilling load were decreased to 1.10 m/h (Table 1).

In Aydin-Horsunlu AKH-2010/1 geothermal drilling work, a total of 1993 meters of wells were drilled. The drilling was performed at a diameter of 17 ½ " for 248.00 meters, a diameter of 12 ¼" for 340.00 meters and a diameter of 8 ½" for 1,412.00 meters. When 8 ½ "drill application values were examined, it was observed that drilling speeds with 12 tons of drilling load and 60 RPM rotation speed, 4.54 m/h of advancement rate was reached. In addition, a rate of 2,12 meters' advancement was achieved with a load value of 6 tons and 50 RPM rotation speed in the same region (Table 2).

Rock bit application parameters, drilling fluid properties and formation characteristics as well as rock bit production quality are important factors for the drilling rate. The performances of the rock bits produced by different companies with the same IADC code are also different.

Table 1. Kutahya-Saphane-Karacaderbent KSU-2 Geothermal Drilling Registration Form [10]

WELL NO: KSU-2	DRILLING MACHINE: WR-6			CITY: KUTAHYA		COUNTY: SAPHANE	FIELD: KARACADERBENT
Drilling rig supervisor :				Drill pipe: 4 1/2"		Mud pump-1:	Pz-8
Drilling person :				Drill PIPE: 3 1/2"		Mud pump-2:	Fm-35
Drilling person :				Drill collar: 8"			
Drilling person :				Drill collar: 6 1/2"			

No	Date of operation	Diameter (inch)	Type	Serial no	Starting depth	Ending depth	Drilling length	Total work hours	Rate of penetration	Formation
1	24.03.2007	17 1/2	Rock-Bit	Old	0.00	113.20	113.20	62.75	1.80	Alluvium, tuff, tuffite, conglomerate, marl
2	03.04.2007	17 1/2	Rock-Bit	277890	113.20	208.90	95.70	58.83	1.68	Conglomerate, claystone, marl
3	12.04. 2007	12 1/4	Rock-Bit	683244	208.90	326.10	117.20	56.58	2.08	Basalt, tuff, tuffite
4	16.04. 2007	12 1/4	Rock-Bit	4110406	326.10	458.00	131.90	105.58	1.25	Basalt, tuff, tuffite
5	22.04. 2007	12 1/4	Rock-Bit	030479	458.00	495.60	37.60	34.83	1.80	Tuff, tuffite
6	24.04. 2007	12 1/4	Rock-Bit	030453	495.60	550.40	54.80	52.83	1.03	Tuff, tuffite
7	27.04. 2007	12 1/4	Insert	0100904	550.40	830.00	279.60	134.00	2.08	Tuff, tuffite
8	17.05. 2007	8 1/2	Insert	307	830.00	1155.15	325.15	141.08	2.30	Tuff, tuffite
9	01.06. 2007	8 1/2	Insert	300	1155.15	1394.60	239.45	128.58	1.86	Tuff, tuffite
10	13.06. 2007	8 1/2	Insert	263	1394.60	1500.00	105.40	95.75	1.10	Tuff, tuffite, conglomerate, sandstone
11	24.06. 2007	8 1/2	Insert	537	1500.00	1600.0	100.00	71.08	1.40	Tuff, tuffite, conglomerate, sandstone

Table 2. Aydin-Horsunlu Geothermal Drilling Registration Form [11]

WELL NO: AKH-2010/1	DRILLING MACHINE: MR-6000/1	CITY: AYDIN	COUNTY: KUYUCAK	FIELD: HORSUNLU
Drilling rig supervisor :	Drill pipe: 4 1/2"	Mud pump-1:	9T-800	
Drilling person :	Drill collar: 8"	Mud pump-2:	9T-800	
Drilling person :	Drill collar: 6 1/2"	Mud pump-3:		

No	Date of operation	Diameter (inch)	Type	Serial no	Starting depth	Ending depth	Drilling length	Total work hours	Rate of penetration	Weight on bit (ton)	Rotation (RPM)	Pressure (PSI)	Pump				Mud		Formation
													No	Collar	Flowrate	Weight	Viscosity		
1	11.03.2010	17 1/2	Mill-Tooth	9499	0.00	248.00	248.00	95.83	2.59	12	60	100	9T-800	6	12.5	1.06	55		Alluvium, conglomerate
2	01.04.2010	12 1/4	Insert	09677	248.00	588.00	340.00	159.00	2.14	12	60	150	9T-800	6	12.5	1.20	60		Mica-schist, granate
3	25.04.2010	8 1/2	Insert	11060	588.00	1014.30	426.30	93.83	4.54	12	60	150	9T-800	6	12.5	1.10	55		Mica-schist, gneiss
4	03.05.2010	8 1/2	Insert	11050	1014.30	1331.50	317.20	81.00	3.92	12	60	250	9T-800	6	12.5	1.10	55		Quartzite, quart-schist
5	08.05.2010	8 1/2	Insert	11054	1331.50	1413.10	81.60	29.67	2.75	14	55	300	9T-800	6	12.5	1.10	55		Phyllite, gneiss, quartzite
6	10.05.2010	8 1/2	Insert	10011	1413.10	1551.50	138.40	54.67	2.53	14	55	350	9T-800	6	12.5	1.10	55		Phyllite, gneiss, quartzite
7	14.05.2010	8 1/2	Insert	273	1551.50	1600.00	48.50	20.25	2.40	14	55	400	9T-800	6	12.5	1.10	55		Gneiss, mica-schist
8	20.05.2010	8 1/2	Insert	276	1600.00	1832.50	232.50	76.58	3.04	12	55	450	9T-800	6	12.5	1.10	55		Phyllite, gneiss, quartzite
9	04.06.2010	8 1/2	Insert	304351	1832.50	1908.00	75.50	35.58	2.12	6	50	500	9T-800	6	12.5	1.10	55		Gneiss, mica-schist
10	07.06.2010	8 1/2	Insert	279	1908.00	2000.0	92.00	40.83	2.25	6	50	500	9T-800	6	12.5	1.10	55		Phyllite, chalk-schist

If it is assumed that a total of 1,200 meters of a borehole with 8½ " diameter is completed with 2 rock bits of the brand a, it is possible to reach the same targeted length of borehole with 5.5 rock bits of the brand c. In order to complete the projected length of borehole, 1 manoeuver should be used in case of using the brand a rock bit and 5 manoeuvers by using the brand c rock bit. The maneuvering time is about 24 hours in 8½ "

drilling work. In this case the lost time from rock bit change will be 1 day for the brand a rock bit and 5 days for the brand c rock bit. If the 1.200-meter progress for 8½ " borehole is planned to be realized and daily drilling cost is estimated to be about 5,000 USD;

Table 3. Performance of different brand rock bits

Rock bit brand	Rock bit diameter (inch)	Drilled length (m)	Working hour (h)	Rate of advancement (m/h)	Usage rate of rock bit (%)	WOB (ton)	RPM
a	8 1/2	611,2	129,5	4,71	80	14-15	50-60
b	8 1/2	371,00	78,17	4,75	80	14	65
****c***	8 1/2	217,33	68,56	3,17	80	14	65

** The brand c has been increased from 50% to 80% since it was changed after use.*

Table 4. Drill meter cost

Rock bit brand	No of rock bits consumed	Number of manoeuvres and lost days	Rock bit cost ($/unit)	Total expenses for rock bits ($)	Cost of lost days ($)	Total cost ($)	Rock bit cost for each meter drilled ($/m)
a	2	1	6.000	12.000	5.000	17.000	**14,17**
b	3,25	3	4.500	14.625	15.000	29.625	**24,68**
c	5,5	5	4.000	22.000	25.000	47.000	**39,16**

When Tables 3 and 4 are examined, the initial cost of the brand a rock bit is 25-30% more expensive than other rock bits, however the cost of each meter drilled is lower. Especially when the maneuvering time is long during the progression of 8½ "diameter boreholes, the high performance brand rock bit selection is important in minimizing the cost of the drilling meter.

5. RESULTS

It is very important to select a rock bit suitable for the formation to be penetrated in order to realize the planned rate of advancement before the drilling operation is started. For this purpose, the drilling engineer should analyze the geological and geophysical studies conducted at the site before the operation begins and obtain detailed information about the possible formation characteristics to be passed. The formation properties are important parameters for both rock bit selection and drilling fluid to be used.

- ✓ If the first basic rule in the drilling of the borehole is to choose a rock bit suitable for the formation to be passed, the second basic rule is to use the drill with the correct parameters.
- ✓ Optimization of drilling work starts with rock bit optimization. The rock bit cost corresponds to 3-5% of the total drilling cost, but the impact on the total drilling cost is 50-60%.
- ✓ During the drilling operations, the drilling engineer will follow the parameters affecting the drilling performance such as changes in torque, rock pieces formed during drilling operation, sludge pump pressures and necessary interventions in order to reduce the cost of drilling and ensure efficient operation.
- ✓ Following the drill performance, the problems that can occur in the rock bit are indicated on the surface. Irregular torque occurs when the drill is overloaded or the drill bit diameter drops. In case of blockage in the drill holes, irregular pump pressure values are read. The pump pressure is regular but the change in the pump stroke number may indicate that the nozzle / drill holes are blocked again.
- ✓ Especially as the depth of the borehole increases, maneuvering (tooling-stroke) times for rock bit exchange will increase. Choosing quality rock bit for regular progression at 8½ "diameter will seriously affect drilling meter cost.

REFERENCES

[1]. Bilgin, N., 1991, Drills used in mines and their operating conditions and economics, Publication of Mining Faculty, Istanbul Technical University, Istanbul (in Turkish).
[2]. Praillet, R., 1990, Blast hole Drilling-Rotary Drilling and The Four Kingdoms. WME, Sept.
[3]. Bilgin, N., Eskikaya, S. & Dincer, T., 1993, Performance Analysis of Rotary Drills with Large Diameter used in Turkish Coal Board, 13. Mining Congress of Turkey (in Turkish)
[4]. Moore, P. L.,1986, Drilling Practices Manual, Second Ed., Oklahoma, USA, pp.363-399
[5]. Paiman, A.M., Al-Askari, M.K.G., Salmani, B., Al-Arazi, B.D. & Masihi, M., 2009, Effect of Drilling Fluid Properties on Rate of Penetration, NAFTA 60 (3) 129-134
[6]. **Warren, T. M., 1987,** Penetration Rate of Performance of Roller Cone Bits, SPE Drilling Engineering, March, 9-18. 8 Maurer, Journal of Petroleum Technology, December, 1433-42
[7]. Junior, D.C., 2007, Challenges and Developments Indirect Measurement of Down Hole Forces affecting Drilling Efficiency
[8]. Ister, T. & Ozdemir, A., 2005, Rock Bit Selection suitable to Formation in accordance with its Cutting Structure, 58. Geology Convention of Turkey, pp 295-296 (in Turkish)
[9]. Serpen, U. 2005, Features of Geothermal Drills and Equipments used, Geothermal Energy Seminar, Publication of Turkish Chamber of Mechanical Engineers E/2005/393-2, pp. 55-66 (in Turkish)
[10]. MTA Drill Report, 2009, General Directorate of Mineral Research & Exploration, Kutahya-Saphane-Karacaderbent KSU-2 Geothermal Drill (in Turkish)
[11]. MTA Drill Report, 2011, General Directorate of Mineral Research & Exploration, Aydin-Horsunlu AKH-2010/1 Geothermal Drill (in Turkish)

ICENS 4TH INTERNATIONAL CONFERENCE ON ENGINEERING AND NATURAL SCIENCE
2-6 May 2018 KIEV UKRAINE

Considerations on Maximum Penetration Levels of Fixed Speed Wind Energy Conversion Systems Operating in Unbalanced Non-Sinusoidal Environments

Alp Karadeniz[1], Murat E. Balci[1], Shady H. E. Abdel Aleem[2]

Abstract

It is well known that unbalanced non-sinusoidal voltages result in high phase currents that may exceed the rated current of the induction motors, and cause an overheating problem for them. As a result, under such unbalanced non-sinusoidal operating conditions, one should determine the maximum permissible loading ratio by intentionally reducing the maximum phase current to its rated value to avoid the motor overheats. In this paper, an approach is implemented to determine the maximum penetration level (MPL) of a fixed speed wind energy conversion system (FSWECS) with squirrel cage induction generator (SCIG) operating in an unbalanced non-sinusoidal distribution system. Further, a Steinmetz compensator (SC) accompanied with single-tuned passive filter (STPF) is proposed to increase the obtained MPL of the FSWECS-SCIG scheme. The simulation results show an excessive reduction of the MPL of the studied system under the unbalanced and non-sinusoidal operating conditions. Besides, the results validate that SC accompanied with the STPF can increase the MPL.

Keywords: Harmonic distortion; imbalance; induction machines; power quality; wind systems.

1. INTRODUCTION

Distributed generation (DG) technologies are small-scale dispersed electrical energy sources placed as close as possible to the customers [1]. The DG units based on photovoltaic (PV) cells and wind turbines are mainly employed in distribution networks since they offer different benefits such as voltage profile improvement, reliability enhancement, electric power loss reduction and energy efficiency increase [2], [3]. Other reasons can promote usage of DG technologies based on the renewable energy sources such as the notable energy crisis in some countries due to the shortage of traditional energy resources, in addition to the increased awareness of global warming and climate change. Altogether, these reasons have forced all the stakeholders in the electric energy sector to deploy usage of the environmentally friendly DG units extensively [4].

In the near past, the DG units were weaker to cause a considerable disturbance in a distribution network. Today, this situation is completely different due to the massive proliferation of DG units all over the world. Hence, excessive penetration or inappropriate DG capacities may cause undesirable effects in the distribution networks such as additional losses and overvoltage [2], [3].

In the literature, determination of the maximum penetration level (MPL) of DG units is handled as an optimization problem by considering bus voltage variation limits or current limitations of the lines/cables and transformers as constraints [5]-[7]. On the other hand, in some recent works [1], [8]-[10], for the DG units with the power electronic-based interfaces, voltage and current harmonic distortion limits stated in the international standards have been further considered as additional constraints to determine the acceptable MPL of the DG units.

[1] *Corresponding author: Balikesir University, Department of Environmental Engineering, 10145, Merkez/Balıkesir, Turkey. akaradeniz@balikesir..edu.tr,mbalci@balikesir.edu.tr*

[2] *Mathematical and Physical Sciences, 15th of May Higher, Institute of Engineering, Helwan Cairo, Egypt, engyshady@ieee.org*

In addition to harmonic pollution, imbalance of voltages and currents is another significant power quality problem that frequently occurs in distribution networks [11]. Uneven distribution of single-phase loads over the three phases, asymmetry of lines and power system faults are the common causes of this problem. One of the power system equipment, which is adversely affected by the unbalanced voltage and/or current, is the induction machine [11]-[13]. Under unbalanced system conditions, they have a poor power factor, torque pulsations, and extra winding losses which cause overheating problems and fast aging of the machines. It is well known that induction machines are widely used in industrial areas as motors. Thus, many studies, in the literature [14]-[19], have aimed to avoid the negative consequences of the unbalanced voltage conditions on the induction motors performance by limiting a maximum loading ratio (widely known as derating factor (DF)). In these studies, DF is generally determined with one of the following ways: (i) use of derating factor curve (or expression) in terms of voltage unbalance level, which is placed in National Electrical Manufacturers Association (NEMA) standard, (ii) equating the ratio between the total power loss and the rated loss to unity and (iii) equating the ratio between maximum rms phase current and the rated one to unity [16], [17].

In today's power systems, due to the large proliferation of nonlinear loads and equipment based on power electronic devices, which draw/inject non-sinusoidal distorted currents, grid voltages are no longer sinusoidal and have distorted waveforms [20]. Similar to the unbalanced supply voltage case, under harmonically distorted voltages, induction motors suffer from torque pulsations, extra losses and overheating, and they should also be derated to avoid these adverse effects [20]-[23]. It can be declared from the literature [23] that when one neglects the skin effect of the windings, under harmonically distorted voltages, the winding loss is directly proportional to the square of the true rms current. This means that the derating procedure could be used to limit overheating of the windings related to the voltage harmonics.

Nowadays, induction generators are employed in wind energy conversion systems (WECS) due to their advantages compared with synchronous generators such as their smaller size, lower cost and higher reliability [24]. The WECS can be divided into three categories: fixed speed, partial variable speed and variable speed WECS. Partial variable and variable speed WECS are able to track the maximum power under variable wind speeds. However, their costs are high because of the power electronics and control circuits' additional cost. As a result, conventionally fixed speed topology with squirrel cage induction generator (SCIG) is still preferred for small to medium WECS. For that reason, the MPLs should be determined to avoid the lifetime reduction of the SCIG included in the fixed speed WECS (FSWECS) under unbalanced non-sinusoidal grid voltages and line currents. Based on that, in this paper, an algorithm is presented to obtain the MPL of FSWECS with SCIG operating in unbalanced non-sinusoidal distribution systems. Further, Steinmetz compensator (SC) accompanied by a single-tuned passive filter (STPF) is proposed to increase the MPL of the FSWECS with SCIG. In the analysis, the conventional d-q model of the SCIG is used [25].

Both oral and poster presentations will be published on a CD in order to be distributed to participants at the time of registration in the conference.

2. MAXIMUM PENETRATION LEVEL OF FSWECS IN UNBALANCED NON-SINUSOIDAL SYSTEMS

In this section, for unbalanced and non-sinusoidal systems, dynamic modeling of FSWECS is presented, and the developed algorithm, which is to find the MPL of the FSWECS under the same system conditions, is further provided.

a. Modeling of FSWECS

The dynamic modeling of the FSWECS is used for analyzing its maximum penetration level under unbalanced non-sinusoidal conditions. As shown in Figure 1, it consists of blades, gearbox, and SCIG. The mechanical power transmitted from the gearbox to the shaft of the SCIG is written in terms of the air density (ρ), the area swept by the rotor (A), power coefficient (Cp), and wind speed (u), as follows:

$$P_M = \frac{1}{2}\rho A u^3 C_p(\lambda) \tag{1}$$

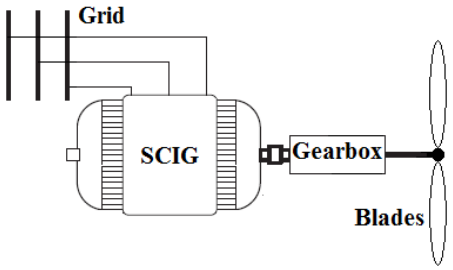

Figure 1. The schematic of FSWECS directly connected to the grid.

The power coefficient (Cp) depends on the tip-speed ratio (λ), which is determined as follows:

$$\lambda = \frac{\omega_m R}{u} \tag{2}$$

where ωm and R are the rotor angular velocity and rotor radius, respectively.

In the analysis, SCIG is modeled using the well-known d-q equivalent circuits shown in Figure 2.

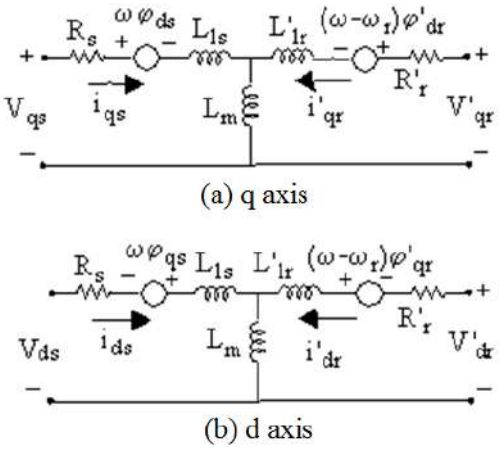

Figure 2. Equivalent circuits of the induction machine, (a) q-axis equivalent circuit and (b) d-axis equivalent circuit.

For the model, equations (3)-(6), the instantaneous d-q axis stator voltages (Vqs and Vds) and instantaneous d-q axis rotor voltages referred to the stator side (V'qr and V'dr) can be expressed in terms of the d-q axis stator and referred rotor magnetic fluxes (φqs, φds, φ'qr and φ'dr), d-q axis stator currents (iqs and ids), d-q axis referred rotor currents (i'qr and i'dr), stator resistance (RS), rotor resistance referred to the stator side (R'r), the reference frame angular velocity (ω), and the electrical angular velocity (ωr), thus:

$$V_{qs} = R_s i_{qs} + \frac{d}{dt}\varphi_{qs} + \omega\varphi_{ds} \tag{3}$$

$$V_{ds} = R_s i_{ds} + \frac{d}{dt}\varphi_{ds} - \omega\varphi_{qs} \tag{4}$$

$$V'_{qr} = R'_r i'_{qr} + \frac{d}{dt}\varphi'_{dr} - (\omega - \omega_r)\varphi'_{dr} \tag{5}$$

$$V'_{dr} = R'_r i'_{dr} + \frac{d}{dt}\varphi'_{dr} + (\omega - \omega_r)\varphi'_{qr} \quad (6)$$

In addition, the magnetic fluxes are written as follows:

$$\varphi_{qs} = L_s i_{qs} + L_m i_{qr} \quad (7)$$

$$\varphi_{ds} = L_s i_{ds} + L_m i'_{dr} \quad (8)$$

$$\varphi'_{qr} = L'_r i'_{qr} + L_m i_{qs} \quad (9)$$

$$\varphi'_{dr} = L'_r i'_{dr} + L_m i_{ds} \quad (10)$$

where Ls, L'r and Lm denote total stator inductance, total rotor inductance referred to the stator side and magnetization inductance, respectively. The two inductance values (Ls, L'r) can be found by summation of the corresponding leakage inductance (Lls and L'1r) and Lm, thus:

$$L_s = L_{1s} + L_m \quad (11)$$

$$L'_r = L'_{1r} + L_m \quad (12)$$

The electromagnetic torque (Te) and its relation with the mechanical torque (Tm) of the shaft can be expressed as follows:

$$T_e = 1.5p\left(\varphi_{ds} i_{qs} - \varphi_{qs} i_{ds}\right) \quad (13)$$

$$T_e - T_m = 2H\frac{d}{dt}\omega_m \quad (14)$$

where p, H and ωm are pole pairs of the machine, inertia constant, and rotor angular velocity, respectively.

The relationships among the line voltages and the d-q voltage components are given in (15) and (16), thus:

$$\begin{bmatrix} V_{qs} \\ V_{ds} \end{bmatrix} = \frac{1}{3}\begin{bmatrix} 2\cos\theta & \cos\theta + \sqrt{3}\sin\theta \\ 2\sin\theta & \sin\theta - \sqrt{3}\cos\theta \end{bmatrix}\begin{bmatrix} V_{abs} \\ V_{bcs} \end{bmatrix} \quad (15)$$

$$\begin{bmatrix} V'_{qr} \\ V'_{dr} \end{bmatrix} = \frac{1}{3}\begin{bmatrix} 2\cos\beta & \cos\beta + \sqrt{3}\sin\beta \\ 2\sin\beta & \sin\beta - \sqrt{3}\cos\beta \end{bmatrix}\begin{bmatrix} V'_{abr} \\ V'_{bcr} \end{bmatrix} \quad (16)$$

where θ is the angular position of the reference frame, and β is the difference between θ and the angular position of the rotor (θr).

By using the d-q current components, the phase currents of the induction machine can be calculated as follows:

$$\begin{bmatrix} I_{as} \\ I_{bs} \end{bmatrix} = \begin{bmatrix} \cos\theta & \sin\theta \\ \dfrac{-\cos\theta + \sqrt{3}\sin\theta}{2} & \dfrac{-\sqrt{3}\cos\theta - \sin\theta}{2} \end{bmatrix}\begin{bmatrix} I_{qs} \\ I_{ds} \end{bmatrix} \quad (17)$$

$$\begin{bmatrix} I'_{ar} \\ I'_{br} \end{bmatrix} = \begin{bmatrix} \cos\beta & \sin\beta \\ \dfrac{-\cos\beta + \sqrt{3}\sin\beta}{2} & \dfrac{-\sqrt{3}\cos\beta - \sin\beta}{2} \end{bmatrix} \begin{bmatrix} I'_{qr} \\ I'_{dr} \end{bmatrix} \quad (18)$$

$$I_{cs} = -I_{as} - I_{bs} \quad (19)$$

$$I'_{cr} = -I'_{ar} - I'_{br} \quad (20)$$

b. *Determination of MPL*

As mentioned before in the introduction section, under unbalanced and non-sinusoidal voltages, the rms phase currents of the induction machine can be considerably higher than its rated current. This means that under such conditions its windings overheat and its useful life will be further reduced. To avoid this problem, it should generate a maximum active power under the unbalanced and non-sinusoidal conditions that its phase currents do not exceed the rated current. To find the maximum permissible active power (P_{Gmax}) of the FSWECS, whose mechanical input power is adjusted by a pitch control, the highest stator phase current is intentionally reduced to the rated current. Thus, *MPL* is expressed as follows:

$$MPL(\%) = \frac{P_{G\,max}}{P_{rated}} \cdot 100 \quad (21)$$

A detailed flowchart of the *MPL* determination algorithm is shown in Figure 3.

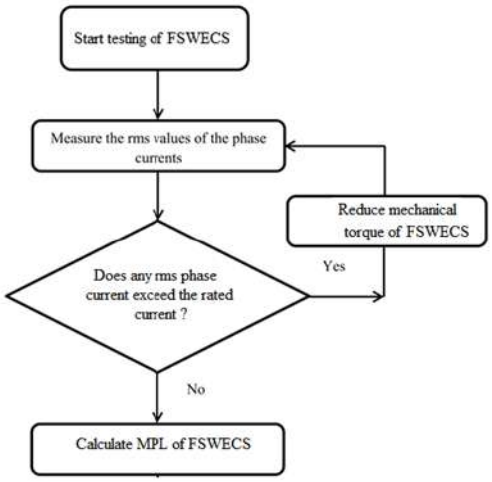

Figure 3. The developed algorithm for determination of the *MPL*.

c. *Methods for Improvement of MPL*

In the literature, several devices are employed to reduce imbalance percentage and mitigate harmonic distortion of voltages and currents in power systems. They are mainly divided into passive compensators, which are based on combinations of passive elements such as resistor-inductor-capacitor (RLC), and active compensators that depend on power electronic-based circuits [20], [26], [27].

The first group includes passive harmonic filters and Steinmetz compensator (SC). While, in the second group, there are several schemes such as the static VAr compensators, static synchronous compensators, active filters and unified power quality conditioners. They have different imbalance and harmonic distortion mitigation capabilities, and, certainly, different investment costs. In general, second group (active) compensators provide better performance than the first group (passive) compensators with regards to imbalance, harmonic distortion and reactive power compensation. However, the active compensators have considerably high costs especially

for high power rating applications when compared to the passive compensators; this explains why passive compensators are still frequently used in today's power systems.

In this study, SC and STPF are considered for the improvement of the MPL in the test system consisting of non-linear and unbalanced loads. Their three-phase equivalent circuits are shown in Figures. 4 and 5, respectively.

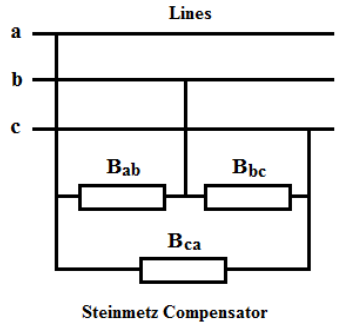

Figure 4. Three-phase equivalent circuit of the Steinmetz compensator at the fundamental frequency.

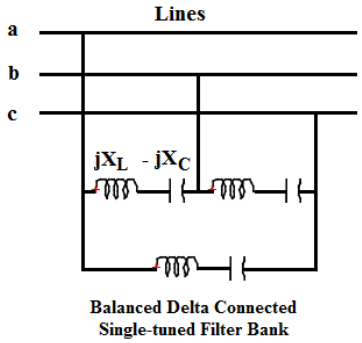

Figure 5. Three-phase equivalent circuit of a balanced delta-connected single-tuned filter bank at the fundamental frequency.

The susceptance values of the Steinmetz compensator at the fundamental frequency can be expressed in terms of the fundamental phase-to-phase active powers (P_{ab1} and P_{cb1}), fundamental phase-to-phase reactive powers (Q_{ab1} and Q_{cb1}), and the fundamental frequency phase-to-phase voltages (V_{ab1}, V_{bc1}, and V_{cb1}) that are measured at the load side [27]:

$$B_{ab} = \frac{1}{3V_{ab1}^2}\left(3Q_{ab1} - \sqrt{3}P_{cb1}\right) \tag{21}$$

$$B_{bc} = \frac{1}{3V_{bc1}^2}\left(\sqrt{3}P_{ab1} + 3Q_{cb1}\right) \tag{22}$$

$$B_{ca} = \frac{1}{3V_{ca1}^2}\left(-\sqrt{3}P_{ab1} + \sqrt{3}P_{cb1}\right) \tag{23}$$

where P_{ab1}, P_{cb1}, Q_{ab1} and Q_{cb1} are expressed as follows:

$$P_{ab} - jQ_{ab} = \left(\overline{V}_{ab1}\right)^* \overline{I}_{a1} \tag{24}$$

$$P_{cb} - jQ_{cb} = \left(\bar{V}_{cb1}\right)^{*} \bar{I}_{c1}, \text{ where } \left(\bar{V}_{cb1} = -\bar{V}_{bc1}\right) \quad (25)$$

It should be noted that the superscripts (_) and (*) denote a complex phasor and conjugate, respectively. In addition to that, negative and positive values of the susceptance indicate whether the susceptance is inductive or capacitive, respectively. These expressions are provided to reduce imbalance level of the load current as well as to compensate the reactive power, at the fundamental frequency. Through the derivation of the susceptance expressions, the load voltage is assumed balanced. So for the unbalanced load voltage condition, these expressions are used to find the Steinmetz compensator's susceptance values iteratively. Particularly, after each iteration, susceptance values are updated by summing its values obtained at the current and previous iteration numbers.

This iterative update will continue until the current unbalance factor $\left(CUF = I_1^{-}/I_1^{+}\right)$, which is the ratio of the fundamental frequency-negative sequence current $\left(I_1^{-}\right)$ to the fundamental-positive sequence current $\left(I_1^{+}\right)$ is to be nil or a negligible value.

On the other hand, the relations among the harmonic tuning order (h_t) and the reactances (X_C and X_L) of the balanced three-phase STPF can be written as;

$$X_L = \frac{X_C}{h_t^2} \quad (26)$$

The X_C value can be calculated by regarding the desired fundamental frequency reactive power compensation, and the h_t value can be selected as the most dominant harmonic current [28].

3. SIMULATION RESULTS

The system under study constitutes of Thevenin voltage source and impedance of the utility side, a power transformer, a single-phase linear load, a six-pulse uncontrolled rectifier, and a wind farm consisting of five FSWECS. The rms voltage and frequency of the Thevenin voltage source are 4.2 kV and 50 Hz, respectively. The resistance and inductive reactance of the Thevenin impedances are equal to 0.01 and 0.1 Ω, respectively. The transformer rating values are specified as 5 MVA, and 4.16 kV/400V, connected as Y/Y, and the ratings of the SCIGs included in the FSWECSs are 0.11 MW, 400 V, 182.5 A, 50 Hz and 1487 rpm. The transformer is modeled by using its well-known T equivalent circuit, and its parameters are given by the block shown in Figure 6. Also, parameters of the SCIG's d-q model are shown in Figure 7. The fundamental active power and power factor (PF) of the single-phase linear load (which is connected between phases a and b) are 0.48 MW and 98.00%, respectively, and the active power and true PF of the six-pulse uncontrolled rectifier are 1.35 MW and 95.00%, respectively.

In the analysis, firstly, the system operates without compensators; this is presented as Case 1 in the results. Case 2 represents the system after compensation using Steinmetz compensator, of which the parameters Bab, Bbc, and Bca are calculated using (21)-(25) as 0.5374, 0.1870 and -0.2182 mhos, respectively. The XCF and ht parameters of the balanced STPF are determined as 5 Ω and 5, respectively, in addition to the Steinmetz compensator, operate collectively. This is presented as Case 3 in the results.

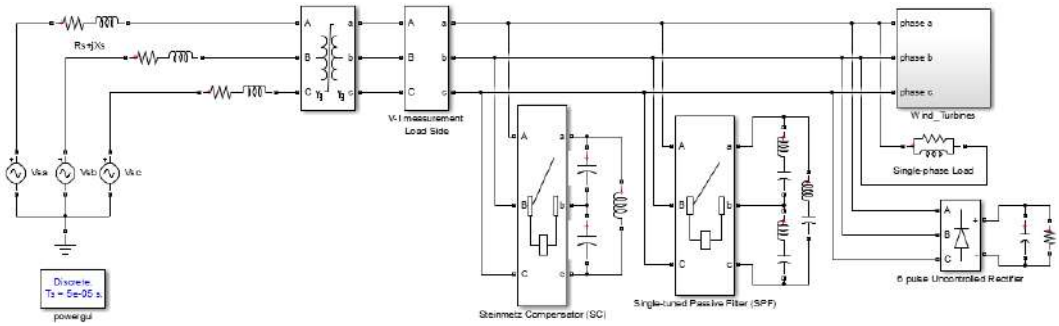

Figure 6. The system under study.

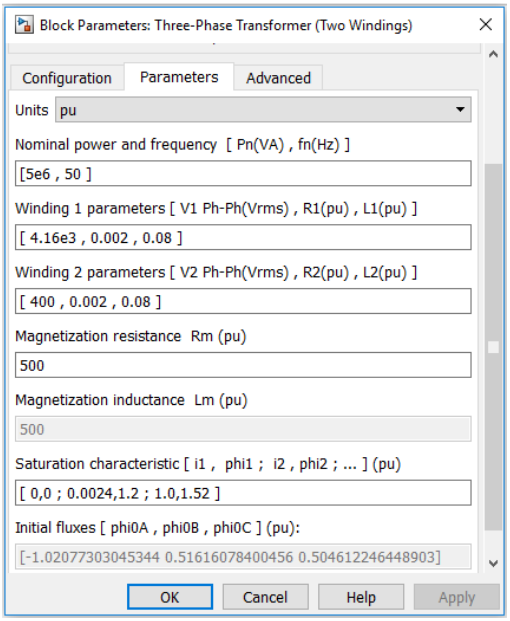

Figure 7. Parameters of the transformer model.

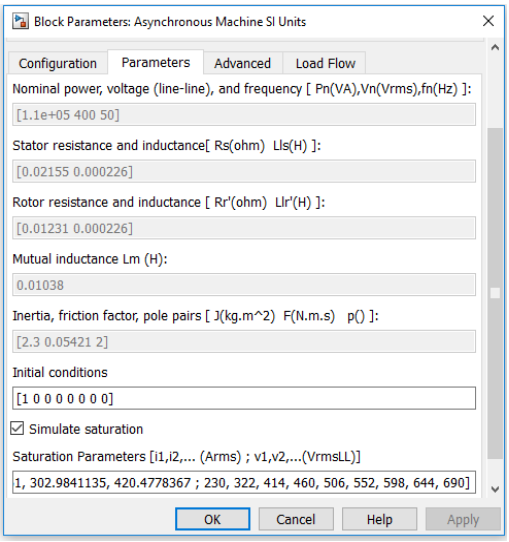

Figure 8. Parameters of the SCIG used in the FSWECS.

For all the considered cases, unbalance factor of the fundamental voltages , CUF, total voltage harmonic distortion values of the phase voltages (THDVa, THDVb and THDVc) and line currents (THDIa, THDIb and THDIc), active power (P) and true PF measured at the load side are presented in Table I. In addition, for the same three cases, the maximum permissible active power generation (Pgmax) as well as MPL of the FSWECS are presented in Table II. Under the determined MPL condition, for the SCIG, Table II also shows the true rms currents (Iga, Igb, and Igc), CUF, THDI values of the phase current, true power factor of the generator (PFg).

Table 1. Power Quality Indices Measured at the Load Side

Parameters	**Case 1**	**Case 2**	**Case 3**
VUF (%)	4.50	--	0.20
CUF (%)	45.50	--	2.30
$THDV_a$ (%)	5.90	10.40	6.38
$THDV_b$ (%)	8.00	8.45	3.00
$THDV_c$ (%)	8.80	14.64	3.97
$THDI_a$ (%)	7.00	18.80	7.95
$THDI_b$ (%)	9.30	18.20	4.37
$THDI_c$ (%)	22.80	31.80	4.48
P (MW)	2.402	2.350	2.385
PF (%)	87.16	96.46	99.66

Table 2. Measurements Obtained for the SCIG

Parameters	**Case 1**	**Case 2**	**Case 3**
I_{ga} (pu)	1.00	0.98	1.00
I_{gb} (pu)	0.68	0.98	0.98
I_{gc} (pu)	0.40	1.00	0.96
CUF (%)	70.00	--	2.06
$THDI_a$ (%)	8.30	16.14	6.94
$THDI_b$(%)	16.50	16.33	3.75
$THDI_c$ (%)	29.50	27.90	4.00
$P_{g\ max}$(MW)	0.059	0.106	0.107
PF_g (%)	66.48	89.07	91.29
MPL (%)	54.09	96.36	98.00

For the system before compensation (Case 1), it is seen from Tables I and II that the three-phase currents and voltages measured at the load side have measured CUF and VUF values as 45.50 and 4.5%, respectively. For the abc phases, the same voltages have THDV values as 5.90, 8.00 and 8.80%, respectively, and the same currents have THDI values as 7.00, 9.30 and 22.80%, respectively. These results point out that the system has considerably unbalanced and non-sinusoidal voltages and currents due to the single-phase and six-pulse uncontrolled rectifier loads. P and PF values of the uncompensated system (Case 1) are 2.402 MW and 87.16%, and this means that the system needs power factor correction in addition to the imbalance reduction and harmonic distortion mitigation. Also, for results of Case 1 given in the same tables, the MPL and PFg values of the SCIG are 54.09% and 66.48%, respectively. In addition, the CUF value of the SCIG's phase currents is 70.00%, and for the abc phases, the THDI values are 8.30, 16.50 and 29.50%, respectively. Pgmax values obtained by the algorithm, that was shown in Figure 3, are 0.059 MW, respectively.

For the system after compensation using Steinmetz compensator (Case 2), it can be figured out from the results that the compensator reduces VUF and CUF, completely. Also, it improves the PF of the system to be 96.46%. The SCIG has balanced phase currents and the improved PFg and MPL values as 89.07% and 96.36%, respectively. However, for both system and SCIG, harmonic amplification occurs as noticed by the high THD values.

Finally, for Case 3, it is seen that the single-tuned filter considerably mitigate the harmonic distortion of the terminal voltages, terminal currents and the SCIG's currents. The imbalance of these currents and voltages are slightly increased due to the presence of the STPF when compared to Case 2. As a result, a comparative analysis of Cases 2 and 3 show that the SCIG has better PFg and MPL values as 91.29% and 98.00%, respectively, in Case 3, for the system using both compensators. In addition, the PF of the system is slightly improved with respect to Case 2.

4. CONCLUSIONS

In this paper, an algorithm is presented to determine the maximum penetration level of fixed speed wind conversion system with squirrel cage induction generator under unbalanced and non-sinusoidal conditions. The simulation results show that the unbalanced non-sinusoidal system conditions considerably reduce the maximum penetration level of the wind system. Accordingly, under all the same system conditions, a Steinmetz

compensator accompanied with a single-tuned passive filter is proposed to increase the reduced penetration level, and the simulation results validate that the proposed compensation scheme can be successfully used under such system conditions.

On the other hand, it is also seen that Steinmetz compensator amplifies the voltage and current harmonics in the system, and the single-tuned filter results in an increment of the voltage and current imbalance. As a result, optimal design of both Steinmetz and single-tuned passive filter should be considered to maximize the maximum penetration level of fixed speed wind conversion systems. This will be investigated in future works.

REFERENCES

[1]. S. Sakar, M. E. Balci, S. H. E. Abdel Aleem, and A. F. Zobaa, "Integration of large- scale PV plants in non-sinusoidal environments: Considerations on hosting capacity and harmonic distortion limits," Renew. Sustain. Energy Rev., vol. 82, pp. 176–186, Feb. 2018.
[2]. R. A. Walling, R. Saint, R. C. Dugan, J. Burke, L. A. Kojovic, "Summary of distributed resources impact on power delivery systems", IEEE Trans. on Power Deliv., vol. 23, No. 3, pp. 1634-1644, Jun. 2008.
[3]. F. H. Guan, D. M. Zhao, X. Zhang, B. T. Shan, Z. Liu, "Research on distributed generation technologies and its impacts on power system", Int. Conf. on Sustainable Power Generation and Supply, pp. 1-6, Apr. 2009, Nanjing, China.
[4]. L. Li, H. Mu, N. Li , M. Li, "Economical and environmental optimization for distributed energy resource system coupled with district energy networks" Energy, vol. 109, pp. 947-960, Aug. 2016.
[5]. S. Conti, S. Raiti, G. Tina, U. Vagliasindi, "Distributed generation in LV distribution networks: voltage and thermal constraints", 2003 IEEE Bologna Power Tech Conference Proceedings, pp. 6, 23-26, June 2003, Bologna, Italy.
[6]. H. M. Ayres, W. Freitas, M. C. De Almeida, and L. C. P. Da Silva, "Method for determining the maximum allowable penetration level of distributed generation without steady-state voltage violations," IET Gener. Transm. Distrib., vol. 4, no. 4, p. 495, 2010.
[7]. R. Viral, D. K. Khatod, "Optimal planning of distributed generation systems in distribution system: a review", Renew. Sustain. Energy Rev., vol. 16, no.7, 5146-5165, Sept. 2012.
[8]. S. Sakar, M. E. Balci, S. H. E. A. Aleem, and A. F. Zobaa, "Hosting capacity assessment and improvement for photovoltaic-based distributed generation in distorted distribution networks," 2016 IEEE 16th International Conference on Environment and Electrical Engineering (EEEIC), Florence, 2016, pp. 1-6.
[9]. N. Santos, V. Cuk, P. M. Almeida, M. H. J. Bollen, P. F. Ribeiro, "Considerations on hosting capacity for harmonic distortions on transmission and distribution systems" Electr. Power Syst. Res, vol. 119, pp. 199-206, Feb. 2015.
[10]. S. Sakar, M. E. Balci, S. H. E. Abdel Aleem, and A. F. Zobaa, "Increasing PV hosting capacity in distorted distribution systems using passive harmonic filtering," Electr. Power Syst. Res., vol. 148, pp. 74–86, Jul. 2017.
[11]. M. H. Albadi, A. S. A. Hinai, A. H. Al-Badi, M. S. A. Riyami, S. M. A. Hinai, R. S. A. Abri, "Unbalance in power systems: Case study", 2015 IEEE International Conference on Industrial Technology (ICIT), Seville, 2015, pp. 1407-1411.
[12]. Ching-Yin Lee, "Effects of unbalanced voltage on the operation performance of a three-phase induction motor", IEEE Trans. on Energy Conv., vol. 14, No. 2, pp. 202-208, Jun. 1999.
[13]. M. E. Balci, M. H. Hocaoglu, A. Koksoy, O. Ozturk, and B. Dursun, "A fixed speed induction generator model for unbalanced power flow analysis," in Proceedings of International Conference on Harmonics and Quality of Power, ICHQP, 2014, pp. 209–213.
[14]. P. Pillay, P. Hoftmann, M. Manyage, "Derating of induction motors operating with a combination of unbalanced voltages and over or under voltages", IEEE Trans. Energy Conv., vol. 17, No. 4, pp. 485–491, Dec. 2002.
[15]. A. Jalilian and R. Roshanfekr, "Analysis of three-phase induction motor performance under different voltage unbalance conditions using simulation and experimental results," Electr. Power Components Syst., vol. 37, no. 3, pp. 300–319, 2009.
[16]. M. S. Kurt, M. E. Balci, S. H. E. Abdel Aleem, "Algorithm for estimating derating of induction motors supplied with under/over unbalanced voltages using response surface methodology," J. Eng., vol. 2017, no. 12, p. 627–633(6), Dec. 2017.
[17]. J. M. Apsley, "Derating of multiphase induction machines due to supply imbalance," IEEE Trans. Ind. Appl., vol. 46, no. 2, pp. 798–805, 2010.
[18]. M. Anwari and A. Hiendro, "New unbalance factor for estimating performance of a three-phase induction motor with under-and overvoltage unbalance," IEEE Trans. Energy Convers., vol. 25, no. 3, pp. 619–625, 2010.
[19]. G. K. Singh, "Power system harmonics research: A survey," Eur. Trans. Electr. Power, vol. 19, no. 2, pp. 151–172, Aug. 2007.
[20]. P. K. Sen, H. A. Landa, "Derating of induction motors due to waveform distortion", 36th Annual Petroleum and Chemical Industry Conference, San Diego, CA, USA, pp. 29-34, 1989.
[21]. C. Y. Lee and W. J. Lee, "Effects of nonsinusoidal voltage on the operation performance of a three-phase induction motor," IEEE Trans. Energy Convers., vol. 14, no. 2, pp. 193–200, 1999.
[22]. G.K. Singh, "A research survey of induction motor operation with non-sinusoidal supply wave forms", Electr. Power Syst. Res., vol. 75, no. 2–3, pp. 200-213, 2005.
[23]. Y. Amirat, M.E.H. Benbouzid, B.Bensaker, R.Wamkeue, "Generators for wind energy conversion systems: state of the art and coming attractions", J. of Electrical Syst.,vol. 3, no. 1, pp 26-38, Mar. 2007.

[24]. Matlab/SIMULINK SimPowerSystems Documents, accessed online from http://www.mathworks.com/help/physmod/powersys/getting-started-with-simpowersystems.html, May 2017.
[25]. J. Dixon, L. Moran, J. Rodriguez, and R. Domke, "Reactive power compensation technologies: State-of-the-art review," Proc. IEEE, vol. 93, no. 12, pp. 2144–2164, 2005.
[26]. T. J. E. Miller, "Reactive power control in electric systems", Wiley-Interscience; 1st edt, 1982.
[27]. S. Y. Lee, C. J. Wu, W. N. Chang, "A compact control algorithm for reactive power compensation and load balancing with static var compensator", Electr. Power Syst. Res., vol. 58, no. 2, pp. 63-70, 2001.
[28]. S. H. E. A. Aleem, M. T. Elmathana, and A. F. Zobaa, "Different design approaches of shunt passive harmonic filters based on IEEE Std. 519-1992 and IEEE Std. 18-2002," Recent Patents Electr. Electron. Eng., vol. 6, no. 1, pp. 68–75, 2013.

BIBLIOGRAPY

Alp KARADENİZ received B.Sc. degree from Eskişehir Osmangazi University (2012), M.Sc.degree from Balikesir University (2015), Turkey. He is a Ph.D. student at Balikesir University since 2015. During 2012-2013 he was a (Control Theory) Master Student at Middle East Technical University, Turkey. Since 2014, he has been with the EEE Dept. of Balikesir University, Turkey. He is working in the field of electric machines, power system analysis, wind power, PV systems and hybrid power systems.

ICENS 4TH INTERNATIONAL CONFERENCE ON ENGINEERING AND NATURAL SCIENCE
2-6 May 2018 KIEV UKRAINE

E-Learning at Work

Volodymyr Boublik[1]

Abstract

Author's experience in teaching software engineering and computer programming based on modern e-learning tools has been summarized. A short historical overview of the problem in the context of distance and blended learning has been suggested. Special interest issues which need more precise solutions have been pointed out. These are calendar and enrollment, forming academic groups, team work, tracking student activities, students review students, antiplagiarism testing and evaluation, internship support.

Key words: distance and blended learning, e-learning, ILIAS, LMS, MOODLE, OpenUSS.

1. INTRODUCTION

Formally the modern e-learning exists for about twenty years. In fact, the phrase "e-learning" was first formally introduced in November 1999 at the TechLearn Conference at Disneyworld by Elliott Masie who was later awarded the number one position on E-learning Industry's Movers and Shakers List in 2017. E-learning as a branch of teaching and learning technology is less than 20 years old. But it is based on approaches which have much longer history and solid roots. There are two aspects in modern e-learning. These are indirect contacts between teacher and student also known as distant education and different kind of technical assistance. As an approach distance education is exactly contemporary with the Babbage machine.

2. PRE-HISTORY

Distance learning started in 1840 as Sir Isaak Pitman in Great Britain introduced education via correspondence. Assignments were distributed to students per post and in the same way they sent their home works. As far as technical assistance is concerned the automated testing began in 1920 as Sidney Pressey invented a mechanical testing machine. By 1936, there were nearly 700 devices patented for educational uses [1]. The way from mechanical testing to programmed teaching took another 30 years and was introduced by B.F.Skinner in the middle of 50-s. Teaching material was divided into small chunk each of them concluded with questions which should be answered by students before proceeding. Moreover, a teaching machine was developed to administer the execution of programmed learning process.

New important movement in programmed learning was inspired by computers created in the middle of the 20th century. Eventually it became clear that computers are the best teaching machines. In the middle of 40-s computers appeared in USA ENIAC Electronic Numerical Integrator and Calculator, University of Pennsylvania,1943 and in UK Alan Turing's Automatic Computing Engine, National Physical Laboratory, London, 1945. Leaving besides USA and UK let us dwell upon the contribution of Kyiv design engineers, and in the early 50-s over the continental Europe. MESM computer, the first universally programmable electronic vacuum tube computer in the Soviet Union, was created in Kyiv, Feofania at Institute of Electrotechnology Ukrainian Academy of Sciences, headed by Prof. S.A.Lebedev. MESM became operational on November 11, 1950. It is worth mentioning that MESM was an electronic vacuum tube computer as Swedish BARK "Binary Arithmetic Relay Calculator" became operational on April 28, 1950 and Zuse's Z4 which was delivered to ETH Zurich on 12 July 1950 were both relay based machines.

In 1957 the Computing Centre was created in Kiev which was later reorganized in 1962 into the Institute of Cybernetics, a leading research institution of the whole country. Parallel to the development

[1] *National University, Kyiv-Mohyla Academy, boublik@ukma.kiev.ua*

computer hardware and software systems, the Institute leaded by Prof. Victor Glushkov provided research in the development and application of teaching machines and programmed learning. A special research team headed by Prof. Kateryna Yuschchenko, Ukrainian Ada Lovelace, developed programmed learning approach for teaching computer programming. Their programmed training workbooks for the most popular programming languages of that time such as FORTRAN and COBOL were widely distributed.

3. TV TEACHING

Parallel to researches in programmed teaching TV learning programs started in many countries on different educational levels with courses for students at secondary schools, vocational training and distance courses for adults. Harvey White, the Professor of Physics at University of California at Berkeley was awarded a grant from Ford Foundation to produce a course consisting of 163 lessons in physics to be broadcasted at PBS station Pittsburgh WQED. Starting with more than 100,000 students from thousands of general school classes throughout the country enrolled in the 1957-1958 academic year, the next year due to the start of Sputnik era motivated more than 150 TV stations all over the world to broadcast the course for millions of students involved [2]. This course has already demonstrated a huge level of scalability and high productivity of teachers. Ukrainian television also used this approach in the late 60-s and Kyiv University organized a very productive feedback channel involving university students to check and evaluate home tasks which were sent to the TV station per post.

4. LEARNING MANAGEMENT SYSTEMS

But a real paradigm shift in programmed training was due to personal computers, their graphical interface, and computer networks. Apple and IBM PC proved in the middle of 70-s the usability of computers for didactical purposes. Many educational projects were launched, mostly in mathematics and sciences. Teachers started programming their courseware on their own. The new innovative approach to teaching might lead to substitution of teachers as a whole. At the end of 90-s, learning management systems (LMS) were introduced. Universities and software industries started the development of their LMSs. The most known pioneer system was Blackboard, which provided a complete solution for course management including exchange of learning contents, testing, communicating, progress tracking, and many more. The turn of the century was a peak of enthusiasm in e-learning. Though there were some critics stating that e-learning introduces nothing innovative but the same teacher centered approach. Another side claimed that teachers and trainers would soon lose their jobs. Industries started using e-learning to cut the costs for introductory training or advanced and further training for their employees. Many universities organized distance online degree programs. The UK Open University is the best known among them. But the main points of interest which will be discussed in this paper are the ways of e-learning support for enhancing the quality of education at regular universities.

5. NAUKMA DEVELOPMENT

The Faculty of Informatics has been gradually getting involved into e-leaning movement since almost last 20 years of this history.

The first step was connected with the development of electronic publishing multimedia approach based on networked facilities. Two chairs Multimedia System Chair and Network Technologies Chair were established in the course of a TEMPUS EU-project “Human Resource Development for Publishing in Ukraine”. The partners of the project were Oxford Brookes University, University of Applied Sciences HTWK Leipzig, National University „Kyiv-Mohyla Academy“ and Ukrainian Academy of Printing. Special courses for electronic and Web-publishing, multimedia, computer graphics and networks were developed and successfully integrated into academic curricula. Academic staff was growing together with students and a sound part of academic staff at the faculty were students at that time. First electronic learning materials and numerous student presentations were developed. The recognition of success was Grand Prix at the Europe wide student competition “Join Multimedia”.

The next step consisted of another TEMPUS EU-Project 2003-2006 “Electronic Multimedia Resource Centre, Ukraine (eMeReCU)” [3] with participation of University of Applied Sciences HTWK Leipzig, National University „Kyiv-Mohyla Academy“, National University „Ostroh Academy“, ABi Associates Ltd London, International Book and Media Agency IBA Berlin. A platform was developed

where electronic learning materials were stored and used national wide. Teachers and students were able to create their own portfolios available at any time from any place.

At the same time the faculty started to distribute ideas of e-learning in Ukraine not only at universities but also among high schools, first of all schools belonging to the Academy network (TEMPUS EU-Project “InterCollegia: Interregional IT-Training Courses for Kyiv-Mohyla Collegia Network” 2005-2008), schools for students with special needs (TEMPUS EU-Project “EduVisIm: Adaptive Information and Communication Technologies for Education of Visually Impaired Students in Ukraine” 2006-2009) [4], as well as to remote areas in the Middle Asia (TEMPUS EU-Projects “InterSCAN: International IT-Training Courses for ShifoCom Secondary Schools Academic Network” in Tajikistan, or “EU-TraceFer: European-Uzbek-Training Centre for Vocational Education Teachers in Ferghana” in Uzbekistan). An impressive cooperation network of European, Ukrainian and Asian universities was created in the course of these projects.

6. ILIAS SYSTEM

Now comes the time to find the universal all-over solution. A very interesting approach was used at Helmut Schmidt University of Hamburg better known as University of the Federal Armed Forces. The University is oriented on military personnel aiming at civil professions after their retying from the army. The main problem of this category of students is a very big gap between graduation from the secondary school and beginning higher education. In order to assist their self-paced study an LMS ILIAS (Integriertes Lern-, Informations- und Arbeitskooperations-System German for “Integrated Learning, Information and Work Cooperation System”) was developed at the University of Cologne partially supported by the German Federal Ministry of Defense [5]. In fact, ILIAS became one of the first practically used university management systems. A prototype was developed since the end of 1997 as part of the VIRTUS project at the University of Cologne. On November 2, 1998, version 1 of the learning management system ILIAS was published and offered at the Faculty of Business Administration, Economic and Social Sciences of the University of Cologne. Due to the growing interest of other universities, the project team decided in 2000 to publish ILIAS as open source software under the GPL. Between 2002 and 2004, a new ILIAS version was completely redesigned and named "ILIAS 3". In 2004, it became the first open source LMS to achieve full Shareable Content Object Reference Model (SCORM) compliance 1.2. SCORM 2004 was achieved with version 3.9 in November 2007. Since 2006 Ukrainian localizations have been developed and introduced at the National Taras Shevchenko University in Kyiv.

There is one single point to notice: ILIAS needs organization, and organization is expensive. In fact, ILIAS needs special maintenance units and specially trained personnel, which is not always available. Today, there are only about 200 registered institutions using the ILIAS system. That is why another platform became a leader on e-learning market. That is a MOODLE system (Modular Object-Oriented Dynamic Learning Environment) which possesses now more than 100 thousand registered sites in more than 200 countries.

7. MOODLE

MOODLE is simply a course management system, which does not pretend to cover the whole university management as ILIAS does. MOODLE allow to create private customized sites for communication between teachers and students. It is able to extend and tailor learning activities with community centered plug-ins. The Faculty of Informatics at National University “Kyiv-Mohyla Academy” made its decision in favor of MOODLE practically as its own private initiative. Today the faculty offers 188 curses of its own stored on distedu portal powered by MOODLE. Other faculties are slowly joining us with 58 courses hosted at our portal.

Unfortunately, the faculty alone was not able to maintain a complete university management system like OpenUSS, developed at the University of Munster. As Prof. Victor Glushkov suggested in the middle of 70-s, the only way to develop p an automatic control system for any enterprise is to build a unique all-over solution instead of a set of partial solutions for each separate task. In fact, many problems arose from using separate systems operating with the same human resources. Student enrollment, calendar planning, lecture schedule, content management is in competence of different offices with all possible contradictions and overlapping. Besides that, there are some problems dealing with insufficiency of MOODLE platform for specific needs of the faculty. First of all, the subject area of computer programming and software development needs some special tools which not always easy

integrated into MOODLE system. That is why some teachers decided to develop LMS on their own as for example e-Xplore Technical English system developed at the Leipzig University of Applied Science.

There is no need to discuss the advantages of the MOODLE system. It can be successfully used in classes and outside of them implementing the idea of blended learning. 7/24 availability, forums, mailing, learning materials, tasks etc. are its well-known advantages. Let us consider some of the problems which might be faced under nearer consideration. Some of them have been solved, other are still waiting for their solution.

7.1. Calendar and enrollment

Once you've planned your course on a weekly basis for the current term, the students get enrolled and the course begins. The next year another starting point should be set. But all starting and ending points for student assignments remain from the previous year. Exactly as some students who have been enrolled before and have completed the course remained enrolled. So, additional information from the dean office concerning eligibility of students enrolled is needed.

7.2. Forming academic groups

If you have a big student contingent (over a hundred students inside of a particular course) you can split them in groups. Normally, we have 5-10 groups in particular subject with a team of teachers working with them. Again, every teacher forms one's group or groups and there is no coherency with the dean office point of view. Some students are left outside of any group, and you are not aware if they are students of current or previous year.

7.3. Team work

One of the advanced modern study technologies consist of wide exploration of student team work throughout the study. A special TEMPUS EU-Project "ITSoftTeam: Redesigning Ukrainian IT curricula by introducing team -oriented modules in Software Engineering" [6] has concentrated on this subject. But MOODLE provides no team working facilities. Special software has been developed to introduce team work in software development process [7]. Another issue deals with creating extra-curriculum communities, some kind of special interest group which also has been created and launched outside of MOODLE http://oop.in.ua/.

7.4. Tracking student activities

MOODLE gives standard information concerning access permissions of particular student to each course unit. But what MOODLE does not control, is the content of these activities. Just by tracking the MOODLE log you cannot get information on whether a student has uploaded one's work or a forum post etc. You are also not able to track student attendance to the classes and restrict their access to tests outside of the class.

7.5. Students review students

Another important direction of software development deals with code review. Normally this is a function of a teacher. But students also should be able to read someone else's source code, test and evaluate it and express their own opinion concerning its quality and possible ways of enhancement. Again, special MOODLE plug-in has been developed to tackle the problem. But one step is still missing. It is the ability of a reviewee to access the review, and ability of a reviewer to access the answer [8]. All these problems are determined by the consequences of the role policy realized in MOODLE: each student has access only to one's own contribution.

7.6. Antiplagiarism

As all students' home work in a form of archived software projects is stored in MOODLE repository, there is a possibility to compare them for uniqueness and find out similar code not only among projects of the current year, but among the entire MOODLE repository. This solution represents some form of an "anti-copy-paste"' policy.

7.7. Testing ad evaluating

Testing and evaluating of students' projects composes a big part of teacher's activities. Special software has been developed to pull each archived project from the MOODLE repository, extract it from the archive, launch a corresponding programming system, run specially prepared tests and suggest an evaluation note [9].

7.8. Tracking grade

MOODLE provides the whole grade information concerning students enrolled in the course. But University ordered format demands filling them in other paper forms.

7.9. Internship support

Internship is an activity outside of MOODLE, which still needs support from e-learning platform. Internship announcement can place their calls for applications; even suggest their own introductory courses attract students interest in internship. Vice versa students can also place their applications. A special Web-portal has been developed to support these activities in the course of DAAD project "Efficient placement of graduates and interns across university-wide databases" http://opplog.com.ua/. It would be a good idea to communicate this portal with MOODLE in order to export the best student projects stored within the system repository to potential employers.

8. CONCLUSION

The items listened above do not cover all aspects of e-learning process. Psychologists, teachers, software engineers, together with experts in different subject areas should combine efforts to outline horizons of future e-learning development. But for the time being , as a conclusion, it can be stated out that in spite of numerous shortcomings, a very positive effect has been achieved and it is impossible to imagine classes in computer programming without MOODLE system. To the conclusion it would be appropriately to recall a part of discussion of Prof. Richard Feynman, Nobel-Prize-Winner, with the Japanese ambassador [10]. Feynman asked: "How Japan had developed itself so rapidly to become such a modern and important country in the world?" The answer was "The people of Japan believed they had only one way of moving up: to have their children educated more than they were. Because of this tendency to learn things all the time, new ideas from the outside would spread through the educational system very easily." By investing both funding and human resources in education, many social and technological problems would be successfully solved.

REFERENCES

[1] Ludy T. Benjamin, Jr. A History of Teaching Machines, American Psychologist, September 1988, Vol. 43, No. 9, 703-712
[2] Harvey Elliott White, Physics: Berkeley, University of California: In Memoriam, Calisphere,1989, pp. 202-205, http://content.cdlib.org/view?docId=hb4p30063r&brand=calisphere
[3] V.Boublik, M.Glybovets, EMERECU — TEMPUS project of creating electronic multimedia resource of educational resources for Ukraine, Academic Records, Pedagogic sciences, 43, 2006, Mykolaiv, pp. 194-195
[4] V.Boublik, M.Glybovets, K.Haenssgen, Expectations and Outcomes of Interregional IT Training for Teachers. Informatics Education: Contribution across the Curriculum, The 3rd International Conference ISSEP 2008, Selected Papers, Poland, Torun, 2008 July 1-4, pp. 108-116
[5] V.Boublik, W.Hesser, E-Learning: Challenges and Perspectives, NaUKMA Academic Records, Computer Science , 36, 2005, pp.58-65
[6] V.Boublik, A.Afonin, S.Borozennyi, Some peculiarities in implementing educational team development of software system, NaUKMA Academic Records, Computer Science, 86, 2008. – pp.73-78
[7] V.Boublik, A.Davydenko, Collaborative methods for e-learning, NaUKMA Academic Records, Computer Science, 190, 2016 pp. 41-46
[8] V.Boublik, N.Drozdovych, Development of collaborative learning environment, NaUKMA Academic Records, Computer Science, 138, – Kyiv, 2012. – pp..76-80
[9] V.Boublik, Towards e-learning for computer programming, NaUKMA Academic Records, Computer Science, 151, – Kyiv, 2013. – pp. 112-115.
[10] Ralph Leighton and Richard Feynman, Surely You're Joking, Mr. Feynman, W.W.Norton, 1985, 322 p.

ICENS 4TH INTERNATIONAL CONFERENCE ON ENGINEERING AND NATURAL SCIENCE
2-6 May 2018 KIEV UKRAINE

Investigation of Flood Risk for Istanbul Gürpınar Stream

Ali Cosar[1], Erdal Kesgin[2], R. İlayda Tan[3], H. İbrahim Demirel[4]

Abstract

Meteorological data with field characteristics and master plans of the site should be well considered for flood risk managements. In this study, flood planning and risk analysis were investigated on the critical cross sections of Gürpınar Stream during flood conditions. These cross sections were considered by Istanbul Water and Sewerage Administration (ISKI). In addition, flood discharges for critical cross-sections were determined with considering Synthetic Unit Hydrograph (SUH). Water levels during flood in the critical sections were simulated with considering flood discharges using DHI MIKE numerical model. This study aims to investigate the flood risk analysis for Gürpınar Stream in İstanbul with the determination of the flood areas.

Keywords: *Flood, Synthetic Unit-Hydrographs (SUHs) Method, Mike*

1. INTRODUCTION

In recent years, damages caused by floods increase as a result of rapid urbanization and industrialization. Flood in rivers is defined as the overflow of the rivers and spreading flows over the adjacent land, called a floodplain that causing damage to the surrounding [1]. The flood risk depends on meteorological conditions and the geological characteristics of the affected area. Uncontrolled urbanization activities without appropriate flood defences, increase the flood risks. In addition, inappropriate development around flood plain, potential impacts of climate change (such as increasing frequency of extreme rainfall events), changing river morphology due to dredging on many rivers are the main reasons for flood disasters

In recent decades urban and agricultural expansion and intensification, often onto historic floodplains, has resulted with the flood disaster. The areas have the risk of flood damages within the certain time periods. Intensive urbanization around these areas also cause damages on infrastructure systems. Flood damages can be caused of life and property losses because of the flood waters and the sediments carried by these floods. Flood control is the work that to reduce or totally prevent effects of flood damage. Flood control systems based on flood protection within acceptable costs considers the occurrence of the largest flood discharge while designing of a structures. Regions around river, especially in dense urban areas, are extremely important in terms of flood planning study without uninterrupted city life. Floods are major disasters that have negative effects on social life and economy. Turkey has the impact of disasters such as earthquakes, floods and forest fires almost every year. In recent years, Turkey has huge losses on human life and property due to floods. Increasing frequency of extreme rainfall due to the climate change causes great numbers of floods and droughts around the world.

In addition, today increasing uncontrolled urbanization activities are the main causes of floods. Intensive urbanization with numerous structures also changes rainfall runoff and almost all of the precipitation flows without mixing into groundwater. Most of the agricultural areas located at the upper part of the river basins are

[1] *Corresponding author: Yildiz Technical University, Department of Environmental Engineering, 34220, Esenler/İstanbul, Turkey.* cosar@yildiz.edu.tr
[2] *Yildiz Technical University, Department of Environmental Engineering,* ekesgin@yildiz.edu.tr
[3] *Yildiz Technical University, Department of Environmental Engineering,* itan@yildiz.edu.tr
[4] *Batman .University,* ibrahimdemirel@gmail.com

used inappropriate, which cause loss of the natural vegetation and higher water levels in the river. This situation causes the flood events with other factors [6].

The design of the flood defence structures to be built for flood protection is determined by the usage status of flood calculations. The knowledge of the peak discharges of the flood could be adequate for the design of a channel or berm construction, while volumes should be known for the flood detention dam and weir project as important criteria. For this reason, the intended design of the work should be well considered according to its aim [7].

This study calculates the peak discharges of flood for time periods using different Synthetic Unit Hydrographs for Istanbul Gürpınar Stream.

2. MATERIALS AND METHODS

Life and property losses are higher, especially in developing and crowded cities due to floods. In order to control the floods in river such places in İstanbul and determine the dimensions of the hydraulic structures for flood defence, it is necessary to identify the flood deflections that may occur. Generally, in the calculation of the flood discharges;

- Observations of flood discharges.
- Rainfall precipitation observations and generating unit hydrographs of floods
- Calculation of floods discharges with the help of empirical formulas etc., three different methods are used [2].

Hydrograph shows the time-dependent variation of the rate of flow (discharge) in a river section. Flood hydrograph shape varies according to the characteristics of rainfall and drainage area. Since the drainage field characteristics are assumed to be constant, similar hydrographs are expected to be obtained from similar precipitations [3]. A unit hydrograph is a hydrograph produced by a precipitation overflow that occurs at a unit height during a given period of time in a drainage field. In this way, by analyzing the various flood hydrographs for the same flow period, the flood hydrograph can be obtained by a known amount of precipitation with the help of known unit hydrographs. Precipitation time, changes in rainfall intensity, size of drainage area, are the factors affecting the shape of the hydrograph. Another factor affecting the shape of the hydrograph is the distribution of rainfall over the drainage area [4]. Hydrograph tends to reach and decline faster from the peak value when the center of the precipitation is close to the downstream section. If the center of the precipitation is close to the upstream, due to the flood routing, the peak is smaller and the transition is smooth. However, the rise and fall in unit hydrograph is slower (Figure 1).

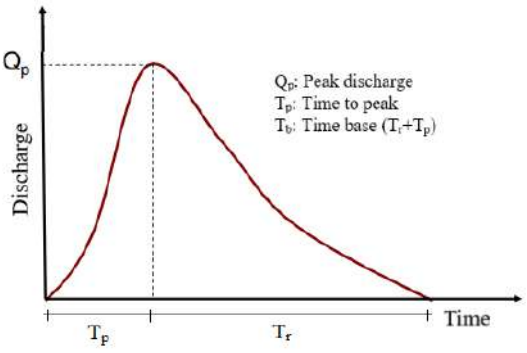

Figure 1. Unit hydrograph

Unit hydrographs can be applied for drainage areas up to 5000 km^2. Areas larger than this value should be examined by dividing the drainage area into smaller areas. This rule is based depends on the location of precipitation center and its regular form with considering the changes of hydrographs [2]. The unit hydrograph is obtained from hydrological observations or using synthetic methods. The unit hydrograph hydrographs can be drawn according to the data obtained from the observations of precipitation stations. Synthetic unit hydrographs can be calculated by using various synthetic methods such as DSI, Mockus, SCS and Snyder method [5].

In this study, the results obtained by calculating the flood discharges in different return period were calculated using DSI, Mockus, SCS, Snyder synthetic unit hydrograph methods and their results were compared.

2.1. Study Area

Gürpınar Stream is located in Istanbul at the European region. Beylikdüzü is surrounded by Esenyurt in the north, Büyükcekmece in the west and Avcılar in the east. The basin of Gürpınar Stream is located Gürpınar, Adnan Kahveci and Dereagzı districts in Beylikdüzü and Pınartepe districts in Büyükcekmece. Figure 2 shows the general view of the Marmara basin and the location of the study area in detailed.

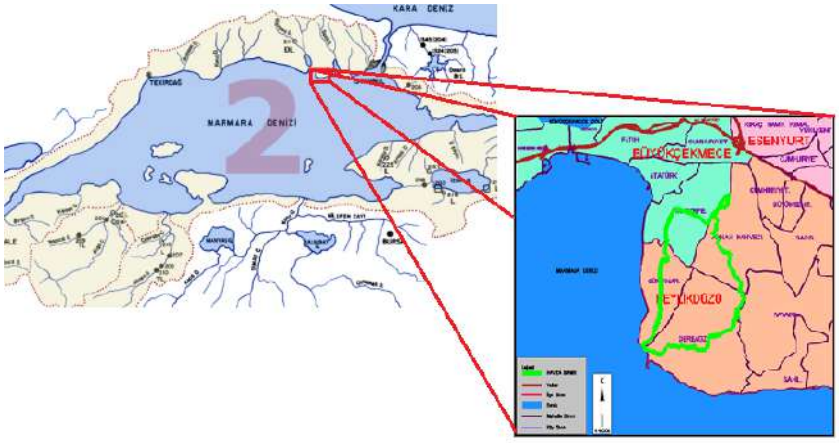

Figure 2. (a) The view of the Marmara Basin (b) location of study area

Satellite maps were used in the study area, obtained from the Water and Sewerage Administration (ISKI). Since these maps are in the ITRF coordinate system, same coordinate system were used in the study. Satellite view of the project area is given in Figure 3.

Figure 3. Satellite image of the project area

Examined maps showed that the study area has higher elevations at the north while lower elevations at the south. These maps also show the urbanized areas around the river. Floodplains of the basin starts from the elevation of 158m and ends at 0m that is the Marmara Sea level. Drainage area of the Gürpınar Stream was calculated as 671.9 ha. Figure 4 shows the location of the Gürpınar Stream where reaches the Marmara Sea. Gürpınar Stream is one of the stream reaches the Marmara Sea with 3.47km and 3.83km with its total and branches lengths, respectively.

Figure 4 The mouth of Gürpinar Stream

The region of Beylikdüzü, which includes Gürpınar Stream, has a population of approximately 220,000 according to data in 2010. According to the master plans for the project area, the basin is mostly covered with residential areas and also includes industrial areas. Thus, the runoff coefficient for the area was taken from the values given by ISKI.

3. RESULTS AND DISCUSSION

The rainfall area in the basin is calculated as 6.72 km^2 from the maps in Figure 3. Precipitation data were obtained from the station located in Florya by the General Directorate of State Hydraulics Works (DSI). The duration of precipitation was taken as the same value of the concentration time in the calculations. Calculated

flood discharges of Gürpınar Stream for different return periods according to the DSI synthetic, Mockus, SCS and Snyder unit hydrograph methods are given in Figure 5, Figure 6, Figure 7 and Figure 8, respectively.

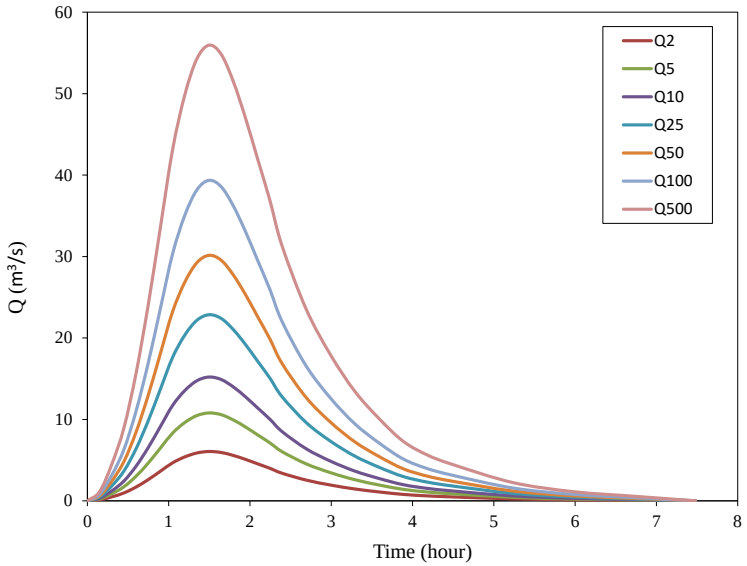

Figure 5. DSI synthetic unit hydrograph for Gürpinar Stream

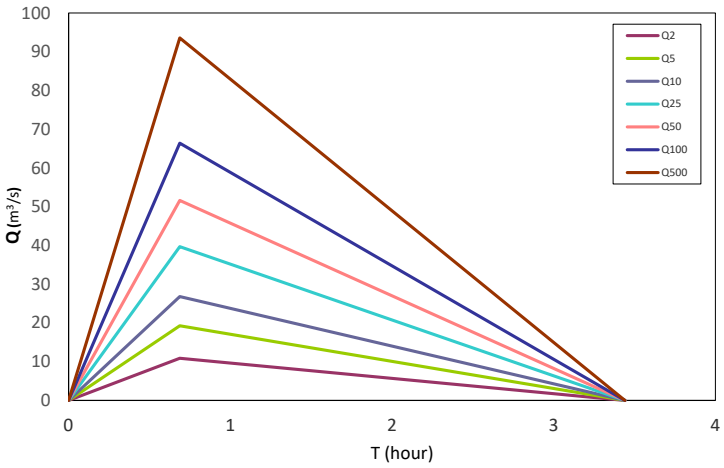

Figure 6. Mockus synthetic unit hydrograph for Gürpinar Stream

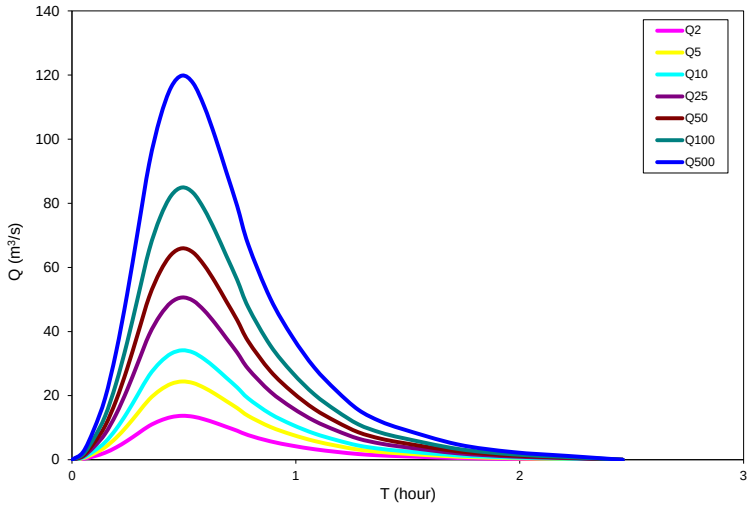

Figure 7. SCS synthetic unit hydrograph for Gürpinar Stream

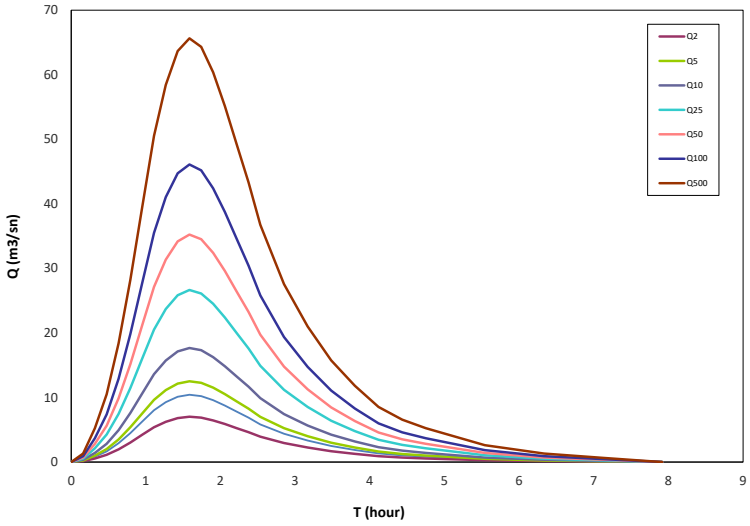

Figure 8. Snyder synthetic unit hydrograph for Gürpinar Stream

The hydrographs obtained by the SCS Synthetic Unit Hydrograph Method are quite different from the hydrographs obtained by the other Synthetic Unit Hydrograph Methods. The hydrographs of the SCS method yielded grater flood discharge for smaller return periods compared to synthetic unit hydrographs determined by DSI, Mockus, SCS and Snyder methods (Figure 9). Thus, DSI, Mockus, SCS and Snyder methods were evaluated in this study. Figure 9 shows the comparisons of the synthetic unit hydrographs for different methods of Gürpınar Basin for the return period of 100 year.

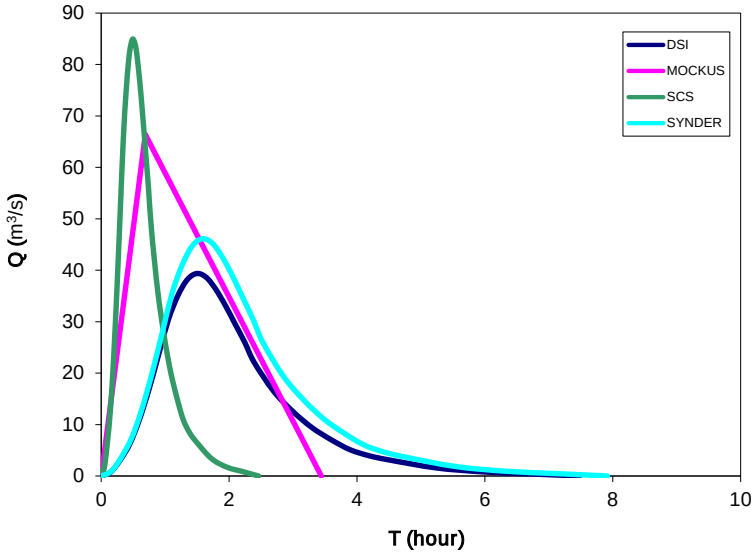

Figure 9. Food hydrographs for Gürpınar Basin with 100 year return period

Table 1 lists the calculated flood discharges with respect to the return periods for different methods. Observations show that the flood is not occurred for 100 year of return period. Figure 10 also shows the discharges for 500 year of return period.

Table 1. Comparison of flood discharges according to different synthetic unit hydrograph methods (m^3/s)

Method	Return Period (year)			
	10	25	100	500
DSI	15.20	22.85	39.36	55.95
MOCKUS	26.84	39.67	66.40	93.58
SCS	34.14	50.62	84.94	119.84
SNYDER	17.68	26.65	46.12	65.65

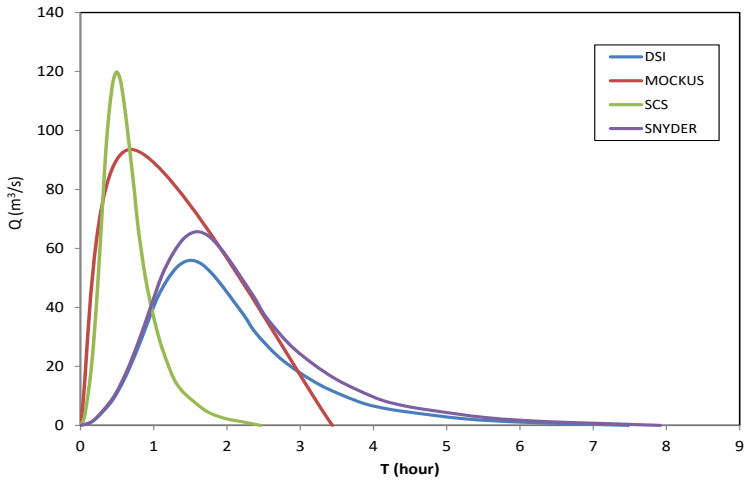

Figure 10. Food hydrographs for Gürpınar Basin with 500 year return period

MIKE Zero numerical model developed by the Danish Hydraulic Institute were used for the determination of flood plains using data obtained from the DSI synthetic unit hydrograph method. For the optimization, different mesh resolutions were tried. An unstructured fine mesh with 8221 triangular elements were used in the numerical model. Boundary conditions are defined as hydrographs obtained for different recurring periods as a function of time and fixed water level for the rivers reaching the sea downstream. Eddy viscosity coefficient is determined as 0.28, manning roughness coefficient is taken as 0.017 in urbanized areas and 0.032 in parks and green areas. The instantaneous water levels (m) obtained for the 500 year return period for Gürpınar as given in Figure 11.

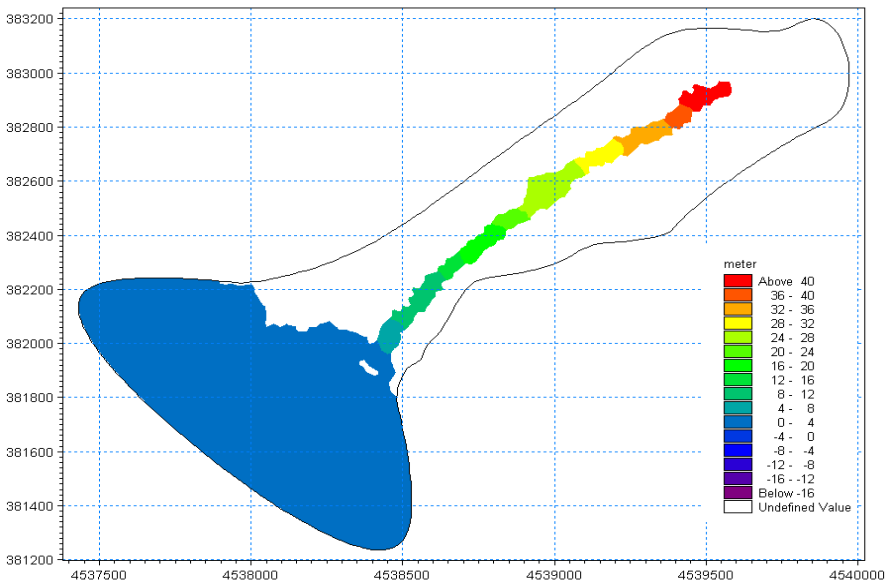

Figure 11. Gürpınar stream's hydrodynamic model mesh (x axis shows longitude (°), y axis shows latitude (°))

4. CONCLUSION

In this study, flood discharge calculations of Gurpinar stream were obtained by using four different methods including DSI, Snyder, Mockus and SCS unit hydrograph methods for different return periods. Following results were obtained:

DSI, Mockus and Snyder synthetic unit hydrographs methods gave similar results.

DSI unit hydrograph method may be more accurate method when compared with Snyder unit hydrograph method because there is more coefficients are taken into consideration in Snyder method than DSI.

In this study area flood discharges are considered using DSI synthetic unit hydrograph method.

Numerical model also showed that the floods for 100 and 500-year return period have no flood risk for trained river sections.

Mockus unit hydrograph method was found with using three different value and it was less sensitive than the other methods. Hence, this method did not preferred for the flood discharge calculations at this study area.

REFERENCES

[1]. Uskay, S., Aksu, S., (2002). "Ülkemizde Taşkınlar, Nedenleri, Zararları ve Alınması Gereken Önlemler", THM, Vol. 420, pp., 4-6.
[2]. Agıralioğlu, N. ve Erkek, C., (1998). "Su Kaynakları Mühendisliği", İstanbul.
[3]. Bayazıt, M., (2003). "Hidroloj", Istanbul.
[4]. Bayazıt, M. ve Önöz B., (2008). "Taşkın ve Kuraklık Hidrolojisi", İstanbul.
[5]. Özdemir, H., (1978). "Uygulamalı Taşkın Hidrolojisi", DSI Press, Ankara.
[6]. ISKI, Istanbul Water and Sewerage Administration. "İstanbul Su Temini, Kanalizasyon ve Drenaj, Atıksu Arıtma ve Uzaklaştırma Master Planı", vol., Section, Yağmur Suyu Drenajı (Kısım A), Istanbul.
[7]. Akdeniz, S., (1998). "Batı Akdeniz Bölgesi Akarsularında Sentetik Birim Hidrograf Metotlarının Uygulanması", Msc. Thesis.

ICENS 4TH INTERNATIONAL CONFERENCE ON ENGINEERING AND NATURAL SCIENCE
2-6 May 2018 KIEV UKRAINE

Treatment of industrial wastewaters with anaerobic membrane bioreactors

Amar Ćemanović[1], Osman Atilla Arikan[1], Abdullah Kizilet[2], Ozer Cinar [3]

Abstract

Anaerobic membrane bioreactors (AnMBR) are wastewater treatment systems with a great potential which has not yet been utilized to its full extent. Membrane bioreactors alone offer significant advantages over conventional activated sludge systems (CAS) - such as low footprint, low sludge production and high treatment efficiency. When compared to aerobic MBRs, AnMBRs offer some additional benefits, the most important being the ability to produce biogas. Additionally, these systems are able to operate under a higher organic loading rate (OLR) and provide important cost savings since aeration is not required. On the other hand, AnMBRs have a higher fouling propensity and hence are generally operated at a lower flux. Research in this technology has experienced an increase in the last two decades, whereby AnMBRs have been utilized for the treatment of a variety of wastewaters and with a focus on different aspects of their operation - mostly treatment efficiency, membrane fouling or biogas production. The advance from lab-scale to pilot- and full-scale systems has been identified as needing special focus in the future. Membrane fouling and its effects on the operation of AnMBRs are the main obstacles that need to be overcome in order for these systems to become widespread. This study offers an overview of the applications of AnMBR technology in the treatment of various types of industrial wastewaters, together with its advantages and challenges that need to be addressed in the future.

Keywords: Industrial Wastewater, Biological Treatment, Anaerobic Membrane Bioreactors, Membrane Fouling

1. INTRODUCTION

In the recent years, membrane bioreactors (MBR) have become more prominent in laboratory scale studies and in full scale wastewater treatment plants. To date, many studies have been conducted using different types of anaerobic reactors in combination with membranes technology. This study evaluates the functionality of the anaerobic membrane bioreactor as an industrial wastewater treatment technology, along with its advantages and drawbacks.

The first application of membrane bioreactor (MBR) technology was in 1969 by Smith et al. [1]. The authors utilized ultrafiltration membranes in a pilot-scale industrial wastewater treatment plant. In the following years, MBR slowly started to be recognized as a viable alternative to conventional systems. The advantages that allowed the MBR technology to thrive are its high treatment efficiency, low footprint (as no settling tank is necessary), pathogen removal potential, low sludge production, potential for water reuse, ease of retrofitting to non-MBR systems etc. [2].

As with all systems, MBRs have certain disadvantages, such as high cost, difficulty operating the system and membrane fouling. Reduction of flux due to clogging of membrane pores over time is an important operational problem. Polymers and microbial products secreted by microorganisms in MBRs accelerate the fouling of membranes, which is the main obstacle that needs to be overcome in order for these systems to become widespread. Various studies have been done to reduce and eliminate the fouling problem. As an example in aerobic processes, the cake layer deposited on the membrane is continuously cleaned with air and as a result fouling is reduced. In anaerobic reactors, the membrane surface can be physically cleaned by recycling of the

[1] *Istanbul Technical University, Department of Environmental Engineering, Maslak/Istanbul, Turkey.*

[2] *Department of Bioengineering and Sciences, Kahramanmaras Sutcu Imam University,46100, Kahramanmaras, Turkey.*

[3] *Corresponding author: Yildiz Technical University, Department of Environmental Engineering, 34220, Esenler/İstanbul, Turkey.* ocinar@yildiz.edu.tr

biogas produced in the reactor [3]. Other common methods to combat fouling include membrane relaxation and backwashing.

Research in this technology has experienced an increase in the last two decades, whereby AnMBRs have been employed for the treatment of various wastewaters and with a focus on different aspects of their operation - mainly treatment efficiency, membrane fouling or biogas production.

2. CURRENT TREATMENT METHODS FOR INDUSTRIAL WASTEWATER

Wastewater emanating from the industry may be treated using different methods, such as physical, chemical, biological or a combination thereof. Physical treatment alone or combined physicochemical methods are most often utilized in the form of pre-treatment. As previously mentioned, certain chemicals are added to initiate coagulation and flocculation of the wastewater particulates, which are then removed by precipitation. Such treatment creates sludge which contains both hazardous matter from the wastewater as well as the chemicals that were added. This presents not only an environmental hazard, which itself requires proper disposal, but also causes additional cost - both for the chemicals added as well as the disposal of the created sludge. Different methods in use include adsorption, ozonation, electrolysis etc., whose main disadvantage is their high cost. Hence, it is generally accepted that biological treatment is the most suitable approach, as long as that the effluent limits can be met.

The parameters predominantly used for industrial wastewater characterization are: COD, BOD, SS (Suspended Solids), DS (Dissolved Solids), color, turbidity, heavy metal content etc. The typical values for COD are in the range of 131 to 17900) [4,5], for pH from 2 to 14 [6,7]), turbidity from 15 to 5700 [8,9]) and often there is a high concentration of color. The diversity of values arises from specificities of the industry in question.

There are many wastewater treatment technologies that are widely used for industrial effluents. The three most prominent technologies are Continuous Stirred Tank Reactor (CSTR), Sequencing Batch Reactor (SBR) and chemical treatment (such as coagulation).

2.1. Continuous Stirred Tank Reactor for industrial wastewater treatment

CSTR is a continuous-flow suspended growth bioreactor, which consists of a completely mixed tank with a wastewater influent stream and a treated effluent containing microorganisms. The wastewater volume in the reactor is fixed and the mixing is adequate to render the concentration for all components uniform throughout the reactor. The effluent is equal in composition to the mixed liquor from inside the reactor [10]. CSTR has many advantages in that it operates in a steady state, is well controllable, has high treatment capacity, large heat transfer areas can be installed etc. In addition, it is particularly suitable for industrial wastewaters as it can tolerate toxic shock loads due to it being completely mixed.

A disadvantage of conventional CSTR systems is a large footprint due to the high volumes of the treatment tank and subsequent settling tank. If the system is aerobic, aeration contributes significantly to the overall operational costs due to the high volume of tanks that need to be supplied with air.

2.2. Sequencing Batch Reactor for industrial wastewater treatment

A fairly new approach for color removal is the use of SBRs [11]. They are a fill-and-draw system (also called batch system) and operate in 5 major phases: fill, react, settle, draw and idle. Their advantage over conventional batch systems is that the sludge performing the treatment is retained from one operation to the next. Further advantages include low build cost, high flexibility and low footprint [12], as all processes happen in the same tank. Flexibility in operation means that every operating cycle can be set up according to specific needs. This is particularly useful for industrial wastewaters, since effluents from different processes can each be treated with different regimes within the same factory.

Significant disadvantages of SBR systems are extreme sludge production and high sludge volume index (SVI) values [13], as well as high levels of maintenance and operator skills that are required.

2.3. Chemical treatment for industrial wastewaters

The most common form of this type of treatment is coagulation. It is performed by the addition of specific chemicals (coagulants) whose function is to neutralize the negative charges on particles, thereby allowing them

to clump together and as such settle at the bottom of the vessel. Many researchers have induced the coagulation of synthetic and real pulp and paper wastewater using various inorganic chemicals (e.g., $FeCl_3$, $FeSO_4$, alum, lime, and $MgCl_2$) alongside components of biological origin [14]. Auxiliary poly-electrolytes are produced by the forced hydrolysis of a simple coagulant, like alum [15].

The process of coagulation is a combination of chemical and mechanical operations and consists of two main stages: (1) fast mixing to disperse coagulant chemicals within the water being treated, and (2) flocculation to band together small particles into well-defined floc by attentive mixing for a prolonged time. The coagulant must be added to raw water and completely dispersed. Commonly used coagulants are mostly salts of iron or aluminum, such as: ferrous sulfate, sodium aluminate etc., but also various polymers [16].

3. MBR SYSTEMS FOR TREATMENT OF INDUSTRIAL WASTEWATER

Membranes employed in MBR systems have a pore size range of 103 - 10-4 µm. With regard to it, the process is called either microfiltration (MF) or ultrafiltration (UF). Another means of categorization of MBR systems is based on the system setup. Namely, the membrane modules may be located in a separate tank (side-stream system) or in the bioreactor tank itself (submerged system). The membrane itself can be in the form of a flat sheet or hollow fibers. If the filtration is performed by a secondary (biological) membrane formed on top of a support material, the technology is called dynamic MBR (DMBR).

All of these variations are an important aspect of wastewater treatment plant operation and design and need to be mindfully chosen based on the needs of the target system. Based on the findings of several studies in the literature about the relative advantages and disadvantages of MBR, DMBR and CAS systems, and overview of their properties is tabulated in Table 1.

Table 1: The comparison of comparatively advantages and disadvantages of MBR, DMBR and CAS

MBR		DMBR		CAS	
Advantages	**Disadvantages**	**Advantages**	**Disadvantages**	**Advantages**	**Disadvantages**
High MLSS	----------	High MLSS	----------	----------	Lower MLSS
Low footprint	----------	Low footprint	----------	----------	Large footprint
Higher volumetric loading	----------	Higher volumetric loading	----------	----------	Lower volumetric loading
Fine control of SRT	----------	Fine control of SRT	----------	----------	Workload for SRT control
----------	Greater operational and process complexity	----------	Greater operational and process complexity	Lower operational and process complexity	----------
Lower sludge production	----------	Lower sludge production	----------	----------	Higher sludge production
----------	Higher capital Low operational costs	Low capital Low operational costs	----------	----------	Higher capital High operational costs
----------	Greater foaming propensity	----------	Greater foaming propensity	Lower foaming propensity	----------
Treated water that reusable	----------	Treated water that reusable	----------	----------	----------
Unlimited by settling due to gravity	----------	Unlimited by settling due to gravity	----------	----------	It is limited by settling due to gravity
----------	High Module Cost	Low module cost	----------	----------	----------
Sample TMP control based on constant flow	----------	----------	Complex TMP control based on constant flow	----------	Indifference
Sample fouling control	----------	----------	Complex fouling control	----------	Indifference
Chemical wash easer applied	----------	----------	Chemical wash not easily applied by taking into account microorganisms	----------	Indifference

Very high physical disinfection performance	----------	Normal physical disinfection performance	----------	----------	Indifference
Affected undirectly by Bulking problem	----------	Affected undirectly by Bulking problem	----------	----------	Affected directly by Bulking problem

MBR and DMBR systems have attracted increasing interest and are becoming more and more favoured over the conventional activated sludge (CAS) system. When comparing CAS, MBR and DMBR reactors, the membranes performing microfiltration (MF) / ultrafiltration (UF) provide excellent solid and liquid separation in the bioreactor, so such systems eventually do not require a secondary clarifier. The higher effluent quality also allows for wastewater reclamation and reuse. MBR and DMBR systems have further advantages such as higher biomass concentration, smaller footprint, lower sludge production and rejection of SS (effluent SS concentration is close to zero) [17]. Their main disadvantage is membrane fouling, but over the years various methods have been developed to minimize and overcome it.

4. ANAEROBIC MBR SYSTEMS FOR TREATMENT OF INDUSTRIAL WASTEWATER

Anaerobic microorganisms are known to grow slower than their aerobic counterparts [18]. Due to the low growth rate, biomass retention is critical for efficient anaerobic treatment. Granular and biofilm-based technologies are being put to use in order to achieve that. The traditional way of obtaining the necessary biomass retention is to ensure that bioreactors operate at high biomass concentrations - therefore, at high organic loading rates. However, under certain conditions such as high salinity or thermophilic temperatures, biofilm and granule formation is not advancing well and a negative effect is observed. AnMBRs can be used to obtain the required sludge retention in unconventional conditions. Such systems work successfully on longer SRTs, maintaining all micro-organisms and allowing them to grow in number. Several research groups have successfully utilized these systems using various conditions and sources of wastewater ([19]-[25]). In most applications, AnMBRs can provide >90% COD removal efficiency. A higher efficiency (>85%) was thus far achieved when treating efflents from the bamboo industry, thin stillage, molasses, slaughterhouses etc. Lower efficiency (>62%) was reported for effluents from pharmaceutical industry, liquid dairy manure, landfill leachate etc. [26].

Anaerobic treatment systems offer several advantages over aerobic systems [27]. Firstly, the operational cost is lower because no energy is spent on aeration. Furthermore, these systems have lower sludge yields and, most importantly, produce methane-rich biogas as a side product. Anaerobic MBRs are especially applicable for strong and highly particulate wastewaters. Currently, however, aerobic treatment is much more widespread, probably due to the complexity of the process control of anaerobic digestion. Moreover, the main drawback of MBR systems in general - membrane fouling - is even more pronounced in AnMBRs due to the small floc size of the biomass [28, 29].

ACKNOWLEDGEMENTS

Author Amar Ćemanović is supported by the Scientific and Technological Research Council of Turkey (Tübitak) through the 2215 Graduate Scholarship Programme.

REFERENCES

[1]. C.V. Smith, D.D. Gregorio and R.M. Talcott, “The use of ultrafiltration membranes for activated sludge separation”, 24th Annual Purdue Industrial Waste Conference, Lafayette, IN pp. 130-1310, 1969.
[2]. C.T.M.J. Frijters, R.H. Vos, G. Scheffer, R. Mulder, Decolorizing and detoxifying industrial wastewater , containing both soluble and insoluble dyes , in a full scale combined anaerobic / aerobic system, Water Res. 40: 1249–1257. doi:10.1016/j.watres.2006.01.013, 2006.
[3]. D.C. Stuckey, Recent developments in anaerobic membrane reactors, Bioresour. Technol. 122: 137–148. doi:10.1016/j.biortech.2012.05.138, 2012.
[4]. G.E Ustun, S.K.A Solmaz and A. Birgul, “Regeneration of industrial district wastewater using a combination of Fenton process and ion exchange-A case study”, Resources Conservation and Recycling, 52, 425-440, 2007.
[5]. A. Rodriguez, G. Ovejero, M.D. Romero, C. Diaz, M. Barreiro and J. Garcia, “Catalytic wet air oxidation of pulp and

paper industrial wastewater using metal supported on carbon nanofibers", Journal of Supercritical Fluids 46, 163-172, 2008.
[6]. W.J Lau, and A.F. Ismail. "Polymeric nanofiltration membranes for pulp and paper dye wastewater treatment: preparation, performance evaluation, transport modelling, and fouling control- a review" Desalination 245, 321-348, 2009.
[7]. D.J Joo,.W.S Shin,.J.H.; Choi, S.J.; Choi, M.C Kim, M.H. Han, T.W Ha, and Y.H.Kim, "Decolorization of reactive dyes using inorganic coagulants and synthetic polymer", Dyes and Pigments, 73, 59-64, 2007.
[8]. Ciabatti, I., Tognotti, F., Lombardi, L., 2010.Treatment and reuse of dyeing effluents by potassium ferrate. Desalination 250, 222e228.
[9]. Bayramoglu, M., Kobya, M., Can, O.T., Sozbir, M., 2004. Operating cost analysis of electrocoagulation of pulp and paper dye wastewater. Separation and Purification Technology 37, 117e125.
[10]. C. P. Leslie Grady, Jr., and Henry C. Lim "Biological Wastewater Treatment: Theory and Applications" 2nd ed. English, Book, Marcel Dekker, 1999.
[11]. I. K. Kapdan and R. Ozturk, "Effect of operating parameters on color and COD removal performance of SBR: Sludge age and initial dye stuff concentration", J. Hazardous Materials, 123, 217-222, 2005.
[12]. R. Ganjesh, G. Balaji, and R. A. Ramanujam, R. A., "Biodegradation of tannery wastewater using sequencing batch reactor Respirometric assessment", J. Bioresource Tech., 97, 1815–1821, 2006.
[13]. D. P., Bernet, D., Nicolas, J., Philipe and R., Moletta, "Effects of oxygen supply methods on the performance of a sequencing batch reactor for high ammonia nitrification" J. Water Env. Res., 72, 195–200, 2000.
[14]. B. H.; Tan, T. T.; Teng, A. K. M Omar, "Removal of dyes and industrial dye wastes by magnesium chloride", Water Res, 34, 597-601, 2000.
[15]. P, Moussas and A. Zouboulis, "A new inorganic–organic composite coagulant, consisting of Polyferric Sulphate (PFS) and Polyacrylamide (PAA)", WaterRes.,;43, 3511–3524, 2009.
[16]. F. R. Spellman, "Mathematics manual for water and wastewater treatment plant operators", 2nd ed., English, Book, Taylor & Francis Group, 2014.
[17]. L. Defrance and M.Y. Jaffrin, "Comparison between filtrations at fixed transmembrane pressure and fixed permeate flux: application to a membrane bioreactor used for wastewater treatment", J. Membr. Sci., 152, 203–210, 1999.
[18]. Y.J. Chan, M.F. Chong, C.L. Law, D.G. Hasell, A review on anaerobic–aerobic treatment of industrial and municipal wastewater, Chem. Eng. J. 155 (2009) 1–18.
[19]. D. Jeison, I. Diaz, J.B. Van Lier, Anaerobic membrane bioreactors: are membranes really necessary?, Electron J. Biotechnol. 11 (2008).
[20]. Z. Huang, S.L. Ong, H.Y. Ng, Feasibility of submerged anaerobic membrane bioreactor (SAMBR) for treatment of low-strength wastewater, Water Sci. Technol. 58 (2008) 1925–1931.
[21]. A. Akram, D.C. Stuckey, Biomass acclimatisation and adaptation during startup of a submerged anaerobic membrane bioreactor (SAMBR), Environ. Technol. 29 (2008) 1053–1065.
[22]. P.J. Van Zyl, M.C. Wentzel, G.A. Ekama, K.J. Riedel, Design and start-up of a high rate anaerobic membrane bioreactor for the treatment of a low pH, highstrength, dissolved organic wastewater, Water Sci. Technol. 57 (2008) 291–295.
[23]. W. Fucks, H. Binder, G. Mavrias, R. Braun, Anaerobic treatment of wastewater with high organic content using a stirred tank reactor coupled with a membrane filtration unit, Water Res. 37 (2003) 902–908.
[24]. F. Meng, H. Zhang, F. Yang, L. Liu, Characterisation of cake layer in submerged membrane bioreactor, Environ. Sci. Technol. 41 (2007) 4065–4070.
[25]. E.R. Cornelissen, S.V. Buggenhout, S.V. Ermen, M. De Smedt, J. Van Impe, J. Koning, Anaerobic treatment of brewery wastewater with an internal membrane bioreactor, Meded. Gent. Fak. Landbouwkd. Toegep. Biol. Wet. 66 (2001) 135–138.
[26]. L. Dvorak, M. Gomez, J. Dolina, "Anaerobic membrane bioreactors—a mini review with emphasis on industrial wastewater treatment: applications, limitations and perspectives." Desalination and Water Treatment 57: 19062–19076, 2016.
[27]. G. Skouteris, D. Hermosilla, P. López, C.Negro, Á. Blanco, "Anaerobic membrane bioreactors for wastewater treatment: A review", Chemical Engineering Journal 198–199 (2012) 138–148.
[28]. D.W. Gao, T. Zhang, C.Y.Y. Tang, W.M. Wu, C.Y. Wong, Y.H. Lee, D.H. Yeh, C.S. Criddle, Membrane fouling in an anaerobic membrane bioreactor: differences in relative abundance of bacterial species in the membrane foulant layer and in suspension, J. Membr. Sci. 364 (2010) 331–338.
[29]. A. Spagni, S. Casu, N.A. Crispino, R. Farina, D. Mattioli, Filterability in a submerged anaerobic membrane bioreactor, Desalination 250 (2010) 787– 792.

ICENS 4TH INTERNATIONAL CONFERENCE ON ENGINEERING AND NATURAL SCIENCE
2-6 May 2018 KIEV UKRAINE

Membrane bioreactors application in textile wastewater treatment

Amar Ćemanović[1], Abdullah Kizilet[2], Ozer Cinar[3]

Abstract

Textile industry is a significant consumer of dyes, with around 50% of dyes produced in the world being textile dyes. Since dye retention is generally less than 50%, most of them are discharged with the wastewater. Such dye-rich textile wastewater is both esthetically unpleasant and harmful to the environment. Current treatment methods most often involve physical/chemical pre-treatment in addition to conventional activated sludge (CAS) treatment in order to achieve the stipulated effluent values. This in turn produces chemical sludge which itself requires proper disposal. Membrane bioreactor (MBR) systems offer better treatment efficiencies combined with a lower sludge production and reduced footprint. Many studies have explored aerobic MBR systems and have reported sufficient COD removal, but insufficient color removal. The most probable cause is the fact that aerobic conditions do not allow for the cleavage of azo-dye molecules, the most common type of dye used in the textile industry. Hence, studies utilizing anaerobic MBR (AnMBR) systems alone or in combination with aerobic MBRs reported satisfactory color removal efficiencies. Additionally, in order to lessen the effect of the commonly encountered fouling problems characteristic for MBRs, some studies applied dynamic MBR (DMBR) systems, which enable higher fluxes together with lower fouling rates. This study offers an overview of the applications of different MBR systems in the treatment of dye-containing textile wastewaters, their advantages and drawbacks as well as perspectives for the future.

Keywords: Textile wastewater, biological treatment, membrane bioreactors, membrane fouling.

1. INTRODUCTION

Textile industry is infamous for its vast water consumption and production of highly colored, strong wastewater. Dye retention in dyeing processes is reported in the range of 2-50% [1] and the unconsumed (reactive) dyes present a significant challenge for treatment systems required to meet strict discharge criteria. The largest class of dyes found in the textile industry are azo dyes, constituting around 70% by weight [2]. Additionally, there are numerous types of chemicals used to enhance dye fixation, such as surfactants and heavy metals, which render the wastewater even harder to treat [3]. Table 1 outlines the main parameters of wastewater produced in the textile industry, with regard to both the type of textile used as well as the process utilized.

Since dyes in water bodies are harmful even at low concentrations, a high level of removal is necessary in order to reduce the effect on the environment to a minimum. However, they are synthesized to be chemically resistant and thus are not readily biodegradable, which can be illustrated by the fact that conventional plants treating municipal wastewater can remove only around 20-30% of color originating from synthetic dyes [4].

[1] *Istanbul Technical University, Department of Environmental Engineering, Maslak/Istanbul, Turkey.*

[2] *Department of Bioengineering and Sciences, Kahramanmaras Sutcu Imam University,46100, Kahramanmaras, Turkey,*

[3] *Corresponding author: Yildiz Technical University, Department of Environmental Engineering, 34220, Esenler/İstanbul, Turkey.* ocinar@yildiz.edu.tr

Table 1: Characteristics of textile wastewater from different processes [3]

Parameter	Fabric type	Desizing	Scouring	Bleaching	Dyeing	Printing
COD (mg/L)	Wool	-	5000 - 90000	-	7920	-
	Cotton	950 - 20000	8000	288 - 13500	1115 - 4585	-
	Synthetic	-	-	-	620	1515
BOD_5 (mg/L)	Wool	-	2270 - 60000	400	400 - 2000	-
	Cotton	-	100 - 2900	90 - 1700	970 - 1460	-
	Synthetic	-	500 - 2800	-	530	590
Color (ADMI)	Wool	-	2000	-	2225	-
	Cotton	64 - 1900	694	153	1450 - 4750	-
	Synthetic	-	-	-	1750	-
Total solids (mg/L)	Wool	-	28900-49300	910	-	-
	Cotton	-	-	2300 - 14400	-	-
	Synthetic	-	-	-	-	150 - 250
	Not specified	7600-42900	-	-	<50000	-
Sulfate (mg/L)	Cotton	-	-	-	1750 - 2690	-
Chloride (mg/L)	Not specified	-	-	90 - 100	26000	-
pH	Wool	-	7.6 - 10.4	6	4.6 - 8	-
	Cotton	8.8 - 9.2	7.2 - 13	6.5 -13.5	9.2 - 10.1	-
	Synthetic	-	8 - 10	-	11.7	-
	Not specified	6 - 8	-	-	-	5 - 8.5
Water usage ($L \cdot kg^{-1}$ fabric)	Wool	-	4 - 77.5	-	40 - 150	280 - 520
	Cotton	-	2.5 - 43	30 - 50	38 - 143	-
	Synthetic	-	17 - 67	-	38 - 143	-
	Not specified	12.5 - 35	-	-	-	20 - 300

2. CURRENT TREATMENT METHODS OF TEXTILE WASTEWATER

Wastewater emanating from the textile industry may be treated using different types of methods, such as physical, chemical, biological or a combination thereof. Physical treatment alone or combined physicochemical methods are most often utilized in the form of pre-treatment. Namely, certain chemicals are added to initiate coagulation and flocculation of the wastewater constituents, which are subsequently removed by precipitation. Such treatment produces sludge which contains both hazardous matter from the wastewater as well as the chemicals that were added. This presents not only an environmental menace, which itself requires proper disposal, but also incurs additional cost - both for the chemicals applied as well as the sludge disposal. Other methods in use include ozonation, adsorption, electrolysis etc. whose main common drawback is the associated high cost. Thus, it is commonly accepted that biological treatment seems to be the most suitable approach, provided that the effluent standards can be met.

The most frequently applied biological treatment method is aerobic biodegradation which, if not complemented by some additional form of treatment, often fails to meet the required discharge parameters. Yurtsever et al. have compared an anaerobic and aerobic system for treating synthetic wastewater containing azo dyes, and reported almost complete color removal using the former, with only 30-50% removal with the latter system [5]. The reason is that aerobic conditions do not enable efficient color biodegradation, so that only partial removal is achieved by adsorption to biomass and/or membrane filtration. Supplementary treatment often involves the use of chemicals which themselves need to be properly removed. Another treatment method relies on anaerobic systems, which are efficient in color removal but in turn yield toxic byproducts.

3. MBR SYSTEMS FOR TREATMENT OF TEXTILE WASTEWATER

The first application of membrane bioreactor (MBR) technology was in 1969 by Smith et al. [6]. The authors utilized ultrafiltration membranes in a pilot-scale industrial wastewater treatment plant. In the coming years, MBR slowly started to gain recognition and popularity, despite its disadvantages which include membrane fouling propensity, difficulty operating the system and high costs. The advantages that allowed the MBR technology to thrive are its high treatment efficiency, low sludge production, low footprint (since no settling tank is necessary), potential for pathogen removal, potential for water reuse, ease of retrofitting to existing systems etc. [7].

Membranes used in MBR systems have a pore size range of 10^3 - 10^{-4} µm. With respect to it, the process is called either microfiltration (MF) or ultrafiltration (UF). Another way to categorize MBR systems takes into

account the system setup. Namely, the membrane modules may be located in the bioreactor tank itself (submerged system) or in a separate tank (side-stream system). Regardless of the mentioned configurations, the membrane itself can be in the shape of a flat sheet or hollow fibers. All of these options are an important aspect of wastewater treatment plant design and operation and need to be thoughtfully chosen based on the specific needs of the system in question.

3.1. Aerobic MBR systems for treatment of textile wastewater

Various studies have explored color removal from textile wastewaters utilizing an aerobic MBR system. Zheng and Liu used an MBR system with a gravity drain and reported 58.7% color removal [8], whereas Brik et al. applied MBR treatment followed by ozonation and attained 93% color removal [9]. Huang et al. employed an aerobic MBR system without post-treatment, and even though the COD removal was satisfactory (80-90%), color removal was only 60-75% [10]. Likewise, Yun et al. reported COD and color removal as 94.8% and 72.9%, respectively [11]. Lorena et al. have directly compared the performance of an aerobic MBR and a conventional activated sludge (CAS) reactor. They reported that COD removal in the MBR was 89-92% as compared to 54-70% in the CAS system, whereas color removal reached 70-73% with the former and only 28% with the latter [12]. These studies suggest that MBR systems, with all its advantages over conventional activated sludge systems, are similarly ineffective in aerobic color removal and hence require additional forms of treatment. As it is known that dyes cannot be degraded aerobically, the presented values of color removal can be attributed to adsorption onto the biomass as well as membrane filtration.

3.2. Anaerobic MBR systems for treatment of textile wastewater

Anaerobic treatment systems offer several advantages over aerobic systems. Firstly, the operational cost is lower since no energy is expended on aeration. Moreover, such systems have lower sludge yields and, most importantly, produce energy-rich biogas as a side product. Anaerobic MBRs are especially suitable for strong and highly particulate wastewaters.

When it comes to anaerobic MBR (AnMBR) systems, Ivanovic and Leiknes reported effective COD and TSS removal from textile wastewater [13], and Saddoud et al. achieved 60% and 30% nitrogen and phosphorus removal, respectively [14]. However, very few studies were conducted on color removal in textile wastewater. In one of them, a decrease in color content of up to 99.2% from synthetic textile wastewater was reported [15]. However, the authors applied relatively low membrane fluxes (~2 LMH) and did not present values for aromatic amines in the effluent. In another study, 86% color removal was achieved, but the authors also did not look into the amount of aromatic amines produced [16].

3.3. Anaerobic-aerobic sequential systems for textile wastewater treatment

As mentioned previously, aerobic treatment alone is ineffective in color removal processes due to the nature of the azo bonds characteristic for azo dyes. Anaerobic conditions allow for the cleavage of the azo bonds since azo-dye molecules act as the final electron acceptor in the microbial electron transport chain. Even though high levels of decolorization are achieved under anaerobic conditions, aromatic amines are created as side products. These compounds constitute a great health hazard due to their known toxicity and carcinogenicity, but fortunately can be entirely biodegraded under aerobic conditions. Hence, complete biological treatment is most effective by utilizing a two-stage anaerobic-aerobic system ([17]-[21]).

When it comes to anaerobic-aerobic sequential systems, research has been conducted on various configurations, but only a very small part involves MBRs. For instance, one research group employed a sequential system utilizing an anaerobic SBR coupled with an aerobic MBR reactor, and reported 83.7 % color removal along with 97.5 % COD removal ([22]-[24]).

Yurtsever et al. utilized a sequential anaerobic-aerobic MBR system for the treatment of textile wastewater, and reported almost complete decolorization in the anaerobic reactor, with some level of recolorization in the aerobic reactor ([25]-[27]).

3.4. Hybrid systems combining MBR with other methods for treatment of textile wastewater

Yan et al. have utilized a hybrid coagulation/MBR system for treatment of real textile dyeing wastewater, whereby the coagulant used was poly-aluminum chloride (PACl). The COD and total phosphate removal were

reported as 90% and 97%, respectively [28]. Furthermore, Qin et al. combined internal microelectrolysis (IE) with an aerobic MBR and achieved very high degradation of brilliant blue dye in wastewater [29]. Grilli et al. employed NF filtration as a post-treatment for a UF MBR system, and noted an increase in COD and color removal as compared to the initial 90-95% and 70%, respectively. In addition, such post-treatment allowed for the effluent to be reused in textile processes [30].

De Jager et al. evaluated both NF and RO as post-treatment of MBR effluent. The results indicated an increase in color removal from 28.6% in the standalone system, to 98.3% and 97.2% in the system with NF and RO post-treatment, respectively [31]. Feng et al. combined Fenton oxidation with MBR for the removal of Reactive Blue 4 (RB4) dye. Fenton oxidation is a chemical treatment method which is able to, among others, decolorize dyes effectively. The authors reported TOC and color removal values as 88% and 90%, respectively [32].

3.5. Membrane fouling in MBR systems

The biggest drawback of the MBR technology is membrane fouling. It is defined as the decrease in permeability due to the occlusion od membrane pores. This is measured either as a decrease in flux (if system is operated in constant-TMP mode) or increase in TMP value (if system is operated in constant-flux mode).

According to the location where fouling occurs, it can be categorized into internal pore fouling or cake layer deposition on the membrane surface. Another categorization is based on the possibility to remove membrane fouling. Hereby, the two principle types are reversible and irreversible fouling. Reversible fouling may further be divided into recoverable and irrecoverable, whereby the former can be removed by simple means, i.e. physical cleaning, backwashing etc., whereas the latter requires the use of chemicals [33].

Fouling propensity is a function of various factors, which can be broadly grouped as: operating conditions of the system; characteristics of: the biomass, the wastewater, the membrane. When it comes to control of membrane fouling, there are two general ways to approach the issue: fouling prevention and membrane cleaning.

Prevention of membrane fouling encompasses various methods. The most commonly carried out method is pre-treatment of the influent wastewater. Another method is close control of parameters in the system, especially the flux level. Some advanced techniques involve electricity-based methods as well as methods in the domain of biological control.

Membrane cleaning is mostly performed physically and/or chemically, or as a combination thereof (such as chemically enhanced backwashing).

3.6. Dynamic MBR systems for treatment of textile wastewater

A variation on MBR systems which is characterized by a lower fouling rate are dynamic MBR (DMBR) systems, which employ biological filtration rather than readily available membranes. Namely, the system is initiated with support material having a much larger pore size than MBR membranes. As solids (including microbial flocs, EPSs, SMPs) accumulate on the surface of the support material, they create a cake layer which functions as a dynamic membrane (DM), also called secondary membrane, with a pore size comparable to that of conventional membranes. The advantage of DMs is that they enable higher fluxes coupled with a lower fouling rate, as well as lower membrane cost because different types of woven/non-woven fabrics and meshes can be used as support for the DM [34]. In addition, it is sufficient to remove the cake layer and have a new layer formed as a way of maintenance, instead of completely replacing fouled membranes as in conventional MBR systems [35]. DMBR systems have been successfully employed for textile wastewater treatment with color removal efficiencies reported in the range of 96-99% ([36]-[38]).

4. PERSPECTIVES FOR THE FUTURE

Future work on utilizing MBR technology for textile wastewater treatment should focus on sequential anaerobic-aerobic systems. The biomass separation efficiency that is possible with MBR technology would effectively prevent mixing of the anaerobic and aerobic cultures, thereby ensuring that both communities operate under preferred oxidative/reductive conditions. Moreover, the final effluent quality may even be sufficient for reuse in the textile industry. Development of such systems, optimized for efficiency and low fouling propensity, would be an important step towards increased use of biological treatment in place of the widespread chemical processes in textile wastewater treatment.

ACKNOWLEDGEMENTS

Author Amar Ćemanović is supported by the Scientific and Technological Research Council of Turkey (Tübitak) through the 2215 Graduate Scholarship Programme.

REFERENCES

[1]. C. O'Neill, F.R. Hawkes, S.R.R. Esteves, et al., "Anaerobic and aerobic treatment of a simulated textile effluent." J Chem Technol Biotechnol, 74: 993–999, 1999.
[2]. H. Zollinger, *Color Chemistry—Syntheses, Properties and Applications of Organic Dyes Pigments*, VCH, New York, NY, 1987.
[3]. I. Bisschops, H. Spanjers, "Literature review on textile wastewater characterization." Environmental Technology 24: 1399–1411, 2003.
[4]. S. Judd, B. Jefferson, "The textile industry," book chapter. *Membranes for Industrial Wastewater Recovery and Re-use*, p. 132-158, Elsevier Science, Amsterdam, The Netherlands, 2003.
[5]. A. Yurtsever, E. Sahinkaya, O. Aktas, et al., "Performances of anaerobic and aerobic membrane bioreactors for the treatment of synthetic textile wastewater." Bioresour. Technol. 192: 564–573, 2015a.
[6]. C.V. Smith, D.D. Gregorio and R.M. Talcott, "The use of ultrafiltration membranes for activated sludge separation", 24th Annual Purdue Industrial Waste Conference, Lafayette, IN pp. 130-1310, 1969.
[7]. S. Judd, "The status of membrane bioreactor technology," Trends in Biotechnology, 26, 2, 109 – 116, 2008.
[8]. X. Zheng, J. Liu, "Dyeing and printing wastewater treatment using a membrane bioreactor with a gravity drain." Desalination, 190: 277–286, 2006.
[9]. M. Brik, B. Chamam, P. Schoberl, et al., "Effect of ozone, chlorine and hydrogen peroxide on the elimination of colour in treated textile wastewater by MBR." Water Sci. Technol. 49: 299–303, 2004.
[10]. R.R. Huang, J. Hoinkis, Q. Hu, et al., "Treatment of dyeing wastewater by hollow fiber membrane biological reactor." Desalination Water Treat. 11 (1–3): 288–293, 2009.
[11]. M.A. Yun, K.M. Yeon, J.S. Park, et al., "Characterization of biofilm structure and its effect on membrane permeability in MBR for dye wastewater treatment." Water Res. 40: 45–52, 2006.
[12]. S. Lorena, C. Marti, S. Roberto, "Comparative study between activated sludge versus membrane bioreactor for textile wastewater." Desalination and water treatment 35(1-3):101-109, 2011.
[13]. I. Ivanovic, T.O. Leiknes, "The biofilm membrane bioreactor (BF-MBR) – a review." Desalination Water Treat. 37, 288–295, 2012.
[14]. A. Saddoud, M. Ellouze, A. Dhouib, et al., "Anaerobic membrane bioreactor treatment of domestic wastewater in Tunisia." Desalination 207, 205–215, 2007.
[15]. A. Spagni, S. Casu, S. Grilli, "Decolourisation of textile wastewater in a submerged anaerobic membrane bioreactor." Bioresour. Technol. 117, 180–185, 2012.
[16]. B.E.L. Baeta, R.L. Ramos, D.R.S. Lima, "Use of submerged anaerobic membrane bioreactor (SAMBR) containing powdered activated carbon (PAC) for the treatment of textile effluents." Water Science & Technology, 65 (9): 1540–1547, 2012.
[17]. C. O'Neill, A. Lopez, S. Esteves, et al., "Azo-dye degradation in an anaerobic–aerobic treatment system operating on simulated textile effluent." Appl Microbiol Biotechnol, 53: 249–254, 2000.
[18]. P. Rajaguru, K. Kalaiselvi, M. Palanivel, et al., "Biodegradation of azo dyes in a sequential anaerobic–aerobic system." Appl Microbiol Biotechnol, 54: 268–273, 2000.
[19]. T. Panswad, A. Techovanich, J. Anotai, "Comparison of dye wastewater treatment by normal and anoxic + anaerobic/aerobic SBR activated sludge processes." Water Sci Technol, 43(2): 355–362, 2001.
[20]. D.T. Sponza, M. Isik, "Decolorization and azo dye degradation by anaerobic/aerobic sequential process." Enzyme Microb Technol, 31(1–2): 102–110, 2002.
[21]. S.A. Ong, E. Toorisaka, M. Hirata, "Decolorization of azo dye (Orange II) in a sequential UASB–SBR system." Sep Purif Technol, 42: 297–302, 2005.
[22]. S.-J. You, J.-Y. Teng, "Anaerobic decolorization bacteria for the treatment of azo dye in a sequential anaerobic and aerobic membrane bioreactor." Journal of the Taiwan Institute of Chemical Engineers 40: 500-504, 2009a.
[23]. S.-J. You, J.-Y. Teng, "Performance and dye-degrading bacteria isolation of a hybrid membrane process." Journal of Hazardous Materials 172: 172-179, 2009b.
[24]. S.-J. You, R.A. Damodar, S.-C. Hou, "Degradation of Reactive Black 5 dye using anaerobic/aerobic membrane bioreactor (MBR) and photochemical membrane reactor." Journal of Hazardous Materials 177: 1112-1118, 2010.
[25]. A. Yurtsever, B. Calimlioglu, M. Gorur, et al., "Effect of NaCl Concentration on the Performance of Sequential Anaerobic and Aerobic Membrane Bioreactors Treating Textile Wastewater." Chemical Engineering Journal ¬287: 456-465, 2015b.
[26]. A. Yurtsever, E. Sahinkaya, O. Cinar, "Treatment of textile wastewater using sequential sulfate-reducing anaerobic and sulfide-oxidizing aerobic membrane bioreactors." Journal of Membrane Science Volume 511: 228-237, 2016a.
[27]. A. Yurtsever, B. Calimlioglu, E. Sahinkaya, "Impact of SRT on the Efficiency and Microbial Community of Sequential Anaerobic and Aerobic Membrane Bioreactors for the Treatment of Textile Industry Wastewater." Chemical Engineering Journal, Volume 314: 378-387, 2016b.

[28]. Z.S. Yan, S.H. Wang, X.K. Kang, et al., "Enhanced removal of organics and phosphorus in a hybrid coagulation/membrane bioreactor (HCMBR) for real textile dyeing wastewater treatment." Desalination Water Treat. 47 (1–3), 249–257, 2012.
[29]. L. Qin, G. Zhang, Q. Meng, et al., "Enhanced MBR by internal microelectrolysis for degradation of anthraquinone dye wastewater." Chem. Eng. J. 210, 575–584, 2012.
[30]. S. Grilli, D. Piscitelli, D. Mattioli, et al. "Textile wastewater treatment in a bench-scale anaerobic-biofilm anoxic-aerobic membrane bioreactor combined with nanofiltration." J. Environ. Sci. Health A Tox. Hazard. Subst. Environ. Eng. 46 (13), 1512–1518, 2011.
[31]. D. De Jager, M.S. Sheldon, W. Edwards, "Membrane bioreactor application within the treatment of high-strength textile effluent." Water Sci. Technol. 65 (5), 907–914, 2012.
[32]. F. Feng, Z. Xu, X. Li, et al., "Advanced treatment of dyeing wastewater towards reuse by the combined Fenton oxidation and membrane bioreactor process." J. Environ. Sci. China 22 (11), 1657–1665, 2010.
[33]. H.-D. Park, I.-S. Chang and K.-J. Lee, Principles of Membrane Bioreactors for Wastewater Treatment, Boca Raton, FL, USA: CRC Press, Taylor and Francis Group, 2015.
[34]. M.E. Ersahin, H. Ozgun R.K. Dereli et al., "A review on dynamic membrane filtration: Materials, applications and future perspectives." Bioresource Technol.; 122:196–206, 2012.
[35]. X.Y. Zhang, Z.W. Wang, Z.C. Wu, et al., "Formation of dynamic membrane in an anaerobic membrane bioreactor for municipal wastewater treatment." Chem Eng J ;165(1):175–83, 2010.
[36]. J.L. Gaddis, H.G. Spencer, S.C. Wilson, "Separation of materials in dye manufacturing process effluent by hyperfiltration." AICHE Symp. Ser. 75 (190): 156–161, 1979.
[37]. G.R. Groves, C.A. Buckley, J.M. Cox, et al.,"Dynamic membrane ultrafiltration for the treatment of industrial effluents for water reuse." Desalination 47: 305–312, 1983.
[38]. R.B. Townsend, M.P.R. Crawdron, F.G. Neytzell, et al., "The potential of dynamic membranes for the treatment of industrial effluents." ChemSA 15 (4): 132–134, 1989.

ICENS

4TH INTERNATIONAL CONFERENCE ON ENGINEERING AND NATURAL SCIENCES

www.icens.eu

EUROPE CONGRESS
www.europecongress.org

Western Michigan University

National University of Public Service

National University of Kyiv-Mohyla Academy

Turkish Airlines

CNR Group